ICAROB 2019

PROCEEDINGS OF THE 2019 INTERNATIONAL CONFERENCE ON ARTIFICIAL LIFE AND ROBOTICS

January 10-13, 2019
B-Con Plaza, Beppu, Oita, JAPAN
24th AROB International Meeting Series

Editor-in-Chief
Masanori Sugisaka
Editors: Yingmin Jia, Takao Ito, Ju-Jang Lee
ISBN 978-4-9908350-4-0

Proceedings of The 2019 International Conference on

ARTIFICIAL LIFE AND ROBOTICS

(ICAROB2019)

January 10-13, 2019
B-Con Plaza, Beppu, Oita, JAPAN
24th AROB International Meeting Series

Editor-in-Chief
Masanori Sugisaka
Editors: Yingmin Jia, Takao Ito, Ju-Jang Lee
ISBN 978-4-9908350-4-0

Contents

SPONSERED

ALife Robotics Corporation Ltd.

ORGANIZED BY

International Steering Committee of International Conference on Artificial Life and Robotics (ICAROB)

SUPPORTED BY

IEEE Fukuoka Section (Japan)

CO-ORGANIZED BY

Chinese Association for Artificial Intelligence (CAAI, P. R. China)

ADVISORY COMMITTEE CHAIR

Moshe Kam (New Jersy Institute of Technology, Former IEEE President, USA)

ADVISORY COMMITTEE

Adam Grzech (Wroclaw University of Technology, Poland)
Bruce Eisenstein (Drexel University, Former IEEE President, USA)
Hidenori Kimura (JST, Japan)
Jeffrey Johnson (The Open University, UK)
Jerzy Świątek (Wroclaw University of Technology, Poland)
Joshua M. Epstein (The Johns Hopkins University, USA)
Kai-Tai Song (National Chiao Tung University, Taiwan)
Masayoshi Tomizuka (University of California Berkeley, USA)
Moshe Kam (New Jersey Institute of Technology, Former IEEE President, USA)
Paul Kalata (Drexel University, USA)
Paul Oh (Drexel University, USA)
Steen Rasmussen (University of Southern Denmark, Denmark)

GENERAL CHAIR

Masanori Sugisaka
(Alife Robotics Corporation Ltd., Japan)

CO-GENERAL CHAIRS

Yingmin Jia (Beihang Univesty, P. R. China)
Takao Ito (Hiroshima University, Japan)
Ju-Jang Lee (Honorary professor, KAIST, Korea)

VICE GENERAL CHAIR

Henrik. H. Lund (Technical University of Denmark, Denmark)
John. L. Casti (International Institute for Applied Systems Analysis, Austria)
Jangmyung Lee (Pusan National University, Korea)
Luigi Pagliarini (Technical University of Denmark, Denmark)
(Academy of Fine Arts of Macerata, Italy)

PROGRAM CHAIRMAN

Makoto Sakamoto (University of Miyazaki, Japan)

CO-PROGRAM CHAIR

Marion Oswald (Technische Universität Wien, Austria)

INTERNATIONAL ORGANIZING COMMITTEE

Akira Fukuda (Kyushu University, Japan)
Andrew Gadsden (University of Guelph, Canada)
Caoli Wang (University of Shanghai for Science and Technology, P. R. China)
Chan Gook Park (Seoul National University, Korea)
Eiji Hayashi (Kyushu Institute of Technology, Japan)
Evgeni Magid (Kazan Federal University, Russia)
Fuzhong Wang (Henan Polytechnic University, P. R. China)
Hazry Desa (University of Malaysia, Perlis, Malaysia)
Hidehiko Yamamoto (Gifu University, Japan)
Hiroki Tamura (University of Miyazaki, Japan)
Hiroshi Kage ((Mitsubishi Electric Corporation, Japan)
Hiroshi Matsuno (Yamaguchi University, Japan)
Jiwu Wang (Beijing Jiaotong University, P. R. China)
Jovana Jovic (CNRS-AIST JRL, Japan, France)
Junping Du (Beijing University of Posts and Telecommunications, P. R. China)
Katsunori Shimohara (Doshisha University, Japan)
Kazuo Ishii (Kyushu Institute of Technology, Japan)
Kevin Voges (Canterbury University, New Zealand)
Kuo-Hsien Hsia (Far East University, Taiwan)
Kuo-Lan Su (National Yunlin University of Science and Technology, Taiwan)
Kyungho Park (Micro-System Programs, RDECOM, ITC-PAC, U.S. ARMY, Japan and USA)
Masao Kubo (National Defense Academy of Japan, Japan)
Masanao Obayashi (Yamaguchi University, Japan)

Maxim Sokolov (Innopolis University, Russia)
Mehta Rajiv (New Jersey Institute of Technology, USA)
Peter Sapaty (Ukrainian Academy of Science, Ukraine)
Pierre Parrend (University of Strasbourg, France)
Qiang Cai (Beijing Technology and Business University, P. R. China)
Takashi Kohno (LIMMS/CNRS-IIS, Institute of Industrial Science, The University of Tokyo, Japan)
Takashi Ogata (Iwate Prefectural Univerity, Japan)
Teruhisa Hochin (Kyoto Prefectural University, Japan)
Tetsuro Hattori (Kagawa University, Japan)
Thi Thi Zin (University of Miyazaki, Japan)
Toru Yamamoto (Hiroshima University, Japan)
Victor Berdonosov (Komsomolsk-on-Amur State University of Technology, Russia)
Yasunari Yoshitomi (Kyoto Prefectural University, Japan)
Yi Chai (Chongqing University, P. R. China)
Yo Horikawa (Kagawa University, Japan)
Yoshifumi Morita (Nagoya Institute of Technology, Japan)
Yoshiro Imai (Kagawa University, Japan)
Zengqiang Chen (Nankai University, P. R. China)

INTERNATIONAL PROGRAM COMMITTEE

Akira Nakamura (AIST, Japan)
Ali Selamat (University of Technology of Malaysia (UTM), Malaysia)
Andre Rosendo (ShanghaiTech University, P. R. China)
Bin Zhang (Beijing University of Posts and Telecommunications, P. R. China)
Arsit Boonyaprapasorn (Chulachomkloa Royal Military Academy, Thailand)
Dongmei Ai (University of Science and Technology Beijing, P. R. China)
Endra Joelianto (Bandung Institute of Technology, Indonesia)
Fengzhi Dai (Tianjin University of Science & Technology, P. R. China)
Haisheng Li (Beijing Technology and Business University, P. R. China)
Haruna Matsushita (Kagawa University, Japan)
Hidetsugu Suto (Muroran Institute of Technology, Japan)
Hiroyuki Iizuka (Osaka University, Japan)
Huailin Zhao (Shanghai Institute of Technology, P. R. China)
Hussein Abbass (University of New South Wales and ADFA, Australia)
Istvan Harmati (Budapest Institute of Technology and Economics, Hungary)
Ivan Tanev (Doshisha University, Japan)
Jiandong Zhao (Beijing Jiaotong University, P. R. China)
Joono Cheong (Korea University, Korea)
Kunikazu Kobayashi (Aichi Prefectural University, Japan)
Lin Li (University of Shanghai for Science and Technology, P. R. China)
Lin Zhao (Qingdao University, P. R. China)
Manabu Yamada (Nagoya Institute of Technology, Japan)

Masahide Ito (Aichi Prefectural University, Japan)
Masayoshi Tabuse (Kyoto Prefectural University, Japan
Masaomi Hatakeyama (University of Zurich, Switzerland)
Norrima Mokhtar (University of Malaya, Malaysia)
Noritaka Sato (Nagoya Institute of Technology, Japan)
Palakorn Tantrakool (King Mongkut's Institute of Technology Thonburi, Thailand)
Ping Wang (North China Electric Power University, P. R. China)
Qinglin Sun (Nankai University, P. R. China)
Satoshi Ikeda (The University of Miyazaki, Japan)
Sanjay S. Joshi (College of Engineering, University of California, USA)
Seong-Ik Han (Dongguk University, Korea)
Shingo Mabu (Yamaguchi University, Japan)
Shumin Fei (Southeast University, P. R. China)
Shyi-Ming Chen (National Taichung University of Education, Taiwan)
Takashi Kuremoto (Yamaguchi University, Japan)
Takayoshi Yamada (Gifu University, Japan)
Taishiro Kishimoto (Keio University, Japan)
Tetsuro Katayama (The University of Miyazaki, Japan)
Thunyaseth Sethaput (Thammasat University, Thailand)
Tieqiu Huang (Beijing Jiaotong University, P.R China)
Toshinori Nawata (Kumamoto National College of Technology, Japan)
Tsunehiro Yoshinaga (Tokuyama National College of Technology, Japan)
Weicun Zhang (University of Science and Technology Beijing, P. R. China)
Xiaoyan Fu (Capital Normal University, P. R. China)
Xuemei Ren (Beijing Institute of Technology, P. R. China)
Yunzhong Song (Henan Polytechnic University, P. R. China)

LOCAL ARRANGEMENT COMMITTEE

Makoto Sakamoto (University of Miyazaki, Japan)
Masanori Sugisaka (ALife Robotics Corporation Ltd., Japan)
Takao Ito (Hiroshima University, Japan)

HISTORY

The International Conference on Artificial Life and Robotics (ICAROB) resulted from the AROB-symposium (International Symposium on Artificial Life and Robotics) whose first edition was held in 1996 and the eighteenth and last edition in 2013. The AROB symposium was annually organized by Oita University, Nippon Bunri University (NBU), and ALife Robotics Corporation Ltd., under the sponsorship of the Science and Technology Policy Bureau, the Ministry of Education, Science, Sports, and Culture (Monbusho), presently, the Ministry of Education, Culture, Sports, Science, and Technology (Monkasho), Japanese Government, Japan Society for the Promotion of Science (JSPS), the Commemorative Organization for the Japan World Exposition ('70), Air Force Office of Scientific Research, Asian Office of Aerospace Research and Development (AFOSR/AOARD), USA. I would like to express my sincere thanks to not only Monkasho (annually fund support from 1996 to 2013) but also JSPS, the Commemorative Organization for the Japan World Exposition ('70), and various other Japanese companies for their repeated support. The old symposium (this symposium has been held every year at B-Con Plaza, Beppu, Oita, Japan except in Oita, Japan (AROB 5th ’00) and in Tokyo, Japan (AROB 6th ’01).) was organized by the International Organizing Committee of AROB and was co-operated by the Santa Fe Institute (USA), RSJ, IEEJ, ICASE (Now ICROS) (Korea), CAAI (P. R. China), ISCIE, IEICE, IEEE (Japan Council), JARA, and SICE. The old AROB-symposium expanded much by absorbing much new knowledge and technologies into it. This history and character of the former AROB symposiums are passed on the current ICAROB conference and to this journal, International Journal of Robotics, Networking and Artificial Life (JRNAL). From now on, ALife Robotics Corporation Ltd. is in charge of management of both the conference and the journal. The future of the ICAROB is brilliant from a point of view of yielding new technologies to human society in the 21st century. We also expect to establish an international research institute on Artificial Life and Robotics in the future with the help of Japanese Government and ICAROB. This conference invites you all.

AIMS AND SCOPE

The objective of this conference is the development of new technologies for artificial life and robotics which have been recently born in Japan and are expected to be applied in various fields. This conference presents original technical papers and authoritative state-of-the-art reviews on the development of new technologies concerning robotics, networking and artificial life and, especially computer-based simulation and hardware for the twenty-first century. This conference covers a broad multidisciplinary field, including areas such as:
Artificial intelligence & complexity
Artificial living
Artificial mind research
Artificial nervous systems for robots
Artificial sciences
Bipedal robot
Brain science and computing
Chaos
Cognitive science
Computational Molecular biology
Computer graphics
Data mining
Disasters robotics
DNA computing
Empirical research on network and MOT
Environment navigation and localization

Evolutionary computations
Facial expression analysis, music recommendation and augmented reality
Foundation of computation and its application
Fuzzy control
Genetic algorithms
Human-welfare robotics
Image processing
Insect-like aero vehicles
Intelligence in biological systems
Intelligent control
Management of technology
Medical surgical robot
Micro-machines
Multi-agent systems
Nano-biology
Nano-robotics
Networking
Neural circuits
Neuro-computer
Neuromorphic Systems
Neuroscience
Pattern recognition
Quantum computing
Reinforcement learning system & genetic programing
Robotics
Software development support method
System cybernetics
Unmanned underwater vehicles
Unmanned Aerial Systems Technologies
Unmanned Aerial Systems designing, controls and navigation
Unmanned Aero vehicles
Virtual reality
Visualization

Hardware-oriented submissions are particularly welcome. This conference will discuss new results in the field of artificial life and robotics

COPYRIGHTS

Accepted papers will be published in the proceeding of The 2019 International Conference on Artificial Life and Robotics (ICAROB 2019) by ALife Robotics Corp. Ltd. Copyright belongs to ALife Robotics Corp. Ltd. Some of high-quality papers in the proceeding will be requested to re-submit their papers for the consideration of publication in an international journal ROBOTICS, NETWORKING AND ARTIFICIAL LIFE under agreement of both Editor-in- Chief Dr. Masanori Sugisaka and 3 reviewers. All correspondence related to the conference should be addressed to ICAROB Office.

ICAROB Office

ALife Robotics Corporation Ltd.
4-Go, 8-Ban, Higshi 2Cyome, Handadai, Oita 870-1108, JAPAN
TEL/FAX：+81-97-597-7760
E-MAIL：
icarob@alife-robotics.co.jp
Home Page：http://alife-robotics.co.jp/

MESSAGES

Masanori Sugisaka
General Chair
(President, ALife Robotics Co., Ltd. Japan)

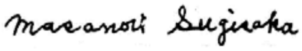

Masanori Sugisaka

General Chair of ICAROB

It is my great honor to invite you all to The 2019 International Conference on Artificial Life and Robotics (ICAROB 2019).
This Conference is changed as the old symposium from the first (1996) to the Eighteenth (2013) annually which were organized by Oita University, Nippon Bunri University(NBU), and ALife Robotics Corporation Ltd. under the sponsorship of the Science and Technology Policy Bureau, the Ministry of Education, Science, Sports, and Culture (Monbusho), presently, the Ministry of Education, Culture, Sports, Science, and Technology (Monkasho), Japanese Government, Japan Society for the Promotion of Science (JSPS), The Commemorative Organization for the Japan World Exposition ('70), Air Force Office of Scientific Research, Asian Office of Aerospace Research and Development (AFOSR/AOARD), USA. I would like to express my sincere thanks to not only Monkasho (annually fund support from 1996 to 2013) but also JSPS, the Commemorative Organization for the Japan World Exposition ('70), Japanese companies for their repeated support.
The old symposium was organized by International Organizing Committee of AROB and was co-operated by the Santa Fe Institute (USA), RSJ, IEEJ, ICASE (Now ICROS) (Korea), CAAI (P. R. China), ISCIE, IEICE, IEEE (Japan Council), JARA, and SICE. The old AROB symposium was growing up by absorbing many new knowledge and technologies into it.
This history and character was inherited also from ICAROB2014(The 2014 International Conference on Artificial Life and Robotics, included a series of ICAROB proceedings in SCOPUS and CPCI now. From now on, ALife Robotics Corporation Ltd. is in charge of management. This year we have The 2019 International Conference on Artificial Life and Robotics (ICAROB2019) (24th AROB Anniversary). The future of The ICAROB is brilliant from a point of view of yielding new technologies to human society in 21st century.
I hope that fruitful discussions and exchange of ideas between researchers during Conference (ICAROB2019) will yield new merged technologies for happiness of human beings and, hence, will facilitate the establishment of an international joint research institute on Artificial Life and Robotics in future.

Yingmin Jia
Co-General Chair
(Professor, Beihang University, R .P. China)

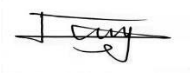

Yingmin Jia

Co-General Chair of ICAROB

It is my great pleasure to invite you to The 2019 International Conference on Artificial Life and Robotics (ICAROB 2019), in B-Con Plaza, Beppu, Oita, Japan from January 10 to 13, 2019.

ICAROB develops from the AROB that was created in 1996 by Prof. Masanori Sugisaka and will celebrate her 24 th birthday in 2019. Doubtless, new mission and big challenges in the field of artificial life and robotics will promote ICAROB to start a new stage and attract wide interests among scientist, researchers, and engineers around the world.

For a successful meeting, many people have contributed their great efforts to ICAROB. Here, I would like to express my special thanks to all authors and speakers, and the meeting organizing team for their excellent works.

Looking forward to meeting you at ICAROB in Beppu and wishing you enjoy your stay in Japan.

Takao Ito
Co-General Chair
(Professor Hiroshima University, Japan)

Takao Ito

Co General Chair of ICAROB

It is my great honor to invite you all to The 2019 International Conference on Artificial Life and Robotics (ICAROB 2019). This Conference is changed as the old symposium (ISAROB) from the first (1996) to the Eighteenth. I am pleased to welcome you to The 2019 International Conference on Artificial Life and Robotics in the wonderful city of Beppu, Oita city, Oita Prefecture, Japan.

The ICAROB has its long history. The former organization of the ICAROB was developed under the strong leadership of the President, famous Professor Masanori Sugisaka, the father of AROB. We gathered many researchers, faculty members, graduate students from all over the world, and published many high-quality proceedings and high-reputational journals every year.

Over the years, dramatic improvements have been made in the field of artificial life and its applications. The ICAROB has becoming the unifying the exchange of scientific information on the study of man-made systems that exhibit the behavioral characteristic of natural living systems including software, hardware and wetware. Our conference shapes the development of artificial life, extending our empirical research beyond the territory circumscribed by life-as-we-know-it and into the domain of life-as-it-could–be. It will provide us a good place to present our new research results, excellent ideas, and valuable information about artificial intelligence, complex systems theories, robotics, and management of technology.

The conference site is B-con Plaza, one of the most famous international convention centers in Kyushu island, Japan. You can find many fantastic scenic spots and splendid historical places in Beppu, Oita city. Enjoy your stay and take your time to visit Beppu, Oita city.

I am looking forward to meeting you in Beppu, Oita city, during the ICAROB 2019 and to sharing the most pleasant, interesting and fruitful conference with you.

Ju-Jang Lee
Co-General Chair
(Honorary professor, KAIST)

Ju-Jang Lee

Co-General Chair of ICAROB

The First International Conference on Artificial Life and Robotics (ICAROB) was held in Oita City, Oita, Japan from Jan. 11th to 13th, 2014. This year's Conference will be held amidst the high expectation of the increasingly important role of the new interdisciplinary paradigm of science and engineering represented by the field of artificial life and robotics that continuously attracts wide interests among scientist, researchers, and engineers around the globe.

Distinguished researchers and technologists from around the world are looking forward to attending and meeting at ICAROB. ICAROB is becoming the annual excellent forum that represents a unique opportunity for the academic and industrial communities to meet and assess the latest developments in this fast growing artificial life and robotics field. ICAROB enables them to address new challenges, share solutions, discuss research directions for the future, exchange views and ideas, view the results of applied research, present and discuss the latest development of new technologies and relevant applications.

In addition, ICAROB offers the opportunity of hearing the opinions of well-known leading experts in the field through the keynote sessions, provides the bases for regional and international collaborative research, and enables to foresee the future evolution of new scientific paradigms and theories contributed by the field of artificial life and robotics and associated research area. The twenty-first century will become the century of artificial life and intelligent machines in support of humankind and ICAROB is contributing through wide technical topics of interest that support this direction.

It is a great honor for me as a Co-General Chair of the 6th ICAROB 2019 to welcome everyone to this important event. Also, I would like to extend my special thanks to all authors and speakers for contributing their research works, the participants, and the organizing team of the 6th ICAROB.

I'm looking forward to meeting you at the 6th ICAROB in Beppu, Oita Prefecture and wishing you all the best.

GENERAL SESSION TOPICS

GS1 Robotics I (3)	GS2 Robotics II (6)
GS3 Complexity (2)	GS4 Poster (5)
GS5 Others (8)	

ORGANIZED SESSION TOPICS

OS1 Intelligent Systems and Control (8)	OS2 Theory and Implementation of Neuromimetic Systems (5)
OS3 Intelligent navigation & Robotics (4)	OS4 Service Robotics (7)
OS5 Business Models and Management (4)	OS6 Software Development Support Method (6)
OS7 Media Information Processing and Artificial Intelligence (4)	OS8 Computational intelligence and cognitive science for human biosignals and human well-being (7)
OS9 Natural Computing and Beyond (3)	OS10 Mathematical Informatics (5)
OS11 Recognition and Control (12)	OS12 Robot Design and Simulation (5)
OS13 System and Control (10)	OS14 Intelligent Control (4)
OS15 Advanced Control (5)	OS16 New development about Control Engineering Education (4)
OS17 Multiagent and Complex Systems (3)	OS18 Data-Driven Control and Diagnosis Control Systems (5)
OS19 Advanced Technology on Sensing Technology, Devices, Application (3)	OS20 Advances in Field Robotics and Sensing System (8)
OS21 Advances in Marine Robotics and It's Applications (5)	OS22 Robot Competitions for Social Contribution (6)
OS23 Kansei and Information Engineering (4)	OS24 Automated content generation for narrative and cognitive contents (5)
OS25 High-Performance Computing for Interactive Content Creation and Rendering (3)	

1/10(Thu.) 17:30-19:30	Welcome Party (Hotel Shiragiku)
1/10(Thu.) - 1/13(Sun.)	ICAROB Secretariat
1/13(Sun.)	Farewell Party (Conference Site: 3F, Meeting Room 31)

TIME TABLE (1/11)

1/11(Fri.)	Conference Room	Meeting Room 31	Meeting Room 32	Meeting Room 33	Meeting Room 1	Meeting Room 4
8:40-	Registration (3F)					
9:00-10:15		OS8 Computational intelligence and cognitive science for human biosignals and human well-being (7) Chair: T. Hiroyasu	OS1-1 Intelligent Systems and Control (4) Chair: Kuo-Hsien Hsia	OS14 Intelligent Control (4) Chair: Yingmin Jia	OS21 Advances in Marine Robotics and It's Applications (5) Chair: Keisuke Watanabe	OS11 Recognition and Control (12) Chair: Fengzhi Dai
10:15-10:30	Coffee break					
10:30-11:00	Opening Ceremony (Conference Room)					
11:10-12:10	Chair: Kuo-Hsien Hsia (H. H. Lund), Chair: Jangmyung Lee (L. Pagliarini) Invited Speech IS1-1, IS1-2(Conference Room) Henrik Hautop Lund, Luigi Pagliarini					
12:10-13:10	Lunch					
13:10-14:10	Chair: Kazuo Ishii Plenary Speech PS-2(Conference room) Masanori Sugiyama					
14:10-14:30	Coffee break					
14:30-15:30			OS1-2 Intelligent Systems and Control (4) Chair: Kuo-Hsien Hsia	OS7 Media Information Processing and Artificial Intelligence (4) Chair: Yasunari Yoshitomi	OS3 Intelligent navigation & Robotics (4) Chair: Chan Gook Park	GS1 Robotics I (3) Chair: Jiwu Wang
15:30-15:50	Coffee break					
15:50-17:50		OS20 (8) Advances in Field Robotics and Sensing System (8) Chair: Eiji Hayashi	OS4 Service Robotics (7) Chair: Evgeni Magid	OS2 Theory and Implementation of Neuromimetic Systems (5) Chair: Timothée Levi	OS18 Data-Driven Control and Diagnosis Control Systems (5) Chair: Takuya Kinoshita	OS13 System and Control (10) Chair: Qiang Wei

Meeting Room 31: Committee waiting room and Rest room

TIME TEBLE (1/12)

1/12(Sat.)	Conference Room	Meeting Room 31	Meeting Room 32	Meeting Room 33	Meeting Room 1	Meeting Room 4
8:40-	Registration					
9:00-9:45			OS17 Multiagent and Complex Systems (3) Chair: Akihiro Yamaguchi	GS3 Complexity (2) Chair: Manabu Sugii	OS9 Natural Computing and Beyond (3) Chair: Marion Oswald	OS19 Advanced Technology on Sensing Technology, Devices, Application (3) Chair: Hiroki Tamura
9:45-10:00	Coffee break					
10:00-11:00		GS4 Poster (5) Chair: Evgeni Magid	OS16 New development about Control Engineering Education (4) Chair: Yoshihiro Ohnishi	OS23 Kansei and Information Engineering (4) Chair: T. Hattori		
11:00-11:10	Coffee break					
11:10-12:10	Chair: Ju-Jang Lee (Y. I. Cho), Chair: Marion Oswald (K. Sumi) Invited sessionIS-2, IS-3 (Conference Room) Young Im Cho, Kaoru Sumi					
12:10-13:10	Lunch					
13:10-14:10	Chair: Akira Nakamura Plenary Speech PS-1 (Conference Room) Kensuke Harada					
14:10-14:30	Coffee break					
14:30-16:00		GS4 Poster	OS15 Advanced Control (5) Chair: Yingmin Jia	OS12 Robot Design and Simulation (5) Chair: QinJian Zhang	OS22 Robot Competitions for Social Contribution (6) Chair: Yasunori Takemura	
16:00-16:20	Coffee break					
16:20-17:50			GS2 Robotics II (6) Chair: Jiwu Wang	OS25 High-Performance Computing for Interactive Content Creation and Rendering (3) Chair: R.P.C. Janaka Rajapakse		
18:30-20:30	Banquet: Hotel Shiragiku					

Meeting Room 31: Committee waiting room and Rest room

TIME TABLE (1/13)

1/13(Sun.)	Meeting Room 31	Meeting Room 32	Meeting Room 33	Meeting Room 1	Meeting Room 4
8:40-	Registration				
9:00-10:30		OS6 Software Development Support Method (6) Chai: Tetsuro Katayama	OS5 Business Models and Management (4) Chair: Takao Ito		
10:30-10:40	Coffee break				
10:40-11:40	Chair: Takao Ito Plenary Speech PS-3(Meeting Room 31) Yingmin Jia				
11:40-12:40	Lunch				
12:40-13:55		OS10 Mathematical Informatics (5) Chair: Makoto Sakamoto	OS24 Automated content generation for narrative and cognitive contents (5) Chair: Jumpei Ono		
Farewell Party (13:55-14:25) Meeting Room 31					

Meeting Room 31: Committee waiting room and Rest room

GS5 Others (8)

no presentation, only papers

The 2019 International Conference on ARTIFICIAL LIFE AND ROBOTICS (ICAROB2019)

January 10 (Thursday)

17:30-19:30 Welcome Party (Hotel Shiragiku)

January 11 (Friday)

10:30-11:00

Opening Ceremony (Conference Room)

Chair: Marion Oswald (Technische Universität Wien, Austria)

Welcome Addresses

1. General Chairman of ICAROB	Masanori Sugisaka (ALife Robotics Co., Ltd., Japan)
2. Co-General Chairman of ICAROB	Yingmin Jia (Beihang University, P. R. China)
3. Co-General Chairman of ICAROB	TaKao Ito (Hiroshima University, Japan)
4. Co-General Chairman of ICAROB	Ju-Jang Lee (KAIST, Korea)
5. Vice General Chair of ICAROB	Henrik Hautop Lund (Technical University of Denmark, Denmark)
6. Vice General Chair of ICAROB	Jangmyung Lee (Pusan National University, Korea)

January 12 (Saturday)

Banquet: Hotel Shiragiku

18:30-20:30

Chair: Takao Ito (Hiroshima University, Japan)

Welcome Addresses

Prof. Kensuke Harada (Osaka University, Japan)

Prof. Yingmin Jia (Beihang University, P.R. China)

Prof. Henrik Hautop Lund (Technical University of Denmark, Denmark)

Prof. Ju-Jang Lee (KAIST, Korea)

TECHNICAL PAPER INDEX

January 11 (Friday)

8:40-Registration

Conference Room
10:30-11:00 Opening Ceremony
Chair: Marion Oswald (Technische Universität Wien, Austria)

11:10-11:40
Invited session IS1-1
Chair: Kuo-Hsien Hsia (Far East University, Taiwan)

IS1-1-1 *Engineering Modular Playware*
Henrik Hautop Lund, Morten Roed Frederiksen, Massimiliano Leggieri
(Technical University of Denmark, Denmark)

IS1-1-2 *User-Friendly Robotics 3 – Playware*
Henrik Hautop Lund, Luigi Pagliarini (Technical University of Denmark, Denmark)

11:40-12:10
Invited session IS1-2
Chair: Jang-Myung Lee (Pusan National University, Korea)

IS1-2-1 *User-Friendly Robotics 1 – AI Software*
Luigi Pagliarini [1,2], Henrik Hautop Lund [1]
([1]Technical University of Denmark, Denmark, [2]Academy of Fine Arts of Macerata, Italy)

IS1-2-2 *User-Friendly Robotics 2– Interfacing Robotics with any user*
Luigi Pagliarini[1,2], Henrik Hautop Lund[1]
([1]Technical University of Denmark, Denmark) ([2]Academy of Fine Arts of Macerata, Italy)

13:10-14:10

Plenary Speech PS-2

Chair: Kazuo Ishii (Kyushu Institute of Technology, Japan)

PS-2 *Toward Life with Partner Robots-Developing robots with the field trial toward the practical use*
Masanori Sugiyama (Toyota Motor Corporation, Japan)

Meeting Room 31
9:00-10:45 OS8 Computational intelligence and cognitive science for human biosignals and human well-being (7)

Chair: Tomoyuki Hiroyasu (Doshisha University, Japan)
Co-Chair: Hiroshi Furutani (Doshisha University, Japan)

OS8-1 *Unified Approach to (1+1) EA on Discrete Linear Functions*
Kenji Aoki, Makoto Sakamoto (University of Miyazaki, Japan)
Hiroshi Furutani, Satoru Hiwa, Tomoyuki Hiroyasu (Doshisha University, Japan)

OS8-2 *A fNIRS study of brain state during letter and category fluency tasks*
Akane Onishi, Satoru Hiwa, Hiroshi Furutani, Tomoyuki Hiroyasu (Doshisha University, Japan)

OS8-3 *Construction of a meditation practice support system leads to a good meditation state: an fNIRS study*
Seika Fujii, Satoru Hiwa, Hiroshi Furutani, Tomoyuki Hiroyasu (Doshisha University, Japan)

OS8-4 *Automated panoramic image creation system for corneal endothelial cells*
Keitaro Kobayashi, Naoki Okumura, Noriko Koizumi, Satoru Hiwa, Hiroshi Furutani, Tomoyuki Hiroyasu (Doshisha University, Japan)

OS8-5 *An fMRI study of the inhibitory effects of the random stimulus-response compatibility task on brain function*
Kei Sahara, Satoru Hiwa, Hiroshi Furutani, Tomoyuki Hiroyasu (Doshisha University, Japan)

OS8-6 *Measurement of brain activity and problem discovery during actual driving*
Seishiro Nakamura, Satoru Hiwa, Kenya Sato, Hiroshi Furutani, Tomoyuki Hiroyasu (Doshisha University, Japan)

OS8-7 Control of driving simulator based on state detection of the driver using Electrocardiogram measurement
Koma Yoshioka, Satoru Hiwa, Kenya Sato, Hiroshi Furutani, Tomoyuki Hiroyasu (Doshisha University, Japan)

15:50-17:50 OS20 Advances in Field Robotics and Sensing System (8)
Chair: Eiji Hayashi (Kyushu Institute of Technology, Japan)
Co-Chair: Kazuo Ishii (Kyushu Institute of Technology, Japan)

OS20-1 *Field Robot and Sensing system*
Eiji Hayashi (Kyushu Institute of Technology, Japan)

OS20-2 *Saliency Map Based on Maximization of Difference between Central and Surround Visions and Its Relationship with Image Feature Points*
Ruugo Mochizuki, Shinsuke Yasukawa, Kazuo Ishii (Kyushu Institute of Technology, Japan)

OS20-3 *Dynamic Wireless Network System using Multiple Drones for Tunnel Applications*
Raji Alahmad, Kazuo Ishii (Kyushu Institute of Technology, Japan)

OS20-4 *Counting Crops under Cultivation using Drone*
Yasunori Takemura[1], Yusuki Hirata[2], Eiji Mizoe[3], Masao Tashiro[4] and Yousuke Nagai[5]
([1]Nishinippon Institute of Technology, [2]Kyushu Institute of Technology, [3]Sky Canvas Co.
[4]Joint Corp. Project Sky-eye, [5]Aruku Aguriculture Service LLC, Japan)

OS20-5 *Soil Compaction and Rolling Resistance Evaluation of a Locomotion System with Adjustable Contact Patches for Applications in the Vineyard*
Enrico di Maria, Kazuo Ishii (Kyushu Institute of Technology, Japan)

OS20-6 *Robot Navigation in Forest Management Based on Graph*
Ayumu Tominaga[1], Ryusuke Fujisawa[1], Eiji Hayashi[1], Abbe Mowshowitz[2]
([1]Kyushu Institute of Technology, Japan, [2]The City College of New York, USA)

OS20-7 *Development of Autonomous Moving System for Field Robot*
Kengo Kawazoe, Eiji Hayashi, Ryusuke Fujisawa (Kyushu Institute of Technology, Japan)

OS20-8 *Development of the sense system that is combined force feedback and vision feedback -Improvement reproducibility of deformation simulation by using LEM-*
Tamon Shigeyama, Eiji Hayashi , Ryusuke Fujisawa (Kyushu Institute of Technology, Japan)

Meeting Room 32
9:00-10:00 OS1-1 Intelligent Systems and Control (4)
Chair: Kuo-Hsien Hsia (Far East University, Taiwan)
Co-Chair: Chung-Wen Hung (National Yunlin University of Science & Technology, Taiwan)

OS1-1 *A Vishay Supercapacitor based Fast Charge Battery*
Chung-Wen Hung, Yi-Chang Yang, Chun-Chu Lin, Li-Sheng Jheng
(National Yunlin University of Science and Technology, Taiwan)

OS1-2 *Multi-Motor Synchronous Control with CANOpen*
Chung-Wen Hung, Roger CL Lee, Bo-Kai Huang, Shit-Ting Yu
(National Yunlin University of Science and Technology, Taiwan)

OS1-3 *Selection Strategy for VM Migration Method*
Yan-Ren Chen, I-Hsien Liu, Keng-Hao Chang, Jung-Shian Li
(National Cheng Kung University, Taiwan)

OS1-4 *VM Migration Placement in Cloud Service*
Yan-Ren Chen, I-Hsien Liu, Keng-Hao Chang, Chuan-Gang Liu, Jung-Shian Li
(National Cheng Kung University, Taiwan)

14:30-15:30 OS1-2 Intelligent Systems and Control (4)

Chair: Kuo-Hsien Hsia (Far East University, Taiwan)

Co-Chair: Chung-Wen Hung (National Yunlin University of Science & Technology, Taiwan)

OS1-5 *Control System for Maintaining Safe Following Distance while Driving*
Kuo-Hsien Hsia, Jia-Hong Cai, Shu-Li Pai (Far East University, Taiwan)
Evgeni Magid (Kazan Federal University, Russia)

OS1-6 *Markerless Indoor Augmented Reality Navigation Device Based on Optical-Flow-Scene Indoor Positioning and Wall-Floor-Boundary Image Registration*
Chian C. Ho, Bo-Kai Wang, Guan-Lung Liao
(National Yunlin University of Science and Technology, Taiwan)

OS1-7 *Development of the handheld gas detector with IoT function.*
Jr-Hung Guo, Kuo-Hsien Hsia, Kuo-Lan Su
(National Yunlin University of Science and Technology, Taiwan)

OS1-8 *Research on Employee Attribute Correlation of Information Security Awareness in Organization*
Tse-Yao Wang (Air Force Institute of Technology, Taiwan)
Fu-Hsiang Wen (National Kaohsiung University of Science and Technology, Taiwan)

15:50-17:35 OS4 Service Robotics (7)

Chair: Evgeni Magid (Kazan Federal University, Russia)

Co-Chair: Kuo-Hsien Hsia (Far East University, Taiwan),

Co-Chair: Kuo-Lan Su (National Yunlin University of Science and Technology, Taiwan)

OS4-1 *Apply 2D Barcode Scanner for Mobile Robot Navigation in Checkerboard Mapping*
Chun-Chi Lai[1], Kuo-Lan Su[1], Chia-Jen Lin[1], Evgeni Magid[2]
([1]National Yunlin University of Science and Technology, Taiwan)
([2]Kazan Federal University, Russia)

OS4-2 *Development of the MyRio Based Mobile Platform*
Bo-Jun Yang[1], Sheng-Jie Liou[1], Jr-Hung Guo[1], Kuo-Lan Su[1], Evgeni Magid[2]
([1]National Yunlin University of Science and Technology, Taiwan)
([2]Kazan Federal University, Russia)

OS4-3 *Modelling Avrora Unior Car-like Robot in Gazebo Environment*
Ksenia Shabalina[1], Artur Sagitov[1], Kuo-Lan Su[2], Kuo-Hsien Hsia[3], Evgeni Magid[1]
([1]Kazan Federal University, Russia)
([2]National Yunlin University of Science and Technology, Taiwan)
([3]Far East University, Taiwan)

OS4-4 *Transfer of learned exploration strategies for a mobile robot from a simulated world to real Environments*
Artur Sagitov[1], Tetsuo Takano[2], Shohei Muto[2], Evgeni Magid[1]
([1]Kazan Federal University, Russia) ([2]Kanazawa University, Japan)

OS4-5 *Extending Gazebo simulator for surgical robotics: tissue and suture modeling*
Artur Sagitov[1], Hongbing Li[2], Evgeni Magid[1]
([1]Kazan Federal University, Russia) ([2]Shanghai Jiao Tong University, China)

OS4-6 *Experiences of Robotics students in Machine Vision course being taught in a foreign language: comprehension, self-efficiency, and active learning strategies improvement*
Tatyana Tsoy, Artur Sagitov, Evgeni Magid (Kazan Federal University, Russia)

OS4-7 *Pilot Virtual Experiments on ArUco and AprilTag Systems Comparison for Fiducial Marker Rotation Resistance*
Aufar Zakiev[1], Ksenia Shabalina[1], Kuo-Lan Su[2], Kuo-Hsien Hsia[3], Evgeni Magid[1]
([1]Kazan Federal University, Russia)
([2]National Yunlin University of Science and Technology, Taiwan)
([3]Far East University, Taiwan)

Meeting Room 33
9:00-10:00 OS14 Intelligent Control (4)
Chair: Yingmin Jia (Beihang University (BUAA), China)
Co-Chair: Weicun Zhang (University of Science and Technology Beijing, China)

OS14-1 *Flock Guiding of Hybrid Agents via Root Block*
Yunzhong Song, Ziyi Fu, Fuzhong Wang (Henan Polytechnic University, China)

OS14-2 *Multiple Model Adaptive Control of Flexible Arm*
Yingzhao Zhang[1], Xiao Wang[1], Handong Li[1], Weicun Zhang[2]
([1]Guizhou University, [2]University of Science and Technology Beijing, China)

OS14-3 *Time-Varying Lyapunov Function for Mechanical Systems*
Bin Zhang[1], Yingmin Jia[2]
([1]Beijing University of Posts and Telecommunications, [2]Beihang University (BUAA), China)

OS14-4 *Optimizing Control Parameters of Space Robot Manipulator for Pulsar X-ray Interference Measurement*
Qiang Chen[1], Hengbin Zhang[1], Xiaomin Bei[1], Hanwen Zhang[2]
([1]Chinese Academy of Space Technology, [2]Beijing Institute of Control Engineering, China)

14:30-15:30 OS7 Media Information Processing and Artificial Intelligence (4)
Chair: Yasunari Yoshitomi (Kyoto Prefectural University, Japan)
Co-Chair: Masayoshi Tabuse (Kyoto Prefectural University, Japan)

OS7-1 *Effectiveness of Data Augmentation in Automatic Summarization System*
Tomohito Ouchi, Masayoshi Tabuse (Kyoto Prefectural University, Japan)

OS7-2 *A System for Posting on SNS Portrait Selected Using Facial Expression Analysis While Writing Message*
Taro Asada[1], Yuiko Yano[2], Yasunari Yoshitomi[1], Masayoshi Tabuse[1]
([1] Kyoto Prefectural University, [2] Nara Guarantee Corporation, Japan)

OS7-3 *A Method Using Wavelet Transform for Judging Character to be Inserted into Image*
Yasunari Yoshitomi[1], Takashi Sato[2], Taro Asada[1], Masayoshi Tabuse[1]
([1] Kyoto Prefectural University, [2] Tokyo Institute of Technology, Japan)

OS7-4 *An Authentication Method for Digital Audio Using Wavelet Transform and Fundamental Frequencies*
Yasunari Yoshitomi[1], Shohei Tani[2], Masaki Arasuna[3], Ryota Kan[4], Taro Asada[1], Masayoshi Tabuse[1]
([1] Kyoto Prefectural University, [2] Fukuchiyama City Hall, [3] Nissay Information Technology Co., Ltd., [4] Shimazu Business Systems Co., Ltd., Japan)

15:50-17:05 OS2 Theory and Implementation of Neuromimetic Systems (5)
Chair: Timothée Levi (The University of Tokyo, Japan)
Co-Chair: Yuichi Katori (Future University Hakodate, Japan)

OS2-1 *Decoding spike patterns of auto-associative memory on spiking neuronal networks*
Naoki Toyoshima, Takashi Kohno (The University of Tokyo, Japan)

OS2-2 *Possible Mechanism of Internal Visual Perception: Context-dependent Processing by Predictive Coding and Reservoir Computing Network*
Hiroto Tamura[1], Yuichi Katori[1,2], Kazuyuki Aihara[1]
([1]The University of Tokyo, [2]Future University Hakodate, Japan)

OS2-3 *Snake robot controlled by biomimetic CPGs*
Damien Blanchard[1], Kazuyuki Aihara[2], Timothée Levi[2]
([1]University of Bordeaux, France, [2]The University of Tokyo, Japan)

OS2-4 *Real-time implementation of ReSuMe learning in Spiking Neural Network*
Xia Yang, Seiji Uenohara, Kazuyuki Aihara, Takashi Kohno, Timothée Levi
(The University of Tokyo, Japan)

OS2-5 *Biomimetic spike-timing based ionic micro-stimulation for neuron culture*
Stephany Mai Nishikawa[1], Farad Khoyratee[1,2], Soo Hyeon Kim[1], Yoshiho Ikeuchi[1], rawr
Kazuyuki Aihara[1], Teruo Fujii[1], Timothée Levi[1]
([1]The University of Tokyo, Japan, [2]University of Bordeaux, France)

OS2-6 *Dynamical network model for visual cortex: hierarchical reservoir computing with bidirectional interactions (withdraw)*
Shohei Takaichi[1], Yuichi Katori[2], Kazuyuki Aihara[1]
([1]The University of Tokyo, [2]Future University Hakodate, Japan)

Meeting Room 1

9:00-10:15 OS21 Advances in Marine Robotics and It's Applications (5)

Chair: Keisuke Watanabe (Tokai University, Japan)

Co-Chair: Kazuo Ishii (Kyushu Institute of Technology, Japan)

OS21-1 *System Development of AUV's Sampling Device Controller Employing MATLAB/Simulink Toolboxes*
Takashi Sonoda[1], Shinsuke Yasukawa[2], Ahn Jonghyun[2], Yuya Nishida[2], Kazuo Ishii[2]
([1]Nishinippon Institute of Technology, [2]Kyushu Institute of Technology, Japan)

OS21-2 *Inspection System for Underwater Structure of Bridge Pier*
Takumi Ueda[1], Hiyoyasu Hirai[1], Kazuki Fuchigami[1], Ryoma Yuki[1], Ahn Jonghyun[1], Shinsuke Yasukawa[1], Yuya Nishida[1], Takashi Sonoda[1], Kazuo Ishii[1], Katsunori Higashi[2], Katsunori Tanaka[2], Tomomasa Ikeda[2]
([1]Kyushu Institute of Technology, [2]West Nippon Expressway Engineering Kyushu, Japan)

OS21-3 *Three-dimensional measurement using laser pattern and its application to underwater scanner*
Yuya Nishida, Tomoya Shinnoki, Shinsuke Yasukawa, Kazuo Ishii
(Kyushu Institute of Technology, Japan)

OS21-4 *Development of Dam Inspection Underwater Robot*
Hiroyasu Hirai, Kazuo Ishii (Kyushu Institute of Technology, Japan)

OS21-5 *Conceptual Design of Small ROV for Sky to Water System*
Keisuke Watanabe, Koshi Utsunomiya, Kazumasa Harada, Nakajima Shuhei
(Tokai University, Japan)

14:30-15:30 OS3 Intelligent navigation & Robotics (4)
Chair: Chan Gook Park (Seoul National University, Korea)
Co-Chair: Jang-Myung Lee (Pusan National University, Korea)

OS3-1 *Trajectory tracking control for a 7-arms robot manipulator*
Wang Jie, Hyun-Hee Kim, Saad abbasi, Min-Cheol Lee (Pusan National University, Korea)

OS3-2 *Estimation tire-rod friction coefficient based on mobile robot*
Ji-Hyeon Kim, Zhang Hongyu, Jang-Myung Lee (Pusan National University, Korea)

OS3-3 *Real-time reflection removal algorithm using stereo camera only*
Do-Kyung Hwang, Jong-Woo An, Jang-Myung Lee (Pusan National University, Korea)

OS3-4 *The Effect of Inertial Measurement Unit on Synthetic Aperture Radar Image Quality*
Soo-Jeong Lee[1], Yong-Gonjong Park[1], Woo-Jung Park[1], Chan Gook Park[1], Jong-Hwa Song[2]
(Seoul National University, Korea[1], Hanwha Systems, Korea[2])

15:50-17:05 OS18 Data-Driven Control and Diagnosis Control Systems (5)
Chair: Takuya Kinoshita (Hiroshima University, Japan)
Co-Chair: Takao Sato (University of Hyogo, Japan)

OS18-1 *A Design Scheme of a Data-driven Predictive-PI Controller*
Yoichiro Ashida, Shin Wakitani and Toru Yamamoto (Hiroshima University, Japan)

OS18-2 *Improvement in Intersample Response of Multirate Regulation Control*
Takao Sato, Natsuki Kawaguchi, Nozomu Araki, Yasuo Konishi (University of Hyogo, Japan)

OS18-3 *Design of a PID Controller using a Fictitious Exogenous Signal for a Fluctuation System*
Masatoshi Kozui, Takuya Kinoshita, Toru Yamamoto (Hiroshima University, Japan)

OS18-4 *Izhikevich Model Based Self-Repairing Control for Plants with Sensor Failures and Disturbances*
Masanori Takahashi (Tokai University, Japan)

OS18-5 *Design of a Data-Driven Controller with Evaluating Controller Performance*
Takuya Kinoshita and Toru Yamamoto (Hiroshima University, Japan)

Meeting Room 4
9:00-10:15 OS11 Recognition and Control (12)
Chair: Fengzhi Dai (Tianjin University of Science and Technology, China)
Co-Chair: Yizhun Peng (Tianjin University of Science and Technology, China)

OS11-1 *Design of feed part control system for rectification process*
Lingran An[1], Fengzhi Dai[1], Yujie Yan[1], Zhongyong Ye[1], Xia Jin[1], Yiqiao Qin[12], Chengcai Wang[3], Kaige Liu[1] ([1]Tianjin University of Science and Technology, [2]Tianjin Tianke Intelligent and Manufacture Technology CO.,LTD, [3]CETC Ocean Information Co., Ltd, China)

OS11-2 *Ultrasonic range finder for vehicle collision avoidance system*
Ying Chen[1], Guowei Yang[1], Fengzhi Dai[1], Yuxuan Zhu[1], Di Yin[1], Yasheng Yuan[1],Yiqiao Qin[12], Ce Bian[12], Chengcai Wang[3], Xinyu Zhang[1] ([1]Tianjin University of Science and Technology, [2]Tianjin Tianke Intelligent and Manufacture Technology CO.,LTD, [3]CETC Ocean Information Co., Ltd, China)

OS11-3 *Chaos synchronization method of Qi system and the circuit design*
Xia Jin[1], Fengzhi Dai[1], Zhongyong Ye[1], Lingran An[1], Yujie Yan[1], Chenglin Zhao[1], Yiqiao Qin[12], Hao Li[3] ([1]Tianjin University of Science and Technology, [2]Tianjin Tianke Intelligent and Manufacture Technology CO.,LTD, [3]CETC Ocean Information Co., Ltd,, China)

OS11-4 *Design of air quality monitoring platform based on Internet of Things*
Yujie Yan[1], Fengzhi Dai[1], Kailun Zhang[1], Wei Wang[2], Jialin Han[1], Yang Li[3], Tianyi Zhang[1] ([1]Tianjin University of Science and Technology, [2]China Institute of Aerospace Engineering , [3]CETC Ocean Information Co., Ltd, China)

OS11-5 *Design of metal weld seam tracking equipment based on image processing*
Yujie Yan[1], Fengzhi Dai[1], Lingran An[1], Xia Jin[1], Zhongyong Ye[1], Yufan He[2], Xinran Guo[3] ([1]Tianjin University of Science and Technology, [2]CETC Ocean Information Co., Ltd, [3]Nanjing University, China)

OS11-6 *The recognition and implementation of handwritten character based on deep learning*
Zhongyong Ye[1], Fengzhi Dai[1], Xia Jin[1], Yasheng Yuan[1], Lingran An[1], Yujie Yan[1], Yiqiao Qin[12], Hao Li[3] ([1]Tianjin University of Science and Technology, [2]Tianjin Tianke Intelligent and Manufacture Technology CO., LTD, [3]CETC Ocean Information Co., Ltd, China)

OS11-7 *Cluster analysis of wine based on three-dim fluorescent spectra characteristic*
Di Yin[1], Fengzhi Dai[1], Yuxuan Zhu[1], Yasheng Yuan[1], Tingting Zhang[1], Ying Chen, Yiqiao Qin[12], Chengcai Wang[3] ([1]Tianjin University of Science and Technology, [2] Tianjin Tianke Intelligent and Manufacture Technology CO., LTD, [3]CETC Ocean Information Co., Ltd, China)

OS11-8 *The control design of the planting device for the hydroponic vegetable*
Yasheng Yuan[1], Fengzhi Dai[1], Zhongyong Ye[1], Yuxuan Zhu[1], Di Yin[1], Tingting Zhang[1], Yiqiao Qin[12], Yang Li[3] ([1]Tianjin University of Science and Technology, [2] Tianjin Tianke Intelligent and Manufacture Technology CO.,LTD, [3]CETC Ocean Information Co., Ltd, China)

OS11-9 *An anti -theft system based on the self-checkout*
Yuxuan Zhu[1], Fengzhi Dai[1], Yasheng Yuan[1], Di Yin[1], Tingting Zhang[1], Ying Chen[1], Ce Bian[12], Yufan He[3] ([1]Tianjin University of Science and Technology, [2]Tianjin Tianke Intelligent and Manufacture Technology CO.,LTD, [3]CETC Ocean Information Co., Ltd, China)

OS11-10 *Case study on communication between embedded linux environment and microcontroller*
Ziheng Gao, Yizhun Peng, Shuo Wang
(Tianjin University of Science and Technology, China)

OS11-11 *Design and implementation of a baby care robot*
Yizhun Peng, Zefan Ge, Kaixuan Geng, Zhou Yang,Rui Yang
(Tianjin University of Science and Technology, China)

OS11-12 *Research on intelligent shopping service robot design*
Shuo Wang, Yizhun Peng, Ruixiang Bai, Ziheng Gao
(Tianjin University of Science and Technology, China)

14:30-15:15 GS1 Robotics I (3)
Chair: Jiwu Wang (Beijing Jiaotong University, China)

GS1-1 *System to decide unit's layout of cell assembly machine by GA (Big Mutation in mutation process)*
Yoshiki Ito, Hidehiko Yamamoto, Takayoshi Yamada (Gifu University, Japan)

GS1-2 *Autonomous decentralized FMS that adopts priority ranking structure based on AGV's lies*
Kento Uejo, Hidehiko Yamamoto, Takayoshi Yamada (Gifu University, Japan)

GS1-3 *CULET: Cubelet Lego Turing Machine*
Ricardo Q. Figueroa, Daniel A. Zamorano, Genaro J. Martínez (Instituto Politécnico Nacional, México), Andrew Adamatzky (University of the West of England, UK)

15:50-17:50 OS13 System and Control (10)
Chair: Qiang Wei (Jianghan University, China)
Co-Chair: Huailin Zhao (Shanghai Institute of Technology, China)

OS13-1 *Research on a non-invasive measuring method of blood glucose concentration based on electrical impedance spectrum*
Tong Yin, Xiaoyan Chen, Meng Du, Hongyi Yin
(Tianjin University of Science and Technology, China)

OS13-2 *Synchronization of Novel 4D Chaotic Systems with Different Control Laws*
Hong Niu (Tianjin University of Science and Technology, China)

OS13-3 *Chaotic characteristics analysis of fractional-order Liu system*
Wengxin Shi, Hongyan Jia (Tianjin University of Science and Technology, China)

OS13-4 *Design and analysis of the multi-robot grouping aggregation algorithm*
Huailin Zhao, Zhen Nie (Shanghai Institute of Technology, China)

OS13-5 *Research of the ARM-based multi-robot aggregation control*
Huailin Zhao, Jingnan Zheng, Zhen Nie, Weiya Zhang, Zonglin Liu
(Shanghai Institute of Technology, China)

OS13-6 *Research on the Trajectory Planning Problem of Robots in Spherical Cutting*
Jun Min, Wenping Jiang, Huailin Zhao (Shanghai Institute of Technology, China)

OS13-7 *Emotional processing between artificial voices and human voices*
Qiang Wei[1], Xiaoyu Zhang[1], Xiao Yang[1], Yixin Lin[2], Qingming Liu[3]
([1]Jianghan University, [2]Huazhong University of Science and Technology, [3]Wuhan Rayson School, China)

OS13-8 *How people are affected by emoticon icon: An ERP study*
Qiang Wei[1], Jingxuan Huang[1], Yu Han[1], Yixin Lin[2]
([1]Jianghan University, [2]Huazhong University of Science and Technology, China)

OS13-9 *Single Chinese character fragments: an ERPs study on orthographic neighborhood effect*
Qiang Wei[1], Yunfei Wang[1], Chen Song[1], Yixin Lin[2]
([1]Jianghan University, [2]Huazhong University of Science and Technology, China)

OS13-10 *Research on embedded electrical impedance measurement system*
Tong Yin, Xiaoyan Chen, Hongyi Yin (Tianjin University of Science and Technology, China)

January 12 (Saturday)

8:40-Registration

Conference Room
11:10-11:40
Invited session IS-2
Chair: Ju-Jang Lee (KAIST, Korea)

IS-2 *A New Machine Learning Algorithm Applicable for Weather Visibility and Food Recognition*
Young Im Cho (Gachon University, Korea)

11:40-12:10

Invited session IS-3

Chair: Marion Oswald (Technische Universität Wien, Austria)

IS-3 *Affective Interactive Systems*

Kaoru Sumi (Future University Hakodate, Japan)

13:10-14:10

Plenary Speech PS-1

Chair: Akira Nakamura (National Institute of Advanced Industrial Science and Technology, Japan)

PS-1 *Motion-Data Driven Grasp/Assembly Planner*
Kensuke Harada[12], Natsuki Yamanobe[2], Weiwei Wan[12], Kazuyuki Nagata[2]
Ixchel G. Ramirez-Alpizar[1], Tokuo Tsuji[3] ([1]Osaka University, [2]National Institute of Advanced Industrial Science and Technology, [3]Kanazawa University, Japan)

Meeting Room 31

10:00-16:00 GS4 Poster (5)

Chair: Evgeni Magid (Kazan Federal University, Russia)

GS4-1 *Relevance Research among Destination Image, Brand Trust, and Satisfaction: Tainan Festival in Taiwan as Example*
Shang-Hui Li, Shu-Fang Hsu, Yi-Tai Shang (Far East University, Taiwan)

GS4-2 *Third-party Logistics Service Supply: Catering Service Trade as Example*
Shu-Fang Hsu, Shang-Hui Li (Far East University, Taiwan)

GS4-3 *Pedal Scale Control Device for Weighing Food Ingredients or Chemical Materials*
Shang-Hui Li, Shu-Fang Hsu, Yi-Tai Shang, Kuan-Ying Chen (Far East University, Taiwan)

GS4-4 *Convolution Neural Network Based Fault Diagnosis of Induction Motors*
Jong-Hyun Lee, In-Soo Lee(Kyungpook National University, Korea)

GS4-5 *Analysis of Value Chain on Food and Beverage Micro-enterprises: Mobile Diner as Example*
Shu-Fang Hsu, Shang-Hui Li (Far East University, Taiwan)

Meeting Room 32
9:00-9:45 OS17 Multiagent and Complex Systems (3)
Chair: Akihiro Yamaguchi (Fukuoka Institute of Technology, Japan)
Co-Chair: Saori Iwanaga (Japan Coast Guard Academy, Japan)

OS17-1 *Different Type of Interaction or Decision Error contribute to Functional Differences*
Saori Iwanaga[1], Masao Kubo[2]
([1]Japan Coast Guard Academy, [2]National Defense Academy of Japan, Japan)

OS17-2 *Evaluation for the Synchronization of the Parade with OpenPose*
Yohei Okugawa, Masao Kubo, Hiroshi Sato, Bui Duc Viet
(National Defense Academy of Japan, Japan)

OS17-3 *Phase shift estimation of the bifurcating neuron from superimposed chaotic spike sequences*
Akihiro Yamaguchi[1], Yutaka Yamaguti[1], Masao Kubo[2]
([1]Fukuoka Institute of Technology, [2]National Defense Academy of Japan, Japan)

10:00-11:00 OS16 New development about Control Engineering Education (4)
Chair: Yoshihiro Ohnishi (Ehime University, Japan)
Co-Chair: Kazuo Kawada (Hiroshima University, Japan)

OS16-1 *Skill Model Estimation of Ability for Reading Drawings*
Kazuo Kawada, Tsukasa Hiyama (Hiroshima University, Japan)

OS16-2 *Learning simulation based on a computational model of neuromodulators*
Yuki Moriguchi, Masayasu Nagamatsu
(Hiroshima University, Japan)

OS16-3 *Estimation of Programming Learning Achievement by Line Tracing Robot*
Yoshihiro Ohnishi[1], Teruyuki Tamai[1], Shinnosuke Mori[1], Kawada Kazuo[2]
（[1]Ehime University, [2]Hiroshima University, Japan）

OS16-4 *Development of Cultivate Computational Thinking using Finger Robot*
Kaito Omata, Shinichi Imai (Tokyo Gakugei University, Japan)

14:30-15:45 OS15 Advanced Control (5)
Chair: Yingmin Jia (Beihang University (BUAA), China)
Co-Chair: Weicun Zhang (University of Science and Technology Beijing, China)

OS15-1 *Pulse Pose Follow Control and Simulation for a 4-DOF Pulse Diagnosis Robot*
Qunpo Liu[1], Guanghui Liu[1], Hongqi Wang[1], Xianzhe Liu[1], Hanajima Naohiko[2]
([1]Henan Polytechnic University, China, [2]Muroran Institute of Technology, Japan)

OS15-2 *A New Adaptive Control System Design Method Based on Neuronetwork Prediction*
Weicun Zhang, Sufang Wang, Yongnan Jia, Qing Li
(University of Science and Technology Beijing, China)

OS15-3 *Mean-square quasi-composite rotating formation control of second-order multi-agent systems under stochastic communication noise*
Lipo Mo[1], Xiaolin Yuan[1], Yingmin Jia[2], Shaoyan Guo[3]
([1]Beijing Technology and Business University, [2]Beihang University (BUAA), [3]South China University of Technology, China)

OS15-4 *Distributed Energy Resource Control Based on Multi-Agent Group Consensus*
Yize Yang[1,2], Hongyong Yang[1], Fan Liu[1], Yuling Li[1], Yuanshan Liu[1]
([1]Ludong University, China, [2]The University of New South Wales, Australia)

OS15-5 *Robust Adaptive Control of Air-to-air Refueling Boom with State-dependent Output Constraints*
Liang Chang, Yingmin Jia (Beihang University (BUAA), China)

16:20-17:50 GS2 Robotics II (6)
Chair: Jiwu Wang (Beijing Jiaotong University, China)

GS2-1 *Automated Guided Vehicle System Analysis in Foam Manufacturing Plant Using Petri-net*
Amornphun Phunopas[1], Wisanu Jitviriya[1], Noppadol Pudchuen[1], Sutee Kumjaikong[1], Songklod Tunsiri[2], Eiji Hayashi[3] ([1]King Mongkut's University of Technology North Bangkok, Thailand, [2]Urban Community, Development College, Thailand, [3]Kyushu Institute of Technology, Japan)

GS2-2 *Preliminary Comparative Experiments of Support Vector Machine and Neural Network for EEG-based BCI Mobile Robot Control*
Yasushi Bandou, Takuya Hayakawa, Jun Kobayashi (Kyushu Institute of Technology, Japan)

GS2-3 *Position Tracking Error Constrained Super-Twisting Dynamic Surface Control with Disturbance Observer for Robot Manipulators*
Seong Ik Han (Dongguk University, Korea Republic)

GS2-4 *Image Processing for Picking Task of Random Ordered PET Drinking Bottles*
Chen Zhu, Takafumi Matsumaru (Waseda University, Japan)

GS2-5 *The Use of Importance Ranks to Derive Suitable Timing of Visual Sensing in Manipulation Task Containing Error Recovery*
Akira Nakamura[1], Kazuyuki Nagata[1], Kensuke Harada[2], Yukiyasu Domae[1]
([1]National Institute of Advanced Industrial Science and Technology (AIST), [2]Osaka University, Japan)

GS2-6-1 *Electronic Measurement and Gamification of Balance Tests*
Yan-Xin Liu, Massimiliano Leggieri, Henrik Hautop Lund
(Technical University of Denmark, Denmark)

GS2-6-2 *Playful Body and Brain Test with the Moto Tiles*
Yan-Xin Liu, Massimiliano Leggieri, Henrik Hautop Lund
(Technical University of Denmark, Denmark)

Meeting Room 33
9:00-9:30 GS3 Complexity (2)
Chair: Manabu Sugii (Yamaguchi University, Japan)

GS3-1 *Extracting Co-occurrence Feature of Words for Mail filtering*
Seiya Temma, Manabu Sugii, Hiroshi Matsuno (Yamaguchi University, Japan)

GS3-2 *Learning Style Classification with Weighted Distance Grey Wolf Optimization*
Duangjai Jitkongchuen, Piyalak Pongtawevirat (Dhurakij Pundit University, Thailand)

10:00-11:00 OS23 Kansei and Information Engineering (4)
Chair: Chair: Tetsuo Hattori (Kagawa University)
Co-Chair: Yoshiro Imai (Kagawa University)

OS23-1 *Color Image Arrangement Based on Histogram Matching Using Smoothed Brightness Histogram (I) --- Overall Smoothing ---*
Yusuke Kawakami, Tetsuo Hattori, Yoshiro Imai, Koji Kagawa, Yo Horikawa (Kagawa University, Japan), R. P. C. Janaka Rajapakse (Tainan National University of the Arts, Taiwan)

OS23-2 *Color Image Arrangement Based on Histogram Matching Using Smoothed Brightness Histogram (II) --- Piecewise Smoothing---*
Yusuke Kawakami, Tetsuo Hattori, Yoshiro Imai, Koji Kagawa, Yo Horikawa (Kagawa University, Japan), R. P. C. Janaka Rajapakse (Tainan National University of the Arts, Taiwan)

OS23-3 *Parameter Estimation Method for Compartment Model - PET Inspection -*
Tetsuo Hattori, Yusuke Kawakami, Yoshiro Imai, Koji Kagawa, Yo Horikawa (Kagawa University, Japan), Hiromichi Kawano (NTT Advanced Technology Company Ltd, Japan)

OS23-4 *Application and Trial Evaluation of Document Writing Support System to Avoid Emotional Misunderstanding*
Shunsuke Doi, Yoshiro Imai, Koji Kagawa, Tetsuo Hattori, Yusuke Kawakami
(Kagawa University, Japan)

14:30-15:45 OS12 Robot Design and Simulation (5)
Chair: QinJian Zhang (Beijing Jiaotong University, China)
Co-Chair: Wei Liu (Beijing Jiaotong University, China)

OS12-1 *Design and Research of Navigation and Dynamics Co- Simulation Platform for Planetary Rover*
Huang Tie-qiu, Zhang Bo-wen, Huang Qian-li (Beijing Jiaotong University, P.R China)

OS12-2 *Research on Application of SFM Method in Virtual Reality Modeling*
Jiwu Wang, Chenyang Li (Beijing Jiaotong University, China)
Min Li (Beijing Forestry University, China)

OS12-3 *Visual SLAM System Design based on Semantic Segmentation*
Jiwu Wang, Yafan Liu, Qinjian Zhang (Beijing Jiaotong University, China)

OS12-4 *Spherical Mobile Robot Designed with Single Omnidirectional Wheels*
Wei Liu, Lian Luo, Jiwu Wang (Beijing Jiaotong University, China)

OS12-5 *An augmented reality implementation method based on Unity3D*
Weixin Zeng, Jiwu Wang (Beijing Jiaotong University, China)

16:20-17:05 OS25 High-Performance Computing for Interactive Content Creation and Rendering (3)
Chair: R.P.C. Janaka Rajapakse (Tainan National University of the Arts, Taiwan)
Co-Chair: Chia-Chen Kuo (National Center for High-performance Computing (NCHC), Taiwan)

OS25-1 *High-Performance Computing for Visual Simulations and Rendering*
Jasmine Wu, Chia-Chen Kuo, Shu-Hsin Liu, Chuan-Lin Lai, Chiang-Hsiang Lien, Ming-Jen Wang, Chih-Wei Wang (National Center for High-performance Computing (NCHC), Taiwan)

OS25-2 *Virtual Reality as an Art Form*
R.P.C. Janaka Rajapakse, Yi-ping Hung (Tainan National University of the Arts, Taiwan)

OS25-3 *Using Quill as a Tool for Real-Time Rendering*
Jasmine Wu, Chia-Chen Kuo, Shu-Hsin Liu, Chuan-Lin Lai, Chiang-Hsiang Lien, Ming-Jen Wang, Chih-Wei Wang (National Center for High-performance Computing (NCHC), Taiwan)

Meeting room 1
9:00-9:45 OS9 Natural Computing and Beyond (3)
Chair: Marion Oswald (Technische Universität Wien, Austria)
Co-Chair: Yasuhiro Suzuki (Nagoya University, Japan)

OS9-1 *Tactile Score: Development and Applications*
Yasuhiro Suzuki (Nagoya University, Japan)

OS9-2 *Tactileology; Haptic Informatics by using Tactile bit, T-bit*
Yasuhiro Suzuki (Nagoya University, Japan)

OS9-3 *Natural Computing and Formal Computing*
Yasuhiro Suzuki (Nagoya University, Japan)

14:30-16:00 OS22 Robot Competitions for Social Contribution (6)
Chair: Yasunori Takemura (Nishinippon Institute of Technology, Japan)
Co-Chair: Kazuo Ishii (Kyushu Institute of Technology, Japan)

OS22-1 *Study on Position Estimation Using Small Size ZigBee Module*
Atsushi Sanada (Nishinippon Institute of Technology, Japan)

OS22-2 *The 4th Tomato Harvesting Robot Competition*
Takayuki Matsuo[1], Takashi Sonoda[2], Yasunori Takemura[2], Kazuo Ishii[3]
([1]National Institute of Technology, Kitakyushu College, [2]NishiNippon Institute of Technology, [3]Kyushu Institute of Technology, Japan)

OS22-3 *End-effector for robotic harvesting of a tomato fruit with calyx*
Binghe Li, Shinsuke Yasukawa, Takuya Fujinaga, Kazuo Ishii
(Kyushu Institute of Technology, Japan)

OS22-4 *Evaluation for Ball Dribbling Mechanism of RoboCup Middle Size League Robot in The World Teams*
Kenji Kimura, Shota Chikushi, Kazuo Ishii (Kyushu Institute of Technology)

OS22-5 *Robot-control method based on personal space*
Kota Kawamoto, Eiji Hayashi, Ryusuke Fujisawa (Kyushu Institute of Technology)

OS22-6 *Recognition method of target objects for autonomous tomato harvesting robot*
Keiji Kamei, Hiroyuki Moriyama (Nishinippon Institute of Technology, Japan)

Meeting room 4
9:00-9:45 OS19 Advanced Technology on Sensing Technology, Devices, Application (3)
Chair: Hiroki Tamura (University of Miyazaki, Japan)
Co-Chair: Keiko Sakurai (University of Miyazaki, Japan)

OS19-1 *The Actual Car Driving Evaluation System using Combined with Eyeball and Face Angle*
Keiko Sakurai, Hiroki Tamura, Koichi Tanno (University of Miyazaki, Japan),
Yukio Hattori (OFA SUPPORT INC, Japan)

OS19-2 *A Study on Speaker Identification Approach by Feature Matching Algorithm using Pitch and Mel Frequency Cepstral Coefficients*
Barlian Henryranu Prasetio, Keiko Sakurai, Hiroki Tamura, Koichi Tanno
(University of Miyazaki, Japan)

OS19-3 *A Study on Breathing and Heartbeat Monitoring System during Sleeping using Multi-Piezoelectric Elements*
Praveen Nuwantha Gunaratne, Chika Yoshida, Keiko Sakurai, Hiroki Tamura, Koichi Tanno,
(University of Miyazaki, Japan)

<u>January 13 (Sunday)</u>

8:40-Registration

Meeting Room 31

10:40-11:40

Plenary Speech PS-3

Chair: Takao Ito (Hiroshima University)

PS-3 *Robust Consensus Control of Multi-vehicle Systems*
Yingmin Jia (Beihang University, P.R.China)

Meeting Room 32

9:00-10:30 OS6 Software Development Support Method (6)

Chair: Tetsuro Katayama (University of Miyazaki, Japan)

Co-Chair: Tomohiko Takagi (Kagawa University, Japan)

OS6-1 *Prototype of an Animated Graphics-Based Training Support Tool for Bug Fixing of Extended Place/Transition Nets*
Tomohiko Takagi, Shogo Morimoto, Yuki Ue, Yoshiro Imai (Kagawa University, Japan)

OS6-2 *Prototype of a Modeling Tool to Convert between Extended Place/Transition Nets and VDM++ Specifications*
Tomohiko Takagi, Ryo Kurozumi (Kagawa University, Japan)

OS6-3 *Application of Pairwise Testing to Test Cases by Boundary Value Analysis in BWDM*
Futa Hirakoba*, Tetsuro Katayama*, Yoshihiro Kita†, Hisaaki Yamaba*, Kentaro Aburada*, Naonobu Okazaki*
(*University of Miyazaki, †Tokyo University of Technology, Japan)

OS6-4 *Development of Library Fescue Extracting Elements of Attributes and Operations of Class Diagram in UML*
Keisuke Mori*, Tetsuro Katayama*, Yoshihiro Kita†, Hisaaki Yamaba*, Kentaro Aburada*, Naonobu Okazaki* (*University of Miyazaki, †Tokyo University of Technology, Japan)

OS6-5 *Tamias: a Syntax File Checker for Parsing Expression Grammar*
Toshihiro Miyaji*, Tetsuro Katayama*, Yoshihiro Kita†, Hisaaki Yamaba*, Kentaro Aburada*, Naonobu Okazaki* (*University of Miyazaki, †Tokyo University of Technology, Japan)

OS6-6 *Implementation of an Arduino Simulator to Support Circuit Design*
Tatsumi Nishida*, Tetsuro Katayama*, Yoshihiro Kita†, Hisaaki Yamaba*, Kentaro Aburada* And Naonobu Okazaki* (*University of Miyazaki, †Tokyo University of Technology, Japan)

12:40-13:55 OS10 Mathematical Informatics (5)

Chair: Makoto Sakamoto (University of Miyazaki, Japan)

Co-Chair: Amane Takei (University of Miyazaki, Japan)

OS10-1 *A Study on Tourism Support Application Using the Virtual Technology*
Masamichi Hori[1], Makoto Sakamoto[1], Takahiro Ishizu[1], Satoshi Ikeda[1], Amane Takei[1], Takao Ito[2], Yu-an Zhang[3] ([1]University of Miyazaki, [2]Hiroshima University, Japan, [3]Qinghai University, China)

OS10-2 *Proposal for Interaction Techniques for Intuitive Virtual Objects Manipulation in Augmented Reality*
Takahiro Ishizu[1], Makoto Sakamoto[1], Takaaki Toyota[1], Masamichi Hori[1], Satoshi Ikeda[1], Amane Takei[1], Takao Ito[2], Yu-an Zhang[3]
([1]University of Miyazaki, [2]Hiroshima University, Japan, [3]Qinghai University, China)

OS10-3 *Two-Dimensional Image Based Body Size Measurement and Body Weight Estimation for Yaks*
Zijie Sun[1], Chen Zhang[1], XiaoFeng Qin[1], Yu-an Zhang[1], Rende Song[2], Makoto Sakamoto[3]
([1]Qinghai University, [2]Yushu Prefecture Animal Husbandry and Veterinary Station, China [3]University of Miyazaki, Japan)

OS10-4 *An efficient structure of organization with complete group guidance*
Satoshi Ikeda[1], Mamoru Yoshimura[1], Makoto Sakamoto[1], Takao Ito[2]
([1]University of Miyazaki, [2]Hiroshima University, Japan)

OS10-5 *Parallel finite element analysis for hyperbolic problems*
Amane Takei,, Makoto Sakamoto (University of Miyazaki, Japan)

Meeting Room 33

9:00-10:00 OS5 Business Models and Management (4)

Chair: Takao Ito (Hiroshima University, Japan)

Co-Chair: Minoru Kumano (University of Miyazaki, Japan)

OS5-1 *Determining the Key Factors of Michinoeki in Yamaguchi Area*
Minoru Kumano[1], Tsutomu Ito[2], Takao Ito[3], Toru Hiraoka[4], Hirofumi Nonaka[5]
([1]University of Miyazaki, [2]Hino Motors, Ltd., [3]Hiroshima University, [4]University of Nagasaki, [5]Nagaoka University of Technology, Japan)

OS5-2 *Discovering the Characteristics of Michinoeki in Japan*
Minoru Kumano[1], Tsutomu Ito[2], Takao Ito[3], Toru Hiraoka[4], Hirofumi Nonaka[5]
([1]University of Miyazaki, [2]Hino Motors, Ltd., [3]Hiroshima University,
[4]University of Nagasaki, [5]Nagaoka University of Technology, Japan)

OS5-3 *An Analysis of Robotic Relationship between Transaction Network and Cross-shareholding Network in Yokokai*
Takao Ito[1], Tsutomu Ito[2], Rajiv Mehta[3], Seigo Matsuno[4], Makoto Sakamoto[5], Satoshi Ikeda[5]
([1]Hiroshima University, Japan, [2]Hino Motors, Ltd., Japan, [3]New Jersey Institute of Technology, U.S.A., [4]Ube National College of Technology, Japan, [5]University of Miyazaki, Japan)

OS5-4 *Technological Discontinuities and the R&D Strategy of Automobile Companies*
Yousin Park[1], Iori Nakaoka[2], Yun-ju Chen[3] ([1]Prefectural University of Hiroshima, [2]National Institute of Technology, Ube College, [3]Shiga University, Japan)

12:40-13:55 OS24 Automated content generation for narrative and cognitive contents (5)
Chair: Jumpei Ono (Vocational School of Digital Arts Sendai, Japan)
Co-Chair: Hiroki Fukushima (Kyushu Womens' University, Japan)
Co-Chair: Takashi Ogata (Iwate Prefectural University, Japan)

OS24-1 *A Method of Haiku Generation Using Deep Learning for Advertising Generation*
Jumpei Ono (Vocational School of Digital Arts Sendai, Japan)
Takashi Ogata (Iwate Prefectural University, Japan)

OS24-2 *The Usage Features of Onomatopoeias in the Recipes in Japanese*
Hiroki Fukushima (Kyushu Womens' University, Japan)

OS24-3 *Storytelling in the Conversation of Aged People*
Yuki Hayashi (Chiba University / Center for Advanced Intelligence Project, Riken, Japan)
Akinori Abe (Chiba University /Dwango Artificial Intelligence Laboratory, Japan)

OS24-4 *Expression of the taste of Japanese sake and metaphor*
Akinori Abe (Chiba University / Dwango Artificial Intelligence Laboratory, Japan)

OS24-5 *An Analysis on Advertising Techniques of Beverages Using Positive Factors of Evaluation Database System*
Yoji Kawamura (Kindai University, Japan)

GS5 Others (8)

GS5-1 *Suppression of Roll Oscillation in Turning of Quadruped Robot by Asymmetric Amplification of Central Pattern Generator Output Waveform*
Makoto Kitani, Ryo Asami, Noritake Sato (Nagoya Institute of Technology, Japan),
Tomofumi Fujiwara, Takahiro Endo, Fumitoshi Matsuno (Kyoto University, Japan),
Yoshifumi Morita (Nagoya Institute of Technology, Japan)

GS5-2 *Tumble avoidance system for rescue robot by estimating the contact points using a 3D depth sensor*
Noritaka Sato, Kotaro Ohshima, Yoshifumi Morita (Nagoya Institute of Technology, Japan)

GS5-3 *Rule based Intrusion Detection System by Using Statistical Flow Analysis Technique for Software Defined Network*
Mahnoor Ejaz, Osama Sohail, Talha Naqash, Zain ul Abideen, Sajjad Hussain Shah
(Bahria University, Pakistan)

GS5-4 *Development of Testbed for SDN to Know Its Feasibility of Deployment on Access Layer*
Rafay Shah, M Osama Shaikh, Talha Shaikh, Tanveer Hussain
(Mehran University of Engineering & Technology, Pakistan)

GS5-5 *Spectrum Sensing using Unsupervised Learning for Cognitive Radio*
Asmara Shaukat, Danish Khan, Talal Arshad, Haseeb Ahmad (PAF-KIET, Pakistan)

GS5-6 *Tracking Secondary User In Cognitive Radio For 5g Communication*
Muhammad Adnan, Muhammad Umair, Sameed bin Junaid
（PAF-KIET, Pakistan）

GS5-7 *Wireless Power Transfer And Data Communication For Biomedical Applications*
Hammad Saleem, Muhammad Awais, Siraj Din, Attequa
(PAF-KIET, Pakistan)

GS5-8 *Feasibility Study Of UAV Implementation In Route Surveying*
D.Hazry, M A Azizan, Safwan Suhaimi, Zulaiha Ramli, Mohamad Syafiq A.K, Zainuddin Hat
(Universiti Malaysia Perlis, Malaysia)

Farewell Party

PS abstracts

PS-1 Motion-Data Driven Grasp/Assembly Planner

Kensuke Harada[1,2], Natsuki Yamanobe[2], Weiwei Wan[1,2], Kazuyuki Nagata[2],
Ixchel G. Ramirez-Alpizar[1], Tokuo Tsuji[3]
([1]Osaka University, [2]National Institute of Advanced Industrial Science and Technology,
[3]Kanazawa University, Japan)

This paper proposes a robotic grasp/assembly planner partially using a motion data. A motion data includes an information on skillful motion which cannot simply be realized by using conventional grasp/assembly planners. We first explain the structure of motion data. Then, we explain the proposed grasp/assembly planner. Finally, we show a numerical example to confirm the effectiveness of our proposed method.

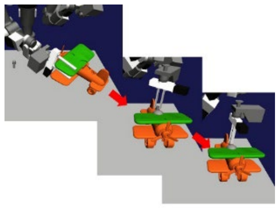

PS-2 Toward Life with Partner Robots - Developing robots with the field trial toward the practical use

Masanori Sugiyama (Toyota Motor Corporation, Japan)

In the near future, robots are expected to be utilized as partners to coexist with people for various social needs. TOYOTA is developing robots aimed to help societies. As a first step, rentals of a rehabilitation robot for walking training at medical institutions have been launched in 2017. Another robot, Human Support Robot, which is aimed for use to support daily living, has been adopted as a standard platform of the domestic environment league at the RoboCup competition since 2017. For the robot development, it is important to learn deeply about the field which the robot is to be actually used. In this presentation, we will show the scene of the field trial toward the practical use of our robots. Also, we will introduce a humanoid robot which is integrated with advanced technologies that would benefit us in the future.

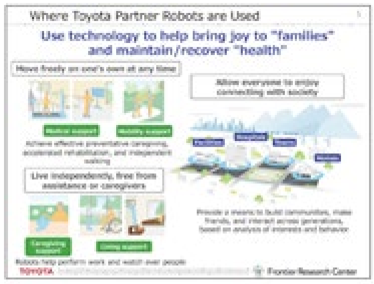

PS-3 Robust Consensus Control of Multi-vehicle Systems

Yingmin Jia (Beihang University, P.R.China)

Consensus control of multi-vehicle systems is to design a coordinated protocol based on the communication topology, so that the multi-vehicle states can reach consensus rapidly and safely to achieve the desired cooperative tasks. Considering parameter variations of vehicles, modelling errors and external disturbances, the corresponding robust consensus control problems should be investigated. To this end, this talk focuses on three basic issues, i.e., single-vehicle maneuverability, multi-vehicle coordination, and disturbance attenuation of control performance of vehicle systems in the uncertain environment, and some recent advances are reviewed. In particular, it is found that most of the existing results are very limited from a practicable point of view because the traditional decoupling control methods are inapplicable to vehicles with varying velocity, the previous coordinated protocols require connectivity of dynamical topologies, and the robust consensus control of multi-vehicle systems with internal uncertainties and external disturbances has not yet fully been studied so far. Doubtless, these limitations make the applications of consensus control theory for multi-vehicle systems to actual objects more difficult, and therefore, it is necessary to develop novel control methods to remove these limitations and all these will be introduced in detail.

IS abstracts

IS1-1-1 Engineering Modular Playware

Henrik Hautop Lund, Morten Roed Frederiksen, Massimiliano Leggieri
(Technical University of Denmark, Denmark)

In this paper, we describe the engineering of modular playware. The modularity of constructing playware systems out of modules may allow the system to be easily transported to be used anywhere, to easily build different bodies and brains, and to allow people to construct and combine the modules to become creative. Hence, the modularity helps fulfilling the Playware ABC. We exemplify the engineering challenges of the hardware, software and communication design of modules through the development of handheld modules for playful rehabilitation. The handheld modules allow for a fun and motivational training of upper extremities, and can be viewed as an extension to the Moto Tiles for lower extremity training, which have proved to be a highly successful playware for prevention and rehabilitation among seniors. The paper outlines the engineering challenges and proposed solutions to make such modular playware for playful upper extremity training.

IS1-1-2 User-Friendly Robotics 3 – Playware

Henrik Hautop Lund, Luigi Pagliarini (Technical University of Denmark, Denmark)

The sustainable The design of playware based on the lessons learned from user-friendly robotics suggests a focus on a number of design criteria to help achieving playware systems that can and will be used according to the Playware ABC by anybody, anywhere, anytime. The design criteria are described in this paper, and they include: modularity, explicit immediate feedback, robustness, simplicity, one-click, design. Each criterion is described based on the lessons learned from user-friendly robotics. We exemplify the use of these design criteria with the development of the playware system, Moto Tiles. The Moto Tiles system is designed as a playful prevention and rehabilitation system for seniors, who are normally not exposed to such high technology systems. The paper discusses how the design criteria allowed for a successful design of a user-friendly system, which is now used daily by tens of thousands seniors all over the globe.

IS1-2-1 User-Friendly Robotics 1 – AI Software

Luigi Pagliarini[1,2], Henrik Hautop Lund[1]
([1]Technical University of Denmark, Denmark) ([2]Academy of Fine Arts of Macerata, Italy)

In this paper we present the trajectory of decades of research in AI and Robotics by highlight the continuity of our method that has always taken into consideration the common user's point of view as a priority. We call such an approach User-Friendly Robotics, and we hereby unravel it by describing our path step-by-step, to see on one side its evolution and on the other its methodological continuity. Therefore, starting from the earliest AI-based application we slowly move-up towards the first Robotics ones to finally describe the last results of our research. We discuss how this User-Friendly Robotics approach leads to solutions that fit particular purposes in society and lead to useful user interaction with technological developments.

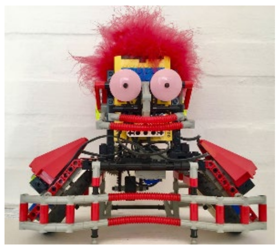

IS1-2-2 User-Friendly Robotics 2– Interfacing Robotics with any user

Luigi Pagliarini[1,2], Henrik Hautop Lund[1]
([1]Technical University of Denmark, Denmark) ([2]Academy of Fine Arts of Macerata, Italy)

In this paper, the second part out of three, we continue presenting the route of our long experience in interfacing AI and Robotics with the public. This paper, in particular, highlights a crucial step we experimented when creating computer based software architecture so to let the common user easily interact with complex behaviour robotics. We define such an approach User-Friendly Robotics, and we hereby describe the principles and the techniques we used to evolve its methodology reporting here the most important case studies we went through, as examples. We then analyse the impact of such method on both science and educational field. Finally, we discuss how this User-Friendly Robotics approach leads to solutions that fit particular purposes in society and lead to useful user interaction with technological developments.

IS-2 A New Machine Learning Algorithm Applicable for Weather Visibility and Food Recognition

Young Im Cho (Gachon University, Korea)

The sustainable Smart City need many intelligent technologies. In this paper, we implement a new Machine Learning algorithm for visibility of weather images. The aim of the research is that to estimate weather visibility using a new machine learning techniques. We use images taken from CCTV cameras as inputs and deep convolutional neural network model to predict results. Our new machine learning algorithm apply to smart life for food recognition, too. We augment many images using a new machine learning algorithm. In this paper, we will detail explain regarding an architecture of the ML model, System Structure, and other essential details.

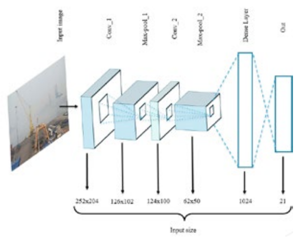

IS-3 Affective Interactive Systems

Kaoru Sumi (Future University Hakodate, Japan)

In this talk, I will present the effect of using emotions in humans and artifacts (computer systems, virtual agents, robots, etc.) interaction. As known as Media Equation, the relationship between humans and artifacts is similar to the social relationship between humans and humans. For example, when a human is helped by an artifact a human want to thank artifacts and return something. Like humans, it is important for artifacts to recognize emotions and express emotions in relation between humans and artifacts. In this talk, I introduce a technique to recognize and express emotions in human interaction with artifacts and show examples of how effective artifacts are when using emotions.

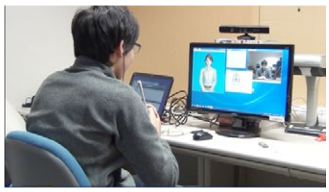

OS abstracts

OS1 Intelligent Systems and Control (8)

OS1-1 A Vishay Supercapacitor based Fast Charge Battery

Chung-Wen Hung, Yi-Chang Yang, Chun-Chu Lin, Li-Sheng Jheng
(National Yunlin University of Science and Technology, Taiwan)

A supercapacitor (SC) power supply management system based on is proposed in this paper. Due to the high charging current characteristics of the SC, means short charging time, the proposed SC-base battery is suitable as a backup battery. The proposed system includes the input voltage, current and temperature protection implemented with analog integrated circuits (IC); and output current limitation circuit. In order to keep output voltage when the SC voltage drops, a boost circuit is used to provide a stable voltage for the load. The circuit design is detailed in this paper, and the experimental results show the proposed system works well.

OS1-2 Multi-Motor Synchronous Control with CANOpen

Chung-Wen Hung, Roger CL Lee, Bo-Kai Huang, Shit-Ting Yu
(National Yunlin University of Science and Technology, Taiwan)

A Brushless DC (BLDC) Motors synchronous control system based on the CANopen protocol is proposed in this paper. Multi-motor control is popular in Robot or automation system, and the synchronization is an important issue, may be the key issue. The CANopen is a solution, due to Process Data Object (PDO) protocol. A Texas Instruments microcontroller TMS320F28069 is used as master to control six BLDC Motors used as slave in this paper. The Master sends synchronization object (SYNC) to slaves base on the communication profile CAN in Automation (CiA) 301 and the motion control profile CiA402. The system suns at 500Kbits/s and 1Mbits/s transmission rate by setting process data object (PDO). The firmware details in this paper to show six-motor synchronous control.

OS1-3 Selection Strategy for VM Migration Method

Yan-Ren Chen, I-Hsien Liu, Keng-Hao Chang, Jung-Shian Li
(National Cheng Kung University, Taiwan)

Virtual machine (VM) live migration occurs frequently in cloud environments. When it is necessary to migrate many VMs, minimizing the migration time is an important concern. Thus, choosing an appropriate strategy to perform VM migration is essential. Accordingly, this paper discusses the advantages and disadvantages of four different migration methods and evaluates their respective migration times and throughputs.

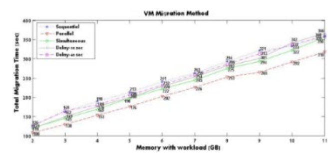

OS1-4 VM Migration Placement in Cloud Service

Yan-Ren Chen, I-Hsien Liu, Keng-Hao Chang, Chuan-Gang Liu, Jung-Shian Li
(National Cheng Kung University, Taiwan)

Smooth and transparent VM migration is essential in maximizing the utilization of cloud resources and ensuring user satisfaction. Previous studies have focused on VM operational procedures, live migration models and efficient migration methods. By contrast, the paper focuses on the fundamental theorems of VM migration. The present study considers two different VM migration problems and proves that they too are NP-complete. In the first problem, subsets of the VM migration groups are migrated to a physical host until their combined resource usage approaches the threshold value of the host. In the second problem, the VM migration groups are migrated simultaneously in such a way as to minimize the total migration time.

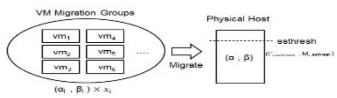

OS1-5 Control System for Maintaining Safe Following Distance while Driving

Kuo-Hsien Hsia, Jia-Hong Cai, Shu-Li Pai (Far East University, Taiwan)
Evgeni Magid (Kazan Federal University, Russia)

Safety is the most important thing while driving. Many traffic accidents occur because of insufficient safe distance. With the advancement of technology, there are cars with a front distance safety warning system. The invention relates to a driving safety distance control system. Some of them are with fixed safe distance regardless of the speed of the car. Other advanced distance detection systems switch between different modes such as high speed and low speed. In this paper, we proposed a driving safety system which can dynamically adjust the safety distance between vehicles depending on the speed and weather conditions. This system can be used to determine and maintain safe distances both in front and rear of a car. This idea has obtained the invention paten of Taiwan. A car with this system can be driven more safely.

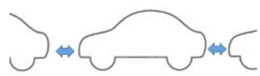

OS1-6 Markerless Indoor Augmented Reality Navigation Device Based on Optical-Flow-Scene Indoor Positioning and Wall-Floor-Boundary Image Registration

Chian C. Ho, Bo-Kai Wang, Guan-Lung Liao
(National Yunlin University of Science and Technology, Taiwan)

For markerless indoor Augmented Reality Navigation (ARN) technology, camera pose is inevitably the fundamental argument of positioning estimation and pose estimation, and floor plane is indispensably the fiducial target of image registration. This paper proposes optical-flow-scene indoor positioning and wall-floor-boundary image registration to make ARN more precise, reliable, and instantaneous. Experimental results show that both optical-flow-scene indoor positioning and wall-floor-boundary image registration have higher accuracy and less latency than conventional well-known ARN methods. On the other hand, these proposed two methods are seamlessly implemented on the handheld Android embedded platform and are smoothly verified to work well on the handheld indoor augmented reality navigation device.

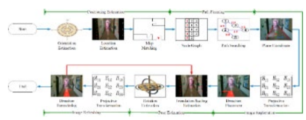

OS1-7 Development of the handheld gas detector with IoT function.

Jr-Hung Guo, Kuo-Hsien Hsia, Kuo-Lan Su
(National Yunlin University of Science and Technology, Taiwan)

Gas detection is very cumbersome because the gas will diffuse and mix with other gases. Therefore, this paper is development a handheld gas detector using a single chip controller. This detector can use a variety of different gas sensors. And use the Fuzzy Analytic Hierarchy Process (fuzzy-AHP) and the Adaptive Fusion Method to improve the correctness and recognition rate of the sensor. In terms of communication, because this gas detection module is hand-held, we use Wi-Fi, LoRa, and wireless communication interfaces such as 433/868/915 Mhz. Let this gas detection module still transmit data while moving. In addition, multiple gas detection modules can be used to form a detection network for large area detection. And we can use the built-in algorithm to do the calibration data for the detection and isolation of network module or sensor. Make this gas detection module more flexible in use.

.

OS1-8 Research on Employee Attribute Correlation of Information Security Awareness in Organization

Tse-Yao Wang (Air Force Institute of Technology, Taiwan)
Fu-Hsiang Wen (National Kaohsiung University of Science and Technology, Taiwan)

Enterprises are attacked by phishing emails, causing significant business losses. The information security protection strategies adopted by enterprises, such as mail filtering, phishing attack website screening and phishing website blacklists, cannot guarantee complete defense. This study attempts to propose another perspective that can reduce the risk of corporate information security. The quality of employees' information security used as an indicator, and the Logistic regression model used as a tool to analyze the key factors that can be used to measure the quality of information security awareness.

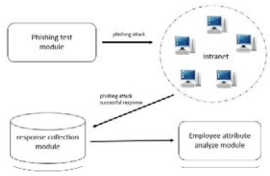

OS2 Theory and Implementation of Neuromimetic Systems (5)

OS2-1 Decoding spike patterns of auto-associative memory on spiking neuronal networks

Naoki Toyoshima, Takashi Kohno (The University of Tokyo, Japan)

Spiking neuronal networks model the electrophysiological activities in Spiking neuronal cells' networks, in which spikes emitted by the neuronal cells transmit information. A well-known application of the spiking neuronal networks is auto-associative memory, in which one of the pre-stored patterns that is mostly similar to the input pattern is retrieved. It is known that the spatio-temporal output spikes are converged to anti-synchronized two groups that correspond to the retrieved pattern and its complement. The spikes in each group are synchronized. For practical use of auto-associative memory on the spiking neuronal networks, it is necessary to convert the spatio-temporal output spikes to digital codes that can be utilized in ordinary digital computer systems. In this manuscript, we propose methods to efficiently do this conversion and extract some more information by additional neurons receiving signals from the neurons in the all-to-all connected network which is a typical configuration for the auto-associative memory.

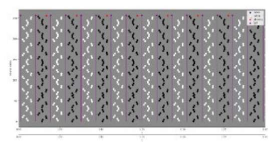

OS2-2 Possible Mechanism of Internal Visual Perception: Context-dependent Processing by Predictive Coding and Reservoir Computing Network

Hiroto Tamura[1], Yuichi Katori[1,2], Kazuyuki Aihara[1]
([1]The University of Tokyo, [2]Future University Hakodate, Japan)

How our brains perceive visual stimuli and generate internal visual images largely remains unknown. Here, we propose a network model by combining the idea of predictive coding and reservoir computing (PCRC). First, we define the context-dependent task by simplifying the process of human's internal visual perception, and then train the PCRC network for the task. In our model, the context represents the category of the visual stimuli, and the network forms different attractor landscapes depending on each context. However, the mismatch between the context and the sensory stimuli induces the perceptual error, which corresponds to the symptoms of the hallucination in dementia with Lewy bodies. Furthermore, we incorporate the parameter representing a sort of neuromodulation into the network model and analyze the influences of the neuromodulation to the stability of the attractor on the network dynamics and performance of the visual perception.

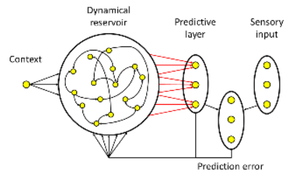

OS2-3 Snake robot controlled by biomimetic CPGs

Damien Blanchard[1], Kazuyuki Aihara[2], Timothée Levi[2]
([1]University of Bordeaux, France, [2]The University of Tokyo, Japan)

Locomotion is one of the most basic abilities in animals. Neurobiologists have established that locomotion results from the activity of half-center oscillators that provides alternation of bursts. Central Pattern Generators (CPGs) are neural networks capable of producing rhythmic patterned outputs without rhythmic sensory or central input. We propose a network of several biomimetic CPGs using biomimetic neuron model and synaptic plasticity. This network is implemented on a FPGA (Field Programmable Gate Array). We designed one unsupervised snake robot using this network of CPG. It is composed of one head wagon and 7 slave wagon. Infrared sensors are also embedded in the head wagon. This robot can reproduce the locomotion of one snake. The hardware robot is also described in this paper.

OS2-4 Real-time implementation of ReSuMe learning in Spiking Neural Network

Xia Yang, Seiji Uenohara, Kazuyuki Aihara, Takashi Kohno, Timothée Levi
(The University of Tokyo, Japan)

Neuromorphic systems are designed by mimicking or being inspired by the nervous system, which realizes robust, autonomous, and power-efficient information processing by highly parallel architecture. Supervised learning was proposed as a successful concept of information processing in neural network. Recently, there has been an increasing body of evidence that instruction-based learning is also exploited by the brain. ReSuMe is a proposed algorithm by Ponulak and Kasinski in 2010. It proposes a supervised learning for biologically plausible neurons that reproduce template signals (instructions) or patterns encoded in precisely timed sequences of spikes. Here, we present a real-time ReSuMe learning implementation on FPGA using LIF Spiking Neural Network (SNN). FPGA allows real-time implementation and embedded system. We show that this implementation can make successful the learning on a specific pattern.

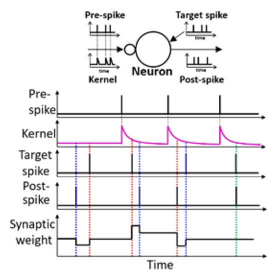

OS2-5 Biomimetic spike-timing based ionic micro-stimulation for neuron culture

Stephany Mai Nishikawa[1], Farad Khoyratee[1,2], Soo Hyeon Kim[1], Yoshiho Ikeuchi[1], Kazuyuki Aihara[1], Teruo Fujii[1], Timothée Levi[1]
([1]The University of Tokyo, Japan, [2]University of Bordeaux, France)

Neurodegenerative diseases influence cognitive and/or motor functions in millions of people worldwide. Neuroprosthesis are used today to support the quality of life but have yet to improve in their power consumption and biocompatibility issues. Here, we propose a novel microfluidic system to investigate the response of the neurons directly stimulated by the potassium ions in biomimetic timing. Unlike the conventional way of stimulating neurons by pipetting or sending electrical stimulus, this biomimetic stimulation system enables precise and rapid control of ion concentration by utilizing microfluidic pneumatic valves, which mimics physiological stimulation in a body. To circumvent these limitations, we propose a new bio-hybrid system. There are three parts that consists this neuro-hybrid system: Spiking Neural Network, neuron culture and ionic micro-stimulation device. By using the system, we demonstrated biomimetic spike-timing based ionic stimulation of the neuron cells with potassium ions and monitored neural activities with a calcium-specific fluorescence indicator.

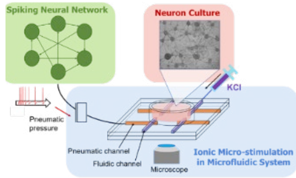

OS2-6 Dynamical network model for visual cortex: hierarchical reservoir computing with bidirectional interactions (withdraw)

Shohei Takaichi[1], Yuichi Katori[2], Kazuyuki Aihara[1]
([1]The University of Tokyo, Japan, [2] Future University Hakodate, Japan)

In visual cortex, there is a feedback connection between high-layer and low-layer. However, the effect of feedback remains poorly understood. We describe a hierarchical neural network model for visual recognition using reservoir computing. We adapt this model to predictive coding of video information. Because input of the network is an image of each frame of video, which is too high dimension for the reservoir computing, we divide the image to patches and integrate divided information in high-layer and send it as feedback.

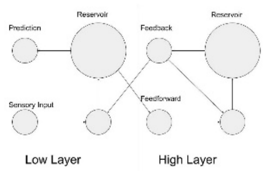

OS3 Intelligent Navigation & Robotics (4)

OS3-1 Trajectory tracking control for a 7-arms robot manipulator

Wang Jie, Hyun-Hee Kim, Saad abbasi, Min-Cheol Lee (Pusan National University, Korea)

This paper proposes a trajectory tracking control based TSMCSPO (terminal silding mode control with sliding perturbation observer) for a 7-arms robot manipulator. The 7-arms robot arm are designed to assemble small parts or packaging. System dynamics, kinematics and inverse kinematics are introduced at first. Because dynamics of this 7-arms robot are difficult to determine precisely with the uncertainties and many nonlinear terms. TSMCSPO are used as a robust controller with the observer for unknown states and perturbation which can estimate the error in obtained system dynamics.

OS3-2 Estimation tire-rod friction coefficient based on mobile robot

Ji-Hyeon Kim, Zhang Hongyu, Jang-Myung Lee (Pusan National University, Korea)

It is very important to estimate the friction coefficient of tire-road for vehicle dynamic control system. For the current dynamic control research, a large amount of experimental data is needed. The theoretical tire model is used to estimate the friction coefficient based on the Gim tire model to improve the tire experience model. Simulation by MATLAB, the simulation results show that the Gim tire model has high precision and can predict the mechanical properties of the tire well.

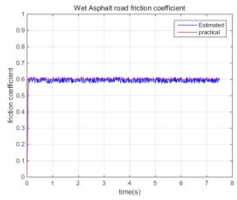

OS3-3 Real-time reflection removal algorithm using stereo camera only

Do-Kyung Hwang, Jong-Woo An, Jang-Myung Lee (Pusan National University, Korea[1])

In this paper, we implemented a light reflection elimination algorithm which is one of the main obstacles of various object recognition systems using vision systems. In other words, this algorithm can be used to remove robotic recognition obstacles from the factory and perform tasks such as locating robots, autonomous vehicles, or unmanned aerial vehicles. This algorithm has been studied with versatility in mind and does not require sensors other than stereo cameras. A brief description of the algorithm is an algorithm that intuitively interprets pixels in HSI space and processes pixels corresponding to light. For intuitive analysis, take an angle, intensity, or other light source (sunlight, fluorescent light, candle) from the camera, then record each pixel value and separate it from a white object (whiteboard, paper, etc.). After pixel operation, object recognition is implemented using the CNN (Convolution Neural Network) method using the YOLO_V2 algorithm

OS3-4 The Effect of Inertial Measurement Unit on Synthetic Aperture Radar Image Quality

Soo-Jeong Lee[1], Yong-Gonjong Park[1], Woo-Jung Park[1], Chan Gook Park[1], Jong-Hwa Song[2] (Seoul National University, Korea[1], Hanwha Systems, Korea[2])

This paper analyzes the effect of inertial measurement unit (IMU) on synthetic aperture radar (SAR) image quality. While operating SAR, it is supposed that an aircraft flies straight and level at a constant speed. Because of atmospheric turbulence and aircraft maneuvers, it deviates from its nominal trajectory. With navigation solutions, the deviations can be compensated through motion compensation procedure. However, uncompensated motion errors generated by IMU errors degrade SAR image quality, such as broadening bandwidth and blurring the image. Since the residual errors depend on the degree of IMU inaccuracies, SAR images and impulse response function (IRF) according to IMU grades are compared with each other. Through this result, the IMU specification is suggested to satisfy given SAR image quality.

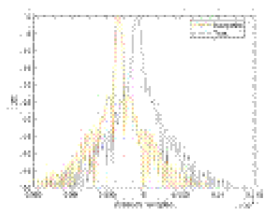

OS4 Service Robotics (7)

OS4-1 Apply 2D Barcode Scanner for Mobile Robot Navigation in Checkerboard Mapping

Chun-Chi Lai[1], Kuo-Lan Su[1], Chia-Jen Lin[1], Evgeni Magid[2]
([1]National Yunlin University of Science and Technology, Taiwan)
([2]Kazan Federal University, Russia)

In this work, a mobile robot is equipped with an industrial barcode scanner which can provide the pose information respect to the tag in the field of view (FOV). For real multiple mobile robot transportation applications, the mobile robot navigation flow is considered to get the global checkerboard type path planning from a remote master server as an input. For the local planner, each robot is applied with a simple path controller to track the global path. The simulation and experimental results show that this implementation has good feasibility and effectiveness for multi- robot co-working such as in a factory area.

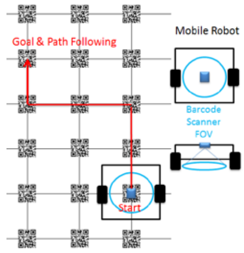

OS4-2 Development of the MyRio Based Mobile Platform

Bo-Jun Yang[1], Sheng-Jie Liou[1], Jr-Hung Guo[1], Kuo-Lan Su[1], Evgeni Magid[2]
([1]National Yunlin University of Science and Technology, Taiwan)
([2]Kazan Federal University, Russia)

The paper develops the MyRio based mobile platform with a robot arm. The structure of the mobile platform uses the Matrix elements. The Matrix element set builds the robot arm with four degrees of freedom. The mobile platform integrates some sensors, three DC servomotors, a RC servomotor, a MyRio based controller, and a vision system. The core of the MyRio based controller is the NI-Single-Board RIO 9606 module. The mobile platform embeds a robot arm on the front side. The driver device of the gripper is a RC servomotor. The vision system of the mobile platform can search and recognize the assigned shape and color that is on the front side of each box using Otsu algorithm. The mobile platform uses the robot arm to catch the ball, and moves to the assigned box simultaneously. In the experimental results, the mobile platform moves to the assigned location from the start location, and uses the vision system to find out the assigned ball, and puts down the ball on another box by the robot arm. Finally, the mobile platform moves to the start location and stop.

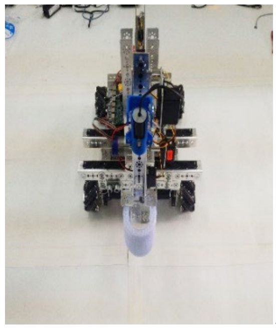

OS4-3 Modelling Avrora Unior Car-like Robot in Gazebo Environment

Ksenia Shabalina[1], Artur Sagitov[1], Kuo-Lan Su[2], Kuo-Hsien Hsia[3], Evgeni Magid[1]
([1]Kazan Federal University, Russia)
([2]National Yunlin University of Science and Technology, Taiwan)
([3]Far East University, Taiwan)

In order to conduct thousands of complicated experiments on autonomous car navigation algorithms it is much safer and cheaper to start algorithm verification within a simulation area given that we succeed to achieve a proper model configuration, which preserves physical properties of underlying objects. This paper focuses on model construction of Avrora Unior mobile robot. Avrora Unior is a Russian car-like mobile robot with Ackermann drive mechanism. For the robot model design we used open source Robot operating system (ROS) and 3D simulator Gazebo. We describe the entire process of modeling and first steps of control implementation for the model.

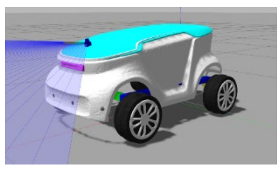

OS4-4 Transfer of learned exploration strategies for a mobile robot from a simulated world to real environments

Artur Sagitov[1], Tetsuo Takano[2], Shohei Muto[2], Evgeni Magid[1]
([1]Kazan Federal University, Russia) ([2]Kanazawa University, Japan)

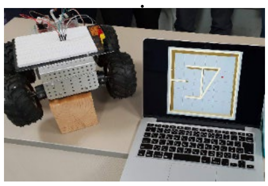

Reinforcement learning based approaches show promises in various robotic applications, but a significant amount of time and resources are required for a robot to learn optimal behavior. Using virtual environments, we could significantly speed up and improve performance of a target task. We implemented a reinforcement learning based exploration algorithm for a mobile robot, training in Gazebo environment and transferring learned strategy to a real robot. We show that it is convenient and appropriate to use simulation to train strategies for mobile robots.

OS4-5 Extending Gazebo simulator for surgical robotics: tissue and suture modeling

Artur Sagitov[1], Hongbing Li[2], Evgeni Magid[1]
([1]Kazan Federal University, Russia) ([2]Shanghai Jiao Tong University, China)

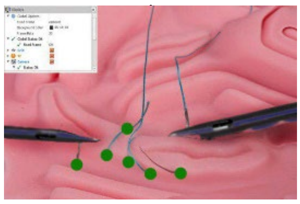

Active use of a simulator as a training tool has proven to be advantageous to a human surgeon, but there is no open source and convenient universal surgery simulation of a robot surgeon. This paper presents an extension of Gazebo simulator for surgical robots using Robot Operating System. We present software architecture that allows modeling robot interaction with different types of tissue and suture. We plan to apply the resulting system for a surgical task of autonomous suturing with different techniques and algorithms to be compared in the same virtual environment.

OS4-6 Experiences of Robotics students in Machine Vision course being taught in a foreign language: comprehension, self-efficiency, and active learning strategies improvement

Tatyana Tsoy, Artur Sagitov, Evgeni Magid (Kazan Federal University, Russia)

Historical development of Russia in the end of 20th century significantly decreased the quality of engineering education. Now, in order to catch up with the developed countries, at Kazan Federal University a novel 2-year Master program in Intelligent Robotics was designed and implemented. The program, which curriculum is based on experience of world leading universities in the field of robotics, targets to educate competitive specialists with competences that are required in the world labor market. Students with various technical backgrounds were enrolled in the program. To follow students' progress in core robotics courses we conducted surveys in the beginning and by the end of each course. This paper presents surveys that were conducted in Machine Vision course. The paper reports results of the survey analysis covering such issues as English language comprehension, self-efficiency, and active learning strategies in the context of Machine Vision.

OS4-7 Pilot Virtual Experiments on ArUco and AprilTag Systems Comparison for Fiducial Marker Rotation Resistance

Aufar Zakiev[1], Ksenia Shabalina[1], Kuo-Lan Su[2], Kuo-Hsien Hsia[3], Evgeni Magid[1]
([1]Kazan Federal University, Russia)
([2]National Yunlin University of Science and Technology, Taiwan)
([3]Far East University, Taiwan)

There exists a large number of fiducial marker system types and both researchers and industry have difficulties to select among this variety a single system that could provide optimal behavior for a particular task. This paper presents design and results of pilot virtual experiments that were conducted in order to compare a performance of two marker systems, ArUco and AprilTag. Experiments were designed to estimate and compare marker systems resistance against rotation with regard to different principal axes in 3D space. Pilot experiment design eliminates influence of external environment, including light conditions, camera resolution, sensor noise, distance between camera and marker, etc. Experiments were implemented in ROS/Gazebo environment. In total over 300,000 virtual experiments were performed and analyzed in order to collect statistically significant data amount.

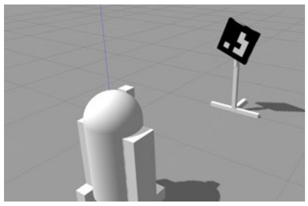

OS5 Business Models and Management (4)

OS5-1 Determining the Key Factors of Michinoeki in Yamaguchi Area

Minoru Kumano[1], Tsutomu Ito[2], Takao Ito[3], Toru Hiraoka[4], Hirofumi Nonaka[5]
([1]University of Miyazaki, [2]Hino Motors, Ltd., [3]Hiroshima University,
[4]University of Nagasaki, [5]Nagaoka University of Technology, Japan)

It is becoming an important issue to improve efficiency in Michinoeki. Thus to find the key determinants is considered as the most urgent task for Michinoeki. This paper proposed a new approach with two steps: to calculate the efficiency using regression model after determing the relevant factors using DEA model. The data are collected from Chugoku area, because Chugoku is the birthplace of Michinoeki. The efficiency of all Michinoeki have been calculated, and the implications have been discussed in this paper.

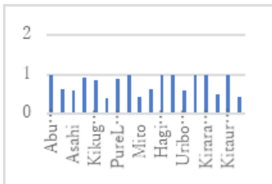

OS5-2 Discovering the Characteristics of Michinoeki in Japan

Minoru Kumano[1], Tsutomu Ito[2], Takao Ito[3], Toru Hiraoka[4], Hirofumi Nonaka[5]
([1]University of Miyazaki, [2]Hino Motors, Ltd., [3]Hiroshima University,
[4]University of Nagasaki, [5]Nagaoka University of Technology, Japan)

World Bank reported that four stages including identification, preparation, appraisal and operation are necessary to improve Michinoeki. Thus to estimate the value of Michinoeki is a crucial issue. As our best knowledge, no research to study the whole Michinoeki although there are 1,107 Michinoeki by April, 2017 in Japan. Nine areas: Hokkaido, Tohoku, Kanto, Hokuriku, Chubu, Kinki, Chugoku, Sikoku, and Kyushu&Okinawa have been divided, eleven basic elements are used as the determinants of the Michinoeki. This paper examined the determinants of the nine areas and found that the key determinants of those nine areas are totally different. It contributes not only to understand the status quo of Michinoeki, but also helpful to find the potential possibility for further development.

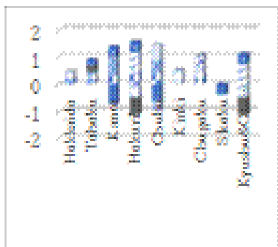

OS5-3 An Analysis of Robotic Relationship between Transaction Network and Cross-shareholding Network in Yokokai

Takao Ito[1], Tsutomu Ito[2], Rajiv Mehta[3], Seigo Matsuno[4], Makoto Sakamoto[5], Satoshi Ikeda[5]
([1]Hiroshima University, Japan, [2]Hino Motors, Ltd., Japan, [3]New Jersey Institute of Technology, U.S.A., [4]Ube National College of Technology, Japan. [5]University of Miyazaki, Japan)

After bubble economy, the relationship of all parts suppliers in the keiretsu have been changed from strong tie to weak tie. One typical thing is relationship of cross shareholdings does not contribute to the transactional relationship. The authors once proved that the relationship between cross share holdings and transactions still remained in Keiretsu of Kyohokai even after the bubble economy. This paper collected the data from Yokokai, a keiretsu of Mazda, and calculated the relationship between cross share holding and transaction to prove the correlationship between cross share holdings and transaction in Yokokai.

OS5-4 Technological Discontinuities and the R&D Strategy of Automobile Companies

Yousin Park[1], Iori Nakaoka[2], Yun-ju Chen[3]
([1]Prefectural University of Hiroshima,
[2]National Institute of Technology, Ube College,
[3]Shiga University, Japan)

This paper focuses on patterns of technological changes and the R&D strategy of automobile companies. Tushman and Anderson (1986) pointed out that there are two types of technological changes. One is incremental technological change which is often generated by existing companies, and the other one is radical technological change which makes great extension in business environment and destroys the order of existing companies. We use the patent information of three automobile companies (Toyota, BYD, Tesla) as the cases on these changes. And we examine our propositions by social network analysis and text analysis. The analysis in this paper include: 1) try to distinguish between the radical and incremental technological changes from R&D projects, and create heat-maps to visualize these changes, 2) make discussion on technological discontinuities and the R&D strategy of automobile companies. In this paper we suppose that patterns of corporate R&D strategy cope with the threat of radical technological changes.

The Network of Patent

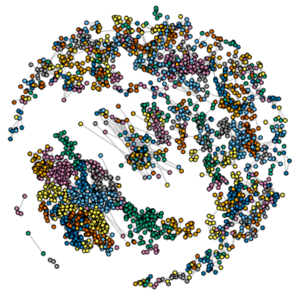

OS6 Software Development Support Method (6)

OS6-1 Prototype of an Animated Graphics-Based Training Support Tool for Bug Fixing of Extended Place/Transition Nets

Tomohiko Takagi, Shogo Morimoto, Yuki Ue, Yoshiro Imai (Kagawa University, Japan)

An EPN (Extended Place/transition Net) is an executable formal model with high representation power for specifications definition and test case generation, but it would not be so easy for most of software engineers to learn and use the EPN efficiently. This paper describes an animated graphics-based training support method and prototype tool for bug fixing of EPNs. The prototype tool gives a trainee a faulty EPN and its animated graphics. The motion of the animated graphics is synchronized with the motion of the faulty EPN. Therefore, it is expected that a trainee can intuitively understand the faulty EPN, and smoothly try to fix a bug (a difference between the faulty EPN and software requirements). The result of bug fixing is checked by the prototype tool.

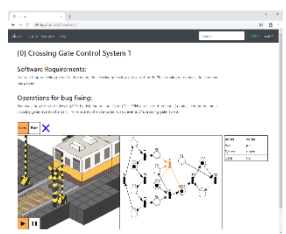

OS6-2 Prototype of a Modeling Tool to Convert between Extended Place/Transition Nets and VDM++ Specifications

Tomohiko Takagi, Ryo Kurozumi (Kagawa University, Japan)

In software modeling, engineers can use EPNs (Extended Place/transition Nets) to define the expected behavior of software. The guards and actions of EPNs are written in VDM++, and thus EPNs can be straightforwardly converted to VDM++ specifications. EPNs provide more abstracted and intuitive view than VDM++ specifications, and VDM++ specifications can be used to generate source codes and test cases. Therefore they give engineers a practical way for model-driven development. VDM++ specifications should be updated along with EPNs, and vice versa. However, it is not so easy for engineers due to their limited time. This paper shows a prototype of a modeling tool that converts (and keep the consistency) between EPNs and VDM++ specifications.

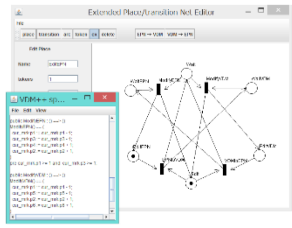

OS6-3 Application of Pairwise Testing to Test Cases by Boundary Value Analysis in BWDM

Futa Hirakoba*, Tetsuro Katayama*, Yoshihiro Kita†,
Hisaaki Yamaba*, Kentaro Aburada*, Naonobu Okazaki*
(*University of Miyazaki, †Tokyo University of Technology, Japan)

In recent years, specifications using specification language become more important. It is necessary to test the developed software, but it takes much time and effort to design test cases manually. So, we developed BWDM(Boundary Value Vienna Develop Method). It generates test cases from VDM++ specifications. In BWDM, test cases are generated by boundary value analysis. However, it is possible to cause a combination explosion by the number of the test cases. In order to solve the above problem, this research extends BWDM so that the pairwise testing can be applied to boundary value analysis. The extended BWDM does not cause the combination explosion, because the pairwise testing only generates test cases which satisfy combinations of two pairs.

Please attach one typical figure in your paper here.

OS6-4 Development of Library Fescue Extracting Elements of Attributes and Operations of Class Diagram in UML

Keisuke Mori*, Tetsuro Katayama*, Yoshihiro Kita†,
Hisaaki Yamaba*, Kentaro Aburada*, Naonobu Okazaki*
(*University of Miyazaki, †Tokyo University of Technology, Japan)

Many modeling tools and development support environments for UML have been developed. And some modeling tools have the function to convert the described model into programs. However, no existing tools can describe all the grammar defined in UML 2.0 specification. Or even if it can be described, the existing tools cannot analyze its meaning correctly. This paper develops library fescue (Feature Elements Section of Class in UML Extraction) extracting elements of attributes and operations of Class Diagram in UML to expand the analyzable range of the grammar defined in UML 2.0 specification. Fescue can parse character strings expressing attributes and operations based on the grammar defined in UML 2.0 specification, and can extract each element from the syntax analysis result. It is confirmed that fescue can parse the components of attributes and operations in a practical time that the existing tools cannot parse.

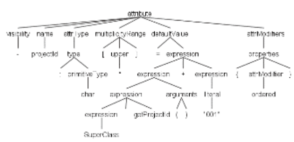

OS6-5 Tamias: a Syntax File Checker for Parsing Expression Grammar

Toshihiro Miyaji*, Tetsuro Katayama*, Yoshihiro Kita†,
Hisaaki Yamaba*, Kentaro Aburada*, Naonobu Okazaki*
(*University of Miyazaki, †Tokyo University of Technology, Japan)

In recent years, Parsing Expression Grammar (PEG) is introduced by Bryan Ford. PEG is not ambiguous because it has ordered choice property. However, it causes “prefix capture”. “Prefix capture” is a problem of hiding the language to be accepted according to the order of choice. Checking syntax files that contain such mistakes confirms the behavior of the parser. However, in confirming the behavior of the parser, it is possible to check only the top level non-terminal symbols, and it is necessary to rebuild the parser for each change in the syntax file. This paper proposes Tamias: a syntax file checker to support checking the syntax files. Tamias has a PEG interpreter which can check all choices and any non-terminal symbols in production rules follows PEG.

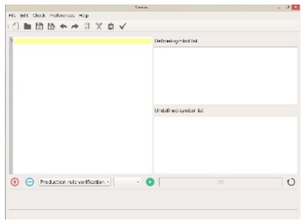

OS6-6 Implementation of an Arduino Simulator to Support Circuit Design

Tatsumi Nishida*, Tetsuro Katayama*, Yoshihiro Kita†,
Hisaaki Yamaba*, Kentaro Aburada*, and Naonobu Okazaki*
(*University of Miyazaki, †Tokyo University of Technology, Japan)

Embedded technologies are used everywhere and are indispensable in our daily life. One of the educational materials to learn embedded technology is Arduino. However, when a beginner designs circuit, it is possible to design circuit that damages Arduino itself or the modules on it. Therefore, this research implements an Arduino simulator that runs on iPad for supporting to design circuit. In this simulator, the circuit on iPad is analyzed to detect the voltage value on the circuit and the risk Arduino itself or the modules being damaged. This feature allows you to visually notify the risk of breakage of Arduino itself or the modules without damaging them. Consequently, this simulator can support to design circuit.

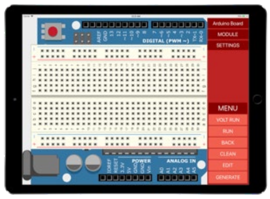

OS7 Media Information Processing and Artificial Intelligence (4)

OS7-1 Effectiveness of Data Augmentation in Automatic Summarization System

Tomohito Ouchi, Masayoshi Tabuse (Kyoto Prefectural University, Japan)

We propose a new data augmentation method in automatic summarization system. A large corpus is required to create an automatic summarization system using deep learning. However, in the field of natural language processing, especially in the field of automatic summarization, there are not many data sets that are sufficient to train automatic summarization system. Therefore, we propose a new method of data augmentation. We use an encoder decoder model with an attention model as automatic summarization system. First, we determine the importance of each sentence in an article using topic model. In order to extend the data, we remove the least important sentence from an input article and use it as a new article. We examine the effectiveness of our proposed data augmentation method in automatic summarization system.

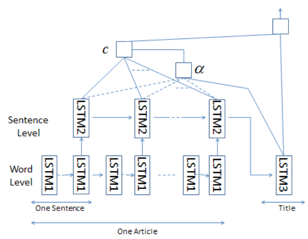

OS7-2 A System for Posting on SNS Portrait Selected Using Facial Expression Analysis While Writing Message

Taro Asada[1], Yuiko Yano[2], Yasunari Yoshitomi[1], Masayoshi Tabuse[1]
([1] Kyoto Prefectural University, [2] Nara Guarantee Corporation, Japan)

We have developed a real-time system for expressing emotion as a portrait selected according to the facial expression while writing a message. The portrait is decided by a hair style, a facial outline, and a cartoon of facial expression. The user selects one hair style and one facial outline before writing a message. The image signal is analyzed by our real-time system using image processing software (OpenCV) and a previously proposed feature parameter. Then the system selects one cartoon expressing one of neutral and happy facial expressions using the facial expression intensity threshold previously decided between these facial expressions. We applied the system to post on an SNS a message and a portrait expressing the facial expression while writing the message. The experimental and questionnaire results suggest that our system can be useful for expressing emotions while writing messages.

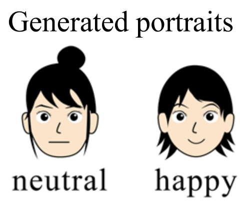

OS7-3 A Method Using Wavelet Transform for Judging Character to be Inserted into Image

Yasunari Yoshitomi[1], Takashi Sato[2], Taro Asada[1], Masayoshi Tabuse[1]
([1] Kyoto Prefectural University, [2] Tokyo Institute of Technology, Japan)

There has been an increase in the number of images on the Internet that contain private information and/or the URL of an illegal Web site. This information might result in a violation of human rights and/or a crime. We previously proposed a method for extracting from an image the region(s) that contain characters. Based on the previously proposed method, we have proposed a method for judging character to be inserted into image using the discrete wavelet transform, the image compression characteristics, and the empirical knowledge that characters have strong vertical and/or horizontal elements. The experimental results show the usefulness of our method.

OS7-4 An Authentication Method for Digital Audio Using Wavelet Transform and Fundamental Frequencies

Yasunari Yoshitomi[1], Shohei Tani[2], Masaki Arasuna[3], Ryota Kan[4], Taro Asada[1],
Masayoshi Tabuse[1] ([1] Kyoto Prefectural University, [2] Fukuchiyama City Hall,
[3] Nissay Information Technology Co., Ltd., [4] Shimazu Business Systems Co., Ltd., Japan)

Recently, several digital watermarking techniques for audio files have been proposed for hiding data in order to protect their copyrights. In general, there is a tradeoff between the quality of watermarked audio and the tolerance of watermarks to signal processing methods, such as compression. For overcoming the inevitable tradeoff, we previously developed an authentication method for digital audio using a discrete wavelet transform. In the present study, we have improved the method by deciding the region to be authenticated in the audio file using the fundamental frequency characteristics. The experimental results show that the method has high tolerance of authentication to cutting small parts in the audio data.

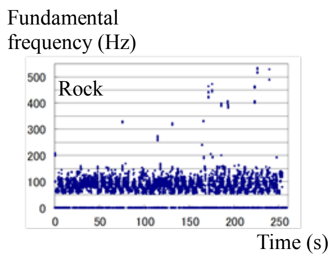

OS8 Computational intelligence and cognitive science for human biosignals and human well-being (7)

OS8-1 Unified Approach to (1+1) EA on Discrete Linear Functions

Kenji Aoki, Makoto Sakamoto (University of Miyazaki, Japan)
Hiroshi Furutani, Satoru Hiwa, Tomoyuki Hiroyasu (Doshisha University, Japan)

We consider the runtime property of discrete linear functions in (1+1) Evolutionary Algorithms. We analyze the process of evolution by means of Markov chain method. This study was motivated by the paper of Jansen treating the runtime property of (1+1) EA on monotonic functions by means of probabilistic theory. As linear functions are special case of monotonic function, we analyze their behavior by Jansen's model, PO-EA. We show that linear functions show almost the same runtime if mutation rate pm is small. On the other hand, in the case of strong mutation, the runtime shows the function specific magnitude. This fact means that higher order mutations play more important roles in the calculation process with stronger mutation.

PO-EA
(1+1) EA
Markov Chain Analysis
↓
Discrete Linear Functions.

OS8-2 A fNIRS study of brain state during letter and category fluency tasks

Akane Onishi, Satoru Hiwa, Hiroshi Furutani, Tomoyuki Hiroyasu (Doshisha University, Japan)

One of the practical issues concerning automated driving vehicles is identifying the state of the driver when switching between manual and automatic control. When switching, it is important to detect the wakefulness and awareness of the driver. In this study, we controlled a driving simulator based on driver state detection. Electrocardiogram (EKG) measurement was used for driver state detection. Heart rate variability analysis (HRV) is a widely known means for estimating sympathetic and parasympathetic activity. We created a Simulink model to calculate SDNN, RMSSD, and LF/HF in real time, which are indicators obtained from the HRV analysis. Based on the model, the state of the driver during the driving simulation was detected. We also created a Simulink model that switches between automatic operation and manual operation of simulated vehicles. By applying these models, construction of a system that safely switches between automatic operation and manual operation is expected.

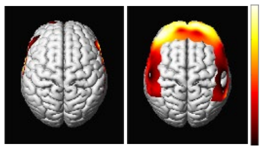

OS8-3 Construction of a meditation practice support system leads to a good meditation state: an fNIRS study

Seika Fujii, Satoru Hiwa, Hiroshi Furutani, Tomoyuki Hiroyasu (Doshisha University, Japan)

Meditation is one methods of realizing a state of mindfulness. By continuing meditation, an improvement of concentration and work efficiency is expected. However, when novices practice meditation, they find it difficult to judge improvements in their practice. Therefore, in this study, a system for supporting novices' meditation practices was formulated. In the proposed system, quantification of and feedback regarding the meditation state based on brain functional information was performed. Brain activity during meditation was measured using functional near-infrared spectroscopy. The brain activity could be measured using this method close to every day. A good brain state during meditation was defined based on previous research. The measured brain state was compared with this good state and the similarity was calculated. The state was then judged on the basis of the similarity and feedback was given when the meditator approached the goal state. The effectiveness of the constructed system was examined.

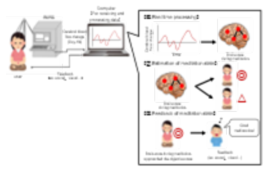

OS8-4 Automated panoramic image creation system for corneal endothelial cells

Keitaro Kobayashi, Naoki Okumura, Noriko Koizumi, Satoru Hiwa, Hiroshi Furutani, Tomoyuki Hiroyasu
(Doshisha University, Japan)

The imaging area of the corneal endothelium imaged by current technology is narrow, mainly observing the central portion. A system for automatically creating a panoramic image based on an imaging video of the corneal endothelium of the mouse was developed. First, still images were extracted from the imaging videos and were convolved with a Laplacian kernel. With the variance of the response as a threshold value, focused images were extracted. By stitching the focus images, panoramic images of the corneal endothelium were created. The reason this method works is that the Laplacian kernel highlights regions of an image containing rapid intensity changes. If the variance is very high, there are huge edges in the image, that is, the image is focused. In this paper, automatically created panoramic images were evaluated by comparison with manually created panoramic images, which were defined as correct images. This system can be applied to the evaluation of the progression of symptoms.

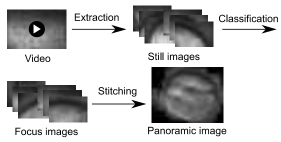

The proposed system

OS8-5 An fMRI study of the inhibitory effects of the random stimulus-response compatibility task on brain function

Kei Sahara, Satoru Hiwa, Hiroshi Furutani, Tomoyuki Hiroyasu (Doshisha University, Japan)

Our behavior is optimized by the brain to suppress unnecessary movement at particular moments. Here, we investigated the differences in inhibition during a spatial stimulus-response compatibility task. The stimulus-response compatibility task is used to investigate brain function while inhibiting movements to accomplish the optimized movements during the compatible and incompatible trials. A previous study investigated inhibitions in specific compatible and incompatible tasks. However, these studies did not consider the inhibition during random events, which is an everyday occurrence in human life. Therefore, in this study, we focused on the differences between specific inhibition and random effect inhibition using three stimulus-response compatibility tasks, comprising the compatible, incompatible, and random tasks. Twenty healthy participants were measured using 1.5-T functional magnetic resonance imaging (fMRI) and the results were analyzed by using activation, brain function network, and behavioral analyses.

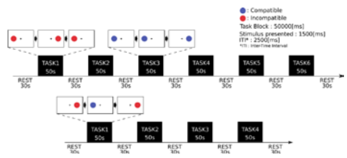

OS8-6 Measurement of brain activity and problem discovery during actual driving

Seishiro Nakamura, Satoru Hiwa, Kenya Sato, Hiroshi Furutani, Tomoyuki Hiroyasu
(Doshisha University, Japan)

In this study, we focused on a system that provides driving support based on a driver's biological parameters. Brain function is one such biological parameter and functional near-infrared spectroscopy (fNIRS) was used to measure brain function. fNIRS is less susceptible to body movements and easier to measure than electroencephalography. In order to compare brain activities during actual vehicle operation and simulated operation, a task performed using a simple course was prepared. In order to quantify the change in cerebral blood flow obtained from each channel, the fractional amplitude low-frequency fluctuations (fALFF), which is an index of local spontaneous brain activity, was calculated. Furthermore, it was z transformed (zfALFF) to allow comparisons between subjects. In addition, to confirm the relationship between driving performance and brain activity, we compared the time series data for driving performance and cerebral blood flow change obtained from each channel. The measurement of brain activity during actual vehicle driving was performed and the results were analyzed. In addition, discussions of the findings and future directions are also included.

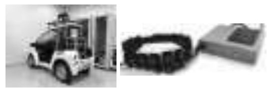

OS8-7 Control of driving simulator based on state detection of the driver using Electrocardiogram measurement

Koma Yoshioka, Satoru Hiwa, Kenya Sato, Hiroshi Furutani, Tomoyuki Hiroyasu
(Doshisha University, Japan)

One of the practical issues concerning automated driving vehicles is identifying the state of the driver when switching between manual and automatic control. When switching, it is important to detect the wakefulness and awareness of the driver. In this study, we controlled a driving simulator based on driver state detection. Electrocardiogram (EKG) measurement was used for driver state detection. Heart rate variability analysis (HRV) is a widely known means for estimating sympathetic and parasympathetic activity. We created a Simulink model to calculate SDNN, RMSSD, and LF/HF in real time, which are indicators obtained from the HRV analysis. Based on the model, the state of the driver during the driving simulation was detected. We also created a Simulink model that switches between automatic operation and manual operation of simulated vehicles. By applying these models, construction of a system that safely switches between automatic operation and manual operation is expected.

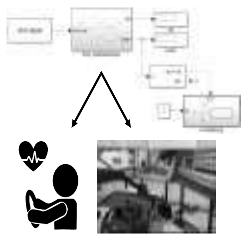

OS9 Natural Computing and Beyond (3)

OS9-1 Tactile Score: Development and Applications

Yasuhiro Suzuki (Nagoya University, Japan)

Unlike music, which can be described by means of a musical score, tactile sense does not have a standard method for transcription. Likewise, tactile sense has no developed principle of composition. Hence, this study developed a method for describing tactile sense, referred to here as the ‘tactile score’. We developed a mutual transformation method between tactile score and haptic vibrations, and then we verified that a hand massage performed according to a tactile score and haptic vibration from a tactile score evoked similar brain activities.

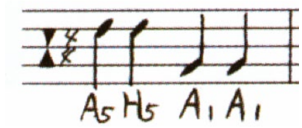

OS9-2 Tactileology; Haptic Informatics by using Tactile bit, T-bit

Yasuhiro Suzuki (Nagoya University, Japan)

Most of Internet of Things, IoT data is time series data, however the time series patterns of tactile sense have not been investigated. Tactile Score is a novel method for describing time sequences of different tactile senses, such as massages. It can not only describe the massages but also tactile senses in multimedia data such as locution, vocalism or rhetoric, etc.; multimedia time series data can be transformed into Tactile Score and we can display tactile senses denoted by Tactile Score by using Tactile Score players. Tactile Score enables us to compose and edit tactile senses. We extract composing principle of time series patterns of tactile senses though analyzing massages; extracted principle has been verified through examining biological responses.

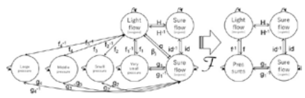

OS9-3 Natural Computing and Formal Computing

Yasuhiro Suzuki (Nagoya University, Japan)

In natural computing, computing substances, such as DNA molecules, cells or ecosystems, observe the result of algorithm and verify it by themselves. Hence, natural computing is primitive in computing and throughout of the evolution from natural computing, it develops “external formal” system to observe and verify and evolve to formal computing system. In this talk, I will briefly address the evolution of computing from natural computing to formal computing and show a novel natural computing framework; thinking about nature by natural computing.

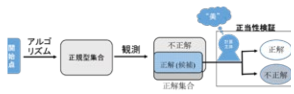

OS10 Mathematical Informatics (5)

OS10-1 A Study on Tourism Support Application Using the Virtual Technology

Masamichi Hori[1], Makoto Sakamoto[1], Takahiro Ishizu[1], Satoshi Ikeda[1], Amane Takei[1], Takao Ito[2], Yu-an Zhang[3]
([1]University of Miyazaki, [2]Hiroshima University, Japan, [3]Qinghai University, China)

Currently, the tourism industry in Miyazaki prefecture has various problems, and various measures are taken. On the other hand, in 2016, virtual technology attracted much attentions such as VR and AR technology. We thought that through the VR and AR technology experience, we could aim for an increase in tourists. Therefore, we will create new applications for smartphones using virtual technology and aim for tourism support. We propose unique features aimed at increasing tourists and creating repeaters. It is a function that allows you to reproduce the scenery anywhere with VR, and to feel the sightseeing experience by AR close.

OS10-2 Proposal for Interaction Techniques for Intuitive Virtual Objects Manipulation in Augmented Reality

Takahiro Ishizu[1], Makoto Sakamoto[1], Takaaki Toyota[1], Masamichi Hori[1], Satoshi Ikeda[1], Amane Takei[1], Takao Ito[2], Yu-an Zhang[3] ([1]University of Miyazaki, [2]Hiroshima University, Japan, [3]Qinghai University, China)

Recently, studies for realizing interaction between users and virtual objects using Augmented Reality (AR) have been actively conducted. However, few previous studies have realized that a user intuitively manipulates virtual objects like clay with their bare hands. In this study, we aim at user's intuitive virtual objects manipulation by realizing basic manipulation on virtual objects with their bare hands. In addition, it is considered that the user feels uncomfortable in the manipulation of the virtual objects because of the occlusion problem in AR, and cannot perform an intuitive manipulation. Therefore, in this study, we solve this problem by performing appropriate hidden surface processing within the range of the user's fingertips.

OS10-3 Two-Dimensional Image Based Body Size Measurement and Body Weight Estimation for Yaks

Zijie Sun[1], Chen Zhang[1], XiaoFeng Qin[1], Yu-an Zhang[1], Rende Song[2], Makoto Sakamoto[3]
([1]Qinghai University, [2]Yushu Prefecture Animal Husbandry and Veterinary Station, China
[3]University of Miyazaki, Japan)

In stock raising, non-contact and non-stress measurement of animal's body size parameters and body weight is a research highlight. Yak's body size parameters and body weight estimated based on body size can reflect yak's growth and development features, production performance and hereditary characters. Therefore, studying the body size measurement and body weight estimation of yaks is an effective approach to promoting scientific breeding and enhancing culture benefits. Traditional manual methods of measuring animal's body size and body weight have such disadvantages as heavy workload and potential safety hazards. This paper firstly acquires the color image of the yak by taking pictures of yaks in Sanjiangyuan. Then, the yak is extracted from the image with the method of foreground extraction based on grey level classified process; after that, the profile curve of the yak is extracted to obtain the temple point and ischium end of the yak with the method of calculating the image edge curvature. Based on that, the marked points for the yak's body height and body dip length are determined; weka based linear regression helps obtain the body weight estimation formula; finally, estimation about the yak's body weight is achieved. Experiments suggest this algorithm is effective to non-contact body size measurement and body weight estimation for yaks in Sanjiangyuan, Qinghai Province.

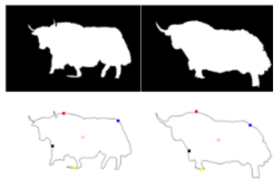

OS10-4 An efficient structure of organization with complete group guidance

Satoshi Ikeda[1], Mamoru Yoshimura[1], Makoto Sakamoto[1], Takao Ito[2]
([1]University of Miyazaki, [2]Hiroshima University, Japan)

The purpose of this paper is to show that the efficient organizational shape when the evaluation criteria is only one, is limited to the three types under the assumption of the communication style called the complete group guidance.

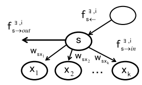

OS10-5 Parallel finite element analysis for hyperbolic problems

Amane Takei, Makoto Sakamoto (University of Miyazaki, Japan)

In this research, we propose a parallel finite element analysis for hyperbolic problems based on an iterative domain decomposition method. In a microwave analysis, the simplified Berenger's PML is developed in which these eight corners are given the average value of all PML's layers. As for accuracy verification of the analysis solver, the absorbing performance of the PML is evaluated by using reflection coefficient based on S parameter. In the accuracy verification, when the maximum side length is set to 1/20 of the wavelength, the error rate of the numerical solution and the theoretical solution is about 1.70 [%] with the PML of 9 layers. So, we have found that proposed method can calculate with high accuracy.

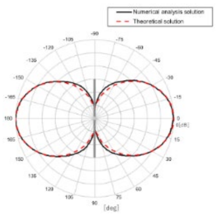

OS11 Recognition and Control (12)

OS11-1 Design of feed part control system for rectification process

Lingran An[1], Fengzhi Dai[1], Yujie Yan[1], Zhongyong Ye[1], Xia Jin[1], Yiqiao Qin[12], Chengcai Wang[3], Kaige Liu[1]
([1]Tianjin University of Science and Technology, [2]Tianjin Tianke Intelligent and Manufacture Technology CO.,LTD, [3] CETC Ocean Information Co., Ltd, China)

This paper completes the structure design of the feed process of the small rectification experimental unit. According to the process requirements, we design the overall scheme of the detection and control system of the main parameters and select the type of the instrument. The system hardware design is based on the CPU222 of Siemens s7-200 PLC and the corresponding input/output module. The lower computer adopts the ladder diagram to complete the program design such as parameter acquisition, scale transformation and PID operation. The monitoring interface of the upper computer adopts configuration the King monitoring software.

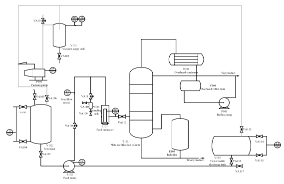

OS11-2 Ultrasonic range finder for vehicle collision avoidance system

Ying Chen[1], Guowei Yang[1], Fengzhi Dai[1], Yuxuan Zhu[1], Di Yin[1], Yasheng Yuan[1],Yiqiao Qin[12], Ce Bian[12], Chengcai Wang[3], Xinyu Zhang[1] ([1]Tianjin University of Science and Technology, [2]Tianjin Tianke Intelligent and Manufacture Technology CO.,LTD, [3]CETC Ocean Information Co., Ltd, China)

In recent years, highway rear-end collision accidents have occurred frequently, causing huge personal injury and property damage. Protective measures such as seat belts and airbags only serve to reduce damage afterwards and do not solve the problem from the source. Therefore, research on the system of vehicle collision avoidance, which actively avoids accidents, is of great significance. The ultrasonic range finder designed based on AT89C51 single-chip microcomputer utilizes the principle of sound wave reflection in the air. It can detect the distance between the vehicle and the obstacle in real time, and immediately alarms beyond the set threshold. Ultrasonic ranging is widely used in automotive anti-collision systems due to its non-contact detection method and simple structure.

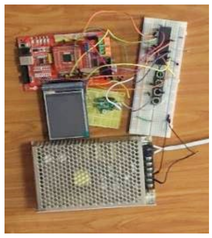

OS11-3 Chaos synchronization method of Qi system and the circuit design

Xia Jin[1], Fengzhi Dai[1], Zhongyong Ye[1], Lingran An[1], Yujie Yan[1], Chenglin Zhao[1], Yiqiao Qin[12], Hao Li[3]
([1]Tianjin University of Science and Technology, [2]Tianjin Tianke Intelligent and Manufacture Technology CO.,LTD, [3]CETC Ocean Information Co., Ltd,, China)

Chaos is a kind of uncertain and random phenomenon that appears in the system. Its dynamic characteristics are rich and interesting. The study of the dynamic characteristics and synchronization methods of Qi chaotic system has fascinated many researchers. In this paper, the dynamic characteristics of Qi chaotic system are analyzed, and the synchronization circuit of Qi chaotic system is designed based on the driving-response chaotic synchronous system and the single-variable feedback perturbation synchronous system, The synchronization circuits of Qi chaotic system are designed respectively, comparing the synchronization curves of the variables simulated by Multisim and the numerical simulation curves obtained by MATLAB, verifying the correctness of the built circuit, and analyzing the advantages and disadvantages between the above two synchronization methods.

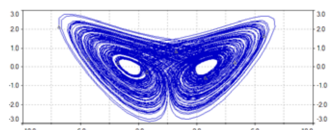

OS11-4 Design of air quality monitoring platform based on Internet of Things

Yujie Yan[1], Fengzhi Dai[1], Kailun Zhang[1], Wei Wang[2], Jialin Han[1], Yang Li[3], Tianyi Zhang[1]
([1]Tianjin University of Science and Technology, [2]China Institute of Aerospace Engineering, [3]CETC Ocean Information Co., Ltd, China)

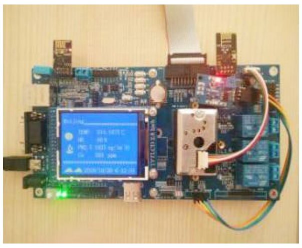

The air quality monitoring platform based on the Internet of Things (IoT) uses the STM32f407 main control module. Data such as temperature, humidity, PM2.5 and carbon monoxide concentration in the atmospheric environment are collected for a long time by each sensor module. Not only the system has the LCD display function, users can also log on to the ESLINK IoT cloud platform to remotely observe the data collection status. The upper limit of each parameter can be set in a specific environment. If the data monitored by the system exceeds the upper limit, the system will alarm. The system has a good application prospect in the environment of office, automobile, factory and so on.

OS11-5 Design of metal weld seam tracking equipment based on image processing

Yujie Yan[1], Fengzhi Dai[1], Lingran An[1], Xia Jin[1], Zhongyong Ye[1], Yufan He[2], Xinran Guo[3]
([1]Tianjin University of Science and Technology,
[2] CETC Ocean Information Co., Ltd, [3]Nanjing University, China)

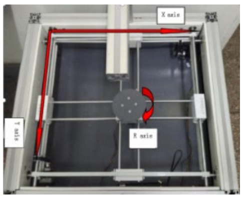

With the development of the intelligent industry, metal automatic welding technology needs to be more popular. The metal weld seam tracking device based on image processing includes two parts of image processing and motion control. The image processing part is developed by the Visual Studio 2013 platform, and the motion control part is controlled by the PID algorithm. Machine vision technology can be used to convert images captured by industrial cameras into vector graphics, which in turn drive the welding table to track metal welds. The device has good control effect and can be well applied in small and medium-sized enterprises.

OS11-6 The recognition and implementation of handwritten character based on deep learning

Zhongyong Ye[1], Fengzhi Dai[1], Xia Jin[1], Yasheng Yuan[1], Lingran An[1], Yujie Yan[1],
Yiqiao Qin[12], Hao Li[3] ([1]Tianjin University of Science and Technology, [2]Tianjin Tianke Intelligent and Manufacture Technology CO., LTD, [3]CETC Ocean Information Co. Ltd, China)

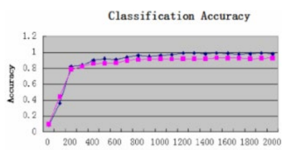

For recognizing handwritten characters, especially the handwritten Chinese characters, this paper uses deep learning techniques to construct convolutional neural networks of different depths to identify character sets containing handwritten digits and Chinese characters, and compares the performance of networks with the same depth and different depths. In the end, the network structure that can be used for identification is finally obtained, and a handwritten character recognition system is implemented based on the network. The recognizing accuracy of the paper reaches 99.18% for the MNIST dataset and 92.02% for the subset of the Chinese dataset HWDB1.1. Compared with other handwritten character algorithms, this paper proves that the used network structure has the application value.

OS11-7 Cluster analysis of wine based on three-dim fluorescent spectra characteristic

Di Yin[1], Fengzhi Dai[1], Yuxuan Zhu[1], Yasheng Yuan[1], Tingting Zhang[1], Ying Chen, Yiqiao Qin[12], Chengcai Wang[3] ([1]Tianjin University of Science and Technology, [2] Tianjin Tianke Intelligent and Manufacture Technology CO., LTD, [3]CETC Ocean Information Co., Ltd, China)

The traditional sensory analysis method can not discriminate different kinds of wine objectively and accurately. The three-dimensional (3D) fluorescence technology has the advantages of strong selectivity, high resolution and direct access to the fluorescence characteristics of the sample. In this paper, the 3D fluorescence spectroscopy five brands of red wine samples. The five characteristic parameters (the mean value, standard deviation, center of gravity coordinates, first order center moment and correlation coefficient) of the 3D fluorescence spectra of these five dry red wine samples are extracted respectively. The results show that the difference of the samples can be distinguished intuitively by extracting the 3D spectral parameters of the different brands. On this basis, the clustering analysis shows that even the same raw material brewing wine is different from the raw material origin and the soil environment. The climate environment will cause an important impact on the composition of the wine.

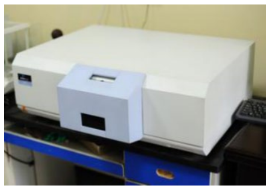

OS11-8 The control design of the planting device for the hydroponic vegetable

Yasheng Yuan[1], Fengzhi Dai[1], Zhongyong Ye[1], Yuxuan Zhu[1], Di Yin[1], Tingting Zhang[1], Yiqiao Qin[12], Yang Li[3] ([1]Tianjin University of Science and Technology, [2] Tianjin Tianke Intelligent and Manufacture Technology CO.,LTD, [3]CETC Ocean Information Co., Ltd, China)

The equipment is designed to household indoor small hydroponic vegetable planting control device. The temperature, humidity, light and carbon dioxide concentration sensors are integrated to the Arduino UNO R3 microcontroller. It is used to detect various parameter data of planting environment. The WIFI module can send the real-time environment variables detected by the sensor to the mobile devices, such as the user's mobile phone, through the wireless network. Moreover, users can also change the corresponding control range of variables according to the planted vegetables through the WIFI module.

OS11-9 An anti -theft system based on the self-checkout

Yuxuan Zhu[1], Fengzhi Dai[1], Yasheng Yuan[1], Di Yin[1], Tingting Zhang[1], Ying Chen[1], Ce Bian[12], Yufan He[3] ([1]Tianjin University of Science and Technology, [2]Tianjin Tianke Intelligent and Manufacture Technology CO.,LTD, [3]CETC Ocean Information Co. Ltd, China)

Nowadays, the imperfection of the anti-theft system impedes the development of self-service cash registers. This paper designs an anti-theft system based on self-service cash registers, which can greatly reduce the theft rate in supermarkets. This anti-theft system adopts Siemens's LOGO!, which is the core of the controller. Moreover, it has massive facilities of anti-theft protection, including radio frequency detection, photoelectric counting, repeated scanning reminder, magnetic detection, video monitoring and anti-theft electronic door. Through the above technologies, the supermarket that uses the self-service cash registers can avoid to some problems, i.e. cash collection leakage, using low price goods to replace that of high price. Multiple facilities are set to jointly protect the safety of goods, effectively reduce theft and loss.

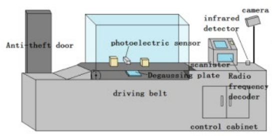

OS11-10 Case study on communication between embedded linux environment and microcontroller

Ziheng Gao, Yizhun Peng, Shuo Wang
(Tianjin University of Science and Technology, China)

In many embedded development scenarios, we need to combine the real-time microcontroller and non-real-time embedded Linux environment for collaborative development. In a high real-time environment (such as: vehicles, production lines), it can complete kinds of features relying on huge Linux ecosystem, such as hot fixable functional modules, improved network communication, easier OTA firmware updates, more efficient algorithm capabilities, and more objects. This paper aims to enumerate and explore several methods that can be used to implement similar duplex communications. For ease of understanding,a single-board computer called Raspberry Pi running Raspbian Linux and an STM32F103 32-bit ARM microcontroller are used in experiment.

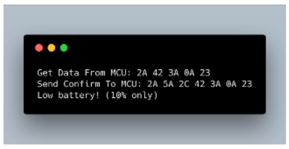

OS11-11 Design and implementation of a baby care robot

Yizhun Peng, Zefan Ge, Kaixuan Geng, Zhou Yang,Rui Yang
(Tianjin University of Science and Technology, China)

Aiming at the shortcoming of single function of traditional pram, this paper proposes an embedded multi-functional intelligent baby care robot. With baby cradle as the carrier, the bionic cradle is realized by combining embedded controller, drive module, motor and various sensors. The babysitting robot has the functions of autonomous following and obstacle avoidance, voice play and real-time picture return, which not only improves the convenience and security of the baby carriage, but also can assist parents to take care of the baby , greatly reducing the burden of parents' parenting.

OS11-12 Research on intelligent shopping service robot design

Shuo Wang, Yizhun Peng, Ruixiang Bai, Ziheng Gao
(Tianjin University of Science and Technology, China)

With the rapid development of the social economy, it’s good to help customers have more efficient and relaxed shopping experience through intelligent means in large commercial centers. In this paper, a shopping service robot project that uses machine vision, deep learning, and IoT is introduced. The robot can help customers complete shopping and complete indoor positioning navigation and autonomous movement intelligently. The robot product is designed to help all customers, especially people with mobility impairments. It will reduce their burden of action, thereby enhancing the user experience and doing special analysis of shopping behavior to help launch more efficient and personalized market planning.

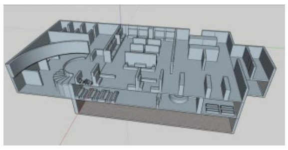

OS12 Robot Design and Simulation (5)

OS12-1 Design and Research of Navigation and Dynamics Co- Simulation Platform for Planetary Rover

Huang Tie-qiu, Zhang Bo-wen, Huang Qian-li (Beijing Jiaotong University, P.R China)

In view of the difficulties in the design of the navigation control system for the exploration of complex and passing missions on Mars and other planets, the overall design idea of the co-simulation platform for the planetary rovers navigation and dynamics is proposed. On the basis of MSC.ADAMS software, the dynamic model of planetary rover in soft soil environment is established through two times of subprogram development. An interactive parallel simulation system is established by using C++, and the cooperative invocation dynamic model and navigation control model are solved to form the closed loop system of co-simulation, and the navigation control system and the dynamic model are realized. Seamless link and parallel efficient solution. Taking the co-simulation of Mars rover as an example, the simulation platform has completed the simulation of Mars rover cruising, crab line, steering, lifting wheel, body lifting and so on in the Martian environment, and can show the moving state of the rover, the contact force of the rover and the driving torque of each mechanism in real time. Due to the high efficiency of the wheel contact model algorithm and the application of parallel multi task processing method, co-simulation can almost achieve real-time. The platform lays an important foundation for the design of navigation control system.

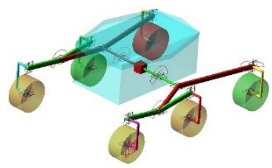

OS12-2 Research on Application of SFM Method in Virtual Reality Modeling

Jiwu Wang, Chenyang Li (Beijing Jiaotong University, China)
Min Li (Beijing Forestry University, China)

Simulation technology has become an important part of design and training. With the development of computer science, Virtual Reality (VR) technology can enable the experiencer to reach the immersion degree that other simulation technologies cannot achieve, and become the focus of military simulation research in various countries. But VR technology also has some shortcomings, such as long modeling period, certain differences between models and real objects. Based on the current technology, this paper proposes a VR technology combined with SFM which can greatly reduce the modeling period and improve the realism of the model to enhance the experience of simulation.

OS12-3 Visual SLAM System Design based on Semantic Segmentation

Jiwu Wang, Yafan Liu, Qinjian Zhang (Beijing Jiaotong University, China)

Visual SLAM is helpful for the development of unmanned platform. But only perceiving the geometric information of the environment is not enough. It is necessary to join the image semantic segmentation with SLAM, which helps to comprehend the scenes and improve the accuracy of pose estimation. Nowdays, the technique of deep learning brings new ideas into traditional SLAM by modeling this problem with convolution neural network.In this approach, we propose a pose estimation technique based on pixel-level multi-target detection, and 2D semantic information are transferred to 3D mapping via correspondence between connective Keyframes. Meanwhile,the semantic information is utilized in other modules for to optimize the visual SLAM system.

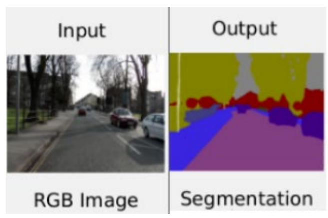

OS12-4 Spherical Mobile Robot Designed with Single Omnidirectional Wheels

Liu Wei, Lian Luo, Jiwu Wang (Beijing Jiaotong University, China)

This paper presents a new spherical mobile robot with a single omnidirectional wheels locating at the ends of the inside vertical diameter of the sphere shell, and the two wheel axes being in orthogonal position. The omnidirectional wheels can roll along the inner surface of the spherical shell, and then drive the spherical shell rolling. The lower omnidirectional wheel is responsible for walking drive, and the upper one for steering drive. The prototype shows the spherical robot moving well.

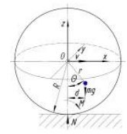

Fig. 1. Eccentric gravitational moment drive

Fig. 2. Omnidirectional wheel

OS12-5 An augmented reality implementation method based on Unity3D

Weixin Zeng, Jiwu Wang (Beijing Jiaotong University, China)

Augmented reality technology uses computer graphics and visual technology to achieve the superposition of virtual objects in real scenes, presenting the sensory effects of real-time interaction. It has broad application prospects and application value, and its popularity has been increasing in recent years. At present, there are two main ways to achieve augmented reality. One is the underlying code, which combines OpenGL and Open CV libraries to realize augmented reality. The second is the secondary development of related content through the corresponding software and SDK package. In this article, we will initially implement augmented reality through Unity 3D and Qualcomm's Vuforia SDK.

OS13 System and Control (10)

OS13-1 Research on a non-invasive measuring method of blood glucose concentration based on electrical impedance spectrum

Tong Yin, Xiaoyan Chen, Meng Du, Hongyi Yin (Tianjin University of Science and Technology, China)

Different from the traditional measurement approach and instruments of blood glucose concentration, we propose a novel measuring method related to electrical impedance spectrum without invasion. A serial experimentations are designed and carried out to detect the electrical impedance amplitudes and phases under 1Hz-10MHz frequencies. Considering the skin contacting impedance and cytomembrane conductivity feature, a simulate circuit is designed and connected in serial with the measuring loop. The measured data were analyzed by an improved Cole-Cole model to derive the relationship between the impedance value and the blood glucose concentration. The results show that the electrical impedance is strong negative correlation to blood glucose concentration, as the blood glucose concentration increases, the impedance value decreases. The conclusion of this research provides a theoretical basis for non-invasive blood glucose surface-measuring.

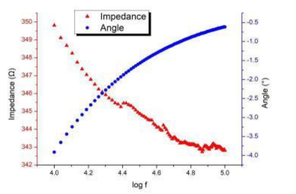

OS13-2 Synchronization of Novel 4D Chaotic Systems with Different Control Laws

Hong Niu (Tianjin University of Science and Technology, China)

In this paper, synchronization of novel four-dimensional(4D) autonomous chaotic systems is studied. Two different control laws are presented, which are based on the strictly positive realness of transfer function matrix and the center translation method respectively. The characteristics of the two control laws, as well as the differences between them, are proposed. Some relevant numerical simulation results, such as the curves of the corresponding synchronization state variables and the errors, are given to illustrate the feasibility and effectiveness of the two control laws.

$$\begin{aligned}
\dot{x}_1 &= a(y_1 - x_1),\\
\dot{y}_1 &= c(x_1 + y_1) + z_1 - x_1 w_1,\\
\dot{z}_1 &= m x_1 - y_1 - h z_1,\\
\dot{w}_1 &= x_1 y_1 - b w_1.
\end{aligned}$$

$$\uparrow$$

$$\begin{aligned}
\dot{x}_2 &= a(y_2 - x_2) + u_{c1},\\
\dot{y}_2 &= c(x_2 + y_2) + z_2 - x_2 w_2 + u_{c2},\\
\dot{z}_2 &= m x_2 - y_2 - h z_2 + u_{c3},\\
\dot{w}_2 &= x_2 y_2 - b w_2 + u_{c4}.
\end{aligned}$$

OS13-3 Chaotic characteristics analysis of fractional-order Liu system

Wengxin Shi, Hongyan Jia (Tianjin University of Science and Technology, China)

The paper analyzes a newly reported fractional-order Liu system based on time-domain approximation and frequency-domain approximation, respectively, and chaotic characteristics of this system are investigated by the phase portrait diagram, Lyapunov exponents diagram and bifurcation diagram. The results of the two approximation methods are consistent, which not only shows chaotic dynamics of the system is reliable, but also is very convenient to utilize chaotic dynamics of the system with fractional-order 0.9.

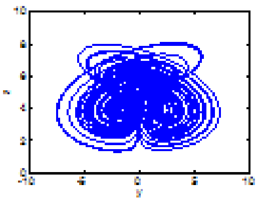

OS13-4 Design and analysis of the multi-robot grouping aggregation algorithm

Huailin Zhao, Zhen Nie (Shanghai Institute of Technology, China)

In this paper, the grouping aggregation problem of multi-robot in simple environment is studied. The grouping algorithm and aggregation algorithm are mainly discussed. Based on two clustering algorithms, K-means and K-medoids, two grouping algorithms are designed. And the noise im-munity and grouping rapidity of these two grouping algorithms are analyzed. Aiming at the problem of aggregation, three kinds of aggregation algorithms are proposed. Taking the center aggregation control as an example, the cooperation and control of each group of robots are studied. Finally, the simulation results of MATLAB shows that the multi-robot grouping and aggregation algorithm is effective.

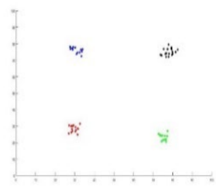

OS13-5 Research of the ARM-based multi-robot aggregation control

Huailin Zhao, Jingnan Zheng, Zhen Nie, Weiya Zhang, Zonglin Liu (Shanghai Institute of Technology, China)

This paper mainly analyzed the basic aggregation problem of multi-robot cooperative system. The algorithm design of multi-robot dynamic aggregation control was discussed. The multi-robot aggregation path planning method in simple environment was discussed. And the kinematics equation of the aggregation algorithm was given at last. Taking the center aggregation control as an example, the cooperation and control of multi-robot are studied. Then we designed a simulation control program on MATLAB for multi-robot system and analyzed the simulation results. Finally, the center aggregation experiment was carried out by using the three car robots. The results show that the multi-robot aggregation algorithm is effective.

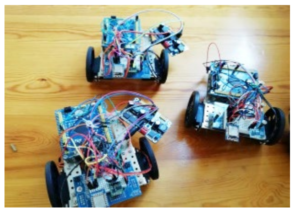

OS13-6 Research on the Trajectory Planning Problem of Robots in Spherical Cutting

Jun Min, Wenping Jiang, Huailin Zhao (Shanghai Institute of Technology, China)

For cylindrical shape cutting of spherical surface vessel a kind of 5-DOF cutting method of cylin-drical shape for spherical surface is provided in this paper. Based on the kinematics model of cutting robot the mathematic relations between cutting tool cylindrical shape and spherical surface are built using Euler transformation and the intersection line model of cylindrical and spherical surface is presented. The robotic cutting trajectory is computed according to the position and attitude relation of robot and spherical sphere and simulations and experiments of cutting trajectory for robot are provided in the end. Experiments results verified the rightness of robot kinematics and cylindrical shape cutting algorithm, and will promote the robot-is application in cutting field.

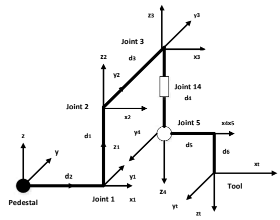

OS13-7 Emotional processing between artificial voices and human voices

Qiang Wei[1], Xiaoyu Zhang[1], Xiao Yang[1], Yixin Lin[2], Qingming Liu[3]
([1]Jianghan University, [2]Huazhong University of Science and Technology,
[3]Wuhan Rayson School, China)

To evaluate the time course of changes in emotional processing between artificial voices and human voices (happy, angry, neutral), the present study examined behavior experience and event related potential component. The emotion arouse of artificial human voice and brain signal were evaluated while the presentation of audio from each conditions (happy, angry, neutral, and artificial voices). The results showed that there were differences in the intensity and the late processing between emotional processing induced by artificial voices and human voices.

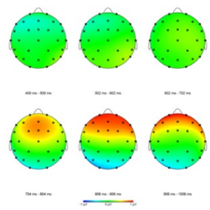

OS13-8 How people are affected by emoticon icon: An ERP study

Qiang Wei[1], Jingxuan Huang[1], Yu Han[1], Yixin Lin[2]
([1]Jianghan University, [2]Huazhong University of Science and Technology, China)

The aim of this study was to investigate the ERP component evoked by emoticon with different attributes and the reaction times during the LDT task. The behavioral results showed that participants demonstrated a positive emotion with a shorter reaction time under both a positive emoticon and a negative emoticon compared to participants under a meaningless emoticon.The results of ERPs indicated the relationship between three ERP components and emotional processing of attention distribution, emotion arousal and emotion valence. Based on these results, we provide evidence for a better understanding of how emoticons improve atmosphere during daily communication.

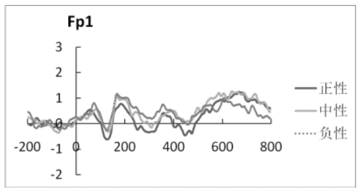

OS13-9 Single Chinese character fragments: an ERPs study on orthographic neighborhood effect

Qiang Wei[1], Yunfei Wang[1], Chen Song[1], Yixin Lin[2]
([1]Jianghan University, [2]Huazhong University of Science and Technology, China)

The aim of study was to discuss family effects and brain activity during the processing of Chinese characters. The study observed the event-related potentials (ERPs) elicited by fragments of Chinese single-character words in Chinese character completion and naming experiment. The result showed that the “Multiple-solution” elicited greater N400 component than the “One-solution”, which index a inhabitation effect. Multiple-solution-word analogy to large families, they are more intense than the false-words and single-words, which are in line with the interaction activation model and have more resources in the cognitive processing process. The glyph processing, the association process, and the memory phase of Chinese characters have an impact. The N400 component may not only mean the integration of the meaning of the word, but may also be related to the process of adjusting the information to adapt to the task.

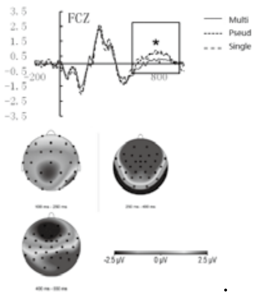

OS13-10 Research on embedded electrical impedance measurement system

Tong Yin, Xiaoyan Chen, Hongyi Yin (Tianjin University of Science and Technology, China)

This paper develops an impedance measurement system based on S3C6410 processor. An OK6410 host board as the controller platform, and an AD5933 chip is used to collect impedance data, and the data is exchanged with the controller with IIC bus protocol. Comparing with the measuring result of the Wayne Kerr 6800B impedance analyzer with the accuracy of 0.05%. The system has the behaviors as lower relative error 0.422% and higher signal-to-noise (SNR) ratio 64.11dB. After calculation, the average absolute error of the impedance phase of the system is 0.527°. The tests results verified that the system is reliable and flexible with a wide application prospect.

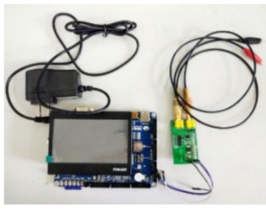

OS14 Intelligent Control (4)

OS14 -1 Flock Guiding of Hybrid Agents via Root Block

Yunzhong Song, Ziyi Fu, Fuzhong Wang (Henan Polytechnic University, China)

The convergent equilibrium of flocking agents is vital importance for their collective behavior, where flock guiding of hybrid agents, which are composed by both first order and second order agents, can only be boiled down to the root node agents, is touched upon here. Both the theoretical analysis and the simulation results are provided to verify the suggested scheme.

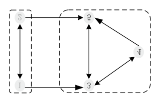

Fig.1 Network consists of 5 nodes

OS14-2 Multiple Model Adaptive Control of Flexible Arm

Yingzhao Zhang[1], Xiao Wang[1], Handong Li[1], Weicun Zhang[2]
([1]Guizhou University, [2]University of Science and Technology Beijing, China)

In this paper, dynamic model of flexible arm is built through Lagrange theory. Then, based on the software SIMULINK, model of flexible arm is established and the state of flexible manipulator under multiple model adaptive control is simulated. Finally, comparing the control effect (like stability, and accuracy) of multiple model adaptive control method with other control methods, Summarize the advantages of MMAC control method.

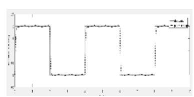

state of flexible manipulator under multiple model adaptive control

OS14-3 Time-Varying Lyapunov Function for Mechanical Systems

Bin Zhang[1], Yingmin Jia[2]
([1]Beijing University of Posts and Telecommunications, [2]Beihang University (BUAA), China)

In this paper, a general method for constructing time-varying Lyapunov functions is provided by using homogeneity theory. Sufficient conditions of uniform asymptotical stability are established for mechanical systems. Different from the existing results on this subject, we remove the periodic restrictions and persistency of excitation restrictions in our work. Robustness properties are also considered in this paper. It is shown that the mechanical systems remain stable after adding higher order perturbing terms. To illustrate the utility of our results, we provide detailed applications on practical systems and numerical results are given.

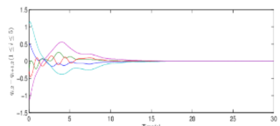

States of the Mechanical Systems.

OS14-4 Optimizing Control Parameters of Space Robot Manipulator for Pulsar X-ray Interference Measurement

Qiang Chen[1], Hengbin Zhang[1], Xiaomin Bei[1], Hanwen Zhang[2]
([1]Chinese Academy of Space Technology, [2]Beijing Institute of Control Engineering, China)

In paper, a pulsar X-ray observation plan of using two detectors installed in two sides of space station is given. Dynamic model of the space robot manipulators and an adapt control method are described. An orthogonal array experimental design method is developed to optimize the control parameters. Simulations are carried out by L_{81} (3^{40}) orthogonal array while fourteen adaptive control parameters are selected. The optimization results show that the parameters expected value could be acquired and computationally efficiency is promoted.

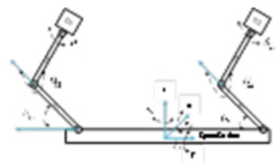

The composition of pulsar x-ray measurement system

OS15 Advanced Control (5)

OS15-1 Pulse Pose Follow Control and Simulation for a 4-DOF Pulse Diagnosis Robot

Qunpo Liu[1], Guanghui Liu[1], Hongqi Wang [1], Xianzhe Liu[1], Hanajima Naohiko[2]
([1]Henan Polytechnic University, China, [2]Muroran Institute of Technology, Japan)

Pulse diagnosis has been proved to have great practical value in the past dynasties. The quality of pulse diagnosis is related to the effect of "syndrome differentiation and treatment" in various clinical departments. The key of high-quality pulse diagnosis is how to dynamically adjust the vertical relationship between the pulse and the sensor. The design adopts a four-degree of freedom manipulator combined with a matrix sensor to form a diagnostic manipulator, which dynamically adjusts the posture of the end sensor of the manipulator by using the flexibility of the manipulator, so as to achieve rapid adjustment and keep the diagnostic pulse sensor perpendicular to the pulse. In this paper, the method of Denavit-Hartenberg is used in kinematics analysis of the manipulator, and Simulations are platformed based on the robot dynamics simulation software V-REP. The simulation results show that the design is feasible.

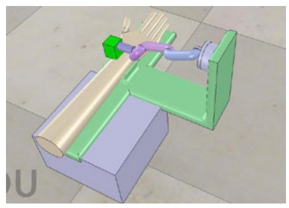

Fig.1 Pulse diagnosis robot

OS15-2 A New Adaptive Control System Design Method Based on Neuronetwork Prediction

Weicun Zhang, Sufang Wang, Yongnan Jia, Qing Li
(University of Science and Technology Beijing, China)

In this paper, a new control system design method is proposed, in which, the controller is designed according to a model with un-modeled uncertainties, an artificial neuronetwork (error back propagation neuronetwork) was adopted to predict the model output error, and the predicted model output error is considered in the control law. This control system design can be used to both linear and non-linear systems. The simulation results verified the effectiveness of the proposed method.

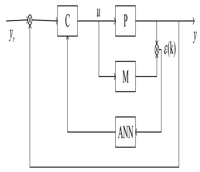

Block diagram of the proposed scheme

OS15-3 Mean-square quasi-composite rotating formation control of second-order multi-agent systems under stochastic communication noise

Lipo Mo[1], Xiaolin Yuan[1], Yingmin Jia[2], Shaoyan Guo[3]
([1]Beijing Technology and Business University, [2]Beihang University (BUAA),
[3]South China University of Technology, China)

This paper mainly concerns the mean-square quasi-composite rotating formation problem of second-order multi-agent systems (MASs) with stochastic communication noises. Firstly, the definition of mean-square quasi-composite rotating formation is proposed. Afterwards, a novel distributed control protocol with time-varying control gains is designed. And then, the origin closed-loop system is translated into an equivalent closed-loop system by taking a proper coordinate transformation. Under some mild assumptions, by means of stochastic differential equation theory, sufficient conditions are deduced for achieving mean-square quasi-composite rotating formation. Eventually, numerical simulations are provided to confirm the effectiveness of the proposed theoretical results.

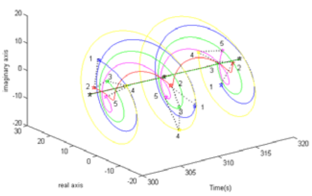

Fig. Local trajectories of the position and moving rotating centers of the MASs.

OS15-4 Distributed Energy Resource Control Based on Multi-Agent Group Consensus

Yize Yang[1,2], Hongyong Yang[1], Fan Liu [1], Yuling Li[1], Yuanshan Liu[1] ([1]Ludong University, China, [2]The University of New South Wales, Australia)

In this paper, a cooperative control strategy of distributed energy resources based on the group consensus of multi-agent systems is proposed. Combining with actual engineering needs, a multi-agent dispatch model of energy networks is designed. Considering the possible adverse effects that may be encountered in actual energy transportation, the matched disturbances and mismatched disturbances are added to simulate the modeling. A group control strategy of distributed energy resources applied to the distribution network is proposed to achieve precise control of energy distribution and safe transportation under multiple disturbances. Finally, the numerical simulation results verify the validity of the model and algorithm.

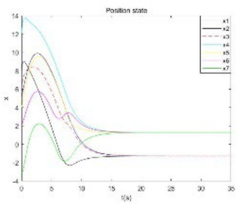

group consensus of distributed energy resources

OS15-5 Robust Adaptive Control of Air-to-air Refueling Boom with State-dependent Output Constraints

Liang Chang, Yingmin Jia (Beihang University (BUAA), China)

In this paper, a robust adaptive controller design method is presented for the uncertain air-to-air refueling boom system with output constraints and disturbance. One advantage of this design method is that the output constraints are state-dependent, which can extend the workspace of the boom while avoiding collision between the boom and the receiver. Backstepping method and barrier Lyapunov function(BLF) are used in this design method. Simulation results show the effectiveness of the proposed controller design method.

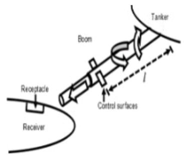

Aerial Refueling Boom

OS16 New development about Control Engineering Education (4)

OS16-1 Skill Model Estimation of Ability for Reading Drawings

Kazuo Kawada, Tsukasa Hiyama (Hiroshima University, Japan)

In Japan, students are studying various drawing educations in junior high school technical education, high school industrial education and university engineering education. However, it is very difficult to read the drawing without understanding trigonometry. Moreover, it is also very difficult to draw wish parts. Because of this, there are many research studies, but these are before-after analysis, and none analysis by time-series data. Therefore, this study aims to develop a new quantitative evaluation method of 3D recognition ability.

OS16-2 Learning simulation based on a computational model of neuromodulators

Yuki Moriguchi, Masayasu Nagamatsu
(Hiroshima University, Japan)

Reinforcement learning, and its biological bases are key to understand human learning. Here we illustrate learning processes of the tower of Hanoi based on the computational model of neuromodulators(Doya, K.2002). The model assumes hypothetical roles for the following parameters of reinforcement learning. 1)Dopamine signals TD error, 2)Serotonin controls discount factor, 3) Noradrenaline controls the inverse temperature, and 4) Acetylcholine controls the learning rate. We have compared the two learning situations. Case a) the reward is given at the goal state only, and Case b) the reward is divided and placed at the intermediate state and goal state. The resulting learning curves shows that b) divided reward enhanced the learning. This result shows an example of learning simulation with a variety of learners who have their own learning characteristics.

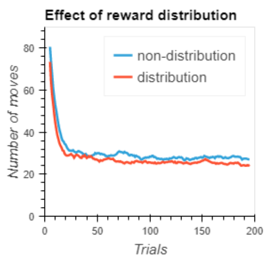

OS16-3 Estimation of Programming Learning Achievement by Line Tracing Robot

Yoshihiro Ohnishi[1], Teruyuki Tamai[1], Shinnosuke Mori[1], Kawada Kazuo[2]
([1]Ehime University, [2]Hiroshima University, Japan)

It is an important problem how to estimate the learning achievement of the programming learning. However, the quantitative evaluation method according to the learning achievement is difficult. This research considers estimation method for the achievement value of the programming learning. The task is given as a course of the line tracing robot. There are multiple courses to be passed. The difficult program can go through a short route. In other words, it is possible to estimate the difficulty level program created by the goal time.

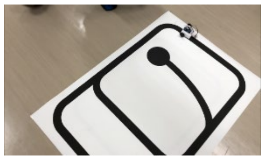

OS16-4 Development of Cultivate Computational Thinking using Finger Robot

Kaito Omata, Shinichi Imai (Tokyo Gakugei University, Japan)

Computational Thinking is one of the necessary skills for children who live in modern times. Therefore, in this research, we aim to design lesson that can cultivate Computational Thinking. In this research, design a lesson that cultivates Computational Thinking by moving a robot to the specified finger state using a finger robot. At that time the children can know that by using the notion of "binary" you can count many numbers by bending and extending your fingers. By using a finger robot, it is thought that children will motivate themselves to teach and to understand easily.

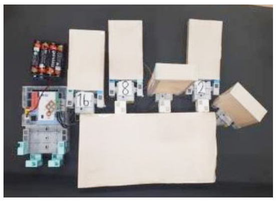

OS17 Multiagent and Complex Systems (3)

OS17-1 Different Type of Interaction or Decision Error contribute to Functional Differences

Saori Iwanaga[1], Masao Kubo[2]
([1]Japan Coast Guard Academy, [2]National Defense Academy of Japan, Japan)

There are many situations where interacting agents can benefit from coordinating their actions, that is, agents gain payoffs by taking the same action as others. These situations can be modeled as coordination games. Another situations is modeled as complementary game, asymmetric coordination games or minority games. In complementary game, agents gain payoffs by taking the different action from others. We deal with these coordination games and asymmetric coordination games as type of interaction and each agent can change the interaction type. And each agent can change the interaction partner. We show that population changes to a mixed population comprised of 80% cooperative agents and 20% complementary agents. A mixed population diversify the collective behavior, type of interaction and preference. There, opposite type of interaction plays a role of small decision error, and it is inefficient to adopt both.

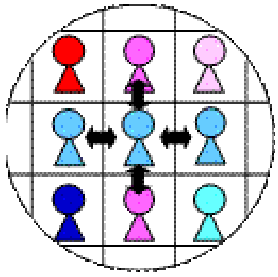

OS17-2 Evaluation for the Synchronization of the Parade with OpenPose

Yohei Okugawa, Masao Kubo, Hiroshi Sato, Bui Duc Viet
(National Defense Academy of Japan, Japan)

In National Defense Academy, parade training is one of our daily training, and is reviewed regularly. However, although the synchronization level of each cadet in the parade is a major factor of the performance, we don't have any objective evaluation methods for the synchronization level. In this research, we propose an objective method focusing on the synchronization level of the parade with OpenPose. OpenPose is capable of measuring many kinds of postures from movies simultaneously, so it is much easier to acquire data than conventional motion analysis with motion capture, and it is suitable for parade analysis, which is a cooperative operation of multiple people. In order to measure the synchronization level, our method is based on the arm swing data of each cadet in the parade, and our results can contribute to objective evaluation methods for cooperative operation, not only parade.

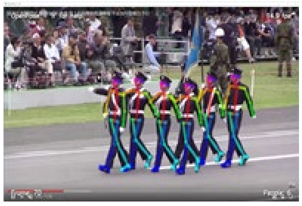

Fig. 1. Analysing a Parade with OpenPose.

OS17-3 Phase shift estimation of the bifurcating neuron from superimposed chaotic spike sequences

Akihiro Yamaguchi[1], Yutaka Yamaguti[1], Masao Kubo[2]
([1]Fukuoka Institute of Technology, [2]National Defense Academy of Japan, Japan)

For the bifurcating neuron, the phase shift value of background oscillation is one of the typical parameters that determine the shape of dynamics (Fig.1 (a)-(c)). In this research, we propose an estimation method of the phase shift value from superimposed chaotic spike sequences generated by the bifurcating neuron. The bifurcating neuron exhibits chaotic inter-spike interval dynamics that depends on the phase shift value of the background oscillation. Therefore, if we correctly estimate each phase shift values from the superimposed chaotic spike sequences, we can characterize the dynamics of the bifurcating neuron and identify each spike sequences from the other superimposed spikes. Fig. 1 (d) shows an example of estimated phase shift values for superimposed three chaotic spike sequences with different phase shift values. In this case, three different phase shift values were correctly estimated and more than 90% of superimposed spikes were also correctly identified.

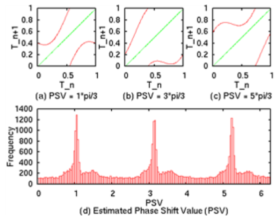

Fig. 1. Estimation of phase shift values.

OS18 Data-Driven Control and Diagnosis Control Systems (5)

OS18-1 A Design Scheme of a Data-driven Predictive-PI Controller

Yoichiro Ashida, Shin Wakitani, and Toru Yamamoto (Hiroshima University, Japan)

PID controllers have been widely employed in real processes. However, for processes with long dead time, the control performance obtained by a PID controller is limited. This is because prediction by a derivative element is not very effective for the processes. For such processes, some predictive controllers have been proposed. Among them, a predictive PI(PIP) controller has only three parameters. Although a PIP controller can be tuned by "trial and error", it is desired to determine control parameters automatically. In this paper, a data-driven design method for a PIP controller is proposed. In the proposed method, control parameters of the PIP controller are calculated automatically from one set of operation data.

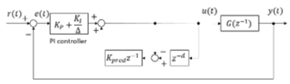

Fig. 1. Block diagram of the predictive PI controller.

OS18-2 Improvement in Intersample Response of Multirate Regulation Control

Takao Sato, Natsuki Kawaguchi, Nozomu Araki, Yasuo Konishi (University of Hyogo, Japan)

This study discusses a multirate regulator system, in which the sampling interval of a plant output is an integer multiple of the holding interval of a control input. A multirate control system is optimized based on a quadratic performance function. In order to improve intersample response, the derived control law is extended using the null-space and/or steady-state constraint. Furthermore, the original performance function is also modified, and the designed control systems are compared quantitatively.

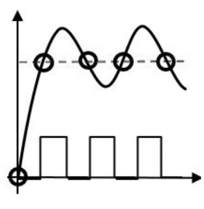

OS18-3 Design of a PID Controller using a Fictitious Exogenous Signal for a Fluctuation System

Masatoshi Kozui, Takuya Kinoshita, Toru Yamamoto (Hiroshima University, Japan)

A lot of industrial machines realize the desired motions by the PID controller. In particular, it is possible to design PID parameters to achieve the desired behavior by the Fictitious Reference Iterative Tuning (FRIT). However, in the steady state, if characteristics of the target system are changed by the operating environment, the desired control performance can not be obtained by the FRIT. In this paper, it is assumed that a disturbance is input when system characteristics are changed by the system switching. The Fictitious Exogenous Signal is calculated by the operational data after the system change. A PID controller tuning by the Fictitious Exogenous Signal is proposed. Moreover, the effect has been verified by numerical example.

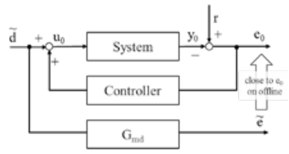

Fig. Block diagram of Fictitious Exogenous Signal.

OS18-4 Izhikevich Model Based Self-Repairing Control for Plants with Sensor Failures and Disturbances

Masanori Takahashi (Tokai University, Japan)

In the previous works, several types of the self-repairing control systems (SRCS) have been developed against unknown sensor failures. The SRCS can automatically detect the failure, and replace the failed sensor with the healthy backup so as to maintain the system stability. This paper presents a new SRCS, whose fault detector is constructed based on a spiking neuron model proposed by E. Izhikevich. In the detector of the SRCS, the sensor failure induces the spikes. Hence, only monitoring the output of the detector makes it possible to find the sensor failure. Also, in this paper, the robustness with respect to disturbances is theoretically analyzed, and it is shown that self-repairing control can be accomplished in the presence of unknown disturbances.

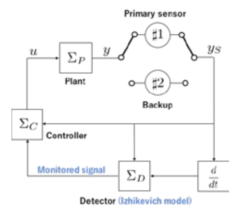

OS18-5 Design of a Data-Driven Controller with Evaluating Controller Performance

Takuya Kinoshita, Toru Yamamoto (Hiroshima University, Japan)

Data-driven controllers have been proposed to achieve the desired control performance without using any system identifications. The effectiveness of these control schemes has been shown through experimental results. For time-variant and nonlinear systems, it is important to evaluate the controller performance and redesign controller when the performance is poor. According to the proposed scheme, the controller performance calculator and controller design are integrated using only input and output data. Furthermore, the controller can be assessed in the transient and steady state.

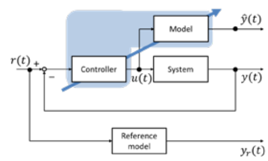

OS19 Advanced Technology on Sensing Technology, Devices, Application (3)

OS19-1 The Actual Car Driving Evaluation System using Combined with Eyeball and Face Angle

Keiko Sakurai, Hiroki Tamura, Koichi Tanno (University of Miyazaki, Japan)
Yukio Hattori (OFA SUPPORT INC, Japan)

The lack of automobile driving standards of persons with brain dysfunction and the increase of car accidents by the elderly are problems. Therefore, research on gaze estimation necessary for vehicle driving evaluation is rapidly developing. In this paper, we proposed the actual car driving evaluation system which can be evaluated by combining eye movements using eye tracking device (TalkEyeLite) and face movement estimated using template matching. In order to the evaluate our proposal method, we carried out the actual car driving experiments. The subjects were one instructor of the car driving school, and five general drivers. We compare the gaze range of the five general subjects and the instructor. As a result, we confirmed that one male in the 40s and one elderly narrow the gaze range.

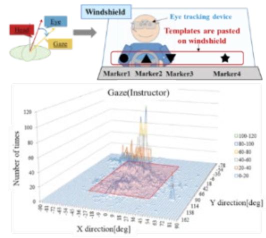

OS19-2 A Study on Speaker Identification Approach by Feature Matching Algorithm using Pitch and Mel Frequency Cepstral Coefficients

Barlian Henryranu Prasetio, Keiko Sakurai, Hiroki Tamura, Koichi Tanno
(University of Miyazaki, Japan)

In this paper, we grouping the words based on the speaker in a sequence of speech in a conversation. There are two speakers in each conversation. The first speech assumed spoken by speaker-1. In recognizing the speakers, we use pitch detection and Mel Frequency Cepstral Coefficients feature extraction with 13 filters. Furthermore, we examine the distance of the second speech vector with the first speech vector using the Feature matching algorithm. Previously, we had experimented on each speaker to find out the mean and variance of the Feature matching. Based on the experimental results, the variance of Euclidean, Mahalanobis and Mahattan Distance are 0.0015, 0.00064, 0.0012. Hence, if the Feature matching value deviates is not more than variance value then the speech is assume spoken by speaker-1. Otherwise, the speech assume spoken by speaker-2.

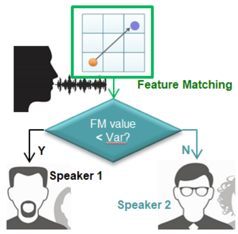

OS19-3 A Study on Breathing and Heartbeat Monitoring System during Sleeping using Multi-Piezoelectric Elements

Praveen Nuwantha Gunaratne, Chika Yoshida, Keiko Sakurai, Hiroki Tamura, Koichi Tanno, (University of Miyazaki, Japan)

We propose a method to monitor breathing and heartbeat during sleeping using piezoelectric elements. First, the signal acquired from the piezoelectric elements during sleeping is separated into a breathing signal and a heartbeat signal using biomedical signal processing software. A method is then proposed to quantify breathing and heartbeat by applying fuzzy theory to the signals. This proposed method is experimentally demonstrated using the following procedure. In the experiment, two subjects slept for one and a half hours. The data from the piezoelectric elements during sleep were extracted. We compared the true value with the count results from these data using the proposed method. The error rate of the breathing count was 0–13%, and the error rate of the heartbeat count was 0–8.2%. The results were non-uniform, and the error rate depended on the subject.

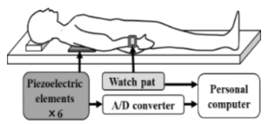

OS20 Advances in Field Robotics and Sensing System (8)

OS20-1 Field Robot and Sensing system

Eiji Hayashi (Kyushu Institute of Technology, Japan)

Labors in which forestry and agriculture and Factory, are working in severe circumstance. So, such workers are necessarily declines and decreases. However, it is important for us to keep going economy, life and nature. Therefore, to prevent a devastation of the forest, the safety and the lack of food and work in harsh environments, we are thinking alternative technologies that a part of severe and dangerous works are taken robot instead of such workers. Something changes are needed that they are seen innovation such as the generation of a new industry by new technologies using AI and intelligent to improve how to recognize and express more and more of the things that we have various desires.

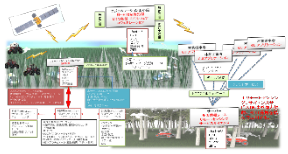

OS20-2 Saliency Map Based on Maximization of Difference between Central and Surround Visions and Its Relationship with Image Feature Points

Ruugo Mochizuki, Shinsuke Yasukawa, Kazuo Ishii (Kyushu Institute of Technology, Japan)

The Saliency map proposed by Itti is a human attention model considering the colors, edge orientations and intensity and designed to have high values in the curious area. In the model, the contrast of Saliency map is not so high and its parameters are adjusted heuristically. The problems to distinguish the front object from background is not suitable. In this research, a Saliency map is proposed to maximize the difference of two images by changing Gaussian filter sizes for the central vision, i.e., the small size Gaussian filtered image, and the surround vision, i.e., the big size Gaussian filtered image. As one of image processing techniques, feature-points extraction methods such as SIFT, SURF are often introduced into object detection and image mosaicking to generate the invariant features against scale and rotation changes. However, these feature points extraction methods have the effects of environments and lighting conditions. The relation between the Saliency map and the feature points extraction is discussed.

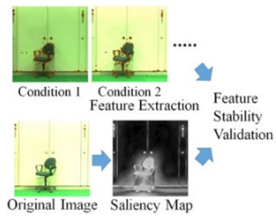

OS20-3 Dynamic Wireless Network System using Multiple Drones for Tunnel Applications

Raji Alahmad, Kazuo Ishii (Kyushu Institute of Technology, Japan)

Tunnels requires inspection and maintenance as their age. Conventional methods depend on special ground vehicles that have many limitations in mobility. UAVs, on the other hand, can overcome these limitations. Communication is of the biggest challenges for UAVs, due to signal attenuation. In this paper, a wireless network system using multi-drones that act as repeaters is proposed. A number of measurements for Wi-Fi signals is conducted to find out the effect of five different scenarios on the signal in virtual tunnel and two scenarios in a real life tunnel. As a result, the signal strength with -64 dBm can provide five Mbps of bandwidth, which is recommended for video streaming. Also, placement of transmitter and receiver is essential for better connection.

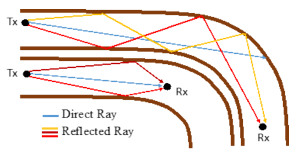

OS20-4 Counting Crops under Cultivation using Drone

Yasunori Takemura[1], Yusuki Hirata[2], Eiji Mizoe[3], Masao Tashiro[4], Yousuke Nagai[5]
([1]Nishinippon Institute of Technology, [2]Kyushu Institute of Technology, [3]Sky Canvas Co. Ltd.,
[4]Joint Corp. Project Sky-eye, [5]Aruku Aguriculture Service LLC, Japan)

In recent years, agricultural workers in Japan are decreasing year by year. Also, rising the average age of agricultural workers is a problem in Japan. As a solution to this problem, there is promotion of new agriculture (smart agriculture) that realizes super-energy saving and high quality production by utilizing robot technology and IoT Technology. The authors are promoting technology by operating forest drone competeton and tomato havevesting robot competition. Throu robot competition, we are currently paying attention to the use of drone in the agriculturel field. In this research, we aim to automatic detect the number of agricultural crops by image processing from image data of aerial photographs taken by drone. In this paper, we will report a method to discriminate agricultural crops by color and to detect the number.

OS20-5 Soil Compaction and Rolling Resistance Evaluation of a Locomotion System with Adjustable Contact Patches for Applications in the Vineyard

Enrico di Maria, Kazuo Ishii (Kyushu Institute of Technology, Japan)

Soil compaction is a form of soil degradation which causes soil erosion, drainage difficulties, hardpan production and loss of nutrients. In order to mitigate this issue, different solutions have been proposed, such as: plough, low ground pressure tires, tracked tractors and controlled traffic farming (CTF). In this work the idea of using a locomotion system with adjustable contact patch is proposed. Two configuration modes are foreseen: wheel mode and track mode. The aim is to reduce the compaction but also optimize the rolling resistance and energy consumption depending on the payload of the robot and the soil conditions. The robot will be used for transporting the grapes harvested in the vineyard. A finite element method model is developed to evaluate the performance of the system in terms of compaction and rolling resistance and experiments in the field are carried out to confirm the model itself.

OS20-6 Robot Navigation in Forest Management Based on Graph

Ayumu Tominaga[1], Ryusuke Fujisawa[1], Eiji Hayashi[1], Abbe Mowshowitz[2] ([1]Kyushu Institute of Technology, Japan, [2]The City College of New York, USA)

This paper addresses the problem of using a mobile, autonomous robot to manage a forest whose trees are destined for eventual harvesting. We have constructed a robotic system enabling an autonomous robot to move between the trees without damaging them and to cut the weeds as it traverses the forest. We proposes the trajectory computation for guidance of the robot in the forest is carried out based on a weighted undirected graph G with trees as vertices. The line graph, L(G) of G will represent the safety paths for guidance of the robot. It is shown that using trees in a forest as environmental landmarks is effective in navigation of forestry autonomous robot.

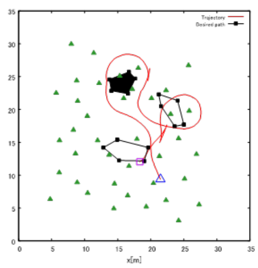

OS20-7 Development of Autonomous Moving System for Field Robot

Kengo Kawazoe, Eiji Hayashi, Ryusuke Fujisawa (Kyushu Institute of Technology, Japan)

SLAM technology is applied to resource management in forestry in artificial forest. From this technology, mapping of trees in artificial forest and automation of growth amount measurement of trees have been realized. Meanwhile, forestry go into a decline by labor shortage in Japanese forestry. And, it has been expected that mechanization and automation of work. We have been developing autonomous moving robot with all-terrain vehicles (ATV). And we designed an obstacle avoidance behavior to move around in the forest. Moreover, by adding a pan angle control actuator to the visual system, we increased the degree of freedom in external situation recognition. This made it possible the robot to the target coordinates specified on the global map based on the obstacle avoidance behavior.

OS20-8 Development of the sense system that is combined force feedback and vision feedback-Improvement reproducibility of deformation simulation by using LEM-

Tamon Shigeyama, Eiji Hayashi , Ryusuke Fujisawa (Kyushu Institute of Technology, Japan)

In the medical treatment and bio-technology field, doctors and researchers need technologies that can accurately perform small-size work. But there are some problems. The operators rely only on sight through the microscope. The operators cannot feel the sense of force. And the operators cannot see the all states of the sample. Our aim is to develop the combined system that that uses both force feedback from the manipulator and visual feedback on a deformation simulation. By reproducing force sense and visual sense of a sample, an operator can feel these sense of a virtual object. For this research, focus on a way to produce a force calculated in simulation of deformation using a haptic device. As the first stage, our simulation of deformation was improved by using LEM (Long Element Method) and evaluated accuracy of a virtual object's deformation.

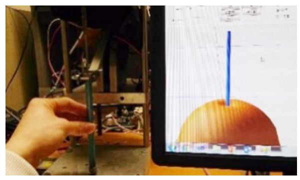

OS21 Advances in Marine Robotics and It's Applications (5)

OS21-1 System Development of AUV's Sampling Device Controller Employing MATLAB/Simulink Toolboxes

Takashi Sonoda[1], Shinsuke Yasukawa[2], Ahn Jonghyun[2], Yuya Nishida[2], Kazuo Ishii[2]
([1]Nishinippon Institute of Technology, Japan, [2]Kyushu Institute of Technology, Japan)

We have developed the sampling device control system for the AUV "Tuna-Sand2" by using MATLAB/Simulink and its toolboxes. The toolboxes are powerful, useful, and functional for developing the robot programming, especially Robotics System Toolbox supports the ROS so that the MATLAB and ROS programs are available for fast developing with high functions and the cloud data communication. Parallel Computing Toolbox can consist a multi-process and parallel computing on script base and Simulink model base program. Stateflow is a powerful tool for design of state transition control method. The toolboxes are employed in the sampling device control system of the AUV. This method with using the toolboxes of MATLAB/Simulink realize the rapid prototyping of the system designs, developments and system test. The developed system mounted on an AUV was powered in several real sea areas.

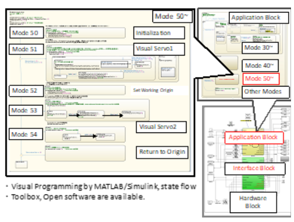

OS21-2 Inspection System for Underwater Structure of Bridge Pier

Takumi Ueda[1], Hiyoyasu Hirai[1], Kazuki Fuchigami[1], Ryoma Yuki[1], Ahn Jonghyun[1], Shinsuke Yasukawa[1], Yuya Nishida[1], Takashi Sonoda[1], Kazuo Ishii[1], Katsunori Higashi[2], Katsunori Tanaka[2], Tomomasa Ikeda[2]
([1]Kyushu Institute of Technology, [2]West Nippon Expressway Engineering Kyushu, Japan)

Inspection of underwater infrastructure of bridge pier is important for bridge maintenance, however, the underwater environment is dangerous and their observation is one of difficult problems. We have been developing the underwater inspection system which consists of an unmanned surface vehicle (USV) and a remotely operated vehicle (ROV). The concepts of the system are (1) Operation is executable with a small number of persons, (2) USV and ROV are controllable from land or bridge, (3) Build 3D model and images for crack detection. The ROV observes the status of whole infrastructure using cameras and control its posture using a depth sensor and IMU sensor. The USV vertically lifts up and down ROV by winch and remotely conduct ROV to infrastructure. USV is installed with GPS, LRF and IMU for horizontal positioning and direction control of the camera. In this paper, we report the results of the inspection operation test by the robot and present issues.

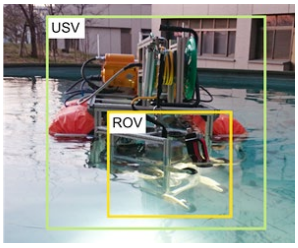

OS21-3 Three-dimensional measurement using laser pattern and its application to underwater scanner

Yuya Nishida, Tomoya Shinnoki, Shinsuke Yasukawa, Kazuo Ishii
(Kyushu Institute of Technology, Japan)

There are many mineral resources on the seafloors energy resources such as methane hydrate, and biological resources such as fish and crustaceans. The accurate amount of the resources needs to be surveyed in detail for making effectiveness use of the resources. In order to measure an accurate volume of the resources, the authors developed a new three-dimensional instrument consisting of a laser projector and a camera. The laser projector irradiates a sharp two-dimensional laser pattern independent the distance to the target object. Our instrument is able to measure three-dimensional shape of the target object using the laser pattern and the principle of light cutting method which is one of active measurement methods.

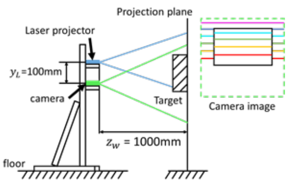

OS21-4 Development of Dam Inspection Underwater Robot

Hiroyasu Hirai, Kazuo Ishii (Kyushu Institute of Technology, Japan)

Maintenances of social infrastructures such as dam, bridge are important subjects. The more aging problem going on, the more the effective inspection methods have been expected. In the inspection of dams, divers observe the conditions of their surface manually, however underwater structure deeper than 30m is limited and their inspections are insufficient. In this paper, we propose the ROV whose functions are video capture, indirect measurement using laser, target depth keeping, heading keeping. The ROV is applied into the dam inspection and showed the effectiveness to find cracks.

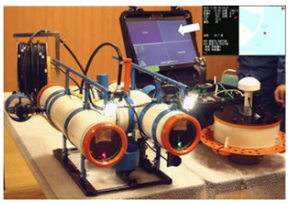

OS21-5 Conceptual Design of Small ROV for Sky to Water System

Keisuke Watanabe, Koshi Utsunomiya, Kazumasa Harada, Nakajima Shuhei
(Tokai University, Japan)

Long term monitoring of an area of coral reef is necessary for investigation of coral bleaching. The researchers usually use underwater cameras to record the reef's present condition using a ROV or diving by themselves. In those cases, they need to hire a boat whose port is not always near the target investigation site where sometimes near a beach. The researcher diving is effective from the viewpoint of precise investigation of a limited spot, however, it is impossible for a diver to investigate wide area simultaneously. To breakthrough these limitations we are considering a new method which uses a combined system of multicopter-USV(Unmanned Surface Vehicle)-ROV. We named this concept as Sky to Water System(SWS). In this paper, we introduce the conceptual design of our Small ROV which can be delivered with its mother USV by a multi-copter from the nearest beach and explain its hardware/software system.

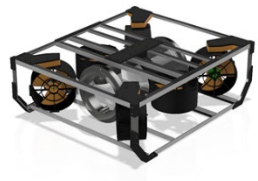

OS22 Robot Competitions for Social Contribution (6)

OS22-1 Study on Position Estimation Using Small Size ZigBee Module

Atsushi Sanada (Nishinippon Institute of Technology, Japan)

The positional information can be used for navigation in controlling a robot, and it is very important information. In this research, we describe the development of a position estimation system using a ZigBee wireless module. GPS is often used for position detection, but high precision measurement is difficult. And also, GPS cannot be used indoors. Furthermore, for position detection by the camera, since it is necessary to analyze by coordinating a plurality of cameras, much cost is required. In this paper, we propose a position estimation system using a low-cost small wireless module. This is to estimate the position based on the radio field intensity with multiple antennas. Since the radio wave intensity is nonlinear with distance and it is difficult to calculate the distance, a neural network is used for distance estimation. As a result, it was confirmed that the distance can be estimated correctly.

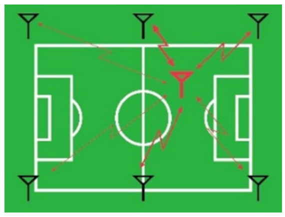

OS22-2 The 4th Tomato Harvesting Robot Competition

Takayuki Matsuo[1], Takashi Sonoda[2], Yasunori Takemura[2], Kazuo Ishii[3] ([1]National Institute of Technology, Kitakyushu College, [2]NishiNippon Institute of Technology, [3]Kyushu Institute of Technology, Japan)

Tomato is one of important fruit vegetables and most tomatoes are produced in the greenhouses, or large-scale farms, where the high temperature and humidity, and long harvest age force the farmer heavy works. With an aim to promote the automation of tomato harvesting, we have organized the tomato harvesting robot competition from 2014. The tomato harvesting robot competition include two divisions which are senior division and junior division. In senior division, free-style robots and rail-style robots had matches. In junior division, robot competition using lego mindstorm was hold. In this paper, we report on the results of the 4th tomato harvesting robot competition.

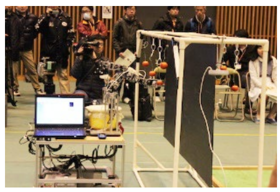

OS22-3 End-effector for robotic harvesting of a tomato fruit with calyx

Binghe Li, Shinsuke Yasukawa, Takuya Fujinaga, Kazuo Ishii
(Kyushu Institute of Technology, Japan)

Tomato fruit harvesting is a labor-intensive process, and therefore robotic automation is required. For tomato fruit harvesting robot, we developed three types of end-effectors (EEs): scissors type, cylinder type and suction-cutting type. It is necessary to harvest the tomato fruit with calyx especially in Japan. Therefore, the proposed EE has a cutter mechanism for cut the peduncle. The results show that the scissors type and the cylinder type EE can cut the peduncle; however, it is difficult to separate one fruit from the cluster. On the other hand, the suction-cutting type can separate and cut one fruit from the cluster and therefore it is useful for harvesting tomato fruit with calyx.

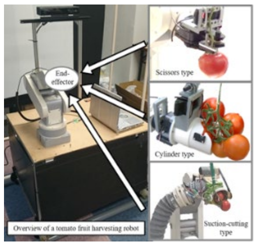

OS22-4 Evaluation for Ball Dribbling Mechanism of RoboCup Middle Size League Robot in The World Teams

Kenji Kimura, Shota Chikushi, Kazuo Ishii (Kyushu Institute of Technology)

RoboCup is a platform designed to promote such research fields as artificial intelligence (AI) and robotics. In recent years, the Middle size league soccer robot has a ball dribbling mechanism. This mechanism controls the ball with two driving rollers and in order to play soccer games well, ball control capability and holding capacity are indispensable. As the result of a survey at the 2017 World Cup, all teams in the world have determined the rollers arrangement heuristically, and no mathematical consideration has been made. In this research, we quantify the slippage between sphere and rollers in order to propose a mathematical model that allows for slippage and evaluate the optimality of the roller arrangement of the world teams.

OS22-5 Robot-control method based on personal space

Kota Kawamoto, Eiji Hayashi, Ryusuke Fujisawa (Kyushu Institute of Technology)

In order for a robot to interact with people, it is necessary for the robot to recognize human emotions and express its own emotions by both verbal and nonverbal communication. Furthermore, in our daily life, we unconsciously adjust our personal space according to the intimacy with others. It is also said that personal space is classified into non-verbal communication. In this research, we analyzed the distance that a person can tolerate when the robot approaches to identify the minimum distance that the person is able to interact comfortably.

OS22-6 Recognition method of target objects for autonomous tomato harvesting robot

Keiji Kamei, Hiroyuki Moriyama (Nishinippon Institute of Technology, Japan)

Recently, the shortage of agricultural workers and depression of its production efficiency have been said in Japan. To solve those problems, the researches that apply the information and robot technology are studied actively. The aim of our research, we focus on the autonomous tomato harvesting robot, and develop the recognition method for target objects. The color identification from a camera and distance measurement between target objects and a robot are key points. To solve those problems, we propose to identify the color based on HSV values and Look-Up-Table and measure the distance for target objects using Depth camera. From the experiments on real field, we succeeded in acquiring the target object from camera and measuring the distance.

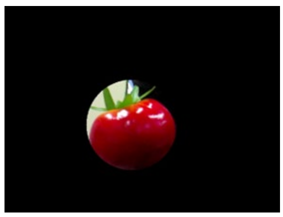

OS23 Kansei and Information Engineering (4)

OS23-1 Color Image Arrangement Based on Histogram Matching Using Smoothed Brightness Histogram (I) --- Overall Smoothing ---

Yusuke Kawakami, Tetsuo Hattori, Yoshiro Imai, Koji Kagawa, Yo Horikawa (Kagawa University, Japan), R. P. C. Janaka Rajapakse (Tainan National University of the Arts, Taiwan)

Although we have already reported that automated color image arrangement by Histogram Matching based on Gaussian Distribution (HMGD) gives good feeling impression if the brightness histogram of the original image has a single peak. However, if there are multiple peaks in the histogram, the HMGD processing does not always bring good results. In this paper, we propose a Histogram Matching method using overall smoothing over the brightness histogram of original image as the reference one instead of using Gaussian distribution. Also in this paper, we present the experimental results.

Left: original image
Right: processed image

OS 23-2 Color Image Arrangement Based on Histogram Matching Using Smoothed Brightness Histogram (II) --- Piecewise Smoothing---

Yusuke Kawakami, Tetsuo Hattori, Yoshiro Imai, Koji Kagawa, Yo Horikawa (Kagawa University, Japan), R. P. C. Janaka Rajapakse (Tainan National University of the Arts, Taiwan)

Although we have already reported that automated color image arrangement by Histogram Matching based on Gaussian Distribution (HMGD) gives good feeling impression if the brightness histogram of the original image has a single peak. However, if there are multiple peaks in the histogram, the HMGD processing does not always bring good results. In this paper, we propose a Histogram Matching method using piecewise smoothing over the brightness histogram of original image as the reference one, after Histogram Analysis by curvature computation. Also in this paper, we present the experimental results.

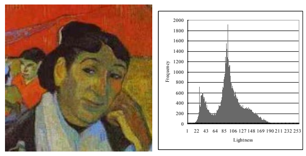

OS23-3 Parameter Estimation Method for Compartment Model - PET Inspection -

Tetsuo Hattori, Yusuke Kawakami, Yoshiro Imai, Koji Kagawa, Yo Horikawa (Kagawa University, Japan), Hiromichi Kawano (NTT Advanced Technology Company Ltd, Japan)

This paper proposes a new general method for parameters estimation in compartment model using DOC (Differentiation of Convolution). In this paper, we apply the DOC method to the parameters estimation in PET (Positron Emission Tomography) inspection especially. Pet inspection is done for getting physiological and biochemical information of organs. The PET camera acquires the image of radioactive distribution inside the human body. In this paper, we make a mathematical analysis of the PET compartment model and describe the DOC method.

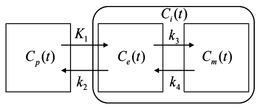

OS23-4 Application and Trial Evaluation of Document Writing Support System to Avoid Emotional Misunderstanding

Shunsuke Doi, Yoshiro Imai, Koji Kagawa, Tetsuo Hattori, Yusuke Kawakami (Kagawa University, Japan)

This paper describes a newly developed system of document designing, handling and self-checking in order for writers to avoid their readers' unnecessary emotional misunderstanding and possible repulsion. It is realized as server-client computing system. The server can obtain user document through the client, scan and separate the regarding document into word-level expressions, check each word while matching it with our sentiment dictionary, calculate the relevant sentimental values for the document and then generate the corresponding radar chart based on emotional axis such as delight, anger, sorrow, pleasure etc. on the relevant user's Web. Document writers utilize such a system before transferring and/or archiving, they can check sentimental values for their documents and recognize how their ones have a lot of emotional feelings. With this facility, the user can check his/her document and recognize whether the document possibly generates readers' unnecessary emotional misunderstanding and moreover repulsion which may occur as a result.

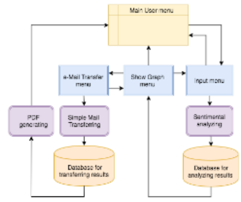

OS24 Automated content generation for narrative and cognitive contents (5)

OS24-1 A Method of Haiku Generation Using Deep Learning for Advertising Generation

Jumpei Ono (Vocational School of Digital Arts Sendai, Japan)
Takashi Ogata (Iwate Prefectural University, Japan)

We tried various approaches to generating story. One of them is haiku generation using deep learning. The method we tried has several tasks, one of which is that only the word time series data is used as learning data. Therefore, the result of learning can be a model similar to generation based on simple word transition probability. Therefore, we will organize the current tasks and try to study the features used for learning and generate by learning results. We also consider how to use the method tried in this paper for advertisement generation. In addition, we consider how to use the attempt in this paper for generating different types of stories.

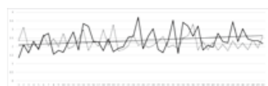

OS24-2 The Usage Features of Onomatopoeias in the Recipes in Japanese

Hiroki Fukushima (Kyushu Womens' University, Japan)

In this study, the author analyzes the co-occurrence tendency of onomatopoeias in the online recipes in Japanese. In Japanese, onomatopoeias are often used to describe faint or vague senses. Especially, onomatopoeias have considerable power to express the sense of taste or sense of odor. Focusing co-occurrence relationships, the author has revealed the roles of onomatopoeias in the tasting description corpus of wine and Japanese sake. In this study, applying the "form-screening method", the author reveales the semantic functions of onomatopoeia in the recipe data. The protocol of form-screening methodology is: First, extract sound symbolic words from the corpus. On the next screening step, all the words extracted in the first step is changed to an screening word. This screening word must be the same word class as extracted words. And finally, analyze the co-occurrence relationships of the screened words using a coding soft.

OS24-3 Storytelling in the Conversation of Aged People

Yuki Hayashi (Chiba University / Center for Advanced Intelligence Project, Riken, Japan)
Akinori Abe (Chiba University /Dwango Artificial Intelligence Laboratory, Japan)

In the conversation of aged people, some people well spoke about their experiences, which was able to attract others. In this paper, we will analyze their skills of storytelling from the viewpoints of the selection of theme, the construction of their story and their vocabulary. In addition, it is also important whether they can attract the other participants' interests. So we will also analyze the transition of topics during a conversation.

OS24-4 Expression of the taste of Japanese sake and metaphor

Akinori Abe (Chiba University / Dwango Artificial Intelligence Laboratory, Japan)

Seto explained "tasting expression" from the aspects of synesthetic expressions (both direction), which are metaphor, metonoymy, and synecdoche. When we express the taste of Japanese sake, we sometimes use the expression "Refreshing scent such as the scent of muskmelon and pear is elegant..." It is rather easy to express the taste by using the well known taste. However, how we controle the path of the metaphor flow? For instance, we frequently use the expression "cheek like apple." Why we assume the colour is red? Similarly, for the taste of the sake, we frequently use the expression "taste like apple." Which apple we assume? In this paper, we will discuss the flow of the metaphor from the aspect of discusion above..

OS24-5 An Analysis on Advertising Techniques of Beverages Using Positive Factors of Evaluation Database System

Yoji Kawamura (Kindai University, Japan)

In the advertising business, the CM Research Institute has constructed an exhaustive evaluation database system of commercial film representation with framework of positive factors. Several factors of positive factors are related to commercial film techniques. By utilizing data on positive factors, it is possible to analyze the outline of the commercial film techniques. In this research, based on the viewing experiment on the communication effect (positive factors, interests, willingness to buy) of 100 commercial films of beverages (can coffee, tea, beer), the characteristics (by brand, by category, history transition, relation between techniques and interest, relation between techniques and willingness to buy) of commercial film techniques are analyzed. This analysis method brings about a lot of knowledge and can be utilized for transient analysis and simultaneous analysis of commercial film techniques using the evaluation database system.

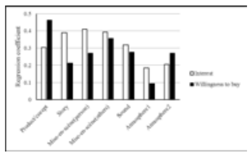

OS25 High-Performance Computing for Interactive Content Creation and Rendering

OS25-1 High-Performance Computing for Visual Simulations and Rendering

Jasmine Wu, Chia-Chen Kuo, Shu-Hsin Liu, Chuan-Lin Lai, Chiang-Hsiang Lien, Ming-Jen Wang, Chih-Wei Wang(National Center for High-performance Computing (NCHC), Taiwan)

Everyone who is involved in film or animation industry knows how rendering can be a nightmare. National Center for High-performance Computing (NCHC) built a render farm that provides a platform for the industry to render their work in a much more efficient timeframe. Over 100 films in Taiwan was rendered using our platform. The newest Render Farm was launched in March of 2018, which allows not only CPU rendering, but also GPU rendering. The throughput is also greatly improved to support complex and large scale simulations. Our Render Farm is currently being used by animation students in Taiwan, as well as companies from the industry. The main goal of this session is to introduce scientific discoveries and technical innovation through prospective computing technology and platform.

OS25-2 Virtual Reality as an Art Form

R.P.C. Janaka Rajapakse, Yi-ping Hung (Tainan National University of the Arts, Taiwan)

After introducing content creations in the immersive environments, the VR content creation process has been changed dramatically. It has enhanced the direct engagements of the artists and reduces the time it takes to get a part from the idea stage to the production stage. Time consuming VR content creation process has been reduced to hours or days. Not only is the time reduced, but the cost is also significantly reduced. The reduced time and cost allows artist to work in near real-time, with the design and production happening at nearly the same time. This section of the session is focused on VR content creation process and its artistic perspectives. Especially, not only concerning VR contents creation in immersive environment is an alternative to find new form of art. And the last part of the speech concerns about the role of VR in the live performance and new form of theater.

OS25 -3 Using Quill as a Tool for Real-Time Rendering

Jasmine Wu, Chia-Chen Kuo, Shu-Hsin Liu, Chuan-Lin Lai, Chiang-Hsiang Lien, Ming-Jen Wang, Chih-Wei Wang (National Center for High-performance Computing (NCHC), Taiwan)

Unity and Unreal are game engines that renders in real-time, and the super computers at NCHC not only supports both, but it also presents a faster frame rate. Rendering is indeed a time consuming procedure, the process of 3D animation takes even longer with more men-power. Quill is a VR illustration and animation tool for the Oculus Rift, which can shorten the traditional 3D animation process done in 3D software, because its 3D models are painted rather than having to go through the process of modeling, texturing, and rigging. This is a great tool to create content for Unity or Unreal, which can then be rendered in real-time by the super computers at NCHC. Another example to demonstrate NCHC's real-time render farm was by performance art. We have high data throughput that can help the performer to do a large scale VFX simulation and to create new kinds of cross-disciplinary performances. As we develop through time, more and more applications can be seen in the near future.

GS abstracts

GS1 Robotics I (4)

GS1-1 System to decide unit's layout of cell assembly machine by GA (Big Mutation in mutation process)

Yoshiki Ito, Hidehiko Yamamoto, Takayoshi Yamada (Gifu University, Japan)

The purpose of this research is to develop a system to decide unit's layout which automatically decides to place a lot of assembled parts, jigs and robot hands of a cell type Assembly Machine by genetic algorithm (GA). The system consists of two modules, the conditions module and GA module. The conditions module reads work data for robot, and sets various parameters required for GA.GA module decides the efficient arrangement place of parts, jigs and robot hands by GA, and outputs the acquired arrangement images. This system proposes the concept of Big Mutation that changes the mutation rate of GA every certain generation. By introducing Big Mutation , the possibility of searching an optimal unit placement increases and the system simulation time is shortened. It is ascertained that the system to decide unit's layout including Big Mutation is useful.

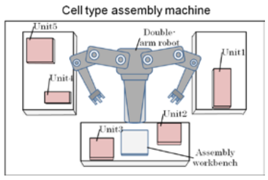

GS1-2 Autonomous decentralized FMS that adopts priority ranking structure based on AGV's lies

Kento Uejo, Hidehiko Yamamoto, Takayoshi Yamada (Gifu University, Japan)

We introduce the model of AGV mind to eliminate path interferences between AGVs when running an autonomous decentralized FMS and carry out behavior controls. The conventional autonomous decentralized FMS believes all information sent by agents as correct. However, the information sent by some agents may be incorrect due to malfunctions. We define this incorrect information as a "lie" and carry out the AGVs action controls which doesn't decrease the outputs of autonomous decentralized FMS even if lies occur. In order to do this, we propose a "priority ranking structure". The proposed method is ①to give a ranking to each AGV according to a lie number, ②to give high ranking AGVs to share jobs. In order to prove the effectiveness, production simulations using priority ranking structure and the conventional research method were carried out. As a result, the productivity of propose method was higher than that of the conventional research method. It is ascertained that the priority structure is useful

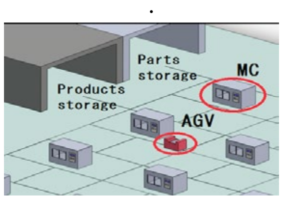

GS1-3 CULET: Cubelet Lego Turing Machine

Ricardo Q. Figueroa, Daniel A. Zamorano, Genaro J. Martínez (Instituto Politécnico Nacional, México)
Andrew Adamatzky (University of the West of England, UK)

In this paper, we show the construction of CULET: a robot that simulates the execution of any 2-symbols Turing machine. CULET is constructed with Cubelets (small autonomous robot-cubes used for teaching basic robotics and programming for kids) and Lego bricks. Cubelets are a kind of high level programming where you do not use traditional code but rather achieves different robots trough the concatenation of blocks, i.e. robots assembled. CULET is designed to performance the read and write of a Turing machine.

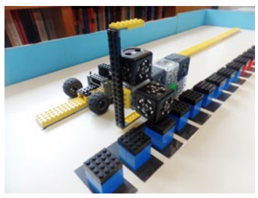

GS2 Robotics II (5)

GS2-1 Automated Guided Vehicle System Analysis in Foam Manufacturing Plant Using Petri-net

Amornphun Phunopas[1], Wisanu Jitviriya[1], Noppadol Pudchuen[1], Sutee Kumjaikong[1], Songklod Tunsiri[2], Eiji Hayashi[3] ([1]King Mongkut' s University of Technology North Bangkok, Thailand, [2]Urban Community Development College, Thailand, [3]Kyushu Institute of Technology, Japan)

The logistic robot is very popular nowadays. The robots run in autonomous, reactive, and parallel situations. These kinds of work are defined as a stochastic problem. We focus on task distribution, routing, scheduling, and queueing. This paper presents a multi AGVs operational analysis in the foam manufacturing plant using the Petri-net. Each robot is designed a role-assignment supervisor with the role of a robot fixed in a zone. According to the work capacity, the supervisor assigns the role of high capacity work to another robot to help in a new zone. To monitor the work situation, the supervisor continually receives feedback information of the system. The analysis is necessary for preventing any failure that can make the central software go down. The results show system management for robotic assistants in the foam manufacturing process.

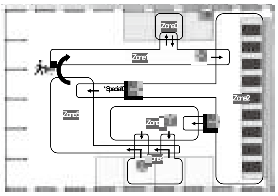

GS2-2 Preliminary Comparative Experiments of Support Vector Machine and Neural Network for EEG-based BCI Mobile Robot Control

Yasushi Bandou, Takuya Hayakawa, Jun Kobayashi (Kyushu Institute of Technology, Japan)

The authors have been developing an EEG-based BCI for mobile robot control, using neural networks that classifies their brain waves to recognize intention of a mobile robot operator. In order to achieve practical classification capability with them, we had applied some techniques, such as Bayesian Optimization for hyperparameters, to the neural network training; however, satisfactory performance of the neural networks has not been obtained yet. Support Vector Machine (SVM) is another machine learning method that demonstrated its usefulness in lots of other studies. In this study, for further development of practical EEG-based BCI for mobile robot control, we have experimentally employed SVM for brain wave classification and compared the performance with the neural networks. This paper presents the comparative results.

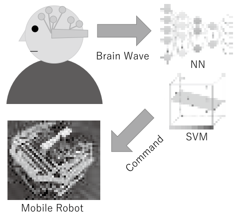

GS2-3 Position Tracking Error Constrained Super-Twisting Dynamic Surface Control with Disturbance Observer for Robot Manipulators

Seong Ik Han (Dongguk University, Korea Republic)

A tracking error constrained dynamic surface control (DSC) with a super-twisting algorithm (STA) and a nonlinear disturbance observer is proposed for robot manipulator systems, where the system dynamics are partially known. The stabilizing controls of the DSC were designed by combining the STA with the virtual tracking errors defined from the DSC design concept. A nonlinear disturbance observer was designed to estimate the unknown nonlinear function and external disturbance instead of using parameterization of the nonlinear function or adaptive law in the conventional STA and DSC schemes. Moreover, a simpler tracking error constraint method is also proposed. The proposed tracking error constrained STA-DSC scheme combined with a nonlinear disturbance observer has better tracking error performance and robustness to uncertainty of robot manipulator system than control systems with a conventional DSC and disturbance observer. The control scheme was evaluated through simulations with the articulated manipulator system.

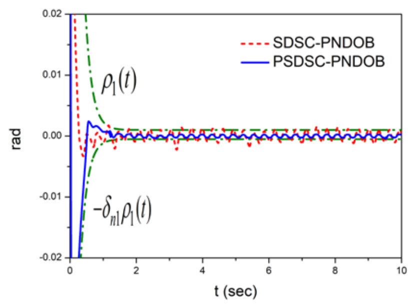

GS2-4 Image Processing for Picking Task of Random Ordered PET Drinking Bottles

Chen Zhu, Takafumi Matsumaru (Waseda University, Japan)

In this research, six brands of soft drinks are decided to be picked up by a 6 degree of freedom robot with a monocular RGB camera. The drinking bottles need to be located and classified with brands before being picked up. The Mask R-CNN, a mask generation network improved from Faster R-CNN, is trained with COCO datasets to detect and generate the mask on the bottles in the image. The Inception v3 is selected for the brand classification task. Around 200 hundred images are taken or found at first; then, the images are augmented to 1500 images per brands by using random cropping and perspective transform. The result shows that the masked image can be labeled with its brand name with at least 85% accuracy in the experiment.

GS2-5 The Use of Importance Ranks to Derive Suitable Timing of Visual Sensing in Manipulation Task Containing Error Recovery

Akira Nakamura[1], Kazuyuki Nagata[1], Kensuke Harada[2], Yukiyasu Domae[1]
([1]National Institute of Advanced Industrial Science and Technology (AIST), [2] Osaka University, Japan)

In general, a manipulation task can be composed of many skill primitives. It is desirable to perform plural visual sensing in most skill primitives as geometric modeling and task planning are performed before execution, and task achievement is confirmed after execution. However, the performance of sensing at all sensing points is difficult because of the restrictions of time and hardware. In this paper, we proposed the addition of importance ranks to the attribute of skill primitives to derive suitable timing to perform visual sensing. The use of the proposed method eases the selection of skill primitives in which visual sensing should be performed. Furthermore, we showed that skill primitives distinguished according to their high importance ranks considerably correlate with those in which error recovery is considered in advance. This characteristic can be used for selecting skill primitives in which error recovery is planned in advance.

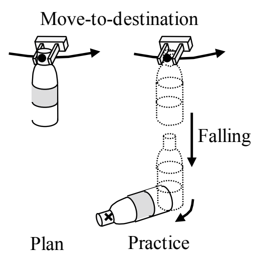

GS2-6-1 Electronic Measurement and Gamification of Balance Tests

Yan-Xin Liu, Massimiliano Leggieri, Henrik Hautop Lund (Technical University of Denmark, Denmark)

We gamified three common balance tests for fall risk diagnosis, Timed Up & Go (TUG), Chair Stand (CS), and Four Square Step Test (FSST), by using the Moto Tiles. The embedded pressure sensor of the Moto Tile was used to detect the movement of subjects and to time the tests. The proposed Moto measurement was compared with traditional stopwatch measurement. A total of 51 samples were analyzed. The intraclass correlation coefficients of the TUG and CS tests were very high (0.98 and 0.94). The FSST was analyzed by Pearson's correlation coefficient and the result also indicated strong correlation (0.79). Based on the results, we concluded that the proposed Moto tests are as reliable as traditional tests.

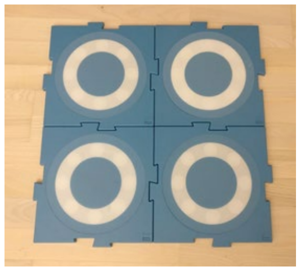

GS2-6-2 Playful Body and Brain Test with the Moto Tiles

Yan-Xin Liu, Massimiliano Leggieri, Henrik Hautop Lund (Technical University of Denmark, Denmark)

We gamified three common balance tests for fall risk diagnosis, Timed Up & Go (TUG), Chair Stand (CS), and Four Square Step Test (FSST), by using the Moto Tiles. The embedded pressure sensor of the Moto Tile was used to detect the movement of subjects and to time the tests. The proposed Moto measurement was compared with traditional stopwatch measurement. A total of 51 samples were analyzed. The intraclass correlation coefficients of the TUG and CS tests were very high (0.98 and 0.94). The FSST was analyzed by Pearson's correlation coefficient and the result also indicated strong correlation (0.79). Based on the results, we concluded that the proposed Moto tests are as reliable as traditional tests. Further, we propose a novel playful body and brain test. The test includes a series of standardized Moto Tiles games, which cover both physical and cognitive abilities. Reference scores of the tests were modeled by data collected from a large number of participants of different ages. The reference scores can be applied to evaluate a user's body and brain abilities in comparison with the average performance at the same age.

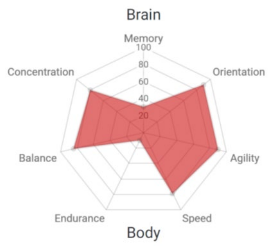

GS3 Complexity (2)

GS3-1 Extracting Co-occurrence Feature of Words for Mail filtering

Seiya. Temma, Manabu. Sugii, Hiroshi. Matsuno (Yamaguchi University, Japan)

Spam mail filters often take advantage of appearance frequency of words in a text for mail classification. However the appearance frequency is one of the most important attribute information with which the mail can be characterized, not a few spam mails can not be distinguished with only the appearance frequency of words. In order to search new attribute information to characterize and classify the mails, we analyzed relationship between words in a text of mails by text data mining. Also we visualized the word network by the co-occurrence and multi-dimensional scaling analysis with the jaccard coefficient in real mails. Co-occurrence network analysis showed important word connections with noun and verb in the same kinds of mails. Multi-dimensional scale analysis showed some word clusters extracted from the same kind of mails. We'll plan to explore how to utilize the result of this study for mail classification.

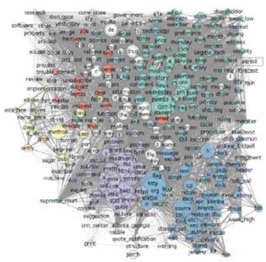

GS3-2 Learning Style Classification with Weighted Distance Grey Wolf Optimization

Duangjai Jitkongchuen, Piyalak Pongtawevirat (Dhurakij Pundit University, Thailand)

The multiclass classification seems to be difficult to improve the performance of the built classification model. This research aims to improve the performance of multiclass classification by using grey wolf optimizer (GWO) algorithm. But in the original GWO, the evolutionary information of population has not been fully utilized, and it is easy to fall into local optimum. The proposed algorithm presents a solution to improve the grey wolf optimizer performance using weighted distance and immigration operation. The weight distance is used for the omega wolves movement is defined from fitness value of each leader (alpha, beta and delta). The proposed technique is based on learning style prediction which addresses multiclass classification problem. The results showed that the proposed technique obtained the higher accuracy rate than other classification techniques. This was implemented to application of learning style prediction which can provide the course materials suitable for learners regarding their learning style.

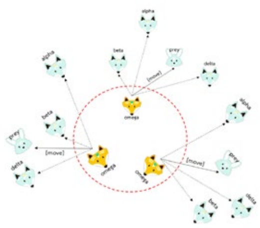

GS4 Poster (5)

GS4-1 Relevance Research among Destination Image, Brand Trust, and Satisfaction: Tainan Festival in Taiwan as Example

Shang-Hui Li, Shu-Fang Hsu, Yi-Tai Shang (Far East University, Taiwan)

In recent years, all local governments of Taiwan have held sightseeing festivals to enhance their popularity, promote their economy, to establish their brand. Tainan, the second biggest city in southern Taiwan, also promotes the various agricultural products and sightseeing to serve customers as the region's annual event. This study took Tainan Festival as an example to explore the relevance of the destination image, brand trust, and satisfaction. The participants for those who took part in 2017 Tainan Festivals, from May to July, were the main subjects on this study. 500 questionnaires were issued, 465 valid questionnaires collected, 93%. The finding results showed that the destination image of Tainan festival activities had a positively effects on satisfaction, brand trust had a positive effects on satisfaction, destination image had a positive effects on brand trust, brand trust had the intermediary effect to the satisfaction and destination image.

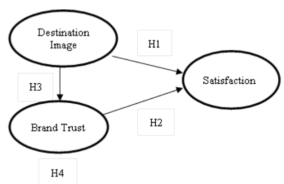

GS4-2 Third-party Logistics Service Supply: Catering Service Trade as Example

Shu-Fang Hsu, Shang-Hui Li (Far East University, Taiwan)

With the development of third-party logistics, refrigeration technology, and transportation which made the food to obtain easily, and improve the quality of food preservation. Now, the catering chefs just ordered his needed foods by line, telephone, fax, or fill the order list etc., to inform the third-party logistics suppliers and there will be someone assigned to the designated location which could save purchasing time and catering chefs don't need to rush around to procure foods. This study analyzed the collected information through literature, in-depth interviews, and observation methods. Third-party logistics suppliers conducted the information, logistics, and cash flow by the different deal due to the different nature of suppliers. Third-party logistics suppliers could be exhaustive on the quality management, logistics activities, interactive mode of trust mechanism, which could not only win the good reputation by the catering chefs, but the professional core competence.

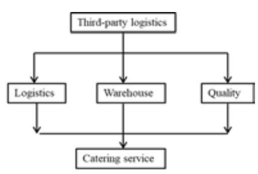

GS4-3 Pedal Scale Control Device for Weighing Food Ingredients or Chemical Materials

Shang-Hui Li, Shu-Fang Hsu, Yi-Tai Shang, Kuan-Ying Chen (Far East University, Taiwan)

Safety and hygiene is one of the most important elements when weighing ingredients or chemical materials. It may cause cross-contamination when preparing them if the operators conduct the scale button and hold the food ingredients or chemical materials by using both hands. The invention relates to a pedal scale control device comprising a scale body and a foot unit. The wireless signal on the foot unit can be connected to the scale body to zero and buckle the function without using of both hands. This invention has obtained Taiwan's invention patent, which is more hygienic and safety for the users when weighing the food ingredients or chemical materials.

GS4-4 Convolution Neural Network Based Fault Diagnosis of Induction Motors

Jong-Hyun Lee, In-Soo Lee (Kyungpook National University, Korea)

Induction motors are one of the most important components for machine and industrial equipment in modern industrial applications. Therefore, it is necessary to develop a fault diagnosis system that detects the operating condition and failure of the induction motor early. This paper presents a induction motor fault diagnosis system using CNN(Convolution Neural Network) model. In the proposed method, the fault diagnosis of the induction motor is performed by using vibration signal data obtained from the induction motor experiment as the input value of convolution neural network model. And then fault diagnosis was made using convolution neural network. In this paper, fault diagnosis of steady state, rotor and bearing failure of induction motor is performed. From the experimental results, it is confirmed that the proposed method is suitable for diagnosis of rotor and bearing failure of induction motor.

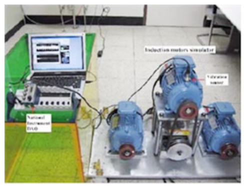

Fig. 1. Experimental environment for fault diagnosis of induction motors

GS4-5 Analysis of Value Chain on Food and Beverage Micro-enterprises: Mobile Diner as Example

Shu-Fang Hsu, Shang-Hui Li (Far East University, Taiwan)

This study was based on the theory of value chain proposed by Porter, 1985, in conjunction with the mobile diner industry from the value activities created in the value chain. The main activity was to analyze the competitive advantage of the mobile diner and the added value to meet customers' need. In this study, the Delphi method was used, and then conducted with interview and observation method on 10 homogeneous mobile diners to gain an in-depth understanding of the development and current situation in southern Taiwan. Exploring their competitiveness, and discovering that the businessmen purchased the necessary food by themselves, which could ensure safety. In terms of marketing and sales, due to the mobility and easy acceptance of customization, the relative value of products and services are relatively improved. This study could provide a practical reference for micro-entrepreneurs who want to invest in food and beverage in the future.

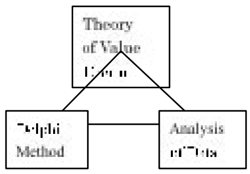

GS5 Others (8)

GS5-1 Suppression of Roll Oscillation in Turning of Quadruped Robot by Asymmetric Amplification of Central Pattern Generator Output Waveform

Makoto Kitani, Ryo Asami, Noritake Sato (Nagoya Institute of Technology, Japan),
Tomofumi Fujiwara, Takahiro Endo, Fumitoshi Matsuno (Kyoto University, Japan),
Yoshifumi Morita (Nagoya Institute of Technology, Japan)

One of control methods for walking of a robot is a central pattern generator (CPG). Using the CPG for a legged robot, it can walk on rough terrain. Kimura et al. developed a quadruped robot "Tekken", which is controlled by the CPG. Tekken can turn by controlling the hip yaw joint. However, when the robot turns by controlling the hip yaw joint, there is a problem that the vibration in the roll direction is large. To solve this problem, we proposed a method of asymmetric amplification of CPG output waveform. We implemented the proposed method on the robot inside the simulator and verified the effectiveness at turning. As a result, we achieved a 43.7% decrease in the roll angle of the robot body than the conventional method. It is assumed that legged robots can turn stably using our proposed method.

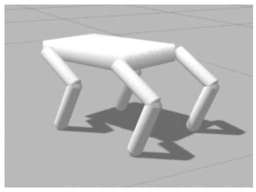

GS5-2 Tumble avoidance system for rescue robot by estimating the contact points using a 3D depth sensor

Noritaka Sato, Kotaro Ohshima, Yoshifumi Morita (Nagoya Institute of Technology, Japan)

Rescue robots are expected to perform works in hazardous areas. However, when the robot runs on a rough terrain, fatal rollover falling sometimes occurs. Therefore, we propose a tumble-risk-assessment system, which reconstructs the environment, estimates the contact points between the ground and the robot, and calculates a normalized energy stability margin (SNE) by using a 3D depth sensor. Moreover, a control system to avoid the tumble situation by moving the sub-crawlers automatically is proposed. In the control system, the SNE is partially differentiated by the angles of the sub-crawlers and the sub-crawlers move to increase the SNE. We implemented the proposed systems to a real robot, carried out experiments, and confirmed the effectiveness of the proposed method.

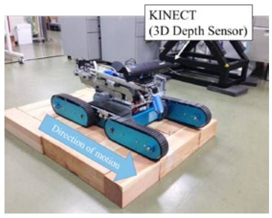

GS5-3 Rule based Intrusion Detection System by Using Statistical Flow Analysis Technique for Software Defined Network

Mahnoor Ejaz, Osama Sohail, Talha Naqash, Zain ul Abideen, Sajjad Hussain Shah
(Bahria University, Pakistan)

Network Security is a vast field making progress around the globe very fast. In every progressing year, developers have implemented different tools, which include Intrusion detection systems. Nowadays Intrusion Detection System (IDS) is one of the popular tools, which are drawing the attention of many researchers. Applying it in Software Defined Networking (SDN) facilitates network management and enables to enhance the productivity of network monitoring. Classifying packets based on their statistics and separating the forward process of network packets from the routing process is the main challenge. In this paper, rule-based classification is done in order to differentiate between viruses and normal packets. Statistical analysis of different network traffic flows are done through which segregation is made and intrusion is detected in Software Defined Networking. The proposed system is experimentally tested on UNB ISCX data,sets

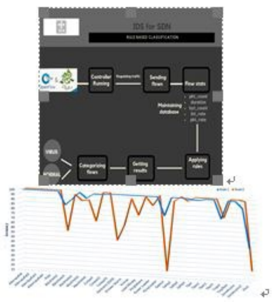

GS5-4 Development of Testbed for SDN to Know Its Feasibility of Deployment on Access Layer

Rafay Shah, M Osama Shaikh, Talha Shaikh, Tanveer Hussain
(Mehran University of Engineering & Technology, Pakistan)

Today, the network requirement of organizations includes enhancing performance, realizing broader connectivity and security regulations. In order to comply with all of these criteria, networking protocols have been evolving significantly over the last few decades. Internet of Things (IoT) has shifted IT from server entity to the network entity. Software Defined Networking (SDN) is a solution of these all problems found in traditional networking. SDN separates control plane from data plane, which makes it easier for an IT Administrator to easily deploy and update regulatory policies. In this project, we have developed a testbed kit using Zodiac-FX Open- Flow Switch for SDN and have tested SDN feasibility on Access Layer. We have also simulated a network of Faculty of Electrical Electronics Computer Engineering (FEECE) of Mehran University of Engineering and Technology (MUET) and have found that SDN performs better than traditional network architecture of FEECE of MUET.

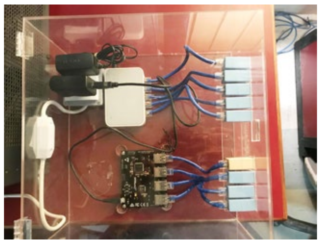

GS5-5 Spectrum Sensing using Unsupervised Learning for Cognitive Radio

Asmara Shaukat, Danish Khan, Talal Arshad, Haseeb Ahmad (PAF-KIET, Pakistan)

Cognitive Radio is the type of wireless communication which has the ability to learn from its surrounding and reconfigure its operating parameters. It uses radio spectrum efficiently by detecting which communication channels are in use and which are not, and instantly move into vacant channels while avoiding occupied ones. This optimizes the use of available radio-frequency (RF) spectrum while minimizing interference to other users. Spectrum sensing is one of the most important tasks performed by the CR. Spectrum sensing refers to the ability of a CR to measure the spectrum activities due to ongoing transmissions over different spectrum bands and to capture the related parameters, it tells us about spectrum usage and existence of primary users in a geographical area. In this work we perform Spectrum sensing using unsupervised learning algorithm (K- mean clustering) and find vacant spectrum.

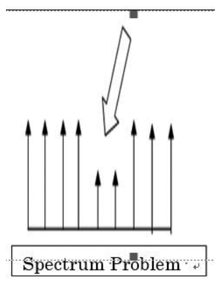

GS5-6 Tracking Secondary User In Cognitive Radio For 5g Communication

Muhammad Adnan, Muhammad Umair, Sameed bin Junaid (PAF-KIET, Pakistan)

Cognitive Radio (CR) is a promising technology which resolves the spectrum scarcity issues and allows secondary user (SU) to use the vacant spectrum space. Many secondary users are allocated different spectrum bands to enhance spectrum utilization. SU co-exists with the PU in the CR network and continuously monitors PU activities in order to use vacant space of PU in the spectrum. The movement of SU in the CR network is random and therefore it is necessary to track the position of SU and measure radio signal strength indicator (RSSI) in order to avoid interference with the PU. In this work, we present the implementation and comparison of two algorithms KALMAN Filter and State Space Least Mean Square (SSLMS) to track the position of SU in the CR network under log distance and log normal shadowing path loss models. Both algorithms track the position of SU by measuring RSSI and Signal to Noise Ratio (SNR) from the PU; however SSLMS gives better performance as compared to KALMAN Filter.

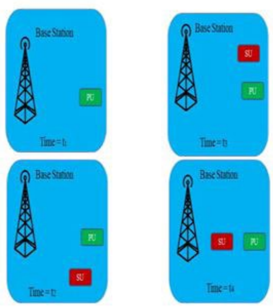

GS5-7 Wireless Power Transfer and Data Communication For Biomedical Applications

Hammad Saleem, Muhammad Awais, Siraj Din, Attequa (PAF-KIET, Pakistan)

A technique of wireless power transfer (WPT) system for biomedical applications with backscattering communication, a rectifier use with active bias mechanism (dependent and independent stages) overcome the diode device losses has been presented in this paper. Apart from conventional and static Vth cancellation technique rectifiers, it achieves more than double efficiency and achieves power loss reduction in both forward and reverse biased conditions it decrease turn on voltage in forward bias condition along with decrease in reverse leakage current during reverse bias condition. Under the input conditions (Vin =1Vp-p coupling coefficient ‘k’=0.01 at 200MHz frequency with transmitter and receiver inductance of 22nH), actively biased differential drive rectifier is able to achieve DC voltage of 880mv for 50kΩ load resistance in dependent stage and achieves DC voltages of 803.2mv for 50kΩ load resistance in independent stage. Regulated output DC voltage is provided under variable coupling conditions and becomes more efficient. Backscattering communication has been performed using switch by changing the resonance frequency of the receiver.

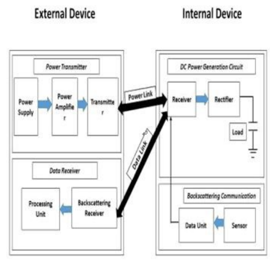

GS5-8 Feasibility Study of UAV Implementation In Route Surveying

D.Hazry, M A Azizan, Safwan Suhaimi, Zulaiha Ramli, Mohamad Syafiq A.K, Zainuddin Hat
(Universiti Malaysia Perlis, Malaysia)

Unmanned Aerial Vehicles (UAVs) are widely used in numerous field and the technology keeps growing. Generally, conventional method use in data collection for engineering work is tedious and requires a lot of manpower. This research focuses on the investigation of the suitability of UAV for route survey. There were three stages: data collection, data processing and data analysis. By using KAMA BETA, the data was collected. For data processing, Pix4Dmapper used for point cloud and AutoCAD 2014 for analysis stage. The result is mainly focused on extracting the road profile and test the point cloud data using RMSE. The result from both method, conventional and UAV from the point cloud data using RMSE show only the small difference.

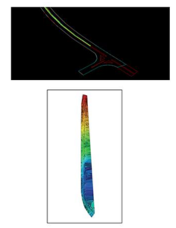

AUTHORS INDEX

Notation of session name

PS: Plenary Session IS: Invited Session, OS: Organized Session, GS: General Session,

Note: 33/90 = (page no. in Technical Paper Index) / (page no. in Abstracts)

[I]

[T]

[Z]

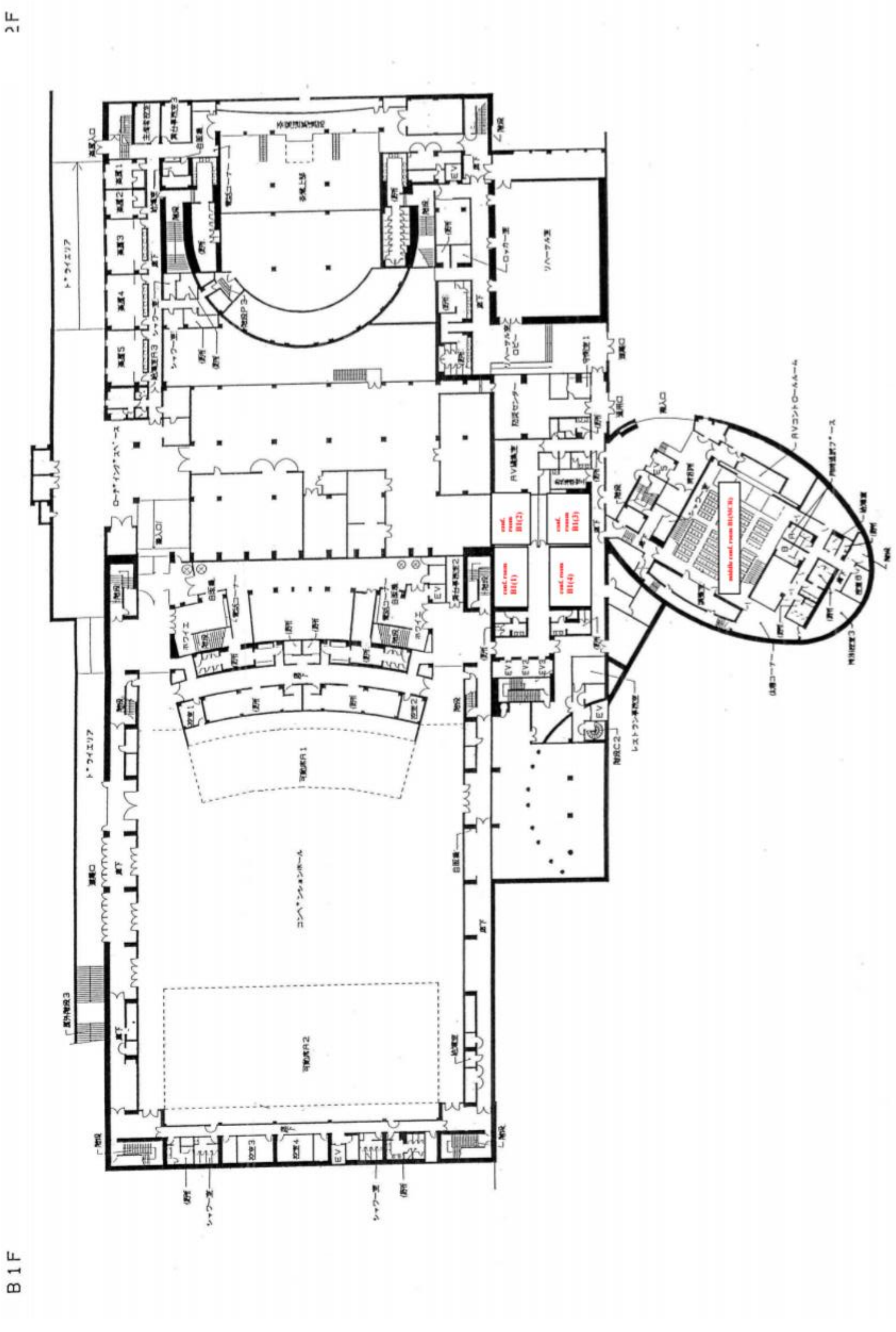

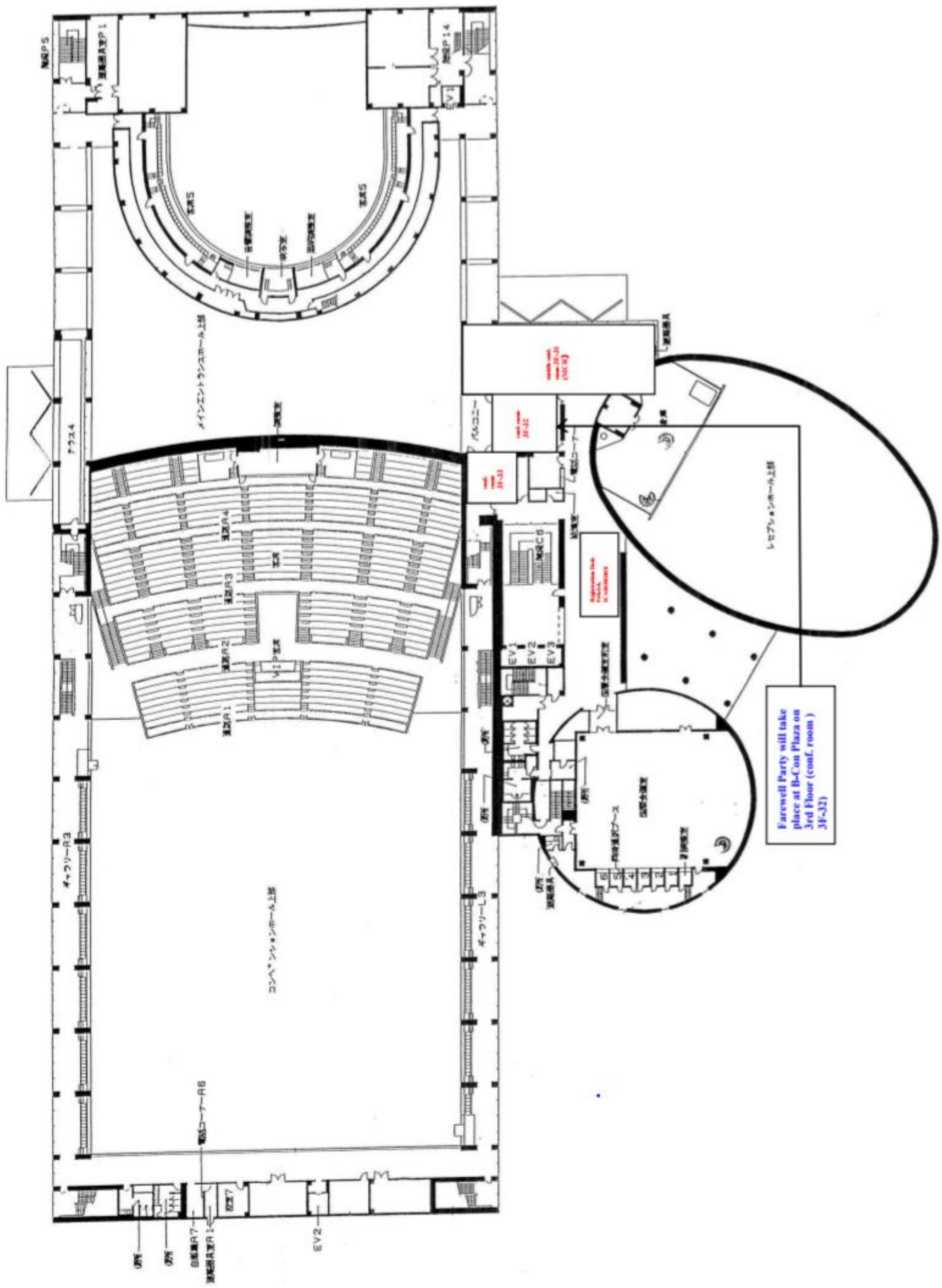
Farewell Party will take place at B-Con Plaza on 3rd Floor (conf. room) 3F-32)

3F

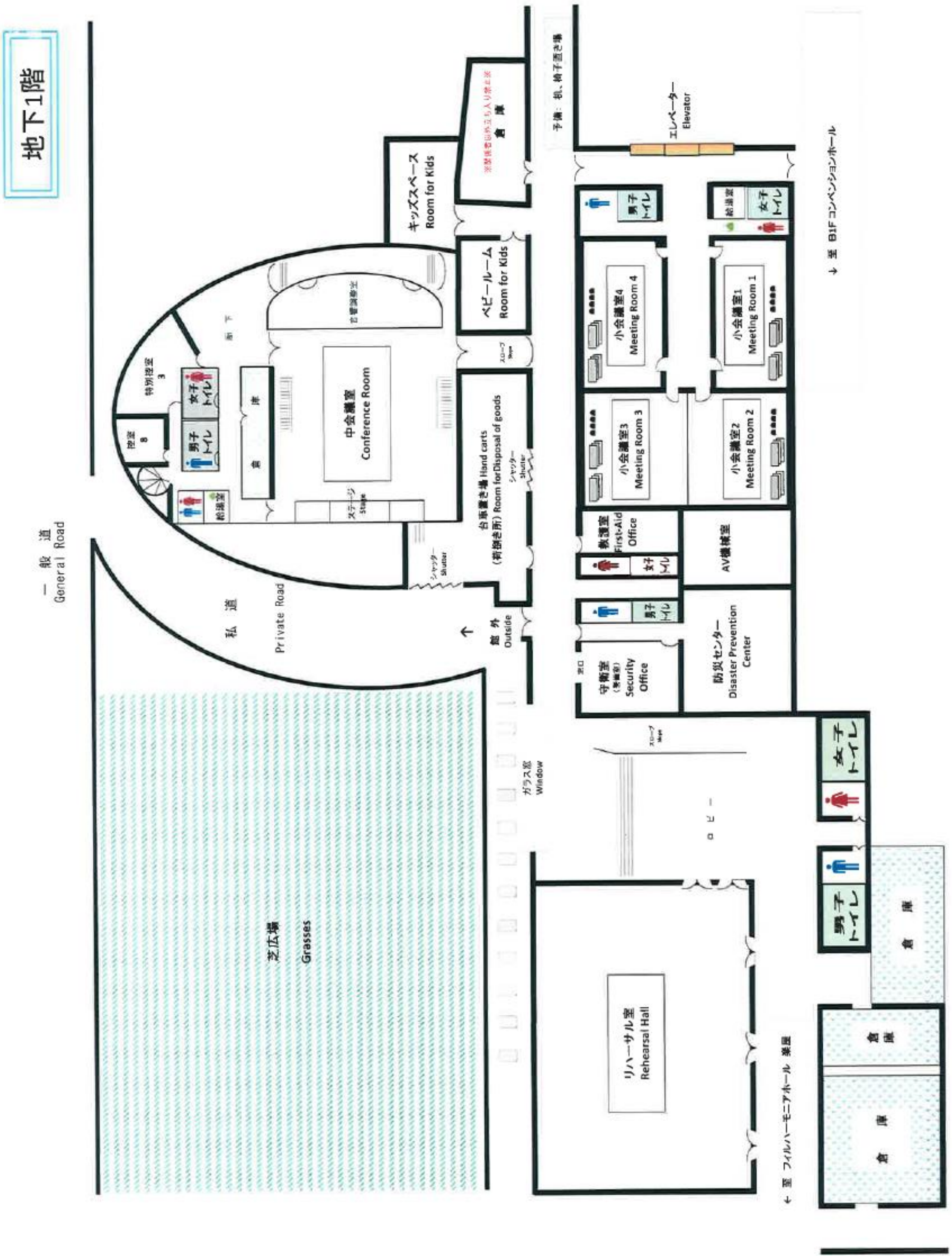
地下1階
一般道
General Road
私道
Private Road
芝広場
Grasses
中会議室
Conference Room
キッズスペース
Room for Kids
ベビールーム
Room for Kids
小会議室4
Meeting Room 4
小会議室1
Meeting Room 1
小会議室3
Meeting Room 3
小会議室2
Meeting Room 2
救護室
First-Aid Office
AV機械室
守衛室
Security Office
防災センター
Disaster Prevention Center
リハーサル室
Rehearsal Hall
エレベーター
Elevator
ロビー
館外
Outside
倉庫

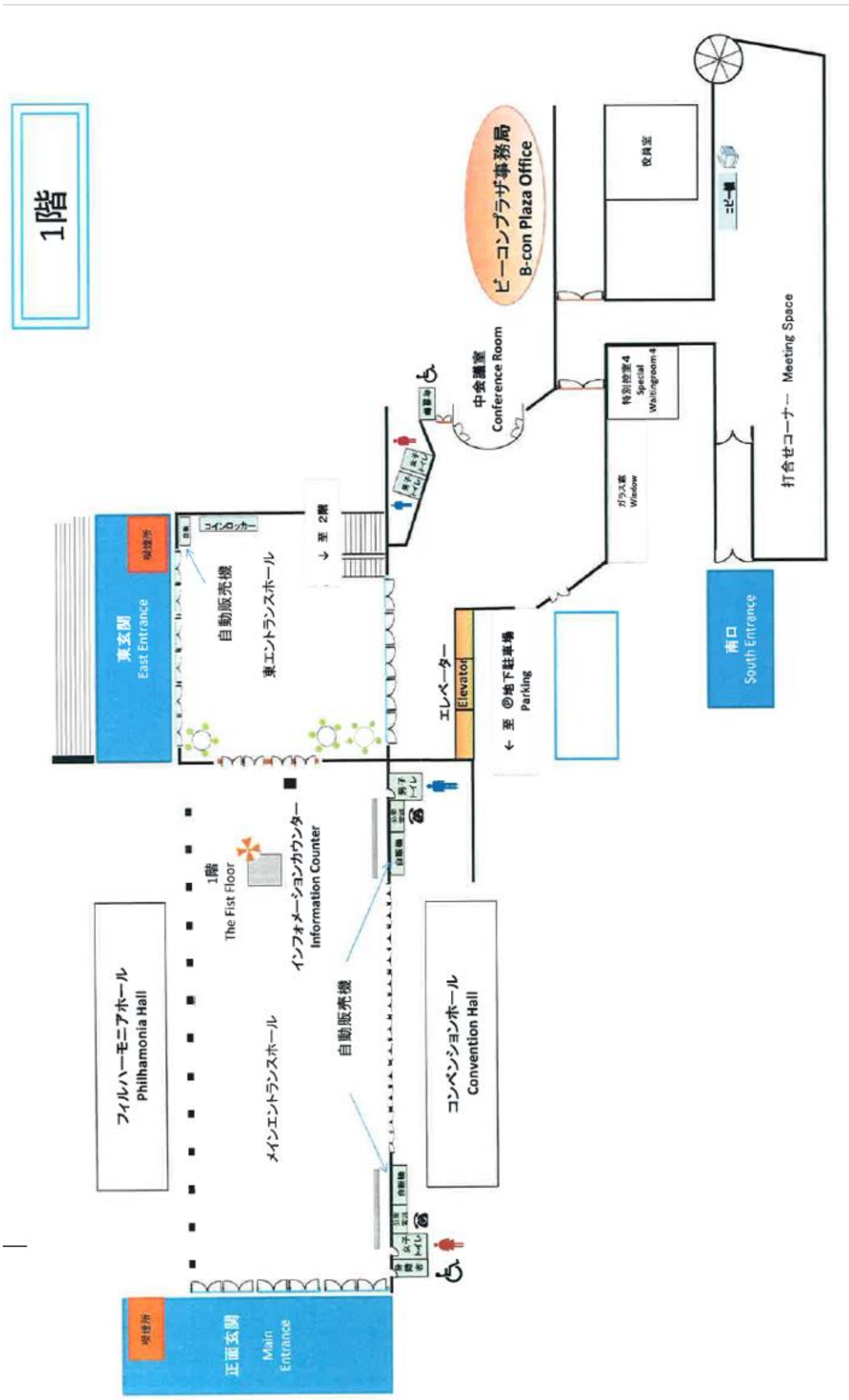
1階
ビーコンプラザ事務局
B-con Plaza Office
中会議室
Conference Room
特別控室4
Special Waitingroom4
打合せコーナー
Meeting Space
ガラス窓
Window
南口
South Entrance
東玄関
East Entrance
コインロッカー
自動販売機
東エントランスホール
至 2階
エレベーター
Elevator
至 地下駐車場
Parking
1階
The Fist Floor
インフォメーションカウンター
Information Counter
フィルハーモニアホール
Philhamonia Hall
メインエントランスホール
自動販売機
コンベンションホール
Convention Hall
正面玄関
Main
Entrance

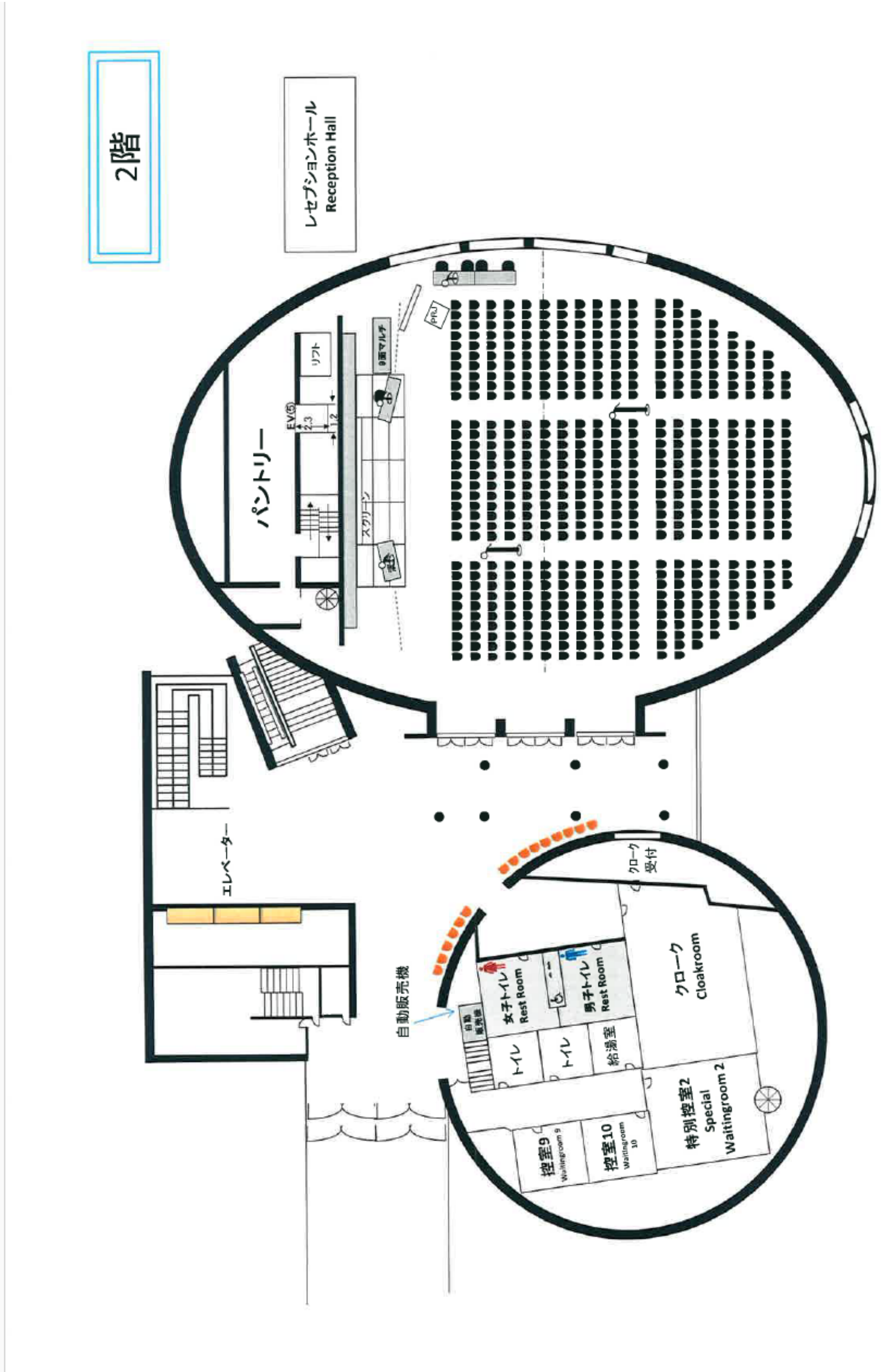

2階
レセプションホール
Reception Hall
パントリー
リフト
スクリーン
エレベーター
自動販売機
クローク受付
クローク
Cloakroom
女子トイレ
Rest Room
男子トイレ
Rest Room
トイレ
トイレ
給湯室
特別控室2
Special
Waitingroom 2
控室9
控室10

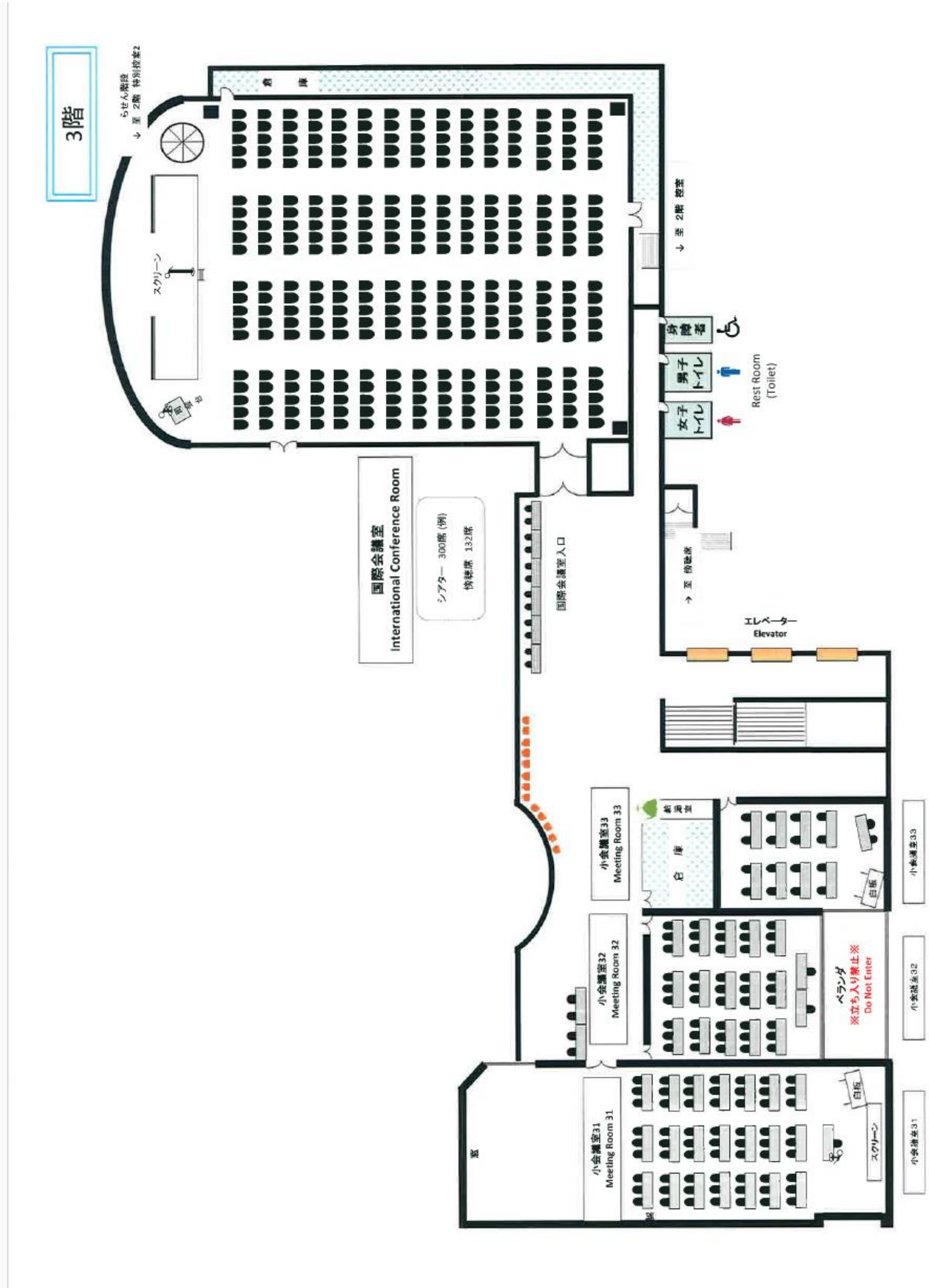
3階
国際会議室
International Conference Room
国際会議室入口
Rest Room
(Toilet)
エレベーター
Elevator
小会議室33
Meeting Room 33
小会議室32
Meeting Room 32
小会議室31
Meeting Room 31
ベランダ
Do Not Enter

Motion-Data Driven Grasp/Assembly Planner

Kensuke Harada[12], Natsuki Yamanobe[2], Weiwei Wan[12]
Kazuyuki Nagata[2], Ixchel G. Ramirez-Alpizar[1], and Tokuo Tsuji[3]
1 Graduate School of Engineering Science, Osaka University, 1-3 Machikaneyama, Toyonaka 560-8531, Japan

2 Intelligent Systems Research Institute, National Institute of Advanced Industrial Science and Technology(AIST), 1-1-1 Umezono, Tsukuba 305-8568, Japan

3 Institute of Science and Technology, Kanazawa University, Kadoma-cho, Kanazawa 920-1192, Japan

E-mail: harada@sys.es.osaka-u.ac.jp, n-yamanobe@aist.go.jp, wan@sys.es.osaka-u.ac.jp, k-nagata@aist.go.jp, ramirez@sys.es.osaka-u.ac.jp, tokuo-tsuji@se.kanazawa-u.ac.jp

Abstract

This paper proposes a robotic grasp/assembly planner using a database of complex and skillfull motion. In our proposed planner, if a skillfull motion is included in the solution path, motion data included in the database is used.

In this paper, we first explain the three-layered structure of the motion data. Then, we explain the proposed grasp/assembly planner. Finally, we show a numerical example to confirm the effectiveness of our proposed method.

Keywords: Robotic assembly, Motion planning, Skillfull motion, Database.

1. Introduction

In factory environment, industrial robots are expected to assemble a product. However, robotic assembly is difficult since a robot has to assemble a variety of objects. Sometimes, a robot has to realize a very skillfull and complex motion.

On the other hand, this research aims to fully automate the product assembly process and proposes a novel robotic grasp/assembly planner. In conventional grasp/assembly planners, we simultaneously planned the grasping posture of a part, the assembly sequence and the motion of a robot. However, conventional grasp/assembly planners can just realize a series of pick-and-place motion of a robot. For the purpose of realizing more complex and skillfull motion by using a grasp/assembly planner, we consider incorporating the database of skillfull motion. The motion data can be generated by using several methods such as human motion capture and robotic motion generation methods. Especially, our motion generation tool utilizes the previously proposed three-layered structure of motion data. In our proposed grasp/assembly planner, if the solution path includes complex and skillfull motion, such motion is realized by using the database of skillfull motion.

This paper briefly outlines our novel grasp/assembly planner using the motion data and shows a simple numerical example. The rest of this paper is organized as follows; we first explain the three-layered data structure in Section 2. The robotic grasp/assembly planner is explained in Section 3. Application of motion data to the grasp/assembly planner is explained in Section 4. A numerical example is shown in Section 5.

2. Three-Layered Data Structure

In this section, we explain the structure of the motion data and method for storing skillfull motion to the database[1]. An assembly task is composed of multiple task elements where each task element is composed of a set of motion sequence. According to this classification, the first, the second and the third layers are respectively named as "work", "task" and "action" layers. Fig. 1 shows an example of assembly of a toy airplane. Since a single action usually includes multiple objects to be assembled, the object held by a robot is named as the "main object" and the object assembled to the main object is named as the "sub object". The following is a set of information included in the database:

・Motion strategy (A sequence of task/motion)
・Human (Identified name etc.)
・Robot (Name, type, hand)
・Object Name
・Object category (e.g., JICFS code)
・Object shape
・Object parameters (Mass, CoG, material, stiffness, etc.)
・Grasping configuration (Main object)
・Fixture configuration (Sub object)
・Time series of the main object's pose w.r.t the sub object
・Control method and its parameters
・Force information applied by the hand

The data can be obtained by several methods such as a human motion capture and a motion generation tool. The data is stored in the YAML format where some examples are shown in Fig. 1.
On the other hand, we have constructed a software tool manually constructing a skillfull motion and store it to the database [1]. Among the three-layered structure of database, our proposed grasp/assembly planner especially uses the action data corresponding to the edge of the AND/OR graph of assembly which will be explained in the next section.

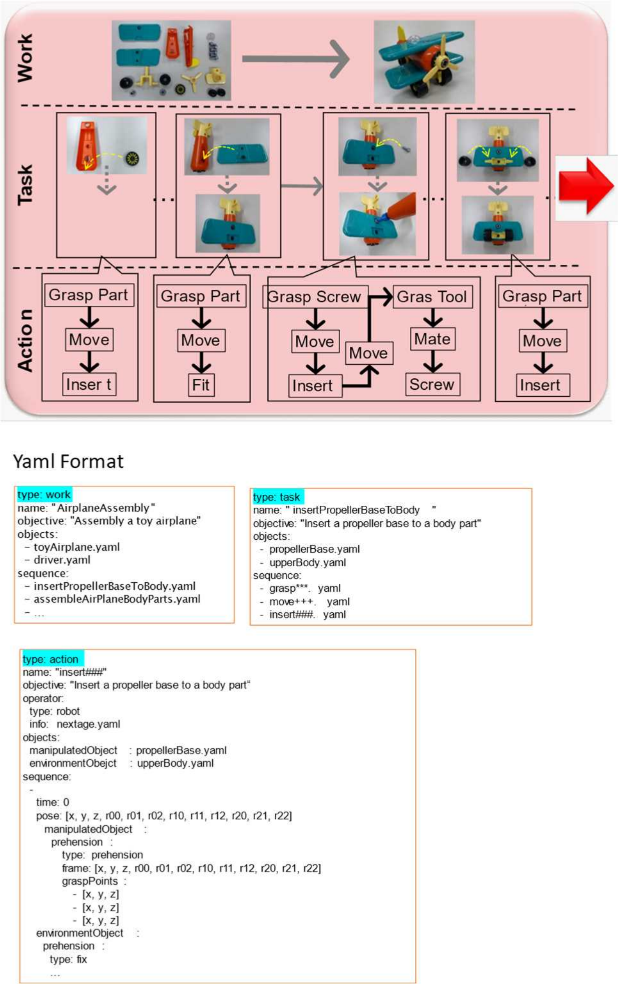

Fig. 1 Three Layered Data Structure and Data Expression using YAML Format

3. Grasp/Assembly Planner Definition

This section shows the overview of the grasp/assembly planner which has proposed in [2,3]. Let us consider a product composed of m parts $P=(P_1,\cdots,P_m)$. Let us also consider assembly of parts by $C=(C_1,\cdots,C_r)$. For example, the assembly C_l composed of the parts P_u, P_v, and P_w can be defined as

$$C_l = \{(P_u, P_v, P_w), (\boldsymbol{T}_{uv}, \boldsymbol{T}_{uw}), (\boldsymbol{n}_{uv}, \boldsymbol{n}_{uw})\} \tag{1}$$

where T_{uv} and $\boldsymbol{n}_{uv}$ denote the homogenous matrix and the approach vector, respectively, of P_v relative to P_u used for an assembly task.

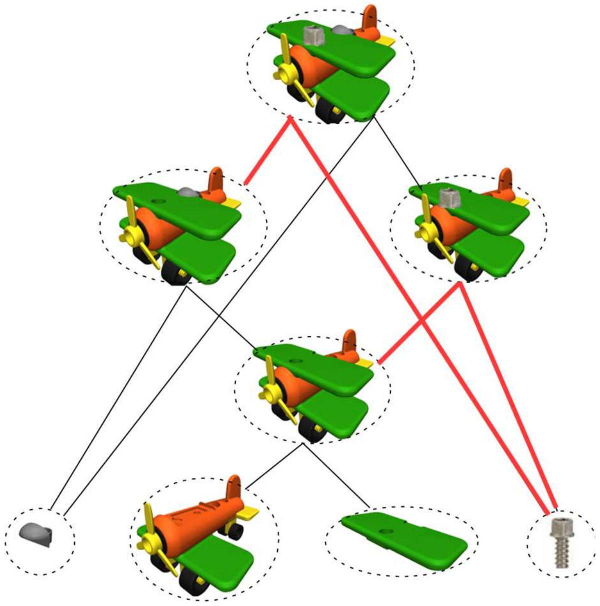

Fig. 2 AND/OR graph of our assembly task where the red lines denote the edges with which the action data is associated.

To assemble a product, a gripper has to grasp an assembly of parts. We consider a set of n grippers $H = (H_1, \cdots, H_n)$ where H_j denotes the j-th gripper. We consider using a grasp planner to calculate a grasping posture where G_{ljk} denotes the k-th grasping posture of the assembly C_l by the gripper H_j. By iteratively calculating grasping posture with changing the approach position, we consider constructing a set of grasping postures $G_{lj}=(G_{lj1}, \cdots, G_{ljk})$ of the assembly C_l grasped by the gripper H_j.

Every possible assembly sequence can be expressed by using the AND/OR graph $G(V, E)$ where the node V is composed of the assembly of parts C_l, $l = 1, \cdots, r$ (Fig. 2). In the grasp/assembly planner introduced in this section, we assume that the AND/OR graph is defined in advance. To obtain robot motion to assemble a given product, we first solve the AND/OR graph[4,5] and obtain a possible assembly sequence. Then, we consider constructing the manipulation graph from the assembly sequence including a set of grasping posture. By solving the manipulation graph, we simultaneously plan grasping posture and robot motion. The method is detailed in our previous papers [2,3].

4. Application of Assembly Motion Data

The grasp/assembly planner explained in the previous subsection just can realize a series of pick-and-place motion. We consider extending this grasp/assembly planner for more complex tasks by using the database of skillfull assembly motion data. In the AND/OR graph shown in Fig.2, the wing is picked by the gripper and put on the body, and then the cockpit can be picked and put on the wing. However, the bolt cannot be assembled to the wing just by using a pick-and-place motion. The edges marked in red shows that the assembly motion data is required for realizing this assembly sequence. We consider associating the action Yaml file corresponding to this assembly sequence. To obtain an assembly sequence, we consider solving the AND/OR graph. If an action Yaml file is associated to the solution edge, we consider using the action Yaml file to generate the robot motion. Otherwise, we consider constructing the manipulation graph and solving it to obtain the robot motion.

5. Result

We consider performing the robotic assembly of a toy airplane. We prepared the skillfull motion of the robot rotating the bolt stored in the database by the YAML format. We first obtained the solution path of the AND/OR graph. Since the solution path includes the screwing motion of the bolt, we used the action YAML data of the screwing motion. The result is shown in Fig. 3. As shown in the figure, when the robot assembles the bolt to the wing, the robot tries to rotate the bolt by using the task motion data.

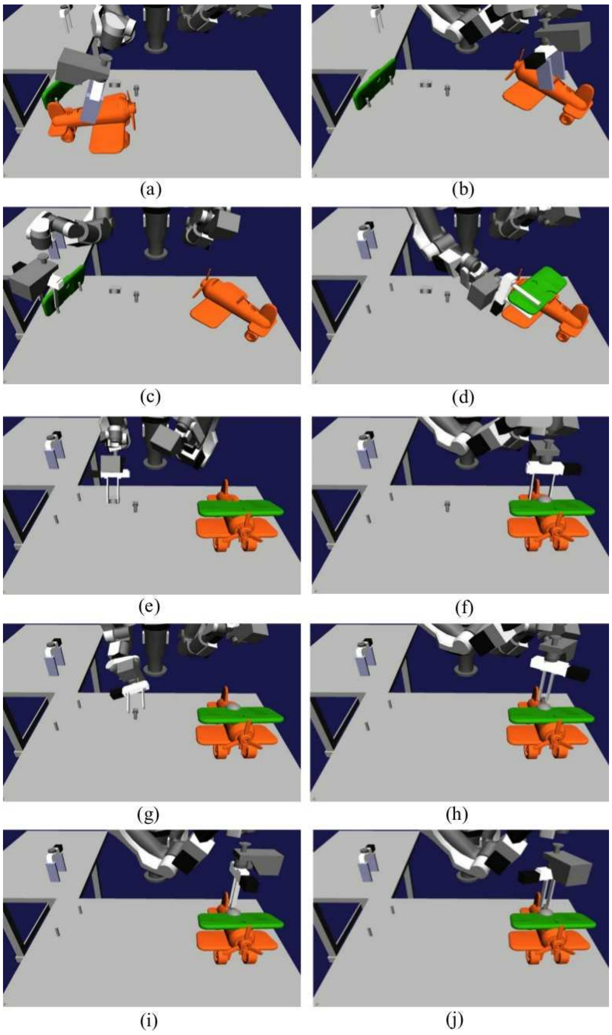

Fig. 3 Simulation result of toy airplane assembly

6. Conclusions

In this paper, we proposed a motion-data driven robotic grasp/assembly planner. A motion data includes an information on skillfull motion which cannot simply be realized by using conventional grasp/assembly planners. This paper first explained the structure of motion data. Then, we explained the proposed grasp/assembly planner. Finally, we showed a numerical example of a toy airplane assembly.

Acknowledgements

This research was conducted under the support of NEDO AI-Robotics Project.

References

1. N. Yamanobe, T. Tsuji, K. Harada, K. Nagata, R. Hanai, and W. Wan, and I.G. Ramirez-Alpizar, "Construction of Cloud Database for Task Motion Generation", *Annual Conf. on the Robotics Society of Japan*, 2016.
2. K. Harada, K. Nakayama, W. Wan, K. Nagata, N.Yamanobe, T. Tsuji, and I.G. Ramirez-Alpizar, "Tool Exchangeable Grasp/Assembly Planner", *Proc. of Int. Conf. on Intelligent Autonomous Systems*, 2018.
3. W. Wan and K. Harada, "Developing and Comparing Single-arm and Dual-arm Regrasp," *Robotics and Automation Letter*, vol. 1, no. 1, pp. 243-250, 2016.
4. L.S.M. de Mello and A.C. Sanderson, "And/Or Graph Representation of Assembly Plans", *CMU Research Showcase*, CMU-RI-TR-86-8, 1986.
5. L.S.M. de Mello and A.C. Sanderson, "Automatic Generation of Mechanical Assembly Sequences", *CMU Research Showcase*, CMU-RI-TR-88-19, 1988.
6. T. Siméon, J.P. Laumond, J, Cortés, and A. Aahbani", Manipulation Planning with Probabilistic Roadmaps", *Int. J. Robotics Research,* vol.23, no.7-8, pp.729-746, 2004.
7. K. Harada, T. Tsuji, and J.-P. Laumond, "A Manipulation Motion Planner for Dual-arm Industrial Manipulators", *Proc. of IEEE Int. Conf. on Robotics and Automation*, pp. 928-934, 2014.

Toward Life with Partner Robots
:
Developing robots with the field trial toward the practical use

Masanori Sugiyama
Toyota Motor Corporation, 1 Toyota-cho
Toyota, Aichi 471-8571, Japan

E-mail: masanori_sugiyama@mail.toyota.co.jp
www.toyota-global.com

Abstract

In the near future, robots are expected to be utilized as partners to coexist with people for various social needs. TOYOTA is developing robots aimed to help societies. As a first step, rentals of a rehabilitation robot for walking training at medical institutions have been launched in 2017. Another robot, Human Support Robot, which is aimed for use to support daily living, has been adopted as a standard platform of the domestic environment league at the RoboCup competition since 2017. For the robot development, it is important to learn deeply about the field which the robot is to be actually used. In this presentation, we will show the scene of the field trial toward the practical use of our robots. Also, we will introduce a humanoid robot which is integrated with advanced technologies that would benefit us in the future.

Keywords: robot, rehabilitation, walking, training, humanoid

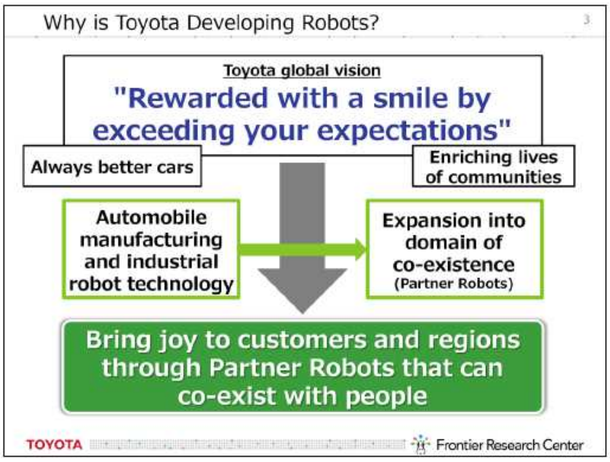

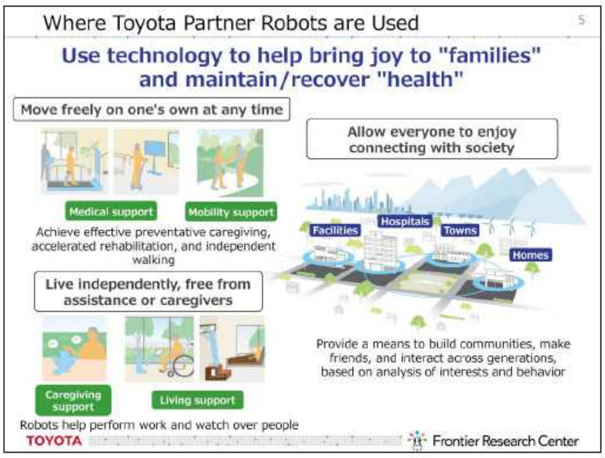

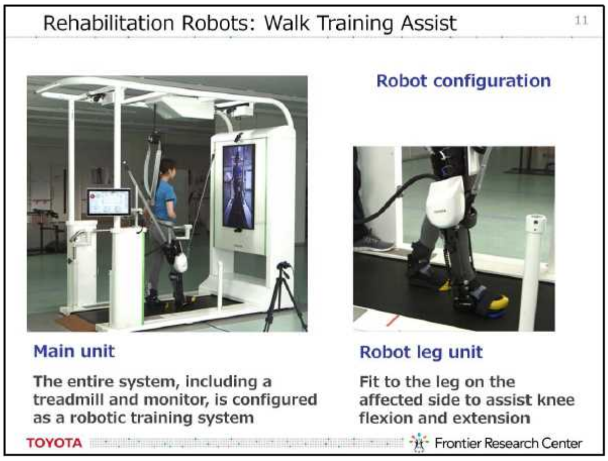
Rehabilitation Robots: Walk Training Assist
11
Robot configuration
Main unit
The entire system, including a treadmill and monitor, is configured as a robotic training system
Robot leg unit
Fit to the leg on the affected side to assist knee flexion and extension
TOYOTA
Frontier Research Center

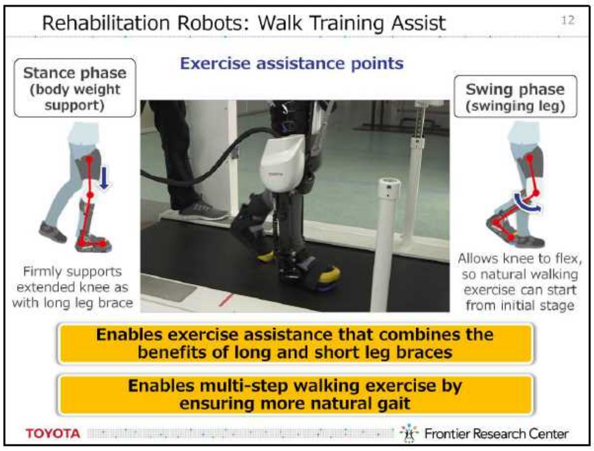
Rehabilitation Robots: Walk Training Assist
12
Exercise assistance points
Stance phase (body weight support)
Swing phase (swinging leg)
Firmly supports extended knee as with long leg brace
Allows knee to flex, so natural walking exercise can start from initial stage
Enables exercise assistance that combines the benefits of long and short leg braces
Enables multi-step walking exercise by ensuring more natural gait
TOYOTA
Frontier Research Center

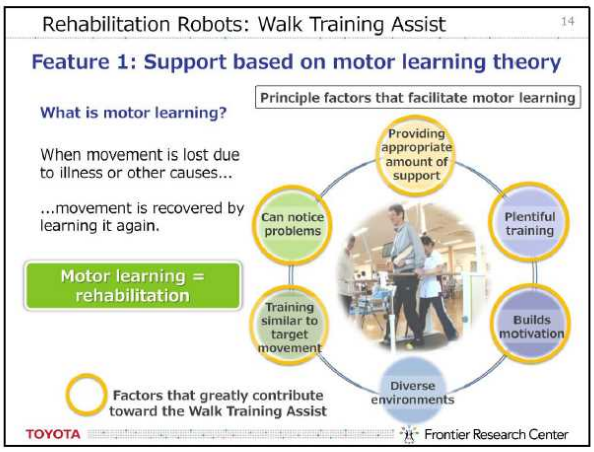
Rehabilitation Robots: Walk Training Assist
14
Feature 1: Support based on motor learning theory
What is motor learning?
Principle factors that facilitate motor learning
When movement is lost due to illness or other causes...
...movement is recovered by learning it again.
Motor learning = rehabilitation
Providing appropriate amount of support
Plentiful training
Builds motivation
Diverse environments
Training similar to target movement
Can notice problems
Factors that greatly contribute toward the Walk Training Assist
TOYOTA
Frontier Research Center

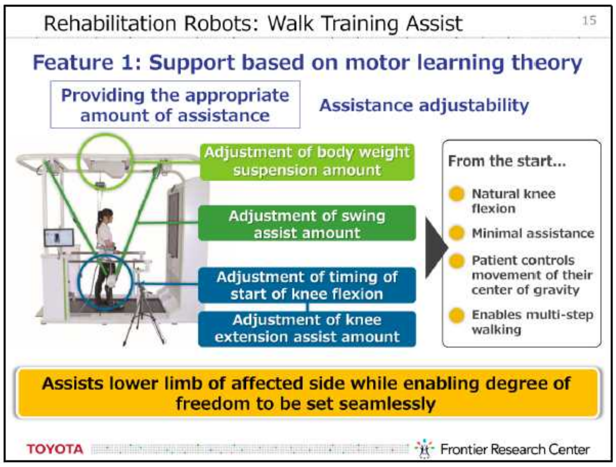
Rehabilitation Robots: Walk Training Assist
15
Feature 1: Support based on motor learning theory
Providing the appropriate amount of assistance
Assistance adjustability
Adjustment of body weight suspension amount
Adjustment of swing assist amount
Adjustment of timing of start of knee flexion
Adjustment of knee extension assist amount
From the start...
Natural knee flexion
Minimal assistance
Patient controls movement of their center of gravity
Enables multi-step walking
Assists lower limb of affected side while enabling degree of freedom to be set seamlessly
TOYOTA
Frontier Research Center

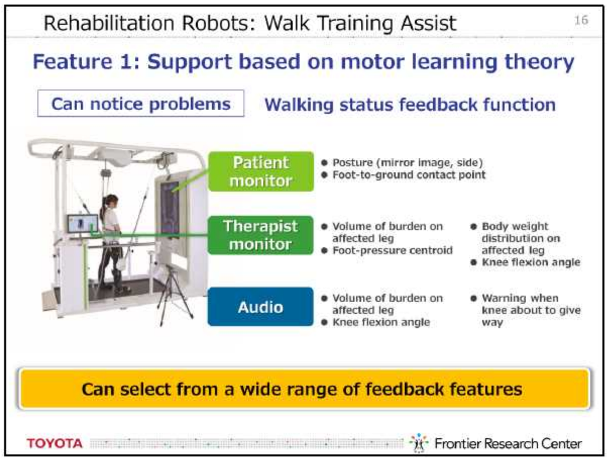
Rehabilitation Robots: Walk Training Assist
16
Feature 1: Support based on motor learning theory
Can notice problems
Walking status feedback function
Patient monitor
Posture (mirror image, side)
Foot-to-ground contact point
Therapist monitor
Volume of burden on affected leg
Foot-pressure centroid
Body weight distribution on affected leg
Knee flexion angle
Audio
Volume of burden on affected leg
Knee flexion angle
Warning when knee about to give way
Can select from a wide range of feedback features
TOYOTA
Frontier Research Center

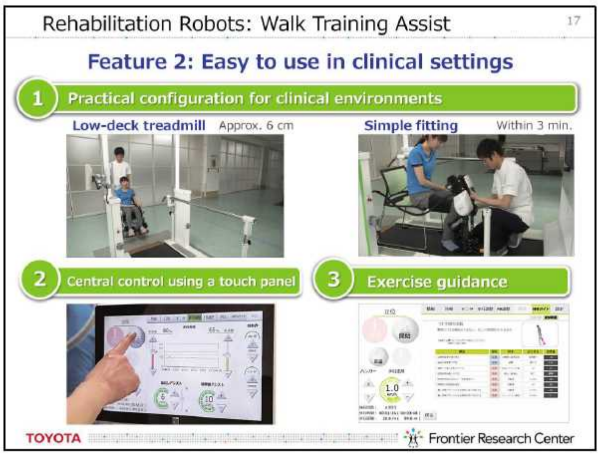
Rehabilitation Robots: Walk Training Assist
17
Feature 2: Easy to use in clinical settings
1 Practical configuration for clinical environments
Low-deck treadmill Approx. 6 cm
Simple fitting Within 3 min.
2 Central control using a touch panel
3 Exercise guidance
TOYOTA
Frontier Research Center

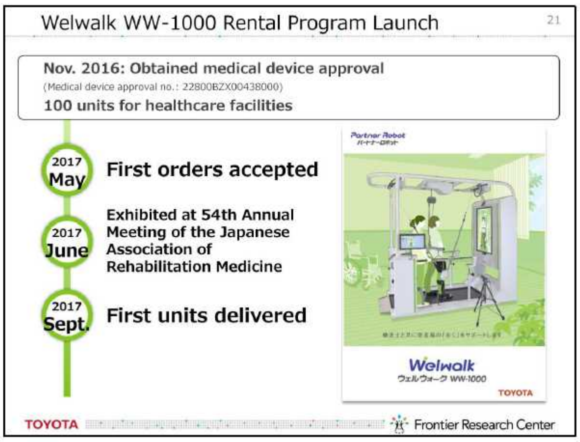
Welwalk WW-1000 Rental Program Launch
21
Nov. 2016: Obtained medical device approval
(Medical device approval no.: 22800BZX00438000)
100 units for healthcare facilities
2017 May
First orders accepted
2017 June
Exhibited at 54th Annual Meeting of the Japanese Association of Rehabilitation Medicine
2017 Sept.
First units delivered
Welwalk
ウェルウォーク WW-1000
TOYOTA
TOYOTA
Frontier Research Center

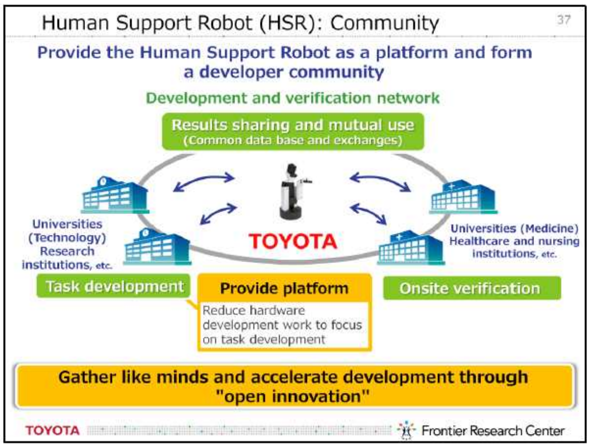
Human Support Robot (HSR): Community
37
Provide the Human Support Robot as a platform and form a developer community
Development and verification network
Results sharing and mutual use
(Common data base and exchanges)
Universities (Technology) Research institutions, etc.
TOYOTA
Universities (Medicine) Healthcare and nursing institutions, etc.
Task development
Provide platform
Onsite verification
Reduce hardware development work to focus on task development
Gather like minds and accelerate development through "open innovation"
TOYOTA
Frontier Research Center

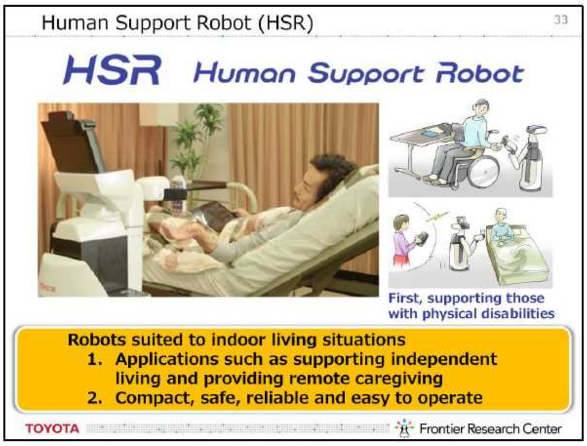
Human Support Robot (HSR)
33
HSR Human Support Robot
First, supporting those with physical disabilities
Robots suited to indoor living situations
1. Applications such as supporting independent living and providing remote caregiving
2. Compact, safe, reliable and easy to operate
TOYOTA
Frontier Research Center


RoboCup World Tournament: Team Competing with HSR
40
A team formed by The University of Electro-Communications and Tamagawa University used the HSR to compete in the 2016 RoboCup @Home World Tournament
RoboCup 2016
LEIPZIG GERMANY
30 JUNE to 3 JULY COMPETITIONS
4 JULY SYMPOSIUM
Won fourth place in the final competition (out of 23 teams) and an Innovation Award
TOYOTA
Frontier Research Center

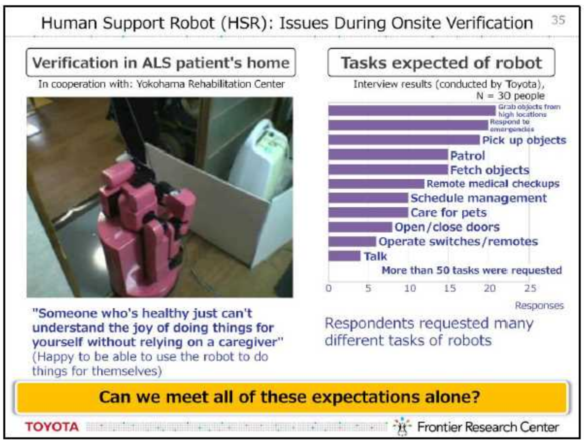
Human Support Robot (HSR): Issues During Onsite Verification
35
Verification in ALS patient's home
In cooperation with: Yokohama Rehabilitation Center
Tasks expected of robot
Interview results (conducted by Toyota), N = 30 people
Grab objects from high locations
Respond to emergencies
Pick up objects
Patrol
Fetch objects
Remote medical checkups
Schedule management
Care for pets
Open/close doors
Operate switches/remotes
Talk
More than 50 tasks were requested
0 5 10 15 20 25
Responses
"Someone who's healthy just can't understand the joy of doing things for yourself without relying on a caregiver"
(Happy to be able to use the robot to do things for themselves)
Respondents requested many different tasks of robots
Can we meet all of these expectations alone?
TOYOTA
Frontier Research Center

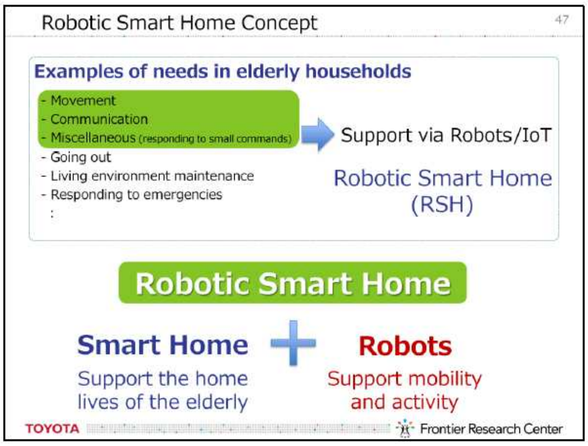
Robotic Smart Home Concept
47
Examples of needs in elderly households
- Movement
- Communication
- Miscellaneous (responding to small commands)
- Going out
- Living environment maintenance
- Responding to emergencies
:
Support via Robots/IoT
Robotic Smart Home (RSH)
Robotic Smart Home
Smart Home
Support the home lives of the elderly
Robots
Support mobility and activity
TOYOTA
Frontier Research Center

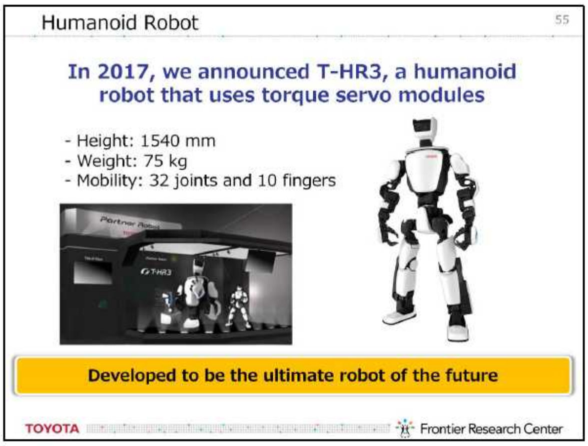
Humanoid Robot
55
In 2017, we announced T-HR3, a humanoid robot that uses torque servo modules
- Height: 1540 mm
- Weight: 75 kg
- Mobility: 32 joints and 10 fingers
T-HR3
Developed to be the ultimate robot of the future
TOYOTA
Frontier Research Center

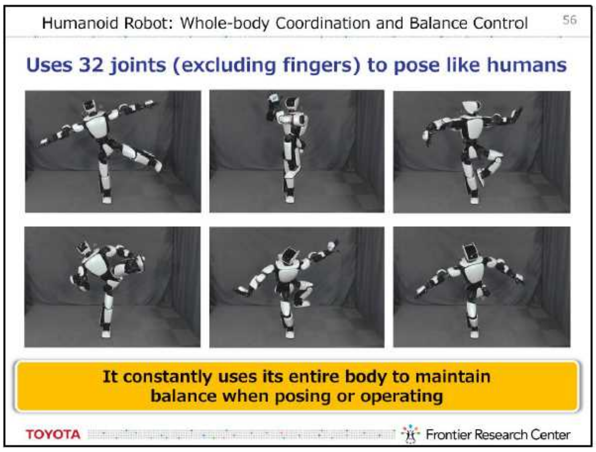
Humanoid Robot: Whole-body Coordination and Balance Control
56
Uses 32 joints (excluding fingers) to pose like humans
It constantly uses its entire body to maintain balance when posing or operating
TOYOTA
Frontier Research Center

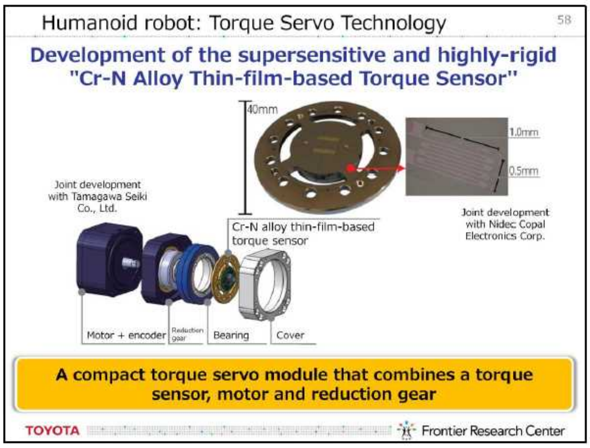
Humanoid robot: Torque Servo Technology
58
Development of the supersensitive and highly-rigid "Cr-N Alloy Thin-film-based Torque Sensor"
40mm
1.0mm
0.5mm
Joint development with Tamagawa Seiki Co., Ltd.
Cr-N alloy thin-film-based torque sensor
Joint development with Nidec Copal Electronics Corp.
Motor + encoder
Reduction gear
Bearing
Cover
A compact torque servo module that combines a torque sensor, motor and reduction gear
TOYOTA
Frontier Research Center

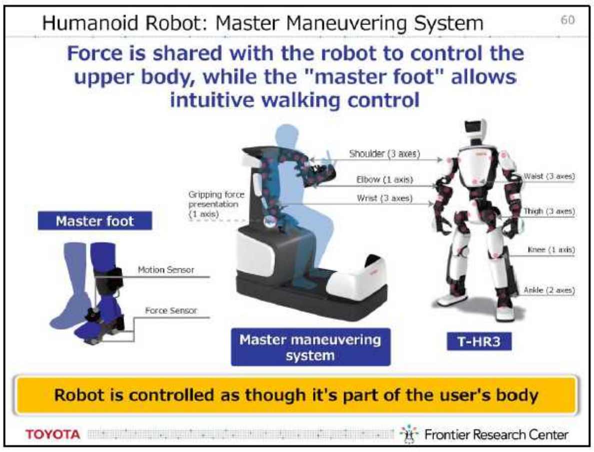
Humanoid Robot: Master Maneuvering System
60
Force is shared with the robot to control the upper body, while the "master foot" allows intuitive walking control
Master foot
Motion Sensor
Force Sensor
Gripping force presentation (1 axis)
Shoulder (3 axes)
Elbow (1 axis)
Wrist (3 axes)
Waist (3 axes)
Thigh (3 axes)
Knee (1 axis)
Ankle (2 axes)
Master maneuvering system
T-HR3
Robot is controlled as though it's part of the user's body
TOYOTA
Frontier Research Center


Humanoid Robot: Master Maneuvering System
61
TOYOTA
Frontier Research Center

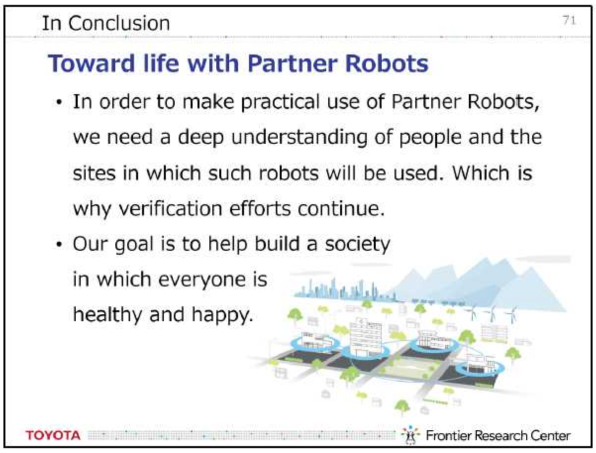
In Conclusion
71
Toward life with Partner Robots
• In order to make practical use of Partner Robots, we need a deep understanding of people and the sites in which such robots will be used. Which is why verification efforts continue.
• Our goal is to help build a society in which everyone is healthy and happy.
TOYOTA
Frontier Research Center

Engineering Modular Playware

Henrik Hautop Lund, Morten Roed Frederiksen, Massimiliano Leggieri
Center for Playware, Technical University of Denmark, Building 326, 2800 Kgs. Lyngby, Denmark

E-mail: hhl@playware.dtu.dk
www.playware.elektro.dtu.dk

Abstract

In this paper, we describe the engineering of modular playware. Constructing playware systems out of individual modules allows the system to be easily transported to be used anywhere, to easily build different bodies and brains, and to allow people to construct and combine the modules in a creative fashion. Thus the modularity helps fulfilling the Playware ABC. We exemplify the engineering challenges of the hardware, software and communication design of modules through the development of handheld modules for playful rehabilitation. The handheld modules allow for a fun and motivational training of upper extremities, and can be viewed as an extension to the Moto Tiles for lower extremity training, which have proved to be a highly successful playware for prevention and rehabilitation among seniors. The paper outlines the engineering challenges and proposed solutions to make such modular playware for playful upper extremity training.

Keywords: Playful technology, Playware, Personal Health Technology, Adaptive Games.

1. Introduction

Playware is defined as intelligent hardware and software that creates play and playful experiences for users of all ages [1, 2], and such playware has been developed for a number of application areas including rehabilitation [3, 4, 5]. Within this area of application, the playware for rehabilitation can be viewed as games for health, though playware puts primary focus on play rather than on games. Playware objects are often designed to match the plug-and-play mentality of modular technology, since such design strategies help facilitate the realization of the concepts of Playware ABC. The Playware ABC entails developing technology for Anybody, Anywhere, Anytime by Building Bodies and Brains, which facilitates that users can Construct, Combine, and Create [6].

Approaching the constructing of playware systems with a focus on modularity, allows the systems to be easily distributed and put to use anywhere, to easily build different bodies and brains, and to allow people to construct and combine the modules to become creative. Hence, modularity often helps when aiming to fulfill the Playware ABC.

Modular playware units act as interactive nodes in a network. The control of the modules can be either fully contained in the embedded systems modules themselves, or the control can, for instance, be divided between on-board control on the embedded system modules and control from a network connected smart device, e.g. tablet or smartphone. In the latter case, communication from the smart device to a server backbone may provide the possibility of data collection and data analysis. In the work presented here, we investigate this latter case and thereby the engineering research examines the division of control between the individual modules and the smart device, and the best strategy for robust communication between them. The focus is working on low level software for controlling the embedded systems; along with the investigation of the on-board sensors and actuators of the boards with the objective of providing playware experiences for the users.

One example of this for lower extremity interaction are the Moto Tiles [4, 7]. For upper extremity interaction, we develop and investigate hand-held modular playware devices. More specifically, for Moto Tiles using NordicRF microchips for developing ANT+ radio communication protocols, and for the hand-held devices using ESP microchips, which provide WiFi connectivity between devices as well as between devices and the Android device. The Internet of Things has opened a new world of possibilities by using protocols that have been around us for a while, such as TCP/IP. The abovementioned ESP chips currently have become the most inexpensive and most accessible choice for this kind of projects involving WiFi communications. Furthermore, the amount of energy consumed by the device, places it as an efficient utility for low-energy and low-cost working contexts. However, using the ESP modules poses a challenge for both the embedded software and the client systems that communicates with them, as they can be error prone and sometimes proves unreliable in fast connect-disconnect scenarios.

Hence the following questions arise:

- What are the software measures needed in order of working around the unpredictability of using inexpensive modules for swift real time communication?
- How can such communication between modular devices be used to create a playware experience by interacting with the users?
- Which sensory modalities and HW implementations can be used reliably to track simple upper body movements in a manner as robust as seen from the sensors of the Moto Tiles in order to provide an equally robust interactive playware e.g. for the elderly performing upper extremity play?

By answering these questions through our research and achieving robust, simple fault tolerant communication between hardware modules, we aim to develop a methodology for designing and adapting playware game activities to motivate people to perform the desired actions. The research methodology [8] is based on iterative prototyping, along with prototyping and testing in laboratory conditions with external probands. Hence, knowledge is built from iterations of synthesis and application. Here, Moto Tiles serves as an example at a much later iteration stage than the hand-held modules at an earlier iteration stage of rapid prototyping, illustrating the research methodology and implementation.

2. Rehab app with handheld modules

The goal of this application is to engage the elderly generation in pulse-increasing activities while having fun. It specifically targets the solar plexus area and focuses on accurate arm movements in a fun and motivating setting, utilizing modules that can be used by Anybody, Anywhere, Anytime according to the Playware ABC (see Fig. 1).

Hardware setup

The current setup consists of custom built ESP modules running NODEMCU/Arduino firmware with custom tailored components to facilitate communication over WiFi. An external barometric pressure-meter has been added to the board to approximate the pressure at different altitude levels. The hardware sensors employed in this project consists of: raw accelerometer data from an onboard accelerometer, and barometric pressure data. In details, we use:

- The ESP8266 Tetra module, which is a low-cost Wi-Fi microchip at 80MHz with 32 kB memory for instruction and 80 kB for user data.
- The Adafruit BME280 I2C Temperature Humidity Pressure Sensor, which measures humidity with ±3% accuracy, barometric pressure with ±1 hPa absolute accuracy (used for altimeter), and temperature with ±1.0°C accuracy. It has a low altitude noise of 0.25m and a fast conversion time.
- The Adafruit 9-DOF Absolute Orientation IMU Fusion Breakout - BNO055, which provides a MEMS accelerometer, magnetometer and gyroscope on a single die with a high speed ARM Cortex-M0 based processor to digest all the sensor data, abstract the sensor fusion and

real time requirements away, and e.g. provide sensor data such as Absolute Orientation (Euler Vector, 100Hz), Three axis orientation data based on a 360° sphere, Absolute Orientation (Quaterion, 100Hz), Angular Velocity Vector (100Hz), Three axis of gravitational acceleration (minus any movement) in m/s^2.

Software setup

ESP firmware

The current iteration of the ESP firmware is utilized towards sending as much sensor data each second as possible. Original versions of the firmware were designed to be more versatile with incoming socket connections to accept incoming messages. However, to gain most of our sensors, the later versions skipped this part and focuses solely on sending out as much information as possible. The cycle is as follows:

1) Once turned on, the ESP module attempts to connect to previously stored WIFI access point.
2) If it fails it will become a hotspot itself and can be accessed at http:://192,168.4.1. Here it attempts to discover any nearby WiFi access points and lets the user select them from a given list. Any selected point is stored along with a user-entered password.
3) When it successfully connects to an access point, it broadcasts its services via MDNS/Bonjour protocols and can be discovered by a client.
4) When a client connects via the MDNS address to the outgoing TCP socket at port 8885, it sends out all given sensor data until the socket connection is broken.
5) The current format for the data transfer is JSON.

Client software

The device(s) is discovered via MDNS browsing software that basically scans the dans after ".local" addresses that match the service profile. Any found device is passed off to a handler thread that establishes the connection. The thread connects to the socket address at port 8886 and starts reading data. Once a complete JSON string is received it is parsed and added to a buffer-queue with sensor readings. The client software was developed both in JAVA for android devices as well as in SWIFT for IOS devices. Both platforms performed equally well in similar fashion.

Improving the level of fault tolerance

During the testing phase of the development of the playware modules, various errors were encountered in different phases of the process flow. Randomly the ESP modules they would fail to detect various onboard sensors during the initialization startup phase. To counter that, a measure was implemented to automatically restart the device, for the state where not all hardware checks had been passed. This could result in a never ending reset loop, so a visual cue was added to indicate the device startup phase (blinking led lights). This meant that a user could manually switch the device off and on again if the automatic restart did not solve the problem.

At the connection phase the modules would arbitrarily fail to connect multiple times. The source of this error might have been interference from other WiFi signals, however this was not verified. As a simple solution, the ESP firmware would allow two attempts at reconnecting before initiating the state WiFi access point. Defining the amount of reconnect attempts that should be allowed, is a tradeoff between how quickly the user should be able to reconfigure the device for a new working context, and how robust the connection phase should seem for an already configured device. Sometimes the ESP devices would disconnect the socket connections without any indication in the embedded software. To resolve that problem, an implementation of idle counters was added to both client and embedded software parts to see whether any data was transmitted or not. If no data was transmitted above a specified threshold amount of times, the ESP modules would enter idle mode and start re-accepting incoming socket connections. The client software would in such case attempt to ping the device to investigate whether the device was still connected to the same network. If the device answered, the client would reconnect. If the device was unresponsive the client notified the user that a module had disconnected.

3. Motion interpretation

The data gathered from the specific sensors are translated into specific movement patterns in two isolated steps. Some parts of the data received from the sensors are rather not precise and needs to be averaged before they can be used. The two steps are detailed in the subsequent sections.

Step 1 Averaging the data

We experimented with different buffer sizes to find a suitable match between speed and accuracy. We measured single runs of each step of the algorithm and found that each iteration takes about 20ms to complete letting us read complete samples at 50hz. However, some fitness arm movements are a lot swifter than a second so we opted for a buffer of 40 samples with a moving frame which seemed to fit our needs. All samples are averaged and we calculate the following data points:

• Average acceleration across x,y,z axis.
• Average rotation across roll, pitch, and yaw.
• Average altitude. Note that this number is already filtered on the ESP device as well using an average of 22 samples.
• A boolean value that determines whether a user defined acceleration threshold has been reached.
• A direction of altitude movement UP, DOWN or LEVEL based on the last 25 calculated average altitudes. If all but three values fall in one category it is determined that a movement in that direction happened.

For the altimeter data, we employed low pass filtering on all raw samples as well as the averages to hinder highly fluctuating output. Note that the sensors are placed inside a ball, why it makes sense to discard x,y, and z as isolated data.

Step 2 Using the information in a health setting.

The system obtains information on roughly what altitude the module is held (with occasional spiking errors), and if it is rotated or not. We employ all these features in a setting that captures the user's imagination (They believe they're tracked 1:1) and at the same time allows a certain movement freedom.

A separate thread handles all movement verification to allow the fetcher thread to gather data as fast as possible. With each looping round it fetches the calculated movement status. A target arm positional state is randomly selected for each controller: UP, DOWN or SIDE and different movement patterns are expected for each of them.

Example - target state UP:

For this state to trigger we expect the user to lift his or hers arm. This entails moving the module up a bit, rotating it a bit and keeping it still at a certain height. These are the signs we look for. With each iteration/measure, we see if the module has rotated. If it has, we increment the rotation counter. Once this value surpasses a fitting threshold, we set a HasRotated value to true. The same goes for correct altitude changes (we make sure the ball moves upwards). Once moved and rotated we expect the user to hold the ball still at the same level.

When that has occurred we accept the target as reached and resets the cycle with a new target state. Note that we could employ pitch, yaw and roll values for each position to assist the algorithm but we found that people shift their wrists around too much when they hold objects, making it impossible to determine if a target position has be reached using that specific data. It simply shifts around too much. The algorithm works well when the values and threshold have been fine tuned so the user don't have to hold still in outer positions too long. In such cases where the algorithm reacts slowly it gets hard to complete longer workouts.

We acknowledge that such slowness holds a certain fitness value, that might suit another perhaps younger audience. All in all the algorithm seems to fit well for the target audience, in that it is very forgiving for people that might not be able to reach outer arm positions or lack strength to move swiftly.

Step 3 game implementation

To make the game fun we have added a very simple scoring system that increments a counter for each correct position reached individually for each arm. As the game is started a progress counter starts crawling across the screen. In 30 seconds the player has to complete as many arm positions as possible. The final score depicts an ability to perform movements and stay coordinated in a stressing situation. It gets increasingly harder when two controllers are used with different target positions for each arm. To facilitate training also the disabled, the game works just as well with a single controller.

Fig 1. Playing the rehab game for upper extremity training with two playware modules in the form of handheld balls.

Fig 2. The interface on the tablet when playing the rehab game for upper extremity training with two playware modules.

4. Future iteration and extension modules

With the calculated sensor data, there are no limits to the type of fitness games that we can make using the relative simple building stones of subsequently employed movements. For this game a high score of multiplayer component would be ideal but the real strength lies in how easy it is to pickup and start using. A developer kit has been made available for computer science classes to develop their own applications with the module and client software.

Fig 3. The tablet interface showing score.

References

1. H. H. Lund, and C. Jessen, "*Playware - Intelligent technology for children's play,*" Technical Report TR-2005-1, June, Maersk Institute, University of Southern Denmark, 2005.
2. H.H. Lund, T. Klitbo, and C. Jessen, "Playware Technology for Physically Activating Play", *Artificial Life and Robotics Journal*, 9:4, 165-174, 2005
3. H. H. Lund, "*Play for the Elderly - Effect Studies of Playful Technology," in Human Aspects of IT for the Aged Population. Design for Everyday Life*. (LNCS Vol. 9194, pp 500-511, Springer-Verlag, 2015)
4. H. H. Lund, and J. D. Jessen, "Effects of short-term training of community-dwelling elderly with modular interactive tiles," *GAMES FOR HEALTH: Research, Development, and Clinical Applications*, 3(5), 277-283, 2014.
5. H.H. Lund, M.D. Pedersen, R. Beck, "Modular robotic tiles: Experiments for children with autism", *Artificial Life and Robotics, 13,* pp. 393-400, 2009.
6. H. H. Lund, H.H. "Playware ABC: Engineering Play for Everybody." *Journal of Robotics Networks and Artificial Life*, *3*(4), 2017
7. http://www.moto-tiles.com (checked: 6/12/2018)
8. H. H. Lund. "Playware Research–Methodological Considerations". *Journal of Robotics, Networking and Artificial Life*, *1*, pp.23-27, 2014

User-Friendly Robotics 3 - Playware

Henrik Hautop Lund, Luigi Pagliarini
Center for Playware, Technical University of Denmark, Building 326, 2800 Kgs. Lyngby, Denmark

E-mail: hhl@playware.dtu.dk luigipagliarini@gmail.com
www.playware.elektro.dtu.dk

Abstract

The design of playware based on the lessons learned from user-friendly robotics suggests a focus on a number of design criteria to help achieving playware systems that can and will be used according to the Playware ABC by anybody, anywhere, anytime. The design criteria are described in this paper, and they include: modularity, explicit immediate feedback, robustness, simplicity, one-click, design. Each criterion is described based on the lessons learned from user-friendly robotics. We exemplify the use of these design criteria with the development of the playware system, Moto Tiles. The Moto Tiles system is designed as a playful prevention and rehabilitation system for seniors, who are normally not exposed to such high technology systems. The paper discusses how the design criteria allowed for a successful design of a user-friendly system, which is now used daily by tens of thousands seniors all over the globe.

Keywords: Playful technology, Playware, Personal Health Technology, User-friendly robotics, Seniors.

1. Introduction

The studies of User-Friendly Robotics [1, 2] led to understanding of how to create interactive technology, which is targeted everyday users who have no prerequisite to understand technological subjects such as robotics and AI. In a number of cases as with the LEGO Mindstorms robots, these users were young children. From a methodological point of view, the background idea is that developing user-friendly systems for young children also leads to an understanding on how to create equally user-friendly systems for any other age group and any other user group with little knowledge of technology.

Indeed, it is interesting how lessons learned from developing user-friendly robotics can be applied to other areas for other users. Based on the developed knowledge, we founded the area of playware. Playware is defined as intelligent hardware and software that creates play and playful experiences for users of all ages [3, 4]. With playware, the technology acts as a play force, which pushes the user into a play dynamics. It is the interactivity with the physical device (in the form of immediate explicit feedback), as learned from the user-friendly robotics, which can be designed to become the play force.

In the same way as in user-friendly robotics, where simple control and understandable interactivity provides the user with a sense of adequacy and achievement to further interact, the interactivity of the playware provides the user with a push (a play force) for further interactivity with the playware, i.e. the user enters into a play dynamics.

Hence, the playware mediates a playful interaction. In order to best possible take advantage from the learning from user-friendly robotics, we develop playware according to the concept of Playware ABC. The Playware ABC concepts entails developing technology for Anybody, Anywhere, Anytime by Building Bodies and Brains, which facilitates that users can Construct, Combine, and Create [5].

2. Design guidelines

The design of playware based on the lessons learned from user-friendly robotics suggests a focus on a number of design criteria to help achieving playware systems that can and will be used by anybody. These design criteria are:

- modularity
- explicit immediate feedback
- robustness
- simplicity
- one-click
- design
- motivation

Modularity
The modularity is based on the learning from distributed and parallel systems such as the artificial neural network control and evolutionary processes. The distribution becomes physical by allowing systems to be composed on many modules that interact with each other. The overall output of the system becomes the emergent behavior when all the modules are interacting with each other. Essentially, the modules can be viewed as intelligent LEGO bricks, as we designed such in the form of I-Blocks [6]. Later, we showed modules of various types and forms, e.g. [7, 8].

Explicit immediate feedback
In order to make interactivity understandable for any user, it is important that there is a feedback from the interaction of the user, and that this feedback is immediate and explicit. This can be a recognizable visual feedback, e.g. a color change on a tile is touched, or a recognizable auditory feedback, e.g. a music instrument change when a Music Tiles cube is turned.

Robustness
The work with Khepera robots, LEGO Mindstorms robots, VIKI humanoids robots, etc. within user-friendly robotics has shown us that it is of crucial importance to develop systems with a robust hardware. Many robotic systems never leaves the research labs and the prototype stage, because they fail to put emphasis on the robustness, and such robustness is of crucial importance for the interaction with the user. If the system has just the slightest glitch in robustness, then the user will reject the system as not understandable, not user-friendly or as a failure.

Simplicity
In order to achieve the crucial robustness, we have learned to focus on simplicity. It is much better to design a simple system that works with the user than to design a more complex technological system, which then may only work 98% of the time. But designing a simple system is not always easy. Actually, it is often more difficult to create simplicity than to add more complexity to the system. To quote Leonardo da Vinci: “Simplicity is the ultimate sophistication”. The simpler the system is, the easier it is for any user to understand and to interact with.

One-click
Related to the simplicity, we have learned also to focus on one-click interaction, both in terms of the physical interaction with robots and interactive playware, and in terms of software interfaces (apps, web-interfaces, etc.). Whenever possible, we recommend to reduce the clicks/interactions to one in order to facilitate the understanding for everybody, and to be able to provide explicit, immediate feedback.

Design
The design of the system is of utmost importance, when users have to interact with the system. The choice of form, material, look, etc. will influence the user acceptance of the system and the user interaction with the system. It should be clear that the physical design of the LEGO invites certain physical interactions, as well as the design of Moto Tiles, Music Tiles cubes, etc. does. With a functional design, some proposed actions by the user are invited by the design.

Motivation
When designing systems that users should interact with, the lessons learned points to the insight that the first and foremost issue is the user motivation to interact with the

system. If the user is not motivated to interact, then it does not matter how good the technology and innovation is, so creating for the user motivation is essential. This is the reason to look towards play. Play is defined as a free and voluntary activity that you do for no other purpose than the play itself and the enjoyment that it brings you. Hence, people have an intrinsic motivation to play. If such intrinsic motivation can be seen also in the interaction with the designed system, then people will interact with the system out of their own free will and for the pleasure that the interaction brings.

3. Experiments

In accordance with the design guidelines, we have designed a number of playware systems for sport, music, play, education, and health. These include MusicTiles and Music Tiles cubes, I-Blocks, intelligent playgrounds, handheld rehab modules, Moto Tiles, etc.

As an example here, we will look more closely at one of these, namely the Moto Tiles [9, 10, 11, 12], since the Moto Tiles system has recently become quite successful worldwide for prevention and rehabilitation among seniors.

Modularity

The original idea of the Moto Tiles was to create *the LEGO bricks for playful physical interaction*, so by its nature, it would be modular. Indeed, a Moto Tiles system is composed of 10 homogeneous modular tiles, which can be attached together to form different patterns on the floor. The modules are interchangeable, so system support can for instance be as simple as to replace one tile with another tile. Also, if one tile should break, the modularity ensures that the system will still work, in this case with 9 tiles. This is important since this ensures that therapists and care workers are always sure to be able to perform a planned training session with the tiles.

Explicit immediate feedback

The Moto Tiles are designed to provide an immediate feedback. When a tile is pressed, the LED ring on the tile may change colour or turn off to jump to another tile. Also, sound from the tablet provides an immediate feedback that signals to the user that the tile has been pressed. The sound can be a simple click sound, an animal sound, a piano sound, a spoken word, etc. Hence, the system has been designed for different modalities of immediate feedback, which are explicit and make the system interaction easily understandable for the user.

Robustness

The Moto Tiles were developed through a series of prototypes over a decade. Some of the prototypes used IR communication between neighbouring tiles, but to ensure robustness this technological solution was skipped in the final *product* development due to robustness issue with the IR neighbor communication sometimes failing. Even if such failure would only happen rarely, it showed in extensive user tests with the prototypes to hamper the user interaction. Likewise, later rounds of the product development introduced static electricity protection of the tiles at a level much higher than the industrial standard in order to provide further robustness of the system.

Simplicity

For achieving robustness of the Moto Tiles, the product development relied upon the principle of simplicity. For instance, to make the system simple, the use of force sensitive resistor (FSR) sensors was substituted with simple membrane switches, providing an on/off press feature instead of the analog reading from FSR sensors. Likewise, the simplification of not installing IR neighbor communication in between the tiles removed the possibility to do automatic topology recognition of the tiles layout, but provided a simpler solution. Further, the tablet interface was designed to make interaction as simple as possible.

One-click

All GUI interface for the Moto app was made to provide a one-click solution, in order to facilitate that even care workers and seniors would be able to use the system easily. Also the physical tiles were designed to allow operation with a one-click strategy. Hence, to start playing with the Moto Tiles, all the user has to do is 1) turn on the tiles, 2) lay the tiles in a pattern on the ground, 3) turn on the tablet and select the Moto app, 4) select a game and press play. All is optimized to provide a kind of one-click strategy on tiles and tablet.

Design
The design of the Moto Tiles was done in collaboration with designers from Henning Larsen Architects to provide a minimal functional design, and designed for "small is smart". This design gives a system, which is easy to store away, transport and set-up anywhere. The charging station is designed to allow tiles to slide easily in and to be carried away. Further, the sounds for the Moto app are designed with sound designers from D4zed for appropriate and understandable sound feedback.

Motivation
We have designed more than 35 games for the Moto Tiles system. All games are designed to be fun and engaging for the users. The playfulness of the games is always the foremost design criteria for the games, and in an iterative fashion [13], the games are developed and tested extensively with seniors to verify whether they provide enjoyment or if they need adjustments to do so. The enjoyment of the seniors in actual training periods with Moto Tiles is validated through qualitative interviews and quantitative measurements in terms of adherence to the training.

Fig 1. Moto Tiles use in group play amongst seniors in Finland.

4. Discussion

Apart from following the design guidelines, the implementation of Moto Tiles in society demanded an extensive effort in scientific effect studies of both the physical effect and cognitive effect on seniors from playing with the Moto Tiles. Even though such important significant effects are presented, it must be noted that the playful aspect related to the motivation is of highest importance in the design process, and as such the health effects are viewed as collateral effects.

References

1. L. Pagliarini and H. H. Lund "*User-Friendly Robotics 1*" ibid
2. L. Pagliarini and H. H. Lund "*User-Friendly Robotics 2*" ibid
3. H. H. Lund, and C. Jessen, "*Playware - Intelligent technology for children's play*," Technical Report TR-2005-1, June, Maersk Institute, University of Southern Denmark, 2005.
4. H.H. Lund, T. Klitbo, and C. Jessen, "Playware Technology for Physically Activating Play", *Artificial Life and Robotics Journal*, 9:4, 165-174, 2005
5. H. H. Lund, H.H. "Playware ABC: Engineering Play for Everybody." *Journal of Robotics Networks and Artificial Life*, *3*(4), 2017
6. H. H. Lund "Intelligent artefacts." *In Proceedings of the 8 th International symposium on artificial life and robotics, ISAROB*, pp. I11-I14. 2003
7. H. H. Lund, P. Marti, and M. Tittarelli. "Remixing playware." In Robot and Human Interactive Communication, 2014 RO-MAN: *The 23rd IEEE International Symposium on*, pp. 49-55. IEEE, 2014.
8. M. Pacheco, M. Moghadam, A. Magnússon, B. Silverman, H. H. Lund, and D. J. Christensen. "Fable: Design of a modular robotic playware platform." In *Robotics and Automation (ICRA), 2013 IEEE International Conference on*, pp. 544-550. IEEE, 2013.
9. H. H. Lund, "Play for the Elderly - Effect Studies of Playful Technology," in Human Aspects of IT for the Aged Population. *Design for Everyday Life*. (LNCS Vol. 9194, pp 500-511, Springer-Verlag, 2015)
10. H. H. Lund, and J. D. Jessen, "Effects of short-term training of community-dwelling elderly with modular interactive tiles," *GAMES FOR HEALTH: Research, Development, and Clinical Applications*, 3(5), 277-283, 2014.
11. H.H. Lund, M.D. Pedersen, R. Beck, "Modular robotic tiles: Experiments for children with autism", *Artificial Life and Robotics*, *13*, pp. 393-400, 2009.
12. http://www.moto-tiles.com (checked: 6/12/2018)
13. H. H. Lund. "Playware Research–Methodological Considerations". *Journal of Robotics, Networks and Artificial Life*, *1*, pp.23-27, 2014

User-Friendly Robotics 1 – AI Software

Luigi Pagliarini[1,2], Henrik Hautop Lund[1]

[1] Centre for Playware, Technical University of Denmark, 2800 Kgs. Lyngby, Denmark
[2] Academy of Fine Arts of Macerata, Via Berardi, 6, 405111 Macerata, Italy

luigipagliarini@gmail.com

Abstract

In this paper, the first part out of three, we present the trajectory of decades of research in AI and Robotics by highlight the continuity of our method that has always taken into consideration the common user's point of view as a priority. We call such an approach User-Friendly Robotics, and we hereby unravel it by describing our path step-by-step, to see on one side its evolution and on the other its methodological continuity. Therefore, starting from the earliest AI-based applications, which are mainly described in this paper, we slowly move-up towards the first Robotics ones to finally describe the last results of our research. We discuss how this User-Friendly Robotics approach leads to solutions that fit particular purposes in society and lead to useful user interaction with technological developments.

Keywords: Playful technology, Playware, User-friendly robotics, Artifcial Intelligence, Artificial Life.

1. Introduction

Approximately a jubilee ago our path towards a user-friendly high-tech tools accidentally started and, basically, has never stopped evolving itself. We improved the criteria of robustness, efficiency and friendliness themselves, and enlarged the domain of application from software to hardware. In the following paper, we describe the essential steps we took, and the technology we developed along the way. We also discuss and highlight the fundamental principles and criteria that, in our opinion, make an AI based artefact, a user-friendly one.

Indeed, we believe that it might be quite hard to define such a field of competencies since it is very multidisciplinary and it includes a quite large set of different aspects, such as user-interaction flow, comprehensibility, simplicity, efficacy, efficiency, aesthetics, and etc. Therefore, this on going process reaches and includes very many different aspects and perspectives that are not always easy to integrate in one single artefact, especially if such an artefact is oriented to more than a single activity, has to reach more than a specific market target, and has to accomplish more than a single goal.

Anyway, the present paper do not aims at being a theoretical one in which we claim a specific hypothesis for HCI (i.e. Human-Computer-Interface) and, on the contrary, it is an attempt for a reportage of our investigations that, one after the other, empirically took us to an successful applicative model of user-oriented tools.

2. AI- based user-friendly software

In 1993 we were part of the research group on Artificial Intelligence and Artificial Life that was commissioned by the Museum of Science of Naples to shape three software that could explain concepts like Neural Networks, Genetic Algorithms and Guided Evolution to a as large population of users as possible. The production of such AI based software - named "Educational Artificial-Life Lab" - was an extraordinary challenge because for the first time we were bringing brand new scientific concepts to the public and we had to find an original way to interface with it.

3. Shape You Brain

The first one [1,2], *Shape Your Brain* (Figure 1), consisted of a simple neural network control system made of eight sensors as sensory input for 8 input neurons, and having 2 output neurons that activate the agent In Shape Your Brain, the task was to develop a control system, a Neural Network in the shape of a Perceptron, so that the agent navigates quickly around in its environment without running into the walls or the central obstacle.

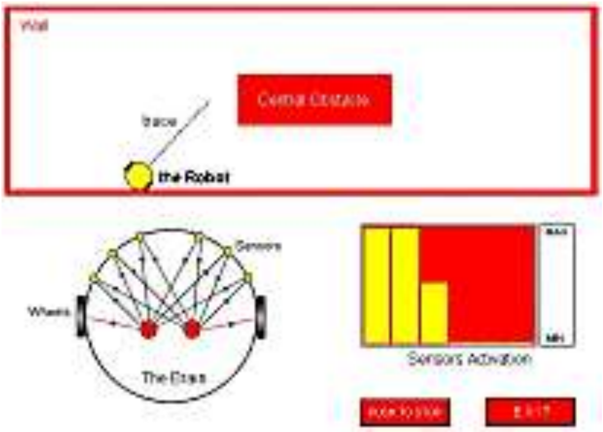

Figure 1. Shape Your Brain, software

The user observes each single step of the agent and for each step is allowed to change the connection weights of the neural network that constitute the control system. In this way, the user experiences how behaviours that are appropriate under some circumstances (e.g., far away from obstacles) are not appropriate under other circumstances (e.g., close to obstacles). To succeed, the user must construct a global behaviour that lets the agent behave appropriately under all circumstances. This is a rather difficult task, since the user has to adjust all connection weights in the neural network that control the agent's. Probably, Shape Your Brain is one of the first Edutainment Electronic Games based on AI ever built.

4. Pet Evolution

The second AI-based software[3], named *Pet Evolution* (Fig. 2) , was similar to Shape Your Brain but, instead of focusing on the direct manipulation of a Neural Network it was thought to guide the users to idea of Genetic Algorithms, therefore, the Darwinian laws. In Pet Evolution the user has to develop the behaviour of the same simple neural network control system agent (i.e. 8 input neurons, and 2 output neurons) so that the agent navigates quickly within its environment without running into the walls or the central obstacle.

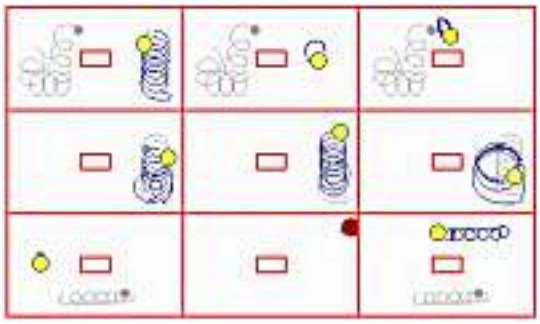

Figure 2. Pet Evolution, software

Instead of a manual tuning of the NN, in this case, a simulated evolution process is used as a developmental tool. A whole population of nine agents is constructed randomly as an initial population. Each agent lives for a number of time steps in the environment with walls and the central obstacle, and the behaviours of all nine agents are shown on the screen. Each agent moves around in the environment leaving a tiny line on its trajectory. From the initial population, the user has to select the three agents that show the best behaviour according to the task of moving around in the environment. Each of the three selected agents makes three copies of its neural network control system, where mutations are applied to a small number of the connection weights. The total of nine mutated copies constitutes a new generation that is permitted to live in the environment. The user selects among these agents, the selected agents reproduce a new generation, the agents of the new generation live in the environment, the user selects again, etc. One experiences the game, Pet Evolution, in a simple way. This tells the careful user that evolution is capable of finding adaptive solutions to difficult problems by such methods as selective reproduction and mutation only. Pet Evolution was one of the first Artificial Life Games ever built in Artificial Life history as well as one of the first Edutainment Electronic Games.

5. Survive!

The third software, called *Survive!* (Fig. 3), was a single person game and consists of a little world where a few artificial organisms and some food pieces are placed. The organisms are small neural networks that navigate in the environment. When an organism reaches a food piece, the food piece is ingested and disappears from the environment. An organism reproduces a child when a certain number of food pieces have been ingested. The number of food pieces ingested by an organism is shown by the organism's size.

If an organism lives for a long period without ingesting any food pieces, the organism dies. When the game starts the only thing a player can do is to administrate a container of food resources in such a way as to keep the population alive as long as possible.

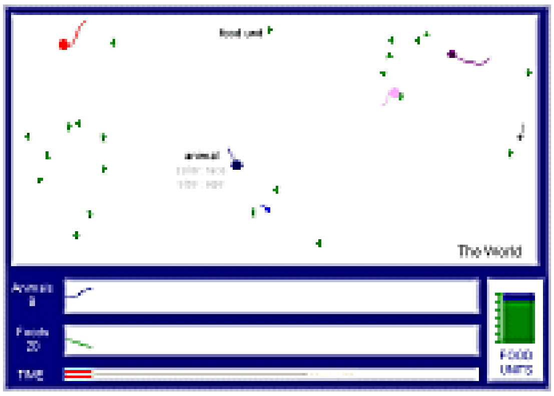

Figure 3. Survive!, software

This process is made more difficult by the fact that the population grows or risks extinction in relation to the quantity of food released and it is very hard to find the right rate of resources to be given. Obviously, this kind of problem-solving enables a child's mind to understand and cope with two important and up to date bio-ecological topics. The first is energy management; the second is the meaning of demographic aspects of life on earth. For these reasons, this game was considered as highly educational in regard to encouraging respect for wildlife and habitats, in such a way that can be termed "easy to understand" and "easy to interact" with [4]. Survive! was one of the first Artificial Life Games ever built in Artificial Life history , too, as well as one of the first Edutainment Electronic Games.

6. Artificial Painter

After this experience, in 1994, we were financed to get involved in a new challenge and design an AI-based and used guided artistic experience. The result was the *Artificial Painter* (AP, Fig. 4) a software package thate uses a Genetic Algorithm on Neural Networks to produce artistic images. The evolution of pictures was based on the user's aesthetic evaluation of a number of pictures shown on the screen. The AP model originates from an inspiration derived from bio-image techniques such as Computed Tomography (CT), Positron Emission Tomography (PET), and Single Neuron Records. All these techniques visualize physiological activities by means of coloured pictures that are used in research and diagnostic [5,6].

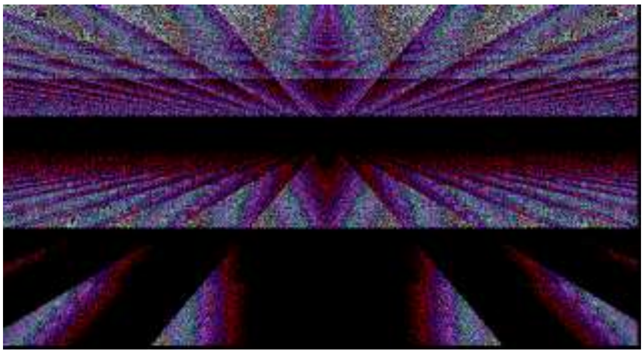

Figure 4. Artificial Painter, software

In a similar way, in AP the techniques of single neuron records are applied on an Artificial Neural Network (ANN) to produce pictures. The Genetic Algorithm is used to lead an evolutionary process that gives the user the possibility of choosing the 'desired' image, i.e. "ANN's brain", amongst many. Chosen images (and underlying ANNs) will be reproduced and, eventually, mutated and the process goes on until the user has reached a satisfactory aesthetical result. Artificial Painter, represents one of the first examples of image evolving simulators in the Electronic Art history (the first one based on neural networks). AP is also considered a milestone in the ALife and AI fields because of its original and innovative conception and for its application in medical field [7].

7. Face-It

One further step towards a user-friendly AI software experience was determinate by the development of *Face-It*, in 1995.

Face-It software package used a Genetic Algorithm to evolve pictures of facial expression. The evolution of pictures was based on the user's evaluation of a number of facial expressions shown on the screen. The Face-It model originated from an inspiration of Leonardo Da Vinci's Facial Studies and Artificial Life techniques of User Guided Evolution of Images, plus Cognitive Science Studies of Recognition of Facial Expressions.

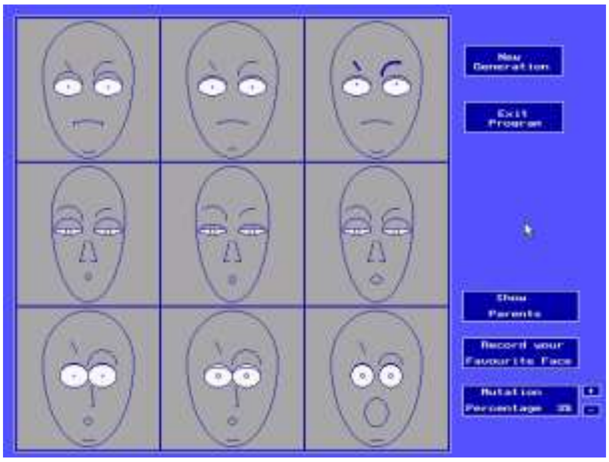

Figure 5. Face-It, software

A Genetic Algorithm works on a population of genotypes. In Face-It, the genotype of each individual is represented by a bit string codifying the values of 33 continuous variables that describe 400.000 possible expressions of, approximately, the same face. Face-It constructs a whole population of individuals. Initially, the genotype of each individual will be set randomly [8,9]. Each individual builds a face that is shown on the screen in front of the user. According to the genotype different faces will appear. The user selects some of the expressions for reproduction by clicking them on with the mouse. Each selected individual (i.e.: expression) will be cloned a fixed number of times and a new generation of faces will appear on the screen. Each clone will be mutated in some randomly chosen parts of the genotype (bit string). The user can decide the average number of genetic mutations. The selection and cloning process can continue until one or more satisfactory expressions are obtained. Face-It, was a clear example of reducing an incredibly complex event, such as face expressions, towards an easy to understand and use artefact.

8. Discussion

This first set of studies clearly traced a way on how to interface complex concepts and machine/software dynamics with human being, regardless of their age and level of competences [7], both in computer science and in general. It is self-evident that since the beginning we concentrated on hiding the level of complexity targeted application and focused on the users' cognitive approach to generic tools, trying to design immediateness within our interactive model. As it will be shown in the following parts we kept on the same path while getting out of virtuality and interfacing with physical agents, robots.

References

1. L. Pagliarini, Insegnare 'Biologia' attraverso l'uso di software di Vita Artificiale. *ECOSOFT International Conference*. Perugia, 15-19 Novembre 1994.
2. Miglino O., Calabretta R., Pagliarini L., Nolfi S., *La vita artificiale come strumento per la didattica delle scienze*. Technical Report, Reparto Sistemi Neurali e Vita Artificiale, Istituto di Psicologia, Roma.1994
3. Pagliarini, L., Rubinacci, F., Lund, H., Sementina, C. I modelli simulati aiutano ad apprendere le tradizionali discipline scolastiche? Atti del Congresso della Sezione di Psicologia Sperimentale (*Proceedings of "Italian Congress of Experimental Psychology*), pp. 76-78, Editrice Democratica Sarda, Sassari, Italy 2001.
4. Miglino, O. Rubinacci, F. Lund, H. H., and Pagliarini, L. "Using artificial life to teach evolutionary biology", in *Cogn Process 5:123-129* (2004).
5. H. H. Lund, L. Pagliarini, O. Miglino Artistic Design with Genetic Algorithms and Neural Network. In *Proceedings of First Nordic Conference on Neural Network*, 9-13/1/95, Vaasa, Finland.
6. H. H. Lund, L. Pagliarini, O. Miglino The Artificial Painter. In *Proceedings of ICANN 1995 International Conference on Artificial Neural Network*, 5-13/6/95, Granada, Spain.
7. L. Pagliarini, H. H. Lund, O. Miglino and D. Parisi Artificial Life: A new way to build educational and therapeutic games. In *Proceedings of ALife V International Conference*, NARA, 15/18-V-1996, Japan, MIT Press(1997).
8. Pagliarini,L., Parisi, D., Il Progetto Face-It. XV Congresso Nazionale della Ricerca di Base in Psicologia (A.I.P.), Capri, 30-IX/2-X 1996.
9. Rubinacci F, Paparone C, Pagliarini L, Matarazzo O, Face-It: Uno strumento di Vita Artificiale per lo studio della genesi delle espressioni facciali delle emozioni, *Atti del Congresso Nazionale dell'AIP* - Sessione di Intelligenza Artificiale e Modelli Connessionisti, Bellaria-Rimini, 16-18 Settembre 2002 (abstract).

User-Friendly Robotics 2– Interfacing Robotics with any user

Luigi Pagliarini[1,2], Henrik Hautop Lund[1]

[1] Centre for Playware, Technical University of Denmark, 2800 Kgs. Lyngby, Denmark
[2] Academy of Fine Arts of Macerata, Via Berardi, 6, 405111 Macerata, Italy

luigipagliarini@gmail.com

Abstract

In this paper, the second part out of three, we continue presenting the route of our long experience in interfacing AI and Robotics with the public. This paper, in particular, highlights a crucial step we experimented when creating computer based software architecture so to let the common user easily interact with complex behaviour robotics. We define such an approach User-Friendly Robotics, and we hereby describe the principles and the techniques we used to evolve its methodology reporting here the most important case studies we went through, as examples. We then analyse the impact of such method on both science and educational field. Finally, we discuss how this User-Friendly Robotics approach leads to solutions that fit particular purposes in society and lead to useful user interaction with technological developments.

Keywords: Playful technology, Playware, User-friendly robotics, Artifcial Intelligence, Robotics Interfaces.

1. Introduction

It is now about 25 years that we are immersed in the study of robots and dynamic systems interfaces. This path almost accidentally started in 1993 [1] has undergone continuous evolution going through ate least three main steps, from full virtual world to mixed realities, to the present where we put all of our effort in hiding the software component as much as possible. At the same time we in parallel enhanced the criteria of robustness, efficiency and friendliness of our method, and enlarged the domain of applications. In the following paper, we describe the intermediate step we took, when moving the control and the evolution of robots behaviour from the researcher/scientist to the common user, trying to depict the fundamental principles and criteria that, in our opinion, make an AI based artefact, a user-friendly one.

We strongly believe, indeed, that the future of high-tech and AI based tools well be grounded on screen disappearance. This consideration leads to an approach toward the idea of “interface” that is necessarily multidisciplinary and it includes a quite large set of different aspects, such as user-interaction flow, comprehensibility, simplicity, efficacy, efficiency, aesthetics, lightness, and etc. Indeed, this process takes into consideration very many different perspectives and aims at including many different features, not always compatible or easy to integrate. Therefore, sometimes, it is a big challenge, especially when one single artefact or interface is oriented to more than a single activity, has to reach more than a specific human target, or to accomplish more than a single goal.

In this paper we present an intermediate step we took when moving the idea of robotics as a field under the control of very experienced users to directly interface with children and not-experienced users. In such passage we inherited the experience maturated in designing AI-based simulators and created different methods to interface with robots in an easy and playful way. We believe that such an example can be of great inspiration for those who are investigating on how to conceive and build new and successful applicative model of user-oriented intelligent tools.

2. Interfacing robots with human beings

In 1997 we started to face a new challenge. The continuous hardware evolution was about to bring into the scientific community a new set of computer boards - like Khepera, as first and LEGO MINDSTORMS and Arduino, later – ideal to assemble autonomous and mobile robots in a relatively cheap way. It clearly was the beginning of a sort of Cambrian age for robotics. We, as part of this on going process started working at the design of new algorithms and to implement new user-oriented interfaces.

3. ToyBot

After such a deep experience in user-friendly AI-based software, our focus moved to robotics applications where an easy to understand and use tool could be combined with robots in action. Since 1997, we produced a quite a amount of artefacts and some of them can be considered exemplar studies that, in a more direct or undirected way, have had a large number of emulations all over the world. In here we will describe the most important ones.

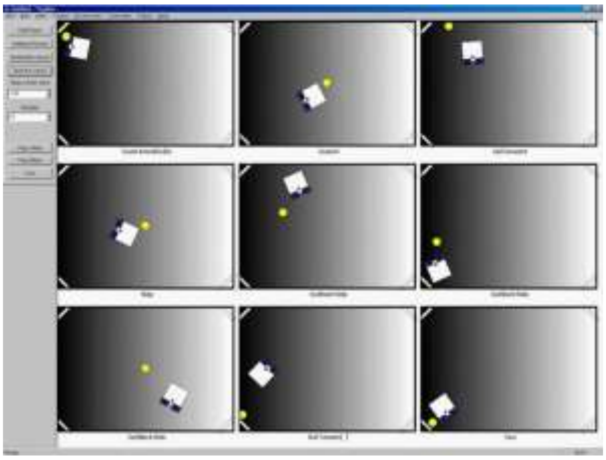

Figure 1. ToyBot, the Simulator for Robots

In 1997 [2] we developed the *ToyBot* project (Fig. 1 and Fig. 2), a research collaboration between the Mobile Robots Group at the Department of Artificial Intelligence, University of Edinburgh (UK) and the Institute of Psychology at National Research Council, Rome (Italy). At that time, a strong limitation of traditional robot kits led to the assumption that to build an intelligent toy-robot (toybot), it was better to program the robot as a sort of "computer with wheels". On the opposite, ToyBot project was based on a different point of view: we considered a mobile toy robot as a little pet moving from the belief that children (and, in general, human beings) would like to play with robots in the same way they do with animals, using direct interaction. Therefore, in our approach, the children-toybots interaction focused only on the "behaviour". In order to permit children to build interesting mobile robots, we tried to avoid any form of "information processing methodology" (i.e.: programming). Artificial Life and Evolutionary Robotics techniques represented a useful solution for our goals. For a specific task designed by the child, we allowed an evolutionary process to design the appropriate robot body plan that the child could assemble. In co-evolution and/or through a user-guided genetic algorithm, the controller of the robot was evolved and downloaded to the robot. The user-guided genetic algorithm consisted of representation of the robots' behaviours on the screen, and the user performed the selection based on the user's own judgement. Re-training in the real world could be done through reinforcement learning.

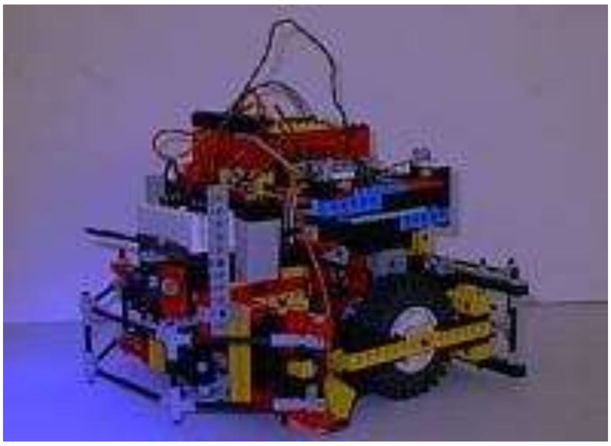

Figure 2. ToyBot, the Robot

The Toybots' behaviours were controlled by Neural Networks, that model the brain of pets. At the end of our project we had children that could develop simple behaviours such as obstacle avoidance, following or avoiding lines on the floor, attraction or fear of light, etc. for LEGO robots. The ToyBot project was a real pioneer in children-oriented games based on robotics. Today a big share of the toy market is taken up by similar approaches.

4. The LEGO Stadium

The LEGO Stadium, or *Stade de Victor LEGO* (Fig. 3 and Fig. 4), was a robot soccer show exhibited, in occasion of RoboCup '98, in "La Villette", La Cite des Sciences et de l'Industrie, Paris (France) [3]. This was actually the very first time the LEGO MINDSTORMS Robotics Invention System was shown in public.

Figure 3. The Stade de Victor LEGO

The LEGO Stadium was fully built with LEGO pieces. The LEGO Stadium consisted of: 1.500 LEGO Spectators making the Mexican Wave, two LEGO Cameramen Operators running up and down along the field and filming the matches, an automatic LEGO Score Board, Rolling Commercials, a synchronized audio system underlining the crucial events in the matches and two of the LEGO Soccer Players, the goalkeepers, that were controlled by LEGO Barcodes with pre-programmed behaviour [4].

Figure 4. The Robot players

Moreover, inside the soccer field we had four LEGO Soccer Players, two for each team, that were able to "introduce" them selves and "sing" their own national anthem. These players, controlled by LEGO MINDSTORMS RCX, had an autonomous behaviour guided by a behaviour-based algorithm.

A placed from above camera was filmed the stadium and downloaded the information to a colour-detector card which, in turn, furnished information on each player and ball positions to each robot that was then able to take, step by step, its strategic decision. The resulting soccer game was an exiting one full of action and lots of goals. The LEGO Stadium show at "La Villette" was a great media event and it is calculated that it was shown to more the 200 million people all over the world, through television shows. A 'preview' of this game was also given as part of a Stockholm Cultural Capital '98 event called Global Tendency Machine in Stockholm in May 1998.

5. Interactive LEGO Football

Moving from this experience we had the intuition that such scheme for behavioural-based robotics could be opened directly to the users/public and a great set of games or professional activity could have been designed. Indeed in 1999, we started building the *Interactive LEGO Football* platform (Fig. 5, 6, 7, 8), a set-up that aimed to be a fully personalized and interactive robotics experience for any user [5,6,7].

Figure 5. Playing the game at MIT Medialab

Therefore, the Interactive LEGO Football (I.L.F.) project was a one-on-one robot soccer game to be played with real robots. The robots use only simple sensors and motors, but a special smart, electronic ball is used to allow the robots to detect it. The robots are programmed with a user-guided behavior-based approach. I.L.F. robot soccer game for children consists of an environmental set-up (field, ball, etc.), LEGO

Mindstorms robots of different colours, and a programming environment.

Figure 6. A Robot player, downloading the control system via infrared

The LEGO robots are premade ones (with two light sensors for ball detection and a switch sensor for crashing detection) so that the children can concentrate their attention on "programming" the behaviour. To let them do so, we built up a behaviour-based algorithm, shown on a very easy-to-understand interface, with photographs and videos of the robot behaviours, where the children have to choose the behavioural sequence the robot will play.

Figure 7. The Behaviour-Based Interface

It is a lot like being the coach of the team and real programming is not needed. Once the child has made his/her choices, he/she can download his/her program into the robot and go and play the game against his/her opponent.

The programming environment has different levels of difficulty that can be accessed accordingly with user's competences. The game was tested at both RoboCup'99 in Stockholm and at the MIT Media Lab MindFest '99, and children from 7 years and up were able to make their own LEGO MINDSTORMS robot soccer players to score within 20-30 minutes and ready to play in small tournaments from within 30 to 60 minutes. I.L.F., under the name of RobocupJunior [8], has become a milestone in children oriented robot games. The same game has also been used in the European RoboCup 2000 event in Amsterdam (Holland) and, in a slightly different version, in RoboCup 2000 in Melbourne (Australia), as part of the RoboCup Jr. setup. At the moment the game is probably one of the most widespread platforms used for educational purposes in the world [9].

Figure 8. RobocupJunior competitions, nowadays

This step represented a sort of breakthrough in robotics since it empirically demonstrated to everybody that there are methods to build and interface robots in such a user friendly way that anybody can access robot's programming and that such "access" can be placed at different levels.

6. Discussion

This second set of studies evidently traced what we can define a breakthrough method on how to interface complex concepts and machine/software dynamics with human being. Since the beginning it become clear to a pretty large number of researchers that such methodology was one of most innovative way to interface robots with people, regardless of their age and level of competences. Indeed, the ILF method was soon inherited by so many research labs, school programs and is, at the moment, one of the most widespread concept for introducing children to robots programming. The basic idea of hiding the level of complexity of the targeted application and focus on the users' cognitive possibilities was, and still is, the right way to go when designing a HCI model.

At this point, there were only a couple goals to be achieved:

A. To enlarge the domain of application of such methodology;

B. To reduce the number of iterations with a computer screen as much as possible.

In the third part of this essay on User-Friendly Robotics we will show the further steps taken towards this direction.

References

1. L. Pagliarini and H. H. Lund "*User-Friendly Robotics 1*" ibid
2. Miglino O, Lund HH, Pagliarini L, Toybots. Allevare robot per apprendere a governare un processo evolutivo. In *Tecnologie Didattiche ITD*, CNR (2002).
3. Lund, H. H., and Pagliarini, L. *Robot Soccer with LEGO Mindstorms*. In Asada and Kitano (eds.) RoboCup'98, LNAI 1604, Springer-Verlag, Heidelberg**.**
4. Lund, H. H., Arendt, J. A., Fredslund, J., and Pagliarini, L. Ola: What Goes Up, Must Fall Down. In *Proceedings of Artificial Life and Robotics (AROB'99)*, ISAROB, Oita.
5. Lund, H. H., and Pagliarini, L. RoboCup Jr. with LEGO Mindstorms. In *Proceedings of Int. Conf. Robotics and Automation 2000 (ICRA2000),* IEEE Press, NJ.
6. Lund, H. H., and Pagliarini, L. (2001) Edutainment Robotics: Applying Modern AI Techniques. In *Proceedings of International Conference on Autonomous Minirobots for Research and Edutainment* (AMIRE-2001).
7. Lund HH, Pagliarini L, Edutainment and Robotic Games for Children. In Proceedings of the 2nd IFAC conference on Mechatronic Systems Mechatronics 2002, Berkeley, California, USA, December 9-11, 2002. Elsevier.
8. https://en.wikipedia.org/wiki/RoboCup_Junior
9. http://junior.robocup.org/events/

A New Machine Learning Algorithm for Weather Visibility and Food Recognition

Young Im Cho[1], Akmaljon Palvanov[2]

[1, 2]*Gachon University, Korea*

[1]*yicho@gachon.ac.kr*
[2]*akmaljon.palvanov@gmail.com*

Abstract

In this paper, we discuss two fundamentally different problems, such as visibility estimation and food recognition using convolutional neural networks. Our focus was revealing limitations of deep convolutional neural networks and methods to tackle with those drawbacks. We propose two dissimilar data-driven approaches for each tasks. The first proposing model designed to estimate the visibility distance from images captured via digital camera. For this task, we use images taken from CCTV cameras as inputs. The second model implemented to recognize dishes from limited images. Additionally, we implemented a graphic user interface as well as special web page that allows users flexibility to operate all operations in real-time. This paper describes both models and other essential details.

Keywords: atmospheric visibility, convolutional neural networks, CCTV, graphic user interface, recognition.

1 INTRODUCTION

Visibility is a degree of ways nicely an observer can view a scene. This consists of how some distance you can see within the surroundings as well as the ability to see the textures and colors of the scene. Haze is the inverse of visibility that is the measure of the inability to view a scene.

Nobody would intentionally agree that poor air great is acceptable. The advantages of correct visibility are apparent. Visibility is a primary and enormously apparent indicator of preferred air excellent. Visibility is distinctly easy to recognize via public. Many humans regard suitable visibility as a figuring out thing for the satisfactory of out of doors existence. As an end result, the community can also decide the effectiveness of environmental control policies to improve air satisfactory by means of visibility.

Experts use special equipment to provide measurement of visibility. These tools themselves and their installation processes are ample expensive and measuring range is also limited. Additionally, the factors mentioned above strongly affects the outcomes.

Hereby, we propose camera and convolutional neural networks (CNN) based approach to estimate visibility as combinations of these methods gives strong superiorities. On the one hand, comparing to tools like visibility meter camera-based visibility measuring is more close to visual method. Also, the technique does not cost expensive, weather conditions like dust and fog etc. can be artificial removed while measuring and can be achieved very accurately results.

CNNs are good at classification and recognizing images as they can learn the relationships between inputs and outputs. The key factors for this ability is large labeled datasets, which support the learning process and novel network architectures with hundreds of millions of parameters. Nevertheless, it is difficult to find suitable dataset always. In this case, data augmentation techniques are widely used. In this work, we study the most common methods to enlarge a dataset consists of limited images.

In order to evaluate the CNNs effectiveness using artificially extended dataset, we selected limited images of Korean dishes. Since input images different in terms of shape, texture, size and color as the Korean dishes lacks any kind of generalized layout.

In contrast, to other types of food such as Indian or Italian, it is more complicated recognizing the images of Korean dishes as the following reasons: images in the same category appear differently; it is complex for modeling dish images because of noise, likely, various backgrounds and textures; a number of high quality and proper images is limited.

We implemented a new deep CNN model for this task. Our model has shown promise results even on a large and diverse image datasets with non-uniform backgrounds.

In the next section, a brief summary of related studies is reviewed. Then, Section 3 presents details of both models and experiments as well as achieved results is given in Section 4. Finally, Section 5 concludes the paper.

2 RELATED WORK

Shengyan et al [1]. proposed visibility estimation based on meteorological laws using digital images. They used deep learning model to artificially extract features from input images. Another approaches for estimating visibility proposed by Sami et al [2] essential properties of these studies are using single camera and evaluate visibility on a basis of daytime light from the input images. In the field of meteorology, one of the main law is Koschmieder's law and many researchers used this function to estimate visibility in both cases, using digital images and using special equipment for visibility estimation, these works have been done in Du et al [3]. Since all these methods use images, as an input quality of the images is vital to get better results, means that degradation of images strongly restricts accurately estimation. This requires essential extra step prior estimate visibility the step is enhancement of the quality of input images. For this situation Dark Channel Prior (DCP) method is widely used. For instance, in poor visibility conditions enhancement of color images proposed by Keong et al [4], in this study, several visibility conditions tested using synthetic images taken via airborne camera. Another effective use of DCP can be seen in Kaiming et al [5]. they used a haze-imaging model to estimate the thickness of the haze then recover quality of the image. Convolutional neural network based dehazing method Boyi et al [6] relies on the re-formulated atmospheric scattering model. In next section we will detailed explain our approach and our techniques.

There have proposed several CNN based food image recognition algorithms. A system based on deep CNN namely DeepFood [7] by Chang et al. analyzes the food image taken by mobile devices and the performance outperformed of previous proposed dietary assessments. In [8] by Yuzhen, five layer CNNs introduced to recognize 5822 food images. It has only 10 classes and overall 90 % accuracy obtained. Another model FoodNet [9] by Paritosh et al. addressed food images recognition using multilayer CNN using the large dataset ETH Food-101. All models mentioned above take advantage of deep CNNs and require large sets of images. Therefore, we addressed to the problem of enlarging dataset from limited images.

3 METHODS

3.1 Datasets

For the task of visibility estimation, we used a set of CCTV images taken by stationary surveillance cameras from four different points in South Korea, near the sea side.

Fig. 1. Samples from the visibility dataset

Atmospheric visibility measurements for those locations was also available. The visibility values are register in the range from 0 to 20000 meters. We assigned 21 classes for each 1 kilometer of visibility (including 0) by dividing the visibility by 1000 and rounding the values. Because of the poor image quality during the night, we decided to use only images from daytime. Examples shown in the Fig. 1.

Limited dataset is a severe problem in case deep CNNs. As we mentioned above, CNNs mostly data-driven and require proper set of images. To overcome this problem, we are proposing an algorithm, which takes single image and applies several augmentation techniques sequentially in order to gain multiple images. The proposing algorithm can give desired number of unlike images with maximum efficiency.

Initially, the system takes single or many images as input(s). Then, normalizes and adjusts the contrast and brightness of the input(s). The normalized image used for generating new images according to the proposing algorithm (image generating functions can be chosen by users).

Some generated inputs might lose their quality during the second step. The reason for reducing the quality is that image resolution will change during the process and zoomed/cropped/scaled image need to quality enhancement. After gaining desired outputs, some images will process using auto-encoder model or image enhancement methods.

Pre-final, quality recovered images will be processed again in order to reduce the similarity of images, to do so we apply random Gaussian noise. In addition, it is done with the contrast, sharpness, color and brightness changes randomly. In the Fig. 2 the proposing dataset enlarger algorithm described.

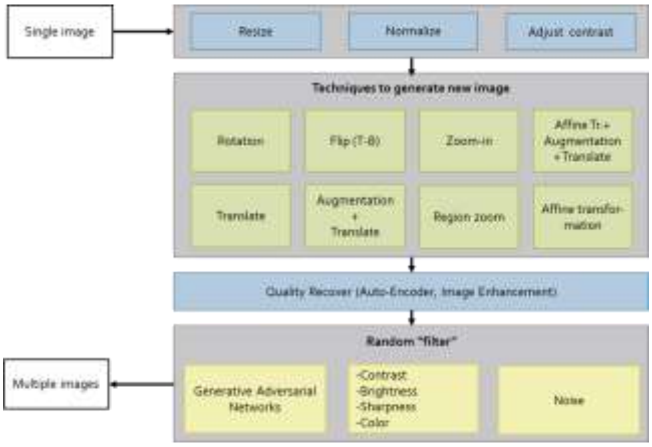

Fig. 2. The proposing dataset enlarger algorithm.

Since, there is no publicly available image datasets for Korean dish recognition, to train our complex food recognition model we have collected a new dataset. The resources for the dataset are taken photos and web images. Our group in daily life collected some partial of the images in this dataset. The Fig. 3 shows example images from the dataset. We selected 50 images for each 23 classes. Images are artificially extended later using the proposed algorithm above, resulting in totally 92000 images.

Fig. 3. Sample images from the food dataset

3.2 Networks

Visibility estimation

Our first model estimates visibility from day time images. Especially, it can classify accurately if there is a foggy weather condition is illustrated. A logical structure of the model for visibility estimation can be seen in Fig. 4.

The first convolutional layer produces 32 feature maps using 5x5 convolutional kernels followed by max-pooling operation. The second convolutional layer produces 64 feature maps using kernel size 3x3. After the last max-pooling operation, feature maps are sent to the dense layer, which includes 1024 neurons. Finally, the last layer is Softmax layer that produces the output. Visibility is complex phenomena as dense fog or low-visibility presented images have almost no features. Fog occupies entire image space as a repercussion everything is abstract, features of objects hidden. In this case, deep CNNs strongly overfits and produces wrong prediction. Therefore, we use only two convolution layers to avoid overfitting.

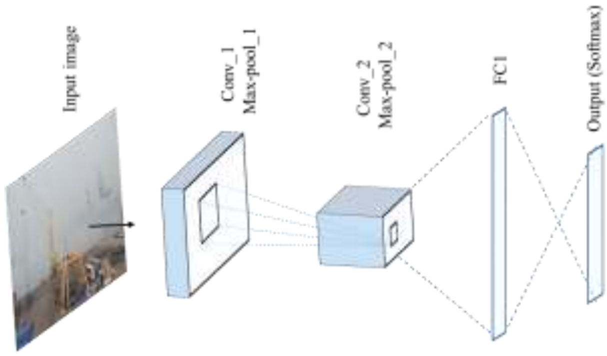

Fig. 4. The logical structure of the CNN model for visibility estimation

Food recognition

Schematic architecture of the model is given in Fig. 5. Initially, the first layer receives 150x150 image as an input and produces 32 feature maps by convolving with the kernel size 9x9. Next, max-pooling operation reduces the dimensionality. The kernel size of 7x7 is used to convolve an output of the previous layer, resulting 64 maps of features. Third and fourth convolution layers produce 128 and 256 feature maps respectively, each followed by max-pooling operation. After the last max-pooling layer, w dense layers employed sequentially each with 512 neurons. Finally, there are 23 Softmax neurons in the output layer, which correspond to the classes of dishes.

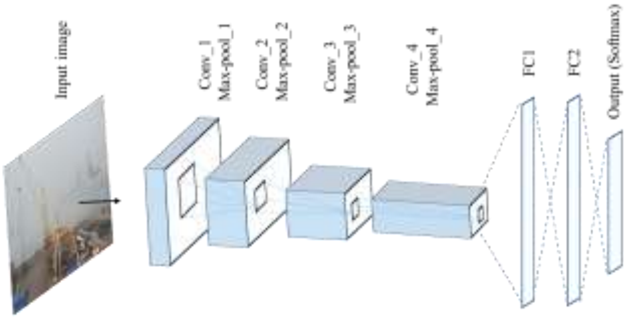

Fig. 5. The logical structure of the CNN model for food image recognition

4 EXPEREMENTS AND RESULTS

Our experiment performed on a high-end server with 64GB of RAM equipped with two Nvidia GeForce GTX 1080 Ti GPUs. We conducted the experiment using Tensorflow machine learning framework. The training process is computationally costly and takes much time. It reads inputs from the memory then shuffles all images then starts training choosing random batches.

A training accuracy presents how perfectly fits every input image to the training data whereas a loss measures the inconsistency between predicted value and actual label.

The evaluation of the accuracy, as well as the loss function over the course of training, is given in figures below.

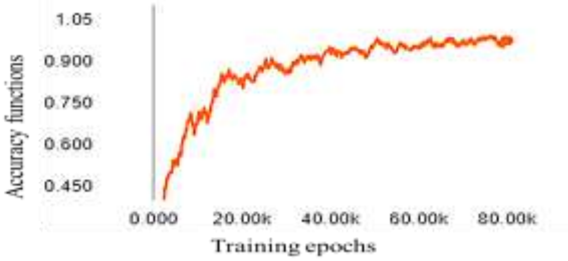

Fig. 6. The accuracy functions over the course of training. The horizontal axis represents training epochs; the vertical axis is the training accuracy functions

As we can see from Fig. 6 during training, our accuracy on random batches approaches 90% of successful visibility classification based in image similarity.

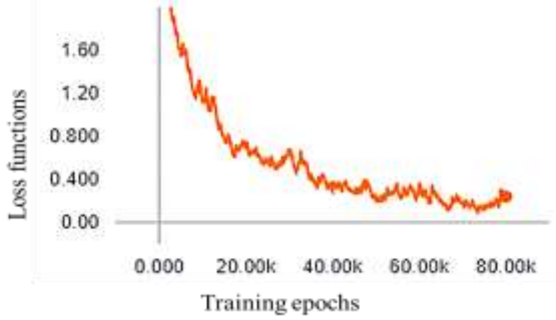

Fig. 7. The evolutions of the loss. The horizontal axis represents training epochs; the vertical axis is the loss function

It is clear from the loss function that the loss successfully reduced to approximately 20%. To perform the evaluation, we developed a java application that selects images from the reference image database and performs an evaluation on each of them separately. The proposing method achieves about 81% classification accuracy on random sample images, which is quiet promising for this problem.

After training the model, we exported the model into a compressed file for deployment. We developed a Java based offline graphic user interface as well as a Java EE based web page for testing the model in real-time. A web based application is designed to run on a remote server accessible over a TCP/IP network such as LAN or the Internet. The application takes a. jpeg or .png image as input, uploads it to the server, loads the trained neural network model and returns the inference result to the clients' web browser.

5 CONCLUSION

To sum up, our studies showed that one of methods to estimate visibility can be done by deep CNN model. I addition, we showed efficient methods to enlarge dataset of limited image to train complex models. We implemented the deep CNN model that recognizes food images and trained it using extended dataset.

ACKNOWLEDGEMENT

This paper is supported by NRF(no: 2018R1D1A1A09084151).

REFERENCES

[1] Shengyan L, Hong F, and Wai-Lun L (2017), Meteorological visibility evaluation on webcam weather image using deep learning features. *International Journal of Computer Theory and Engineering*

[2] Sami V, Jari H (2015), Image based visibility estimation during day and night. *Computer Vision - ACCV* 2014, pp. 277-289

[3] Du K, Wang K, Shi P, Wang Y (2013), Quantification of atmospheric visibility with dual digital cameras during daytime and nighttime. *Atmos*, pp. 2121–2130

[4] Keong, John P. Oakley (2002), Enhancement of color images in poor visibility conditions. *Proceedings 2000 International Conference on Image Processing*, Canada

[5] Kaiming H, Jian S, Xiaoou T (2011), Single image haze removal using dark channel prior. *IEEE Transactions on Pattern Analysis and Machine Intelligence*

[6] Boyi L, Xiulian P, Zhangyang W, Jizheng W, Dan F (2017) AOD-Net: All-in-one dehazing network. *IEEE International Conference on Computer Vision*

[7] Chang L, Yu C, Yan L, Guanling Ch, Vinod V, Yunsheng M (2016), DeepFood: Deep Learning-Based Food Image Recognition for Computer-Aided Dietary Assessment. *ICOST*

[8] Yuzhen L (2016), *Food Image Recognition by Using Convolutional Neural Networks*, CSE803 final project

[9] Paritosh P, Akella D, Bappaditya M, Puhan N (2017), FoodNet: Recognizing Foods Using Ensemble of Deep Networks. *IEEE Signal Processing Letters*, pp. 1758-1762

Affective Interactive Systems

Kaoru Sumi
Future University Hakodate,
*Hakodate,Hokkaido 041-8655, Japan**

E-mail: kaoru.sumi@acm.org
www.fun.ac.jp

Abstract

Known as Media Equation, the relationship between humans and artifacts is similar to the social relationship between humans and humans. For example, when a human is helped by an artifact, the human wants to thank the artifact and give something in return. Like humans, it is important for artifacts to recognize emotions and express emotions when interacting with humans. This talk introduces a technique to recognize and express emotions in human and artifact interaction, and shows examples of how effective artifacts are when using emotions.

Keywords: affective computing, affective learning, human agent interaction

This talk introduces human and artifact interaction, which occurs with computer systems, virtual agents, robots, etc. What are the information elements that are important for us to consider in the relationship between human and artifact?

In our previous study, it was shown that the expressions and words of the character agent have an important role in persuasive technology [1]. Persuasive technology [2] is technology that artifacts use to persuade humans. It is said that if a user recognizes the presence of something in a computer, he or she will respond to it according to the normal social rules. Thus, it is important to present emotions of artifacts in order to change the behavior of humans.

According to the concept “Media Equation”, people treat computers, televisions, and new media as real people and places, thereby making the users uncomfortable if an agent behaves in a disagreeable manner [3]. It is said that the relationship between humans and artifacts is similar to the social relationship between humans and humans. Because of this, for artifacts to be used successfully, it is important that the artifacts both recognize human emotions and show emotion.

Therefore, our research group has been studying interaction using emotions. If artifacts can recognize human emotions dynamically, it will be possible to provide very fine-grained services.

In recent years, we have become able to identyfy emotions using various devices in various ways. For example, devices which can detect things such as heart rate, skin potential, facial expression, brain waves, and gestures have become familiar. There are various methodologies for emotion recognition, but methodologies for emotional expression are limited. For example, since many robots do not change their expressions, there is no flexibility in expressing emotions, so we often conduct experiments using character agents. We have developed a counseling system [4][5], a customer service learning system [6], a job interview system [7], and a programming learning support system [8][9][10] in our research on interactive systems using emotion. These studies were developed to examine interactive systems between a human and an artifact.

References

1. Kaoru Sumi and Mizue Nagata: *Evaluating a Virtual Agent as Persuasive Technology, Psychology of Persuasion*, Janos Csapó and Andor Magyar eds., Nova Science Publishers.2010.
2. B.J.Fogg: *Persuasive Technology –Using Computers to Change What We Think and Do-*, Elsevier, 2003.
3. Reeves, Byron and Clifford Nass *The Media Equation: How People Treat Computers, Television, and New Media Like Real People and Places*, Cambridge University Press, 1996.
4. Kaoru Sumi: *Spoken Dialogue Agent Applications using Emotional Expressions, Emotions and Technology: Communication of Feelings for, with, and Through Digital Media*, Elsevier (2015).
5. Kaoru Sumi: Human Computer Interaction via Affective Computing, *Journal of Robotics, Networking and Artificial Life*, Vol. 3, Number 2, Atlantis Press (2016.9).
6. Kaoru Sumi, Ryuji Ebata: *A Character Agent System for Promoting Service-Minded Communication, Intelligent Virtual Agents*, Lecture Notes in Computer Science, LNAI8108, pp.438, Springer (2013.8).
7. Kaoru Sumi, Kodai Morita: Spoken Dialogue Agent System for Writing Resumes while Practicing Job Interviews: Theory and Practice of Computation: Proceedings of Workshop on Computation: Theory and Practice WCTP2015, World Scientific (2016)
8. Thomas James Z. Tiam-Lee and Kaoru Sumi: Analyzing Facial Expressions and Hand Gestures in Filipino Students' Programming Sessions, *2017 International Conference on Culture and Computing, Culture and Computing 2017*, Kyoto, Japan, September 10-12, 2017, pp75-81,(2017.9).
9. Thomas James Tiam-Lee and Kaoru Sumi: Procedural Generation of Programming Exercises with Guides Based on the Student's Emotion, *IEEE SMC* 2018 (2018.10).
10. Thomas James Z. Tiam-Lee and Kaoru Sumi: Adaptive Feedback based on Student Emotion in a System for Programming Practice, *International Conference on Intelligent Tutoring Systems*, Volume 10858 of the Lecture Notes in Computer Science, pp.243-255, (2018.6)

A Vishay supercapacitor based fast charge battery

Chung-Wen Hung[1]*, Yi-Chang Yang[2], Chun-Chu Lin[2], Li-Sheng Jheng[1]

[1] Department of Electrical Engineering
National Yunlin University of Science and Technology
No. 123 University Rd. Section 3, Douliu, Yunlin 640, Taiwan
[2] Vishay (Taiwan) Ltd.
233 Baoqiao Rd., Xindian District, Sindian City District, New Taipei City 23145, Taiwan,
Corresponding author: *wenhung@yuntech.edu.tw

Abstract

A supercapacitor (SC) power supply management system based on is proposed in this paper. Due to the high charging current characteristics of the SC, means short charging time, the proposed SC-base battery is suitable as a backup battery. The proposed system includes the input voltage, current and temperature protection implemented with analog integrated circuits (IC); and output current limitation circuit. In order to keep output voltage when the SC voltage drops, a boost circuit is used to provide a stable voltage for the load. The circuit design is detailed in this paper, and the experimental results show the proposed system works well.

Keywords: *fast charge, supercapacitor; current limiting circuit.*

1. Introduction

Due to energy crisis and global warming issues, a global ban on the sales of traditional internal combustion engine (ICE) vehicles is considered these years. [1] The alternative solution is electric vehicle (EV) with more environmentally friend, but the energy storage is an issue. The disadvantages of the current electrochemical cell battery solution are not only long charging times and short battery life, but also easy damaged in non-monotonic consumption. [2] A SC based battery is new direction, because of almost no limited charging current, and free non-monotonic consumption. However, the SC based battery product for EV is not so popular, due to its lower energy density. It is suitable used in high frequency charging and discharging situation, or as a backup battery, such in automatic guided vehicle (AGV) and electric turret truck. When the battery under exchanging, a system is turnoff and its electronic system parameters are lost, it means long reboot time. A SC based battery management system for backup function is proposed in this paper, to maintain stable power supply when the battery is replaced.

Table 1. Vishay SC specifications [3]

Item	Value
Category temperature range	-40°C ~ +85°C
Rated voltage	2.3V ~ 2.7 V
IP (MAX. PEAK CURRENT)	35 A

The specification of Vishay SC used in paper is different from normal capacitor and electrochemical cell, as shown in Table 1. [3] Vishay SC provide many features, which is suitable for EV. Such as: “Double 85 degree”, Vishay is only supplier to provide temp / humidity 85-degree test of EDLC type SC. Moreover, its safe function without bulging of sealing. The protection specification proposed in this paper is based on these value, including: the temperature, voltage, chagrining and discharging current protection.

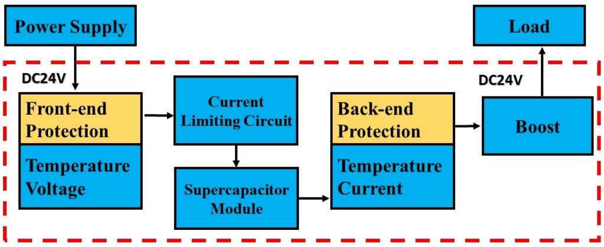

Fig. 1. System architecture diagram.

2. System Architecture

The system architecture is shown in Fig. 1. It includes five blocks: front-end protection, current limiting circuit, SC module, back-end protection and boost. The SC module serves as a storage element, and the current limiting circuit is adopted to limit the inrush charging current, and the boost circuit is used to provide a stable output voltage.

2.1. Over-temperature protection circuit:

When the SC is charged and discharged, the temperature of the SC will gradually increase. In order to prevent damage, a temperature sensor is installed in the SC block. With operational amplifiers (OPA) comparing, when the temperature voltage exceeds the threshold's, the front-end protection circuit switch immediately disconnected protection switch to perform the protection function.

Table 2. Current-limiting circuit component specifications

Item	Value
P-MOSFET1	J376
Capacitor C1	4400uF
Diode D1	RURG5060
R1	100K Ohm
R2	20k Ohm
R3	2 Ohm

2.2. Over-voltage protection circuit:

In charging input, when the charging voltage of the SC exceeds the SC maximum tolerable voltage, again, the protection circuit will immediately disconnect protection switch to prevent overcharging. If the input voltage exceeds the limitation voltage of SC, its lifetime will be shortened and even be damaged the circuit. Therefore, installing overvoltage protection circuit is necessary.

2.3. Over-current protection circuit:

When the output current exceeds the SC withstand current, SC life will be shorted. A shunt is used to transfer output current to the corresponding voltage in over-current protection circuit. Similarly, the protection circuit will immediately disconnect switch when Over-current.

3. Circuit Designed

3.1. Voltage Balance Method of SC

The voltage limitation of SC is extremely low, only 2.7V. In order to provide 24 V output, 11 SCs are connected in series, as shown in Fig. 2 (a). [4] The voltage balance method of the SC is necessary to keep the same voltage of each series SC. In high frequency charging and discharging application, the parallel resistor method is most common and simplest method. A resistor, 100KΩ, is paralleled with each SC, as presented in Fig. 2(a). Its advantages are low-cost and simple, but the resistance will continue to consume energy, means poor device efficiency.

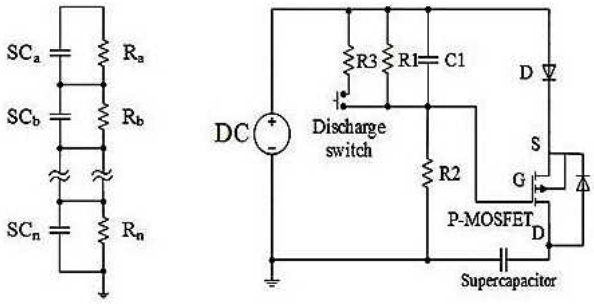

(a) Balancing circuit (b) Current limiting circuit

Fig. 2. Voltage balancing and Current limiting circuit

3.2. Current limiting circuit

The proposed Current limiting circuit is shown in Fig. 2 (b). A diode, D and a P-MOSFET provide the charging path. A Resister, R2, and a capacitor, C1, construct a charging circuit, and V_{C1} equal to V_{SG}, what is used to control SC charging current. In the initial stage, means the voltage of SC is zero, the V_{C1} is charging slowly, and the SC charging current is limited less than maximum. The V_{C1} is charged to approach to the voltage divided by R1 and R2, which is higher than threshold voltage and totally turns on the switch. Note, the ratio of R1 and R2 is fixed to 4.7 for keep the maximum turn on voltage. Now, the SC is charged in low current, due to the high V_{SC}. Moreover, R3 and switch provide a discharging rout. The Table 2. shows a typical parameter and value of components in the proposed Current limiting circuit.

3.3. Boost circuit:

The output boost circuit is shown in Fig. 3, and its specification is described in Table 3. Note, the input range is from 6 to 24V, because the SC voltage will always decrease when discharging. The load current is set into 2 and 4.5 A, which are required from users of electric turret truck for backup battery solution. Table 4. shows the part number and value of circuit components used in the boost circuit, these the part number and value are calculated based on the specifications in Table 3.

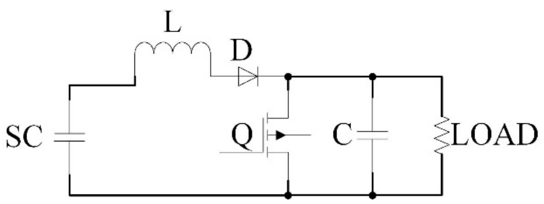

Fig. 3. Boost circuit

Table 3. Boost circuit specifications

Item	Value
Input Voltage	6 V~24 V
Output Voltage	24 V
Load Current	2 A/4.5 A
Po_max	108W
Frequency	200K Hz

Table 4. Boost component specifications

Item	Value or Part number
Inductor L1	25uH
Output filter capacitor C1	220uF
Power Switch Q1	IRF0642
Diode D1	F15S60S
Controller	LM3478 IC [5]

4. Experimental results.

Table 5. is the protection specification. Due the maximum withstand voltage of a SC is 2.7V, the total voltage of 11 series SC is 29.7V. The overvoltage protection value is set to 28V. The current limiting could be set less than specification's value.

Table 5. Protection circuit specification

Item	Value
Overvoltage Protection	28 V
Overcurrent Protection	25 A
Current Limiting Protection	15 A
Temperature Protection	80°C

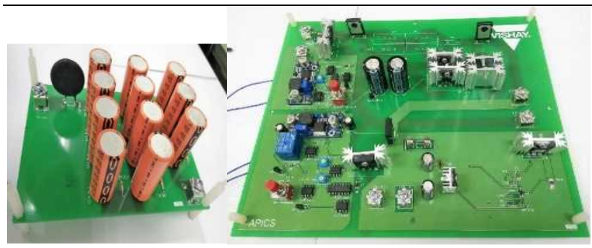

(a) Series SC block (b) Control system block

Fig. 4. Photo of circuit

4.1. *Experimental Circuit*

The photos of system are present in Fig. 4, and left and right are SC and Control system blocks, respectively. In the control system block, Fig. 4 (b), the upper left is the front protection circuit, the upper right is the current limiting circuit, the lower left is the back-end protection circuit, and the lower right is the boost circuit.

4.2. *Current Limit Test*

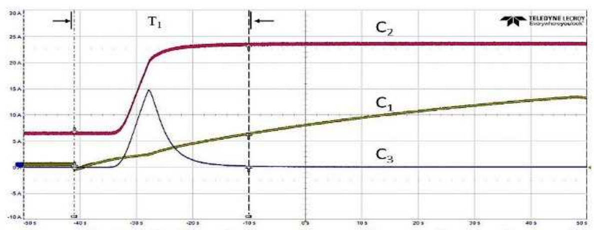

(a)Current limiting current 14.83A

C_1 (5V / *div*), C_2 (5V / *div*), C_3 (5A / *div*), t: 10s /div

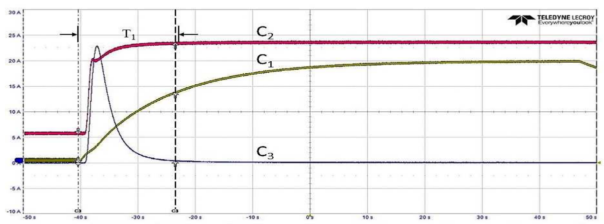

(b) Current limiting current 22.9A

C_1 (5V / *div*), C_2 (5V / *div*), C_3 (5A / *div*), t: 10s /div

Fig. 5. Current Limit Circuit Experiment Section

With the components in Table 6, the operation of the input charging current is captured, as shown in Fig. 5.

The channel C_1, C_2 and C_3 is the V_{SG} voltage, SC voltage, and the input current, respectively. In (a)/(b), the maximum current about 14.83A / 22.9A, and T_1 is initial charging time is about 30 /16 seconds depended on different RC combinations. The initial charging time is set by adjusting the resistor value ofR1 and R2 in Table 6, and the C is fixed to 4400uF. The target charging current is limited to 15A, so choose R1 = 100kΩ and R2 = 20kΩ.

Table 6. Current limiting circuit test

R1(k Ω)	R2(k Ω)	CURRENT(A)	TIME(Sec)
470	100	7.53	83
360	75	8.2	67
240	48	10.35	55
120	24	14.57	38
100	**20**	**14.83**	**30**
75	15	15.75	27
62	12	16.66	21
30	6.2	20.1	18
18	3.6	22.9	17
12	2.4	23.0	16

4.3. Over-current test

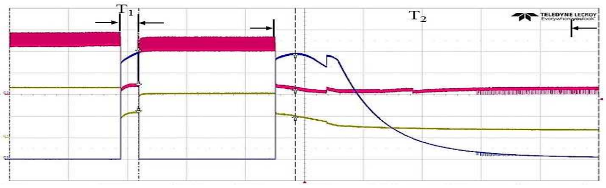

Fig. 6. Over-current circuit test section
C_1 (10V / *div*), C_2 (10V / *div*), C_3 (5A / *div*), t: 2s /div

Fig. 6 shows the over-current protection operation. Channel C_1, C_2 and C_3 represent the SC's voltage, the DS voltage, and the SC current, respectively. In the first, the SC is fully charged, and system discharges to a DC load. When the protection current is exceeded, the post-protection switch is turned off. T_1 in Fig. 6 show the switch is turned off, due to discharging current larger than 25A. Moreover, T2 presents the power supporting time from fully charging SC to out of energy with output current under control.

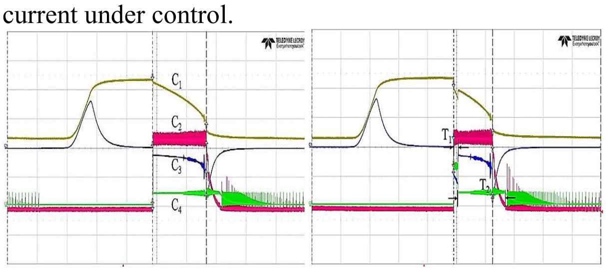

(a) Load 2A (b) Load 2A + 4.5A

Fig. 7. Test output voltage and current

C_1 (10V / *div*), C_2 (10V / *div*), C_3 (10A / *div*), C_4 (5A / *div*), t: 10s /div

Fig. 7 shows that the SC is output by the boost circuit to supply the load. Again, channel C_1, C_2, C_3 and C_4 represent the SC voltage, the output voltage, the SC current, and the output current. The target voltage of 24V can be maintained for 19 seconds under 2A load current. And, in Fig. 7 (b), output is 6.5A load first for T1,1 second, then the 2A output maintains about 13 seconds, T2.

5. Conclusions.

A Vishay SC base fast charge battery is proposed in this paper. 11 SCs are connected in parallel to perform a backup battery. The over voltage protection, over temperature protection, and SC voltage balance are discussed. High input current limitation is implemented to provide the high charging current and protect function. To keep constant output voltage, a boost circuit is adopted. The experiment results show the proposed system workable. The capacity of energy storage could be increased when series SCs are connected in parallel and component parameters are modified.

Acknowledgements

This work is partially supported by the Vishay (Taiwan) Ltd; and also by Ministry of Science and Technology, ROC, under contract No. MOST 107-2221-E-224-054. and 106-2622-E-224-017-CC3

References

[1] A. Petroff, "These countries want to ban gas and diesel cars," https://money.cnn.com/2017/09/11/autos/countries-banning -diesel-gas-cars/index.html

[2] L. Kouchachvili, W. Yaïci and E. Entchev, Hybrid battery/supercapacitor energy storage system for the electric vehicles, *Journal of Power Sources* **375**, 2018, pp. 237-248.

[3] Vishay, "225 EDLC CAP™ Ruggedized Electrical Double Layer Energy Storage Capacitors", *225 EDLC ENYCAP™ datasheet*, 27, Mar. 2018.

[4] C. Ionescu, A. Vasile and R. Negroiu, "Investigations on balancing circuits for supercapacitor modules," *2016 39th International Spring Seminar on Electronics Technology (ISSE)*, Pilsen, 2016, pp. 521-526.

[5] TEXAS INSTRUMENTS, "LM3478 High-Efficiency Low-Side N-Channel Controller for Switching Regulator", *LM3478 datasheet*, Dec. 2017.

Multi-Motor synchronous control with CANopen

Chung-Wen Hung[*,1], Roger CL Lee[2], Bo-Kai Huang[1], Shih-Ting Yu[1]

[1] *Department of Electrical Engineering*
National Yunlin University of Science and Technology
No. 123 University Rd. Section 3, Douliu, Yunlin 640, Taiwan
[2]*Naroller Electionics Co., Ltd.*
6F., No578, Sec. 1, Minsherg N. Rd., Guishan Dist., Taoyuan City 333, Taiwan
Corresponding author: [*]wenhung@yuntech.edu.tw

Abstract

A Brushless DC (BLDC) Motors synchronous control system based on the CANopen protocol is proposed in this paper. Multi-motor control is popular in Robot or automation system, and the synchronization is an important issue, may be the key issue. The CANopen is a solution, due to Process Data Object (PDO) protocol. A Texas Instruments microcontroller TMS320F28069 is used as master to control six BLDC Motors used as slave in this paper. The Master sends synchronization object (SYNC) to slaves base on the communication profile CAN in Automation (CiA) 301 and the motion control profile CiA402. The system suns at 500Kbits/s and 1Mbits/s transmission rate by setting process data object (PDO). The firmware details in this paper to show six-motor synchronous control.

Keywords: CAN bus, CANopen, Brushless DC Motors

1. Introduction

Multi-motor synchronized control is a important and key issue in Robot or automation system. How a communcation protocal supports synchroniztion is discuused in many literatures. [1] mentioned CAN communication for complex in-vehicle networks can reduce the cost of hardware configuration and maintenance. [2] is similar to [1], but the CANopen protocol is adopted and supports compatibility. The master communicate with the devices form different manufacturers. CAN is also widely used in the industrial field due to the better error mechanism and high transmission rate.[3] The CANopen protocol also defines device specifications for industrial devices. This paper will refer to the Network Management (NMT) Object, which CANopen basic communication specification is mentioned in [4] and [5]. The Service Data Object (SDO) is used to ask or set parameter for any single node. And the PDO is the object communication code for instant communication and the SYNC synchronization command. The target of the paper is the synchronous control of six BLDC motors, through the basic communication specification CiA 301 [6] and the motion device specification CiA 402 [7]. The CAN peripheral of TI TMS320F28069, master, is used to handle the CAN communication, and the CANOpen protocol is peformed by program. The parameters of target speed, acceleration and deceleration on the Maxon EPOS4 motor drive could be set and synchronous controled. The speed mode of the CiA 402 is used to achieves position control of the motor. The updating rate for six motors synchronous control will be discussed in this paper.

2. System Architecture

The system architecture is shown in Fig.1. The system includes a mater (TI's TMS320F28069), CAN driver (Renesas' R2A25416SP) and motor drivers (Maxon's EPOS4) with motors.

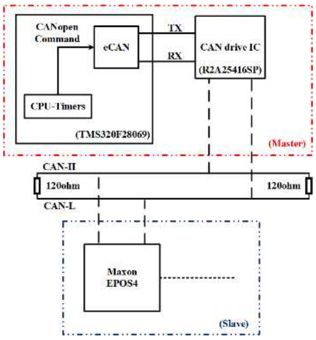

Fig. 1. System architecture diagram

2.1. *Master- TI TMS320F28069*

The build-in peripherals of TMS320F28069, CAN module and timer, are used in the CAN master. Due to digital format of CAN module signal, a driver is necessary to convert signal to differential signals of CAN-H and CAN-L. These two wires are connected directly to CAN bus. The timer is sued to trigger CPU to set the new target speed, acceleration and deceleration values of the slaves every fixed time interval.

2.2. *Slave- Maxon EPOS4 drive*

The Maxon EPOS4 is adopted in system to drive motor, the CAN communication interface is built in, and the CiA 301 and 402 object specifications are support by thid driver. In this paper, it is selected as the slaves to receive the target speed, acceleration or deceleration from the master for motor control.

2.3. *CAN Transport Packets*

The CAN2.0A format is shown in Fig.2, what is used in CANopen protocol. This format is also used in this paper, it is the key of calculate communication capability, later. However, the format includes stuffing bit, and this bit stuffing mechanism is sued to detect short even. The maximum of stuffing bits generated by the bit stuffing mechanism is discussed in [8], as shown in Eq. (1). The first 4 bits of the 11bits ID of the arbitration field in a single complete packet are defined as the control code, and the else 7 bits specified in the following are the node ID. These 11 bits are collectively referred to as the communication object identifier(COB-ID), and is followed by corresponding format specifications for the data sections in the packet.

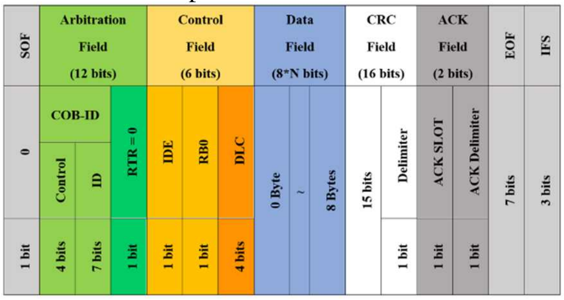

Fig. 2. Base of CAN data frame format

$$\text{stuff bit}_{\max} = 8 + 2 * \text{DLC} \tag{1}$$

3. Software Architecture

In the CANopen CiA 301 protocol, a master must arrange communication relationships between a transmit- and a receive-PDO with SDO. [6] is stipulated that the NMT must be used to control the working state of the device before using the SDO or PDO. Each device has a working state machine. The master controls the working state of the node through the NMT. As shown in Table 1, if people like to use SDO, the node working state have be set into the pre-operation mode. If PDO, the node in operation mode is necessary.

Table 1. States and Communication Objects [6]

	Pre-Operational	Operational	Stopped
NMT	√	√	√
PDO		√	
SDO	√	√	
SYNC	√	√	

In the master, the timer is used to trigger master to update the parameters of the PDO mapping to the device periodically. These parameters are the motion device state machine control object, such as the target speed object, the acceleration object, and the deceleration object. The data type of each object is also shown in Table 2.

Table 2. Data format of the object [7]

Object	Data type
6040h: Control word	UNSIGNED16 (2 Bytes)
60FFh: Target velocity	INTEGER32 (4 Bytes)
6083h: Acceleration	UNSIGNED32 (4 Bytes)
6084h: Profile deceleration	UNSIGNED32 (4 Bytes)

3.1. *Implementation Process data object*

In this paper, PDO is used for parameter setting and synchronous control. The NMT object communication code is used to set the working state of the node, and the NMT object includes the single or broadcast mode. Due to multiple nodes in the proposed system, the working state of all nodes is set to the operation mode in the broadcast mode. When the working state of node is the pre-operation mode, the node could process the SDO object. It is necessary for the PDO usage, the PDO mapping function of the node muse be set by SDO in advance. The SDO is only use in a point-to-point scheme. A node has to respond the SDO send from the master in 1 ms, as shown in Fig. 3(a).
After completing the PDO setting, the working mode of a node needs to be set to the working mode, and then the PDO function is valid. Note, it is important, when the nodes receive the PDO from the master, the nodes will wait for the SYNC command from the master to start to achieve the command. Here, this SYNC is a broadcast signal without data, and the all of motors can start simultaneously, as shown in Fig. 3(b).

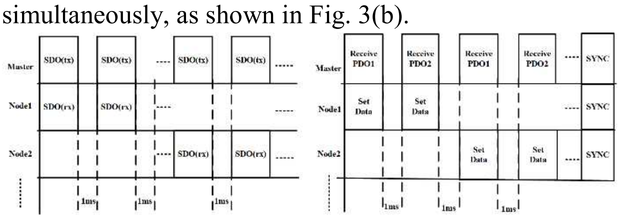

(a) SDO (b)PDO

Fig. 3. sequence in time

3.2. *Comapre SDO with PDO for synchronized control*

The Fig. 4 shows the comparison of SDO and PDO for synchronized control with three parameters, which lengths are 1, 2 and 4 bytes. Because the SDO has a specific format in the data field when setting the object parameter to a node. Three packets are necessary, due to setting three object parameters in SDO mode. After setting, the node will return 4 bytes of response to the master. However, after PDO mapping function is performed in SDO mode, only 8 bytes of one packet is required to set object parameters.

4. Experimental results

The Fig. 5 presents the system diagram of the experiment. As mentioned above, the master, TI TMS320F28069, and CAN driver in red dash box. The blue dash box shows the salve, and every slave includes a Maxon drive and a BLDC motor. Obviously, the CAN bus is sued to link master and all salves in parallel.

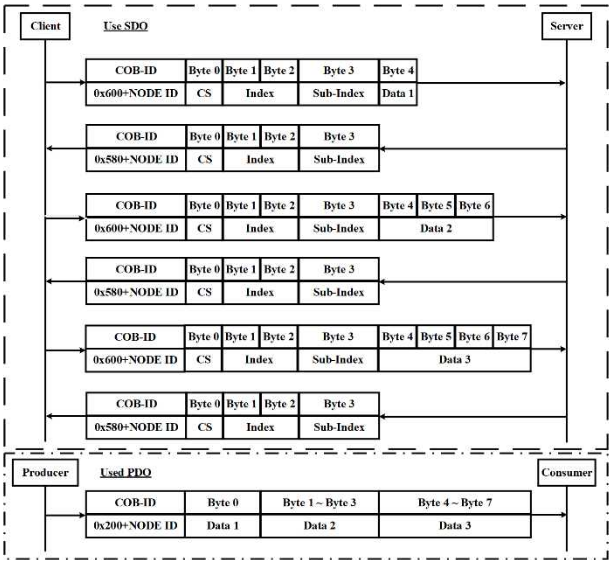

Fig. 4. SDO vs PDO [5]

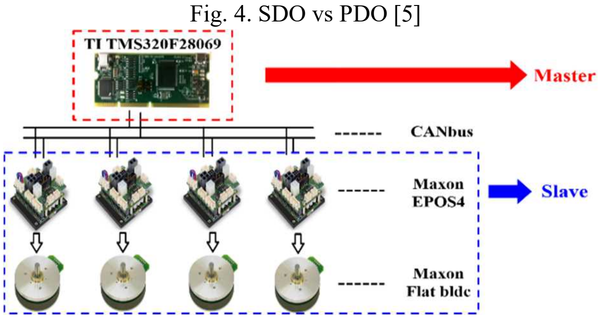

Fig. 5. Experiment system

4.1. *Method of updating speed commands*

The system minimize requirement is that every slave is updated the driver commands every 0.1 second for synchronized control. These commands are the target speed, acceleration, deceleration and control word, and these four parameters are arranged into two groups of PDO, means two PDO mapping. When the all slaves (named consumer in PDO mode) received all PDO parameters from the master (named producer in PDO mode), and then the master sends a broadcast SYNC signal to trigger all salves.

4.2. *Node Capacity Calculation*

To make sure how many slaves could be control synchronously in the proposed system, the node capacity calculation is necessary. As discussed previously, CANopen follows the packet format of CAN2.0A, which is present in Fig. 1. The length of the minimum packet which never includes any data byte is 47 bits, which includes the IFS (Inter-frame Space) field already. The length of a packet depends on the object. The packet's length without stuff bit can be calculated from Eq. (2). Moreover, in the actual situation, the stuff bit must be considered, and its length could get from Eq. (3).

$$\text{CAN data bits}_{\text{no stuff bit}} = 47 + 8 * \text{DLC} \quad (2)$$

$$\text{CAN data bits}_{\text{stuff bit}} = 55 + 10 * \text{DLC} \quad (3)$$

In SDO mode, the maximum number of nodes controlled synchronously in 0.1 second is derived as (4). Note, the 8 ms is the extra inter-frame space requested by Maxon for 8 packets. First, the SDO_Packet_Length equals to the length of 4 parameter SDO packets plus 4 response packets. Note, the parameter SDO packet includes the minimums length (55 bits), 4 bytes (CS, index, and sub-index) and data bytes as shown in Table 2, and the exact bit number can get from Eq. (3). Moreover, the response packet is fixed to 4 bytes plus 55 bits. Finally, the SDO packet is equal to 900 bits. And node number can be get from (4).

$$\text{Node number}_{\text{SDO}} = \frac{0.1(\text{s})}{\frac{\text{SDO\_Packet\_Length}}{\text{baud rate}} + 8(\text{ms})} \quad (4)$$

On the other hand, the PDO equation is more complex, as shown in Eq. (5). The one SYNC packet (55 bits) is necessary for every 0.1 S, so is 1ms (extra inter-frame space). Due to the two PDO mapping groups, the 2 ms is the extra inter-frame space for two packets. Next, PDO_Packet_Length includes 2 PDO packets. The data of the first PDO pocket is 8 bytes, and second's is 6 bytes. In short, PDO_Packet_Length is equal to 250 bits.

$$\text{Node number}_{\text{PDO}} = \frac{0.1(s) - \frac{\text{sync}}{\text{baud rate}} - 1(ms)}{\frac{\text{PDO\_Packet\_Length}}{\text{baud rate}} + 2(\text{ms})} \quad (5)$$

The calculation results are present in Table 3 for the different communication mode and different baud rates

Table 3. Maximum number of nodes

	SDO	PDO
500kbits/s	10	39
1Mbits/s	11	43

4.3. *Experimental Results of Position Control*

(a) Initial (b) Finish

Fig. 6. Position experiments

The 4.3. Experimental Results of Position Control is shown in Fig. 6, and (a)/(b) is the initial/finish status. This experiment run in the PDO mode. From left to right, the first and third motors are controlled in the same commands, and the second's and fourth's are in the other sane commands. They are synchronous stopped at the same two positions. The results show the proposed CANopen synchronous control is workable.

5. Conclusions

This paper proposes a multi-node synchronization control system. The system includes the CiA 301 and the CiA 402 of the CANopen protocol and use the PDO and SYNC object for synchronization control. The protocol is detailed and the capacity is calculated in the paper. Finally, the experimental results shown the proposed system work well.

Acknowledgements

This work is partially supported by the Vishay (Taiwan) Ltd; and also by Ministry of Science and Technology, ROC, under contract No. MOST 107-2221-E-224 -054. and 106-2218-E-150-001-

References

[1] D. Q. Wang, S. Gao, Y. Q. Chen, Y. Wang and Q. Liu, "Intelligent Control system based on CAN-bus for car doors and windows," *2009 3rd International Conference on Anti-counterfeiting, Security, and Identification in Communication*, Hong Kong, 2009, pp. 242-245.

[2] G. Livint, V. Horga, M. Ratoi, M. Albu and G. Chiriac, "Implementing the CANopen protocol for the distributed control of a hybrid electric vehicle," *2009 8th International Symposium on Advanced Electromechanical Motion Systems & Electric Drives Joint Symposium*, Lille, 2009, pp. 1-6.

[3] W. Li, G. Lijin and L. Zheyuan, "Design of STM32-Based CANopen Motion Control Master in Transfer Robot," *2013 Third International Conference on Instrumentation, Measurement, Computer, Communication and Control*, Shenyang, 2013, pp. 1609-1612.

[4] Yang Fan, R. Chen and Z. Chen, "Communication of the wind turbine testing system based On CANopen protocol," *2011 IEEE Power Engineering and Automation Conference*, Wuhan, 2011, pp. 162-165.

[5] B. K. Huang, *"Design and implementation of micro-stepping motor driver with CANopen"* Master Thesis, National Yunlin University of Science and Technology, June 2017.

[6] CANopen Application layer and communication profile, CiA DS301, *Version*: 4.0.2, Feb. 13, 2002, pp. 15-114.

[7] CANopen Device Profile Drives and Motion Control, CiA DS402, *Version* 2.0, Jul. 26, 2002, pp. 14-174.

[8] Holger Zeltwanger(2008), C. H. GE, "*CANopen: das standardisierte, eingebettete Netzwerk*(Chinese Edition)," Beijing University of Aeronautics and Astronautics Press, Jul. 1, 2011, pp. 1-123.

Selection Strategy for VM Migration Method

Yan-Ren Chen, I-Hsien Liu, Keng-Hao Chang
Department of Electrical Engineering / Institute of Computer and Communication Engineering, National Cheng Kung University, Tainan City, 70101, Taiwan

Chuan-Gang Liu
Department of Applied Informatics and Multimedia, Chia-Nan University of Pharmacy and Science, Tainan City, 71710, Taiwan

Jung-Shian Li
Department of Electrical Engineering, National Cheng Kung University, Tainan City, 70101, Taiwan
E-mail: {yrchen, ihliu, khchang}@cans.ee.ncku.edu.tw, chgliu@mail.cnu.edu.tw, jsli@mail.ncku.edu.tw
www.cans.ee.ncku.edu.tw

Abstract

Virtual machine (VM) live migration occurs frequently in cloud environments. When it is necessary to migrate many VMs, minimizing the migration time is an important concern. Thus, choosing an appropriate strategy to perform VM migration is essential. Accordingly, this paper discusses the advantages and disadvantages of four different migration methods and evaluates their respective migration times and throughputs.

Keywords: *VM migration, Sequential, Delay, Parallel, Simultaneous.*

1. Introduction

VM migration plays a critical role in cloud computing in satisfying user demand for computing resources while simultaneously meeting the needs of the operator for energy savings, load balancing, periodic maintenance, and so on. VM migration can be performed using four different methods, namely sequential, delay, parallel, or simultaneous. In sequential migration, migration of a VM is performed only once the migration of the previous VM on the same server has been completed. In delay migration, the VMs are located on different servers and a small delay is introduced between their migration. In parallel migration, multiple VMs located on the same physical server are migrated at the same time. Finally, in simultaneous migration, VMs located on different physical servers are migrated at the same time. In practice, the migration times of the four methods may vary widely. Thus, the choice of an appropriate migration method is essential to minimize the total migration time under different VM memory loads, migration link bandwidths, page dirtying rates, and so on.

2. Background and Related work

2.1. *VM Migration Techniques*

Virtualization platforms generally utilize either a pre-copy live migration approach [1, 2] or a post-copy live migration approach [3, 4]. Of the two methods, the pre-copy method results in a shorter downtime, while the post-copy method results in a shorter total migration time. In [5], [6], the authors showed that the overall migration time for Stages 0 ~ 5 of the pre-copy method comprises four components, namely the Pre-Migration Overhead (Stages 0 & 1), the Stage 2 Overhead, the Stage 3 Overhead, and the Post-Migration Overhead (Stages 4 & 5). Among these components, the Stage 0/1/4/5 overhead time is static but not constant.

Consequently, under the same VM migration conditions, the overhead times of the pre-and post-copy migration methods are slightly different.

2.2. *Migration Performance Indicators*

Common migration performance indicators include the total migration time, the migration down time, and the total number of VM migrations. The total migration time measures the elapsed time between the start of the first VM migration process and the end of the final VM migration process. The authors in [5-7] investigated the effects of various factors on the total migration time, including the migration link bandwidth, the frequency of dirty memory pages, the VM memory size, and so on. The migration down time measures the time for which service is interrupted during the migration process, and should be minimized in order to maintain user satisfaction. Finally, the number of VM migrations indicates the total number of VMs migrated, and should be reduced to the minimum number possible to minimize the impact of the migration process.

2.3. *TCP Window Size*

VMware [8] prescribes the use of the transmission control protocol (TCP) to establish a connection for VM migration and transmit the corresponding migration traffic. TCP is a synchronous transmission protocol with good reliability and completeness. The TCP window size used to transmit the migration packets is assigned a minimum value of (CWND, RWND), i.e., sendwin=min(cwnd,rwnd). The authors in [9] presented a scheme for lowering the value of ssthresh in order to enter the congestion avoidance stage early. However, the system suffered an insufficient startup problem accordingly. The authors in [10] considered a serial transfer process rather than parallel server request

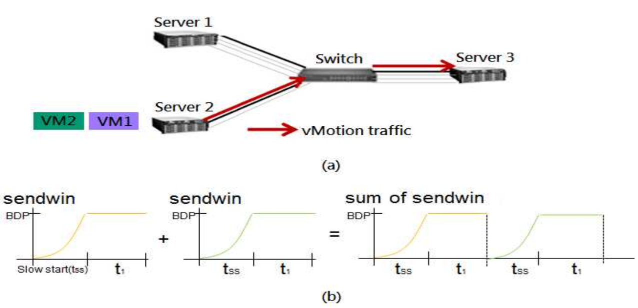

Fig.1. (a) Sequential Method (b)Sum of Sendwin

units (SRU) transmissions. However, the method resulted in a low bandwidth utilization rate during the slow start cycle.

3. VM Migration Methods and Window Size

3.1. *Sequential Method*

Figure 1(a) shows a typical example of the sequential VM migration process. Let bandwidth delay product (BDP) be the product of the link bandwidth and the round-trip time. Assume that VM1 and VM2 have the same memory size and page dirtying rates (i.e., t_{ss}+t_1 is constant). Furthermore, assume that TCP ssthresh is larger than BDP. Thus, sendwin is equal to BDP in the slow start phase. The sum of sendwin for the two VMs is then obtained as shown in Figure 1(b).

In the sequential migration method, there is no overlap between the migrations of VM1 and VM2, respectively. Consequently, the sum of sendwin in Figure 1(b) does not exceed BDP. As a result, the throughput is not degraded by overflows at the switch buffer. However, the bandwidth cannot be fully utilized during the slow start phase and the migration overheads of the two VMs cannot be processed at the same time. Consequently, the total migration time is increased. Furthermore, the operator cannot explicitly configure the time at which each VM migration task is to be performed. In other words, the sequential migration method lacks versatility.

3.2. *Parallel Method*

As shown in Figure 2(a), in the parallel migration method, VM1 and VM2 are located on the same server and are transmitted at the same time over a single connection. The sendwin size of each VM is thus reduced to (1/2)BDP. Consequently, the sum of sendwin is equal to BDP, as shown in Figure 2(b). It is seen in Figure 2(b) that t'_{ss} is less than t_{ss}. In other words, the

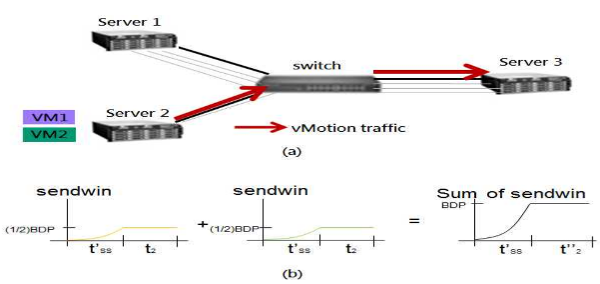

Fig.2. (a) Parallel Method (b)Sum of Sendwin

parallel migration method improves the bandwidth usage during the slow start phase. In addition, the migration overheads of the two VMs can be processed at the same time. Hence, the total migration time is reduced.

3.3. *Simultaneous Method*

Figure 3(a) illustrates the simultaneous migration method, in which the migrations of VM1 and VM2, which are located on different servers, are executed in a many-to-one communication mode. Assuming that the links between the source servers and the switch have the same bandwidth, the sum of sendwin reaches BDP after just t', as shown in Figure 3(b). Notably, t' is less than t_{ss}. In other words, the migration process results in a long overlap time between the transmissions of the two VMs. Consequently, the switch buffer easily overflows; resulting in packet drops and a significant reduction in the throughput. Thus, the total migration time of the simultaneous migration process is longer than that of the parallel migration process.

3.4. *Delay Method*

As shown in Figure 4(a), the delay migration method is similar to the simultaneous migration method other than for the fact that a short delay is introduced between the migrations of the two VMs. The delay method reduces the overlap time of the multiple TCP connections (see

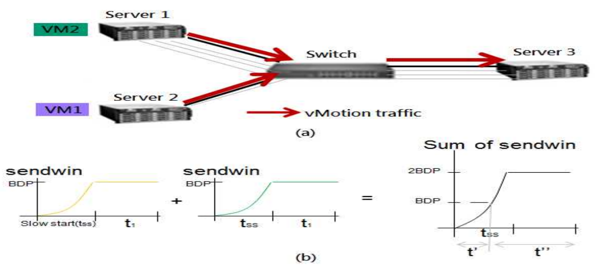

Fig.3. (a) Simultaneous Method (b)Sum of Sendwin

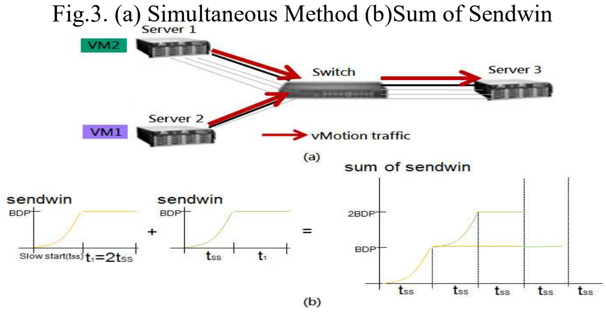

Fig.4. (a) Delay Method (b)Sum of Sendwin

Figure 4(b)), and therefore smooths the traffic volume and improves the throughput. However, the total migration time is usually much longer than that of the simultaneous migration method.

4. Performance Experiments and Analysis

4.1. *Experiment Environment*

Migration experiments were performed using three HP ProLiant DL380 G6 physical servers (two sources and a destination) and hypervisor VMware vSphere 5.5 software. The experiments replicated the network architectures and migration methods shown in Figs. 1(a)~4(a). Each VM was configured to have eight virtual CPUs and 14 GB of virtual RAM. Memory testing tool was used to increase the memory loads of the VMs in the range of 2 ~ 11 GB. The total migration time of the VMs under different loads was measured.

4.2. *Experiment Results*

Figure 5 shows the experimental results obtained for the variation of the total migration time with the VM memory load for each of the considered migration methods. The results support the following main conclusions:

(1) The migration methods can be ranked in terms of the total migration time (shortest to longest) as follows: Parallel < Simultaneous < Delay < Sequential.

(2) For a memory load of 11 GB, the total migration time of the simultaneous method is close to that of the sequential method.

(3) The delay method generally results in a longer total migration time than the simultaneous method. However, the performance of the delay method depends on the delay time applied. For example, given a memory load of 11 GB and a delay time of 120 seconds, the delay method results in a shorter total migration time than the simultaneous method.

Figure 6 shows the throughputs obtained for each of the four migration methods given a VM memory load of 4 GB. The migration methods can be ranked in terms of the throughput performance (high to low) as follows: Parallel ≈ Sequential > Delay > Simultaneous.

4.3. *Migration Selection Strategy*

Based on the experimental results presented above for

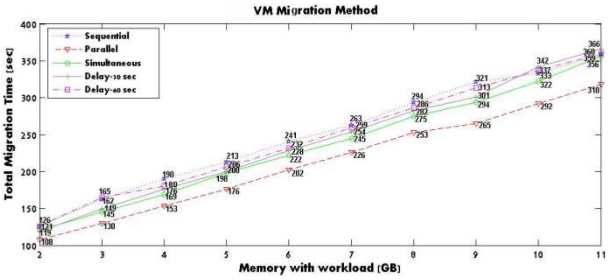

Fig.5. Total migration times of different VM migration methods.

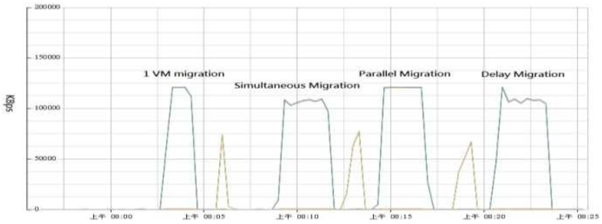

Fig. 6. Throughputs obtained under different VM migration methods.

the total VM migration time, the following migration selection strategies are proposed:

(1) Selection strategy 1: If the switch-server 3 link bandwidth is much higher than that of the source-switch links:

Selection order: Simultaneous -> Parallel -> Delay ->Sequential method

(2) Selection strategy 2: If the bandwidths of the links between the switch and the servers (sources and destination) are the same:

Selection order: Parallel -> Simultaneous -> Delay ->Sequential method.

5. Conclusion

This paper has analyzed the migration time and throughput performance of four different VM migration methods (sequential, delay, parallel, and simultaneous) under different VM memory loads. In general, the results have shown that when the link bandwidth of the migration destination is much higher than that of the source(s), the simultaneous method results in the shortest migration time. By contrast, if the link bandwidth of the migration destination is equal to that of the source(s), the parallel migration method provides the shortest total migration time.

Acknowledgements

This work was supported by the MOST (Ministry of Science and Technology), Taiwan under contracts numbers MOST 107-2218-E-006-036- and MOST 107-2221-E-006-140-.

References

1. Virtual Machine Live Migration Overview, Microsoft TechNet,https://technet.microsoft.com/en-us/library/hh831435(v=ws.11).aspx, 21 August. 2013.
2. Christopher Clark, Keir Fraser, Steven Hand, Jacob Gorm Hansen, Live Migration of Virtual Machines, https://www.usenix.org/legacy/event/nsdi05/tech/full_papers/clark/clark.pdf
3. Hines, Michael R., and KartikGopalan, Post-copy based live virtual machine migration using adaptive pre-paging and dynamic self-ballooning, *ACM SIGPLAN/SIGOPS international conference on Virtual execution environments*. *ACM*, 2009, pp. 51-60.
4. Michael R. Hines, Umesh Deshpande, Kartik Gopalan, Post-Copy Live Migration of Virtual Machines, http://osnet.cs.binghamton.edu/publications/hines09postcopy_osr.pdf
5. Sherif Akoush, Ripduman Sohan, Andrew Rice, Andrew W. Moore and Andy Hopper, Predicting the Performance of Virtual Machine Migration, *IEEE International Symposium on Modeling, Analysis & Simulation of Computer and Telecommunication Systems (MASCOTS),* 2010, pp. 37-46.
6. Mohamed Esam Elsaid, Christoph Meinel, Live Migration Impact on Virtual Datacenter Performance : Vmware vMotion Based Study, *International Conference on Future Internet of Things and Cloud (FiCloud)*. 2014, pp. 216-221.
7. Felix Salfner, Peter Troger, Andreas Polze, Downtime Analysis of Virtual Machine Live Migration, *The Fourth International Conference on Dependability,* ISBN: 978-1-61208-149-6. 2011, pp. 100-105.
8. "VMware vSphere5.1 vMotion Architecture, Performance and Best Practices." VMware TECHNICAL WHITE PAPER, Available at: https://www.vmware.com/iles/pdf/techpaper/VMware-vSphere51-vMotion-Perf.pdf.
9. A. Phanishayee, E. Krevat, Y. Vasudevan, D. G. Andersen, G. R. Ganger,G. A. Gibson and S. Seshan, Measurement and Analysis of TCP Throughput Col/apse in Cluster-based Storage Systems, *The 6th USEUNTX Conference on File and Storage Technologies (FAST 2008)*, 2008. pp. 12:1-12:14 [Online].
10. Shigeyuki Osada, Kazutoshi Kajita, Yukinobu Fukushima and Tokumi Yokohira, TCP Incast Avoidance Based on Connection Serialization in Data Center Networks, Communications, 19th Asia-Pacific Conference((APCC)), 2013, pp. 142–147.

VM Migration Placement in Cloud Service

Yan-Ren Chen, I-Hsien Liu, Keng-Hao Chang
Department of Electrical Engineering / Institute of Computer and Communication Engineering, National Cheng Kung University, Tainan City, 70101, Taiwan

Chuan-Gang Liu
Department of Applied Informatics and Multimedia, Chia-Nan University of Pharmacy and Science, Tainan City, 71710, Taiwan

Jung-Shian Li
Department of Electrical Engineering, National Cheng Kung University, Tainan City, 70101, Taiwan
E-mail: {yrchen, ihliu, khchang}@cans.ee.ncku.edu.tw, chgliu@mail.cnu.edu.tw, jsli@mail.ncku.edu.tw
www.cans.ee.ncku.edu.tw

Abstract

The present study considers two different VM migration problems and proves that they too are NP-complete. In the first problem, subsets of the VM migration groups are migrated to a physical host until their combined resource usage approaches the threshold value of the host. In the second problem, the VM migration groups are migrated simultaneously in such a way as to minimize the total migration time.

Keywords: *VM, Live Migration,* NP-Completeness.

1. Introduction

Generally speaking, problems can be classified as either Unsolvable, Intractable, Non-Deterministic Polynomial (NP), or Polynomial (P). This study focuses on the particular case of NP problems. In other words, the problem solution can be calculated in exponential time and verified in polynomial time. When a problem belongs to NP and some NP-complete (NPC) problems can be solved by this problem, then the problem is also a NPC problem. NP-hard problems are one type of NP problem for which it still has not found a polynomial complexity of the decision algorithm, and polynomial complexity of the decision algorithm does not exist. NP-hard problems are a particular class of NP problem to which every problem in NP can be translated, and each solution to such a problem gives a fast solution to every other problem in NP. Problems which are both NP and NP-hard are referred to as NP-Complete (NPC).

2. Background and Related work

2.1. *NP-Completeness*

In [1-3], the authors proposed various methods for proving that problems belong to NPC. These methods typically involve three main steps:
(1). Prove that the problem under consideration belongs to an NP problem (i.e., B∈NP).
(2). Select an already known NPC problem. (i.e., EXACT-COVER, SAT, Bin Packing, and so on).
(3). Transform (reduce) the selected NPC problem to the problem under consideration.
Common NPC problems include the Satisfiability Problem [3], the 0-1 Knapsack problem [2], the Hamiltonian Cycle, and so on. Taking the Knapsack problem for illustration purposes, Lagoudakis [2] reviewed various algorithms for solving the 0-1 Knapsack problem and showed by reference to the

EXACT-COVER and SAT problems that they all belong to NPC.

The nature of the VM migration problem (i.e., NP-complete or NP-hard) has attracted significant attention in the literature. The authors in [4] proved that VM migration flow over the delivery path is NP-complete by reference to the Hamiltonian Cycle problem. The authors also proposed a method for minimizing the number of delivery flow under the migration process and showed by reference to the Bin Packing problem that this too was NP-complete. Kangkang et al. [5] reported that for both off-line and online scenarios, the author-defined total completion time minimization VM placement problem was an NP-hard problem. However, no formal proof was provided to substantiate the claim. The authors in [6] showed that the problem of placing VMs on a physical host with both a minimal cost and a minimal response time is NP-hard. However, while a heuristic algorithm was proposed for its solution, the NP-hardness of the problem was not formally presented. Zhang et al. [7] used a software-defined networking (SDN) technique to minimize the network flow resumption time during VM migration. The flow migration problem was transferred to a Disjoint Path Problem and shown to be NP-complete. The authors in [8] considered a network-aware VM migration (NetVMM) problem and showed that it is a variant of the well-known NP-complete multiple-knapsack problem.

3. Proposed Scheme

3.1. *A subset of the VM migration groups is migrated to a physical host until their resource usage approaches the threshold value of this physical host → NPC problem*

Assume that a subset of the VM migration groups on multiple source hosts are to be migrated to a single physical host, as shown in Figure 1. For the migration process to be successful, the total resource requirements of the selected subset of VM migration groups must be less than the designated threshold resources of the destination host. The related notations are listed in Table 1.

As discussed in the following, the migration of the subset of VM migration groups to the physical host until the usage resource load approaches the threshold value

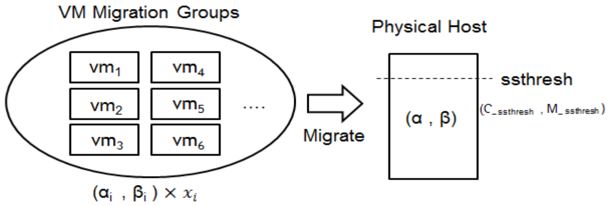

Fig.1. VM migration to destination host

Table 1 Notations used in Section 3.1

Notation	Description
C	CPU resources of physical host.
M	Memory resources of physical host.
c(u)	CPU loads of migrated VMs
m(u)	Memory loads of migrated VMs
VM	Total VM migration group (i.e., VM = $\{vm_1, vm_2, ..., vm_{n-1}, vm_n\}$)
C_ssthresh	Threshold value of CPU resources of physical host
$M_{\_ssthresh}$	Threshold value of memory resources of physical host

of the host is an NP problem. In general, a non-deterministic algorithm is one which, for the same input, a different result is obtained every time. For the VM migration problem considered here, the total usage resources of the VMs to be migrated must be less than the remaining resources of the destination host before migration. Furthermore, the migration process should continue until the VM migration resource usage just approaches (but does not exceed) the threshold value of the physical host. This problem can be verifiable in polynomial time. Hence, the migration of a subset of the VM migration groups to a physical host until their resource usage approaches the threshold value of this physical host belongs to NP.

Let the migration problem be transformed using the Sum of Subset problem (a known NPC problem). In the Sum of Subset problem, there exist n integers, of which a particular subset of n can be found for which the sum of the subset is equal to M. For example, given a set A = $\{a_1, a_2, a_3, ..., a_p\}$, the aim of the Sum of Subset problem is to find the subset of A, denoted as Sub_A=$\{ a_1, a_4, a_5, a_6 \}$, for which the sum of Sub_A is M. In the VM migration problem, the host resources and the usage resources of the VMs are both given. When Sub_A contains a subset of A ⇔ usage resource of partial VM in this group that satisfies equation (1). Thus, the VM migration problem can be formulated as the following Sum of Subset problem:

$$\sum_{u\in \text{subset VM}} c(u) \le C_{\_ssthresh} * C \text{ and } \sum_{u\in \text{subset VM}} m(u) \le M_{\_ssthresh} * M. \quad (1)$$

Assuming that |A| = n objects, then u = {ui, i = 1, ..., n}. Let the selection factor have the following form:

$$\text{if } x_i = \begin{cases} 1 & \text{if VM is selected} \\ 0 & \text{otherwise} \end{cases} . \quad (2)$$

The resource usage of the VMs can thus be obtained as

$$\text{VM\_Resource\_usage}\{\, C_i, M_i \,\}=\{\, \sum_{i=1}^{n} x_i \times c(u_i)\ ,\ \sum_{i=1}^{n} x_i \times m(u_i)\,\} \approx \{C_{\_ssthresh} * C, M_{\_ssthresh} * M\}\,. \quad (3)$$

Equation (3) gives the correspondence between A and VM and between VM and the load. The corresponding complexity is O (np^2) polynomial time. Thus, the migration problem belongs to NP-complete.

3.2. *Minimizing the simultaneous migration time (i.e., non-preemptive schedule) is a NPC problem*

VM migration can be performed in four different modes, namely *sequential*, *parallel*, *simultaneous*, or *delay*. In the simultaneous VM migration process, multiple VMs are migrated simultaneously to different physical servers, as shown in Figure 2. In many-to-one communications, many TCP connections compete for the same fixed resources of the switch and router during the migration process, and thus buffer overflows readily occur and cause packet losses. In order to facilitate the discussion, assume that congestion and retransmission do not occur and $B>b_1+b_2+b_3+\ldots+b_n$, where B, b_1, b_2,…, b_n are the link bandwidths. Under this condition, the overall migration time can be reduced by moving more than one VM at the same time. However, when consolidating the VMs at the source host side into batches for migration, it is first necessary to check whether the resources at the destination side are sufficient to enable the migration to be successfully completed. As described in Section 3.1, this problem is verifiable in polynomial time. Consequently, the simultaneous migration of multiple VMs on different hosts to multiple destination hosts belongs to NP.

Let the simultaneous VM migration problem shown in Figure 2 be transformed to the Minimum Finish Time Non-Preemptive Schedule problem (a known NPC problem). The related notations are listed in Table 2.

The Minimum Finish Time Non-Preemptive Schedule problem assumes that each task is not interrupted during execution and seeks a schedule which achieves a completion time less than or equal to a pre-set value. For example, assume that the processors are capable of performing parallel processing (i.e., each processor is capable of processing each task) and, in the case of identical processors, the tasks are performed in parallel. For such a scheduling scenario, the completion time is equal to the time at which the final task is completed. In other words, the completion time can be expressed simply as

$$C\_T = \underbrace{\overbrace{\underbrace{\max(T_j)\,|_{batch\,1}^{j=1:k1}}_{\text{k1 tasks}} + \underbrace{\max(T_j)\,|_{batch\,2}^{j=k1+1:k2}}_{\text{k2-k1 tasks}} + \ldots + \underbrace{\max(T_j)\,|_{batch\,m}^{j=kp+1:n}}_{\text{n-kp tasks}}}^{\text{n tasks}}}_{\text{m processors}}$$

There exists a one-to-one mapping between the Minimum Finish Time Non-Preemptive Schedule problem and the VMs on the physical hosts. Suppose that VM_migrate is distributed as follows:

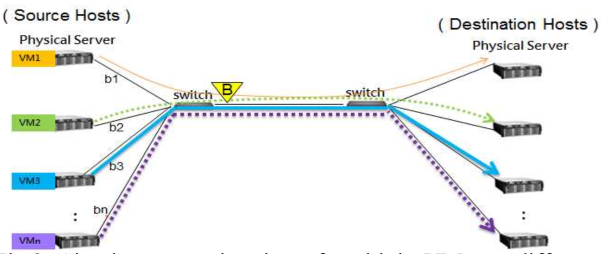

Fig.2. Simultaneous migration of multiple VMs on different hosts

Table 2 Notations used in Section 3.2

Notation	Description
m	Number of processors (i.e. m≧2)；expressed as $P=[p_1,p_2,\ldots p_m]$
n	Number of tasks；expressed as $J=[j_1,j_2,\ldots j_n]$
C_T	Completion time value
T	Set of processing times of various tasks；expressed as $T=[t_1,t_2,\ldots,t_n]$
N	Number of VMs to be migrated
M	Number of physical hosts
$VM_{\_dist}$	Distribution of N VMs on physical host; expressed as VM_dist =$[N_1,N_2,\ldots N_M]$
$VM_{\_migrate}$	Subset of VM_dist to be migrated

$$VM_{migrate}=\{\overbrace{[\text{Subset\_1 of } VM_{dist}]}^{\text{Physical Host 1}}, \overbrace{[\text{Subset\_2 of VM\_dist}]}^{\text{Physical Host 2}}, \overset{\cdots\cdots}{\ldots\ldots} \overbrace{[\text{ Subset\_m of VM\_dist}]}^{\text{Physical Host m}}\}$$

where Subset_1 of VM_{dist} , Subset_2 of VM_{dist} and…$Subset_m$ of VM_{dist} is VM_{dist} are the subsets of VMs assigned to Physicals Hosts 1, 2 and m, respectively.

In other words, the VMs are consolidated into several batches, and all of the VMs in one batch are migrated to the target host at the same time. The VM migration time consists mainly of migration overheads and the transfer time itself. Thus, for each batch of VMs, the migration time can be expressed as

$$T_{\text{migration time\_batch}} = \max(\text{each of VM migration time (Overheads + transfer time)})|_{\text{batch}}$$

The total migration time is equal to the sum of the migration times of the individual batches, i.e.,

$$T_{\text{total\_migration\_time\_batch}} = T_{\text{migration\_time\_batch 1}} + T_{\text{migration\_time\_batch 2}} + \ldots + T_{\text{migration\_time\_batch m}}$$

The correspondence between the minimum of the simultaneous migration time and the Minimum Finish Time Non-Preemptive Schedule problem is given by: processors↔physical host resource, tasks↔VMs (where each VM cannot be interrupted as it migrates) ↔ each task cannot be interrupted as it executes. In other words, the output of the minimum of the simultaneous migration time problem can be transformed to the output of the Minimum Finish Time Non-Preemptive Schedule problem. Thus, the following relation equation is obtained for the Minimum Finish Time Non-Preemptive Schedule problem:

$$T' = \sum \max (T_j)\ |_{\text{batch 1,...,batch m}}$$

Minimizing the simultaneous VM migration time is similar to solving the non-preemptive schedule for processing a set of tasks in such a way as to achieve the minimum finish time. The Minimum Finish Time Non-Preemptive Schedule problem is known to be NPC. From the transform above, it is seen that the simultaneous migration time for the migration operation of VM vMotion $\leq_p$ minimum finish time of the non-preemptive schedule problem. In other words, the problem of determining the simultaneous migration time for VM vMotion is polynomial time reducible to the minimum finish time non-preemptive schedule problem. Therefore, the simultaneous VM migration problem is also an NPC problem.

4. Conclusion

This study has proven that VM migration is an NPC problem by reference to two known NPC problems, namely the Sum of Subset problem and the Minimum Finish Time Non-Preemptive Schedule problem.

Acknowledgements

This work was supported by the MOST (Ministry of Science and Technology), Taiwan under contracts numbers MOST 107-2218-E-006-036- and MOST 107-2221-E-006-140-.

References

1. Robert J. FOWLER, Michael S. PATERSON and Steven L. TANIMOTO, 1981. Optimal Packing and convering in the plane are NP-Complete, *INFORMATION PROCESSING LETTERS, Vol. 12, Iss. 3*, 1981, pp. 133-137.
2. Michail G. Lagoudakis, *The 0–1 Knapsack Problem--An Introductory Survey,* citeseer. nj. nec. com/151553. html, 1996.
3. Jun Gu, Paul W. Purdom, John Franco, Benjamin W. Wah, Algorithms for the Satisfiability (SAT) Problem: A Survey, https://www.cs.toronto.edu/~chechik/courses03/csc2108/algorithms-for-satisfiability.pdf, 1997.
4. Lei Cui, JinpengHuai, Jianxin Li, Chunming Hu, Bo Li, TianyuWo, Hussain Al-Aqrabi, Lu Liu , VMScatter: Migrate Virtual Machines to Many Hosts, *In: VEE'13, ACM 978-1-4503-1266-0/13/03,*. 2013, pp. 63-72.
5. Kangkang Li, Huanyang Zheng, and Jie Wu, Migration-based virtual machine placement in cloud systems, *Cloud Networking (CloudNet), IEEE 2nd International Conference*, 2013, pp 83-90.
6. Rajalakshmi Shenbaga Moorthy et al, An Effective Mechanism for Virtual Machine Placement using Aco in IAAS Cloud, IOP Conference Series: *Materials Science and Engineering*, 225012227, Vol. 225 , Issue 1, pp. 012227, 2017, https://doi.org/10.1088/1757-899X/225/1/012227.
7. Sai Qian Zhang, Pouya Yasrebi, Ali Tizghadam, Hadi Bannazadeh, Alberto Leon-Garcia, Fast Network Flow Resumption for Live Virtual Machine Migration on SDN, *2015 IEEE 23rd International Conference on Network Protocols*, 2015, pp. 446-452.
8. 7. Weizhe Zhang, Shuo Han, Hui He, Huixiang Chen, Network-aware virtual machine migration in an overcommitted cloud, Future Generation Computer Systems, 2016, pp. 428-442.

Control System for Maintaining Safe Following Distance while Driving

Kuo-Hsien Hsia
Department of Electrical Engineering, Far East University
No.49, Zhonghua Rd., Xinshi Dist., Tainan City 74448, Taiwan (R.O.C.)

Jia-Hong Cai
Department of Electrical Engineering, Far East University
No.49, Zhonghua Rd., Xinshi Dist., Tainan City 74448, Taiwan (R.O.C.)

Shu-Li Pai
Global Learning and Assessment Development, Greater China
Room 402, Building 2, No. 78, Maizidian Street, Chaoyang District, Beijing 100020, China
E-mail: khhsia@mail.feu.edu.tw, vic1004210564@gmail.com, dosg1222@qq.com
www.feu.edu.tw

Evgeni Magid
Laboratory of Intelligent Robotic Systems (LIRS), Intelligent Robotics Department, Higher Institute for Information Technology and Intelligent Systems, Kazan Federal University, Russia

Abstract

Safety is the most important issue while driving. Many traffic accidents occur because of insufficient safe distance. With the advancement of technology, there are cars with a front distance safety warning system. Some of them are with fixed safe distance regardless of the speed of the car. Other advanced distance detection systems switch between different modes such as high speed and low speed. In this paper, we proposed a driving safety system which can dynamically adjust the safe distance between vehicles depending on the speed and weather conditions. This system can be used to determine and maintain safe distances both in front and rear of a car. This idea has obtained an invention patent of Taiwan. A car with this system can be driven more safely.

Keywords: Driving safety, safe distance, driving speed, weather conditions.

1. Introduction

Living in this era, transportation is inseparable from people's daily lives. Many people often drive to work or travel. For some people, driving is their work. So, driving safety is an absolutely important part for them. According to the annual report of the Freeway Bureau, Ministry of Transportation and Communications (MOTC), Taiwan, the reasons for the top ten accidents on the super highway of Taiwan in 2015 are as follows:[1]

(i) Not maintaining the driving safety distance (50.5%)
(ii) Not appropriately changing lanes or directions (12.8%)
(iii) Not paying attention to the state in front of the car (10.3%)
(iv) Other violations that caused accidents (8.0%)
(v) Backing the car without accordance with regulations (2.2%)
(vi) Wheel shedding or tire burst (1.8%)

(vii) Loading goods not safely fixed (1.3%)
(viii) Drunk driving (1.1%)
(ix) Vehicle parts falling (0.7%)
(x) Not maintaining driving safety interval (0.6%)

Traffic accident analysis reports in many countries have similar conclusions. Statistics of traffic accidents show one of the most common causes of traffic accidents to be the "failure to observe a safe distance behind another vehicle.[2]" There are three safe distance required in car-following[3]: front safe distance, rear safe distance, and lateral safe distance, as shown in Fig. 1. Everybody knows that keep safe distance in driving is very important. Considering the three safe distances, the front distance can almost completely controlled by the driver. Studies have shown that leaving more space between vehicles helps to reduce traffic accidents and allows for smoother traffic.[4]

There are many factors that may have influence on safe distance. For example, speed of the vehicle, driver's attentiveness, size and condition of the vehicle, road surface, and weather conditions are all factors of the driving safety distance. An article of WHO (World Health Organization) shows that speed has been identified as a key risk factor in road traffic injuries, influencing both the risk of a road crash as well as the severity of the injuries that result from crashes.[5] A good suggestion for keeping safe driving distance is "two-second rule." The rule is that a driver should ideally stay at least two seconds behind any vehicle that is directly in front of his or her vehicle.[6] However, counting seconds may cause distracting for the driver. Another guiding rule about safe distance (in meter) on the super highway in Taiwan is half of the speed (in km/h) for small cars and speed minus 20 for large cars.

With the advancement of technology, there are cars with a front distance safety warning system. Some of them are with fixed safe distance regardless of the speed of the car. Other advanced distance detection systems switch between different modes such as high speed and low speed. However, from earlier discussions we know that the safe following distance closely regards to the speed of the vehicle. In this paper, we will propose a driving safety system which can dynamically adjust the safe distance between vehicles depending on the speed and weather conditions.

2. System Architecture

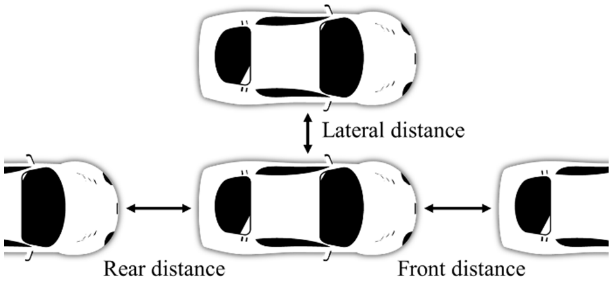

Fig. 1. Distances that should be concerned by the driver.

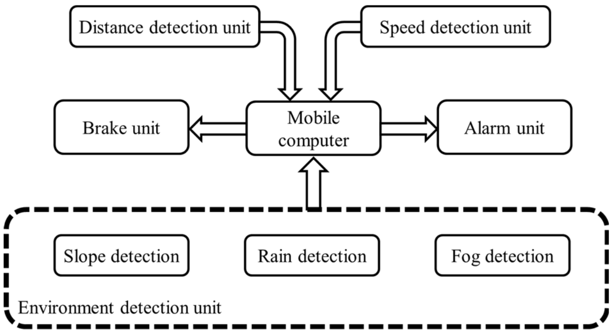

Fig. 2. System architecture of the proposed system.

Our system is primarily designed to alert drivers when there is insufficient safe distance from the vehicle in front. The system architecture is shown in Fig. 2. We modified the rule of safe distance promulgated by the Freeway Bureau, MOTC, Taiwan by considering the environment parameters such as uphill/downhill, heavy rain, and thick frog. Hence the driving safety distance can be adjusted dynamically. The function of the safety distance in front of the car is shown as Eq. (1).

$$d = f(v, r, g, s) = \begin{cases} \frac{v}{2} * (1 + r + g + s) & \text{for small car} \\ (v - 20) * (1 + r + g + s) & \text{for large car} \end{cases} \quad (1)$$

where $0 \le r, g, s \le 1$.

Here d is the safe distance, v is the speed of the car, r is the status of rain, g is the status of frog, and s is the slope of uphill or downhill. The parameter r is 0 when it is not a rainy day, and is 1 when it is heavy rain. The parameters of g and s are defined in similar way. For example, a small car is driven on the highway at a speed of 110 km per hour, with clear weather and non-uphill/downhill sections, the safety distance should be 55 meters. For the same speed but in the downhill section, the safety distance should be more than 55 meters.

This system can be integrated into the driving computer to form a complete driving safety system, or it can be an independently-operated driving safety assistant system. For the integrated system, the system can remind the driver to slow down or automatically activate the brake system to force the deceleration when the safety distance is insufficient. For an independently operated system, the system can only alert the driver to slow down without any mandatory action.

The alarm unit can include an audio alert and a light alert. The sound or light warning in the car can remind the driver to properly slow down to avoid the danger of chasing. If there is a light warning at the rear of the vehicle, it can alert the driver of the rear car that the safety distance to the front vehicle and the vehicle in front can be reminded that it is insufficient. It is recommended that the rear vehicle should be properly decelerated.

This structure has been awarded the invention patent of Taiwan with certificate No. I594215 in August 2017.

3. Experimental Simulation

To promote our patent concept, we constructed a simple simulation experiment system. An HT66F50 is used as the central processing unit of the system. An ultrasonic sensor is used as the front distance detector. We use a sliding-type variable resistor to simulate the throttle acceleration system. In order to detect that the car is on an uphill or downhill state, we use two mercury switches configured as inverted V-type, as shown in Fig. 3, to detect the attitude of the car. If the front switch is closed and the rear one is open, then the car is on a downhill slope. If both switches are closed, then the car is on a horizontal road. However, due to the acceleration will affect the action of the mercury switch, the mercury switch is not suitable for use on actual cars to detect uphill or downhill. An alternative way for the uphill/downhill detection is to use the relationship between throttle and speed changes. Our experimental car for simulation is shown in Fig. 4. All circuits are packed into the cabin of a model car. An LCD for display the message of simulation result is mounted on the roof of the model car. Fig. 5 shows that the car speed is at 76 to 77 km/h. No rain and no frog is detected at that time. By (1), we know that the safe distance should be 38 meters, as shown in the LCD display. Fig. 5 shows that

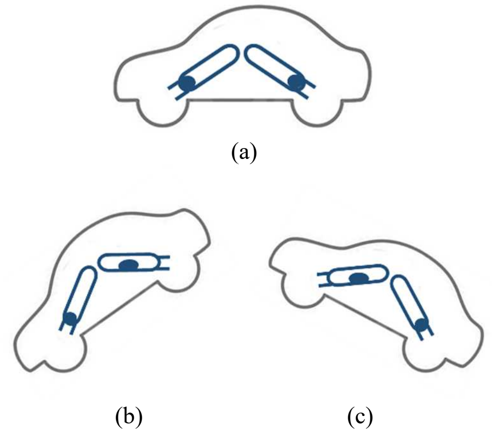

Fig. 3. Car attitude. (a) Horizontal, (b) Downhill, (c) Uphill.

Fig. 4. Our experimental car for simulation.

Fig. 5. An experimental result of dynamic adjustment of safe distance.

the detected front distance is 20 meters, and hence the alarm system will be activated.

4. Discussions and Conclusions

In this paper, we proposed a driving safety system which can dynamically adjust the safe distance between vehicles depending on the speed and weather conditions. This system can be used to determine and maintain safe distances both in front and rear of a car. Our technology has the following characteristics:

- The safe distance will be automatically adjusted with the speed and weather conditions. The faster the speed or the poor weather conditions, the longer the safe distance is.
- The safe distance will be automatically adjusted with the road slope. The safe distance of the downhill road will be automatically extended.
- With the front distance detection system, the vehicle can be alerted when the safe distance is insufficient, to remind the driver to decelerate properly to avoid the occurrence of chasing.
- If the system is mounted with the automatic brake assisting system, the brake deceleration can be automatically started in the case of insufficient safe distance to improve the road safety.
- With the rear distance detection system, in the case of insufficient safe distance of the rear vehicle, the driver should promptly accelerate or change the lane to avoid collision in the case of inconspicuous driving.
- The technology can also be applied to the automatic following system, which can keep the distance of vehicles in a safe region to improve the driver's acceptance of the following system.
- In addition to being integrated into the safety design of a new car to improve the safety factor of the vehicle, the technology can also be used for retrofitting old vehicles as a driving safety facility.
- This technology is applicable to the automobile manufacturing industry and the automobile maintenance industry. The installation on the vehicle can greatly improve the driving safety factor.
- The technology can also be applied to locomotives or various types of moving vehicles to improve the safety factor of the vehicle.

This idea has obtained an invention patent of Taiwan. We deeply believe that a car with this system can be driven more safely.

References

1. *2015 National Road Accident Review Analysis Report*, Freeway Bureau, MOTC, Taiwan, July 13, 2016. (in Chinese)
2. L. Zemanek and J. Prnka, The issue of observance of safe following distance between vehicles in Germany, *Eur. Scientific J.* **Special Edition**, 2015, pp. 448-461.
3. D. Qu, X. Chen, W. Wang and X. Bian, Modeling of car-following required safe distance based on molecular dynamics, *Math. Problems in Eng.* **2014**(604023), 2014, pp. 1-7.
4. S. H. Chacon, *The Effect of Driver Behavior on Freeway Traffic Flow*, Dept. Operations Res. & Financial Eng., Princeton University, 2008.
5. *Road Safety – Speed,* available at: http://www.who.int/violence_injury_prevention/publications/road_traffic/world_report/speed_en.pdf, cited: Sep. 20, 2018.
6. *Two-second rule*, available at: https://en.wikipedia.org/wiki/Two-second_rule, cited: Sep. 20, 2018.

Markerless Indoor Augmented Reality Navigation Device Based on Optical-Flow-Scene Indoor Positioning and Wall-Floor-Boundary Image Registration

Chian C. Ho, Bo-Kai Wang, and Guan-Lung Liao
Department of Electrical Engineering, National Yunlin University of Science and Technology
Douliou, Yunlin County 64002, Taiwan
E-mail: futureho@yuntech.edu.tw, m10312027@yuntech.edu.tw, b10012153@yuntech.edu.tw
www.yuntech.edu.tw

Abstract

For markerless indoor Augmented Reality Navigation (ARN) technology, camera pose is inevitably the fundamental argument of positioning estimation and pose estimation, and floor plane is indispensably the fiducial target of image registration. This paper proposes optical-flow-scene indoor positioning and wall-floor-boundary image registration to make ARN more precise, reliable, and instantaneous. Experimental results show both optical-flow-scene indoor positioning and wall-floor-boundary image registration have higher accuracy and less latency than conventional well-known ARN methods. On the other hand, these proposed two methods are seamlessly implemented on the handheld Android embedded platform and are smoothly verified to work well on the handheld indoor augmented reality navigation device.

Keywords: augmented reality, indoor positioning, image registration, navigation.

1. Introduction

With the rapid development and wide deployment of emerging technologies in ubiquitous computing field, personal navigation system that can accommodate to perform well outdoors and indoors have drawn more and more interest. This is because personal navigation device offering personal destination awareness anywhere and anytime is essential to versatile ubiquitous computing applications, like outdoor and indoor path directions, outdoor and indoor information guide, outdoor and indoor marketing advertisement, outdoor and indoor social networking, and so on.

However, conventional 2D (birdview) or 3D (overlook) virtual-model navigation devices are not intuitive enough to guarantee the proper perception alignment between virtual-model navigation scenario and real-world navigation situation. Besides, conventional 2D (birdview) or 3D (overlook) virtual model navigation devices fail to be evolved into the ever-growing wearable see-through devices, like eyeglasses, helmet, or goggles. Even worse, staring at 2D (birdview) or 3D (overlook) virtual model navigation devices on driving or on foot might cause careless accidents or dangerous occurrences.

Augmented Reality Navigation (ARN) technology is the best alternative choice and becomes more and more fascinating in ubiquitous computing applications since it can lay real-world navigation directions over what users are actually seeing in front of themselves in the true world.[1-8] In general, according to the object-tracking principles, ARN technologies can be divided into three main categories: 1) marker, 2) markerless, and 3) positioning. The marker ARN technology is the most reliable one tracking the registered objects and projects the computer graphics onto the registered objects based on distinctive markers or landmarks.[1,2] Nevertheless, a large amount of deployment of distinctive markers or

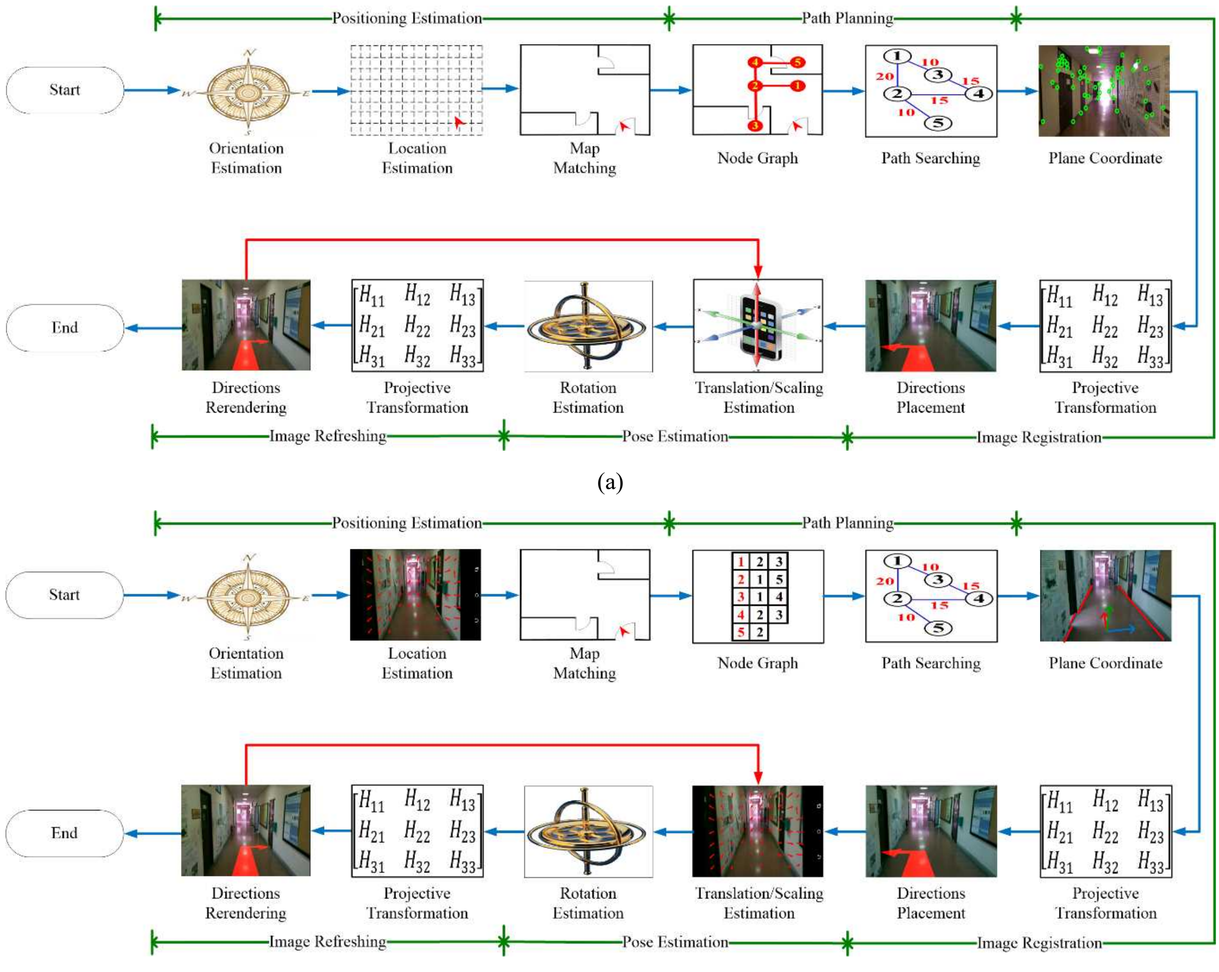

Fig. 1. Flowchart of (a) typical and (b) proposed markerless indoor ARN technologies.

landmarks for marker ARN technology are very expensive and unrealistic. The markerless ARN technology simply on the cost-effective basis of natural or plain features, like points, lines, corners, textures, is actually recognized as the most practical but difficult one.[3-5] The positioning (a.k.a. markerless) ARN technology is the most common and used one depending only upon the available location coordinate from outdoor Global Positioning System (GPS) or specific indoor Wireless Sensor Networking (WSN) infrastructure.[6-8]

Due to the markerless characteristic of main playground of outdoor and indoor real-world environments, most of recent research activities and interests in ARN technologies focuses on markerless issue, especially for indoor scenarios.[9-11] Fig. 1 (a) shows the algorithm flowchart of typical markerless indoor ARN device. In Fig. 1 (a), first of all, the indoor ARN device has to finish the estimation of location coordinate through external radio positioning infrastructure (e.g., WiFi, Bluetooth LE, RFID) or internal inertial positioning unit at the step of location estimation, in the stage of positioning estimation. Meanwhile, the indoor ARN device also finishes the estimation of orientation angle through fusion of digital compass and Inertial Measurement Unit (IMU) sensors at the step of orientation estimation, in the stage of positioning estimation. Then, the indoor ARN device matches the estimated location coordinate and orientation angle of the targeted device onto the built 2D map at the step of map matching, in the stage of positioning estimation. Next, the indoor ARN device has to build the critical nodes on the built 2D map at the step of node graph, in the stage of path planning, and has to finish the shortest or fastest navigation path evaluation to the destination on the built

2D map at the step of path searching, in the stage of path planning. After accomplishing the floor plane registration (including camera pose initialization) at the step of plane coordinate, in the stage of image registration, and Homography-based 2D-to-3D projective transformation of the map and navigation path at the step of projective transformation, in the stage of image registration, the indoor ARN device can accurately project the ARN path directions onto the markerless real-world floor plane through elaborate floor region segmentation at the step of directions placement, in the stage of image registration. Afterward, when the camera (viewing) pose of the indoor ARN device varies, the translation/scaling and rotation variations of camera (viewing) coordinate in real-world coordinate can be properly evaluated at the steps of translation/scaling estimation and rotation estimation, respectively, in the stage of pose estimation. Finally, the ARN path directions on the screen of the indoor ARN device can be rotated and deformed properly in object (image) coordinate at the step of projective transformation, in the stage of image refreshing, so as to be closely stuck onto the markerless real-world floor plane through elaborate camera pose estimation at the step of directions rerendering, in the stage of image refreshing.

Among stages of the algorithm flowchart of the typical markerless indoor ARN device in Fig. 1 (a), the accuracy and reality of the ARN path directions is actually sensitive and vulnerable to these three stages of positioning estimation, pose estimation, and image registration, especially to these three steps of location estimation, translation/scaling estimation, and plane coordinate. For markerless indoor ARN technology, camera pose is inevitably the fundamental argument of positioning estimation and pose estimation, and floor plane is indispensably the fiducial target of image registration. Thus this paper concentrates to address on issues of camera pose estimation and floor plane registration in the subsequent sessions.

This paper is organized as follows. Section 2 reviews pros and cons of conventional well-known camera pose estimation methods for the markerless indoor ARN device, like frame-to-frame planar homographies and feature-based optical flow. In addition, Section 2 also reviews pros and cons of conventional well-known floor plane registration methods for the markerless indoor ARN device, like Otsu binarization floor plane registration and moving-average binarization floor plane registration. Section 3 presents optical-flow-scene indoor positioning and wall-floor-boundary image registration to improve the accuracy and reality of the ARN path directions. Section 4 compares the experimental results between these proposed two methods and conventional well-known methods. Section 5 demonstrates the implementation results of Android-based portable indoor ARN device based on proposed optical-flow-scene indoor positioning and wall-floor-boundary image registration. Finally, Section 6 draws brief conclusions and future work.

2. Conventional Methods

There are many conventional camera pose estimation methods and floor plane registration methods applied to for the indoor ARN device in the past 10 years. But these conventional methods are rightly the dominant factors to degrade the accuracy and reality of markerless indoor ARN technologies.

2.1. *Conventional camera pose estimation methods*

Single planar homography can thoroughly interpret the relation between a real plane in 3D real-world coordinate and its projective plane on the 2D image coordinate, so frame-to-frame planar homographies[10, 12-15] can estimate the camera pose variation and some depth information when the camera is rotated or translated. It is the most popular and reliable method for camera pose estimation. However, the accuracy and reliability of camera pose estimation of frame-to-frame planar homographies depends deeply upon the accuracy and reliability of feature detection of the fiducial projection planar surface, e.g. floor plane. In addition, it is difficult to guarantee to detect correct and enough distinctive features on the fiducial projection planar surface frame by frame when the camera is sometimes rotated or translated dramatically.

Another widely-used camera pose estimation method is feature-based optical flow. Feature-based optical flow is more efficient and effective to track the distinctive features and estimate the pose variation, but it can not estimate the depth information and viewpoint rotation.[10, 13, 15]

2.2. *Conventional floor plane registration methods*

All conventional floor plane detection or floor plane segmentation methods can be sorted into 2 main categories: 1) Otsu binarization floor detection and 2) moving-average binarization floor detection.[15-18]

The binarization threshold of Otsu binarization floor detection is decided by the illumination statistical distribution result of the scene. It can perform well and readily on low-contrast scenes, but not on high-contrast scenes. Because the illumination of the floor plane under high-contrast scenes is almost deeply dark.

On the other hand, the binarization threshold of moving-average binarization floor plane detection is determined by a series of averages of different lines on the full-scale scenes. Although it can perform better on high-contrast scenes than Otsu binarization floor detection, its computation complexity is too high to meet the real-time requirement, especially on complicated-background scenes.

3. Proposed Methods

This paper proposes optical-flow-scene indoor positioning and wall-floor-boundary image registration to improve these three stages of positioning estimation, pose estimation, and image registration of typical markerless indoor ARN technologies, especially to improve these three steps of location estimation, translation/scaling estimation, and plane coordinate, illustrated in Fig. 1(b).

3.1. *Proposed optical-flow-scene indoor positioning method*

Optical-flow-scene indoor positioning method with only monocular RGB camera can solve the location estimation and translation/scaling estimation effectively and efficiently. Fig. 2 illustrates the transformation model of camera pose estimation from 2D image-plane coordinate onto 3D real-world coordinate in proposed optical-flow-scene indoor positioning method, and how to work out the camera pose estimation issue. In Fig. 2, *C* means the known location of the faraway wall or obstacle, along Y_r axis of 3D real-world coordinate. *h* represents the height difference between some real-world pixel and the middle point of real-world field, along Z_r axis of 3D real-world coordinate. *V* and *V'* are the present and displaced real-world location of the camera, along Y_r axis of 3D real-world coordinate, respectively. *f* implies the focal length of the camera. *w* denotes the height difference between some optical flow pixel (*P*) and the middle point of optical flow field on the present image plane, and *w'* denotes the height difference between some optical flow pixel (*P'*) and the middle point of optical flow field on the displaced image plane, along Y_i axis of 2D image-plane coordinate. *d* indicates the real-world displaced distance of the camera, that is the location difference between *V* and *V'*, along Y_r axis of 3D real-world coordinate. The unit of all variables above is centimeter.

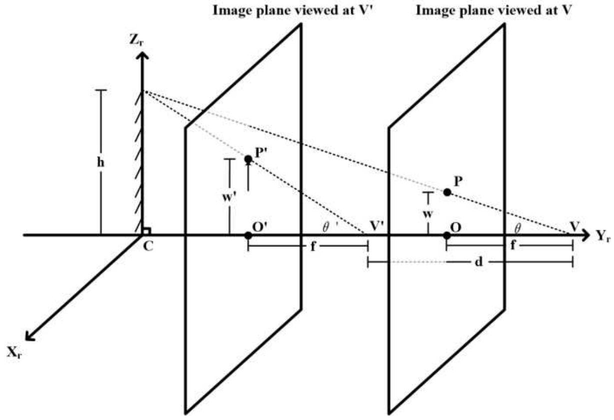

Fig. 2. Transformation model of camera pose estimation of proposed optical-flow-scene indoor positioning method.

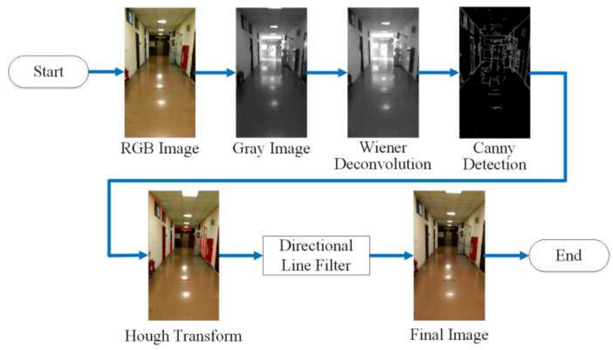

Fig. 3: Flowchart of proposed wall-floor-boundary image registration method.

Therefore, the real-world forward/backward displaced distance of the camera can be elaborately evaluated by (1)-(3), along Y_r axis of 3D real-world coordinate, while $(V - C)$ is given from the difference between known locations of the faraway wall (or obstacle) and the present camera on the real-world map.

$$\frac{(V-C)}{h}=\frac{f}{w}=>h=\frac{w(V-C)}{f} \tag{1}$$

$$\frac{V'-C}{h}=\frac{f}{w'}=>V'=C+\frac{hf}{w'} \tag{2}$$

$$d=V-V'=(V-C)-\frac{hf}{w'}=(V-C)-(\frac{f}{w'})(\frac{(V-C)}{f})w=(V-C)(1-\frac{w}{w'}) \tag{3}$$

As for the real-world horizontal or slightly vertical displaced distance of the camera can be proportional and reversely evaluated by the horizontal or slightly vertical displaced distance of some optical flow pixels on the image plane.

3.2. *Proposed wall-floor-boundary image registration method*

Fig. 3 illustrates the algorithm flowchart of proposed wall-floor-boundary image registration. The detailed descriptions on Fig. 3 will be explained step-by-step as follows. Wiener Deconvolution filter is a key preprocessing method for floor detection, because it can blur and simplify the background details. Then, strong features of edges or contours can be preserved inherently.

Because the floor plane usually has fewer edges or contours than the furniture or the wall decorations, edge detector or contour detector can extract non-floor regions smoothly and easily. Hough transform stands for Probabilistic HoughLine Transform. It is an efficient and effective way to detect the extremes of edge-lines. In order to detect the representative edge-line features, Directional Line filter is intended to reduce a number of noisy points or unconnected lines in a curve that is approximated by a series of points. After acquiring the end dots (extremes) of edge-lines exactly, the contours connected by every end dots are rightly the border of floor segmentation.

4. Experimental Results

Table 1 shows Localization error and execution time comparison between conventional RFID indoor positioning, conventional WiFi indoor positioning, conventional feature-based optical flow indoor positioning, and proposed optical-flow-scene indoor positioning, under various indoor spaces of (a) laboratory, (b) corridor, and (c) lobby. From Table 1, it is evident that proposed optical-flow-scene indoor positioning has much higher localization accuracy and less execution latency than conventional camera pose estimation methods, especially under high-obstructed environments.

Table 2 shows the coverage accuracy and execution time comparison between conventional Otsu binarization floor detection, conventional moving-average binarization floor detection, and proposed wall-floor-boundary detection. From Table 2, it is obvious that proposed wall-floor-boundary detection has much higher coverage accuracy and less execution latency than conventional floor detection registration methods, especially under high-contrast environments.

Table 1. Localization error and execution time comparison between proposed optical-flow-scene indoor positioning and conventional camera pose estimation methods under various indoor spaces of (a) laboratory, (b) corridor, and (c) lobby.

(a)

Laboratory (11m)		
Method	Localization error	Execution time
RFID	0.972 m	0.524 sec
Wi-Fi	0.712 m	0.372 sec
Feature-Tracking Optical Flow	0.773 m	0.209 sec
Optical Flow Field	**0.463 m**	**0.124 sec**

(b)

Corridor (14m)		
Method	Localization error	Execution time
RFID	0.532 m	0.481 sec
Wi-Fi	0.698 m	0.371 sec
Feature-Tracking Optical Flow	0.721 m	0.198 sec
Optical Flow Field	**0.526 m**	**0.112 sec**

(c)

Lobby (21m)		
Method	Localization error	Execution time
RFID	0.482 m	0.453 sec
Wi-Fi	0.643 m	0.312 sec
Feature-Tracking Optical Flow	0.877 m	0.203 sec
Optical Flow Field	**0.441 m**	**0.113 sec**

Table 2. Accuracy and execution comparison between various floor plane detection methods.

Floor Detection Methods	Coverage Accuracy	Execution Performance
Otsu binarization	40%	7.19 fps
moving-average binarization	65%	2.85 fps
wall-floor-boundary	**88%**	**6.22 fps**

5. Android Implementation

Android embedded platform with rich HW/SW features is the best choice to implement and verify the portable markerless indoor ARN device. The proposed optical-flow-scene indoor positioning and wall-floor-boundary image registration methods are smoothly integrated into the portable markerless indoor ARN device and are certainly verified to work well.

6. Conclusions

Although Visual Simultaneous Localization And Mapping (VSLAM) also can improve the issues of positioning estimation, pose estimation, and image registration, this paper proposes and implements two more effective and efficient methods, optical-flow-scene indoor positioning and wall-floor-boundary image registration, to make markerless indoor ARN device more precise, reliable, and instantaneous.

Acknowledgements

This work was supported in part by Ministry of Science and Technology, Taiwan, under Grant MOST 106-2221-E-224-053.

References

1. Jongbae Kim and Heesung Jun, Vision-based location positioning using augmented reality for indoor navigation, *IEEE Transactions on Consumer Electronics*, vol. 54, no. 3, Aug. 2008, pp. 954–962.
2. O. Mohareri and A. B. Rad, Autonomous humanoid robot navigation using augmented reality technique, in *Proceedings of 2011 IEEE International Conference on Mechatronics (ICM)*, Apr. 2011, pp. 463–468.
3. S. DiVerdi and T. Hollerer, Heads up and camera down: a vision-based tracking modality for mobile mixed reality, *IEEE Transactions on Visualization and Computer Graphics*, vol. 14, no. 3, May–Jun. 2008, pp. 500–512.
4. H. Hile and G. Borriello, Positioning and orientation in indoor environments using camera phones, *IEEE Computer Graphics and Applications*, vol. 28, no. 4, Jul.–Aug. 2008, pp. 32–39.
5. T. Oskiper, M. Sizintsev, V. Branzoi, S. Samarasekera, and R. Kumar, Augmented reality binoculars, *IEEE Transactions on Visualization and Computer Graphics*, vol. 21, no. 5, May 2015, pp. 611–623.
6. A. D. Cheok and Li Yue, A novel light-sensor-based information transmission system for indoor positioning and navigation, *IEEE Transactions on Instrumentation and Measurement*, vol. 60, no. 1, Jan. 2011, pp. 290–299.
7. R. Hervas, J. Bravo, and J. Fontecha, An assistive navigation system based on augmented reality and context awareness for people with mild cognitive impairments, *IEEE Journal of Biomedical and Health Informatics*, vol. 18, no. 1, Jan. 2014, pp. 368–374.
8. B. H. Thomas and C. Sandor, What wearable augmented reality can do for you, *IEEE Pervasive Computing*, vol. 8, no. 2, Apr.–Jun. 2009, pp. 8–11.
9. A. I. Comport, E. Marchand, M. Pressigout, and F. Chaumette, Real-time markerless tracking for augmented reality: the virtual visual servoing framework, *IEEE Transactions on Visualization and Computer Graphics*, vol. 12, no. 4, Jul.–Aug. 2006, pp. 615–628.
10. T. Lee and T. Hollerer, Multithreaded hybrid feature tracking for markerless augmented reality, *IEEE Transactions on Visualization and Computer Graphics*, vol. 15, no. 3, May–Jun. 2009, pp. 355–368.
11. Y.-G. Kim and W.-J. Kim, Implementation of augmented reality system for smartphone advertisements, *International Journal of Multimedia and Ubiquitous Engineering*, vol. 9, no. 2, Sep. 2014, pp. 385–392.
12. G. Simon and M.-O. Berger, Pose estimation for planar structures, *IEEE Computer Graphics and Applications*, vol. 22, no. 6, Nov./Dec. 2002, pp. 46–53.
13. S. J. D. Prince, K. Xu, and A. D. Cheok, Augmented reality camera tracking with homographies, *IEEE Computer Graphics and Applications*, vol. 22, no. 6, Nov./Dec. 2002, pp. 39–45.
14. M. Maidi, M. Preda, and V. H. Le, Markerless tracking for mobile augmented reality, in *Proceedings of IEEE International Conference on Signal and Image Processing Applications*, Nov. 2011, pp. 301–306.
15. G. C. Barcelo, G. Panahandeh, and M. Jansson, Image-based floor segmentation in visual inertial navigation, in *Proceedings of IEEE International Instrumentation and Measurement Technology Conference (I2MTC)*, May 2013, pp. 1402–1407.
16. Ma Ling, Wang Jianming, Zhang Bo, and Wang Shengbei, Automatic floor segmentation for indoor robot navigation, in *Proceedings of International Conference on Signal Processing Systems (ICSPS)*, vol. 1, Jul. 2010, pp. V1-684–V1-689.
17. L. F. Posada, K. K. Narayanan, F. Hoffmann, and T. Bertram, Floor segmentation of omnidirectional images for mobile robot visual navigation, in *Proceedings of IEEE/RSJ International Conference on Intelligent Robots and Systems (IROS)*, Oct. 2010, pp. 804–809.
18. F. G. Rodriguez-Telles, L. Abril Torres-Mendez, and E. A. Martinez-Garcia, A Fast Floor Segmentation Algorithm for Visual-Based Robot Navigation, in *Proceedings of International Conference on Computer and Robot Vision (CRV)*, May 2013, pp.167–173.

Development of a Handheld Gas Detector with IoT Function

Jr-Hung Guo
Department of Electrical Engineering, National Yunlin University of Science & Technology
No. 123, University Road, Section 3, Douliou, Yunlin 64002, Taiwan

Kuo-Hsien Hsia
Department of Electrical Engineering, Far East University,
No.49, Zhonghua Rd., Xinshi Dist., Tainan City 74448, Taiwan

Kuo-Lan Su, Chien-Wei Liu
Department of Electrical Engineering, National Yunlin University of Science & Technology,
No. 123, University Road, Section 3,Douliou, Yunlin 64002, Taiwan
E-mail: g9710801@yuntech.edu.tw, khhsia@mail.feu.edu.tw, {sukl, m10512059}@yuntech.edu.tw

Abstract

Gas detection is very cumbersome because the gas will diffuse and mix with other gases. A handheld gas detector with IoT function using a single-chip controller will be developed in this paper. This detector consists of a variety of different gas sensors. Adaptive fusion method is used to integrate sensing information from different sensors to improve the correctness and gas identification of this detector. Since this gas detection module is hand-held, we use wireless communication interfaces such as Wi-Fi and LoRa with bands at 433/868/915 MHz to enable this gas detector to be able to transmit data while moving. In addition, multiple gas detection modules can be used to form a detection network for large area detection. A built-in algorithm can assist in the correction and isolation of data from modules or sensors in the detection network. Therefore, the gas detecting module can be more flexible in use.

Keywords: Handheld gas detector, Gas detection, Adaptive Fusion Method.

1. Introduction

Harmful gas detection is always a hot research topic. The main reason is that the environment in which we live is full of harmful gases from various industries or daily life. Easy to diffuse or mix with other gases is an important feature of gas, so how to properly detect harmful gases is very difficult. There have been many studies in this issue in the past. For example, José Luis Herrero et al. proposed the use of electronic nose and web architecture to form a system for detecting harmful gases [1]. Jasmine Pramila Devadhasan et al. developed a gas sensor array that can be connected to a smart phone [2]. Ayushi Paliwal et al. developed a sensor for coating Au on a ZnO surface using a surface plasmon resonance (SPR) technique to detect CO [3]. Sören Dierks and Andreas Kroll used remote sensing and sensor data fusion to detect methane gas leakages [4]. From these previous studies we know that the detection of harmful gases is very difficult and costly. In this paper, we will develop a handheld gas detector with gas sensors easily bought in the market and integrate multiple communication interfaces to form the architecture of Internet of Things (IoT). These sensors used in this paper and the gases that they can detect are summarized in Table 1.

All sensors except TGS825 can detect multiple gases. Hence an output of a sensor may correspond to different concentrations of different gases. How to distinguish different gases from the output signal is the key of the entire detection system. In this paper, the sensor signals are distinguished by a curve fitting method. The redundant management method is used to confirm and determine the gas concentration. Also the Adaptive Fusion Method is used to improve the correctness and the recognition rate of the sensor. In addition, multiple detectors can form a gas sensing network via wireless communication interface and IoT technology. This can increase the accuracy of the gas detection system and solve the gas diffusion problem simultaneously.

2. System Architecture

The gas detector developed in this paper is based on an 8051 series single-chip, and is combined with the sensor signal processing circuit, communication interface, and other peripheral circuits. The block diagram of the gas detector is shown in Fig. 1. Up to 8 gas sensors can be connected for this detector. The results sensed by each sensor are first passed through the signal processing circuit and then sent to the A/D converter in the single chip for digitization before operation and processing.

Due to the handheld design, we integrate a 433/868/915 MHz tri-band multi-channel RF interface, a Wi-Fi interface and a LoRa interface for wireless communication. With this design, the detector can transmit the data or calculation results of the sensors to the host computer during moving. In addition, there are also wired communication interfaces such as UART (Universal Asynchronous Receiver/Transmitter) and Ethernet communication interface. Hence the application of the whole module can be more flexible.

In addition, we use uIP [5] in the detector to handle the network communication of the detector. The goal of uIP is to enable an 8-bit or 16-bit microcontroller to communicate over the network using the TCP/IP protocol. It can provide basic UDP and TCP services. The code size of uIP is only a few kilobytes, and it only requires a few hundred bytes of RAM to run. Fig. 2 is a block diagram of uIP.

In the detector we use the TCP and UDP protocols in uIP. These two protocols are the most commonly used in network communications. So we can develop different applications according to the needs, or use the TCP protocol to directly store the data of the detector into the database. In addition, we set up Web Server in the detector, so users can directly use the browser to operate the detector, such as controlling the I/O, or setting the sensor type or threshold. This makes the detector very convenient to use and manage.

Table 1. Sensor characteristics table.

	HS129	HS130	HS131	HS133	HS134	HS135	TGS825	TGS826	MQ2	MQ3	MQ4	MQ5	MQ6	MQ7	MQ8	MQ9
Alcohol	●	●	●	●	●	●		●	●	●	●	●	●	●	●	
Ammonia								●								
CH4	●		●	●					●	●	●	●	●	●	●	●
CO	●				●				●	●	●	●	●	●	●	●
CO2						●										
H2	●				●		●	●	●		●	●	●	●	●	●
i-C4H10		●				●		●								
LPG	●		●	●					●	●	●	●	●	●	●	●
Smoke			●	●		●			●		●					
propane									●							
benzine										●						
hexane										●						

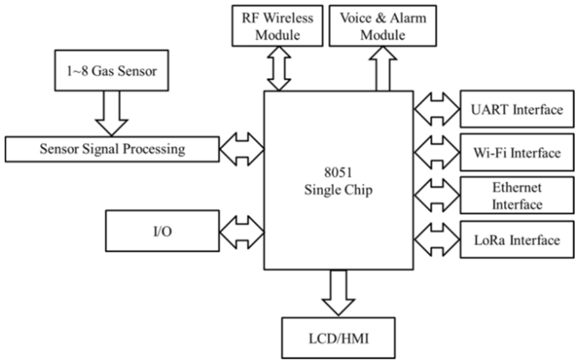

Fig. 1. Handheld Gas Detector Hardware Block Diagram.

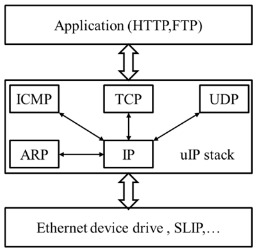

Fig. 2. Stack Structure of uIP.

3. Hardware and Software

The main board of this gas detector is shown in Fig. 3. We use a modular design for this gas detector, so either the communication interface, the display module or the human machine interface can be replaced as needed. In addition, 10 I/Os are reserved for applications or extensions. An expansion board for gas sensors, as shown in Fig. 4, are designed for easily replacing or installing required gas sensors as needed. The well-assembled gas detector with cover and LCD display is shown in Figure 5.

The monitoring system is developed by VB.NET. It can graphically display the real-time data of the connected gas detector, and store the data in the database system. In addition, this monitoring system can also be used to set the gas detector I/O or gas sensor parameters to make the use of gas detectors more convenient. The monitoring system is shown in Fig. 6.

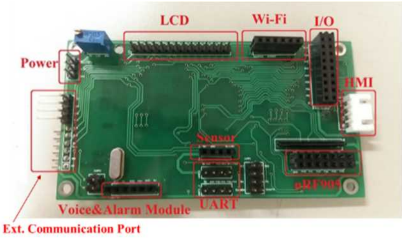

Fig. 3. Main board of the gas detector.

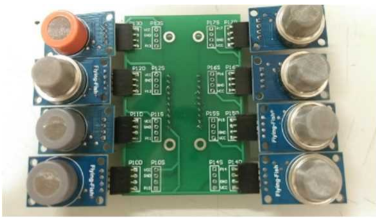

Fig. 4. Extension board for gas sensors.

Fig. 5. Well-assembled hand-held gas detector.

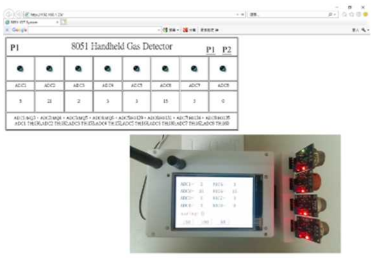

(a) Handheld Gas Detector with Web Interface.

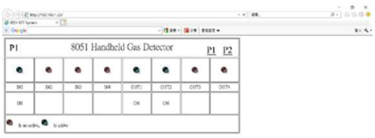

(b) Handheld Gas Detector I/O Status in Web Interface.

Fig. 6. Handheld Gas Detector Web Interface.

4. Experimental Results

We developed a handheld gas detector using an 8051 single chip with multiple communication interfaces combined with an easy to buy gas sensor. Two gases at an environment of 26.2ºC and 57.8% humidity are tested. We use the MQ2 sensor as an example to illustrate how R_O is obtained. The voltage on R_O with R_O and R_L in series connection in the air under known condition is 1V, and the variable resistance R_L of the gas sensor is 5.1KΩ. The voltage divider rule gives: $5V*5.1K/(R_O+5.1K) = 1V$ resulting in $R_O \approx 20.4K$. So R_O is set as 20K for simplicity in the experiment. Applying voltage divider rule to R_S and R_L in series, the voltage on R_S is $5V*5.1K/(R_S+5.1K)$. The A/D value can be obtained by multiplying the voltage by 5.1. Table 2 summarizes the data for MQ2. Data for other sensors can be obtained in the same way.

For the first test gas, the measured data is summarized as Table 3. From the characteristics of each sensor, we can have the result as Table 4. It can be seen from Table

Table. 2. MQ2 Sensor characteristics table.

R_S/R_O	R_S	Voltage on R_S	A/D Value
0.1	2	3.592	183.192
0.2	4	2.802	142.902
0.3	6	2.297	117.147
0.4	8	1.947	99.297
0.5	10	1.689	86.139
0.6	12	1.491	76.041
0.7	14	1.335	68.085
0.8	16	1.209	61.659
0.9	18	1.104	56.304
1	20	1.016	51.816
2	40	0.565	28.815
3	60	0.392	19.992
4	80	0.299	15.249
5	100	0.243	12.393
6	120	0.204	10.404
7	140	0.176	8.976
8	160	0.154	7.854
9	180	0.138	7.038
10	200	0.124	6.324
15	300	0.084	4.26
20	400	0.063	3.2
50	1000	0.025	1.293
100	2000	0.012	0.64

Table 3. Sensed data of Experiment 1.

ID	Sensor	A/D value	R_S/R_O
ADC1	MQ2	120	about 0.29
ADC2	MQ3	22	about 2.7
ADC3	MQ4	86	about 0.5
ADC4	MQ5	150	about 0.18
ADC5	MQ6	83	about 0.53
ADC6	MQ7	33	about 1.8
ADC7	MQ8	235	about 11.75
ADC8	MQ9	110	about 0.32

4 that the detection results of more than half of the gas sensors indicate that the gas is most likely to be LPG. Moreover, all of MQ2, MQ5, MQ6, and MQ9 can detect LPG, and the sensed concentration is quite close to 5000 ppm except for MQ2. The rest of the gas sensors are not specifically designed for LPG detection, and the detected gas concentration is also quite different from them. So it can be concluded that this gas is most likely to be LPG.

For the second test gas, the measured data is summarized as Table 5. By applying the same analysis procedure as what had done for the previous test gas, we found that the test gas should be alcohol.

5. Conclusion

We developed a handheld gas detector with multiple communication interfaces. This detector uses gas sensors easily bought on the market. In addition, we designed a sensor connector (extension board) to make this gas detector more convenient to use. We use multiple communication interfaces on the gas detector and use uIP to enable the detector to communicate via TCP/IP and UDP. Therefore, we use the TCP/IP protocol to establish a Web Server on the detector, allowing the user to monitor the status of the detector through the browser. Finally, we developed a monitoring system to monitor the gas detector. In the monitoring system, all connected detectors can be monitored in real time, and the data of these detectors can be instantly stored in the database. Hence the entire detection system can be used in a more convenient way. In the future, we will continue to reduce the size of the detector and strengthen the function of the monitoring system. A web-based monitoring system will also be developed, and it is hoped that it will be applied in various fields requiring gas detection in the future.

Table 4. Gas analysis of Experiment 1.

Sensor	Possible Gas	Concentration (ppm)
MQ2	LPG	about 8K
	propane	about 9K
MQ3	Benzine	about 0.5
MQ4	CH4	about 7.5K
MQ5	LPG	about 5K
MQ6	LPG	about 5K
MQ7	CO	about 40
MQ8	Alchohol	about 1K
MQ9	LPG	about 5K

Table 5. Sensed data of Experiment 2.

ID	Sensor	A/D value	R_S/R_O
ADC1	MQ2	23	about 2.45
ADC2	MQ3	179	about 0.11
ADC3	MQ4	2	about 38
ADC4	MQ5	2	about 38
ADC5	MQ6	20	about 2.9
ADC6	MQ7	193	about 0.09
ADC7	MQ8	17	about 3.5
ADC8	MQ9	225	about 0.05

References

1. J. L. Herrero, J. Lozano, J. P. Santos, J. A. Fernández and J. I. S. Marcelo, A web-based approach for classifying environmental pollutants using portable E-nose devices, *IEEE Intell. Syst.* **31**(3) (2016) 108-112.
2. J. P. Devadhasan, D. Kim, D. Y. Lee and S. Kim, Smartphone coupled handheld array reader for real-time toxic gas detection, *Analytica Chimica Acta* **984** (2017) 168-176.
3. A. Paliwal, A. Sharma, M. Tomar and V. Gupta, Carbon monoxide (CO) optical gas sensor based on ZnO thin films, *Sensors and Actuators B: Chemical* **250** (2017) 679-685.
4. S. Dierks and A. Kroll, Quantification of methane gas leakages using remote sensing and sensor data fusion, *2017 IEEE Sensors Applications Symposium* (*SAS*), (Glassboro, New Jersey, 2017) 1-6.
5. A. Dunkels. Full TCP/IP for 8-bit architectures. *The First International Conference on Mobile Systems, Applications, and Services* (*MOBISYS '03*), (San Francisco, California, 2003) 85-98.

Research on Employee Attribute Correlation of Information Security Awareness in Organization

Tse-Yao Wang
Department of Aviation & Communication Electronic, Air Force Institute of Technology,
No. 198. Jieshou W. Rd., Gangshan Townwhip
Kaohsiung County, 820, Taiwan (R.O.C.) *

Fu-Hsiang Wen
PHD program in Engineering Science and Technology,
Department of Engineering at National Kaohsiung University of Science and Technology,
1 University Rd., Yanchao,
Kaohsiung, Taiwan (R.O.C.)
E-mail: harry0716@gmail.com, rsbmb751@gmail.com
www.afats.khc.edu.tw, www.nkust.edu.tw

Abstract

Enterprises are attacked by phishing emails, causing significant business losses. The information security protection strategies adopted by enterprises, such as mail filtering, phishing attack website screening and phishing website blacklists, cannot guarantee complete defense. This study attempts to propose another perspective that can reduce the risk of corporate information security. The quality of employees' information security used as an indicator, and the Logistic regression model used as a tool to analyze the key factors that can be used to measure the quality of information security awareness.

Keywords:. Phishing, Logistic regression, Information security awareness.

1. Introduction

Information security threats have become an enormous potential business risk for companies. Enterprises rely on the Internet to support day-to-day operations, and the use of IT tools has become a target for potential attackers. Regarding the most commonly used e-mail system, it is already an essential daily application system for modern enterprises. Implementing phishing email attacks against email is the most commonly used attacking pipeline for cyber attackers. This low-cost and easy-to-implement cyber attack technology can penetrate by the official communication activities and private communication activities of employees in the organization. Once the attacker successfully penetrates, it will launch further attacks. Although the email filtering strategy deployed in the enterprise security protection framework, the success factors of such attacks are often not the weakness of information technology, but whether the employees in the organization have a high level of information security awareness.

In the context of armed phishing attacks where technology cannot drip, the focus of corporate protection should not be on the priority of technology but should focus on providing the establishment of corporate security culture. The information security awareness of employees is the cornerstone of the enterprise's asset security culture. Understanding the information security awareness of employees has become an information security issue worth studying.

2. Literature Review

The primary method of phishing email attacks is to send carefully designed emails to the victim's email address to entice the victim to click on the malicious URL link or open the attachment file containing the malicious program, causing the victim's computer. The malware is implanted, and the attacker completes the purpose of manipulating the victim's computer [1]. Although the technical level of phishing attacks is not high, many protection measures proposed for such attacks, such as mail filtering and phishing blacklisting strategies. However, it is still not useful to completely block such attacks. Given this, some researchers have proposed to research the role of the injured party in the analysis of the role of the injured party in the form of data analysis. The research on demographic characteristics analysis has attracted much attention.

The most critical step in the successful implementation of the phishing attack is whether the target victim chooses to trust the content indication of the email and complete the click action on the hyperlink provided by the content. Therefore, individual differences in trust relationships become essential indicators of observation. A demographic analysis of victims of phishing attacks from previous studies indicates that gender and age are two significant predictors of observation [3]. Other studies have found that it is easier to get a letter sent by the opposite sex than a letter sent by the same sex [5], and it is easier to submit personal information on the phishing website. An analysis of the age of the victims indicates that ethnic groups between the ages of 18 and 25 have higher rates of hooking than those of other age groups [3]. The general view is that information security curriculum training can help to raise awareness of information security. Some studies have looked at how responsive to phishing email attacks after training in information security courses. The results of the study showed that after the implementation of the training course, the subjects were more alert to phishing attacks [4]. Similar anti-phishing training studies have also pointed out that training courses are equally valid for increasing risk awareness among men and women [6]. On the other hand, when the training system provides a presentation of security cues, it will affect the participants' willingness to participate in the training (in the case of non-forced training), and regarding the content of the training course, the research finds that the picture presented. Better than the effect of a large number of text prompts [7].

Most of the subjects studied in the previous study were analyzed by students [5][4]. However, in recent studies, the subjects of the survey are not limited to college students [3][2][6], and the scope of sampling is closer to ours. Real world observation. Also, the analysis methods used for fishing sensitivity often use regression analysis [3] or chi-square independence test [5] to explain the independent variables (such as gender, age) and phishing sensitivity. Whether there is a lack of significance between sexes, although the above methods can test the crucial factors affecting fishing sensitivity, there is still no further explanation for the interaction between variables.

3. Research methodology

In order to verify that information security awareness has a positive impact on corporate information security protection, we try to propose a phishing attack design experiment to analyze the key factors affecting employee information security awareness within the organization, and the quality of information security awareness of employees within the organization. Can it become an important indicator of corporate information security risks? We also hope to explore further whether the impact of information security awareness on information security risks is a direct or indirect relationship. Through the research and analysis of the above issues, we can obtain a measurement method that can measure information security awareness and the information security risk of enterprises.

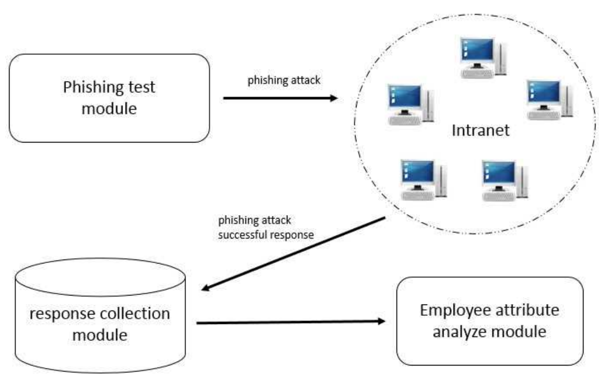

Fig. 1. Phishing attack test architecture.

4. Analytical Method

This study will use the Logistic regression model analysis method to explore the relationship between candidate auto-variables and dependent variables and identify the key factors that lead to the quality of information security awareness among employees.
Logistic regression formula:

$$E(y) = \frac{e^{\beta_0 + \beta_1 x_1 + \beta_2 x_2 + ... + \beta_p x_p}}{1 + e^{\beta_0 + \beta_1 x_1 + \beta_2 x_2 + ... + \beta_p x_p}}$$

.

References

1. Christian Ludl, Sean McAllister, Engin Kirda, and Christopher Kruegel, “On the Effectiveness of Techniques to Detect Phishing Sites”, Detection of Intrusions and Malware, and Vulnerability Assessment Lecture Notes in Computer Science Volume 4579, 2007, pp 20-39.
2. Michael Workman,“wisecrackers: a Theory-Grounded investigation of phishing and pretext social engineering threats to information security”, Journal of the American Society for Information Science and Technology, Volume 59, Issue 4, 15 February 2008, pages 662–674.
3. Steve Sheng, Mandy Holbrook, Ponnurangam Kumaraguru, Lorrie Cranor, Julie Downs, “Who falls for phish? A demographic analysis of phishing susceptibility and effectiveness of interventions”, Proceedings of the SIGCHI Conference on Human Factors in Computing Systems, CHI 2010, April 10-15, 2010, Pages 373-382 .
4. Ronald C. Dodge Jr., Curtis Carver, Aaron J. Ferguson, “Phishing for user security awareness”, Computers & Security, Volume 26, Issue 1, February 2007, Pages 73–80.
5. Tom Jagatic, Nathaniel Johnson, Markus Jakobsson, and Filippo Menczer, “Social phishing”, Communications of the ACM, Volume 50, Issue 10, October 2007, Pages 94-100.
6. Ponnurangam Kumaraguru, Justin Cranshaw, Alessandro Acquisti, Lorrie Cranor, Jason Hong, Mary Ann Blair, Theodore Pham, ” school of phis：a real-word evaluation of anti-phishing training”, Symposium on Usable Privacy and Security(SOUPS) 2009, July 15-17, 2009, Article No. 3.
7. Ponnurangam Kumaraguru, Steve Sheng, Alessandro Acquisti, Lorrie Faith Cranor, Jason Hong ,“Teaching Johnny not to fall for phish”, ACM Transactions on Internet Technology (TOIT), Volume 10 Issue 2, May 2010, Article No. 7.

Decoding spike patterns of auto-associative memory on spiking neuronal networks

Naoki Toyoshima
Graduate School of Engineering, The University of Tokyo, 7-3-1 Hongo, Bunkyo-ku, Tokyo113-8656, Japan

Takashi Kohno
Institute of Industrial Science, The University of Tokyo, 4-6-1 Komaba, Meguro-ku, Tokyo 153-8505, Japan
E-mail: tnaoki@sat.t.u-tokyo.ac.jp, kohno@sat.t.u-tokyo.ac.jp

Abstract

Spiking neuronal networks model the electrophysiological activities in neuronal cells' networks. One of their applications is auto-associative memory, in which one of the pre-stored patterns mostly similar to the input pattern is retrieved. In correctly retrieved states, neurons generate spikes periodically in two anti-synchronized groups that correspond to the retrieved pattern. In this manuscript, we propose methods to evaluate the retrieved spatio-temporal spike patterns by adding neurons that receive spikes from the original auto-associative memory network.

Keywords: spiking neuronal networks, auto-associative memory, synchronization, spatio-temporal spike patterns

1. Introduction

Researches aiming to realize information processing systems that incorporate excellent characteristics of the brain can be roughly classified into neuro-inspired and neuromimetic systems. In the neuro-inspired systems, the dynamical properties in the neuronal cells' networks in the brain is ultimately abstracted. For example, the conventional artificial neural networks (ANNs) are a discrete time system. On the other hand, the neuromimetic systems try to mimic the dynamical properties as precisely as possible.

Spiking neuronal networks (SNNs) are one of the neuro-mimetic systems. They model the electrophysiological activities in the neuronal cells' networks, in which spikes emitted by the neuronal cells code information. They are composed of spiking neuron models which take the dynamics of the membrane potential of the neuronal cells into account. Circuit implementation of SNNs that aims to simulate them efficiently in terms of power consumption and execution speed is called silicon neuronal networks (SiNNs)[1].

Auto-associative memory is a well-known application of both SNNs and ANNs. In this task, one of the pre-stored patterns that is mostly similar to the input pattern is expected to be retrieved. On SNNs, the retrieved pattern is a spatio-temporal spike pattern in which the synchrony between the spikes can be utilized to detect its accuracy.[2] Therefore, in order to realize practical SiNN circuit modules for the auto-associative memory, it is necessary to develop methods to interpret the spatio-temporal spike patterns as digital codes. Conventionally, some measures such as the overlap and phase synchronization index have been used for their evaluation, which require relatively complex calculation including the exponent.

In this research, we propose methods to efficiently interpret the spatio-temporal spike patterns in the auto-associative memory by some additional SNNs to the original auto-associative memory SNN. By using SNNs, we expect the interpretation will be realized power-efficiently in the future by implementation using ultralow power analog SiNNs.

In the following sections, we first explain the SNN

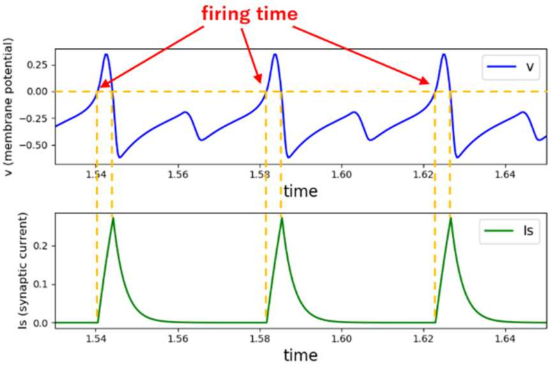

Fig. 1. A sample waveform of membrane potential v and corresponding synaptic current I_s

model used in this work. We describe two methods to interpret the spatio-temporal spike patterns and their simulation results, and then conclusion.

2. Model

2.1. *Digital Spiking Silicon Neuron (DSSN) model*

Generally, spiking neuron models represent the dynamics of the membrane potential as differential equations. DSSN model[3] is one of the qualitative spiking neuron models optimized for digital circuit implementation. It qualitatively reproduces various neuronal activities by relatively simple equations. It is represented as 2-variable differential equations as follows.

$$\frac{dv}{dt} = \frac{\phi}{\tau}(f(v) - n + I_0 + I_{stim}), \quad (1)$$

$$\frac{dn}{dt} = \frac{1}{\tau}(g(v) - n), \quad (2)$$

where

$$f(v) \equiv \begin{cases} a_n(v + b_n)^2 - c_n (v < 0) \\ -a_p(v - b_p)^2 + c_p (v \geq 0) \end{cases}, \quad (3)$$

$$g(v) \equiv \begin{cases} k_n(v - p_n)^2 + q_n (v < r) \\ k_p(v - p_p)^2 + q_p (v \geq r) \end{cases}, \quad (4)$$

where, v represents the membrane potential and n represents the abstract activity of the ionic channels. I_{stim} represents a stimulus input from synaptic models. These equations are designed to reduce the number of multiplications which consume an amount of circuit resources.

When I_{stim} is low, membrane potential v converges to constant value (the resting potential). However, when I_{stim} is higher than a particular threshold, the model shows repetitive firing as shown in Fig. 1.

Our synaptic model[4] is represented as a differential equation as follows.

$$\frac{dI_s}{dt} = \begin{cases} \alpha(1 - I_s)(v > 0) \\ -\beta I_s (v \leq 0) \end{cases}, \quad (5)$$

where I_s is the synaptic current, α and β are constants, and v is the membrane potential of the pre-synaptic neuron. Figure 1 shows a sample waveform of membrane potential v and corresponding synaptic current I_s. It models the transmitter release in chemical synapses. Stimulus current I_{stim} in Eq. (1) is calculated by the following equation.

$$I_{stim}^i = \sum_{j=1}^{N} W_{ij} I_s^j + I^i, \quad (6)$$

where W_{ij} represents connection weight from j_{th} neuron to i_{th} neuron in the network, and I^i represents an arbitrary stimulus applied by the experimenter.

2.2. *Auto-associative memory*

The auto-associative memory is a distributed memory scheme in which one of the pre-stored patterns that is mostly similar to the input pattern is to be retrieved. In this research, we use N-dot binary (black/white) patterns and a N-neuron all-to-all connected network of DSSN. Each pixel in the pattern corresponds to each DSSN. Patterns are stored by the correlation learning[5], in which W_{ij} is determined as follows.

$$W_{ij} = \begin{cases} \frac{1}{p}\sum_{u=1}^{p} x_i^u x_j^u \ (i \neq j) \\ 0 (i = j) \end{cases}, \quad (7)$$

where x_i^u is the value of the i_{th} pixel in the u_{th} stored pattern (black: +1, white: -1), and p is the number of the stored patterns.

In the associative memory on SNNs, it is known that the spatio-temporal spike patterns converge to anti-synchronized two groups that correspond respectively to black and white pixels in the retrieved pattern when a stored pattern is correctly retrieved[2]. The degree of synchronization depends on the input patterns. Example patterns are shown in Fig. 2 (high synchrony) and Fig. 3 (low synchrony). In these raster plots, a dot is placed at a point that corresponds to the firing time and the neuron index of each spike. Generally, input patterns farther from the nearest stored pattern make the synchronization more incomplete.

3. Decoder network

In order to interpret the spatio-temporal spike patterns of the auto-associative memory, following two problems have to be solved.

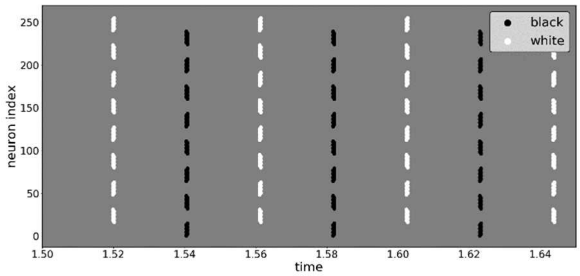

Fig. 2. Raster plot of a retrieved state with high synchrony

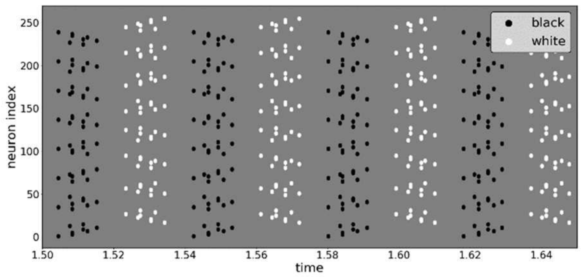

Fig. 3. Raster plot of a retrieved state with low synchrony

1. Which of the anti-synchronized neuron groups corresponds to the black dots ?
2. To which group does each neuron belong ?

3.1. *Dummy neuron*

We add a neuron to solve the first problem. The learning process is modified so that the neuron is always synchronized with the black group regardless of the input pattern. We call it a dummy neuron.

The dummy neuron is introduced as follows. First, a black pixel (a dummy pixel) is added to each of the stored patterns each of which is composed of *N* pixels. These patterns with *(N+1)* pixels are stored in a network of *(N+1)* neurons by ordinary correlation learning. The dummy neuron is a $(N+1)_{th}$ neuron which corresponds to the dummy pixel. The dummy pixel is also added to the input pattern. The dummy pixel is black in all of the stored patterns, thus the dummy neuron is always synchronized with the black group. The connection weights from the original network to dummy neuron are calculated by the following equation based on Eq. (7).

$$W_{N+1,i} = \frac{1}{p}\sum_{u=1}^{p} x_i^u \,. \tag{8}$$

Connection weights from dummy neuron to the original network are fixed to zero because it is not mandatory for the retrieval process in the original network. Figure 4 is a raster plot with the dummy neuron represented by red dots. It is synchronized with the black group.

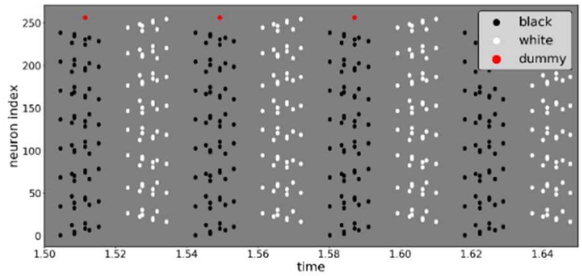

Fig. 4. Raster plot with dummy neuron (red dots)

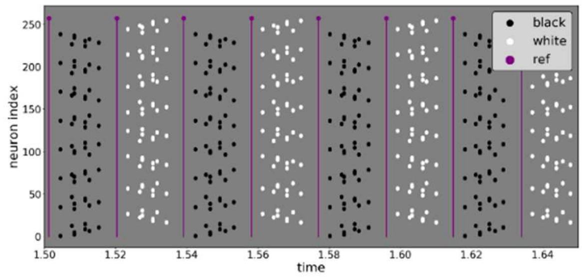

Fig. 5. Raster plot with reference neuron (purple dots and lines)

3.2. *Reference neuron*

Another neuron is introduced to solve the second problem. When the original network is in the anti-synchronized states, the new neuron repetitively fires in the blank periods between the two anti-synchronized neuron groups. Therefore, the two groups can be separated by the firing times of this neuron. We call this neuron a reference neuron. Figure 5 is a raster plot where the spikes of the reference neuron are represented by purple dots and lines. We can see the two neuron groups corresponding to black and white are correctly separated by these lines.

The mechanism of the reference neuron is as follows. In Fig. 6, the black and white plots represent I_s of the neurons in the network. In anti-synchronized states, the average of all neurons' I_s (the orange plot) has its peaks at the centers of the two anti-synchronized groups and its bottom at the blank period between them. Thus, the negated average (the yellow plot) with a bias can be used to stimulate the reference neuron so that it fires at the blank periods repetitively as shown in Fig. 7. The purple plot is membrane potential *v* of the reference neuron.

Stimulus input I_{stim} of the reference neuron is calculated by the following equation.

$$I_{stim}^{ref} = A \cdot \left(\frac{-1}{N} \sum_{i=1}^{N} I_s^i \right) + B, \tag{9}$$

where *N* is the number of neurons in the network and I_s^i represents synaptic current of i_{th} neuron in the original network. Positive constants *A* and *B* are appropriately selected so that the reference neuron correctly works.

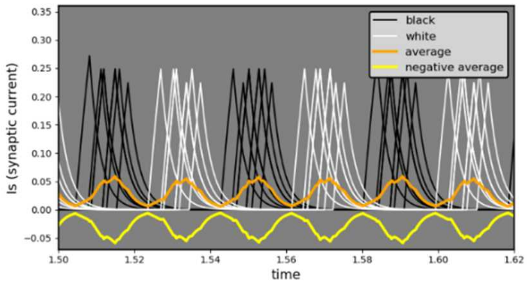

Fig. 6. I_s of the neurons in the network (the black and white plots), the average of all neurons' I_s (the orange plot), the negated average of all neurons' I_s (the yellow plot)

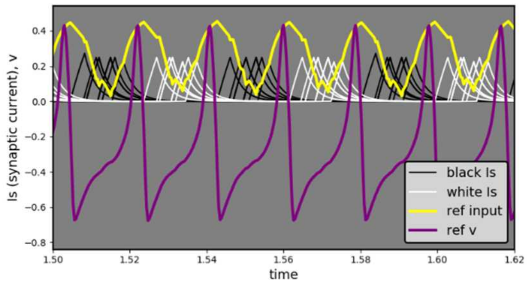

Fig. 7. I_s of the neurons in the network (the black and white plots), the negated average of all neurons' I_s with a bias (the yellow plot), membrane potential v of the reference neuron (the purple plot)

4. Result

We executed simulations with many input patterns to check whether the proposed methods correctly work. The number of pixels in the stored pattern (N) is 256. We used four patterns shown in Fig. 8 as the stored pattern set. Any pair of the patterns in the set is orthogonal to each other. We generated input patterns inserting errors by inverting randomly selected pixels in the stored patterns. For each error rate of 10%, 20%, 30%, 400 input patterns (100 patterns for each stored pattern) were generated. Figure 9 shows examples of the input patterns based on the stored pattern 1.

With all of the input patterns, the network converged to anti-synchronized states and all of these states were correctly interpreted as one of the stored patterns by the dummy neuron and the reference neuron. However, when the error rate is 30%, some of the interpreted patterns were different from the one from which the input pattern was generated.

5. Conclusion

In this manuscript, we proposed two methods, the dummy neuron and the reference neuron, to interpret the spatio-temporal spike patterns. We confirmed that these methods work correctly by simulations using many

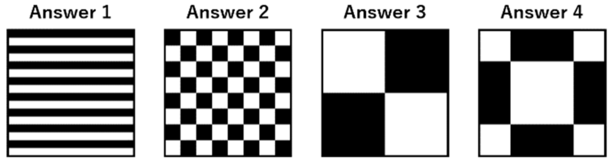

Fig. 8. The stored pattern set used in the simulation

Fig. 9. Examples of the input patterns based on the stored pattern 1

input patterns.

When error rate of the input pattern is higher than 30%, the network sometimes converged to stable repetitive firing states which could not be interpreted as any of the stored patterns as well as different from the original pattern. As the future works, we will develop methods to detect such undesirable stable states by additional SNNs.

Acknowledgement

This research was supported by JST SICORP and JSPS Grants-in-Aid for Scientific Research "Fund for the Promotion of Joint International Research".

References

1. Kohno. T, Li. J, and Aihara. K, Silicon neuronal networks towards brain-morphic computers, Nonlinear theory and its applications, *IEICE*, vol. 5, no. 3, (2014) pp. 379-390
2. Li. J, Katori. Y, and Kohno. T, An FPGA-based silicon neuronal network with selectable excitability silicon neurons, *Frontiers in Neuroscience,* vol. 6, Article. 183, pp. 1-13 (2012).
3. Kohno. T and Aihara, K, Digital spiking silicon neuron: concept and behaviors in gj-coupled network, *Proceedings of ISAROB, (2007)* OS3–OS6.
4. Destexhe. A, Mainen. Z. F, and Sejnowski. T. J, Kinetic models of synaptic transmission, *Methods in Neural Modeling*, 2nd Edn (1998), pp. 1–25.
5. Hopfield. J. J, Neural Networks and Physical Systems with Emergent Collective Computational Abilities, *Proc. Natl. Acad. Sci. USA*, vol. 79, (1982) pp. 2554-2558

Possible Mechanism of Internal Visual Perception: Context-dependent Processing by Predictive Coding and Reservoir Computing Network

Hiroto Tamura
*Graduate School of Engineering, The University of Tokyo**

Yuichi Katori
Future University Hakodate†
Institute of Industrial Science, The University of Tokyo‡

Kazuyuki Aihara
Institute of Industrial Science, The University of Tokyo‡
E-mail: hiroto0324@sat.t.u-tokyo.ac.jp, katori@fun.ac.jp, aihara@sat.t.u-tokyo.ac.jp

Abstract

The predictive coding is a widely accepted hypothesis on how our internal visual perceptions are generated. Dynamical predictive coding with reservoir computing (PCRC) models have been proposed, but how they work remains to be clarified. Therefore, we first construct a simple PCRC network and analyze the nonlinear dynamics underlying it. Since the influence of contexts is another important factor on the visual perception, we also construct PCRC networks for the context-dependent task, and observe their attractor-landscapes on each context.

Keywords: visual system, perception, predictive coding, reservoir computing, context, nonlinear dynamics.

1. Introduction

It is widely known that what we see is not the visual sensory input as it is. Instead, our brains integrate the sensory inputs and reconstruct the internal image in the manner we can easily understand. For example, although the actual visual input is 2D and received by both eyes, what we see is the 3D vision as one image. However, exactly how the internal visual perceptions are generated in the visual cortex has provoked much debate.

The predictive coding is one of the most accepted hypotheses on the internal perception. In the predictive coding framework, a perceived image is not merely the integrated visual sensory input, but the result of the prediction made by the internal generative model. The predictive coding also assumes that the generative model is optimized to minimize the residual error between the prediction and the actual sensory input. In particular, the hierarchical predictive coding model[1] postulates that the top-down signals from the higher-order area carry the predictions of lower-level neural activities, whereas the bottom-up signals from the lower-order area carry the residual errors between the predictions and the actual lower-level activities, so that the ascending signals have much less redundancy.

However, this model is only suitable for static visual inputs and cannot deal with temporally changing visual images, or movies. Then Fukino et al.[2] proposed the

*7-3-1 Hongo, Bunkyo-ku, Tokyo 113-8656, Japan
†116-2 Kamedanakano-cho, Hakodate, Hokkaido 041-8655, Japan
‡4-6-1 Komaba, Meguro-ku, Tokyo 153-8505, Japan

predictive coding with reservoir computing (PCRC) model, which can predict the temporally changing auditory inputs, implementing the generative model by the dynamical reservoir. Furthermore, the hierarchical PCRC models for more complex auditory inputs were proposed by Ara and Katori.[3,4]

Here, the reservoir computing[5] refers to a type of the recurrent neural network (RNN) approach with a simple learning strategy. When the reservoir computing networks are trained, only the output connections are modified, and the recurrent and feedback connections are fixed with randomly given values.

However, precisely how these PCRC models[2,3,4] work largely remains to be clarified. Moreover, these conventional models cannot perceive unlearned inputs. In addition, they are not exactly driven by the prediction error but by the sum of the error and their own prediction, which is equal to the original sensory input.

In this study, therefore, we first modify them and construct a simple one-layer PCRC network exactly driven by the prediction errors, which can perceive even unlearned inputs. Then we analyze the nonlinear dynamics underlying the trained network, in order to clarify the mechanism of the behavior.

The influence of contexts, which refers to situations, goals, and relevant past experiences, is another important factor on the visual perception. For example, even identical sensory stimuli can result in very different perceptions depending on contexts. Indeed, RNN models for context-dependent tasks have been proposed.[6]

Therefore, we also construct a PCRC network for a simple context-dependent perception task. We analyze the trained network again, in order to reveal how the network perceives the sensory stimuli on each context. We further construct a PCRC network which can perceive more high-dimensional visual inputs, in order to show that the proposed network can be a possible mechanism of the visual perception. We observe that the mismatch between the context and the type of sensory stimuli induces the perceptual error, which exhibits complex visual features.

2. Simple PCRC

In this section, we construct a simple one-layer PCRC network exactly driven by the prediction errors. We also analyze the nonlinear dynamics underlying the trained network to elucidate how it works.

2.1. *Network architecture and dynamics*

We use a leaky-integrator RNN, defined by the equation:

$$\tau\dot{\boldsymbol{x}} = -\boldsymbol{x} + W^{REC}\boldsymbol{r} + W^{FB}\boldsymbol{z} + W^{IN}(\boldsymbol{d}-\boldsymbol{z}), \quad (1)$$

where τ is the membrane time constant, N is the number of neurons, $\boldsymbol{x}(t) \coloneqq (x_1(t),\dots,x_N(t))^{\mathrm{T}} \in \mathbb{R}^N$ represents the membrane potentials or activities of the neurons at time $t \in \mathbb{R}$, and $\boldsymbol{r} \coloneqq (\phi(x_1),\dots,\phi(x_N))^{\mathrm{T}} \in \mathbb{R}^N$ represents the firing rates of the neurons with $\phi(x) \coloneqq \tanh(x)$. $W^{REC} \in \mathbb{R}^{N\times N}$ is a random recurrent connectivity matrix, whose elements are sampled i.i.d. from $\mathcal{N}(0, g^2/N)$ with the parameter $g \in \mathbb{R}$. M is the dimension of the input and output. The output of the network $\boldsymbol{z} \coloneqq W^{OUT}\boldsymbol{r} \in \mathbb{R}^M$ represents the prediction and is fed back through weights $W^{FB} \in \mathbb{R}^{N\times M}$, whose elements are independently and uniformly sampled from $[-1, 1]$. The residual error between the target (or sensory input) $\boldsymbol{d}(t) \in \mathbb{R}^M$ and the prediction $\boldsymbol{z}(t)$ is fed through weights $W^{IN} \in \mathbb{R}^{N\times M}$, whose elements are independently and uniformly sampled from $[-1, 1]$. The output weights $W^{OUT} \in \mathbb{R}^{M\times N}$ are initially set to all zero, and modified during training. Note that the last term is unique to the PCRC network. This network architecture is illustrated in Fig. 1, though contexts are ignored in this section.

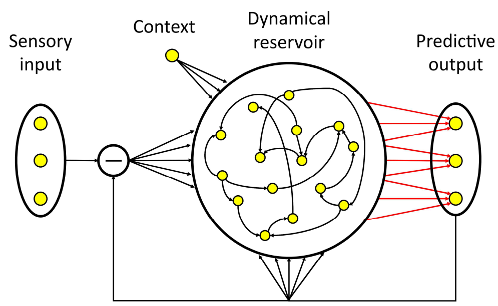

Fig. 1. Schematic chart of the one-layer PCRC network architecture. Only the output weights (red) are modified during training.

In order to simulate this dynamics numerically, we introduce the discrete-time version of Eq. (1), derived by Euler method:

$$\boldsymbol{x}(n+1) = \boldsymbol{x}(n) + \frac{\delta}{\tau}[-\boldsymbol{x}(n) + W^{REC}\boldsymbol{r}(n) + W^{FB}\boldsymbol{z}(n) + W^{IN}(\boldsymbol{d}(n)-\boldsymbol{z}(n))], \quad (2)$$

where $n \in \mathbb{Z}$ is the discrete time step, δ is the small time interval, and other notations follow Eq. (1).

Throughout this paper, we use $N = 1000, g = 1.2, \tau = 100$ msec, and $\delta = 10$ msec. In this section, we use $M = 2$ for visibility of the dynamics.

2.2. *Task*

We present the constant vectors $\boldsymbol{d}^1, \ldots, \boldsymbol{d}^{N_D} \in \mathbb{R}^M$ in turn as the sensory inputs to the network, where N_D is the number of trials. The network is trained to keep outputting the target $\boldsymbol{d}^i$ until the next target $\boldsymbol{d}^{i+1}$ is presented, at each i th tial. Each sensory input $\boldsymbol{d}^i$ is presented for 0.2 sec, and its elements are independently and uniformly sampled from $[1, 2]$.

Since the network actually receive the prediction error $\boldsymbol{d}^i - \boldsymbol{z}(t)$ as the input, it is required to decode this error into the original sensory input $\boldsymbol{d}^i$. This corresponds to the framework of the predictive coding.

2.3. *Learning rule*

We train W^{OUT} by FORCE (Fast Order Reduced and Controlled Error) learning algorithm,[7] which is based on the recursive least square filter. Its update rule is:

$$\boldsymbol{e}(t) := W^{OUT}(t - \Delta t)\boldsymbol{r}(t) - \boldsymbol{d}(t), \quad (3)$$

$$\boldsymbol{s}(t) := P(t - \Delta t)\boldsymbol{r}(t)\left(1 + \boldsymbol{r}^{\mathrm{T}}(t)P(t - \Delta t)\boldsymbol{r}(t)\right)^{-1}, \quad (4)$$

$$P(t) = P(t - \Delta t) - \boldsymbol{s}(t)\boldsymbol{r}^{\mathrm{T}}(t)P(t - \Delta t), \quad (5)$$

$$W^{OUT}(t) = W^{OUT}(t - \Delta t) - \boldsymbol{e}(t)\boldsymbol{s}^{\mathrm{T}}(t), \quad (6)$$

where the initial value for $P(t) \in \mathbb{R}^{N \times N}$ is given by

$$P(0) = \frac{1}{\alpha} I, \ (\alpha \in \mathbb{R}). \quad (7)$$

In this algorithm, the inverse of $P(t)$ is a running estimate of the autocorrelation matrix of the firing rates $\boldsymbol{r}(t)$ plus a regularization term:

$$P^{-1}(t) = \int \boldsymbol{r}(t')\boldsymbol{r}^{\mathrm{T}}(t')dt' + \alpha I. \quad (8)$$

Throughout this paper, we use $\alpha = 0.02$ and $\Delta t = \delta$.

2.4. *Results and analysis*

We trained the network for 1000 trials. (i.e., $N_D = 1000$.) At each trial in the test phase, the sensory input $\boldsymbol{d}^i$ is presented for 1.0 sec. As shown in Fig. 2, the training resulted in almost perfect performance. Fig. 2 also shows that at the beginning of each ith trial, the prediction error $\boldsymbol{d}^i - \boldsymbol{z}(t)$ is fed to the network as a sharp pulse, but it immediately decays to zero and the network settles into a fixed point $\bar{\boldsymbol{x}}^i$ where $\boldsymbol{z}(t) \equiv \boldsymbol{d}^i$.

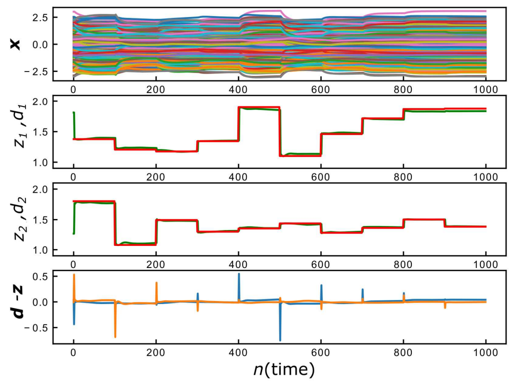

Fig. 2. The response of the trained network in the test phase. The 1st row represents the activities of the reservoir $\boldsymbol{x}(t)$, red plots in the 2nd and 3rd row represent the target $\boldsymbol{d}(t)$, green plots in the 2nd and 3rd row represent the output $\boldsymbol{z}(t)$, and the 4th row represents the prediction error $\boldsymbol{d}(t) - \boldsymbol{z}(t)$.

In order to reveal the underling mechanism of this behavior, we analyze the nonlinear dynamics of the trained network. In what follows, we regard the term $W^{IN}(\boldsymbol{d} - \boldsymbol{z})$ as the external force and separate it from the network's own dynamics, because of its pulse-like behavior. i.e., we here analyze the dynamics:

$$\tau \dot{\boldsymbol{x}} = -\boldsymbol{x} + W^{REC}\boldsymbol{r} + W^{FB}\boldsymbol{z}\,. \quad (9)$$

Following the approach of Sussillo and Barak[8], we define the scalar function $q(\boldsymbol{x}) := |\dot{\boldsymbol{x}}|^2/2$, which is near to zero if $\boldsymbol{x}$ is an approximate fixed point, or a slow point. Fig. 3A shows that almost all the q values at the end of trials are very low, and the corresponding slow points are located on a 2D-manifold in the phase space. Fig. 3A also shows that at the beginning of each ith trial, the pulse-like prediction error $\boldsymbol{d}^i - \boldsymbol{z}(t)$ drives the trajectory out of the 2D-manifold, but in the subsequent relaxation phase, the trajectory is attracted by the 2D-manifold, and the projection of the trajectory onto the manifold corresponds to the total movement $\boldsymbol{d}^i - \boldsymbol{d}^{i-1}$.

Furthermore, by analyzing the linearized system around each slow point on the 2D-manifold, we uncover the stability of this manifold. Linearizing Eq. (9) around the slow point $\bar{\boldsymbol{x}}$ $(q(\bar{\boldsymbol{x}}) \simeq 0)$, we obtain the dynamics about the perturbation $\delta\boldsymbol{x} := \boldsymbol{x} - \bar{\boldsymbol{x}}$:

$$\dot{\delta\boldsymbol{x}} = \frac{1}{\tau}[-I + (W^{REC} + W^{FB}W^{OUT})R'(\bar{\boldsymbol{x}})]\delta\boldsymbol{x}, \quad (10)$$

where $R'_{ij}(\bar{\boldsymbol{x}}) := \delta_{ij}\phi'(\bar{x}_i)$.

As for almost all the slow points, the linearized systems around them have only eigenvalues with the negative real part, as shown in Fig. 3B. This suggests that almost all the slow points are locally stable, and the 2D-manifold composed of them attracts any trajectories in the vicinity of it. Nevertheless, this manifold attractor is not fully continuous and there is a slow flow on it. Then the trajectory on the manifold is attracted by the specific slow point on the manifold where the output $\boldsymbol{z}(t)$ is near to but not equal to the target $\boldsymbol{d}^i$, which leads to the little prediction error shown in Fig. 2.

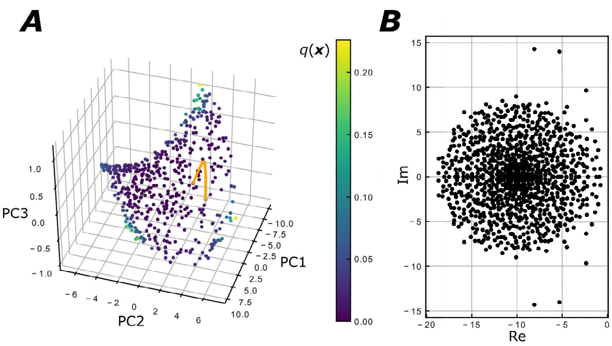

Fig. 3. **(A)** The locations of the slow points $\bar{\boldsymbol{x}}^i$ for the entire target range $\boldsymbol{d}^i \in [1,2]^2$ in 3D PCA (Principal Component Analysis) space. The color scale of each slow point represents the value of $q(\bar{\boldsymbol{x}}^i)$. The orange points represent an example of the trajectory of $\boldsymbol{x}(t)$ during a trial. **(B)** A typical example of the eigenvalue spectrum of the Jacobian at slow points on the 2D-manifold.

Up to this point, the trained network has exhibited the performance only on the discontinuously changing sensory inputs. Here we show that the same network can also perceive the continuously changing sensory inputs. For example, Fig. 4A shows that the network output succeeded in following the sinusoidal input. In this case the network trajectory $\boldsymbol{x}(t)$ keeps travelling around the 2D-manifold in the phase space, as shown in Fig. 4B. This behavior results from the balance between the attracting force from the 2D-manifold and the driving force by the prediction error $\boldsymbol{d}(t) - \boldsymbol{z}(t)$. Even in the general case, the same mechanism enables the network to perceive the continuously changing input.

Throughout this section, we have shown the case of $M = 2$ for simplicity, but the same scenario holds for the case of general M.

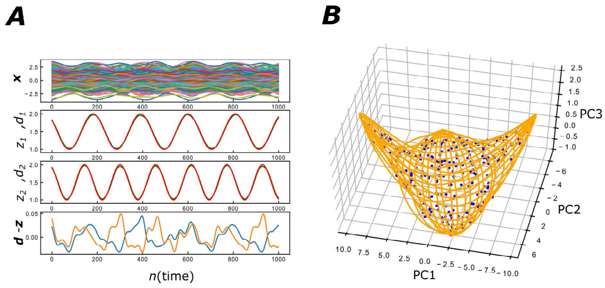

Fig. 4. The response of the trained network to a continuously changing sensory input. **(A)** The activities of the reservoir $\boldsymbol{x}(t)$ (the 1st row), the target $\boldsymbol{d}(t)$ (red plots in the 2nd and 3rd row), the output $\boldsymbol{z}(t)$ (green plots in the 2nd and 3rd row), and the prediction error $\boldsymbol{d}(t) - \boldsymbol{z}(t)$ (the 4th row). **(B)** The trajectory of $\boldsymbol{x}(t)$ (orange) and the 2D-manifold composed of the stable slow points (blue) in 3D PCA space.

3. Context-dependent PCRC

In this section, we construct a simple PCRC network for the context-dependent perception task. We also analyze the trained network to elucidate how it switches the processing depending on contexts.

3.1. *Network architecture and dynamics*

We add to Eq. (1) the term of the context signal from external modules:

$$\tau\dot{\boldsymbol{x}} = -\boldsymbol{x} + W^{REC}\boldsymbol{r} + W^{FB}\boldsymbol{z} + W^{IN}(\boldsymbol{d} - \boldsymbol{z}) + W^{CON}\boldsymbol{c}, \qquad (11)$$

where the context $\boldsymbol{c}(t) \in \mathbb{R}^L$ is fed through weights $W^{CON} \in \mathbb{R}^{N\times L}$, whose elements are independently and uniformly sampled from $[-1, 1]$. In this section we use $M = 4$ and $L = 2$ for simplicity, and the other settings follow section 2.

3.2. *Task and learning rule*

We present the constant vectors $\boldsymbol{d}^1, \dots, \boldsymbol{d}^{N_D} \in \mathbb{R}^M$ in turn as the sensory inputs to the network, and train the network to keep outputting each given constant vector until the next target is presented. We also present the context $\boldsymbol{c}^1 \coloneqq (0, 1)^{\mathrm{T}}$ during the 1st to $N_D/2$ th trials, and the context $\boldsymbol{c}^2 \coloneqq (1, 0)^{\mathrm{T}}$ during the $N_D/2 + 1$ th to N_Dth trials, respectively. Each sensory input $\boldsymbol{d}^i$ is presented for 0.2 sec, and its elements are given as $\boldsymbol{d}^i = \left(d_1^i, 1/d_1^i, d_2^i, 1/d_2^i\right)^{\mathrm{T}}$ on the context $\boldsymbol{c}^1$ and $\boldsymbol{d}^i = \left(d_1^i, d_2^i, d_2^i/2, d_1^i/2\right)^{\mathrm{T}}$ on the context $\boldsymbol{c}^2$, respectively. At each trial d_1^i and d_2^i are independently and uniformly sampled from $[1,2]$. Note that the essential dimension of the input is $M/2$ on each context, but the trained network is required to switch the type of processing depending on contexts.

We train W^{OUT} by FORCE learning algorithm used in section 2.

3.3. *Results and analysis*

We trained the network for 1000 trials on each context $\boldsymbol{c}^1$ and $\boldsymbol{c}^2$. (i.e., $N_D = 2000$.) At each trial in the test phase, the sensory input $\boldsymbol{d}^i$ is presented for 1.0 sec. As shown in Fig. 5A, the training resulted in almost perfect performance, and the pulse-like prediction error drives the network from one slow point to another, as with the context-free case in section 2. Fig. 5B shows that the two different 2D-manifold attractors are formed for the contexts $\boldsymbol{c}^1$ and $\boldsymbol{c}^2$, respectively. This suggests that the network switches its attractor-landscape depending on contexts, and the same mechanism as section 2 enables the network to perceive the sensory inputs on each context.

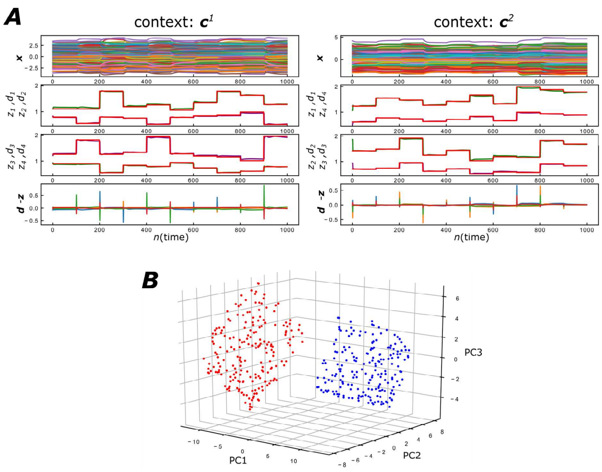

Fig. 5. The context-dependent response of the trained network. **(A)** The activities of the reservoir $\boldsymbol{x}(t)$ (the 1st row), the target $\boldsymbol{d}(t)$ (red plots in the 2nd and 3rd row), the output $\boldsymbol{z}(t)$ (green and purple plots in the 2nd and 3rd row), and the prediction error $\boldsymbol{d}(t) - \boldsymbol{z}(t)$ (the 4th row). (Left: context $\boldsymbol{c}^1$. Right: context $\boldsymbol{c}^2$.) **(B)** The locations of the slow points $\bar{\boldsymbol{x}}^i$ for the entire target range $(d_1^i, d_2^i) \in [1,2]^2$ in 3D PCA space. (Blue: on the context $\boldsymbol{c}^1$. Red: on the context $\boldsymbol{c}^2$.)

We next evaluate the performance of the trained network when the type of the sensory input ($\boldsymbol{d}^i = (d_1^i, 1/d_1^i, d_2^i, 1/d_2^i)^{\mathrm{T}}$ or $(d_1^i, d_2^i, d_2^i/2, d_1^i/2)^{\mathrm{T}}$) does not match the context. In this case, we present each sensory input $\boldsymbol{d}^i$ for 5.0 sec. Fig. 6 shows that the context mismatch keeps the prediction errors apart from zero, so that the network fails to perceive the sensory inputs, but nevertheless the network trajectories sometimes settle into slow points.

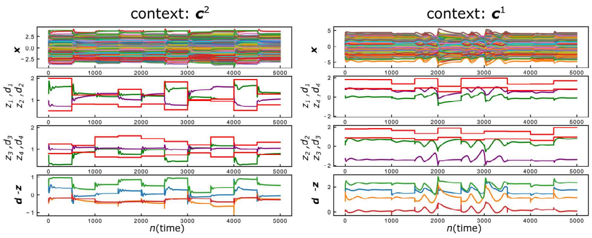

Fig. 6. The perceptual errors induced by the context mismatch. (Left: $\boldsymbol{d}^i = (d_1^i, 1/d_1^i, d_2^i, 1/d_2^i)^{\mathrm{T}}$ on the context $\boldsymbol{c}^2$. Right: $\boldsymbol{d}^i = (d_1^i, d_2^i, d_2^i/2, d_1^i/2)^{\mathrm{T}}$ on the context $\boldsymbol{c}^1$.)

4. Context-dependent PCRC for Visual Data

In this section, we construct a context-dependent PCRC network which can perceive more high-dimensional visual inputs, in order to demonstrate that the proposed network can be a possible mechanism of the visual perception. We also observe the complex features of the perceptual error induced by the context mismatch.

4.1. *Network architecture, task, and learning rules*

The network architecture and settings follow those of section 3, except the dimension of the input and output: $M = 20$.

We use the MNIST (Mixed National Institute of Standards and Technology) data set, which is widely used for handwritten numeral recognition tasks, as the high-dimensional visual sensory stimuli. As the preprocessing, we first compress the MNIST data whose labels are “0” or “1” into 20 dimension, using the NMF (Non-negative Matrix Factorization). We next randomly choose one of the compressed MNIST data as the sensory input $\boldsymbol{d}^i$ and present it to the network for 0.2 sec at each i th trial. At the same time, we present the context $\boldsymbol{c}^1$ if $\boldsymbol{d}^i$ has “0” label, and the context $\boldsymbol{c}^2$ if $\boldsymbol{d}^i$ has “1” label, respectively. (i.e., each context represents the category of the visual sensory input.) We train the network to keep outputting the presented sensory input $\boldsymbol{d}^i$ during each trial. In the test phase, we present to the network unlearned compressed MNIST data as the sensory inputs.

The trained network is required to form slow points that correspond to even unlearned MNIST data in its phase space.

We use the FORCE algorithm again during training.

4.2. *Results and analysis*

We trained the network for 2000 trials on each context $\boldsymbol{c}^1$ and $\boldsymbol{c}^2$. (i.e., $N_D = 4000$.) At each trial in the test phase, we present a randomly chosen unlearned MNIST data for 5.0 sec as the sensory input $\boldsymbol{d}^i$. Fig. 7A shows that the training network almost succeeded in perceiving unlearned MNIST inputs, and the pulse-like prediction error drives the network from one slow point to another, as with the case above. Fig. 7B shows that the two different manifold attractors are formed for the "0" label and "1" label MNIST inputs respectively, but in the 3D PCA space we cannot observe the actual shapes of these manifolds.

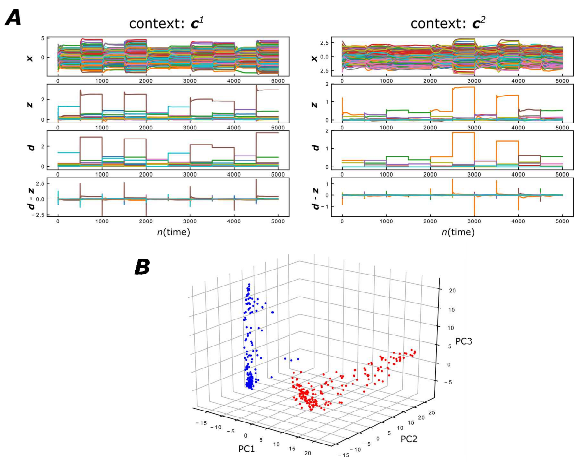

Fig. 7. The context-dependent response of the trained network to unlearned MNIST inputs. **(A)** The activity of the reservoir $\boldsymbol{x}(t)$, the output $\boldsymbol{z}(t)$, the target $\boldsymbol{d}(t)$ and the prediction error $\boldsymbol{d}(t) - \boldsymbol{z}(t)$. (Left: context $\boldsymbol{c}^1$. Right: context $\boldsymbol{c}^2$.) **(B)** The locations of the slow points $\bar{\boldsymbol{x}}^i$ in 3D PCA space on the context $\boldsymbol{c}^1$ (red) and on the context $\boldsymbol{c}^2$ (blue), respectively.

We next evaluate the performance of the trained network when the label of the sensory input does not match the context. As shown in Fig. 8, the context mismatch keeps the prediction errors apart from zero, but nevertheless the network trajectories settle into slow points.

We further visualize these errored predictions $\boldsymbol{z}$ at slow points and compare them with the original inputs $\boldsymbol{d}$, by inversely transforming the output $\boldsymbol{z}$ into the dimension of the original MNIST data, using the matrix generated in NMF. As a result, in the errored predictions, the original sensory inputs and the predictions for the wrong label MNIST image overlap each other, as illustrated in Fig. 9.

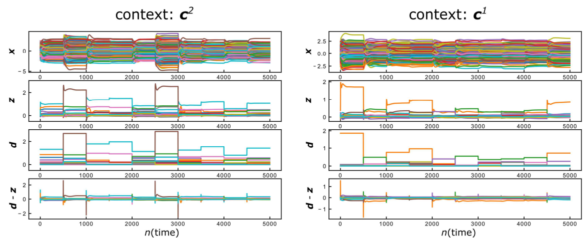

Fig. 8. The perceptual errors induced by the context mismatch. (Left: label "0" data are presented on the context $\boldsymbol{c}^2$. Right: label "1" data are presented on the context $\boldsymbol{c}^1$.)

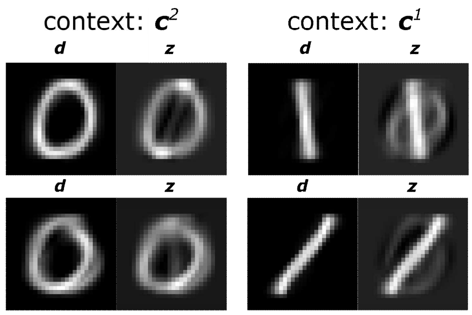

Fig. 9. The examples of the visualized comparison between the original inputs $\boldsymbol{d}$ and errored predictions $\boldsymbol{z}$ on the context mismatch. (Left: label "0" data are presented on the context $\boldsymbol{c}^2$. Right: label "1" data are presented on the context $\boldsymbol{c}^1$.)

5. Discussion

We first proposed the simple one-layer PCRC network driven by the prediction error, which can perceive even unlearned inputs. We analyzed the nonlinear dynamics underling the trained network, and revealed that the network perceives the sensory stimuli using the low-dimensional manifold attractor in its phase space. Since low-dimensional manifold attractors have been also observed in the trained RNNs in previous studies,[6,8,9] it can be a natural strategy for RNNs to use them for the information processing.

Next, we constructed the simple PCRC network for the context-dependent task, and observed that the different attractor-landscape is formed on each context. Throughout this study, we used the PCRC networks with only one layer and assumed the context signals to be fed from the external module, for simplicity. However, the hierarchy plays a key role in the predictive coding framework,[1] and how the context signals are generated remains to be clarified. Therefore, it is our future work to build the hierarchical PCRC model composed of the one-layer networks which are analyzed in this study, and incorporate the modules which generate the context signals inside the model.

Finally, we constructed the context-dependent PCRC network for the compressed MNIST data task, and demonstrated that the proposed network can be a possible mechanism of the visual perception. The perceptual errors induced by the context mismatch exhibited complex features, and interestingly, they share some common features with the symptoms of the hallucination in dementia with Lewy bodies,[10] in which the patients see other people who are not there on the background which actually exists there. It is also our future work to study the relation between these perceptual errors.

Acknowledgements

The authors are grateful to T. Kohno for useful discussions. This paper is partially supported by AMED under Grant Number JP18dm0307009, NEC Corporation, and JSPS KAKENHI Grant Number JP16K00246, and also based on results obtained from a project subsidized by the New Energy and Industrial Technology Development Organization (NEDO).

References

1. R. P. Rao and D. H. Ballard, Predictive coding in the visual cortex: a functional interpretation of some extra-classical receptive-field effects, *Nat. Neurosci.* **2**(1) (1999) 79-87.
2. M. Fukino, Y. Katori and K. Aihara, A Computational Model for Pitch Pattern Perception with the Echo State Network, in *2016 Int. Symp. Nonlinear Theory and Its Application* (Yugawara, Japan, 2016), 271-274.
3. K. Ara and Y. Katori, Hierarchical network model of auditory information processing using dynamical predictive coding, in *23rd Int. Conf. Artificial Life and Robotics* (Beppu, Japan, 2018), 41-46.
4. Y. Katori, Network model for dynamics of perception with reservoir computing and predictive coding, *Advances in Cognitive Neurodynamics* (VI), Chapter 11 (Springer Nature Singapore Pte Ltd, Singapore, 2018).
5. M. Lukoševičius and H. Jaeger, Reservoir computing approaches to recurrent neural network training, *Computer Science Review* **3**(3) (2009), 127-149.
6. V. Mante, D. Sussillo, K. V. Shenoy and W. T. Newsome, Context-dependent computation by recurrent dynamics in prefrontal cortex, *Nature* **503**(7474) (2013), 78-84.
7. D. Sussillo and L. F. Abbott, Generating coherent patterns of activity from chaotic neural networks, *Neuron* **63**(4) (2009), 544-557.
8. D. Sussillo and O. Barak, Opening the black box: low-dimensional dynamics in high-dimensional recurrent neural networks, *Neural Comput.* **25**(3) (2013), 626-649.
9. C. Beer and O. Barak, Dynamics of dynamics: following the formation of a line attractor, *arXiv*:1805.09603 (2018).
10. D. Collerton, J. P. Taylor, I. Tsuda, H. Fujii, S. Nara, K. Aihara and Y. Katori, How can we see things that are not there? Current insights into complex visual hallucinations, *Journal of Consciousness Studies* **23**(7-8) (2016), 195-227.

Snake robot controlled by biomimetic CPGs

Damien Blanchard
IMS, University of Bordeaux, France
Talence, 351 cours de la Libération, 33400, France

Kazuyuki Aihara
IIS, The University of Tokyo, Japan
Tokyo, 4-7-1 Komaba, Meguro-ku, 153-8505, Japan

Timothée Levi
IIS, The University of Tokyo, Japan
Tokyo, 4-7-1 Komaba, Meguro-ku, 153-8505, Japan

E-mail: damien.blanchard@u-bordeaux.fr, kohno@sat.t.u-tokyo.ac.jp, aihara@sat.t.u-tokyo.ac.jp, levi@sat.t.u-tokyo.ac.jp
www.iis.u-tokyo.ac.jp/ja/

Abstract

Locomotion is one of the most basic abilities in animals. Neurobiologists have established that locomotion results from the activity of half-center oscillators that provides alternation of bursts. Central Pattern Generators (CPGs) are neural networks capable of producing rhythmic patterned outputs without rhythmic sensory or central input. We propose a network of several biomimetic CPGs using biomimetic neuron model and synaptic plasticity. This network is implemented on a FPGA (Field Programmable Gate Array). We designed one unsupervised snake robot using this network of CPG. It is composed of one head wagon followed by seven slave wagons. Infrared sensors are also embedded in the head wagon. This robot can reproduce the locomotion of one snake.

Keywords: snake robot, CPG, biomimetic, spiking neural network, locomotion.

1. Introduction

Locomotion is one of the most basic abilities in animals. Neurobiologists have established that locomotion is created by Central Pattern Generator (CPG) activity that produces alternating bursts[1]. Most rhythmic movements are programmed by CPG (Central Pattern Generator) networks[2]. CPGs are neural networks capable of producing rhythmic patterned outputs without sensory input. CPGs can be found in animal locomotion such as swimming in salamander[3] or lamprey[4], and cardiac pulsation system in leech[5, 6].

Usually, in the field of robotics, CPGs are made using simple neuron models[7] or simple oscillators[8], which are not biological time scales and which are considered as bio-inspired systems rather than biomimetic systems. These models provide sinusoidal oscillations and cannot reproduce biomimetic CPGs which have variability in performance. As our aim is to replicate biological behavior, we developed biomimetic CPGs using digital neuromorphic system.

2. Biomimetic CPGs in digital neuromorphic system

2.1. *CPG neural network*

The biomimetic CPG is based on the neural network system that controls the heartbeat of a leech[6]. This simple network uses 8 excitatory neurons with 12 inhibitory synapses, making it an ideal candidate for our applications.

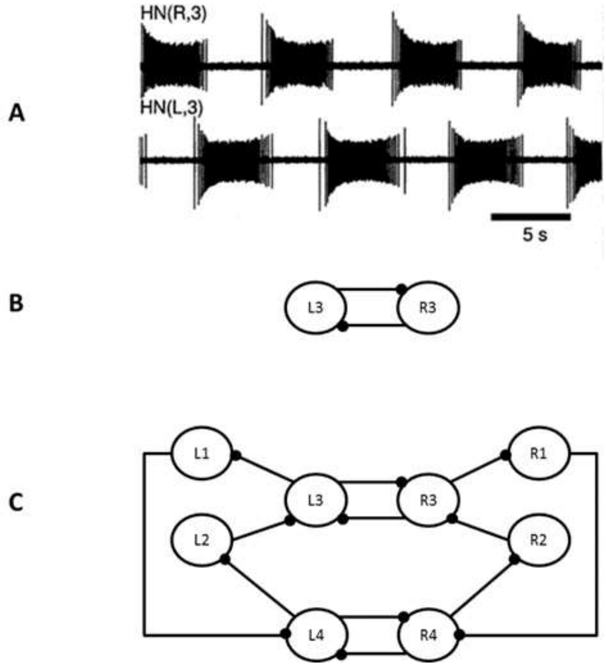

Fig. 1. Electrical activity of the neural system of the Heartbeat of the Leech. Neurons are represented by circles. Inhibitory synapses are represented by black dots. A: Electrical Activity from the Leech [HILL 2003]. B: Diagram of an Elemental Oscillator of the Heart of the Leech. C: Diagram of the Segmental Oscillator of the Heart of the Leech.

2.2. *Simplification of the model*

To design this CPG (Segmental Oscillator in Figure 1.C C), Hill's neural network diagram[6] was used.

The network designed by Hill uses the Hodgkin-Huxley model[9] and complex equations for synapses. First work was to simplify this model by applying Izhikevich neurons[10]. Using the short-term synaptic plasticity[11] and the Izhikevich Regular Spiking neurons, the activity of Hill's model was reproduced.

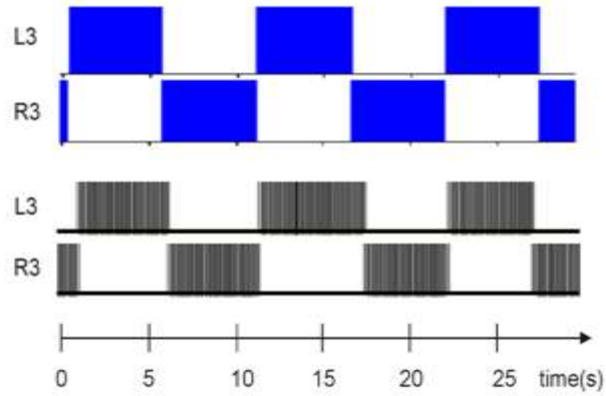

Fig. 2. Comparison of CPG activity between Hill's model (in blue) and our model (in black)

Even though the model was simplified, the same behavior and characteristics as the biological CPGs was successfully reproduced. The important point is to allow a variability in the characteristics of the CPGs. Percentages of variability can be controlled by adjusting the parameters of short-term synaptic plasticity.

By changing the parameters of the inhibitory synapses, it is possible to obtain different periods and cyclic ratios. This is very important especially for closed-loop experiments and to reproduce locomotion activities for robotics. A single parameter pair manages the modification of the period and of the duty cycle. The possible period interval in seconds is quite wide [0.3s; 35s].

2.3. *Implementation in digital neuromorphic system*

Biomimetic CPGs[12, 13, 14, 15] are implemented in a digital platform: CMOD A7-A35 Xilinx Artix-7 FPGA (Field Programmable Gate Array). The neural network implementation architecture operates on a single computation core. This real-time digital system requires few resources and low power consumption[16, 17, 18, 19]. Table 1 summarizes the stated resources.

Table 1. Utilization of the resources for the implementation of biomimetic CPGs

Kintex-7	Utilization	Available	Percentage
LUT	7786	20800	**37.43**
FF	3299	41600	**7.93**
BRAM	50	50	**100**
DSP	40	90	**44.44**

Figure 3 describes the CMOD A7 FPGA board where CPGs with different period are implemented.

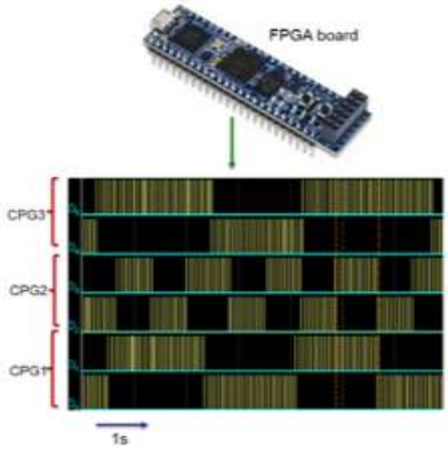

Fig. 3. Three different CPGs with different period (1,7s, 3,6s and 5s). The output are from the scope.

As we implemented the biomimetic CPGs in the FPGA board, we design the structure of the snake robot which embedded the FPGA board.

3. Snake robot

3.1. *Design*

The snake robots is composed of 7 wagons (like spinal cord) and 1 locomotive (mimics the brain).

Biomimetic CPGs will control the different motors of the wagons. As the output of the FPGA board is 3.3V with low current, a power driver for the motors and a VHDL module for converting the CPGs to PWM (Pulse Width Modulation) to control motor speed needs to be added. The PWM frequency should be between 100 Hz and 200 kHz. The duty cycle of the PWM controls the speed of the motor. Pololu_DRV8835 was used for the power driver. Motors are DG01D with a 0.8 kg.cm couple and a no load speed of 90 rpm.

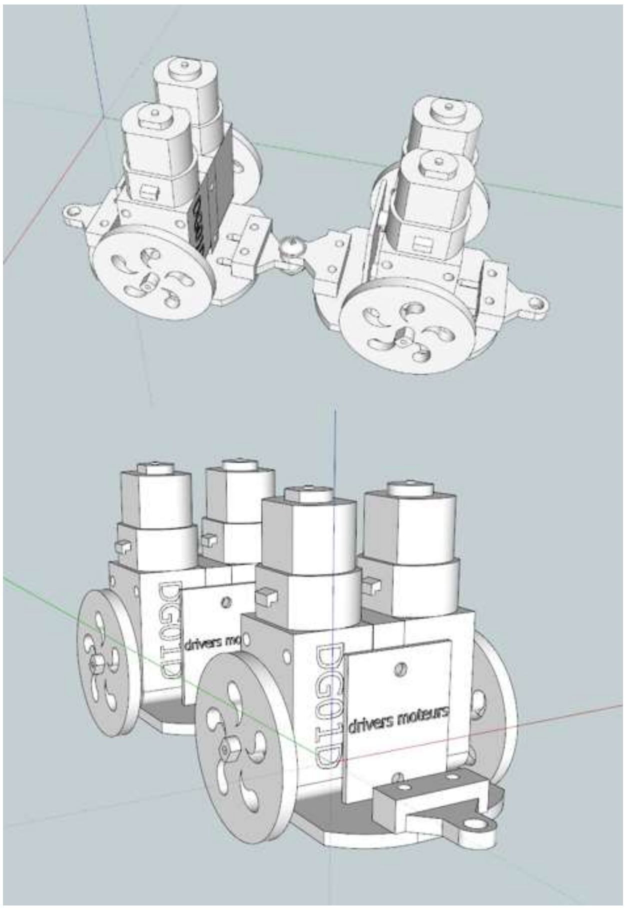

Fig. 4. 3D view of the wagon design

All the distance between the different wagons and the possible movement angle can be tuned with mechanical structure. Figure 5 shows how the tuning is possible.

Fig. 5. The orange screw allows the tuning of distance of the different wagons but also the angle for the movement.

The design of electrical connection and components for the locomotive and for the wagon is described in figure 6.

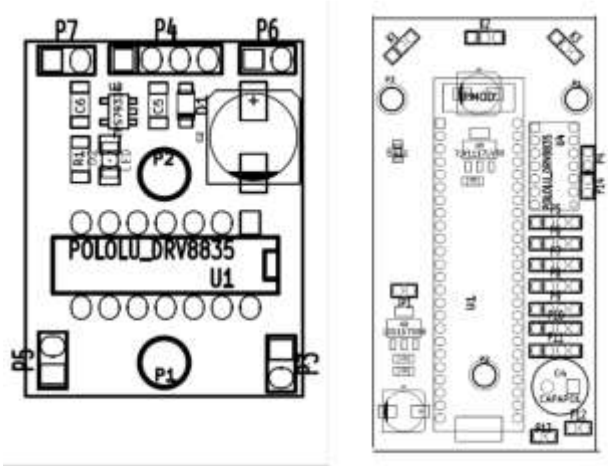

Fig. 6. On the left, the electrical circuit of the wagon. On the right, the electrical circuit of the locomotive with the FPGA board.

The locomotive system has 3 IR sensors for detecting the different obstacles and then send stimulus to CPGs for modifying duty cycle and period. The tuning of the duty cycle allows the movement and the tuning of period allows the speed or the stop of the robot.

3.2. *Results*

Height CPGs were implemented (one for the locomotive and 7 for the wagons). Enable input are connected to each wagon to choose which ones are working for simulating a lesion of the spinal cord.

The CPGs are connected for allowing forward locomotion like we can find in animal locomotion[20]. Fig. 7 describes this CPG network and the forward locomotion.

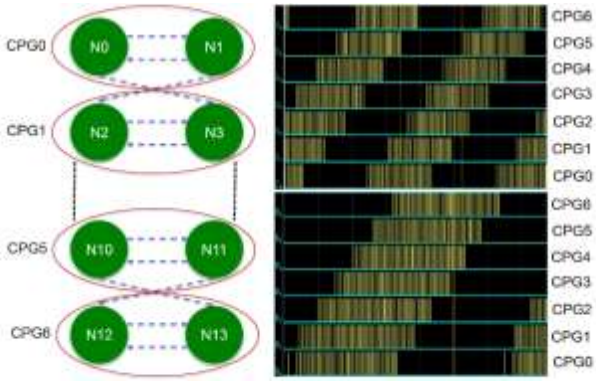

Fig. 7. Forward locomotion with two examples of speed using a chain of 7 CPGs for the 7 wagons. Time axis is one second by division. Signal are the left neuron (N0, N2, N4, N6, N8, N10 and N12) of each CPG.

The final snake robot is 59 cm long and works with real-time biomimetic CPGs and mimics the snake locomotion. Figure 8 shows the final snake robot picture.

Fig. 8. Picture of the snake robot with the locomotive and the 7 wagons.

4. Conclusion

This article describes the design of a snake robot. This robot is controlled by real-time network of biomimetic CPGs. This system can be used in robotic applications[21] for a closer behavior to biological animals. It can also be used in bio-hybrid robotics (biomimetic CPGs can be replaced by in vitro cell culture). We previously showed that our system can be connected to biological neurons[22, 23]. Another advantage is that the real-time systems can simulate multiple CPG topologies and simulate different hypothesis and protocol treatments for biomedical applications such as spinal cord injury[24] and neuroprosthetics[25].

Acknowledgements

Authors thank Social Cooperation Program for Brain-Morphic AI to Resolve Social Issues, IIS, U Tokyo.

References

1. T. Brown, On the nature of the fundamental activity of the nervous centres; together with an analysis of the conditioning of rhythmic activity in progression and a theory of the evolution of function in the nervous system. *Journal of Physiology*, 48, 18-46, 1914
2. E. Marder and D. Bucher, Central pattern generators and the control of rhythmic movements. *Current Biology* 11, 986-996, 2001
3. A. Ijspeert, A. Crespi, D. Ryczko, J. Cabelguen, From swimming to walking with a salamander robot driven by a spinal cord model. *Science*, 315, 1416-1420, 2007

4. AH. Cohen et al., Modelling of intersegmental coordination in the lamprey central pattern generator for locomotion. *Trends in Neuroscience*. 15, 434–438, 1992
5. GS. Cymbalyuk, Q. Gaudry, MA. Masino, R.L. Calabrese, Bursting in Leech Heart Interneurons: Cell-Autonomous and Network-Based Mechanisms. *J. Neuroscience*, 22, 10580-10592, 2002
6. AA. Hill, J. Lu, MA. Masino, OH Olsen, RL Calabrese, A model of a segmental oscillator in the leech heartbeat neuronal network, *J Comput Neurosci*., 10, 281-302, 2001
7. S. Amari, Characteristic of the random nets of analog neuron-like elements, *IEEE Trans. on System, Man and Cybernetics*, 2, 643-657, 1972
8. B. Van Der Pol, The heartbeat considered as a relaxation oscillation, and an electrical model of the heart. *Philosophical Magazine*, 6, 763–775, 1928
9. AL. Hodgkin, AF. Huxley, A quantitative description of membrane current and its applications to conduction and excitation in nerve, *The Journal of Physiology*, 117, 500-544, 1952
10. E.M. Izhikevich, Simple model of spiking neurons. *IEEE Transactions on Neural Networks*, 14, 1569- 1572, 2003
11. E.M. Izhikevich and G. Edelman, Large-scale model of mammalian thalamocortical systems, *Proceedings of the National Academy of Sciences of the United States of America*, 105, 3593-3598, 2008
12. J.H. Barron-Zambrano and C. Torres-Huitzil, FPGA implementation of a configurable neuromorphic CPG-based locomotion controller, *Neural Netw*.45, 50–61, 2013.
13. C. Li, R. Lowe, T. Ziemke, Humanoids Learning to Walk : a Natural CPG-Actor-Critic Architecture, *Frontiers in Neurorobotics*, 7:5, 2013
14. E. Donati, F. Corradi, C. Stefanini, G. Indiveri, A spiking implementation of the lamprey's Central Pattern Generator in neuromorphic VLSI, *IEEE BioCAS 2014*,2014
15. C. Qi et al., A real-time FPGA implementation of a biologically inspired central pattern generator network, *Neurocomputing*, 244, 63-80, 2017
16. M. Ambroise, T. Levi, S. Joucla, B. Yvert, S. Saïghi, Real-time biomimetic Central Pattern Generators in an FPGA for hybrid experiments. *Frontiers in Neuroscience*, 7, 215, 2013
17. M. Ambroise, T. Levi, Y. Bornat, S. Saïghi, Biorealistic spiking neural network on FPGA, *47th Annual Conference on Information Sciences and Systems* CISS, 1-6, 2013
18. F. Grassia, T. kohno, T. Levi, Digital hardware implementation of a stochastic two-dimensional neuron model, *Journal of Physiology Paris*, 110:4, 409-416, 2016
19. T. Levi, Y. Guo, K. Aihara, T. Kohno, Study of real-time biomimetic CPG on FPGA: behavior and evolution, *JRNAL*, 4:4, 299:302, 2018
20. T. Matsuo, T. Yokoyama, D. Ueno, K. Ishii, Biomimetic Motion Control System Based on a CPG for an Amphibious Multi-Link Mobile Robot, *Journal of Bionic Engineering*, 91-97, 2008
21. T. Levi, T. Nanami, A. Tange, K. Aihara, T. Kohno, Development and Applications of Biomimetic Neuronal Networks Toward BrainMorphic Artificial Intelligence, *IEEE Transactions on Circuits and Systems* II, 65:5, 577-581, 2018
22. S. Joucla et al.,, Generation of locomotor-like activity in the isolated rat spinal cord using intraspinal electrical microstimulation driven by a digital neuromorphic CPG, *Frontiers in neuroscience*, 10, 2016
23. T. Levi et al., Biomimetic neural network for modifying biological dynamics during hybrid experiments, *Journal on Artificial Life and Robotics*, May 2017
24. M. Capogrosso et al., A brain–spine interface alleviating gait deficits after spinal cord injury in primates, *Nature*, 539, 284-288, November 2016
25. T. Levi, P. Bonifazi, P. Massobrio, M. Chiappalone, Closed-loop systems for next-generation neuroprostheses, *Frontiers in Neuroscience*, 12-26, 2018

Real-time implementation of ReSuMe learning in Spiking Neural Network

Yang Xia*
Graduate School of Engineering, The University of Tokyo, Japan
Tokyo, 4-7-1 Komaba,Meguro-ku,153-8505, Japan

Seiji Uenohara
IIS, The University of Tokyo, Japan
Tokyo, 4-7-1 Komaba,Meguro-ku,153-8505, Japan

Kazuyuki Aihara
IIS, The University of Tokyo, Japan
Tokyo, 4-7-1 Komaba,Meguro-ku,153-8505, Japan

Timothée Levi
IIS, The University of Tokyo, Japan
Tokyo, 4-7-1 Komaba,Meguro-ku,153-8505, Japan

E-mail:xiayang@sat.t.u-tokyo.ac.jp, uenohara@sat.t.u-tokyo.ac.jp, aihara@sat.t.u-tokyo.ac.jp, levi@sat.t.u-tokyo.ac.jp
www.iis.u-tokyo.ac.jp/ja/

Abstract

Neuromorphic systems are designed by mimicking or being inspired by the nervous system, which realizes robust, autonomous, and power-efficient information processing by highly parallel architecture. Supervised learning was proposed as a successful concept of information processing in neural network. Recently, there has been an increasing body of evidence that instruction-based learning is also exploited by the brain. ReSuMe is a proposed algorithm by Ponulak and Kasinski in 2010. It proposes a supervised learning for biologically plausible neurons that reproduce template signals (instructions) or patterns encoded in precisely timed sequences of spikes. Here, we present a real-time ReSuMe learning implementation on FPGA using Leaky Integrate-and-fire (LIF) Spiking Neural Network (SNN). FPGA allows real-time implementation and embedded system. We show that this implementation can make successful the learning on a specific pattern.

Keywords: Spiking neural network, ReSuMe, LIF, FPGA

1. Introduction

Neuromorphic systems are designed by mimicking or being inspired by the nervous system, which realizes robust, autonomous, and power-efficient information processing by highly parallel architecture. There are three common methods to realize the neuromorphic circuits, which are software[1 2 3], analog hardware[4 5 6 7] and digital hardware[8 9 10 11 12]. Software can implement simple neuron model but a large scale neural network with complex neuron model cannot be realized in real-time. The power consumption is also quite important (kW for supercomputer). For hardware implementation, compared to analog circuits, digital implementations consume more power but they are convenient to modify, more portable and lower cost for implementation with FPGA devices.

Supervised learning was proposed as a successful concept of information processing in neural network[13]. Recently, there has been an increasing body of evidence that instruction-based learning is also exploited by the brain.

Remote Supervised Method (ReSuMe) is a new supervised learning method for Spiking Neural Networks. The main reason for the study of ReSuMe is the need to invent an effective learning method to control the movement of people with physical disabilities. However, the in-depth analysis of ReSuMe method shows that this method is not only suitable for motion control tasks, but also suitable for other practical applications, including modeling, identification and control of various non-stationary and non-linear objects[14 15].

In this paper, we present a real-time ReSuMe learning implementation on FPGA using Leaky Integrate-and-fire (LIF) Spiking Neural Network (SNN). FPGA allows real-time implementation and embedded system[16].

We show that this implementation can make successful the learning on a specific pattern.

2. Method

This section proposed three methods that applied to the ReSuMe learning implementation on FPGA, which are LIF-neuron model, Postsynaptic potential (PSP) and Spike response model (SRM), as well as ReSuMe algorithm.

2.1. *LIF neuron model*

The LIF neuron is one of the simplest spiking neuron models. Due to the convenience with which it can be analyzed, simulated especially implemented in digital silicon neural network, the LIF neuron is very popular[17]. A neuron is modeled as a "leaky integrator" of its input *I*(t):

$$\tau_m \frac{dv}{dt} = -v(t) + RI(t) \tag{1}$$

where *v(t)* represents the membrane potential at time *t*, τ_m is the membrane time constant and *R* is the membrane resistance. This equation describes a simple resistor-capacitor (*RC*) circuit where the leakage term is due to the resistor and the integration of *I(t)* is due to the capacitor that is in parallel to the resistor. The spiking events are not explicitly modeled in the LIF model. Instead, when the membrane potential *v(t)* reaches a certain threshold v_{th} (spiking threshold), it is instantaneously reset to a lower value v_r (reset potential) and the leaky integration process described by Eq. (1) starts a new with the initial value v_r.

Consider the case of constant input: *I(t) = I*. We assume v_r= 0. The solution of Eq. (1) is then given by:

$$v(t) = RI\left[1 - \exp(-\frac{t}{\tau_m})\right] \tag{2}$$

Here *v(t)* is in an exponential decay. In discrete digital sequential circuit, a linear decay method is usually used to optimize computing process for saving hardware resources.

$$dv = [-v + RI]\frac{dt}{\tau_m} \tag{3}$$

Eq. (3) describes the computing equation of *dv,* then solution *v* = *v* + *dv* obviously.

2.2. *Postsynaptic Potential and Spike Response Model*

By considering a single postsynaptic neuron *i* with a membrane potential u_i at time t , a simplified SRM is defined[17].

$$u_i(t|\mathrm{X}, y_i) \coloneqq \sum_j w_{ij} \sum_{t_j^f \in x_j} \epsilon(t - t_j^f) \tag{4}$$

This SRM signifies a dependence of the neuron's membrane potential on its presynaptic input pattern X from n_i synapses. An output spike occurs at a time t_j^f. The term of Eq. (4) describes a weighted summation of the pre-synaptic input: the w_{ij} corresponds to the synaptic weight from a presynaptic neuron *j*, the kernel ϵ refers to the shape of an evoked PSP. The PSP kernel evolves according to

$$\epsilon(s) = \frac{1}{C}\int_{S'=0}^{\infty} \exp(-\frac{s'}{\tau_m})\alpha(s-s')ds'\Theta(s) \tag{5}$$

The term $\Theta(s)$ is the Heaviside step function defined such that $\Theta(s) = 1$ for $s \geq 0$ and $\Theta(s) = 0$. Here we approximate the postsynaptic current's time course by an exponential decay[18].

$$\alpha(s) = \frac{q}{\tau_s}\exp(-\frac{s}{\tau_s})\Theta(s) \qquad (6)$$

For a further simplified computer in digital circuit, the exponential decay $\alpha(s)$ substitute the PSP kernel evolves $\epsilon(s)$ approximately.

2.3. *ReSuMe architecture and algorithm*

An implementation of ReSuMe in the Liquid State Machine (LSM) architecture is proposed as an example[19]. The Liquid State Machine consists of a large, fixed "reservoir" network - the neural microcircuit (NMC) from which the desired output is obtained by training the suitable output connection weights.

In the implementation of ReSuMe method, the original LSM approach has been modified. The modified architecture consists of a set of input neurons N^{in}, the *NMC* structure, a set of learning neurons N^{l} with a total number k and a corresponding set of teacher neurons N^{d} (see Fig.1). NMC receives signal $s^{in}(t)$ from N^{in} and transforms it into a vector of signals $\hat{S}_i^{in}(t)$ which i is presented to the learning neurons $n_i^l \in N^l$. The teacher neurons N^{d} are not directly connected with any other structure.

Since we focus more on the ReSuMe learning implementation itself on this paper, so we generated pre-

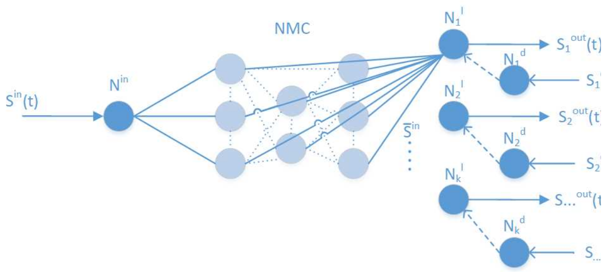

Fig. 1. ReSuMe implemented in the modified Liquid State Machine Architecture.

synapse to the learning neuron as NMC output.

The modification algorithm, which adjusts weights between pre-spike and post-neuron, is applied according to the following simplified equation:

$$\frac{d}{dt}w_{ki}(t) = [S^d(t) - S^d(t)] *$$

$$[a^d + \int_0^\infty W^d(s^d)S^{in}(t - s^d)ds^d] \qquad (5)$$

The Fig.2 shows a specific weights update process.

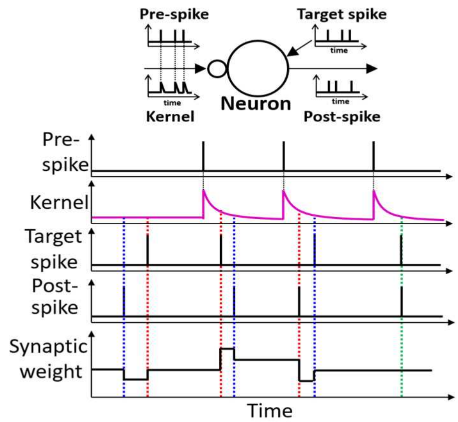

Fig. 2. An example waveform of synaptic weight updating in ReSuMe learning process.

3. Implementation

These section proposed implementation of above methods we introduced above with results showed in waveforms.

3.1. *Implementation of LIF neuron*

We implement LIF Neuron with VHDL language in FPGA. By adjusting the size of dt and matching different time constant, our LIF Neuron can work at very high clock frequency (10 kHz), which means that its calculation accuracy is very high and the real-time requirement is realized.

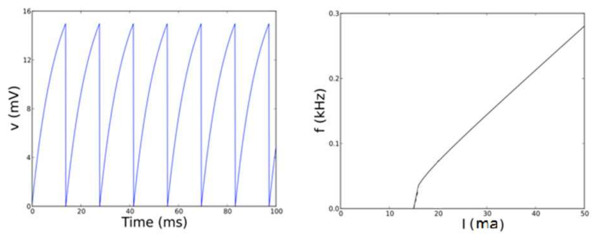

Fig. 3. Stimulation of a LIF neuron by a constant input current: the time-course of the membrane potential, *v(t)* with 15 mV threshold and 20 mA current *I* (left); *f-I* curve for a LIF neuron (right).

3.2. *Implementation of PSP and SRM*

As we introduced in 2.2, we use simplified exponential decay to achieve RSM and PSP. Because post neurons are connected to 500 pre-synaptic inputs, hardware resources are still unacceptable if 500 exponential operations (even in linear decay) are performed in the same clock cycle. We adopt time division multiplexing, and use two-stage pipeline to complete 500 sets of PSP operations in 1000 clock cycles (actually 501 cycles, remaining standby, theoretically supporting input ceiling of 999), just using one multiplier and one adder.

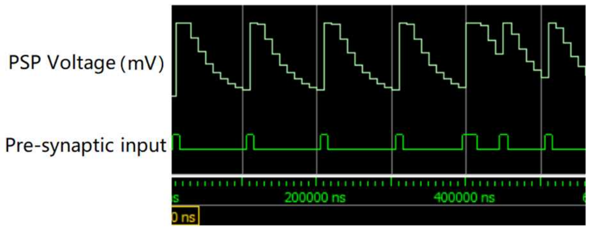

Fig. 4. Waveform of PSP process in which indicates once pre-synaptic input spikes, the PSP starts an exponential decay.

3.3. *Implementation of ReSuMe learning*

ReSuMe we implemented includes an exponential attenuation (linear attenuation) which attribute to change of parameter k. Each time teacher input spike or post-synaptic neuron spike arrives, weight is updated. 500 exponential operations are performed. We use 500 clock cycles, time division multiplexing to achieve this change, and update weight in real-time so that PSP and RSM modules are used to calculate the correct weight instantly.

3.4. *Architecture of ReSuMe learning*

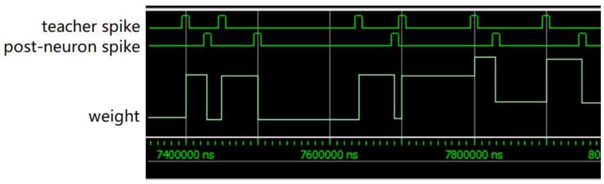

Fig.5. Waveform of ReSuMe weight adjusting process which achieves the ideal functions as showed in Fig.2

The overall hardware architecture of ReSuMe learning is shown in Fig. 6. We use LIF Neuron as post-synaptic neuron, equipped with ReSuMe learning module, and 500 pre-synaptic inputs are connected to post-synaptic neuron. Each connection is operated by PSP and summarized by RSM.

3.5. *Results and discussion*

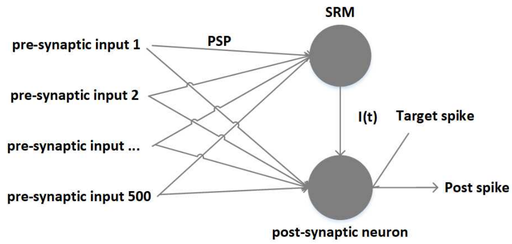

Fig. 6. Architecture of ReSuMe learning.

Firstly, we simulate the actual learning waveform of ReSuMe. As shown in Fig. 7, we have completed the learning of 500 input data containing target patterns and random patterns. Post neurons can spike the location of each pattern with a minimal delay in 2-4 time steps. Here time step means cycle of computing and input patterns. For example, if clock frequency is 100 MHz and computing needs 1000 cycles under our implementation, the time step is 0.01 ms. Then we tested different input pattern groups, and completed real-time test and verification on the FPGA.

4. Conclusion

This paper introduces the advantages of using devices such as FPGA to realize the digital neural network.

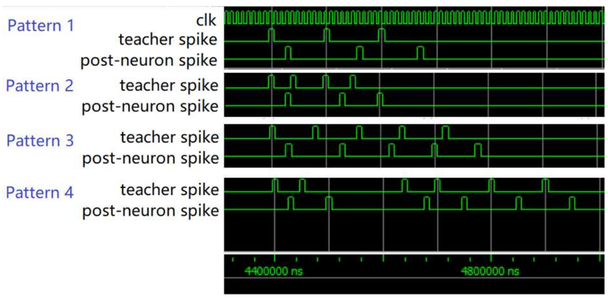

Fig. 7. Waveform of different input patterns and their ReSuMe learning process. The third result shows that the minimum spike interval is 5 time steps.

Methods of LIF neuron, PSP and RSM module as well as ReSuMe learning are described and illustrated on hardware implementation. Then the overall framework of ReSuMe learning is elaborated, with the different output data due to different inputs analyzed.

Acknowledgements

Authors would like to thank Prof. Takashi Kohno, from IIS, the University of Tokyo.

References

1. M.-O. Gewaltig and M. Diesmann, M., NEST (NEural Simulation Tool), *Scholarpedia* 2:1430 (2007).
2. M.L. Hines and N.T. Carnevale, NEURON: a tool for neuroscientists, *The Neuroscientist* 7 (2001) pp. 123-135.
3. D. Goodman and R. Brette, The Brian simulator, Frontiers *in Neuroscience* 3(2) (2009) pp. 192-197.
4. A. Natarajan ans J. Hasler, Hodgkin-Huxley Neuron and FPAA Dynamics, *IEEE Trans Biomed Circuits Systems*, 12(4) (2018), pp. 918-926.
5. F. Grassia, L. Buhry, T. Levi, J. Tomas, A. Destexhe and S. Saïghi, Tunable neuromimetic integrated system for emulating cortical neuron models, Frontiers *in Neurosciences*, 5:134 (2011).
6. N. Qiao, H. Mostafa, F. Corradi, M. Osswald, F. Stefanini, D. Sumislawska, G. Indiveri, A reconfigurable on-line learning spiking neuromorphic processor comprising 256 neurons and 128K synapses, *Frontiers in neuroscience*, 9:141(2015).
7. J. Schemmel, L. Kriener, P. Muller, K. Meier, An Accelerated Analog Neuromorphic Hardware System Emulating NMDA- and Calcium-Based Non-Linear Dendrites, *Proceedings of the International Joint Conference on Neural Networks* (2017)
8. R. Wang, G. Cohen, K. Stiefel, T. Hamilton, J. Tapson, and A. Van Schaik, A., An FPGA Implementation of a Polychronous Spiking Neural Network with Delay Adaptation*, Frontiers in Neuroscience*, 7:1–14(2013).
9. P. Merolla et al., *A million spiking-neuron integrated circuit with a scalable communication network and interface*, *Science*, 345:6197(2014) pp. 668-673.
10. M. Ambroise, T. Levi, S. Joucla, B. Yvert and S. Saïghi, Real-time biomimetic Central Pattern Generators in an FPGA for hybrid experiments, *Frontiers in Neurosciences,* 7:215(2013).
11. Grassia F, Kohno T, Levi T, Digital hardware implementation of a stochastic two-dimensional neuron model, *Journal of Physiology Paris*, 110:4(2016), pp. 409-416.
12. Grassia F, Levi T, Doukkali E, Kohno T, Spike pattern recognition using artificial neuron and Spike-Timing-Dependent Plasticity implemented on a multi-core embedded platform, *Journal of Artificial Life and Robotics*, 23:2(2018), 200-204
13. S. Ghosh-Dastidar, H. Adeli, A new supervised learning algorithm for multiple spiking neural networks with application in epilepsy and seizure detection, *J. Neural Networks*, (2009).
14. A. Kasin´ski and F. Ponulak, Experimental demonstration of learning properties of a new supervised learning method for the spiking neural networks, *Lecture Notes in Computer Science*, Vol. 3696, (2005), pp. 145–153.
15. M. Kraft, A. Kasin´ski and F. Ponulak , Design of the spiking neuron having learning capabilities based on FPGA circuits, *Proceedings of the 3rd International IFAC Workshop on Discrete-Event System Design*, (Rydzyna, Poland, 2006),pp. 301–306.
16. L. Kechiche, L. Touil, and B. Ouni, Toward the Implementation of an ASIC-Like System on FPGA for Real-Time Video Processing with Power Reduction, *International Journal of Reconfigurable Computing*, vol. 2018(2018)
17. W. Gerstner, and W. Kistler, *Spiking Neuron Models: Single Neurons, Populations*, *Plasticity*, Cambridge University Press (2002).
18. B.Gardner and A.Gruning, *PLOS ONE | DOI : 10.1371 / journal.pone.0161335*(2016).
19. W. Maass, T. Natschlaeger, H. Markram. Computational models for generic cortical microcircuits, *Computational Neuroscience: A Comprehensive Approach*, (Chapman and Hall/CRC, Boca Raton, 2004), pp. 575–605.

Biomimetc Spike Timing Based Ionic Micro-Stimulation for Neuron Culture

Stephany Mai Nishikawa
Institute of Industrial Science, The University of Tokyo, Japan
Farad Khoyratee
IMS Lab, University of Bordeaux, France
Soo Hyeon Kim
Institute of Industrial Science, The University of Tokyo, Japan
Yoshiho Ikeuchi
Institute of Industrial Science, The University of Tokyo, Japan
Kazuyuki Aihara
Institute of Industrial Science, The University of Tokyo, Japan
Teruo Fujii
Institute of Industrial Science, The University of Tokyo, Japan
Timothée Levi
Institute of Industrial Science, The University of Tokyo, Japan
IMS Lab, University of Bordeaux, France

E-mail: stephany@iis.u-tokyo.ac.jp, levi@sat.t.u-tokyo.ac.jp
www.iis.u-tokyo.ac.jp

Abstract

Neurodegenerative diseases are incurable and debilitating conditions that influence cognitive and/or motor functions in millions of people worldwide. Neuroprosthesis are used today to support the quality of life but have yet to improve in their power consumption and biocompatibility issues. For the future realization of neuroprosthesis, understanding the neurophysiological behaviors and the investigations on the interaction of neuronal cell assemblies is therefore essential. Here, we propose a novel microfluidic system to investigate the response of the neurons directly stimulated by the potassium ions in vitro in biomimetic timing.

Keywords: Ionic micro-stimulation, Neurons, Spiking Neural Network, Microfluidics

1. Introduction

Most of neurodegenerative diseases are incurable and debilitating conditions that influence cognitive and/or motor functions in millions of people worldwide. Neuroprosthesis are used today to support the quality of life but have yet to improve in their power consumption and biocompatibility issues. To realize a neuroprosthesis that are close to biological behavior, understanding the neurophysiological behaviors and the investigations on the interaction of neuronal cell assemblies is therefore essential. Often being silicon based, this kind of neuromorphic engineering is called biomimetic artificial neural systems [1], [2], [3]. The main goal of such systems is to design tools for biomedical applications including neuroprosthesis and to understand the human nervous system. This project reveals a new bio-hybrid system which includes a real-time Spiking Neural Network (SNN) and biomimetic ionic micro-stimulation coupled to living 'in vitro' neuron culture. To simplify the interactions with biological neurons and to reduce the bio-compatibility issues, we designed a biomimetic ionic micro-stimulation using microfluidic techniques and ionic exchange. Furthermore, to obtain a stimulation close to biological one, a neuromorphic system called Spiking Neural Network (SNN) is used. Firstly, the SNN was integrated in a digital platform FPGA. Then, the spike-timing coming from SNN system is used for triggering the microfluidic ionic micro-stimulation to make the stimulation the closest to biological behavior.

2. Biomimetic spike-timing based microfluidic system

There are three parts that compose the neuro-hybrid system (Fig. 1): (1) Spiking Neural Network (SNN), (2) neuron culture and (3) ionic micro-stimulation in microfluidic system. This system characterizes the neural network and its evolution by using biomimetic spike-timing based ionic stimulation. Each part will be described in detail throughout this article.

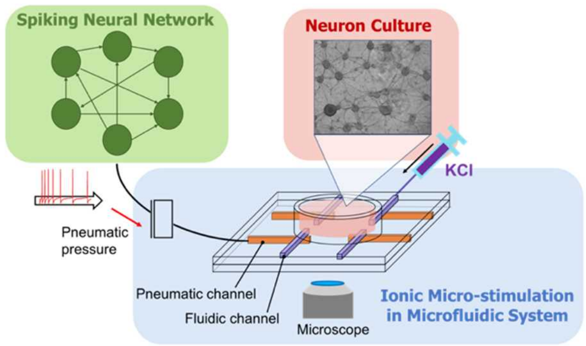

Fig. 1. Neuro-hybrid system with real-time digital SNN (green), biomimetic ionic micro-stimulation in microfluidic system (blue) and biological neuron culture (pink). SNN electrical output is converted into air pulse.

3. Spiking Neural Network (SNN)

The biomimetic SNN network is a neuromorphic system that is the closest detailed level of analogy to the nervous system [4]. A network of silicon neurons is connected via silicon synapses under plasticity rules. In neuro- hybrid experiments, spike timing and shape of the action potential (AP) must reproduce the same dynamics of a biological nerve impulse. This tunable biomimetic system works in real time and is based on Hodgkin-Huxley (HH) formalism [5] which is the most bio-plausible neuron model. We integrated the SNN in a digital platform FPGA. This spike timing-based system, SNN, was connected to the air pressure controller to trigger ionic micro-stimulation on the microfluidic device with stimulation closer to biological behavior.

4. Ionic micro- stimulation in microfluidic device

This device is structured with fluidic channels and pneumatic channels that allow the control of a stimulation sent to the neurons. The structure is described in Fig. 2 [7]. This device has four fluidic channels to input potassium chloride (KCl) of 10mM with each having a pneumatic valve to control the stimulation timing. The channels are equipped with ion selective permeable membrane (Sigma-Aldrich, Nafion® perfluorinated resin solution 5wt.%) to mimic the chemical exchange of biological neurons. It also has an integrated cell dish for the placement of living neurons with a thinness of less than 5mm allowing the observation through microscope during calcium imaging.

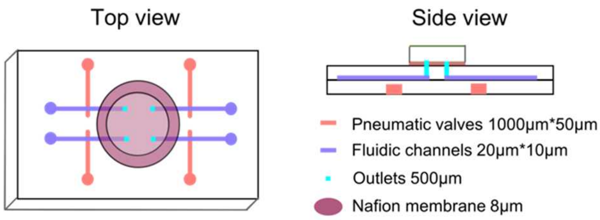

Fig.2. Structure of ionic micro-stimulation device. Set of four fluidic channels with under layer of pneumatic channel. The crossing of these two different types of channels will allow to control the input of solution in fluidic channel.

5. Neuron Culture

This bio-hybrid system contains 'in vitro' primary cultures of mice hippocampal neurons. Neurons were carefully dissected from embryos and were prepared as described [6]. Neurons isolated from embryonic day 17 ICR mouse were plated in Neurobasal medium. They were used in this experiment after two weeks of maturation inside the cell dish of the microfluidic device.

6. Results

6.1. *Integration of Spiking Neural Network into FPGA*

Regular and simplified equations of biomimetic SNN are implemented on a FPGA [8]. Electrical activities of different classes of cortical neurons can be simulated in biological time scale with strong correlation between hardware simulations (Fig.3. red) and software simulations (Fig.3. blue). The Central pattern generators (CPGs) provide bursts of spikes with frequency, variability and spike width in the ranges that are commonly observed in nature [9]

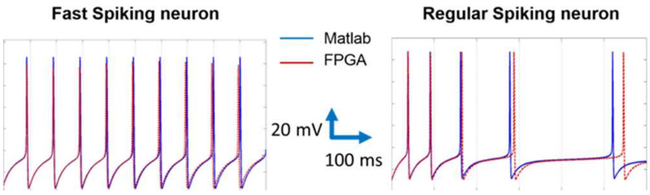

Fig. 3. Comparison between model (blue) and FPGA (red). FPGA implementation and Matlab software simulations are nearly similar.

6.2. *Micro stimulation in the microfluidic system*

After two weeks of cell maturation, neuronal activities were visualized by calcium imaging with Fluo-4 AM (Molecular Probes, United States). To observe the spatial and temporal changes in calcium resulting from spontaneous activity, the raw sequences were processed to observe changes in fluorescence intensity of when the biomimetic ionic micro-stimulation is activated (Fig. 4).

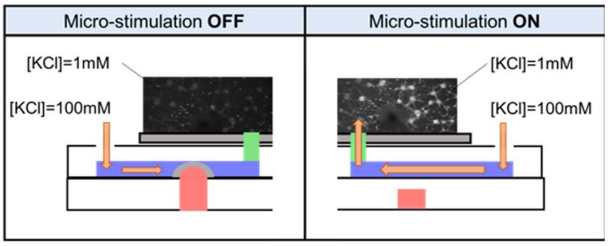

Fig. 4. Bio-hybrid experiments using biomimetic ionic micro-stimulation. When micro-stimulation is ON, the neuron culture is active. Calcium imaging technique is used for detecting neuronal activity.

When the 250ms length pulse of ON/OFF were sent to the pneumatic valve, the ionic stimulation was received by the neurons which in turn were stimulated by potassium ion. This was confirmed by staining the neurons with calcium imaging. The neural activities (Fig.5.) successfully responded accordingly to the programmed ionic stimulation of 250ms. When the pneumatic microvalve is open, the fluorescent intensity increases. On the other hand, when it closes, the fluorescent decreases. During when the pneumatic valve is closed, the neurons activity returns back to its original intensity range.

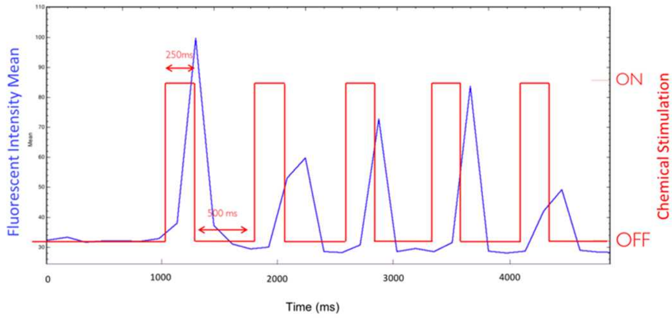

Fig. 5. Stimulations were sent to the device with neuron culture. After calcium imaging, the activity was seen accordingly to the programmed air pulse sent to the pneumatic valve.

After this successful stimulation, the device was integrated with the Spiking Neural Network (SNN) to acquire a more bio-inspired stimulation. This was done by connecting the SNN implemented FPGA unit to the valve of the air controller.

6.3. *Neural response to spike-timing based micro-stimulation*

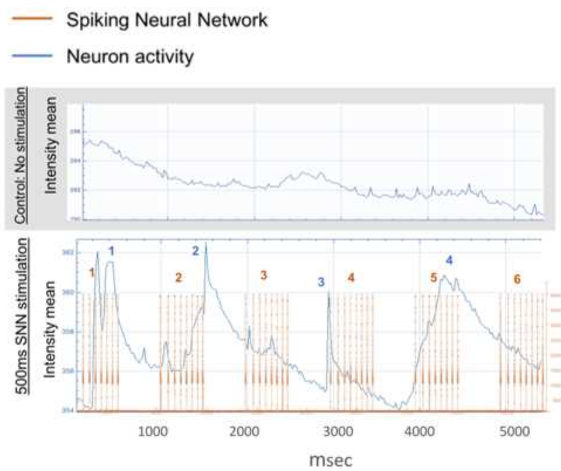

Fig.6. After calcium imaging, the neural activity without any stimulation (top) and during the stimulation using SNN system (bottom) were recorded. The top graph shows the control activity of neurons at resting state. The bottom graph shows the neural activity when CPGs-based burst-like stimulations were sent for 500ms. Images were taken at 200ms frame rate and the fluorescent intensity mean was plotted. The neural activity is visualized when the florescent intensity increased spontaneously. Activity was seen accordingly to the programmed spikes with added delays of approx. 250ms each spike.

The matured neurons were stained with calcium specific fluorescence to visualize the neural activity. The SNN stimulation sent has 8 bust-like spikes for 500ms with 500ms of no signals between stimulation. Fluorescence response observed shows a timely neural activity. However, there were delays in the response time for neuron activity (Fig. 6.). This may have been caused by the insufficient performance of the camera that was used.

7. Conclusion

Our device can generate a biomimetic stimulation accordingly to the sequenced air pressure programmed with Spiking Neural Network (SNN). The activity of neurons observed through calcium imaging showed timely response to SNN signals sent with certain delays.

The neural response was as expected when triggering the stimulation manually and by programmed air pressure of 250ms with air pressure controller. During the 500ms of OFF stimulation, the neural activities decreased as its fluorescent intensity diminished. On the other hand, as we integrated the Spiking Neural Network in the system, delays in response time for the activity of neuron after each stimulation were observed. However, during this recording, the computer had error for insufficient working space (RAM) and the recording showed some lags. This might have caused the error of response time in neural activities.

In the future, we will try to record the neural activity with a camera capable of capturing higher frame rate per second without having a lag during the recording of the neurons. On the other hand, the next step of our work is to create a closed-loop bio-hybrid system where the recorded neuronal activity is used as a feedback for SNN.

References

[1] M. Mahowald, R. Douglas , "A Silicon neuron,", *Nature*, 354, 515-518, 1991

[2] G. Indiveri et al., "Neuromorphic silicon neuron circuits ", *Frontiers in neuroscience,* 5, 73, 2011

[3] M. Ambroise, T. Levi, S. Joucla, B. Yvert, S. Saighi, "Real-time biomimetic Central Pattern Generators into FPGA for hybrid experiments," *Frontiers in Neuroscience*, **7**, 215, 2013

[4] M. Ambroise, T. Levi, Y. Bornat, S. Saighi, "Biorealistic spiking neural network on FPGA", *47th Annual Conference on Information Sciences and Systems (CISS)*, 1-6, Baltimore, US, 2013

[5] AL. Hodgkin and AF. Huxley, "A quantitative description of membrane current and its applications to conduction and excitation in nerve," *The Journal of Physiology*, 117, 500-544, 1952

[6] G. Brewer, J. Torricelli, E. Evege, P. Price, "Optimized survival of hippocampal neurons in B27-supplemented Neurobasal, a new serum-free medium combination,“ *J Neurosci Res*, 35, 567–576, 1993

[7] S.M. Nishikawa, S.H. Kim, Z. Luo, T. Kirihara, Y. Ikeuchi, T. Fujii and T. Levi, "Biomimetic microfluidic neurons for Bio-hybrid experiments", *Artificial Life and Robotics*, 2018

[8] T. Levi, F. Khoyratee, S. Saighi, Y. Ikeuchi, "Digital implementation of Hodgkin–Huxley neuron model for neurological diseases studies", *Artificial Life and Robotics*, Artificial Life and Robotics 23 (1), 10-14, 2018

[9] M. Ambroise et al., Biomimetic neural network for modifying biological dynamics during hybrid experiments, Journal on Artificial Life and Robotics, 22:3, 398-403, September 2017

Trajectory Tracking Control for a 7-Arms Robot Manipulator

Wang Jie
Department of Mechanical Engineering, Pusan National University,

Hyun-Hee Kim, Saad abbasi and Min-Cheol Lee*
School of Mechanical Engineering, Pusan National University,
*635-4Jangjeon 2 dong, Geumjeong-gu, Busan, 609-735,South Korea**
E-mail: wj@pusan.ac.kr, saadjamshed93@gmail.com,mclee@pusan.ac.kr
me.pusan.ac.kr

Abstract

This paper proposes a trajectory tracking control method based SPO (sliding perturbation observer) for a 7-arms robot manipulator. The 7-arms robot manipulator is designed to assemble small parts or packaging in industrial manufacturing. System dynamics modeling is introduced at first. The dynamics of this 7-arms robot is difficult to determine precisely caused by its uncertainties and many nonlinear terms through mathematical analysis. An experimental identification process using signal compression method is applied to divide the linear term from integrated dynamics with non-linear terms and uncertainties. Estimation of the non-linear terms and uncertainties for compensating the real dynamics is obtained by SPO. Controller sliding mode control is designed based on estimation perturbation.

Keywords: manipulator, robust controller, sliding mode control, perturbation observer.

1. Introduction

Multi-axis robot arm are wildly used for industrial area, such as parts assembly, automatic welding in vehicle manufacturing, pre-arrangement etc. Usually, those kinds of robots are requested for an accurate trajectory tracking. However, caused by those multi-axis arms the traditional controller without consideration of dynamics such as PID is not proper. Many robust controllers based on system dynamics model are designed with robust performance. In [1], a linear control logic LQR is combined with PID to control a flexible manipulator. Sliding mode control (SMC) is the most used one. The designed nonlinear control input which restrains the error states within sliding surface that ensures an outstanding performance for a nonlinear system. In [2], a robust controller SMC based SMCSPO is designed to control a hydraulic manipulator with showing an excellent performance in tracking. Before designing and applying the above mentioned controllers, system dynamics is necessary modeled at first. In this research, a 7 arms manipulator is designed to simulate the assembling work which mainly focus on trajectory tracking. The dynamics of this manipulator is modeled using signal compression method [3]. Signal compression method uses an equivalent impulse signal which is obtained from an similar impulse signal filtering by a time delay filter, then given as a tracking reference to the object system. This identification process is introduced at first in this paper. However, as same as mostly used identification method, signal compression method only estimates the divided linear terms without any reflection from nonlinear terms in original system dynamics. Therefore, compensation for the nonlinear terms and uncertainties which are not identified is necessary. Kalman fiter can estimate uncertainties which is well known caused by its high accuracy in low frequency area [4]. SPO has the similar algorithm with kalman fiter, but derived from state space, which also has outstanding estimation performance in low frequency area [5]. In this paper, we use the SPO to observe the perturbation which contains the nonlinear terms in dynamics, identification errors, uncertainties and disturbance. The estimated perturbation is used for designing a robust controller such as sliding mode control. This paper is organized as following: signal compression method for system modeling is introduced in section 2, the perturbation design is shown in section 3, we conclude this work in section 4.

2. Dynamics Modeling

Signal compression method is used for dynamics identification. In this method, an equivalent impulse signal is generated to implement on an objective system as the desired trajectory. The equivalent impulse signal is obtained by passing a time delay filter from a designed impulse signal. The expanded impulse signal is available to apply on the real system. Then, the response output is filtered by the inverse of the time delay filter. The result after the inverse time delay filter is supposed as the real response which is from the origin impulse signal to the linear system. The system can be modeled when we change the model dynamics to match the correlation with the output signal from real experiment. This logic is shown in figure. 1.

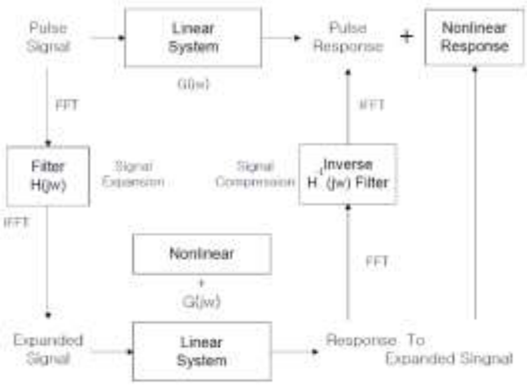

Fig. 1. Signal Compression Method Logic.

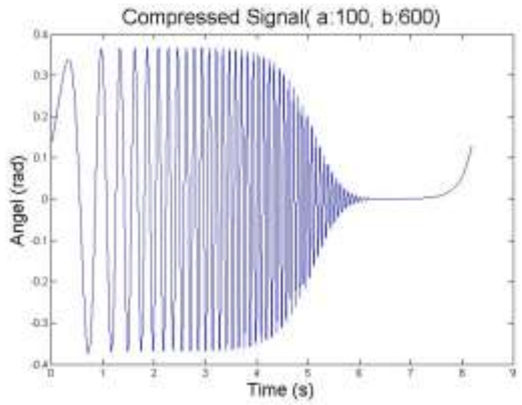

Fig. 2. Expanded Impulse Signal.

The expanded signal is shown in figure.2. It obtained from the designed impulse signal in Eq.(1) passed by an time delay filter with following function in Eq.(2):

$$
\begin{aligned}
&P(n) = 60\exp[-(\frac{n}{a})^{12}],\ 0 \le n \le N/2-1 \\
&P(n) = 0,\ n = N/2 \qquad\qquad (1) \\
&P(n) = P(N-n),\ N/2+1 \le n \le N-1
\end{aligned}
$$

$$
\begin{aligned}
&H(n) = \exp[-\frac{12n^2}{b}j],\ 0 \le n \le N/2-1 \\
&H(n) = 0,\ n = N/2 \qquad\qquad (2) \\
&H(n) = H(N-n),\ N/2+1 \le n \le N-1
\end{aligned}
$$

The robot manipulator are shown in figure.3. The experiment of signal compression method is accomplished with an simple P controller (Kp=10) which logic is shown in figure(4).

Fig. 3. Real System .

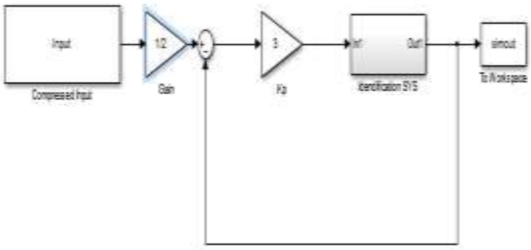

Fig. 4. Expanded Impulse Signals.

The output from compression signal of link7 is shown in Fig .5. In Fig . 6, the result of real system output passed by the invers filter of Eq. (2) and model result with same process are shown. All links modeling result are shown in Table.1 with the assumption of their dynamics are a simple 2 order linear system.

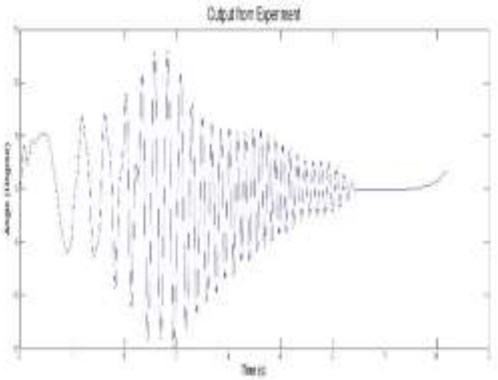

Fig. 5. Real System Response(link7).

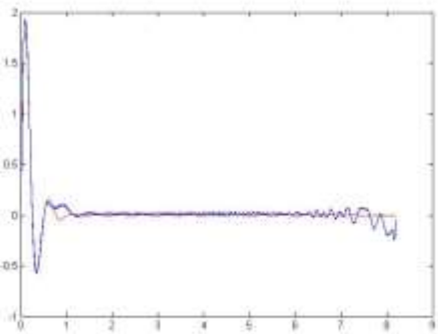

Fig. 6. Correlation of Real System Response with Modeled System Response Result(link 7).

Table 1. Result of Medeling

	ζ	ω_n	2nd order.Model
1	0.642	6.864	$\frac{4.711}{s^2-8.813s}$
2	1.521	2.937	$\frac{0.8626}{s^2-8.934s}$
3	0.324	7.628	$\frac{5.819}{s^2-4.943s}$
4	0.61	5.521	$\frac{3.048}{s^2+6.736s}$
5	0.346	12.469	$\frac{15.55}{s^2+8.629s}$
6	0.37	13.21	$\frac{17.45}{s^2+9.776s}$
7	0.35	12.502	$\frac{15.63}{s^2+8.751s}$

3. Controller

In this section, we define the perturbation in a mathematic equation. Before defining perturbation, the dynamics of a general robot system is normally defined as

$$\ddot{x}_j = f_j(\mathbf{x}) + \Delta f_j(\mathbf{x}) + \sum_{i=1}^{n} [(b_{ji}(\mathbf{x}) + \Delta b_{ji}(\mathbf{x}))u_i] + d_j(t)$$
$$j = 1, \ldots, n. \tag{3}$$

where $\mathbf{x} \overset{\Delta}{=} [\mathbf{X}_1 \ldots \mathbf{X}_n]^{\mathrm{T}}$ is the state vector and $\mathbf{X}_j \overset{\Delta}{=} [x_j, \dot{x}_j]^{\mathrm{T}}$. The terms $f_j(\mathbf{x})$ correspond to linear driving terms while $\Delta f_j(\mathbf{x})$ corresponds to the nonlinear driving terms, their parameters, dynamic modeling, and dynamic uncertainties. The components b_{ji} and Δb_{ji} represent the elements of the control gain matrix and their uncertainties, while d_j is the external disturbance and u_j is the control input. It is assumed that the terms f_j and b_{ji} can be obtained after system identification. Perturbation is introduced simply in the introduction that contain the nonlinear terms in dynamics, identification errors, uncertainties and disturbance as shown in Eq. (4).

$$\Psi_j(\mathbf{x}, t) = \Delta f_j(\mathbf{x}) + \sum_{i=1}^{n} [\Delta b_{ji}(\mathbf{x}) u_i] + d_j(t). \tag{4}$$

The observer contains states are shown in Eq. (5).

$$\begin{aligned}
\dot{\hat{x}}_{1j} &= \hat{x}_{2j} - k_{1j}\,\mathrm{sat}(\tilde{x}_{1j}),\\
\dot{\hat{x}}_{2j} &= \alpha_3 \bar{u}_j - k_{2j}\,\mathrm{sat}(\tilde{x}_{1j}) + \hat{\Psi}_j,\\
\dot{\hat{x}}_{3j} &= \alpha_{3j}^2 (\bar{u}_j + \alpha_{3j}\hat{x}_{2j} - \hat{x}_{3j}),\\
\hat{\psi}_j &= \alpha_{3j}(\alpha_3 \hat{x}_{2j} - \hat{x}_{3j}).
\end{aligned} \tag{5}$$

The stability of SPO is proved in [6]. The perturbation estimation is used to design a robust controller. In here, we use sliding mode control with its combination of SPO.

4. Experiment and Conclusion

The experiment is designed for trajectory tracking on the Windows based RTX software (real time operating system). The application interface is made from MFC API and shown in Fig. 7. It also can plot the movement of link 7.

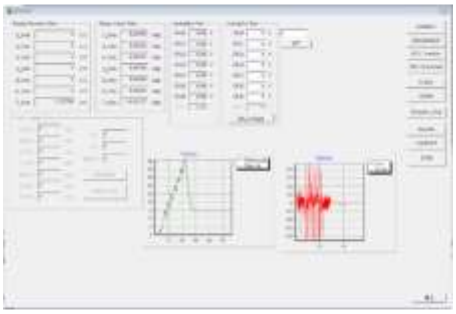

Fig. 7. Real Time Tracking Result Using SMCSPO for link 7.

In Fig. 8, the reference trajectory of link 2 with blue line and real trajectory with red line are presented. The error between them is shown in Fig. 9.

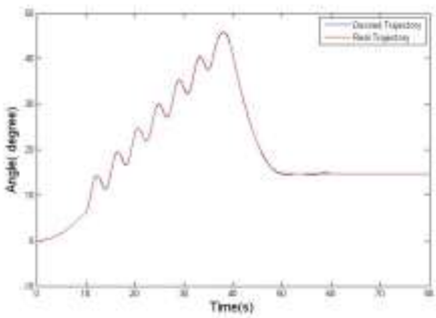

Fig. 8. Tracking Result Using SMCSPO of link 2.

The tracking error shows within the limit about 0.3 degree. It verifies the sliding mode control with proposed perturbation estimation has outstanding performance fora multi-arm robot which dynamics is obtained by signal compression method approximately.

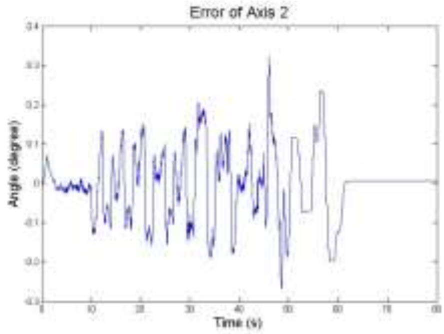

Fig. 9. Error in Tracking Result of link 2.

Acknowledgments

This research was supported by the MOTIE (Ministry of Trade, Industry & Energy), Korea, under the Industry Convergence Liaison Robotics Creative Graduates Education Program supervised by the KIAT (N0001126) and the National Research Foundation of Korea (NRF) grant funded by the Korea Government (MSIP) (No.NRF-2012M2B2B 1055503).

References

1. Yun, Yuan, and Yangmin Li. "Active vibration control based on a 3-DOF dual compliant parallel robot using LQR algorithm." *Intelligent Robots and Systems*, 2009. IROS 2009. *IEEE/RSJ International Conference on. IEEE*, 2009.
2. Wang, Jie, Karam Dad, and Min Cheol Lee. "Bilateral Control of Hydraulic Servo System Based on SMCSPO for 1DOF Master Slave Manipulator." *alife-robotics*, (2017), *International Conference on Artificial Life and Robotics*.
3. Lee, Min Cheol, and Nobuharu Aoshima. "Identification and its evaluation of the system with a nonlinear element by signal compression method." *Transactions of the Society of Instrument and Control Engineers* 25.7 (1989): 729-736.
4. Wan, Eric A., and Rudolph Van Der Merwe. "The unscented Kalman filter for nonlinear estimation." *Adaptive Systems for Signal Processing, Communications, and Control Symposium 2000. AS-SPCC*. The IEEE 2000. Ieee, 2000..
5. Lee, Min Cheol, et al. "Reaction force estimation of surgical robot instrument using perturbation observer with SMCSPO algorithm." *Advanced Intelligent Mechatronics (AIM)*, 2010 IEEE/ASME International Conference on. IEEE, 2010.
6. Jie, Wang, Karam Dad, and Min-Cheol Lee. "SMCSPO based force estimation for a hydraulic cylinder." *Control, Automation and Systems (ICCAS)*, 2017 *17th International Conference on*. IEEE, 2017.

Estimation tire-rod friction coefficient based on mobile robot

Ji- Hyeon Kim
Dep. of Electronic Eng., Pusan National University, 2,Busandaehak-ro 63beon-gil Geumjeong-gu Busan, 46241, Republic of Korea

Zhang Hongyu
Dep. of Electronic Eng., Pusan National University, 2,Busandaehak-ro 63beon-gil Geumjeong-gu Busan, 46241, Republic of Korea

Jang-myoung Lee
Dep. of Electronic Eng., Pusan National University, 2,Busandaehak-ro 63beon-gil Geumjeong-gu Busan, 46241, Republic of Korea

E-mail : jihyeon1696@pusan.ac.kr, zhanghy0218@pusan.ac.kr, jmlee@pusan.ac.kr

www.pusan.ac.kr

Abstract

It is very important to estimate the friction coefficient of tire-road for vehicle dynamic control system. For the current dynamic control research, a large amount of experimental data is needed. The theoretical tire model is used to estimate the friction coefficient based on the Gim tire model to improve the tire experience model. Simulation by MATLAB, the simulation results show that the Gim tire model has high precision and can predict the mechanical properties of the tire well.

Keywords: simulation, dynamic control, Gim tire, frcition

1. Introduction

Logistics robots are growing in non-manufactured environments due to the surge in online shopping. Shipping robots, which are robots that deliver goods to customers indoors or within five kilometers of the city, are growing exponentially. Among the major technologies related to logistics robots such as hardware, driving, awareness and operation, we are going to study stability of driving when transporting goods.

We studied how safe it was to be off the road depending on the various conditions in the city center. As the interface between the vehicle and the road, the tire shape in different driving environments makes different characters dynamic response in the vehicle. It is important information for safe driving and dynamic control of tire force, but they are limited by the friction coefficient [1], and the tire model is roughly. It can be divided into three types: empirical model, semi-empirical model and theoretical model.[2,3] The empirical model has a high amount of access to specific tires for semi-empirical models, but often requires a large amount of experimental data, so the versatility is low, the cost is high, and it brings great It is inconvenient to have a widely accepted model of the Magic Formula proposed by pacejka and a semi-empirical model of uniform tires describing the 6-component force characteristics of tires proposed by Academician Guo Konghui[4]. The theoretical model is to establish the relationship between the tire force and the parameters through the mathematical description of the mechanical properties of the tire. The most representative pure theoretical model is the Gim tire model. The tire has a simple formula and does not require data fitting. And the characteristics of the tire force can be used to quickly and easily obtain the friction coefficient of the tire.

2. Gim tire model

The Gim tire model is based on the concept of an "interacting spring", which itself is considered to be a series of three-dimensional elastic elements that transmit forces in the radial, transverse, and longitudinal directions, each of which has three 3D elastic elements. The contact area between the tire and the ground, which is orthogonal to the center axis, interacts with each other, can be assumed to be a rectangular area. [5,6]The relationship between the length l of the grounding wire and the free radius r of the wheel and the radial deformation δ is

$$r^2 = \left(\frac{1}{2}\right)^2 + (r-\delta)^2 \tag{1}$$

Because r >> δ , so

$$l = \sqrt{8r\delta} \tag{2}$$

2.1 Simulation Implementation of Gim Tire Model

Regardless of the tire roll angle, depending on the longitudinal and lateral forces of the tire, there are two forms of braking and driving, respectively, which defines the longitudinal slip ratio as

$$S_X = \frac{V_X - V_C}{V_X} > 0 \text{ (Braking situation)} \tag{3}$$

$$S_s = \frac{V_X - V_C}{V_X} < 0 \text{ (Drive situation)} \tag{4}$$

Where: Vc is the circumferential speed of the tire; Vx is the longitudinal speed of the wheel.
Define the lateral slip ratio as

$$S_a = (1-|S_s|)|\tan a| \text{ (Braking situation)} \tag{5}$$

$$S_a = |\tan a| \tag{6}$$

Where: α is the wheel side angle, α = arctan(VY /VX);VY is the lateral speed of the wheel.

2.2 Model force characteristics under the combined action of longitudinal force and lateral force

The tire-ground adhesion coefficient is related to the slip rate of the tire surface relative to the ground. If the combined effect of longitudinal and lateral forces is taken into account, the integrated adhesion coefficient of the wheel is defined as

$$\mu = \mu_0(1 - As_{sa}) \tag{7}$$

Where: u0 is the static friction coefficient of the tire and the road surface.
A is the adhesion coefficient reduction factor $A=(1-\mu_1/\mu_0)/s_1;s_{sa}$ Synthetic slip rate to reflect the longitudinal slip and lateral offset of the tire, $s_{sa} = \sqrt{s_s^2 + s_a^2}$, The two-point friction coefficient (0, μ0) and (s1, μ1) obtained by the test ,Synthetic slip ratio.

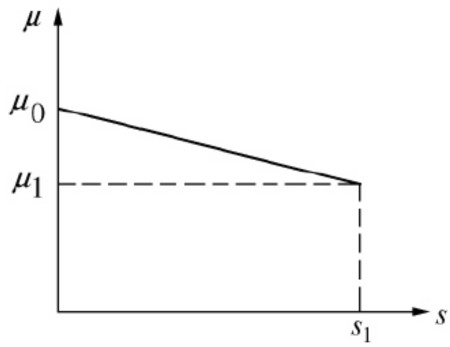

Fig. 1. Synthetic slip ratio

At the same time, considering the combined action of the longitudinal force and the lateral force, the synthetic adhesion coefficient μ can be decomposed into the longitudinal adhesion coefficient μ_x and the lateral adhesion coefficient μ_y corresponding to the longitudinal force and the lateral force using the friction circle concept. From the concept of friction circle, we know

$$\left(\frac{\mu_x}{\mu}\right)^2 + \left(\frac{\mu_y}{\mu}\right)^2 = 1 \tag{8}$$

Then the longitudinal adhesion coefficient of the wheel is

$$\mu_x = \left(\frac{\mu s_s}{s_{sa}} \right) = \mu \cos \beta \quad (9)$$

The lateral adhesion coefficient of the wheel is

$$\mu_y = \left(\frac{\mu s_a}{s_{sa}} \right) = \mu \sin \beta \quad (10)$$

Where: β is the slip direction angle and is a function of the longitudinal slip ratio s_s and the lateral slip ratio s_a.
Contact area rolling-sliding critical point is

$$s_n = \frac{1}{3\mu F_Z} \sqrt{(C_S s_s)^2 + (C_a s_a)^2} \quad (11)$$

Longitudinal critical slip rate of elastic deformation of tire

$$s_{sc} = \frac{3\mu F_Z}{C_S} \quad (12)$$

Tire lateral critical slip ratio

$$s_{sa} = \frac{C_S}{C_a} \sqrt{s_{sc}{}^2 + s_s{}^2} \quad (13)$$

Where: F_Z is the wheel normal load; C_S , C_a are the longitudinal and lateral (lateral) stiffness of the tire.
Defined $l_n = l - s_n, l_n$ as the dimensionless value of the tire grounding wire length, regardless of the tire returning moment characteristics, the longitudinal force between the tire and the road surface is

$$F_x = C_S s_S l_n{}^2 + \mu_x F_z (1 - 3l_n{}^2 + 2l_n{}^3)(s_s < s_{sc}) \quad (14)$$

$$F_x = \mu_y F_z (s_a \geq s_{sc}) \quad (15)$$

3. Simulation Implementation of Gim Tire Model

Simulink is an important component of MATLAB. It provides a dynamic system modeling, simulation and comprehensive analysis integration environment, which is widely used in the dynamic simulation and design of complex simulation and design of control systems.
In the establishment of the Gim tire model, the tire model is divided into four modules, namely four different subsystems, namely the slip rate subsystem, the critical slip rate subsystem, the road adhesion coefficient subsystem, and the tire force system, the total system input, the wheel angular velocity w, and the wheel linear velocity v, the tire side yaw angle, and the vertical load, and the system output is the longitudinal and lateral ground friction of the tire.

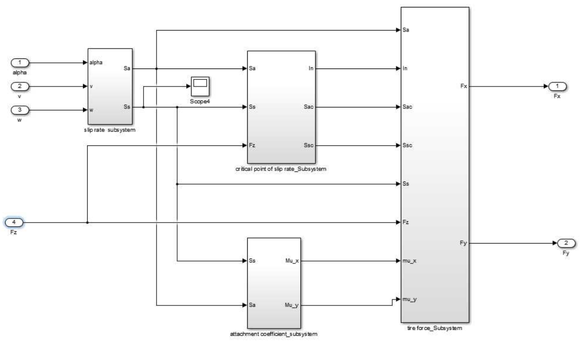

Fig. 2. Gim tire model Simulink block

3.1 Slip rate subsystem

Vehicles on the road have brake and drive two patterns, and both of the calculation of the slip rate varied, therefore need to use the tire rolling radius R, and the input of the wheel speed v, and the angular velocity w logic judgment, the system uses two switch modules, to determine the wheel in driving or braking mode, and then the slip rate is calculated using the corresponding formula.

3.2 The critical slip rate subsystem

The longitudinal and lateral friction coefficients of tires are determined according to the given road surface comprehensive adhesion coefficient and longitudinal and transverse slip conditions.

3.3 The road adhesion coefficient subsystem

This module is to calculate the tire ground wire length, dimensionless value of tire and the longitudinal critical slip ratio of the elastic deformation and lateral critical slip ratio, the module switching function is used to determine the lateral critical slip ratio, namely when the actual wheel longitudinal slip ratio is greater than its critical point indicates that the wheel is in pure sliding state, means the wheel lateral critical slip ratio of 0.

3.4 The tire force system

The module USES the calculated values to determine the longitudinal and lateral forces of the final tire F_x and F_y .
Because we only care about the change in the coefficient of friction in a straight line, we don't care about the third and fourth part.

4. Model verification and simulation analysis

In order to validate the established model of tire features a description of the precision of this experiment in dry concrete Liu Min (measured 0.8 road surface friction coefficient, μ_0 = 1.14) on tire force characteristics in laboratory test data to validate the theoretical tire model, the experiment of tire in the case of side-slip Angle of 0 to determine the coefficient of friction, you known, the mobile robot in the execution of the longitudinal force to perform the friction, so we only pay attention to the change of the longitudinal coefficient of friction, We carry the data measured by the mobile robot on the actual road into the model for analysis.

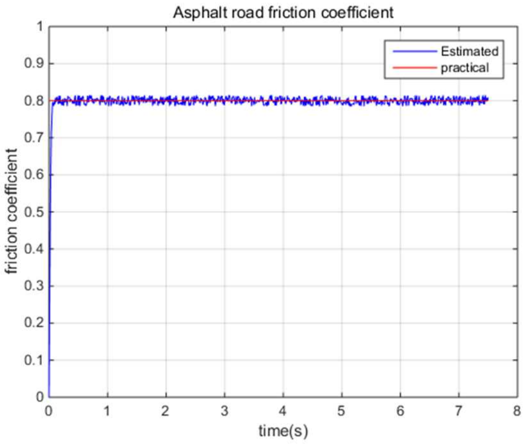

Fig. 3. Asphalt road friction coefficient

From figure 3 estimates with the actual friction coefficient of friction coefficient by contrast, one has good matches, although have certain deviation estimates and actual values, but estimates range is around the actual road friction coefficient, estimate the tendency of the friction coefficient and the actual value is the same, it is verified the model established in this paper, the calculation of the tire force is credible, Gim tire model can effectively predict the tire mechanical characteristics. The possible reason for the data fluctuation is that the mobile robot is light in mass and slow in speed, which is greatly affected by the flatness of the ground.

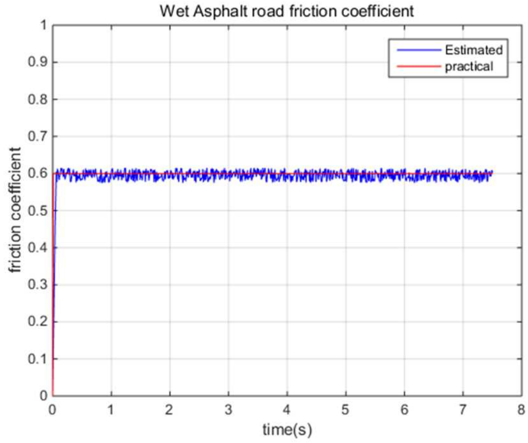

Fig. 4. wet Asphalt road friction coefficient

In the figure above, the friction coefficient of the mobile robot on the wet road surface is compared with the actual value. It can be seen that this model can also measure the friction coefficient well in the wet environment.

5. Conclusion

Tire has a very important role in vehicle dynamics model, is an important part of vehicle dynamic control system, this paper study was conducted based on Simulink simulation, the simulation, compared to the estimated value and actual value of the Gim tire model has good performance ability, in the following study will be in the Segway VDC (vehicle dynamic control system) in the further research

Acknowledgements

This research was funded and conducted under 『the Competency Development Program for Industry Specialists』 of the Korean Ministry of Trade, Industry and Energy (MOTIE), operated by Korea Institute for Advancement of Technology (KIAT). (No. N0001126, HDR program for Industrial convergence/connected for creative robot human resource development)

References

1. Changsun Ahn Huei Peng, H.Eric Tseng. Estimation of Road Friction for Enhanced Active Safety System: Dynamics Approach Proceedings of 2009 American Control ConferencesR. Loren and D. B. Benson (eds.), *Introduction to String Field Theory*, 2nd edn. (Springer-Verlag, New York, 1999).

2. Pacejka H B, Bakker E.Magic formula tyre model [J]. Vehicle systems Dynamics 1993R. Loren and D. B. Benson, Deterministic flow-chart interpretations, *J. Comput. System Sci.* **27**(2) (1983) 400–433.
3. Pacejka H B, Besselink I J M. formula tyre model with transite properties [J]. Vehicle systems Dynamics 1997
4. Guo K H, Lu D, Ren. A unified non-steady non-linear tyre model under complex wheel motion inputs including extreme operating conditions [J]
5. Gim G, Nikravesh P. An analytical model of pneumatic tyres for vehicle dynamics simulations. Part 1[J]. Pure Slips, internationals Journal of Vehicle Design, 1990
6. Gim G, Nikravesh P. An analytical model of pneumatic tyres for vehicle dynamics simulations. Part 1[J]. Comprehensive Slips, internationals Journal of Vehicle Design, 1991

Real-time reflection removal algorithm using stereo camera only

Do-kyung Hwang
Dep. of Electronic Eng., Pusan National University, 2,Busandaehak-ro 63beon-gil Geumjeong-gu Busan, 46241, Republic of Korea

Jong-woo An
Dep. of Electronic Eng., Pusan National University, 2,Busandaehak-ro 63beon-gil Geumjeong-gu Busan, 46241, Republic of Korea

Jang-myoung Lee
Dep. of Electronic Eng., Intelligent Robot Laboratory, 2,Busandaehak-ro 63beon-gil Geumjeong-gu Busan, 46241, Republic of Korea

E-mail: dokyung7379@pusan.ac.kr, jmlee@pusan.ac.kr
www.pusan.ac.kr

Abstract

In this paper, we implemented a light reflection elimination algorithm which is one of the main obstacles of various object recognition systems using vision systems. In other words, this algorithm can be used to remove robotic recognition obstacles from the factory and perform tasks such as locating robots, autonomous vehicles, or unmanned aerial vehicles. This algorithm has been studied with versatility in mind and does not require sensors other than stereo cameras. Algorithm that intuitively interprets pixels in HIS(Hue ,Saturation, Intensity) space and processes pixels corresponding to light. For intuitive analysis, take an angle, intensity, or other light source (sunlight, fluorescent light, candle) from the camera, then record each pixel value and separate it from a white object (whiteboard, paper, etc.). After pixel operation, object recognition is implemented using the CNN(Convolutional Neural Network) method using the YOLO(You Only Look Once)_V2 algorithm[5]

Keywords: Light less, Pixel analysis, Object detection, reflections removal, CNN, YOLO(You Only Look Once).

1. Introduction

One of the big problems in the field of image recognition is the detection problem due to light. In order to solve the problem of light recognition, researches on shadow removal technique[3], removal of light reflected in water during rain[2], and removal of afterimage using time difference motion in edge channel are being studied. However, it is difficult to apply these studies in an industry where real - time image recognition is required.

For example, removing shadow, removing afterimages using time-lag motion in the edge channel results in elimination of objects (such as a person or a vehicle that should actually be collected) that should not be removed, On the contrary, whe0n the light is removed in the rain, the object is considered more. However, considering the object, the light reflection component itself is not removed much. In this study, considering the marketability, we came to the study with general purpose in mind. This algorithm is divided into two major stages.
First, white objects and light reflection components are distinguished in the HSI channel through pixel analysis, And then processes the distinct Light Pixel components.

2. Pixel analysis

First, the first step is to analyze the pixel values in the HSI channel [1]. In the HSI channel, the RGB values are different depending on the original color, saturation, and brightness. Assuming that the y-axis reference is brightness and the degree of brightness is expressed as 0 ~ 128, RGB color is expressed as shown in Fig.1.

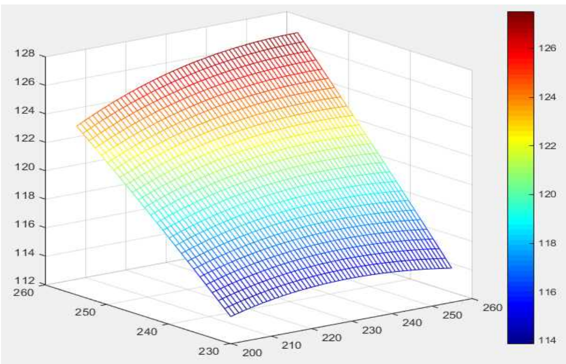

Fig. 1-

In this paper, to derive the supernatural components of light, several angles and various light sources are photographed in the color space as shown in Fig. 1, and the pixel values corresponding to the light are derived.. Then, layers are constructed based on the collected data, and the pixel values extracted by the layer information are processed by 0 to discriminate.
Fig. 2 show the result of light separation in a situation where various objects are placed.

In the case of Fig 2, I took a picture with a ZED stereo camera when the sunlight penetrated strongly through

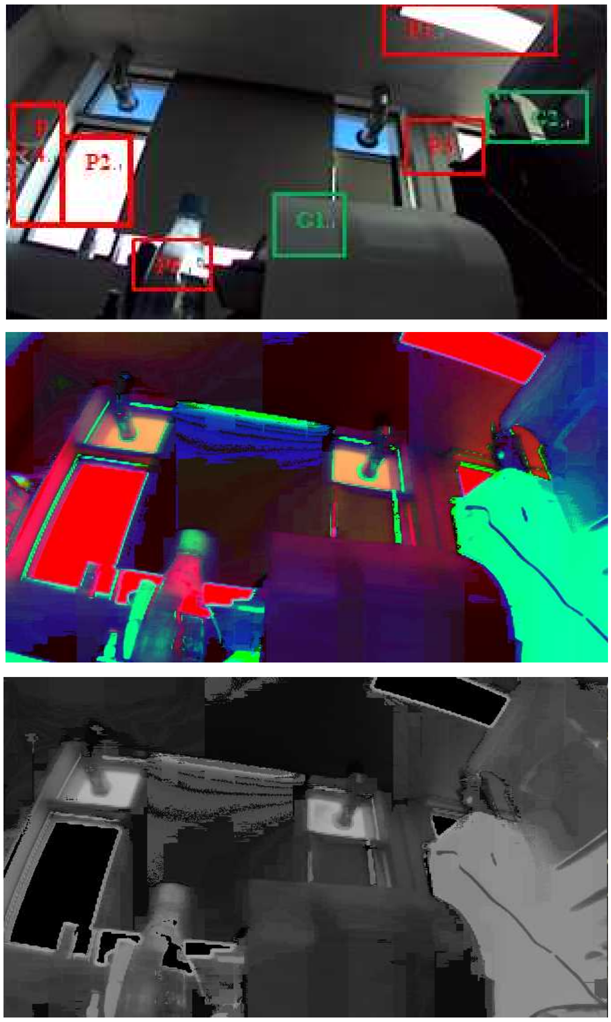

Fig. 2-

the window at 7 o'clock in the morning, and I analyzed various situations in a single photograph by adding a fluorescent light source. In Figure 2, light separates into red boxes and white objects into green boxes..
The meaning of each point is P1, P2 is the light source (fluorescent light, sunlight) P3 Weak sunlight P4 is the weak sunlight on the white wall P5 is the sunlight passing through the plastic water bottle and G1 and G2 are white paper and white glass bottles.

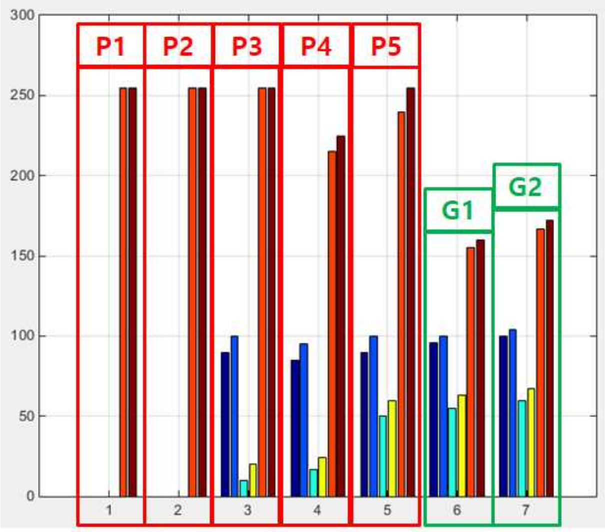

Fig. 3.

Fig. 3 shows the :el values for the example Point in Fig. 2. In the light sources P1 and P2, R channel value is 255, G and B channel value are 0
It is possible to confirm that the R channel value of the light material transmitted through the remaining object is relatively high. On the other hand, G1 and G2, which are white objects, have a relatively low R channel value and relatively high G and B channel values.[4] The method proposed in this paper distinguishes between bright objects and white objects in the same way as the analysis in Fig. 3, and shoots bright objects and white objects with various angles and brightness to construct a large number of Data tables and layers about light

3. Experiment

In order to test the performance of the algorithm, we experimented with the recognition rate by placing an object named H in front of the window in an environment where the window is very sunny at 2:00 pm. For object detection, YOLO_v2 algorithm was used and total 800 pieces of learning data and 500,000 pieces of learning data were used, and in an additional situation, the environment is configured so that the light noise can enter more intensely in the presence of a fluorescent lamp in a relatively bright corridor.

The camera used in the experiment was ZED stereo Cam, Increase the distance to H in the red arrow direction as shown in Fig 4. We collected data about when applying the algorithm presented in this paper and when not applying it.

Words)

Fig. 4.

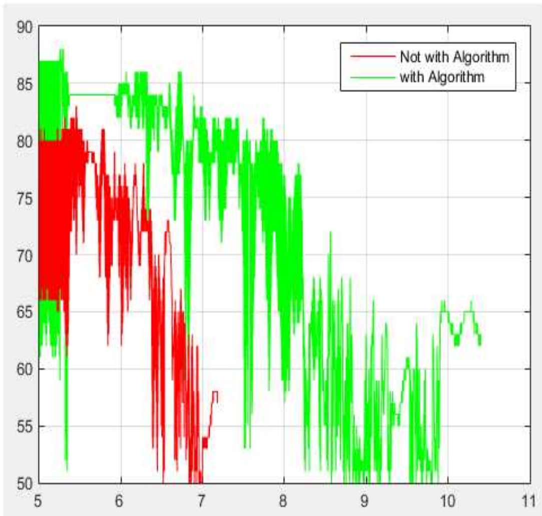

Fig. 5.

The y axis in Fig. 5 is the detection rate for the object, and the x axis is the detection distance.
Fig. 5 shows the difference in detection rate and detection distance when applying the algorithm (green line) and when not applying it (red line).

4. Restore

However, if you treat the Pixel of light as '0', the object may be processed as '0' when there is light on the object. In this case, we present a method for restoring objects using surrounding pixel information and color correction.[1] The basic perimeter Pixel information usage method follows eq. (1).

$$\frac{\sum\left[\sum_{n=x-1}^{x+1}\sum_{m=y-1}^{y+1} p(n,m)\right]}{p(x,y)_{count}} \qquad (1)$$

Fig. 6 below shows a restored object using surrounding pixel information.

Fig. 6

5. Conclusion

Although this algorithm has been studied in consideration of versatility, it is impossible to restore the shape of objects such as small letters due to light. Therefore, robots that perceive that the range of objects is simply limited, or peripheral pixels may be applicable in simple fields. These problems will require more research or results from some media that can block light.

Acknowledgements

This research was funded and conducted under『the Competency Development Program for Industry Specialists』of the Korean Ministry of Trade, Industry and Energy (MOTIE), operated by Korea Institute for Advancement of Technology (KIAT). (No. N0001126, HDR program for Industrial convergence/connected for creative robot human resource development)

This research was financially supported by the Ministry of trade, Industry and Energy (MOTIE), Korea Institute for Advancement of Technology (KIAT) through the Robot Business Belt Development Project (A012000009)

.

References

1. Taeha Um and Wonha Kim, Dehazing in HSI Color Space with Color Correction (*JBE* Vol. 18, No. 2, March 2013) pp. 85–104
2. Sang-Woong Lee, Removing Lighting Reflection under Dark and Rainy Environments based on Stereoscopic Vision (*Journal of KIISE* Vol. 37, No. 2, February, 2010) pp. 104–107
3. Byeong-Ju Han and Jae-young Sim, Single image based shadow removal algorithm (*IPIU* 2015 Vol. 27 February, 2015)
4. Bong-hwa Song and Hyung-Je Cho, *Vehicle Recognition in the Forward Direction and the Trace of Movements for Collision Prediction* (Institute of Image Culture and Content in Dongguk University 2008 Vol.1 2018) pp.101–114
5. Joseph Redmon, Santosh Divvala, Ross Girshick and Ali Farhadi, You Only Look Once: *Unified, Real-Time Object Detection*

The Effect of Inertial Measurement Unit on Synthetic Aperture Radar Image Quality

Soojeong Lee[1], Yong-gonjong Park[1], Woo Jung Park[1], Chan Gook Park[1], Jong-Hwa Song[2] and Chang-Sik Bae[2]

[1]Department of Mechanical & Aerospace Engineering/Automation and Systems Research Institute, Seoul National University, 1 Gwanak-ro, Gwanak-gu, Seoul 08826, Republic of Korea

[2]Hanwha Systems, 491-23 Gyeonggidong-ro, Namsa-myeon, Cheoin-gu, Yongin-si, Gyeonggi-do 17121, Republic of Korea

Abstract

This paper analyzes the effect of inertial measurement unit (IMU) on synthetic aperture radar (SAR) image quality. While operating SAR, it is supposed that an aircraft flies straight and level at a constant speed. Because of atmospheric turbulence and aircraft maneuvers, it deviates from its nominal trajectory. With navigation solutions, the deviations can be compensated through motion compensation procedure. However, uncompensated motion errors generated by IMU errors degrade SAR image quality, such as broadening bandwidth and blurring the image. Since the residual errors depend on the degree of IMU inaccuracies, SAR images and impulse response function (IRF) according to IMU grades are compared with each other. Through this result, the IMU specification is suggested to satisfy given SAR image quality.

Keywords: synthetic aperture radar (SAR), inertial measurement unit (IMU), SAR image quality, impulse response function (IRF)

1. Introduction

Synthetic aperture radar (SAR) is a radar system providing high resolution images by synthesizing the received radar signals. During SAR operation, the aircraft is supposed to fly straight and level at a constant speed. While moving, it transmits and at the same time collects received signals through the whole time, called as synthetic aperture time (SAT). By post-processing such as range Doppler algorithm (RDA), the collected signals are synthesized to make the phases coherent.[1, 2] Because of this step, SAR antenna can get the same effect as using longer antenna, meaning the higher resolution. However, it is impossible for an aircraft to fly the nominal trajectory because of atmospheric turbulence and aircraft maneuvers. Therefore, before image formation the deviations should be measured and compensated. With measured navigation solutions, motion compensation (MOCO) such as pulse repetition frequency (PRF) control and range shift compensates the deviations, resulting in better image quality than without MOCO.[3] However, due to inertial measurement unit (IMU) errors the difference between actual position and measured one is generated. This, uncompensated motion errors degrade SAR image quality, for example, broadening bandwidth and blurring the image.[4, 5]

MOCO such as PRF control is known to be essential before SAR image processing to improve SAR image quality. Therefore, researches about MOCO are widely done.[3, 6, 7] At the same time, the uncompensated motion error is concerned.[4, 8–11] Especially, the effect according to the error term such as constant, linear, quadratic and cubic terms are studied.[4, 9–11]

Since residual errors depend on the degree of IMU inaccuracies,[8] in this paper SAR images and impulse response function (IRF) according to IMU grades are compared to each other. Through this result, the IMU specification is suggested to satisfy given SAR image quality.

This paper is organized as follows. Section 2 explains the navigation method before SAR operation and the relationship between phase error and position error. Section 3 provides the specific values of IMU specifications used in the simulation and compare the resultant images and IRF according to IMU grades. Section 4 concludes the paper and suggests the IMU specification to satisfy given SAR image quality.

2. Residual Errors by IMU Inaccuracies

In this section, the navigation algorithms during simulation and the relationship between phase error and position error are explained.

2.1. *EGI/IMU integrated navigation algorithm*

Because of the aircraft structure, the SAR antenna and the global positioning system (GPS) receiver cannot be mounted in the same position. IMU which is mounted with the GPS receiver on the center of gravity is designated as IMU 1. The other IMU mounted on the SAR antenna is designated as IMU 2. During SAR operation, to compare SAR image quality according to IMU inaccuracies, only inertial navigation system (INS) with IMU 2 is performed. Before SAT, to estimate the bias of accelerometer and gyroscope of IMU 2, EGI/IMU integrated navigation algorithm is applied. EGI/IMU integrated navigation is as follows: embedded GPS/INS (EGI) system is implemented with IMU 1. The navigation solution from EGI system is considered as GPS data in EGI/IMU integrated navigation algorithm. Then, another EGI system is performed with IMU 2 and the previous EGI data. However, since the IMU 2 is mounted in the other position, at the measurement update in EGI/IMU integrated system, the lever arm effect should be considered.[5] Through this system, the bias of accelerometer and gyroscope of IMU 2 can be estimated before operating SAT, resulting in the reduced residual errors.

2.2. *Position error equation with initial errors*

Phase error of the received signal causes the degradation of SAR image, such as defocusing. Therefore, if the relationship between phase error and position error is clarified, the effect of IMU inaccuracies on SAR image quality can also be clarified. To obtain expression for that, several steps are carried out as below.

First, the relationship between the phase error and the range error is widely known as Eq. (1). Since the range error here is motion error in range direction, it does not stand for the position error commonly mentioned. As in Ref. 5, the range error can be expressed as Eq. (2).

$$\phi = -\frac{4\pi}{\lambda}\Delta R \tag{1}$$

$$\Delta R = -\mathbf{\Delta p}\cdot\boldsymbol{\eta}_{\mathbf{LOS}} \tag{2}$$

The error contributions in short term according to error sources are summarized in Table 1, sorted into error type.[12] Then, the position error can be derived as Eq. (3). Because in short term, quadratic error term is dominant, Eq. (3) can be simplified as Eq. (4). Lastly, Eq. (5) is derived from Eq. (1), (2), (4) to represent the relationship between phase error and IMU errors.

$$\begin{aligned}\Delta p_N = \Bigg\{&\left(\delta p_N\right)^2 + \left(\delta v_N t\right)^2 + \left(\frac{1}{2}g\varphi_N t^2\right)^2 \\ &+\left(\frac{1}{2}\nabla_N t^2\right)^2 + \left(\frac{1}{6}g\rho_E\varphi_D t^3\right)^2 + \left(\frac{1}{6}g\varepsilon_N t^3\right)^2\Bigg\}^{\frac{1}{2}}\end{aligned} \tag{3}$$

$$\Delta p_N \approx \frac{1}{2}\sqrt{\left(g\varphi_N\right)^2 + \nabla_N{}^2}\, t^2 \tag{4}$$

$$\phi = \frac{4\pi}{\lambda}\times\left[\left(\eta_1+\eta_2+\eta_3\right)\times\frac{1}{2}\sqrt{\left(g\varphi_N\right)^2+\nabla_N{}^2}\, t^2\right] \tag{5}$$

where ϕ is phase error, λ is wavelength, ΔR is range error, $\mathbf{\Delta p}$ is position error vector, $\boldsymbol{\eta}_{\mathbf{LOS}}$ is line-of-sight unit vector, and $\eta_1, \eta_2, \eta_3, p_N, p_E, p_D$ are elements of vector $\boldsymbol{\eta}_{\mathbf{LOS}}$, $\mathbf{\Delta p}$ respectively. t is time, g is gravitation constant, and ρ_E is Earth rotation rate. δp_N is initial position error, δv_N is initial velocity error, φ_N

Table 1. Position error due to each error source of navigation

Error type	Error source	Position error value
Constant	Initial position error	δp_N
Linear	Initial velocity error	$\delta v_N t$
Quadratic	Initial tilt, Accelerometer bias	$\frac{1}{2}g\varphi_N t^2$, $\frac{1}{2}\nabla_N t^2$
Cubic	Initial azimuth error, Gyroscope bias	$\frac{1}{6}g\rho_E\varphi_D t^3$, $\frac{1}{6}g\varepsilon_N t^3$

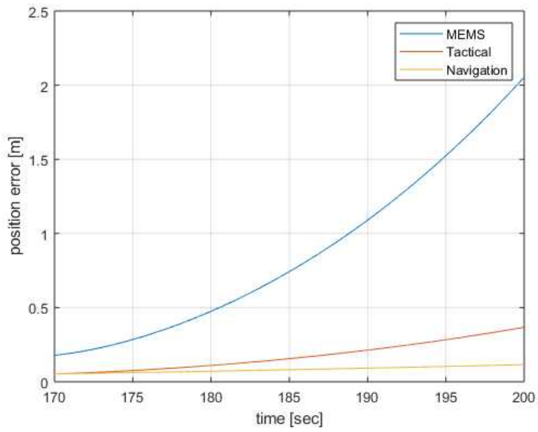

Fig. 1. Position error during SAR operation

is initial tilt, ∇_N is accelerometer bias, φ_D is initial azimuth error, and ε_N is gyroscope bias.

3. Simulation

To compare the effect of IMU on SAR image quality, simulations are performed. In this section, simulation conditions, the chosen IMUs specification and results are described. 30 cm resolution and peak sidelobe ratio (PSLR) are chosen as the requirements of SAR image quality.

3.1. *Simulation conditions*

The simulation is implemented for 200 seconds in 200 m/s at an altitude of 7,600 m and during the last 30 seconds SAR is operated. The sampling frequency of GPS is 1 Hz and IMU 1, IMU 2 are 200 Hz, respectively. GPS with 10 cm white Gaussian noise is used. IMU 1 in the same position as GPS receiver has 10 μg accelerometer bias and 0.005 deg/hr gyroscope bias. 50 Monte Carlo simulations are implemented. For image formation, spotlight SAR mode is chosen and the PRF is 4,000 Hz.

Table 2. IMU on SAR antenna specifications

IMU 2	Accelerometer		Gyroscope	
	Bias [μg]	*Velocity random walk [μg]*	*Bias [deg/hr]*	*Angular random walk [deg/√hr]*
ADIS 16460	200	20	8	0.12
ADIS 16488A	70	7	5.1	0.26
HG 9900	25	2.5	0.003	0.002

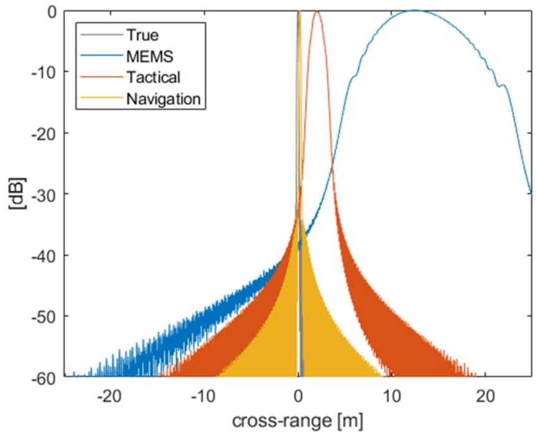

Fig. 2. Impulse Response Function

3.2. *IMU specifications*

To compare the effects of IMU inaccuracies, different grades of IMU are selected: microelectromechanical systems (MEMS) grade IMU, tactical grade IMU and navigation grade IMU. For each grade of IMU, ADIS 16460, ADIS 16488A, HG 9900 are selected to obtain specific values of IMU specifications and they are listed in Table 2. Fig. 1 shows the position error during SAR operation according to IMU.

3.3. *Resultant images and IRF*

By point target simulation, spotlight SAR is implemented. Fig. 2 shows IRF according to IMU grades. IRF with MEMS grade IMU is distorted and broadened much more than tactical and navigation grade IMU. IRF with tactical grade is asymmetric and shifts from true value. IRF with

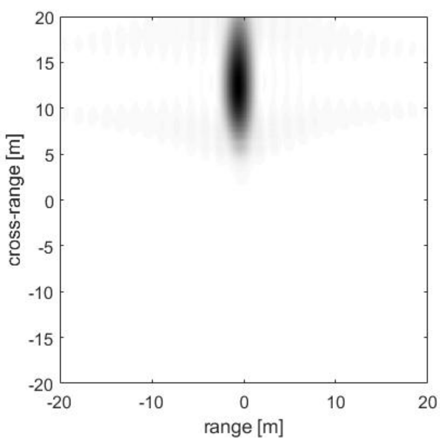

Fig. 3. SAR image with MEMS grade IMU

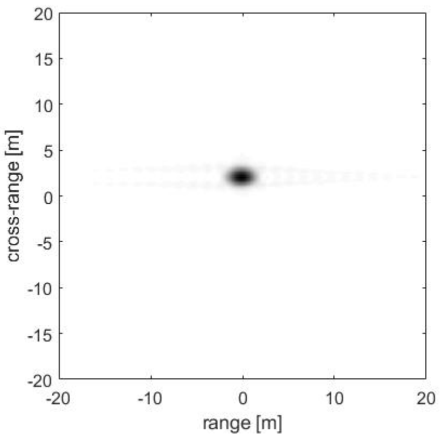

Fig. 4. SAR image with tactical grade IMU

navigation grade shifts less than IRF with tactical grade, but it also has asymmetric sidelobe. Figs. 3–5 show resultant SAR images. As expected with IRF results and Table 3, Fig. 3 is defocused and broadened much as compared to Figs. 4, 5.

4. Conclusion

In this paper, the effects on SAR image quality according to IMU grades are compared. To satisfy the given SAR image quality requirements with pure navigation, navigation grade IMU is recommended. If tactical grade IMU should be used, then auxiliary sensor has to be added to improve the image quality. In future work, to satisfy the given SAR image quality with only tactical grade IMU, the effect of autofocus on alleviating quadratic and cubic term errors will be considered.

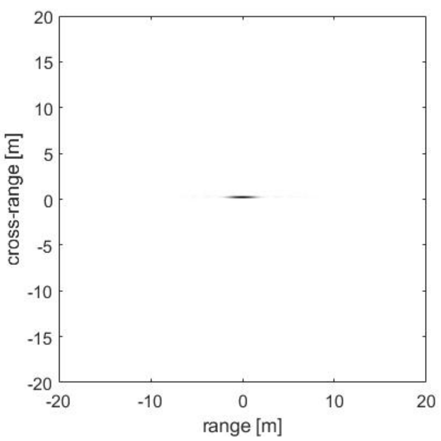

Fig. 5. SAR image with navigation grade IMU

Table 3. SAR image quality

IMU Grade	Resolution [cm]	PSLR [dB]
MEMS	815	-12.14
Tactical	110	-23.51
Navigation	14	-28.71

Acknowledgements

This work was supported by a grant-in-aid of HANWHA SYSTEMS (Project number 0418-20180054).

References

1. A. Moreira, P. Prats-Iraola, M. Younis, G. Krieger, I. Hajnsek, and K. P. Papathanassiou, A tutorial on synthetic aperture radar (*IEEE Geoscience and Remote Sensing Magazine, 2013*), pp. 6–43.
2. M. Elhefnawy and W. Ismail, *Fundamentals of synthetic aperture radar systems* (*International Journal of Emerging Technology and Advanced Engineering*, vol. 5, 2015), pp. 172–178.
3. G. E. Haslam and A. Damini, Specifying the allowable latencies in the application of SAR motion corrections (*Proc. EUSAR '96, European Conf. on Synthetic aperture radar, Koenigwinter, Germany,* 1996), pp. 26–28.
4. S. Buckreuss, Motion errors in an airborne synthetic aperture radar system (*European Transactions on Telecommunications*, vol. 2, 1991), pp.655–664.
5. A. Kusk, J. Dall, and E. L. Christensen, *Estimating sensor motion in airborne SAR* (Ph.D. Thesis, Technical University of Denmark, 2006).
6. E. Zaugg and D. Long, *Generalized SAR processing and motion compensation* (2008).
7. D. H. Kim, S. H. Park, and K. T. Kim, SAR motion compensation using GPS/IMU (*The Journal of Korean Institute of Electromagnetic Engineering and Science*, vol. 22, 2011), pp. 16–23.
8. E. P. Velikanova, A. A. Geltser, Z. T. Erdyneev, and N. V. Panokin, Analysis of accuracy requirements for an inertial navigation system in synthetic aperture radars (*Gyroscopy and Navigation*, vol. 8, 2017), pp. 129–135.
9. Y. Mao, M. Xiang, L. Wei, and S. Han, The effect of IMU inaccuracies on airborne SAR imaging (*Journal of Electronics* (China), vol. 28, 2011), pp. 409–418.
10. G. E. Haslam and B. Reid, Motion sensing requirements for synthetic aperture radar (*IEEE Proc. vol. 1, 1983*), pp. 126–131.
11. G. Fornaro, G. Franceschetti, and S. Perna, Motion compensation errors: effects on the accuracy of airborne SAR images (*IEEE Transactions on Aerospace and Electronic Systems*, vol. 41, 2005), pp. 1338–1352.
12. D. H. Titterton, and J. L. Weston, Strapdown inertial navigation technology – 2nd Edition (*The Institution of Electrical Engineers*, 2004).

Apply 2D Barcode Scanner for Mobile Robot Navigation in Checkerboard Mapping

Chun-Chi Lai
Bachelor Program in Interdisciplinary Studies, National Yunlin University of Science and Technology, 123 University Road, Section 3,
Douliou, Yunlin 64002, Taiwan, R.O.C.

Kuo-Lan SU
Department of Electrical Engineering, National Yunlin University of Science and Technology, 123 University Road, Section 3,
Douliou, Yunlin 64002, Taiwan, R.O.C.

Chia-Jen Lin
TECO Electric & Machinery Co., Ltd., 4F, No.3, Park St.,
Nan-Kang, Taipei 11503, Taiwan R.O.C.
E-mail: cclai@yuntech.edu.tw, jeromy@teco.com.tw

Evgeni Magid
Laboratory of Intelligent Robotic Systems (LIRS), Intelligent Robotics Department, Higher Institute for Information Technology and Intelligent Systems, Kazan Federal University, Russia

Abstract

In this work, a mobile robot is equipped with an industrial barcode scanner which can provide the pose information respect to the barcode tag in the field of view (FOV). For real multiple automated guided vehicle (AGV) transportation applications, the mobile robot navigation flow is considered to get the global checkerboard type path planning from a remote master server as an input. For the local planner, each robot is applied with a simple path controller to track the global path. The simulation and experimental results show that this implementation has good feasibility for multi robot co-working in a factory area.

Keywords: Automatic Guided Vehicle, 2D Barcode Code Navigation.

1. Introduction

For a traditional automated guided vehicle (AGV) control system that usually follows a magnetic tape for routine tasks. At a later time, two-dimensional barcode tags were researched as a popular AGV positioning solution after Amazon acquired Kiva Systems [1] which was the most notable commercial success of AGV fleet management system. The Kiva robots are operated within in a zone where the 2D barcode tags were affixed to the ground as checkerboard map. Without driving over the 2D barcode tags, the proximity of the 2D barcode tag can be detected and identified via the image processing system that allow Kiva system to get high quality positioning information.

B. Dzodzo et al. [2] had applied the 2D bar codes mounted on ceiling for requirements in facilities where floors and walls are in constant damaging contact with equipment and personnel. Also, there were many researches and commercial approaches which placed the 2D codes on the walls, ceilings as well as floors [3], [4], [5], [6].

In this work, a mobile robot is equipped with an industrial barcode scanner which can directly provide the pose information respect to the tag in the field of view (FOV). For multiple AGV transportation applications, the navigation flow is considered to get the global checkerboard type path planning from a remote master server as an input. For the local planner, each robot is applied with a path controller to track the global path. The simulation and experimental results show that this implementation has good feasibility for multi robot co-working.

2. System Description

Fig. 1 (a) shows a differential wheeled robot platform that was built in our laboratory. The movement of differential wheeled robot is based on two separately servo driven wheels placed on either side of the robot. The differential wheeled robot platform is the most popular type in AGV applied. Due to it can thus change its direction by varying the relative rate of rotation of its wheels and hence does not require an additional steering motion.

Fig. 1 (b) shows an industrial optical scanner [7]. This device will detect 2D barcode tags which are typically glued onto the floor in a grid as shown in the left of Fig. 2. The individual 2D barcode tags are numbered consecutively and include position information. It can be used together with a colored tap affixed to the floor and code tags printed with 2D barcode.

In the right of Fig. 2 shows the 2D barcode tags of AGV positioning system. A 2D barcode tag contains position information in addition to a specific number. A cross in the center of the 2D barcode tag marks the zero point. The X and the Y axes are marked starting from the zero point. The black arrow indicates the positive axis and the white arrow indicates the negative axis. So the read head reports the position of the AGV in relation to the zero point of the 2D tag to the motion controller.

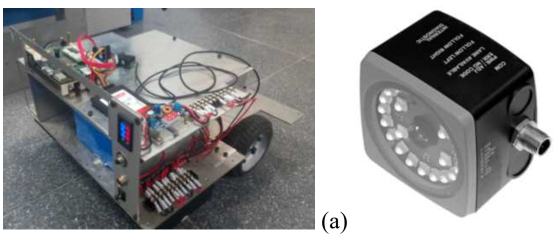
(a) (b)

Fig. 1. (a) a differential wheeled robot platform equipped with an industrial PC (b) the optical reading head (PGV 100 serial) for barcode tag identification

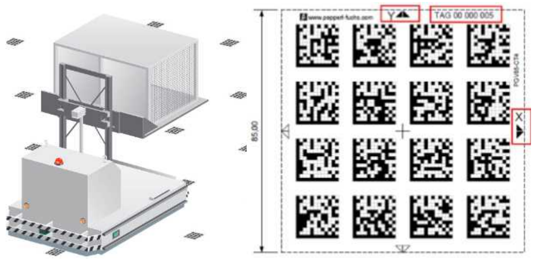

Fig. 2. Automated guided vehicle with 2D barcode tag

3. Frame Transformation in ROS

In this section we take an overview of Robot Operating System (ROS). Base on ROS framework and utilities, we can integrate the control and positioning system quickly. Besides, it is necessary to induce the coordinate transform between tag in map (world coordinate) and the odometry coordinate. So the transform tree in ROS will be completed for AGV navigation.

3.1 *Robot Operating System*

Robot Operating System (ROS) is a software frame work for robotics research and development. It applies a peer-to-peer topology for communication between robot processes and it provides tools for robot software development. For more information about ROS, the online wiki [8] is available. For the sake of completeness, some common concepts are listed as below:

- Nodes are ROS processes that perform computation. Nodes can communicate with each other using messages.
- Topics are named medium over which nodes exchange messages. Multiple nodes can publish / subscribe to a predefined topic.
- Subscriber is wrapped in a node which listens to the messages that are published to a topic.
- Publisher is wrapped in node which sends to a topic for other nodes can subscribe.
- roscore is a collection of nodes that are pre-requisites of a ROS-based system. roscore starts a ROS master node. So we must have a roscore running in order for nodes to communicate.
- TF in ROS is a package that lets the user keep track of multiple coordinate frames over time. TF maintains the relationship between coordinate frames in a tree structure buffered in time, and lets

the user transform points, vectors, etc., between any two coordinate frames at any desired point in time.

3.2 *Coordinate Transform from Barcode Scanner*

Fig. 3 shows the TF tree relationship in this work. The barcode scanner is attached in the robot with a pose transformation respect to the robot center (base_link). In general, the odometry will accumulate the encoder pulses from wheels and transfer it as displacement and rotation from the robot center respect the initial zero odometry coordinate frame. If there is no wheel drift error, the odometry coordinate frame will be the same as the world map coordinate frame. However in real situation, the wheel drift will accumulate to increase the positioning error. So we need the barcode scanner to get the real world's position, and re-align the drift between the odometry and world map.
In Fig. 4, the cross m' presents the world's coordinate center and the cross o' presents the odometry's coordinate center. The blue arrow presents the AGV's pose {xo, yo, Φo} in odometry coordinate frame. When the barcode scanner attached in the AGV that identifies the barcode tag on the floor, we will convert it as global position information such as {xm, ym, Φm}. So we can calculate the coordinate drift {xd, yd, α} between the world map and odometry frames.

$$R = \sqrt{xo^2 + yo^2} \tag{1}$$
$$\beta = \tan^{-1}\frac{yo}{xo} \tag{2}$$
$$\alpha = \Phi m\text{-}\Phi o \tag{3}$$
$$xa = R\cos(\beta + \alpha) \tag{4}$$
$$ya = R\sin(\beta + \alpha) \tag{5}$$
$$xd = xm - xa \tag{6}$$
$$yd = yd - ym \tag{7}$$

From the above equation (3), (6) and (7) the coordinate drift {xd, yd, α} will be calculated if we have the input {xo, yo, Φo} and {xm, ym, Φm}. In ROS framework, we need to create a transfer node to publish the /tf topic between odomety and world map for the TF tree's completion such as shown in Fig. 3.

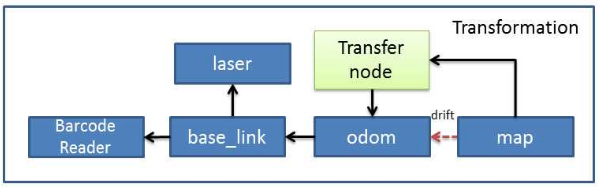

Fig. 3. Coordinate transformation (TF) in ROS.

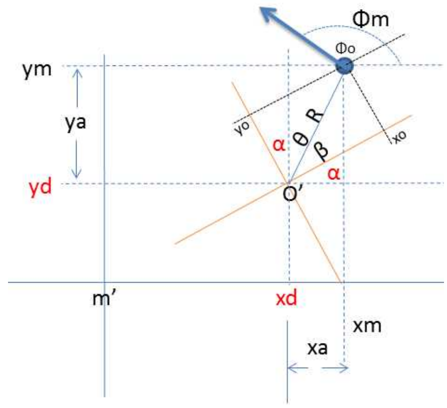

Fig. 4. Coordinate Transform between world (map) and odometry.

4. Action Server Mechanism for Navigation

In ROS based system, if we would like to send a request to a node to execute a task, and also receive a reply to the request. This can currently be achieved via ROS actionlib package. Fig. 5 shows the Action Server node that is designed in this work. The global path receiver is a template function to subscribe the goal messages from the Action Client. The goal would be a pose stamped array message that contains the path information for robot sequential moving in the world. When Action Server has received the goal, the local path follower will calculate the motion command and publish the cmd_vel topic. And another servo control node will subscribe the topic for handling AGV to follow the global path. Also the Action Server will give the feedback as the state reply to tell the Action Client about the incremental progress of the goal. For moving the platform, this will be the robot's current pose along the path. Finally, a result is sent from the Action Server to the Action Client upon completion of the goal. This is different than feedback, since it is sent exactly once.

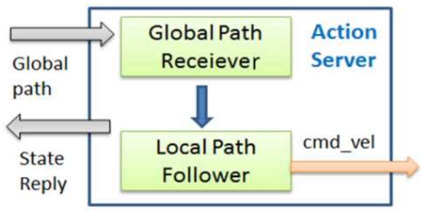

Fig. 5. An Action Server framework for AGV navigation

5. Fleet Management Framework

A fleet management system [9] primarily concerns itself with managing a group of vehicles to meet the goals and objectives obtained from an enterprise computer system. In this paper, we primarily implement a simplified fleet management system using ROS multi master system. To implement a multi master system, a package called multimaster_fkie [10] is needed and can be easily installed. Fig. 6 shows the simple fleet management framework in this study. The major task of the path planning server is to handle all the AGV's path planning and send the path message via wireless network to each AGV.

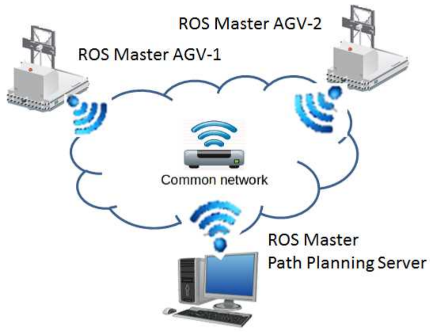

Fig. 6. Fleet management framework

6. Experiment Results and Conclusions

The experiment is firstly simulated and demonstrated in ROS rviz user interface for verifying the system integration. For convenient, a robot platform model named (turtlebot-waffle) is pre-loaded as shown in Fig. 7 (a) and the blue line presents the global path which was published from the remote ROS master. Fig. 7 (b) shows the Action Server was handling robot's orientation for global path following. Fig. 7 (c) shows that robot had reached the goal.

In this work, we have demonstrated the methodology and integration the mobile robot navigation in checkerboard mapping based on the 2D barcode scanner. The direction for future work therefore includes optimal management strategy to improve the efficient when numerous robots are co-working in the same time.

7. References

1. Kiva system overview. http://www.kivasystems.com/solutions/system-overview
2. B. Dzodzo et al., Realtime 2D code based localization for indoor robot navigation, in *IEEE International Conference on Robotics and Biomimetics* (ROBIO), 2013. p. 486-492.
3. J. Huh et al., Mobile robot exploration in indoor environment using topological structure with invisible barcodes, in *ETRI journal* , 2007, 29(2), p.189–200.
4. S. Zhao et al., Robot autonomous localization based on single artificial landmark, in *Journal of Shandong University (Engineering Science)*, 2007, 37.4, p.39-44.
5. G. Lin, X. Chen, A Robot Indoor Position and Orientation Method based on 2D Barcode Landmark. *JCP*, 2011, 6.6, p.1191-1197.
6. H. Kobayashi, A new proposal for self-localization of mobile robot by self-contained 2d barcode landmark, in Proceedings of *IEEE SICE Annual Conference,* 2012, p. x2080-2083.
7. Position Guided Vision (PGV): https://www.pepperl-fuchs.com/global/en/
8. Robot Operation System (ROS): http://wiki.ros.org/
9. A. Singhal et al., Managing a fleet of autonomous mobile robots (AMR) using cloud robotics platformm. In *IEEE European Conference on Mobile Robots (ECMR)*, 2017, p. 1-6.
10. Juan et al., Multi-master ros systems, *Institut de Robotics and Industrial Informatics*, 2015.

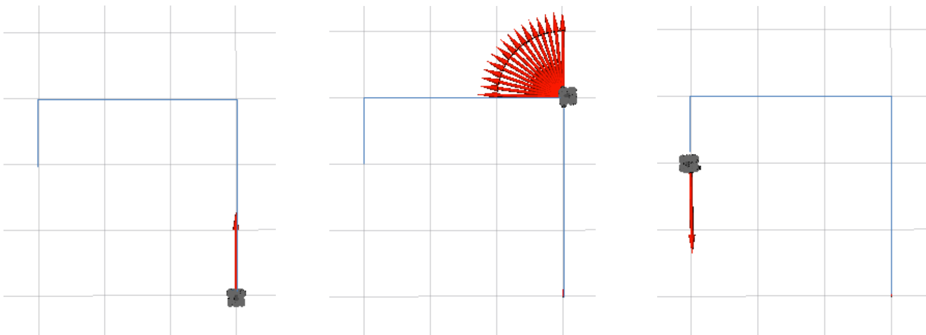

(a) robot received the global path (b) robot turned in the check point (c) robot reached the goal

Fig. 7. The robot executed the path following task which was published from remote server.

Development of the MyRio Based Mobile Platform

Jr-Hung Guo*, Bo-Jun Yang and Kuo-Lan Su
Graduate of Electrical Engineering, National Yunlin University of Science & Technology, Yunlin 64002, Taiwan, ROC..
E-mail:g9710801@yuntech.edu.tw, sukl@yuntech.edu.tw

Evgeni Magid
Laboratory of Intelligent Robotic Systems (LIRS), Intelligent Robotics Department, Higher Institute for Information Technology and Intelligent Systems, Kazan Federal University, Russia

Abstract

The paper develops the MyRio based mobile platform with a robot arm. The structure of the mobile platform uses the Matrix elements. The Matrix elements build the robot arm with four degrees of freedoms, too. The mobile platform integrates some sensors, four DC servomotors, two DC motors, two RC servomotors, a MyRio based control box, and two vision devices. The core controller of the MyRio-1900 control box is the NI-Single-Board RIO 9606 module. The mobile platform embeds a robot arm on the frond side. The driver device of the gripper is a RC servomotor. The developed mobile platform uses ultrasonic sensors to detect the obstacles. Trapezoidal acceleration and deceleration algorithm and Proportional-Integral-Derivative (PID) algorithm are used for precise motion control of each DC servomotor. A vision device of the mobile platform can search and recognize the shape and color of the assigned billiard ball. The other recognizes the symbol of each QR code. These vision devices are fixed on the frond side of the mobile platform, and recognize the assigned object using Otsu algorithm. In the experimental results, the mobile platform tests the positioning function of the Proportional-Integral-Derivative (PID) algorithm for each DC servomotor. Then we implement the movement precious of the mobile platform.

Keywords: MyRio, DC servomotors, NI-Single-Board RIO 9606 module, Otsu algorithm.

1. Introduction

An autonomous mobile platform usually works for a predefined task. The remote user can control the mobile platform doing the assigned task, too. In practice, a human wants the mobile platform to do the assigned task, such as catching an exploder and moving a dangerous object. Many mobile platforms have been widely applied in many fields, too. Such as factory automation, dangerous environment detection, office automation, hospital, entertainment, farm automation and security management system. There are some successful examples, such as ASIMO, PEPPER, NAO, QRIO and AIBO. We have been designed an intelligent mobile robot to do patrol autonomously and auto-recharging process [1,2]. In the paper, we design a mobile platform to finish some assigned tasks with a robot arm using the MyRio control system, and test the fundamental functions on the motion control.

In the past literatures of the robotic research, many experts research stable walking on uneven terrain. Su et al. have designed a mobile robot to solve the problems such that the robots can move from the start point to the target point on uneven terrain. [3]. Peng et al. designed a where/track mobile platform to search and rescue in dangerous environment. The motion modes of the mobile platform can be switched alternatively to adapt on different ground situations [4]. Guo et al developed a mobile platform, based on KNR controller. The mobile robot embed a robot arm with four degrees of freedom, and used of light sensors and touch sensors for line tracking and detects the initial location [5]. Su et al developed a mobile based robot arm using KNRm system. The developed mobile platform uses the vision device to recognize the position of the assigned object, and uses ultrasonic sensors to detect the distance of object and obstacle [6,7].

The paper is organized as follows: Section II describes the system architecture of the mobile platform and the robot arm, and explains the functions of the MyRio-1900 control box. Section III explains the hardware devices of the mobile platform. Section IV presents the experimental results of the motion control for the mobile platform using PID control method. Section VI presents the brief concluding remarks.

2. System Architecture

The system architecture of the mobile platform is shown in Fig. 1. The system contains two parts; one is the laptop and the other is a mobile platform. The laptop can program motion trajectories and recognize color and size of each object using NI LabVIEW software. The monitor interface system is developed on the laptop. The mobile platform contains five parts. There are structure and motors, image system, sensory system, power and drivers and control methods.

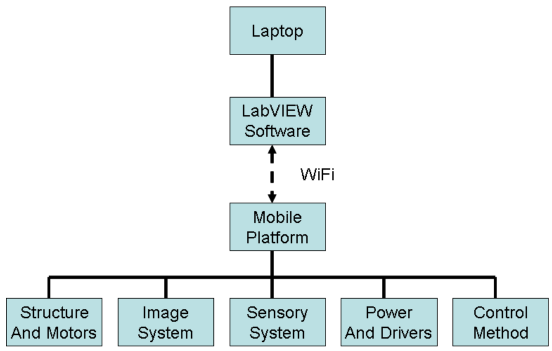

Fig 1. System architecture

The structure of the mobile platform is built by some Tetrix elements. We use three type DC motors to drive the mobile platform with a robot arm. One is four DC servomotors to control the motion trajectories of the mobile platform; two DC motors and two RC servomotors to build the robot arm. The image system uses WSR LifeCam Cinema Video Camera to search the positions of selected billiard balls, and uses Logitech C310 camera to recognize the style of each QR code. The main element of the sensor system is some ultrasonic sensors to be fixed on the frond side of the mobile platform. The ultrasonic sensors can detect the distance from the obstacle.

The main controller of the mobile platform is a MyRio control box to program the control methods. The hardware device of the MyRio-1900 control box is shown in Fig.2. The length, width and height are about 15cm, 10cm and 3cm. The control box displays the function of each connective pin. Users can select the needed element to connect with the control box for the assigned task. In order to achieve the purpose of accurate positioning, the core controller of the box is Xilinx Zynq-7010 to be a SoC system (a ARM-Cortex-A9 and a FPGA chip). The driver device of each DC servomotor uses the Tetrix DC motor expansion controller.

Fig. 2 MyRio-1900 control box

The control method uses PID control law and trapezoidal acceleration and deceleration algorithm to control each DC servomotor, and tune the mobile platform to follow the programmed trajectories. The controller of the KNRm system computes each compensator signals (P, I and D) according to the error signals as following：

$$e = SP - PV \quad (1)$$

$$u(t) = K_c\left[e + \frac{1}{T_i}\int_0^t e\,dt + T_d\frac{de}{dt}\right] \quad (2)$$

SP is desired value, and PV is measured value. The e is the error value to be the desired value minus the measured value. K_c is the proportional constant, T_i is integral time constant, and T_d is derivative time constant.

3. Mobile Platform

The structure integration of the mobile platform uses Matrix element shown in Fig. 3(a). The mobile platform can uses four DC servomotors to connect four mecanum wheels moving on the programmed motion paths. The MyRio system controls each DC servomotor through the DC servomotor driver is shown in Fig. 3(b), and programs the rotation range according to the feedback signal of the encoder sensor. The controller of the MyRio box uses PID control law and trapezoidal acceleration and deceleration algorithm to control each DC servomotor, and tune the mobile platform to follow the programmed trajectories, and finish the precision position.

The driver elements of the robot arm are two DC motors and two RC servomotors. The robot arm fixes on the frond side of the mobile platform, and is driven by the MyRio controller shown in Fig. 4. The structure of the robot arm is built using Tetrix elements. The image system is embedded on the top of the gripper to recognize position and color of the billiard ball, and searches the assigned billiard ball on the competition playground. Then the mobile robot moves approach to the assigned billiard ball, and catches the ball using the gripper of the robot arm, and moves the billiard ball to put down on the assigned position of the QR code.

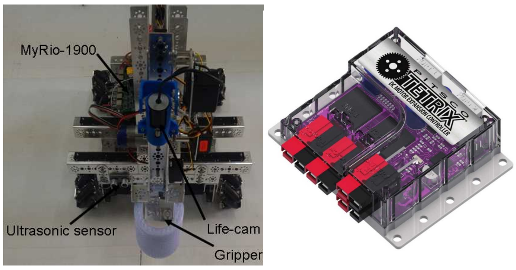

(a) (b)

Fig. 3 The mobile platform

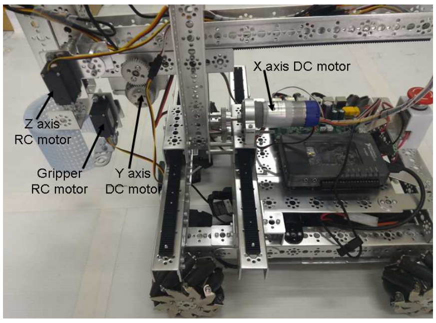

Fig. 4 The robot arm

4. Experimental Results

We implement the experimental results on the competition playground using the mobile platform (length 4m and width 2m). The pre-processing program of the PID control method for each DC servomotor using LabView software shown in Fig. 5. We set the rotation angle of the DC servomotor to be 180 degree. Then we program the driver software of the DC servomotor using LabVIEW language shown in Fig. 6. In the experimental result, the DC servomotor makes the red label on the top of the wheel shown in Fig. 7(a). Then we run the programmed software to control the wheel turning 180 degree. We can see the label to go down shown in Fig. 7(b).

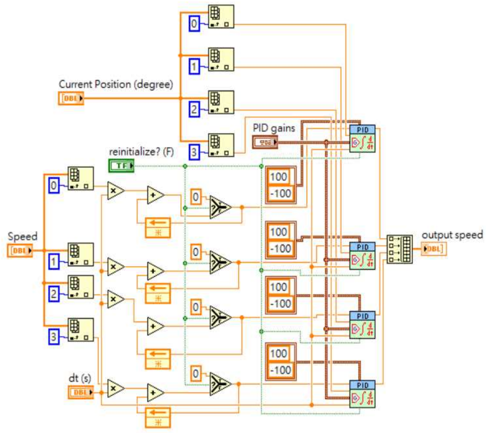

Fig. 5 PID control method program of LabVIEW

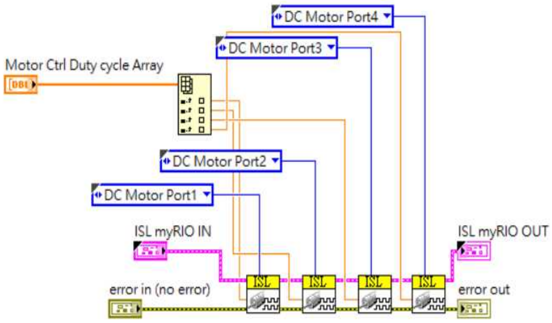

Fig. 6. Driver program of LabVIEW

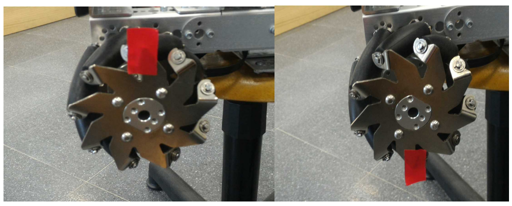

(a) (b)

Fig. 7. Experimental result

Then we test the motion precision of the mobile platform, and program the software using the LabVIEW system shown in Fig.8. We set the parameters of the PID Control method $K_C = 2.0$, $T_i = 0.0$, and $T_d = 0.00085$ shown in Fig. 9. Now we implement these parameters to control the mobile platform moving 50cm. We can see the initial position to be zero (the center of the rear wheel) shown in Fig. 10(a). Then the mobile platform moves to stop at the assigned position. We can see the stop position to be about 49.7 cm shown in Fig. 10(b). The speed curve of the mobile platform uses the Trapezoidal acceleration and deceleration algorithm shown in Fig. 11.

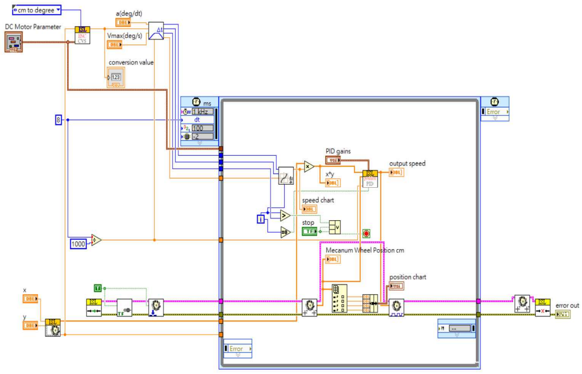

Fig. 8. Motion control program of LabVIEW

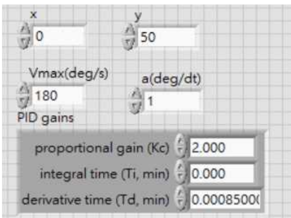

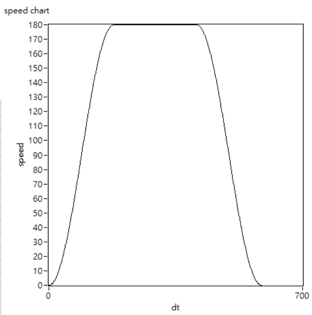

Fig. 9. Parameter values of PID Fig. 11. Speed curve

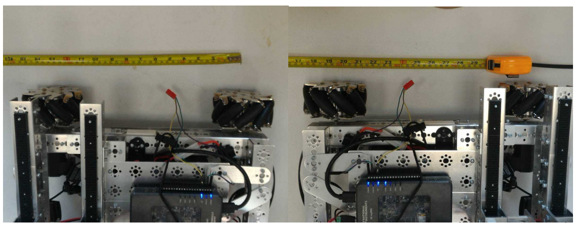

(a) (b)

Fig. 10. Experimental result of motion control

5. Conclusion

We designed a mobile platform with a robot arm using MyRio-1900 control box, and used the Tetrix elements to construct the mobile platform. The core controller of the MyRio box programs trapezoidal acceleration and deceleration algorithm and PID algorithm to control each DC servomotor of the mobile platform. The platform used two vision devices. One is WSR LifeCam Cinema Video Camera; the other is Logitech C310 camera. In the experimental results, the mobile platform can finished the precision position of each DC servomotor, and moved to the assigned distance very successfully. In future, they will finish various tasks with the image recognition function.

Acknowledgment

This work was supported by the Ministry of Science and Technology of Taiwan (MOST 107-2221-E- 224-053).

References

1. K. L. Su, Y. L. Liao, J. H. Guo and C. Y. Chung, Implement of the Auto-docking Processing for Mobile Robots, *The Innovative Computing, Information and Control – Express Letters (ICIC-EL)*, Vol.5, No.1, pp.31-36, 2014.
2. S. H. Chia, J. H. Guo, K. L. Su and B. Y. Li, Team Mobile Robots Based Intelligent Security System, *Applied Mathematics & Information Science*, Vol.7, No.2L, pp.435-440, 2013.
3. S. T. Su, C. H. Chen and K. L. Su, "Develop a Mobile Robot Moving on Uneven Terrain," The Innovative Computing, Information and Control – *Express Letters , Part B, (ICIC-ELB)*, Vol.6, No.2, 2015, pp.459-464
4. A. Peng, Y. Zhou, J. Hu and Y. Ou, "Mechanical design for wheer/track transform mobile platform-search and rescue robot," *IEEE Internation Conference on Robotics and Biomimetics*. P.1787, 2014
5. J. H. Guo, K. H. Hsia, K. L. Su and J. T. Wang, Development of the Mobile Robot With a Robot Arm, *International Conference on Industrial Technology(ICIT)*, Taipei, Taiwan, March 14-17, pp.1648-1653, 2016.
6. J. H. Li, K. H. Hsia, J. H. Guo and K. L. Su, "Development of the KNRm System Based Mobile Robot," *The Innovative Computing, Information and Control – Express Letters, Part B, (ICIC-ELB*), Vol.9, No.3, 2018, pp.185-194.
7. J. H. Li, J. H. Guo and K. L. Su, "Implementation of the Mobile Based Robot Arm for Image Recognition," *International Conference on Artificial Life and Robotic*s, Beppu, Oita, Japan, Feb. 1-4, 2018, pp.58.

Avrora Unior Car-like Robot in Gazebo Environment

Ksenia Shabalina[1], Artur Sagitov[1], Kuo-Lan Su[2], Kuo-Hsien Hsia[3], Evgeni Magid[1]
[1]Laboratory of Intelligent Robotic Systems (LIRS), Intelligent Robotics Department, Higher Institute for Information Technology and Intelligent Systems, Kazan Federal University, 35 Kremlyovskaya street, Kazan, Russia Federation
[2]Department of Electrical Engineering, National Yunlin University of Science and Technology, Taiwan
[3]Department of Electrical Engineering, Far East University, Taiwan
E-mail: ks.shabalina@it.kfu.ru, sagitov@it.kfu.ru, sukl@yuntech.edu.tw, khhsia@mail.feu.edu.tw, magid@it.kfu.ru
http://kpfu.ru/robolab.html

Abstract

Experiments are valuable tool of robust control algorithms design, but experiments tend to be expensive. In order to conduct thousands of complex experiments with autonomous car navigation algorithms it is safer and cheaper to start algorithm verification within a simulation, relying on a proper robot model, which preserves physical properties of underlying objects. In this paper we present the design of Avrora Unior mobile robot model, which is a Russian car-like robot with Ackermann steering geometry, and describe the process of modeling its kinematics and dynamics. Robot model was designed within open source robotics framework ROS for Gazebo simulator.

Keywords: car-like robot, non-holonomic robot, simulation, Avrora Unior, Gazebo, ROS.

1. Introduction

In the past decades a broad use of simulations became an essential part in robotics research field. We highlight the following reasons of using simulation in robotics: real experiments with robots are expensive while simulations are cheap; simulation experiments take less time than real experiments and are always safer than experiments in real world; simulations allow testing novel concepts and algorithms even if required hardware is not available for a user; simulations help to quickly detect and correct gross errors in algorithms; finally, simulations could provide fairly reasonable testing of experimental setups. Those reasons apply to all robot types and tasks.

A simulator became a very progressive tool that can be used to reproduce complicated environments (e.g., water); they can use user-defined physics with dynamic changes, which makes it possible to construct and use a robot model behaving very close to a real robot. Gazebo is the one of the most popular 3D simulator of robots, which was successfully used to simulate UAVs[1] and UGVs[2,3]. It could be used as an environment for performing various experiments: testing basic robot motions, path planning and collaboration with other robots[4], manipulation[5], modeling USAR scenarios[6] etc. Other specialized simulators (e.g., UWSim[7]) could help simulating water environments for AUV robots.

In our research we develop autonomous car navigation and locomotion algorithms for mobile robot Avrora Unior (Fig.1), and use Gazebo simulator to construct the robot model and to test control algorithms before performing experiments with the real robot.

2. Avrora Unior Car-like Robot

Avrora Unior robot is a car-like mobile robot that was created by Russian company Avrora Robotics (Fig. 1). Originally, this robot was designed for students' training in the field of autonomous driving, and such purpose clearly influenced technical design of the robot. Due to a small size and relatively low weight (~43,5 kg) of the robot, it is a safe solution for testing and validating algorithms for autonomous driving both in indoor and outdoor environments. As it is a small robot, it could be easily moved around the laboratory room by two students. Moreover, Avrora Unior provides Ackermann drive mechanism that is used in real cars. Table 1 and Table 2 show linear dimensions and weight parameters of the robot, respectively. The robot consists of body panels (robot shell), chassis (metal backbone), power source (lead acid battery), sensors and control unit (laptop Acer TravelMate P2). Another significant advantage of this robot is an open source software and off-the-shelf hardware.

Hardware could be easily replaced, upgraded or new elements could be retrofitted (e.g., sensors). The robot has preinstalled Linux Ubuntu 16.04 LTS operating system with ROS Kinetic. The vanufacturer also provides open source steering and drive control packages.

Fig. 1. Avrora Unior car-like robot.

Table 1. Robot dimensions.

Dimension	Dimension (m)
Rim diameter	0.204
Wheel diameter	0.26
Wheel width	0.11
Lateral length of the entire robot	1.112
Robot height	0.57
Robot width	0.65

3. Robot Operating System Environment

Robot Operating System (ROS) is a popular open source framework for collaborative robot software development. The framework is composed of atomic units (packages), which aim to solve particular problems in domain or provide particular functionality for a certain robot(s). All existing packages in ROS could be improved by a user and a new package could be added and described in a special knowledge base.

Table 2. Weight of Avrora Unior robot parts.

Element	Weight (kg)
Wheel	0.9
Shell of the robot	8.5
Cover	3.0
Hokuyo weight	0.16
Kinect weight	0.45
The entire robot	43.5

Gazebo provides an open source 3D simulator integration with ROS that can properly simulate a various types of existing robot models (including AUVs, UGVs, manipulators, etc.) and allows creating custom robots. Gazebo evaluates world physics and a robot model interaction. Developers can test their algorithms with a proper robot model in a virtual environment a desired number of times, modify the environment (e.g., add or remove obstacles) to explore algorithm's strengths and weaknesses before conducting field experiments with expensive equipment. In addition, Gazebo provides customizable plugins that simulate various types of sensors. For our robot model we used standard sensor plugins after a number of necessary adjustments. Gazebo supports robot model in SDF and URDF formats and allows importing STL and DAE meshes for objects.

4. Gazebo Robot Model

This section describes the process of modeling. We present the architecture of the model package, discuss key elements and their characteristics, cover joint geometry of the model and sensor specifications.

4.1. *Architecture*

Using *avrora_ros* name for our metapackage we decomposed the model into several individual packages: *avrora_description, avrora_gazebo, avrora_control*. This decomposition of the model provides a convenient and effective division of main functional parts of the robot model. Package *avrora_description* contains general description of the model for ROS framework: robot URDF (Universal Robotic Description Format) representations, component meshes and materials of the model. Package *avrora_gazebo* contains configurations of the model that should be loaded into Gazebo simulator. Package *avrora_control* contains configuration of the model joints' settings and geometry: joint type, PID controller values and ROS controller settings.

Our project uses URDF model representation format, which is a XML format file that describes a robot model with a help of special tags. The main tags, which are used for describing virtual structure of a robot, are link and joint tags. Links (robot elements) are connected with a joints, generating a tree-structured representation.

4.2. *Core elements*

We selected several link elements (i.e., core components) to represent our model: *base_link, right_steer_link, right_steer_wheel, right_drive_wheel, left_steer_link, left_steer_wheel, left_drive_wheel*. In order to make the model visually similar to real Avrora Unior robot we applied meshes for those links (the meshes are the courtesy of Avrora Robotics company) with corresponding inertial parameters (Fig. 2).

Link *base_link* represents the outer shell (or the body) of the robot. Links *right_steer_link and left_steer_link* describe the parts of Ackermann steering mechanism actuating the front wheels (*right_steer_wheel and left_steer_wheel*, respectively). Links *right_drive_wheel* and *left_drive_wheel* represents the rear driven wheels.

All links in the model were scaled to proportions and dimensions of the real robot. To adapt inertial characteristics of the robot to the model, we calculated simplified inertial tensor for all links. We substituted compound meshes of a *base_link* with a solid cuboid object, steer wheel links, rear and front wheels as a solid cylinder to calculate approximated link inertia tensors.

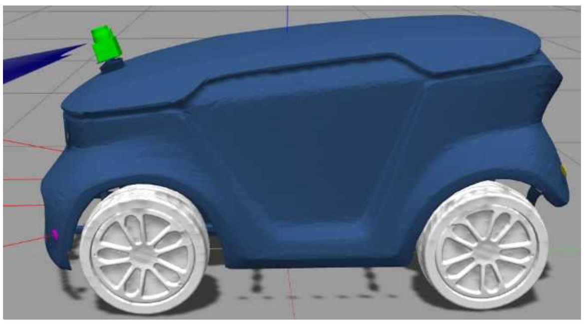

Fig. 2. Avrora Unior model in ROS/Gazebo environment.

4.3. *Joints, motors and transmission*

URDF format provides several types of joints: prismatic, revolute, continuous, floating and fixed. In our model we used three type of joints: fixed, revolute and continuous. Fixed joints attach rigidly two links with each other and in our model we used these joints to rigidly attach robot sensors to the main body. Continuous type allows rotation of a joint around a specified axis without upper and lower limits on the angle of rotation. Those type of joints in the model (*left_steer_wheel_joint, left_drive_wheel_joint, right_steer_wheel_joint, right_drive_wheel_joint*) were used to connect the wheels to the chassis. Revolute joints allow constrained rotation around a specified axis within upper and lower limits. We used revolute type joints for steering joints (*left_steer_joint* and *right_steer_joint*), to implement Ackermann steering geometry for model steering control (Fig. 3). The axis of rotation in both joints is Y-axis. Such joint configuration is a base for implementation of Ackerman drive mechanism for Avrora Unior model.

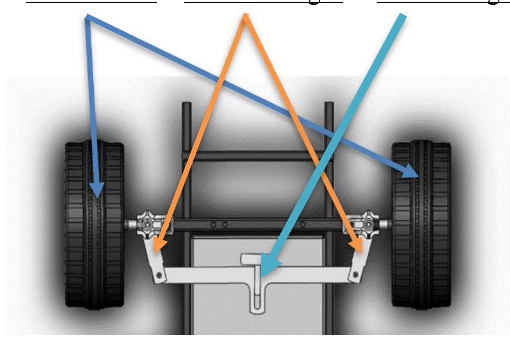

Fig. 3. Avrora Unior chassis scheme.

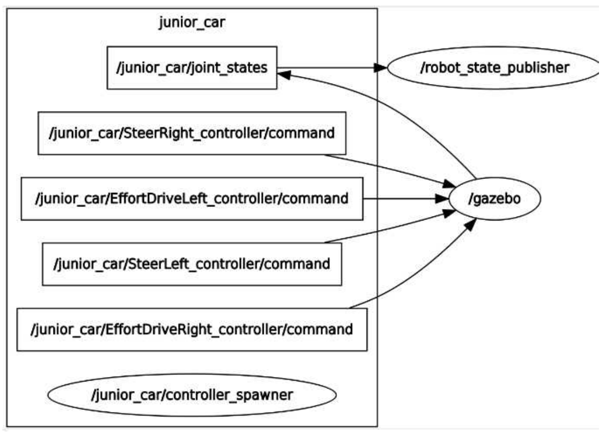

Fig.4. *rqt_graph* of Avrora Unior model topics (sensor's topics are not visualized).

We approximate Ackermann geometry by moving the steering pivot joints steering to angles (between steering kingpins and the centre of the front axle) that are calculated from a desired steer angle as Eq. 1:

$$\begin{cases} \delta_{1l} = c_\delta * \delta_{st}, \delta_{1r} = arc\cot\left(cot(\delta_{1l}) - \frac{2B}{l_1}\right) when\ \delta_{st} > 0 \\ \delta_{1r} = c_\delta * \delta_{st}, \delta_{1l} = arc\cot\left(cot(\delta_{1r}) + \frac{2B}{l_1}\right) when\ \delta_{st} < 0 \end{cases} \quad (1)$$

where δ_{st} is the input angle, c_δ = 0.5, B is a half of the wheelbase, l_1 is the wheel linkage length. As a result, we have four continuous joints providing wheel rotation in X-axis direction (linear motion on the plane) and two revolute joints to replicate steering mechanism of Ackerman drive system.

Since there are only two motor driven wheels in Avrora Unior and a motor actuated steering mechanism, we configured the following ROS control joint controllers: position controllers *SteerRight_controller* and *SteerLeft_controller* (ROS *JointPositionController*), effort controllers *EffortDriveRight_controller* and *EffortDriveLeft_controller* (ROS *JointEffortController*). Controllers' topic visualization is showed in Figure 4.

4.4. *Sensor Simulation*

Table 3 presents the list of sensors of the real robot, their implementation in ROS framework and Gazebo environment. The model sensors were placed in the same positions as the real robot sensors in order to further match real sensor data. All Gazebo sensor plugins were configured to fit specifications of real robot sensors. We visualize sensor data with Rviz software.

5. Conclusions and Future Work

In this paper, we presented car-type Avrora Unior robot modeling. We used ROS environment and Gazebo robotics simulator. To construct the model, we used URDF format, which is supported by Gazebo. Core elements of Avrora Unior model were imported from mesh files provided by the manufacturer. Appropriate joint controllers for Ackermann steering and sensor simulations were added. As part of our future work, we are preparing a proper setup of the PID parameters of joint controllers and developing an improved Ackermann drive system. After successful modelling the cooperative path finding tasks will be applied in simulated within Gazebo urban environments[8] prior to real world testing.

Table 3. Sensors and plugins.

Sensor	ROS package	Gazebo plugin
LIDAR	hokuyo_node	laser_controller
Microsoft Kinect	freenect_stack	camera_plugin
GPS	ur_nmea_driver	novatel_gps_sim
Proximity	ur_rangefinder_driver	Sonar
IMU	myahrs_driver	imu_plugin

Acknowledgements

Part of the work was performed according to the Russian Government Program of Competitive Growth of Kazan Federal University.

References

1. A., Sagitov and Y., Gerasimov, Towards DJI Phantom 4 Realistic Simulation with Gimbal and RC Controller in ROS/Gazebo Environment. In *Int. Conf. on Developments in eSystems Engineering*, (2017), pp. 262-266.
2. I., Afanasyev, A., Sagitov, E., Magid. ROS-based SLAM for a Gazebo-simulated mobile robot in image-based 3D model of indoor environment. In *Int. Conf. on Advanced Concepts for Intelligent Vision Systems*, (Springer, Cham, 2015), pp. 273-283.
3. M., Sokolov et al., Modelling a crawler-type UGV for urban search and rescue in Gazebo environment, *In IEEE Int. Conf. on Artificial Life and Robotics (2017).*
4. W., Yao et al., A simulation system based on ros and gazebo for robocup middle size league, *In IEEE Int. Conf. on Robotics and Biomimetics,* (2015), pp. 54-59.
5. W., Qian et al., Manipulation task simulation using ros and gazebo, *In IEEE Int. Conf. on Robotics and Biomimetics,* (2014), pp. 2594-2598.
6. S., Kohlbrecher et al., Robocuprescue 2014-robot league team hector Darmstadt (Germany), *RoboCupRescue* (2014).
7. O., Kermorgant, A dynamic simulator for underwater vehicle-manipulators, In *Int. Conf. on Simulation, Modeling, and Programming for Autonomous Robot*s (Springer, Cham, 2014), pp. 25-36.
8. A. Andreychuk and K. Yakovlev. Applying MAPP Algorithm for Cooperative Path Finding in Urban Environments. In *Int. Conf. on Interactive Collaborative Robotics*, (2017), pp. 1-10.

Transfer of learned exploration strategies of a mobile robot from a simulated to real environments

Artur Sagitov[1], Tetsuto Takano[2], Shohei Muto[3], Evgeni Magid[1]
[1]Laboratory of Intelligent Robotic Systems (LIRS), Intelligent Robotics Department, Higher Institute of Information Technology and Intelligent Systems, Kazan Federal University, 35 Kremlyovskaya street, Kazan, 420008, Russia
[2]Department of Electronic Information Sciences, Kanazawa University, Kanazawa, Japan
[3]Department of Mechanical Science and Engineering, Kanazawa University, Kanazawa, Japan
E-mail: E-mail: sagitov@it.kfu.ru, shohei0625@stu.kanazawa-u.ac.jp, magid@it.kfu.ru
http://kpfu.ru/robolab.html

Abstract

Reinforcement learning based approaches show promises in various robotic applications, but a significant amount of time and resources are required for a robot to learn optimal behavior. Using virtual environments, we could significantly speed up and improve performance of a target task. We implemented a reinforcement learning based exploration algorithm for a mobile robot, training in Gazebo environment and transferring learned strategy to a real robot. We show that it is convenient and appropriate to use simulation to train strategies for mobile robots.

Keywords: navigation, algorithm, mobile robots, reinforcement learning, exploration.

1. Introduction

Reinforcement learning is a field of machine learning where an agent learns a behavior by interactions within particular environment. All interactions are being graded and the goal of an agent is to achieve maximum possible cumulative grade. Method is inspired by how humans are taught in schools, i.e., taking tests and exams and receiving positive or negative feedback. In robotics, such method presents a way to design and implement complex behavior that are hard to conceptualize. Our initial goal was to build a simple mobile robot that autonomously explores an environment based upon reinforced learning algorithm, without any human interventions.

Major obstacle to be considered using reinforced learning is an amount of time that should be spent for learning optimal behavior, as real trials are slow and costly. One of the possible solution to this problem is the idea of incorporating simulations of a real environment. This process is self-correcting and can improve by obtaining information from real world trials to correct the simulated environment.

One of the major frameworks for reinforcement learning research is OpenAI Gym[1]. This framework provides an easy way to debug and benchmark an algorithm under a variety of different environments. Zamora et al. extended OpenAI Gym functionality with interfaces to Robot Operating System (ROS) and the Gazebo simulator, to simplify the integration with the robotic hardware to validate existing reinforcement learning algorithms in real environments[2].

Our custom mobile robot was integrated into ROS and Gazebo environment with control interfaces on both real and virtual robots unified. The robot was trained using Q-Learning algorithm. Reward increased if it had explored previously unsearched areas on the map and decreased if it had a collision with the walls. With the training completed in the simulation, resulting strategy is easily transferred to the real robot.

2. Related Work

Mathematical concepts of reinforcement learning began when optimal control framework for Markov decision process proposed by Bellman[3] was reformulated by Sutton[4] and Watkins[5]. In recent years, reinforcement learning has become an important method in robotics[6]. It was applied to locomotion[7,8], manipulation[9-12] and autonomous vehicle control[13]. Combining reinforcement learning with general-purpose neural networks shown significant potential, including real-time control of 7 degree-of-freedom manipulators[14-16]. Using large and deep neural networks have made it possible for robots to master complex manipulations with minimal manual engineering, though it is still unknown whether this can be easily applied to an arbitrary task[17-18].

In a study[19] deep neural network (combination of convolutional networks and a long short-term memory network) learns to self-calibrate from a history of previously set of actions and observations. Learning from multiple simulated samples that had consisted of trajectories and objectives, this network was able to learn controlling a robotic arm successfully, achieving goals being set from various frames of reference and using a non-calibrated camera.

3. System Setup

We used OpenAI gym-gazebo extension for a virtual robot and a virtual environment. Gym-gazebo is a combination of OpenAI Gym, ROS and Gazebo. OpenAI provides interface for implementation and testing of an algorithm that will controls real and virtual robot in the Gazebo simulation[20].

3.1. *Learning Robot*

The target for the experiments was a custom-build mobile robot being controlled through a mounted Arduino Uno microcontroller (Fig.1). This learning robot is a four-wheel mobile robot that was controlled by 4 DC motors (one per wheel, two motors on each side), with a spring amortization on each wheel. Velocity controller was implemented for each axis using *ros_control* package. Robot uses differential steering for taking turns and can make complete in-place (pivot) rotations by creating difference in velocities of the left or right side wheels. Sensory information was provided by Hokuyo LIDAR (UTM-30LX) mounted on the top of the frame.

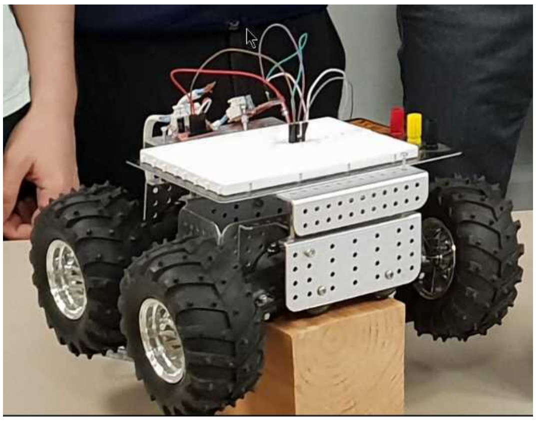

Fig. 1. Learning robot.

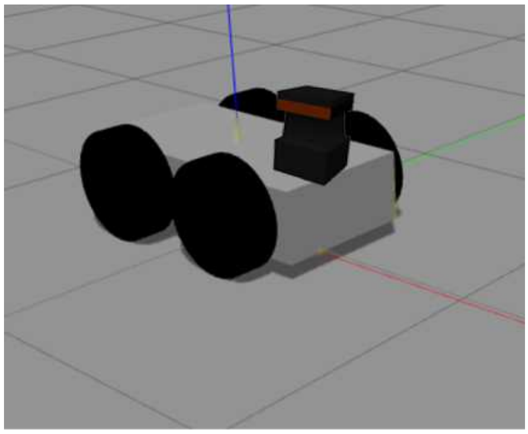

Fig. 2. Virtual learning robot in Gazebo.

ROS package *rosserial* provided a ROS communication protocol over Arduino's UART interface and allowed publishing and subscribing to ROS messages, publishing coordinate frame transforms and accessing ROS system time. The robot control and sensor processing was implemented using *rosserial* protocol by wrapping standard ROS serialized messages and multiplexing multiple topics over to the microcontroller. We implemented virtual representation of the learning robot for the Gazebo simulator, including controller interfaces, controller managers, transmissions and hardware interfaces to match exactly with the real robot (Fig.2), using the same approach that we had exploited in our previous research on crawler robot modelling[21].

3.2. *Learning algorithm*

We implemented multi-step Q-Learning method to facilitate learning of exploration strategy. Q-learning is a widely used reinforcement learning method introduced by Watkins[5] that uses formulated policies, constructing robot strategy by defining action to take under what circumstances with probabilistic transitions and rewards.

We assumed exploration strategy as a finite Markov decision process (FMDP). Using Q-learning we searched for a strategy that is optimal in a sense that it maximizes an expected value of a total reward (area explored) over all successive steps. Starting from an initial point in decision space, Q-learning can find optimal action-selection strategy given formalized FMDP. Reward was used to provide the reinforcement and in our case it measured an added explored space after an action taken.

Learning robot have a set of states S, and a set of possible actions in this state A. When action $a \in A$ is selected, the robot makes transitions from one state to another state. With each action robot takes from a particular state a reinforcing reward will be changed. When a number of steps reaches a predefined limit or the robot gets stuck we calculate a final reward.

The robot tries to maximize its total reward by adding a maximum reward achievable from future states to the reward for achieving its current state, affecting current action selection given a possible future reward. A total potential reward, which is defined as a weighted sum of expected values of rewards of all future actions starting from the current state, is taken as an objecting function.

At each step, we update the quality function:

$$Q(s_t, a_t) \leftarrow Q(s_t, a_t) + \alpha \left[r_t + \gamma \max_{\alpha} Q(s_{t+1}, a_t) - Q(s_t, a_t) \right], \quad (1)$$

where parameters α (learning rate) and γ (discount factor) are hyperparameters that determine the influence of new information and possible future rewards.

We implemented four possible actions in each state: forward motion (both axes 0.2 m/s), left turn (left axis -0.1 m/s, right axis 0.1 m/s), right turn (left axis 0.1 m/s, right axis -0.1 m/s) and backward motion (both axes -0.2 m/s). The robot was severely penalized if it made a contact with a wall. As soon as a current action was achieved, a new goal was provided and a reward was issued based upon a change of explored territory area.

3.3. *Exploration environment*

As a test for our setup, we selected a standard gym-gazebo labyrinth *GazeboCircuit2TurtlebotLidar-v0*. This environment consists of a simple straight lined circuit with five right turns and one left turn (Fig.3). We used a LIDAR sensor to localize and map the environment, using no other positioning information.

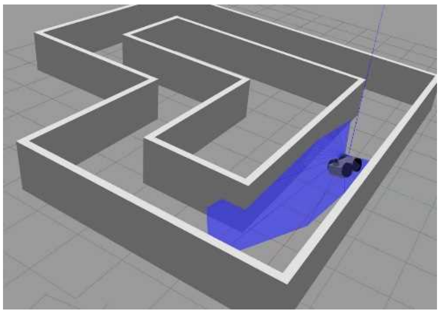

Fig. 3. Testing environment in ROS Gazebo.

4. Results

Our setup allowed us to get around 10 times faster than real time simulation; thus, our virtual robot could perform ten times more learning trials than the real robot. 5000 trials were completed within around 6 hours. Figure 4 demonstrates that the robot exploration strategy significantly improved over time, as the average total reward over time increased.

Even with training performed entirely in a simulator different from a real world, we have obtained exploration strategies, which perform well on the physical robot. We attribute successful transfer to randomizations of simulated environment and unified control interface between real and virtual robot.

We observed several factors that contributed to the difference between the simulation and the reality during executions: the real robot exhibits a lateral and longitude wheel slip, accumulates wheel velocity inaccuracies and is more prone to collisions when driving near the walls.

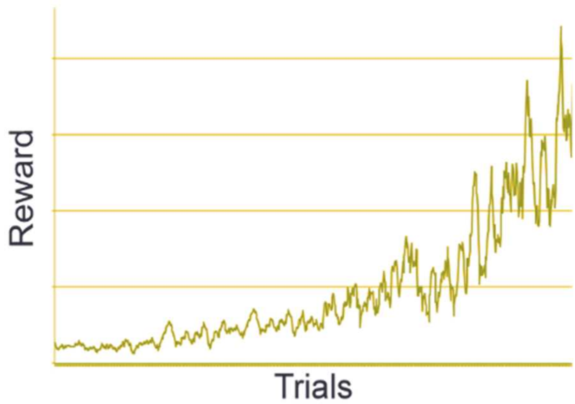

Fig. 4. Reward after trials.

5. Discussion and Future Work

There are several ways we are trying to improve the learning process. In the order of priority, we list:

1. Verify the approach for more complicated robots.
2. Speed up simulation for robots using multiple computers.
3. For complex environments, make simulation run at a faster speed.
4. Further diversify environments and add multiple robots.
5. Implement additional tools for calculating performance metrics for different algorithms.
6. Make automatic recommendations from the resultant strategy.

6. Conclusion

Reinforcement learning plays a significant role in the growing field of machine learning and, in order to overcome difficulties, robotics simulator like Gazebo is shown saving costs and speeding up the learning process. We have shown that reinforcement learning algorithms are capable of learning complex exploration skills from scratch and without purposefully designed trajectories, but our method has a number of limitations, such as simplified robot and test environment. We have plans to address these issues in the future.

Acknowledgements

This work was supported by the Russian Foundation for Basic Research (RFBR), project ID 18-58-45017. Part of the work was performed according to the Russian Government Program of Competitive Growth of Kazan Federal University.

References

1. G. Brockman, et.al., OpenAI gym (arXiv preprint, arXiv:1606.01540, 2016).
2. I. Zamora, et.al. Extending the OpenAI Gym for robotics: a toolkit for reinforcement learning using ROS and Gazebo (arXiv preprint arXiv:1608.05742, 2016).
3. R. Bellman, A Markovian decision process, in *Journal of Mathematics and Mechanics* (1957) pp. 679-684.
4. R.S. Sutton, Temporal credit assignment in reinforcement learning, (PhD Thesis, University of Massachusetts, Amherst, MA., 1984).
5. C.J.C.H. Watkins, Learning from Delayed Rewards (Ph.D. thesis, Cambridge University, 1989).
6. J.Kober, J.A. Bagnell, J. Peters, Reinforcement learning in robotics: A survey, in *The Int. J. of Robotics Research*, 32, (2013), pp. 1238-1274.
7. N. Kohl and P. Stone, Policy gradient reinforcement learning for fast quadrupedal locomotion, in *Int. Conf. on Robotics and Automation* 3 (2004), pp. 2619-2624.
8. G. Endo, J. Morimoto, T. Matsubara, J. Nakanishi, and G. Cheng, Learning CPG-based biped locomotion with a policy gradient method: Application to a humanoid robot, in *Int. J. of Robotic Research*, **27**(2) (2008), pp. 213–228.
9. J. Peters and S. Schaal, Reinforcement learning of motor skills with policy gradients, in *Neural Networks*, **21**(4) (2008), pp. 682–697.
10. E. Theodorou, J. Buchli, and S. Schaal, Reinforcement learning of motor skills in high dimensions, in *Int. Conf. on Robotics and Automation* (2010) pp. 2397-2403.
11. J. Peters, K. Mulling, and Y. Altun, Relative entropy policy search, in *AAAI Conference on Artificial Intelligence* (2010), pp. 1607-1612.
12. M. Kalakrishnan, L. Righetti, P. Pastor, and S. Schaal, Learning force control policies for compliant manipulation, in *Int. Conf. on Intelligent Robots and Systems* (2011), pp. 4639-4644.
13. P. Abbeel, A. Coates, M. Quigley, and A. Ng, An application of reinforcement learning to aerobatic helicopter flight, in *Advances in Neural Information Processing Systems* (2006) pp. 1-8.
14. P. Pastor, H. Hoffmann, T. Asfour, and S. Schaal, Learning and generalization of motor skills by learning from demonstration, in *Int. Conf. on Robotics and Automation* (2009), pp. 763-768.
15. J. Schulman, S. Levine, P. Moritz, M. Jordan, and P. Abbeel, Trust region policy optimization, in *Int. Conf. on Machine Learning* (2015), pp. 1889-1897.
16. S. Levine, C. Finn, T. Darrell, and P. Abbeel, End-to-end training of deep visuomotor policies, *J. of Machine Learning Research*, **17**(1) (2016), pp. 1334-1373.
17. M. Deisenroth and C. Rasmussen, PILCO: a model-based and data efficient approach to policy search, in *Int. Conf. on Machine Learning* (2011), pp. 465-472.
18. T. Moldovan, S. Levine, M. Jordan, and S. Abbeel, Optimism-driven exploration for nonlinear systems, in *Int. Conf. on Robotics and Automation* (2015), pp. 3239-3246.
19. F. Sadeghi, A. Toshev, E. Jang and S. Levine, Sim2Real Viewpoint Invariant Visual Servoing by Recurrent Control, in *IEEE Conf. on Computer Vision and Pattern Recognition* (2018), pp. 4691-4699.
20. I., Afanasyev, A., Sagitov, E., Magid. ROS-based SLAM for a Gazebo-simulated mobile robot in image-based 3D model of indoor environment. In *Int. Conf. on Advanced Concepts for Intelligent Vision Systems*, (Springer, Cham, 2015), pp. 273-283.
21. M., Sokolov et al., Modelling a crawler-type UGV for urban search and rescue in Gazebo environment, *In IEEE Int. Conf. on Artificial Life and Robotics (2017).*

Extending Gazebo simulator for surgical robotics: tissue and suture modeling

Artur Sagitov[1], Hongbing Li[2], Natalia Schiefermeier-Mach[3], Evgeni Magid[1]
[1]Laboratory of Intelligent Robotic Systems, Intelligent Robotics Department, Kazan Federal University, Kazan, Russia
[2]Department of Instrument Science and Engineering, Shanghai Jiao Tong University, Shanghai, China
[3]Health University of Applied Sciences Tyrol, Innsbruck, Austria
E-mail: sagitov@it.kfu.ru, natalia.schiefermeier-mach@fhg-tirol.ac.at, magid@it.kfu.ru
http://kpfu.ru/robolab.html

Abstract

Active use of a simulator as a training tool has proven to be advantageous to a human surgeon, but there is no open source and convenient universal surgery simulation of a robot surgeon. This paper presents an extension of Gazebo simulator for surgical robots using Robot Operating System. We present software architecture that allows modeling robot interaction with different types of tissue and suture.

Keywords: robotic surgery, tissue modelling, suture modelling, Gazebo, ROS.

1. Introduction

Robotic surgery field experiences exponential growth and emerging new techniques present new challenges for training of surgeons. We note the increase in quality of robotic surgery simulations and incorporation of those into modern surgical training curriculum. Simulators have proven to be advantageous in a practice, but they are designed for a human training and it is not possible to use those for developing autonomous procedures.

Surgery simulation is an interactive physical simulation that involves rigid and deformable objects. Simulation development engages various applied mathematics branches including numerical analysis, geometric modeling, computational mechanics, collision detection, and rendering, while their computational efficiency is achieved with compound algorithms and multi-threading that take full advantages of modern hardware capabilities. Therefore, developing surgical simulations is a challenging task that requires an expertise in all of the aforementioned areas. One of the ways to address this is combining available separate domain frameworks into a single modular package.

We used Gazebo simulation as a base for our surgery robot simulation because of its support for robot operating system (ROS)[1], but a number of changes were required as Gazebo is not capable of deformable objects simulation. Gazebo consists of two main components: a server and a client. The server evaluates physics of the environment: entire state of each object being involved in the simulation, forces and velocities of each object and external controllers' input. The client uses server output to displays the environment in a graphical user interface in order to provide visualization and control. The server can use different physics' engines each being optimized for different use cases. We have selected Bullet physics engine for existing soft body routines and had to implement a new external plugin for Gazebo in order to add soft body modeling to Gazebo.

Modern vector graphics editors and computer games use a special data structure that represents all entities - a scene graph, which contains different object representations in the scene. In our simulation we organize objects, their relations and algorithms in a hierarchical data structure that is similar to scene graphs. Each object is decomposed into a set of properties: state vectors, mass, forces, constraints, topology, integration scheme, and solving process. Simulation algorithms can be customized for each component individually as well as for physical models themselves. A physical object is represented as a combination of four models: internal model, inertial model, collision model and visual model. We propagate forces and movements between the models concurrently during the simulation.

2. Related Work

In a field of rigid body simulations for robotics there is a number of different products, including an open-source software Gazebo[2], proprietary V-REP, WorkspaceLt, RoboticSimulation, Webots and others. Those simulators rely on different physics engines (e.g., Open Dynamics Engine (ODE), Bullets, DART or NVidia PhysX) and are fast and efficient in rigid-body simulations and easy to use. The main disadvantage from our perspective is that very few of them are capable of modeling realistic soft bodies. Usually soft object modelling involves a use of structural multi-physics tools such as ComSol. As those tools use continuous mechanics algorithms the disadvantage of this method is a slow computational speed and the requirement of deep understanding of the physical processes behind.

Modeling soft objects is an active field of research, and a number of methods exist for soft tissue deformation in a surgical simulation. Mass-spring models (MSM) approximate a soft tissue as a set of point masses being interconnected with massless elastic springs. Advantages of MSM are their easy implementation and efficient evaluation. Disadvantages include difficulty in distribution of material properties and dependency of deformation upon a selected discretization topology[3]. When deformation accuracy is a concern, a finite element method (FEM) is considered. FEM represents a soft tissue model as a continuous object and constructs built-in equations to model complex mechanical behavior of soft tissues. Equations approximating geometric and material properties being involved in deformation are numerous, which makes FEM computationally expensive; moreover, it can become numerically unstable. To address the issue of the computational efficiency of FEM model reductions[4], tensor pre-computation[5], multi-grid solvers[6] and domain decomposition[7] could be applied. FEM that is used in real time surgical simulations often uses simplified linearized equations for material law and strain computation. These simplifications are applicable for small deformations and cause significant errors for large deformations[8]. To correct for large scale deformations a geometric nonlinear tensor-mass model has been applied[9] but it imposes complicated computations using quadratic formulations of strain. To address geometric nonlinearity involving rotational deformations FEM could be supplemented with a co-rotational formulation[10]. In meshless method[11] a deformation could be evaluated without explicit node connections with a penalty of additional computations of node adjacency metric at each iteration. Lack of explicit topology is also an issue[12]. Formulation of Lagrangian dynamics for FEM taking into account geometric and material nonlinearities method[13] depends upon constant topology of an object as it uses precomputations, and has shown numerical stability with only small time steps. To address deformation nonlinearity method of hyperelastic mass links a new approach[14] was proposed that provides fast computation, but as of now is applicable only for homogenous objects[15]. Boundary element method[16] was unable to address objects anisotropic and heterogeneous properties. Using specialized hardware, such as Graphics Processing Unit (GPU), could be used to handle computational load[17]. Simulation framework SOFA[18] was developed with a focus on deformable objects and complex interactions, and can simulate a large variety of models, including rigid-bodies, MSM and FEM with hyperelastic masses.
Our implementation for Gazebo simulator is a somehow intermediate approach between simple game physics engines and a complicated FEM analysis.

3. Tissue and suture models

Both tissue and suture are represented as soft deformable bodies. Assuming suture simple geometry, we directly use a default 2D discretization for solving constitutive equations. The tissues are a 3D object and to construct a mechanical model we had to discretize the tissue domain. We use CGAL (an efficient geometric C++ library) to generate a hexahedral polygonal mesh from 3D model. We adjusted discretization parameters to have the best deformation accuracy given selected limit of volume elements to address the performance. Discretization example is presented in Fig.1.

Deformable objects' behavior is a subject to the laws of continuum mechanics for material modeling, Lagrangian multipliers for constraints solving, and Signorini problem for contact resolution. Internal forces of a simulated object are dependent on a current state and a sum of all known external forces. Amount of deformation depends only on external loads. We use Hooke's law for this dependency because of computation time constraints. Deformation is treated as purely elastic behavior. Each tissue type specifies Young modulus and Poisson's ratio as parameters. When a potential contact with a robot end-effector has been detected, we measure the distance between the robot and an obstacle at a contact point. Using contact mechanics, we find an area of the contact patch and find a displacement vector by resolving Signorini problem.

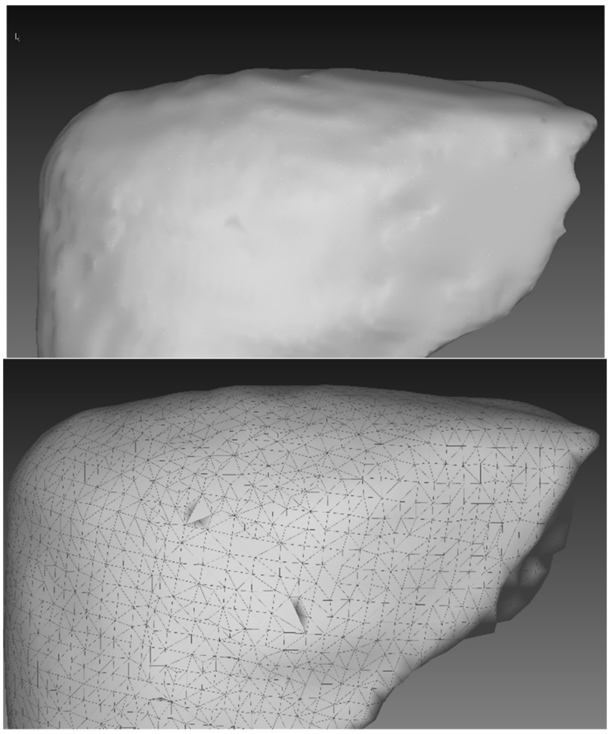

Fig. 1. Model discretization and triangulation

4. Gazebo integration

A scene contains the robot and its environment and is described within XML file. Soft tissues are defined using an extension of URDF format with components for discretization options, contact configuration and options for numerical integration and rendering. Using a synchronized tissue model, we collect force vectors and contact points from different representations to obtain an entire system. Applying our Gazebo plugin, we connect the Gazebo world and the soft tissue to allow interaction with other objects. Plugin synchronizes locations of each of soft body nodes between different representations. Rendering module of the plugin utilizes the state of the physical simulation to render a visualization because Gazebo does not have deformable meshes rendering capability. We render our meshes using custom OGRE renderer as a plugin to Gazebo that is implemented through *rendering::visual* class.

In our current configuration of the plugin we allow interaction of a rigid body object (manipulator) with a soft tissue in a realistic manner. Behavior of the simulated soft tissue is sensitive to parameter selection, mechanical parameters and tissue topology which should be specified manually.

5. Examples of abdomen simulation

We are using abdomen models available from OpenHELP phantom, which are designed with realistic anatomy and material characteristics, for our autonomous suturing system prototype testing[19]. Using plugin for each of the tissue type, abdomen models were imported to Gazebo with proper mechanical properties. Model of the interaction is represented on Fig. 2.

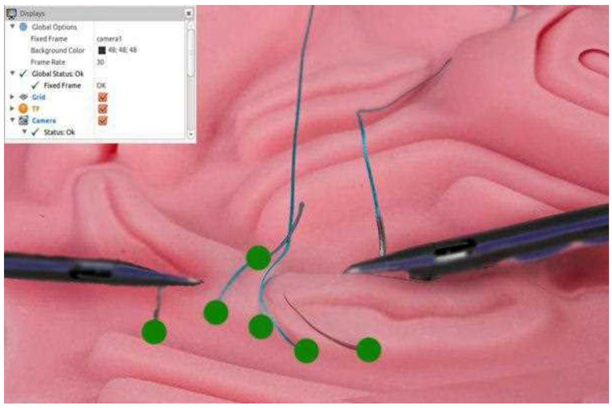

Fig. 2. Integrated model in Gazebo

We used a custom manipulator to interact with the soft tissue to observe the interaction results. The interaction simulation took around 5 seconds for 1 real time second (time step of 5ms, 10000 mesh nodes) using Haswell-E i7-5820K. The complete soft tissue model therefore was successfully implemented for

Gazebo, although the performance should be improved further.

6. Conclusions

We developed and implemented a new soft tissue Gazebo plugin with an emphasis on performance and have achieved an acceptable level of usability. The plugin demonstrates realistic interaction with soft tissue. As a future work, we consider to improve performance with a GPU-based approach and to allow for complex elastic interactions' simulation. We intend to turn this plugin into a basis for long-term developments in robot surgery automation.

Acknowledgements

This work was supported by the Russian Foundation for Basic Research and the Government of the Republic of Tatarstan, project ID 18-48-160037. Part of the work was performed according to the Russian Government Program of Competitive Growth of Kazan Federal University.

References

1. A. Sagitov, T. Tsoy, H. Li, E. Magid. Automated open wound suturing: detection and planning algorithm. *J. of Robotics, Networking and Artificial Life*, Volume 5, Issue 2, September 2018, pp. 144 - 148
2. N. Koenig and A. Howard, Design and use paradigms for gazebo, an open-source multirobot simulator, in *Proc. of Conf. on Intelligent Robots and Systems*, vol. 3 (2004).
3. Y. Duan, W. Huang, H. Chang, W. Chen, J. Zhou, S.K. Teo, Y.Su, C.K. Chui, S. Chang, Volume preserved mass-spring model with novel constraints for soft tissue deformation, in *IEEE J. Biomed. Health Inform.*20 *(1),* (2016), pp. 268–280.
4. C. Yang, S. Li, Y. Lan, L. Wang, A. Hao, H. Qin, Coupling time-varying modal analysis and FEM for real-time cutting simulation of objects with multi-material sub-domains, in *Comput. Aided Geom.* Des.43, (2016), pp. 53–67.
5. S. Cotin, H. Delingette, N. Ayache, Real-time elastic deformations of soft tissues for surgery simulation, *IEEE Trans. Vis. Comput. Graphics,* 5 (1), (1999), pp. 62–73.
6. D. Weber, J. Mueller-Roemer, C. Altenhofen, A. Stork, D.W. Fellner, Deformation simulation using cubic finite elements and efficient p-multigrid methods, in *Comput. Graphics* UK 53, (2015), pp. 185–195.
7. J. Huang, X. Liu, H. Bao., B. Guo, H.Y. Shumb, An efficient large deformation method using domain decomposition, in *Comput. Graphics* UK30 (6), (2006), pp. 927–935.
8. Y. Payan, Soft Tissue Biomechanical Modeling for Computer Assisted Surgery, vol. 11. (Springer*,* Berlin, 2012).
9. S. Xu, P. X. Liu, H. Zhang, A nonlinear viscoelastic tensor-mass visual model for surgery simulation, in *IEEE Trans. Instrum.* Meas.60, (2011), pp. 14–20.
10. R. Plantefève, I. Peterlik, N. Haouchine, S. Cotin, Patient-specific biomechanical modeling for guidance during minimally-invasive hepatic surgery, in *Ann. Biomed.* Eng.44, (2016), pp. 139–153.
11. G.Y. Zhang, A. Wittek, G.R. Joldes, X. Jin, K. Miller, A three-dimensional nonlinear meshfree algorithm for simulating mechanical responses of soft tissue, in *Eng. Anal. Bound.* Elem.42, (2014), pp. 60–66.
12. V.P. Nguyen, T. Rabczuk, S. Bordas, M. Duflot, Meshless methods: a review and computer implementation aspects, in *Math. Comput. Simul.*79 (3), (2008), pp. 763–813.
13. K. Miller, G. Joldes, D. Lance and A. Wittek, Total Lagrangian explicit dynamics finite element algorithm for computing soft tissue deformation, in *Int. J. Numer. Methods Biomed.* Eng.23 (2), (2007), pp. 121–134.
14. F. Goulette, Z.-W. Chen, Fast computation of soft tissue deformations in real-time simulation with Hyper-Elastic Mass Links, in *Comput. Methods Appl. Mech.* Eng.295, (2015), pp. 18–38.
15. J. Zhang, Y. Zhong, and C. Gu, Ellipsoid bounding region-based ChainMail algorithm for soft tissue deformation in surgical simulation, in *International Journal on Interactive Design and Manufacturing*, vol. 12, no. 3, (2018), pp. 903-918.
16. P.Wang, A.A. Becker, I.A. Jones, A.T. Glover. S.D. Benford. C.M. Greenhalgh, M. Vloeberghs: Virtual reality simulation of surgery with haptic feedback based on the boundary element method, in *Comput. Struct*. 85 (7–8), (2007), pp. 331–339.
17. S.F. Johnsen, Z.A. Taylor, M.J. Clarkson, J. Hipwell, M. Modat, B. Eiben, L. Han, Y. Hu, T. Mertzanidou, D.J. Hawkes, S. Ourselin, NiftySim: a GPU-based nonlinear finite element package for simulation of soft tissue biomechanics, in *Int. J. Comput. Assist. Radiol. Surg.10* (7), (2015), pp. 1077–1095.
18. F. Faure, C. Duriez, H. Delingette, J. Allard, B. Gilles, S. Marchesseau, H. Talbot, H. Courtecuisse, G. Bousquet, I. Peterlik, S. Cotin, SOFA: A Multi-Model Framework for Interactive Physical Simulation, Soft Tissue Biomechanical Modeling for Computer Assisted Surgery, 11, Studies in *Mechanobiology, Tissue Engineering and Biomaterials,* (Springer, 2012), pp. 283-321.
19. A. Sagitov, H. Li, E. Magid. Toward automated open wound suturing using haptic feedback: detecting wounds and planning the suture. *Int. Conf. on Artificial Life and Robotics*, (2018), pp. 208-211.

Experiences of Robotics students in Machine Vision course being taught in a foreign language: comprehension, self-efficiency, and active learning strategies improvement

Tatyana Tsoy, Artur Sagitov, Evgeni Magid

Laboratory of Intelligent Robotic Systems (LIRS), Intelligent Robotics Department, Higher Institute of Information Technology and Intelligent Systems, Kazan Federal University, 35 Kremlyovskaya street, Kazan, 420008, Russia

E-mail: {tt, sagitov, magid}@it.kfu.ru

www.kpfu.ru/robolab.html

Abstract

Crisis in Russia in 1990s significantly decreased engineering education quality. To catch up with developed countries, a novel 2-year master program in Intelligent Robotics was designed and implemented at Kazan Federal University based on world leading universities' experience. The program targets to educate competitive specialists with competences that are required by world labor market. To follow students' progress in core robotics courses we conducted surveys. The paper reports survey analysis that was conducted in Machine Vision course and covered such issues as English language comprehension, self-efficiency, and active learning strategies.

Keywords: Engineering education, robotics education, postgraduate studies, master program, Machine Vision, motivation.

1. Introduction

We are evidencing comprehensive digitalization and automation of all aspects of our daily life, including healthcare[1], economics[2], etc. Social and demographic challenges that developed countries are recently facing force us to develop technologies at accelerated pace in order to replace human labor with robotic systems (RS). Consequently, world demand for specialists in robotics is growing rapidly and creating new challenges for up-to-date engineering education.

According to Robotics Russian Association, robot density in 2014 was 66 RS per 10 000 workers while in developed countries the automation level is significantly higher, e.g., 478 RS in Korea, 314 RS in Japan, 292 RS in Germany, 164 RS in US[3]. To catch up with developed countries Russian government started long-term investments into engineering education and establish new higher education programs.

As a result of these efforts, a new master program in Intelligent Robotics was launched in September 2017 at Higher Institute of Information Technology and Intelligent Systems of Kazan Federal University, and its syllabus was designed to consider local employers' requirements[4]. After establishing the pilot program, we continue conducting student feedback surveys about our courses and to update the courses aiming for further effectiveness improvement. This paper presents analysis of Machine Vision course survey that was conducted in the (first) Fall semester of 2017-2018 academic year.

2. Postgraduate robotics studies

The master program targets to educate highly skilled experts in the field of Intelligent Robotics using modern set of robotic equipment that includes various types of robots and broad selection of sensors and cameras. Along with technical skills in robotics we provide postgraduate students with such courses as Social Robotics and Communication Skills as serious robotics projects are always a team work and soft skills are a must in order to successfully implement a project.

Before opening the master program in Intelligent Robotics at KFU, we had started our surveys among bachelor students in order to understand motivation, evaluate environment of teaching in English and an opportunity to allow complicated material explanations in Russian considering the fact that all students were Russian native-speakers[4]. Further to have a regular update and improve our master program based on feedback from students we continued conducting surveys with students that are enrolled in Intelligent Robotics master program on the core courses of our syllabus such as Introduction to Robotics[8], Sensors and Sensing, Robot Operating System (ROS)[5] and Machine Vision.

3. Curriculum of Computer Vision Course

Machine Vision is one of the essential disciplines in the master program curriculum as visual feedback is very important for robots especially in industry where wide range of visual systems is applied[6]. In the last decade vision systems become more available due to technological improvements and progressively decreasing costs, which provided more facilities for developing new applications and using robots in production. In our curriculum we take into account that vision-assisted robots taking over a number of manufacturing jobs such as quality control, precision manufacturing and product sorting. Additionally, they also play a significant role human-robot collaboration and multi-agent robotics.

According to survey results no respondent studied Machine Vision subject before entering the program, either at educational organizations or by self-studying. Before launching the program, we anticipated this fact and designed Machine Vision curriculum assuming that students do not possess any knowledge in this field. Thus, the curriculum consisted of the following topics:

1. *Image formation*: optics, cameras, and representations.
2. *Image transformations*: sampling, color spaces, convolutions, linear filters, and histograms.
3. *Nonlinear filtering*: median filter, Fourier and Laplace transforms, frequency analysis, and transfer function.
4. *Feature Detectors*: feature points and matching, gradient, edge and corner detection, Harris detector, Canny and Sobel filters.
5. *Stereovision:* calibration, epipolar geometry, homography, stereo disparity, structure from motion, and optical flow.
6. *Recognition*: Machine learning in computer vision, neural networks, and image categorization.

By completing the course successfully, the participant was expected to possess the following skills:

- understand theoretical and practical aspects of image manipulation, formation, measurement, and analysis;
- implement methods of image matching and alignment;
- determine geometric relations between 2D images and the 3D environment;
- know and able to apply object and scene recognition, image categorization;
- design architecture of computer vision applications.

4. Research Method and Analysis

The surveys assist us to analyze attitude, motivation, and challenges that students faced during Machine Vision course in the first semester of the master program, which lasted 1.5 astronomical hours, and was run 18 weeks. We conducted initial survey after the first class and a final survey in the end of the course before a final test. The initial survey included 49 questions that referred to students' expectations from the course and previous experience, while the final survey included 39 questions and questioned about new in-class experience. A number of identical questions in both surveys allowed observing dynamics of English language and motivation. The surveys were conducted in Russian via on-line Google forms. The questions contained statements, open-ended and multiply choice questions. Each statement was presented on a 5-point scale with optional answers: strongly disagree (SD), disagree (D), no opinion (NO), agree (A) and strongly agree (SA), which appear along X-axis in Fig. 1-6. Y-axis of Fig. 1-6 indicate percentage of the respondents that selected the corresponding options. We applied the same research method that we had used in our previous papers[4,5,7,8]. For the analysis we selected 9 respondents with technical background who participated in both initial and final surveys.

4.1. *English language comprehension*

Machine Vision classes were taught in English to Russian native speakers considering that students had some history of studying English language at school and university. English language comprehension was assumed the main milestone for effective teaching, however, the students did not meet significant difficulties with receiving information in English[4,5]. As Fig.1 demonstrates, the tendency of using English with less anxiety was positively progressive by the end of the course. A special language environment was created for the students to feel comfortable and perceive material more effectively. Figure 2 depicts a reflection on the opportunity to ask for explanations in Russian if a student could not understand the material in English, and the tendency was positive toward the course end.

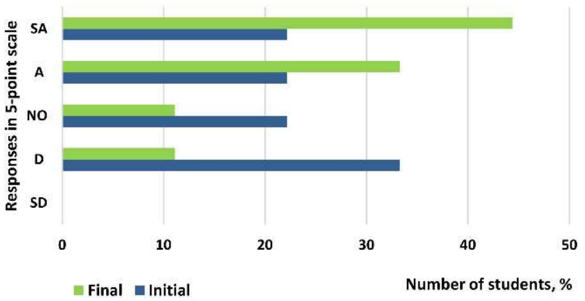

Fig. 1 I do not worry if I make mistakes while speaking English during classes.

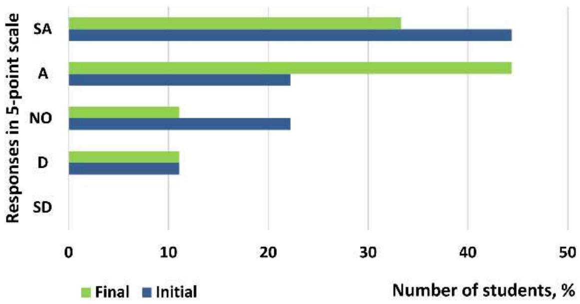

Fig. 2 I am not afraid if I do not understand when the teacher speaks English, because I can ask for explanations in Russian.

4.2. *Self-efficiency*

In the end of the course majority of students (11,1% SA and 44,4% A vs. 44,4% NO) considered the course was the most difficult for them in comparison with other courses. Even though 55,5% of the students considered it to be the most difficult one in both initial and final surveys, 88,8% of them disagreed with the statement "I think, I will not be able to learn the subject no matter how much efforts I put". Moreover, responding "If a lecture content is difficult I would avoid learning the material" statement, the students replied 66,6% SD and 33,3% D in the beginning of the course and 77% SD, 11,1% NO, 11,1% A by the end of the course, which supports the conclusion that despite difficulty of the course more students shifted to be more self-efficient while learning the material. Figure 3 shows that during the course 77,7% of the students thought that they will pass the final examinations successfully.

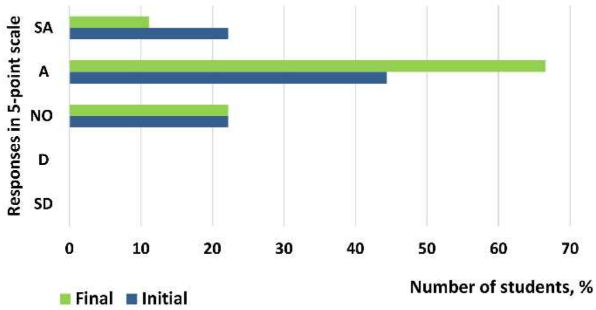

Fig. 3 I am sure I will successfully pass Machine Vision course.

4.3. *Active learning strategies*

During the course the students not only passively digested the material but also actively learned it using extra sources (Fig. 4). One of the motivation components to study the subject could be related to students' plans after graduation as it is shown in Fig. 5: 100% of the students (66,6% SA, 33,3%A) realized the importance of studying the subject since they believed that they are going to use this knowledge in a future job.

Moreover, 6 out of 9 respondents would like to connect their future with robotics, while 3 did not decide yet. However, even with that high motivation the course was not an easy one for the respondents as 77,7% (66,6% SD and 11,1% D) disagreed with the statement that they would study the course independently rather than participate in the classes (Fig. 6), which adds credits to self-efficiency where students considered the subject the most difficult among other courses.

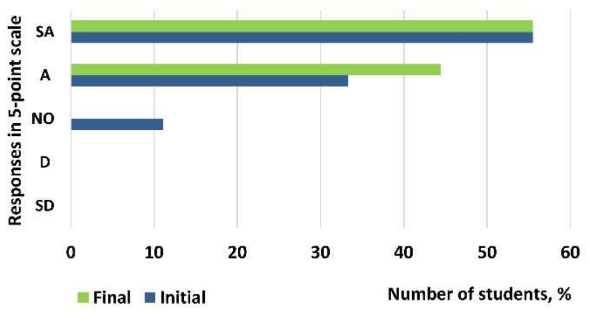

Fig. 4 If I do not understand new material of Machine Vision course, I shall try to find extra sources myself to understand it.

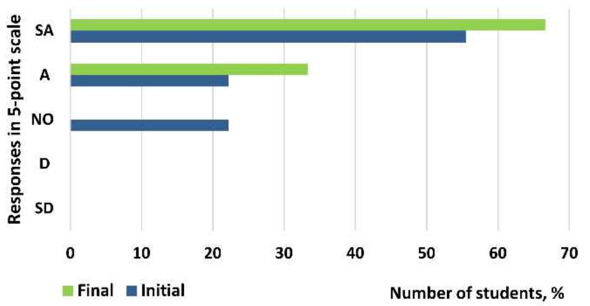

Fig. 5 I think that studying Machine Vision course is important, because I shall use this knowledge in my future job

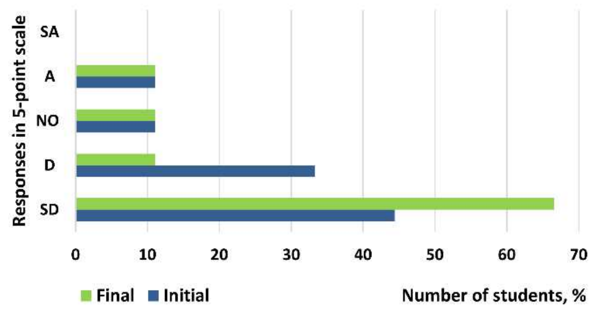

Fig. 6 If I had an opportunity not to take Machine Vision class I would have better learned it by myself.

5. Conclusions

Analysis of surveys among postgraduate students of Machine Vision course showed positive results in the course material comprehension in English while having an opportunity to ask for additional explanations in Russian. Despite the fact that the course was evaluated as the most difficult one among others, the students applied significant self-efficiency to learn the subject and used active learning strategies while possessing high motivation to study the course because the vast majority of the respondents associated their future career with robotics. Next we plan to develop new surveys in order to evaluate master program in Intelligent Robotics courses content comprehension along with conducting continuous surveys to track students' needs and to follow the robotics area global market employers' requirements.

Acknowledgements

This work was supported by the Vladimir Potanin Foundation, project ID GK180000602. Part of the work was performed according to the Russian Government Program of Competitive Growth of Kazan Federal University.

References

1. A. J. Aljaaf, C. Mallucci, D. Al-Jumeily, A. Hussain, M. Alloghani, J. Mustafina. A Study of Data Classification and Selection Techniques to Diagnose. *Applications of Big Data Analytics: Trends, Issues, and Challenges*, Springer (2018), p 121-134.
2. R. C. Brown. Made in China 2025: Implications of Robotization and Digitalization on MNC Labor Supply Chains and Workers' Labor Rights in China. *Tsinghua China L. Rev*. (2016), 9, 186.
3. Russian National Association of Robotics Market Participants. Analytical Research: World Market of Robotics (January, 2016). http://www.robotunion.ru/ru/
4. T. Tsoy, L. Sabirova, & E. Magid, (2017). Towards Effective Interactive Teaching and Learning Strategies in Robotics Education. *IEEE Int. Conf. on Developments in eSystems Engineering* (2017), pp. 267-272.
5. T. Tsoy, L. Sabirova, & E. Magid. Effective robotics education: Surveying Master Program Students Experiences in Robot Operating System Course. *IEEE Int. Conf. on Developments in eSystems Engineering* (2018).
6. L. Pérez, Í. Rodríguez, Í., N. Rodríguez, R. Usamentiaga, R., & D. García, D. (2016). Robot guidance using machine vision techniques in industrial environments: A comparative review. *Sensors*, 16(3), 335.
7. T. Tsoy, L. Sabirova, M. Abramsky, E. Magid. Establishing Effective "Teaching for Robotics: a comparison study of Bachelor students participated in Introduction to Robotics course". *Int. Conf. on Artificial ALife and Robotics*, pp. 212-215, 2018.
8. T. Tsoy, L. Sabirova, E. Magid. "Effective robotics education: Surveying Master Program Students Experiences in Introduction to Robotics Course", *Int. Conf. on Mechanical, System and Control Engineering*, vol. 220, 2018.

Pilot Virtual Experiments on ArUco and AprilTag Systems Comparison for Fiducial Marker Rotation Resistance

Aufar Zakiev, Ksenia Shabalina, Evgeni Magid
Laboratory of Intelligent Robotic Systems (LIRS), Intelligent Robotics Department, Higher Institute of Information Technology and Intelligent Systems, Kazan Federal University, 35 Kremlyovskaya street, Kazan, 420008, Russia
E-mail: zaufar@it.kfu.ru, ks.shabalina@it.kfu.ru, magid@it.kfu.ru
http://kpfu.ru/robolab.html

Abstract

There exists a large number of fiducial marker system types and both researchers and industry have difficulties to select among this variety a single system that could provide optimal behavior for a particular task. This paper presents design and results of pilot virtual experiments that were conducted in order to compare a performance of two marker systems, ArUco and AprilTag. Experiments were designed to estimate and compare marker systems resistance to rotation with regard to different principal axes in 3D space. Pilot experiment design eliminates influence of external environment, including light conditions, camera resolution, sensor noise, distance between camera and marker, etc. Experiments were implemented in ROS/Gazebo environment. In total over 300,000 virtual experiments were performed and analyzed in order to collect statistically significant data amount.

Keywords: robotics, fiducial marker system, recognition algorithms, experimental comparison, ROS, Gazebo.

1. Introduction

Fiducial marker systems (FMS) are systems of planar graphical markers that are designed to be detected by corresponding machine vision algorithms. FMS are widely used in physics, medicine, robotics, augmented reality, metrology, robotics, etc. Broad range of robotic tasks including navigation[1], localization[2], mapping[3] and camera calibration[4] use FMS as a main element. Our long-term goal is to calibrate several Russian robots, including humanoid AR-601 robot (Fig. 1), and FMS usage is way to accomplish this task in automated manner. Modern FMSs have different designs and are developed for various purposes: each of them has its own advantages and drawbacks. Therefore, a suitable FMS choice requires to compared systems for various criteria, paying attention to criteria that are important for a particular task of interest. Our goal is to auto calibrate robot cameras: markers are placed on the humanoid robot's manipulator (e.g., palm) and the humanoid observes this marker in order to estimate and programmatically eliminate camera distortions. For this task the FMS should be resistive to manipulator rotations and partial occlusions being caused by marker overlap with various objects (e.g., robot's parts).

Early approach to systematically compare the FMSs was conducted through multiple manual experiments in order to estimate different markers' resistance to rotation and overlapping (both systematic and arbitrary). However, this approach has a number of significant disadvantages, which make manual experiment results hardly reproducible:

- Overwhelming time consumption. Multiple iterations are required in order to collect statistically significant amount of data.
- Complexity of experiments' fairness control. Multiple environment conditions, e.g., inclination angle, marker position with regard to a camera, lighting conditions, etc. are hard to monitor and control.
- Limited hardware choice. Hardware has unavoidable noises and often do not possess desired properties, e.g., camera resolution, lens distortion level, optical sensor sensitivity, etc.

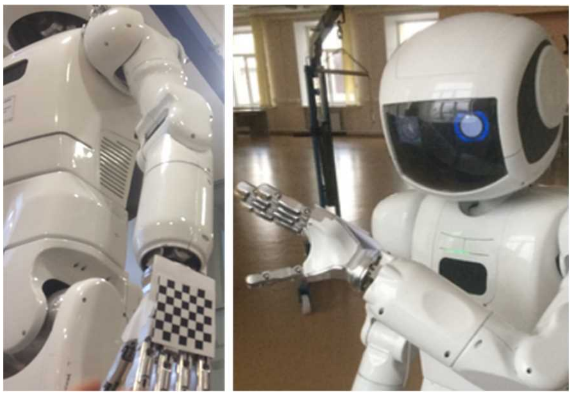

Fig. 1. Fiducial marker placement on robot manipulator (left); marker observation by robot (right).

This paper presents virtual experiments design and ArUco[5] and AprilTag[3] systems comparison for rotation resistance results. Section 2 presents previous research results. Section 3 briefly describes ROS/Gazebo virtual environment used for experiments. Section 4 is dedicated to experiment setup; Section 5 shows experiment results. Finally, Section 6 concludes our work.

2. Related Work

As it was mentioned, in our previous research[6, 7] we had conducted manual experiments with several fiducial marker systems. We had chosen AprilTag, ARTag and CALTag[8] for comparison and designed our experiments to validate their resistance to rotations, systematic occlusions and arbitrary overlaps. These experiments were conducted using Genius FaceCam 1000X web-camera first to get data about FMS applicability on low-cost equipment. Then experiments were continued with AR-601 humanoid robot, using its integrated Basler acA640-90gc cameras. The experiment results analysis revealed that AprilTag and ARTag are resistive to marker rotations, however, are very sensitive to marker edge overlaps. This could be explained by the detection algorithm sequence: one of the first steps is edge detection, and if it fails, the entire detection process stops. On the opposite, CALTag demonstrated high detection rate on various rotation angles and different occlusions.

3. ROS/Gazebo environment

Robot Operating System (ROS) is a fast-growing framework for robotics development. Its architecture consists of *nodes* and *topics* between them for communication. Such distributed structure allows creating various data and command flow schemas, making sensor data analysis and robot motion control easy. ROS is distributed in the form of minimally functional units called *packages.*

The following FMS have their detection algorithms encapsulated in ROS packages: AprilTag, ArUco, Alvar[9] and ChiliTag[10]. Actually, ArUco is universal detection library, that could be used to detect ArUco markers and, in addition, AprilTag, ARTag[11,12], ARToolKitPlus[13], and ARToolKitPlusBCH (Binary Coded Hexadecimal). Gazebo is 3D-simulator that could be integrated with ROS as a tool to visualize simulations and apply real world properties, including light and collision processing to the objects within the simulation.

4. Experiment Setup

We created two robots in virtual environment: a robot-performer with marker and R2D2-like robot with a camera. The robot-performer is designed to modify a marker appearance between distinct detections: it rotates the marker for a predefined angle within user-defined angle limits (the scheme is shown in Fig. 2). The robot with the camera simulates a static camera stand (Fig. 3). Numerous experiment parameters were kept constant through all the experiments (see Table 1) in order to eliminate their influence on comparison results.

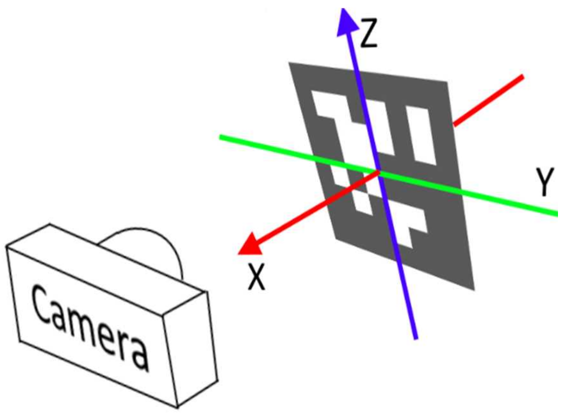

Fig. 2. Virtual experiment rotation scheme.

Table 1. Virtual experiment constant parameters.

Parameter	Value
Camera resolution	640 x 480 px.
Camera distortion level	0 (ideal lens)
Camera noise level	0 (ideal device)
Distance	2 m.
Rotation range (X-axis)	[-180˚; +180˚)
Rotation range (Z-axis)	[-90˚; +90˚]
Marker side size	0.4 m
Light angle of incidence	45˚
Light spectrum	White light
Light conditions	Uniform at whole marker area

Rotation experiments flow works as follows:

1. The robots spawn at constant distance from each other. Initially, the marker inclination angle around a (particular) rotation axis is zero.
2. The logger waits for a half of second for the marker detection.
3. The logger logs an inclination angle and a result of detection procedure.
4. The robot-performer rotates the marker for 1 degree around a user-defined axis (X-axis or Z-axis).
5. If the rotation limit is not reached, the algorithm goes to step #2; else the experiment ends.

The logger logs all results twice: first output goes to a console, second goes to a file with proper name including tag family (e.g., ArUco), tag type (e.g., 25h7), tag ID, the distance to the camera and the date of the experiment.

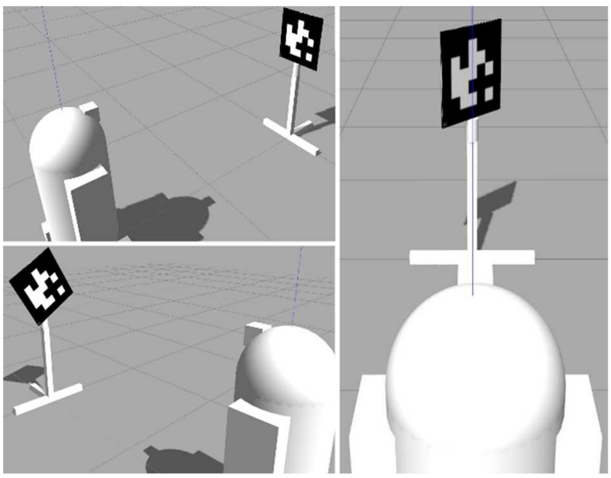

Fig. 3. Virtual experiment design: initial marker position (top left); rotated 30 degrees around X-axis (bottom left); rotated 45 degrees around Z-axis (right).

5. Experimental Results

All markers of a selected type are tested to collect statistically significant amount of data: 100 ArUco (type is 25h7) markers and 242 AprilTag (type is 25h7) markers. Markers of this type have 25 encoding pixels and Hamming distance between any of them is equal or more than 7. Equal marker types eliminated difference between FMS encoding properties and encoded data amount. Experiments were conducted with each distinct marker twice to collect reliable data about each detection angle. Experiment results are presented in Table 2.

Table 2. Average detection rate through all the markers in rotation experiments by FMS type and rotation axis.

Marker family and type	Rotation axis x	Rotation axis z
AprilTag – 25h7	99.94%	69.96%
ArUco – 25h7	99.97%	86.07%

The experiment results allow concluding that AprilTag family markers are practically insensitive to X-axis rotations; however, ArUco family markers have significantly better resistance to Z-axis rotations. In addition, failed detections distributions for each marker family are presented in Fig. 4 and Fig. 5.

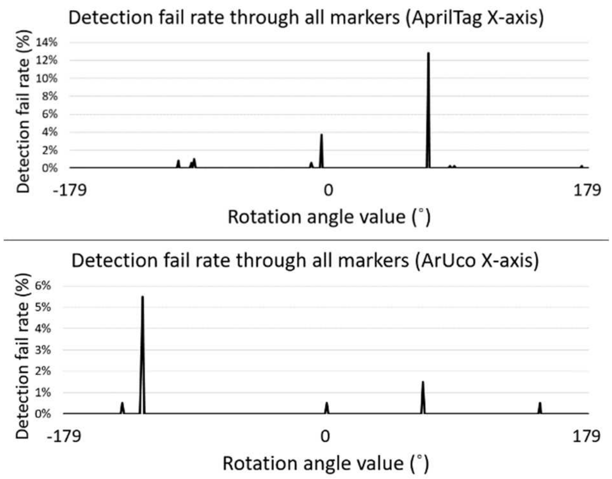

Fig. 4. Virtual experiment results for X-axis rotation: detection rates through all markers depending on rotation angle for AprilTag (top) and ArUco (bottom).

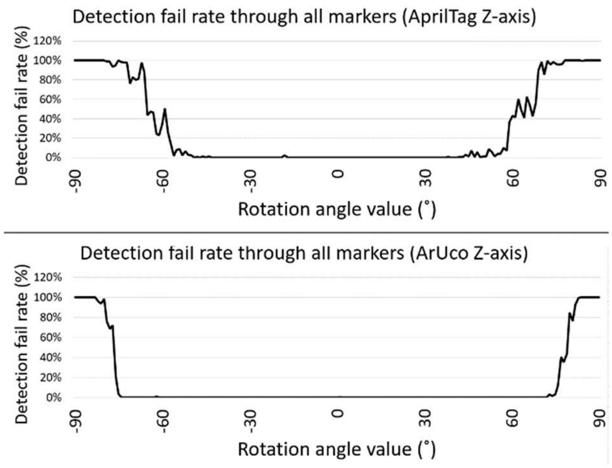

Fig. 5. Virtual experiment results for Z-axis rotation: detection rates through all markers depending on rotation angle for AprilTag (top) and ArUco (bottom).

Z-axis diagrams show a rather predictive FMS behavior: increasing rotation angle decreases marker area that is visible to the camera, leading to unsuccessful detections. Both FMSs showed highest resistance to rotations around X-axis: nearly ideal detection rate has been logged for all rotation angles.

6. Conclusions and Future Work

This paper presents a set of pilot experiments with AprilTag and ArUco marker systems in virtual environment and their performance comparison for rotations. The created virtual environment could be used as a framework for further comparative research because new FMS addition to the project is easy. In addition, the virtual environment experiments could be easily distributed for multiple cores: this gives a chance to qualitatively peer-review and reproduce these experiments without limitations. Our future work concentrates on different FMS comparison for their resistance to occlusions (both systematic and arbitrary) and exploring dependence of maximum detection distance on camera resolution.

Acknowledgements

This work was supported by the Russian Foundation for Basic Research (RFBR), project ID 18-58-45017. Part of the work was performed according to the Russian Government Program of Competitive Growth of Kazan Federal University.

References

1. R. Kuriya, T. Tsujimura and K. Izumi, Augmented reality robot navigation using infrared marker, in *Proc. 24th IEEE Int. Symposium on Robot and Human Interactive Communication*, (2015), pp. 450-455.
2. V. Dhiman, J. Ryde and J. J. Corso, Mutual localization: Two camera relative 6-DOF pose estimation from reciprocal fiducial observation, in *Proc. IEEE/RSJ Int. Conf. on Intelligent Robots and Systems*, (2013), pp. 1347-1354.
3. E. Olson, AprilTag: A robust and flexible visual fiducial system, in *Proc. IEEE Int. Conf. on Robotics and Automation*, (2011), pp. 3400-3407.
4. M. Fiala, Comparing ARTag and ARToolKit Plus Fiducial Marker Systems, in *Proc. IEEE Int. Workshop on Haptic Audio Visual Environments and their Applications*, (2005), pp. 148-153.
5. F. J. Romero-Ramirez, R. Muñoz-Salinas and R. Medina-Carnicer, Speeded Up Detection of Squared Fiducial Markers, in *Image and Vision Computing* (2018).
6. A. Sagitov, K. Shabalina, R. Lavrenov and E. Magid. Comparing fiducial marker systems in the presence of occlusion, in *Proc. Int. Conf. on Mechanical, System and Control Engineering*, (2017), pp. 377-382.
7. K. Shabalina, A. Sagitov, L. Sabirova, H. Li, and E. Magid. ARTag, AprilTag and CALTag Fiducial Systems Comparison in a Presence of Partial Rotation: Manual and Automated Approaches, *Lecture Notes in Electrical Engineering*.
8. B. Atcheson, F. Heide, W. Heidrich. CALTag: High Precision Fiducial Markers for Camera Calibration, in *Vision, Modeling, and Visualization Workshop*, vol.10, (2010), pp. 41-48.
9. C. Woodward, S. Valli, P. Honkamaa and M. Hakkarainen, Wireless 3D CAD viewing on a PDA device in *Proc. 2nd Asian International Mobile Computing* (Langkawi, Malaysia, 2002), pp. 83-87.
10. Q. Bonnard, S. Lemaignan, G. Zufferey, A. Mazzei, S. Cuendet, N. Li and P. Dillenbourg, Chilitags: Robust Fiducial Markers for Augmented Reality (Switzerland, 2013).
11. M. Hirzer, Marker Detection for Augmented Reality Applications, *Seminar/Project Image Analysis Graz*, (2008), pp. 1-25.
12. M. Fiala, ARTag, a fiducial marker system using digital techniques, *Computer Vision and Pattern Recognition*, vol.2, (2005), pp. 590-596.
13. D. Wagner and D. Schmalstieg, Artoolkitplus for pose tracking on mobile devices (2007), pp. 139-146.

Determining the Key Factors of Michinoeki in Yamaguchi Area

Minoru Kumano
Faculty of Regional Innovation, University of Miyazaki
1-1 Gakuendai-Nishi, Miyazaki, 889-2192 Japan
E-mail: kumano@cc.miyazaki-u.ac.jp

Tsutomu Ito
Hamura Plant, Hino Motors, Ltd.,
5-2-1 Midorigaoka, Hamura City, Tokyo, 205-8601, Japan
E-mail: fw.eldorado.500cuin@gmail.com

Takao Ito
Graduate School of Engineering, Hiroshima University
1-4-1 Kagamiyama, Higashi Hiroshima, 739-7527
E-mail: itotakao@hiroshima-u.ac.jp

Toru Hiraoka
Department of Information Systems, University of Nagasaki
1-1-1, Manabino Nagayo, Nishisonogi, Nagasaki, 815-2195, Japan
E-mail: hiraoka@sun.ac.jp

Hirofumi Nonaka
Department of Information Management System Engineering, Nagaoka University of Technology
1603-1, Kamitomioka, Nagaoka, Niigata, 940-2188, Japan
E-mail: nonaka@kjs.nagaokaut.ac.jp

Abstract

It is considered as the most urgent issues for Michinoeki to find the key determinants and to measure its efficiency. This paper proposed a new approach with two steps: to calculate the efficiency using DEA model after determining the relevant factors using regression model. The data are collected from Yamaguchi area, because Yamaguchi is the birthplace of Michinoeki in Japan. The contribution of this paper are: 1) identified the key factors of Michinoeki in Yamaguchi area, and 2) calculated the efficiencies of the Michinoeki, and 3) proposed a four cell matrix model to make judge of the position of Michinoeki for their further development. Based on the findings, the managerial implications are discussed, the study limitations are identified and directions for further research are suggested.

Keywords: DEA model, Four cell matrix model, Michinoeki, Efficiency.

1. Introduction

A plethora of studies of Michinoeki from the viewpoints of break function, information dispatch function, regional cooperation function, and disaster prevention function have been published in the past decades. Based on our investigation, the studies associated with efficiency calculation to improve their management quality are still sparse. This paper proposes a new approach with two steps: to calculate the efficiency using DEA model after determining the relevant factors using multivariate regression model. The data are collected from the Michinoeki in Yamaguchi area, because Yamaguchi area is the exact birthplace of Michinoeki in Japan. The contribution of this paper are: 1) identified the key factors of Michinoeki in Yamaguchi area, and 2) calculated the efficiencies of the Michinoeki, and 3) proposed a four cell matrix model to make judge of the position of Michinoeki for their further development. Based on the findings, the managerial implications are discussed, the study limitations are identified and directions for future research are suggested.

This paper is structured as follows: Section 2 introduces the background of this research. In section 3, the paper explicates data collection and the models of multivariate regression model and DEA model to identify the key factors and efficiency of Michinoeki using selected variables. Section 4 shows the results and discusses our findings. The conclusions and directions for future research and managerial implications are proffered in the final section.

2. Background

Michinoeki is well-known for its four-function model. Today Michinoeki plays important roles in regional economic revitalization in Japan. Recently many studies of Michinoeki have been published. Regional economic revitalization is main part of Abenomics [1]. Mitsuhashi analyzed the economic background of Michinoeki [2]. Ogata et al. explained the relationship between Michinoeki and regional revitalization based on the viewpoint of business model [3]. Hiraoka et al. discussed the relationship between the number of customers and information associated with agriculture, forestry, and fisheries of Michinoeki [4]. Furthermore, Kumano et al. discovered successful determinants of Michinoeki in Chugoku area using regression model [5]. All of these researches show that it is becoming an important issue to calculate efficiency to improve the quality of Michinoeki. Thus to find the key determinants and to measure its efficiency are considered as the most urgent tasks for Michinoeki. This paper will focus on the discovering the determinants, and calculating the efficiency of Michinoeki in Yamaguchi area. The number of Michinoeki reached 23 as of July 21, 2017. They are shown in Table 1.

Table 1 Michinoeki List in Yamaguchi Area.

1	Abu Town	13	Niho no Sato
2	Hagi Okan	14	Hagi Seamart
3	Asahi	15	Ganjoju Onsen
4	Aio	16	Uribo no Sato Katamata
5	Yutori Park Tamagawa	17	Hotaru Kaido Nishi no Ichi
6	Sazanseto Towa	18	Kirara Ajisu
7	Kikugawa	19	Hagi Sansan Sammi
8	Happiness Fukue	20	Kitaura Kaido Hohoku
9	Chomonkyo	21	Solene Shunan
10	Pure Line Nishiki	22	Kaminoseki Kaikyo
11	Ofuku	23	Shiosai Ichiba Houfu
12	Mitou	24	Senzakitchen*

*Semzakitchen has been opened in 2018 fiscal year.

The geographic distribution map of Michinoeki in Yamaguchi area is shown as in Figure 1.

Fig. 1 Geographic distribution map of Michinoeki.

3. Data Collection and Models

The data in 2015 used in this paper are collected from the database of the headquarter of Michinoeki to calculate the efficiency of Michinoeki in Yamaguchi area. Under the advices from the experts of Michinoeki, twelve variables are selected as the determinants of the Michinoeki in this paper. They are: square meters of land space (SMLS), weekdays' traffic near the station (WTNS), holidays' traffic near the station (HTNS), operating cost (OC), total parking number (TPN), total number of the restroom (TNR), square meters of free rest place (SMFRP), number of the selling items (NSI), number of local products items (NLPI), number of the registered farmers (NRF), square meters of facilities space (SMFS) and population of the city located (PCL). The SMLS and OC could be considered as the determinants of variables of information dispatch function, the WTNS, HTNS, NSI, NLPI, PCL, and NRF are designed as the indexes of regional cooperation function, the TPN, TNR, SMFRP and SMFS will play important role in break function and disaster prevention function. Sales revenue and number of purchasers are selected as the performance of Michinoeki. Thus, this leads to the formation of the following regression equation:

$$y = a_1 SMLS + a_2 WTNS + a_3 HTNS + a_4 OC + a_5 TPN + a_6 TNR + a_7 SMFRP + a_8 NSI + a_9 NLPI + a_{10} NRF + a_{11} SMFS + a_{12} PCL + \varepsilon \quad (1)$$

After determining the key factors of the Michinoeki, the efficiency will be calculated using the following DEA model [6-7].

$$\max \quad \theta = \frac{\sum_r^s u_r y_{rj}}{\sum_{i=1}^m v_i x_{ij}} \ (j = 1, 2, \dots, n) \quad (2)$$

Subject to

$$\frac{\sum_r^s u_r y_{rj}}{\sum_{i=1}^m v_i x_{ij}} \le 1 \ (j = 1, 2, \dots, n) \quad (3)$$

$$u_r \ge 0 \ (r = 1,2, \dots, s) \quad (4)$$

$$v_i \ge 0 \ (i = 1,2, \dots, m) \quad (5)$$

4. Calculation and Discussions

The relationship between the twelve variables and sales revenue and the number of purchasers are calculated respectively. The key factors are finally determined using backward delamination method. The results are shown as in Table 2.

Table 2 Results of the regression models of sales and number of the purchasers.

	Models			
	Sales Revenue		Number of the Purchasers	
	Standardized coefficient	Probability	Standardized coefficient	Probability
SMLS	-	-	-	-
WTNS	-	-	-	-
OC	-	-	-0.3402	0.0436
TPN	0.6486	0	0.7271	0.0004
TNR	-	-	-	-
SMFRP	0.2412	0.0128	-	-
NSI	-	-	-1.2853	0.0107
NLPI	-	-	1.4318	0.0059
NRF	-	-	-	-
SMFS	0.4165	0.0128	0.7997	0
PCL	0.548	0.0002	0.1327	0.0506
Intercept	0	0.0011	0	0.0006
R^2		0.94610		0.97644
multiple R^2		0.97268		0.0.98815
Adjusted R^2		0.90969		0.96604
AIC		445.97		207.33
DW Ratio		2.2853		2.6311

The determinants of those two models are different. The adjusted R square of sales revenue and number of purchases are 0.9069 and 0.96604 respectively. Four variables and six variables are significant statistically. The four variables in the model of sales revenue are: TPN, SMSRP, SMFS, and PCL, and the six variables of number of purchasers are: OC, NSI, NPLI, SMFS, and PCL. Accordingly, regional cooperation function, break function, and disaster function are becoming much important rather than information dispatch function because Yamaguchi is the birthplace of Michinoeki with long history.

The efficiency of the 23 Michinoeki in Yamaguchi area are calculated using DEA model based on our results. The efficiency of Yutori Park Tamagawa, Chomonkyo, Kitaura Kaido Hohoku, and Shiosai Ichiba Houfu can not be calculated because of lack of data. It is illustrated as Fig. 2.

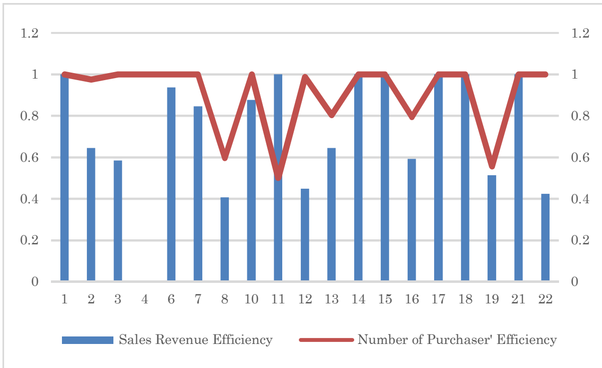

Fig. 2. Efficiency of the 23 Michinoeki.

The correlation coefficient of sales revenue and number of purchasers is 0.318, not significant statistically. Thus, no significant statistically correlation between those tow results exits. In order to find the future direction of these Michinoeki, a four cell matrix is proposed based on the efficiency of sales revenue and number of purchasers in this paper. It is reported in Fig. 3.

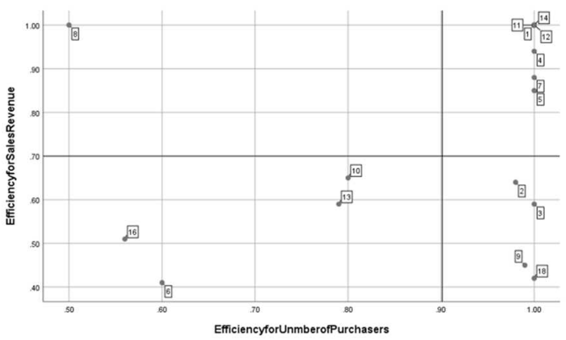

Fig. 3 The positions of the Michinoeki.

The Michinoeki located in the 4th quadrant could be excellent because they have high efficiency of sales revenue and the number of purchases both. The Michinoeki located in the 2nd quadrant could be considered as sales oriented one because they have high efficiency of sales revenue even with low efficiency of number of purchase. The Michinoeki located in the 3rd quadrant could be poor because there are still rooms to improve. The Michinoeki located in the 4th quadrant could be called visitors oriented because the efficiency of the number of purchasers are lower. Accordingly, Abu Town, Hagi Seamart, Ganjoju Onsen, Hotaru Kaido Nishi no Ichi, Kirara Ajisu, Solene Shunan, and Sazanseto, Pure Line Nishiki, and Kikugawa are considered as excellent Michinoeki while Niho no Sato, Uribo no Sato Katamata, Hagi Sansan Sammi, and Hapiness could be the poor Michinoeki. Ofuku could be sales revenue oriented Michinoeki while Hagi Okan, Asahi, Mitou, and Kaminoseki Kaikyo could be visitors oriented Michinoeki.

5. Conclusion

The relationship between twelve variables and sales revenue and number of purchasers are calculated and discussed. Only four and six variables are significant statistically for model of sales revenue and number of purchasers, respectively. The 18 Michinoeki could be divided into four groups, Abu Town and other 8 Michinoeki are excellent, and Niho no Sato and other 3 could be poor. Ofuku needs to improve its efficiency of number of purchaser while Hai Okan and other 3Michinoeki need to improve their efficiency of sales revenue. More qualitative support for these conclusions is required. Furthermore, only one-year Data set is not sufficient. Much more data set and investigation is required.

References

1. Successful examples of regional revitalization, http://www.kantei.go.jp/jp/singi/sousei/meeting/top_seminar/h29-01-13-haifu4.pdf#search=%27%E5%9C%B0%E6%96%B9%E5%89%B5%E7%94%9F+%E4%BA%8B%E4%BE%8B%27, retrieved April 20, 2018.
2. Masakuni Mitsuhashi, Why is regional revitalization difficult? http://news.yahoo.co.jp/feature/499, retrieved September 20, 2018.
3. J. Ogata, D. Nozokito, H. Murata, and K. Yamamoto, Developing Michinoeki using Michinoeki: an analysis based business model, http://www.waseda.jp/sem-inoue/file/archives/2015_sotsuron_roadsidestation.pdf#search=%27%5B5%5D+%E7%B7%92%E6%96%B9%E7%B4%94%E4%B8%80%E9%83%8E%E3%83%BB%E8%8E%85%E6%88%B8%E5%A4%A7%E5%9C%B0%E3%83%BB%E6%9D%91%E7%94%B0%E5%B8%86%E3%83%BB%E5%B1%B1%E6%9C%AC%E5%92%8C%E5%B8%8C%EF%BC%8C%E3%80%8C%E9%81%93%E3%81%AE%E9%A7%85%E3%80%8D%E3%81%AB%E3%82%88%E3%82%8B%E5%9C%B0%E5%9F%9F%E6%B4%BB%E6%80%A7%E5%8C%96%E2%80%95%E3%83%BC%E3%83%93%E3%82%B8%E3%83%8D%E3%82%B9%E3%83%A2%E3%83%87%E3%83%AB%E3%81%AE%E8%A6%B3%E7%82%B9%E3%81%8B%E3%82%89%E3%81%AE%E5%88%86%E6%9E%90%E2%80%95%27, retrieved September 10, 2018.
4. Toru Hiraoka, Shiori Nishimura, Hirofumi Nonaka, Takao Ito, and Minoru Kumano, A Correlation Analysis between the Number of Customers and Information Related to the Agriculture, Forestry, and Fisheries of Michi-no-eki in Japan, *Journal of the Institute of Industrial Applications Engineers*, Vol.6, No.4, pp.173-178, Oct. 2018.
5. M. Kumano, T. Ito, T. Ito, T. Hiraoka, H. Nonaka, M. Hirota, Discovering Successful Determinants of Efficiency of Michinoeki in Chugoku Area, *Proceedings of The 2018 International Conference on Artificial Life and Robotics*, 352-354, B-Con Plaza, Beppu, Oita, Japan, February 1-4, 2018.
6. Farrell M. J., The Measurement of Productive Efficiency, *Journal of the Royal Statistical Society*, Series A (General) Vol. 120, No. 3, 253–290, 1957, Royal Statistical Society (Wiley).
7. Charnes A. Cooper W. W. Rhodes E., Measuring the efficiency of decision-making units, *European Journal of Operational Research*, 2, 429–444, 1978, North-Holland Publishing Company.

Discovering the Characteristics of Michinoeki in Japan

Minoru Kumano
Faculty of Regional Innovation, University of Miyazaki
1-1 Gakuendai-Nishi, Miyazaki, 889-2192 Japan
E-mail: kumano@cc.miyazaki-u.ac.jp

Tsutomu Ito
Hamura Plant, Hino Motors, Ltd.,
5-2-1 Midorigaoka, Hamura City, Tokyo, 205-8601, Japan
E-mail: fw.eldorado.500cuin@gmail.com

Takao Ito
Graduate School of Engineering, Hiroshima University
1-4-1 Kagamiyama, Higashi Hiroshima, 739-7527
E-mail: itotakao@hiroshima-u.ac.jp

Toru Hiraoka
Department of Information Systems, University of Nagasaki
1-1-1, Manabino Nagayo, Nishisonogi, Nagasaki, 815-2195, Japan
E-mail: hiraoka@sun.ac.jp

Hirofumi Nonaka
Department of Information Management System Engineering, Nagaoka University of Technology
1603-1, Kamitomioka, Nagaoka, Niigata, 940-2188, Japan
E-mail: nonaka@kjs.nagaokaut.ac.jp

Abstract

It is a crucial issue to estimate the Michinoeki today. As our best knowledge, no research to estimate the Michinoeki using the data set for all Michinoeki although 1,107 Michinoeki have been established by April , 2017 in Japan. We divided Japan into nine areas, and examined the determinants of the nine areas. We found that the key characteristics of those nine areas are completely different. This paper contributes are: 1) understanding the status quo of Michinoeki, 2) finding the potential possibility for their further development. Based on the findings, the managerial implications are discussed, the study limitations are identified and directions for further research are suggested.

Keywords: Michinoeki, revitalization, sales revenue, number of purchasers.

1. Introduction

Michinoeki is considered as one of the important models for revitalization of regional economy. Maryvonne once indicated that "Michinoeki can be an effective tool for reducing poverty because they address social issues and benefit local residents directly" [1]. Today, Michinoeki developed fast not only in Japan, but also in Kenya and China. According to our investigation, no research to estimate the characteristics of Michinoeki using data set of whole Japan although 1,107 Michinoeki have been established by April, 2017 in Japan. Using data drawn from 1,107 Michinoeki in Japan, this research attempts to shed light on discovering the characteristics of the Michinoeki to improve the quality of management.

This paper is structured as follows: Section 2 introduces the background of this research. In section 3, the paper explicates data collection and multivariate regression model using specific eighteen variables selected from the data set of whole Japan. Section 4 shows the results and discussions on our findings. The conclusions and directions for further research and managerial implications are proffered in the final section.

2. Background

Michinoeki are located along major national highways with four functions of 1) providing free parking space, restrooms, 2) spreading information, 3) allying with regional society, and 4) preventing disaster. Accordingly, the four-function model of Michinoeki could be illustrated in Fig. 1.

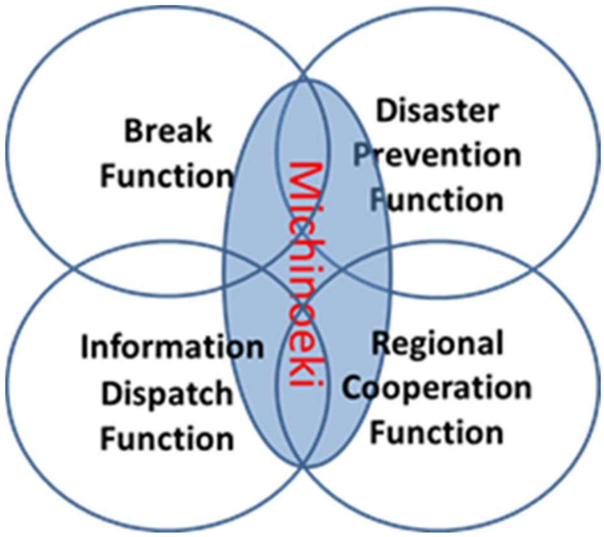

Fig. 1 Four-function model of Michinoeki.

A plethora of theories and analyses of Michinoeki from the four viewpoints have been published in the past decades. Ogata et al. explained the relationship between Michinoeki and regional revitalization based on the viewpoint of business model [2]. Kumano et al. discovered successful determinants of Michinoeki in Chugoku area using regression model [3]. Hiraoka et al. analyzed the relationship between the number of customers and information associated with agriculture, forestry, and fisheries of Michinoeki [4]. Furthermore, Kumano et al. identified the determinants of Michinoeki in Kyushu area, Japan [5]. As our best knowledge, no research to estimate the characteristics of all Michinoeki although 1,107 Michinoeki have been established by April, 2017 in Japan. In order to discover the characteristics of Michinoeki, we divided Japan into nine areas, they are: Hokkaido, Tohoku, Kanto, Hokuriku, Chubu, Kinki, Chugoku, Shikoku, and Kyushu & Okinawa. Furthermore, eighteen basic variables are selected from the database as the determinants of the Michinoeki. This paper focused on examining the determinants of the nine areas and finding the key characteristics of those nine areas.

3. Data Collections and Model Building

The data of 2015 are collected from the database of the headquarter of Michinoeki. In this paper, eighteen variables are selected as the determinants to express the four functions in Michinoeki. They are: 1) square meters of land space (SMLS), 2) number of standard-sized car parking lot(NSSCPL), 3) number of large vehicles (NLV), 4) square meters of parking area (SMPA), 5) total number of the restroom (TNR), 6) square meters of free rest place (SMFRP), 7) total seats of the free rest place (TSFRP), 8) weekdays' traffic near the station (WTNS), 9) holidays' traffic near the station (HTNS), 10) population of the city located (PCL), 11) operating cost (OC), 12) number of the agriculture and marine products (NAP), 13) number of the local products (NLP), 14) number of the selling items (NSI), 15) number of original products (NOP), 16) number of the registered farmers (NRF), 17) square meters of the facilities for marine products (SMFMP), and 18) square meters of facilities space (SMFS). SMLS, SMPA, SMFAP, SMFS and OC could be considered as the determinants of the function of spreading information and preventing disaster. NSSC, NLV, TNR, SMFPR, TSFRP, WTNS, and HTNS are designed as the indexes of providing free parking space and restrooms. PCL, NAP, NLP, NSI, NOP, and NRF will play important role in allying with regional society. Sales revenue and number of purchasers are selected as the performance of Michinoeki. Thus, this leads to the formation of the following multivariate regression equation:

Table 1 Results of standardized coefficients of the eighteen variables and sales revenue.

	1	2	3	4	5	6	7	8	9	10	11	12	13	14	15	16	17	18
Hokkaido	-0.28	0.30					0.19	0.42					-0.66		0.23	0.15	0.92	
Tohoku					-0.22		0.40			0.26						0.32	0.44	
Kanto		2.07			-1.30		-0.19		0.30		-0.17		0.33		0.12	0.18		
Hokuriku			-0.61	-0.45			1.25	1.34	-0.64			-21.82	22.33	0.49	-0.43			0.21
Chubu	-0.25	0.20	0.14	0.17										0.78	0.10			
Kinki	-1.10	0.66						-1.02	1.18		0.57	0.54	-0.78	0.83	-0.49			
Chugoku			0.36							0.35		0.58			-0.44	0.38		0.52
Sikoku		-0.91	0.64	1.30	-1.20	1.02			-0.20	-0.19	-0.28		1.21	-0.49	0.12	-0.15		
Kyushu & Okinawa		-0.16	0.17			0.21		-0.50	0.55	-0.19		0.55		0.40		-0.22	0.48	0.22

Table 2 Results of standardized coefficients of the eighteen variables and number of purchasers.

	1	2	3	4	5	6	7	8	9	10	11	12	13	14	15	16	17	18
Hokkaido	-0.21	0.24		0.30	-0.36		0.39								0.33	0.20	0.56	
Tohoku	-0.27				-0.24		0.47			0.21						0.35	0.42	
Kanto	-1.19	3.52			-1.89	0.42	-0.64	0.35					0.56					0.29
Hokuriku			-0.37				0.73	1.26	-1.05					0.83	-0.46			0.32
Chubu	-0.49	0.53	0.36				0.17			-0.15	0.27			0.41	0.18			
Kinki		-1.45	0.43	1.09	0.87			-3.21	3.03	0.49			-1.06			1.36		
Chugoku				0.16		-0.31				0.38						0.33	0.46	0.44
Sikoku		-1.08	0.54	1.44	-1.02	1.00		-0.23		-0.32	-0.25		0.86		0.09	-0.16		
Kyushu & Okinawa				0.30				-0.42	0.42					0.21			0.82	

$$y = a_1 SMLS + a_2 NSSC + a_3 NLV + a_4 SMPA + a_5 TNR + a_6 SMFRP + \mathrm{a}_7 \text{ TSFRP} + a_8 WTNS + a_9 HTNS + a_{10} PCL + a_{11} OC + a_{12} NAP + \mathrm{a}_{13} \text{ NLP} + a_{14} NSI + a_{15} NOP + a_{16} NRF + a_{17} SMFAP + a_{18} SMFS + \varepsilon \tag{1}$$

4. Calculation and Discussions

The standardized correlation coefficients between the eighteen variables and sales revenue and number of purchasers are calculated respectively. The results are shown as in Table 1 and Table 2.

Based upon Table 1 and Table 2, we find following results. First, the correlation coefficients of 1) square meters of land space (SMLS) are all negative. The possible reason is that the scales of all Michinoeki are big enough because the first purpose of Michinoeki is to provide free space for visitors. Second, the correlation coefficients of 17) square meters of the facilities for marine products (SMFMP), and 18) square meters of facilities space (SMFS) are all positive. Thus, the scales of the shop of marine products and the scale of the facilities space contribute not only the sale revenue, but also the number of purchasers. Third, 17) square meters of the facilities for marine products (SMFMP) has strong impact on the performance of Hokkaido, Tohoku, and Kyushu & Okinawa. Kyushu & Okinawa are strong effected by not only 17) square meters of the facilities for marine products (SMFMP), but also 9) holidays' traffic near the station (HTNS). Thus, it will be considered that the performance is effected by SMFMP and HTNS both, differs from Hokkaido and Tohoku. Fourth, the highest value of Kanto is 2) number of standard-sized car parking lots(NSSCPL), thus the traffic will be considered as one of the characteristics of Kanto. Fifth, the key determinants of Hokuriku, Chubu, Chugoku, and Kinki are 13) number of the local products (NLP), 14) number of the selling items (NSI), 12) number of the agriculture and marine products (NAP), and 9) holidays' traffic near the station (HTNS). Kanto and Shikoku are effected by 4) square meters of parking area (SMPA) and 2) number of standard-sized car parking lot (NSSCPL). Thus different area has its different specific characteristics. The key determinants of each area are listed in Table 3.

Table 3 Key determinants of each Michinoeki.

Area	Key Determinants	
Hokkaido	Square meters of the facilities for marine products (SMFMP)	Weekdays' traffic near the station (WTNS)
Tohoku	Square meters of the facilities for marine products (SMFMP)	Total seats of the free rest place (TSFRP)
Kanto	Number of standard-sized car parking lot(NSSCPL)	
Hokuriku	Number of the local products (NLP)	
Chubu	Number of the selling items (NSI)	
Kinki	Holidays' traffic near the station (HTNS)	
Chugoku	Number of the agriculture and marine products (NAP)	Square meters of facilities space (SMFS)
Sikoku	Square meters of parking area (SMPA)	
Kyushu & Okinawa	Number of the agriculture and marine products (NAP)	Holidays' traffic near the station (HTNS)

5. Conclusions

The relationship between eighteen variables and sales and number of purchasers are calculated and discussed. Different area has its different specific characteristics. For instance, the sale revenue of Hokkaido, Tohoku, and Kyushu & Okinawa are all depend on the square meter of the facilities for marine products, but the influence of Tohoku is weak than Hokkaido, Kyushu and Okinawa are affected by the square meter of the facilities for agriculture products and holidays traffic near the station both. However, much more qualitative support for our conclusion is required. Moreover, only one fiscal year data set is not sufficient. Much more data set and investigation is required.

References

1. Guidelines for Roadside Stations "Michinoeki", p.7, http://documents.worldbank.org/curated/en/753051468137999706/pdf/356830Guidelin1de0stations01PUBLIC1.pdf#search=%27woeld+bank+Michinoeki%27, retrieved November 10, 2018.
2. J. Ogata, D. Nozokito, H. Murata, and K. Yamamoto, Developing Michinoeki using Michinoeki: an analysis based business model, http://www.waseda.jp/sem-inoue/file/archives/2015_sotsuron_roadsidestation.pdf#search=%27%5B5%5D+%E7%B7%92%E6%96%B9%E7%B4%94%E4%B8%80%E9%83%8E%E3%83%BB%E8%8E%85%E6%88%B8%E5%A4%A7%E5%9C%B0%E3%83%BB%E6%9D%91%E7%94%B0%E5%B8%86%E3%83%BB%E5%B1%B1%E6%9C%AC%E5%92%8C%E5%B8%8C%EF%BC%8C%E3%80%8C%E9%81%93%E3%81%AE%E9%A7%85%E3%80%8D%E3%81%AB%E3%82%88%E3%82%8B%E5%9C%B0%E5%9F%9F%E6%B4%BB%E6%80%A7%E5%8C%96%E2%80%95%E3%83%BC%E3%83%93%E3%82%B8%E3%83%8D%E3%82%B9%E3%83%A2%E3%83%87%E3%83%AB%E3%81%AE%E8%A6%B3%E7%82%B9%E3%81%8B%E3%82%89%E3%81%AE%E5%88%86%E6%9E%90%E2%80%95%27, retrieved September 10, 2018.
3. M. Kumano, T. Ito, T. Ito, T. Hiraoka, H. Nonaka, M. Hirota, Discovering Successful Determinants of Efficiency of Michinoeki in Chugoku Area, *Proceedings of The 2018 International Conference on Artificial Life and Robotics*, 352-354, B-Con Plaza, Beppu, Oita, Japan, February 1-4, 2018.
4. Toru Hiraoka, Shiori Nishimura, Hirofumi Nonaka, Takao Ito, and Minoru Kumano, "A Correlation Analysis between the Number of Customers and Information Related to the Agriculture, Forestry, and Fisheries of Michi-no-eki in Japan", *Journal of the Institute of Industrial Applications Engineers*, Vol.6, No.4, pp.173-178, Oct. 2018.
5. M. Kumano, T. Ito, and T. Ito, A Determinants Analysis of the Michinoeki in Japan, *International Journal of Economics and Management Systems*, Vol. 2, pp.287-291, November, 2017.

An Analysis of Robotic Relationship between Transaction Network and Cross-shareholding Network in Yokokai

Takao Ito
Graduate School of Engineering, Hiroshima University
1-4-1 Kagamiyama, Higashi Hiroshima, 739-7527
E-mail: itotakao@hiroshima-u.ac.jp

Tsutomu Ito
Hamura Plant, Hino Motors, Ltd.,
5-2-1 Midorigaoka, Hamura City, Tokyo, 205-8601, Japan
E-mail: fw.eldorado.500cuin@gmail.com

Rajiv Mehta
School of Management, New Jersey Institute of Technology, University Heights,
Newark, New Jersey, 07102-1982, U.S.A.
E-mail: kumano@cc.miyazaki-u.ac.jp

Seigo Matsuno
Department of Business and Administration, NIT, Ube College,
2-14-1, Tokiwadai, Ube, Yamaguchi, 755-0096, Japan
E-mail: hiraoka@sun.ac.jp

Makoto Sakamoto and Satoshi Ikeda
Faculty of Engineering, University of Miyazaki,
1-1 Gakuen Kibanadai-Nishi, Miyazaki, 889-2192, Japan
E-mail: sakamoto@cc.miyazaki-u.ac.jp,and bisu@cc.miyazaki-u.ac.jp

Abstract

Cross shareholdings is one of the typical characteristics of Keiretsu. It contributes to maintain good transaction relationships among memberships. However, cross shareholdings as reflected by the percentage and amount of stock cross ownership is being abandoned. As a result, carmakers are losing control of their parts suppliers. This paper calculate the relationship between transaction and cross shareholdings, and tested the relationship between inter-firm relationship and corporate performance. Based on the findings, the managerial implications are discussed, the study limitations are identified and directions for further research are suggested.

Keywords: inter-firm relationship, transaction, cross shareholding.

1. Introduction

Keiretsu was considered as one of the useful models to improve corporate performance. Widely accepted as being successful, Keiretsu is made-up of affiliated organizations that are ordered and characterized by long-term continuous rationality, trade exclusivity, and information concealment. After bubble economy, Keiretsu has been changed from trade exclusive to market competition. And cross shareholdings is no more considered as one of the contribution resources of transaction. Thus, the new changes begs the following questions: What is the status quo of the inter-firm relationships between cross shareholdings and transaction? Does the robotic relationship between transaction network and cross shareholding network hold? Robotic relationship is defined if the cross shareholding relationships are automatically affected by the inter-firm's transaction relationships. It means that cross shareholdings relationships continue contribute to the interfirm transaction relationships. It will provide managerial implications that can be used as guidelines in formulating corporate strategy. Accordingly, this paper makes a unique contribution to extant thought by: 1) calculating the degree of all firms in Yokokai, 2) analyzing the correlation between cross shareholdings and transaction, 2) Discovering the relationship between degree and corporate performance in order to shed light on the robotic relationship between transaction and cross shareholdings.

This paper is structured as follows. Section 2 reviews the literature focusing on network analysis. In section 3, the paper explicates the calculation of degree and regression model. Section 4 discusses managerial implication emerging from our findings. Section 5 will mention limitations and provide directions for future research.

2. Background

Inter-firm relationship is one of main issues in corporate management. Many researches have been published recently. Takeshi and Noro published a paper on strengths and weakness of Keiretsu [1]. Ts. Ito et al. proposed a new approach called Fragility to calculate the inter-firm relationship in Yokokai [2]. Furthermore, Ta. Ito et al. did a empirical research on inter-firm capital relationship in Yokokai using IDE spatial model [3]. All these researches focused on analyzing inter-firm within a single network. As a well-known fact, all economic behaviors are associated with each other. Keiretsu is composed of multiple networks, such as transaction network and cross shareholdings network. All of these networks are interactively work with each other. Based on our investigation, the studies associated with interaction among multiple networks is still sparse. Thus, this paper will shed light on the correlation between networks of cross shareholdings and transactions, and calculate relationship between network indexes and corporate performance.

3. Data Collection and Model

To calculate the correlation between networks of cross shareholdings and transactions, data for fiscal year 1997 and 2004 were drawn from Mazda's Yokokai keiretsu. The detailed information of those two years are shown in Table 1 and Table 2.

The network relationships among the companies were identified through graph modelling. A tie shows the percentage of the transaction and/or cross shareholdings between each pairs of firms.

The degree is calculated as follows.

$$C_D(p_k) = \sum_{i=1}^{n} a(p_i, p_k)$$
$$i = 1, 2, \dots, n; k = 1,2, \dots, m \qquad (1)$$

where

$a(p_i, p_k)$=1; if and only if p_i and p_k are connected by a line

= 0; otherwise

4. Calculation and Discussions

We first calculated the index of degree for all firms in Yokokai in 1997 and 2004 respectively. And we calculated correlation matrix between transaction and cross shareholdings. The results are shown in Table 3 and Table 4.

Table 3 and Table 4 show that all correlation coefficients are significant statistically. Transaction outdegree is negatively associated with transaction indegree (-0.4691 in 1997 and -0.5652 in 2004) same as the relation between transaction outdegree and transaction indegree (-0.4648 in 1997 and -0.3268 in 2004). It means more selling, less purchasing holds. Both of the correlation coefficients between transaction indegree and cross shareholdings outdegree are negative in 1997 and 2004 (0.4013 in 1997 and 0.7368 in 2004). It means more invest, more selling holds. The capital relationship contributes its transaction still remains even in 2004, this contradicted with the traditional viewpoint. Thus, the robotic relationship between transaction and capital holds. The correlation coefficients between transaction outdegree and cross shareholdings indegree is

Table 1 Total number of Banks and Finance Institutions, and Suppliers including carmakers in Yokokai in 1997.

	Total Number in Yokokai before Removing Singletons			Total Number in Yokokai after Removing Singletons		
	Total number	Banks and Finance Institutions	Suppliers including Car-makers	Total number	Banks and Finance Institutions	Suppliers includi Car-makers
Transaction	201	0	201	122	0	122
Cross shareholding	254	53	201	122	27	95

Table 2 Total number of Banks and Finance Institutions, and Suppliers including carmakers in Yokokai in 2004.

2004	Total Number in Yokokai before Removing Singletons			Total Number in Yokokai after Removing Singletons		
	Total number	Banks and Finance Institutions	Suppliers including Car-makers	Total number	Banks and Finance Institutions	Suppliers includi Car-makers
Transaction	188	0	188	91	0	91
Cross shareholding	224	36	188	101	36	65

Table 3 Correlation matrix of out-degrees and in-degrees of Transaction and Cross shareholdings in 1997.

	Transaction Outdegree	Transaction Indegree	Cross shareholdings Outdegree	Cross shareholdings Indegree
Transaction Outdegree	1	-0.4691	-0.4648	-0.3718
		0	0	0.0013
Transaction Indegree	-0.4691	1	0.4013	0.8561
	0		0.0005	0
Cross shareholdings Outdegree	-0.4648	0.4013	1	0.2945
	0	0.0005		0.012
Cross shareholdings Indegree	-0.3718	0.8561	0.2945	1
	0.0013	0	0.012	

Table 4 Correlation matrix of out-degrees and in-degrees of Transaction and Cross shareholdings in 2004.

	Transaction Outdegree	Transaction Indegree	Cross shareholdings Outdegree	Cross shareholdings Indegree
Transaction Outdegree	1	-0.5652	-0.3268	0.4475
		0	0.0079	0.0002
Transaction Indegree	-0.5652	1	0.7368	-0.3802
	0		0	0.0018
Cross shareholdings Outdegree	-0.3268	0.7368	1	-0.2193
	0.0079	0		0.0792
Cross shareholdings Indegree	0.4475	-0.3802	-0.2193	1
	0.0002	0.0018	0.0792	

-0.3718 in 1997 and 0.4475 in 2004 respectively. It means "more capital accepted, less selling" in 1997 has been change to "more capital accepted, more selling " in 2004. Furthermore, the correlation coefficients between cross shareholdings-outdegree and cross shareholdings indegree is 0.2945 in 1997 and -0.2193 in 2004 respectively. It means "more invest, more capital accept" in 1997 has been change to "more invest, less capital accept " in 2004.

Furthermore, we calculated the regression model between transaction outdegree, transaction indegree, Cross shareholding outdegree, and cross shareholdings indegree and sales revenue, one of the corporate indexes. The four variables were all significant in 1997 while only two variables of Transaction indegree and cross shareholding outdegree are significant statistically. The adjusted R square of 0.95375 in 2004 is higher than 0.65336 in 1997. The standardized coefficients of are illustrated as in Fig. 2.

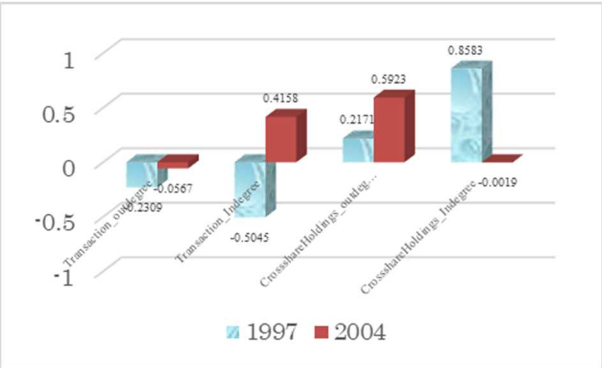

Fig. 2. Standardized Coefficients of outdegree and indegree of transaction and cross shareholdings.

Fig. 2. provides that transaction indegree in 2004 contributes to its sales revenue positively while it was negative in 1997. The more capital accept, the more sales holds. It will be considered all investment are selected to invest only for the powerful supplier. And consequently cross shareholdings contributes to sales revenue is much higher.

5. Conclusion

In this paper, we calculated 1) degree, one of the network indexes, 2) correlation coefficients of outdegree and indegree of transaction and cross shareholdings networks, and verified the relationship between the four variables and sales revenue using regression model. Based upon our findings, more invest, more selling holds. Thus works even in 2004. Accordingly, a certain robotic relationship between transaction and cross shareholdings holds. However, it is not sufficient to prove the robotic relationship between transaction and cross shareholding. Much more data sets are required to shed light on the real relationship between the transaction and cross shareholdings and discover the mechanism of robotic behavior in Keiretsu.

References

1. Akira Takeshi, and Yoshihisa Noro, Keiretsu Divergence in the Japanese Automotive Industry: Why Have Some, But Not All, Gone? CEAFJP Discussion Paper Series 17-04, http://ffj.ehess.fr/upload/Discussion/CEAFJPDP-17-04.pdf#search=%27Keiretsu+Divergence+in+the+Japanese+Automotive+Industry%3A%27 retrieved Oct. 10, 2018.
2. Ts. Ito, K. Takahashi, K. Morikawa, Ta. Ito, R. Mehta, S. Matsuno, and M. Sakamoto, Fragility in Network Systems: An Empirical Investigation, *Journal of Robotics, Networking and Artificial Life*, Vol.4, Issue 1, pp.81-86, Atlantis Press, July 2017.
3. Ta. Ito, Ts. Ito, K. Takahashi, M. Sakamoto, S. Ikeda, and R. Mehta: An Empirical Research on Inter-firm Capital Relationship in Yokokai Using IDE Spatial Model, *Journal of Robotics, Networking and Artificial Life*, Volume 2, Issue 2, pp. 125-131, Atlantis Press, September 2015.

Technological Discontinuities and the R&D Strategy of Automobile Companies

Yousin Park
Dept. of Business Administration, Prefectural University of Hiroshima,
1-1-71 Ujina-Higashi, Minami-ku, Hiroshima City, Hiroshima Pref., 734-8558, Japan
ecventure@pu-hiroshima.ac.jp

Iori Nakaoka
Dept. of Business Administration, National Institute of Technology, Ube College,
2-14-1 Tokiwadai, Ube City, Yamaguchi Pref., 755-8555, Japan
nakaoka@ube-k.ac.jp

Yunju Chen
Faculty of Economics, Shiga University,
1-1-1, Banba, Hikone City, Shiga Pref.,734-8558, Japan
yun-chen@biwako.shiga-u.ac.jp

Abstract

This paper focuses on patterns of technological changes and the R&D strategy of automobile companies. Tushman and Anderson (1986) pointed out that there are two types of technological changes. One is incremental technological change which is often generated by existing companies, and the other one is radical technological change which makes great extension in business environment and destroys the order of existing companies. We use the patent information of three automobile companies (Toyota, BYD, Tesla) as the cases on these changes. And we examine our propositions by text analysis and social network analysis. The analyses in this paper include the followings: 1) To distinguish between the radical and incremental technological changes from R&D projects, and create heat-maps to visualize these changes, 2) To discuss on technological discontinuities and the R&D strategy of automobile companies. In this paper we suppose that patterns of corporate R&D strategy cope with the threat of radical technological changes.

Keywords: technological discontinuities, radical technological change, R&D strategy of automobile companies, patent analysis,

1. Introduction

This paper focuses on patterns of technological changes and the impact of technological breakthroughs on environmental conditions. Tushman and Anderson (1986) point out that there are two types of technological changes [1]. One is incremental technological change which is often generated by existing companies, and the other one is radical technological change which makes great extension in business environment and destroys the order of existing companies.

Nowadays, traditional automobile industry is faced with new challenges due to radical technological change such as the development of electric vehicle. New entrants, such as Tesla and BYD, are competing with existing companies in research development. We suppose that some features of R&D management help these entrants to keep their competitive advantage.

In this paper, we use the patent information of three automobile companies (Toyota, BYD, Tesla) as the cases on these changes. And we examine our propositions by text analysis and social network analysis. The analyses in this paper include the following: 1) To distinguish between the radical(product) and incremental(process) technological changes from R&D projects, and create heat-maps to visualize these changes, 2) To discuss on technological discontinuities and the R&D strategy of automobile companies. In this paper we suppose that patterns of corporate R&D strategy cope with the threat of radical technological changes.

2. Background

2.1Technological discontinuities

Abernathy(1978) described that a dynamic model of innovation includes a pattern of sequential and cross-sectoral change in product innovation, process innovation, and organizational structure. Firms that are new to a product area will exhibit a fluid pattern of innovation and structure. As the market develops, a transitional pattern will emerge. Finally, the market stabilizes, fostering a specific pattern of behavior. [1].

Tushman and Anderson(1986) demonstrate that technology evolves through periods of incremental change punctuated by technological breakthroughs which enhance or destroy the competence of firms in an industry. These breakthroughs, or technological discontinuities, significantly increase environmental uncertainty and munificence. They point out that while competence-destroying discontinuities are initiated by new firms and are associated with increased environmental turbulence, competence-enhancing discontinuities are initiated by existing firms and are associated with decreased environmental turbulence. Therefore, a radical innovation that can create new businesses and transform or destroy existing ones [2].

Anderson and Tushman(1990) suggest that the key punctuation points are technological discontinuities and dominant designs; these delimit eras of ferment and eras of incremental change [3]. Firms must develop diverse competences both to shape and deal with technological evolution.

2.2 The overview of automobile industry

Table 1 Market value of world top automobile companies

Company	Stock price	Market Cap
Toyota	$52	172.1billion
Daimler AG	$73	78.3billion
Tesla Inc	$364	59.7billion
BMW	$94	56.8billion
SAIC Motor Corp	$5	53.2billion
General Motors	$34	51.9billion
Honda	$28	50.3billion
Volkswagen	$154	45.5billion
Ford	$11	43.3billion

Source: Factset (Jun 2017)

Although as a new entrant, Tesla gives confidence and expectation to investors. Table 1 shows the market value of world top automobile companies. From this table, we can see that Tesla in the United States is valued higher in corporate value than GM in the stock market in 2017. In addition, China's BYD has attracted attention for the global production of electric vehicles.

In this paper we discuss the patterns of R&D strategies of Toyota, Tesla and BYD. Because the advent of electric vehicles in the automobile industry may be product innovation and is also possible to become technological innovation of competence-destroying discontinuities to existing firms like Toyota. To test this hypothesis, we make a comparison among R&D strategies of Toyota, BYD and Tesla by social network analysis.

3. Methodology and data

In the following sections, the trends of R&D strategies of automobile companies are analyzed. Patent documents are archived in Patent integration. All patents are classified according to three kinds of classification codes, IPC (International Patent Classification), FI (File Index) and F-term (File Forming Term). FI and F-term are classification codes for segmentalizing IPC in Japan. IPC codes in table 2 are the most frequently used in electric vehicle. This paper utilizes all patents (Japan, America, China, and WIPO) of automobile companies and we pay special attention to their IPC which is related to electric vehicle described in “IPC B60L”. Patents which are based on F-term and IPC related to electric vehicle and published by each company are extracted and collected

Table 2 IPC of patents related to electric vehicle

IPC codes	Contents
B60L	PROPULSION OF ELECTRICALLY-PROPELLED VEHICLES
B60L1/00-3/12	Supplying electric power to auxiliary equipment of electrically-propelled vehicles
B60L7/00-13/00	Electrodynamic brake systems for vehicles in general
B60L15/00-15/42	Methods, circuits or devices for controlling the propulsion of electrically-propelled vehicles

(Source) World Intellectual Property Organization

from the patent information. In order to examine target companies' R&D strategies and the change of core researchers in their R&D organizations, we visualize their patent information in 3 steps, and then diagrams can be created by these analyses.

First, count the number of patent publications related to electric vehicle of each target company. Second, conduct social network analysis and calculate network centrality. Third, create heat maps of core member in R&D projects.

3.1. *An approach based on the number of patent publications*

Fig. 1 shows that Toyota is overwhelmingly more than other two companies in the number of patent applications. The reason is that the R&D investment amount of Toyota is as 10 times as the other two.

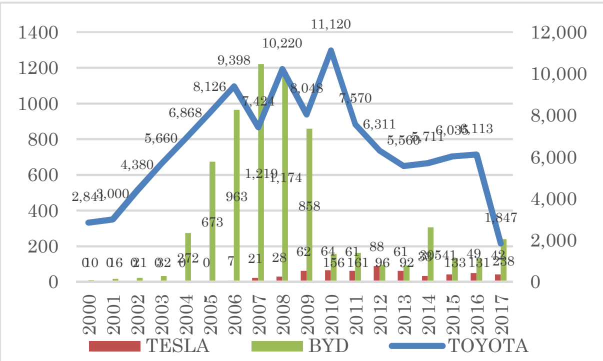

Fig. 1 The number of patents applications of the three companies

3.2. *An approach by the text analysis.*

We visualize their R&D strategies associated with co-applicant of patent publication by social network analysis and calculate network centrality (degree, betweenness, closeness). Fig 2, 3, 4 show the network of patent co-applicant of Toyota, BYD and Tesla in 2016.

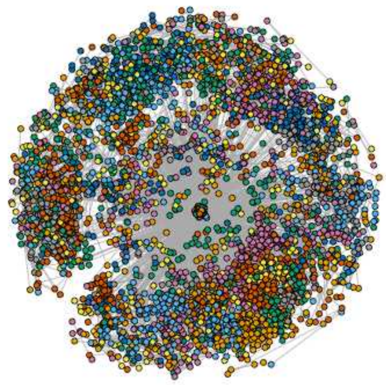

Fig.2 Network of patent applicant of Toyota

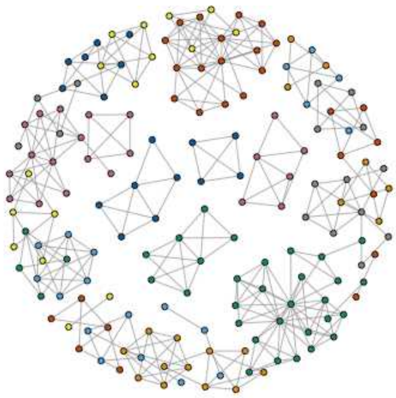

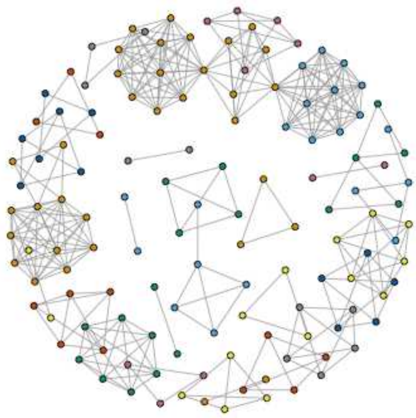

Fig. 3 Network of patent applicant of BYD
Fig. 4 Network of patent applicant of Tesla

3.3. *An approach by core rigidities.*

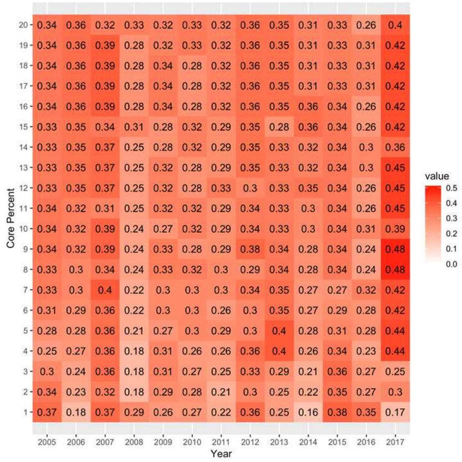

Fig. 5 Core rigidities of Toyota

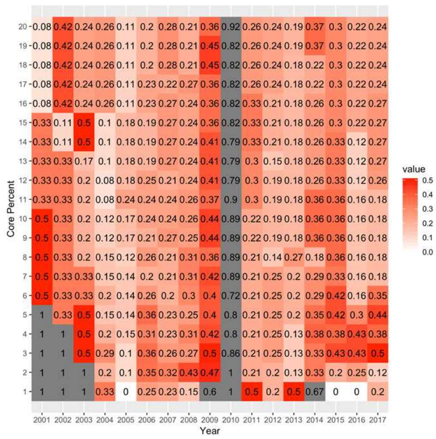

Fig. 6 Core rigidities of BYD

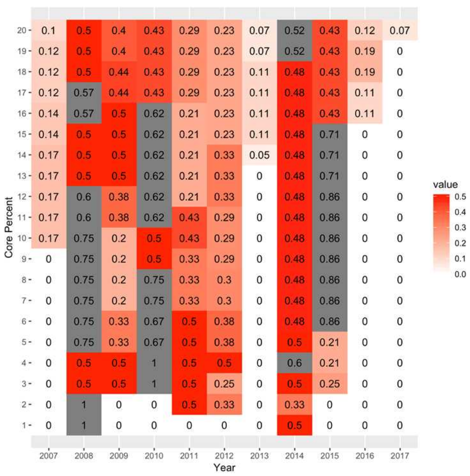

Fig. 7 Core rigidities of Tesla

Fig. 5, 6, 7 illustrate the core rigidities of these three companies. The score of core rigidities means that core members have been continuously active in R&D projects. In pattern of heat maps, we find that Toyota has exploited core member every year and taken an improvement of R&D capabilities. BYD and Tesla have changed core member per 2-3 years and taken an exploration of R&D capabilities.

4. Conclusions

We discuss that patterns of corporate R&D strategy cope with the threat of radical technological changes such as electric vehicle. We find the similarities and differences in the R&D strategies of three companies. Why has each company taken different R&D strategies? For Toyota, whose core product has been gasoline engine, has adopted R&D strategy that leveraged this. BYD whose core competence has been battery technology, developed FHV of world in 2009. Recently BYD has focused on the development of EV. Tesla may have been reorganized R&D strategy by mass production of Model X since 2014 and development of Model S as a new car.

Therefore, the hypotheses on R&D strategy of each firms seem to be related to their business domain and core competence. In the case of business domain, we think that the decision of vertical integration or horizontal specialization affects a firm's profit and competitive advantage. The analyses we have made on Chinese ICT companies, prove our hypotheses [4]. For automobile companies, we should also pay attention to the decision of vertical integration or horizontal specialization.

References

1. W. J. Abernarthy, *The productivity dilemma*, Baltimore, MD: Johns Hopkins University Press (1978).
2. M. L. Tushman and P. Anderson, "Technological Discontinuities and Organizational Environments" *Administrative Science Quarterly*, 31, pp. 439-465 (1986).
3. P. Anderson and M. L. Tushman, "Technological discontinuities and dominant designs: A cyclical model of technological change" *Administrative Science Quarterly*, 35, pp. 604-633 (1990).
4. Y. Chen, Y. Park and I. Nakaoka "A Comparison Study on the Vertical Integration and Horizontal Specialization of Chinese ICT Companies" *Journal of Robotics, Networking and Artificial Life*, Vol.4, No.4, pp. 317-321 (2018)

Prototype of an Animated Graphics-Based Training Support Tool for Bug Fixing of Extended Place/Transition Nets

Tomohiko Takagi
Faculty of Engineering and Design, Kagawa University
2217-20 Hayashi-cho, Takamatsu-shi, Kagawa 761-0396, Japan

Shogo Morimoto
Graduate School of Engineering, Kagawa University
2217-20 Hayashi-cho, Takamatsu-shi, Kagawa 761-0396, Japan

Yuki Ue
Graduate School of Engineering, Kagawa University
2217-20 Hayashi-cho, Takamatsu-shi, Kagawa 761-0396, Japan

Yoshiro Imai
Faculty of Engineering and Design, Kagawa University
2217-20 Hayashi-cho, Takamatsu-shi, Kagawa 761-0396, Japan
E-mail: takagi@eng.kagawa-u.ac.jp, s17g483@stu.kagawa-u.ac.jp,
s18g459@stu.kagawa-u.ac.jp, imai@eng.kagawa-u.ac.jp

Abstract

This paper describes an animated graphics-based training support method and prototype tool for bug fixing of EPNs (Extended Place/transition Nets). The prototype tool gives a trainee a faulty EPN and animated graphics. The motion of the animated graphics is synchronized with the motion of the faulty EPN. Therefore, it is expected that a trainee can intuitively understand the faulty EPN, and smoothly try to fix a bug. The result of bug fixing is checked by the prototype tool.

Keywords: Training Support, Software Modeling, Place/Transition Net, Bug Fixing

1. Introduction

Formal models in graphical and mathematical languages can give unambiguous abstracted representation of the behavior of software. In software development, they are useful to define specifications, generate program codes, and generate test cases systematically. For example, in Ref. 1, time Petri nets are used to model real-time software and generate test cases that focus on its state transition and timing properties. Ref. 2 shows a prototype tool to generate boundary value test cases from formal specifications written in VDM++[3].

In our previous study, an EPN (Extended Place/transition Net) that is a combination of a PN (Place/transition Net) and VDM++ was proposed and introduced into test case generation[4] and evaluation[5]. The PN is a kind of Petri nets that can be used to model software from the viewpoint of its basic state transition. The advantage of the EPN for the PN is that some complex and essential aspects such as guards and actions on transitions can be written in VDM++, and a state of software is closely expressed as a marking and values of instance variables. The EPN is executable on a tool, and software engineers can confirm the abstracted behavior of software before beginning its implementation. However, it would not be so easy for most of software engineers to learn and use the EPN efficiently. In general, a formal model with higher representation power requires software engineers to gain higher degree of expertise and experience, which will prevent the spread of the formal model in actual software development. There are only a limited number of software engineers skilled in formal modeling, and they are too busy to train unskilled software engineers. Therefore, a training support tool should be established to solve this problem.

In this study, we are planning to develop a tool to support the training of formal modeling using EPNs. Different support methods should be constructed based on the difference of trainees' achievement. First, we classified the trainees' achievement into the following two levels.

- Level 1: A trainee has gained the ability to understand the behavior of software from a given EPN, and fix a bug (that is, a difference between the EPN and true software requirements).
- Level 2: A trainee has gained the ability to construct an EPN from given software requirements.

As the first step of this study, we have constructed an animated graphics-based training support method and prototype tool to achieve the level 1. This paper shows this method, functions of the prototype tool, and discussion about its effectiveness. The prototype tool gives a trainee a faulty EPN and its animated graphics. The faulty EPN is an EPN that includes an intended bug, and the animated graphics illustrate the behavior of software based on the faulty EPN. The motion of the animated graphics is linked to (that is, synchronized with) the motion of the faulty EPN. Therefore, it is expected that a trainee can intuitively understand the faulty EPN, and smoothly try to fix a bug. The prototype tool checks the result of bug fixing, and evaluates each trainee's achievement.

The rest of this paper is organized as follows. In section 2, we propose an animated graphics-based training support method. Section 3 illustrates the functions of the prototype tool that the core of the proposed method has been implemented into. Section 4 gives discussion about effectiveness based on trial application of the prototype tool, and finally section 5 shows conclusion and future work.

2. Training Support Method

In this section, we propose an animated graphics-based training support method for bug fixing of EPNs. This method consists of (1) creation of exercises, (2) work on exercises, and (3) evaluation.

2.1. *Creation of exercises*

A trainer, that is, a skilled software engineer creates exercises for trainees. Each exercise consists of software requirements that was written in a natural language, an original EPN that was correctly constructed based on the software requirements, a faulty EPN that was constructed by inserting an intended bug into the original EPN, operations to fix the intended bug of the faulty EPN, and animated graphics that illustrate the behavior of software based on the faulty/fixed EPN.

An intended bug can be created by applying existing mutation operators to an original EPN. A good exercise includes an intended bug that cannot be easily found and is likely to be made in actual software development.

The operations for bug fixing are defined as a pair (or pairs) of a kind of existing mutation operators, and the number of times to apply the mutation operator to a faulty EPN. For example, when (arc addition, 2) is defined as operations, correct bug fixing can be achieved by adding two arcs somewhere to a faulty EPN. In other words, the intended bug of the faulty EPN would be created by (arc deletion, 2).

The motion of animated graphics needs to be synchronized with the motion of the faulty/fixed EPN that is shown as the change of its current state (that is, its current marking and values of instance variables) and the highlighting of a recently fired transition. Trigger of motion in the animated graphics is the fire of a transition in the faulty/fixed EPN; on the contrary, trigger of the fire of a transition can be the result of motion in the animated graphics. The definition of the trigger in an EPN and its animated graphics is one of trainer's tasks.

2.2. *Work on exercises*

A faulty EPN and its animated graphics are given to a trainee. As mentioned above, the motion of the animated graphics is linked to the motion of the faulty/fixed EPN.

In more detail, the following procedure is automatically performed based on the trigger definitions.

(i) In the faulty/fixed EPN, each transition is checked whether it can fire or not. A transition is fireable, if all from-places of the transition contain the required number of tokens, and the guard of the transition is true. If there are no fireable transitions, it will be a failure that was caused by an intended bug or an incorrect bug fix, and this procedure is terminated.

(ii) If a trigger event occurs in the animated graphics, a transition relating to the trigger event is identified in the faulty/fixed EPN. If the transition is fireable, corresponding motion in both of the faulty/fixed EPN and the animated graphics is invoked, and then this procedure returns to (i). If the transition is not fireable, it will be a failure that was caused by an intended bug or an incorrect bug fix, and this procedure is terminated.

(iii) A fireable transition is randomly selected, and then corresponding motion in both of the faulty/fixed EPN and the animated graphics is invoked. This procedure returns to (i).

If the above-mentioned procedure is terminated, all the motion is stopped, and then, the faulty/fixed EPN and the animated graphics return to their initial states.

It is expected that a trainee can intuitively understand a faulty EPN from its animated graphics. If the trainee has found the difference between the faulty EPN and given software requirements, he/she tries to remove an intended bug from the faulty EPN. The trainee can modify the faulty EPN by using only the operations for bug fixing that have been given in the exercise. Modification to the faulty EPN is reflected on the animated graphics, and thus the trainee can confirm the result of his/her bug fixing by viewing the synchronous motion of the fixed EPN and its animated graphics.

2.3. *Evaluation*

When a trainee has finished his/her bug fixing, the fixed EPN is compared with the original EPN. If they are the same, it is judged as correct bug fixing. If they are not the same, it is judged as incorrect bug fixing, and the trainee is suggested to retry the exercise.

The time taken for the completion of correct bug fixing, and the number of incorrect bug fixing are recorded in order to evaluate not only trainees' achievement but also the quality of exercises.

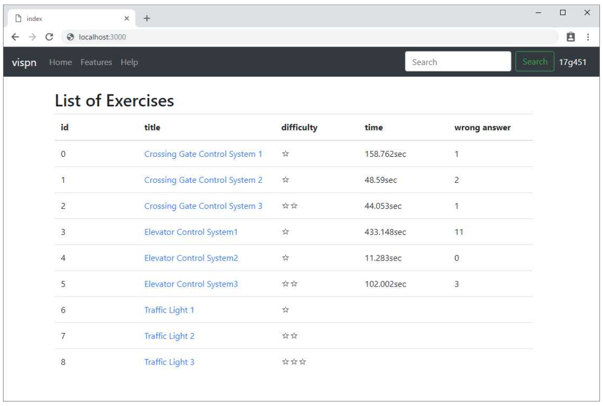

Fig. 1. Top page providing the list of exercises.

3. Prototype of a Training Support Tool

The core of the training support method proposed in the previous section has been implemented as a prototype tool. This section illustrates its functions.

The prototype tool has been constructed as a Web application in order that trainees can use it easily. The aim of this prototyping is to evaluate the effectiveness of animated graphics against understandability of EPNs, and thus it does not include the implementation of functions to help the creation of exercises. Also, only model-based mutation operators[6] are introduced to prepare faulty EPNs and operations for bug fixing.

First, a trainee needs to log on to the prototype tool by using a Web browser, and select an arbitrary exercise on a top page shown in Fig. 1. The top page provides the information about each exercise, including its title, degree of difficulty that was supposed by a trainer, time taken for the completion of correct bug fixing, and number of incorrect bug fixing.

Soon after clicking a title of a desired exercise on the top page, a trainee receives a corresponding training page. A training page consists of software requirements, animated graphics, a faulty EPN, operations for bug fixing, and some buttons (an "Answer" button, a "Retry" button, buttons for operations for bug fixing, and so on). When selecting "Crossing Gate Control System"[7] from the list shown in Fig. 1, the trainee receives the training page shown in Fig. 2. The animated graphics are formed from map chips (blocks to form a map, such as rails and a road) and motion objects on the map (such as a train

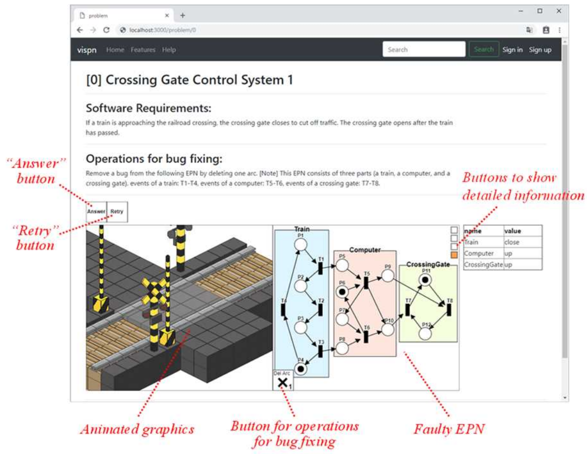

Fig. 2. Training page (initial state).

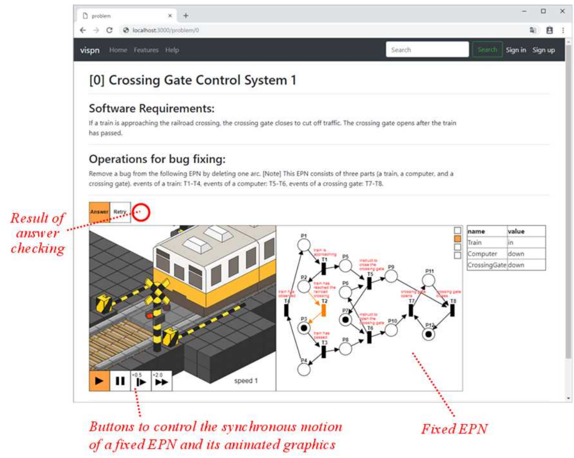

Fig. 4. Training page (answering a correct bug fix).

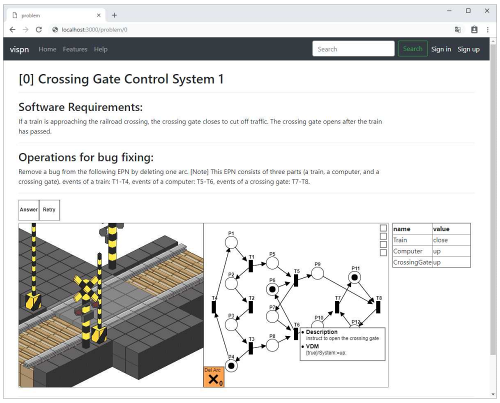

Fig. 3. Training page (modifying a faulty EPN).

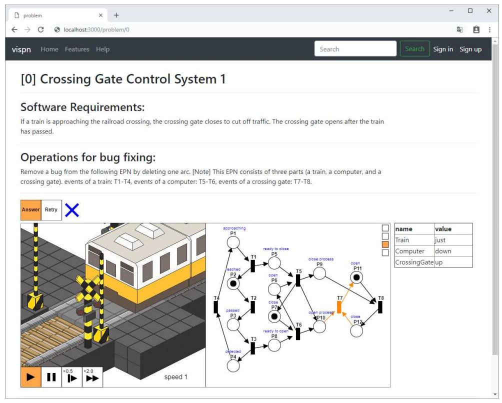

Fig. 5. Training page (answering an incorrect bug fix).

and a crossing gate). The operation for bug fixing in this exercise is (arc deletion, 1), and therefore a "X" button to apply a mutation operator of arc deletion only once is provided on the pane that contains the faulty EPN of the crossing gate control system. The trainee pushes the "X" button, and clicks an arc of the faulty EPN to delete it. In Fig. 3, the arc from T5 to P10 has been deleted from the faulty EPN. The number on a button for operations for bug fixing tells how many times its mutation operator needs to be applied to a faulty EPN, and it decreases with application, as shown in Fig. 2 and Fig. 3. A button for operations for bug fixing becomes unavailable if its number reaches 0. Also, a trainee can push the "Retry" button to undo all his/her operations at any time.

Soon after pushing the "Answer" button, the trainee is notified whether his/her bug fix is correct or not. Additionally, the training page shows the synchronous motion of the fixed EPN and its animated graphics. The motion can be controlled by using fast/normal/slow play buttons and a stop button. Fig. 4 and Fig. 5 give the screen shots of the training page on the subject of the crossing gate control system, just after pushing the "Answer" button. In Fig. 4, the trainee has successfully fixed the intended bug, and the synchronous motion of the fixed EPN and its animated graphics shows that the crossing gate closes with the approach of a train. On the other hand, in Fig. 5, the crossing gate does not close in spite of the approach of a train, since the trainee has failed in bug fixing. The trainee can undo his/her incorrect bug fixing, and retry this exercise by pushing the "Retry" button.

Note that a trainee cannot view the synchronous motion of a faulty/fixed EPN and its animated graphics before pushing the "Answer" button in the prototype tool, which will encourage a trainee to carefully view and think about the EPN at first. When a trainee cannot understand a given faulty EPN, he/she pushes the "Answer" button without any modification and can view the synchronous motion.

4. Discussion

This section gives discussion about effectiveness based on trial application of the prototype tool.

We created six exercises on the subject of a crossing gate control system and an elevator control system, and set them to the prototype tool. After that, a graduate student who is studying a test case generation technique based on EPNs in our laboratory worked on the exercises on the prototype tool. As a result of this trial application, he succeeded in all bug fixing. His average time to finish correct bug fixing is about 133 seconds, and his average number of incorrect bug fixing is three. Finally, we and the graduate student entered a free discussion, and the following opinions were obtained:

- The prototype tool is of high quality, and animated graphics seem to accelerate trainee's understanding for EPNs.
- However, some exercises have lower degree of difficulty, since same original EPNs and their animated graphics are reused to reduce the cost of creating exercises.
- Trainer's effort will be largely devoted to creating animated graphics, and a technique and tool need to be developed to support it.
- The quality of intended bugs will depend on the degree of expertise and experience of a trainer. Heuristic approaches such as a genetic algorithm will be able to be applied to support/automate the creation of good intended bugs.
- A trainee will not know which exercise to select. It is better that the prototype tool can suggest appropriate exercises for each trainee, according to his/her achievement.
- It will be better to allow a trainee to view the synchronous motion from the first.
- Some user interfaces should be improved.

5. Conclusion and Future Work

In this paper, we have proposed an animated graphics-based training support method for bug fixing of EPNs, and showed a prototype tool that the core of the proposed method has been implemented into. As a result of trial application of the prototype tool, we found that animated graphics seem to accelerate trainee's understanding for EPNs, but the cost to create good exercises is not small. To improve this problem, we will construct a technique and tool to assist the creation of animated graphics and intended bugs. Also, we plan to develop a function to suggest appropriate exercises automatically for each trainee, according to his/her achievement.

Acknowledgements

This work was supported by JSPS KAKENHI Grant Number JP17K00103.

References

1. I. Ho and J. Lin, Generating Test Cases for Real-Time Software by Time Petri Nets Model, in *Proc. of 8th Asian Test Symposium (ATS)* (Nov. 1999), pp.295-300.
2. T. Katayama, H. Tachiyama, Y. Kita, H. Yamaba, K. Aburada and N. Okazaki, BWDM: Test Cases Automatic Generation Tool Based on Boundary Value Analysis with VDM++, *Journal of Robotics, Networking and Artificial Life (JRNAL)*, Vol.4, No.2 (Sept. 2017), pp.110-113.
3. J. Fitzgerald, P.G. Larsen, P. Mukherjee, N. Plat and M. Verhoef, *Validated Designs for Object-Oriented Systems*, (Springer-Verlag London, 2005).
4. T. Takagi and T. Katayama, Negative Test Case Generation from an Extended Place/Transition Net-Based Mutants, in *Proc. of International Conference on Artificial Life and Robotics (ICAROB)* (Feb. 2018), pp.513-516.
5. T. Takagi, S. Morimoto and T. Katayama, Development of a Tool for Extended Place/Transition Net-Based Mutation Testing and Its Application Example, *Journal of Robotics, Networking and Artificial Life (JRNAL)*, Vol.4, No.2 (Sept. 2017), pp.168-174.
6. T. Takagi, R. Takata, Z. Furukawa, F. Belli and M. Beyazıt, Metrics for Model-Based Mutation Testing Based on Place/Transition Nets, in *Proc. of Joint Conf. of 21st Int. Workshop on Software Measurement and 6th Int. Conf. on Software Process and Product Measurement (IWSM-MENSURA)* (Nov. 2011), pp.7-10.
7. N.G. Leveson and J.L. Stolzy, Safety Analysis Using Petri Nets, *IEEE Transactions on Software Engineering*, Vol.13, No.3 (Mar. 1987), pp.386-397.

Prototype of a Modeling Tool to Convert between Extended Place/Transition Nets and VDM++ Specifications

Tomohiko Takagi
Faculty of Engineering and Design, Kagawa University
2217-20 Hayashi-cho, Takamatsu-shi, Kagawa 761-0396, Japan

Ryo Kurozumi
Faculty of Engineering, Kagawa University
2217-20 Hayashi-cho, Takamatsu-shi, Kagawa 761-0396, Japan
E-mail: takagi@eng.kagawa-u.ac.jp, s15t225@stu.kagawa-u.ac.jp

Abstract

In software modeling, after converting an EPN (Extended Place/transition Net) to a VDM++ specification, engineers will repeatedly modify the EPN or the VDM++ specification. However, it is not so easy for engineers to keep the consistency between them, since it is a time-consuming task. To address this problem, we are developing a prototype of a modeling tool including the generators between an EPN and a VDM++ specification. This paper shows functions of the prototype, discussion about effectiveness, and so on.

Keywords: Software Modeling, Place/Transition Net, VDM++ Specification

1. Introduction

Software modeling is the activity to construct a requirements specification that represents the abstracted structure and/or behavior of software to be developed, and it plays an important role in the development of high-quality software. In software modeling, software engineers can use EPN (Extended Place/transition Net)[1] that is a directed graph-based formal modeling language. An EPN specification, that is, a requirements specification that has been drawn based on EPN is also called an EPN. EPN is useful to define the complex behavior of software in which some modules work concurrently. It has higher representation power than traditional place/transition net, because of the introduction of guards and actions. A guard and action can be attached to each transition of an EPN, and they are written in VDM++[2] that is a text-based formal modeling language in VDM (Vienna Development Method), and thus an EPN can be straightforwardly converted to a VDM++ specification.

Both of EPNs and VDM++ specifications are abstracted, unambiguous, and executable requirements specifications, but EPNs provide more abstracted and intuitive view than VDM++ specifications. Both can be used to create test cases[1,3], and also can be converted to source codes. Therefore, they will give software engineers a practical way for model-driven development.

After converting an EPN to a VDM++ specification, software engineers will repeatedly modify the EPN or the VDM++ specification. In order to keep the consistency between them, the VDM++ specification should be updated along with the EPN, and vice versa. However, it is not so easy for software engineers due to their limited time. A technique and tool are needed to address this problem.

This paper shows a prototype of a modeling tool that converts and keeps the consistency between EPNs and

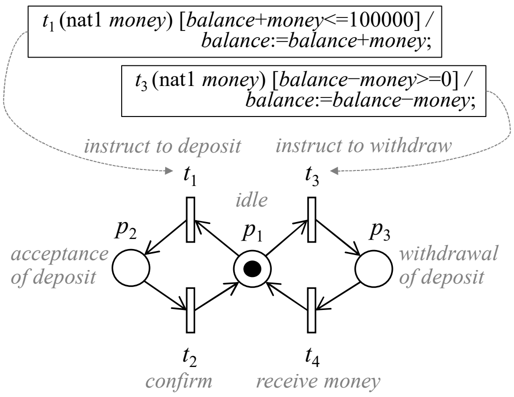

Fig. 1. EPN of simple account management.

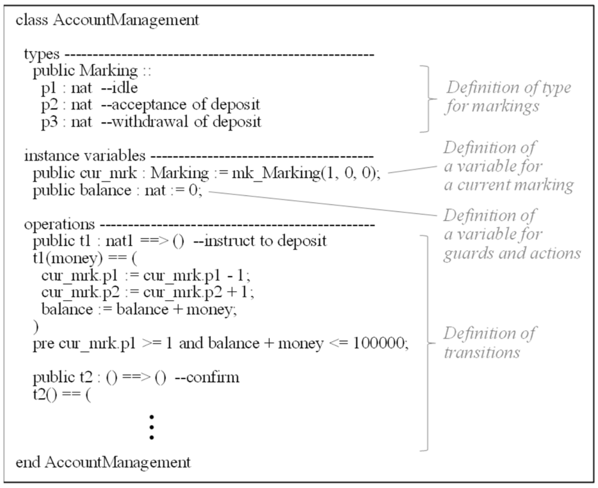

Fig. 2. VDM++ specification based on an EPN.

VDM++ specifications. In section 2, we describe the overview of software development using EPNs and VDM++ specifications, and illustrate functions of the prototype of the modeling tool. Section 3 gives discussion about its effectiveness, and finally section 4 shows conclusion and future work.

2. Conversion between EPNs and VDM++ Specifications

In this section, we describe the overview of software development using EPNs and VDM++ specifications, and clarify the scope of this study. After that, we illustrate functions of the prototype of the modeling tool.

2.1. *Overview of software development using EPNs and VDM++ specifications*

The basic processes of software development we suppose in this study are as follows.

(i) An EPN is constructed based on software requirements. It consists of six kinds of element, that is, places (representing the state of each module), tokens (representing the current state of each module), transitions (representing the state transition that is triggered by an event), arcs (representing the change of tokens by the firing of a transition), guards (representing the additional condition for a transition to be fireable), and actions (representing the data processing in a transition). A state of software is expressed as a marking and values of instance variables.
An example of an EPN that represents simple account management is given in Fig. 1. It has three places, one token, four transitions, and eight arcs. The transitions t_1 and t_3 have guards and actions. For example, t_1 can be fired, if the from-place p_1 holds a token and the guard "*balance* + *money* <= 100000" is satisfied. Also, when it is fired, the action "*balance* := *balance* + *money*;" is executed. "*balance*" is an instance variable that can be accessed from all the guards and actions in the EPN. "*money*" is an event parameter of nat1 type that represents an input from a user, and it can be accessed from the guard and action of t_1 only.
Tools and techniques for EPN are used in this process.

(ii) A VDM++ specification is constructed based on the EPN in order to refine the requirements specification. The guards and actions in the EPN have been written in VDM++, and thus the EPN is straightforwardly converted to a VDM++ specification. Fig. 2 shows an example of a VDM++ specification that is converted from Fig. 1. The refinement is performed based on the converted VDM++ specification, and its results are reflected to the EPN. Software engineers can return to the process (i) at any time. Tools and techniques for VDM++ are used in this process.

(iii) The implementation is performed based on the EPN or VDM++ specification, that is, source codes are written based on skeleton codes that are converted from the EPN or VDM++ specification. Software engineers can return to the processes (i) and (ii) at any time, if they find any problems. Tools and techniques for EPN or VDM++ are used to generate the skeleton codes, and common programming environments are used to complete the implementation.

(iv) Software testing is performed based on the EPN, VDM++ specification and others. Software engineers can return to the processes (i), (ii) and (iii) at any time, if they find any problems. Tools and techniques for EPN, VDM++ and others are used in this process.

The scope of this study is the processes (i) and (ii).

2.2. *Functions of the prototype of the modeling tool*

We are developing a prototype of a modeling tool to support the processes (i) and (ii) that have been discussed in section 2.1. The screen shot of the prototype is shown in Fig. 3. It consists of the following functions (including functions under construction).

Editor of an EPN

The EPN editor with GUI (Graphical User Interface) allows a user (that is, a software engineer) to intuitively construct an EPN. The user puts places, tokens, transitions, and arcs on the drawing pane shown as (A) in Fig. 3, and then edits their attributes including guards and actions on the attribute pane shown as (B) in Fig. 3. The editor can highlight the parts that will include structure errors, such as isolated places and transitions. The user can keep his/her EPN on file.

Generator from an EPN to a VDM++ specification

A VDM++ specification can be generated from an EPN that has been constructed on the EPN editor. The generator is invoked from the GUI of the EPN editor. The generation is executed based on the coding pattern shown in Fig. 2. If the generator finds any problems on the EPN, it stops the generation and gives error messages to the user. A VDM++ specification generated is sent to and shown in the VDM++ specification editor discussed below.

Editor of a VDM++ specification

The VDM++ specification editor with GUI allows a user to refine a VDM++ specification given from the above-mentioned generator. The editor can highlight some keywords of VDM++ and parts that will include syntax

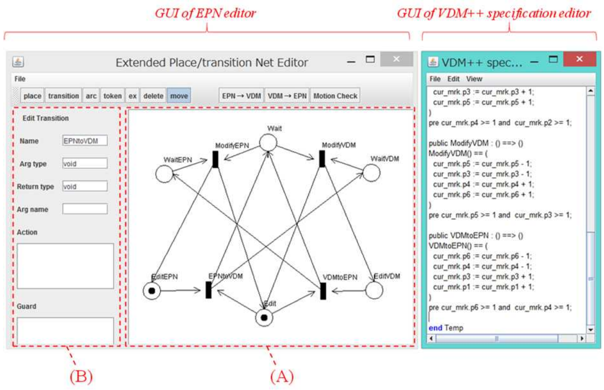

Fig. 3. Prototype of the modeling tool.

errors. The user can keep his/her VDM++ specification on file.

Generator from a VDM++ specification to an EPN

An EPN can be generated from a VDM++ specification that has been constructed on the VDM++ specification editor. The generator is invoked from the GUI of the EPN editor, and it parses the VDM++ specification. Note that the generator can accept only a VDM++ specification based on the coding pattern shown in Fig. 2. If the generator finds any problems on the VDM++ specification, it stops the generation and gives error messages to the user. An EPN generated is sent to and shown in the EPN editor, and it can be modified on the editor.

3. Discussion

This section gives discussion about the effectiveness of the prototype.

The key functions to achieve the aim of this study are the generators between an EPN and a VDM++ specification. When a user has modified an EPN, he/she can immediately update a VDM++ specification by using the generator from an EPN to a VDM++ specification. Also, when a user has modified a VDM++ specification, he/she can immediately update an EPN by using the generator from a VDM++ specification to an EPN. However, both of the generators are invoked by manual operation. It is better that they are automatically invoked in order to reduce software engineers' effort and surely keep the consistency.

The prototype does not provide a function to execute an EPN and VDM++ specification on its GUI. As already mentioned, the advantage of EPNs and VDM++ specifications is to be executable, and EPNs provide more abstracted and intuitive view than VDM++ specifications. Therefore, a function to execute an EPN on the EPN editor should be developed so that a user can check a requirements specification effectively. It will be useful also to support model-based testing in a software testing process.

The quality of a requirements specification affects the quality of software as a final product. The requirements specification in this study is written in EPN and VDM++, and thus techniques and tools for EPN and VDM++ need to be introduced into the prototype in order to effectively improve the quality of the requirements specification from the viewpoint of both EPN and VDM++.

4. Conclusion and Future Work

In this paper, we have discussed a prototype of a modeling tool that converts and keeps the consistency between EPNs and VDM++ specifications. The prototype has four functions, that is, (a) the editor of an EPN, (b) the generator from an EPN to a VDM++ specification, (c) the editor of a VDM++ specification, and (d) the generator from a VDM++ specification to an EPN. The key functions to achieve the aim of this study are (b) and (d). When a user has modified an EPN, he/she can immediately update a VDM++ specification by using (b). Also, when a user has modified a VDM++ specification, he/she can immediately update an EPN by using (d).

In our future study, the prototype will be improved so that (b) and (d) can be automatically invoked in order to reduce software engineers' effort and surely keep the consistency. Also, we plan to develop a function to execute an EPN on the EPN editor, which will be useful to check a requirements specification.

Acknowledgements

This work was supported by JSPS KAKENHI Grant Number JP17K00103.

References

1. T. Takagi and T. Katayama, Negative Test Case Generation from an Extended Place/Transition Net-Based Mutants, in *Proc. of International Conference on Artificial Life and Robotics (ICAROB)* (Feb. 2018), pp.513-516.
2. J. Fitzgerald, P.G. Larsen, P. Mukherjee, N. Plat and M. Verhoef, *Validated Designs for Object-Oriented Systems*, (Springer-Verlag London, 2005).
3. T. Katayama, H. Tachiyama, Y. Kita, H. Yamaba, K. Aburada and N. Okazaki, BWDM: Test Cases Automatic Generation Tool Based on Boundary Value Analysis with VDM++, *Journal of Robotics, Networking and Artificial Life (JRNAL)*, Vol.4, No.2 (Sept. 2017), pp.110-113.

Application of Pairwise Testing to Test Cases by Boundary Value Analysis in BWDM

Futa Hirakoba*, Tetsuro Katayama*, Yoshihiro Kita†,
Hisaaki Yamaba*, Kentaro Aburada*, and Naonobu Okazaki*
*University of Miyazaki, Japan, †Tokyo University of Technology, Japan
hirakoba@earth.cs.miyazaki-u.ac.jp, kat@cs.miyazaki-u.ac.jp, kitayshr@stf.teu.ac.jp,
yamaba@cs.miyazaki-u.ac.jp, aburada@cs.miyazaki-u.ac.jp, oka@cs.miyazaki-u.ac.jp

Abstract

BWDM is a test case generation tool for the VDM++ specification. The existing BWDM could cause a combinatorial explosion of the generated test cases. To reduce the number of test cases, there is PICT: a pairwise testing tool. However, BWDM cannot call PICT library. Hence, we have developed PICT-wrapper. It is an interface to connect PICT and BWDM. We extend BWDM in that PICT-wrapper is embedded. The extended BWDM eliminate the possibility of the combinatorial explosion.

Keywords: software testing, boundary value analysis, pairwise testing, formal methods, VDM++, PICT

1. Introduction

As the importance of software in society is increasing, specifications using specification languages become more important.[1] It is necessary to test the developed software, but it takes much time and effort to design test cases manually. So, we developed BWDM (Boundary Value Vienna Develop Method).[2, 3]

In BWDM, test cases are generated by boundary value analysis and symbolic execution from VDM++ specification. However, it is possible to cause a combinatorial explosion by the number of the test cases because the existing BWDM generate by all combinations when boundary value analysis. There is a pairwise testing[4] as an effective testing method to reduce the total number of the combinations. According to Ref. 4, there are very few defects occurring in three or more factors. Therefore, combination testing is effective for two factors. (To find the defects occurring in three or more factors, you should test with other techniques.) And, to test combinations of only two factors is called pairwise testing. In order to solve the above problem in the existing BWDM, this research extends BWDM so that the pairwise testing can be applied to boundary value analysis in BWDM. In applying the pairwise testing, we use PICT (Pairwise Independent Combinatorial Testing Tool) developed by Microsoft Corporation.[5] We have developed PICT-wrapper. It is an interface to connect PICT and BWDM. And, we have extended BWDM in that PICT-wrapper is embedded.

2. The existing BWDM

BWDM has the following features.

- Test cases generation by symbolic execution.[2]
- Test cases generation by boundary value analysis.[3]

In symbolic execution, it is expected that the test cases generated by symbolic execution can cover the all execution flow. Test cases generated by boundary value analysis can be used for boundary testing. By using BWDM, efficiency of software development for VDM++ specification can be improved.

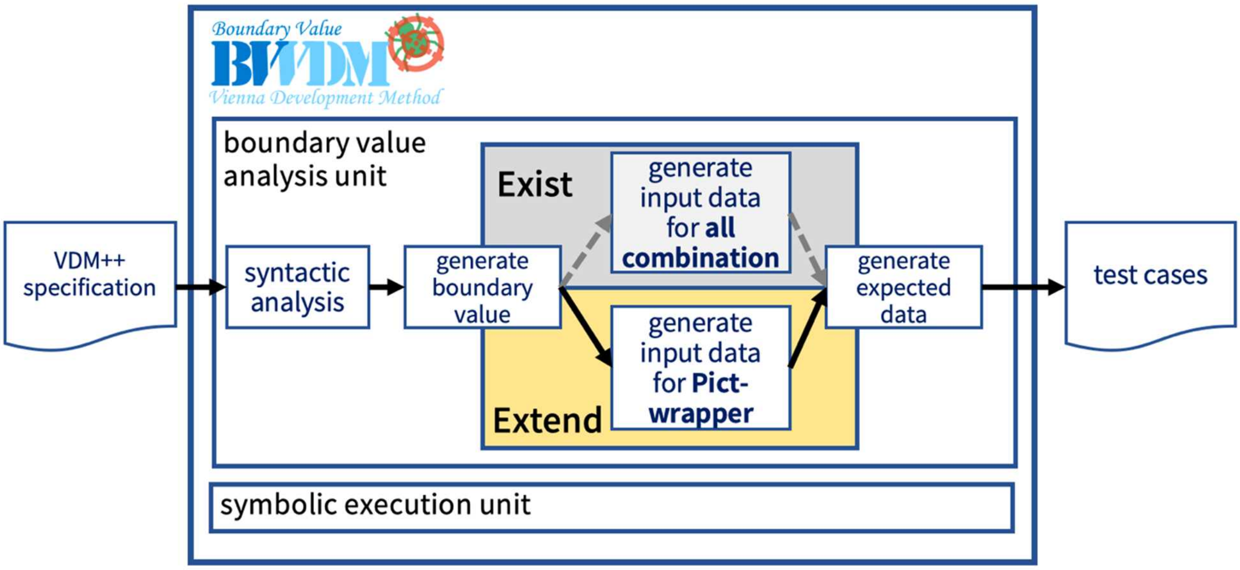

Fig. 1. The flow of the extended BWDM.

However, there is a problem with BWDM. In generating test cases by boundary value analysis, the number of the generated test cases is determined by multiplying values of each that the factors can take. For example, in the case of factors (6, 6, 2, 4, 5, 7), BWDM generates 10,080 test cases. That is, a combination explosion may occur. In this paper, we extend BWDM to solve this problem.

3. The extended BWDM

We have developed PICT-wrapper. It is an interface to connect PICT and BWDM. And, we have extended BWDM in that PICT-wrapper is embedded. The details are described below.

3.1. *PICT-wrapper*

Although PICT is a CLI tool, it also provides an API (PICT library), which can be used from C++ programs. However, since the existing BWDM is written in Java, it cannot call the PICT library. Therefore, as a preparation for extension of BWDM, we develop another PICT library that can be called from Java programs using JNA (Java Native Access).[6] We call it PICT-wrapper. The functions mainly used in the PICT-wrapper are shown below.

- PictAddParameter - Registering factors and levels to PICT
- PictGenerate - Generating of combination data
- PictGetNextResultRow - Getting generated data

3.2. *Application of pairwise testing*

Fig. 1 shows the flow of the extended BWDM. In the boundary value analysis unit, it extracts boundary values of minimum and maximum values of types for each argument accordance with conditional expression in the function of VDM++ specification. In the existing BWDM, all combinations of boundary values generated for each argument are generated as input data in boundary value testing.

In the extended BWDM, input data are generated by applying the pairwise testing using the PICT-wrapper described in Section 3.1. Specifically, it inputs parameters that can be taken by factor obtained by boundary value generation into the PICT-wrapper. In the pairwise testing, by focusing on a pair of two factors, a combination testing of all pairs is executed. Here, in the PICT-wrapper by changing its setting, it is also possible to make N pairs of factors.

The input data generation algorithm of the PICT-wrapper that received boundary value data is shown below. The flow of the PICT-wrapper using this algorithm is shown in Fig. 2. PICT-wrapper generates

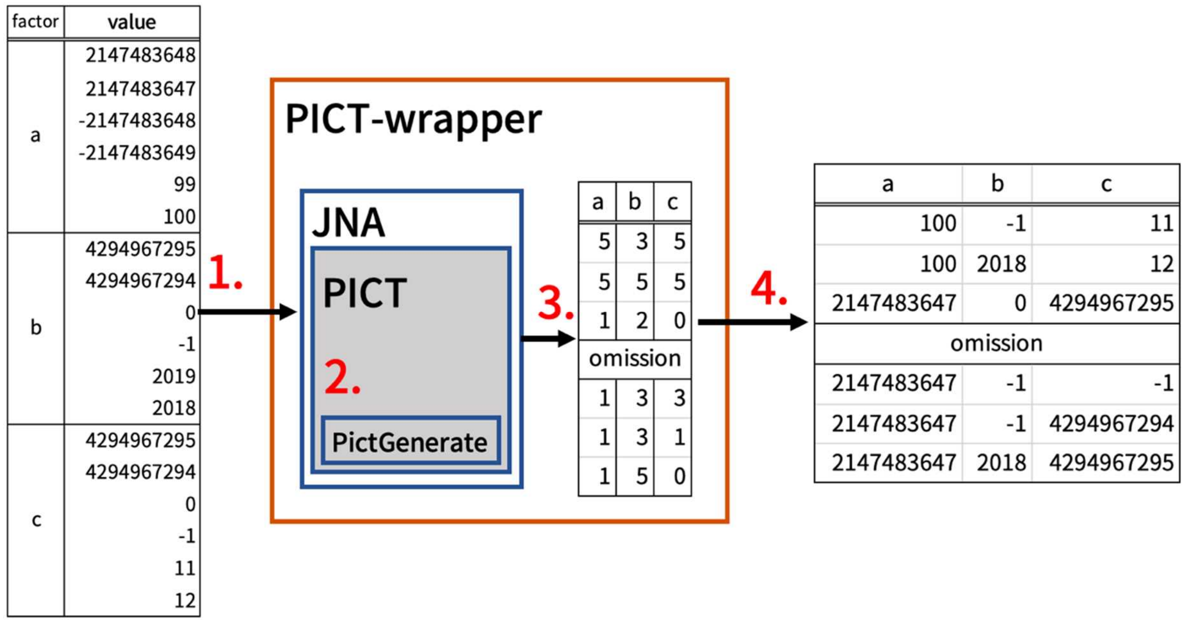

Fig. 2. The flow of PICT-wrapper.

Table 1. Application result.

Number	Input			Expected output
1	100	-1	11	Undefined Action
2	100	2,018	12	"a is 100 or more and c is 12 or more"
3	2,147,483,647	0	4,294,967,295	Undefined Action
~	~	~	~	~
38	2,147,483,647	-1	-1	Undefined Action
39	2,147,483,647	-1	4,294,967,294	Undefined Action
40	2,147,483,647	2,018	4,294,967,295	Undefined Action

test data, using factors and values of each factor, which are given by boundary value analysis result, as arguments.

i. By using PictAddParameter, register factors and levels in PICT.
ii. By using PictGenerate, generate combination data to which the pairwise testing was applied.
iii. By using PictGetNextResultRow, acquire one combination data generated by step ii. The acquired data is an index of parameters that can be taken by the factors.
iv. Generate output data of PICT-wrapper using parameters corresponding to the index of data acquired by step iii.

4. Application example

The results of applying a VDM++ specification to the extended BWDM is shown in Table 1. In the VDM++ specification, the factor is 3, the level is a function of (6, 6, 6).

In the existing BWDM, 216 test cases were generated. In the extended BWDM, 40 test cases are generated test cases. The number of the generated test cases can be reduced. In addition, it was confirmed that 40 test cases can cover all combinations of pairs of two factors.

5. Evaluation

We confirm that the extended BWDM can reduce the number of test cases compared to existing BWDM. In experiment of the comparison, we input function of factor 7 and level (6, 8, 6, 8, 8, 6, 6) into BWDM. A comparison of generation results is shown in Table 2. The execution environment is macOS 10.13.6 (CPU: Intel

Table 2. Comparison of the generation result.

	Number of generated test cases	Execution time(sec)
The existing BWDM	663,552	6.767146152
The extended BWDM	78	0.88973152

Core i5 2.3 GHz, RAM: 16 GB). The formula used for comparison is shown below.

$$Reduction\ rate(\%) = \frac{A - B}{A} \times 100 (1)$$

where

A is Total test cases generated by the existing BWDM.
B is Total test cases generated by the extended BWDM.

From Table 2 and Eq. (1) the number of generated test cases could be reduced by (663,552 - 78) / 663,552 × 100 = 99.98(%). The existing BWDM generated a huge number of test cases. But, the extended BWDM generated a practical number of test cases. Therefore, the extended BWDM can eliminate possible to cause a combination explosion of test cases. Furthermore, test case generation time could be shortened (see Table 2). As a result, the extended BWDM is more highly practical.

However, the extended BWDM cannot use a part of features of PICT library. For example, the extended BWDM cannot set a constraint of a specific combination. The restriction of the specific combination means a combination which must be tested or a combination which does not need to be tested. In order to conduct flexible testing, it is necessary to deal with it in future. Also, since BWDM still has few VDM++ syntax that can be applicable to it, it is necessary to expend its applicable range, In the case of A boundary value analysis for the extended BWDM, it can't be analyze conditional expression that contains two or more variables. By solving these problems, BWDM will become more practical.

6. Conclusion

In this paper, we have extended BWDM. The purpose is to eliminate the possibility of the combinatorial explosion occurring in the number of test cases generated from boundary value analysis results. The extended BWDM performs boundary value analysis on the VDM++ specification, applies a pairwise testing, and automatically generates test cases. As an evaluation result, we confirmed the extended BWDM can eliminate possibility to cause the combination explosion of the test cases generated from the boundary value analysis result. Therefore, the extended BWDM is more highly practical. Also, the extended BWDM is expected to improve the efficiency of the test process because the test cases for a function including many factors and many levels have become a practical number.

The future issues are as follows.

- Expanding an applicable range of BWDM.
- Corresponding to a constraint of the specific combination.
- Corresponding to boundary value analysis of conditional expression including two or more variables.

References

1. Anne E. Haxthausen, *An introduction to formal methods for the development of safety-critical application*, DTU Informatics Technical University of Denmark, pp.1-32 (2010).
2. Hiroki Tachiyama and Tetsuro Katayama, *Structure Recognition Method of If-Then-Else Expression in BWDM using VDM++ Specification*, IPSJ/SIGSE Software Engineering Symposium, pp.130-137 (2017) (in Japanese).
3. Hiroki Tachiyama, Tetsuro Katayama, et al., *Prototype of Test Cases Automatic Generation Tool BWDM Based on Boundary Value Analysis with VDM++*, International Conference on Artificial Life and Robotics, pp.275-278 (2017).
4. D. Richard Kuhn, Dolores R. Wallace and Albert M. Gallo, *Software fault interactions and implications for software testing,* IEEE Transactions on Software Engineering, Vol. 30, pp.418-421 (2004).
5. Microsoft Corp., *Microsoft/pict Pairwise Independent Combinatorial Testing*, https://github.com/Microsoft/pict (last accessed on 2018/11/07)
6. *java-native-access/jna Java Native Access*, https://github.com/java-native-access/jna (last accessed on 2018/11/07)

Development of Library Fescue Extracting Elements of Attributes and Operations of Class Diagram in UML

Keisuke Mori*, Tetsuro Katayama*, Yoshihiro Kita†,
Hisaaki Yamaba*, Kentaro Aburada*, and Naonobu Okazaki*
**University of Miyazaki, Japan, †Tokyo University of Technology, Japan*
hirakoba@earth.cs.miyazaki-u.ac.jp, kat@cs.miyazaki-u.ac.jp, kitayshr@stf.teu.ac.jp,
yamaba@cs.miyazaki-u.ac.jp, aburada@cs.miyazaki-u.ac.jp, oka@cs.miyazaki-u.ac.jp

Abstract

No existing UML tools can describe all the grammar defined in UML 2.0 specification. This paper develops library fescue (Feature Elements Section of Class in UML Extraction) extracting elements of attributes and operations of Class Diagram in UML to expand the analyzable range of the grammar defined in UML 2.0 specification. It is confirmed that fescue can parse the components of attributes and operations that the existing tools cannot parse.

Keywords: UML, Class Diagram, Attribute, Operation, Syntax Analysis

1. Introduction

In object-oriented software development, UML[1] (Unified Modeling Language) is widely used as a standard model notation for problem analysis and specification description. Therefore, many modeling tools and development support environments for UML have been developed, and some modeling tools have the function to convert the described model into programs. However, no existing tools can describe all the grammar defined in UML 2.0 specification[2] (hereinafter called the Specification).

This paper develops library fescue (Feature Elements Section of Class in UML Extraction) extracting elements of attributes and operations of Class Diagram in UML for expanding the analyzable range of the grammar defined in the Specification. The two functions to realize this purpose are needed as follows:

- Parsing grammar defined in the Specification
- Extracting each element from parsing result

2. The Attribute and The Operation in Class Diagram

Figure 1 shows the BNF (Backus Naur Form) of the attribute and the operation of the Class Diagram defined in the Specification. The attribute is defined as a nonterminal symbol <attribute>, and the operation is defined as a nonterminal symbol <operation>. The attribute and the operation of Class Diagram are defined comprehensively in the Specification, but some undefined items remain.

13 nonterminal symbols undefined in the nonterminal symbols in Fig. 1 are as follows:

- name
- parameter-name
- attr-type
- type-expression
- return-type
- attr-constraint
- oper-constraint
- value-specification
- default
- integer
- attribute-name
- oper-name
- param-property

```
<attribute> ::= [<visibility>] ['/'] <name> [':'
    <attr-type>] ['['<multiplicity>']'] ['='
    <default>] ['{' <attr-modifier> [','
    <attr-modifier>]* '}']

<operation> ::= [<visibility>] <name> '('
    [<parameter-list>] ')' [':' <return-type>]
    ['{' <oper-property> [',' <oper-property>]*
    '}']

<visibility> ::= '+' | '-' | '#' | '~'

<attr-modifier> ::= 'readOnly' | 'union' |
    'subsets' <attribute-name> | 'redefines'
    <attribute-name> | 'ordered' | 'unique' |
    <attr-constraint>

<oper-property> ::= 'redefines' <oper-name> |
    'query' | 'ordered' | 'unique' |
    <oper-constraint>

<parameter-list> ::= <parameter> [','
    <parameter>]*

<parameter> ::= [<direction>] <parameter-name>
    ':' <type-expression> ['[' <multiplicity>
    ']'] ['=' <default>] ['{' <parm-property>
    [',' <parm-property>]* '}']

<direction> ::= 'in' | 'out' | 'inout' | 'return'

<multiplicity> ::= <multiplicity-range> [['{'
    <order-designator> [','
    <uniqueness-designator>] '}'] | ['{'
    <uniqueness-designator> [','
    <order-designator>] '}']]

<multiplicity-range> ::= [<lower> '..'] <upper>

<lower> ::= <integer> | <value-specification>
<upper> ::= '*' | <value-specification>
<order-designator> ::= 'ordered' | 'unordered'
<uniqueness-designator> ::= 'unique' | 'nonunique'
```

Fig. 1. The BNF of the attribute and the operation of Class Diagram defined in the Specification.

This paper defines all undefined nonterminal symbols in the Specification to exactly accept the Specification. In this paper, explanation about <name> and <parameter-name>, and definition of the grammar are as follows.

In the Specification, <name> is defined as the *name* of the attribute and the operation, and <parameter-name> is defined as the *name* of the parameter in the operation. The name in the Specification is defined as the name of the String type had by the NamedElement class, which is the generalization relation between the Attribute class having <name> and the Parameter class having <parameter-name>. String type is one of the primitive type in the Specification, and is not based on a specific character and a character string length. In term of syntax analysis, this paper defines <name> and <parameter-name> as an arbitrary character string excluding characters such as symbols (e.g. colon and parenthesis) and spaces (e.g. space character and tab character) that may be accepted as other nonterminal symbols.

```
attribute
    :   visibility? divided? name attrType?
        multiplicityRange? defaultValue?
        attrModifiers?
    ;

operation
    :   visibility? name parameterList
        returnType? operProperties?
    ;
```

Fig. 2. Root nodes of defined grammar in ClassFeature.g4.

3. The Grammar File

This paper describes the grammar file ClassFeature.g4 needed for ANTLR[3] used in Section 4 based on the grammar defined in Section 2. The described grammar file is 320 lines. Figure 2 shows the root nodes of the defined grammar in the grammar file. Also, Table 1 shows the relationship of nonterminal symbols in Fig. 1 and nonterminal symbols in Fig. 2.

From Table 1, it can be seen that all items of terminal or nonterminal symbols of the attribute and the operation in Fig. 1 are defined by the respective nonterminal symbols in Fig. 2.

4. Fescue

This paper develops library fescue[4] (Feature Elements Section of Class in UML Extraction), which is an element extraction of the attribute and the operation. Fescue is based on the parser generated by ANTLR from the grammar file described in Section 3. Fescue is written in Java programming language.

Fescue instantiates each nonterminal symbol in the grammar file described in Section 3 when fescue is entered and scans a character string representing an attribute or an operation. The class structure in fescue is a tree structure because it is modeled on the structure of the syntax tree generated by the parser. An instance corresponding to a higher nonterminal symbol has a function of extracting each instance corresponding to a lower nonterminal symbol. Basically, fescue is developed as the Java class file structure based on the nonterminal symbols defined in Section 2 and Section 3. Here, due to restrictions of the programming language, some structures are partially changed.

Table 1. Relationship of nonterminal symbols in Fig. 1 and nonterminal symbols in Fig. 2.

Nonterminal Symbol in Fig. 2		Nonterminal Symbol in Fig. 1	
attribute	visibility	<attribute>	<visibility>
	divided		‘/’
	name		<name>
	attrType		‘:’ <attr-type>
	multiplicityRange		‘{‘ <multiplicity> ‘}’
	defaultValue		‘=’ <default>
	attrModifiers		‘{‘ <attr-modifier> [‘,’ <attr-modifier>]* ‘}’
operation	visibility	<operation>	<visibility>
	name		<name>
	parameterList		‘(‘ <parameter-list> ‘)’
	returnType		‘:’ [<return-type>]
	operProperty		‘{‘ <oper-property> [‘,’ <oper-property>]* ‘}’

```
- projectId : char [*] = SuperClass.getProjectId() + "001" {ordered}
```

Fig. 3. Example: a statement of attribute of one line.

```
+ calculateProjectPoint(in projectId : char [*] = "Project number 001", parameters : double
    [(lowCount-1)..*] = instances.searchParameters(true, instances.getProjectId()).get() {readOnly}) :
    double {query, redefines SuperClass.calculate()}
```

Fig. 4. Example: a statement of operation of one line.

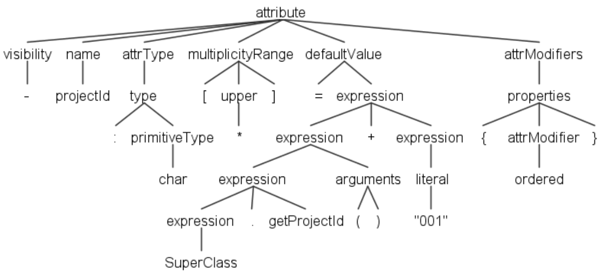

Fig. 5. Syntax tree of the statement in Fig. 3.

For example, the attribute in Fig. 2 has seven nonterminal symbols, but Attribute class in fescue has a relationship with the next six classifiers.

- Visibility enumeration
- Type class
- Name class
- MultiplicityRange class
- DefaultValue class
- Property interface

There is not a class corresponding to the nonterminal symbol “divided”. This is the reason for a structure that Attribute class has as a boolean “isDivided” field. Furthermore, Attribute class has List type Property interface as nonterminal symbol “attrModifiers”.

Fescue is executed by the test code written in JUnit5[5] and JaCoCo[6], and C1 coverage is measured in fescue. In all classes generated by fescue, C1 coverage of class files other than the syntax analyzer files automatically generated by ANTLR is 100%. The number of items being testing with the fescue library is 4000 or more. In addition, automatic build and automatic test using Travis CI[7] are carried out, and now all test cases are passed. As a result, it is confirmed that fescue can extract all terminal symbols in the syntax analysis result (see Subsection 5.1).

5. Evaluation

This paper evaluates the grammar file in Section 3, and describes related research. Hereinafter, a character string representing an attribute is called an attribute sentence, and a character string representing an operation is called an operation sentence.

5.1. *Evaluation of grammar file*

As an application example, an attribute sentence and an operation sentence are entered to a grammar test which is a function of ANTLR, and its syntax tree is generated. Figure 3 shows the applied attribute sentence, and Figure

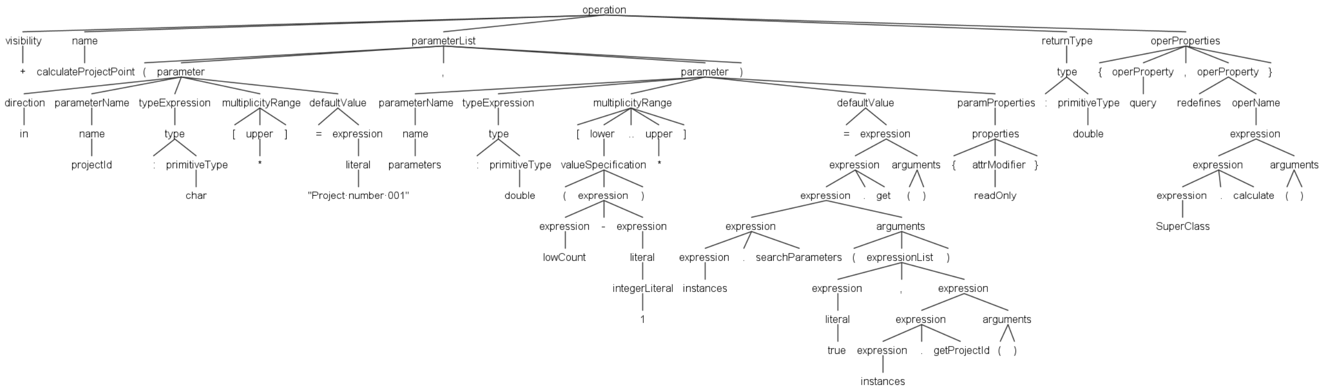

Fig. 6. Syntax tree of the statement in Fig. 4.

4 shows the applied operation sentence. In addition, Figure 5 shows the syntax tree of the statement in Fig. 3, and Figure 6 shows the syntax tree of the statement in Fig. 4.

Even if any existing tool is entered the character strings in Fig. 3 and Fig. 4, it does not output correct parsing results (see Subsection 5.3). Looking at each node of depth one from the root nodes in Fig. 5 and Fig. 6, it is confirmed that each node corresponds with each nonterminal symbol in Fig. 2. Similarly, it is also confirmed that each node deeper than depth one corresponds with each terminal or nonterminal symbol. Therefore, it is confirmed that the correct syntax tree can be generated for all terminal symbols in Fig. 5 and Fig. 6. As a result, the grammar file in the paper is useful because it can analyze attribute sentences and operation sentences which cannot be analyzed by the existing tools.

5.2. *Related research*

BlueJ[8] is an IDE (Integrated Development Environment) for supporting to learn Java. It can execute coding Java and editing Class Diagram simultaneously.

When comparing BlueJ and fescue, BlueJ cannot edit attributes and operations with the character string defined in the Specification. BlueJ is an IDE targeting Java, and if you want to edit the attributes and operations of the Class Diagram, you must edit the Java code. Fescue can parse attribute sentences and operation sentences. Hence, you can edit them in the Class Diagram.

6. Conclusion

This paper has developed library fescue, which is an element extraction of attributes and operations due to expanding the analyzable range of the grammar defined in the UML 2.0 specification. This paper has described ANTLR grammar file which is based on the BNF of the attribute and the operation in the UML 2.0 specification.

It is confirmed that fescue can extract all terminal symbols of attributes and operations which cannot extract by the existing UML tools.

Therefore, fescue developed in this paper can extract all terminal symbols. If fescue is incorporated into the existing UML tools, the incorporated tools are expected to expand grammar which can analyze. As a result, fescue is useful because the incorporated tools are useful for converting the described model to programming language.

Future works are as follows:

- Application to definition grammar with UML 2.5.1
- Acceptance of OCL grammar in prop-modifier of attribute, oper-property, and param-property of operation

References

1. *Welcome To UML Web Site!,* http://www.uml.org/ (accessed 2018-11-12).
2. Object Management Group, *The Unified Modeling Language 2.0 Specification*, Ohmusha, 2006 (in Japanese).
3. Terence Parr, *The Definitive ANTLR4 Reference*, The Pragmatic Bookshelf, 2012.
4. *fescue*, https://github.com/morichan/fescue/ (accessed 2018-11-12).
5. *JUnit 5*, https://junit.org/junit5/ (accessed 2018-11-12).
6. *EclEmma – JaCoCo Java Code Coverage Library*, https://www.jacoco.org/jacoco/ (accessed 2018-11-12).
7. *Travis CI – Test and Deploy Your Code with Confidence*, https://travis-ci.org/ (accessed 2018-11-12).
8. Michael Kolling and Bruce Quig, The BlueJ system and its pedagogy, in *Computer Science Education*, Vol. 13, No. 4, pp. 208–213, (2014).

Tamias: a Syntax File Checker for Parsing Expression Grammar

Toshihiro Miyaji*, Tetsuro Katayama*, Yoshihiro Kita†,
Hisaaki Yamaba*, Kentaro Aburada*, and Naonobu Okazaki*
**University of Miyazaki, 1-1 Gakuen-kibanadai nishi, Miyazaki, 889-2192 Japan*
†Tokyo University of Technology, 1404-1 Katakuramachi, Hachioji City, Tokyo 192-0982, Japan
E-mail: miyaji@earth.cs.miyazaki-u.ac.jp, kat@cs.miyazaki-u.ac.jp, kitayshr@stf.teu.ac.jp,
yamaba@cs.miyazaki-u.ac.jp, aburada@cs.miyazaki-u.ac.jp, oka@cs.miyazaki-u.ac.jp

Abstract

Parsing Expression Grammar (PEG) proposed by Bryan Ford has the higher expressive ability than traditional BNF, but it also has problems such as prefix capture. "Prefix capture" is a problem of hiding the language to be accepted according to the order of choice. To support checking syntax files including such mistakes, this paper proposes Tamias: a syntax file checker to support checking the PEG syntax files. Tamias has PEG interpreter which can check production rules of PEG. It can verify the behavior of production rules and measure the reach rate of choices.

Keywords: Syntax Analysis, Parser, Parsing Expression Grammar, Packrat Parsing

1. Introduction

BNF (Backus-Naur Form) can express type-2 grammar (CFG: Context-Free Grammar) in the Chomsky hierarchy. Although BNF is traditionally used in the syntax definition of programming languages, it is possible to describe ambiguous grammar (e.g. dangling-else problem). The ambiguous grammar is not allowed programming languages because the compiler would interpret multiple languages. Unfortunately, it has been proved that there is no algorithm to judge that the CFG contains ambiguous grammar.[1,2]

On the other hand, Parsing Expression Grammar (PEG) introduced by Bryan Ford[3] is not ambiguous grammar because it has ordered choice property. However, the ordered choice causes "prefix capture".[4] "Prefix capture" is a problem of hiding the language to be accepted according to the order of choice. Checking syntax files that contain such mistakes usually confirms the behavior of the parser generated by the parser generator. However, in confirming the behavior of the parser, it is possible to check only the top level non-terminal symbols, and it is necessary to rebuild the parser for each change in the syntax file. To support checking syntax files, this paper proposes Tamias: a syntax file checker to support checking the PEG syntax files.

2. Parsing Expression Grammar and its parsing technique

Parsing Expression Grammar (PEG) is a formal grammar, introduced by Bryan Ford in 2004.[3] PEG is deterministic. Therefore, it is suitable for the syntax definition of the programming languages, and it was found that not only the Context-Free Grammar (CFG) but also a part of the Context-Sensitive Grammar (CSG) can be expressed.

2.1. *Definition of PEG*

A PEG G is defined by the 4-tuples:

$$G = (V_N, \Sigma, R, e_S)$$

where

1. V_N is a finite set of non-terminal symbols.
2. Σ is a finite set of terminals ($\Sigma \cap V_N = \phi$).

3. R is a finite set of production rules.
4. e_S is a parsing expression called the start expression.

The production rule is described in the form of "$A = e$" (where $A \in V_N$, e is a parsing expression). A parsing expression is an instruction for an input string given by users and is described by a non-terminal symbol or a terminal symbol. A parsing expression can use operators. When the input string s is applied to the parsing expression e, e matches the substring of s and indicates "success" or "failure". s has a pointer p representing the reading position. If e indicates success, e consumes the substring of s (i.e. advances p by the length of the substring). Also, if e indicates failure, let s applies the next parsing expression.

2.2. *Packrat parsing technique*

Packrat parsing is one of parsing techniques that can parse PEG. [5] It is a top-down parsing technique proposed by Bryan Ford in 2002. Ford solved the problem that the parsing time of PEG including a backtracking increases exponentially with linear time by memoization of the parsing result.

2.3. *Prefix capture*

"Prefix capture" is a problem of hiding the language to be accepted according to the order of choice. For example, the grammar "A = ('+' / '++')[a-z]" does not accept the language "++i". The reason is that parsing "[a-z]" fails after parsing "+" of the language "++i". To solve this problem, the order '+' and '++' is reversed. Thus, it is difficult to understand prefix capture immediately.

3. Tamias

Tamias is a syntax file checker to support checking the syntax files for PEG. Tamias has three areas: a text editor area, a list of non-terminal symbols, and a production rules check area. Tamias has PEG interpreter which can check all choices and any non-terminal symbols in production rules according to PEG. Also, Tamias can parse without building a parser. A checking method using a PEG interpreter can be selected from the production rules check area. There are two methods of checking the production rules, "production rules verification" and "reach rate measurement". Both methods require one testable symbol and one input string. A testable symbol refers to a non-terminal symbol from which a terminal symbol can be derived. Tamias recursively searches and extracts testable symbols from the grammar described in the text editor area.

3.1. *Production rules verification*

Production rules verification can confirm whether the input string is accepted by the production rule. In one verification, production rules verification requires an expected output in addition to one testable symbol and one input string. The users can select whether the specified input string is accepted or rejected. Tamias displays the comparison result between the expected output and the output of PEG interpreter. If the expected output and the actual output are equal, "Passed" is displayed. Otherwise, "Failed" is displayed.

3.2. *Reach rate measurement*

Reach rate measurement calculates the rate of success of parsing in the ordered choice of the selected production rule. The reach rate is obtained by assigning two or more check results in one production rule to the following calculating formula:

$$\text{Reach rate [\%]} = \frac{\text{Parsing success choices}}{\text{All choices}} \times 100 \qquad (1)$$

3.3. *PEG interpreter*

PEG interpreter is an interpreter that executes parsing for PEG described in text editor in Tamias. PEG interpreter requires a testable symbol and an input string. PEG interpreter shows the output of the parsing expression after parsing. By selecting testable symbols, PEG interpreter can check not only top level non-terminal symbols.

4. Implementation of PEG interpreter

4.1. *Data used in the PEG interpreter*

- Production rules
  Production rules are rules obtained from non-terminal symbols that can be derived from testable symbols. One production rule is expressed as a pair of a non-terminal symbol and a parsing expression.
- Input string
  Input string has a string and a pointer that expresses a reading position.
- Lookup table
  Lookup table stores the reading position of the input string. The row of the lookup table corresponds to

Algorithm 1 PEG interpreter

```
Input: nt: testable symbol ∈ non-terminal symbol, s: input string
Output: success or failure
function PARSE(nt, s)
    ex ← parsing expression corresponding to nt
    if nt is stored in the lookup table then
        s consumes the stored value
        return success
    end if
    for choice in ordered choices in ex do
        if SEQUENCE(choice, s) is success then
            Memoize the reading position of s
            return success
        end if
        Memoize failed reading position of s
        return failure
    end for
end function
function SEQUENCE(choice, s)
    Get the current reading position of s
    for parsing expression in choice do
        if parsing by operator is success then
            s backtrack to the previous position
            return failure
        end if
    end for
    return success
end function
```

Fig. 1. PEG interpreter algorithm

the parsing processing, and the column corresponds to the reading position of the input string.

4.2. *PEG interpreter algorithm*

The algorithm of the PEG interpreter is shown in Fig.1. It recursively is executed until parsing of the terminal symbol.

5. Experiment and Discussion

We confirm that PEG interpreter can parse correctly by using grammar representing addition and multiplication and grammar including prefix capture.

5.1. *Production rules verification*

We confirm the production rules verification method by using grammar representing the addition and multiplication below:

Sum = Product '+' Product / Product Product = Value '*' Value / Value Value = [0-9]

We write the grammar in the text editor area of Tamias and check the two languages "1+2*3" and "*2" in the production rules check area. Next, we selected "accept" as the expected output in both languages. The experimental results are shown in Fig.2.

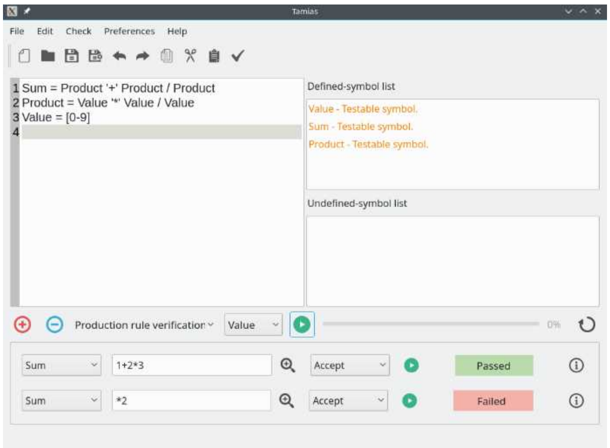

Fig. 2. Result of executing production rules verification

As shown in Fig.2, the check result of the language "1+2*3" according to the grammar was "Passed". On the other hand, the check result of the language "*2" not conforming to the grammar was "Failed". Therefore, the production rules verification can check the grammar correctly.

5.2. *Reach rate measurement*

We confirm the reach rate measurement method by using grammar "A = ('+' / '++')[a-z]" including prefix capture. However, since Tamias does not currently support input of parsing subexpression, we write the following grammar into the text editor area of Tamias.

A = Op Id Op = '+' / '++' Id = [a-z]

Next, we measure the reach rate of "A" using two languages "+i" and "++i". Finally, we reverse the choices of "Op" and measure the reach rate of "A" using the same languages. The experimental results are shown in Fig.3.

As shown in Fig.3, the reach rate is not 100% in the grammar including prefix capture. In contrast, the reach rate is 100% in the grammar excluding prefix capture. Therefore, from the formula of reach rate (section 3.2 (1)):

$$\text{Parsing success choice} = \text{All choices}$$

it can be proved that prefix capture has not occurred for all input strings.

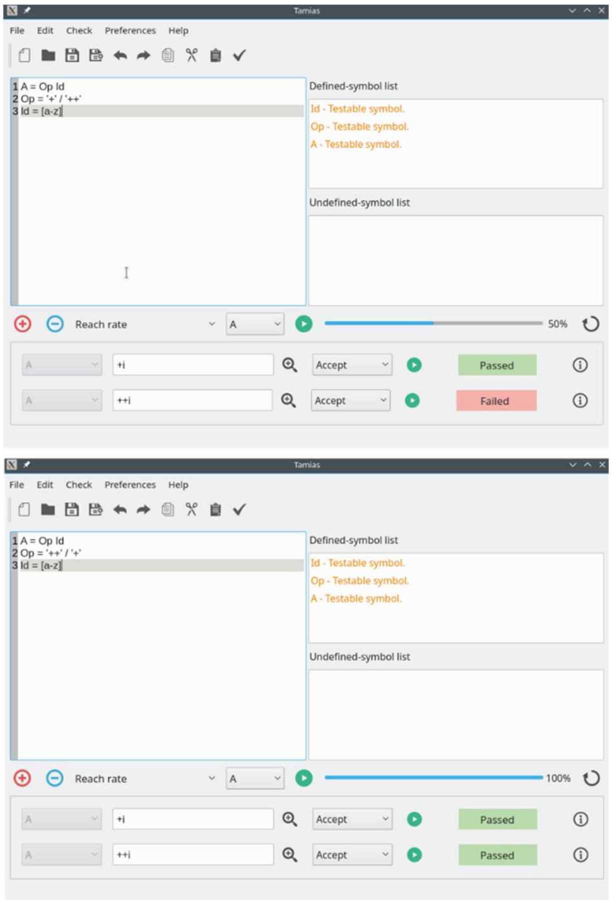

Fig. 3. Two results of executing reach rate measurement

6. Related Research

Honda et al. proposed a PEG debugger to support development of PEG.[6] The PEG debugger has functions such as setting breakpoints, executing steps, displaying stack trace, and so on. The PEG debugger can check the behavior for one input and the occurrence of prefix capture. However, the PEG debugger cannot prove that prefix capture has not occurred for any input string.

Mori et al. proposed a parser generator that can composite parsers and implemented its prototype.[7] In the traditional method, when part of the syntax in PEG was changed, it was necessary to rebuild the corresponding parser. The proposed method can generate a parser that can deal with the problem of the traditional method. Tamias solves the problem of rebuilding the parser by implementing a PEG interpreter.

7. Conclusions

In this paper, we have proposed Tamias: a syntax file checker to support checking the syntax files for PEG. Tamias has PEG interpreter which can check all choices and any non-terminal symbols in production rules according to PEG. Tamias can check the production rules and can measure reach rate of choices by using PEG interpreter. In the production rules verification, Tamias compares the expected output with the output of the PEG interpreter and displays the result. In the reach rate measurement, Tamias can check that the grammar does not contain prefix capture.

The experiment with a grammar representing addition and multiplication showed that Tamias can compare the expected output by users with actual output by PEG interpreter without building a parser. The experiment with a grammar including prefix capture showed that Tamias can prove that prefix capture has not occurred for any input strings by measuring reach rate.

Therefore, Tamias can support checking PEG syntax files. A future work is to improve Tamias to support parsing subexpression described by parentheses.

References

1. David G Cantor, On the ambiguity problem of Backus systems. *Journal of the ACM (JACM),* Vol.9, No.4, pp.477-479, 1962.
2. Robert W Floyd, On ambiguity in phrase structure languages. *Communications of the ACM,* Vol.5, No.10, pp.526-534, 1962.
3. Bryan Ford, Parsing expression grammars: a recognition-based syntactic foundation. *ACM SIGPLAN Notice,* Vol. 39, pp.111-122. ACM, 2004.
4. Roman R Redziejowski, Parsing expression grammar as a primitive recursive-descent parser with backtracking. *Fundamenta Informaticae,* Vol.79, No.3-4, pp.513-524, 2007.
5. Bryan Ford, Packrat parsing:: simple, powerful, lazy, linear time, functional pearl. *ACM SIGPLAN Notices,* Vol.37, pp.36-47. ACM, 2002.
6. Shun Honda et.al., Implementing and Evaluating a Debugger for Supporting Development of PEGs, *JSSST*, Vol.32, pp.1-6, 2015. (in Japanese)
7. Kensuke Mori et al., Composition of parsers for incremental Parsing Expression Grammars., *JSSST*, Vol.30, pp.641-650, 2013. (in Japanese)

Implementation of an Arduino Simulator to Support Circuit Design

Tatsumi Nishida*, Tetsuro Katayama*, Yoshihiro Kita†,
Hisaaki Yamaba*, Kentaro Aburada*, and Naonobu Okazaki*
**University of Miyazaki, 1-1 Gakuen-kibanadai nishi, Miyazaki, 889-2192 Japan*
†Tokyo University of Technology, 1404-1 Katakuramachi, Hachioji City, Tokyo 192-0982, Japan
E-mail: nishida@earth.cs.miyazaki-u.ac.jp, kat@cs.miyazaki-u.ac.jp, kitayshr@stf.teu.ac.jp,
yamaba@cs.miyazaki-u.ac.jp, aburada@cs.miyazaki-u.ac.jp, oka@cs.miyazaki-u.ac.jp

Abstract

Embedded technologies are used everywhere. One of the educational materials to learn the embedded technologies is Arduino. When a beginner designs circuit, it is possible to design the circuit that damages Arduino itself or the modules on it. Therefore, this research implements an Arduino simulator that runs on iPad for supporting to design a circuit. In this simulator, the circuit on iPad is analyzed to detect the value of voltage on the circuit and the risk that Arduino itself or the modules are damaged.

Keywords: embedded technologies, Arduino, simulator, iPad

1. Introduction

Embedded technologies are used everywhere and are indispensable in our daily life.[1] For example, there are cars, car navigation systems, air conditioners, televisions, and so on. As the demand for embedded software increases, its development is also diversifying. One of the educational materials to learn the embedded technologies is Arduino. Arduino is used around the world as learning kits.[2,3] We can learn embedded technologies by designing a circuit and controlling the circuit by programming.

The learning kits that summarize sensors and jumper wires are also on the market, and Arduino has the advantage that even a beginner who have never designed a circuit can easily develop it. However, when a beginner designs a circuit, it is possible to design the circuit that damages Arduino itself or the modules on it.

Therefore, this research implements an Arduino simulator ADVIS (Arduino VIrtual Simulator) that runs on iPad for supporting to design a circuit. In ADVIS, the circuit on ADVIS is analyzed to detect the value of voltage on the circuit and the risk that Arduino itself or the modules are damaged. These features can support to design a circuit on Arduino.

2. Arduino Uno

Arduino has various kinds such as Arduino Uno, and Arduino Leonardo, and so on. ADVIS developed in this paper simulates Arduino Uno.

Fig.1 shows an overview of Arduino Uno. Arduino Uno is a digital input / output device equipped with 8 bits microcomputer. Arduino Uno itself has 32KB flash memory. Therefore, even if it is turned off, the program can be saved in it. Arduino Uno flows electric current of 20 mA of current from each output pin. Based on the above specifications, the value of the electric current flowing from each output pin of ADVIS is 20 mA.

In Arduino, depending on the circuit designed by a user, it is possible to design the circuit that damages Arduino itself on it. Specifically, there are the followings.

- A risk of overvoltage when output pins are connected

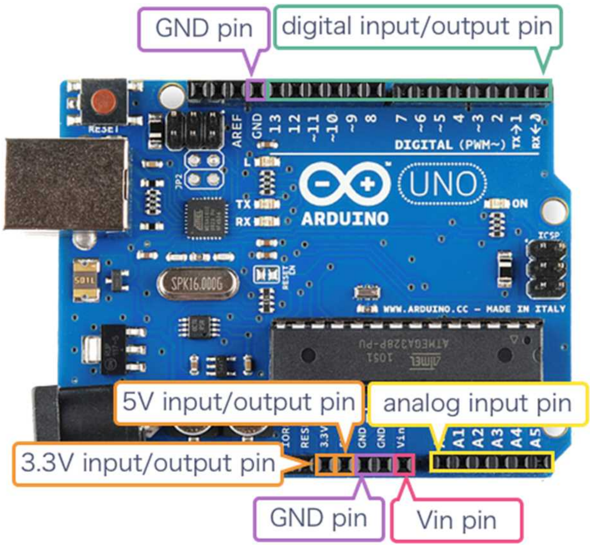

Fig. 1. An overview of Arduino Uno

- A risk of damaging the blocking diode in the Arduino itself when the voltage exceeding 3V is sent to the input pin
- A risk of overcurrent if the input pin receives an electric current exceeding 200mA

In the implementation of ADVIS in this paper, only the first and second risks as above can be detected.

3. Arduino simulator ADVIS

The requirements of ADVIS is as follows.

- iPad Pro 12.9 (2nd generation)
- iOS 10+

Fig.2 shows an overview of ADVIS. ADVIS consists of the following three parts.

- Circuit design part
- Module selection part
- Menu part

3.1. *Circuit design part*

In the circuit design part, a circuit is designed using jumper wires, LEDs, and resistors.

3.2. *Module Selection part*

In the module selection part, a module to be handled in for the circuit design part is selected. ADVIS can handle jumper wires, LEDs, and resistors only. The LED has a resistance value of 100Ω, and when a voltage of 3 V or more flows, the LED lights up in green. The resistor has a resistance value of 150Ω.

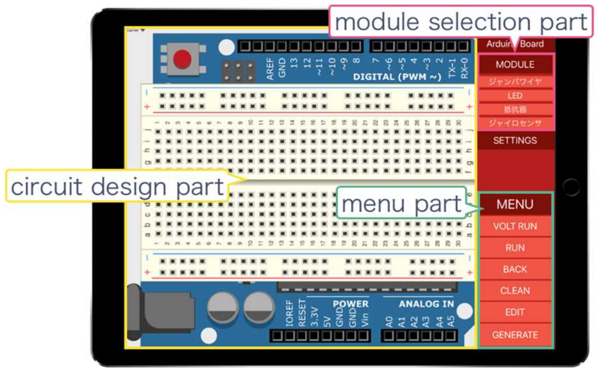

Fig. 2. An overview of ADVIS.

3.3. *Menu part*

In the menu part, it is implemented the "CLEAR" function, the "BACK" function, the "RUN" function, and the "VOLT RUN" function.

Using the "Clear" function removes all modules that are placed in the circuit design part and returns to the initial state.

Using the "BACK" function returns the circuit design part to its previous state. Here, immediately after using the "CLEAR" function, you cannot use the "BACK" function.

Using the "RUN" function, the designed circuit is executed to detect the risk of module breakage. Fig.3 shows an example of the "RUN" function (Here, the image is edited for easy-to-read). When the risk of a module breakage is detected, highlight the input pin of the module in red.

Using the "VOLT RUN" function displays the value of voltage on the designed circuit. Fig.4 shows an example of the "RUN" function (Here, the image is edited for easy-to-read).

3.4. *Function of ADVIS*

In ADVIS, in addition to the risk of damaging the Arduino itself described in Section2, the risk of damaging the module can be detected. It's target module is only LED. LED is damaged if it receives voltage more than 3V.

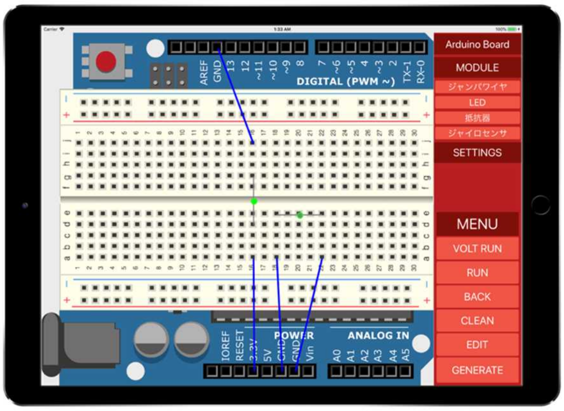

Fig. 3. Example of the “RUN” function

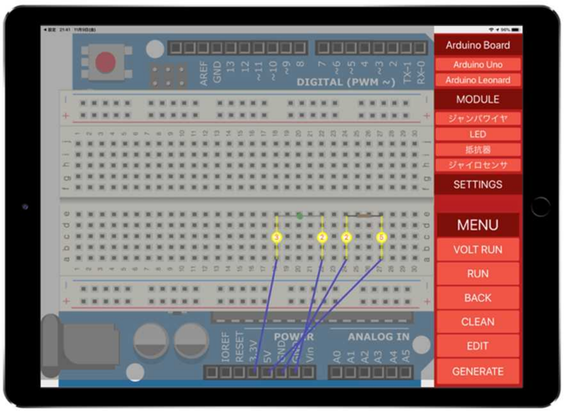

Fig. 4. Example of the “VOLT RUN” function

4. Verification if ADVIS

It is confirmed that ADVIS can simulates correctly the designed circuit. The followings are verified.

- Displaying of the value of voltage on the circuit
- Detecting a risk of Arduino itself being damaged
- Detecting a risk of module being damaged

4.1. *Displaying of value of voltage on the circuit*

To display the value of voltage on the circuit, it can be displayed by using the “VOLT RUN” function. As an example, connect 5V pin and Vin pin to the breadboard respectively. Fig.5 shows the result that the “VOLT RUN” function is executed.

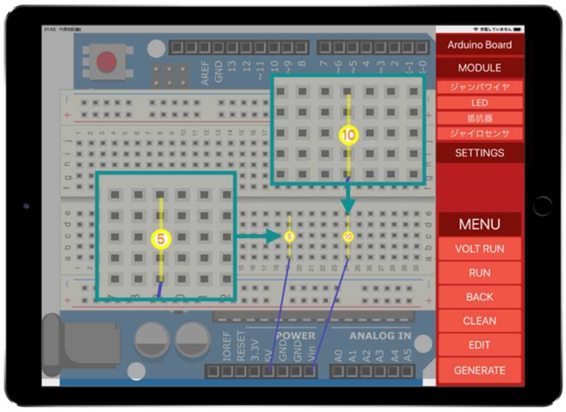

Fig. 5. Displaying the value of voltage on the circuit

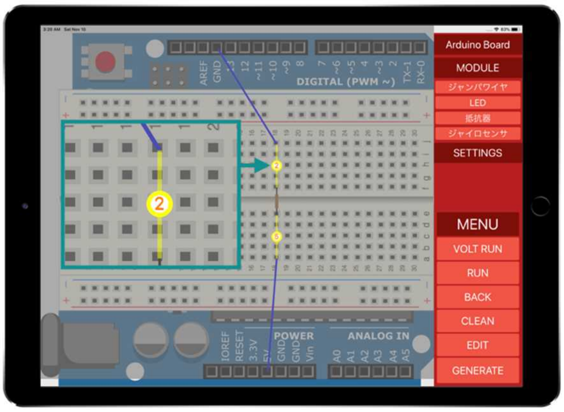

Fig. 6. Displaying of value of voltage using resistor

From Fig.5, 5V is displayed on the circuit connected to the 5V pin, and 10V is displayed on the circuit connected to the Vin pin.

Next, the resistor and the 5V pin to the breadboard are connected. Fig.6 shows the result that the "VOLT RUN" function is executed.

From Fig.6, 5V is displayed on the circuit, and 2V, which is calculated from Ohm's law ($V = 0.02 \times 150$), is displayed on the circuit.

Therefore, it can be confirmed that ADVIS displays the value of voltage.

4.2. *Detecting a risk of Arduino itself being damaged*

In order to detect where there is a risk of corruption of Arduino itself, it can be displayed by using the "VOLT RUN" function. As an example, connect 5 V pin and Vin

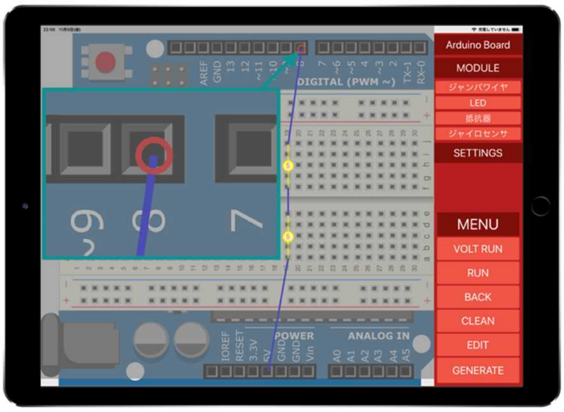

Fig. 7. Detecting a risk of Arduino itself being damaged

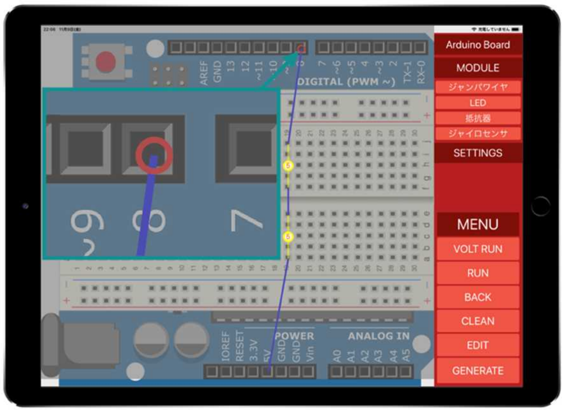

Fig. 8. Detecting a risk of the module being damaged

pin to input / output pins. In this circuit because the voltage exceeding 3V is followed to the input pin, there is a risk that the blocking diode of the Arduino itself will be damaged. Fig.7 shows the result that the "VOLT RUN" function is executed.

From Fig.7, ADVIS can display the Arduino input / output pins in red when the risk that the Arduino itself is damaged is detected.

4.3. *Detecting a risk of module being damaged*

In order to detect where there is a risk of corruption of modules, it can be displayed by using the "RUN" function. As an example, connect the LED to the 5V pin. In this circuit, there is a risk of damaging the LED because it receives the value of voltage higher than 3V. Fig.8 shows the result that the "RUN" function is executed.

From Fig.8, ADVIS can display the input pin in red when the risk that the module is damaged is detected.

5. Conclusion

This research has implemented an Arduino simulator ADVIS (Arduino VIrtual Simulator) that runs on iPad for supporting to design a circuit. The implemented ADVIS has the following functions.

- Designing a circuit
- Visualizing the value of voltage in the circuit
- Detecting a risk of Arduino itself being damaged
- Detecting a risk of module being damaged

Consequently, ADVIS can support to design a circuit. Future issues are as follows.

- Save function of the designed circuit
- Circuit control by programming
- A function to automatically generate a program based on the designed circuit
- Implementation of resistors with various values and other modules

References

1. Masayuki Hirayama: Software Engineering for Embedded System, Current State of Embedded Software Development, IPSJ Magazine, Vol. 45, No. 7, pp. 677-681, 2004 (in Japanese).
2. P. Jamieson, "Arduino for teaching embedded systems. are computer scientists and engineering educators missing the boat?", *Proc. FECS*, pp. 289-294, 2010.
3. Mohammed El-Abd, A Review of Embedded Systems Education in the Arduino Age: Lessons Learned and Future Directions, International Journal of Engineering Pedagogy, Vol. 7, No.2, pp.79-93, 2017.

Effectiveness of Data Augmentation in Automatic Summarization System

Tomohito Ouchi, Masayoshi Tabuse
Graduate School of Life and Environmental Sciences, Kyoto Prefectural University,
1-5 Shimogamohangi-cho, Sakyo-ku, Kyoto 606-8522, Japan
E-mail:t_ouchi@mei.kpu.ac.jp, tabuse@kpu.ac.jp

Abstract

We propose a new data augmentation method in automatic summarization system. A large corpus is required to create an automatic summarization system using deep learning. However, in the field of natural language processing, especially in the field of automatic summarization, there are not many data sets that are sufficient to train automatic summarization system. Therefore, we propose a new method of data augmentation. We use an encoder-decoder model with an attention mechanism as automatic summarization system. First, we determine the importance of each sentence in an article using topic model. In order to extend the data, we remove the least important sentence from an input article and use it as a new article. We examine the effectiveness of our proposed data augmentation method in automatic summarization system.

Keywords: automatic summarization, data augmentation, encoder-decoder model, attention mechanism.

1. Introduction

In recent years, the amount of information on the net of the world has increased exponentially, and it is expected to become 44 ZB in 2020[1]. Under the circumstance, the technique of automatic summarization becomes indispensable for efficient selection of information. Therefore, we first tried to start studying converting English articles that account for the majority of the information on the net into Japanese summaries. However, there is no large corpus in which English articles and Japanese summaries are set. Therefore, we considered whether the technique of data augmentation commonly used in image processing can be applied to natural language processing.

Several studies have applied data augmentation to natural language processing. A method of adding noise to an intermediate vector[2], and a method of data augmentation by generating a dialect sentence correspond to each given standard sentence[3]. However, both methods are adapted to document classification, yet none have been adapted to automatic summarization. The nature of automatic summarization is that there is little influence on the summary that is generated whether there is redundant part or not. Further, in image processing, data may be expanded by changing the background. This assumes that the background has no direct impact on the target task. Therefore, we focused on change of background which is one of data expansion of image processing, and expanded data by deleting redundant sentences of original article in automatic summary.

Automatic summarization is classified into two approaches. One is an extractive summarization in which words, phrases or sentences of input articles are directly extracted and combined to create a summary. The other is an abstractive summarization in which an input article is temporarily converted to an intermediate vector and then a summary is generated based on the intermediate vector. In extractive summarization, there is a problem of how to connect extracted words, phrases or sentences. And there is also the possibility that in extractive summarization it is unknown what the directive word is pointing at. On the other hand, in abstractive summarization, since it is generated from an internal semantic representation, there is a possibility that it becomes one integrated summary. It also learns grammatical information, so it is easy to connect words and phrases in contrast to an extractive summarization. However, the abstract summarization needs to be learned with a large number of pairs of input articles and generation summaries, which takes time and effort to prepare the corpus.

In this research, we examine whether data augmentation is effective in abstractive summary. As a method of data augmentation, an article excluding the sentence with the lowest importance level in the input article is also learned. Our abstractive summary is a model obtained by adding an attention mechanism to the encoder-decoder model. The proposed model and the method of data augmentation are described in Section 2. Experiment and evaluation are described in Section 3, discussion and summary are given in Section 4.

2. Our Model

In this section, we describe the model used in this research and the method of data augmentation.

2.1. *Attention-based Encoder-decoder model*

The basic form of the model used in our study is an encoder-decoder model combining two RNNs. RNN is used to process time series data, and updates the hidden state with input x_t at a certain time *t* and the hidden state $h_{(t-1)}$ at the previous time as inputs of RNN.

$$h_t = \sigma(Wx_t + Uh_{t-1} + b) \qquad (1)$$

W, *U* and *b* are parameters and they are the same at each time step, respectively. σ is an activation function. Figure 1 shows a simple encoder-decoder model.

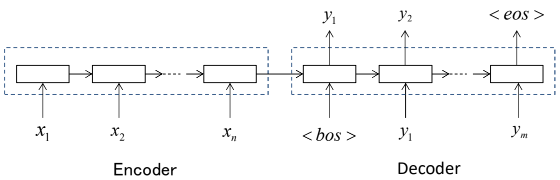

Fig.1 Encoder-Decoder model. $x_i, y_i \in \{0,1\}^V$, V is the number of vocabulary. x_i and y_i are vectors encoding of 1-of-k representation.

We put each word of the input article in RNN sequentially and the hidden vector created. When the last word of the input article is inputted, the encoder outputs the intermediate vector and decoder outputs word by word using the intermediate vector. After inputting the word as a 1-of-k vector, we embed the vector to the lower dimensional vector with an embedding matrix. However, since the number of words of the target input article is several hundreds, the information of the word entered at the beginning is hard to be transmitted to intermediate vector. Therefore, we use LSTM unit, which is resistant to gradient elimination and gradient explosion. We make LSTM on the encoder side bidirectional. As a result, it becomes multi-layered LSTM. This model is shown in Figure2.

$x_{k,l}$ represents the *l*-th word of the *k*-th sentence. n_k represents the number of words of the *k*-th sentence.

However, this model cannot reflect information well

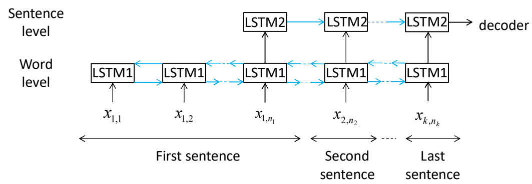

Fig.2 proposed model (encoder side only)

because the intermediate vector has a fixed number of dimensions regardless of the length of the input article. Therefore, we used the attention mechanism which uses information of the input words when the system generates words. Figure 3 shows attention-based model.

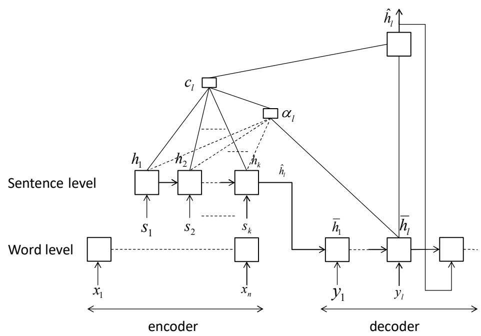

Fig.3 Attention-based model. State of generating the (l +1)-th word on decoder side

The attention-based model is expressed by the following formula.

$$\alpha_l = softmax(h_1 \cdot \overline{h}_l, h_2 \cdot \overline{h}_l, \cdots h_k \cdot \overline{h}_l) \quad (2)$$

$$c_l = \sum_{K=1}^{k} h_K \cdot \alpha_{l,K} \quad (3)$$

$$\hat{h}_l = (c_l, \overline{h}_l)^T W_C \quad (4)$$

$$y_{l+1} = \arg\max(softmax(\hat{h}_l W_h)) \quad (5)$$

$\overline{h}_l$ represents the hidden state of the *l*-th word of the generated summary. In equation (2), *softmax* function is applied to the inner product of the hidden state of each sentence and the hidden state of the generated summary word, and creates a α_l indicating which sentence is how important. In equation (3) we take a weighted average on it. In Equation (4), c_l and $\overline{h}_l$ are rearranged and converted into a hidden vector $\hat{h}_l$. In Equation (5), $\hat{h}_l$ is converted into a vector of vocabulary number dimensionality, *softmax* is applied, and the word id having the maximum value is returned.

2.2. *Data augmentation method*

We measure the importance for each sentence of the input article and use the article generated excluding the lowest important sentence as new data.
Refer to [4] for how to determine importance for each sentence in the input article. First, a topic model is created from the English Wikipedia full text, and the sentence weight is determined for each topic of the input article. Then, the sum of sentence weights for all topics is taken as the final weight of the sentence, and it was taken as the importance of the sentence.

$$b_{t,i} = \frac{W_{t,i}}{\sqrt{N_i}} \quad (6)$$

$$b_i = \sum_t b_{t,i} \quad (7)$$

Firstly the weight $b_{t,i}$ of the sentence *i* with respect to the topic *t* is examined. In Equation (6), $b_{t,i}$ multiplies the sum $W_{t,i}$ of an importance of the words constituting the sentence *i* by the inverse of the square root of the total number N_i of words as a coefficient. This coefficient is for weighting sentences that are not influenced by the sentence length. In Equation (7), we let the sum of $b_{t,i}$ be the final weight of sentence *i*.

3. Experiment and Evaluation

In this section, we evaluate the effectiveness of the data augmentation proposed in Section 2.

3.1. *Dataset*

We used CNN news story dataset [5]. This data set is a total article number of 92,579 articles, multiple summaries are attached to each article. In the experiment, we used the first abstract as a reference summary. Also, I tried learning with 45,000 articles and 90,000 articles.

3.2. *Parameter settings*

1-of-k vector of both encoder and decoder was embedded to 300 dimensional vectors. So, the input of LSTM at the word level encoder and the input of LSTM of the decoder were both 300 dimensions. Since the LSTM at the word level encoder is bidirectional, the output is 600 dimensions. So, the input of LSTM at the sentence level encoder was 600 dimensions, and the output was 300 dimensions. The final output of the attention-based model was also set to 300 dimensions. We used pre-learned word2vec [6] for the initial value of the embedding matrix and a transformation matrix to be transformed from the vector into a vector of vocabulary number dimensionality. Adam was used as a learning algorithm. In addition, beam search was used as a searching algorithm of generated sentences. The maximum summary length was 50 and the beam size was set to 16.
In the case of 90,000 articles for learning, it took 1.5 days without data augmentation and 3 days with data augmentation.

3.3. *Evaluation method*

ROUGE [7] is used as a general evaluation method of automatic summarization, which is evaluated by matching of reference summary and generated summary word. We used ROUGE-1, ROUGE-2, ROUGE-L, ROUGE-W. ROUGE-1 and ROUGE-2 evaluate unigram and bigram coincidence, respectively. ROUGE-L evaluates matching the longest common subsequence. ROUGE-W is also almost the same, but it evaluates matching of continuing longest common subsequence.

3.4. *Result*

Evaluation of our data augmentation using by ROUGE is shown in Table 1 and 2. f, r, p in the Table represent F value, recall and precision, respectively.

Experiments were performed by recognizing 1,000 test data not used for training data. The same test data was used in all cases.

	ROUGE−1 f	ROUGE−1 r	ROUGE−1 p	ROUGE−2 f	ROUGE−2 r	ROUGE−2 p
original	0.1064	0.1050	0.1116	0.0436	0.0436	0.0438
extended	**0.1149**	**0.1138**	**0.1197**	**0.0452**	**0.0451**	**0.0457**

	ROUGE−l f	ROUGE−l r	ROUGE−l p	ROUGE−w f	ROUGE−w r	ROUGE−w p
normal	0.1571	0.1540	0.1641	0.0975	0.0782	0.1350
extended	**0.1639**	**0.1612**	**0.1705**	**0.1008**	**0.0812**	**0.1386**

Table 1 Results on 45,000 articles. “original” is original data and “extended” is extended data.

	ROUGE−1 f	ROUGE−1 r	ROUGE−1 p	ROUGE−2 f	ROUGE−2 r	ROUGE−2 p
normal	0.1375	0.1348	0.1447	**0.0774**	**0.0738**	**0.0756**
extended	**0.1445**	**0.1420**	**0.1514**	0.0724	0.0722	0.0730

	ROUGE−l f	ROUGE−l r	ROUGE−l p	ROUGE−w f	ROUGE−w r	ROUGE−w p
normal	0.1253	0.1235	0.1302	0.0743	0.0599	0.1023
extended	**0.1359**	**0.1345**	**0.1406**	**0.0795**	**0.0641**	**0.1091**

Table 2 Results on 90,000 articles.

3.5. *Discussion*

Except for ROUGE-2 value of 90,000 articles, results of “extended” data were better than ones of “normal” data. The reason for this result is that using the augmentation data the system learn not only original articles but also articles with less important sentences removed, so it learn which sentences are important or not. Therefore, the model with extended data learned more information of sentences.

4. Conclusion

Although the degree of accuracy improvement by the data augmentation was lower than the degree of accuracy improvement by setting 45,000 articles to 90,000 articles, it was able to confirm that there was an effect. As a future task, since the rouge value in this model is still low, we want to improve it.

References

1. Data Growth, Business Opportunities, and the IT Imperatives, http://www.emc.com/leadership/digital-universe/2014iview/executive-summary.htm
2. Dongxu Zhang, Zhichao Yang, “Word Embedding Perturbation for Sentence Classification” arXiv : 1804.08166vl (2018).
3. I. Saito, J. Suzuki, K.Nishida, K. Sadamitsu, S. Kobashikawa, Ryo. Masumura, Y. Matsumoto, J. Tomita “Improving Neural Text Normalization with Data Augmentation at Character- and Morphological Levels” Proceedings of the 8th International Joint Conference on Natural Language Processing, 257-262 (2017).
4. H.Sigematsu, I.Kobayashi “Generation of abstracts considering importance of potential topics” The Association for Natural Language Processing (2012) (In Japanese).
5. How to Prepare News Articles for Text Summarization, https://machinelearningmastery.com/prepare-news-articles-text-summarization/
6. https://code.google.com/p/word2vec/
7. Lin C. W., “ROUGE: A Package for Automatic Evaluation of Summaries”, Proceeding of the ACL-04 workshop, Vol.8 (2004).
8. F. Shinmura, Y. Kawanishi, D. Deguchi, I. Ide, H. Murase and H. Fujiyoshi, “Pedestrian’s Inattention Estimation based Recognition of Texting While Walking from In-Vehicle Camera Images”, *IEICE Technical Report,* 83–88 (2015).
9. A. Krizhevsky, I. Sutskever and G. E. Hinton, “ImageNet Classification with Deep Convolutional Neural Networks”, *Advances in Neural Information Process. Systems 25,* 1097–1105 (2012).

A System for Posting on SNS Portrait Selected Using Facial Expression Analysis While Writing Message

Taro Asada[1], Yuiko Yano[2], Yasunari Yoshitomi[1], Masayoshi Tabuse[1]
1: Graduate School of Life and Environmental Sciences, Kyoto Prefectural University,
1-5 Nakaragi-cho, Shimogamo, Sakyo-ku, Kyoto 606-8522, Japan
E-mail: t_asada@mei.kpu.ac.jp, {yoshitomi, tabuse}@kpu.ac.jp}
http://www2.kpu.ac.jp/ningen/infsys/English_index.html
2: Nara Guarantee Corporation,
163-2 Horencho, Nara 630-8668, Japan

Abstract

We have developed a real-time system for expressing emotion as a portrait selected according to the facial expression while writing a message. The portrait is decided by a hair style, a facial outline, and a cartoon of facial expression. The system selects one portrait expressing one of neutral, subtly smiling and smiling facial expressions using two thresholds on facial expression intensity. We applied the system to post on an SNS a message and a portrait expressing the facial expression.

Keywords: Facial expression analysis, Real-time system, Mouth area, Portrait, Writing messages, OpenCV.

1. Introduction

Recently, social network services (SNSs) have become very popular as communication tools on the Internet. A message, a static image, or a moving image can be posted on Twitter. However, information about our real emotions cannot be posted on Twitter while writing a message. As a result, a message might be misunderstood by a receiver. It was reported that such a misunderstanding on a message on LINE caused bullying at a school.[1]

In this paper, we propose a real-time system for expressing three kinds of emotions as a portrait selected according to the facial expression while writing a message. For generating a portrait, a user selects one hair style and one facial outline before writing a message. The image signal is analyzed by our real-time system using image processing software (OpenCV)[2] and a previously proposed feature parameter (facial expression intensity)[3]. Then the system selects one cartoon expressing one of neutral, subtly smiling and smiling facial expressions using the facial expression intensity thresholds previously decided for these facial expressions. The portrait selection method used in this paper is based on a previously reported method.[4]

2. Proposed System and Method

2.1. *System overview and method outline*

In this system, a webcam moving image captured in real-time is analyzed via the following process.

The proposed method consists of (1) extracting the mouth area, (2) calculating the facial expression feature vectors, (3) determining the facial expression intensity and calculating its average value while writing a message, (4) selecting hair style and facial outline of portrait by a user, and (5) posting the message and an automatically selected portrait for the message on Twitter. The details of these steps are explained in the following subsections.

2.2. *Mouth area extraction*

The mouth area is selected for facial expression analysis because it is where the differences between neutral and smiling facial expressions appear most distinctly. We use the mouth area extraction method which is described in our reported research[5] and is briefly reviewed in this subsection.

Moving image data while writing message are changed from RGB to YCbCr image data, and then the face area is extracted from the YCbCr image as a rectangular shape, and the lower 40% portion of the face area is standardized. Next, the mouth area is extracted from that portion.

2.3. *Facial expression intensity measurement*

We use the facial expression intensity measurement method which is described in our reported research[5] and is reviewed in this subsection.

For the Y component of the selected frame, the feature vector for the facial expression is extracted for the mouth area. The extraction is performed by using a two-dimensional discrete cosine transform (2D-DCT) for each 8 × 8-pixel section. Two 8×8-pixel sections at each of the left and right lower corners are not included for this measurement, because these sections might cause errors due to the appearance of the jaw and/or neck line(s) there.[5]

To measure the feature parameters of the facial expressions, we select low-frequency components from the 2D-DCT coefficients for use as the facial expression feature vector elements. However, the direct current component is not included. In total, 15 feature vector elements are obtained. The facial expression intensity is defined as the norm difference between the facial expression feature vectors of the reference and target frames. In this study, the first 20 continuous frames of mouth area data successfully extracted after the webcam recording begins are treated as reference frame candidates. The reference frame selection method is explained in detail in Ref. 6.

2.4. *Selecting hair style and facial outline of portrait*

For generating a portrait of a user, the user selects (1) one gender (male or female), (2) one hairstyle among seven ones for each gender (for female, see Fig.1) and (3) one facial outline among four ones for each gender, and registers them beforehand in the proposed system.

Fig. 1. Selectable hair styles for female.

2.5. *Posting a message and an automatically selected portrait for the message on Twitter*

Facial expression intensity is measured using our previously discussed method.[7] A portrait is generated by the proposed system using a cartoon of facial expression, a hairstyle and a facial outline which are selected beforehand by the user. The cartoon is automatically selected by comparing the average value of facial expression intensity and two thresholds decided experimentally beforehand. Then the message and the selected portrait are posted on Twitter when the user presses a button of the proposed system. In this system, three portraits, expressing neutral, subtly smiling and smiling facial expressions, are used (see Fig. 2).

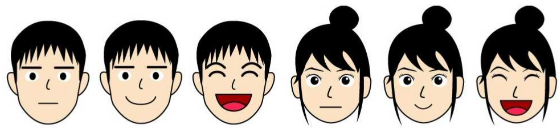

(a) (b) (c) (d) (e) (f)

Fig. 2. Each example for male or female portrait expressing neutral (a and d) , subtly smiling (b and e), and smiling (c and f) facial expressions.

3. Experiment

3.1. *Conditions*

The experiment was performed on a Dell XPS 9350 PC equipped with an Intel Core i7-6560U 2.2 GHz central processing units (CPUs) and 8.0 GB of random access memory (RAM). The Microsoft Windows 7 Professional operating system (OS) was installed on the PC and Microsoft Visual C++ 2008 and 2013 Express Editions were used as the development language. CoreTweet,[6] as a library, and the Twitter API were used to post a message and portrait on Twitter.

First, the condition of the preliminary experiment[4] for a preparation of this experiment is reviewed in this subsection. We had performed experiments with one male (subject A in his 20s) and five females (subjects B to F in their 20s) under the two conditions listed below.

As an initial condition in the experiment, the subjects had been instructed to maintain a neutral facial expression and face forward without speaking for about five seconds just after the start of the experiment. After the initial state of a neutral facial expression had been terminated, the subjects had been requested to intentionally respond with one of two types of facial expressions (Experiment P1, neutral; Experiment P2, big smile) and write a message, '友達から貰ったこのぬいぐるみかわいくない' (in Japanese), which means, 'This stuffed toy, a present from a friend, is pretty, isn't it?' Experiments P1 and P2 had been performed two times for each subject. In each experiment, facial expression intensity measurements had been performed for each subject during writing a message for 35 seconds and then the average facial expression intensity for that message had been calculated.

In this study, in order to distinguish between the neutral, subtly smiling and smiling facial expressions on the basis of average facial expression intensity while writing message, a threshold between neutral and subtly smiling expressions was set as the intermediate value of 12 average facial expression intensities of the six subjects for neutral (Experiment P1), and then one between subtly smiling and subtly smiling expressions was set as that for big smile (Experiment P2).

In this study, three experiments (Experiments 1, 2, 3) were performed with two males (subject G in his 20s, subject H in his 40s) and one female (subject I in her 20s). After the initial state of a neutral facial expression was terminated, the subjects were requested to intentionally respond with three types of emotions (Experiment 1, neutral; Experiment 2, subtly smiling; Experiment 3, smiling) and wrote a same message as that in Experiments P1 and P2. In each experiment, facial expression intensity measurements were performed for 35 seconds and then the average facial expression intensity for that message for each subject was calculated, after which both the message and the portrait expressing the facial expression while writing the message were posted on Twitter.

3.2. *Results and discussion*

Table 1 shows the average of facial expression intensity under the condition of Experiment P1 and P2 for each subject. In Table 1, the values subtracted by the average of facial expression intensity for 10 seconds in the time range of 1 to 11 seconds just after starting the experiment are shown. The intermediate values of facial expression intensities in Experiments P1 (neutral) and P2 (big smile) were 0.37 and 1.37, respectively (table 1). Therefore, the two thresholds for distinguishing between the three types of facial expressions were respectively determined as 0.37 and 1.37. Thus, in the proposed system, a facial expression having an average facial expression intensity under 0.37 is judged to be a neutral facial expression, one 0.37 or higher and under 1.37 is judged to be a subtly smiling expression, and one 1.37 or higher is judged to be a smiling expression.

Table 1. The average of facial expression intensity under the condition of Experiment P1 (neutral) and P2 (big smile).[4]

Subject	A		B		C	
1st or 2nd	1	2	1	2	1	2
Neutral	0.38	0.44	0.36	0.17	-0.4	0.51
Big smile	1.48	3.1	0.29	1.01	0.68	3.4
Subject	**D**		**E**		**F**	
1st or 2nd	1	2	1	2	1	2
Neutral	0.4	0.34	0.16	0.38	0.66	-0.06
Big smile	0.45	1.85	0.83	1.25	12.96	11.98

Tables 2 shows the average of facial expression intensity under the condition of Experiments 1, 2 and 3 for each subject. The values in Table 2 were calculated in the same manner as that for Table 1. Figs. 3 to 5 show changes in facial expression intensity of mouth area and mouth image at the characteristic timing point for each subject. As shown in Tables 2 and 3, our proposed system distinguished among the three types of facial expressions (neutral, subtly smiling, smiling) at the accuracy of (8/9). Our system misjudged as a smiling facial expression for a subtly smiling one of subject I (Tables 2 and 3).

Table 2. The average of facial expression intensity under the condition of Experiments 1, 2 and 3.

Subject	G	H	I
Exp. 1	0.13	0.07	0.26
Exp. 2	0.87	1.26	1.78
Exp. 3	10.36	1.83	7.9

Table 3. Generated portraits for subjects G and I under the condition of Experiments 1, 2 and 3.

Exp.	1		2		3	
Subject	G	I	G	I	G	I
Portrait	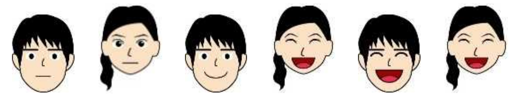					

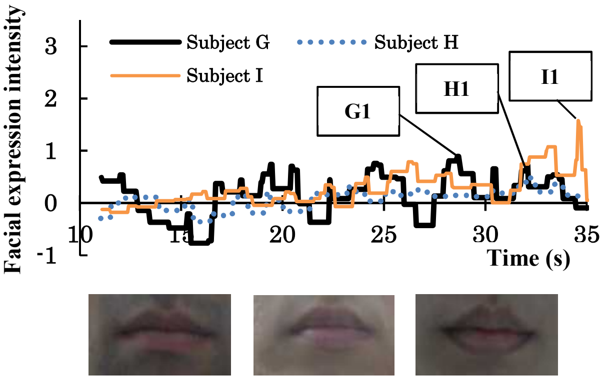

G1 H1 I1

Fig. 3. Changes in facial expression intensity of mouth area for subjects G, H and I (upper graph). Mouth images are shown for three moments during Experiment 1 (G1, H1, I1), as indicated on the graph (lower images).

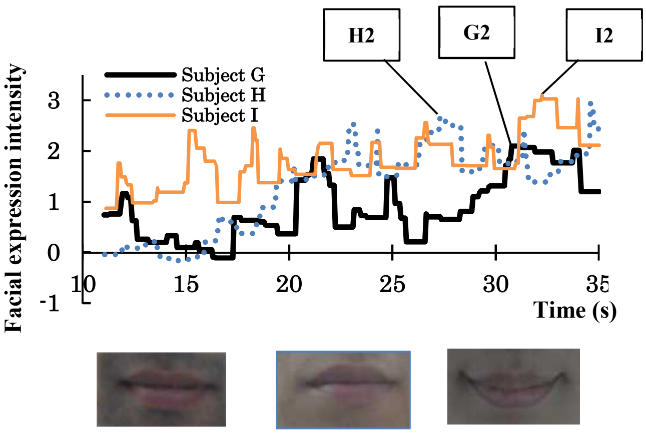

G2 H2 I2

Fig. 4. Changes in facial expression intensity of mouth area for subjects G, H and I (upper graph). Mouth images are shown for three moments during Experiment 2 (G2, H2, I2), as indicated on the graph (lower images).

4. Conclusion

Herein, we have developed a real-time system for expressing three emotions (neutral, subtly smiling, smiling) as the portraits generated according to the facial expression while writing a message. We applied the system to the posting on Twitter of both a message and a portrait. The improvement of the system for a subtly smiling judgement is one of the next targets.

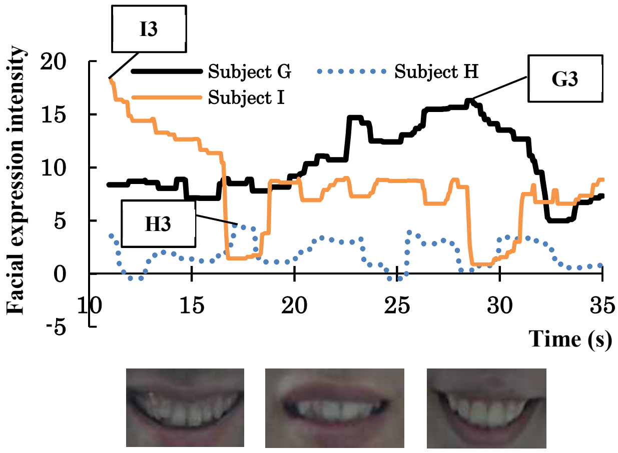

G3 H3 I3

Fig. 5. Changes in facial expression intensity of mouth area for subjects G, H and I (upper graph). Mouth images are shown for three moments during Experiment 3 (G3, H3, I3), as indicated on the graph (lower images).

Acknowledgements

We would like to thank the subjects for their cooperation in the experiments.

References

1. K. Takeuchi, *Sumaho Jidai ni Taiou Suru Seitoshidou・Kyouiku Soudan* (Honnomori Shuppan, Tokyo, 2014). (in Japanese)
2. Open CV. http://opencv.org/ Accessed 13 December 2017.
3. T. Asada, Y. Yoshitomi, R. Kato, M. Tabuse, and J. Narumoto, Quantitative evaluation of facial expressions and movements of persons while using video phone, *J. Robotics, Networking and Artif. Life* **2**(2) (2015) 111-114.
4. T. Asada, Y. Yano, Y. Yoshitomi, and M. Tabuse, Portrait selection system using facial expression analysis while writing messages on SNS (in Japanese), in *Proc. of Human Interface Symposium 2018* (Ibaraki, Japan, 2018), pp. 219-222.
5. Y. Yoshitomi, T. Asada, K. Mori, R. Shimada, Y. Yano, and M. Tabuse, Facial expression analysis and its visualization while writing messages, *J. Robotics, Networking and Artif. Life* **5**(1) (2018) 37-40.
6. R. Shimada, T. Asada, Y. Yoshitomi, and M. Tabuse, Real-time system for horizontal asymmetry analysis on facial expression and its visualization, in *Proc. of The 2017 Int. Conf. on Artif. Life and Robotics* (Oita, Japan, 2017), pp. 120-123.
7. T. Asada, K. Mori, R. Shimada, Y. Yoshitomi, and M. Tabuse, Facial expression analysis in real time while writing messages (in Japanese), in *Proc. of Human Interface Symposium 2017* (Osaka, Japan, 2017), pp. 469-472.
8. CoreTweet. https://github.com/CoreTweet/ Accessed 20 December 2017.

A Method Using Wavelet Transform for Judging Character to be Inserted into Image

Yasunari Yoshitomi[1], Takashi Sato[2], Taro Asada[1], and Masayoshi Tabuse[1]
1: Graduate School of Life and Environmental Sciences, Kyoto Prefectural University,
1-5 Nakaragi-cho, Shimogamo, Sakyo-ku, Kyoto 606-8522, Japan
E-mail: {yoshitomi, tabuse}@kpu.ac.jp, t_asada@mei.kpu.ac.jp}
http://www2.kpu.ac.jp/ningen/infsys/English_index.html
2: School of Engineering, Tokyo Institute of Technology,
2-12-1 Ookayama, Meguro-ku, Tokyo 152-8550, Japan

Abstract

There has been an increase in the number of images on the Internet that contain private information and/or the URL of an illegal Web site. This information might result in a violation of human rights and/or a crime. Based on a previously proposed method, we propose a method for judging whether characters have been inserted into an image using the discrete wavelet transform, the image compression characteristics, and the empirical knowledge that characters have strong vertical and/or horizontal elements.

Keywords: Character insertion judgement, Image compression characteristics, Internet, Private information, URL of illegal Web site, Wavelet transform.

1. Introduction

There has been an increase in the number of images on the Internet that contain private information and/or the URL of an illegal Web site. This information could result in a violation of human rights and/or a crime. It is very time-consuming and inefficient to detect such information by inspecting each individual Web page, but there is no existing automatic method for checking images for such information. To achieve such a method, the first step is to extract from the image the regions that contain characters. An algorithm for extracting such regions has received considerable attention in the field of computer vision research,[1-3] but it falls far short of practical application. For overcoming the problem, we proposed a method for extracting from an image the regions that contain characters.[4]

In the present paper, based on the previously proposed method,[4] we propose a method for judging whether characters have been inserted into an image.

2. Wavelet Transform of Image Signals

The image is first decomposed into four subbands: 1LL, 1LH, 1HL, and 1HH. The subbands labeled 1LH, 1HL, and 1HH represent the finest-scale wavelet coefficients. Fig. 1 shows the level 1 decomposition, in which the image is decomposed into four subbands that share the same scale.

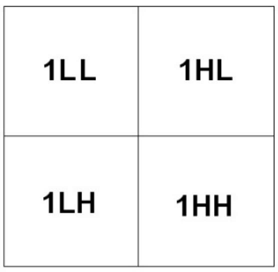

Fig. 1. Mallat division.

In general, the wavelet coefficients for these three domains (HH, HL, and LH) are called the elements of the multiresolution representation, whereas the wavelet coefficients of the other domain (LL) are called the elements of the multiresolution analysis. For further information on the DWT, see Ref. 5.

3. Method for Character Domain Extraction from Image

Fig. 2 shows the flowchart of our previously proposed method,[4] and Fig. 3 shows an example of input and output images for our system for character domain extraction. The algorithm of our previously proposed method is reviewed in this section because it is very important for the present study.

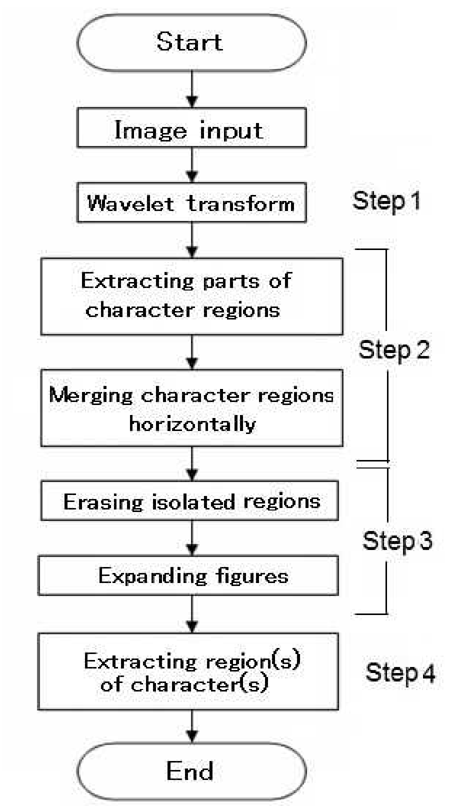

Fig. 2. Flowchart of previously proposed method.[4]

Fig. 3. Input image (left) and output image (right).[4]

Step 1: The RGB elements of the input image (Fig. 3) are transformed into YCrCb elements (Fig. 4). This is followed by applying DWT to each element to obtain the 1HL and 1LH elements, which correspond to the vertical and horizontal elements, respectively (Fig. 4).

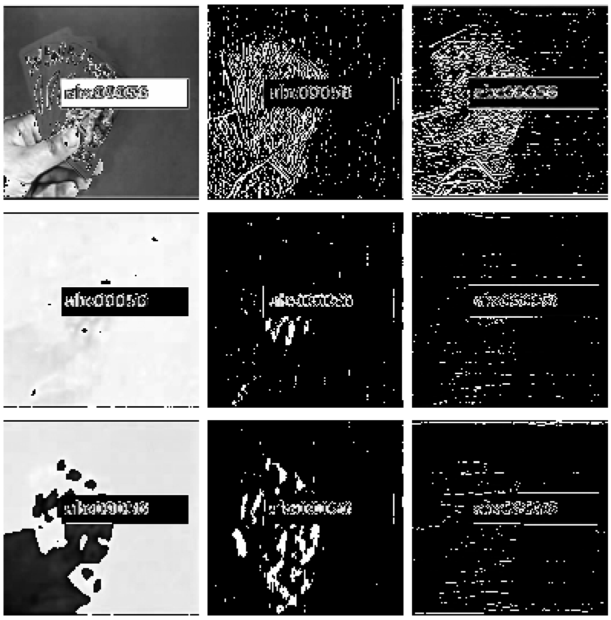

Fig. 4. 1HL (top row center) and 1LH (top row right) elements for the Y element (top row left); 1HL (middle row center) and 1LH (middle row right) elements for the Cr element (middle row left); and 1HL (bottom row center) and 1LH (bottom row right) elements for the Cb element (bottom row left); all obtained from the input image (Fig. 3).[4]

Step 2: A segmentation is performed for both the 1HL and 1LH elements, using each threshold (Fig. 5). Then, the scattered regions that have values of 255 in the binary image for each of YCrCb elements are horizontally merged by changing to the value 255 all the pixels having the same horizontal coordinate as a pixel already having the value 255.

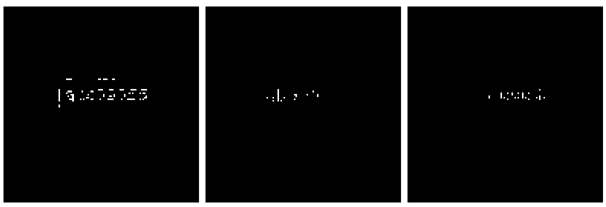

Fig. 5. Binary images obtained for both 1HL and 1LH elements for the Y, Cr, and Cb elements of the related images in Fig. 4; left: Y; center: Cr; right: Cb.[4]

Step 3: Isolated regions are erased and regions with the value 255 are expanded.
Step 4: A mask is generated for extracting from the initial RGB image those areas that contain characters. This is done by using a logical summation to merge the regions with the value 255 in the binary images obtained for the Y, Cr, and Cb elements. Finally, the output RGB image is generated by changing to white the color of any pixel for which the value of the corresponding pixel on the mask image is 0; this leaves only the regions containing characters on the RGB image.

The threshold in Step 2 was set to be half the minimum value for each element, but not higher than -40. The threshold is determined on the basis of the sharpness of the sharpest domain in the image. In cases of the input image having character regions, the threshold might be determined on the basis of the sharpness of characters. For further information on our previously proposed method, see Ref. 4.

4. Image Compression Characteristics of Output Images of Our System

We have discovered that output images of our system[4] for character domain extraction have a tendency to be small after compression by the JPEG technique when the input image has character regions. Fig. 6 shows an example of compression characteristics of an output image. The upper left image (Lena) in Fig. 6 was selected from the Standard Image Database (SIDBA). The lower left image was produced by writing several black characters ("abc09056") on the upper left image. The background of the characters was white. As shown in Table 1, we can judge whether characters are written on the image by focusing on the reduction in JPEG format image size when applying our previously proposed method[4] to the image. Fig. 7 shows the relationship between the sizes of JPEG format input and output images transformed from 24-bit 256×256 pixel BMP form. Several images used for creating Fig. 7 were selected from SIDBA. Others were gathered from the Internet. Then, several black characters ("abc09056") were written on the original images in a way similar to that shown in Fig. 6. In Fig. 7, images with character regions appear below those without character insertion.

Fig. 6. JPEG format image (left) transferred from a BMP format input image and JPEG format image (right) transferred from a BMP format output image with (bottom) or without (top) a character region.

Table 1 Size of JPEG format image (Fig. 6) transformed from 24-bit 256×256 pixel BMP form.

Character insertion	Input	Output
Without	28	19
With	29	4

(KB)

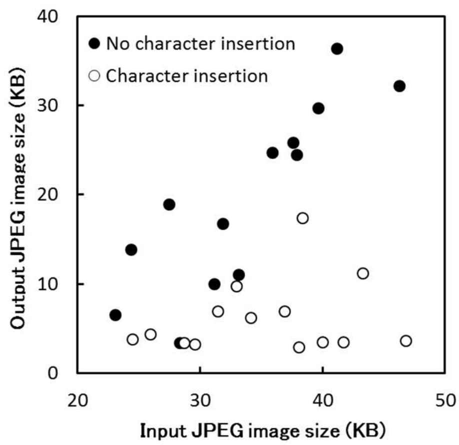

Fig. 7. Relationship between sizes of JPEG format input and output images.

5. Proposed Method for Character Insertion Judgment

Firstly, an image database is produced by collecting images with or without character insertion from a database like SIDBA or the Internet. All images in the image database are input into our system[4] for character domain extraction, and then the input and output images of our system are transformed into JPEG format images. The two-dimensional feature vector space whose components are a pair of JPEG format sizes of the input and output images of the system is prepared as teacher data. A test image is judged as to whether it has character regions as follows:

Step I A pair of JPEG format sizes of input and output images of the system is obtained for a test image. Go to step II.
Step II When the size of the output image is the constant obtained in case of an all-white image, the test image is judged as having no character regions. Otherwise, go to step III.
Step III In the two-dimensional feature vector space whose components are a pair of JPEG format sizes of the input and output images of our system, the test image is judged using teacher data and a pattern recognition technique as to whether it has character regions.

6. Experiments

6.1. *Conditions*

The standard images selected from the Standard Image Database (SIDBA) and other images obtained from the Internet were prepared in 24-bit 256×256 pixel BMP form for evaluation of the proposed method. The numbers of teacher and test images as original images are 15 and 16, respectively. Several black characters ("abc09056") were written on the original images; the backgrounds of the characters are white. We used the Daubechies wavelets for the DWT. The experiment was performed in the following environment: personal computer, DELL OPTIPLEX790 (CPU: Intel(R) Core(TM)i7-2600 3.40 GHz; main memory: 4.00 GB); OS, Microsoft Windows 7 Professional; development language, Microsoft Visual C++ 6.0.

In the process of segmentation in Step 2, which was described in Section 3, the pixels in the binary images were set to 255 when the values of the 1HL or 1LH elements were below their particular thresholds; otherwise, the pixels were set to 0. In the process of segmentation in Step 3, as described in Section 3, regions with 50 or fewer pixels were erased; this expansion of the larger regions was performed five times.

By the proposed method described in Section 5, the test data are judged as to whether the image has character regions. As the pattern recognition technique in Step Ⅲ described in Section 5, the *k*-nearest neighbor algorithm (*k*=3) was used.

6.2. *Results and discussion*

According to Step Ⅱ, one test image was correctly judged as having no character regions because the size of the output image was the constant (1.61 KB) obtained in the case of an all-white image. Then, according to the criterion in Step Ⅲ, 25 test images were correctly judged as to whether they had character regions. The 5 other test images were misjudged. As a result, the accuracy of the character insertion judgment by Steps II and Ⅲ was 83.9% (26/31). The image compression characteristics of the output images of our system are due to the JPEG algorithm, mainly the Huffman coding.

7. Conclusion

A method for judging whether characters have been inserted into an image was developed based on our previously proposed method;[4] this method uses the discrete wavelet transform and the empirical knowledge that characters have strong vertical and/or horizontal elements. In the proposed method, we utilize image compression characteristics of output images of our system.[4] Our experimental results show the usefulness of the proposed method.

References

1. H. Hirano and M. Okabe, Detection of text area inserted by image editing (in Japanese), in *IPSJ SIG Notes,* vol. 2012-CVIM-183, no. 9, (Japan, Koganei, 2012), pp. 1–8.
2. K. Ashida, H. Nagai, M. Okamoto, H. Miyao, and H. Yamamoto, Extraction of characters from scene images (in Japanese), *Trans IEICE* **J88-D-II**(9) (2005) 1817–1824.
3. S. Masuko, T. Hoshi, and H. Hirano, A system for searching texts in images by using reliability factor and saliency (in Japanese), *J. IPSJ* **51**(9) (2010) 1520–1529.
4. T. Taniguchi and Y. Yoshitomi, Method for character domain extraction from image using wavelet transform, *J. Robotics, Networking and Artif. Life* **2**(2) (2015) 103–106.
5. D. Inoue and Y. Yoshitomi, Watermarking using wavelet transform and genetic algorithm for realizing high tolerance to image compression, *J. IEEJ* **38**(2) (2009) 136–144.

An Authentication Method for Digital Audio Using Wavelet Transform and Fundamental Frequencies

Yasunari Yoshitomi[1], Shohei Tani[2], Masaki Arasuna[3], Ryota Kan[4], Taro Asada[1], and Masayoshi Tabuse[1]
1: Graduate School of Life and Environmental Sciences, Kyoto Prefectural University,
1-5 Nakaragi-cho, Shimogamo, Sakyo-ku, Kyoto 606-8522, Japan
E-mail: {yoshitomi, tabuse}@kpu.ac.jp, t_asada@mei.kpu.ac.jp}
http://www2.kpu.ac.jp/ningen/infsys/English_index.html
2: Fukuchiyama City Hall, 13-1 Miki, Fukuchiyama, Kyoto Prefecture 620-8501, Japan
3: Nissay Information Technology Co., Ltd., 5-37-1 Kamata, Ohta-ku, Tokyo 144-8721, Japan
4: Shimazu Business Systems Co., Ltd., 1 Kuwahara-cho Nishinokyo, Nakagyo-ku, Kyoto 604-8442, Japan

Abstract

Several digital watermarking techniques for audio files have been proposed for hiding data in order to protect their copyrights. There is a tradeoff between the quality of watermarked audio and the tolerance of watermarks to signal processing methods, such as compression. In order to overcome the inevitable tradeoff, we previously developed an authentication method for digital audio. We have improved the method by determining the region to be authenticated in the audio data by using the fundamental frequency characteristics.

Keywords: Authentication, Audio, Copyright protection, Wavelet transform, Fundamental frequency.

1. Introduction

Recent progress in digital media technology and distribution systems, such as the Internet and cellular phones, has enabled consumers to easily access, copy, and modify digital audio. Several digital watermarking (DW) techniques for audio files have been proposed for hiding data in order to protect their copyrights. In general, there is a tradeoff between the quality of watermarked audio and the tolerance of watermarks to signal processing methods, such as compression.

In previous research,[1] to essentially overcome this issue, we developed an authentication method for digital audio to protect the copyrights. In contrast to DW, no additional information is inserted into the original audio by the previously proposed method, and the digital audio is authenticated using features extracted using a discrete wavelet transform (DWT) and characteristic coding of the previously proposed method.[1] However, the region to be authenticated in the audio data is decided by the fixed length and the fixed starting time from the beginning of the audio data. Therefore, the authentication tolerance to clipping of the audio data is insufficient for practical use.

In the present study, to overcome this issue, we have improved the method by determining the region to be authenticated in the audio data by using the fundamental frequency characteristics.

2. Observed Phenomenon Underpins the Authentication Method

The procedure and algorithm of our previously proposed method[1] is reviewed in this section, because it is very important for the present study.

It has been observed that when a DWT is applied to audio data, in the histogram of the wavelet coefficients of the multi-resolution representation

(MRR), the center of the distribution is very close to zero.[2] We exploited this phenomenon in order to develop an authentication method for audio data.[1] For further information on the DWT used, see Refs. 3 and 4.

3. Authentication Ratio

We set the authentication parameters as described below.[1,5]

In Fig. 1, $Th'(\text{minus})$ was chosen so that it divides the nonpositive wavelet coefficients (S'_m in total frequency) into two equal groups, and similarly $Th'(\text{plus})$ was chosen so that it divides the positive wavelet coefficients (S'_p in total frequency) into two equal groups. Next, the values of the parameters $T1'$–$T4'$, which control the authentication precision, were chosen such that the following conditions were satisfied:

1) $T1' < Th'(\text{minus}) < T2' < 0 < T3' < Th'(\text{plus}) < T4'$.
2) The value of S'_{T1}, the number of wavelet coefficients in $(T1', Th'(\text{minus}))$, is equal to S'_{T2}, the number of wavelet coefficients in $[Th'(\text{minus}), T2')$, i.e., $S'_{T1} = S'_{T2}$.
3) The value of S'_{T3}, the number of wavelet coefficients in $(T3', Th'(\text{plus})]$, is equal to S'_{T4}, the number of wavelet coefficients in $(Th'(\text{plus}), T4')$, i.e., $S'_{T3} = S'_{T4}$.
4) $S'_{T1} / S'_m = S'_{T3} / S'_p$.

In the present study, the values of both S'_{T1} / S'_m and S'_{T3} / S'_p are set to 0.3, which is the same setting used for creating the code for the original audio data.[1] When preparing the authentication codes, the wavelet coefficients V' for each MRR sequence are divided as shown in Fig. 1 into three sets, which are defined as follows:

- $F = \{V' \mid V' \in V'^{AC}, V' < Th'(minus)\}$
- $G = \{V' \mid V' \in V'^{AC}, Th'(minus) \le V' \le Th'(plus)\}$
- $H = \{V' \mid V' \in V'^{AC}, Th'(plus) < V'\}$,

where V'^{AC} is the set of wavelet coefficients from the target audio data that is used to create the authentication code.

The wavelet coefficients V'_i are then classified according to the following rules with the flags f_i used in creating the original code $\boldsymbol{C}$:

When $f_i = 1$ and $V'_i \in G$, b'_i is set to 0.

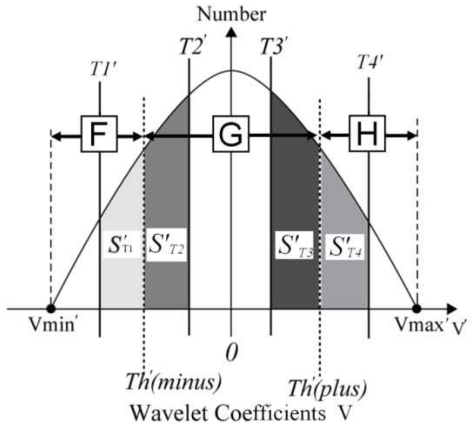

Fig. 1. Three sets (F, G, and H) of MRR wavelet coefficients used for authentication.[1]

When $f_i = 1$ and $V'_i \in (F \cup H)$, b'_i is set to 1.

When $f_i = 0$, b'_i is set to 0.5.

Note that the value 0.5 can be chosen arbitrarily, since the value of b_i that is the bit for creating the code for the original audio data[1] does not influence the method's performance. Finally, this sequence of b'_i values is used to form the authentication code C'.

The authentication ratio AR (%) is defined as follows:

$$AR = \frac{100 \sum_{i=1}^{N} f_i \left(1 - |b_i - b'_i|\right)}{\sum_{i=1}^{N} f_i}, \tag{1}$$

where N is the number of wavelet coefficients chosen to create the authentication code for the original audio data.[1] As can be seen in equation (1), neither b_i nor b'_i influences the value of AR when $f_i = 0$, which occurs when the corresponding V_i that is the wavelet coefficient of the original audio is not selected for coding in the original audio data.[1]

To use the proposed method, we need to store the flags f_i and the original code $\boldsymbol{C}$ for each copyrighted file that we want to protect. When calculating (1) in order to authenticate audio data, we do not use the original audio data; instead, we use the flags f_i and the code $\boldsymbol{C}$ for that file.[1]

4. Fundamental Frequency Characteristics of Audio Data

Fig. 2 shows the fundamental frequency of the first entry of the rock music genre category in the music database RWC for research purposes.[6] As shown, several local maximums

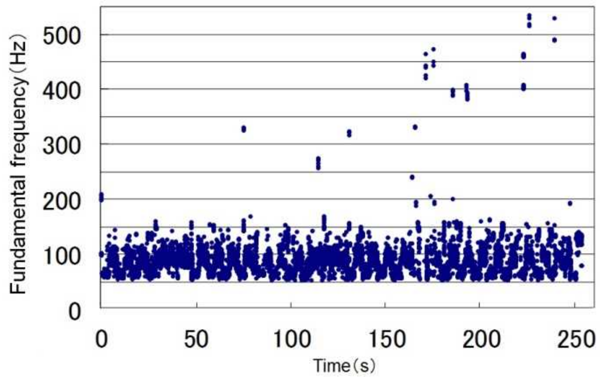

Fig. 2. Fundamental frequency of audio data.

of the fundamental frequency exist within the stream of the music. We have proposed a method for determining the region to be authenticated in the audio data by using local maximums of the fundamental frequency of the audio data, as described in the next section.

5. Proposed Method for Determining the Region to be Authenticated in the Audio Data

The audio data clipping procedure for the authentication is as follows:

Step 1: The fundamental frequency $f(i)(i=1,2,3\ldots,n)$ at the start time index i is measured every 0.01 seconds from the beginning to the end of T seconds of the original audio data, i.e., $n=100T$. Then, the absolute value of difference $ADF(i)=|f(i+1)-f(i)|$ is calculated for all $i(i=1,2,3,\ldots,n-1)$.

Step 2: The sum $S(i)=\sum_{j=0}^{999} ADF(i+j)$ is calculated for all $i(i=1,2,3,\ldots,n-999)$.

Step 3: The start time indexes i are determined by whether the value of $S(i)$ is among the top 10 of all $S(k)$ under the restriction $|i-j|\geq 1000$ for all j such that $S(i)<S(j)$.

Step 4: For the start time indexes i selected in Step 3, 10 seconds of audio data are clipped for the authentication.

6. Experiments

6.1 Conditions

An experiment was performed in the following computational environment: the personal computer was a DELL OPTIPLEX CF-SX1 (CPU: Core i7-2600 Duo, 3.40 GHz; main memory: 4.0 GB); the OS was Microsoft Windows XP; the development language was Microsoft Visual C++ 6.0.

Five music audio files, namely, the first entry of each of five genre categories—classical, jazz, popular, rock, and hiphop—in the music database RWC used for research purposes,[6] were copied from CDs onto a personal computer as WAVE files with the following specifications: 44.1 kHz, 16 bits, and monaural. For each music audio file selected from the database, 10 sets of 10-second clips of music audio were produced using the proposed method described in Section 5.

For investigating the authentication tolerance to clipping, audio test data were produced by clipping one region from each music audio file selected from the database. The clipped regions were specified by all combinations of the lengths 0.01, 0.1, 0.5, 1.0, 2.0, 3.0, and 4.0 seconds and the starting times 0, 5, and 10 seconds (from the beginning of the original audio data), resulting in 21 clipping conditions. Then, for each audio test data file produced from each original audio data file, 10 sets of 10-second clips of music audio were produced using the proposed method described in Section 5, and the authentication procedure was performed using the previously proposed method.[1] The highest value of the authentication ratio of the original audio data to the audio test data (hereinafter referred to as *HAR*) of AR as described in Section 3 among those of the 100 combinations of the 10 clips of the original data and the 10 clips of test data was calculated.

As another method for comparison (hereinafter referred as AMFC), we chose audio data from the classical music genre category and produced one 10-second clip whose starting time gave the highest fundamental frequency for 0.01 seconds among those in the audio data. Next, the clipping regions from the beginning of the original audio data were specified by the lengths 0.00001, 0.00005, 0.0001, 0.0002, 0.0003, 0.0004, 0.0005, 0.001, and 0.01 seconds. Then, the calculation of AR for the original audio data and the audio data after clipping by the above each length was performed for one 10-second clip whose starting time from the beginning of the audio data was decided by the above method for the original audio data. For the DWT, we used Daubechies wavelets. Level 8 was chosen based on an analysis of preliminary experiments.[1]

6.2 Results and discussion

Tables 1 and 2 respectively show the *AR* values for AMFC and the *HAR* values for the proposed method. As shown in Table 1, AMFC showed poor authentication tolerance to clipping: clipping 0.01 seconds of audio caused *AR* to decline to 65.88%. On the other hand, as shown in Table 2, the authentication tolerance to clipping of the audio data was improved by adopting the proposed method.

Table 1. *AR* with AMFC for clipping from the beginning of original classical audio data.

Clipping length (s)	*AR*(%)
0.00001	100
0.00005	100
0.0001	99.22
0.0002	96.84
0.0003	87.75
0.0004	84.98
0.0005	78.66
0.001	69.57
0.01	65.88

Table 2. *HAR* (%) with the proposed method under the 21 clipping conditions. Starting time for the test data from the beginning of the original audio data: (a) 0, (b) 5, and (c) 10 seconds.

(a)		Music				
		classical	jazz	popular	rock	hiphop
Clipping length (s)	0.01	100	100	100	100	100
	0.1	100	100	100	100	85.49
	0.5	98.82	99.60	99.17	99.61	78.04
	1.0	98.08	98.81	92.24	98.43	80.63
	2.0	73.12	86.67	99.17	95.29	80.63
	3.0	67.19	89.33	100	93.37	80.63
	4.0	94.25	90.40	95.01	69.41	71.76

(b)		Music				
		classical	jazz	popular	rock	hiphop
Clipping length (s)	0.01	95.62	98.82	96.40	99.72	94.90
	0.1	96.16	94.12	92.52	87.06	90.91
	0.5	82.75	89.02	93.91	84.71	83.40
	1.0	91.78	80.63	77.25	77.47	75.29
	2.0	86.03	74.67	75.10	95.44	73.52
	3.0	79.73	72.19	85.77	77.65	86.17
	4.0	64.38	71.76	76.28	74.12	73.12

(c)		Music				
		classical	jazz	popular	rock	hiphop
Clipping length (s)	0.01	100	100	100	100	100
	0.1	96.44	100	100	99.61	100
	0.5	97.65	99.61	98.42	97.63	99.60
	1.0	93.70	86.27	96.08	95.65	94.47
	2.0	88.77	66.40	91.70	93.73	88.54
	3.0	80.00	73.33	80.29	87.84	91.70
	4.0	64.84	73.87	79.45	79.61	76.28

When 5-second clip was used for narrowing the 10-second clip decided as the region to be authenticated in the audio data, *HAR* was much improved, being almost 100% for all the clipping conditions used in this experiment. Even for a clipping length of 4.0 seconds, *HAR* improved to 100% except under one condition for classical audio data: clipping from a starting time of 5 seconds from the beginning of the original audio data. In the exceptional case, *HAR* was 76.25%.

7. Conclusion

In general, there is a tradeoff between the quality of watermarked audio and the tolerance of watermarks to signal processing methods, such as compression. To overcome this inevitable tradeoff, we previously developed an authentication method[1] for digital audio using a DWT. In the present study, we have improved the method by determining the region to be authenticated in the audio file by using the fundamental frequency characteristics. The experimental results show that the method has a high authentication tolerance to clipping small parts from the audio data.

References

1. Y.Yoshitomi, T.Asada, Y.Kinugawa, and M.Tabuse, An authentication method for digital audio using a discrete wavelet transform, *J. Inf. Sec*. **2**(2) (2011) 59–68.
2. S. Murata, Y. Yoshitomi, and H. Ishii, Optimization of embedding position in an audio watermarking method using wavelet transform, in *Abstracts of Autumn Research Presentation Forums of ORSJ* (Japan, Tokyo, 2007), pp. 210–211. (in Japanese)
3. D. Inoue and Y. Yoshitomi, Watermarking using wavelet transform and genetic algorithm for realizing high tolerance to image compression, *J. IEEJ* **38**(2) (2009)136–144.
4. T. Taniguchi and Y. Yoshitomi, Method for character domain extraction from image using wavelet transform, *J. Robotics, Networking and Artif. Life* **2**(1) (2015) 103–106.
5. R. Fujii, Y. Yoshitomi, T. Asada, and M.Tabuse, An Authentication method using a discrete wavelet transform for a recaptured video, *J. Robotics, Networking and Artif. Life* **3**(2) (2016) 107–110.
6. M. Goto, H. Hashiguchi, T. Nishimura, and R. Oka, RWC music database: Database of copyright-cleared musical pieces and instrument sounds for research purposes”, *Trans. IPSJ* **45**(3) (2004) 728–738. (in Japanese)

Unified Approach to (1+1) EA on Discrete Linear Functions

Kenji Aoki
Information Technology Center, University of Miyazaki, 1-1 Gakuen-kibanadai-nishi
Miyazaki, 889-2192, Japan

Makoto Sakamoto
Faculty of Engineering, University of Miyazaki, 1-1 Gakuen-kibanadai-nishi
Miyazaki, 889-2192, Japan

Hiroshi Furutani
Innovative Computing Research Center, Doshisha University, 1-3 Tataramiyakodani
Kyoto, 610-0394, Japan

Satoru Hiwa and Tomoyuki Hiroyasu
Faculty of Life and Medical Sciences, Doshisha University, 1-3 Tataramiyakodani
Kyoto, 610-0394, Japan
E-mail: aoki@cc.miyazaki-u.ac.jp
www.miyazaki-u.ac.jp

Abstract

We consider the runtime property of discrete linear functions in (1+1) Evolutionary Algorithms, PO-mutation and Jansen's model, PO-EA. We analyze the process of evolution. This study was motivated by the paper of Jansen treating the runtime property of (1+1) EA on monotonic functions by means of probabilistic theory. As linear functions are special case of monotonic function, we analyze their behavior. We show that the (1+1) EA can obtain an optimum solution at a stable hitting time for discrete liner functions. When the mutation rate is weak, on the order of 1 / l, most monotonic functions behave similarly and can be approximated well by the PO-mutation model.

Keywords: Evolutionary algorithm, Discrete linear function, (1+1) EA, PO-mutation, PO-EA

1. Introduction

Discrete optimization covers one area of optimization for the mathematical and applied aspects of integer programming and combinatorial optimization. Usually, most studies deal with each optimization problem individually. However, there are some researchers who try to capture several properties of optimization function $f(x)$ that make it tractable. In the continuous optimization, a function can be minimized efficiently, if it is convex [1]. On the other hand, a function is maximized efficiently, if it is concave.

In the area of discrete optimization, there are such properties which make optimization tasks easier. One of them is submodularity, which has many interesting properties [2]. Another one is monotonicity, and monotonic submodular functions have recently been studied extensively in computer science. This paper focuses on the monotonic functions, leaving the submodularity for the future trial.

Jansen [3] introduced the partially ordered evolutionary algorithm (PO-EA) model and analyzed its performance in linear functions. Later, this algorithm was expected to simulate the optimization of monotonic functions [4, 5]. PO-EA is a pessimistic model of the true optimization process. One may consider PO-EA as a model to derive an upper bound on the expected hitting time for monotonic functions.

In this study, we analyze the expected hitting time of (1+1) EA, PO-mutation and PO-EA. Without loss of generality, we assume the optimum binary string is $\{1\}^l$, and use EAs on discrete liner functions as a representative monotonic function. Colin et al. have shown that PO-EA can be divided into two parts [5], which named PO-mutation and ZeroMax models. PO-mutation model contains mutations which increase the fitness of every monotonic function. By using computer experiment, we calculate the expected hitting times of optimum for (1+1) EA, PO-mutation and PO-EA on discrete linear functions. By this analysis, we can see the contributions of (1+1) EA, PO-mutation and PO-EA at hitting time, and understand the mechanism of the optimizing process of EAs.

2. Mathematical models of EAs

In discrete optimization, mathematical models for evolutionary algorithms (EAs) have attracted the interest of many researchers [6]. For the theoretical analysis of EAs, one usually chooses (1+1) EA as the first trial. A detailed overview of these studies are presented in [7]. This paper treats the optimization of monotonic functions within the framework of evolutionary algorithms.

If we are given a ground set $L = \{1, 2, \ldots, l\}$ and a set function $f: A \rightarrow R$ for all subsets $A \subseteq L$, the monotonic function has the property of $f(A) \leq f(B)$ if $A \subseteq B$ and $B \subseteq L$. This function covers a wide range of discrete optimization. A set function can be equivalently described by pseudo-Boolean function. For example, with $l = 5$, a set $A = \{1, 2, 4\}$ is equivalent to a binary string (1, 1, 0, 1, 0). We use the notation of binary strings in the following. OneMax function is one of most frequently studied monotonic functions. Mülenbein carried out a pioneering study by using Markov chain for analyzing the time evolution of states in EA [8]. He derived the expected hitting time T of the optimum for OneMax function on (1+1) EA. For large string length l and mutation rate $p_m = c / l$, the result is approximately given by $T \approx e^c / c \cdot l \ln(l / 2)$.

Furutani et al. also analyzed the expected hitting times of EAs by applying Markov chain and random local search (RLS) [9]. The behavior of this Markov chain is completely determined by the transition matrix P of an absorbing Markov chain [10]. The explicit form of absorbing Markov chain for OneMax problem is presented in [9]. Using this expression of P, we showed that the expected runtime of RLS algorithm is H_1 / p_m steps. Here, p_m is mutation rate, and H_1 is the first Harmonic number. The runtime of this chain is approximately given by $l \log(l)$ if we use $p_m = 1 / l$.

3. Evolutionary Algorithms

3.1. *(1+1) Evolutionary Algorithm*

Evolutionary Algorithm ($\mu + \lambda$) came from Evolutionary Strategy developed by Rechenberg and Schwefel, where μ and λ are numbers of parent solutions and offspring solutions, respectively. We choose the parameters $\mu = 1$ and $\lambda = 1$ for simplicity. Though (1+1) EA seems too simple for an analysis, it has attracting properties. As Wegener states that [2],

(1) it is efficient for many problems,
(2) it can not get stuck in a local optimum, and
(3) the analysis of it reveals many tools that can be used in more practical algorithms.

The algorithm of (1+1) EA is given by Algorithm 1.

Algorithm 1 (1+1) EA

1: Initialize $\boldsymbol{x} \in \{\mathbf{0}, \mathbf{1}\}^{\boldsymbol{l}}$ uniformly at random.
2: Create $\boldsymbol{x}'$ by flipping one each bit in $\boldsymbol{x}$ with probability $\boldsymbol{p_m}$.
3: Select if $\boldsymbol{f}(\boldsymbol{x}') \geq \boldsymbol{f}(\boldsymbol{x})$ then $\boldsymbol{x} := \boldsymbol{x}'$.
4: Go to 2 until a termination condition is fulfilled.

3.2. *PO-mutation Algorithm*

Colin et al. have shown that PO-EA can be divided into two parts [5]. Ma et al. have named it PO-mutation and ZeroMax models [11]. They treated two selection conditions, $(x' \geq x)$ and $\{(x' \ngeq x)$ AND $(f(x') \leq f(x))\}$, separately. We call the first condition as PO-mutation model, and the second condition as ZeroMax model, respectively. PO-mutation has a role of driving force for approaching the optimum solution. On the contrary, ZeroMax model works as a resistance against the move to the optimum. Please note that ZeroMax model has a condition $(x' \ngeq x)$, which makes its power smaller than OneMax model. The algorithm of PO-mutation is given by Algorithm 2.

Algorithm 2 PO-mutation

1: Initialize $\boldsymbol{x} \in \{\mathbf{0}, \mathbf{1}\}^{\boldsymbol{l}}$ uniformly at random.
2: Create $\boldsymbol{x}'$ by flipping one each bit in $\boldsymbol{x}$ with probability $\boldsymbol{p_m}$.
3: Select if $\boldsymbol{x}' \geq \boldsymbol{x}$ then $\boldsymbol{x} := \boldsymbol{x}'$.
4: Go to 2 until a termination condition is fulfilled.

It should be mentioned that the PO-mutation model is designed to study the convergence properties of PO-EA. Since the selection process of Algorithm 2 assumes that $\{1\}^l$ is the optimum string, this model cannot be applied to real problems whose optimum strings are not known.

3.3. *PO-EA*

Jansen introduced the partially ordered evolutionary algorithm (PO-EA) model [3]. The algorithm of PO-EA is given by Algorithm 3.

Algorithm 3 PO-EA
1: Initialize $\boldsymbol{x} \in \{\mathbf{0}, \mathbf{1}\}^{\boldsymbol{l}}$ uniformly at random.
2: Create $\boldsymbol{x}'$ by flipping one each bit in $\boldsymbol{x}$ with probability $\boldsymbol{p_m}$.
3: Select if $(\boldsymbol{x}' \geq \boldsymbol{x})$ OR $\{(\boldsymbol{x}' \not\leq \boldsymbol{x})$ AND $(\boldsymbol{f}(\boldsymbol{x}') \leq \boldsymbol{f}(\boldsymbol{x}))\}$ then $\boldsymbol{x} := \boldsymbol{x}'$.
4: Go to 2 until a termination condition is fulfilled.

The difference of three algorithms are Selection in the step 3.

4. Discrete Linear Function

As a test function, we apply discrete linear function *f*(*x*)

$$f(x) = a_1x_1 + a_2x_2 + \cdots + a_ix_i$$

$$f(x) = \textstyle\sum_{i=1}^{l} a_i\, x_i, \quad x_i \in \{0,1\}, \qquad (1)$$
$$a_i = (1+s)^i, \qquad 0 \leq s \leq 1,$$

where x is a binary string of length l. We consider the maximization problem of this function. The optimum solution is $x_{opt} = \{1\}^l$. If $s = 0$, then $a = 1$ and $f(x) = \sum_{i=1}^{l} x_i$. That is to say OneMax function. If $s = 1$, then $a_i = 2^i$, i.e. binary number.

Since many studies suggested that the mutation probability of $p_m = 1 / l$ may be the best choice, we carried out our analysis using this value.

5. Numerical Experiment

In this section, we compare the first hitting time of the numerical experiments of (1+1) EA, PO-mutation and PO-EA with s=0.0, 1.0 and 0.5. We used the mutation rate $p_m = 1 / l$. The length of string is $l = 100$, and we performed 10,000 runs for each parameter set, and averaged over them.

Figure 1 shows the time dependence of probability of the first hitting time of optimum solution in (1+1) EA, PO-mutation and PO-EA with $s = 0.0$. These lines are the

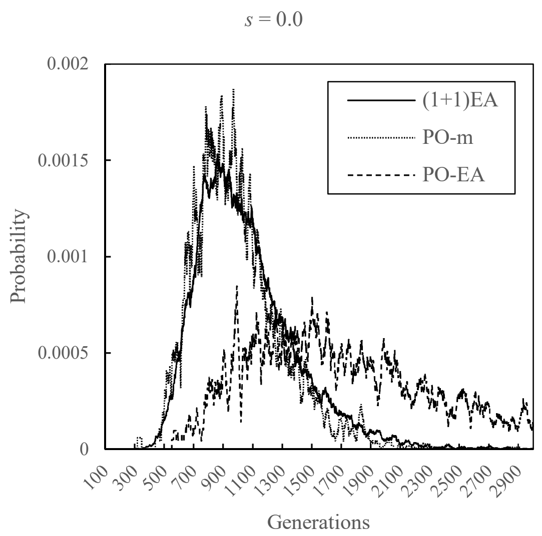

Fig. 1. Distribution of the first hitting time of optimum solution in (1+1) EA, PO-mutation and PO-EA with $s = 0.0$. The solid line is the result of (1+1) EA calculation. The dotted line is the result of PO-mutation calculation. The dashed line is the result of PO-EA calculation.

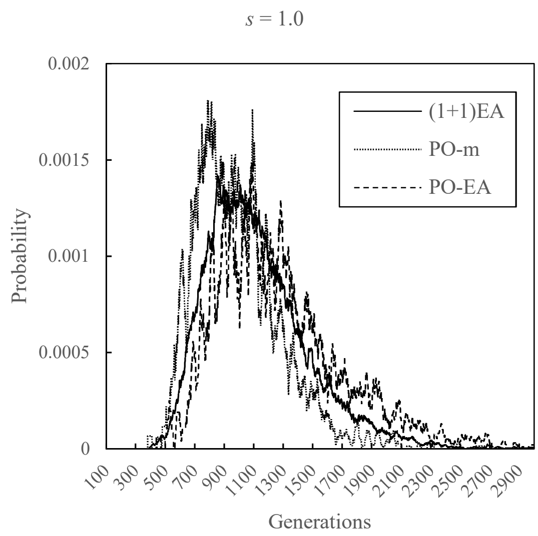

Fig. 2. Distribution of the first hitting time of optimum solution in (1+1) EA, PO-mutation and PO-EA with $s = 1.0$. The solid line is the result of (1+1) EA calculation. The dotted line is the result of PO-mutation calculation. The dashed line is the result of PO-EA calculation.

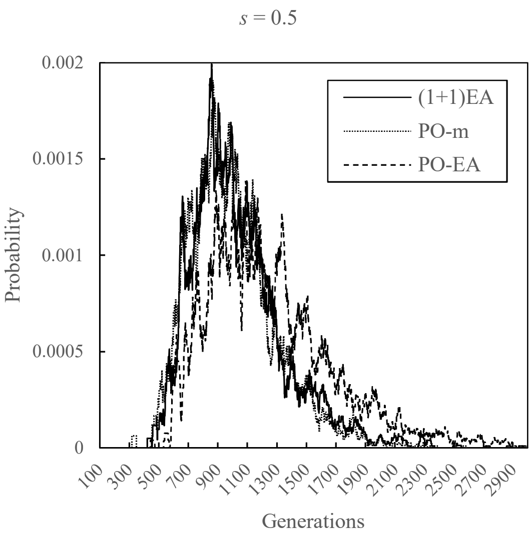

Fig. 3. Distribution of the first hitting time of optimum solution in (1+1) EA, PO-mutation and PO-EA with s = 0.5. The solid line is the result of (1+1) EA calculation. The dotted line is the result of PO-mutation calculation. The dashed line is the result of PO-EA calculation.

results of numerical calculation. The result is moving averaged with window size of 30. The dotted line is the result of PO-mutation calculation. The dashed line is the result of PO-EA calculation. In Fig.1, the waveforms of (1+1) EA and PO-mutation are similar, but PO-EA is behind the other. The mean of the first fitting times in (1+1) EA, PO-mutation and PO-EA are 1069, 1014 and 1976, respectively.

Figure 2 shows the time dependence of probability of the first hitting time of optimum solution in (1+1) EA, PO-mutation and PO-EA with s = 1.0. The dotted line is the result of PO-mutation calculation. The dashed line is the result of PO-EA calculation. In Fig. 2, the peak of the first hitting time is delayed in order of PO-mutation, (1+1) EA and PO-EA. The mean of the first fitting times in (1+1) EA, PO-mutation and PO-EA are 1136, 1008 and 1295, respectively.

Figure 3 shows the time dependence of probability of the first hitting time of optimum solution in (1+1) EA, PO-mutation and PO-EA with s = 0.5. The dotted line is the result of PO-mutation calculation. The dashed line is the result of PO-EA calculation. In Fig. 3, as in Fig. 1, the waveforms of (1+1) EA and PO-mutation are similar. PO-EA is behind the other, but it is not as late as Fig. 1. The mean of the first fitting times in (1+1) EA, PO-mutation and PO-EA are 1050, 1018 and 1280, respectively.

6. Summary

In this paper, we studied time behavior of (1+1) EA, PO-mutation and PO-EA to understand how evolutionary computation works for discrete liner functions. We demonstrate that the (1+1) EA can obtain an optimum solution at a stable hitting time for discrete liner functions. When the mutation rate is weak, on the order of 1 / *l*, most monotonic functions behave similarly and can be approximated well by the PO-mutation model. These studies can help to understand the working mechanism of Evolutionary Algorithms, and give some suggestions to design algorithms for other problems.

References

1. Boyd S, Vandenberghe L (2004) *Convex optimization*. Cambridge University Press, Cambridge
2. Fujishige S (2005) *Submodular functions and optimization*, 2nd edn. Elsevier, Amsterdam
3. Jansen T (2007) *On the brittleness of evolutionary algorithms. Foundations of Genetic Algorithms* 2007. Springer, Lecture Notes in Computer Science, New York, pp 54–69 (4436)
4. Doerr B, Jansen T, Sudholt C, Winzen C, Zarges C (2013) Mutation rate matters even when optimizing monotone functions. *Evol Comput* 21:1–12
5. Colin S, Doerr B, Férey G (2014) Monotonic functions in EC: anything but monotone! In: *Proceedings of the 2014 annual conference on genetic and evolutionary computation*, pp 753–760
6. Auger A, Doerr B (eds) (2011) Theory of randomized search heuristics. *World Scientific*, Singapore
7. Oliveto PS, Yao X (2011) Runtime analysis of evolutionary algorithms for discrete optimization, chapter 2. Theory of randomized search heuristics. *World Scientific*, Singapore, pp 21–52
8. Mülenbein H (1992) How genetic algorithms really work I. Mutation and hillclimbing. *Parallel Probl Solving Nat* II:15–26
9. Furutani H, Tagami H, Sakamoto M, Du Y (2014) Markov chain analyses of random local search and evolutionary algorithm. *J Robot Netw Artif Life* 1:220–224
10. Iosifescu M (1980) *Finite Markov processes and their applications*. Wiley, New York
11. Ma Q, Zhang Y, Yamamori K, Furutnai H, Hiwa S and Hiroyasu T (2018) Markov chain analysis of evolutionary algorithms for monotonic functions. *Artif Life Robot*

An fNIRS study of brain state during letter and category fluency tasks

Akane Onishi,
Hiroshi Furutani, Tomoyuki Hiroyasu and Satoru Hiwa
Faculty of Life and Medical Sciences, Doshisha University, 1-3 Tatara Miyakodani
Kyotanabe-shi, Kyoto-fu 610-0394, Japan

shiwa@mail.doshisha.ac.jp

Abstract

Verbal fluency tasks (VFT) can be categorized into the letter fluency task (LFT) that evaluates the ability to generate words starting with a particular letter, and the category fluency task (CFT) that involves recall of words that belong to semantic categories. In this study, we investigated the differences in brain activity during LFT and CFT in healthy subjects. Brain activity in the frontal and the temporal region was measured using functional near-infrared spectroscopy (fNIRS) with 40 channels. We observed more prominent brain activity when performing LFT than CFT.

Keywords: Verbal fluency task, letter fluency task, category fluency task, fNIRS, brain activity

1. Introduction

Functional near-infrared spectroscopy (fNIRS) is a technique that measures metabolic changes in hemoglobin oxygen *in vivo*, using near-infrared light. fNIRS detects changes in concentration of oxy-hemoglobin, deoxy-hemoglobin, total hemoglobin, and measures alteration in cerebral blood flow caused by neural activity[1,2]. Brain function measurement using fNIRS is noninvasive, has excellent temporal resolution, and is performed under routine conditions. In recent times, fNIRS as a tool in advanced medicine is attracting attention. fNIRS examination using verbal fluency task (VFT) is widely being used in diagnosis of depression symptoms. VFT is a task that requires to generate as many words within a category or starting with a given letter as possible within a time limit. In the letter fluency task (LFT), words are recalled from particular letter. In the category fluency task (CFT), words are recalled from semantic categories. The characteristics of brain activity in VFT are different in depression, bipolar disorder and schizophrenia, therefore, diverse activating tasks are used for different disorders. It has been pointed out that VFT tests not only the semantic memory related to vocabulary but also many cognitive functions such as effective vocabulary search power, information processing speed, and executive function[3]. There are several studies on brain activity differences in LFT and CFT of healthy subjects and patients with a mental illness[4,5,6,7,8]. However, only a few studies compare LFT and CFT as such. In this study, brain activities during LFT and CFT were compared in healthy subjects. We hypothesized a difference in brain activity between LFT and CFT and therefore, the purpose of the current study was to investigate the brain status of the two versions of the VFT over a wide area of the frontal and bilateral temporal brain regions using 40 channels of fNIRS.

2. Material and methods

2.1. *Study participants*

Healthy subjects (average age 22.35 ± 0.93, 17 males, 3 females, right-handed) were recruited for this study. All the participants performed LFT and CFT, and brain activity during each task was measured using fNIRS. The study was approved and conducted as per the ethical guidelines of the Institue.

2.2. *Experiment procedure*

In the experiment, a block-design VFT (letter and category version) was performed. The experimental design is shown in Fig. 1. It consisted of 60 seconds of pre-task rest followed by 60 seconds of task period. Participants were initially instructed to watch a cross at the center of the computer screen during the experiment. The task section began with three tasks (a, ka, shi / animals, fruits, sports). This was explained to the participants by the computer as audible instructions. The content of the task was determined from the frequency of use of letters and previous studies[8,9]. During LFT, participants were instructed to generate as many words as possible starting with the displayed letters, while during CFT, participants were instructed to generate as many words which would fit in the presented category. The two tasks were done consecutively and the participants were explained about the order at the beginning of the experiment. The total number of correct words generated during the task was recorded as an indicator of VFT performance.

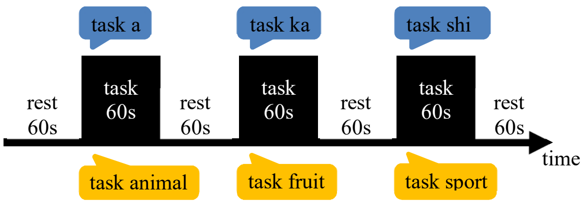

Fig. 1. Experimental design

2.3. *NIRS instrument*

In this study, a 40-channel fNIRS device (LABNIRS, Shimadzu Corporation, Kyoto) was used. The distance between the irradiation probe and the light receiving probe was set to 3.0 cm. In order to minimize the artifacts, the participants were instructed to avoid voluntary movements. The experimental set-up is shown in Fig. 2. The sampling frequency was set at 37.037 Hz. After data acquisition, three-dimensional (3D) coordinates of each light source and detector were measured using a 3D digitizer (FASTRAK, Polhemus, Vermont, USA). Subsequently, these were input to the SPM-fNIRS toolbox for spatial registration, and the layout of each channel and Montreal Neurological Institute (MNI) coordinates was created.

Fig. 2. Experimental set-up

2.4. *Data processing*

fNIRS data was band-pass filtered using 0.01-0.1 Hz. fNIRS data from 9 participants were excluded due to a variation of 0.01 mM*cm in 0.1 seconds. fNIRS data was were band-stop filtered (physiological noise removal) using 0.12 - 0.35 Hz, and with 0.7 - 1.5 Hz after artifact correction based on moving standard deviation and spline interpolation. Next, trend removal was performed using a high pass filter based on the discrete cosine transform set. General linear model (GLM) analysis was used for extraction of the active regions in the brain. Using the hemodynamic response function (HRF), a blood flow alteration model was created as shown in Fig. 3. Statistical significance in brain activity between the two groups was examined using the regression coefficient obtained by regression analysis of blood flow alteration model and measurement data. All the calculations and modeling was done using the SPM-fNIRS toolbox.

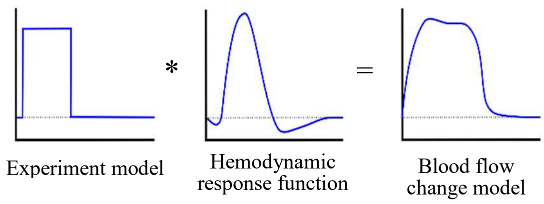

Fig. 3. Creation of blood flow alteration model

3. Results

Brain activation analysis was performed with 11 fNIRS data. Regions with maximum activity for LFT and CFT are represented in Table. 1 and 2, respectively. Group analysis results are shown in Table. 3 and 4. Brain activity observed during LFT performance was higher than during CFT.

Table. 1. Activated brain region (LFT) (FWE, $p<0.05$)

Region	Number of people
Precentral L	10
Precentral R	10
Frontal Sup L	8
Frontal Sup R	8
Frontal Mid L	10
Frontal Mid R	8
Frontal Mid Orb L	7
Frontal Inf L	10
Frontal Inf R	10
Postcentral L	9
Postcentral R	9
SupraMarginal L	8
SupraMarginal R	9
Angular R	7
Temporal Sup L	8
Temporal Sup R	8
Temporal Mid L	8
Temporal Mid R	6
Temporal Inf L	7

Table. 2. Activated brain region (CFT) (FWE, $p<0.05$)

Region	Number of people
Precentral L	7
Precentral R	7
Frontal Sup L	7
Frontal Sup R	6
Frontal Mid L	7
Frontal Mid R	7
Frontal Inf L	7
Frontal Inf R	7
Postcentral L	7
Postcentral R	6
SupraMarginal L	6
SupraMarginal R	6
Temporal Sup L	6
Temporal Mid L	6
Temporal Inf L	6

Table. 3. Group analysis result (LFT) (FWE, $p<0.05$)

Region
Rolandic Oper L
Temporal Sup R
Frontal Inf Tri L
Frontal Inf Tri R

Table. 4. Group analysis result (CFT) (FWE, $p<0.05$)

Region
Frontal Inf Tri R
Caudate R

4. Discussion

In this study, brain activation was investigated based on the change in hemoglobin concentration measured during VFT performance in healthy subjects. An extensive activation in the frontal and temporal brain regions including Broca's areas was observed during the VFT performance. In particular, LFT augmented the brain activation compared to CFT. During CFT, participants would search for words by utilizing the concept of associations such as already existing vehicles. On the other hand, in LFT, words were searched from the notion of phonology which is rarely used in daily life. In other words, participants suppress the recall of related words and perform complex word searches[10]. The results of this study suggest that LFT requires more activation of brain regions than CFT. As shown in Table 1 and 2, four regions are activated exclusively during LFT. The regions include angular gyrus R (R-ANG), middle temporal gyrus R (R-MTG), superior temporal gyrus R (R-STG), and orbital part of inferior frontal gyrus L (L-ORB) as shown in Fig. 4. Amongst these four regions, ANG is located at the junction of the occipital, temporal, and parietal regions and is regarded as an important interface for communicating and integrating information with various brain regions[11,12]. Several studies have associated ANG with memory, meaning, memory consciousness, default mode network (DMN)[13]. MTG, on the other hand, is activated with a more difficult phonological task and plays an important role in controlling semantic search[14]. Co-activation of ANG and MTG observed during LFT suggests their role in word searches that suppresses related word remembrance.

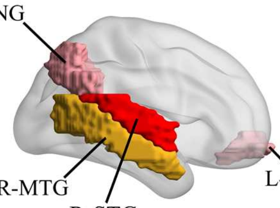

Fig. 4. Brain regions activated only during LFT

5. Conclusion

Currently, several ongoing studies are investigating the difference in brain activity between LFT and CFT in healthy subjects and patients with a mental illness. However, there are only a few studies that compare LFT and CFT as such. Therefore, in this study, the brain activities during LFT and CFT were compared only in healthy subjects. The results from 11 healthy subjects established an increase in LFT activation compared to CFT. Our results suggest that co-activation of ANG and MTG makes it possible to search words with related word recall suppressed.

6. References

1. S. Heinzel, F.G. Metzger, A.-C. Ehlis, R. Korell, A. Alboji, F.B. Haeussinger, K. Hagen, W. Maetzler, G.W. Eschweiler, D. Berg, et al., "Aging-related cortical reorganization of verbal fluency processing: a functional near-infrared spectroscopy study," *Neurobiology of aging*, vol. 34, no. 2, pp. 439-450, 2013.
2. G. Strangman, D.A. Boas and J.P. Sutton, "Non-invasive neuroimaging using near-infrared light," *Biological psychiatry*, vol. 52, no. 7, pp. 679-693, 2002
3. C.E. Bokat and T.E. Goldberg, "Letter and category fluency in schizophrenic patients: a meta-analysis," *Schizophrenia research*, vol. 64, no. 1, pp. 73-78, 2003.
4. A.-C. Ehlis, M.J. Herrmann, M.M. Plichta and A.J. Fallgatter, "Cortical activation during two verbal fluency tasks in schizophrenic patients and healthy controls as assessed by multi-channel near-infrared spectroscopy," *Psychiatry Research: Neuroimaging*, vol. 156, no. 1, pp. 1-13, 2007.
5. K. Ikezawa, M. Iwase, R. Ishii, M. Azechi, L. Canuet, K. Ohi, Y. Yasuda, N. Iike, R. Kurimoto, H. Takahashi, et al., "Impaired regional hemodynamic response in schizophrenia during multiple prefrontal activation tasks: a two-channel near-infrared spectroscopy study," *Schizophrenia research*, vol. 108, no. 1-3, pp. 93-103, 2009.
6. Y. Kubota, M. Toichi, M. Shimizu, R.A. Mason, C.M. Coconcea, R.L. Findling, K. Yamamoto and J.R. Calabrese, "Prefrontal activation during verbal fluency tests in schizophrenia a near-infrared spectroscopy (nirs) study," *Schizophrenia research*, vol. 77, no. 1, pp. 65-73, 2005.
7. K. Marumo, R. Takizawa, M. Kinou, S. Kawasaki, Y. Kawakubo, M. Fukuda and K. Kasai, "Functional abnormalities in the left ventrolateral prefrontal cortex during a semantic fluency task, and their association with thought disorder in patients with schizophrenia," *Neuroimage*, vol. 85, pp. 518-526, 2014.
8. C.-J. Huang, P.-H. Chou, H.-L. Wei and C.-W. Sun, "Functional connectivity during phonemic and semantic verbal fluency test: a multichannel near infrared spectroscopy study," *IEEE Journal of Selected Topics in Quantum Electronics*, vol. 22, no. 3, pp. 43-48, 2016.
9. T. Hatta, A. Kanari, M. Mase, Y. Nagano, T. Shirataki and S. Hibino, "Strategy effects on word searching in japanese letter fluency tests: Evidence from the nirs findings," *Reading and Writing*, vol. 22, no. 9, pp. 1041-1052, 2009.
10. S.V. Tupak, M. Badewien, T. Dresler, T. Hahn, L.H. Ernst, M.J. Herrmann, A.J. Fall-gatter and A.-C. Ehlis, "Differential prefrontal and frontotemporal oxygenation pat-terns during phonemic and semantic verbal fluency," *Neuropsychologia*, vol. 50, no. 7, pp. 1565-1569, 2012.
11. P. Hagmann, L. Cammoun, X. Gigandet, R. Meuli, C.J. Honey, V.J. Wedeen and O. Sporns, "Mapping the structural core of human cerebral cortex," *PLoS biology*, vol. 6, no. 7, p.e159, 2008.
12. D. Tomasi and N.D. Volkow, "Association between functional connectivity hubs and brain networks," *Cerebral cortex*, vol. 21, no. 9, pp. 2003-2013, 2011.
13. M.L. Seghier, "The angular gyrus: multiple functions and multiple subdivisions," *The Neuroscientist*, vol. 19, no. 1, pp. 43-61, 2013.
14. J. Davey, H.E. Thompson, G. Hallam, T. Karapanagiotidis, C. Murphy, I. De Caso, K. Krieger-Redwood, B.C. Bernhardt, J. Smallwood and E. Jefferies, "Exploring the role of the posterior middle temporal gyrus in semantic cognition: Integration of anterior temporal lobe with executive processes," *NeuroImage*, vol. 137, pp. 165-177, 2016.

Construction of a meditation practice support leads to a good meditation state: an fNIRS study

Seika Fujii*
Satoru. Hiwa, Hiroshi. Furutani, Tomoyuki. Hiroyasu
Faculty of Life and Medical Sciences, Doshisha University, 1-3 Tatara Miyakodani
Kyotanabe-shi, Kyoto-fu 610-0394, Japan

tomo@is.doshisha.ac.jp

Abstract

In this study, we constructed a system to quantify a meditation state based on brain function information and feedback that is based on the functional near-infrared spectroscopy (fNIRS). In the system, the meditation state is fed back to the user in real time. The system informs the user via sound when it judges that a good meditation is being performed. The meditation experiment was conducted using this system. As a result, user's brain state at meditation were visualized.

Keywords: meditation, neurofeedback, real-time, dynamic functional connectivity analysis, fNIRS.

1. Introduction

Kabat-Zinn defined mindfulness as "to actively pay attention and consciousness without value judgment at this moment"[1]. Meditation brings a person to a state of mindfulness, which typically has the effect of reducing stress and improving concentration[2]. These effects have been neuroscientifically verified using non-invasive brain function imaging equipment such as functional magnetic resonance imaging (fMRI)[3,4]. On the other hand, it is not easy for a novice who has just begun meditation to judge whether they are achieving a good or bad state of meditation, and it is thus difficult to experience those effects mentioned above. It would be beneficial if there were a system that could support novices' meditation practices and improve the effects of meditation. In this study, we constructed a system to quantify the meditation state based on brain function information and feedback that is based on functional near-infrared spectroscopy (fNIRS), which is one of the non-invasive brain function imaging devices used to study the effects of meditation. In our previous study, we defined the meditation meta-state as one that is peculiar to meditation. This meditation meta-state is determined by measuring the time series obtained from multiple channels made by the fNIRS, obtaining the correlation of time series data between channels, and finally expressing it in a matrix. A meditation meta-state derived from the data of a practitioner is defined, the similarity is obtained by data of the brain state under meditation and real-time processing, and by definition that meditation is done better if the similarity is high, meditation state is fed back in real time. By doing this, users can objectively recognize their meditation state, and it becomes possible to experience the feeling of meditation. Features of the constructed system exist in this feedback method. The system alerts the user when the meditation is being performed well while the user is in the process of meditating. In other words, the system praises the user.
Although this mechanism inhibits meditation, the act of returning from a wandering state to a mindful state is essential in mindfulness training. At the same time, by giving feedback to users immediately after a good meditation state, the motivation to continue with their practice is maintained. In the following sections, we explain the analysis method used to construct the system,

the creation method of the meditation meta-state, and the specifications of the proposed system.

2. Proposed System

2.1. *Functional Connectivity Analysis*

The fNIRS device measures changes in cerebral blood flow (CBF). If the changes in CBF between two regions are measured and found to be similar, it is considered that those regions are functionally coordinated and active. In this way, cooperative and active regions are nodes, and the cooperativeness of brain function connectivity can be represented as a network that has a thick line to connect regions with a high degree of cooperation. As shown in Fig. 1, the network representation can be put into the form of a matrix. This series of analyses is called functional connectivity (FC) analysis. In previous studies related to meditation, FC analysis is often used[5]. The FC analysis is summarized as follows. First, a correlation coefficient of the time series data between two regions is calculated and correlation coefficients are calculated for all measurement points, and a correlation coefficient matrix is created. The correlation coefficient indicates the degree of cooperation. Finally, thresholding is performed on this correlation coefficient matrix and a FC matrix that shows a stronger degree of cooperation is obtained. Furthermore, the brain state of the user during meditation changes from moment to moment[4]. Dynamic FC analysis is used to capture the changing brain state to construct the system. In dynamic FC analysis, a fixed-length window of time is used, and the FC analysis is performed on the amount of CBF that changes within that window[6]. Concerning the width of this window, a certain overlap is kept, and the FC analysis is similarly performed while moving the window on the time axis. As a result, a dynamic brain function network is observed.

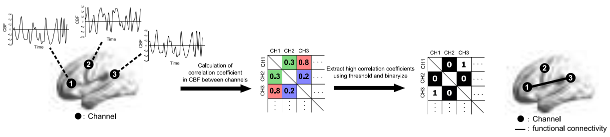

Fig. 1 Process of functional connectivity analysis

2.2. *Definition of meditation meta state*

To quantify the meditation state of a user, a reference indicator is necessary. In this study, the brain state peculiar to meditation is called the meditation meta-state, and a corresponding matrix is created. The meditation meta-state is used as a reference indicator. The procedure for calculating the meditation meta-state is as follows. To measure brain activity, the amount of CBF change across 116 channels was measured using the ETG-7100 fNIRS system (Hitachi, Ltd.). Data for five meditation practitioners (45.6 ± 0.7 years old, cumulative practice time 3,910 ± 2,228 hours) were used for a meditation meta-state. The meta-state was constructed from changes in CBF during their five-minute meditation practice. Using dynamic FC analysis, the FC commonly seen among all five practitioners was defined as the meditation meta-state. A region with meta-state Fig. 2 was shown. From Fig. 2, it is suggested that the meditation meta-state indicates one’s state during meditation.

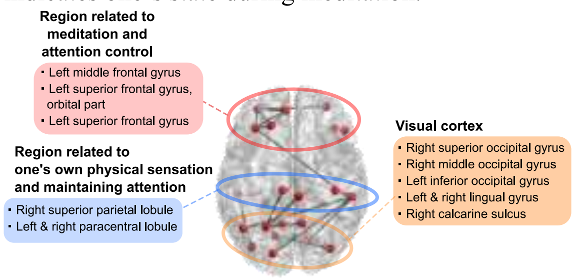

Fig. 2 Brain regions containing the mediation meta-state

2.3. *Estimation of brain state during meditation*

The change in the amount of CBF obtained using the fNIRS was analyzed and the meditation state of the user was determined. Fig. 3 shows the procedure used for estimating the state of the brain during meditation. A window of 60 seconds was used to analyze the change in the amount of CBF. First, physiological noise was removed by the moving average and FC matrix was calculated. Then, in the matrix, Fisher's Z transformation was performed so that the correlation coefficient became a normal distribution, and an edge density of 15% was set as a threshold value of the correlation coefficient. The number of connection was kept constant. This matrix is defined as the state of the brain during the meditation of a user, and the similarity between this matrix and the meta-state was calculated. The degree of similarity was set as a ratio (occurrence) so that the connection of the meta-state is included in the FC of a user.

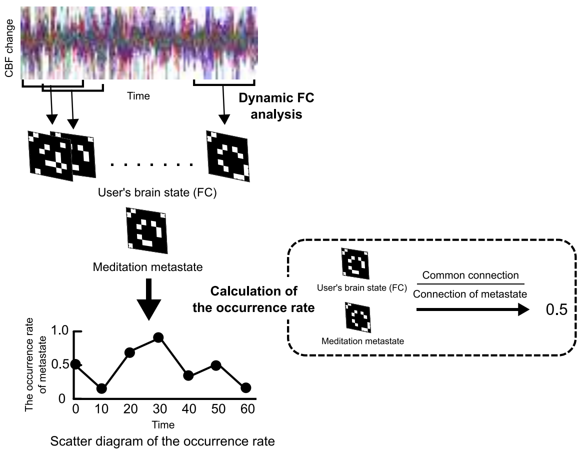

Fig. 3 The process of estimating the meditation state

2.4. *Feedback*

The system feeds information regarding the meditation state back to the user. Feedback is important in that it informs you when you are in an excellent meditation state. In other words, it praises the user. To realize this, feedback is made available to the user if the following conditions are simultaneously satisfied at the point that the meditation meta-state is attained:

- The current occurrence is larger than the one that was calculated immediately before.
- The current occurrence is 1^{st} or 2^{nd} is largest among the last five.

When the occurrence is higher than the one immediately preceding, it indicates that the meditation state is improved. Furthermore, within the most recent (5 times) occurrences, the taming with relatively high occurrence is calculated. When these conditions are met, it is judged that the user's meditating brain state has approached the target state and a sound is heard. The user is thus informed that their meditative state has improved.

2.5. *Real-time system*

We assumed that it is essential to provide feedback of the meditation state during the user's meditation practice. For that purpose, the changes in CBF are processed in real time and fed back to the user. In the constructed system, brain function is measured by the ETG-7100, and the processes of sections 2.3 and 2.4 are performed in real time. Feedback is given to the user according to the meditation state determined by the processing result of section 2.3.

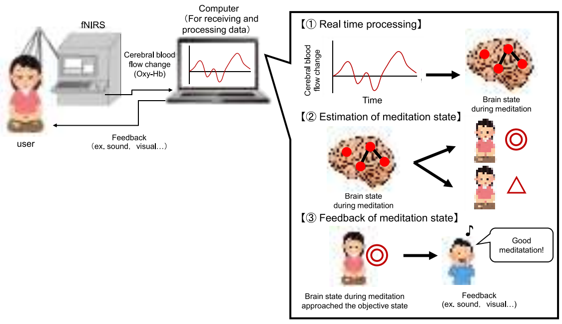

Fig. 4 System overview

3. Materials & Methods

3.1. *Participants*

The participants comprised four male (with a mean age of 23.0 years, SD 0.8 years) who were novices in meditation. Each subject was evaluated every three days for four days at a time (range 2018/6/13 - 6/25; 12: 00 - 17: 00). Furthermore, the subjects were randomly divided into two groups (two in each group). One group received feedback from the system based on changes in the amount of CBF, and one group received feedback at random moments (two each).

3.2. *Protocol*

The experimental design is shown in Fig. 5.

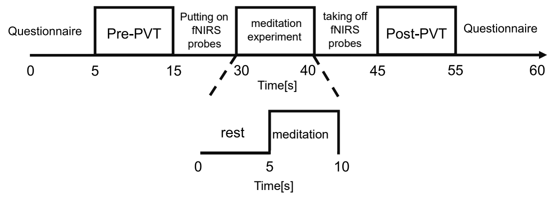

Fig. 5 Experiment protocol

Subjects responded to a questionnaire before and after the experiment. A psychomotor vigilance task (PVT) was also conducted before and after the meditation experiment to measure their attention control abilities. After the PVT, the meditation experiment was started. In the meditation experiment. Participants kept their eyes closed and the breath counting method was used. Counting one's breath is one of the meditation practices that novices can easily do. The feedback sound identified the state in which the last meditation was done, and participants were instructed to maintain that state.

3.3. *fNIRS data and behavioral acquisition*

Changes in CBF across the whole brain 116 CH were measured using the ETG-7100. PVT was used for examining changes in the attention control abilities of participants with or without the system. When a white circle was displayed at the center of a screen, the participants were instructed to press a key quickly. Reaction time (RT) is the amount of time between the moments when a white ring is shown and when the participant presses the key.

4. Results & Discussion

4.1. *Occurrence of meditation meta state*

Fig. 6 shows a graph of the transition of occurrences in both the feedback group and the false feedback group within 10 minutes of the meditation experiment.

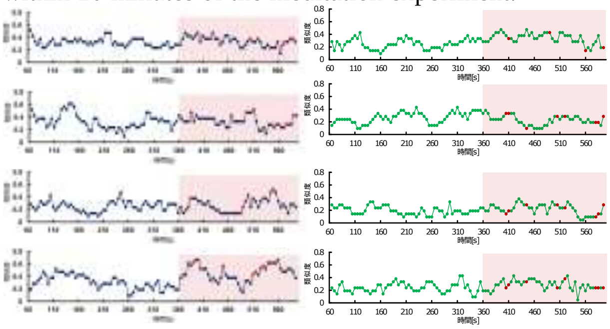

Subject A (Feedback group)   Subject C False Feedback group)

Fig. 6 Changes in the occurrence of subject A and subject C: the first to fourth measurements

4.2. *RT in the PVT*

Fig. 7 shows the relationship between RT of each PVT. As shown in Fig. 7, there was no difference between the groups. Kaul et al. reported that RT in PVTs improved by doing meditation for 40 minutes[7]. In other words, attention control abilities may be enhanced by meditation with or without feedback.

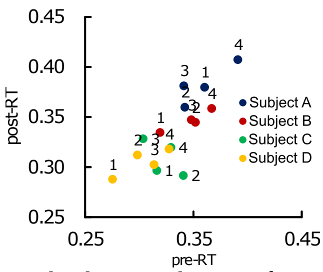

Fig. 7 The relationship between the RTs of pre- and post-PVT of all subjects

5. Conclusion

By practicing meditation, the effects of reduced stress and improved concentration are experienced. However, for a novice, it is difficult to recognize and affect one's state during meditation. Therefore, we constructed a system that feeds back the meditation state to the user in real time by using fNIRS. In the system, the state of brain function during meditation is expressed as a network by a dynamic FC analysis. The data of experts was used as a reference indicator of a good meditation state, and it was defined as the meditation meta-state. For the brain state of a user, the extent to which the meditation meta-state is contained was defined as an occurrence. By setting conditions on the occurrence, the reachability of the target state was evaluated. A feedback system was built to inform the user via an audible sound when it estimates that a good meditation is being performed. The meditation experiment was then conducted using the system. As a result, one's state at rest and one's state at meditation were visualized. In this experiment, there was no difference between the feedback group and the control group obtained. The system has been further modified, and new validation experiments need to be done.

References

1. M.A. Killingsworth and D.T. Gilbert, "A wandering mind is an unhappy mind," *Science*, vol. 330, no. 6006, pp. 932–932, 2010.
2. J. Smallwood and R.C. O'Connor, "Imprisoned by the past: unhappy moods lead to a retrospective bias to mind wandering," *Cognition & Emotion*, vol. 25, no. 8, pp. 1481–1490, 2011.
3. Kabat-Zinn, Jon and Hanh, Thich Nhat, "Full catastrophe living: Using the wisdom of your body and mind to face stress, pain, and illness," *Delta*, 2009.
4. Y.-Y. Tang, B.K. Hölzel and M.I. Posner, "The neuroscience of mindfulness meditation," *Nature Reviews Neuroscience*, vol. 16, no. 4, pp. 213-225, 2015.
5. W. Hasenkamp, C.D. Wilson-Mendenhall, E. Duncan and L.W. Barsalou, "Mind wandering and attention during focused meditation: a fine-grained temporal analysis of fluctuating cognitive states," *Neuroimage*, vol. 59, no. 1, pp. 750-760, 2012..
6. V.D. Calhoun, R. Miller, G. Pearlson and T. Adalı, "The chronnectome: time-varying connectivity networks as the next frontier in fMRI data discovery," *Neuron*, vol. 84, no. 2, pp. 262–274, 2014.
7. P. Kaul, J. Passafiume, R.C. Sargent and B.F. O'Hara, "Meditation acutely improves psychomotor vigilance, and may decrease sleep need," *Behavioral and brain Functions*, vol. 6, no.1, p.47, 2010.

Automated Panoramic Image Creation System for Corneal Endothelial Cells

Keitaro Kobayashi, Naoki Okumura, Noriko Koizumi,
Satoru Hiwa, Hiroshi Furutani, Tomoyuki Hiroyasu
Doshisha University, 1-46 Tataratodani Kyotanabe-shi,
Kyoto, 610-0394, Japan
tomo@is.doshisha.ac.jp
www.doshisha.ac.jp

Abstract

In this study, we propose a method for observing the quality of corneal endothelial cells for the entire cornea by capturing panoramic images from motion pictures. Panoramic images were generated by concatenating the focused images extracted from the moving images using the Tenengrad focus evaluation function. These panoramic images were evaluated to confirm the usefulness of this approach. As a result, Improvements in the capacity to observe changes in the state of these cells could be observed.

Keywords: Panoramic image, corneal endothelial cell, focused image extraction, Tenengrad,

1. Introduction

One cause of corneal disorders is endothelial cell reduction[1]. These cells do not have a regenerative function[2]. Therefore, if the number of these cells is decreased through trauma or illness, a corneal disorder occurs, which results in declining vision for the patient. The primary treatment for this disorder is a corneal transplants sourced from a donors. One problem, however, is an insufficient number of donors. Primary treatment for corneal disorders involves either the transplantation of all corneal layers, or only the endothelium[4]. Both methods require a corneal donor. In Japan, there are currently about 20,000 people with a corneal disorder but the annual number of corneal transplants is limited to 2,800 and 1,200 of these use imported corneas. Due to this chronic donor shortage, there is an interest in treatments that regenerate corneal endothelial cells, without the need for a donor[3] This involves either treatment by culturing these cells outside the body before transplantation[4-6] or the use of eye drops[7]. Currently, medical research on the use of eye drops is assessed by observing changes to the number of endothelial cells before and after treatment using a specular microscope. However, the imageable range of these observations is narrow and only the central part of the cornea can easily be evaluated despite the eye drops affecting the entire cornea[8]. This study proposes a method for observing changes to the number corneal endothelial cells for the entire cornea by capturing panoramic images from motion pictures. The utility of this system for evaluating changes to corneal disorders is also assessed.

2. Panoramic image creation

The proposed system captures panoramic images using moving images of the corneal endothelial cells. This makes it is possible to observe the condition of all cells. Fig. 1 shows the procedure used. First, video images were obtained of the corneal endothelium using a contact type specular microscope. Second, focused images were extracted from the moving images. Finally, the images were combined using software called AutoStitch™ [9] to generate a panoramic image.

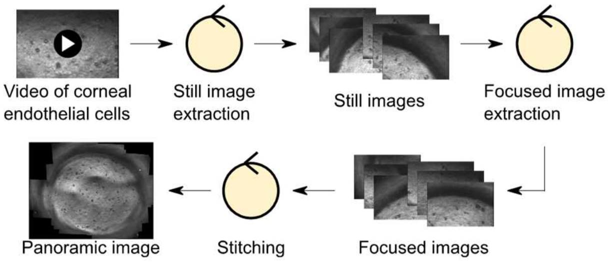

Fig. 1. Proposed system

2.1. *Image extraction*

The panoramic image was generated by concatenating the focused images extracted from the moving images. In general, the edges of the captured objects in the focused images were unclear due to the shaking of the camera, which causes blurring. Therefore, images were extracted using the Tenengrad focus evaluation function[10] (Eq. (1)).
.

$$\varphi_{x,y} = \sum_{(i,j)\in\Omega(x,y)} \left(G_x(i,j)^2 + G_y(i,j)^2 \right) \quad (1)$$

Where, Gx and Gy are image gradients in the x and y directions, respectively, calculated by convolving the target image with the Sobel operator. This filter emphasizes specific areas of the image that undergo a sudden change in brightness. Fig. 2 shows that a higher value for the Tenengrad focus evaluation function relates to images with clearer edges. In contrast, Fig. 3 shows that the value of the function is smaller for blurred images.

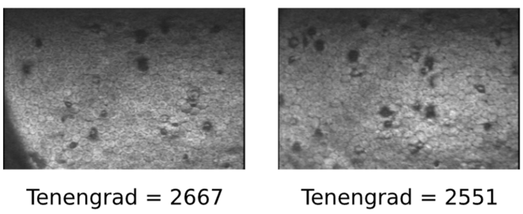

Fig. 2. Tenengrad focus evaluations for focused images

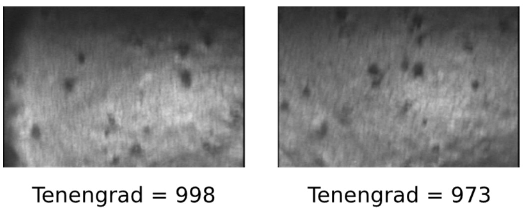

Fig. 3. Tenengrad focus evaluations for blurred images

2.2. *Image stitching*

AutoStitch™ is free software that automatically generates panoramic images from input images. The Scale-Invariant Feature Transform (SIFT) was used to extract features when aligning these images. There were two options for the synthesis algorithm, including linear or multiband blending. Multiband blending, which is a pyramid-based method, was used for this study.

2.3. *Experimental Method*

Ten corneal endothelial videos (size: 720 × 480 pixels, frame rate: 30 fps, magnification: 200 times) were captured from mice provided by the tissue engineering laboratory of the Graduate School of Biomedical Sciences, Doshisha University. These videos followed an S-shaped path using a contact type specular microscope. First, still images (size: 720 × 480 pixels) were extracted from each video at 30 frames per second. The extracted still images were then labeled using the Tenengrad focus evaluation function and divided equally into 50 groups. Images with the highest function value in each group were then extracted as focused images. A panoramic image was then generated by linking these images with AutoStitch™. This panorama was then observed to assess the usefulness of this approach.

2.4. *Result and discussion*

Figs. 4 and 5 show examples of panoramic images generated by this method. In Fig. 4, it was difficult to observe changes to the state of the cells in the upper left section of the image. This was because an overexposed image (Fig. 6) was extracted as one of the focused images. Thus, a focused image with a lower Tenengrad focus evaluation function value was substituted to generate a new panoramic image (Fig. 7). This confirms that it is possible to link alternative images if one is overexposed. An image with ≥ 1000 pixels, having a brightness value ≥ 250 was determined to be overexposed. However, difficulties still remained when attempting to observe changes to the state of the cells at the time of linking. Thus, the image in Fig. 7 was flattened using histogram equalization. This was shown to be useful for observing the changes to the cells. Fig. 5 shows another example where excluding the lower right of the imaged cornea had been connected. It was confirmed using Fig. 9 that the state of the cell was only partially extracted in the focused image. Fig. 10 shows the same panorama generated after manually deleting the focused image. The improvement in the clarity of the cells that can be observed when comparing Fig.8 and Fig.10 suggests that this is a useful and necessary method for extracting focused images that can observe changes in the state of all cells.

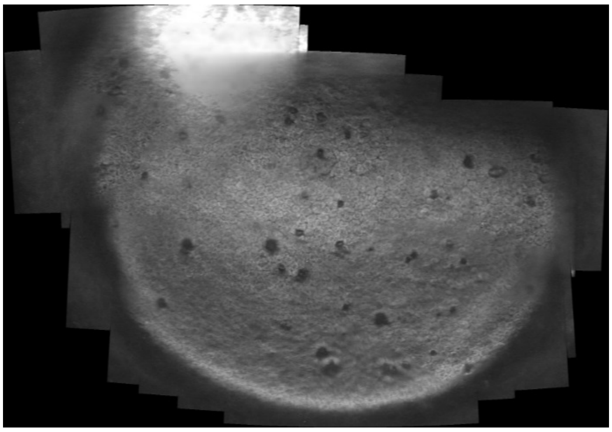

Fig. 4. Panoramic image 1

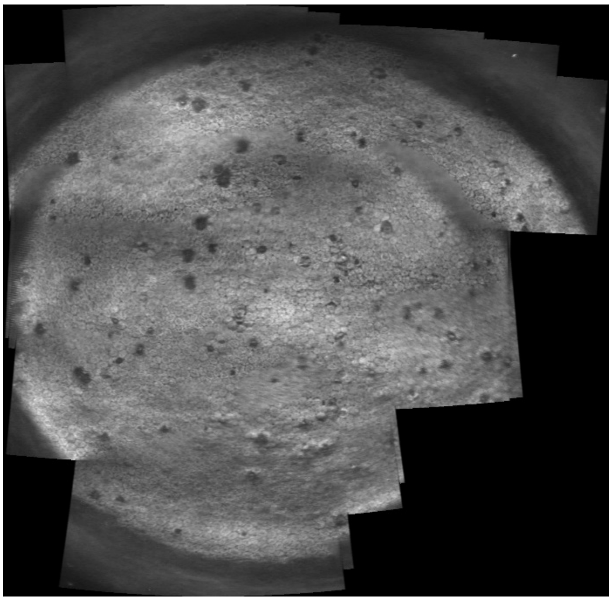

Fig. 5. Panoramic image 2

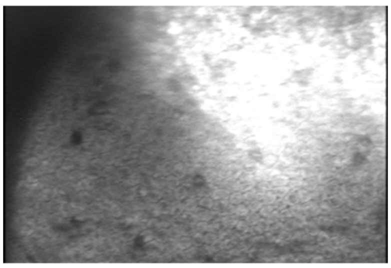

Fig. 6. Overexposed image

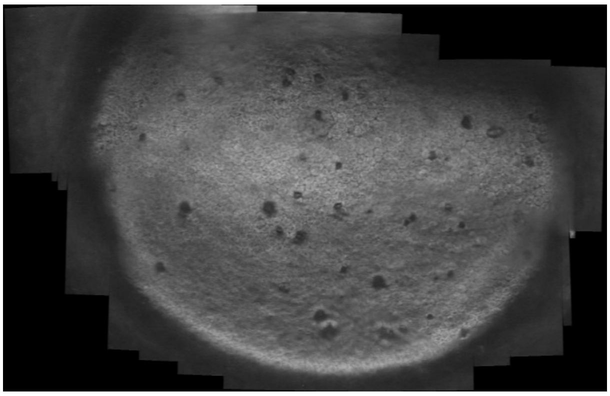

Fig. 7. Panoramic image 1 after deleting the overexposed image

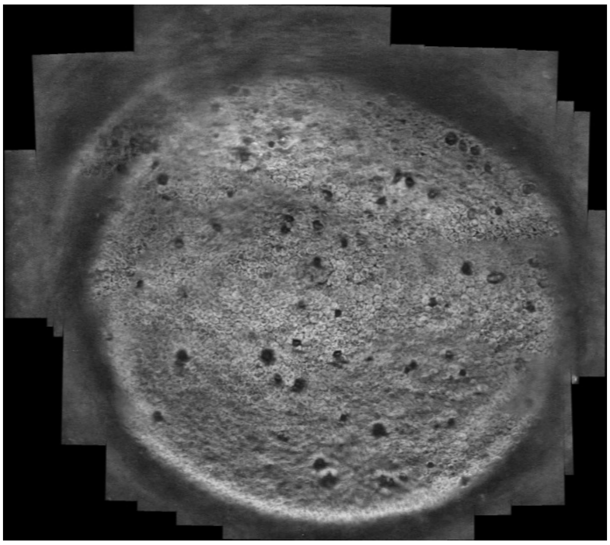

Fig. 8. Panoramic image 1 after histogram equalization

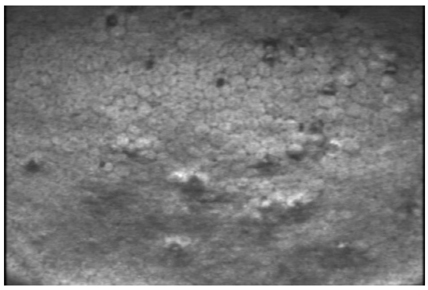

Fig. 9. A partially focused image

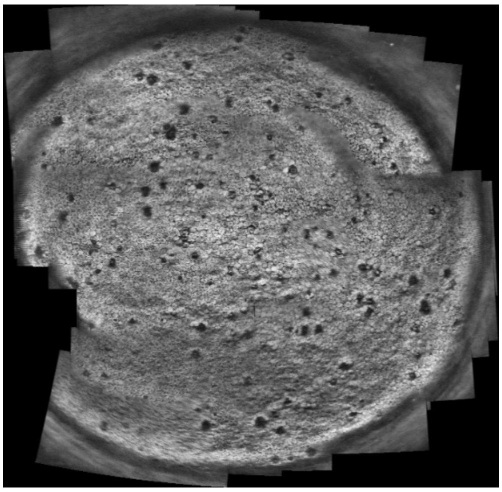

Fig. 10. Panoramic image 2 after manually deleting the partially focused image

3. Conclusion

In medical research examining the effectiveness of the treatment of corneal disorders with eye drops, there is a problem when attempting to evaluate images of sections other than the central portion of the cornea. Therefore, a method for capturing a panoramic image from moving images was proposed. To confirm the usefulness of this approach, these panoramic images were evaluated. Improvements in the capacity to observe changes the state of these cells could be observed as a result. Thus, it is concluded that this method is useful.

References

1 Gain, P. *et al.* Global Survey of Corneal Transplantation and Eye Banking. *JAMA Ophthalmol* **134**, 167-173, doi:10.1001/jamaophthalmol.2015.4776 (2016).

2 Joyce, N. C. Proliferative capacity of the corneal endothelium. *Prog Retin Eye Res* **22**, 359-389, doi:S1350946202000654 [pii] (2003).

3 Tan, D. T., Dart, J. K., Holland, E. J. & Kinoshita, S. Corneal transplantation. *Lancet* **379**, 1749-1761, doi:10.1016/S0140-6736(12)60437-1 (2012).

4 Koizumi, N. *et al.* Cultivated corneal endothelial cell sheet transplantation in a primate model. *Invest Ophthalmol Vis Sci* **48**, 4519-4526, doi:48/10/4519 [pii]10.1167/iovs.07-0567 (2007).

5 Okumura, N. *et al.* Rho kinase inhibitor enables cell-based therapy for corneal endothelial dysfunction. *Sci Rep* **6**, 26113, doi:10.1038/srep26113 (2016).

6 Kinoshita, S. *et al.* Injection of cultured cells with a ROCK inhibitor for bullous keratopathy. *N Engl J Med* **378**, 995-1003 (2018).

7 Koizumi, N. *et al.* Rho-associated kinase inhibitor eye drop treatment as a possible medical treatment for Fuchs corneal dystrophy. *Cornea* **32**, 1167-1170, doi:10.1097/ICO.0b013e318285475d (2013).

8 Tanaka, H. *et al.* Panoramic view of human corneal endothelial cell layer observed by a prototype slit-scanning wide-field contact specular microscope. *Br J Ophthalmol*, doi:10.1136/bjophthalmol-2016-308893 (2016).

9. M. Brown and D. Lowe, Automatic Panoramic Image Stitching using Invariant Features, *International Journal of Computer Vision*, 74(1) (2007) 59-73

10. J. Tenenbaum, *Accommodation in Computer Vision*. Stanford University PhD. Thesis (1970)

An fMRI study of the inhibitory effects of the random stimulus-response compatibility task on brain function

Kei Sahara, Hiroshi Furutani, Tomoyuki Hiroyasu, and Satoru Hiwa
Faculty of Life and Medical Sciences, Doshisha University, 1-3 Tatara Miyakodani Kyotanabe-shi, Kyoto-fu 610--0394, Japan

shiwa@mail.doshisha.ac.jp

Abstract

The Stimulus-Response Compatibility (SRC) task is typically used in a congruent control study. In this study, we used 3 conditions to investigate the differences between inhibition processes in incidental events. Congruent and incongruent conditions are common in SRC tasks. However, the incidental conditions are not investigated. We hypothesize that the random condition has the strongest inhibition processes in congruent control processes. We used fMRI to investigate brain function and analyzed the data using activation analysis and behavior analysis.

Keywords: Stimulus-Respond Compatibility task, functional Magnetic Resonance Imaging, Behavior analysis, Activation analysis

1. Introduction

To successfully interact with our environment, we must select appropriate behavioral responses given our current environmental situation and particular goals[1]. Cognitive control processes include a series of mechanisms (e.g., working memory, attentional control, inhibitory control, cognitive flexibility, problem-solving, and planning) that allow flexible and adaptive behavior in response to environmental demands by implementing specific goal-directed action[2]. The stimulus-response compatibility (SRC) paradigm is typically used in the study of cognitive control[3]. SRC tasks usually require inhibition of irrelevant features specified in task instructions, which indicate the required response[4]. In general, the SRC task contains 2 conditions: a congruent condition and an incongruent condition. There are a number of previous studies investigating various behavior analyses and activation analyses of SRC tasks. SRC tasks have several styles, each using a different type of stimulus (e.g., numerical association target, pitch association target)[5]. In this study, we used a spatial SRC task using a visual stimulus. A spatial SRC is known as a psychological phenomenon in which an overlap of spatial properties between stimuli and responses leads to faster and more accurate responses[6]. Furthermore, we used a 3rd condition, a random condition which contains both SRC task conditions (congruent, incongruent), to investigate inhibitions during incidental events. Therefore, in this study, we hypothesized that the 3rd condition, the random condition, has the strongest inhibiting effect in all conditions. We used behavior analysis, activation analysis, and connecting analysis to investigate the differences among the three conditions.

2. *Methods*

2.1. *Subjects*

A total of 20 healthy young adults (age range: 21-25 years, average age: 22.3±1.05, 4 females) participated in this fMRI study. One participant was excluded due to inaccurately responding during multi-tasks. Therefore, the final number of participants was 19 (age range: 21-25, average age: 22.26±1.07, 4 females). Each participant's dominant hand was established by the Edinburgh handedness inventory (Oldfield, 1971). Seventeen participants were right-handed and 2 participants were ambidextrous. Before participating in the study, all participants received information and instruction about the protocol.

2.2. *Stimuli*

There were 2 visual target stimuli, which consisted of blue and red dots. The blue dot indicated the congruent task, for which participants were instructed to respond to the target stimulus with their ipsilateral hand. The red dot indicated the incongruent task, for which participants were instructed to respond to the target stimulus with their contralateral hand. The target stimuli appeared on both sides of the fixation stimulus during the experiment and the participants responded by pressing buttons on a pad.

2.3. *Experiment protocol*

In this study, we had 3 tasks: the congruent task, the incongruent task, and the random task.. The congruent and incongruent tasks contained only blue or red dots, respectively, as the target stimuli. The random task contained both blue and red dots as the target stimuli. The 3 tasks were divided into 2 sessions. Session 1 contained 6 task blocks, and only one task (congruent/incongruent) was presented per block. The task appeared 3 times randomly throughout the session. Session 2 contained 4 task blocks, which contained all random tasks (congruent). In both sessions, there were 20 trials in each block, and the target stimuli were presented for 1000 ms, with an inter-stimulus interval (ISI) of 1500 ms. During the 30000 ms rest periods participants were instructed to stare at the fixation stimulus.

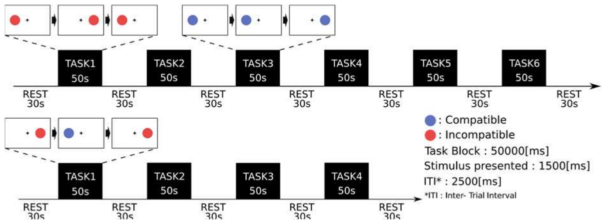

Fig. 1 Experimental protocol: (A) Congruent and incongruent condition session, (B) Random condition

2.4. *fMRI data acquisition*

Images were acquired with a 1.5 Tesla MRI scanner (Hitachi Echelon Vega). Functional images were imaged by gradient-echoplanar imaging (EPI) pulse sequence (TR = 2500 ms, TE = 40 ms, FA = 85°). Images were preprocessed by SPM12 (ASHBURNER, John, *et al.* SPM12 manual. *Wellcome Trust Centre for Neuroimaging, London, UK*, 2014.), which included realignment for correction of head movements, slice timing correction, co-registration for adjusting the functional and structural images, normalization to adjust the EPI images into normalized MRI brain images, and smoothing of activation images. The results were labeled by Automated Anatomical Labeling (AAL).

2.5 *Behavior data analysis*

The behavior data during the experiments were analyzed in MATLAB (Guide, MATLAB User's. "The mathworks." *Inc., Natick, MA* 5 (1998): 333.). We compared the mean reaction times (RT) among the 3 conditions (congruent, incongruent, and random) by using an ANOVA test ($P<0.001$) and Bonferroni test.

2.6 *fMRI data analysis*

The functional brain images were analyzed by SPM12. For one level analysis we fit the preprocessed image data into a general linear model (GLM) for fMRI model specification. After model estimation, we compared the congruent, incongruent, and random conditions to the rest condition and each conditions. We then ran a 2 level analysis to compare each condition to the others to estimate the differences of inhibition in each condition.

3. Results and Discussion s

3.1. *Behavior data analysis*

In the behavior data analysis, a one-way between subjects ANOVA was conducted to compare the effect of mean RTs among the congruent, incongruent, and random conditions (Figures 2 and 3). There was a significant effect of RT for all 3 conditions [$F(2,187) = 65.75$, $p<0.001$].

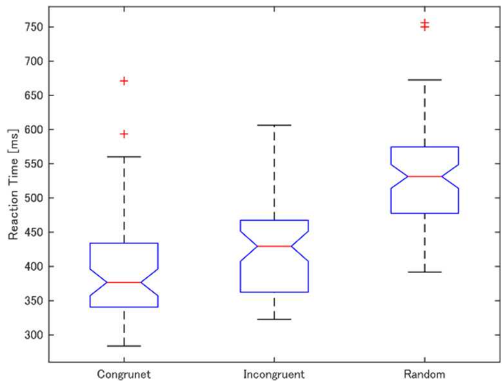

Fig. 2 The results of mean RTs ANOVA in 3 conditions.

The Bonferroni post-hoc test indicated that the mean score for the random condition (M = 535.06, SD = 8.59) was significantly different from the congruent condition (M = 393.85, SD = 9.92) and the incongruent condition (M = 427.49, SD = 9.92). However, there was no significant difference between the congruent condition and the incongruent condition. The random condition had the longest mean RT. This result suggests that we observed a Simon effect in the random condition. The Simon effect appears in incompatible trials and reflects an interference from a proponent response based on the stimulus position[4]. Therefore, we show that the random condition has the strongest inhibition, indicated by the behavior analysis.

3.2. *fMRI data activation analysis*

The result of the image data analyzed in 2 level (uncorrected, $p<0.001$) had 3 comparisons: congruent vs rest, incongruent vs rest, and incongruent vs congruent (Table 1).

congruent vs rest	incongruent vs rest	incongruent vs congruent
Precentral_R	Postcentral_R	Calcarine_R
Cerebellum_ Crus2_R	Rolandic_Oper_L	Precentral_L
Occipital_Inf_L	Postcentral_L	Frontal_Inf_Tri_R
Hippocampus_R	Heschl_R	Frontal_Sup_Medial_R
Rolandic_Oper_R	Heschl_L	
Postcentral_L	Calcarine_R	
Occipital_Mid_L	Precentral_L	
Heschl_R	Rolandic_Oper_R	
	Caudate_L	
	Insula_R	
	Temporal_Sup_L	

Table. 1 The results of the 2 level (uncorrected, $p<0.001$) activation analysis.

There were no signs of activation in random vs rest, random vs congruent, or random vs incongruent comparisons. We then checked the results of the 1 level analysis to see if there was any region which was commonly activated in all 19 participants. First, in the random vs rest comparison, the most commonly activated region was the right postcentral gyrus (12 participants), which is known as a primary receptor of general bodily sesantion[8]. The second most common region was the right superior temporal gyrus (STG) (9 participants), which is known as the main auditory region and also functions in visual processing of moving stimuli[9]. The medial frontal gyrus, middle occipital gyrus, middle temporal gyrus (MTG), and superior frontal gyrus (SFG) were commonly activated in 8 participants. The medial frontal gyrus plays a role in performance monitoring, which allows for performance adjustments on subsequent trials[10]. The middle occipital gyrus is involved in visual processing[11]. The MTG has many functions, including semantic retrieval, semantic memory, and functions as a semantic control network or as a default mode network (DMN)[12]. The SFG is reported to be involved in several networks: a DMN, cognitive execution network, motor control networks, and is also involved in execution of working memory and attention[13]. Second, in the random vs congruent comparison, the most common region was right MTG (11 participants). The second most common regions were the right lingual gyrus, the right STG, and the left MTG (8 participants). The lingual gyrus is involved in higher order analysis of visual stimuli[14]. Third, in the random vs incongruent comparison, the most commonly activated region was the left middle frontal gyrus (MFG) (12 participants), and the second most common region was the left MTG (9 participants). The MFG is involved in a ventral frontoparietal network for attentional processes[15].

4. *Conclusion*

In this study, we used a random condition to investigate inhibition during incidental events during a spatial SRC task. We analyzed behavioral and fMRI data from 19 healthy participants. The behavioral data show a significant difference in the mean RT between the resting condition and the congruent and incongruent conditions. This result suggests that the random condition has the strongest inhibition out of all the conditions. The activation analysis showed only 3 comparisons having differences in activated regions via the 2 level analysis, which included the congruent vs rest, incongruent vs rest and incongruent vs congruent comparisons. Therefore, we went back to the 1 level analysis to observe which regions were active in the rest comparisons: the random vs rest, random vs congruent, and random vs incongruent comparisons. In the 1 level comparisons, we could observe differences in activation of functional regions related to cognitive control processes, such as the medial frontal gyrus, MTG, and MFG. The results suggest that the random condition has the strongest inhibition, as assessed by the behavior analysis, and we can observe activity in regions that are related to cognitive control processes.

References

1. Eric H. Schumacher, Mark D'Esposito, Neural Implementation of Response Selection in Humans as Revealed by Localized Effects of Stimulus-Response Compatibility on Brain Activation, *Human Brain Mapping* **17:193-201** (2002)
2. Chan, R. C. K., Shum, d., Toulopoulou, T. &Chen, E. Y. H. Assessment of executive functions: review of instruments and identification of critical issues. Arch. Clin. *Neuropsychol*. **23(2)**, 201-216 (2008)
3. Zhang, H. Zhang, J. & Kornblum, S. A parallel distributed processing model of stimulus-stumulus and stumulus-response compatibility. *Cogn. Psychol*. **38**, 386-432 (1999).
4. Jesus Cepon, Santiago Galdo-Alvarez, Fernando Diaz, Cognitive control activity is modulated by the magnitude of interference and pre-activation of monitoring mechanisms, *Scientific Report* **6:39595** (2016)
5. Weis, T., Estner, B., Krick, C. M., Reith, W., & Lachmann, T. (2015). SNARC meets SPARC in fMRI—Interdependence of compatibility effects depends on semantic content. *Neuropsychologia*, *77*, 331-338.
6. Cieslik, E. C., Zilles, K., Kurth, F., & Eickhoff, S. B. (2010). Dissociating bottom-up and top-down processes in a manual stimulus–response compatibility task. *Journal of neurophysiology*, *104*(3), 1472-1483.
7. Oldfield, R. C. (1971). The assessment and analysis of handedness: the Edinburgh inventory. Neuropsychologia, 9(1), 97-113.
8. Webb, W., & Adler, R. K. (2016). *Neurology for the Speech-Language Pathologist-E-Book*. Elsevier Health Sciences.
9. Xu, J., Wang, J., Fan, L., Li, H., Zhang, W., Hu, Q., & Jiang, T. (2015). Tractography-based parcellation of the human middle temporal gyrus. *Scientific reports*, *5*, 18883.
10. Ridderinkhof, K. R., Ullsperger, M., Crone, E. A., & Nieuwenhuis, S. (2004). The role of the medial frontal cortex in cognitive control. *science*, *306*(5695), 443-447.
11. Zhang, B., He, S., & Weng, X. (2018). Localization and Functional Characterization of an Occipital Visual Word form Sensitive Area. *Scientific reports*, *8*.
12. Xu, J., Wang, J., Fan, L., Li, H., Zhang, W., Hu, Q., & Jiang, T. (2015). Tractography-based parcellation of the human middle temporal gyrus. *Scientific reports*, *5*, 18883.
13. Li, W., Qin, W., Liu, H., Fan, L., Wang, J., Jiang, T., & Yu, C. (2013). Subregions of the human superior frontal gyrus and their connections. *Neuroimage*, *78*, 46-58.
14. Machielsen, W. C., Rombouts, S. A., Barkhof, F., Scheltens, P., & Witter, M. P. (2000). FMRI of visual encoding: reproducibility of activation. *Human brain mapping*, *9*(3), 156-164.
15. Cieslik, E. C., Zilles, K., Kurth, F., & Eickhoff, S. B. (2010). Dissociating bottom-up and top-down processes in a manual stimulus–response compatibility task. *Journal of neurophysiology*, *104*(3), 1472-1483.

Measurement of brain activity and problem discovery during actual driving

Seishiro Nakamura
Graduate School of Life and Medical Science, Doshisha University, 1-3 Tatara Miyakodani Kyotanabe, Kyoto, Japan[*]

Satoru Hiwa, Kenya Sato, Hiroshi Furutani, Tomoyuki Hiroyasu
Doshisha University, Japan[†]

tomo@is.doshisha.ac.jp

Abstract

Currently, a system that performs driving support based on the biological information of a driver has attracted attention. Brain function is one of the sources of biological information, and we used fNIRS for brain function measurement. We used a simple course to operate an actual vehicle, and fNIRS measured the brain activities during the driving. The measured cerebral blood flow change data included artifacts of the driver's body motion and car body vibration. The removal of artifacts was performed using CBSI.

Keywords: fNIRS, CBSI, driving, brain activity

1. *Introduction*

Although the number of traffic accident deaths has decreased, further reduction is expected. Reduction of accidents has been realized by improved safety performance of the car. There are two aspects to the safety of a car: Passive safety and Active safety, as discussed below.

Passive safety utilizes equipment to minimize injury when an accident occurs. An example of Passive safety is a seat belt or Supplemental Restraint System Airbag (SRS) Airbag. Early seat belt designs restrained the driver in the vicinity of the waist, but the upper body was not restrained. When an accident occurred, the upper body of the driver hit the steering wheel and the dashboard, and the driver was more likely to be injured. Subsequently, a three-point seatbelt was developed, making it possible to reduce the movement of the upper body. As another example of passive safety, structures were designed to absorb the shock of collisions at the front and rear ends of the car, making the safety of the occupant's living space more robust, thus improving safety of the driver.

Another safety feature, Active safety, is a technology to reduce the occurrence of accidents. Vehicle control devices, such as the Anti-Lock Braking System (ABS) and Electronic Stability Control (ESC), are examples of Active safety. ABS is a system that prevents the vehicle from becoming uncontrollable by preventing the tire from locking during braking. Electronic stability control technology was developed to make four-wheel independent control possible. For example, the ESC independently controls the braking devices of all the wheels and controls the generation and suppression of the rotational motion of the vehicle body. With such a wheel braking system, sudden skidding of the vehicle can be eliminated.

The application of existing technology to the development of new, preventive safety systems has advanced. One of them is a driving support system. The driving support system monitors the external environment of a car and prevents accidents. The driving support system may, however, cause malfunctions due to various factors. In order to further improve the driving support system, it is necessary to have the system monitor not only the external environment of the vehicle, but also the internal environment and the biological condition of the driver. One cause of traffic accidents is the distraction of the driver. Therefore, by incorporating the biological information of the driver, it is expected that we can reduce the number of traffic accidents by detection of changes in driving behavior, and deterioration of physical condition. With regard to biological information, human behavior is controlled by the brain, so the interest in brain function is increasing. Noninvasive brain function imaging devices, such as functional magnetic resonance imaging (fMRI), electroencephalogram (EEG), and functional Near infra-red spectroscopy (fNIRS), are used to measure brain function. fNIRS observes changes in hemoglobin in the brain. Near-infrared light has relatively high bio-permeability. fNIRS is less susceptible to body movements and more accessible than EEG for measuring brain electrical activity.

Human "cognition," to obtain information with eyes and ears, and "judgment," to process cognitive information in the brain, results in movement of "hands and feet" to "operate" the car. In car driving, cognition, judgment, and operation are three essential elements. In this study, the relationship between operation and brain activity was examined. In the experiments, brain activities were measured during driving of the vehicle, and the discovery of the task and its examination were carried out.

2. *Brain function measurement by fNIRS*

In this study, brain function measurement was performed by fNIRS to acquire driver information. fMRI has a high spatial resolution, making it possible to observe specific brain activity. However, the body must be kept motionless at the time of measurement, and the flexibility of the experiment is low. On the other hand, EEG is widely used and has a high spatial resolution, but it is susceptible to electrical noise. Therefore, we concluded that fMRI and EEG are not suitable for measuring brain activities during car operation, especially in contraindicated cases. Since fNIRS can measure without restraining the human, and uses near-infrared light harmless to the living body, it is highly safe.
The wavelength of near-infrared light used for fNIRS is 700 to 1000 nm.

Near-infrared light has high bio-permeability. Hemoglobin easily absorbs near-infrared light. Oxygenated hemoglobin and deoxidized hemoglobin have different absorption coefficients. fNIRS measures oxyhemoglobin and deoxygenated hemoglobin using near-infrared light with two different wavelengths. In this study, the frontal lobe brain function was measured by the fNIRS device (Spectratech Inc.) composed of 16 channels. The equipment used is shown in Fig.1.

Fig. 1 NIRS device (OEG-16, Spectratech Inc.)

3. *Method of removing artifacts of driver and car body motion*

In this experiment, the brain activity of the actual driver and the movement of the car were measured. Using the results, we examined the effects of body movement and car body vibration on cerebral blood flow. The cerebral blood flow time series data were bandpass filtered as preprocessing. A band of 0.008 - 0.09 [Hz] is considered to be a frequency band related to the activity, and the bandpass filtering was configured for this band. After that, the correlation between OxyHb data of the cerebral blood flow time series and DeoxyHb data was calculated. In general, OxyHb data and DeoxyHb data derived from brain function are anti-correlated, and when the correlation value is high, there is a high possibility that driver and car body artifacts exist in measurement data. CBSI was adopted as a method to eliminate the influence of body movement. At CBSI, artifacts of motion are removed by the following method.

$$x_0 = \frac{1}{2}(x - \alpha y)$$
$$y_0 = -\frac{1}{\alpha}x_0$$

x, y, x_0, y_0 are the measured OxyHb data, DeoxyHb data, real OxyHb data, and DeoxyHb data. Through the above processing, transients and artifacts of the car body movement are removed.

4. *Outline of the experiment*

In this experiment, the brain activity of the driver and the movement of the car were measured. The following experiment was conducted.

4.1. *Human subject of the experiment*

The subject of this experiment was one graduate student in his early 20 s, holding a regular driving license. His physical and visual impairments were within the correctable range. Prior to the experiment, the experimental procedures and experimental protocol details were explained to the subject. In addition, the subject agreed to participate in the experiment.

4.2. *Experimental devices*

The vehicle used for the experiment was a compact, one-seater electric vehicle (ultra-small EV "COMS": Toyota Auto Body、Fig. 2).

Fig. 2 COMS (Toyota Auto Body)

Information, such as the steering angle and amount of brake pedal stroke, was acquired from the Controller Area Network (CAN) of this vehicle. The OEG 16 (Spectaratech Inc.) was used to measure brain activity. The sampling frequency was 1.53 [Hz]. The total number of channels of brain activity in the forehead of the subject was 16. The subject entered the vehicle wearing the OEG16 sensors, and attached a seatbelt. The OEG 16 controller was fixed to the car body so that operations other than driving were not performed during driving.

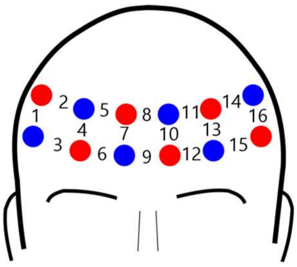

Fig.3 Channel placement

4.3. *Experimental design*

In this experiment, brain activity and driving operation during driving of the car were measured. In the driving task, the subjects drove the course, weaving in and out, between the pylons.

The subject drove five turns of the circumferential circuit as shown in Fig.4.

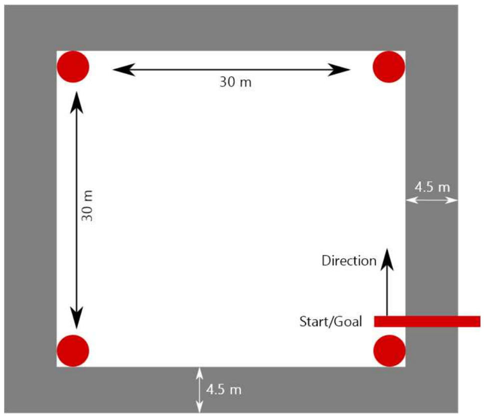

Fig.4 Driving Course Setting

We conducted questionnaires on subjects before and after the experiment. Question items before the experiment are age, sex, latest driving day, license retention years, previous day's sleeping hours, dominant handedness, corrective vision, pleasure/discomfort degree, fatigue degree, and sleepiness degree. Question items after the experiment were the four items of pleasantness/discomfort degree, fatigue degree, drowsiness level, and ease of driving. Three question items related to ease of driving were ease of bending, braking effectiveness, and ease of acceleration. The Visual Analog Scale (VAS) method was used for the subject’s responses to the degree of pleasure/discomfort, fatigue, and drowsiness, respectively.

5. *Results*

The correlation value between OxyHb and DeoxyHb in each channel is shown in Fig.5. Most of the correlation values between OxyHb and DeoxyHb are close to 1.0 (red part). This result shows that the time series of oxygenated hemoglobin and deoxygenated hemoglobin are largely similar. Therefore, this blood flow change is not caused by brain activity. That is, it was a change in blood flow caused by the driver's body movement and vehicle body movement.

In order to confirm this, an acceleration sensor was attached to the subject's head to detect the motion of the subject's head. When driving, the subject would always points his / her face in the traveling direction. Also, the car was shaking by the undulation of the road surface.

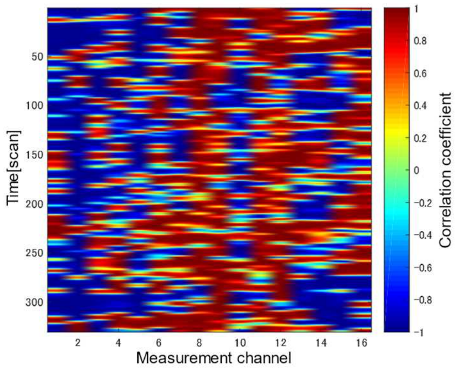

Fig.5 Correlation Coefficient Values between OxyHb data and DeoxyHb before CBSI

The possibility that this shake affected the motion of the subject was confirmed.

For this data, CBSI was applied. Correlation between OxyHb data to which CBSI was applied and DeoxyHb data, to which only the bandpass filter was applied, was calculated and the results are shown in Fig.6.As a result, the state in which the correlation value is close to 1.0 decreases.

Here, the cerebral blood flow change amount of CH8

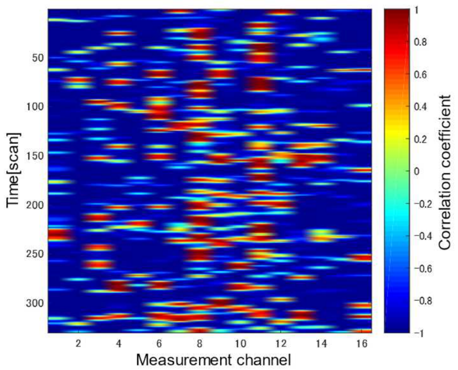

Fig. 6 Correlation Coefficient Values between OxyHb data and DeoxyHb after CBSI

is shown in Fig.7. Extreme blood flow change disappears and the amplitude decreases. This result indicates that the body motion of the driver and the vibration of the vehicle body were removed.

6. Conclusion

In this research, a driving support system using biological information was developed. Utilizing a small electric car, the effectiveness of the developed system was examined. In this experiment, problems were found when measuring brain activity during driving. In car operation, the correlation value between OxyHb and DeoxyHb of all

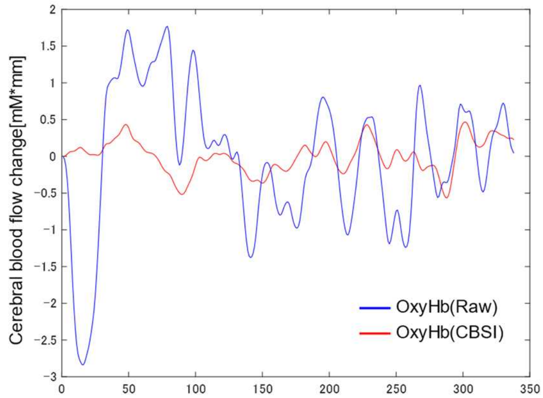

Fig. 7 Cerebral blood flow change of channel 8

CHs was close to 1.0. This indicates that the measured fNIRS data had artifacts of driver's body movement or vehicle body vibration. In this study, CBSI was applied as a method of removing artifacts. As a result, the artifacts of body movement of the driver or vibration of the vehicle body were removed.

In the future, we will further reduce these artifacts during driving and measure brain activity during driving.

References

1. National Police Agency, Traffic Accident Statistics （ 2016.10 ）," 2016 . http://www.e-stat.go.jp/SG1/estat/List.do?lid=000001163223
2. M. Tanishita, H. Miyoshi and M.Sano, *Cost-benefit analysis of automobile safety regulations, "Technical report*, ITEC working Paper Series 06-16", Doshisha University Technology and International Cooperation Center, 2006
3. S. Kusakabe, T. Kobuse, K. Okada and K. Nomura, Performance evaluation of automobile, vol. 135, no. 2, pp. 99-102, 2015.
4. T. IINUMA, \MRI principle and equipment, "*Clinical surgery*", vol. 43, no. 11, pp. 1569-1574, 1988.
5. Y. Inoue, About near-infrared spectroscopy," *Medical Image Information Society Journal*, vol. 27, no. 4, pp. 98-101, 2010.
6. S. Miyauchi, M, Misaki, S. Kan, T.Koike, K. Iwata, S. Takahama, Simultaneous measurement of fMRI-EEG and sleep research, "*Cognitive neuroscience*", vol. 9, no. 1, pp. 49-55, 2007.
7. Xu Cui, Signe Bray, Allan L. Reiss, Functional near infrared spectroscopy (NIRS) signal improvement based on negative correlation between oxygenated and deoxygenated hemoglobin dynamics, "*Neuroimage*", vol.49, no. 4, pp.3039-3046, 2010

Control of driving simulator based on state detection of the driver using Electrocardiogram measurement

Koma Yoshioka
*Graduate School of Life and Medical Science, Doshisha University, 1-3 Tatara Miyakodani Kyotanabe, Kyoto, Japan**

Satoru Hiwa, Kenya. Sato, Hiroshi. Furutani, Tomoyuki. Hiroyasu
Doshisha University, 1-3 Tatara Miyakodani Kyotanabe, Kyoto, Japan

tomo@is.doshisha.ac.jp

Abstract

One of the problems posed by automatic vehicles is the state of the driver at the time of switching between manual and automatic systems. In this research, the driving simulator was controlled based on detection of the driver's state by electrocardiogram measurements. A Simulink model that calculates the indicators of the driver's state obtained from real-time heart rate variability analysis was constructed in the driving simulator to assess the usefulness of the proposed system.

Keywords: driver detection, ECG, heart rate analysis, stress

1. Introduction

In a completely automatic vehicular operation, all conventional driving activities such as recognition, judgment, and other manual operations are solely performed by the system. This research adopts the definition of the Society of Automotive Engineers (SAE) for an automatic vehicular operation, which is characterized by varying levels depending on technology. SAE categorizes automatic operation in six levels— 0 to 5. At level 0, the system runs manually. At levels 1–2, the vehicle is currently in practical use. At level 3, all acceleration/deceleration, steering, and ambient monitoring are performed by the system, and from level 4, the vehicle is in fully automatic operation. Automatic operation is bypassed during emergencies, when the driver is required to immediately assume manual control of the vehicle (takeover) [1]. The critical point exists during levels 2 and 3, where a safe and smooth takeover [2] should be performed by the driver instantly. Thus, the state of the driver at these levels is very important, and a system capable of monitoring the driver's state during manual takeover will essentially lead to prevention of accidents normally caused by dozing off, and mistakes caused by excessive tension.

In this research, we developed a driver-state detection system, via a real-time driving simulation, which is capable of controlling the simulated vehicle based on the driver state that is measured by the electrocardiogram (ECG). The system conducts an analysis of real-time variations in heart rate (HR) from the ECG signal to determine the state of the driver, and gains control of the driving simulator (DS) based on the analysis.

2. Detection of the driver's state

In this section, we will first define the driver who

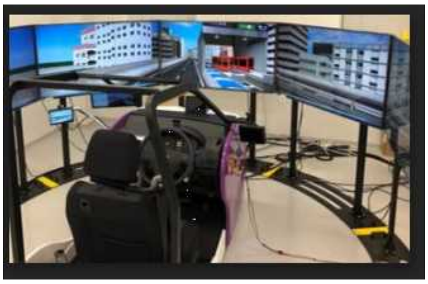

operates the DS during the simulation.

2.1. *DS configuration*

Figure 2. The driving simulator (DS) FORUM8 UC-win/Road, by FORUM 8

Figure 1 shows the UC-win / Road of FORUM 8 company used in the simulation.

The DS is composed of 42-inch flat monitors installed in the front, left and right front, and left and right for a total of five locations. In addition, there are smaller monitors installed at eight more locations, three of which were at the side mirrors and the room mirror. During the simulation, the image of the driver's seat viewpoint was displayed. The driver's seat was equipped with handle steering, accelerator, brake, handbrake, gear, and turn signal where operations similar to real automatic cars were possible. The overall system configuration is illustrated in Figure 2.

The DS is controlled by a DS Controller (PC1) installed with the UC-win / Road software. The automatic operation control system is constructed in the Driving Agent (PC 2), which performs automatic operation control based on the DS vehicle information transmitted by PC 1. In addition, PC 2 receives a processing signal based on the driver's biological information acquired from a third computer (PC 3), or the system's biomedical information controller. For example, PC 3 controls PC 2 based on the biometric measurement results, and switching between automatic operation and manual operation is performed.

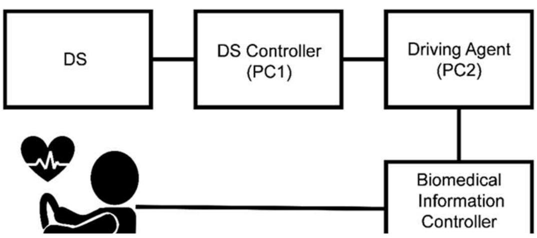

Figure 1. Overall configuration of the system

2.2. *State detection*

The ECG instrument was used to detect the driver's condition during the simulation. ECG measurements can be noninvasive and continuous. The autonomic nervous activity of the driver was estimated through an analysis of variations in HR shown by the ECG results.

2.1.1. *ECG measurements*

All ECG equipment were manufactured by g.tec, whose products are easily operated via MathWorks Simulink. The biometric instrument came from g.USBamp. A g.GAMMA box was used as the active electrode converter with a sampling frequency of 256 Hz, and the g.GAMMA clip was the active electrode. A Kendall electrode was the electrode used for placement on the skin. The three-point induction method was employed for the ECG measurement.

2.2.2. *Analysis of R variations*

The peak of the waveform obtained from electrocardiography is called an R wave. The instant at which an R wave is generated can be likened to a moment of a heartbeat. The interval at which R waves are generated is called the R – R interval (RRI). RRI is not constant but is continually fluctuating, hence the term HR variability. HR variability analysis is widely known as a method of estimating the autonomic nervous activity of a person. In general, autonomic nerves are divided into sympathetic and parasympathetic nerves. Sympathetic activities result to increased HR and decreased HR variability, while parasympathetic activities lead to decreased HR and increased HR variability [3]. Time and frequency domain analyses performed in this study were based on HR variability. Time domain analysis is an analysis in which constant RRI values of time series are applied directly [4].

The HR, the standard deviation of the RRI (the standard deviation of normal-to-normal RR intervals: SDNN), and the root mean square of the difference between two consecutive RRI values of successive differences (RMSSD) were used for the autonomic activity analysis. HR increases when sympathetic nerves dominate, while SDNN and RMSSD increase when the parasympathetic nerves dominate. In the frequency domain analysis, the estimated value of the spectrum is calculated for the data in which the RRI time series data is resampled at regular intervals. Estimation of power spectral density was performed on the RRI data resampled at 1 Hz using the periodogram method. The spectrum estimation value can be roughly divided into a low frequency (LF) and a high frequency (HF). The LF band is within the 0.05 – 0.15 Hz range, while HF band is within the 0.15 – 0.40 Hz. Power was integrated into each band, and the ratio of the total value, LF / HF, was used as the activity index of the sympathetic nerve.

3. DS control from ECG real-time analysis

The system, which switches the DS manual operation to automatic operation, was developed based on ECG results for estimation of the driver's autonomic nerve activity. The system is described in the succeeding subsection.

3.1. *The system and its functions*

PC 3, the computer conducting the ECG measurement and real-time analysis for the DS, was connected to PC 2 for control of the automatic operation system.

The state of the driver was monitored in the PC 3. When PC 3 detects a state of tension in the driver, it instantly commands PC 2 to switch the DS to automatic operation.

3.2. *Simulink model*

Figure 3 illustrates the ECG real-time analysis model, which consists of two functions.

The first function is ECG signal acquisition, achieved by employing a g.USBamp block of the g.tec proprietary model. The Unbuffer block was used for the buffered data, and a data type conversion block was used to convert the data to double type.

The second function is the real-time analysis model. It uses the raw ECG signal as input data to calculate the HR, SDNN, RMSSD, LF / HF in real time.

From the calculated index, the state of the driver is estimated for a possible system switch from manual operation to automatic operation. Estimation is done by the LF/HF ratio. Figure 4 shows the automatic operation command transmission model, which sends the switch command to the computer receiver when the specified LF/HF threshold value is exceeded. From Figure 4 , the

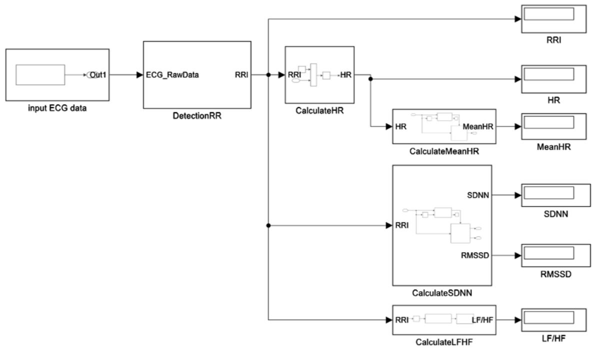

Figure 3. ECG real-time analysis model

manual operation is performed when the input is equal to zero. Otherwise, when the input is 1, the switch command for automatic operation is transmitted to the system via a UDP communication.

Along with the switch command, it is also possible to simultaneously transmit a command limiting the vehicle speed. The automatic driving system accepts data encoded in ASCII and characterized in bytes.

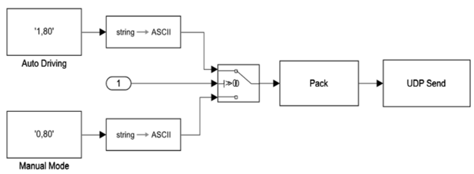

Figure 4. Automatic operation instruction model

4. Evaluating the usefulness of the ECG real-time analysis model

To validate the usefulness of the real-time analysis model, we compared the simulation results with those of the batch process. R wave detection was performed by real-time processing of the ECG data in a 3-minute resting period.

The participants were 8 healthy males, all at 23 years of age. After measurement, batch processing was employed for R-wave detection. The correlation coefficient of the RRI time series data detected in both real-time processing and batch processing were compared. All of the 8 data in both processes showed a correlation coefficient of 1.0. From this, it was suggested that both models could produce similar results.

5. Discussion on the driver-state estimation method

The procedures of the driver-state estimation are as follows:
① ECG measurement of the driver while at rest.
② Calculation of the average HR, LF/HF, SDNN, and RMSSD values at rest.
③ Comparison of each indicator by real-time analysis during experiment with its average value at rest.
④ The output for each indicator whose real-time analysis is sympathetically dominant over that at rest is 1.
⑤ The output 1 is added.

Because there are four indicators, the possible maximum output value is 4, while the possible minimum value is 0.

Figure 5 shows the value of the estimated time series change of stress for the driver. The peak, high-stress state

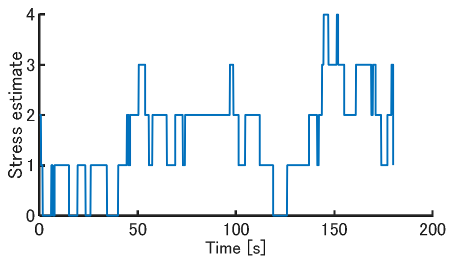

Figure 5. Time series change of stress value

for the subjects occurred at around 150 seconds from the analysis. This means that the subjects experienced maximum tension at that time. The estimation method gives an insight on the state of tension of the driver based on behavior and objective data.

6. Conclusions

There have been a wide range of automatic driving techniques developed in the recent years, which also attracted vast research on automatic driving systems.
Because the switching of systems from automatic to manual arises during critical levels of vehicular operations, in this case within levels 2 – 3 of the SAE definition, the issue is how the driver could ensure a safe and smooth takeover to prevent pre-conceived accidents or mistakes.

Realizing that the state of the driver is important during the takeover, this study proposed a system that monitors the driver's state of tension or autonomic nerve condition using heart rate variability analysis from a system's channel, which sequentially communicates a switch command to another channel for an effective manual-to-automatic operation shift.

The system was validated through a driving simulator and real-time ECG measurements analysis. It was proven that the real-time analysis model is useful for heart variability analysis because it gives the same results as for offline analysis.

7. References

1. A. Eriksson and N.A. Stanton, "Takeover time in highly automated vehicles: noncritical transitions to and from manual control," *Human factors*, vol. 59, no. 4, pp. 689-705,2017.
2. U U.E. Manawadu, H. Hayashi, T. Ema, T. Kawano, M. Kamezaki and S. Sugano, " Tactical-level input with multimodal feedback for unscheduled takeover situations in human-centered automated vehicles," in 2018 *IEEE/ASME International Conference on Advanced Intelligent Mechatronics (AIM)IEEE*, pp. 634-639 2018.
3. G.G. Berntson, J.T. Bigger, D.L. Eckberg, P. Grossman, P.G. Kaufmann, M. Malik, H.N. Nagaraja, S.W. Porges, J.P. Saul, P.H. Stone, et al., "Heart rate variability: origins, methods, and interpretive caveats," *Psychophysiology*, vol. 34, no. 6, pp. 623-648, 1997.
4. T.F.o.t.E.S.o.C.t.N.A.S.o.P. Electrophysiology, "Heart rate variability: standards of measurement, physiological interpretation, and clinical use," *Circulation*, vol. 93, no. 5, pp. 1043-1065, 1996.

Tactile Score; Development and Applications

Yasuhiro Suzuki
Graduate School of Informatics, Nagoya University, Furocho Chikusa
*Nagoya City, Aichi Prefecture 464 0814, JAPAN**
E-mail: ysuzuki@nagoya-u.jp
www.ysuzuki.info

Abstract

Unlike music, which can be decribed by means of a music score, tactile sense does not have a standard method for transcription. Likewise, tactile sense has no developed principle of composition. Hence, this study developed a method for describing tactile sense, referred to here as the 'tactile score'. We developed a mutual transformation method between tactile score and haptic vibrations, and then we verified that a hand massage performed according to a tactile score and haptic vibration from a tactile score evoked similar brain activities.

Keywords: List four to six keywords which characterize the article.

1. Introduction

Tactile sense[1] is sometimes called 'the first sense'; it is the first sense formed in hu-mans during development as a foetus. Tactile sense is associated with intimacy and empathy. It plays an important role in the somatic systems in its application of attention as a method of changing consciousness and improving knowledge. However, whereas visual media are systematized with colors and their combinational principles, such as color circles, and music in auditory media is systematized with the combinational principles of theories of harmonics, there has been no such a combinational principle for tactile sense.

Since criticism by Kant[2], many aestheticians have nearly given up thinking about beauty rationally although artists have been constructing beauty in various fields, such as music composition, dancing, and graphics. Prominent aesthetician Richard Shusterman[3] introduced the concept of Somaesthetics based on Baumgarten's Aesthetica[4], which proffered the belief that the body has its own aesthetic principles and a natural discerning ability: […] the body (of another or even one's own) can provide beautiful sensory perceptions or (in Kant's famous terminology) repre-sentations.). Shusterman pointed out that aesthetics is not a written knowledge but the sum of body experiences:

W*hen we are moved by a great artwork, it changes our blood pressure, heart rate, brain activities, etc. When we see a great artwork, if our body does not response to it, that means that the piece is not a great artwork for us person-ally. In other words, our body experiences judge the beauty of things. Such an enlarged view of aesthetics would give more systematic attention to the body's crucial roles in aesthetic perception and experience, including the aesthetic dimensions of body therapies, sports, martial arts, cosmetics, etc., that re-main marginalized in academic aesthetic theory.*[3]

2. Tactile Score

The massage, which is composed of a sequence of various tactile senses of movements of hands on the body, is a form of haptic engineering that humankind has been developing for more than 4,000 years. For this reason, we chose to investigate the massage to devise a method of describing the tactile sense.

Through our investigation, we found the massage to be composed of pressure, area of contact or touching, and velocity of the movement of the massager's hands. We modelled our tactile description on the musical score[5]. In staff notation of the tactile note, we defined the third line as the basic pressure—the basic pressure with which we might hold a baby or delicate, breakable objects. Hence, the basic pressure is not defined absolutely but may change from person to person or for different types of massage. We also defined the parts of the hand used in massaging and the kinds of stroke used when massaging.

For example, the fingertip to the first joint is 1, the second joint is 2, the third joint is 3, the upper part of the palm is 4, the centre of the palm is 5, and the bottom of the palm is 6. Thus, a flowing motion from a fingertip to the third joint is denoted as '1–3'.

For massage strokes, we analysed the method of massaging in face therapy and the stroking action of the hands' movements. We assigned these as A, a, N, and n, where A stands for the massage stroke of drawing a circle on the cheek, and N stands for a massage stroke of drawing a line, a stands for a smaller circle on the check and n also a shorter line than N. For example, A5 illustrates drawing a circle on the cheek with the centre of the palm.

1.1 Principle of Creating Tactile Sense of Massaging

Having developed a workable method for describing massages, we are now able to compose massages. We have created various tactile scores and performed them, and have examined and determined the comfortable massages. We synthesized these experiments and experiences of massaging for customers and obtained the common characteristics of a comfortable massage as follows:

$$Const.=S\times P\times V$$

,where S is the area of touching, P is the pressure of the massage, and V is the velocity of hand movement. For instance, draw a circle on the back of your hand using your fingertip strongly and then draw a circle on the back of your hand using your palm with the same movement velocity; if you massage with the same pressure, it will not be comfortable, but if you massage more softly, it will be comfortable. As S decreases and V remains constant, and P becomes stronger,

Const. = S × P × V is preserved; this will generate a comfortable massage. This experimentally obtained principle has been confirmed through experiments and mathematical analysis using category theory.

2 Experimental Aesthetics of Tactile Sense

To verify the obtained principle, we examined and compared the effectiveness of massages that were, in principle, correctly or incorrectly composed. We analysed salivary alpha-amylase, because this protein enzyme increases when a person suffers from stress. We also examined the small face effect (improved elasticity and smoothness) and improvements in the skin condition, based on changes in the brightness of the skin.

We compared the values of the stress markers before and after the massage. When the massage was principally correct, the values of the stress markers decreased, and when it was incorrect, the values increased. This finding confirmed that people feel comfortable when a massage is principally correct and can recognize a principally incorrect massage.

We then set out to verify the effectiveness of the massages as beauty treatments. We took photos before and after the principally correct massage and compared the shape and brightness of the face using image processing. The processed findings indicated that the shape of the face tended to shrink, especially around the cheeks, and that the brightness of the facial image tended to be heightened. These results were obtained through experiments using a part of the same face therapy massage that has been requested by and performed on more than 200,000 customers in our beauty shops; its effectiveness has therefore been validated by social experiments. The human body distinguishes beautiful and non-beautiful haptic sensations. People experience the beauty of their own bodies with physical senses, as proven by a range of indicators from the salivary alpha-amylase levels[6] to enhanced brightness or 'glows' to improved elasticity, relaxation, and skin condition improvements. If this appeal to the beauty of personal experience seems strangely idiosyncratic, consider the remarks of Jean-Marie Guyau: *To breathe deeply, sensing how one's blood is purified through its contact with the air and how one's whole circulatory system takes on new activity and strength, this is truly an almost intoxicating delight whose aesthetic value can hardly be denied (in Guyau, J.-M. (1884). Les problèmes de l'esthétique contemporaine (11th ed.) (pp. 20–21).*

The principle of creating pleasurable tactile sense, which we extracted and codified, shows how to compose beautiful haptic sensations in art and design.

3 Mutual Transformation of Haptic Tactile Scores and Haptic Vibrations

Haptic media, like a hand massage, is a personal media; no one can massage thousands of people simultaneously, display a massage in a gallery, or broadcast a massage through television or over the internet and obtain the same results as those for the individual receiving the massage. This does not mean that tactile sensations cannot be communicated. To do this, we attempted to bridge the gap between haptic sensation in the physical environments and the digital world of bits and bytes.

To transform the haptic media of the massage (personal media) into mass media, we transformed tactile scores into haptic vibrations[7]. There are several ways of performing such transformations. In this work, we show the case where only the pressure changes, and not the size of the contact area. Based on research on haptic impressions and frequencies, stronger pressure corresponds to a lower frequency, whereas weaker pressure, to a higher frequency relative to the frequency of the aforementioned standard pressure, which we signify with the third line in the tactile score.

For example, in transforming the following music score (Re, Re, So, So; with quarter notes) into tactile

score, we set the sine wave at 40 Hz frequency and define the difference of each half-tone as 5 Hz. When the tempo of the tactile score is one second for each quarter note, this tactile score is transformed into the sequence of a sine wave of 30 Hz (= 40 – 5 x 2 Hz) for 1 sec, 30 Hz for 1 sec, 50 Hz (= 50 + 5 x 2 Hz) for 1 sec, and 50 Hz for 1 sec.

Using this transformation, we can also obtain the tactile score from the sound input. When the first inputted sound is analysed by Fourier analysis and frequencies, we obtain the amplitudes and their durations; based on the obtained results, we can define the frequency that corresponds to the basic pressure and the amplitude, which corresponds to the halftone.

For example, it is obtained as follows: (the highest frequency – lowest frequency) / 12 = the pressure of half tone, where we differentiate of the range of frequencies into an octave (twelve half-tones). Using this algorithm, we can create a tactile score automatically from music, natural sounds, noise, etc. To verify the transformation method from tactile score to haptic vibration, we examined the effect of transformed vibrations from tactile score on the human body. Preliminary examinations showed that the human body distinguishes the quality of vibrations, and this affects activities of the brain.

Thus, the transformed vibration from a tactile score may produce the same effect as a hand massage according to the tactile score. We examined brain activity using near infrared spectroscopy (NIRS)[8] (specifically, Pocket NIRS Duo, *DynaSence*, Co. Ltd.). We examined how hand massages composed through tactile scores affect brain activities and found that well-designed hand massages created through correctly composed tactile scores, with the codified composing principle, evoke brain activities higher than those produced by incorrectly composed massages.

The result of the experiment indicated that haptic vibration transformed from a correctly composed tactile score evoked brain activities that were statistically significantly higher than sine waves and the control.

4 Applications of Tactile Score

Construction of a transformation system from tactile notation to vibrotactile has expanded related research on the scores. For example, by using this technique to extract tactile notation from songs and convert it into vibrotactile sense, it is possible to take out haptic sense inherent in music and obtain tactile sense corresponding to songs. Unlike the traditional so-called "beat" bass enhancement and tactileization (such as Body Sonic), the appeal to emotion increases in music without beats such as Enka and majestic classic. This new music - haptic media is of interest from acoustic experts, and commercialization of major sound manufacturers and reproducers is under way (Patent No. 6322780, 6401758). Also, at the request of NTT, I designed the vibration tactile extracted from the music for the hearing-impaired person (Tsukuba Technical University Dance Team) (for the event "Nico-Nico Chokaigi, 2018"), and from animation and same touch It was also used for video work that generated vibration tactile sense (exhibition Haptic TV, ICC museum, Tokyo). This media has attracted attention from music specialists and develops to collaborative research and has created a technology to foster presence by combining inaudible vibration haptic sense with music and has started distribution business of this media.

In addition, we have found that it is an active haptic presentation device that can obtain various tactile sensations when the user operates by combining new material and vibrating tactile sense with a major manufacturer of electronic component equipment. We have started a collaborative research project (Vibration Medicine project) that applies a series of vibrational haptic technology to improve insomnia related to lower brain dysfunction with major drug development manufacturer. Depending on progress, we plan to develop to demonstration experiments in cooperation with local governments within a few years. The interactions in the information environment have been digital (coupled or not) so far. What is important in the future is the quality of interaction. For example, "Thank you" for print is "Thank you" regardless of the depth of gratitude. The quality of information changes as it changes type / pictograph, handwritten character, telephone and interaction quality.

In the future, everything will be digitally linked by Internet of Things, IoT etc. This domain enables mutual action of emotion and emotion in the information environment by enriching the link quality while utilizing this growing link as a social infrastructure, its significance and ripple effect are great. Moreover, even in the direct interaction between humans, as well as playing instruments while watching the score, you can perform a high quality massage by touching, combine tactile information technology and direct interaction, By monitoring speech and facial expressions and smoothing human relationships, it is expected to improve the environment of emotional labor (high nurse, care giver, call center, etc) with high staff turnover rate.

In addition, by giving vibratory tactile sensation generated from the talent of expert's massage in preparatory research to the face, stress markers (amylase concentration in saliva) decrease, blood flow increase at the terminal (limb) Mire, a questionnaire suggests improvement of sleep state. This result suggests that vibratory tactile sensation can be improved by improving lower brain dysfunction (disorders such as respiration, sleep, mood) and exercise effects of patients who have been bedridden for a long time (from rising blood flow in hands and feet) It is expected to have a high ripple effect as a new medical device that can be used cheaply and easily at home.

Acknowledgement

This research has been supported by Grant in Aid for Scientific Research (KAKENHI) No:15K00268 and 16H03093

References

1. Serino, A. & Haggard, P. Touch and the body. *Neuroscience and Biobehavioral Reviews* (2010). doi:10.1016/j.neubiorev.2009.04.004
2. Kant. *Crítica de la razón pura*. *critica de la razon pura* (2005). doi:10.1109/ICRA.2013.6630904
3. Shusterman, R. Muscle memory and the somaesthetic pathologies of everyday life. *Hum. Mov.* (2011). doi:10.2478/v10038-011-0001-2
4. Gregor, M. J. Baumgarten's Aesthetica. *Rev. Metaphys.* (1983). doi:10.2307/20128010
5. Suzuki, Y., Watanabe, J. & Suzuki, R. Tactile score, a knowledge media of tactile sense for creativity. *Smart Innov. Syst. Technol.* (2012). doi:10.1007/978-3-642-29934-6_56
6. Nater, U. M. *et al.* Stress-induced changes in human salivary alpha-amylase activity - Associations with adrenergic activity. *Psychoneuroendocrinology* (2006). doi:10.1016/j.psyneuen.2005.05.010
7. Suzuki, Y., Suzuki, R., Watanabe, J., Yoshida, A. & Shigeru, S. Haptic vibrations for hands and bodies. *SIGGRAPH Asia 2015 Haptic Media Contents Des.* (2015). doi:10.1145/2818384.2818389

Tactileology; Haptic Informatics by using Tactile bit, T-bit

Yasuhiro Suzuki
Graduate School of Informatics, Nagoya University, Furocho Chikusa
*Nagoya City, Aichi prefecture 464-081, JAPAN**
E-mail:ysuzuki@nagoya-u.jp
www.ysuzuki.info

Abstract

With the progress information technology, IT our interaction has become dense through information space. On the other hand, the interaction of tactile "interaction" is getting loose. Therefore, we conceived an academic field that integrates with the digital information space by systematically studying and informing the tactile interaction. Therefore, we will create a tactile information processing system that outputs a sense of touch by inputting tactile, converting it into a talent, converting it into a tactile score, using a method "touches" for describing tactile interactions as an intermediate language. In this area, the tactile interaction which has been tacit knowledge so far is informed and integrated with the existing academic arts and industrial infrastructure, enriching tactile interaction in the society at large including the information space It is expected to become.

Keywords: Tactileology, Tactile bit, Tbit, Tactile Communications

1. Introduction

Developments of information technologies, IT such as Social Network Services, SNS, Internet of Things, IoT[1] and so on have transformed interaction space from real world to cyberspace. Interactions in cyberspace do not limit by time and borders; we will hesitate to make a phone all in midnight, while we will send e-mail in every time and we have to pay international postal fee to send a letter to abroad, while we do not have to pay such fees to send e-mail to abroad. In the past, individuals interacted via mass media such as newspapers and TV. SNS enabled individuals to interact directly.

Direct interaction allowed information and capital to flow between individuals. This personal information and the flow of capital have changed the social structure greatly. For example, there are disappearance of personal shops due to the development of electronic commerce such as Amazon, rationalization of customer service and practical application of automatic driving in public transportation. Through the development of IT, the interaction in the information space becomes dense while the direct interaction in the real space becomes sparse.

The disappearance of direct interaction between individuals by IT also occurs in the medical field. In 2011, Abraham Verghese[2], Stanford University Medical School professor gave a lecture entitled "Power of Doctor's Hand" at Technology Entertainment Design, TED Global. In the lecture he said that “ *I joke, but I only half joke, that if you come to one of our hospitals missing a limb, no one will believe you till they get a CAT scan, MRI or Orthopedic consult*.” (CAT: Computed Axial Tomography, MRI: Magnetic Resonance Imaging). And he alarmed the present situation that only the data was biased in the medical field and the "interaction" between the doctor and the patient is getting thin. He predicted that "[…] *the most important innovation, I think, in medicine to come in the next 10 years, and that is the power of the human hand -- to touch, to comfort, to diagnose and to bring about treatment."* Although, ten years have passed since this lecture, such medical innovation as his prediction has not occurred during this time.

1.1. *Related works in Tactile Sense*

Tactile sense has been investigated in cell biology (mainly tactile receptors)[3], neuroscience[4], psychology[5], cognitive science[6], virtual reality (VR)[7] , robotics[8] and so on. In physiology and neuroscience, response pathways and mechanisms for tactile stimuli have been studied [9]. However, there are no studies that designed the tactile stimulus itself. In psychology studies are being conducted on illusion[10] and phantom limbs[11] (pain in parts that should have been cut off), relationships with perception [12], emotion and relationships with affordance [13], and so on.

In informatics, Susumu Tachi et.al. (Keio University, JAPAN) have been developed various tactile interfaces and applied for Virtual Reality, VR system, such as the tele-existence system[14] (system that makes people and objects of remote areas feel as if they are nearby). They also develop Tactile Toolkit [15] that records sound (such as fricatives) when they are in contact with objects and reproduces them with a vibrotactile presentation device (using the same method for Nintendo-Alps Electrics company). In overseas, Hiroshi Ishii (Massachusetts Institute of Technology, MIT USA) et.al. have been conducting research project "tangible bit"[16 17] which can be touched directly, and it is well known for many years.

Massage is a time-varying tactile used from the ancient times (depicted on the mural paintings of the Egyptian era) over time and region. Hippocrates who is one of the founder of Western medicine pointed out the medical effect of massage, but massage is still only one of alternative therapies, as compared with surgical science and internal medicine which was subsequently established as Western medicine.

A lot of research has been conducted in nursing and physiotherapy in Japan, and overseas the National Center for Complementary and Integrative Health (NCCIH) of the National Institutes of Health has been leading research on massage since 1991. In the review of massage, it has shown that massage gives effect on pain relief[18], mental health [19], infants [20] (weight gain) etc. In addition, immune function of breast cancer patients [21], the quality of life of diabetes patients [22], relationship with blood glucose level [23], etc. have been reported.

Regardless of domestic and overseas research, massage research is mainly clinical research, and studies that have stepped into massage techniques are commonly described in natural language. In nursing science, Kawashima Midori (Nihon Red Cross Nursing University) systemizes the hands, advocates "TE-ARTE" and establishes associations and conducts practice and dissemination activities.

Conventional studies of time-varying tactile sensations (massage), unified methods that can describe arbitrary massages as tactile notes have not been proposed, and the provision of technologies with high reproducibility with quality control is difficult.

We know the importance of touching directly; such as shaking hands and hugs. The importance of the power of human hands is a common recognition beyond our time and region among us. The sense that supports "people's contact" and "power of human hands" is "tactile".

2. Tactile Score

Hence, I conceived a research that informs the tactile interaction and integrates with tactile information and information environment. This research can utilize traditional tactile research in information environment (nursing, physical therapy, engineering, etc.) information environment. The sensitivity on frequency of sound of tactile sense is not high compared with auditory sense but for tactile receptors sensing pressures and their patterns are important to detect sharpness or roughness of object to touch; of course, there are another important ability to sense e.g. temperature, pain, etc. However, in order to describe tactile sense, not only pressures but also should consider another characteristic; hence we have been considered in massaging, which is the most common products of haptic engineering and possesses long history.

To investigate the method of massage, we take massaging to be composed of pressure, the area of touching, and the velocity of the movement of hands. In staff notation of the tactile note, we define the third line as the basic pressure; the basic pressure is the pressure when we hold a baby or an expensive jewel very carefully.

Hence, the basic pressure is not defined absolutely but may change from person to person or for different types of massage. We also define the part of the hand used in massage and the kind of stroke when massaging. For example, the fingertip to the first joint is 1, the second joint is 2, the third joint is 3, the upper part of the palm is 4, the center of the palm is 5 and the bottom of the palm is 6; when we flow from a fingertip to the third joint, this is denoted as ``1-3". For massage strokes, we analyze the method of massaging and strokes of hands movements; we symbolize each stroke as, etc. For example, the symbol stands for the massage stroke of drawing a circle on the cheek.

3. Tactile bit, T-bit

Tactile can be translated into language by using Tactile Score. Tactile sensation is included in the senses. For example, sculpture is called visual tactile, and has been discussed in aesthetics, philosophy, and so on. The sound texture is expressed tactilely like "soft voice" or "hard sound (heavy metal)". Also, tactile in taste is called texture. Therefore, when describing the tactile sense included in the five senses with Tactile Score, Tactile Score becomes a sensory language.

Tactile Score describes discrete time change of pressure. When describing five senses with Tactile Score, only the time change of what corresponds to "pressure" in each sense is described. Therefore, even if the sense is described by Tactile Score, not all tactile sense is described. This is similar to music score in music. The music score is a discretizing description of the temporal change of the pitch. Therefore, the music score does not describe all of the music. However, music score is an important way of describing music. By using music score we can record, save, edit and distribute music, making possible the birth of composers.

Tactile scores describe tactile symbols and quantify them. Symbolized and quantified tactile sensations can be processed with conventional information processing systems and artificial intelligence systems. Therefore, the tactile information informed by Tactile Score is called Tactile bit, T-bit. When tactile sense of five senses is described by T-bit, that is, Tactile Score, T-bitized tactile sense becomes input to the conventional information system. Then, by outputting the result of information processing as Tactile Score and converting Tactile Score to tactile sense, it is possible to construct a system that inputs tactile information, performs information processing, and outputs tactile sense.

3.1. *Information search by using T-bit*

Fig. 1. Demonstration of information search by using T-bit, a user make a voice; when a user talks to the system, the user have massage with the extracted vibrotactile sense (photograph is J.Yamagiwa, the president of Kyoto University).

We constructed a haptic search system using T-bit.This system uses only T-bitized tactile information without using language information for information retrieval. The retrieved information is also outputted as tactile sense. This system processes tactile input and outputs tactile sense, which is completely different from the conventional information retrieval system (Fig 1.). This system converts the user's voice into T-bit and analyzes its touch quality. Touch quality is a concept used in tactile science, and it is defined by two-dimensional touch sense in the vertical direction and the horizontal direction. The vertical direction is expressed as "hardness" and "softness", and the horizontal direction is expressed as "smoothness" and "roughness". This system evaluates as "Soft" if the variance of the Tactile Score used in the T-bitization (the strength of the pressure) is large, "Hard" if not, and if the envelop of the Tactile Score is smooth "Smooth", if it is jagged, it is evaluated as "rough". By quantifying each tactile, the T-bit tactile is mapped on a two-dimensional plane.

We have calculated the touch quality of hundreds of T-bit music data and constructed a touch database. This database stores music and its touch quality (this system won the president of Kyoto University prize in *Kyoto University Interdisciplinary Research Idea Contest 2017*).

3.2. *Toward Tactileology by using T-bit*

Previous tactile studies have studied the tactile sense when integrating time. On the other hand, this research corresponds to tactile research when time is differentiated. In addition, tactile sense has been mainly described in natural language, but in this research its described by symbol (score). Chemistry and mathematics were once described in natural languages, but eventually the description by chemical formulas and algebraic symbols became to be used and it made a dramatic progress. This research by Tactile Score makes dramatic progress in tactile research and application.

Acknowledgement

This research was supported by JSPS KAKENHI, Grant in Aid for Scientific Research No. 15K00268

References

1. Saracco, R. The internet of things. in *IEEE Technology Time Machine Symposium on Technologies Beyond 2020, TTM 2011* (2011). doi:10.1038/scientificamerican1004-76
2. Verghese, A. A touch of sense. *Health Aff. (Millwood).* (2009). doi:10.1377/hlthaff.28.4.1177
3. Lumpkin, E. A., Marshall, K. L. & Nelson, A. M. The cell biology of touch. *Journal of Cell Biology* (2010). doi:10.1083/jcb.201006074
4. Graczyk, E. L. *et al.* The neural basis of perceived intensity in natural and artificial touch. *Sci. Transl. Med.* (2016). doi:10.1126/scitranslmed.aaf5187
5. Bauer, A., Hagenburger, J., Plank, T., Busch, V. & Greenlee, M. W. Mechanical pain thresholds and the rubber hand illusion. *Front. Psychol.* (2018). doi:10.3389/fpsyg.2018.00712
6. Nonomura, Y. *et al.* How to identify water from thickener aqueous solutions by touch. *J. R. Soc. Interface* (2012). doi:10.1098/rsif.2011.0577
7. Kilteni, K., Groten, R. & Slater, M. The Sense of Embodiment in virtual reality. *Presence: Teleoperators and Virtual Environments* (2012). doi:10.1162/PRES_a_00124
8. Kappassov, Z., Corrales, J. A. & Perdereau, V. Tactile sensing in dexterous robot hands - Review. *Rob. Auton. Syst.* (2015). doi:10.1016/j.robot.2015.07.015
9. Vallbo, Å. & Johansson, R. S. Properties of cutaneous mechanoreceptors in the human hand related to touch sensation. *Hum. Neurobiol.* (1984). doi:10.1007/s00406-006-0654-6
10. Tsakiris, M., Prabhu, G. & Haggard, P. Having a body versus moving your body: How agency structures body-ownership. *Conscious. Cogn.* (2006). doi:10.1016/j.concog.2005.09.004
11. Moseley, G. L. I can't find it! Distorted body image and tactile dysfunction in patients with chronic back pain. *Pain* (2008). doi:10.1016/j.pain.2008.08.001
12. Dargahi, J. & Najarian, S. Human tactile perception as a standard for artificial tactile sensing--a review. *The international journal of medical robotics + computer assisted surgery : MRCAS* (2004). doi:10.1002/rcs.3
13. Lee, B. & Macgregor, C. G. The Emotional Impact of Surface and Prototyping Properties in Product Design. *Proc. Hum. Factors Ergon. Soc. Annu. Meet.* (2010). doi:10.1177/154193121005402003
14. Tachi, S. Telexistence and Retro-reflective Projection Technology (RPT). *Proc. Virtual Real. Int. Conf.* (2003).
15. Pohl, I. M. . & Loke, L. . Touch toolkit: A method to convey touch-based design knowledge and skills. in *TEI 2014 - 8th International Conference on Tangible, Embedded and Embodied Interaction, Proceedings* (2014). doi:10.1145/2540930.2540957
16. Ishii, H. & Ullmer, B. Tangible bits. in *Proceedings of the SIGCHI conference on Human factors in computing systems - CHI '97* (1997). doi:10.1145/258549.258715
17. Ishii, H., Lakatos, D., Bonanni, L. & Labrune, J. B. Tangible Bits: Beyond Pixels. *Interactions* (2009). doi:10.1145/1347390.1347392
18. Frey Law, L. A. *et al.* Massage Reduces Pain Perception and Hyperalgesia in Experimental Muscle Pain: A Randomized, Controlled Trial. *J. Pain* (2008). doi:10.1016/j.jpain.2008.03.009
19. Plews-Ogan, M., Owens, J. E., Goodman, M., Wolfe, P. & Schorling, J. Brief Report: A pilot study evaluating mindfulness-based stress reduction and massage for the management of chronic pain. *J. Gen. Intern. Med.* (2005). doi:10.1111/j.1525-1497.2005.0247.x
20. Field, T., Diego, M. & Hernandez-Reif, M. Preterm infant massage therapy research: A review. *Infant Behavior and Development* (2010). doi:10.1016/j.infbeh.2009.12.004
21. Hernandez-Reif, M. *et al.* Breast cancer patients have improved immune and neuroendocrine functions following massage therapy. *J. Psychosom. Res.* (2004). doi:10.1016/S0022-3999(03)00500-2
22. Ezzo, J., Donner, T., Nickols, D. & Cox, M. Is Massage Useful in the Management of Diabetes? A Systematic Review. *Diabetes Spectr.* (2001). doi:10.2337/diaspect.14.4.218
23. Sajedi, F., Kashaninia, Z., Hoseinzadeh, S. & Abedinipoor, A. How effective is Swedish massage on blood glucose level in children with diabetes mellitus? *Acta Med. Iran.* (2011).

Natural Computing and Formal Computing

Yasuhiro Suzuki
Graduate School of Informatics, Nagoya University, Furocho Chikusa
*Nagoya City, Aichi prefecture 464-0814, JAPAN**
E-mail: ysuzuki@nagoya-u.jp
www.ysuzuki.info

Abstract

The basis of natural calculation is considered. In order to that algorithm, programming, calculation are redefined. From the redefinition, it is shown that the observation is indispensable for calculation. Considering from the new definition, the calculation can be divided into Natural Computing and Formal Computing. Natural Computing is the primitive computation and all computations occur as Natural Computing. And Natural Computing evolves to Formal Computing. We reconsider the research on artificial intelligence using the results of this study and suggest a future direction of progress.

Keywords: Foundation of Natural Computing, Observation of Computing, Formal Computing, Artificial Intelligence

1. Introduction

Algorithm is an order of executions; so, there are many algorithms in nature. In general, elements in nature, including human, cannot predict the future, but we can predict that DNA would replicate itself, growth of cell through cell cycles and how the ecosystem recover after being destroyed by the flood.

Why can we predict them? Because we (not only human) know algorithms and how they will work. Computing is composed of algorithm, the observation of computing and its verification; where observation is how "decode" the result of algorithm and the verification guarantee the legitimacy of computing; for example, result of algorithm (addition) of 1 + 1 can be 2 or 10, if the method of observation is decimal system, we can observe 2 and 10; if it is binary system, we can observe 10 but cannot 2; in decimal observation, we can verify 2 is correct, while 10 is not correct and in binary observation, we can verify 10 is correct. In this example, we used formal observation and verification that have given by mathematics.

However, most of computing in nature does not have formal system to observer and verify. This is fundamental difference of formal computing from natural computing. In natural computing, computing substances, such as DNA molecules, cells or ecosystems, observe the result of algorithm and verify it by themselves. Hence, natural computing is primitive in computing and throughout of the evolution from natural computing, it develops "external formal" system to observe and verify and evolve to formal computing system.

2. What is Algorithm?

When you buy potatoes, carrots and onions in the grocery store and make an account at the cash register. In the register, the total is displayed as 0 yen at the beginning, but the total amount changes as the price of potatoes, carrots and onions are added, when all are finally added and the consumption tax is added at the end, the total amount will not change.

When the state change due to action becomes steady, that state is called normal form. As in this example, the normal form includes not only the case where the state change stops but also a dynamic steady state like the computing process of the circumference ratio.

2.1. *Algorithm*

In the case where the order of action is determined beforehand when the state changes with action, or in the case where the order of action occurs from the process of change, such order is called an algorithm.

In the grocery store example, the addition order of "potato + carrot + onion" corresponds to the algorithm. In chemical reactions, the order of reaction speed occurs relatively, and the state changes in that order, so the order is the algorithm.

Changing the order of algorithms is called programming. For example, if you buy 4 potatoes, 1 onion and 3 ginsengs, adding efficiency one by one is not efficient, so change the order of action with "potato x 4 + carrot x 3 + onion" this is programming. Also for chemical reactions, catalysts and enzymes are used to change the order of reaction rates, which is also programming.

2.2. *Observation of Computing*

When the way to observe the state change by the algorithm is defined, the system becomes computing. Observations are defined by predefined correct answer sets and intersection sets of normal type sets. An element included in this intersection set becomes a correct candidate. For example, when searching for the shortest path of a maze by using slime molds, the normal type group becomes the state of slime mold[1] after a certain period of time. In some cases, it may have reached from the entrance to the exit, various state changes such as stopping on the way, splitting into multiple parts, stopping at the entrance, etc. are all normal types.

Here, if the correct answer set is "an individual that has reached from the entrance to the exit", the correct answer candidate is "an individual that has reached from the entrance to the exit of the maze" among the various regular forms. From the viewpoint of the observing computing entity, these will be entering at least in the maze.

On the other hand, there is no way to know whether slime mold acted "unravel the maze" or not. Slime molds are just a state change, not even more or less. Therefore, the assertion that "slime mold has an intelligence to solve the maze", "slime mold is clever" is an arbitrary part of the computing entity observing the behavior of slime mold as such. If the correct answer set by the computing entity is "the slime divides into two", this time, "regular division slime mold" will be selected for the normal type set.

Although individuals reaching from the entrance to the exit were chosen as correct candidates by observation, since not all of them are passing through the shortest route, it is necessary to verify the correctness of the correct candidate. For this purpose, the computing entity investigates the shortest path length of the maze in advance, and the individual that is the shortest path length among the correct candidate is "correct answer".

2.3. *Subjective verification and objective verification*

In the case where verification of validity is performed outside the computing subject (the subject performing computing), it is called "objective verification". In addition, when the subject of verification itself conducts validation, it is called "subjective verification". "Objective" here is an objective to the computing entity.

The shortest path search using slime mold is a computing using organisms of slime molds and verification is objectively performed (by the shortest path length). Hamiltonian path search by DNA computing[2] and DNA origami[3] are also objective verification.

In addition, when the subject of computing is not human, for example, in DNA replication system, the replication result is subjected to objective verification by thermodynamic calibration[4], and even if protein is inactivated due to replication error, objective verification is carried out by evolutionary selection. Meanwhile, in graphics and composition using computers, since the work is produced by subjective observation by the drawer (verification of correct answer set) it is subjective verification. Even with the same computing entity, there are cases where objective verification and subjective verification are used together by replacing the verification system.

3. Computational Aesthetics

How is "verification" in the case of subjective verification carried out? In the case of objective verification, verification is carried out by an external mechanism such as mathematics outside the computing entity, but subjective verification does not have a reason like mathematics. In that case, it is beauty to become the base of the verification. Here, beauty is the beauty in a broad sense including arts, comfort, comfort, stability, safety and other computing entities. All criteria that judge "good" are called beauty[5].

3.1. *Computational Aesthetics of Alberto Giecometti*

French artist, Giacometti (Alberto Giacometti: 1901 - 1966)[6] is known for sculptural works sculpted to the limit, his work is like a bone, but there is a rich and expansive presence if fulfilled. Philosopher Isaku Yanaihara served as a model for sculptural works of Giacometti and left a conversation with him during the work making a note.

In the process of making sculpture, Giacometti scrapes extra clay, eventually all the clay is scraped and nothing is gone, and as Giacometti tries to capture Yanaihara with a graphic, there is still no satisfaction with the giant meter Return to sculpture.

What is interesting in this case is that computing does not halt because the subjective verification continues to be incorrect, so that calculation continues even if the computing "case (canvas or clay)" eventually disappears. There were no external noises (the date of Yanaihara's return home was decided), etc. There was no shaky subjective verification and the calculation continued until the correct answer was reached.

If the computing entity is an electronic computer or a robot, calculation cannot be continued once the enclosure is exhausted. However, even if the chassis disappears, if we can take the algorithm and the verification system to a moving case in some way, we can continue the calculation while moving from the case to the case until we get the correct answer. Such a calculation system has already been realized and implemented in natural systems. That is, we are biological systems.

4. Natural Computing and Formal Computing

Computing is "state change due to order of action and its observation", which is not done only by computers or human beings.

For example, natural selection in evolution is objective verification. However, even without assuming Darwinian evolution, subjective verification is repulsion, attraction and structural stability / instability in substance interaction. If the interaction between the substances is stable (aesthetic state) the substances constitute the structure and if it is unstable (in a state not beautiful) the structure cannot be maintained. Therefore, even if we do not assume objective verification like Darwin evolution[7], the stability and instability of interaction between substances becomes subjective verification.

Since the computational system that subjectively verifies is more primitive, the computing that performs "state change by order of action and observation + subjective verification" is called natural computing. On the other hand, computing that perform objective verification are called formal computing.

5. Natural Computing and Formal Computing

We defined computing with subjective verification as natural calculation. Natural systems including human beings in general, natural calculations are ubiquitous.

For example, it is said that wine[8] called wine today is discovered to have been naturally fermented by collapsed grape where the grapes are clustered by chance, and that "delicious liquid" In order to reproduce the trial and error it may have been repeated variously, such as crushing the grapes etc. on the spot and adding water.

The trial and error of winemaking is "state change of the grape liquid by order of action", and the normal form is "the unnoticeable liquid" obtained as a result of the state change. And the observation system is the correct set of our taste. Therefore, winemaking can be regarded as a computing system (wine computing system in the following).

If the wine computing system is natural computing, even a suspicious liquid (correct answer candidate) that cannot be said to be very wine, it becomes wine if it becomes "correct answer" as a result of subjective verification of the calculation subject.

However, that "liquid that the computing entity verified with wine" would be considered "incorrect" from other subjective verification systems (i.e. those who taste that wine).

When observing with many people, it is necessary to modify (program) the algorithm so that wines that many subjective verification systems observe as "correct answers" can be brewed. The subjective verification system becomes a group and constitutes objective, so natural computing evolves to formal computing.

Attempts to change natural computing to formal computing by evolving from a subjective verification system to an objective verification system is a general method of natural science.

In many cases, a big discovery comes from an irrational intuition such as intuition and experience by one scientist. Objective verification is difficult when the novelty of the discovery is high. Therefore, we repeatedly make "a phenomenon that might be a big discovery" and make efforts to enable objective verification.

There, attempts have been made to move from a natural calculation system to a formal calculation system, and as a result, a perfectly rational form calculation system is constructed (in many cases in the case of mathematics or physics) or a consultative formal computing is constructed (Wine computing).

6. Future Natural Computing and Artificial Intelligence

Computer science started by fusion of formal calculation and natural calculation. Computer science and mathematics involve natural calculations (human recognition), so it is difficult to construct a completely rational formal calculation system.

For example, research on artificial intelligence has many difficulties. Many difficulties arise to develop intelligence which is natural computing to formal computing (such as frame problem[9] and semantic processing in natural language processing[10])

In recent years, by changing the direction of artificial intelligence research to controversial formal computing (statistics / use of corpus in natural language processing, etc.), a new development has begun to appear.

In the future, artificial intelligence will develop as controversial formal computing that incorporates the interaction with the environment, not rational formal computing by "pure intelligence[11]".

Acknowledgement

This research has been supported by Grant in Aid for Scientific Research (KAKENHI) No:15K00268 and 16H03093

References

1. Nakagaki, T., Yamada, H. & Tóth, Á. Maze-solving by an amoeboid organism. *Nature* (2000). doi:10.1038/35035159
2. Adleman, L. Computing with DNA. *J. Comput. Biol.* (1995). doi:10.1089/cmb.1995.2.1
3. Rothemund, P. W. K. Design of DNA origami. in *IEEE/ACM International Conference on Computer-Aided Design, Digest of Technical Papers, ICCAD* (2005). doi:10.1109/ICCAD.2005.1560114
4. Bennett, C. H. Dissipation-error tradeoff in proofreading. *BioSystems* (1979). doi:10.1016/0303-2647(79)90003-0
5. Suzuki, Y. in *SpringerBriefs in Applied Sciences and Technology* (2019). doi:10.1007/978-4-431-56844-5_1
6. Gaff, J. *Alberto Giacometti*. *Artists in their time* (2002).
7. Darwin, C. *On the Origin of Species by Means of Natural Selection*. *D. Appleton and Company* (1859). doi:10.1126/science.146.3640.51-b
8. Piškur, J., Rozpedowska, E., Polakova, S., Merico, A. & Compagno, C. How did Saccharomyces evolve to become a good brewer? *Trends in Genetics* (2006). doi:10.1016/j.tig.2006.02.002
9. McCarthy, J. & Hayes, P. J. in *Readings in Artificial Intelligence* (1981). doi:10.1016/B978-0-934613-03-3.50033-7
10. Ng, H. T. & Zelle, J. Corpus-Based Approaches to Semantic Interpretation in NLP. *AI Mag.* (1997). doi:10.1609/aimag.v18i4.1321
11. Searle, J. R. Chinese Room Argument. *MIT Encycl. Cogn. Sci.* (1999). doi:10.4249/scholarpedia.3100

A Study on Tourism Support Application Using the Virtual Technology

Masamichi Hori[1]
[1] *Graduate of Engineering, University of Miyazaki,*
1-1 Gakuenkibanadai-nishi Miyazaki-shi, Miyazaki, 889-2192, Japan

Makoto Sakamoto[2*], **Takahiro Ishizu**[1], **Satoshi Ikeda**[2], **Amane Takei**[2], **Takao Ito**[3], **Yu-an Zhang**[4]
[2] *Faculty of Engineering, University of Miyazaki,*
1-1 Gakuenkibanadai-nishi Miyazaki-shi, Miyazaki, 889-2192, Japan

[3] *Graduate School of Engineering, Hiroshima University,*
1-3-2 kagamiyama Higashihiroshima-shi, Hiroshima, 739-8511, Japan

[4] *Department of Computer Technology and Application, Qinghai University,*
251 Ning Da Lu, Xining, Qinghai, 810000, China

**Corresponding Author*
E-mail:sakamoto@cs.miyazaki-u.ac.jp
http://www.miyazaki-u.ac.jp/

Abstract

Currently, the tourism industry in Miyazaki prefecture has various problems, and various measures are taken. On the other hand, in 2016, virtual technology attracted much attentions such as VR and AR technology. We thought that through the VR and AR technology experience, we could aim for an increase in tourists. Therefore, we will create new applications for smartphones using virtual technology and aim for tourism support. We propose unique features aimed at increasing tourists and creating repeaters. It is a function that allows to reproduce the scenery anywhere with VR, and to feel the sightseeing experience by AR close.

Keywords: Augmented reality, Virtual reality, Smartphone application, Traditional culture, Sightseeing.

1. Introduction

Due to the popularization of mobile terminals and the emergence of interactive technology, the tourism industry is changing drastically. In order to be a tourist destination that is attractive and win the competition, it is essential to improve unique experiences and value-added services. Miyazaki Prefecture · Takachiho Town is one of the most famous sightseeing places in Japan, but it has various problems and countermeasures have been taken [1]. Especially, it is urgent to introduce new technology. In 2016 and 2017, the virtual technology called AR, VR, MR showed great excitement and it was the year when it became commonly recognized. AR associates with real-world content and extends them. VR can gain unrealistic experiences in a new world on computers. These are found in a wide range of fields such as advertisement, tourism, education and entertainment [2] [3]. In this study, we will link virtual technology and tourism industry and aim to solve problems related to sightseeing of Takachiho. Specifically, we provide functions that make it easy to experience images that reproduce beautiful landscapes by VR technology, and that enable "take-away" of tourism experiences through AR technology.

1.1. *Background*

The tourist site that is the target of this study is Takachiho Town, Miyazaki Prefecture. Takachiho Town is located at the northernmost tip of Miyazaki Prefecture the center of Kyushu. It has a beautiful natural treasure Takachiho Gorge, a great change due to the four seasons, and it is blessed with wonderful nature. Takachiho Gorge and Akimoto shrine are shown in Figure 1. The history of the town is old and there are reports that there were villages since about 4000 BC [4]. It is a place where God descended in Japanese mythology and is regarded as a land with considerably deep connection with the birth of Japan. There are Kagura, born from the Amanoiwato legend of Japanese mythology, and land that is related to myths. In recent years as a power spot attracts attention from a wide range of age groups.
Especially the Akimoto area called Okutakachiho focuses on people living in the village. And they are doing have tourists experience village-specific experiences activities. Tourists can eat cuisine using regional ingredients, and can visit shrines and sacred trees standing in majestic nature. In 2016, it was selected as a good example of the "treasure of Discover rural mountain fishing village" designated by the Ministry of Agriculture, Forestry and Fisheries, and it is thought that tourists will further increase in the future [5].
However, as a change in the environment surrounding tourism, Miyazaki prefecture states that the population declines, the declining birthrate and aging, intensified competition, and the development of information and communication technology are left behind.
The number of sightseeing tourists is at a lower level [6] than at peak hours. Creating attractive sightseeing sites that want to visit many times, and sending out information using media, ICT, and SNS are issues.

Fig.1 Takachiho Gorge(left), Akimoto shrine(right).

1.2. *Literature review*

Major use of AR in tourist spots is to combine with mobile terminals as a guide tool. It is AR use as a bridge connecting tourist spots with visitors. "ToARist: An Augmented Reality Tourism App created through User-Centred Design" [7] is an AR application design with an emphasis on discussion with users. This study was revealed what visitors really wanted in the AR display, and how the AR navigation should be displayed. "Augmented Reality and Gamification in Heritage museums" [8] conducted a definition and analysis of AR communication model and noise at the museum, and approached better experience. Furthermore, adding the game elements revealed that the depth of the AR system will increase.
As a study of the meta-viewpoint of introducing AR, there is "How can Tourist Attractions profit from Augmented Reality?" [9]. This study revealed the AR profit model through collaboration with stakeholders in the field and showed the possibility to introduce AR with minimal risk.
The impact on sightseeing in the AR application "Pokèmon GO" which became one of the keywords in 2016 is great. According to the official report, the collaboration event with Miyagi Prefecture in November 2016 mobilized about 100,000 people in 11 days, tourism consumption amount of 2 billion yen [10], the collaboration event with Tottori Prefecture in November 2017 mobilized about 89,000 people in 3 days, tourism consumption amount of 1.3 billion yen and PR effect 500 million yen [11]. Players visit sightseeing spots triggered by content capabilities, leading to attraction discovery and economic activities. It is a characteristic result of AR based on reality.
"Virtual Reality and Implications for Destination Marketing" [12] is investigating how promotional contents of VR technology will affect the image of tourist spots. It is said that it will have a good influence on most items including the effectiveness of advertisement, also highly likely to share experiences of destinations and advertisements themselves.
"Virtual reality, presence, and attitude change: Empirical evidence from tourism" [13] is a survey on VR tourist content targeting 1,000 people, regarding the presence of the VR experience, it showed that the attitude towards the destination of the consumer is positive and VR is effective.

2. Method

We will explain the method used to create the application.

2.1. *3DCG modeling*

About 3DCG model production cooperate with vocational schools in Miyazaki prefecture. The 3DCG model to be produced is shown in Figure 2. It is a reproduction model of God appearing in Kagura, the character of Takachiho's special product, and hawk inhabiting Takachiho.

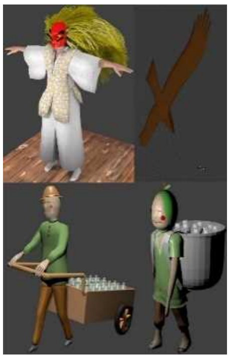

Fig.2 Bird's eye view of Tadikarao (upper left), hawk (upper right), "chihomaro" character (bottom).

2.2. *System*

We chose Unity 3d as a software that can produce applications for mobile from the viewpoint of future development and application creation that is not bound by OS. We used Blender for model creation. The device used is an Android smartphone.

2.2.1. *VR*

We use smartphone and VR glasses certified by google card board to realize VR function. We installed a simple VR function by attaching it to a smartphone. Figure 3 shows the VR glasses. With this function, can see the state of Takachiho reproduced with 3DCG. Figure 4 shows the state of the VR space.

Fig.3 VR glasses.

Fig.4 VR takachiho.

2.2.2. *AR*

The markerless type is inputting a natural image (an image having a use other than a marker). We'd like to run it as an application alone, and implement it on a mobile terminal, especially on a smartphone. When recognizing the pamphlet of Kagura, God dances and when recognizing the "Chihomaro" package , the character is displayed. As "takeaway" of the unique function, when recognize the hand, dance Kagura on the palm of the hand. Figures 5 show the state of AR.

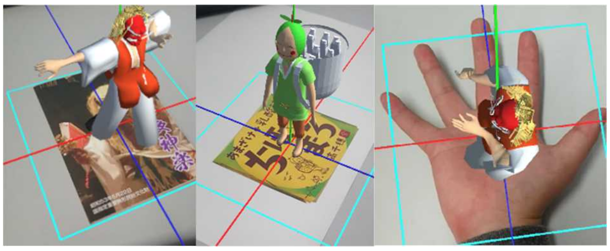

Fig.5 Pamphlet recognize (left), package recognize (center), "take away" hand dance (right).

2.3. *Experimet*

Application experience and questionnaire survey are conducted for five 20's. The task is done for 3 minutes and we respond to questionnaires about 6 items (scale of 1 to 5) and 1 free opinion. Items are about virtual technology and sightseeing, about contents, and so on.

3. Result and Discussion

In the item "Would you like to visit your destination after experiencing virtual technology?", the score is 4.2 points. By experiencing virtual technology, we think that stimulating tourism motivation and being able to feel tourism more closely. "Would you like to share virtual technology contents?" is positive result. Virtual technology is generally known, furthermore we also think that using a simple VR glasses or a markerless type AR can easily produce a share effect. There is an opinion that prioritize enjoy the sightseeing experience in destination over virtual technology. However, we think can provide a special tourism experience by applying the guidance and shooting with the virtual character by AR. "Is it easy to prepare for experiencing virtual technology?", "Is the operation of VR · AR good?", "Contents fulfillment level" were negative point. It is because there were work to put a burden on the user such as attaching VR glasses to devices and obtaining natural images to be recognized by the AR. Also, about the operation of the virtual technology, it was not possible to smoothly read the hand at the AR, which led to a negative opinion. It is necessary to revise the complete markerless AR on the smartphone.

4. Conclusion

In this study, we created tourism support application using two virtual technologies, VR technology and AR technology. VR function can simulate the tour of Takachiho. In AR technology, we implemented a markerless type AR that displays 3DCG models by reading pamphlets and packages. Also, as a unique function, the 3DCG model can dance on the palm by complete markerless AR. This function is called "takeaway" and is aiming for the share effect.
Based on the evaluation results, we found that by introducing virtual technology to tourism support, we will affirm the attitude towards the destination. Easy to share with simple making, can aim to create new tourists and repeat customers. There is a positive opinion in the AR function at the tourist resort, there is a possibility that it can provide a unique experience. As the contents enhancement, improvement of interactivity when experiencing VR, and the AR function that takes a commemorative shooting with the 3DCG model. By applying stamp rally type gamification, can aim not only use applications before sightseeing and after sightseeing but also use applications during sightseeing.

Acknowledgements

Miyazaki multimedia vocational school people are very busy, thank you hearty thank you for your cooperation in 3DCG modeling and advice etc. Also, the Miyazaki Tourism Convention Association, Inc., abc Corporation, Inc., Phoenix Seagaia Resort Co., Ltd., people in the Akimoto district who took care of me in the interview, other prefectures within the prefecture We would like to express my gratitude to all concerned parties in each municipality.

References

1. Heisei27 July Miyazaki Prefecture Tourism Promotion Plan ~ Toward revival of tourism miyazaki ~. [Online] Official website of Miyazaki Prefecture https://www.pref.miyazaki.lg.jp/kanko-suishin/kense/shingikai/documents/37281_20180613084219-1.pdf (accessed 2018/11 / 1).
2. Takashi Kurida, Kiyoshi Kiyokawa, Takashi Okuma, "*Fundamentals, Development and Practice of AR Technology*", Science Information Publishing, 2015, pp 377-385.
3. Zenji Nishikawa, Katsuomi Kobayashi, Yaseinootoko, izm, Kazuya Hiruma, "*VR contents development guide*", MDN Corporation, 2017, pp18-33.
4. Overview of Takachiho | Introduction / History of the town | administrative information | Takachiho cho [Online] Takachiho cho information official website. http://www.town-takachiho.jp/administration/history/outline.html (accessed 2018/11/1).
5. Takachiho Mura Council "Treasure of Discover Rural Farm Village (Mura)" was selected. | What's New | Takachiho-cho Tourist Association [Online] Takachiho cho information official website. http://takachiho-kanko.info/news/detail.php?log=1479688433 (accessed 2018/11/1).
6. Miyazaki Prefecture tourist statistics survey result in Heisei27. [Online] Official website of Miyazaki Prefecture https://www.pref.miyazaki.lg.jp/kanko-suishin/kanko/miryoku/documents/26823_20161226163703-1.pdf (accessed 2018/11/1).
7. Williams, M, Yao, KKK and Nurse, JRC et al., "ToARist: An augmented reality tourism app created through user-centred design", *31st British Human Computer Interaction Conference*, 2017.
8. Ramy Hammady, Minhua Ma, Nicholas Temple, "Augmented Reality and Gamification in Heritage Museums.", *Serious Games*, Vol. 9894, pp 181-187, Springer, Cham, 2017.
9. Eleanor E Cranmer, M. Claudia tom Dieck, Timothy Jung, "How can Tourist Attractions profit from Augmented Reality?", *Augmented Reality and Virtual Reality - Empowering Human, Place and Business*, pp 21-32, Springer, Forthcoming, 2017.
10. About the number of tourists etc. of Pokèmon GO related events - Official website of Miyagi Prefecture. [Online] Miyagi Prefecture official website. https://www.pref.miyagi.jp/release/ho20161219-6.html (accessed 2017/12/1).
11. Number of participants in "Pokémon GO Safari Zone in Tottori Sand Dunes" and Economic Effect. [Online] Tottori prefecture official website. http://www.pref.tottori.lg.jp/271365.htm (accessed 2018/11/1).
12. Griffin Tom, Giberson Juleigh, Lee Seung Hwan (Mark), Guttentag Daniel, Kandaurova Maria, Sergueeva Ksenia, Dimanche Frédéric, "Virtual Reality and Implications for Destination Marketing", *Travel and Tourism Research Association: Advancing Tourism Research Globally*, 29, 2017.
13. Iis P. Tussyadiah, Dan Wang, Timothy H. Jung, M.Claudia tom Dieck, "Virtual reality, presence, and attitude change: Empirical evidence from tourism" (2018). *Tourism Management* Vol 66, Pages 140-154, 2018.

Proposal for Interaction Techniques for Intuitive Virtual Objects Manipulation in Augmented Reality

Takahiro Ishizu, Makoto Sakamoto*, Takaaki Toyota, Masamichi Hori, Satoshi Ikeda and Amane Takei
Faculty of Engineering, University of Miyazaki,
Miyazaki-City, Miyazaki, Japan

Takao Ito
Graduate School of Engineering, Hiroshima University,
Hiroshima-City, Hiroshima, Japan

Yu-an Zhang
Department of Computer Technology and Applications, Qinghai University,
China
E-mail: hm14002@student.miyazaki-u.ac.jp, fruits2000jp@yahoo.co.jp

**Corresponding Author*
E-mail:sakamoto@cs.miyazaki-u.ac.jp
http://www.miyazaki-u.ac.jp/

Abstract

Recently, studies for realizing interaction between users and virtual objects using Augmented Reality (AR) have been actively conducted. However, few previous studies have realized that a user intuitively manipulates virtual objects like clay with their bare hands. In this study, we aim at user's intuitive virtual objects manipulation by realizing basic manipulation on virtual objects with their bare hands. In addition, it is considered that the user feels uncomfortable in the manipulation of the virtual objects because of the occlusion problem in AR, and cannot perform an intuitive manipulation. Therefore, in this study, we solve this problem by performing appropriate hidden surface processing within the range of the user's fingertips.

Keywords: augmented reality, intuitive manipulation, virtual objects, gesture interaction, occlusion problem.

1. Introduction

Augmented reality (AR) is a technique of superimposing information generated by a computer on perceptual information that we receive from real space.

In recent years, technique for realizing interaction between a user and virtual objects in AR has attracted attention.

In interaction technology in AR, it is necessary for the user to be able to intuitively manipulate the virtual objects.

Since the main means of the interaction with the objects in real life is hand, it should also be possible for hand to manipulate virtual objects in the virtual space for intuitive manipulation [1].

Kato et al. [2] introduced soft body virtual objects by using a physics engine, reflected the action of crushing on the virtual object with the user's bare hand in the virtual space, and realized the deformation manipulation of virtual objects by interaction with the user.

Suzuki et al. [3] realized a move manipulation of rigid body virtual objects by interaction with the user.

However, it was not realized that after deforming the virtual object, moving or join the virtual object while maintaining that shape.

In this study, we realize to intuitively perform user's manipulation such as deformation of virtual object, maintenance of shape after deformation, joining, and so on, aiming for more advanced interaction between a user and virtual objects.

We believe that this study is useful, for example, by applying this study to modeling work of 3DCG, so that it can be more intuitively.

2. Proposal

In this paper, we propose a method to create new virtual objects and a method to distinguish whether the user wants to grasp or wants to move the virtual object. In this way, we realize that the user creates a virtual object, deforms it, moves it while maintaining the deformed state, and joins the two virtual objects.

Moreover, we perform a hidden surface processing to allow the user to recognize the context of the user's hand and the virtual objects.

2.1. *System Component*

We make it possible to realize the interaction of the user and the virtual objects by adopting the Leap Motion Controller specialized for acquisition of three-dimensional coordinates of fingers and introducing soft body virtual objects.

This system consists of a Web camera for real image acquisition and marker recognition, the Leap Motion Controller for obtaining three-dimensional coordinates of fingers, and PC for performing arithmetic processing and video output. In this system, we use network programming to prevent interference between the Leap Motion Controller and the Web camera [4]. In this system, we perform acquisition processing of three-dimensional coordinates of fingers with the Leap Motion Controller on the server side. And we perform acquisition processing of image with the Web camera, physical calculation, and video output on the client side.

As shown in the Fig.1, we place the paper on which the AR marker is printed and the Leap Motion Controller, and observe the paper with the Web camera. The virtual objects are displayed by recognizing the AR marker.

In this system, we use virtual objects that can be physically computed using the physics engine (Bullet Physics) [5].

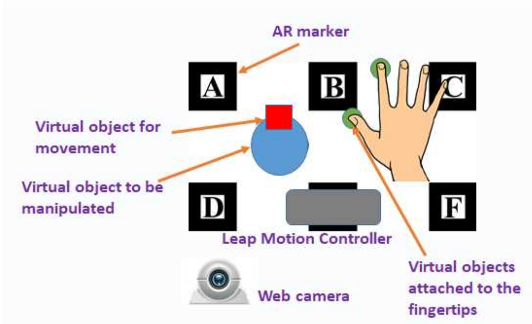

Fig.1. System Component

3. Hidden Surface Processing

In AR, a virtual object superimposed on the image of the real space later. For this reason, even when the virtual object is located deeper than the real object, the virtual object is not hidden by the real object, and it is displayed as if the object is always in front . This is called an occlusion problem in AR, and when the user manipulates the virtual object, the user cannot recognize the anteroposterior relationship between the virtual object and the user's hand correctly [6]. For this reason, we think that the user feels uncomfortable visually and cannot perform an intuitive manipulation. Therefore, in this paper, we solve this problem by hidden surface processing of hands and the virtual object in the virtual space, using three-dimensional coordinates of fingers obtained with the Leap Motion Controller and recognizing hand region from skin color region in RGB image obtained with Web camera

4. Manipulation of Virtual Object

In this section, we will explain the manipulation of virtual objects by bare hand to realize more intuitive interaction between a user and virtual objects.

4.1. *Generation of Virtual Object*

The user can newly generate a “virtual object to be manipulated”, which size is desired by user by gesture of index fingers of both hands (Fig.2).

The procedure will be described below.

(i) This system acquires the three-dimensional coordinates by putting the user's index finger of the right hand on the Leap Motion Controller.
(ii) This system acquires the three-dimensional coordinates by putting the user's left index finger on the Leap Motion Controller while keeping the state of Step 1.
(iii) The user away the own left index finger with the Leap Motion Controller.
(iv) This system determines the size of the “virtual object to be manipulated” based on the value when the index finger of both hands comes closest and generate the object.

4.2. *Deformation and Moment of The Virtual Object*

It is difficult to distinguish whether the user wants to grasp or wants to move the virtual object. Therefore, this system performs deformation of the virtual object when the user's palm is downwards, and movement of the virtual object when the user's palm is upward. This system decides that the palm is upward when the user's little finger, ring finger, middle finger, index finger, thumb line up from the left of the Leap Motion Controller.

In this system, deformation and movement manipulations on virtual object are performed with only the right hand.

The user turns the palm downwards and crush the “virtual object to be manipulated” with the thumb and index finger, whereby the user's “virtual objects attached to the fingertips” and “virtual object to be manipulated” collide with each other, and the “virtual object to be manipulated” can be deformed (Fig.3).

The user can move “virtual object to for movement” which hold the representative coordinate of “virtual object to be manipulated” by turning the user's palm upwards and moving his/her hand near the virtual object (Fig.4). Since “virtual object for movement” is attached to “virtual object to be manipulated” in advance, “virtual object to be manipulated” can be moved by moving “virtual object for movement”.

In the case where two virtual objects are generated, this system obtains the Euclidean distance between the center of the hand and each “virtual object for movement” of each of the two virtual objects and selects a closer “virtual object for movement” as the moving target.

4.3. *Joining of The Virtual Objects*

The user prepares two virtual objects in advance. The user brings one “virtual object to be manipulated” closer to the other “virtual object to be manipulated”.

Since collision determination between “virtual object to be manipulated” is not performed in this system, when two “virtual object to be manipulated” continue closer to each other, they eventually overlap each other. And when reaching a fixed distance, the two virtual objects join together (Fig.5).

Fig.2. Create Object

Fig.3. Deform Object

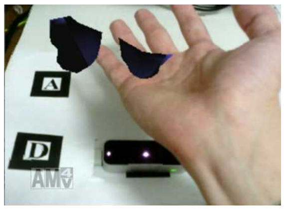

Fig.4. Move Object

Fig.5. Join Objects

5. Evaluation

We investigated the interaction with the virtual object using this system by questionnaire to evaluate whether it is intuitive or not and to extract this system's improvement point. We asked six university students of subjects to perform basic manipulations on virtual objects shown in Fig.2 to Fig.5.

5.1. *Experiment Method*

After having the subject trial this system, we conducted a question form questionnaire on each item of “good point”, “difficult point” in manipulation, and “improvement point” in this system, and we evaluated this system.

5.2. *Experiment Result*

The questionnaire result was as follows.

As for "good point", there was some opinions such as "manipulation method is intuitive and easy to understand", and "movements of the hands was reflected in the system".

As for "difficult point", there are some opinions such as "it is difficult to join two virtual objects", "it is difficult to grasp the sense of distance with the virtual object", and "when the hand is manipulated at a low position from the desk, the virtual object does not react in user's gesture".

As for "improvement point", there are some opinions such as "I want feedback when crushing virtual objects", "I want functions that can be transformed into arbitrary figures such as cones and rectangular parallelepipeds by gesture" and "I want a manipulation function to cut off virtual objects".

6. Consideration

First, we consider "good point". From the "good point", we found that the interaction manipulation with the virtual object incorporating the gesture is intuitive. Therefore, we believe that it is possible to superimpose the physical phenomenon such as deformation object by hand in the real space on the virtual objects.

Next, we consider "difficult point". We think that the reason why the cause of the opinion that "it is difficult to grasp the sense of distance with the virtual object" is that when the user manipulates the virtual object, an error occurs due to a delay in the position information of the finger acquired with the Leap Motion Controller, and the user feels a sense of incompatibility.

We think that the reason why the cause of the opinion that "it is difficult to join two virtual objects" is that in this system, the coupling of virtual objects are joined when the two virtual objects approach within a certain distance, similarly to the reason that "it is difficult to grasp the sense of distance with the virtual object", an error occurs between the position of the finger on the real space and the position of the finger on the virtual space.

We think that the reason why the cause of the opinion that "when the hand is manipulated at a low position from the desk, the virtual object does not react in user's gesture" is that when the hand is in a low position, the hand covers the Leap Motion Controller, and the coordinates of the fingertips cannot be acquired we considered.

7. Conclusion

In this study, we realized a more intuitive manipulation between a user and virtual objects by creating new virtual objects and distinguishing whether the user wants to grasp or wants to move the virtual object.

In the evaluation experiment, we asked six subjects to perform the basic manipulation on the virtual objects and conducted a questionnaire survey. As a result of the experiment, it was shown that by using this system, it is possible to intuitively perform the interaction manipulation with the virtual objects.

In our future work, we will address the issues of "difficult point" and add functions pointed out in "improvement point" so that it can more intuitively interact with virtual objects. Furthermore, we think that it is necessary to increase the precision of interaction, such as enabling finer deformation of virtual objects.

References

1. V. Buchmann, S. Violich, M. Billinghurst and A. Cockburn. "FingARtips-Gesture Based Direct Manipulationin in Augmented Reality". *Proc. International Conf. on Computer Graphics and Interractive Techniques*, pp.212-221, 2004.
2. S. Kato, S. Ishigaki, S. Suzuki and M. Sato. "A Study on Presentation of Softness of Virtual Object in Gripping Motion with Bare". *Journal of The Institute of Image Information and Television Engineers*, 2017, VoL 71, No. 3, pp.J121-J124.
3. H. Suzuki , S. Suzuki and M. Sato . "Visual Improvement of AR System Focusing on Grasping Motion with Bare Hands". *Journal of The Institute of Image Information and Television Engineers*, 2014, VoL 68, No. 7, pp. J299-J301.
4. U. Imamura, et al. "*The proposal and development of the novel technology with Augmented Reality*". Future University Hakodate 2011 System Science Practice Group Report, 2012.
5. F. Fujisawa. "Information media experiment, Application development using physics engine". [Online] http://slis.tsukuba.ac.jp/~fujisawa.makoto.fu/lecture/iml/ (accessed 2018-03-17).
6. K. Reiji and S. Makoto. "Development of A System enabling Display of Gripping the AR Object Using Leap Motion Controller". *The 29th Annual Conference of the Japanese Society for Artificial Intelligence*, 2015.

Two-Dimensional Image Based Body Size Measurement and Body Weight Estimation for Yaks

Zijie Sun
Department of Computer Technology and Applications
Qinghai University, 810016, Xining China
Chen Zhang
Department of Computer Technology and Applications
Qinghai University, 810016, Xining China
Xiaofeng Qin
Department of Computer Technology and Applications
Qinghai University, 810016, Xining China
Yu-an Zhang*
Department of Computer Technology and Applications
Qinghai University, 810016, Xining China
Rende Song
Yushu Prefecture Animal Husbandry and Veterinary Station
Yushu Qinghai, 815000, China
Makoto Sakamoto
Faculty of Engineering
University of Miyazaki, Miyazaki City 889-2192 Japan

Abstract

non-contact acquisition of the body size and weight of the animals is one of the hot research topics in the animal husbandry sector. In this paper, the yaks were photographed in the Sanjiangyuan Region, and their body weight was estimated by foreground extraction, identification of measuring points, linear regression and other methods.

Keywords: Sanjiangyuan; yak; image; foreground extraction; body size; body weight.

1. Introduction

Yak is a kind of unique cattle which lives at an altitude of above 3000m, mainly on the Qinghai-Tibet Plateau and adjoining mountains and in the subalpine regions. Yak can adapt to extreme ecological conditions such as high & cold environment and oxygen-deficient environment[1], and is essential to animal husbandry economy on the Qinghai-Tibet Plateau. China is the biggest yak breeding country in the world, and accounts for 92% [2]. Specifically, Qinghai Province raises 4.9 million yaks, and accounts for 38% in China [3].

With the improvement of information perception technology and precision breeding level, the livestock body size and body weight are more acquired by non-contact and high-precision methods [4]. As the yaks occupy a special position on the Qinghai-Tibet Plateau, yak research is particularly important. During yak research, it is particularly important to measure yak body size and body weight. In this paper, the color images of the yaks were preliminarily processed, and then the yak images were identified through gray scale classification. By identifying the processed images, 4 points for measuring the body height and body steep length were marked based on curvature calculation results. Finally, the actual body size of the yaks was obtained based on the camera imaging principle. The body weight formula for the yaks was given after linear regression using weka, and the actual body weight of the yaks was finally estimated.

2. Foreground Extraction

The experiments showed that the gray scale of the dark yaks was the lowest in the gray-scale images, so the pixel points of which the gray scale was greater than 150 basically were not those of the dark yaks. Based on

* Corresponding author: Yu-an Zhang,e-mail:2011990029@qhu.edu.cn

the yak images (Figure 1), Figure 2 gave the gray scales of the images with different colors, with 50 gray scales as a unit, in which the gray scale of the red part, yellow part, blue part, white part and black part was [0,50], [51,100], [101,150], [151,200] and [201,255] respectively.

It can be seen that the red part basically showed the body type of the yaks. Based on this, the dark yak images may be extracted from the color images.

2.1. *Background Removal*

During image background removal, we firstly passivized the images based on the Gaussian blur algorism for which the formula was shown below:

$$f(x, y) = \frac{1}{2\pi\sigma^2} e^{-\frac{x^2+y^2}{2\sigma^2}} \quad (1)$$

3*3 Gaussian convolution kernels were generated based on Formula 1 (standard deviation σ=1). Afterwards, the pictures were convolved by 3*3 Gaussian convolution kernels after compression and graying for image blunting and subsequent processing [5]. One threshold value for background removal was determined, and the pixels around the images were traversed. It was determined whether the pixels were background pixels based on the tolerance [6]. The background was removed if the answer was affirmative, otherwise retained.

Fig. 1. Yak Image.

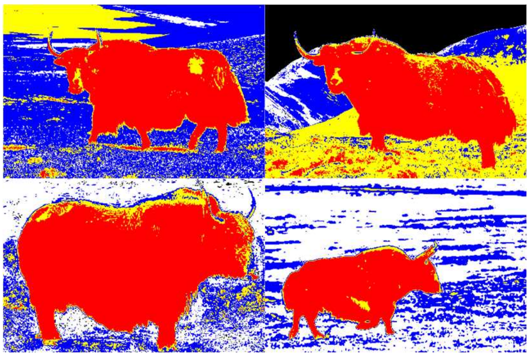

Fig. 2. Gray Scale Classification of Yak Image.

2.2. *Classification*

After image background removal, the gray scales of the images were classified, and the yak center points in the images were calculated. The images were continuously iterated by the flood fill method, until the images became smooth [7].

Figure 3 showed the classified images and center points. The gray scale of the red part, yellow part, blue part and white part was [0, 50], [51,100], [101,150] and [151,200] respectively; the black part showed removed background; the pink part showed the yak center points pre-determined by the system in the images. Upon determination, the overall shape of the yaks was determined through extension from the center points.

After yak image foreground was extracted through classification, the extracted yak images perhaps were unsmooth. Therefore, the images can be dilated and then eroded.

Fig. 3. Classified Image and Center Point.

Final yak foreground images were shown in Figure 4.

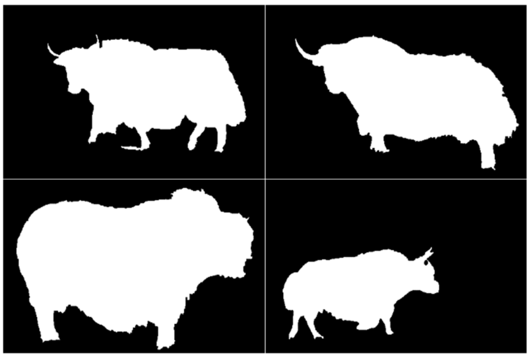

Fig. 4. Final Yak Foreground Image.

3. Identification of Measuring Point

According to traditional yak body size measurement standards, the body steep length referred to the distance from the point of shoulder to the point of the buttocks, as shown in TX-C Segment of Figure 5. The body steep length was measured by a measuring stick. If the body weight was estimated according to the body size, the body steep length may be measured by a tape. The body height referred to the vertical distance from the point of sideburns to the ground, as shown in T-G Segment of Figure 5. The body height may be measured by a measuring stick [8]. Once the point of buttocks, point of shoulder and point of sideburns were accurately found out, the body steep length and body height of the yaks can be accurately acquired [9-10].

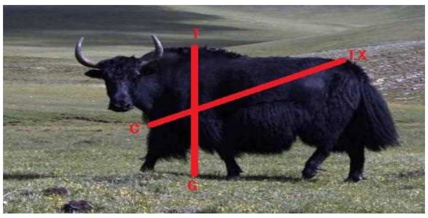

Fig. 5. Body Height and Body Steep Length of Yak.

After the binary foreground images of the yaks were obtained, the edges of the binary yak images were firstly extracted, and the yak center points were calculated. After the standing direction of the yaks was known through communication with the users, the images can be divided into 4 parts, and points TX, C, T and G (Figure 5) were determined respectively. The body height and body steep length of the yaks were finally obtained.

When marking the points in the images, we firstly extracted the edges of the images (Figure 4), and then calculated the yak center points.

3.1. *Identification of Point of Sideburns (Point T)*

After the center points and image edges of the yaks were determined, it can be determined that the point of sideburns was at the upper left or upper right of the center point according to the head direction of the yaks. Extensive experiments showed that the point of sideburns of the yak was at the maximum point of curvature of the contour curve for the yaks which formed an angle of 30°-60° to the yak center point in the yak curve contour map.

During curvature calculation, one triangle can be formed by one contour point of the area where the points of yak sideburns were located and two adjacent points, as shown in Figure 6. Three sides and perimeter P of the triangle were calculated. The area S of the triangle was obtained according to the Heron's formula, and the curvature K was calculated [11]. In Figure 6, the calculation formula for P can be given according to the geometrical relationships.

$$P = a + b + c \tag{2}$$

In the formula (2), P referred to perimeter, and a, b, c referred to three sides of the triangle. S may be expressed as follows:

$$S = \sqrt{\mathrm{P}(P-a)(P-b)(P-c)} = \frac{abc}{4R} \tag{3}$$

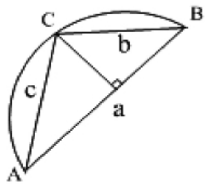

Fig. 6. Determination of Point of Sideburns of Yak.

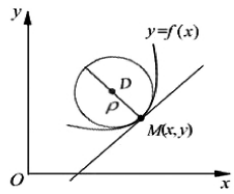

Fig. 7. Determination of Curvature.

In which, R referred to radius of circle.

In Figure 7, the calculation formula for curvature K was shown below:

$$K = \frac{1}{\rho} = \frac{1}{R} \tag{4}$$

Thus:

$$K = \frac{4\sqrt{P(P-a)(P-b)(P-c)}}{abc} \quad (5)$$

Through the above steps, the curvature K of 3 non-collinear points can be obtained.

3.2. *Identification of Lowest Point (Point G)*

Upon determination of the center point, it can be determined that Point G of the yaks was at the lower left or lower right of the center point according to the standing direction and center points of the yaks. Afterwards, the lowest point can be determined only by traversing the images.

3.3. *Identification of Point of Buttocks (Point TX)*

Upon determination of the center points, it can be determined that the point of the buttocks was at the lower left or lower right of the center point according to the standing direction and center points of the yaks. Extensive experiments showed that the point of the buttocks of the yaks was at the minimum point of curvature of the contour curve for the yaks which formed an angle of 10° - 40° to the yak center point in the yak curve contour map[12].

3.4. *Identification of Point of Shoulder (Point C))*

Upon determination of the center points, it can be determined that the point of shoulder was at the lower left or lower right of the center point according to the standing direction and center points of the yaks. Extensive experiments showed that the point of shoulder of the yaks was at the boundary point with an angle of 50° - 80° to the yak center point and with the shortest distance to the center point.

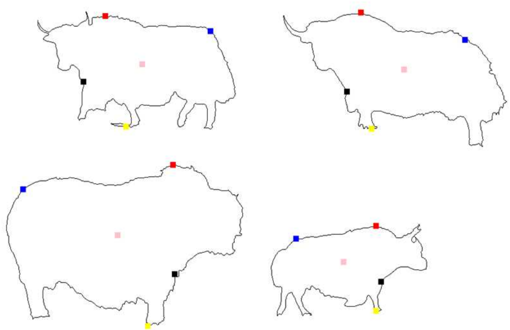

Fig. 8. Final Yak Foreground Image.

Final measuring points of the yak images were shown in Figure 8, in which the point of sideburns (Point T), lowest point (Point G), point of the buttocks (Point TX), point of shoulder (Point C) and center point were shown in red, yellow, blue, black and pink respectively.

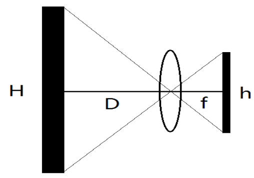

Fig. 9. Camera Shooting Structure.

4. Estimation of Body size and Weight of Yaks

The camera shooting structure was shown in Figure 9. In Figure 9, H referred to actual object height; h referred to the object height on the image sensor; D referred to the distance from the camera lens to the object; and f referred to lens focal length. Therefore, we can obtain the actual height based on this principle.

4.1. *Calculation of Body Steep Length and Body Weight of Yaks*

An image consists of pixels. Pixel is the smallest unit of the image represented by a sequence of numbers. The pixels can be deemed as indivisible units or elements in the entire images [13]. Therefore, we can obtain the actual length H of the measured object according to Formula 6.

$$H = \frac{LvD}{f} \quad (6)$$

We shall obtain the sensor size and resolution of this type of camera to calculate the actual length v represented by each pixel. The area size of each pixel can be calculated by dividing the sensor area of this type of camera by its resolution. The actual length represented by each pixel can be obtained through square root calculation. Further, the actual body height and body steep length of the yaks were obtained according to Formula 6.

4.2. *Calculation of Body Weight of Yaks*

The actual body weight of the yaks can be estimated according to the actual body height and body steep length of the yaks.

The body height, body steep length and body weight of 597 yaks (0.5-5.5 years) were manually measured in the Yushu Region, and linear regression was performed using weka , so as to obtain the formula for estimation of the body height and body steep length of the yaks:

$$W=2.6123*H+1.3334*S-242.4778 \quad (7)$$

In Formula 7, W referred to body weight; H referred to body height; S referred to body steep length.

5. Advantages & Disadvantages

According to this algorithm, two-dimensional images of the yaks were firstly identified based on classification processing ideas, and the yak images were extracted from the pictures by the flood fill method. Then, the center points and standing direction of the yaks were determined, and the measuring points of the yak images were finally obtained through curvature analysis. The body height and body steep length of the yaks were obtained based on the camera imaging principle. After the formula for estimation of the body height and body steep length of the yaks was obtained by performing linear regression using weka, the body weight of the yaks was finally estimated. Through detection, this algorithm had good effects for estimation of the body weight of the yaks. But under the impacts of various external factors, following disadvantages possibly existed during actual detection:

1) During image identification, it needed to manually determine whether the yak head faced left or right.
2) If the images were not accurately identified, identification accuracy of the measuring points would be affected.
3) If the measuring distance was inaccurate, the accuracy of body weight estimation would be affected.
4) This algorithm was affected by standing postures of the yaks. If the yak body was inclined in the yak images, the final measurement accuracy would be affected.

6. Conclusion

According to this algorithm, the gray scales were firstly classified, and then the positions of the yaks in the images were preliminarily determined by background removal, Gaussian blur, average processing and flood fill and other methods. The yak images were extracted from the pictures through extension from the yak center point. Afterwards, the yak measuring points were determined according to the center point and head direction of the yaks as well as the curvature of the yak contour curve map. Finally, the actual body height and body steep length of the yaks were obtained based on the camera imaging principle, and the body weight of the yaks was calculated.

7. Acknowledgements

This work is supported by Science and Technology Project in Qinghai Province (No. 2017-ZJ-717); Modern agriculture (cow calf) industrial technology system project (CRA-37); National natural fun projects (No.61640206);

References

1. Editorial Board of Chinese Yak Science, China Yak Science (Chengdu: Sichuan Science and Technology Press, 1989).
2. Wang, Q., Breeding Management Measures for Domestication of Purebred Wild Yaks, *Abstracts of Animal Husbandry & Veterinary Medicine(4)*, 18-18.
3. Yang Shi, B.J., Bao, S.K., Zhao, S.N., et al. Observation of Greenhouse + Supplementary Feeding Effects of Yaks in North Pastoral Areas of the Qinghai Lake in Cold Season, *Heilongjiang Journal of Animal Science & Veterinary Medicine.* **16** (2014) 124–124.
4. Zhang, L.N., Wu, P. Algorithm of sheep body dimension measurement and its applications based on image analysis. *Computers and Electronics in Agriculture.* (2018) 33-35.
5. Réti, Z. Deblurring images blurred by the discrete gaussian. *Applied Mathematics Letters*, 8(8), (1995) 29-35.
6. María, M., & Lópezálvarez, M. A. Removing Background Color from Blueprints. *Color and Imaging Conference.* (Vol.volume 2011) pp.48-51(4)
7. Kang, H., Lee, S. H., Lee, J. Image segmentation based on fuzzy flood fill mean shift algorithm. *Fuzzy Information Processing Society (pp.1 - 6). IEEE* (2010)
8. Measurement and Analysis of Body Weight and Body Size of Yaks in Sanjiangyuan Region. (2017)
9. Blum, H., A transformation for extracting new descriptors of shape. Models Percept. *Speech Visual Form 19, 362–380. China Cattle Science,* (1967) 43(1), 14-17.
10. Blum, H., Biological shape and visual science (part I). *J. Theor. Biol.* 38 (2), (1973) 205–287.
11. Zhao, J.M., Zhao, Z.X., Li, Q., Kinect Sensor Based Body Size Measurement Method for Sheep. *Jiangsu Agricultural Sciences*, 43(11), (2015) 495-499.
12. Jiang, J., Yue, W., Cao, M.Z. Research on Machine Vision Based Body Size Measurement Method for Sheep. *Journal of Inner Mongolia University of Science & Technology*, 34(4), (2015) 322-327.
13. Zhang Z G, Dong F L, Zhang Q C, et al. Fabrication of pixelated polarizer array and its application in polarization enhancement. *Acta Physica Sinica*, (2014), 63(18): 184204(1-10).

An efficient structure of organization with complete group guidance

Satoshi Ikeda*

Department of Computer Science and System Engineering, Miyazaki University, Japan,
bisu@cs.miyazaki-u.ac.jp

Mamoru Yoshimura*

Graduate School of Engineering, Miyazaki University, Japan,
hf11031@student.miyazaki-u.ac.jp

Makoto Sakamoto*

Department of Computer Science and System Engineering, Miyazaki University, Japan,
sakamoto@cs.miyazaki-u.ac.jp

Takao Ito†

Graduate School of Engineering, Hiroshima University, japan,
itotakao@hiroshima-u.ac.jp

Abstract

In this paper, we show model that an efficient organizational shape with one criterion can be classified into three types by using a new mathematical.

Keywords: Hierarchical organization, Mathematical model, Discrete combination optimization

1. Introduction

In [1,2], we proved using a mathematical model that an efficient shape of a hierarchical organization with only one criterion is limited to three types, see Fig.1 .

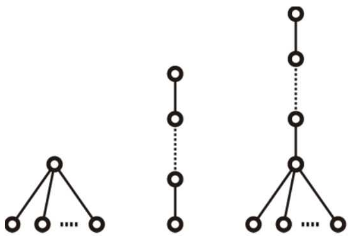

Fig.1. Three types of efficient trees when evaluation criteria is one.

Subsequently, the mathematical model for evaluating the shape of the organization has been generalized more realistically[3,4]. Although the basic idea of the total output to the outside of the organization as an evaluation value has not changed, the major improvements in the revised mathematical model are the following two points.

(a) Contribution of the members for a given organization can be categorized as the internal contribution to maintain the organization and the external contribution to realize the purpose of the organization in society.
(b) For any fixed organization, the sum of the effort each person spends is constant, but its influence is different depending on how to take a communication style.

The ratio of one's external contribution effort to the total of one's effort is called the external output coefficient. In the mathematical model of [3,4] with one

*University of Miyazaki, 1-1, Gakuen Kibanadai Nishi, Miyazaki, 889-2192
†University of Hiroshima, 1-4-1, Kagamiyama, Higashi-Hiroshima, 739-8527

evaluation criterion under the assumption that the external output coefficient takes a constant $\alpha \in [0,1]$ independent of member, previous results in [1,2] correspond to $\alpha = 0$ and the communication style called "the complete group guidance".

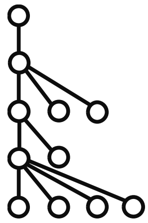

Fig.2. A bruch graph.

When the number of evaluation criteria is one, in the paper [3,4], we showed that the structure of an efficient organization becomes pass-like shape in the case that personal ability value of organization members is high. This is an extension of the results of [1,2] to the case of the model of [3,4] in part. However, in general it was not known whether the results of [1,2] could be extended to the case of the model of [3,4]. We expected that the results could be extended in the general case, but in reality it was not. In [5], by simulation experiments, Yoshimura et al. showed that an efficient tree is generally a brush tree shape, see Fig.2, when the number of evaluation criteria is one. After much consideration, we concluded that the efficient tree shape as shown in Fig.1 may depend on the communication style.

The purpose of this paper is to show that the efficient organizational shape when the evaluation criteria is only one, is limited to the three types shown in Fig.1 under the assumption of the communication style called the complete group guidance.

2. Mathematical Model

2.1. *Notations and Tree Graph as Hierarchical Organization*

Suppose that $G = (V(G), E(G))$ is a graph. Throughout this paper, a graph is always finite, directed and simple, with order $n = |V(G)| (n \geqq 2)$ and size $m = |E(G)|$.

For $u \in V(G)$, by $N(u) = \{v | \{u, v\} \in E(G)\}$, we denote the set of vertices adjacent to u, and call $\deg(u) = |\ N(u)\ |$ the degree of $u \in V(G)$. For an arbitrarily fixed rooted tree T with its root r and leaves $L(T)$, we denote

$$\deg^* s = \begin{cases} \deg s & \text{if } s \in \{r\} \cup L(T), \\ \deg s - 1 & \text{otherwise.} \end{cases}$$

For a rooted tree T with $V(T) = S$, we define natural partial ordering $\$(S,<)\$$ that so-called the tree-order associated with T. That is, the root $r \in S$ of T is the least element and the leaves of T are the maximal elements in this partial order. This ordering will be considered as the expression ``depth": if $x < y$, we say x lies below y in T. Note that the root r is the least element, and that the leaves of T are its maximal elements in this partial order.

Suppose that $S = \{s_1, s_2, \cdots, s_n\} (n \geq 2)$ and $\mathcal{A}$ ($|\mathcal{A}| \geqq 1$) are finite sets. Through this paper, $\mathcal{A}$ is the set of the evaluation measures. And S is interpreted as the set of members of a given organization, which consists of $s_1, s_2, \cdots, s_n$. There are many rooted trees with S as vertices. After that, we identify each rooted tree as its corresponding organization tree. Let $\mathcal{T}(S)$ be the set of rooted trees with S as its elements.

2.2. *External Contribution and Internal Contribution*

For a given S and $i \in \mathcal{A}$, we define $\{\varphi_i\}_{i \in \mathcal{A}}$ by

$$\varphi_i : S \to R^+ \equiv \{x \in R |\ x > 0\} \quad \text{for} \quad i \in \mathcal{A}$$

We call $\varphi_i(s)$ the personal ability of $s \in S$ with respect to $i \in \mathcal{A}$. And we call $(S, \{\varphi_i\}_{i \in \mathcal{A}})$ an evaluation system. According to the idea of 1-3, the evaluation function of a given evaluation system 1 $(S, \{\varphi_i\}_{i \in \mathcal{A}})$ is defined as follows. For $i \in \mathcal{A}$, total output of $s \in S$ that written by $f^{\alpha,i}_{s\to}$ is the product of s's personal ability $\varphi_i(s)$ and s's input that written by $f^{\alpha,i}_{s\leftarrow}$. That is,

$$f^{\alpha,i}_{s\to} = \varphi_i(s)\, f^{\alpha,i}_{s\leftarrow}.$$

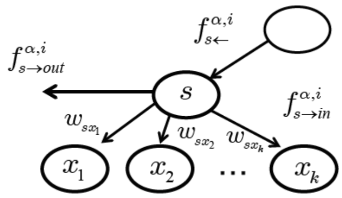

Fig.3. Input and output for $s \in S$

For $i \in \mathcal{A}$, s's total output $f^{\alpha,i}_{s\to}$ is classified into s's external output $f^{\alpha,i}_{s\to out}$ and s's internal output $f^{\alpha,i}_{s\to in}$, see Fig.3. That is

$$f^{\alpha,i}_{s\to} = f^{\alpha,i}_{s\to out} + f^{\alpha,i}_{s\to in}.$$

For the subordinate $s \in S$ who received instructions from his superior, it is necessary to transmit appropriate instructions $f^{\alpha,i}_{s\to in}$ as superior to his own subordinates, while s as subordinate carries out the instructions $f_{s\to out}^{\alpha,i}$, see Fig.3.

We assume that the ratio of s's external output to s's total output is a constant independent of $s \in S$. Through this paper, we denote the ratio of $f_{s\to out}^{\alpha,i}$ to $f_{s\to}^{\alpha,i}$ as $\alpha \in [0,1]$ for any $s \in S$. That is,

$$\text{external output } f_{s\to out}^{\alpha,i} : \text{ internal output } f_{s\to in}^{\alpha,i} = \alpha : 1-\alpha$$

for any $s \in S$. We call α the external output coefficient and call $1-\alpha$ the internal output coefficient.

2.3. *Weights' Policy*

For a given organizational structure tree T, we assume that the value of the input for subordinate $x \in N(s)$ with $x > s$ is obtained by multiplying its weight $\{w_{sx}^i\}$ to $f_{s\to in}^{\alpha,i}$, see Fig.3 again. Where

$$0 \le w_{sx}^i \le 1$$

for any $s \in S \setminus L(T), x > s$ of $x \in N(s)$ and

$$1 \le \textstyle\sum_{x\in N(s),x>s} w_{sx}^i \le \deg^* s$$

for any $s \in S \setminus L(T)$. Therefore, the total contribution of $s \in S \setminus L(T)$ for the organization can be expressed by

$$\left(\textstyle\sum_{x\in N(s),x>s} w_{sx}^i\right) f_{s\to in}^{\alpha,i} + f_{s\to out}^{\alpha,i}.$$

We assume that $(w_{sx}^i)_{x\in N(s),x>s}$ for $s \in S \setminus L(T)$ is a sequence depending only on $\deg^* s$ and $i \in \mathcal{A}$. That is, for $s, s' \in S \setminus L(T)$ s,s' and $i \in \mathcal{A}$, $\deg^* s = \deg^* s'$ implies that $(w_{s'x}^i)_{x\in N(s'),x>s'}$ is a permutation of $(w_{sx}^i)_{x\in N(s),x>s}$. Thus, for a fixed $\deg^* s$ and $i \in \mathcal{A}$, the selection that we can do is which weight to assign whom. We call the way of the determination *a weights' policy*. For any weights' policy, we assume that if $\deg^* s \ge \deg^* s'$ for $s, s' \in S$,

$$w_{sx1}^i \ge w_{sx2}^i \ge \cdots \quad \text{and} \quad w_{s'x'1}^i \ge w_{s'x'2}^i \ge \cdots,$$

then $(w_{sx}^i)_{x\in N(s),x>s}$ *and* $(w_{s'x'}^i)_{x'\in N(s'),x'>s'}$ satisfy

$$w_{sxj}^i \le w_{s'xj}^i$$

for $j = 1,2,\cdots,\deg^* s'$.

2.4. *Communication Style*

The weights' policy is a parameter determined by the communication style in the organization. Typical ones are the following two cases;

(1) Complete Individual Guidance (CIG)
$\sum_{x\in N(s),x>s} w_{sx}^i = 1$ for any $s \in S \setminus L(T)$.

(2) Complete Group Guidance (CGG)
$\sum_{x\in N(s),x>s} w_{sx}^i = \deg^* s$ for any $s \in S \setminus L(T)$.

The case of (1) CIG is an organization like a secret society. Since a superior gives an instruction to his/her subordinates individually, the members of the organization do not know about each other's work. In such organizations, when new member joins the organization, or a member of the organization leave the organization, its efficient organization can not be constructed unless the existing organization is broken once.

On the other hand, the case of (2) CGG is an open organization. The characteristic of an organization with such a communication style is that it is stable in the sense that there is no need to significantly change the composition of the whole organization when new member joins it. Roughly speaking, the reason why CGG has such a property is that when we convert T to

$$T' = T - xs + ys$$

for $T, T' \in \mathcal{T}(S)$, $s, x, y \in S$, $s \in N(x)$, $s > x$, the evaluation function is affected only by the part of the up closure of s, see Fig.4.

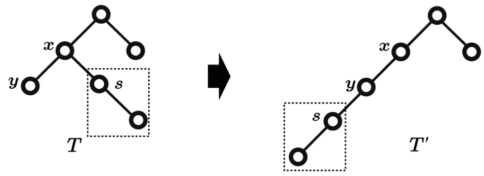

Fig.4. Conversion from T to T'

CIG and CGG are extreme cases, the general style is intermediate between them.

2.5. *Evaluation Function*

To summarize so far, for a given evaluation system $(S, \{\varphi_i\}_{i\in\mathcal{A}})$, a rooted tree T with root r and $V(T) = S$, $s \in S$, $i \in \mathcal{A}$ and an external output coefficient $\alpha \in [0,1]$, $f_{s\leftarrow}^{\alpha,i}$ and $f_{s\to}^{\alpha,i}$ denote the input and the output of $s \in S$, respectively. And $f_{s\to out}^{\alpha,i}$ and $f_{s\to in}^{\alpha,i}$ denote the external and the internal outputs of $s \in S$ for the organization, respectively. Then we define the follows;

$$f_{s\to}^{\alpha,i} = \varphi_i(s)\, f_{s\leftarrow}^{\alpha,i}$$

$$f_{s\leftarrow}^{\alpha,i} = \begin{cases} 1 & \text{if } s = \text{root}, \\ w_{p(s)s}^i\, f_{p(s)\to in}^{\alpha,i} & \text{otherwise.} \end{cases}$$

Where $\{w_{xy}^i\}$ denote the weights from $x \in S \setminus L(T)$ to $y \in N(x)$ with respect to $i \in \mathcal{A}$ in anarbitrarily fixed T. And $p(s)$ denotes the parent node (as superior) of $x \in S$

on T. Under the assumption of extenal and internal output, we define

$$f_{s\to in}^{\alpha,i} = \begin{cases} 0 & \text{if } s \in L(T), \\ (1-\alpha) f_{s\to}^{\alpha,i} & \text{otherwise,} \end{cases}$$

$$f_{s\to out}^{\alpha,i} = \begin{cases} f_{s\to}^{\alpha,i} & \text{if } s \in L(T), \\ \alpha f_{s\to}^{\alpha,i} & \text{otherwise.} \end{cases}$$

$$f_{s\to}^{\alpha,i} = f_{p(s)\to in}^{\alpha,i} + f_{p(s)\to out}^{\alpha,i},$$

For a given evaluation system $(S, \{\varphi_i\}_{i\in\mathcal{A}})$ an external output coefficient $\alpha \in [0,1]$ and a given weights' policy, let T be a rooted tree graph with $V(T) = S$. Then we will evaluate the rooted tree T as organization model by

$$\Phi^{(\alpha)}(T) = \sum_{i\in\mathcal{A}} \Phi^{(\alpha,i)}(T), \Phi^{(\alpha,i)}(T) = \max_{\{w_{xy}^i\}} \sum_{i\in\mathcal{A}} f_{s\to out}^{(\alpha,i)}(T)$$

Here $\{w_{xy}^i\}$ shall be taken about all the possible combinations under the given weights' policy. For a given $(S,\backslash\{\ \{\varphi_i\}_{i\in\mathcal{A}})$ and $\alpha \in [0,1]$, we call $\Phi^{(\alpha)}(T)$ *the ability value of* T. Under a given weights' policy, $T_{opt}^{(\alpha)}$ is an efficient tree for a given external output coefficient $\alpha \in [0,1]$, if $\max_{T\in\mathcal{T}(S)} \Phi^{(\alpha)}(T)$ is attained by $\Phi^{(\alpha)}(T_{opt}^{(\alpha)})$. Here $\mathcal{T}(S)$ denotes the set of rooted tree graph with $V(T) = S$.

3. Results

Theorem 1. Under the setting of Complete Group Guidance, suppose that $(S, \{\varphi_i\}_{i\in\mathcal{A}})$ is an evaluation *system such that* $S = \{\ s_1, s_2, \cdots,\ s_n\}$ *with*

$$\varphi_i(s_1) \geq \varphi_i(s_2) \geq \cdots \geq \varphi_i(s_n)$$

for some $i \in\mathcal{A}$. Assume that $\max_{T\in\mathcal{T}(S)} \Phi^{(\alpha,i)}(T)$ is attained by $T_{opt}^{(\alpha,i)}$, then we have the followings.

(a) Asuume that $\varphi_i(s_n) \geq 2/(1-\alpha)$, then we see that one of $T_{opt}^{(\alpha,i)}$ is the path graph in Fig.5(1).

(b) Asuume that $\varphi_i(s_2) \leq 1/(1-\alpha)$, then we see that one of $T_{opt}^{(\alpha,i)}$ is the star graph in Fig.5(2).

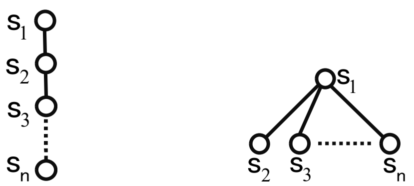

(1) $T_{opt}^{(\alpha,i)}$ as a path graph (2) $T_{opt}^{(\alpha,i)}$ as a star graph

Fig.5. An efficient organization structure.

The typical form of an efficient tree with respect to some $i \in\mathcal{A}$ is a path graph or star graph as in Theorem1. In general, we can show that the form of $T_{opt}^{(\alpha,i)}$ becomes the form which seems to have put these two figures together.

For a given $(S, \{\varphi_i\}_{i\in\mathcal{A}})$ and its organizational structure tree T, let us define

$$D_2(T) = \{s \in S |\ \deg^*(s) \geq 2\}$$

Theorem 2. Under the setting of CGG, suppose that $(S, \{\varphi_i\}_{i\in\mathcal{A}})$ is an evaluation system. Assume that $\max_{T\in\mathcal{T}(S)} \Phi^{(\alpha,i)}(T)$ is attained by $T_{opt}^{(\alpha,i)}$ for some $i \in\mathcal{A}$, then we have the followings.

(a) $|D_2(T_{opt}^{(\alpha,i)})|$ is equal to 0 or 1.

(b) Putting $D_2(T_{opt}^{(\alpha,i)}) = \{x\}$ when $|D_2(T_{opt}^{(\alpha,i)})| = 1$, then we see that

$$\left\{s \in S \middle| s > x \ in\ T_{opt}^{(\alpha,i)}\right\} = L(T_{opt}^{(\alpha,i)}).$$

The general form of the most efficient tree $T_{opt}^{(\alpha,i)}$ which theorem2 insists on is shown in Fig.6.

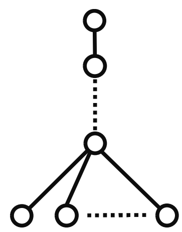

Fig.6. General form of $T_{opt}^{(\alpha,i)}$ for some $i \in \mathcal{A}$.

References

1. S.Ikeda, An Efficient Structure of Organization, *International Interdisciplinary Workshop on Robotics, Ecosystem, and Management*(2010), pp.72-78.
2. S.Ikeda, T.Ito and M.Sakamoto, Discovering the efficient organization structure: horizontal versus vertical, *Artificial Life and Robotics*(2011), vol.15, 4, pp.478-481.
3. S.Ikeda, T.Ito, M.Sakamoto, A Mathematical Model of Hierarchical Organization, *Proceedings of the international conference on Pure Mathematics and Applied Mathematics*(2015), pp423-432.
4. S.Ikeda, T.Ito, M.Sakamoto, T.Ito, An Evaluation Model of Internal and External Contributions in Hierarchical Organizations, *International Journal of Mathematical Models and Methods in Applied Sciences*(2015), Vol.9, pp.636-645.
5. M. Yoshimura, T. Ito, M. Sakamoto, T. Ito, Y. Shinano, S. Ikeda, An efficient structure of organization with complete individual guidance, *Proceedings of the 2018 International Conference on Artificial Life and Robotics*(2018), vol.23,pp.264-267.

Parallel finite element analysis for hyperbolic problems

Amane Takei and Makoto Sakamoto
Department of Electrical and System Engineering, University of Miyazaki, 1-1 Gakuen Kibanadai-Nishi Miyazaki, 889-2192, Japan
E-mail: takei@cc.miyazaki-u.ac.jp
www.miyazaki-u.ac.jp/english/

Abstract

With the expansion of electromagnetic field analysis using computers, large spaces that include complex shapes have also become an analysis target, and the development of a high-accuracy analysis is required for these problems. Therefore, in the present study, Berenger's PML for hyperbolic problems, which is currently the most effective absorbing boundary condition, is applied to the parallel finite element method based on the domain decomposition method, which is an effective analysis method for the high-frequency band. As a basic study, we developed an analysis solver using a parallel finite element method based on the iterative domain decomposition method. In verifying the accuracy of the analysis solver, we analyzed TEAM Workshop Problem 29, which is a benchmark problem, and confirmed that a highly accurate solution is obtained. Next, a model with Berenger's PML added to the dipole antenna model is used as an analysis object, and the absorption performance of the PML is evaluated using a reflection coefficient based on the S parameter. Moreover, the accuracy of the antenna analysis is evaluated by comparing the directivity of the dipole antenna with the theoretical solution. As a result, the effectiveness of the proposed method for high-frequency analysis is confirmed.

Keywords: Iterative domain decomposition method, Parallel finite element method, Berenger's PML, Large-scale analysis, Microwave analysis.

1. Introduction

In the present study, Berenger's PML for hyperbolic problems like a high-frequency electromagnetic field analysis, which is currently regarded as the most effective absorbing boundary condition, is applied to the parallel finite element method, which is an analysis method that is capable of computing large-scale problems. We then show that the parallel finite element method is effective as an analysis method for a microwave band by calculating the problem dealing with an open domain and evaluating the solution's accuracy. First, as a basic study, we developed a three-dimensional electromagnetic field analysis solver using a parallel finite element method based on the iterative domain decomposition method. In order to verify the accuracy of the developed analytical solver, we calculate TEAM Workshop Problem 29, which is a benchmark problem, and evaluate the accuracy of the analytical solver. Next, a model with a PML added to the dipole antenna is used as the analysis object, and the absorption performance of the PML is evaluated using a reflection coefficient based on the *S* parameter. Moreover, by comparing the directivity of the dipole antenna with the theoretical solution, evaluations of the accuracy and performance of the antenna analysis are performed. As a result, we confirmed the effectiveness of this method for microwave analysis.

2. Numerical analysis

We analyze TEAM Workshop Problem 29[1] in order to verify the accuracy of the developed analytical solver.[2] TEAM 29 is a benchmark problem and involves a resonator model. The resonator is cylindrical and has a diameter of 1.9 [m] and a height of 1.45 [m]. In the analysis, a dielectric phantom having a relative permittivity ε_r of 80 and an electric conductivity σ of 0.52 [S/m] is positioned, and the resonance state is investigated. The analysis domain boundary is a perfect conductor. The analysis model is shown in Fig. 1. Table 1 shows the specifications of the TEAM 29 model. The highest calculation efficiency is achieved when the number of elements contained in one subdomain is approximately 170, and the number of partial domains is determined such that the number of elements contained in one subdomain is equal to 170.

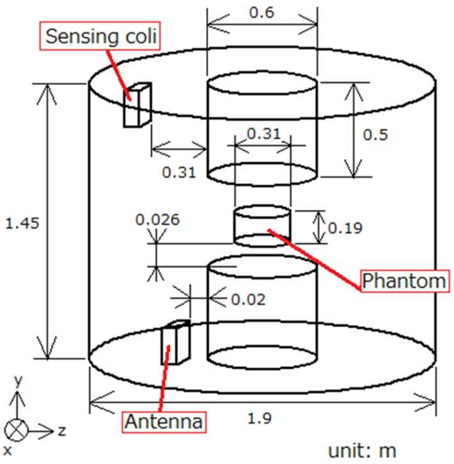

Fig. 1. TEAM 29 cavity resonator model

Table 1. TEAM 29 model data.

No. of Elements	DOFs	No. of Subdomains
121,277	149,668	100×7

The results of the analysis of TEAM 29 are subjected to frequency response analysis in order to confirm the accuracy of the developed analytical solver. In order to detect the resonant frequency and compare solutions with actual measurements, the frequencies of some range are analyzed. The frequency band of 60 [MHz] to 140 [MHz] is calculated for 2-MHz steps, and the response for every frequency step is investigated. In addition, calculations near the resonance frequency are performed in 0.4-MHz intervals. The computing environment used in the present study is a 25-PC cluster equipped with Intel Core i7-2600K multi-core CPUs (total: 100 cores) and 32 GB memory is used. The compiler used is the gcc. In addition, Message Passing Interface (MPI) is used for the parallelization library. The average calculation time per frequency step and the averagely used memory are shown in Table 2. Fig. 2 shows the frequency response of the magnetic field. The measured and calculated values are shown in Table 3.

Table 2. Specifications of the TEAM 29 model.

No. of Elements	DOFs	No. of Subdomains
121,277	149,668	100×7

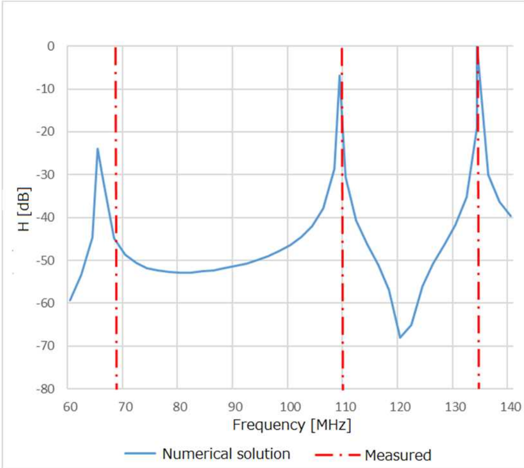

Fig. 2. Numerical and measured frequency response analysis results

Table 3. Resonance frequencies (Units: [MHz]. The error rate [%] between measured data and the numerical solution is shown in parentheses.)

Resonance mode	Measured data	FDTD 25-mm mesh	Result
1st	68.6	67 (2.33)	65.6 (4.37)
2nd	110	110	109.0 (0.91)
3rd	134	134	134.4 (0.30)

As shown in Fig. 2, a solution resonating around the resonance frequency of the actually measured value is obtained. In the comparison of the measured and calculated values, the error rate is 4.37 [%] in the 1st mode, 0.91 [%] in the 2nd mode, and 0.30 [%] in the 3rd mode. As the mode increases, the error rate decreases. However, it is the same tendency as the analysis result obtained by the FDTD method. Moreover, the error rate is less than 5 [%], and a solution with high accuracy is obtained.

Therefore, the solution obtained by the developed solver is proven to have a sufficiently high accuracy. Moreover, in the analysis of the dipole antenna applying the PML described in the following sections, the error tolerance index is defined as 5 [%] in order to evaluate the accuracy.

3. PML

3.1. *Berenger's PML*

The PML can be used to create an absorbing boundary by surrounding the analysis domain with a PML. From the viewpoint of the accuracy of the obtained solution, the PML is currently the most effective absorbing boundary condition. Although Berenger's PML is originally proposed as an absorbing boundary condition for the FDTD method, in the present study, we apply a finite element method dealing with an unstructured grid, we propose a simplified method omitting the directionality of electric conductivity given to the PML and confirm its effectiveness.

Berenger's PML stacks several PMLs outside the analysis domain and gradually sets a large value of electric conductivity according to the outer layer so that the outermost wall can be surrounded with a perfect conductor wall without reflecting electromagnetic waves. Fig. 3 shows a schematic diagram of Berenger's PML absorbing boundary.

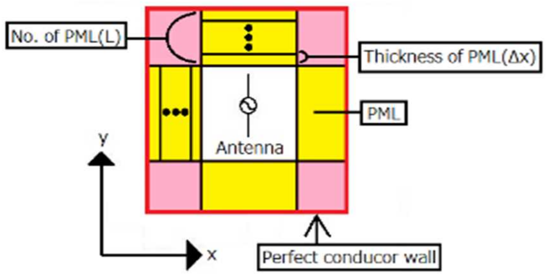

Fig. 3. PML absorbing boundary

In this paper the distribution of the electric conductivity for PML is expressed as follows:

$$\sigma = \sigma_{max}\left[\frac{\left(L-\hat{L}(x)\right)\Delta x}{L\Delta x}\right]^M \quad (1)$$

where Δx is the thickness of PML 1, L is the number of layers of the PML, $\hat{L}(x)$ is a coefficient determined by position x, and $\hat{L}(x)$ = 0 at the position of the Lth layer, $\hat{L}(x)$ = 1 at the position of the (L-1)th layer, and $\hat{L}(x)$ = L -1 at the position of the first layer.

Moreover, σ_{max} is the maximum value of the electric conductivity for the PML, and M is the degree distribution of electric conductivity. This equation is used to determine the electric conductivity of each layer of the PML.

The parameters to be determined as the parameters of the PML are the thickness Δx of PML 1, the number L of PML layers, the maximum electric conductivity σ_{max} of the PML, the degree M distribution of the electric conductivity, the reflection coefficient R [dB] between the PML of the outermost layer, and the perfect conductor wall. The reflection coefficient R is approximated as follows:

$$|R(\phi)| \cong exp\left[-\frac{2\sigma_{max}L\Delta x}{(M+1)\varepsilon_0 c}\cos\phi\right] \quad (2)$$

where ϕ is the incident angle of the electromagnetic wave, and c is the speed of light. Since we cannot decide the incident angle for an arbitrary incident wave, ϕ = 0, a reflection coefficient for perpendicular incidence is used as a reference. Moreover, since the M that gives the distribution of the electric conductivity causes the calculation accuracy to deteriorate if the change of the electric field in the PML is too steep, M is approximately 2 to 4. If the number of layers L is too large, more memory will be required, and if L is too small, it will not function adequately as an absorbing boundary. There are many cases where the concrete number of L is set to 4 to 16. The thickness Δx of PML 1 is a constant thickness of all layers.

We set the reflection coefficient R(0) according to the required accuracy. Upon determining the above parameters, the maximum electric conductivity σ_{max} is given as follows:

$$\sigma_{max} = -\frac{(M+1)\varepsilon_0 c}{2L\Delta x}\ln|R(0)| \quad (3)$$

In the present study, we construct a PML using (1) through (3) with L = 9, M = 4, and Δx = λ/10. However, in order to reduce the analysis scale, we examine the optimum value of L in the next section.

3.2. *Numerical results*

We assign the PML to the dipole antenna model. The analysis domain is a cube of length 0.6 [m] so that the distance from the antenna to the innermost PML matches the wavelength. The current density is applied to the antenna as a current source as follows:

$$I(y) = I_0 \cos\left(\frac{2\pi}{\lambda} y\right) \quad : -l \leq y \leq l \tag{4}$$

where I_0 = 0.08 [A/m^2], λ is the wavelength, and l is the length from the feeding point to the antenna tip.
The analysis frequency is 1 [GHz], and the length of the antenna is 0.15 [m], which is the half wavelength. Here, mesh division is performed so that the maximum side length of the element is 1/20 of the wavelength. The analysis domain's boundary is a perfect conductor. Fig. 4 shows a schematic diagram of the dipole antenna model.

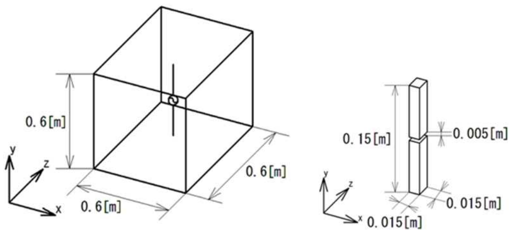

(a) Analysis domain (b) Antenna

Fig. 4. Dipole antenna model

We assign PMLs to the domain boundary as shown in Fig. 4(a). The plane portion of the PML at the domain boundary overlaps a number of flat plates according to the number of layers, and the corner portion of the PML is one rectangular parallelepiped or cube. The boundary of the outermost layer of the PML is a perfect conductor wall. We perform performance evaluation by setting the thickness of one layer to be 0.03 [m] and the PML to have L = 9 (hereinafter a PML with L layers is abbreviated as PML(L)). Table 4 lists the number of elements and the degree of freedom of the analysis model.

Table 4. Number of elements and DOFs of the dipole antenna model

	PML(0): Perfect conductor wall	PML(9)
No. of Elements	4,669,759	26,899,669
DOFs	5,506,368	31,703,550

In (3), we set L = 9, Δx = 0.03, M = 4, and $R(0)$ = -120 [dB], which yields the maximum electric conductivity σ_{max} to PML(9). In addition, we decide the electric conductivity of each layer using (1). In this study, we set the average value of each layer to the electric conductivity of the corner portion. We evaluate the performance of the PML based on the reflection coefficient obtained using the S_{11} parameter[3]. The observation point of the S_{11} parameter is on the x-axis 1 cm inside of the PML. The computing environment is the same as in the section 2. Table 5 lists the reflection coefficient, the CPU time, and the memory size.

Table 5. Results for reflection coefficient, CPU time, and memory size

	PML(0): Perfect conductor wall	PML(9)
Reflection coefficient [dB]	0	-18.65
CPU time [s]	1,278	18,787
Memory size [MB/core]	44.3	227.3

When the domain boundary is PML(0), i.e., when it is a perfect conductor wall, S_{11} = 1, so that the reflection coefficient is 0 [dB]. On the other hand, when the domain boundary is PML(9), the reflection coefficient is -18.65 [dB]. The design target reflection coefficient of the antenna, for example, is generally approximately -10 to -20 [dB], and in the present study, we use a reflection coefficient of approximately -10 to -20 [dB][3]. Thus, PML(9) can obtain sufficient absorption performance. On the other hand, in comparing with PML (0), PML (9) increases the amount of memory used and computation time, depending on the absorbing layer applied. Fig. 7 shows a visualization diagram of the electric field obtained by analysis.

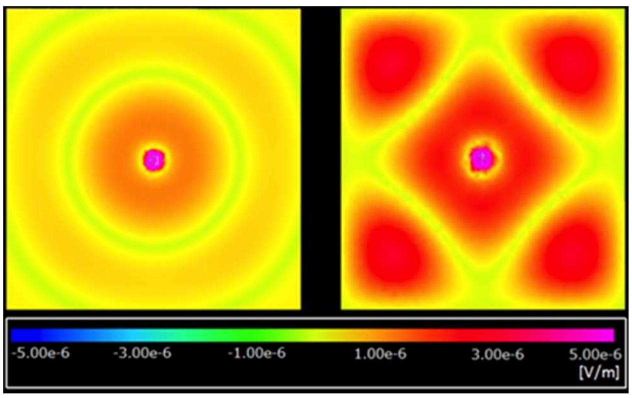

Fig. 5. **V**isualization of the analysis result (electric field) (Left: PML(9), Right: PML(0) (perfect conductor wall))

In Fig. 5, the left-hand side shows PML(9) at the boundary edge and the electric field propagates from the dipole antenna to the free space. On the other hand, the right-hand side of Fig. 5 shows the mode when the dipole antenna is enclosed by a perfect conductor wall.

Next, we perform the directivity evaluation of the dipole antenna by error evaluation using the theoretical solution in the far field. The error evaluation of the far field uses the E plane.

The theoretical solution[3] of the far field of the E plane is as follows:

$$E_\theta = j60I\frac{e^{-jkr}}{r} \cdot \frac{\cos\left(\frac{\pi}{2}\cos\theta\right)}{\sin\theta} \qquad (5)$$

where j is the imaginary unit, I is the current, and r is the distance from the feeding point. The approximate distance r to the far-field peak of the Fresnel's region ($2\,l^2/\lambda < r$) is 0.250 [m], if the dimension l (= 0.150 [m]) of the dipole antenna is not ignored. Moreover, k is the wave number and is given by $k = 2\pi/\lambda$. The directivity evaluation is performed by comparing the numerical analysis solution with the theoretical solution on the E plane. Fig. 6 shows a plot of the numerical analysis solution e_θ and the theoretical solution E_θ in increments of 1 [deg].

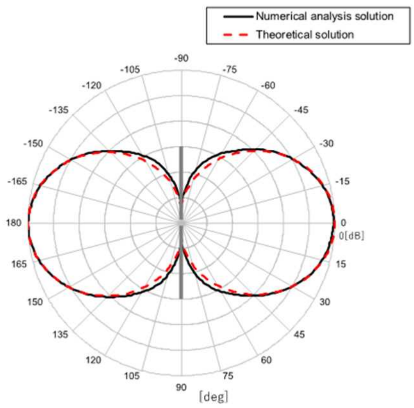

Fig.6. Numerical and theoretical solutions in the E plane

The directivities of the numerical and theoretical solutions agree very well. The range of θ, which is the far field far beyond the Fresnel's region, can be expressed by (6). The lower limit θ_{Min} is $\arcsin(2\,l^2\,/\,r\lambda) + 90 \cong -57$ [deg], and the upper limit θ_{Max} is $90 - \arcsin(2\,l^2\,/\,r\lambda) \cong 53$ [deg]. The average error rate E_{err} in this range is obtained by (7). As a result, the average error rate is 1.70 [%], and it is shown that a highly accurate solution can be obtained.

$$\arcsin\left(\frac{2\,l^2}{r\lambda}\right) + 90 \leq \theta \leq 90 - \arcsin\left(\frac{2\,l^2}{r\lambda}\right) \qquad (6)$$

$$E_{err} = \frac{\sum_{i=\theta_{Min}}^{\theta_{Max}} \frac{|e_i - E_i|}{E_i}}{\theta_{Max} - \theta_{Min} + 1} \times 100 \quad [\%] \qquad (7)$$

In the calculations shown in Fig.5, we used a dipole antenna model with PML(9). Here, we find the optimum L from the average error rate in the far field and the reflection coefficient of PML(L) by a parameter study using the number of PMLs. The computing environment is the same as in the section 2. Table 6 shows the number of elements for each L, the number of degrees of freedom of the edge, the error rate, the reflection coefficient, the calculation time, and the number of iterations of the COCG method applied to the interface problem.

Table 6. Numerical model data and results

	PML(9)	PML(8)	PML(7)
No. of elements	26,899,669	24,184,687	21,533,641
DOFs	31,703,550	28,506,352	25,383,890
Average error rate [%]	1.70	3.81	12.87
Reflection coefficient [dB]	-18.65	-15.79	-15.04
CPU time [h]	5.22	3.77	2.81
No. of iterations	46,508	37,755	30,695
Memory size [MB/core]	227.3	204.6	182.6

From Table 6, PML(9) is the case with the best far field accuracy. When the allowable range of the error rate is less than 5 [%], which is the allowable range of numerical analysis error, since PML(7) has a reflection coefficient of less than -15 [dB], the PML functions sufficiently. However, the error rate exceeded the allowable range. We can find that PML(8) is optimal because it has a better calculation time and iteration count than PML(9).

4. Conclusion

In the present paper, we propose a simplified method that omits the directionality to Berenger's PML hyperbolic problems like a high-frequency electromagnetic field analysis and gives the average value of the electric conductivity of each layer at the corner of the model. Performance evaluation reveale that sufficient absorption performance can be obtained. In the accuracy verification by directivity evaluation of the dipole antenna, when the maximum element side length is set to 1/20 of the wavelength and the PML to be given is set to 9 layers, the error rate of the numerical solution and the theoretical solution is about 1.70 [%]. It is found that a highly accurate solution can be obtained. In addition, when the tolerance range of the far-field error rate that is considered to be sufficiently practical is set to less than 5 [%], an eight-layer PML is found to be optimal. In addition, the usefulness of the proposed method for a frequency band of 1.2 GHz or higher, which is used in microphones and mobile phones, is demonstrated.

Acknowledgements

The present study was supported in part by a JSPS Grant-in-Aid for Scientific Research (Basic Research (B), 17H03256). The computer environment used in the present study was supported in part through a JST Adaptable and Seamless Technology transfer Program (A-STEP (Search Type), AS262Z02631H).

References

1. TEAM Workshop, Tucson, AZ, USA, 1998.
2. A. Takei, S. Sugimoto, M. Ogino, S. Yoshimura, H. Kanayama: Full Wave Analyses of Electromagnetic Fields with an Iterative Domain Decomposition Methodm, *IEEE Transactions on Magnetics*, 46:8 (2010), 2860-2863.
3. Fujikura LTD. Homepage: http://www.fujikura.co.jp/eng/

Design of feed part control system for rectification process

Lingran An[1], Fengzhi Dai[1*,] Yujie Yan[1], Zhongyong Ye[1], Xia Jin[1], Yiqiao Qin[12], Chengcai Wang[3], Kaige Liu[1]

[1] *College of Electronic Information and Automation,*
Tianjin University of Science and Technology, China;

[2] *Tianjin Tianke Intelligent and Manufacture Technology CO.,LTD, China;*

[3] *CETC Ocean Information Co., Ltd, Beijing 100041, China*
*E-mail: * daifz@tust.edu.cn*
www.tust.edu.cn

Abstract

This paper completes the structure design of the feed process of the small rectification experimental unit. According to the process requirements, we design the overall scheme of the detection and control system of the main parameters and select the type of the instrument. The system hardware design is based on the CPU222 of Siemens s7-200 PLC and the corresponding input/output module. The lower computer adopts the ladder diagram to complete the program design such as parameter acquisition, scale transformation and PID operation. The monitoring interface of the upper computer adopts King View monitoring software.

Keywords: rectifying column, feed, PLC, PID

1. Introduction

The rectification operation makes use of the different volatility of different components of the mixed liquid under the same pressure, causes the partial vaporization and condensation of different components in the column, and finally the complete separation is obtained[1].

This design is mainly aimed at the feed part of the rectifying column. There are three feed states of rectifying column: superheated steam, supercooled liquid mixed in Vapor-liquid phase and saturated liquid. In chemical research, how to select the feeding port is mainly studied. When the component becomes heavier, the feeding port should change downward to increase the reflux ratio, and when the component becomes lighter, the feeding port should change upward to reduce the reflux ratio[2]. Feed quantity, temperature, pressure and material balance are the important factors that affect the rectifying column[3].

The design idea of feed part control system of rectification process is as follows:

Firstly, the technological process of rectifying column and feed process is analyzed, and the process pipeline and control flow chart are drawn. Then, the detection and control points of the feed control system are determined to achieve the ideal rectification effect, and the instrument selection is completed.

Next comes the design of the hardware part of the control system. We mainly complete the selection of PLC modules and the hardware wiring of the system.

Finally, the design of the software part of the control system. We use STEP7 programming software to write the control program of the lower computer through the ladder diagram programming language, so as to realize the collection and processing of field data, and control the communication between the field equipment and the upper computer. The upper computer adopts the monitoring software (such as King View) which is compatible with the selected PLC to monitor the control process.

2. Overall scheme design

2.1. Analysis of process flow and control

The process pipeline and control flow chart of feeding part are shown in fig.1. We add the mixture into the feed tank V102, open the valve VA107, and the feed pump P102 feeds the raw material into the feed preheater E101 to heat the raw material. The feed flow meter FIC101 detects the feed flow in order to control its variation range. We open the valve VA112 to allow the raw steam generated by the feed preheater to enter the rectifying column T101. TIC101 detects the feed temperature and controls the heating temperature of the feed preheater to obtain the target product. The raw materials and steam entering the rectifying column are subsequently reflux and reboiler treated to produce light component products and recombinant sub-products. After the rectification experiment, the residual liquid in the raw material tank was taken back to the tower kettle discharge tank V105 for recycling and utilization by vacuum pump P101 and vacuum buffer tank V101.

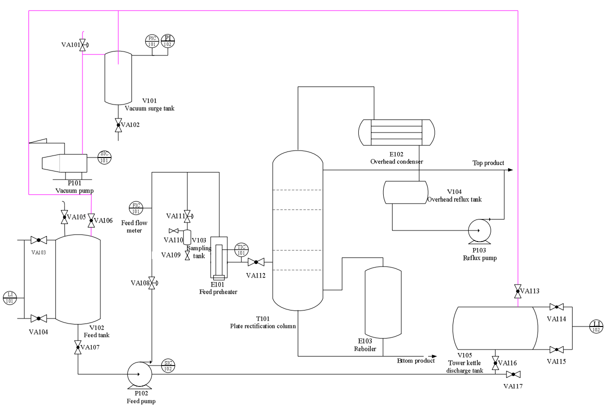

Fig.1. The process pipeline and control flow chart of feeding part

2.2. Determination of detection scheme

First, we select the detection points. There are many factors influencing the feed in the process of rectification, among which the temperature of feed and the flow rate of feed are the important factors influencing the whole process of rectification. The variation range of feed temperature will directly affect the vapor-liquid equilibrium of the whole rectifying column. The variation range of feed quantity should be controlled within a reasonable range to achieve the ideal rectification effect. In addition, the liquid level of the raw material tank should be tested in order to add the raw material in time. Therefore, detection points include feed flow (FIC101), feed temperature (TIC101) and feed tank level (LI101).

Next is the selection of the measuring instruments. For the flow detection point FIC101, we choose differential pressure flow transmitter, which is an intelligent differential pressure flow meter based on the monocrystalline silicon differential pressure sensor. It can display feed flow in real time and realize remote transmission, which is convenient for remote real-time monitoring. For the temperature detection point TIC101, we choose the Pt100 temperature sensor, which not only has the analog signal output function of the transmitter, but also can increase the digital communication function. For the liquid level detection point LI101, we choose the input level transmitter, which is a pressure sensor to measure the liquid level. The essence of liquid level measurement is to change the pressure differential into 4 ~ 20mA standard signal by sensor and amplifying circuit and then output it.

2.3. Determination of control scheme

According to the selected detection points, we determined two control points. First is the flow control point FIC101, which controls the feed flow by controlling the speed of the feed pump. Next is the temperature control point TIC101, which controls the temperature of the feed preheater by controlling the heating power of the heating rod.

Finally, the selection of actuators is completed according to the selected control points. For FIC101, the frequency converter is the one that controls the speed of raw material pump, so we choose Siemens MM440 frequency converter. For TIC101, we chose solid state voltage regulator to control the power of heating rod.

3. Hardware design

The input and output points of this control system include: 2 digital input points (start and stop switches), 2 digital output point (2 control relays), 3 analog input points (feed temperature, feed rate and feed tank level), 2 analog output points (voltage of the solid-state voltage regulator and frequency of the frequency converter). Therefore, the CPU222 module is selected, which has 8 native digital inputs and 6 native digital outputs, allowing up to 2 I / O expansion modules. One EM231 analog expansion input modules and an EM232 analog expansion output modules are selected as required. The hardware wiring diagram is shown in Fig.2.

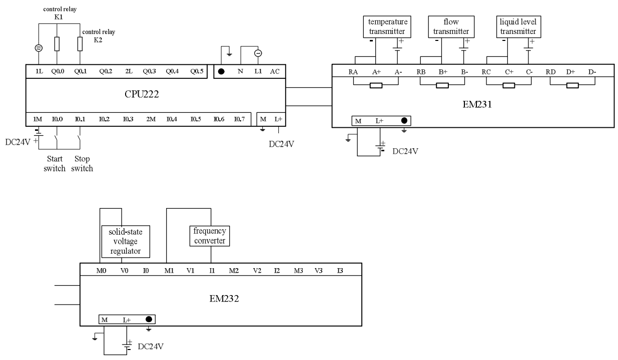

Fig.2. The hardware wiring diagram

4. Programming software design

The control layer of the control system of feed part of rectification process is the PLC system. It is used to receive on-site data and control the site equipment according to the pre-designed control strategies, while send the on-site data and equipment state to the PC machine. This design selects the S7-200 series PLC as the controller, and the programming software uses the STEP 7-Micro/WIN software of the German SIEMENS company.

4.1. The main program design

The PLC program is designed in a structured way. The main program completes all functions of the system, and calls each module in turn according to the system requirements and subroutine functions. The data conversion and scale conversion subroutine is used to process and store the collected data. Some of the data and the set value are compared to calculate the deviation, which is used for the PID operation of the program generated by the PID instruction wizard. The control output conversion subroutine is used to transform the data after PID operation and output it to the executor. The flow chart of the main program is shown in fig.3.

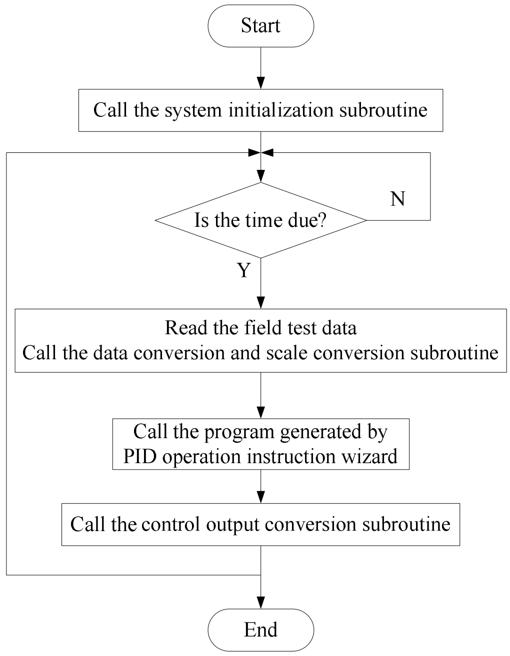

Fig.3. The flow chart of the main program

4.2. PID operation subroutine design

In practical engineering, the ratio, integral and differential control is the most widely used regulator control law, referred to as PID control, also known as PID regulation[4].

In S7-200CN, PID command is a method to realize PID function[5]. In STEP7-Micro/WIN V4.0, we can use the wizard to generate a PID instruction or program, and then call it in the main program. After completing the configuration of the PID loop through the wizard, the specified PID regulation subroutine PIDx_INIT and interrupt program PID_EXE will be automatically generated. The PIDx_INIT instruction performs the PID function based on the inputs and outputs we have previously set in the PID wizard, and it can be invoked every time the scan is performed. In this design, feed temperature control system and feed flow control system adopt PID wizard to generate the instructions[6].

5. Monitoring software design

This design adopts kingview6.55 monitoring system software. Generally, such a system can be divided into three layers: control layer, monitoring layer and management layer. PLC and PC are connected by PC-PPI cable hardwire, and the monitoring software of PC is communicated with PLC through PPI[7].

First of all, we complete the definition of the external equipment and the communication between the Kingview6.55 and the external equipment in the software. Secondly, we define the variables in the control system. Finally, we design the configuration screen, which includes the drawing of the screen and the connection of the animation, etc. Our configuration screen is divided into three pages, namely, main interface for feed monitoring, production report and data curve, and is equipped with the start and stop button, screen switch button, user login and exit button, etc. The main monitoring interface after login is shown in fig.4.

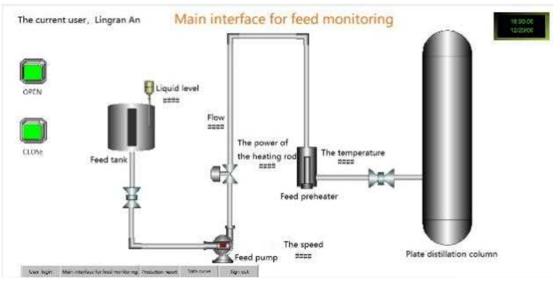

Fig.4. The main monitoring interface after login

6. Summary and prospect

This design adopts DCS control system based on programmable controller Siemens S7-200. Its contents mainly include the overall scheme design of the feed part of the rectification process control system and the design of hardware and software.

The detection and control points selected in this design are for the feed part of the rectification process, and the complete rectification process should also include the reflux part and the reboiler part. Therefore, the selection of parameters, algorithms, software and hardware is relatively simple and cannot meet the complete rectification control requirements. Adaptive control algorithm, predictive control algorithm, inferential control algorithm and robust control algorithm can be developed for the complete rectification control, or intelligent control methods such as neural network and fuzzy control can be considered for the rectification column.

Acknowledgement

The research is partly supported by the "13th Five-Year" comprehensive investment and basic research business fee items of China (000040192).

References

1. Fuxue Liu, Research and application of rectification column, *Chinese Petroleum and Chemical Standards and Quality*, 2011, 9: P199.
2. Chuanbo Yu, Correctly understand the proper feed position and q value of rectification column, *Higher Education in Chemical Engineering*, 2008, 2: P60-P68.
3. Kejing Li, Briefly discuss the design of process control scheme of rectification column, *Petrochemical Industry Application*, 2013, 9: P120-P124.
4. Xueyong Shi, Realization of PID control in the liquid level of distillation tower kettle, *Science and Technology Economic Guide*, 2017, 3: P72.
5. Jianfang Jiang, Siemens S7-200 PLC engineering application technology tutorial, *China Machine Press*, 2010: P184-P197.
6. Huailin Zhao, Masanori Sugisaka, Leilei Cui, Guanglin Shi, Research on the intelligent control algorithm for a soft joint actuated by Mckibben muscles, *Artificial Life and Robotics* (ISSN1433-5298), Vol.14, No.1, 2009, P85-P88.
7. Yahui Mu, The practical technology of Kingview software, *Yellow River Water Conservancy Press*, 2012: P34-P35.

Ultrasonic Range Finder for Vehicle Collision Avoidance System

Ying Chen[1], Guowei Yang[1], Fengzhi Dai[1*], Yuxuan Zhu[1], Di Yin[1], Yasheng Yuan[1],Yiqiao Qin[12], Ce Bian[12], Chengcai Wang[3], Xinyu Zhang[1]

[1] *College of Electronic Information and Automation,*
Tianjin University of Science and Technology,China

[2] *Tianjin Tianke Intelligent and Manufacture Technology CO.,LTD, China*

[3] *CETC Ocean Information Co., Ltd, Beijing 100041, China)*
*E-mail: * daifz@tust.edu.cn*
www.tust.edu.cn

Abstract

In recent years, highway rear-end collision accidents have occurred frequently, causing huge personal injury and property damage. Protective measures such as seat belts and airbags only serve to reduce damage afterwards and do not solve the problem from the source. Therefore, research on the system of vehicle collision avoidance, which actively avoids accidents, is of great significance. The ultrasonic range finder designed based on AT89C51 single-chip microcomputer utilizes the principle of sound wave reflection in the air. It can detect the distance between the vehicle and the obstacle in real time, and immediately alarms beyond the set threshold. Ultrasonic ranging is widely used in automotive anti-collision systems due to its non-contact detection method and simple structure.

Keywords: Ultrasonic, Vehicle collision avoidance, AT89C51, Distance detection

1. Introduction

Traffic accidents caused by vehicles are one of the most influential factors in human society. On average, one person in the world died of road traffic accidents every 60 seconds, and one person was injured in a road accident every 5 seconds.[1] Road traffic safety has become a concern of all countries in the world.

When the whole world is threatened by road traffic accidents, airbags, seat belts and other devices are beneficial to reduce the harm of people in traffic accidents, but they are passive anti-collision measures for emergency protection after the event, and the effect is small, and Personal injuries and economic losses will still occur after the accident.

Therefore, with the development of the computer and electronical technology, it is an irresistible trend to make the multiple intelligent agents cooperate with each other to complete a specific complex task.[2] Research on the car collision avoidance system that can play an active protective role is very urgent. This design is mainly applied to the anti-collision system based on the ultrasonic ranging method. Ultrasonic ranging is not affected by light, surrounding magnetic fields, or gas properties compared to other methods. Especially in the air, due to the slow circulation speed in the air, the echo signals contained in the direction of structural information transmission are easy to detect, the resolution is high, and the accuracy is higher than other methods. Has a broad market development prospects and practicality of life.

2. Hardware selection

The system is divided into ultrasonic transmitting module, signal receiving module, single chip processing module, LED display and sound and light alarm module.

The ultrasonic ranging system adopts the transmission and reception separation method. The transmission and reception separation have two advantages: one is that the transmission and reception signals do not overlap, the pure reflection signal is received by the probe; the second is that the receiving probe is selected at a suitable position to prevent The loss and interference caused by the reflected object on the ultrasonic surface enhances the reliability of the system. According to design requirements and comprehensive factors, TCT40-16T/R ultrasonic distance sensor (T is the transmitting sensor and R is the receiving sensor). At the same time, the main controller selects AT89C51 microcontroller, LED digital display adopts dynamic scanning mode.

2.1. Main control chip

The main chip uses the low-power, high-performance 8-bit microcontroller AT89C51 chip as the main controller of the ultrasonic ranging system. The chip contains 4kBytes ISP, which can repeatedly erase 1000 flash memories. The main features are as follows.

- The 8031 CPU is compatible with the MCS-51;
- Full static operation: 0~33MHz;
- Three program memories;
- Serial channel;
- There are 32 programmable I/O lines;
- Contains 16 16-bit timer/counters;
- 6 interrupt sources;
- Programmable 128 * 8-bit built-in RAM;3

AT89C51 is shown in the Fig.1.

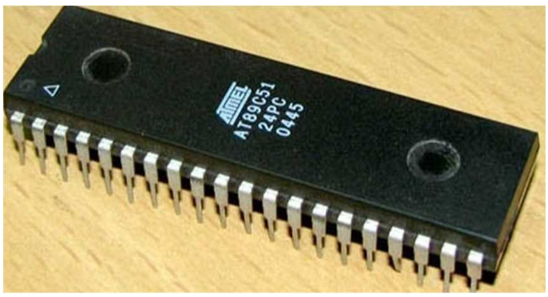

Fig.1. ILI9341 touch screen

2.2. NE555

The 555 timer is composed of three 5KΩ resistors, a voltage divider and voltage comparators C1 and C2, and a basic RS flip-flop and discharge tube TD. The 555-time circuit and external components form a 40kHZ multi-resonant circuit, while the microcontroller controls the output of the NE555 to drive the ultrasonic transducer.

- Frequency 100kHz
- Power supply voltage 4.5V~16V
- Supply current 10mA
- Working temperature 0°C~70°C[4]

NE555 is shown in the Fig.2.

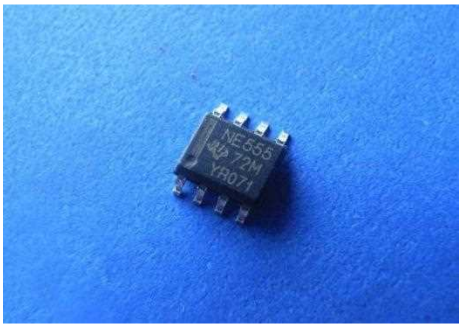

Fig.2. NE555

2.3. CX20106A

Cx20106 is an infrared demodulation integrated circuit produced by Sony Corporation of Japan. It is packaged in 8-pin single-row in-line plastic package. It contains preamplifier, auto-biasing, passband filtering, peak detection and Schmitt shaping output. The function is to demodulate the encoded signal and send it to the microprocessor for processing.[5] the parameters of the pins and the transmission frequency of the corresponding transmitting circuit. CX20106A is shown in Fig.3.

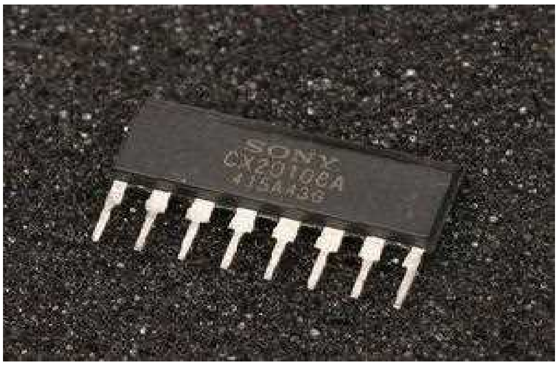

Fig.3. CX20106A

3. System circuit module design

The system circuit is mainly divided into 5 modules.

3.1. Single chip microcomputer and its peripheral circuits

The main chip uses a single piece of AT89C51. The AT89C51 chip and peripheral circuits form the smallest system, which is the central module of the entire ultrasonic ranging system. The 40kHZ transmission frequency is provided to the software for processing by the microcontroller P3.2. After the received echo is processed by the AT89C51 information, the measurement distance is on the LED display, and the data displayed by the P0 port and the port 2 are LED display. The dynamic scanning method is displayed. If the measurement distance is lower than the safety distance set in advance (for example: 1m or 0.5m), the alarm circuit is activated to issue an alarm signal, and the alarm circuit is controlled by the P2.4 buzzer output port.

3.2. Ultrasonic transmitting circuit

The ultrasonic transmitting circuit needs to output an electrical signal during operation to enable the ultrasonic transducer to emit ultrasonic waves. In order to increase the transmission capacity of the ultrasonic wave, it can be transmitted over a longer distance. It is necessary to increase the voltage of the signal.[6] Therefore, the ultrasonic transmitting portion mainly includes a square wave generator and a boosting circuit. At the same time, the microcontroller is used to control the NE555, and the 3-pin output is used to drive the ultrasonic transducer.

3.3. Ultrasonic receiver module

The ultrasonic receiving circuit can amplify, filter and shape the weak electric signal received by the ultrasonic probe, and output a step signal, prompting the AT89C51 to calculate the ultrasonic transmission time interval t in the air. The echo signal shaping is output as a square wave signal, and then input to the input terminal P3.2 of the external interrupt 0 of the microcontroller, and the specific time of receiving the ultrasonic echo is calculated to determine the propagation time t of the ultrasonic wave in the air.

3.4. Display circuit

This design uses a four-in-one common anode digital tube SM410564 as a display device. The most common one is the P0 port, the common end of the P2 port P2.0 --- P2.3 vfour pins, because the driving capacity of the P2 transistor is limited, so the digital tube is not directly connected to the public port P2, but can pass P2 The port controls three transistors to turn the digital tube power on and off.

3.5. Ultrasonic receiver module

Connect the speaker, transistor and resistor to the P23 microcontroller pin, and the other end of the buzzer is grounded to form an audible alarm circuit.

4. Test results and summary

Real distance (m)	0.2	0.5	1.0	2.0	4.0	5.0
Measuring distance (m)	0.22	0.52	0.99	2.02	4.03	4.96
Error (m)	0.02	0.02	-0.01	0.02	0.03	-0.04

It can be seen that the ultrasonic can guarantee the accuracy of the measurement within a certain measurement range. As the distance of the obstacle increases, the detection sensitivity of the ultrasonic ranging system will decrease, and the measured distance will have an error. After the actual test, the error range is kept around 3 to 5 cm, which is negligible in the automobile collision avoidance system.

The ultrasonic sensor is used to convert the distance information into an electrical signal and transmit it to the working module for processing. Timely detection of the distance between the vehicle and the obstacles in front of the vehicle and behind the vehicle is a novel active safety protection system. The NE555 timer and CX20106A demodulator used in the design improve the measurement accuracy and intelligence of the system. In addition, the alarm device is inexpensive and easy to install. The designed ranging system has low cost, good performance and practicality. It's handy to operate.

Acknowledgement

The research is partly supported by the "13th Five-Year" comprehensive investment and basic research business fee items of China (000040192).

References

1. Zuohan Wang, Reducing Traffic Accidents: More Active and Passive Safety Technologies Need to Be Adopted, *Commercial Vehicles,* 2010, 4: p96 - p97.
2. Huailin Zhao, Yangguang Guo, Masanori Sugisaka, Design of the Multi-Car Collaboration System, *the 2017 International Conference on Artificial Life and Robotics (ICAROB 2017), Jan. 19-22, 2017*, Miyazaki, Japan, p186 - p190.
3. Xuemei Dian, Application of Ultrasonic Ranging in Automobile Reverse Collision Avoidance System, Artificial Intelligence and Identification Technology, 2007, 10: p83～p85.
4. Xinghua Peng, *Research and application of ultrasonic range finder* (Hubei, Hubei University, 2013)
5. Chengjian Lu, *Functional Model of 555 Timer and Its Application*（Yulin, Journal of Yulin Teachers College, 2006)
6. Derong Tan, Yuanjie Wu, *Research on Key Technologies of Vehicle Anti-collision Collision Active Safety System* (Taiyuan: Taiyuan University of Technology, 1998)
7. Lei Li, Honghao Hu, *Ultrasonic Sensor Design Based on AT89C51 Single Chip Microcomputer* (Shanghai: Fudan University, 1999)
8. Guirong Qu, Principle and Maintenance of Infrared Demodulator CX20106A (Beijing: Institute of Electronic Design, University of Science and Technology Beijing, 1997)
9. Hongtao Tan, Xueping Zhang. The principle of single-chip design range finder and its simple application, *Journal of Computer Applications*, 2004, 18: p94 - p95.

Chaos synchronization method of Qi system and the circuit design

Xia Jin[1], Fengzhi Dai[1*], Zhongyong Ye[1], Lingran An[1], Yujie Yan[1], Chenglin Zhao[1], Yiqiao Qin[12], Hao Li[3]

[1]College of Electronic Information and Automation, Tianjin University of Science and Technology, China

[2]Tianjin Tianke Intelligent and Manufacture Technology CO.,LTD

[3] CETC Ocean Information Co., Ltd, Beijing 100041, China

daifz@tust.edu.cn

Abstract

Chaos is a kind of uncertain and random phenomenon that appears in the system. Its dynamic characteristics are rich and interesting. The study of the dynamic characteristics and synchronization methods of Qi chaotic systems has fascinated many researchers. In this paper, the dynamic characteristics of Qi chaotic system are analyzed, and the synchronization circuit of Qi chaotic system is designed based on driving-response chaotic synchronous system and single-variable feedback perturbation synchronous system, The synchronization circuits of Qi chaotic system are designed respectively, comparing the synchronization curves of the variables simulated by Multisim and the numerical simulation curves obtained by MATLAB, Verifying the correctness of the built circuit., and analyze the advantages and disadvantages between above the two synchronization methods.

Keywords: Qi system, Chaotic synchronization, Circuit simulation, DSP builder

1. Introduction

The term chaos originally represented the state of the universe when it was not formed. For the origin of the universe, many astronomers firmly believed that the chaos theory stated that the universe gradually evolved from the initial chaotic state to the vast space full of laws and theorems today. Chaos is a random phenomenon that appears in a nonlinear system that determines the system. Chaos is unpredictable and uncertain, but what is interesting is that it can also be expressed in simple formulas. More and more people begin to study its related characteristics and strive to apply it to real life. As chaos is separated from physics into a single discipline[2], more and more research results have enriched people's vision. People are more convinced that chaos research will have a positive and far-reaching impact on human production and life in the near future.

2. Chaotic synchronization

Chaotic synchronization[3], that is, two systems with different initial conditions, whose orbits change with time and merge into one orbit. Chaotic synchronization can also be said to be a kind of chaotic control. So far, people have found that a variety of synchronization methods have been studied, and these synchronization methods have continuously promoted the application of chaotic systems. These methods can achieve good results in chaotic synchronization. In this paper, the two methods control of driving response and univariate coupling control[1] are used to design the synchronization circuit of Qi chaotic system. The correctness of the two synchronization methods is proved by analyzing the simulation results. And compare the two synchronization methods, and give the method and theoretical support for the application based on Qi chaotic system.

3. Driver response synchronization for Qi chaotic systems

This section synchronizes the driving response of the Qi chaotic system, and builds the modeling diagram based on the DSP builder in the FPGA development module[7]. Let the continuous differential equations of the Qi chaotic system be:

$$\begin{cases} \dot{x_1} = a(y_1 - x_1) + y_1 z_1, \\ \dot{y_1} = c x_1 - y_1 - x_1 z_1, \quad (1) \\ \dot{z_1} = x_1 y_1 - b z_1, \end{cases}$$

In this paper, the y variable is used as the driving signal, and the x variable is used as the driving response signal. Use the DSP builder module to draw the modeling diagram in the Simulink template as follows:

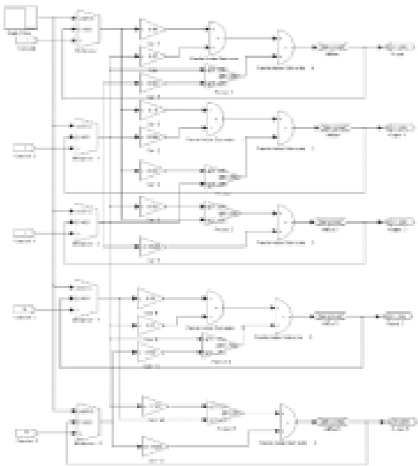

Fig.1.Synchronous modeling of driving response with Y as the driving variable

The initial value of the drive system is (1, 1, 1) and the initial value of the response system is (10, 10). The modeling diagram is simulated to obtain the chaotic trajectory curves of the two systems x and z variables as shown in the following figure.

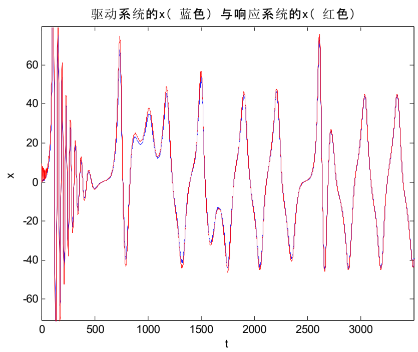

Fig.2. Chaos trajectory of variable X in both systems

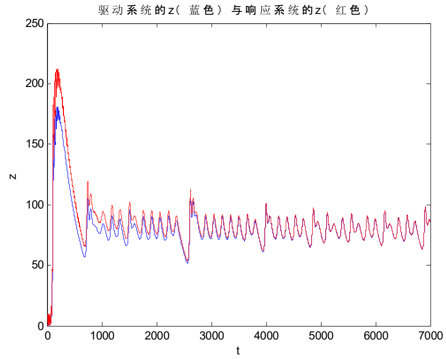

Fig.3. Chaos trajectory of variable Z in both systems

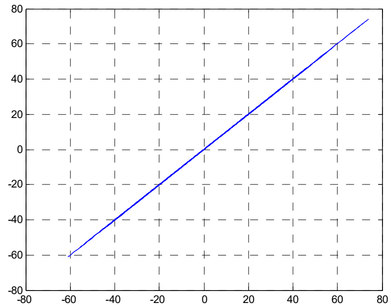

Fig.4.State synchronization diagram of variables X in both systems

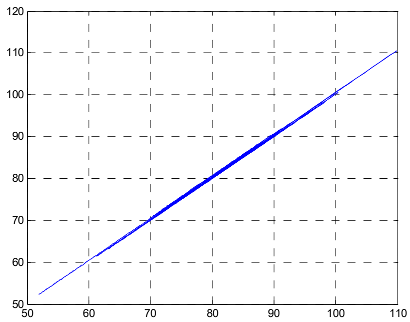

Fig.5. State synchronization diagram of variables Z in both systems

It can be seen from the above figure that the chaotic trajectory[4] of the drive system and the response system is synchronized after a period of time, and the synchronization time between the two system x variables is very short, the state synchronization diagram shows a complete 45 degree slash, and the two system z variables Although it can be synchronized, but the synchronization time is relatively long, the 45-degree diagonal line displayed in the state synchronization diagram has a prominent part, which is incoherent, and the actual synchronization effect is not as good as the synchronization effect of the x variable. The synchronization effect of the response system variable x is shorter than the synchronization effect of the variable z, and the synchronization time is short and the precision is high. Therefore, if the variable y is selected as the driving signal for the synchronization of the driving response of the Qi system, the x variable is used as the effective signal for practical application.

4. Univariate coupling synchronization for Qi chaotic systems

In this section, the univariate coupling synchronization[5] of the Qi chaotic system is performed, and the y variable perturbation is used for synchronization.

The response system is:

$$\begin{cases} \dot{x_2} = a(y_2 - x_2) + y_2 z_2, \\ \dot{y_2} = cx_2 - y_2 - x_2 z_2 + k(y_1 - y_2), \\ \dot{z_2} = x_2 y_2 - bz_2, \end{cases} \quad (2)$$

Design the analog circuit using Multisim as shown in the figure below:

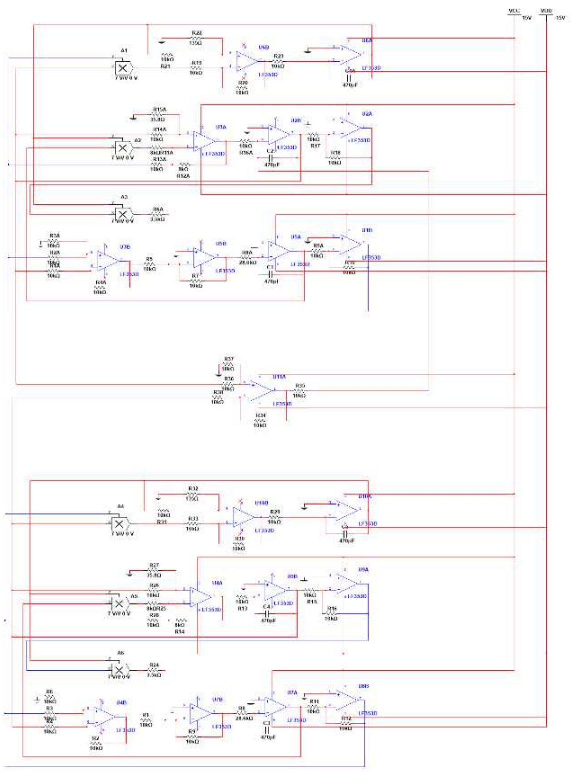

Fig.6.A circuit that synchronizes with a Y variable perturbation

The feedback gain is taken as 100, and the Matlab simulation diagram is as follows:

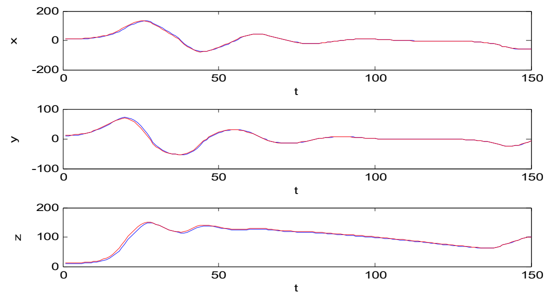

Fig.7.Two systems X, Y, Z variable trajectory

According to the simulation diagram, this synchronization method is effective, and the two systems can be synchronized, the synchronization time is less than 50, and the synchronization precision of the x variable is high, and the synchronization time is short. The corresponding variables of the drive system are subtracted from the corresponding variables of the response system, and the error graph and state synchronization diagram are obtained for the circuit simulation. The results are shown in the following figure:

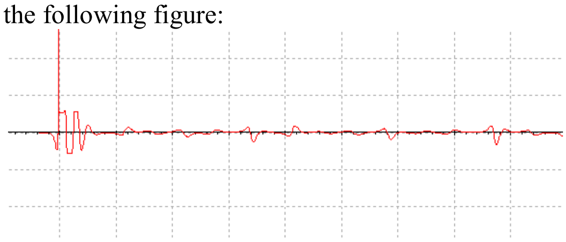

Fig.8.X1-x2 error graph

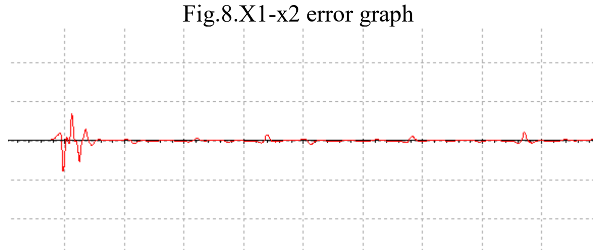

Fig.9.Y1-y2 error graph

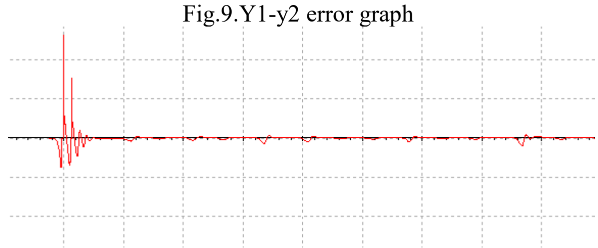

Fig.10.Z1-z2 error graph

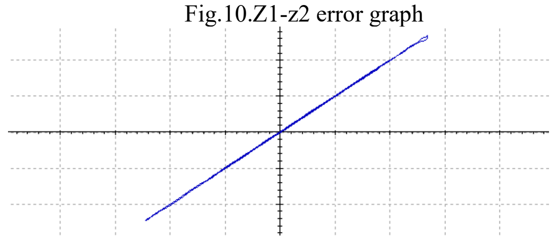

Fig.11. State synchronization diagram for variable x1-x2

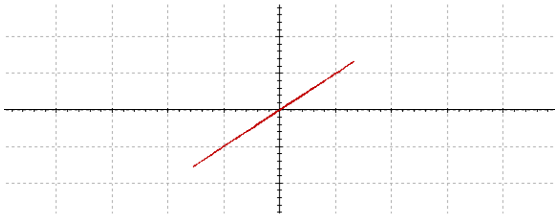

Fig.12.State synchronization diagram of the variable y1-y2

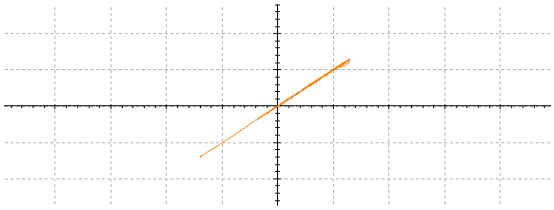

Fig.13. State synchronization diagram of the variable z1-z2

It can be seen from the synchronization error graph between the three variables of the two systems that the perturbation with the variable y can synchronize the two Qi chaotic systems. By observing the state synchronization diagram of the three variables in the dynamic process, the state synchronization diagram of the x variable is uniform with the state synchronization diagram of the other two variables, and the 45degree diagonal line is uniform, although there are errors at both ends of the oblique line, but the oblique line Obvious and precise, it proves that the synchronization effect is good. The 45-degree slash of the y variable's state synchronization diagram is clearly visible and the synchronization effect is also good. The state synchronization diagram of the z variable has a very thin slash at the lower left end, but the upper right end is very thick, the distribution is uneven, and the synchronization effect is not good. The Lyapunov exponent calculated by Matlab is $\lambda_1 = -14.9805$, $\lambda_2 = -28.3155$, $\lambda_3 = -95.3522$. The conditional Lyapunov exponent with all negative values proves that the two chaotic systems can reach the synchronization state.

5. Testing and conclusion

By comparing the driving response synchronization method with and univariate coupling synchronization method, it can be seen that the driving response[6] synchronization method is simple and easy to understand. For the synchronization of the Qi chaotic system, the operation is convenient and easy to succeed, and the final result is also ideal, but in the face of other indecomposable system is powerless and has certain limitations. The univariate coupling synchronization method is applicable widely, without decomposing the system, high synchronization precision and high speed, but the feedback coefficient k needs to be researched and obtained, and at least two variables need to be feedback perturbed when facing a hyperchaotic system. Increased the complexity.

References

1. Zhong Q, Zhang C. Chaos Control of a New Chaotic Dynamical System and Its Application. Lecture Notes in Electrical Engineering, 2014, 163:1465-1472.
2. Chen Y, Li S G, Liu H. Synchronization of fractional-order chaotic systems based on adaptive fuzzy control. Acta Physica Sinica, 2016.
3. Nijmeijer H J C H. Nonlinear chaos control and synchronization. Handbook of Chaos Control, Second Edition. Wiley - VCH Verlag GmbH & Co. KGaA, 2007.
4. Yong-Jian L. Combined Synchronization Control of Hyper-chaotic Systems. College Mathematics, 2011.
5. Zelinka I, Senkerik R, Navratil E. Investigation on realtime deterministic chaos control by means of evolutionary algorithms. IFAC Proceedings Volumes, 2006, 39(8):190-196.
6. Senkerik R. Optimization of feedback control of chaos by evolutionary algorithms. Analysis & Control of Chaotic Systems. 2006.
7. Tuna M , Can Bülent Fidan. Electronic circuit design, implementation and FPGA-based realization of a new 3D chaotic system with single equilibrium point. Optik - International Journal for Light and Electron Optics, 2016, 127(24):11786-11799.

Design of Air Quality Monitoring Platform Based on Internet of Things

Yujie Yan[1], Fengzhi Dai[1*], Kailun Zhang[1], Wei Wang[2], Jialin Han[1], Yang Li[3], Tianyi Zhang[1]

[1] College of Electronic Information and Automation,
Tianjin University of Science and Technology, China

[2] Department of Electronic and Control Engineering,
North China Institute of Aerospace Engineering , China

[3] CETC Ocean Information Co., Ltd, Beijing 100041, China
*E-mail: * daifz@tust.edu.cn*
www.tust.edu.cn

Abstract

The air quality monitoring platform based on the Internet of Things (IoT) uses the STM32f407 main control module. Data such as temperature, humidity, PM2.5 and carbon monoxide concentration in the atmospheric environment are collected for a long time by each sensor module. Not only the system has the LCD display function, users can also log on to the ESLINK IoT cloud platform to remotely observe the data collection status. The upper limit of each parameter can be set in a specific environment. If the data monitored by the system exceeds the upper limit, the system will alarm. The system has a good application prospect in the environment of office, automobile, factory and so on.

Keywords: Internet of Things, STM32f407, PM2.5, sensor

1. Introduction

With the development of industry, environmental problems have become more and more serious, especially air pollution has seriously affected people's lives. Traditional meteorological monitoring stations are bulky, susceptible to environmental and time constraints, and their communication networking costs are high and deployment is difficult. At present, it is hoped that a low-cost portable atmospheric monitoring device can obtain air quality information in real time. The monitoring equipment can be accurately monitored in the home, in the car, in the workplace[1], etc.

The air quality monitoring platform developed by this design can be applied to various occasions, and can monitor the temperature, humidity, PM2.5, CO and other concentration changes in the air in real time, and can monitor the current data information on the LCD screen and terminal equipment. The system has an alarm function, and when a certain parameter exceeds the set range, it can immediately alert the user. The system has low cost, high precision, convenient use and certain market application prospects.

2. Hardware structure design

The hardware data acquisition part mainly uses each sensor node to monitor the atmospheric environment quality in real time, and transmits the detected environmental data information to the network layer in real time, and displays it on the LCD display in real time. The environmental monitoring hardware system uses STM32F407 as the main control chip for signal processing, and each sensor module performs sensing signal extraction. The signal conditioning circuit shapes, amplifies, and filters the circuit waveform to condition the data into a signal that the microprocessor can process.

The A/D signal acquisition module performs signal acquisition, and the MCU part performs signal processing analysis. The overall hardware design of the system is shown in the Fig.1.

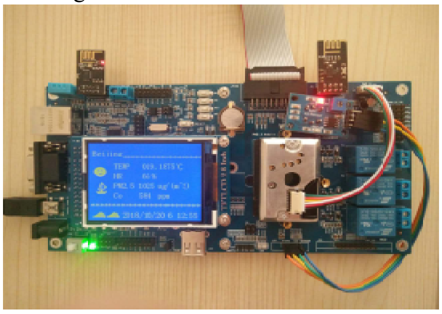

Fig.1. Hardware design of the system

2.1. STM32F407 master chip

The main control chip adopts high-performance 32-bit ARM M4 architecture series chip STM32F407. The chip's clock speed is up to 168MHz, integrating single-cycle DSP instructions and floating point units. The processing capacity is up to 210DMIPS, which is about 200 times that of a normal 8-bit microcontroller.

2.2. Wireless Communication Technology

The wireless communication technologies currently used in the market include Bluetooth technology, Zigbee technology, and WIFI technology. WIFI (Wireless Fidelity) is a certification standard for wireless LAN products consisting of Access Point and wireless network cards[2]. WIFI technology is easy to integrate with existing wired Ethernet networks[3].

The ESP8266 is an ultra-low power UART-WIFI pass-through module designed for mobile devices and IoT applications. The user's physical device can be connected to a WIFI wireless network for Internet or LAN communication for networking. The hardware schematic is shown in the Fig.2.

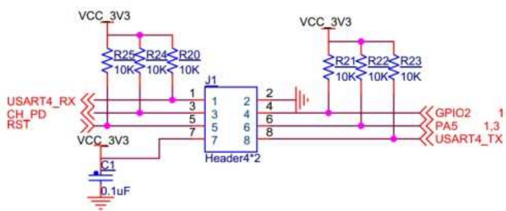

Fig.2. WIFI hardware schematic

2.3. Humidity sensor module

This design uses the DHT11 temperature/humidity sensor, which is a temperature and humidity composite sensor with a calibrated digital signal output. It uses dedicated digital module acquisition technology and temperature and humidity sensing technology to ensure high reliability and stability[4]. The sensor consists of a resistive wet sensor and an NTC temperature sensor connected to a high performance 8-bit microcontroller. The calibration coefficients are stored in the OTP memory as a program, and these calibration coefficients are called internally during the processing of the detection signal. The single-wire serial interface makes system integration easy and fast. The product is a 4-pin single-row pin package for easy connection. The circuit principle of DHT11 interface is shown in the Fig.3.

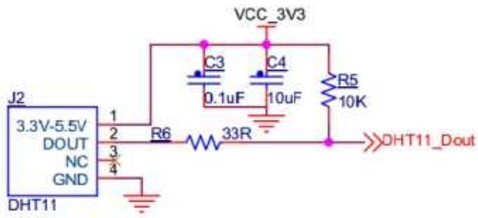

Fig.3. DHT11 hardware schematic

2.4. Carbon monoxide collection module

This design uses the MQ-7 carbon monoxide concentration monitoring sensor, which is a dual signal output (analog output and TTL level output). The TTL output valid signal is low level (when the output is low, the signal light is on, it can be directly connected to the single chip); the analog output is 0~5V, the higher the concentration, the higher the voltage[5]. The sensor has high sensitivity and good selectivity to carbon monoxide, and has a long service life and reliable stability. The MQ-7 sensor hardware schematic is shown in the Fig.4.

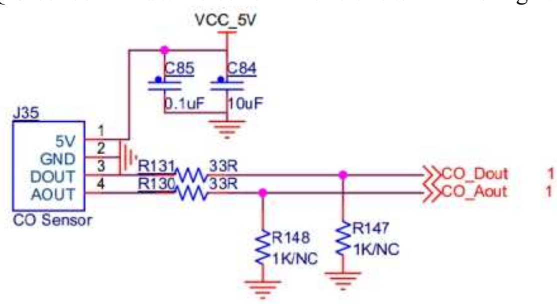

Fig.4. MQ-7 sensor hardware schematic

2.5. Temperature acquisition module

With the DS18B20 temperature sensor, only one port line is required to connect the microprocessor to the two-way communication between the microprocessor and the DS18B20. The working power supply is 3.0~5.5V/DC, no external components are needed in use; the measurement results are serially transmitted in 9~12 digits; multi-point networking function is supported[6]. To achieve multi-point temperature measurement, if the number is too much, the power supply voltage will be too low, resulting in unstable signal transmission. The hardware schematic of the DS18B20 temperature sensor is shown in the Fig.5.

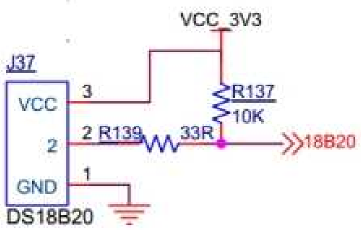

Fig.5. DS18B20 temperature sensor

2.6. PM2.5 acquisition module

The GP2Y1010AU0F optical dust concentration detection sensor is designed to sense dust particles in the air. An infrared light-emitting diode and a phototransistor are placed diagonally inside, so that it can detect the reflected light in the air. Even very small particles such as tobacco smoke can be detected, and tiny particles of 0.8 micron or more can be measured to perceive phlegm and pollen produced by tobacco, house dust and the like. The sensor has a very low current consumption and can be used up to 7VDC. The sensor output is an analog voltage whose value is proportional to the dust concentration. The hardware schematic is shown in the Fig.6.

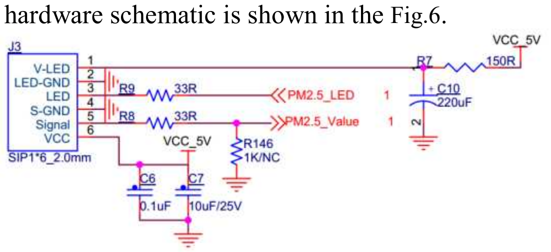

Fig.6. GP2Y1010AU0F hardware schematic

2.7. LCD display module

The LCD9341 with 320*240 pixels displays the data collected by each sensor. Generally, there are three ways to connect the liquid crystal display to the main chip: serial port connection, SPI bus connection and SRAM memory interface. The LCD panel of the project development board uses the SRAM interface, which is equivalent to the LCD connected to the memory interface of the main chip. Therefore, accessing the LCD is equivalent to accessing the memory of the main chip by accessing the three buses (data bus, address bus and control Bus) implementation. The hardware schematic of LCD9341 is shown in the Fig.7.

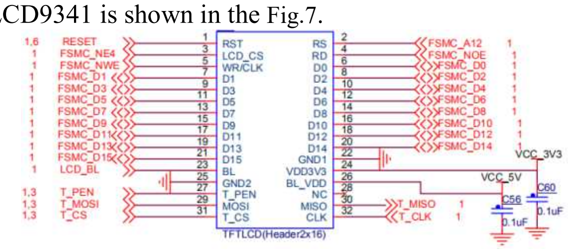

Fig.7. The hardware schematic of LCD9341

3. Software design

3.1. Temperature acquisition humidity realization

The temperature sensor DS18B20 is a digital temperature sensor that does not require AD conversion. The sensor converts temperature to digital up to 93.75ms at 9-bit resolution and temperature to up to 750ms at 12-bit resolution for even more accurate results. This design selects 12-bit data representation. The upper 5 bits are sign bits, the lower 4 bits are fractional parts, and the others are integer bits. After parsing this data, the temperature is obtained. According to the read and write timing of the DS18B20, the program realizes the reset, initialization, read and write data of the sensor and the conversion function of the read data.

3.2. Program implementation of humidity acquisition

The humidity sensor DHT11 is also a digital temperature/humidity sensor that does not require AD conversion. DHT11 should use the GPIO port of the MCU for initial configuration, set the required GPIO port pin (PA4) to general push-pull output, no pull-up pull-down, 50MHz output mode, so that the DHT11-DATA pin of the MCU is set to none. Pull-up pull-down input mode. The single-bus data format communication between the microprocessor and the DHT11 takes about 4ms. The data is divided into fractional part and integer part. The complete data transmission is 40bit, and the high position is first out. After the user MCU sends a start signal, the DHT11 switches from the low power mode to the high speed mode. After waiting for the host start signal to end, the DHT11 sends a response signal, sends 40 bits of data, and triggers a signal acquisition, and the user can select to read part of the data.

3.3. Program implementation of carbon monoxide and PM2.5 acquisition

The mq-7 and GP2Y1010AU0F for collecting carbon monoxide and PM2.5 are analog sensors, and the output is analog, so the acquired analog signal needs to be converted into a digital signal. There are 3 ADCs in the STM32F407zgtx, a total of 24 channels, each ADC is 12 bits, corresponding to the converted digital range from 0 to 4095. In this project, for MP2.5, channel 10 of ADC1 is selected; Co selects channel 4 of ADC3. When programming the ADC converter, it includes several functions such as initialization, turning on AD conversion, waiting for the end of AD conversion, and obtaining the conversion result.

3.4. Program implementation of wireless communication module

Software programs include WIFI initialization functions, connect WIFI, establish connections, disconnect, and send data functions. A macro API_KEY defined in the program is the connection key obtained after the cloud platform is successfully registered. After the module initialization is completed, the WIFI connection is implemented by the customized esp8266_link_wifi() function, where the first parameter of the function is the network name to be connected, and the second parameter is the connection password. The status of the corresponding device in the ESLINK IoT cloud platform is obtained by the download_sensor_status() function. The parameters of the function include the IP address of the connection route, one or more device numbers, and API_KEY. Upload the data collected by each sensor to the cloud platform through the upload_device_datas() function. The function has six parameters: the IP address of the connection route, the device number, the API_KEY, the array of sensor numbers, and the data collected by each sensor. The array and size are composed.

4. Conclusion

After the system is running, the actual changes of each parameter can be monitored on the IoT cloud platform. Take the data waveform monitored by the temperature sensor as an example, as shown in the Fig.8. It can be seen that the system can monitor temperature changes and generate waveforms in real time over a certain period of time.

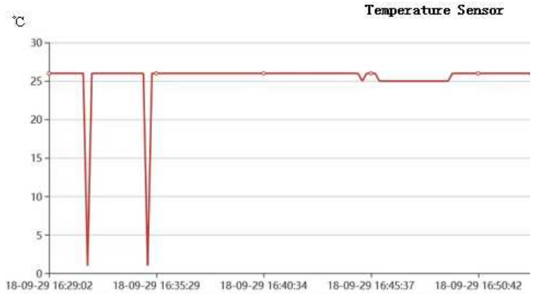

Fig.8. Temperature data waveform

Acknowledgement

The research is partly supported by the "13th Five-Year" comprehensive investment and basic research business fee items of China (000040192).

References

1. Hongyu Xu, Huangfei Shen. Design of multi-point temperature detection system based on STM32. *Electronic Science and Technology*, 2016, 5: P158-P161.
2. Jincheng Wu, Chengcheng Zeng, Jingrui Sun. PM2.5 Monitoring System Based on STM32F407 Wireless Intelligent Network. *Journal of Tianjin Normal University*, 2017, 6: P62-P66.
3. Huailin Zhao, Shunzhou Wang, Yunxiang Liu, Xuyao Hao, Design of an Intelligent Housekeeping Robot Based on IOT, *Journal of Information and Communication Engineering*, Vol.2(2), 2016, P114-P118.
4. Na Liu, Temperature and Humidity Measurement and Control System Based on ZigBee Module Granary. *Microcontrollers & Embedded Systems*, 2016, 5: P69-P72.
5. Xiaoping Ding. Design and Research of CO Detection and Alarm System Based on Wireless Network (Jiangsu, Suzhou University, 2013)
6. Kai Li, Chen Xu, Research on temperature controller design based on DS18B20. *Science and Technology Innovation*, 2018, 7: P163-P165.

Design of Metal Weld Seam Tracking Equipment Based on Image Processing

Yujie Yan [1], Fengzhi Dai [1*], Lingran An [1], Xia Jin [1], Zhongyong Ye [1], Yufan He[2], Xinran Guo[3]

[1] *College of Electronic Information and Automation, Tianjin University of Science and Technology, China;*

[2] *CETC Ocean Information Co., Ltd, Beijing 100041, China*

[3] *School of Government, Nanjing University*

*E-mail: * daifz@tust.edu.cn*
www.tust.edu.cn

Abstract

With the development of the intelligent industry, metal automatic welding technology needs to be more popular. The metal weld seam tracking device based on image processing includes two parts of image processing and motion control. The image processing part is developed by the Visual Studio 2013 platform, and the motion control part is controlled by the PID algorithm. Machine vision technology can be used to convert images captured by industrial cameras into vector graphics, which in turn drive the welding table to track metal welds. The device has good control effect and can be well applied in small and medium-sized enterprises.

Keywords: automatic welding, image processing, Visual Studio 2013, motion control, PID

1. Introduction

In the traditional welding industry, most welders use manual welding methods. And because of the large amount of smoke, arc and high temperature generated during the welding process, this will directly damage the welder's health. Moreover, the manual welding operation is labor intensive, and it is difficult for the welder to ensure the welding quality under a long working condition[1].

The development of industry has promoted the rise and application of automatic welding technology. Currently, teaching welding robots are the most widely used. However, the welding process is easily affected by many factors, and the complex products processed by the teaching-type welding robot are difficult to meet the process precision. The intelligent weld seam tracking device designed in this paper can collect the image information of the workpiece to be welded by industrial camera. A weld seam edge vector that can be recognized by the control system is obtained by image processing techniques. Finally, the motion control system controls the welding table motion based on the weld edge information to achieve automatic tracking and tracing of the weld. The device has high control precision and can be applied to small and medium-sized enterprises, and has certain market prospects.

2. The hardware structure design

The overall frame of the automatic seam tracking equipment is made of aluminum alloy and iron alloy, and the equipment is equipped with hardware such as industrial cameras and lenses. The control part is composed of STM32F407 main control board, three stepping motors and motor drive. Three stepping motors control the X, Y and R axes respectively. Two motors control the X and Y axes for two-dimensional linear motion, and one motor controls the R axis for planar rotation motion to achieve three-degree-of-freedom motion control. The mechanical structure model of the automatic seam tracking equipment established by SOLIDWORKS modeling software is shown in Fig.1.

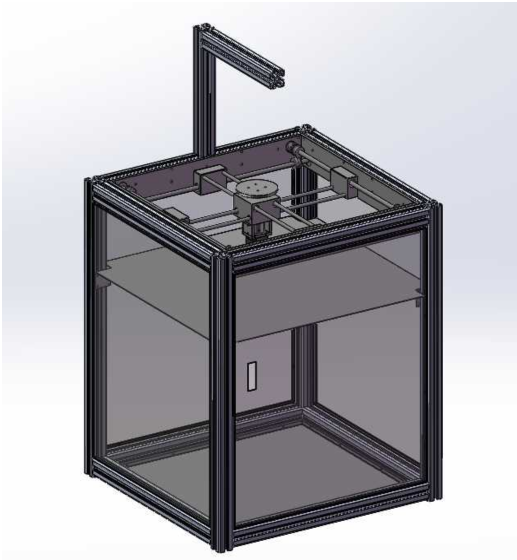

Fig.1. The design of the mechanical structure model

2.1. Industrial camera module

Industrial camera is one of the important modules of image acquisition system. Its performance will directly affect the quality of the captured weld image, which will affect the subsequent image processing. Industrial cameras work by capturing a pattern with weld information, converting the pattern signal into a digital signal, and finally storing it on a computer as a digital signal[2].

Industrial cameras can be divided into CCD (Charge Coupled Device) cameras and CMOS (Complementary Metal Oxide Semiconductor) cameras. Among them, CMOS cameras have a large light sensing range and low cost, and have good guarantees in terms of safety, radiation resistance and transmission speed. This design uses DH-HV3151UC industrial camera, as shown in Fig.2. This camera belongs to the USB2.0 series of cameras, with high resolution and clarity. It does not require an additional image capture card during use, and it is very convenient to communicate with the computer.

Fig.2. DH-HV3151UC industrial camera

2.2. Camera lens module

The lens is very important to the camera, no lens camera can not shoot any information. The lens is composed of a series of prisms. The incident light passes through the prism group, and a series of transformations such as convergence focus occurs, and finally an image is formed on the photosensitive element. The optical system of the lens is very important for the control of light, and the photosensitive element is also imaged by the transformed light. Therefore, the choice of lens will have a direct impact on the quality of the image captured by the system. When selecting the lens of an industrial camera, the following parameters are mainly considered: focal length, resolution, depth of field, aperture. In this design, the industrial camera mainly collects images of metal workpieces that need to be welded for subsequent image processing. Therefore, the M0824-MPW2 fixed focus lens is used here, as shown in Fig.3.

Fig.3. Camera lens module

2.3. Stepper motor selection

The stepping motor converts the pulse signal into angular displacement or linear displacement, rotates according to the set angle, and runs step by step according to the received pulse signal. When the motor is working normally, only the number and frequency of the pulse signals will affect its motion, regardless of the load. The number of pulse signals affects the angular displacement of the motor, and the frequency of the pulse signal affects the speed and acceleration of its rotation, thereby regulating and positioning the system[3].

According to the internal structure of the motor, it can be roughly divided into three types: Variable Reluctance (VR), Permanent Magnet (PM) and Hybrid Stepping (HS). The unit uses a 36GP27B-42H250C13 two-phase hybrid stepper motor to adjust the motion of the entire weld tracking device. Fig.4 shows the appearance of the motor.

Fig.4. Two-phase hybrid stepper motor

2.4. Motor drive module

The stepper motor must be matched to the corresponding motor drive for precise motion. The motor driver divides its motion step angle into several small steps by controlling the phase current of the input motor to realize the subdivision drive[4]. This design uses the matching M420B stepper motor driver, as shown in Fig.5 below. This type of stepper motor driver has the following features:

• High performance, low price, compact form factor and easy installation;

• The power supply voltage is 18~40VDC, and the driving current is 0.25~2A;

• Automatic semi-flow function; maximum dynamic 128 subdivision;

• Photoelectric isolation signal input, motor noise optimization function;

• Bipolar constant current chopping mode with chopping frequency up to 100KHZ.

Fig.5. Motor drive module

2.5. Main control chip

The main control chip adopts high-performance 32-bit ARM M4 architecture series chip STM32F407. The chip's clock speed is up to 168MHz, integrating single-cycle DSP instructions and floating point units. The processing capacity is up to 210DMIPS, which is about 200 times that of a normal 8-bit microcontroller[5]. This allows the automatic seam tracking device to quickly process the acquired information and output the results of the analysis to the actuator.

3. Image acquisition and processing

Before the weld seam is controlled and tracked, image acquisition and processing are first required. Before this, the entire device needs to be initialized. After that, the industrial camera is called to perform image acquisition on the metal characters, and the captured image is read and judged by the computer. If the image fails to be read, the industrial camera needs to be recalled to capture the image and read the image until the image is successfully read.

After successfully reading the target image, it is necessary to perform a series of processing on the image, and finally obtain the vector coordinates of the edge of the image weld. The image processing process mainly includes image denoising of images, threshold segmentation of images, contour extraction and filtering of images, skeleton refinement and extraction of image edges, and final bitmap vectors.

In this design, the collected image is filtered and denoised by a median filtering method, and the denoised welded image is subjected to threshold processing using the Otsu method. The Suzuki85 algorithm is selected to extract the edge of the pre-processed weld image. After the edge image of the weld image is obtained, the skeleton extraction of the image is required, and the Zhang fast parallel refinement algorithm is selected[6]. Since the ultimate goal of image processing is to provide the subsequent weld tracking control system with control information that it can recognize, the edge image of the weld image is finally bitmap vectorized.

4. Weld seam tracking system workflow

After image processing, the control system determines the starting point of the weld to track the weld by identifying and calculating weld vector information. And by controlling the motion trajectory of each coordinate axis, the welding workbench is moved to achieve the purpose of tracking and describing the weld seam. During the seam tracking process, the arm above the device is fixed. During the movement, the welding station can perform the three-axis linkage of the X-axis, the Y-axis and the R-axis according to the motion information provided by the control system. The X-axis controls the left and right movement of the welding table, and the theoretical stroke can reach 1200 mm; The Y axis controls the back and forth movement of the welding table, the theoretical stroke is 1600mm; the R axis rotates by driving the indexing plate. The welding table is driven to rotate, and the indexing accuracy can reach 0.2° . Fig.6 below shows the distribution of each motion axis on the plane of the welding table.

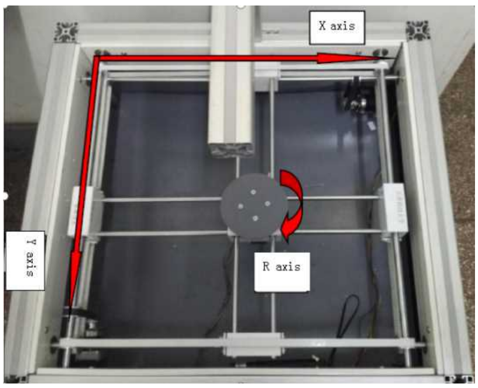

Fig.6. Distribution of each motion axis

Acknowledgement

The research is partly supported by the "13th Five-Year" comprehensive investment and basic research business fee items of China (000040192).

References

1. Zhiwei Luo, Lixiu Li. Research on automatic welding guidance of industrial robot based on vision. *Welding Technology*, 2018, 8: P69-P73.
2. Wenju Zhou, *Research and application of online high-speed detection and precise control based on machine vision* (Shanghai, Shanghai University, 2014)
3. Xiaolei Du. Design of electric lifting window based on AT8989S52 single chip microcomputer. *Mechanical & Electrical Technology*, 2018, 5: P19-P21.
4. Qi Shimeng, Yan Huasong, Huang Wenhui. Design of Robot Gripper Control System Based on Stepper Motor. *Instrument Technique and Sensor*, 2018, 9: P61-P65.
5. Hao Zeng, Wei Zhang, Sikai Zheng. Image Remote Acquisition Terminal Based on STM32F407. *Industrial Control Computer*, 2014, 11: P81-P83.
6. Fengzhi Dai, Jinbin Zhao, Huailin Zhao. The application of resonance algorithm for image segmentation. *Applied Mathematics and Computation,* Vol.194 (2), 2007, P453–P459.

The recognition and implementation of handwritten character based on deep learning

Zhongyong Ye[1], Fengzhi Dai[1*], Xia Jin[1], Yasheng Yuan[1], Lingran An[1], Yujie Yan[1], Yiqiao Qin[12], Hao Li[3]

[1] *College of Electronic Information and Automation,*
Tianjin University of Science and Technology, China;

[2] *Tianjin Tianke Intelligent and Manufacture Technology CO.,LTD, China;*

[3] *CETC Ocean Information Co., Ltd, Beijing 100041, China*
*E-mail: * daifz@tust.edu.cn*
www.tust.edu.cn

Abstract

This paper mainly focuses on the recognition of handwritten characters, especially handwritten Chinese characters. Using deep learning technology constructs a deep convolution neural network to identify the character set of handwritten Chinese characters, compares the performance differences of the same depth network, and finally gets the network structure which can be used for recognition, and realizes the recognition system of handwritten characters based on the network. By comparing with other hand writing characters, the engineering application value of the network structure used in this paper is proved, and finally the handwriting character recognition system based on this model also embodies the feasibility of the network structure in this paper.

Keywords: Deep learning, Machine learning, Pattern recognition, Handwriting character recognition, Convolution neural network

1. Introduction

Deep Learning is a deep-seated network structure based on multiple hidden layers proposed in recent years, which is used to study and deal with some popular problems in the field of machine learning, such as image retrieval and image recognition[1].

At present, although there are more application of deep learning technology to solve the application of handwritten digital character recognition, but in the field of handwritten Chinese character recognition, it is more traditional method based on artificial feature extraction. Because Chinese character strokes are more complex than other common characters English letters or Arabic numerals, and handwritten Chinese characters are more varied because of the different styles and habits of personal writing, Therefore, the recognition of handwritten Chinese character characters has always been a hot research problem in the field of machine learning.

2. Application of deep convolution neural network in handwritten Chinese character recognition

2.1. Data preparation and preprocessing

Because this paper is aimed at the recognition of handwritten Chinese characters, the sample data using handwritten Chinese characters set is also used from the HWDB1.1 database to obtain some of the data samples. In this experiment, the sample data HWDB1.1 divided into 4 sub-datasets, that is, Ten classification, Hundred classification, Thousand classification, 3755 classification of the dataset will be named Set1, Set2, Set3 and Set4 respectively. The composition of each dataset is as follows in table 1.

Table 1 Composition of the data sets

Set name	Writer1	Writer2	Training	Testing	Total
Set1	240	60	2400	600	3000
Set2	240	60	24000	6000	30000
Set3	240	60	240000	60000	300000
Set4	240	60	901200	225300	1126500

In table 1, set name represents the data name of four child datasets, Writer1 that the number of people writing training samples, that is, the sampling source of the training sample, came from a different 240 persons, Writer2 represents the number of people who wrote the test sample, The training column represents the total number of training samples in the dataset, Testing column indicates the total number of samples used for testing in the dataset, and the last column represents the total number of samples used to experiment with the dataset.

2.2. Model structure and its improvement method

The network used in the design of this paper is improved on the basis of Alexnet deep convolution neural network. It contains five convolution layers, 3 of which are followed by a pool layer with a maximum sampling, followed by 3 full-attached layers, and the last Oftma classifier with 1000 output nodes, and if the input layer is not included, the total number of layers of the network reaches 8 layers, the network structure is shown in Fig.1.

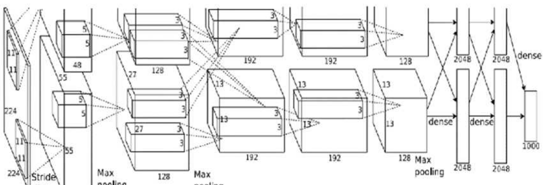

Fig.1. Alexnet Network structure diagram

In this paper, the main improvement of the Alexnet network is to adjust the number of convolution nuclei in the convolution layer, reduce the number of convolution layer, and adjust the number of the full connection layer, according to the performance of their own computer to readjust the network training parameters, the specific improvement is as follows:

1. Reduce the dimension of the input layer from 3 to 1, because for handwritten Chinese characters, the image can be grayscale to get a single-channel picture, it does not have the same as high-resolution natural images, in the RGB three channels have a wealth of information.

2. Change the number of convolution cores in the first convolution layer from the original 96 to 60, and the corresponding pooling layer changes accordingly.

3. Remove the first fully connected layer and connect the final output layer with only one full-connection layer.

4. Change the number of output nodes of the final classifier to 10,100,1000 and 3755, respectively, that is, the datasets used are Set1, Set2, Set3, and Set4, respectively. The structure obtained by the network through the above 1,2,3 step is named CNNet, and because its final output node is slightly different, it is named CNNet1, CNNet2, CNNet3 and CNNet4 respectively.

3. Experimental results and analysis

3.1. The influence of calculating mean image on the result in preprocessing

In this experiment, in order to verify whether the mean processing of images in preprocessing will have an impact on the training of the network, under the condition that the relevant parameters of the network are unchanged, the network CNNet3 obtained by the improvement of the Alexnet network are preprocessed by mean calculation Set3 Training and Training sample SeT3 without mean calculation preprocessing are trained, and the relevant results of the two training models are shown in Fig.2.

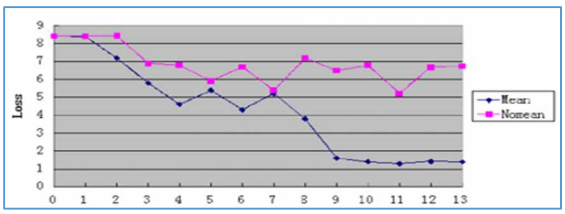

Fig .2 Relationship between calculating mean value and network convergence in preprocessing

The horizontal coordinates in the figure represent the number of iterations of the network, that is, the number of training times, the longitudinal coordinates represent the loss value of the network model.

3.2. network related training parameter settings

Using the strategy of the relevant parameters in Le Net5, the learning rate is increased from 0.01 to 0.02, which is equivalent to increasing the step length, The decrease of the gradient descent method is increased, and the network oscillation is avoided, thus crossing the local minimum point and approaching the larger extremum point. Finally, it is proved by experiments that the value of batch_size is reduced to 64 o'clock, the network can converge at a faster speed, and the classification accuracy is high, which proves that the network also achieves the optimal solution, so this paper sets the Batch_size to 64 and the learning rate to 0.01.

3.3. Experimental results and analysis of four data sets and mnist in Cnnet

After adjusting the relevant parameters of the network so that the network can converge, the four sub-datasets Set1, set2, set3 and Set4 of HWDB1.1 handwriting characters are trained with four sub-networks of Cnnet respectively. For cnnet networks with higher complexity (more convolution nuclei and deeper network structures), the recognition rate of handwritten Chinese characters is higher, and their ability to express the sample features is much higher than that of the simpler convolution neural network Net2, that is, more sample categories can be classified.

Although the convolution network with shallow accuracy has increased more, the complexity of cnnet network is higher on the network convergence, and the following table 2 is the comparison between Net2 and cnnet networks in convergence.

Table 2 Comparison of convergence times between Net2 and Cnnet

Set name	Net2	CNNet
Set1	6100	48000
Set2	11600	84000
Set3	14300	123000
Set4	-	179000

Under the same experimental conditions[6 7], cnnet is much higher than the Net2 network in the number of iterations required to make the network converge. Taking the training of DataSet Set4 as an example, the number of samples used for training has reached more than 900,000, and each image size is larger, the network each training weight needs to be used in the sample batch that is batch_size also larger. Coupled with the need for all the test sample data after each 10,000 iterations to verify the classification accuracy of the network, it takes nearly 4 days for the network cnnet to be fully trained on the training Set 4, so that the time spent on each parameter is enormous, This is also a major disadvantage for deep convolution neural networks compared to simple convolution neural networks.

4. System design and implementation

4.1. System structure and design

1. System Framework and related modules

This system architecture adopts BS structure as shown in Fig.3, that is, users only need to have simple interaction with the browser, most of the core business of the system is on the server side. The system of this paper uses Python-based Tornado web framework:

Fig.3. BS architecture diagram

According to the different division of functions, the system can be divided into the following modules: input module, model information loading module, model classification module, result mapping module and the final output module, the system flow chart composed of these modules is shown in Fig.4.

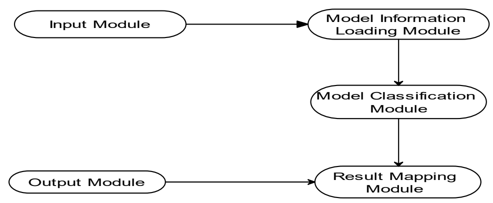

Fig 4 Overall module flow chart of the system

2. Core class Design

The main modules of this system are model loading, model classification and result mapping module, so each module corresponds to design a corresponding core class, complete the main functions of the module.

(1) Load model module; (2) Model classification module; (3) Result mapping module.

4.2. Data-related preprocessing operations

The model used in this system is CNNet3, the input image is a single channel grayscale image, and the test picture which has been processed does not need to be grayscale, but if the color image of RGB is entered, it needs to be preprocessed by grayscale.

There are many ways to grayscale, such as the component method, which uses the pixel value of one of the channels of RGB as the grayscale value; Mean method, the average of three channels is used as the grayscale value; Weighted average method, that is, according to a certain weight to the RGB three components weighted, this paper uses the third Way, which represents the grayscale image, respectively, the input image of three sub-vectors, the grayscale formula is as follows:

$$f(x,y) = 0.30(x,y) + 0.59(x,y) + 0.11(x,y) \quad (1)$$

The G component weight is set to the highest, the lowest part of B component is the human eye to green sensitivity is the highest, and the blue sensitivity is the lowest. The input of the system is a multi-formatted character picture, and the correct characters in the picture are obtained by entering the picture. However, in the network model, the initial result of the output is the corresponding character category in the training sample data, and the corresponding transformation is carried out in the mapping module. Therefore, the mapping relationship between characters and categories must be established first in the implementation of this system, as shown in Fig.5.

Fig.5 Mapping relationships for datasets

The CNNet3 network model is used in the system, that is, the output node is 1000. You need to establish the first 1000 classes of the DataSet as shown in the map. As shown in the figure, class_000 represents the first classification of the sample set, in which the folder is the same character dataset, corresponds to the first character "丁" in the mapping file and marks it as n1001.

Acknowledgement

The research is partly supported by the "13th Five-Year" comprehensive investment and basic research business fee items of China (000040192).

References

1. Rong Zhang, Weiping Li, Tong Mo, Review of Deep Learning, *Information and Control*, 2018, 5: P385-P397.
2. Bing Shun, Dehui Kong, Wenhui Zhang, Wenhao Jia, Survey on Human Action Recognition From Depth Maps, *Journal of Beijing University of Technology*, 2018, 10: P1353-P1366.
3. Shengyi Zhou, Techniques Review of Deep Learning, *Information Technology Exploration*, 2018, 10: P116-P117.
4. Anqi Liu, Shuai Zhang, Xinfang Chang, Bingkun chen, Real time human action recognition and monitoring method based on deep learning, *Heilongjiang Science*, 2018, 10: P14-P16.
5. Kai Yang, Youchun Xu, XiangBi An, Yonglei Li, Kunpeng Liu, Vehicle Detection Method Based on Deep Learning, *Army Military Transportation Academy*, 2018, 7: P58-P61.
6. Youwen Huang, Chaolun Wan, Human behavior recognition algorithm based on deep learning, *Artificial Intelligence*, 2018, 10: P1-P5.
7. Qicheng Mei, Wenge Lv, Research on Commodity Image Recognition Based on Deep Learning, *Mechanical and Electrical Engineering technology*, 2018, 9: P27-P151.
8. Huailin Zhao, Zheng Wu, Xiaoxing Wang. A Multi-robot Rescuing System. *The 2018 International Conference on Artificial Life and Robotics* (ICAROB 2018), Feb.1-4, 2018, Beppu, Japan, P582-586.

Cluster Analysis of Wine based on Three-dim Fluorescent Spectra Characteristic

Di Yin [1], Fengzhi Dai [1*], Yuxuan Zhu [1], Yasheng Yuan [1], Tingting Zhang [1], Ying Chen, Yiqiao Qin [12], Chengcai Wang [3]

[1] *College of Electronic Information and Automation, Tianjin University of Science and Technology, China;*

2 Tianjin Tianke Intelligent and Manufacture Technology CO.,LTD
3 CETC Ocean Information Co., Ltd, Beijing 100041,
*China E-mail: * daifz@tust.edu.cn*
www.tust.edu.cn

Abstract

The traditional sensory analysis method can not discriminate different kinds of wine objectively and accurately. The three-dimensional (3D) fluorescence technology has the advantages of strong selectivity, high resolution and direct access to the fluorescence characteristics of the sample. In this paper, the 3D fluorescence spectroscopy five brands of red wine samples. The five characteristic parameters (the mean value, standard deviation, center of gravity coordinates, first order center moment and correlation coefficient) of the 3D fluorescence spectra of these five dry red wine samples are extracted respectively. The results show that the difference of the samples can be distinguished intuitively by extracting the 3D spectral parameters of the different brands. On this basis, the clustering analysis shows that even the same raw material brewing wine is different from the raw material origin and the soil environment. The climate environment will cause an important impact on the composition of the wine.

Keywords: Characteristic parameters; Clustering analysis; Wine; Three-dimensional fluorescence spectroscopy

1. Introduction

Wine has always been popular with people and is famous for its elegance and noble. In recent years, because some non-standard productions, wine trace components exceed the standard, so infected and invaded by some harmful elements that are harmful to human body, such as biogenic amine, ochratoxin and other harmful substances. These harmful substances can cause headaches, abnormal heart rate, and may even cause cancer.

Different brands of wine have different trace components. With the development of chemical analysis techniques, some analytical techniques such as feeling evaluation, gas chromatography, ultraviolet absorption spectrometry and infrared spectrometry have been appearing constantly, although which can meet the needs of wine detection on a certain basis, there are also some shortcomings such as complex processing, consuming measurement, high cost, sensitivity and inaccuracy. Fluorescence spectrometry is an efficient and accurate analytical method, Because of the characteristics of high measurement accuracy, small sample size and high resolution, it is very convenient to solve the shortcomings of the traditional methods, such as many and tedious analysis process.

In this paper 3 kinds of different brands of Wine as the research object, carries on the analysis using three-dimensional fluorescence spectra of high sensitivity. Wine contains many complex components. It is difficult to study certain ingredients. Therefore, the fluorescence spectra of wine under different excitation wavelengths are determined in this paper, and the three-dimensional fluorescence spectra are constructed according to the original data. The three-dimensional fluorescence spectra of five different wine samples from three brands were studied, and three characteristic parameters were extracted. The clustering method was used to analyze the data. On this basis, the three-dimensional fluorescence spectra characteristics of wine samples were extracted to effectively distinguish different brands of wine.

2. Experiment

2.1. Experimental device

This experiment uses the LS-55 spectrofluorimeter of PerkinElmer company of America, and the light source is pulsed xenon lamp. The cuvette is a 1cm quartz liquid cell with stopper. This consists of 5 units, namely, light source, monochromator, sample cell, detector and display.

2.2. Experimental method

Because of the fluorescence quenching of five samples from three different brands, the selected wine samples need to be diluted before they can be measured in a cuvette. The dilution of the wine samples in this experiment is 20 times. In this paper, the excitation wavelength is set from 250nm and the interval is 5nm to 350nm , the emission wavelength ranges from 200 to 700 nm, and the scanning speed is 1000 nm/min. Under these conditions, two-dimensional fluorescence data are obtained.

2.3. Data processing and analysis

The measured two-dimensional fluorescence spectrum data are normalized, smooth filtering, synthesized three-dimensional fluorescence spectra and three-dimensional contour map, and curved surface fitting and characteristic parameters are made by using the program of MATLAB (number of fluorescent peaks, position, peak wavelength of main fluorescence，optimal excitation wavelength).

2.4. Three dimensional fluorescence spectra of wines of different brands

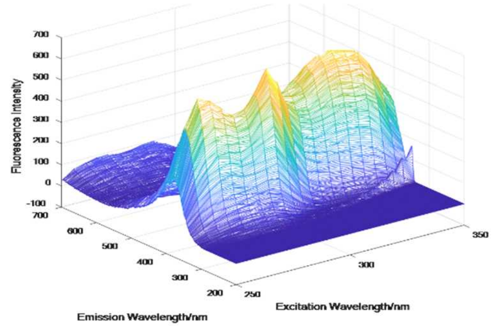

Fig.1 Great Wall Dry Red Wine

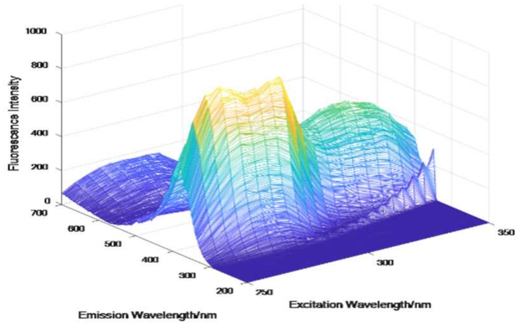

Fig.2 Great Wall Cabernet Dry Red Wine

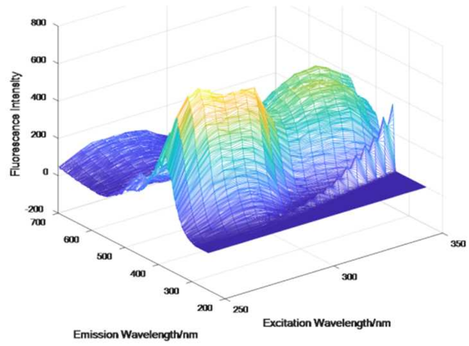

Fig.3 Changyu Dry Red Wine

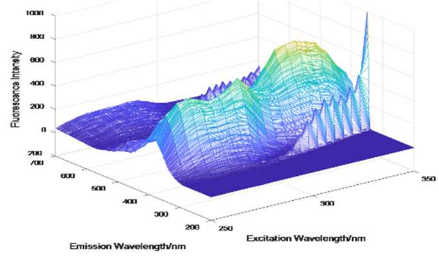

Fig.4 Changyu Dry Red Wine (premium wine)

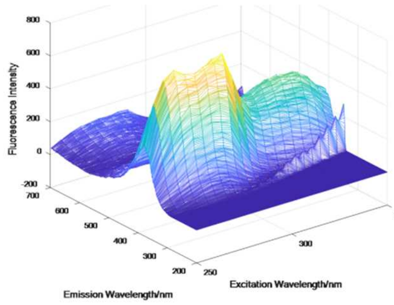

Fig.5 Arabella Dry Red Wine

Table1 Characteristic parameters of 3D fluorescence spectra of samples

sample	wave peak number	peak position	fluorescence intensity	optimum excitation wavelength (/nm)
1	3	260/376.5	619.6	290
		290/375	680.3	
		325/418.5	637.2	
2	3	265/372.5	941.3	265
		290/374.5	908.5	
		330/429	567.6	
3	3	265/372.5	710.5	265
		290/373	625.7	
		335/423	483	
4	3	290/374	651.2	325
		325/419.5	783.4	
		265/375	587.2	
5	3	265/376.5	757.3	290
		290/374.5	772.8	
		335/418.5	455.1	

These figures show three-dimensional fluorescence spectra of five kinds of wines: Great Wall Dry Red Wine, Great Wall Cabernet Dry Red Wine, Changyu Dry Red Wine, Changyu Dry Red Wine(premium wine) and Arabella Dry Red Wine. From the comparison of the spectra of the samples, there is an obvious fluorescence peak in the range of 260 nm/375 nm, and the band of 260 nm/375 nm has the best excitation wavelength.

From table 1, we can see the corresponding comparison, Changyu Dry Red Wine and Great Wall Cabernet Dry Red Wine are the best excitation wavelengths of 265nm. However, Great Wall Dry Red Wine and Arabella Dry Red Wine are the best excitation wavelengths of 290nm. This is because the grapes detected in the brand wine are made from the same grape variety Cabernet Sauvignon grapes. Although the location of wave peaks is the same, their optimal excitation wavelengths are quite different. It is due to the different content of trace fluorescent substances in wines from different regions. It is mainly distinguished by the location of fluorescence peaks. According to the intensity and number of fluorescence peaks, the characteristic substances of different brands of wine can also be distinguished.

The difference of brands can not be seen from the atlas, so it can not be directly distinguished by the map. Therefore, we need to extract the characteristic parameters of the map to see the differences, and then classify them by cluster analysis.

3. Clustering analysis

3.1. The concept of cluster analysis

"Birds of a feather flock together". As an important branch of statistics, clustering analysis has been widely applied in various fields. This is mainly based on distance based clustering analysis. The software used in this experiment is SPSS 19. To analyze the trace components of different brands of wines and calculate the similar distance between wines by various methods. After repeated tests and combined with the data of this subject, the data measured by Euclidean distance analysis can be used to obtain better clustering results.

3.2. Feature data extraction

Table2 Extraction of characteristic parameters of 3D fluorescence spectra

number	mean value	standard deviation	abscissa of center of gravity	vertical coordinates of center of gravity	first order center moment	correlation coefficient
1	118.2692	168.566	302.5984	430.1101	-1.33e+05	-3.12e+05
2	149.9626	204.2795	295.6212	430.4683	-1.27e+05	-3.59e+05
3	156.788	171.6284	300.0153	441.7986	-1.33e+05	-3.52e+05
4	140.4287	177.1754	303.6513	437.7785	-1.33e+05	-3.64e+05
5	118.0955	165.4325	296.6428	428.3699	-1.27e+05	-3.50e+05

3.3. Clustering results

The purpose of cluster analysis is to cluster different brands of wines using extraction parameters. And accurate classification of different brands of wines. Five kinds of wine data were used in this paper. The distance between samples was Euclidean distance and hierarchical clustering method was used for clustering.

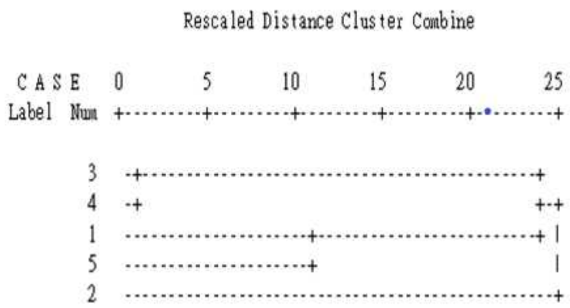

Fig.6 Dendrogram

It can be seen from Figure 6 that the Euclidean distance between two samples of Changyu is small, and the difference between them is small. The sample 1,5,2 has a larger Euclidean distance, which indicates that the difference between samples is large.

4. Conclusion

In this paper, the 3D fluorescence spectroscopy five brands of red wine samples. It was found that the 3D fluorescence spectra of wine brewed with Cabernet Sauvignon were basically the same, and could not be directly distinguished by spectral comparison. The five characteristic parameters (the mean value, standard deviation, center of gravity coordinates, first order center moment and correlation coefficient) of the 3D fluorescence spectra of these five dry red wine samples are extracted respectively. The results show that the difference of the samples can be distinguished intuitively by extracting the 3D spectral parameters of the different brands. On this basis, the clustering analysis shows that even the same raw material brewing wine is different from the raw material origin and the soil environment. The climate environment will cause an important impact on the composition of the wine.

Acknowledgement

The research is partly supported by the "13th Five-Year" comprehensive investment and basic research business fee items of China (000040192).

References

1. Masanori Katsuyama,Nobuhito Ohte. Determining the sources of stormflow from the fluorescence properties of dissolved organic carbon in a forested headwater catchment[J]. Journal of Hydrology,2002,268(1).
2. Yawei Hou, Huailin Zhao. Handwritten Digit Recognition Based on Improved BP Neural Network. The 13th Chinese Intelligent Systems Conference (CISC2017), Oct.14-15, 2017. Mudanjiang, China. P63-70.
3. Jianlei Yang,Tuo Zhu. *Study on discrimination system of distilled spirits based on three-dim fluorescent spectra technique.* (Jiangnan University, 2009)
4. Yuan Yan, Jin-Gou, Xu,Zhu-Guang Lin,Yi-Bin Zhao,Le-Tian Wang,Guo-Zhen Chen. *Study on total luminescence spectra. Application of the Monte-Carlo method to three-dimensional synchronous fluorescence spectrometry.*(Analytica Chimica Acta,1995)
5. Jiaman Wang, Liang Ma, Yuhao Zhang, Tao Jiang. *Investigation of the interaction of deltamethrin (DM) with human serum albumin by multi-spectroscopic method. Journal of Molecular Structure*,(2017)
6. Yuan Yan, Jingou Xu, Guozhen Chen, *Total integration method of three-dimensional fluorescence spectrometry* (Chinese Science Bullentin,1997)
7. Jian Wang,Renguang Zuo,Jef Caers. *Discovering geochemical patterns by factor-based cluster analysis.* (Journal of Geochemical Exploration,2017)

The Control Design of the Planting Device for the Hydroponic Vegetable

Yasheng Yuan[1], Fengzhi Dai[1*], Zhongyong Ye[1], Yuxuan Zhu[1], Ying Chen[1], Di Yin[1], Tingting Zhang[1], Yiqiao Qin[12], Yang Li [3]

[1] College of Electronic Information and Automation,
Tianjin University of Science and Technology, China;

[2] Tianjin Tianke Intelligent and Manufacture Technology CO.,LTD;

[3] CETC Ocean Information Co., Ltd, Beijing 100041, China
E-mail: [*] daifz@tust.edu.cn
www.tust.edu.cn

Abstract

The equipment is designed to household indoor small hydroponic vegetable planting control device. The temperature, humidity, light and carbon dioxide concentration sensors are integrated to the Arduino UNO R3 microcontroller. It is used to detect various parameter data of planting environment. The WIFI module can send the real-time environment variables which detected by the sensor to the mobile devices, such as the user's mobile phone. And, users can also change the control range of variables according to the planted vegetables through the WIFI module.

Keywords: WIFI, remote control and monitoring, hydroponic vegetable, single chip

1. Introduction

Planting Hydroponic vegetables use the certain nutrient solution, rather than use the soil. With the expansion of the city and the reduction of agricultural land[1], the technology of Hydroponic vegetables is more and more important.

Compared with traditional farming, hydroponic cultivation of vegetables can greatly reduce the waste of labor force in terms of physical strength, and the crop of hydroponic cultivation can grow rapidly, the matrix and material of hydroponic vegetables can reduce the harm of plant bacteria[2]. The nutrient solution of hydroponic vegetables can be recycled, thus reducing environmental pollution.

In conclusion, the equipment is designed to create a small hydroponic vegetables control device which can automatically detect environmental parameters and make adjustment, which can enrich our life and free our hands. This design adopts the Arduino UNO R3 and the Arduino Extended Edition to connect the sensors and controllers. In addition, this design adopts the WIFI module, and the WIFI main module connects to the server through the MQTT protocol, which can control the controller and collect the environmental information[3]. This design has high practical value in small hydroponic vegetable planting.

2. The hardware structure design

Intelligent devices are mainly responsible for data collection and the control of environmental parameters, so the size is better to be small. Therefore, this design adopted the Arduino Sensor Shield extension plate to place the single chip[4], the various sensors and a series of controllers.

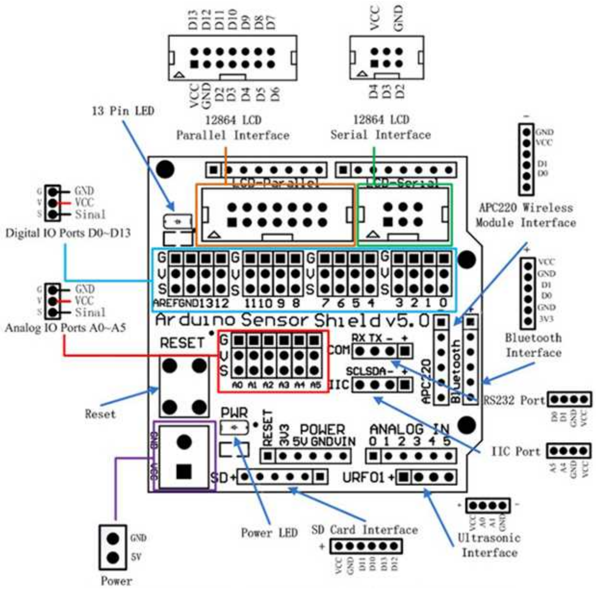

Fig.1 Arduino Sensor Shield Functional Diagram

2.1. Hydroponic box design

In this device, the hydroponic box is designed by the soildworks software. The hydroponic box can be planting six vegetables, the upper cover can be opened to changing vegetables and replace the nutrient solution, the fan and light supplement lamp are installed on the wall, and the humidification device is installed into the box.

the design of hydroponic box is shown in the Fig.2.

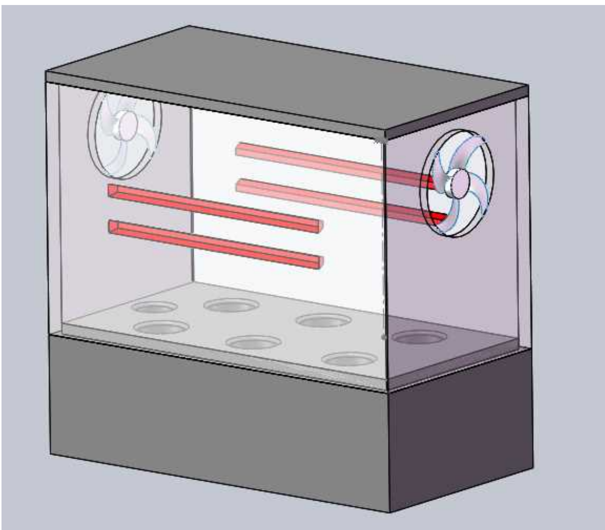

Fig.2. hydroponic box design

2.2. WIFI module

The design adopts the WIFI module of ESP8266, and it comes with a core MCU. The MCU has the built-in RAM, ROM, support RTOS, and reaches the maximum clock speed of 80 MHz. The WIFI module has the following characteristics:

- Built-in 10-bit high-precision ADC, with a complete TCP / IP protocol stack.
- Supports Cloud Server Development / Firmware and SDK for fast on-chip programming.
- Support the UART/GPIO data communication interface.
- Support Smart Link intelligent networking.

The WIFI module is shown in Fig.3.

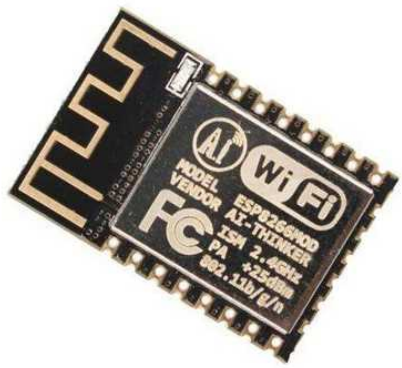

Fig.3. WIFI module

2.3. Main control chip

In this design, the external MCU is Arduino UNO R3, and the Arduino board is based on Atmel's ATMEGA 328 MCU. It can be simply fixed the sensors and various electronic components. It has the following characteristics:

- Input voltage: there is no need for external power supply or external connect USB 5.0V~9.0V voltage input.
- Output voltage: 5.0V voltage output, 3.3v voltage output and external power supply input.
- Support ICSP downloads and TX/RX.
- Operating temperature range: - 40 ° C to + 85 ° C.

The design of the main control chip is shown in Fig.4.

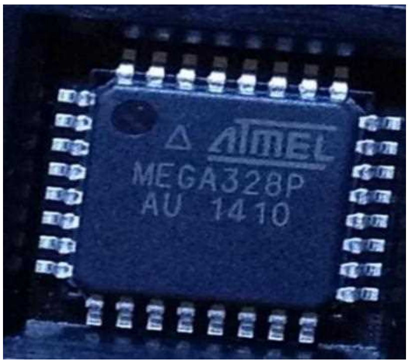

Fig.4. ATMEGA 328P chip

3. System circuit module design

In the circuit design, this design adopts a boost module, temperature and humidity module, carbon dioxide module and ambient light sensor module. These modules greatly improve the function of the device.

3.1. Boost module

The universal input voltage of boost module is 3V ~ 32V, and the better working voltage range is 5V ~ 32V. The universal output voltage is 5V ~ 35V. It built-in 4A high efficiency MOSFET, which can make full use of conversion efficiency. The high switching frequency is 400KHZ, so it can achieve a better effect[5].

3.2. Design of connection circuit for temperature and humidity module

The design adopts the temperature and humidity compound sensor DHT11. It has humidity measurement elements to measure humidity and NTC temperature measurement elements to measure temperature, and its correction factor is stored in OTP memory by program[6]. DHT11 has four pins, one pin is the temperature and humidity data output pin, the other three pins are connected to VCC, GND and floating[7]. The DHT11 is a temperature and humidity sensor, and its measurement accuracy is very high. The accuracy of temperature measurement is about 2℃, and the accuracy of humidity measurement is about 5%. Its signal transmission distance can reach to 20 meters.

3.3. Design of connection circuit for ambient light sensor module

The design adopts the ambient light sensor BH1750. It is a digital ambient light sensor. It is possible to detect wide range at high resolution. (1 ~ 65535Lux). BH1750 has five pins, one pin is the IIC bus clock pin, one pin is the IIC bus data pins, one pin is the IIC device address pin, the other two pins are connected to VCC and GND.

3.4. Design of connection circuit for carbon dioxide module

The design adopts the carbon dioxide sensor MG811. It using solid electrolyte battery principle to measure carbon dioxide, it have simulate output and TTL level output, and better sensitivity of carbon dioxide, it is also can better identify the content of carbon dioxide in the air, carbon dioxide gas sensitive element test concentration in the range of 350 ~ 10000 parts per million, working conditions for the environment temperature: - 40 ℃ ~ 70 ℃, humidity: ≤95%RH.

4. Introduction of functional module

With the functional modules, we can easily control and monitor the hydroponic vegetable planting equipment.

4.1. The carbon dioxide regulator design

We adopt the ventilation fan as the carbon dioxide controller. When the concentrations of carbon dioxide in the device is too high, the ventilation fan working, which can effectively adjust the concentrations of carbon dioxide in this device.

4.2. The humidity regulator design

We adopt the atomized tablets to increase the humidity and supplement the nutrient solution. The atomized tablet has low price, low driving voltage and high conversion frequency[8]. It adopts atomized tablet intermediate spray, 5um ultra-fine spray aperture and 740 ultra-dense spray holes. Most importantly, it is easy to operate.

4.3. The ambient light regulator design

We adopt the LED grow light as the light regulator design. It can promote photosynthesis and promote plant growth.

4.4. The temperature regulator design

The temperature regulation of this equipment is mainly divided into two parts: the temperature increasing device and the temperature decreasing device.

The temperature increasing device adopts the ceramic heating slice. Ceramic heating plate is a temperature heating element, which has the features of simple use, quick temperature rise, more secure, uniform heating, long life and high heating temperature. The temperature decreasing device is a fan. It has the following characteristics:

- The air flow which near the outlet of the fan is mostly flocculated, which can rapidly cool down the air flow through the tuyere if there is more heat.
- When the fan starts blowing, according to the direction of the wind, positive pressure can be formed around the air outlet in the closed environment, which can avoid the external environment dust entering the device.

4.5. Wireless module design

This design uses a wireless Mesh network for ad hoc network communication. With the mobile-phone APP NetAssist, the WIFI module of this design can access to the Internet. We can send different instructions to change and adjust the growth environment of different vegetables. It can also query the environment parameters of the current device in real time.

5. Testing and conclusion

By the test of the hydroponic vegetable planting control device, the following data are obtained: WIFI module can through the APP to choose the environment parameters of plants. The above data shows that the device can basically meet the needs of device to control different kinds of hydroponic vegetables.

By using temperature and humidity module，carbon dioxide module and ambient light sensor module, environmental parameters such as temperature, humidity, light and carbon dioxide concentration can be can be real-time transmitted to the user.

By using controller, the equipment can be controlled when the equipment detects the environmental parameters not conform to the setting range.

The tests included the stability and speed of the WIFI module, the sensitivity of the controller, and the accuracy of the sensor. The test results show that the device can basically meet the user's control and monitoring.

Acknowledgement

The research is partly supported by the “13th Five-Year” comprehensive investment and basic research business fee items of China (000040192).

References

1. Hannes Jochen König, Sandra Uthes, Johannes Schuler, etc. Regional impact assessment of land use scenarios in developing countries using the FoPIA approach: Findings from five case studies. *Journal of Environmental Management*,2013,12.
2. Jane Tavares, Koon-Hui Wang, Cerruti R.R. Hooks. An evaluation of insectary plants for management of insect pests in a hydroponic cropping system. *Biological Control*,2015,9.
3. Huailin Zhao, Shunzhou Wang, Yunxiang Liu, Xuyao Hao, Design of an Intelligent Housekeeping Robot Based on IOT. *Journal of Information and Communication Engineering. Vol.2(2)*, 2016, P114-118.
4. Hanafy M. Omar. Enhancing automatic control learning through Arduino-based projects[J]. *European Journal of Engineering Education*,2018,4.
5. Linlin Tang. *Design and implementation of intelligent monitoring system for vegetable greenhouses* (Shandong, Shandong university, 2010).
6. Di Li, Based on Arduino's smart greenhouse surveillance system design, Journal of electronic science and technology. 2017,1: P81-P85
7. Jean-Christophe Cuilliere, Vincent Francois, Remi LacroisLi, A new approach to automatic and a priori mesh adaptation around circular holes for finite element analysis, *Computer-Aided Design*, 2016.
8. V. Vanhoorne, E. Peeters, B. Van Snick, J.P. Remon, C. Vervaet. Crystal coating via spray drying to improve powder tabletability. *European Journal of Pharmaceutics and Biopharmaceutics*,2014.

An anti-theft system based on the self-checkout

Yuxuan Zhu[1], Fengzhi Dai[1*], Yasheng Yuan[1], Di Yin[1], Tingting Zhang[1], Ying Chen[1], Ce Bian[12], Yufan He [3]

[1] College of Electronic Information and Automation,
Tianjin University of Science and Technology, China;

[2] Tianjin Tianke Intelligent and Manufacture Technology CO.,LTD;

[3] CETC Ocean Information Co., Ltd, Beijing 100041, China
*E-mail: * daifz@tust.edu.cn*
www.tust.edu.cn

Abstract

Nowadays, the imperfection of the anti-theft system impedes the development of self-service cash registers. This paper designs an anti-theft system based on self-service cash registers, which can greatly reduce the theft rate in supermarkets. This anti-theft system adopts Siemens's LOGO!, which is the core of the controller. it has massive facilities of anti-theft protection, including radio frequency detection, photoelectric counting, repeated scanning reminder, magnetic detection, video monitoring and anti-theft electronic door. Through the above technologies, the supermarket that uses the self-service cash registers can avoid to some problems, i.e. cash collection leakage, using low price goods to replace that of high price. Multiple facilities are set to jointly protect the safety of goods, effectively reduce theft and loss.

Keywords: LOGO!, anti-theft system, repeated scanning reminder, radio frequency detection

1. Introduction

During the holidays, there are many customers in the supermarket. When they finish shopping and decide to check out, they need to wait in long lines. This phenomenon makes low efficiency. Therefore, the self-checkout plays an important role in the supermarket. But at present, only a small number of self-checkout systems have been accessed in China. Even though the self-checkout is becoming more and more mature in foreign countries, the manufacturing cost is very expensive and the security system of self-checkout is unperfect. Theft often occurs. The imperfection of the anti-theft system hinders the development of the self-checkout.

There is not a self-service cash register with perfect anti-theft function in domestic and foreign supermarkets. Using a self-service cash register with a sophisticated anti-theft system can save time for consumers and reduce manual charges for supermarkets. The development of relevant apps can provide better publicity to the supermarkets, which can not only benefit the supermarkets but also facilitate the customers.

2. Function introduction

The article describes an anti-theft system based on the self-checkout which can well solve the theft behaviors in supermarket that uses the self-service cash register. This anti-theft system adopts Siemens's LOGO!, which is the core of the controller. Moreover, it has massive facilities of anti-theft protection, including radio frequency detection, photoelectric counting, repeated scanning reminder, magnetic detection, video monitoring and anti-theft electronic door. Some thefts, i.e. cash collection leakage, using low price goods to replace that of high price, can start the alarm equipment. At the same time， through the thermal infrared body sensor to connect the LOGO! which can control conveyor to work or stop. These functions can effectively save power resources. Moreover, multiple facilities are set to jointly protect the safety of goods, effectively reduce theft and loss.

Self-service cash register has three modules: cashier cover, scanning and payment. The anti-theft system is composed of electric control cabinet, control equipment, camera and anti-theft detection door. The working process of the system is to turn on the switch and press the button to start work. If the buzzer alarms, the security personnel will verify the situation and shut down the system to restart. If the alarm lamp alarms, the monitoring room staff will verify the situation and the alarm lamp will be delayed to close.

The design of the anti-theft system based on the self-checkout is shown in Fig.1.

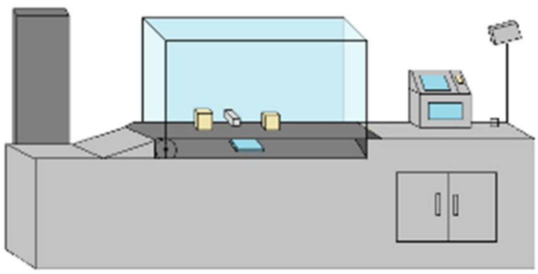

Fig.1.The anti-theft system based on the self-checkout

3. Function module introduction

This anti-theft system adopts Siemens's LOGO!, which is the core of the controller. It has massive facilities of anti-theft protection, including radio frequency detection, photoelectric counting, repeated scanning reminder, magnetic detection, video monitoring and anti-theft electronic door.

3.1. Count detection

The LOGO! controls the work of the photoelectric sensor probe. When the goods is sanned and passed through the conveyor belt, the photoelectric counter adds. Through the LOGO! determine whether the goods has been scanned by the photoelectric sensor. If the goods is not scanned, the counter is added and the alarm device is activated, and the security personnel comes to check. At the same time, it will send the instructions to the video monitoring room to make the monitoring personnel pay attention. If the goods is scanned, the count is cleared. This method can found the situation that the customer takes the goods without scanning the code

3.2. The reminder of rescanning

When the barcode reader in the cash register detects the same item, it will send the signal to the video monitoring room, which will attract the attention of the staffs in the monitoring room, and check whether the customer has scanned the barcode of the same item, and whether there is an undesirable phenomenon of low price goods replacing the high price.

3.3. radio-frequency technique

The anti-theft system designed in this paper improves the decoder and combines the decoder with the radio frequency decoder. When the bar code is swept, the decoder works automatically to fuse the rf label. The radio frequency detection door is placed in the channel. If the radio frequency signal is detected, the alarm device on the radio frequency detection door will send out an alarm to alert the security guards near the door.

3.4. Detection of magnetic

The demagnetization plate is added into the conveyor belt, which can automatically demagnetize the goods on the conveyor belt. The magnetic detection door is also installed in the passageway to prevent customers from carrying the goods that haven't been paid for.

3.5. Smart conveyor belt

Using thermal infrared human induction technology, it can detect if there is someone before the cash register, and send the detection signal to the LOGO! to control the conveyor belt work or stop, effectively saving power resources.

4. Operating principle

There are three parts in the anti - theft system includes mechanical, monitoring and electronic. The mechanical part includes conveyor belt; The monitoring part includes the camera, monitor and radio frequency detection door; The electrical component includes switches. There are five inputs and three outputs. The input variables include the buttons of start and stop, infrared detector, code scanner and photoelectric sensor. Moreover, output variables include conveyor belt switch, buzzer alarm and alarm lamp. Above is the control core of this security system.

The actual working principle is when the customer walks into the checkout, the infrared detector detects the input signal and controls the conveyor belt to open. After the customer scans the goods, the counter will add one. When the customer puts the goods on the conveyor belt and the goods pass the photoelectric sensor, the counter will add another and reset. If someone steals goods, that is, goods are not scanned, the buzzer alarm begins to alarm. When the customer repeatedly scans the same bar code, the alarm light in the monitoring room will alarm, reminding the monitoring personnel to monitor whether there is any behavior of replacing the high-priced goods with cheap goods. The scanning device is equipped with a rf decoder. Valuable goods with rf soft label can only pass through the rf detection door after the scanning soft label is invalid. The magnetic device is installed under the conveyor belt, so that the original magnetic goods in the supermarket must be sent out through the conveyor belt to prevent theft.

5. Technical implementation

5.1. Control requirements

Turning on the switch and press the open button. If the signal is detected by the infrared detector, the conveyor will turn on. When the goods are scanned, the counter will be increased by one. When the goods pass the photoelectric sensor, the counter will be increased by one again. At that time, the alarm will not alarm and the counter will reset. When the counter is not added or reset normally, the alarm system will be activated to alarm the theft.

5.2. I/0 list

Table1 Inputs

I_1	I_2	I_3	I_4	I_5
Photoelectric sensor	Infrared detector	code scanner	stop button	start button

Table2 Outputs

Q_1	Q_2	Q_3
alarm light	buzzer alarm	conveyor

The control principle of the logo! is shown in Fig.2.

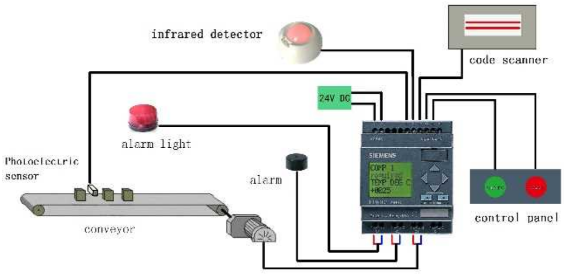

Fig.2. The control principle of the logo!

6. Conclusion

At present, the anti-theft system of self-service cash registers at home and abroad is very imperfect, with many loopholes, which has caused great losses to supermarkets and affected the development of self-service cash registers. The anti-theft system developed based on the self-service cash registers of supermarkets. With the application of new technology in the field of anti-theft, it can well improve the phenomenon of serious loss, promote the promotion of cash registers, and at the same time, take an important step towards the realization of supermarket automation. To this end, the system has the following highlights.

6.1. The low rate of theft

In order to reduce the theft rate, multiple anti-theft detection is adopted, such as code sweeper, photoelectric sensor, radio frequency detection, degaussing plate, synchronous count, to prevent the leakage of goods; When the same bar code is scanned repeatedly, the alarm light in the monitoring room will alarm, reminding the monitoring personnel to monitor whether to replace the high-priced goods with cheap ones. The rf decoder is combined with the decoder. Only when the rf soft label fails when the decoder is scanned, it can pass the rf test door. Installing demagnetizer at the conveyor belt for anti-theft detection.

6.2. Humanized design

The appearance and structure of the self-service cashier system is similar to the traditional cashier desk. The open touch screen panel is installed to display the commodity information. The external structure of the anti-theft system is mainly composed of conveyor belt, which will not bring inconvenience to customers but help them to deliver the goods.

6.3. Energy conservation and low consumption

The main electric consuming device of the equipment is the conveyor belt. The system is detected by the infrared detector, which makes the conveyor belt turn off when no one uses it, greatly saving electricity.

6.4. Stable operation

Siemens's LOGO! has high reliability and extreme reliability, with data maintenance function, can ensure that when the equipment suddenly power down, the data is saved safely.

6.5. Convenient equipment installation

Siemens's LOGO! has almost no wiring requirements, and it only needs to press the button to write and change the program, which is highly portable and can adapt to different requirements.

Acknowledgement

The research is partly supported by the "13th Five-Year" comprehensive investment and basic research business fee items of China (000040192).

References

1. Meng Liu, Kai Fu, Analysis and design of self-service checkout terminal in large supermarkets, Industrial design, 2018, 1: P47 – P48.
2. Yingang Fu, Design and implementation of information appliance control platform (Shangdong, Shandong University of Science and Technology, 2007)
3. Sinuo Liu, Analysis and design of self-service shopping cashier system, Modern industrial economy and informatization,2017,7: P18- P20.
4. Yaling Tang, Ling Ma, Haitao Song, Analysis and design of supermarket self-service cash register system,2017,4: P128.
5. Xiaona Kong, Design and implementation of self-pay system based on RFID technology, Computer-Aided Design, 2016.
6. Shunzhou Wang, Huailin Zhao, Weiren Wang, Huijun Di, Xueming Shu. Improving Deep Crowd Density Estimation via Pre-Classification of Density. The 24th International Conference on Neural Information Processing (ICONIP2017), Nov.14-18, 2017, Guangzhou, China. P260-269. (EI)
7. Huailin Zhao, Yangguang Guo, Sugisaka Masanori, Design of the Multi-Car Collaboration System, the 2017 International Conference on Artificial Life and Robotics (ICAROB 2017), Jan. 19-22, 2017, Miyazaki, Japan, p186-190.

Case Study on Communication between Embedded Linux Environment and Microcontroller

Ziheng Gao, Yizhun Peng *, Shuo Wang

College of Electronic Information and Automation,Tianjin University of Science and Technology, China

Binhai International Advanced Structural Integrity Research Centre， Tianjin University of Science and Technology,China

*E-mail: * pengyizhun@tust.edu.cn*

Abstract

In many embedded development scenarios, we need to combine the real-time microcontroller and non-real-time embedded Linux environment for collaborative development. In a high real-time environment (such as: vehicles, production lines), it can complete kinds of features relying on huge Linux ecosystem, such as hot fixable functional modules, improved network communication, easier OTA firmware updates, more efficient algorithm capabilities, and more objects. This paper aims to enumerate and explore several methods that can be used to implement similar duplex communications. For ease of understanding, a single-board computer called Raspberry Pi running Raspbian Linux and an STM32F103 32-bit ARM microcontroller are used in experiment.

Keywords: communication, embedded, real-time, Raspberry Pi, ARM

1. Introduction

IoT (Internet of things) has become closer to people's daily life, such as smart speakers and remoting control table lamps. As the working basis of the intelligent equipment to meet the products' demands, embedded development is more complicated. Lots of terminal equipment need to connect the Internet to run high computational tasks and high IO tasks. They will be used to develop deep learning models online for predictions.

Excellent native support for huge ecosystems and asynchronous tasks in an embedded Linux environment can accommodate all of the above. In addition, native compatibility of different types of scripting languages optimizes workflow.

However, traditional embedded development must operate in a real-time environment to meet reliability and other requirements. Obviously, the contradiction between them cannot be solved in the same environment. Therefore, using two controllers to process real-time and non-real-time tasks separately is a good solution.

Communication is an inevitable problem between two controllers. This article focuses on how to build a complete and reliable communication solution. We ran the Raspbian Linux distribution of the single-board computer Raspberry Pi and the 32-bit ARM microcontroller-STM32F103 as an example. It is worth mentioning that Raspbian is a customized version of Debian. It was created to accommodate the ARM commands of the Raspberry pi. Essentially, it's a full-featured Linux distribution.

2. Choices

The communication protocol is an inevitable part when it comes to communication. The protocol is also divided into application layer protocols and underlying protocols according to the level. Firstly, we will consider the most comprehensive multi-layer communication protocol stack, such as the TCP/IP[1] stack, which is used widely in Internet, and the CAN bus, which is commonly used in industrial control. This article will introduce four communication protocols.

2.1 Ethernet protocol

Ethernet is one of the most popular computer LAN technologies[2]. The advantage is that the ecosystem and protocol stack is mature. For example, TCP/IP is well known, but its standard topology is the bus topology.

2.2 CAN bus

The Controller Area Network is a feature-rich automotive bus standard based on the Broadcast Communication Mechanism. According to the content of the message, message Identifier is used to define the priority of content and messages for delivery. It is a multi-master serial bus standard for connecting ECUs[4]. The CAN network includes multiple ECU nodes which can be input/output devices, embedded devices that include CAN interchangers or gateways. It is concluded that CAN bus communication is generally applicable in large industrial equipment, but the disadvantages in the underlying two-machine communication are similar to Ethernet.

2.3 I²C bus

Inter-Integrated Circuit is a serial communication bus that uses a master-slave architecture. For simple two-wire communication, serial data line (SDA) and serial clock line (SCL) are recommended to use when the amount of data is not large and data structure is not responsible.

2.4 Serial communication bus: SPI and UART

Serial communication is essentially on the bus and other data channels and continuously performs the communication process of the above single process. The corresponding method is parallel communication. This article only describes two examples of 5SPI and UART.

2.4.1 Serial Peripheral Interface

SPI is a high-speed, full-duplex, synchronous, serial communication bus, working in master-slave mode, independent transceiver. The SPI bus consists of SCLK (serial clock), SDI (serial data input) and SDO (serial data output). CS.SPI is a protocol that allows a master device to initiate a synchronous communication with serval slave devices. The data lines of the SPI for input and output are independent, so it is allowed to complete the input and output of data at the same time.

2.4.2 Universal Asynchronous Receiver Transmitter

UART is a two-wire, full-duplex, asynchronous serial communication bus. There are only two lines, one for sending and one for receiving. The timing requirements for both parties are relatively strict, and the communication speed is not very fast. However, it is simple and easy, and it is suitable for transmitting data between two better-performing controllers.

3. CASE

3.1 Choose plan

The use of serial communication UART to implement the two-machine communication we describe is a very cost-effective opinion. Below, we will explain how to make this solution practical by designing a simple two-machine communication protocol. We will use the above-mentioned single-board computer Raspberry Pi and STM32F103 microcontroller to demonstrate.

3.2 Implementation plan

3.2.1 Configuration

On the Raspberry Pi[8], we will use the highly acclaimed Python to finish the programming. The Raspberry Pi 3 Model B has two sets of UART serial ports, one hardware serial port for Bluetooth, and one software serial port for GPIO pins. For performance considerations, we have to exchange them. Then, we need bind the GPIO pins to the hardware serial port instead of BT. Specific steps are as follows[9]:

A. Turn off the onboard Bluetooth feature. The steps are as described above.

B. Restore the serial port and set it as a universal serial port. Edit document: */boot/config.txt* at the end of the document, add a statement: *dtoverlay=pi3-miniuart-bt* .

Edit document:*/boot/cmdline.txt*,next step replace the contents of the document with the following:

dwc_otg.lpm_enable=0

console=ttyl

root=/dev/mmcblk0p2

rootfstype=ext4

elevator=deadline

fsck.repair=yes rootwait

Above we have completed the basic configuration of the serial port.

3.2.2 Programming

A. Reference the pyserial[6] library for serial programming. It has been shown in the figure1.

PySerial encapsulates the serial communication module and supports different platforms such as Linux, Windows and BSD. Also, it is a python support module. This module encapsulates the access rights of the serial port. The module named "Stand" will automatically select the appropriate backend.

B. On the STM32[7], the communication part code is as figure 2.

```
import serial
com=serial.Serial('COM7',9600)
com.write('on')
```

Fig1. pyserial library for serial programming

```
void USART1_IRQHandler(void)
{
    u8 Res;
#if SYSTEM_SUPPORT_OS
    OSIntEnter();
#endif

    if(USART_GetITStatus(USART1, USART_IT_RXNE) != RESET)
    {
        Res =USART_ReceiveData(USART1);

        if((USART_RX_STA&0x8000)==0)
        {
                if(Res==0x40)
                    USART_RX_STA|=0x8000;
                else
                {
                    USART_RX_BUF[USART_RX_STA&0X3FFF]=Res ;
                    USART_RX_STA++;
                    if(USART_RX_STA>(USART_REC_LEN-1))USART_RX_STA=0;
                }
            }
        }

#if SYSTEM_SUPPORT_OS
    OSIntExit();
#endif
}
```

Figure 2: the communication part code

3.2.3 Design

A. After solving the problem of how to initiate communication on both sides, it is necessary to design a set of application layer communication protocol to unify the standard of multi-party hardware communication. In order to make the communication content can be recognized bilaterally. Also, easy to increase or decrease the modification function. This article thinks that the protocol standard needs to meet the following.

- The unit of communication content is a message frame, including the frame header, the message body, and the end of the frame, all of which are ASCII characters.
- The message body includes a variety of data, each of which has its corresponding flag, data body, separator between the data and the data body, and a separator between the data.
- Each type of data is distinguished by a identifier, and the meaning and data type of its representative are negotiated in advance.
- The final assembled message frame can be divided, recognized, converted, and processed in the form of a string or an array of characters as both ends.

B. As an example, this article will introduce a set of application layer communication protocols designed in a vehicle project.

Basic definition of interface:

a. Serial communication using the UART protocol, the baud rate is 115200.

b. In the form of a packet, the header is defined as *(ASCII code 0x2A) and the trailer is defined as # (ASCII code ox23)

The data in data packet must have an identifier,

a)Which is any uppercase letter in ASCII, followed by the data body.

b) The data identifier is separated from the data body by ':' (ASCII code 0x3A)

c) Multiple data is separated by ',' (ASCII code 0x2C) in the same package.

Identifier	Type	Description	When
A	null	Package of sync request, empty body	Request micro-controller sync data
B	uint8	Battery level of percentage system	Battery level is updated
M	uint8	Motor state, 1-5 means go/back/left/right/stop	Motor state (need) update
R	string	RFID Tag's UID of ten system	Sensor have read a new tag
Z	null	Sync header, empty body, represent the frame used by sync data	The micro-controller receive request('A' package)

Figure 3: The custom identifier

Data return confirmation and synchronization: In order to make the communication reliable, two ends can send the packet back to the secondary station after receiving the data that needs to be consistent at both ends. Besides, aim to synchronize the upper and lower data, the logical state can still obtain the underlying state after the restart, and the bottom layer should send all the latest data to the logical end the synchronization data frame flag 'Z' should be added to the header of the post back message. The certain example is as figure 4.

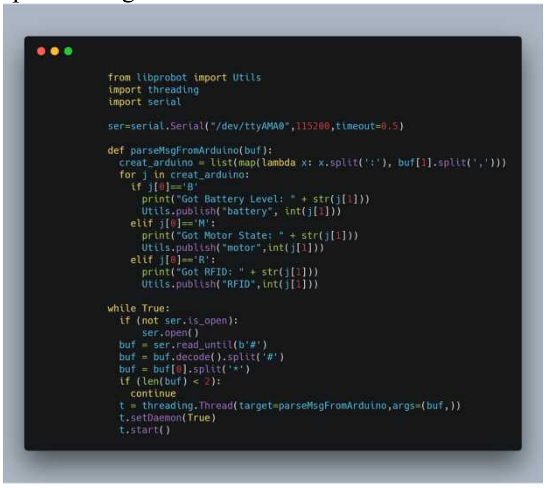

```
from libprobot import Utils
import threading
import serial

ser=serial.Serial("/dev/ttyAMA0",115200,timeout=0.5)

def parseMsgFromArduino(buf):
  creat_arduino = list(map(lambda x: x.split(':'), buf[1].split(',')))
  for j in creat_arduino:
    if j[0]=='B'
      print("Got Battery Level: " + str(j[1]))
      Utils.publish("battery", int(j[1]))
    elif j[0]=='M':
      print("Got Motor State: " + str(j[1]))
      Utils.publish("motor",int(j[1]))
    elif j[0]=='R':
      print("Got RFID: " + str(j[1]))
      Utils.publish("RFID",int(j[1]))

while True:
  if (not ser.is_open):
      ser.open()
  buf = ser.read_until(b'#')
  buf = buf.decode().split('#')
  buf = buf[0].split('*')
  if (len(buf) < 2):
    continue
  t = threading.Thread(target=parseMsgFromArduino,args=(buf,))
  t.setDaemon(True)
  t.start()
```

Figure 4.Certain example of programming

4. Conclusion

The above is an implementation scheme that we proposed and completed. We use the UART serial port as the transport layer protocol to design the application layer protocol.

5. Acknowledgement

This research was partially supported by Student's Platform for Innovation and Entrepreneur Training Program, the Ministry of education of China （201810057019）. We are also very grateful to Yang Jiasheng for his help in the revision of the manuscript.

REFERENCE:

1. LiMing. Research and development of embedded TCP/IP protocol stack. Computer engineering and Application, 2002, (8): 18-19
2. IEEE 802.3-2015 Ethernet protocol official document
3. CJ1W Defined CAN Unit Operational Manual
4. Wang Weixin. Principle and interface technology of single chip microcomputer: China Agriculture Press,2013.08
5. Song Qinhua. Shipboard Electronic Countermeasure. Comparison of online programming mechanism between SPI and UART, 2015, (10): 66-67
6. pySerial 3.0 documentation. https://pythonhosted.org/pyserial/.
7. Wang Wei. Design of communication system without host computer based on STM32F103. Tianjin Polytechnic University,2017.
8. Raspberry official technical documents. https://www.raspberrypi.org/blog/.
9. THE RASPBERRY PI UARTS. https://www.raspberrypi.org/documentation/configuration/uart.md.

Design and implementation of a baby care robot

Yizhun Peng, Zefan Ge *, Kaixuan Geng, Zhou Yang, Rui Yang

College of Electronic Information and Automation, Tianjin University of Science & Technology, China

Binhai International Advanced Structural Integrity Research Centre，Tianjin University of Science and Technology,China

** gezefan@mail.tust.edu.cn*
www.tust.edu.cn

Abstract

Aiming at the shortcoming of single function of traditional pram, this paper proposes an embedded multi-functional intelligent baby care robot. With baby cradle as the carrier, the bionic cradle is realized by combining embedded controller, drive module, motor and various sensors. The babysitting robot has the functions of autonomous following and obstacle avoidance, voice play and real-time picture return, It not only enriches the function of pram, but also improves the convenience and safety of pram, and can assist the parents to take care of the baby, which greatly reduces the parents' burden of parenting.

Key words: robot, autonomous follow, obstacle avoidance, Voice play interface, real-time picture transmission

1. Introduction

Now China has become the largest child carrier producer in the world [1]. But with the rapid development of science and technology, the traditional baby carriage with single function can not meet the needs of parents very well. In order to relieve the pressure of parents to take care of children, an embedded intelligent child-care system is designed and embedded in the baby carriage, which makes the existing ordinary baby carriage become an intelligent baby-care robot. It can help parents to take care of children, Parents spend less time in taking care of babies and making babies grow healthier and healthier. For example, when the baby is awake and crying, the traditional baby carriage must have someone waiting beside the baby carriage to cradle and coax the baby to sleep at all times, so it can not do other things. The simulation automatic cradle realized by the motor control of this product can automatically complete the work without delaying the work of parents; When the baby wakes up, the baby needs to be accompanied, cars can play parents' recordings,Tang poems, children's songs and so on to accompany them in early childhood education[2]. Car-mounted cameras can send pictures of babies back to the computer or mobile terminal in real time, so that parents can see the situation of babies with their mobile phones whenever they are cooking or busy. At the same time, the baby carriage also has the function of autonomous follow and obstacle avoidance. It not only improves the convenience and safety of the baby carriage, but also helps parents to take care of the baby, and greatly reduces the burden of parenting[3].

This product breaks through the capability range of the existing baby carriage with artificial intelligence technology, so that parents can take care of the baby without affecting their work. It also enables parents to have more independent space and free time, so that intelligent childcare can lead the trend of the times [4].

2. The overall scheme design

The modular embedded intelligent child-rearing system is based on Arduino single-chip computer, using baby cradle car as the carrier, combined with drive module, motor and a variety of sensors. As shown in Fig. 1 is a high-definition camera, which is used to monitor the baby's condition and upload the video to the terminal; 2, 3, 4, 5 and 6 are photoelectric sensors, in which 2, 3, 4 and 5 are placed in the upper, middle and lower layers in front of the baby carriage respectively to avoid obstacles; 6 are placed above the rear of the baby carriage for independent follow-up of the baby carriage; 7 are motor-driven. Module, drive motor to provide power for baby carriage. The sensor information transmission signal is analyzed to drive the circuit to control the motor movement.

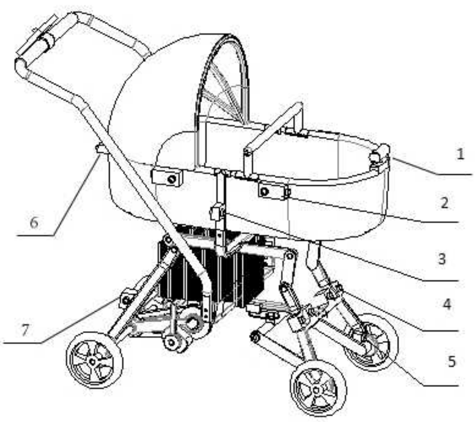

Fig.1. overall layout of the baby care robot

(1. Hd camera, 2-6. photoelectric sensor, 7. motor drive module)

2.1. Main control chip

ATmgea328p MCU of Atmel Company has the advantages of high performance, high cost performance, rich peripherals and low power consumption[5].The microcontroller based on Atmel 8-bit AVR RISC combines 32 kB ISP flash memory and read-write capability, 1 kB EEPROM, 2 kB SRAM, 23 general I/O lines, 32 general working registers, 3 flexible timers/counter of compare mode, internal and external interrupts, serial programmable USART, byte-oriented 2-wire serial interface, SPI serial port, 6-channel 10-bit A/D converter (8 channels encapsulated by TQFP and QFN/MLF), Programmable Watchdog Timer with internal oscillator, and five software alternative power-saving modes. The device operates between 1.8-5.5 volts. The throughput of the device is close to 1 MIPS per MIPS. This design uses the Arduino serial microcontroller with ATmgea328p kernel as the controller of the robot.

The Arduino ecosystem includes a variety of development boards, modules and expansion panels. Among them, UNO R3 is the most suitable entry and the most functional Arduino development board. It is a microcontroller board based on ATmega328P. It has 14 digital input/output pins (6 of which can be used as PWM output), 6 analog inputs, 16MHz crystal clock, USB connection, power jack, ICSP connector and reset button. It only need to connect computer through USB data line to power supply, program download and data communication.The main control chip is shown in the Fig. 2.

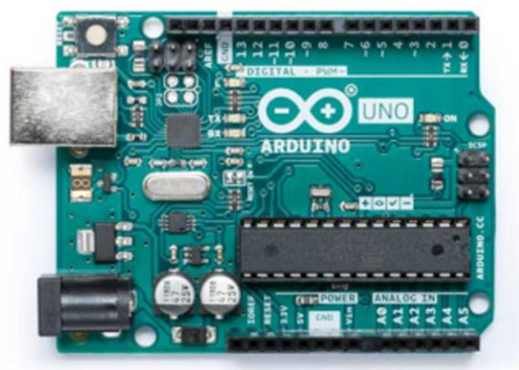

Fig.2. The Arduino UNO R3 real figure

2.2. The Photoelectric sensor

This design uses photoelectric sensor to realize automatic following and obstacle avoidance. The sensor model is E18-D80NK, as shown in Fig.3.

Fig.3. The photoelectric sensor physical map

E18-D80NK infrared photoelectric switch, also known as diffuse reflection obstacle avoidance sensor module proximity switch, is a photoelectric sensor which integrates transmission and reception. The emitted light is modulated and sent out, and the receiver demodulates the reflected light. The interference of visible light is avoided effectively. The use of lenses also makes it possible for the sensor to detect up to 80 cm distances (due to the characteristics of infrared light, different colors of objects can detect different maximum distances; white objects are farthest, black objects are nearest). The sensor has many advantages, such as long detection distance, less visible light interference, low price, easy assembly and easy use. It can be widely used in many occasions such as obstacle avoidance of robots, pipeline parts and so on. Its working voltage is 5V DC power supply, driving current is 100mA, working environment temperature is - 25 C - 55 C, standard detection object illumination requirements are below 1000LX, incandescent lamp 3000LX, effective detection distance for opaque objects is 3 - 80cm,the distance of the obstacle can be detected by adjusting the adjustable potentiometer at the end of the sensor.The working principle of photoelectric sensor is to control by converting the change of light intensity into the change of electric signal. When the sensor detects obstacles in front, the red indicator lights up at the rear of the sensor, and the return value of the single chip computer is 0, which outputs low level. When there are no obstacles in front of the sensor, the single chip computer outputs high level 1. The single chip computer determines whether there are obstacles in front of the sensor by collecting the return value of the sensor. The sensor has three lines: brown, blue and black. The Brown connects to 5V pin of MCU, the blue connects to the ground pin of MCU, and the black connects to the digital pin of MCU. The return value of the sensor can be read out by the serial port monitor of MCU to judge whether there is an obstacle in front of it.

2.3. The recording and playback module

The nested recording and playback module in the baby carriage plays the role of early education. This module can not only record parents'voices and play them to infants, but also play children's songs, Tang poems, fairy tales and so on. It can accompany infants all the time and teach them early6.

This module is composed of speech recording circuit, audio power amplifier circuit and audio decoding circuit. Language recording circuit is essentially an analog data acquisition system. Using DTAS (direct analog storage) technology, the recorded and played information can be directly recorded in EEPROM inside the chip, so that the existing analog data can be well preserved. Effective components, reduce the distortion of sound quality, improve the quality of recording and playing, and get the natural and realistic sound reduction effect. The working principle of this module is to decode the read signal through the audio decoding circuit to get the digital signal. Then the digital signal is converted into analog signal by the digital-to-analog converter. The analog audio is amplified by the audio power amplifier circuit. Finally, the low-pass filter is sent to the headphone output port.

2.4. The video monitoring module

The video monitoring module is composed of high-definition camera, ESP8266 control board and mobile phone (computer) APP7. The camera is inside the cradle car to capture the baby's status in real time and transmit the image to the connected control board. Finally, we can see the video taken by the camera through the mobile phone (computer) terminal to understand the baby's status. . This module has two working modes: when the parents are close to the baby stroller, for example, when the baby sleeps in the bedroom in the same house and the parents cook in the kitchen, we can create hot spots through the WIFI module of ESP8266 main control board and transmit picture data under the same LAN. When parents are far away from the baby stroller, for example, when parents want to see the baby's condition at work, they can also view it through the terminal, but they need a cloud server. First, the master board uploads the data collected by the camera to the cloud server, and then the parents download the video from the cloud to watch locally using the mobile terminal8.

2.5.Motor control system

The system consists of Arduino main control board, drive circuit, motor and coder. The system block diagram is shown in Fig. 4.

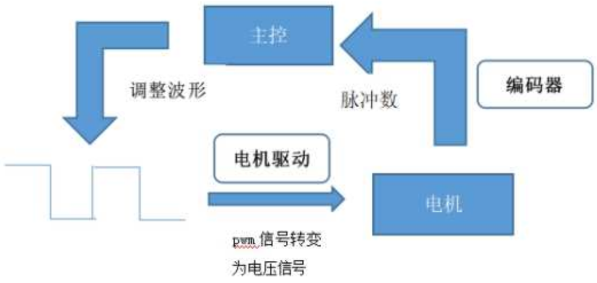

Fig.4. The motor control system

The main control board transmits one-wave signal to the motor driving circuit, and the motor driving circuit changes the voltage at both ends of the motor according to the square-wave signal, so as to control the motor speed. Then the motor speed is monitored in real time by the encoder and the pulse count is transmitted back to the main control to realize the closed-loop feedback system,and then the PID algorithm is used to adjust the duty ratio to achieve the set speed of the motor.

2.6 Data acquisition and processing

In this module, ADC is used to collect sensor data, and the data collected directly from the sensor is not accurate because it is susceptible to external interference. Therefore, according to different types of sensor data, mean filtering, weighted recursive average filtering, median filtering, Kalman filtering, dithering filtering and first-order lag filtering are carried out to improve the data accuracy.

3. Mechanical structure design

We use embedded mechanical structure to combine intelligent modules with baby carriage, which makes the traditional baby carriage multi-functional and intelligent, and optimizes the mechanical structure of baby carriage on the original basis.

3.1. Interactive part embedded structure

In the mechanical part of human-computer interaction, in order to achieve the purpose of easy use and simplicity, we analyzed a number of solutions for structural design, and finally chose the first one, as shown in Table 1.

Table 1 structure plan and analysis

Plan 1: use threaded fitting to link each component.	**Advantages**	**The material is easy to obtain, convenient to use, simple in structure, reliable in link and convenient in assembly and disassembly.**
	Disadvantages	The joint is easy to cause careless scratches, low pressure, and easy to rot and leak at the thread.
Plan 2: use buckle structure to link all parts.	Advantages	The assembly is simple, fast, saving time, saving material cost, and the finished product is not easy to be damaged artificially.
	Disadvantages	Customer disassembly time consuming.
Plan 3: use the pin link scheme	Advantages	Links are simple and easy to replace.
	Disadvantages	The reliability of the link is not high enough.

In order to achieve the purpose of good strength and light weight in the selection of mechanical structural materials, we analyzed several schemes for the selection of materials, and finally selected the first one, as shown in Table 2.

Table 2 material selection plan and analysis

Plan 1: use 3D to print materials.	**Advantages**	**Strong development and short R & D cycle.**
	Disadvantages	The production cycle is long and the R & D cost is high.
Plan 2: use of aluminum metal materials	Advantages	The technology is mature, and the cost of mass production is low.
	Disadvantages	The metal itself is heavier.
Plan 3: use of carbon fiber materials	Advantages	The quality is light and the intensity is good.
	Disadvantages	The price is high.

3.2. Structural design of each module

In view of the monitoring, real-time and reasonable structure of some sensors located in the baby carriage, we have set up a special slot for the sensor, and use the embedded installation method to ensure the ease of use and convenience of the sensor above. Because the sensors in the lower part need to take into account the characteristics of safety and intelligence, a surround mechanical structure is specially designed to ensure that they have the function of safe escort while having an intelligent experience.

In order to make the display part run stably and cope with the unfavorable weather environment in general, a set of protective structure with waterproof and preventing accidental impact damage is designed for the display and its surrounding components. On the premise of satisfying the function, the control part is specially designed to make it more ergonomic and bring users a better experience.

3.3. Motor performance analysis and drag structure design

In order to ensure the mechanical properties and structural stability of the traction part of the motor, ANSYS is used to carry out mechanical analysis of the mechanism. After analyzing various schemes, the direct traction structure with the best performance is selected. The traction mechanism diagram is shown in Fig. 5.

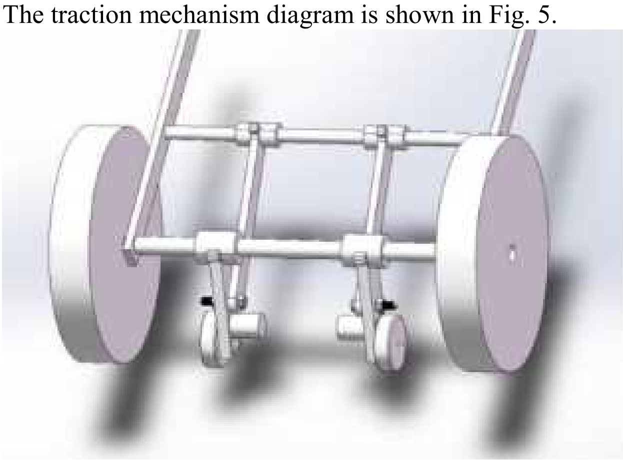

Fig.5. Motor drive mechanism diagram

Then, the performance of the motor was analyzed, and multiple types of motors were selected for comprehensive comparison analysis to test the motor's mechanical performance. The analysis results are shown in table 3.

Table 3 motor performance analysis

Name	**torque**	**Motor weight**	**Advantages and disadvantages**
42BYGH 40-1704A stepper motor	0.48N*m	360g	The amount of movement is accurate, the speed is uniform, the structure is stable, and the noise is low.
			Torque is small and drag is difficult.
N-F-0321 Gear motor	5.16M*m	146g	Light weight, high torque, good for dragging.
			External encoder control is required.
AB42 Planetary reducer	10N*m	400g	Light weight, high torque, good for dragging.
			External encoder control is required.
HB860H stepper motor	8.5 N*m	400g	Large torque can travel on complex ground.
			The price is high and the noise is high.

Under the condition of synthetically analyzing the load and torque that the stator rotor and shaft of the motor need to bear and reducing the cost as far as possible, the N-F-0321 deceleration motor is chosen as the power source of the traction part of the baby carriage9.

The motor operation scheme generally includes gear drive, belt drive and direct traction drive. Through the analysis of table 4, we finally choose the motor direct traction mode of scheme 3.

Table 4 motor drive scheme and analysis

Plan	**The advantages and disadvantages**	
Plan 1: use the gear drive scheme	advantages	Gear transmission is stable, transmission ratio is accurate, reliable, high efficiency, long service life, using a wide range of power, speed and size.
	disadvantages	Heavy weight, noise, transmission distance is small, often need lubrication, and most of the baby carriages on the market can not directly match the gears.
Plan 2: use belt drive scheme	advantages	The belt has good elasticity, it can relieve impact and vibration in work, smooth movement and no noise. When the load is too large, the belt slips on the wheel, so it can prevent other parts from being damaged and play a role of safety protection. The belt is an intermediate part. It can select the length according to the need in a certain range to adapt to the larger working conditions of the center distance requirement. The structure is simple, easy to manufacture, easy to install and maintain, and low in cost.
	disadvantages	Transmission by friction can not transmit high power, and cause sliding loss and delay loss easily.

Plan 3: scheme of direct traction with motor	advantages	Simple and easy to use, flexible structure, can be applied to a variety of complex environments.
	disadvantages	The traction tire of motor is easy to slide on the smooth road when rotating.

4. function introduction

Modular embedded intelligent child care system is composed of two main functions: safety monitoring and self motion. The product is nested on a baby carriage to be a baby care robot. The robot's physical diagram is shown in Fig. 6 below.

Fig. 6. The robot physical map

Baby care robot is a multi-functional baby carriage, which can not only take care of the baby carefully, but also ensure the safety of the baby efficiently. It can provide a safe and comfortable environment for infants. The system consists of several modules, such as bionic automatic cradle module, automatic tracking module for infant parents, intelligent autonomous obstacle avoidance module and early education module, which can effectively, comprehensively and real-time protect infants and provide them with a comfortable environment. Environmental Science. Its mechanical aspect uses a new type of mechanical structure, through the motor rotation to provide power for the baby carriage, can effectively reduce the pressure of the cart. Baby care robot, the first car in the baby's life, gentle, considerate, intelligent and omnipotent, all-round care of the baby's safety. The intelligent system of baby care robot meets the needs of infant growth.

4.1. Bionic automatic cradle function

When a baby is awake and crying, parents usually use rocking cradle to coax the baby to sleep or stop crying, but this requires parents to stay beside the baby carriage and not be able to do their own thing, and sometimes distracted by urgent things. We designed a bionic automatic cradle for this situation, the model. The block adopts fully automatic technology, which can automatically swing with the most suitable frequency and amplitude, simulate the scene of parents shaking the baby to sleep, help the baby sleep better and more comfortably, and parents can also take time to do other things.

4.2. Self following and obstacle avoidance functions

The photoelectric sensor is used to realize the function of independent following and obstacle avoidance of the baby carriage. The photoelectric sensor is installed at the rear of the baby carriage. The algorithm is used to realize the function of automatic following. When the rear sensor detects the parents, the baby carriage begins to move forward. When the left sensor detects the parents, the baby carriage turns right differently, and when the rear is right. When the side sensor detects the parent, the baby carriage turns left. In the process of movement, if the front sensor of the baby carriage detects obstacles, the baby carriage immediately stops moving. The photoelectric sensor in front of the baby carriage is divided into three layers: upper, middle and lower, which can detect obstacles of different heights. This function can very well assist parents to take baby strollers out, especially for the elderly to take children out, which can provide great convenience and safety.

4.3. The function of early childhood education

An early education module is embedded in the baby carriage, which includes recording and playback, poems, children's songs, fairy tales and other functions. When the baby is awake, we can not only play the audio recorded in advance by parents to accompany the child, but also play children's songs, poems, fairy tales and so on to enlighten the infant's early education. At the same time, the baby is not alone when it is alone.

4.4. The real time video return function

The baby carriage is equipped with a high-definition camera facing the baby. We can view the video captured by the camera in real time from the terminal of the mobile phone or computer, and we can see the baby's condition anytime and anywhere. Whether you are cooking in the kitchen, going out to buy food, or missing your baby, you can always pick up your mobile phone to check the baby's condition. This function has brought great convenience to parents.

5. summary

With the change of time, technological means are also developing rapidly. More and more behaviors and work can be replaced by robots, which is an irresistible trend. More detailed escort robots will be developed. With the development of artificial intelligence, robots are becoming more and more intelligent, and they can do more and more things. Service-oriented robots will be full of people in all aspects. By that time, care robots need to be more capable and more humane.

References

1. Wenjie Wang. Design and research of a new type of baby carriage. Tianjin University of Science and Technology, 2017.
2. Yanhui Chen, Xiaoqi Li. Design of an intelligent baby carriage. science and technology innovation guide, 2014,11 (27): 53-54.
3. Zhihan Li, Yicheng Shi, Ying Wang. Design and Research of Multifunctional Intelligent Baby Car. Digital Technology and Applications, 2018,36 (03): 174-175.
4. Saishai Li, Yue Qiu,Bowen Sun . Research on Intelligent Baby Car Design Based on Emotional Design Theory. Industrial Design, 2018 (08): 30-31.
5. Mengting Liu, Fan Wu, Zhiqin Chen. Design of aerial reconnaissance six-axis rotary-aircraft based on ATmega-328p and Android.Electronic world,2016(18):147-148.
6. Qiuming Wang, Chaoyang Zhu, Qiuyu Xu, Yuxuan Sun. Intelligent baby carriage design. Information and computer (theoretical version), 2017 (21): 110-111.
7. Binqi Liu, Haitao Liu. Design of Intelligent and Safe Baby Car for Data Communication Based on STM32. Science and Technology and Innovation, 2018 (16): 62-63+67.
8. Qijun Zou, Sunjia Wei, Shiji Yu, Huijin Chen. An intelligent design of baby carriage. Popular Science and Technology, 2015, 17 (06): 5-6+12.
9. Sen Li, Yicai Tian, Ming Tan, Fanghui Gao, Wanzhao Zhao. Smart Following Baby Cart Design Based on STM32. China Science and Technology Information, 2018 (09): 81-82+12.

Research on Intelligent Shopping Service Robot Design

Shuo Wang[1,2], Yizhun Peng *[1,2], Ruixiang Bai[1], Ziheng Gao[1,2]

1.College of Electronic Information and Automation,Tianjin University of Science and Technology, China

2.Binhai International Advanced Structural Integrity Research Centre， Tianjin University of Science and Technology,China

** pengyizhun@tust.edu.cn*

Abstract

With the rapid development of the social economy, it is good to help customers have more efficient and relaxed shopping experience through intelligent means in large commercial centers. In this paper, a shopping service robot project that uses machine vision, deep learning, and IoT is introduced. The robot can help customers complete shopping and complete indoor positioning navigation and autonomous movement intelligently. The robot product is designed to help all customers, especially people with mobility impairments. It will reduce their burden of action, thereby enhancing the user experience and doing special analysis of shopping behavior to help launch more efficient and personalized market planning.

Keyword: feature recognition, Artificial neural networks, indoor positioning navigation, machine vision

1. Introduction

With the in-depth development of artificial intelligence, the current research on smart shopping carts (robots) is also deepening. There are some innovative designs such as a large shopping cart based on traditional ergonomics, a smart shopping cart system that can automatically follow up, a smart shopping cart based on RFID technology, etc[1-3].

This paper aim to design a shopping service robot to optimize shopping and entertainment experience. The main designing features are as follows.

(1) The robot is designed to result in implementing object follow with the use of machine vision to identify feature description.

(2) The inertial navigation system module uses the same feature color block identification method. The INS (Inertial Navigation System) module is calibrated to improve indoor positioning accuracy under known indoor map conditions.

(3) Artificial neural networks (ANN) are used to train the contours of customers. The color block recognition feature in machine vision is used to reduce the weight of the training model to improve the accuracy of object tracking.

The above scheme can realize automatic tracking of customers, indoor positioning navigation and autonomous movement. Robots can combine recommendations and systems to create clear, personalized route recommendations to reduce barriers to customers' shopping experience.

2. Design

2.1. Feature recognition module

2.1.1 Color feature

Color feature is a significant and intuitive underlying feature of the image with RST (rotation, scale and translation) invariance. This article designs a method for color feature resolution and image feature extraction. The specific method is to use a small unit method combining different characteristic color values to form a characteristic color block. The color feature[4] mainly uses the HSV space. The HSV is the representation method of the point of the RGB color space in the inverted cone. The method can achieve simple, fast linear transformation and better clustering[5] effect.

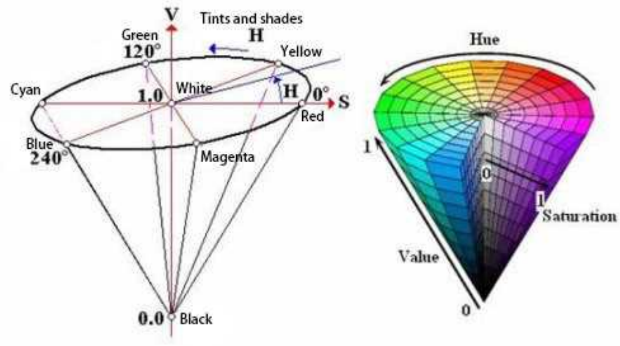

Fig 1. HSV space

2.1.2 Image color feature extraction

This design uses feature color blocks as visual recognition objects to achieve robotic automatic tracking accuracy improvement and correct indoor positioning navigation. In addition, the convolutional neural network is used to identify and optimize the recognition object in identification of the feature color block. thereby it improved the recognition speed and accuracy. We design to use the feature extraction of the neural network to identify the feature values of the color blocks and then obtain the image information according to the arrangement and combination of the color feature values in the image[6].

In this section, image color recognition is used to identify and analyze preset different color feature blocks. HSV color space and color image advantages are used to improve the accuracy of recognition resolution. CNN network training is used to identify recognition models under different actual conditions to improve recognition efficiency.

2.2. Indoor position navigation module

The design uses the combination of inertial navigation system and machine vision to improve the accuracy of indoor positioning on inertial navigation. The basic principle of inertial navigation is to read the linear acceleration and angular velocity by accelerometer and gyroscope respectively and establish the navigation coordinate system[7], as shown in Figure 2. Figure 3 is a flow chart showing the speed and position of the robot body in the navigation coordinate system by solving the quaternion attitude.

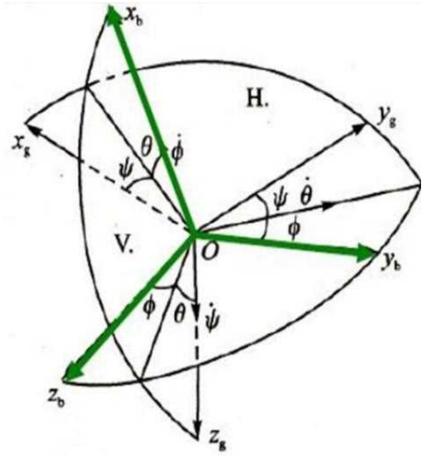

Fig 2. Navigation coordinate system

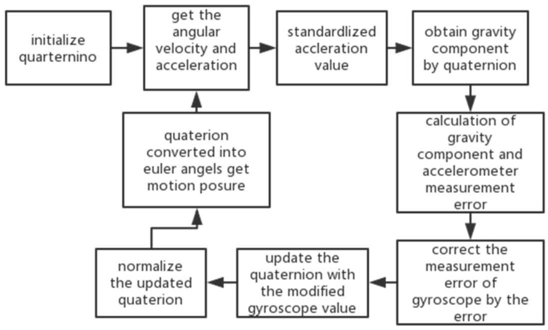

Fig 3. Navigation coordinate system by solving the quaternion

2.2.1 Error analysis

Since the accelerometer and gyroscope in the mems inertial device are essentially sensors, there is a large error in the actual use of the device[8]. The calibration principle of accelerometer and gyroscope is as follows.

1) Accelerometer calibration principle

$$a' = a * scale + bias \tag{1}$$

(a' is the measured value of the accelerometer, a is the ideal value, scale is the accelerometer scale factor, and bias is the zero-point decimation)

2) Gyro calibration principle

$$gyro' = gyro * scale + bias \tag{2}$$

2.2.2 Actual error correction scheme

Actually, the robot cannot automatically recalibrate at regular intervals. As time pasting, temperature drift will become more and more obvious. These factors will increase the positioning error[9]. So, we set up I^2C communication between MPU6050 and Raspberry Pi, and then configure the I^2C address of Raspberry Pi and MPU6050. We can read and write the MPU6050 register by reading and writing the MPU6050 register. We also use the quaternion algorithm to convert the acceleration and angular velocity values of the three axes into Euler angles and establish the inertial navigation coordinate system to obtain the speed and position of the robot body .

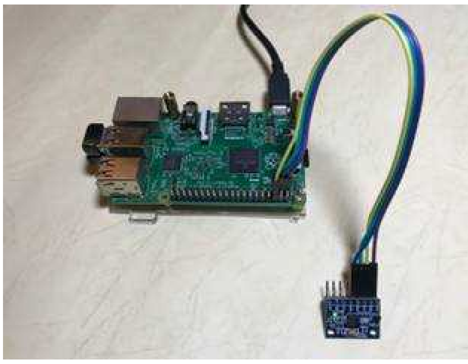

Fig 4. Hardware connection diagram

We use the CNN image DHF feature extraction algorithm in machine vision to identify the preset feature patches. We obtain the image feature information according to the corresponding unique coordinate information. We store it in the memory of the Raspberry pi and replace the coordinate information in the mpu6050 with it. This updates the coordinates of the robot, improving the accuracy of navigation.

2.3. Human contour recognition module

This paper mainly adopts the way of extracting human body contour from sequence image as the main recognition model of robot recognition customer and add color block feature to improve the recognition accuracy. The dual feature recognition training mode has certain robustness.

2.3.1 Extraction of human contour features

This article uses Gabor feature information to extract the character(customer)contour in the image. The steps are as follows:

a. The input tested picture calculates the Gabor wavelet characteristics in eight direction.
b. The RGB and Ga or features of the image are used as input values, and the contour of the human body is calculated using the expectation maximization algorithm to obtain a human body mask.
c. Perform morphological processing such as noise removal and open- loop calculation on the output of step b to obtain a more accurate human mask.
d. The mask generated in step c is phase-operated with the original image to extract the contour features of the customer image.

2.3.2 Use CNN for identification training

By consulting a large number of references[10,11,12,13], we know that methods such as learning classifiers, using a large number of feature blocks and probability enhancement trees and using sparse coding gradient features to detect and identify contours have been used.

We use Convolutional Neural Networks (CNN) to identify the contours of the characters that have been extracted and the color block features. Firstly, we design to construct a 14four-layer neural network, where the size of the input layer is 45 × 45 × 3, and the size of the four-layer convolutional layer is 45 × 45 × 32, 22 × 22 × 48, 11 × 11×16 and 5×5×128. The first fully connected layer size is 128 and the last layer size is 101. Among them, four convolutional layers and two fully connected layers are used for parameter learning and the remaining layers are randomly initialized[15]. Its structure is shown in Figure 5.

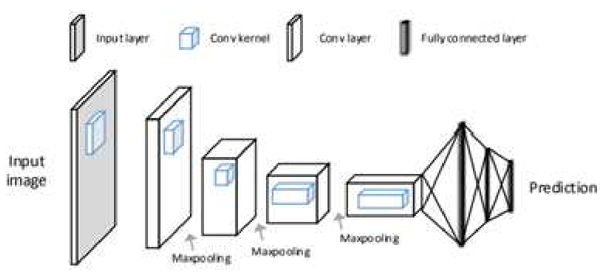

Fig 5: CNN structure diagram

2.3.3 Experimental effect training

We use the specific person pictures collected in the supermarket scene as the data set to extract the contour features and color block recognition features of the customers in the image. There are 500 images in total, of which 200 are for training, 200 for testing and 100 for inspection. In order to evaluate the classification results, a correct recognition rate (PCR) is introduced as an evaluation index, which is defined as follows

$$PCR = \frac{T}{N} \times 100\% \tag{3}$$

T is the number of correctly identified samples and N is the total number of test samples.

If the CNN only recognizes the contour features of the customer, the average correct recognition rate is 80% after multiple training verifications. If the recognition of the color patch feature is added, the correct recognition rate of CNN can reach 90%, and the training effect of the model is significantly improved. Moreover, the recognition effect of CNN is more ideal than the single feature recognition method in the environment of uneven illumination, which shows that the dual feature recognition enhances the robustness of CNN.

3. Conclusion

In a separate module test, the basic expected effect can be achieved in an ideal environment. Due to the large amount of computation, it is impossible to put all the functions on the Raspberry Pi processor. So, we plan to use cloud services to solve the problem and move some of the operations to the cloud.

Acknowledgement

The study was partially supported by Student's Platform for Innovation and Entrepreneur Training Program, the Ministry of education of China(201810057019). We thank Wu Peishu for his help in greatly improving the manuscript. We are also very grateful to Yang Jiasheng for his help in the revision of the manuscript.

References

1. JiangChao. The principle and algorithm of automatic following system for Internet supermarket shopping cart. *Electronic technology and software engineering*, 2018, (11): 1-2
2. WangChongning. Analysis of innovative design of large supermarket shopping cart based on Ergonomics. *Industrial Design*, 2016, (1): 33-35
3. LiYun. Research and design of intelligent shopping cart based on RFID Technology. *Internet of things technology*, 2014, (7): 18-19
4. PanYongsheng. A new multi feature fusion method for image retrieval. *Science and technology and Engineering*, 2014, 14(15):219-223
5. ZhengQiang. A new color feature extraction method in image retrieval. *National Conference on new computer technology and computer education*. 2009.
6. LiQin. Image depth level feature extraction algorithm. *Pattern recognition and Artificial intelligence*, 2017, 30(2): 127-136.
7. HeChao. *Error compensation of MEMS sensor for Strapdown Inertial Navigation System*. Harbin Institute of Technology. Master's degree thesis, 2010.
8. YuRongnan. Design of two order complementary filter attitude solver. *Journal of zhejiang university of technology*,2017,45(4):417-420.
9. FengXinyu. *Design of four rotor UAV*. Beijing: Tsinghua University Press, 2017.
10. SunDong. Recognition of human contour features based on support vector machine. *Scientific and technological information*, 2009, (8): 53-55
11. D.R.Martin,C.Fowlkes, D.Tal,and J.Malik.A database of human segmented natural images and its application to evaluating segmentation algorithms and measuring ecological statistics.*In Proc.ICCV*,pages 416-425,2001.
12. P.Dollar,Z.Tu,and S.Belongie.Supervised learning of edges and object boundaries. *In Proc.CVPR,volume* 2,pages 1964-1971,2006.
13. Z.Tu.Probabilistic boosting-tree: Learning discriminative models for classification, recognition, and clustering. *In Proc. ICCV*, volume 2, pages 1589-1596. *IEEE*,2005.
14. Alex Krizhevsky. *ImageNet Classification with Deep Convolutional Neural Networks*
15. X.Ren and L.Bo.Discriminatively trained sparse code gradientsfor contour detection. *In Proc. NIPS*.

Design and Research of Navigation and Dynamics Co- Simulation Platform for Planetary Rovers

Huang Tieqiu
School of Mechanical, Electronic and Control Engineering
Beijing Jiaotong University
Beijing, China

Zhang Bowen
School of Mechanical, Electronic and Control Engineering
Beijing Jiaotong University
Beijing, China

Huang Qianli
The High School Attached to Beijing Jiaotong University,
Beijing, China

Abstract

In view of the high demand for the design of navigation control system for the complex mission of Mars and other planets which will be carried out in our country in the near future, the overall design idea of the combined simulation platform for navigation and dynamics of the planet vehicle is put forward. On the basis of MSC-ADAMS software, the dynamic model of planetary rover in soft soil environment was established through the secondary development of subroutine. C++ was used to establish an interactive parallel simulation system, and the dynamic model and navigation control model were co-invoked for parallel calculation to form a co-simulation closed-loop system, so as to realize seamless connection and parallel efficient calculation between the navigation control system and the dynamic model. Because of the high efficiency of the wheel soil contact model algorithm and the adoption of parallel multitasking method, the co-simulation can reach almost real time. The platform lays an important foundation for the design of navigation control system.

Keywords: planetary rover; co-simulation; dynamics of terrain-vehicle; dynamics of multibody systems

1. Introduction

Mars terrain is more complicated than the moon, and the requirements for the passing of the planetary rover are getting higher and higher. At the same time, the design of navigation and control system has put forward with a higher demand. There is an urgent need to develop a planetary vehicle simulation platform with the ability to establish a planetary vehicle dynamics model and to be efficient, real-time and stable.

At present, a variety of simulation tools for planetary vehicles have been developed by relevant foreign research institutions aiming at planetary wheel soil action. Yen [1] and Jain [2]et al. developed a ROAMS (Rover Analysis, Modeling and Simulation) planetary vehicle virtual simulation platform, and had been applied to the US Mars exploration program, which contains multiple sub-modules; Patel[3] et al. developed RMPET(Rover Mobility Performance Evaluation Tool) simulation software on the basis of Bekker[4] theory, which is used to study the rotations of the planet vehicle and calculate the settlement amount, movement resistance, slip rate, hook traction and so on of the planet rover; Bauer[5-6] et al. based on Bekker theory, developed a RCAST(Rover

conceptual, Analysis and Simulation Tool) tool with the AS2TM model of soil rotation; Feng[7] et al. have developed Artemis(ADAMS-based Rover Terramechanics and Mobility Interaction Simulator).
In China, Huang Tieqiu[8] et al. proposed a modular co-simulation model of lunar rover based on Adams and C/C++ language of multi-body dynamics software. Jiang Lei [9] et al. constructed the simulation analysis software for the 3D visualization of the lunar rover with Pro/E secondary development technology, the Vortex physics engine and the OSG graphical visualization object; Xu Yawei[10] and Shao Zheng[11] have established a lunar rover simulation platform with Bekker theory and AS2TM wheel-soil interaction model, and Ding Liang[12] has designed a comprehensive planetary vehicle simulation system through Matlab and SpaceDyn toolkits. However, the seamless link and the parallel efficient calculation between navigation control system and dynamic model are not realized.
In order to solve the problems in the design of planetary vehicle navigation system, this paper puts forward the overall design idea of the navigation and dynamics co-simulation platform on planetary vehicle. On the basis of dynamic simulation software MSC.ADAMS, we developed subroutines with the formula of Bekker wheel-soil action, and a virtual prototype of the planetary vehicle with the interaction of the soil contact was programmed to simulate the vehicle to obtain more accurate results of the performance evaluation of the vehicle. By studying the interface between command and data flow between dynamics and navigation control system, an interactive parallel simulation control system was established by C++, which seamlessly linked the navigation control system and dynamics model of the planetary vehicle. Then it can form a co-simulation platform to realize efficient co-simulation of navigation control and dynamics.

2. Architecture of Simulation Platform

Fig. 1 is the general framework of the simulation platform, including the planetary vehicle multi-body dynamics model, the wheel soil action model, the interactive parallel simulation system and the 3D dynamic image and data display system.

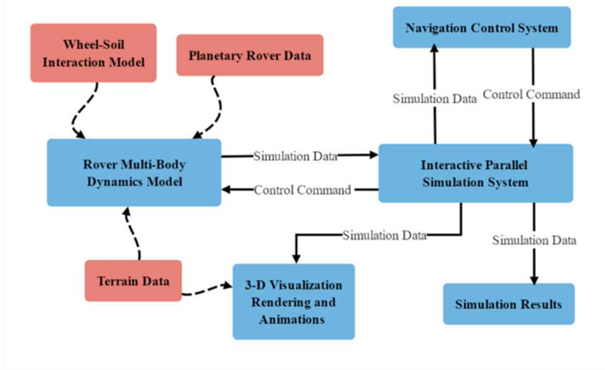

Fig.1 Architecture of Simulation Platform

2.1. *Rover Model*

By consulting relevant literatures, the active suspension planetary vehicle configuration of the article[13] is selected. Traditional rocker-steering frame suspension of the planet vehicle has good obstacle performance, but can not cross the obstacles and subsidence. The active suspension Planet vehicle is based on the traditional rocker-steering frame suspension planetary vehicle to eliminate a certain degree of freedom in the suspension and can adjust the suspension geometry. T The active suspension structure not only inherits the good pass-through peace and smoothness of the rocker-steering frame suspension, but also realizes the working conditions such as lifting the vehicle body, lifting wheels and the creep.

2.2. *Wheel-Soil Interaction Model*

Bekker theory model is widely used. Based on Bekker's theory of ground mechanics, the research on the passing of American planetary vehicle is not universal, so it needs to be rationalized and modified according to different application background conditions.
During the rotation of the wheel around the axis, there is a trend of movement relative to the ground, and the ground produces friction on the wheel, which is the fundamental reason for the wheel to move forward, also known as adhesion. The magnitude of the wheel is closely related to the movement trend of the wheel relative to the ground, and the motion of the wheel relative to the ground is described by the slip ratio. The solution formula of adhesion force P is as follows:

$$P = (c_0 \cdot A + W \cdot \tan\varphi_0)\cdot[1 - \frac{k}{sl}\cdot(1 - e^{-\frac{sl}{k}})] \quad (1)$$

Where c0 is soil cohesion, A is plate contact area, W normal load on wheel, φ0 is soil internal friction angle, k is Bernstein–Goriatchkin's parameter of a load–sinkage curve, s is slip ratio, l is wheel length of a contact area.

Since the slip ratio is 0 or tends to 0 when the wheel is stationary, the adhesion formula (1) is not usable at this time. For this reason, the formula for correcting the adhesion is obtained by the formula (2) within the range permitted by the guaranteed error:

$$P = \begin{cases} (c_0\cdot A + W\cdot\tan\varphi_0)\cdot[1-\frac{k}{sl}\cdot(1-e^{-sl/k})] & (s<s_{\min}) \\ (c_0\cdot A + W\cdot\tan\varphi_0)\cdot[1-\frac{k}{s_{\min}l}\cdot(1-e^{-sl/k})]\cdot\frac{s}{s_{\min}} & (s<s_{\min}) \end{cases} \quad (2)$$

Where smin is correction factor of slip ratio.

The Bekker theory uses the following formula to describe the external (due to soil compaction) motion resistances:

$$R_c = \frac{(3W)^{\frac{2n+2}{2n+1}}}{(3-n)^{\frac{2n+2}{2n+1}}\cdot(n+1)\cdot(k_c + b\cdot k_\varphi)^{\frac{1}{2n+1}}\cdot D^{\frac{n+1}{2n+1}}} \quad (3)$$

Where n is Bekker sinkage coefficient, D is wheel overall diameter, b is wheel width, kc 、 kφ are Bekker's cohesive and frictional moduli of soil deformation of a load–sinkage curve.

However, when the speed of wheel increases to a certain value, the external (due to soil compaction) motion resistances does not increase with the increase of speed. In order to reflect this phenomenon and ensure the continuity of force, the resistance Rc is correlated with the velocity, and the formula is obtained by modifying the formula (3).

$$R_c = \begin{cases} \frac{(3W)^{\frac{2n+2}{2n+1}}}{(3-n)^{\frac{2n+2}{2n+1}}\cdot(n+1)\cdot(k_c+b\cdot k_\varphi)^{\frac{1}{2n+1}}\cdot D^{\frac{n+1}{2n+1}}}\cdot(1+a_1\cdot s) & (v\ge v_0) \\ \frac{(3W)^{\frac{2n+2}{2n+1}}}{(3-n)^{\frac{2n+2}{2n+1}}\cdot(n+1)\cdot(k_c+b\cdot k_\varphi)^{\frac{1}{2n+1}}\cdot D^{\frac{n+1}{2n+1}}}\cdot(1+a_1\cdot s)\cdot\frac{v}{v_0} & (v<v_0) \end{cases} \quad (4)$$

Where a1 is correction coefficient of slip ratio, v0 is judgment factor of velocity.

Drawbar pull DP is actually the real power of the wheel. The formula is:

$$DP = P - Rc \quad (5)$$

2.3. *Dynamic Model of Planetary Vehicle Drive System*

ADAMS subroutine is an effective tool to extend dynamic model capability. Through the secondary development of subroutine, the modeling and calculation of motor control torque and MOTION drive unit can be realized.

PID algorithm is a widely used motor drive control algorithm, based on PID algorithm for the secondary development of SFOSUB subroutine, can achieve wheel drive modeling simulation while monitoring motor current, voltage and so on.

Because the method of establishing MOTION driving unit is adopted to realize the modeling and simulation of active suspension, according to the working mode of active suspension, the motion-controlling subroutine MOTSUB is redeveloped to realize the dynamic modeling and simulation of active suspension drive.

2.4. *Natural Terrain*

Natural terrain is an essential part of the simulation platform, this paper constructs the natural terrain environment of the platform through the C + + language subroutine. Natural terrain environment is established by dividing grids, as shown in Fig.2 :(a) The terrain is divided into square grids with equal spacing;(b) The vertices of each lattice give the coordinate value to represent the height of the terrain point;(c) The three-dimensional vertices of the lattice are connected diagonally.

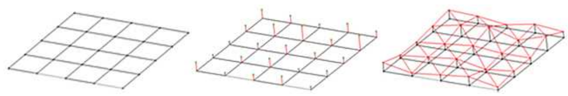

Fig.2 Natural Terrain

2.5. *Interactive Parallel Simulation System*

The simulation platform should make up the closed-loop simulation with the planetary vehicle navigation system, which has high requirements for the real-time simulation. A "bridge" is established between the platform and the navigation system to realize the closed-loop simulation, and the interactive parallel simulation system transmits the command of the navigation control system to the multi-body dynamics model of the planetary vehicle. Then the simulation data is transferred to the navigation control system to realize the seamless link between the navigation control system and the dynamic model of the planetary vehicle.

Real-time simulation is one of the most difficult problems in platform building. How to improve the efficiency of program execution and satisfy the real-time performance of simulation is an urgent problem to be solved in establishing an interactive parallel simulation control system.

Through the research, it is found that the efficiency of program execution can be greatly improved by using multithreading parallel mode, that is, instruction and simulation data transmission and state display operation are independent. In order to solve the data transmission between different threads, the memory mapping method is adopted to map the shared data to a piece of memory space, and the data is read by the token method to ensure the integrity and real-time of the data.

To establish an interactive parallel simulation system, it is necessary to clarify the interface between each module and the navigation control system under the functions of establishing the body system of the planetary vehicle, the simulation of the contact dynamics of the wheel soil, the simulation of the drive of the planet car, the measurement and output of the dynamics and kinematics results, and to establish the data communication.

3. Rover Simulation

By using the soil characteristic parameters shown in Table 1[14], an accurate control strategy is developed to simulate the various working conditions of the planet vehicle in the simulation of Mars surface environment.

are three core technologies of augmented reality technology, including three-dimensional registration technology, display technology and intelligent interaction technology[5].

Table 1: Soil Properties

Soil Properties	Figure
n	1.0
c_0	0.017 N/cm^2
φ_0	35°
k	1.78 cm
k_c	0.14 N/cm$^{(n+1)}$
k_φ	0.82 N/cm$^{(n+2)}$

The active suspension motion mode is achieved by the combination of the angle adjustment mechanism, the clutch and the drive mechanism, and the steering mechanism maintains the zero position.

As shown in Fig.3 is the lifting condition of the planetary vehicle body. Lifting wheel, creep and other working conditions are based on the vehicle body lift to achieve.

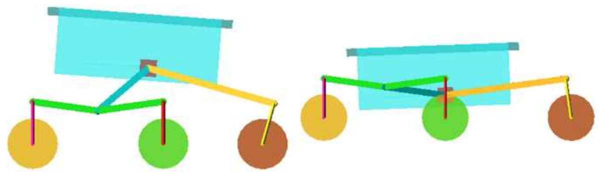

Fig.3 Body lifting

When a wheel of a planetary vehicle fails or needs to cross an obstacle, the wheel can be lifted as shown in Fig.4. During the simulation, we found that when the height of the car body is low, the body may touch the ground, so the height of the body needs to be raised before lifting the wheel.

Fig.4 Wheel lifting

The peristaltic mode of the planetary vehicle is a complex working condition. In the process of lifting and lifting the body, the wheels move together to make the planet rover wriggle, as shown in Fig.5.

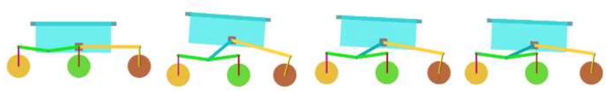

Fig.5 Creep of rover

4. Conclusion

Aiming at the dilemma of the design of navigation control system in the near future exploration of Mars and other planets, this paper puts forward the overall design idea of the co-simulation platform of planetary vehicle navigation and dynamics. Through the development of MASC.ADASM software two times, the efficient joint simulation platform of planetary vehicle navigation control system and dynamics is established by using multithreaded Parallel computing mode, which successfully combines the contact Dynamics model of wheel soil, the dynamic model of multi-rigid body of planetary vehicle and the navigation control system.

References

[1] Yen J, Jain A, Balaram J. ROAMS: Rover Analysis, Modeling and Simulation[C]//*Proceedings of the Fifth International Symposium on Artificial Intelligence, Robotics and Automation in Space*, Paris: European Space Agency, 1999, 249-254.

[2] Jain A, Balaram J, Cameron J, et al. Recent developments in the ROAMS planetary rover simulation environment[C]//*IEEE Aerospace Conference Proceedings, Big Sky: IEEE,* 2004, 861-876.

[3] Patel N, Ellery A, Allouis E, et al. Rover mobility performance evaluation tool (RMPET): a systematic tool for rover chassis evaluation via application of bekker theory[C]//*Proceedings of the 8th ESA Workshop on Advanced Space Technologies for Robotics and Automation*, 2004, 251-258.

[4] Bekker M G. Introduction to terrain-vehicle systems[M]. Translation Group of Introduction to terrain-vehicle systems. Beijing: *China Machine Press*, 1978(in Chinese).

[5] Bauer R, Leung W, Barfoot T. Development of a dynamic simulation tool for the ExoMars rover[C]//*Proceedings of the 8th International Symposium on Artificial Intelligence, Robotics and Automation in Space*, Paris: European Space Agency, 2005, 1-8.

[6] BAUER R, BARFOOT T, LEUNGW, et al. Dynamic Simulation Tool Development for Planetary Rovers[J]. *International Journal of Advanced Robotic Systems*, 2008, 5(3): 311-314.

[7] ZHOU F, ARVIDSON R E, BENNETT K. Simulations of Mars Rover Traverses[J]. *Journal of Field Robotics*, 2013, 31(1): 141-160.

[8] Huang Tieqiu, Xing Yan, Teng Baoyi. A New Mode of Co-Simulation Based on Adams and C/C++ Language[J]. *Aerospace Control*, 2011, 29(1): 63-66(in Chinese).

[9] Jiang Lei, Guo Jianjuan. Simulation Algorithm of Lunar Rover Based on Vortex[J]. *Transactions of the Chinese Society for Agricultural Machinery*, 2012, 43(s1): 352-356(in Chinese).

[10] Xu Yawei, Chen Jianxin, Liu Liangdong, et al. A Simulation Tool for Dynamics and Control of a Lunar Rover in Soft Soil Environment[J]. *Aerospace Contrd and Application*, 2008, 34(6): 52-57(in Chinese).

[11] Shao Zheng. *Study on Virtual simulation Platform of Tyre-soil Interaction for Lunar Rover Based on Virtual Reality Technology*[D]. Shenyang: Northeastern University, 2008(in Chinese).

[12] Ding Liang. *WHEEL-SOIL INTERACTION TERRAMECHANICS FOR LUNAR/PLANETARY EXPLORATION ROVERS: MODELING AND APPLICATION*[D]. Haerbin: Harbin Institute of Technology, 2010(in Chinese).

[13] Gao Haibo, Zheng Junqiang, Liu Zhen, et al. Xu Yawei, Chen Jianxin, Liu Liangdong, et al. A Simulation Tool for Dynamics and Control of a Lunar Rover in Soft Soil Environment[J]. *ROBOT*, 2017, 39(2): 140-150(in Chinese).

[14] Liu Xingjie, Su Bo, Jiang Lei, et al. Research on Soil Mechanical Properties of Martian Surface Soil[J]. *Manned Spaceflight,* 2016, 22(4): 459-465(in Chinese).

Research on Application of SFM Method in Virtual Reality Modeling

Jiwu Wang
School of Mechanical, Electronic and Control Engineering
Beijing Jiaotong University
Beijing, China

Chenyang Li
School of Mechanical, Electronic and Control Engineering
Beijing Jiaotong University
Beijing, China
E-mail: jwwang@bjtu.edu.cn, 17121244@bjtu.edu.cn
www.bjtu.edu.cn

Abstract

Virtual Reality (VR) technology has been widely used in digital cities, industrial simulation, training, etc. And virtual environment modeling is one of the most important parts in the process. When modeling virtual environment based on reality scene, using conventional methods to modeling is complicated and the model was made is different from the real scene due to the high complexity of reality scene. Applying SFM method to VR environment modeli- ng based on reality scene was proposed in this paper, which can improve the realism of the VR environment, reduce the modeling steps and shorten the modeling time.

Keywords: Virtual Reality, SFM method, modeling, Unity.

1. Introduction

Virtual Reality (VR) is an artificial media space built by computer, which is virtual with a sense of reality although. VR enables people to enter a virtual environment through multimedia sensor interaction devices with an immersive feeling. With external devices, such as helmets and data gloves, users see an interactive dynamic 3D view formed by multi-source information. VR has been applied in many fields such as aviation, aerospace, automobile manufacturing, education, etc.

VR technology uses computer to generate a virtual world with realistic three-dimensional visual, auditory, tactile and other sensory forms. The first problem to be solved during the process is virtual environment modeling, that is, the construction problem of virtual world. Using conventional methods to modeling, the modeling process is very complex and the realism of the obtained model cannot be guaranteed.

2. Introduction of conventional virtual reality simulation modeling methods

The Conventional VR environment modeling has been carried out in many research, which are shown as follows:

(1)Using VB, C++, OpenGL graphics library and other tools to develop, in which the process is complex and the workload is large. These methods are not very satisfactory as the processes are not convenient and the obtained models are not realistic enough.

(2)Using VR software (such as WTK and VRML) to modeling complex 3D graphics is very difficult and time-consuming, the obtained model is also not satisfied [1].

(3)Considering these methods above, Bing Dang [2] used Multigen Creator simulation modeling software to complete the creation of virtual campus environment through five stages: data acquisition, data pre-processing, create model, model optimization and scene integration. This method uses digital technology to obtain geographic coordinates from the plan of AutoCAD format, obtain the height and 3D geometric feature data of each building through architectural design, and finally collect the campus texture information by ground photography to complete the establishment of 3D model. The model is built as shown in Fig 1.

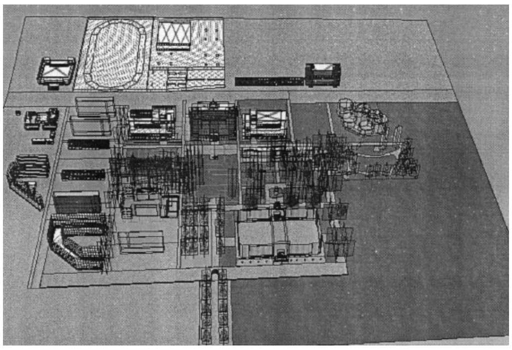

Fig. 1. 3D model of campus

It can be seen that the modeling of the real scene completed by the method basically restores the actual campus scene. But the model is relatively simple and not realistic enough so the user cannot feel sufficient immersion. It is not appropriate to modeling virtual environments based on reality scene.

3. Application of SFM Method in VR Modeling

Major headings should be typeset in boldface with the first letter of important words capitalized.

3.1. *Instruction of SFM*

The SFM (Structure from Motion) method is a method of recovering camera parameters and three-dimensional information with numerical methods by detecting matching feature point sets in multiple uncalibrated images. The SFM method detects the set of feature points to be matched in the image to restore the positional relationship between the cameras firstly with low image requirement. At the same time, the camera sequence can be self-calibrated during the reconstruction process using the image sequence, eliminating the step to pre-calibrate the camera. Moreover, the robustness of the motion method is also extremely strong due to the advancement of various feature point extraction and matching techniques. Another great advantage of the SFM method is that it can reconstruct large-scale scenes and the number of input images can reach million level, which is very suitable for 3D reconstruction of natural terrain and urban landscape.

Using the SFM method for 3D reconstruction, images or videos captured by various devices can be used as input, and multiple images captured from different perspectives can be restored to their three-dimensional structure. Taking a bear model as an example, the main processing flow is shown in Fig 2.

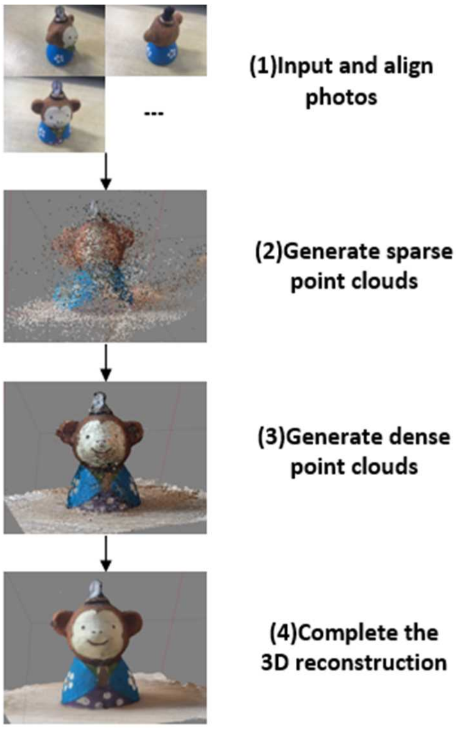

Fig. 2.the process of SFM

As you can see from Fig 2, SFM is mainly divided into four steps:

(1)Input and align photos: input the images of the captured models or scenes into the SFM program to complete the alignment of the images. In the process of alignment, the feature points in each photo are extracted firstly, and the feature points are extracted, where the shape or texture information is more prominent in the

photo, and then the feature points between the photos are matched. After the matching is completed, the positional relationship between the cameras is calculated by the different positions of the feature points in the photo.
(2) Generate sparse point cloud: The three-dimensional coordinates of each feature point in the three-dimensional space can be solved by the basic principle of stereo vision based on the positional relationship between the feature point and each camera. Then, according to the texture information of each point, a coefficient point cloud with color information is generated.
(3) Generate dense point cloud: According to the obtained sparse point cloud, by using the PMVS tool to perform interpolation between points, a new point is generated in the sparse point cloud, thereby generating a dense point cloud.
(4) Complete the 3D reconstruction: According to the result of the dense point cloud, the triangulation of the point cloud is performed. The adjacent three points are used to form a facet, before which the outliers in the generated dense point cloud need to be performed. The culling operation ensures that the final 3D reconstruction has no defects, and facets generated by the triangulation process are connected to form the final 3D reconstruction model.
SFM method restored the shape and texture information of the model very well with high realism, which only requires little operation in the generation process of the 3D model. Modeling can be done manually, which reduces the modeling process and time and increases the realism of the model.

3.2. *Application of SFM method in VR modeling*

Please After the modeling is completed, the material information can be exported through a type 3D format file such as OBJ, and the texture file of the model is also exported as a picture, and the exported model and texture information are respectively shown in Fig 3, Fig 4.

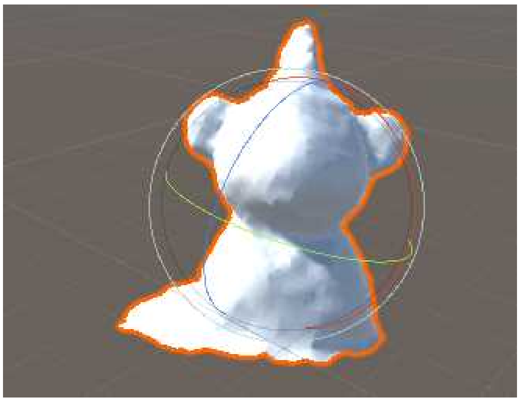

Fig. 3.the material information of model.

Fig. 4.the texture information of model.

It can be seen that the model basically restores the realistic three-dimensional information, but he number of texture files can only be one due to the limitation of the Unity software in the subsequent work. Therefore, the derived model only contain positive texture information, which is also the shortcoming of the current SFM method modeling and needed to be improved in the future. This shortcoming only has an impact on the modeling of the model, while modeling the scene can get all the texture information.
The files obtained in the above steps can be imported into the Unity3D[3] software successively to complete the subsequent edit of the VR. The imported model is shown in Fig 5.

Fig. 5.the model in Unity3D.

4. Conclusion

The application of the SFM method to reality-based VR environment modeling is discussed in this paper. Compared with the conventional modeling method, the advantages of SFM method are shown as flowing:
(1). Reduce the difficulty of modeling with less operation. Using the SFM method to modeling only needs to take a multi-angle photos of the real environment in the early stage, and then input photos into the program, in which the modeling can be operated step by step. Compared with the conventional methods, the operation is very simple and requires little on modeling skill in SFM method
(2). Reduce the modeling cycle with less modeling steps. The SFM method needs less operation steps than the conventional method, and the time period is also shorter, which can be even faster on a computer with a high-performance GPU.
(3).The realism of obtained model is higher. Compared to conventional method modeling, the texture information modeled by the SFM method comes from a photo rather than a manual selection of tones, so a higher degree of realism can be obtained when the texture is finally mapped onto the model.
There is also a disadvantage to improve in the future of the SFM method: only the positive information of the model can be mapped on the model as the number limitation of input texture file of Unity.

References

1. Fengwei Yuan, Biwen LI, Bin He. Accurate Modeling of VR Based on SolidWorks-VRML [J]. *MECHANICAL & ELECTRICAL ENGINEERING MAGAZINE*, 2007,24(10):103-105.
2. Bing Dang. *Research on virtual scene generation in Virtual Reality* [D].Beijing: Beijing Jiaotong University,2010.
3. Unity3D [EB/OL], http://unity3d.com/.

Visual SLAM System Design based on Semantic Segmentation

Jiwu Wang
School of Mechanical, Electronic and Control Engineering, Beijing Jiaotong University
Beijing, China

Yafan Liu
School of Mechanical, Electronic and Control Engineering, Beijing Jiaotong University
Beijing, China
E-mail: jwwang@bjtu.edu.cn, 17121246@bjtu.edu.cn
www.bjtu.edu.cn

Abstract

Visual SLAM is helpful for the development of unmanned platform. But only perceiving the geometric information of the environment is not enough. It is necessary to join the image semantic segmentation in SLAM, which helps to comprehend the scenes and improve the accuracy of pose estimation. Nowadays, the technique of deep learning brings new ideas into traditional SLAM by modeling this problem with convolution neural network.In our approach, we propose a pose estimation algorithm based on pixel-level multi-object detection, and 2D semantic information are transferred to 3D mapping via correspondence between connective Key frames. Meanwhile,the semantic information is utilized in other modules for to optimize the visual SLAM system.

Keywords: Multi-object detection, Semantic segmentation, Pose estimation, Semantic mapping

1. Introduction

SLAM (Simultaneous Localization and Mapping), it means that the robot acquires effective information of the surrounding environment via the sensors carried by the robot in the process of continuous movement, and completing map construction and real-time pose estimation.[1] The contribution of traditional SLAM is that "Where am I now?"; "What is the structure of my environment?". But the traditional SLAM can't answer that: "What are the characteristics of the objects in the surrounding environment?"; "How can I get that target position? At present, the technique of deep learning brings new ideas into traditional SLAM by modeling this problem with convolution neural network. From the perspective of algorithm, there are still three difficulties in the implementation of traditional visual SLAM.

First, the accuracy of feature point extraction and matching algorithms needs to be improved. In fact, there is no feature extraction and matching algorithm with good performance and efficiency. As we all known, feature point extraction algorithm can consider SIFT>SURF>ORB>FAST in performance, and FAST>ORB>SURF>SIFT in efficiency.[2] Furthermore, the Direct method is less tolerant to illumination due to the strong assumption of gray value, and the application scenario is relatively simple. The Direct method can hardly perform loop closing because it does not extract environmental features.

Second, reducing back-end optimized data is also a difficulty for SLAM. The relationship between the image coordinates and the spatial coordinates of the feature points is non-linear. These matches also introduce a number of constraint relationships that complicate the calculation of the variables to be estimated, while also controlling the computation time to the allowable range.

Third, loop closing part is often prone to loss matching (called False Negative) or False Positive. When a false negative occurs, the purpose of the loop closing part cannot be achieved (a closed loop cannot be formed) ; when a false positive occurs, the problem is more complicated and directly leads to a loop-back error (the robot loses itself).

acing the challenges of these problems, we believe that the future development of SLAM is either to combine with state-of-art deep learning or to adopt new sensors (such as Event Camera: the difference between the Event Camera and the traditional camera is that it records changes in the scene, not a fixed scene). Therefore, in this paper, our approach abandons the inherent idea of the traditional SLAM, proposes a pose estimation algorithm based on multi-object detection, and implements an environmental semantic map that combines the semantic information of key frames with the 3D point cloud map. The core technology adopted is the semantic segmentation and deep-learning object detection technology .

2. Semantic SLAM Overview

Based on the traditional feature point ORB-SLAM framework, this paper applies the image information obtained by object detection and the semantic information of key frames to pose estimation and semantic map construction in visual SLAM system.

The overall system can be divided into four modules: object detection, key frame semantic segmentation, camera pose estimation and semantic map construction , as shown in Figure 1. The image acquisition device is the RGBD sensor (KINECT 2), which can obtain RGB image and Depth image of surrounding environment.

Firstly, the Single Shot Multi-Box Detector (SSD) algorithm is used to detect objects on RGB sequence images. The unsupervised semantic segmentation algorithm is used to semantically segment selected key frames. At the same time, Depth information, object detection results and semantic segmentation information are simultaneously transmitted into the pose calculation module for current Camera pose estimation. Secondly, a locally sparse 3D point cloud mapping is performed according to the obtained continuous camera pose. Finally, the 3D point cloud map is merged with the semantic information on the 2D key frames to construct a globally consistent semantic map. At the same time, the results of object detection and the semantic information of key frames will also optimize the back-end and complete loop-back detection to achieve a more perfect SLAM system.

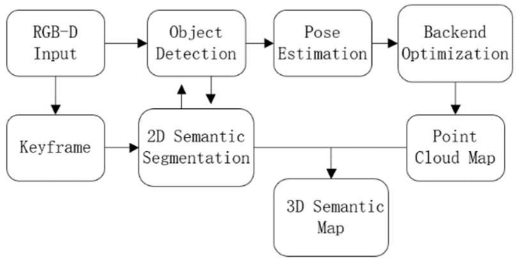

Fig. 1. Semantic SLAM Overview

3. Pose Estimation

The deep learning algorithm is the mainstream target recognition algorithm in the field of computer vision. It relies on multi-layer neural network to learn the hierarchical feature representation of images. Compared with the traditional object recognition method, it can achieve higher accuracy. At the same time, deep learning can also semantically segment images, build a semantic knowledge base of the environment, and improve robot service capabilities and human-computer inter-action capabilities.

In the field of visual SLAM, a hierarchical image feature extraction method based on deep learning has appeared in recent years,[3] and it has been successfully applied to SLAM pose estimation and closed-loop detection. However, most of them do not perform as well as ORB-SLAM. Therefore, this paper breaks through the tradition and proposes a pose estimation method based on pixel-level multi-object detection combined with object recognition and ORB feature points. The specific implementation methods are as follows:

(i) Using the state-of-art deep learning algorithm to perform object recognition and semantic segmentation on selected key frames in the image sequence. Then, the semantic information is weighted to each pixel in the image to filter the effective pixels that have a positive effect on the object detect-ion, thereby improving the accuracy of the object detection.

(ii) The system adopts different pose estimation schemes depending on the working environment. In the scene where the identifiable object is rich, the camera pose estimation will be directly based on the center point of the detected objects; and in the scene where the identifiable object is less, the feature point matching will be accelerated by the semantic information to calculate the camera pose.

3.1. *Multi-object scene pose estimation*

A flowchart of a method for performing pose calcul-ation based on identifiable object semantic information is shown in Figure 2.

First, the target detection module extracts the position and category of the identifiable object in each frame of the sequence. Second, the extracted object center module extracts a center point from the semantic pixel

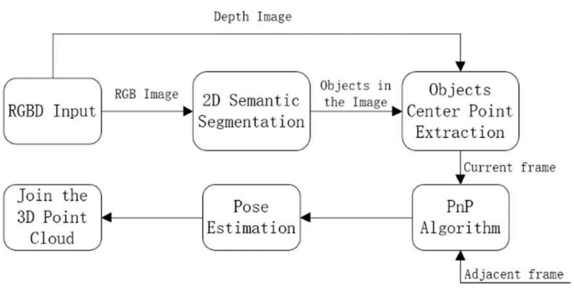

Fig. 2. Pose estimation algorithm flow chart

recognition frame of each object in the image, and the depth information of the center point in the corresponding depth image can be easily obtained. If there are enough similar objects between the front and back frames, and the pixel coordinates and depth information of the center point of the object between the two frames in the respective camera coordinate system are known, the pose estimation between the two frames can use the Perspective n Points(PnP) algorithm. The object detection algorithm to be adopted by this module is based on Single Shot Multi-box Detector(SSD) algorithm.[4] As one of the main target detect-ion algorithm frameworks, SSD object detection network has obvious speed advantage compared with Faster R-CNN,[5] and has obvious accuracy advantage compared with You Only Look Once(YOLO).[6]

3.2. *Sparse scene pose estimation*

As mentioned above, the implementation of the simplest P3P algorithm requires at least four feature points, so pose estimation based on multi-object detection requires determining at least four targets in the environment. But sometimes the environmental information is relatively simple, such as corridors, walls without textures, and so on. Therefore, when there are less than 4 identifiable objects in the environment scene, we propose a feature point matching acceleration algorithm based on semantic segmentation.

In the semantic SLAM system, we know that the feature points are mostly concentrated on the surface of the object with texture. When each frame of the image is semantically segmented, it is equivalent to the classify the feature points of ORB. Therefore, when the brute force matching algorithm is applied to the feature point set with the same semantic label, not only can the searching range of force matching be reduced, but also the matching accuracy can be improved. On the other hand, according to the positional relationship of the same object in the image between adjacent frames, we can easily eliminate the mismatched points and improve the accuracy of matching. Therefore, for an unknown scene where the identifiable object is sparse, we can use the ORB feature point matching algorithm with semantic label to achieve the desired effect.[7]

In summary, the pose estimation algorithm based on multi-object detection combines the continuity of ORB-SLAM with SSD convolutional neural network to improve the accuracy of semantic segmentation. Then, in the case of crossing the low-level features, the pose estimation of the camera is performed directly based on the identifiable objects in the scene.

4. Semantic Mapping

At the front-end of SLAM, Our approach is to use unsupervised convolutional neural network algorithm to obtained semantic information of every frame which are projected to globally consistent 3D map from a real-time SLAM system. as shown in Figure 3.

The 3D map is constructed by a series of keyframes combined with the depth information acquired by the RGBD camera. At the same time, the semantic information obtained by keyframes in this process is also

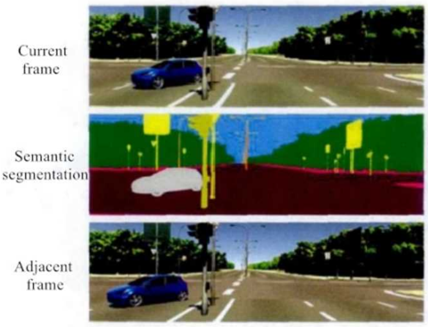

Fig. 3. Semantic segmentation

integrated into the 3D map. Since the 3D map should have globally consistent depth information, it will be re-optimized based on the geometry information in the environment.[8]

The specific implementation of our method is to create a 3D scene map with consistent label information online by moving the robot with the RGBD camera in an unknown scene. The method is divided into two separate processes, as shown in Figure 4. First, a valid keyframes is selected from the sequence of image frames captured by the RGBD camera, and the 3D map is reconstructed using the selected keyframes in conjunction with the pose map generated by SLAM process. Secondly, the 2D semantic segmentation pro-cess predicts pixel-level classification on key frames, and uses this classification to create a local optimal depth estimate for each key frame, and obtains the correspondence between the pixels and voxels marked in the 3D point cloud. Our approach can ultimately achieve global optimal 3D semantic segmentation and real-time updates of 3D point clouds to generate glob-ally consistent 3D maps.

5. Conclusions

SLAM is a outstanding topic in the field of computer vision. The study of SLAM technology combined with deep learning is the emerging direction in the future. This

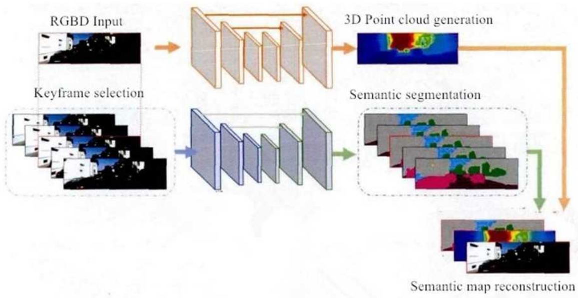

Fig. 4. Overview of Semantic mapping

paper points out the technical difficulties of the traditional SLAM, and summarizes the development prospects of the traditional SLAM method and the deep learning SLAM method. Facing the current challenges, this paper proposes a simultaneous location and mapping program based on semantic segmentation. our method combines pose estimation, object detection and semantic segmentation by using convolutional neural networks algorithm, and then makes great progress.

References

1. Petillot Y, Salvi J, et al. *The SLAM problem: a survey* [M]. AMSTERDAM: IOS PRESS, 2008:363.
2. Cadena C, Carlone L, Carrillo H, et al. Past, Present, and Future of Simultaneous Localization and Mapping: Toward the Robust-Perception Age[J]. *IEEE Transaction on Robotics*, 2016,32(6):1309-1332.
3. Han J, Zhang D, Cheng G, et al. Advanced Deep-Learning Techniques for Salient and Category-Specific Object Detection: A Survey[J]. *IEEE Signal Processing Magazine*, 2018, 35
4. Jia Y, Shelhamer E, Donahue J, et al. Caffe: *Convolutional Architecture for Fast Feature Embedding*[J]. 2014.
5. Ren S, He K, Girshick R, et al. Faster R-CNN: Towards Real-Time Object Detection with Region Proposal Networks[J]. *IEEE Trans Pattern Anal Mach Intel*l, 2017,39(6):1137-1149.
6. Redmon J, Divvala S, Girshick R, et al. You Only Look Once: Unified, Real-Time Object Detection[M]//*IEEE Conference on Computer Vision and Pattern Recognition.* 2016:779-788.
7. ChaoHua YAN. *Deep Semantic Simultaneous Localization and Mapping*[D]. Zhejiang University,2018.
8. Li X, Belaroussi R. *Semi-Dense 3D Semantic Mapping from Monocular SLAM*[J]. 2016.

Spherical Mobile Robot Designed with Single Omnidirectional Wheel Method

Liu Wei
School of Mechanical, Electronic and Control Engineering
Beijing Jiaotong University
Beijing, China

Lian Luo
School of Mechanical, Electronic and Control Engineering
Beijing Jiaotong University
Beijing, China

Jiwu Wang
School of Mechanical, Electronic and Control Engineering
Beijing Jiaotong University
Beijing, China

Abstract

This paper presents a new spherical mobile robot driven by single omnidirectional wheel. The physical model is that an arc rail is built inside the sphere shell, and the arc rail can rotate around a spherical diameter freely. It supports one driving omnidirectional wheel and keeps the driving omnidirectional wheel touching the inside of the sphere shell. The touching friction force drives the sphere rolling forward or backward. Steering drive can drive the omnidirectional wheel moving along the arc rail, that causes the spherical mobile robot steering left or right. The omnidirectional wheel and the steering drive working together can realize the omnidirectional movement in any direction. The structure of the spherical mobile robot is described in detail, and its motion and dynamics models are built. The preliminary analysis is carried out by dynamic software and shows that the spherical mobile robot can achieve omnidirectional motion well.

Keywords: Spherical mobile robot, Omnidirectional wheel, Omnidirectional motion.

1. Introduction

The sphere is concise shape with the smallest surface area, the largest volume, and rolling in all direction. It is the most excellent shape existing in the universe, and the best rolling body that every animal likes to play with. The typical characteristics of the sphere are: 1) when no friction and air resistances, an ideal sphere with uniform density will be kept moving forward straightly and smoothly by the inertia force and moment of inertia; 2) when the mass centroid close to the sphere center, the position attitude is in stable, and when the mass centroid away from the center, the sphere has a strong tendency to self-stabilization, etc. The characteristics of spheroid inspire the enthusiasm of scholars to invent many kinds of spherical robots. Since the spherical robot concept first appeared, it was considered as a new technology to lead the industrial revolution like implementation in planet-moon exploration, military usage, and inevitably arising the demand of the toy entertainment industry[1, 2].

Through literature and patents review, there are several types of representative spherical robots, and according to their physical driving principles, the current spherical robots with omnidirectional motion performance could be divided into two typical categories: 1) Inertia moment driving type [3, 4, 5, 6], the principle is to rely on the rotating inertia moment to drive the omnidirectional rolling of a spherical robot, but the inertia moment needs the rapid rotation like spinning gyroscope to acquire enough driving force. 2) Eccentric torque drive type, its principle is to rely on the motion of eccentric mass centroid producing the eccentric torque on the fulcrum, and the eccentric torque drives the spherical robot rolling. The invention of drive mechanism with eccentric torque driving the spherical robot has been very rich[7, 8, 9,]. One of the earliest and concise spherical robots is invented and researched by Halme etc.(1996) [5]. Its driving mechanism is made up of a driving wheel, a steering shaft and a balance wheel. One of recent and most concise spherical robots is reported by Liu Wei etc.(2018).It has two independent driving omnidirectional wheels located at each end of the inside vertical diameter of the sphere shell, and the two wheels' axes are in orthogonal position. Both omnidirectional wheels can roll on the inner surface of the spherical shell by their friction forces. The lower omnidirectional wheel is responsible for walking drive, and the upper one for steering drive.

Although there are many mechanisms to realize the eccentric torque drive principle, their physical model can be described briefly as shown in Figure 1. Supposing the only resistance is the rolling resistance torque $\boldsymbol{T_f}$,, the torque $\boldsymbol{T}$ caused by mass centroid is considered to drive or steer the robot rolling. The distance $\boldsymbol{r}$ which from the sphere center to the mass centroid $\boldsymbol{m}$ directly determines the quantity of the driving torque $\boldsymbol{T}$, that is $\boldsymbol{T=m \cdot g \cdot r \sin(a)}$. When $\boldsymbol{T} > \boldsymbol{T_f}$, the spherical robot will start to move and increase speed. When $\boldsymbol{T} = \boldsymbol{T_f}$, the spherical robot will move uniformly. When $\boldsymbol{T}<\boldsymbol{T_f}$, the spherical robot will reduce speed until stop.

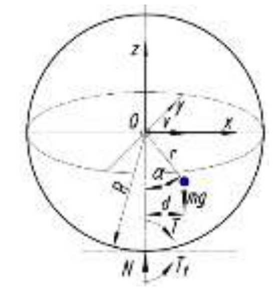

Figure 1 Principle of eccentric torque drive

This paper proposes a novel and concise spherical robot mechanism with only one omnidirectional wheel to drive the eccentric torque overcome the rolling resistance torque. The spherical robot can realize the omnidirectional motion in any direction. The omni wheel is arranged by a series of small rollers around the circumference which are perpendicular to the driving direction. When omni wheel drives, its rollers can slide laterally on the wheel periphery. The lateral rolling of small rollers does not interfere its circumferential driving function. The mechanism is shown in Figure 2. The spherical robot driven by one omni wheel will be analyzed as following in several aspects as mechanism composition, motion and dynamics analysis etc.

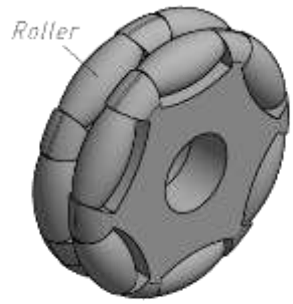

Figure 2 Omni wheel

2. Mechanism

The spherical mobile robot includes an omnidirectional wheel, driving motor, arc rail, chassis, support wheels, steering motor, side wheels, springs and spherical shell, as shown in Figure 3. The lower end is the Driving omnidirectional wheel, and it produces friction at the inner surface of the spherical shell under the co-function of two forces of gravity and spring pre-pressure. The upper end is the steering omnidirectional wheel, and it produces friction at the inner surface of the spherical shell with the function of the spring pre-pressure. The sphere centroid deviates from the center of the sphere (distance r). When driving the omnidirectional wheel, the generated rolling friction is transmitted to the frame, which causes the frame swing forwards or backwards. The steering omnidirectional wheel rolls sideways (left or right direction), and it does not hinder the driving of the driving, so that the generated eccentric torque drives the spherical shell to roll backwards or forwards. Similarly, when driving the upper omnidirectional wheel, the generated rolling friction is transmitted to the frame, causing the frame to swing towards left or right. At this time, the driving omnidirectional wheel rolls sideways without hindering the steering drive, thereby generating an eccentric moment to drive the sphere shell move leftwards or rightwards.

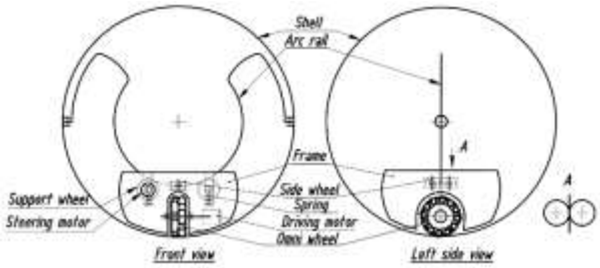

Figure 3 Drive mechanism of biorthogonal omni wheels

3. Function analysis

First, the coordinate system ***G-XYZ*** is established on the ground, and the coordinate system ***O-xyz*** is established on the spherical robot. As shown in Figure. 4, since the spherical shell always rotates with respect to the frame, the ***O-xyz*** coordinate system is fixed to the frame of the sphere centroid. Parameters are set as follows: ***m*** is the mass of all the parts or mechanisms in the spherical shell, ***r*** is the distance between this mass and the sphere centroid, ***M*** is the mass of the spherical shell, t is the wall thickness of the spherical shell, f_{rr} is the rolling resistance of the spherical shell, far is the air resistance, ***V*** is the speed of the sphere, w is the angular velocity of the sphere. Now we suppose that the rolling contact of the whole system is pure rolling (that is, temporarily excluding the influence of sliding), so that a series of simplified dynamic analysis can be performed. Here, a model could be constructed for the motion of the spherical robot, and it could be decomposed into the following phases: start-up phase, uniform phase, obstacle phase, take-off phase and landing phase.

The sample mechanism uses two motors to control the forward/backward and turn right/left. In order to reduce the height of centroid, the control system, the power supply and the drive motor of the upper omnidirectional wheel are all arranged away from the center of the sphere (sphere centroid?). In order to ensure that the upper and lower omni-direction wheels are always on the vertical diameter, an important task needs to be completed before the frame components are installed into the spherical shell - static balance.

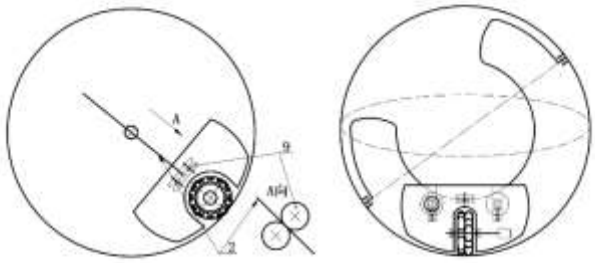

Figure 4 Run pose and steering pose

4. Conclusion

The spherical robot's driving scheme makes use of the characteristics of the omnidirectional wheel to simplify the driving structure, and it can better increase the distance from the center of mass to sphere center so as to generate a maximized eccentric driving torque. This orthogonal arrangement makes the walking omnidirectional wheel and steering omnidirectional wheel independent at both force direction and motion direction, which is very conducive to the control system.

(1). Reduce the difficulty of modeling with less operation. Using the SFM method to modeling only needs to take a multi-angle photos of the real environment in the early stage, and then input photos into the program, in which the modeling can be operated step by step. Compared with the conventional methods, the operation is very simple and requires little on modeling skill in SFM method

References

1. Rhodri H A, Julian F v. Rolling in nature and robotics: a Review[J]. *Journal of Bionic Engineering*, 2006, 3(4):195-208.
2. Deng Zongquan, Yue Ming. Overview of the development of spherical robots[J]. *Robotics and applications*, 2006 (3) ,27-31.
3. Bhattacharya S, Agrawa S K. Spherical rolling robot: a design and motion planning studies, *Proceedings of the IEEE International conference on Robotics and*

Automation[C]. San Francisco， CA， April， 2000， 835~839.

4. Joshi V A，Banavar R N，Hippalgaonkar R，Design and analysis of a spherical mobile robot [J]，*Mechanism and Machine Theory*，2010，45(2) :130-136
5. Halme A, Schonberg T, Wang Y. Motion control of a spherical mobile robot. *4th IEEE International Workshop on Advanced Motion Control*, Mie, Japan, 1996, 1,259–264.
6. Javadi A H A, Mojabi P. Introducing august: A novel strategy for an omnidirectional spherical rolling robot. *IEEE International Conference on Robotics and Automation*, Washington, DC, USA, 2002, 3527–3533.
7. Batten C. Wentzlaff D. Kickbot， A Spherical Autonomous Robot. Massachusetts Institute of Technology people.csail.mit.edu/wentzlaf/documents/Batten. 2001. Class.Kickbot.pdf，2006，3，20
8. Jaimez M，Castillo J J，Garcia F，et al，Design and Modelling of Omnibola ©，A Spherical Mobile Robot [J]，*Mechanics Based Design of Structures and Machines*，2012，40 (4): 383-399
9. Otani T et a1，Position and attitude control of a spherical rolling robot equipped with a gyro[A]，*International Workshop on Advanced Motion Control*[c]，Istanbul，Turkey：IEEE，2006，416—421

An Augmented Reality Implementation Method Based on Unity3D

Jiwu Wang
School of Mechanical, Electronic and Control Engineering
Beijing Jiaotong University
Beijing, China

Weixin Zeng
School of Mechanical, Electronic and Control Engineering
Beijing Jiaotong University
Beijing, China
E-mail: jwwang@bjtu.edu.cn, 17121253@bjtu.edu.cn
www.bjtu.edu.cn

Abstract

Through computer graphics and visual technology achieving the superposition of virtual objects in real scenes, augmented reality technology is able to present the sensory effects of real-time interaction. It has broad application prospects and application value. At present, there are two main ways to achieve augmented reality. One is the underlying code, which combines OpenGL and OpenCV libraries to realize augmented reality. The second is the secondary development of related content through the corresponding software and SDK package. In this article, augmented reality will initially be completed through Unity 3D and Qualcomm's Vuforia SDK.

Keywords: Augmented Reality, Vuforia SDK, Modeling, Unity3D.

1. Introduction

Augmented reality technology is a technology developed on the basis of virtual reality technology, which uses computer graphics and computer vision to superimpose virtual objects into real scenes, allowing users to perceive a real scene and virtual scenes seamlessly. Meanwhile, with the new environment, the user is presented with a sensory effect of real-time interaction[1].

Augmented reality was first applied in the military field. But with the continuous development in recent years, it has been widely applied to more fields. In the medical field, doctors can use augmented reality technology to accurately locate the patient's lesions for easy surgery. In the field of television broadcasting, important data on the sports field in the live sports competition can be superimposed on the TV screen through augmented reality, providing more information to the audience. In the field of education, augmented reality technology will change the traditional education model and create a more vivid and interesting learning scene for students. Augmented reality has broad application prospects and great application value, therefore it has very significant research significance[2].

2. Background

Many research institutes at home and abroad have achieved certain results in the direction of augmented reality. The first pioneer in the world to study augmented reality was Ivan Sutherland[3]. In 1992, Steven Feiner published a paper on the prototype of the AR system at the International Conference on Graphic

Images, which was subsequently widely cited by the American Computer Society[4]. In 1999, the University of Washington released the open source augmented reality development kit-AR Tool Kit. With the release of this development kit, a large number of augmented reality applications are beginning to emerge. In 2014, Google launched "Google Glass". In addition to the functions of sending messages, taking photos, talking, viewing maps, video chats, setting calendar reminders, etc. through voice control, its most prominent feature is the use of augmented reality technology to attach environment information on display devices. In 2015, Microsoft released the AR head-up Microsoft HoloLens, which is not subject to any restrictions - no cables, earpieces, and no need to connect to a computer. Microsoft HoloLens has the features of holograms, high-definition lenses, stereos, and more, allowing you to see and hear holograms around you. Apple announced the ARKit at WWDC 2017, which helps us implement AR technology in the easiest and fastest way.

3. Implementation Methods

There are three core technologies of augmented reality technology, including three-dimensional registration technology, display technology and intelligent interaction technology[5].

- Three-dimensional registration. In order to realize the combination of virtual and real, the position of the augmented reality real-time tracking camera is calculated for the position of the camera image and the position of the virtual image appearing in the real scene.
- Display technology. Depending on the real world, virtual images or models present a virtual and fused world to the user.
- Real-time interaction. This refers to an interaction between the user and the virtual object, and the information flow and feedback can be timely and effective between the two. The main implementation methods of augmented reality are two categories in the general direction. The first is through the underlying code, and the second is the secondary development of related content through the corresponding software and SDK package.

3.1. *Underlying Code*

Relatively speaking, OpenCV realizes the recognition and positioning of Marker, and then superimposes virtual objects under the camera image through OpenGL to realize augmented reality. As shown in FIG.1, the feature points in the real-time scene are extracted by using a related feature point extraction algorithm. Then, the relevant feature point data is obtained after detection and description, and the Hamming distance is used for matching, and the RANSAC algorithm filters the matching points to obtain the final matching point data. Then, according to the conversion of the coordinate information, the position of the virtual information in the real scene is determined, thereby realizing the augmented reality[6].

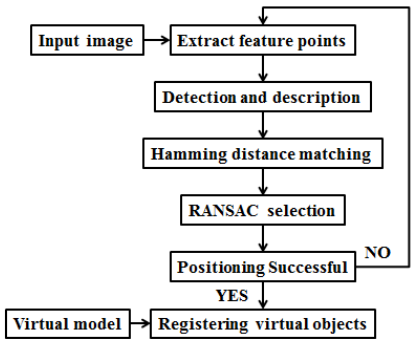

Fig. 1. Underlying implementation

3.2. *Secondary Development*

With some mainstream AR SDKs, such as Easy AR, Vuforia[7], Metaio, AR Kit and so on, the implementation of augmented reality is achieved through the related AR engine. Users of the AR SDK need to know the functions that the SDK can implement, the platforms they support, and the stability of implementation. Secondary development is currently a mainstream choice for AR development, not only to achieve faster results, but also to build practical applications.

4. Achievement Based on U3D

Augmented Reality have been achieved through Unity3D[8] and Qualcomm's Vuforia SDK.

4.1. *Unity3D*

Unity3D is not only a 3D animation software, but also a a very compatible platform. It is capable of making games as well as realizing virtual reality and augmented reality. We chose it because it is compatible with many development environments and offers a variety of plugins that are necessary for later higher levels of development.

4.2. *3ds Modeling*

Fig. 2. 3D model of Knight

Figure 2 shows the 3D model named Knight. Using 3D modeling software called 3ds Max to build 3D model, it can be exported to a format file that Unity3D can open.

4.3. *AR Engine*

At this point, we should focus on implementing augmented reality with Unity3D. In some SDKs such as AR Kit, Smart AR, Easy AR and Vuforia, we choose Vuforia to create a location-based AR application with no markup type, which can meet the requirements of Unity3D. This SDK can provide a AR-camera which could realize the superposition of virtual objects in real scenes. Meanwhile, the SDK can make identify map which is able to be identified by the AR-camera. Based on this SDK, we will add location-based functions and other functions. Figure 3 shows one of the identify map.

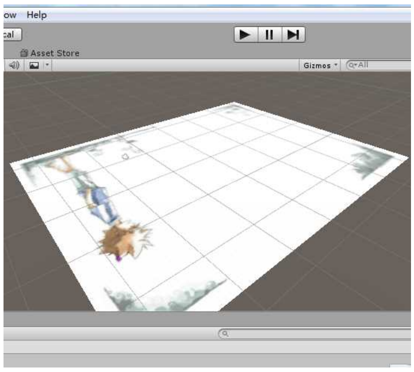

Fig. 3. Identify map

5. Experiment and Results

This experiment uses Win10 system, and the graphics card model is GTX960. The software is Unity3D-2018.2.10-f1, and the development kit is Vuforia-unity-6-2-10.

5.1. *Building Environment*

In our research, we first import the Vuforia SDK into U3D and then apply the AR Camera and Image Target. When we get the KEY under Vuforia's official website, we make a recognition map and import it, and then import the 3D model generated by 3ds Max.

5.2. *Results*

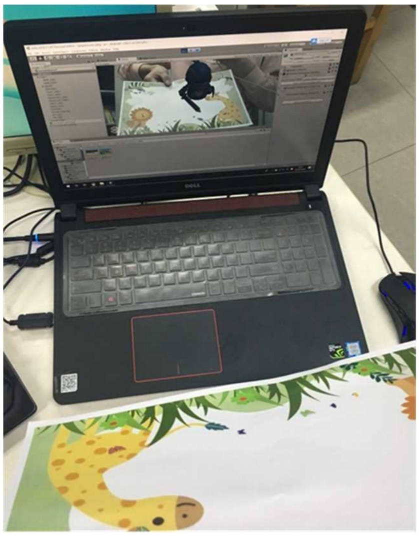

Fig. 4. Displaying the Knight Model by AR

Figure 4 shows the experimental results. U3D is able to display the Knight model above the recognition map and let the model do some action. Once the natural image inside the camera being read, the model will continue to be displayed even if the position changes or the angle changes. In addition, the Knight is able to complete some designed actions when the Knight is displayed. However, when the recognition map is too close to the camera, the model will appear outside the screen and cause invisibility.

6. Conclusion and Future Work

In this study, we tried to make an application using Unity3D. Future tasks include advanced application features such as adding instruction windows, implementing some instructions, the creation of other models, and some of the problems actually used. We hope to achieve more functionality in the future work.

References

[1] T Ronald, Azuma. A survey of augmented reality Presence, *J.* 6(4) (1997)355-385.
[2] Xiyu Wang and Fengjun Zhang, Research status and development trend of augmented reality technology, *J. Science and technology guide*, 36(10) (2018)75-83.
[3] I E Sutherland, The ultimate display, *Proceedings of IFIP*, *J.* 65(2) (1965)506-508.
[4] S Feiner, B Macintyre and D Seligmann, Annotating the real world with knowledge-based graphics on a see-through head-mounted display, *J. Conference on Graphics Interface*, (1992)78-85.
[5] Yin Hou, Augmented reality technology review, *J. Computer measurement and control*, 25(2) (2017)1-8.
[6] Yue Wang and Shusheng Zhang, Model-based augmented reality unmarked three-dimensional registration tracking method, *J. Journal of Shanghai Jiaotong University*, 52(1) (2018)83-90.
[7] Vuforia [EB/OL], http://developer.vuforia.com/.
[8] Unity3D [EB/OL], http://unity3d.com/.

Research on a Non-Invasive Measuring Method of Blood Glucose Concentration Based on Electrical Impedance Spectrum

Tong Yin [1], Xiaoyan Chen [1*], Meng Du[1], Hongyi Yin[1]

[1] College of Electronic Information and Automation,
Tianjin University of Science and Technology, China;

*E-mail: * cxywxr@tust.edu.cn*
www.tust.edu.cn

Abstract

Different from the traditional measurement approach and instruments of blood glucose concentration, we propose a novel measuring method related to electrical impedance spectrum without invasion. A serial experimentations are designed and carried out to detect the electrical impedance amplitudes and phases under 1Hz-10MHz frequencies. Considering the skin contacting impedance and cytomembrane conductivity feature, a simulate circuit is designed and connected in serial with the measuring loop. The measured data were analyzed by an improved Cole-Cole model to derive the relationship between the impedance value and the blood glucose concentration. The results show that the electrical impedance is strong negative correlation to blood glucose concentration, as the blood glucose concentration increases, the impedance value decreases. The conclusion of this research provides a theoretical basis for non-invasive blood glucose surface-measuring.

Keywords: blood glucose concentration, impedance spectroscopy, non-invasive glucose measurement

1. Introduction

The blood glucose concentration is one of the key indicators reflecting the condition of diabetic patients. At present, the most common testing method is acupuncture measurement before and after meal invasively, which bring great pain to the patients with potential dangers of infection[1]. Compared with the common invasive method, non-invasive blood glucose concentration measuring has the advantages of no acupuncture and no pains with simple and quick operation. Non-invasive blood glucose concentration measuring has an important application value of monitoring the blood glucose change in time and of visualizing the abnormally glucose metabolism rapidly[2].

There are four categories of non-invasive glucose monitoring technologies involving electromagnetic waves in development[3]: near infrared (NIR) spectroscopy, far infrared (FIR) spectroscopy, optical rotation of polarized light, and electrical impedance spectrum (EIS) etc. The first three techniques are with relative weak changes, limited resolution and insufficient precision due to glucose imprinted to the signals registered[4]. EIS has been tested over a period of time for non-invasive glucose concentration monitoring.

EIS has a unique standing among numerous modern methods used for physical and chemical analyses of material, because it can investigate the relaxation processes of complex systems in an extremely wide range of characteristic times from 10^{-12} to 10^{4}s. EIS is especially sensitive to intermolecular interactions and, is able to monitor cooperative processes[5].

This aim of this research is to explore a new way that detecting the blood glucose concentration non-invasively by EIS method on the surface of body. The concentration of electrolytes in the blood and tissues changes with glucose concentration, which in turn causes an imbalance in electrolyte concentration between blood and tissue fluid. This causes the ions to move in a directional manner, and the electrical properties of the cell membrane change with the concentration of ions passing through the cell membrane. From a macro perspective, the impedance of the human body will also change accordingly. On the biological principle, it indicates a hopeful direction for non-invasive blood glucose measuring.

2. The relationship deduction of glucose and cell membrane capacitance

An increasing concentration of glucose in blood induces significant reactions in blood and human tissues. It is known that the concentration of sodium decreases and potassium increases due to the active transport of ions and water movement from the tissue and blood cells, such as erythrocytes, into the vascular system. It can be understood on the cellular level that glucose uptake through membrane transporters (GLUTs) requires controlling the electrolyte balance to maintain osmolality and cell sizes[5].

Ping. S proposed and verified the relationship between cell membrane capacitance (C_{mem}) and blood glucose concentration (C_{glu}) by Michaelis-Menten equation as

$$C_{mem} = C_{mem,0}\left[1 + \frac{N_{tot}\left(\mu_{glu}^2 - \mu_{free}^2\right)}{3kT\varepsilon_0\varepsilon_{mem,0}\left(1+{K_m}/{c_{glu}}\right)}\right] \quad (1)$$

Major headings should be typeset in boldface with the first letter of important words capitalized.

When the blood glucose concentration is zero, the cell membrane capacitance is defined as $C_{mem,\ 0}$. According to the experimental data in[6], when the blood glucose concentration of the human body is 5 mmol/L, C_{mem}=1.12 $C_{mem,\ 0}$; When the blood glucose concentration of the human body is 20 mmol/L, C_{mem}=1.37 $C_{mem,\ 0}$. Substituting this result into formula (1), the relationship between cell membrane capacitance and blood glucose concentration is

$$\frac{C_{mem}}{C_{mem,0}} = 1 + \frac{0.53}{1+{8.57}/{C_{glu}}} \quad (2)$$

According to the experimental data in[7], the cell membrane capacitance value is 1 μF/cm^2 when the blood glucose concentration is zero. In this paper, a rectangular electrode of 16 cm^2 is selected for simulation test, so $C_{mem,\ 0}$=16μF. Bring $C_{mem,\ 0}$ into formula (2) to obtain cell membrane capacitance values corresponding to blood glucose levels of different concentrations, as shown in Fig. 1. The specific values are shown in Table 1.

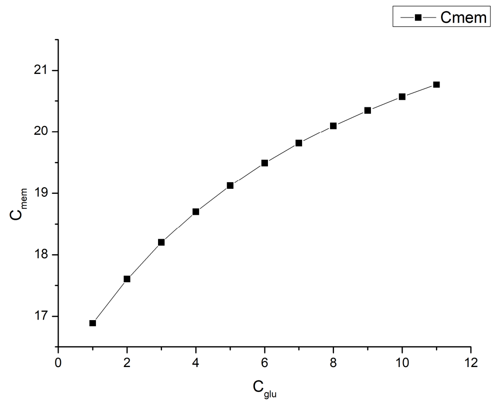

Fig. 1. The relationship between C_{glu} and C_{mem}. As the C_{glu} increases, C_{mem} shows an upward trend.

Table 1. Corresponding values between blood glucose concentration (C_{glu}) and cell membrane capacitance (C_{mem})

C_{glu}(mmol/L)	C_{mem}(μF)
0	16.0000
1	16.8861
2	17.6045
3	18.1988
4	18.6985
5	19.1245
6	19.4921
7	19.8125
8	20.0941
9	20.3438
10	20.5665
11	20.7665

From Fig. 1, at the change stage of 3 to 10 mmol/L in human blood glucose concentration, the cell membrane capacitance changes very rapidly, and this change is more obvious than that caused by other substances to the cell membrane capacitance. When the cell membrane capacitance changes, the influence of other substances can be ignored. Therefore, the impedance index can be used to indicate the blood glucose reasonably.

3. Equivalent circuit model

3.1. *Establishment of human body equivalent circuit model*

To simulate the effects of different blood glucose concentrations on impedance spectroscopy measurements, we established a human equivalent circuit model. In an alternating electric field, the biological tissue has greater impedance at the lower frequency. The capacitive impedance characteristic of biological tissues was discovered by scholar Philippson in 1920, who established a corresponding bio-impedance equivalent circuit model.

The single cell equivalent circuit model of biological tissue is shown in Fig. 2(a). R_i, R_m and R_e are the equivalent resistances of intracellular fluid, cell membrane and extracellular liquid respectively. C_i, C_m and C_e are theirs equivalent capacitance. According to the existing research theory, at low frequencies (generally <1MHz), the values of C_i and C_e are small, so the capacitive reactance is large and can be treated as an open circuit; at this time, R_m is large and can also be regarded as an open circuit. Through the above-described conversion processing, a simplified biological tissue cell equivalent circuit model as shown in Fig. 2(b) can be obtained. Since a large number of cells are combined in a certain manner, biological tissues or organs are formed. So biological tissue can be called a collection of multiple cells. Therefore, the equivalent circuit model shown in Fig. 2(b) can also represent the entire biological tissue, and R_i, R_e, and C_m represent the internal liquid resistance, the external liquid resistance, and the membrane capacitance of the entire biological tissue, respectively. This is named the three-element circuit model of biological tissue [8].

Due to the detecting electrodes and skin contacting, it is also necessary to consider the effect of contact impedance. Therefore, we established a novel human equivalent circuit model as shown in Fig. 3.

R_d represents the contact impedance, R_i is the internal liquid resistance of the human body, R_e is the liquid resistance, and C_{mem} is the cell membrane capacitance. According to the experimental data in[9], we set R_d=1kΩ, R_i=500Ω, R_e=500Ω.

According to the Laplace transform in the circuit theory, the corresponding real and imaginary parts of the impedance can be obtained as:

$$R = \frac{R_d+R_e+(R_e*R_d+R_i*R_e+R_i*R_d)*\omega^2*C_{mem}^2*(R_e+R_i)}{1+\omega^2*C_{mem}^2*(R_e+R_i)^2} \quad (3)$$

$$I = \frac{-R_e^2*\omega*C_{mem}}{1+\omega^2*C_{mem}^2*(R_e+R_i)^2} \quad (4)$$

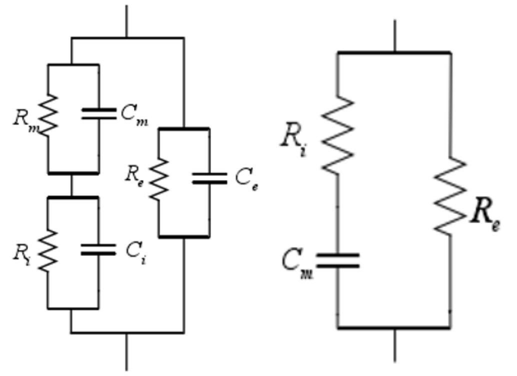

Fig. 2. Biological tissue equivalent circuit model

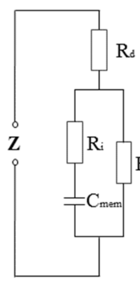

Fig. 3. Human equivalent circuit model

3.2. *Simulation of the equivalent circuit model*

In this paper, the impedance of the human body equivalent circuit model is completed under twelve different equivalent blood glucose concentrations (C_{glu}=0,1,2,3,4,5,6,7,8,9,10,11). Spectral simulation with a measurement frequency range of 0Hz-100MHz. A curve of blood glucose concentration and impedance spectrum as a function of frequency is then obtained. Impedance measurement at different blood glucose concentrations was simulated by the human equivalent circuit model of Fig. 3.

The situation shown in Fig. 4 is C_{glu} = 5 mmol/L. It can be seen by Fig. 4 that above 100Hz the impedance keep at 1250Ω stably. Therefore, in order to show the results clearly, the high frequency band is out of consideration, and the change segment is displayed.

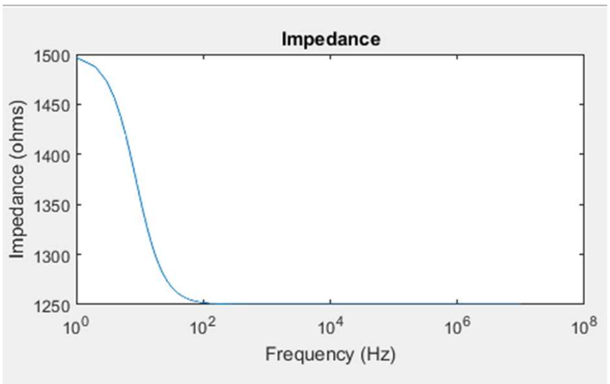

(a)

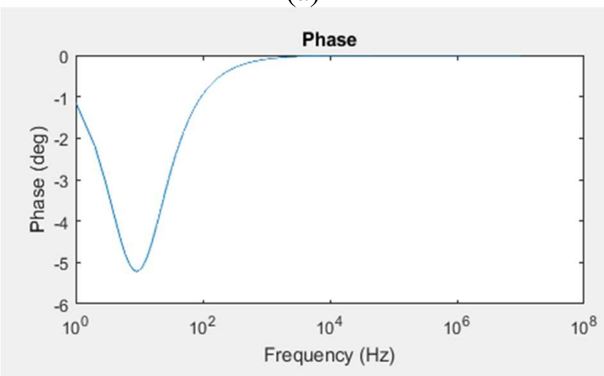

(b)

Fig. 4. (a) The curve of the model impedance value with frequency when C_{glu}=5 mmol/L, the ordinate is the impedance value, and the abscissa is the frequency of the logarithmic display; (b) The curve of the model Phase value with frequency when C_{glu}=5 mmol/L, the ordinate is the phase value, and the abscissa is the frequency of the logarithmic display.

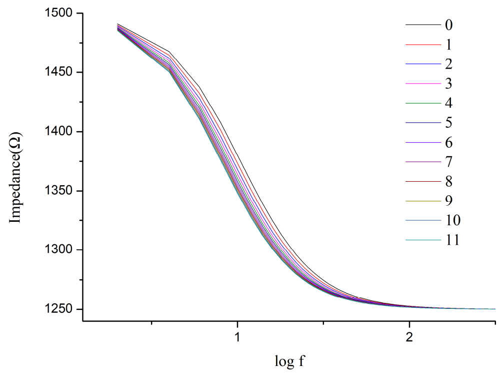

Fig. 5. The relationship between frequency and impedance at different blood glucose concentrations.

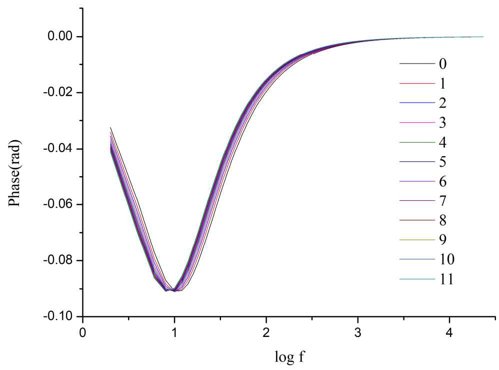

Fig. 6. The relationship between frequency and phase at different blood glucose concentrations.

The corresponding values of C_{mem} and C_{glu} in the model simulation are shown in Table 1.

The data obtained by simulation in MATLAB, for each C_{mem}, $_0$ we obtain the corresponding impedance and phase values at different blood glucose concentrations as shown in Fig. 5 and Fig. 6.

As it can be seen from the above figures, as the blood glucose concentration increases, the impedance value at the same frequency decreases. However, as the blood glucose concentration increases, the speed of impedance value decreases slowly. At the same time, the change of impedance value is not obvious in the blood glucose range of the human body. The impedance changes reflecting the changes of blood glucose, which are highly demanding on the accuracy of the device, and some influencing factors can cause errors in the measured results. With the change of blood glucose concentration, the phase value is negatively correlated with the phase size before the corner frequency; after the corner frequency, it is positively correlated with the phase size. These trends indicate it is unreliable to measure the impedance or phase values of human tissue individually. Because the impedance of a single frequency point carries less physiological and pathological information, there are many factors affected.

3.3. *Simulation experiments*

Use the Wayne Kerr 6500B impedance analyzer to test the human equivalent circuit model shown in Fig. 7. Set C_{mem} as 20, 21, 22μF separately. The blood glucose concentration corresponding to the measured capacitance is shown in the following Table 2. The frequency range is 20Hz-10MHz.

Table 2. Blood glucose concentration (C_{glu}) corresponds to cell membrane capacitance (C_{mem})

C_{mem}(μF)	C_{glu}(mmol/L)
20	7.651786
21	12.31322
22	20.73387

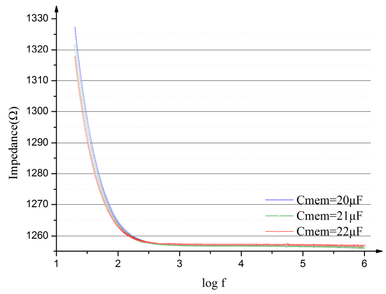

Fig. 7. The relationship between frequency and impedance at different Capacitance value.

In order to reflect the trend change, the following Fig. intercepts the data before 1 MHz. It can be seen that as the blood glucose concentration increases, the impedance value decreases.

4. Data processing and result analysis

Table 3. Diagnostic criteria of blood glucose values and corresponding C_{mem} before and after meal

z	C_{glu} minimum (mmol/L)	C_{glu} maximum (mmol/L)	C_{mem} minimum (μF)	C_{mem} maximum (μF)
Hypoglycemia		4.6		18.9619
Normal glucose	4.6	7.8	18.9619	20.0406
Abnormal glucose metabolism	7.8	11.1	20.0406	20.7854
Diabetes	11.1		20.7854	

4.1. *Blood glucose diagnostic standard simulation*

Different blood glucose concentration standards corresponding to different diagnostic results are obtained and shown in Table 3. According to formula (2), the corresponding C_{mem} values are calculated.

The C_{mem} value is brought into the human body equivalent circuit model shown in Fig. 3, and the impedance measurement is simulated at different blood glucose concentrations. The impedance value (a) and the phase value (b) thus obtained are as shown in the following Fig. 8.

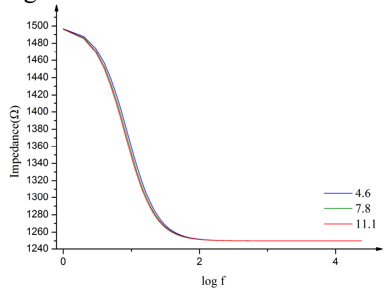

(a)

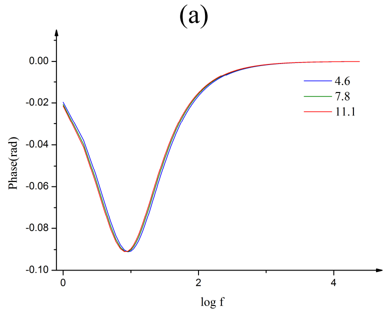

(b)

Fig. 8. The relationship between frequency, impedance and phase under diagnostic criteria.

4.2. *Analysis based on Cole-Cole theory*

In order to accurate describe the equivalent circuit model of biological tissues, Cole KS and Cole RH have conducted in-depth research in this regard. They summed up a set of actual biological tissue electrical impedance theory, the Cole-Cole theory [9-10], and used it to describe the dielectric model of biological tissue. The basic content of the Cole-Cole theory is that the trajectory of the electrical tissue's electrical impedance in the complex plane is a circular arc in the fourth quadrant, and the center of the circle is not on the real axis but in the first quadrant.

The measurement of bio-impedance is essentially to obtain the characteristic parameters in the impedance trajectory map. It can be seen from the above analysis that as long as an excitation electric signal of a certain frequency is applied to the biological tissue and the output signal flowing through the biological tissue is simultaneously measured, the impedance amplitude at the frequency can be calculated by the relevant demodulation algorithm. If the excitation power signal is operated in a sweep mode, the entire impedance circle can be obtained by curve fitting. On the impedance plot, the impedance value at any frequency point can be obtained. Based on this theory, the Cole-Cole chart and its electrical characteristic parameters of the human equivalent circuit model are obtained from the real and imaginary parts of the impedance and the phase and impedance values. Corresponding Cole-Cole biological tissue electrical impedance characteristic equation is.

$$Z = R_\infty + \frac{R_0 - R_\infty}{1 + jw\frac{1}{2\pi fc}} \quad (5)$$

The Im axis represents the imaginary part of the impedance, and the Re axis represents the real part value. f_c represents the frequency value when the imaginary part is maximum. R_0 represents the electrical impedance of biological tissue at a frequency of zero. R_∞ represents the electrical impedance of biological tissue at infinite frequency. These scatter points in the figure are calculated at frequencies from 10 Hz to 20 MHz, in which the impedance changes from 150Ω to 1250Ω. Fitted into a circle by these scatter plots and it can be seen that it is normative. According to the measured real and imaginary parts of the impedance, the Cole-Cole circle is fitted through Python using the weighted average method, and the following Fig. 9 shows the Cole-Cole circle fitted at C_{glu}=5 mmol/L.

The change trend of the characteristic parameter fc has a great correlation with the change of the blood glucose concentration. From the data in the Table 4, the magnitude of fc has an inverse correlation with the magnitude of the blood glucose concentration. The higher blood glucose concentration, the smaller value of fc corresponding to the impedance spectrum.

A polynomial fit was performed by MATLAB to obtain a correspondence between C_{glu} and f_c:

$$f_c = -0.001C_{glu}^3 + 0.0316C_{glu}^2 - 0.4229C_{glu} + 9.7647 \quad (6)$$

The coefficient of determination R^2 = 0.9999, which means that the fitting effect is excellent. The characteristic frequency f_c in the impedance spectrum can reflect the change of human blood glucose concentration to a certain extent, and it is possible to realize non-invasive blood glucose monitoring based on impedance spectrum method.

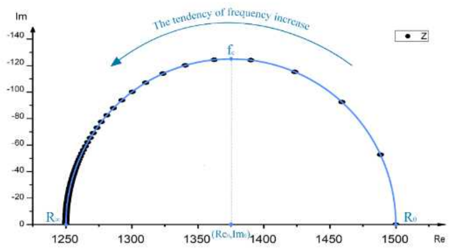

Fig. 9. The Cole-Cole impedance circle

Table 4. Impedance spectrum characteristic parameters and corresponding blood glucose concentration

Diagnosis	f_c(Hz)	C_{glu}(mmol/L)
Hypoglycemia	9.04	2
Hypoglycemia	8.511	4
Normal glucose	8.165	6
Abnormal glucose metabolism	7.92	8
Abnormal glucose metabolism	7.738	10
Diabetes	7.597	12

5. Conclusion

As the glucose concentration changes, the binding of glucose to the transporter changes the capacitance of the cell membrane. The transport of glucose into cells by transporters is a macroscopic change in the impedance of the human body. Considering the skin contacting impedance and cell membrane conductivity feature, a simulate circuit is designed and connected in serial with the measuring loop. The measured data were analyzed by an improved Cole-Cole model to derive the relationship between the impedance and the blood glucose concentration. The results show that the electrical impedance is strong negative correlation to blood glucose concentration, especially the characteristic frequency fc, as the blood glucose concentration increases, the impedance value decreases. The conclusion of this research provides a theoretical basis for non-invasive blood glucose surface-measuring.

Acknowledgment

The authors would like to thank the EIT research group from Tianjin University of Science and Technology. This paper was supported by a grant from the National Natural Science Foundation of China (Grant No.61301246) and a grant from the Science and Technology Project of Tianjin (12JCYBJC19300). It was also supported by the Reform in Education from Tianjin Municipal Education Commission of China (171005704B).

References

1. A. G. A. Aggidis, J. D. Newman, G. A. Aggidis, Investigating pipeline and state of the art blood glucose biosensors to formulate next steps[J]. *Biosensors and Bioelectronics*, 2015, 74, 243-262.
2. D. Klonoff, Noninvasive blood glucose monitoring. *Diabetes Care* 20, 1997, 433-443.
3. T. Koschinsky, L. Heinemann, Sensors for glucose monitoring: technical and clinical aspects. *Diabetes Metab*, 2001, 17, 113-123.
4. I. Harman-Boehm, A. Gal, A. M. Raykhman, et al., Noninvasive glucose monitoring: a novel approach[J]. *Journal of Diabetes Science and Technology*, 2009, 3(2), 253-260.
5. A. Caduff, E. Hirt, Y. Feldman, Z. Ali, L. Heinemann, First human experiments with a novel non-invasive, non-optical continuous glucose monitoring system[J]. *Biosensors and Bioelectronics*, 2003, 19(3), 209-217.
6. Y. Hayashi, L. Livshits, A. Caduff, et al., Dielectric spectroscopy study of specific glucose influence on human erythrocyte membranes[J]. *Journal of Physics D: Applied Physics*, 2003, 36(4), 369.
7. P. Shap, X. D. Zhang, X. C. Zhang, Biological Tissue Impedance Model for Blood Glucose Monitoring (*Acta Lase ｒ Biology Sinica, China*). 2016, 25(03), 250-256.
8. L. Livshits, A. Caduff, S. Talaryms, The role of GLUT1 in the sugar-induced dielectric response of human erythrocytes[J]. *The Journal of Physical Chemistry B*, 2009, 113 (7), 2212-2220.
9. Y. D. Chen, Y. T. Cao, Y. M. Gao, S. H. Pun, P. U. Mak, M. I. Vai, Y. R. Li, M. Du, Experimental study on contact impedance of intra-body communication transmitter[J]. *Journal of Biomedical Engineering Research*, 2010, 29(1), 13-17.
10. H. Beving, L. E. G. Eriksson, C. L. Davey, et. al., Dielectric properties of human blood and erythrocytes at radio frequencies (0.2-10 MHz); dependence on cell volume fraction and medium composition[J]. *European Biophysics Journal*, 1994, 23 (3), 207-215.
11. K. S. Cole, R. H. Cole, Dispersion and absorption in dielectrics I. Alternating current characteristics[J]. *The Journal of chemical physics*, 1941, 9(4), 341-351.
12. K. S. Cole, R. H. Cole, Dispersion and absorption in dielectrics II. Direct current characteristics[J]. *The Journal of Chemical Physics*, 1942, 10(2), 98-105.

Synchronization of Novel 4D Chaotic Systems with Different Control Laws

Hong Niu

College of Electronic Information and Automation,

Tianjin University of Science & Technology, China

E-mail: spots@163.com
www.tust.edu.cn

Abstract

In this paper, synchronization of novel four-dimensional(4D) autonomous chaotic systems is studied. Two different control laws are presented, which are based on the strictly positive realness of transfer function matrix and the center translation method respectively. The characteristics of the two control laws, as well as the differences between them, are proposed. Some relevant numerical simulation results, such as the curves of the corresponding synchronization state variables and the errors, are given to illustrate the feasibility and effectiveness of the two control laws.

Keywords: novel 4D chaotic system, chaos synchronization, strictly positive realness of transfer function matrix, center translation method

1. Introduction

Chao synchronization has been one of the major subjects in nonlinear dynamics.[1-4] It has great engineering significance and application prospect in signal processing, secure communication and so on.

In this paper, the synchronization of two identical novel 4D chaotic systems with different initial values is studied via two different control laws based on the strictly positive realness of transfer function matrix and the center translation method.

2. Review of the Novel 4D Chaotic System

The novel 4D chaotic system has been discussed in Ref. 5. It is formulated as

$$\begin{aligned}\dot{x} &= a(y-x),\\ \dot{y} &= c(x+y)+z-xw,\\ \dot{z} &= mx-y-hz,\\ \dot{w} &= xy-bw,\end{aligned} \tag{1}$$

where $a = 25$, $b = 3$, $c = 18$, $m = 19$ and $h = 14$. The phase portraits of the system (1) are shown in Fig. 1(a)-(f).

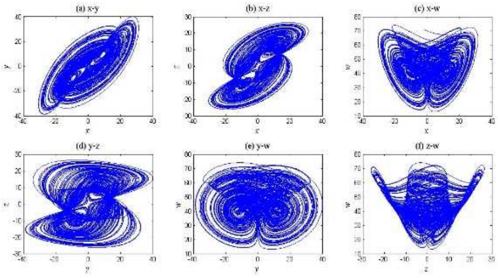

Fig. 1. Phase portraits of the novel 4D chaotic system: (a) *x*-*y*; (b) *x*-*z*; (c) *x*-*w*; (d) *y*-*z*; (e) *y*-*w*; (f) *z*-*w*

3. Chaos Synchronization Based on Strictly Positive Realness of Transfer Function Matrix

3.1. Corollary and Theorem

Corollary 1.[1-3] *Consider the system*

$$\dot{\boldsymbol{x}} = A\boldsymbol{x} + B\boldsymbol{u}, \tag{2}$$

$$\boldsymbol{y} = C\boldsymbol{x}. \tag{3}$$

Let $\boldsymbol{G}(s) = C(sI\text{-}A)^{-1}B$ *be a p×p transfer function matrix, where I is a n×n identity matrix, and* (A,B) *is controllable and* (A,C) *is observable. Then,* $\boldsymbol{G}(s)$ *is strictly positive real if there exist matrices* $P = P^{\mathrm{T}} > 0$ *and* $Q = Q^{\mathrm{T}} < 0$ *such that*

$$A^{\mathrm{T}}P + PA = Q, \tag{4}$$

$$B^{\mathrm{T}}P = C. \tag{5}$$

Theorem 1.[1-3] *Consider the system*

$$\dot{\boldsymbol{e}} = A\boldsymbol{e} + B\left(\boldsymbol{u} + \boldsymbol{u}_c\right), \tag{6}$$

$$\boldsymbol{y} = C\boldsymbol{e}, \tag{7}$$

$$\boldsymbol{u}_c = -K\boldsymbol{y} = -KC\boldsymbol{e}, \tag{8}$$

where $\boldsymbol{u}$ *is the nonlinear part which is packaged as the external input of the system (6) and* $\boldsymbol{u}_c$ *is the controller to be designed. The system (6)-(7) is asymptotically stable at the origin* $\boldsymbol{e} = \boldsymbol{0}$ *if there exist matrices K,* $P = P^{\mathrm{T}} > 0$ *and* $Q = Q^{\mathrm{T}} < 0$*, such that* $\boldsymbol{G}(s) = C[sI\text{-}(A\text{-}BKC)]^{-1}B$ *is strictly positive real.*

3.2. Design of Synchronization Controller

Consider the system (1) as the drive system. The response system is given by

$$\begin{aligned}
\dot{x}_2 &= a\left(y_2 - x_2\right) + u_{s1} + u_{c1},\\
\dot{y}_2 &= c\left(x_2 + y_2\right) + z_2 - x_2 w_2 + u_{s2} + u_{c2},\\
\dot{z}_2 &= m x_2 - y_2 - h z_2 + u_{s3} + u_{c3},\\
\dot{w}_2 &= x_2 y_2 - b w_2 + u_{s4} + u_{c4},
\end{aligned} \tag{9}$$

where

$$\boldsymbol{u}_s = \begin{bmatrix} u_{s1} & u_{s2} & u_{s3} & u_{s4} \end{bmatrix}^{\mathrm{T}}$$

and

$$\boldsymbol{u}_c = \begin{bmatrix} u_{c1} & u_{c2} & u_{c3} & u_{c4} \end{bmatrix}^{\mathrm{T}}$$

are structure compensator and synchronization controller to be designed. The function of the structure compensator $\boldsymbol{u}_s$ is to compensate the structure difference between the drive and the response systems so that the two chaotic attractors can be synchronized under the control of the synchronization controller $\boldsymbol{u}_c$.

Let

$$\begin{aligned}
\boldsymbol{e} &= \begin{bmatrix} e_1 & e_2 & e_3 & e_4 \end{bmatrix}^{\mathrm{T}}\\
&= \begin{bmatrix} x_2 - x & y_2 - y & z_2 - z & w_2 - w \end{bmatrix}^{\mathrm{T}}
\end{aligned}$$

be the synchronization error and $\boldsymbol{u}_s = \boldsymbol{0}$. Then the error system is formulated as

$$\begin{aligned}
\dot{e}_1 &= a\left(e_2 - e_1\right) + u_{c1},\\
\dot{e}_2 &= c\left(e_1 + e_2\right) + e_3 - \left(x_2 w_2 - x w\right) + u_{c2},\\
\dot{e}_3 &= m e_1 - e_2 - h e_3 + u_{c3},\\
\dot{e}_4 &= \left(x_2 y_2 - x y\right) - b e_4 + u_{c4}.
\end{aligned} \tag{10}$$

Hence,

$$\boldsymbol{u} = \begin{bmatrix} 0 & -\left(x_2 w_2 - x w\right) & 0 & x_2 y_2 - x y \end{bmatrix}^{\mathrm{T}},$$

$$A = \begin{bmatrix} -a & a & 0 & 0\\ c & c & 1 & 0\\ m & -1 & -h & 0\\ 0 & 0 & 0 & -b \end{bmatrix},$$

$$B = I,$$

where I is a 4×4 identity matrix. Let $P = P^{\mathrm{T}} = I$. From (5), $C = B^{\mathrm{T}}P = I$. Obviously, $((A\text{-}BKC),B)$ is controllable and $((A\text{-}BKC),C)$ is observable.

Let the synchronization controller $\boldsymbol{u}_c$ be

$$\begin{aligned}
\boldsymbol{u}_c &= \begin{bmatrix} u_{c1} & u_{c2} & u_{c3} & u_{c4} \end{bmatrix}^{\mathrm{T}} = -KC\boldsymbol{e}\\
&= \begin{bmatrix} -k_1 e_1 & -k_2 e_2 & -k_3 e_3 & -k_4 e_4 \end{bmatrix}^{\mathrm{T}},
\end{aligned} \tag{11}$$

where k_1, k_2, k_3, $k_4 \geq 0$. Then,

$$\begin{aligned}
&\left(A - BKC\right)^{\mathrm{T}} P + P\left(A - BKC\right)\\
&= \begin{bmatrix} f_{11} & f_{12} & f_{13} & 0\\ f_{21} & f_{22} & 0 & 0\\ f_{31} & 0 & f_{33} & 0\\ 0 & 0 & 0 & f_{44} \end{bmatrix} = F,
\end{aligned}$$

where

$$\begin{aligned}
f_{11} &= -2\left(k_1 + a\right),\\
f_{22} &= -2\left(k_2 - c\right),\\
f_{33} &= -2\left(k_3 + h\right),\\
f_{44} &= -2\left(k_4 + b\right),\\
f_{12} &= f_{21} = a + c,\\
f_{13} &= f_{31} = m.
\end{aligned}$$

Comparing with the matrix Q in Ref. 5 which is formulated as

$$Q=\begin{bmatrix} q_{11} & q_{12} & q_{13} & 0 \\ q_{21} & q_{22} & q_{23} & 0 \\ q_{31} & q_{32} & q_{33} & 0 \\ 0 & 0 & 0 & q_{44} \end{bmatrix},$$

where

$$\begin{aligned} q_{11} &= -2n_1(k_1+a), \\ q_{22} &= -2n_2(k_2-c), \\ q_{33} &= -2n_3(k_3+h), \\ q_{44} &= -2n_4(k_4+b), \\ q_{12} &= q_{21} = an_1+cn_2, \\ q_{13} &= q_{31} = mn_3, \\ q_{23} &= q_{32} = n_2-n_3. \end{aligned}$$

It is easy to find that the matrix F is totally equal to the matrix Q, when $n_1 = n_2 = n_3 = n_4 = 1$. It has been proven that the matrix Q is negative definite when

$$k_2 > \frac{h(a+c)^2}{4ah-m^2}+c > \frac{(a+c)^2}{4a}+c$$

while $k_1 = k_3 = k_4 = 0$ under the condition that $n_1 = n_2 = n_3 = n_4$. Therefore, it can also make the matrix F negative definite. From Corollary 1 and Theorem 1, the transfer function matrix of system (10) $\boldsymbol{G}(s) = C[sI-(A-BKC)]^{-1}B$ is strictly positive real, and the error system (10) will be asymptotically stable at the origin $\boldsymbol{e} = \boldsymbol{0}$ such that the states of the response system (9) are synchronized with those of the drive system (1) under the control of the synchronization controller $\boldsymbol{u}_c$.

Let $k_2 = 45$ and $k_1 = k_3 = k_4 = 0$, and substitute them into the synchronization controller $\boldsymbol{u}_c$, then

$$\begin{aligned} \boldsymbol{u}_c &= \begin{bmatrix} u_{c1} & u_{c2} & u_{c3} & u_{c4} \end{bmatrix}^{\mathrm{T}} \\ &= \begin{bmatrix} 0 & -45e_2 & 0 & 0 \end{bmatrix}^{\mathrm{T}}. \end{aligned} \tag{12}$$

3.3. Numerical Simulation

Remark 1. *The initial values of the drive system (1) and the response system (9) are* $(x_0, y_0, z_0, w_0) = (1, 1, 1, 1)$ *and* $(x_{20}, y_{20}, z_{20}, w_{20}) = (5, 4, 7, 8)$ *respectively in this paper.*

The curves of the errors and the synchronized state variables are shown in Fig. 2 and Fig. 3. The horizontal axis t expresses the solution interval of differential equations, so the variable t is a dimensionless quantity. The definition of t is all the same in this paper. From Fig. 2 and Fig. 3, it can be seen that the errors e_1, e_2, e_3 and e_4 converge to zero asymptotically and rapidly and the state variables are synchronized well. It demonstrates that the response system (9) and the drive system (1) have been synchronized under the control of the synchronization controller $\boldsymbol{u}_c$.

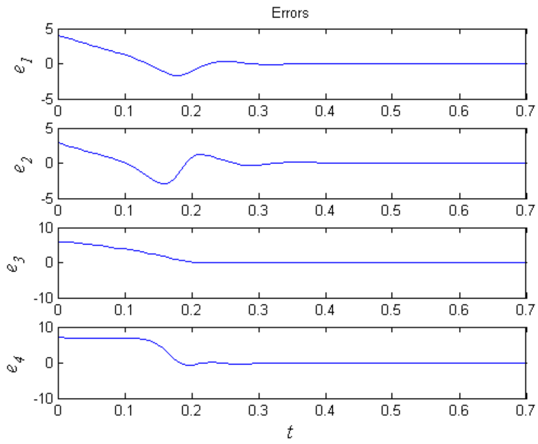

Fig. 2. Curves of errors

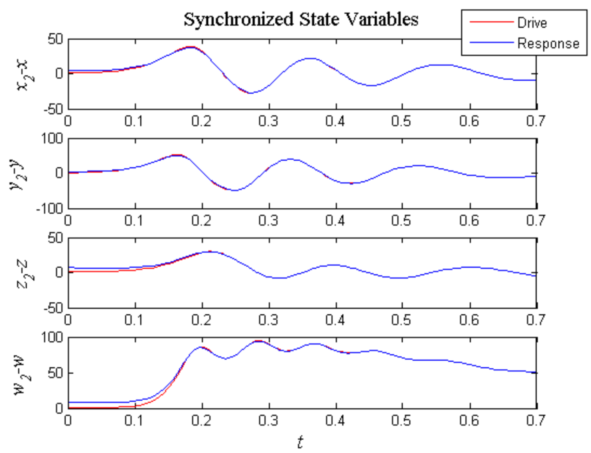

Fig. 3. Curves of synchronized state variables

4. Chaos Synchronization Based on Center Translation Method

4.1. Formulation of Error System

The error system is formulated as[3-4]

$$\begin{aligned}
\dot{e}_1 &= a(e_2 - e_1) + u_{c1}, \\
\dot{e}_2 &= c(e_1 + e_2) + e_3 - e_1 e_4 + u_{c2}, \\
\dot{e}_3 &= m e_1 - e_2 - h e_3 + u_{c3}, \\
\dot{e}_4 &= e_1 e_2 - b e_4 + u_{c4},
\end{aligned} \tag{13}$$

where the synchronization controller $\boldsymbol{u}_c$ is the same as that in (11). In fact, a structure compensator $\boldsymbol{u}_s$ is added to the response system (9), such that the error system (13) is equivalent to the response system (9) whose center is moved to $\boldsymbol{X} = [x\ y\ z\ w]^{\mathrm{T}}$.

4.2. Design of Synchronization Controller

Comparing the error system (13) with the controlled system (2) in Ref. 5, it can be found that their formulations are identical. It has been confirmed in detail in Ref. 5 that the system, such as the error system (13), is globally asymptotically stable at the origin as long as

$$k_2 > \frac{h(a+c)^2}{4ah - m^2} + c > \frac{(a+c)^2}{4a} + c,$$

while $k_1 = k_3 = k_4 = 0$. Thus, the synchronization controller $\boldsymbol{u}_c$ in the error system (13) is the same as that in (12).

4.3. Design of Structure Compensator

From (1), (9) and (13), the structure compensator $\boldsymbol{u}_s$, which is difficult to find directly, can be calculated as

$$\boldsymbol{u}_s = \begin{bmatrix} 0 & x_2 w + x w_2 - 2xw & 0 & 2xy - x_2 y - x y_2 \end{bmatrix}^{\mathrm{T}}.$$

In fact, from the construction procedure of the error system (13), it can be found that the design of the structure compensator can be omitted whatever the structure of the drive system is. Thus, if the state variables of the drive system and their derivatives are known or can be estimated via state observer, the synchronization controller $\boldsymbol{u}_c$ can be designed from the structure of the response system. It simplifies the synchronization procedure.

4.4. Numerical Simulation

The curves of the errors and the synchronized state variables are shown in Fig. 4 and Fig. 5. The two figures show that the errors e_1, e_2, e_3 and e_4 converge to zero asymptotically and rapidly and the state variables are synchronized well. It demonstrates that the response system (9) and the drive system (1) have also been synchronized under the control of the structure compensator $\boldsymbol{u}_s$ and the synchronization controller $\boldsymbol{u}_c$. Comparing Fig. 4 and Fig. 5 with Fig. 2 and Fig. 3, it can be found that the convergence time in Fig. 4 and Fig. 5 is a little longer than that in Fig. 2 and Fig. 3.

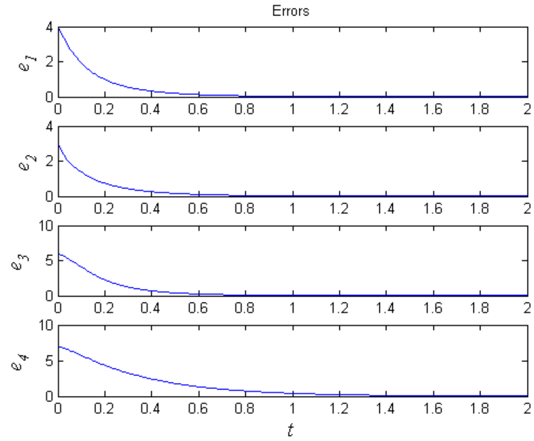

Fig. 4. Curves of errors

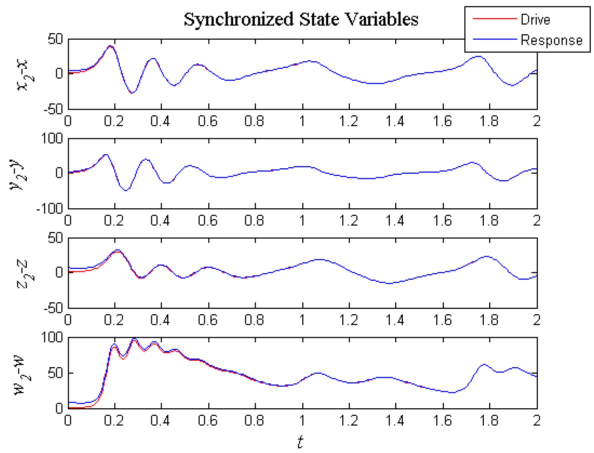

Fig. 5. Curves of synchronized state variables

5. Conclusion

The most difference between the two control laws is the global asymptotic stability of error system. The control law based on the center translation method makes the error system globally asymptotically stable at the origin, while the control law based on the strictly positive realness of transfer function matrix only makes the error system asymptotically stable at the origin. Whether the nonlinear part of the error system could be packaged as the external input, as described in Theorem 1, still needs to be analyzed and proven mathematically. Meanwhile, the proof of the control law based on the center translation method is rigorous and its design procedure is much more straightforward. However, a nonlinear structure compensator is hidden in the formulation of the error system of the control law based on the center translation method. It makes the circuit implementation of this control law complex and difficult. In contrast, the most advantage of the control law based on the strictly positive realness of transfer function matrix is that there is no structure compensator and the synchronization controller is linear, so the circuit implementation of this control law is direct and easy. In brief, there are both advantages and disadvantages in the two control laws. More researches would be established to conquer the disadvantages of the two control laws.

Acknowledgements

The research is supported by the Innovation Fund for the Young Teachers of Tianjin University of Science & Technology.

References

1. Hong Niu and Guoshan Zhang, Synchronization of chaotic systems with variable coefficients, *Acta Physica Sinica*, 62(3): 105-115, 2013.
2. Hong Niu, Guoshan Zhang and Jiankui Wang, Synchronization of Chua's circuits based on strictly positive realness, *26th Chinese Control and Decision Conference*, Changsha, China, 2014.5.31-6.2.
3. Hong Niu, Guoshan Zhang and Jiankui Wang, Chaos synchronization of Chua's circuit and Lorenz system based on strictly positive realness, *Proceedings of the 33rd Chinese Control Conference*, Nanjing, China, 2014.7.28-7.30.
4. Hong Niu, On synchronization of 5D hyperchaotic system and 3D chaotic system with variable coefficient, *Dynamical Systems and Control*, 5(2): 41-47, 2016.
5. Hong Niu, Analysis and control of a novel 4D chaotic system, *The 2017 International Conference on Artificial Life and Robotics*, Miyazaki, Japan, 2017.1.19-1.22.

Chaotic characteristics analysis of fractional-order Liu system

Wengxin Shi *, Hongyan Jia

College of Electronic Information and Automation,
Tianjin University of Science and Technology, China;

*E-mail: * 10161740075@qq.com*

Abstract

The paper analyzes a newly reported fractional-order Liu system based on time-domain approximation and frequency-domain approximation, respectively, and chaotic characteristics of this system are investigated by the phase portrait diagram, Lyapunov exponents diagram and bifurcation diagram. The results of the two approximation methods are consistent, which not only shows chaotic dynamics of the system is reliable, but also is very convenient to utilize chaotic dynamics of the system with fractional-order 0.9.

Keywords: Chaotic characteristic, fractional-order system, time-domain approximation, frequency-domain approximation

1. Introduction

Since chaotic behavior was found to exit in fractional-order Chua's circuit in 1995[1], the theory and application of fractional-order chaos has been attracting more and more interest of research in recent two decades[2-6]. According to Poincare-Bendixon theorem, it is impossible for a continuous autonomous integer-order system to be found to be chaotic when the order of the system is less than three[7-8]. However, for many fractional-order systems, the obvious advantage is that chaotic dynamics can occur when the order of the system is less than three, such as the fractional Rössler system [9], the fractional modified Duffing system[10], and so on [11-13]. Which provide an opportunity for researchers to find more chaotic dynamics in some lower dimensional systems. In addition, when studying secure communications based on integer-order chaotic systems, the parameters and initial values of the chaotic systems are generally selected as key secrets of secure communication. However, for fractional-order chaotic systems, the remarkable advantage is the order of fractional-order chaotic systems can also be used as key secrets of secure communication besides the parameters and initial values of the chaotic systems [14-16]. Therefore, the research on fractional-order chaotic systems not only help researchers to find more chaotic dynamics and enrich the theory of chaos, but also provide more suitable physical model or tools for application such as secure communication.

Generally speaking, computing the solutions of fractional-order systems is very difficult, so some approximation methods are always used to investigate the dynamics of fractional-order systems. So far as we know, the time-domain approach and the frequency-domain approach are two kind of common approximation methods which are always adopted. In literature, some fractional-order systems have been investigated based on frequency-domain approach[2,5,7,17,18] and other fractional-order systems have been investigated based on time-domain approach[4, 19-24]. However, it is seldom that a fractional-order system is simultaneously investigated to show chaotic dynamics based on both of the approximation methods. We find that it is insufficient to investigate chaotic characteristics of the fractional-order systems in either, because each of approximation methods has own merits and demerits. Therefore, it is necessary to use these two approximation methods to analyze and display chaos for a fractional-order system.

Recently, a fractional-order system named as the fractional-order Liu system is reported, and its chaotic attractor is found by phase portraits and Electronic Workbench Basics simulation[25-27]. In this paper, the fractional-order Liu system is further discussed, the difference from the research in[25-27] is that chaotic characteristics of the fractional-order Liu system are analyzed in detail by showing the Lyapunov exponents diagram and bifurcation diagram, based on time-domain approximation and frequency-domain approximation, respectively. The results of the two approximation methods are consistent.

2. Bifurcation analysis for the fractional-order Liu system

Recently, a fractional-order system was reported by Zhang et al, and Chen et al, in 2007 and 2008, in Ref[25-27], respectively. The fractional-order Liu system is described as

$$\begin{cases} \dfrac{d^q x}{dt} = f_1(x, y, z) = a(y - x), \\ \dfrac{d^q y}{dt} = f_2(x, y, z) = bx - cxz, \\ \dfrac{d^q z}{dt} = f_3(x, y, z) = -dz + gx^2, \end{cases} \tag{1}$$

Where $a, b, c, d, g \in R$, $(x, y, z) \in R^3$ and $0 < q < 1$, parameter q is called as the fractional order. Although its chaotic attractor has been found by discussing phase portraits and Electronic Workbench Basics simulation in Ref[25-27], it is insufficient to analyze the chaotic dynamics underlying the system, therefore, here we further discuss its chaotic characteristic.

As described above, when studying some fractional-order systems numerically, the time-domain approximation and the frequency-domain approximation are two kinds of mainly methods to be adopted to investigate chaotic dynamics, and each of them has its own merits and demerits. Generally, compared with the time-domain approximation, the frequency-domain approximation is more practical to implement and utilize the fractional-order systems. However, the time-domain approximation is more accurate than the frequency-domain approximation when showing chaotic behaviors of the fractional-order systems. Therefore, in order to further analyze the chaotic characteristics, the system (1) is exclusively investigated based on both time-domain approximation and frequency-domain approximation.

2.1 Bifurcation analysis based on time-domain approximation

In this paper, the advised Adams-Bashforth-Moulton method in Ref [4] and [24] is adopted to numerically analyze chaotic behavior of system (1), and thus for the initial values x_0, y_0, z_0 and step length h, on the basis of the above method, the fractional-order four-wing system (1) can be written as following discrete form

$$\begin{cases} x_{n+1} = x_0 + \dfrac{h^q}{\Gamma(q+2)}[f_1(x_{n+1}^p, y_{n+1}^p, z_{n+1}^p) + \sum\limits_{j=0}^{n} \beta_{j,n+1} f_1(x_j, y_j, z_j)], \\ y_{n+1} = y_0 + \dfrac{h^q}{\Gamma(q+2)}[f_2(x_{n+1}^p, y_{n+1}^p, z_{n+1}^p) + \sum\limits_{j=0}^{n} \beta_{j,n+1} f_2(x_j, y_j, z_j)], \\ z_{n+1} = z_0 + \dfrac{h^q}{\Gamma(q+2)}[f_3(x_{n+1}^p, y_{n+1}^p, z_{n+1}^p) + \sum\limits_{j=0}^{n} \beta_{j,n+1} f_3(x_j, y_j, z_j)], \end{cases} \tag{2}$$

Where

$$\begin{cases} x_{n+1}^p = x_0 + \dfrac{1}{\Gamma(q)} \dfrac{h^q}{q} \sum\limits_{j=0}^{n} ((n+1-j)^q - (n-j)^q) f_1(x_j, y_j, z_j), \\ y_{n+1}^p = y_0 + \dfrac{1}{\Gamma(q)} \dfrac{h^q}{q} \sum\limits_{j=0}^{n} ((n+1-j)^q - (n-j)^q) f_2(x_j, y_j, z_j), \\ z_{n+1}^p = z_0 + \dfrac{1}{\Gamma(q)} \dfrac{h^q}{q} \sum\limits_{j=0}^{n} ((n+1-j)^q - (n-j)^q) f_3(x_j, y_j, z_j), \end{cases}$$

$$\beta_{j,n+1} = \begin{cases} n^{q+1} - (n-q)(n+1)^q, & j = 0 \\ (n-j+2)^{q+1} + (n-j)^{q+1} - 2(n-j+1)^{q+1}, & 1 \le j \le n \\ 1, & j = n+1 \end{cases}, \quad i = 1,2,3$$

here the error for the time-domain approach is about $O(h^r)$, $r = \min(2, 1+q)$.

Fixing parameters $b = 40$, $c = 10$, $d = 2.5$, $g = 4$, initial values $x_0 = 1, y_0 = 1, z_0 = 1$, and fractional-order $q = 0.9$, based on time-domain approach, the Lyapunov exponents diagram and bifurcation diagram of system (1) are obtained, as shown in Fig.1(a) and Fig.1(b), respectively. It can be seen that chaos exists in the system (1) with fractional-order $q = 0.9$ for the parameter interval $a = [2.3, 20]$ in Fig.1. For a=6, based on time-domain approach, the phase portraits of chaotic attractor are obtained to further show chaotic dynamics of system (1), as shown in Fig.2.

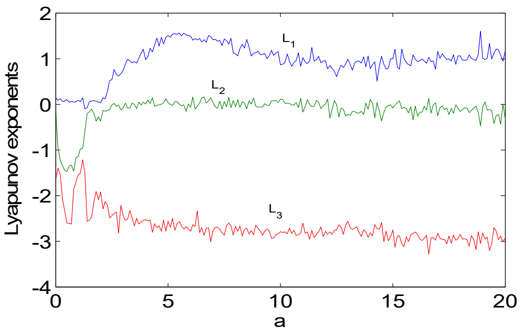

(a) Lyapunov exponents diagram

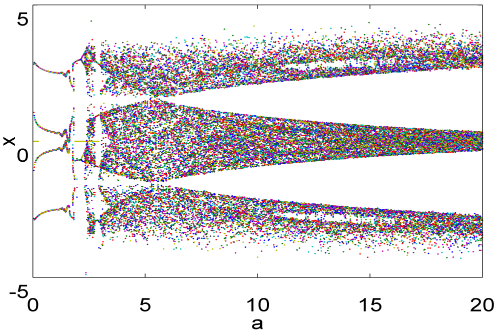

(b) Bifurcation diagram

Fig.1 Lyapunov exponents diagram and bifurcation diagram of system (1) based on time-domain approach

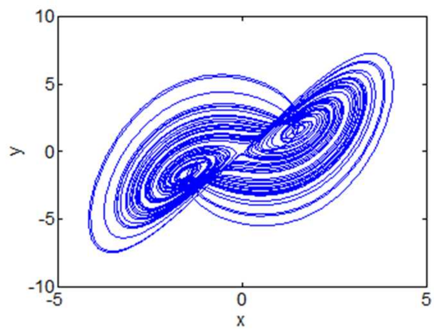

(a) Phase portrait in $x-y$ plane

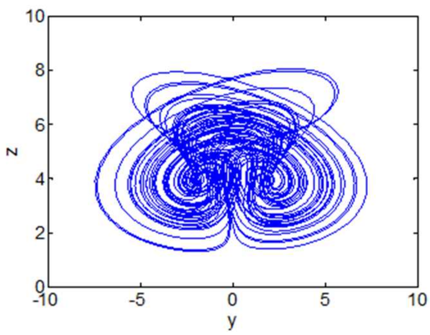

(b) Phase portrait in $y-z$ plane

Fig.2 Chaotic attractors of system (1) based on time-domain approach

2.2 Bifurcation analysis based on frequency-domain approximation

In this paper, the frequency-domain approach [7] is adopted as well, which was also used in literatures [25-27], and the approximation function with an error of 2 dB is listed as follows

$$\frac{1}{s^{0.9}} = \frac{2.2675(s+1.292)(s+215.4)}{(s+0.01292)(s+2.154)(s+359.4)} \tag{3}$$

Under the same condition, $b=40$, $c=10$, $d=2.5$, $g=4$, initial values $x_0=1, y_0=1, z_0=1$, and fractional-order $q=0.9$, based on frequency-domain approach, the Lyapunov exponents diagram and bifurcation diagram of system (1) are also obtained, as shown in Fig.3(a) and Fig.3(b), respectively. It can be also seen that chaos exists in the system (1) with fractional-order $q=0.9$ for the parameter interval $a=[2.8, 20]$ in Fig.3. For a=6, based on frequency-domain approach, the chaotic attractor has been obtained to further show chaotic dynamics in the system (1), as shown in Fig.4.

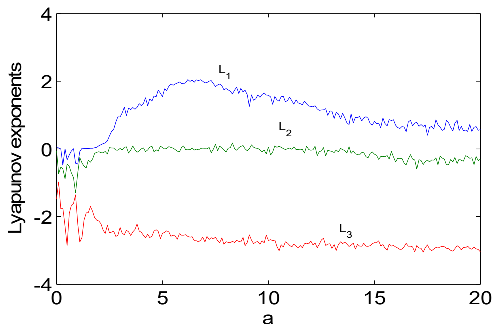

(a) Lyapunov exponents diagram

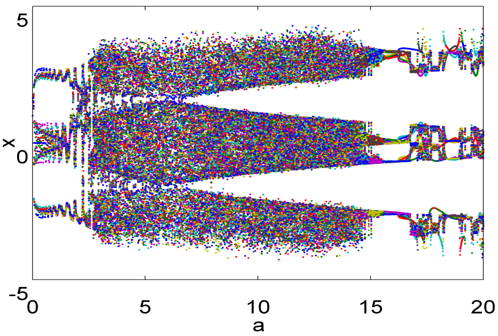

(b) Bifurcation diagram

Fig.3 Lyapunov exponents diagram and bifurcation diagram of system (1) based on frequency-domain approach

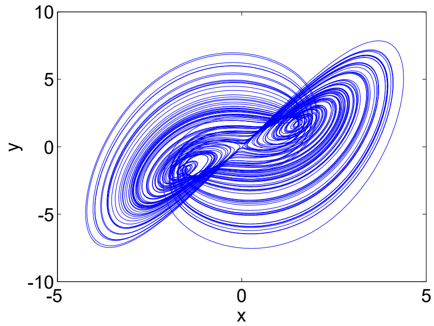

(a) Phase portrait in $x-y$ plane

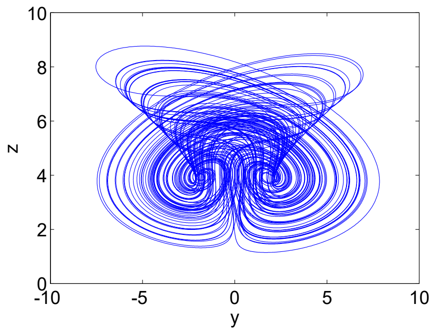

(b) Phase portrait in $y-z$ plane

Fig.4 Chaotic attractors of system (1) based on frequency-domain approach

By comparing the numerical results from the frequency-domain approach and those from the time-domain approach, respectively, we conclude that chaos indeed exists in the chaotic dynamic of system (1) with fractional-order 0.9, no matter whether adopting frequency-domain approach or time-domain approach. What's more, the numerical results from the two approaches are very coincident except for some tiny difference.

3. conclusion

The paper analyzes a newly reported fractional-order Liu system based on time-domain approximation and frequency-domain approximation, respectively, and chaotic characteristics of this system are investigated by the phase portrait diagram, Lyapunov exponents diagram and bifurcation diagram. And the results of the two approximation methods are consistent. The work in this paper not only show chaotic dynamics of system (1) is reliable, but also is very convenient to utilize chaotic dynamics of system (1).

Acknowledgements

The research is partly supported by the Research Fund for the National Natural Science Foundation of China (Grant No.61573199). It is also supported by the Young Scientists Fund of the National Natural Science Foundation of China (Grant No.11202148).

References

1. Hartley T T, Lorenzo C F, Killory Qammer H. Chaos in a fractional order Chua's system [J]. *IEEE Transactions on Circuits & Systems I Fundamental Theory & Applications*, 1995, 42(8): 485-90.
2. Grigorenko I, Grigorenko E. Chaotic dynamics of the fractional Lorenz system [J]. *Physical Review Letters*, 2003, 91(3): 034101.
3. Deng W H, Li C P. Chaos synchronization of the fractional Lü system [J]. *Physica A Statistical Mechanics & Its Applications*, 2005, 353(1): 61-72.
4. Diethelm K, Ford N J, Freed A D. A predictor-corrector approach for the numerical solution of fractional differential equations [J]. *Nonlinear Dynamics*, 2002, 29(1-4): 3-22.
5. Lu J G, Chen G R. A note on the fractional-order Chen system [J]. Chaos Solitons & Fractals, 2006, 27(3): 685-8.
6. Dadras S, Momeni H R. Control of a fractional-order economical system via sliding mode [J]. *Physica A Statistical Mechanics & Its Applications*, 2010, 389(12): 2434-42.
7. Ahmad W M, Sprott J C. Chaos in fractional-order autonomous nonlinear systems [J]. *Chaos Solitons & Fractals*, 2003, 16(2): 339-51.
8. Lu J G. Chaotic dynamics of the fractional-order Lü system and its synchronization [J]. *Chinese Physics B*, 2006, 59(2): 301-5.
9. Li C, Chen G. Chaos and hyperchaos in the fractional-order Rössler equations [J]. *Physica A Statistical Mechanics & Its Applications*, 2004, 341(1–4): 55-61.
10. Ge Z M, Ou C Y. Chaos in a fractional order modified Duffing system [J]. *Chaos Solitons & Fractals*, 2007, 34(2): 262-91.
11. Huang X, Zhao Z, Wang Z, et al. Chaos and hyperchaos in fractional-order cellular neural networks [J]. *Neurocomputing*, 2012, 94(3): 13-21.
12. Hosseinnia S H, Magin R L, Vinagre B M. *Chaos in fractional and integer order NSG systems [M]*. Elsevier North-Holland, Inc., 2015.
13. Aghababa M P. Chaotic behavior in fractional-order horizontal platform systems and its suppression using a fractional finite-time control strategy [J]. *Journal of Mechanical Science & Technology*, 2014, 28(5): 1875-80.
14. Sheu L J. A speech encryption using fractional chaotic systems [J]. *Nonlinear Dynamics*, 2011, 65(1-2): 103-8.

15. Kiani-B A, Fallahi K, Pariz N, et al. A chaotic secure communication scheme using fractional chaotic systems based on an extended fractional Kalman filter [J]. Communications in Nonlinear Science & Numerical Simulation, 2009, 14(3): 863-79.
16. Sheu L J, Chen W C, Chen Y C, et al. A two-channel secure communication using fractional chaotic systems [J]. World Academy of Science Engineering & Technology, 2010, 72(1): 248.
17. Jia H Y, Chen Z Q, Qi G Y. Topological horseshoe analysis and circuit realization for a fractional-order Lü system [J]. Nonlinear Dynamics, 2013, 74(1-2): 203-12.
18. Charef A, Sun H H. Fractal system as represented by singularity function [J]. IEEE Transactions on Automatic Control, 2002, 37(9): 1465-70.
19. Tavazoei M S, Haeri M. Limitations of frequency domain approximation for detecting chaos in fractional order systems [J]. Nonlinear Analysis Theory Methods & Applications, 2008, 69(4): 1299-320.
20. Tavazoei M S, Haeri M. Unreliability of frequency-domain approximation in recognising chaos in fractional-order systems [J]. Let Signal Processing, 2007, 1(4): 171-81.
21. Deng W H. Numerical algorithm for the time fractional Fokker-Planck equation [J]. Journal of Computational Physics, 2007, 227(2): 1510-22.
22. Zhou P, Wei L J, Cheng X F. A novel fractional-order hyperchaotic system and its synchronization [J]. Chinese Physics B, 2009, 18(7): 2674-9.
23. Petras I. Chaos in the fractional-order Volta's system: modeling and simulation [J]. Nonlinear Dynamics, 2009, 57(1-2): 157-70.
24. Li C P, Peng G J. Chaos in Chen's system with a fractional order [J]. Chaos Solitons & Fractals, 2004, 22(2): 443-50.
25. Chen X R, Liu C X, Wang F Q, et al. Study on the fractional-order Liu chaotic system with circuit experiment and its control [J]. Acta Physica Sinica, 2008, 57(3): 1416-22.
26. Lu J J, Liu C X. Realization of fractional-order Liu chaotic system by circuit [J]. Chinese Physics B, 2007, 16(6): 1586-90.
27. Xu Z, Liu C X. Realization of fractional-order Liu chaotic system by a new circuit unit [J]. Chinese Physics B, 2008, 17(11): 4033-8.

Design and Analysis of Multi-robot grouping aggregation algorithm

Huailin Zhao*
School of electrical and Electronic Engineering,Shanghai Institute of technology, No. 100, Haiquan Road, Fengxian District, Shanghai 201418,China

Zhen Nie
School of electrical and Electronic Engineering,Shanghai Institute of technology, No. 100, Haiquan Road, Fengxian District, Shanghai 201418,China

E-mail: zhao_huailin@yahoo.com, hbniezhen@foxmail.com
www.sit.edu.cn

Abstract:

In this paper, the grouping aggregation problem of multi-robot in simple environment is studied. The grouping algorithm and aggregation algorithm are mainly discussed. Based on two clustering algorithms, K-means and K-medoids, two grouping algorithms are designed. And the noise immunity and grouping rapidity of these two grouping algorithms are analyzed. Aiming at the problem of aggregation, three kinds of aggregation algorithms are proposed. Taking the center aggregation control as an example, the cooperation and control of each group of robots are studied. Finally, the simulation results of MATLAB shows that the multi-robot grouping and aggregation algorithm is effective.

Keywords: multi-robot; clustering; grouping aggregation; swarm intelligence

1.Introduction

The multi-robot collaboration system is a frontier topic in the field of artificial intelligence [1]. From the control point of view, the multi-robot collaboration system is a typical distributed control system [2-4], and its goal is to build large complex systems which included software and hardware systems into small, easy-to-manage systems that communicate and coordinate with each other. The research of multi-robot collaboration system involves the knowledge, goals, skills, planning of robots and how to make robots coordinate actions to solve problems, and the idea of swarm intelligence is emphasized. The multi-robot collaboration system forms a complex system through communication, coordination, and cooperation among autonomous robots. The major applications include formation flying of multi-UAV, clusters of warehousing logistics robot, competitions of robot team, large-scale robotic rescue systems, etc. Some Examples in nature are dancing fish, flying birds, and so on.

Aggregation is the basic problem of multi-robot system consistency [5-6], and it is also an optimizing measure [7], and the grouping aggregation is a special case of aggregation problem. Group aggregation is a motion planning of the robots randomly distributed in space, which are divided into many groups according to a specific grouping rule, and then each group of robots adjust the motion states through communication and cooperation between each other, finally they gather together, or in the desired area to complete the aggregation. In the end, all the robots formed a multi-group gathering situation, the idea of swarm intelligence is emphasized.

After the comparative analysis of two clustering algorithms, K-means and K-medoids, an efficient grouping aggregation algorithm is designed based on K-means algorithm. The feasibility of multi-robot grouping aggregation is verified by MATLAB simulation experiment. And the multi-robot distributed coordination and grouping aggregation control are realized.

2.Analysis and design of grouping algorithm

Grouping aggregation is divided into two steps, grouping task and aggregation task. The grouping task is to complete the group division of each robot according to a specific grouping rule. This study designed and analyzed a grouping algorithm based on two clustering algorithms, K-means and K-medoids.

(1) The K-means algorithm is a clustering algorithm which is the simplest and most commonly used in unsupervised learning. It is a center-based clustering algorithm [8-9]. The K-means algorithm completes the grouping task by minimizing the distance between each sample and the center of the cluster. The initial centers of each cluster were randomly selected.

In the Euclid space, a set of n-dimensional samples $X=\{x_1,x_2,x_3\cdots x_i\cdots x_n\}$ (representing n robots) is given, where $x_i \in R^n$. The K-means algorithm divides all samples into k clusters $C=\{c_i, i=1,2,\cdots,k\}$. The Euclidean distance is chosen as the criterion for the distance, the equation is expressed as follows.

$$d(a,b)=\|a-b\| \qquad (1)$$

where a, b represents two points in the Euclid space, which are two n-dimensional data.

In determining the similarity of the samples, the samples are divided into the clusters with the highest similarity according to the following equation (the similarity is based on the distance between the samples and the centers, and the smaller the distance, the higher the similarity).

$$c_i=\arg\min_{C}\sum_{i=1}^{k}\sum_{x_j\in X}\left\|x_j-\mu_i\right\|^2 \qquad (2)$$

Where μ_i is the center of ith cluster.

The k-means algorithm needs to re-divide the cluster and update the centers iteratively. When the Square Error Sum is converged, the K-means algorithm ends. The equation of Square Fitting Error Sum is given by

$$J=\sum_{i=1}^{k}\sum_{j=1}^{n}d_{ij}\left\|x_j-\mu_i\right\|^2 \qquad (3)$$

Where $d_{ij}=\begin{cases}1, x_j\in c_i\\ 0, x_j\notin c_i\end{cases}$ 。

(2) The K-medoids algorithm uses the point closest to the cluster center as the center of the cluster [10-11]. There are many forms of K-medoids algorithm, the most classic one is the PAM algorithm. The basic idea is:

Firstly, k samples are randomly selected from n samples as k initial centers; then Euclidean distance is calculated according to the equation (1), and the initial clustering is performed according to the principle of minimum distance; Finally, center points are replaced by non-center points repeatedly to improve the clustering quality. The post-replacement clustering quality is estimated by a cost function (4), which measures the average dissimilarity degree between the object and its reference object. In the process of substitution, the least cost is selected for replacement, and cluster again until the cluster no longer changes. The cost function is expressed as follows:

$$TC_{ih}=\sum_{j=1}^{n}C_{jih} \qquad (4)$$

Where TC_{ih} is the total cost after the center point o_i replaced by non-central point o_h ; C_{jih} is the cost of o_j after o_i is replaced by o_h . If the total cost is negative, it means that the average dissimilarity degree within the clusters becomes smaller after the replacement. So o_i can be replaced by o_h . Otherwise, it cannot be.

Under the requirement, to achieve the grouping aggregation, the grouping is the premise of the aggregation, and the quality of the grouping directly affects the aggregation of the robots. Therefore, the two grouping algorithms are further studied, mainly analyzing the noise immunity and the calculation rapidity.

(1) The analysis of the noise immunity

The noise immunity is the first factor to be considered in system design, and it is the key to system security under abnormal conditions. In order to test the noise immunity of the two algorithms, 20 samples were set to simulate 20 robots randomly placed in space, and they were divided into two groups by K-means and K-medoids respectively. Another abnormal sample was added as noise.

As mentioned earlier, the K-means algorithm is a center-based clustering algorithm, so the position of the center is an important criterion for the quality of the grouping. The experimental results are shown in Fig.1. Fig.1(a) shows the results of grouping without noise. The samples were well divided into two groups by the k-means algorithm, and the grouping effect was well. Fig.1(b) shows that when the noise point c appeared, although the grouping task was completed, the center was obviously deviated. If the noise is more intense, the center deviation would be larger. Due to the deviation of the center, the grouping of the two samples, a and b, has changed. If the noise is more intense, the grouping results of more samples would be affected. It can be seen that the K-means algorithm is sensitive to noise. If the sample contains abnormal points, it would seriously affect the grouping result.

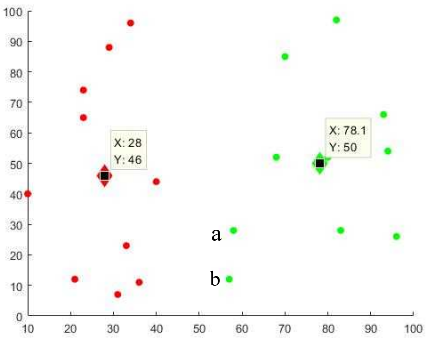

(a)

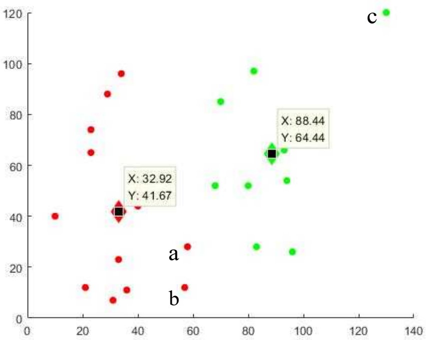

(b)

Fig.1. The test of noise immunity of K-means algorithm: (a) the grouping result without noise; (b) the grouping result with noise

The K-medoids algorithm uses the point closest to the cluster center as the center point of the cluster, thus effectively avoiding the phenomenon that the center of the K-means algorithm changes due to the deviation of the noise. The simulation of grouping results is shown in Fig.2. Fig.2(a) shows the grouping result without noise, and the grouping result was good. Fig.2(b) shows the grouping result when the noise point c appeared, and the grouping task was still completed. Because the center was instead of the sample closest to the center. Therefore, there is no center deviation, and the grouping result was not affected. It can be seen that the K-medoids algorithm has strong noise immunity.

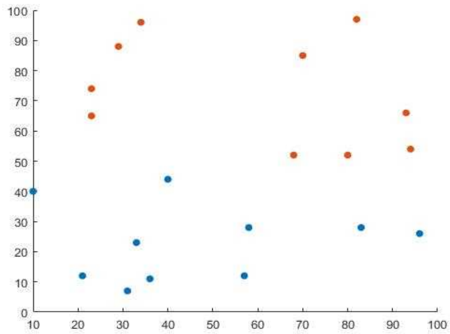

(a)

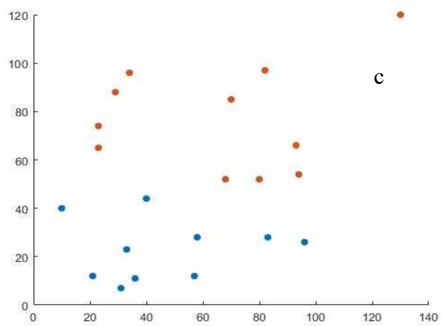

(b)

Fig.2. The test of noise immunity of K-medoids algorithm: (a) the grouping result without noise; (b) the grouping result with noise

(2) The analysis of the calculation rapidity

The K-means algorithm a center-based clustering algorithm. In the calculation process, only the average of the robot coordinates should be calculated. The time complexity is $O(nkt)$ for k<<n, t<<n. Where n is the number of samples, k is the number of clusters, and t is the number of iterations. The K-medoids algorithm uses the point closest to the cluster center as the center of the cluster. In the calculation process, the distance and total cost between any two points are constantly calculated. The time complexity is $O(n^2kt)$ for *k<<n, t<<n*. Where n is

the number of samples, k is the number of clusters, and t is the number of iterations. Obviously, the time complexity of the k-medoids algorithm is greater than k-means algorithm. When a large number of samples or a large k should be deal with, the calculation speed will be slow, which seriously affects the grouping efficiency.

Through the comparison and analysis, the K-means algorithm is simple and fast. Although the noise immunity is not as good as the K-medoids algorithm, when the sample is large, a few noise has little effect on the K-means algorithm. The K-medoids algorithm has strong noise immunity, but when there are a large number of samples, the calculation speed is slow due to the large time complexity. Since this grouping aggregation will process a large amount of data, the K-means algorithm was decided.

3.Analysis and design of aggregation algorithm

As mentioned earlier, the aggregation problem is that multi-robots randomly distributed in the space adjust the motion states through communication and cooperation between each other, finally they gather together, or in the desired area to complete the aggregation. Aiming at the aggregation task requirements of this topic, three aggregation control algorithms were designed and analyzed in this paper:

1) Selecting a robot from each group as leaders, as shown in Fig.3(a). The basic idea of this algorithm is to pre-set a leader robot, and other robots are called followers [12-13]. In the process of aggregation, the leader controls the motion path, and the followers keep a certain angle and distance with the leader, finally all robots aggregate at the position of the leader. After careful analysis, the aggregation has some defects. On the one hand, because the algorithm doesn't make full use of the advantages of distributed systems, when the leader robot goes wrong, it will cause all robots fail to aggregate. On the other hand, because the control of the system is relatively simple, the follower or leader robot may be lost in the process of motion in the complicated reality environment. The aggregation task failed.

2) Selecting the neighboring robot as the reference point, as shown in Fig.3(b). Each robot finds its own target position in the whole aggregation movement through the position information of neighboring robots. The limitation of this method is that a large amount of communications is required, and each robot needs to spend more time for communication, and the result of the formation control is not satisfactory.

3) Selecting the center of group as the reference point, as shown in Fig.3(c). This selection method is called center algorithm. During the aggregation process, multiple robots form a geometric figure. According to the geometric figure, the geometric center is calculated. Each robot uses takes the center as a reference point to adjust the direction and speed, and move to the reference point. During the aggregation movement, the system constantly updates the reference points, and finally all robots reach a same point. the aggregation task is end. This algorithm is simple and practical. The system is convergent. The advantages of the distributed control system are fully reflected.

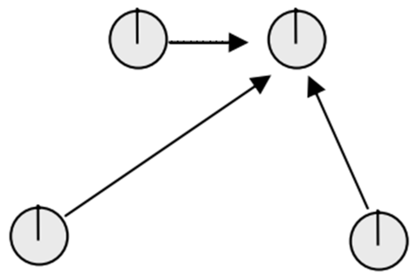

(a)

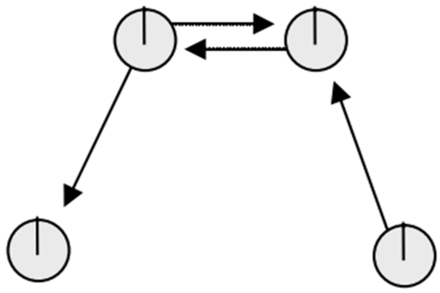

(b)

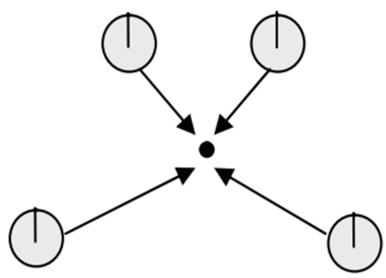

(c)

Fig.3. Three different aggregation algorithms:(a) Selecting a robot from each group as leaders; (b) Selecting the

neighboring robot as the reference point; (c) Selecting the center of group as the reference point.

Comparing the three aggregation algorithms, this study intends to use the center algorithm for aggregation control. The center calculation equations are expressed as follows:

$$x_c = \sum_{i=1}^{n} x_i / n \quad , \quad y_c = \sum_{i=1}^{n} y_i / n \qquad (5)$$

Where (x_i , y_i) is the 2-D coordinate of the current position for the i^{th} robot, and (x_c , y_c) is the center coordinate.

During the aggregation process, the system periodically updates the center position and notifies all robots. Each robot makes motion planning according to its current position and new center position. The motion planning equation is given by

$$X_i(k+1) = X_i(k) + v_i(k+1) \cdot T \qquad (6)$$

Where T is the sampling period, X_i is the motion state of i^{th} robot, v_i is the velocity of i^{th} robot.

4.Calculation process of grouping aggregation algorithm

As mentioned earlier, to complete the packet aggregation task, the first thing should be done is grouping operation, and the next is the aggregation operation. The specific process is as follows.

According to the grouping requirements, the robot updates the position of the center of the group in real time, and calculates the distance to the centroid, grouped according to the nearest distance principle. The specific algorithm flow is as follows:

(1) choose k robots from all robots randomly as the initial group center;

(2) The Euclidean distance between each robot and the group center are calculated, and assign them to the group with the closest center according to the nearest distance principle;

(3) Calculate the mean of all objects in each group as the new center, and calculate the Square Error Sum. Repeat from step 2 until the Square Error Sum is converged.

After the grouping operation is completed, the aggregation operation is started. According to the requirements of center algorithm, the center position of each group should be real-time updated and notified each robot in the group. Each robot adjusts the speed and direction according to its current position and new center position, then moves to the center. The specific algorithm flow is as follows:

(1) Each robot initializes its position, and reads and saves the current position;

(2) The robots in the group communicate with each other to inform the position information. The center coordinates are calculated according to the position coordinates of all robots. Then each robot calculates its own speed and direction of motion based on its own coordinate and center coordinate. Finally, the robots move to the center of the group.

(3) Repeat from step 1 until al robots in each group enter a small range.

5.Simulation analysis

According to the grouping aggregation control algorithm, the research group carried out simulation analysis on the MATLAB. In order to facilitate the observation of the simulation results and analysis, the simulation environment which is a two-dimensional with a length of 100 and a width of 100 was first configured. 60 robots were randomly set up in the grid. It was intended to divide them into 4 groups and achieve group aggregation. The specific two-dimensional grid and the initial position of the robot are shown in Fig.4.

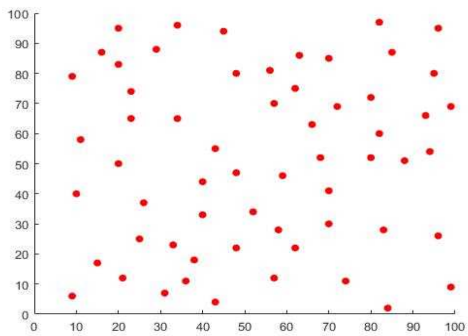

Fig.4. The specific two-dimensional grid and the initial position of the robot

The multi-robot system is first divided into four groups according to the K-means algorithm, and the aggregation motion starts after the grouping is completed.

During the grouping process, the centers are updated after each grouping and grouped again according to the nearest distance principle. Fig. 5(a) shows that the four sample points were randomly selected as the initial centroid, and the first grouping was completed. Fig.5(b) and Fig. 5(c) were the repeated grouping process of the robot, and the diamonds showed the real-time position of the centers. The grouping result was as shown in Fig. 5(d), and there was a good effect

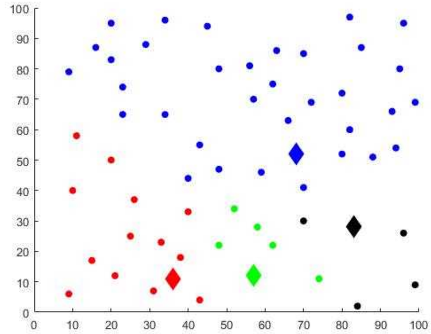

(a)

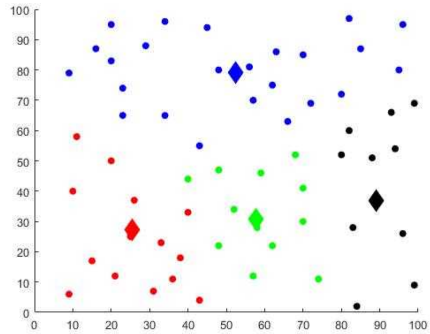

(b)

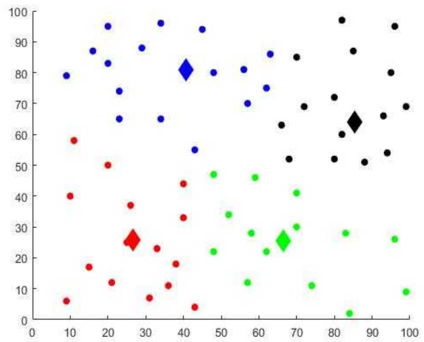

(c)

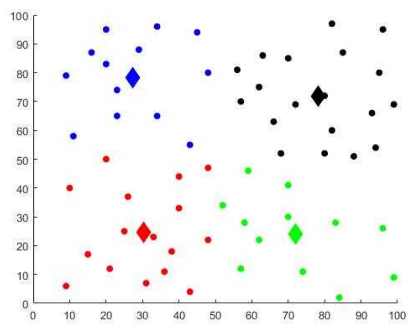

(d)

Fig.5. The simulation of grouping process

In the process of aggregation control, the robots of each group moved from the initial position to the center of each group. During the aggregation motion, the centers were updated in each sampling period (the sampling period T was set 1 second). The Fig.6(a) to Fig.6(e) correspond to a sampling period in the aggregation process, respectively. Fig.6(d) shows that the robots have gathered within a small range. Fig.6 (e) shows that the motion state of the robots was slightly adjusted relative to Fig.6(d), but it was still within a small range, so that the aggregation task was completed.

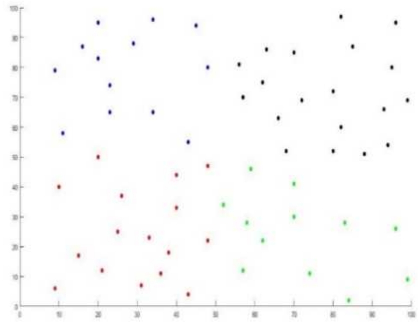

(a)

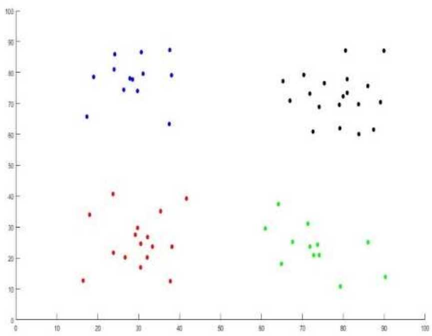

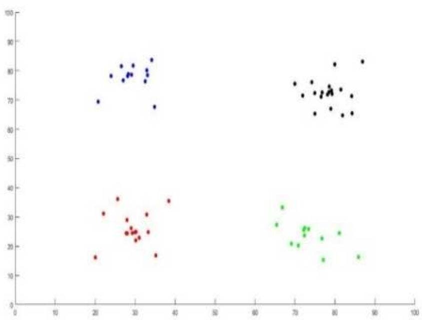

(b)

（c）

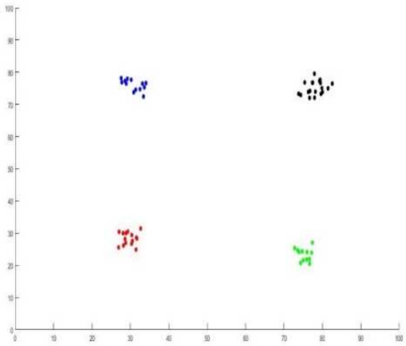

(d)

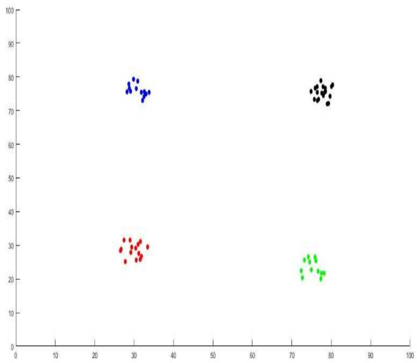

(e)

Fig.6. The Simulation of aggregation process

6. Conclusion

This topic takes multi-robot system as the research object, and takes grouping aggregation as the main task, and realizes the grouping and aggregation control of multi-robot in simple environment. The research group designed the center grouping algorithm and the center aggregation algorithm based on K-means algorithm. The MATLAB simulation analysis shows the detailed process of grouping operation and aggregation operation, which verifies the feasibility of the grouping aggregation algorithm. The algorithm embodies the swarm intelligence in a certain degree.

References

1. Huailin Zhao, Yangguang Guo, Masanori Sugisaka. Design of the Multi-Car Collaboration System[C], *the 2017 International Conference on Artificial Life and Robotics (ICAROB 2017)*, 2017.01, Japan. 186-190.
2. Wei Tingting. Research on the surround control problem of multi-agent system [D]. *University of Electronic Science and Technology of China*, 2014.
3. Shi Xiaoxing. *Research on Formation and Coordination of Group Robots* [D]. Lanzhou University of Technology, 2011.
4. Dimos V. Dimarogonas, Kostas J. Kyriakopoulos Connectedness. Preserving Distributed Swarm Aggregation for Multiple Kinematic Robots[C]. *IEEE Transactions on Robotics*, VOL. 24, NO. 5, OCTOBER 2008, 1213-1223.
5. Huailin Zhao, Wei Ren. Consensus Problem of Distributed Multi-agent Systems[C], *Proceedings of the 2015 International Conference on Artificial Life and Robotics (ICAROB 2015)*, 2015.01, Japan. 201-206.
6. Huailin Zhao, Zheng Wu, Xiaoxing Wang. A Multi-robot Rescuing System[C]. *The 2018 International Conference on Artificial Life and Robotics (ICAROB 2018)*, 2018.02, Japan. 582-586.
7. Zhu Guoqing. *Study on Control on strategy for Self-Organized Formation of Swarm Robotics Systems*[D]. Shandong University, 2017.
8. Wang Qian, Wang Cheng, Feng Zhenyuan, Ye Jinfeng. Review of K-means clustering algorithm [J]. *Electronic Design Engineering*: 2012, 4:21-24
9. Yang Ping, Guo Chunyang, Li Cuiming. Swarm Robots Aggregation Formation Control Based on K-means Clustering Algorithm[J]. *Modular Machine Tool & Automatic Manufacturing Technology*, 2012, 8:89-92.
10. Wang Zhongqiang, Li Gui, Han Ziyang, Zheng Xinlu. Research and Implementation Based on K-medoids Clustering Algorithm[J]. *Silicon Valley*:2011,1:80-81
11. Xia Ningxia, Su Yidan, Yu Xi. Efficient K-medoids clustering algorithm[J].Application Research of Computers:2010,12:4517-4519
12. Wang Wenming, Zhou Shuai. Research on Multi-Robot Cooperative Control and Formation Method[J]. Netinfo Security: 2014, 6:59-66.
13. Luo Jing, Liu Chenglin, Liu Fei. Pilot-following formation and obstacle avoidance control of multi-mobile robots[J]. CAAI Transactions on Intelligent Systems, 2017, 12(2): 202-212.

Research of the ARM-based Multi-robot aggregation Control

Huailin Zhao
School of electrical and Electronic Engineering, Shanghai Institute of technology, No. 100, Haiquan Road, Fengxian District, Shanghai 201418,China
Jingnan Zheng
School of electrical and Electronic Engineering, Shanghai Institute of technology, No. 100, Haiquan Road, Fengxian District, Shanghai 201418,China
Zhen Nie
School of electrical and Electronic Engineering, Shanghai Institute of technology, No. 100, Haiquan Road, Fengxian District, Shanghai 201418,China
Weiya Zhang
School of electrical and Electronic Engineering, Shanghai Institute of technology, No. 100, Haiquan Road, Fengxian District, Shanghai 201418,China
Zonglin liu
School of electrical and Electronic Engineering,Shanghai Institute of technology, No. 100, Haiquan Road, Fengxian District, Shanghai 201418,China
E-mail: zhao_huailin@yahoo.com, hbniezhen@foxmail.com
www.sit.edu.cn

Abstract

This paper mainly analyzed the basic aggregation problem of multi-robot cooperative system. The algorithm design of multi-robot dynamic aggregation control was discussed. The multi-robot aggregation path planning method in simple environment was discussed. And the kinematics equation of the aggregation algorithm was given at last. Taking the center aggregation control as an example, the cooperation and control of multi-robot are studied. Then we designed a simulation control program on MATLAB for multi-robot system and analyzed the simulation results. Finally, the center aggregation experiment was carried out by using the three car robots. The results show that the multi-robot aggregation algorithm is effective.

Keywords: Multi-robot; Aggregation Control; Motion planning; Swarm intelligence.

1. Introduction

The multi-robot collaboration system is a frontier topic in the field of artificial intelligence [1]. From the control point of view, the multi-robot collaboration system is a typical distributed control system [2-4], and its goal is to build large complex systems which included software and hardware systems into small, easy-to-manage systems that communicate and coordinate with each other. The research of multi-robot collaboration system involves the knowledge, goals, skills, planning of robots and how to make robots coordinate actions to solve problems, and the idea of swarm intelligence is emphasized. The multi-robot collaboration system forms a complex system through communication, coordination, and cooperation among autonomous robots. The major applications include formation flying of multi-UAV, clusters of warehousing logistics robot, competitions of robot team, large-scale robotic rescue systems, etc. Some Examples in nature are dancing fish, flying birds, and so on.

Aggregation is the basic problem of multi-robot system consistency [5-6], and it is also an optimizing measure [7]. The aggregation problem is that the robots are distributed in space adjust the motion states through communication and cooperation between each other, finally they gather together, or in the desired area to complete the aggregation. The research team has realized the cooperation and aggregation of two robots [8]. However, the Wi-Fi communication between the two robots was indirectly realized by the host computer, otherwise the bidirectional communication cannot be realized. So the cost of the system is high. Because there are only two robots, there is not much swarm intelligence. This topic intends to design and utilize three intelligent cars based on ARM, and a distributed control system is formed by these cars. This system does not require host computers as transfers, and any two machines can communicate directly with each other. The project intends to design an effective algorithm of aggregation control to achieve multi-machine distributed coordination and aggregation, which reflects certain swarm intelligence and lays a foundation for the research of large-scale multi-robot distributed control system.

2. Analysis and design of aggregation algorithm

As mentioned earlier, the aggregation problem is that multi-robots randomly distributed in the space adjust the motion states through communication and cooperation between each other, finally they gather together, or in the desired area to complete the aggregation. For a multi-machine system consisting of n robots. For a multi-machine system consisting of n robots, a typical kinematics equation of aggregate control is expressed as follows.

$$\dot{x}_i(t) = u_i(t),\ i = 1,\cdots,n \qquad (1)$$

Where $\dot{x}_i(t)$ is the state variable of ith robot, $u_i(t)$ is the control input of ith robot.

$$u_i(t) = \sum_{j=1}^{n} a_{ij}(t)\left[x_j(t) - x_i(t)\right] \qquad (2)$$

Where $a_{ij}(t)$ is coefficient of the system.

It can be seen from equation (2) that the farther the robot is from other robots, the greater the control effect. Based on the above basic theory, three aggregation control algorithms were designed and analyzed for the aggregation task requirements of this topic:

1) Selecting a robot from each group as leaders, as shown in Fig.1(a). The basic idea of this algorithm is to pre-set a leader robot, and other robots are called followers [9-10]. In the process of aggregation, the leader controls the motion path, and the followers keep a certain angle and distance with the leader, finally all robots aggregate at the position of the leader. After careful analysis, the aggregation has some defects. On the one hand, because the algorithm doesn't make full use of the advantages of distributed systems, when the leader robot goes wrong, it will cause all robots fail to aggregate. On the other hand, because the control of the system is relatively simple, the follower or leader robot may be lost in the process of motion in the complicated reality environment. The aggregation task failed.

2) Selecting the neighboring robot as the reference point, as shown in Fig.1(b). Each robot finds its own target position in the whole aggregation movement through the position information of neighboring robots. The limitation of this method is that a large amount of communications is required, and each robot needs to spend more time for communication, and the result of the formation control is not satisfactory.

3) Selecting the center of group as the reference point, as shown in Fig.1(c). This selection method is called center algorithm. During the aggregation process, multiple robots form a geometric figure. According to the geometric figure, the geometric center is calculated. Each robot uses takes the center as a reference point to adjust the direction and speed, and move to the reference point. During the aggregation movement, the system constantly updates the reference points, and finally all robots reach a same point. the aggregation task is end. This algorithm is simple and practical. The system is convergent. The advantages of the distributed control system are fully reflected.

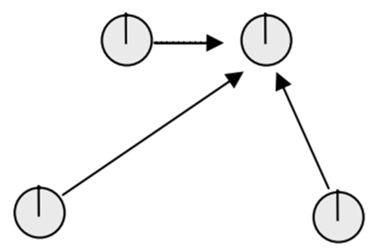

(a)

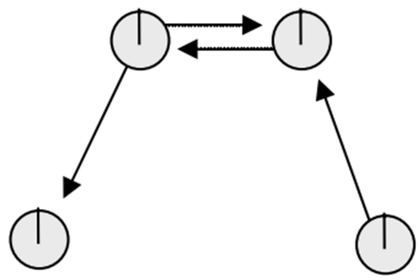

(b)

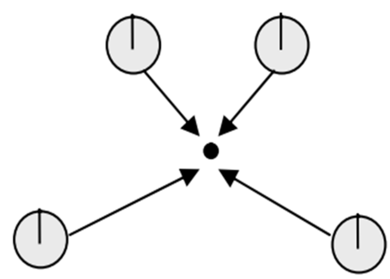

(c)

Fig.1 Three different aggregation algorithms:(a) Selecting a robot from each group as leaders; (b) Selecting the neighboring robot as the reference point; (c) Selecting the center of group as the reference point.

Comparing the three aggregation algorithms, this study intends to use the center algorithm for aggregation control. The center calculation equations are expressed as follows:

$$x_c = \sum_{i=1}^{n} x_i / n \quad , y_c = \sum_{i=1}^{n} y_i / n \qquad (3)$$

Where（x_i , y_i) is the 2-D coordinate of the current position for the i[th] robot, and (x_c , y_c) is the center coordinate.

During the aggregation process, the system periodically updates the center position and notifies all robots. Each robot makes motion planning according to its current position and new center position. The motion planning equation is given by

$$X_i(k+1) = X_i(k) + v_i(k+1) \cdot T \quad (4)$$

Where T is the sampling period, X_i is the motion state of i[th] robot, v_i is the velocity of i[th] robot.

3. Calculation process of center aggregation algorithm

According to the requirements of center algorithm, the center position of each group should be real-time updated and notified each robot in the group. Each robot adjusts the speed and direction according to its current position and new center position, then moves to the center. The specific algorithm flow is as follows:

(1) Each robot initializes its position, and reads and saves the current position;

(2) The robots communicate with each other to inform the position information. The center coordinates are calculated according to the position coordinates of all robots. Then each robot calculates its own speed and direction of motion based on its own coordinate and center coordinate. Finally, the robots move to the center of the group.

(3) Repeat from step 1 until al robots in each group enter a small range.

4. Robot motion control system

In the multi-machine cooperation system, each robot is an intelligent individual. When cooperation is needed, every robot communicates with each other. Otherwise, each robot independently completes the motion planning. The distributed control of the whole system is realized.

The main controller of each robot uses the STM32 [11-12], and the WIFI module is additionally configured to realize the communication cooperation. The GPS module is configured to read the real-time location. The INS is configured to achieve azimuth adjustment. Fig. 2 shows the robot motion control system.

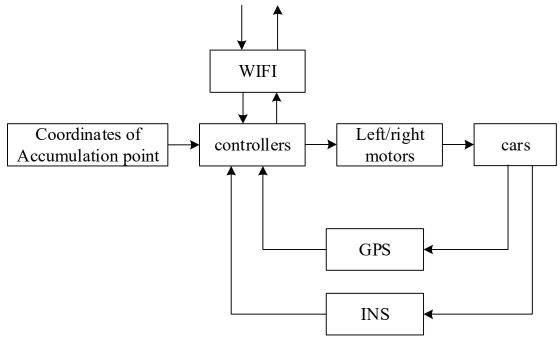

Fig.2 The robot motion control system

As mentioned earlier, any two robots in the system can communicate directly with each other by Wi-Fi, and no longer require the host computers as transfers. The reason is that we have configured two Wi-Fi modules for each car, one dedicated to sending signal and the other dedicated to receiving signal. In this way, the two-way communication of each robot is realized, and the host computers are no longer require, thereby greatly reducing the system cost.

5. Simulation analysis

According to the grouping aggregation control algorithm, the research group carried out simulation analysis on the MATLAB. The simulation environment which is a two-dimensional with a length of 100 and a width of 80 was first configured. The initial positions of three robots were randomly set, and their coordinates are (1,1), (100,50), (5,80). The specific two-dimensional grid and the initial position of the robot are shown in Fig.3(a).

In the process of aggregation control, the robots moved from the initial position to the center. During the aggregation motion, the centers were updated in each sampling period (the sampling period T was set 1 second). The Fig.3(b) to Fig.3(f) correspond to a sampling period in the aggregation process, respectively. Fig.6(e) shows that the robots have gathered within a small range. Fig.6 (f) shows that the motion state of the robots was slightly adjusted relative to

Fig.6(e), but it was still within a small range, so that the aggregation task was completed.

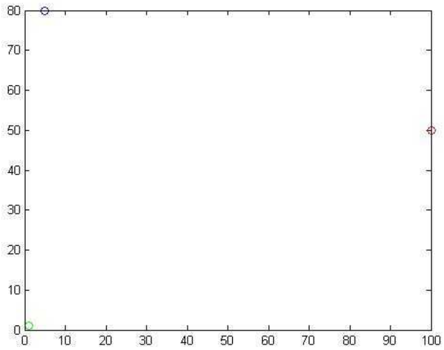

(a)

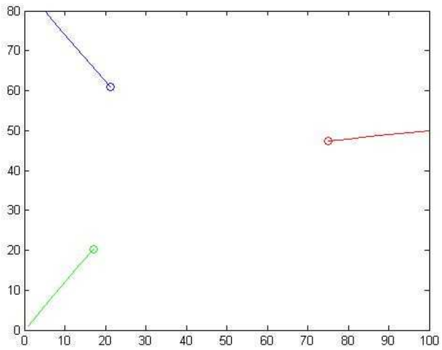

(b)

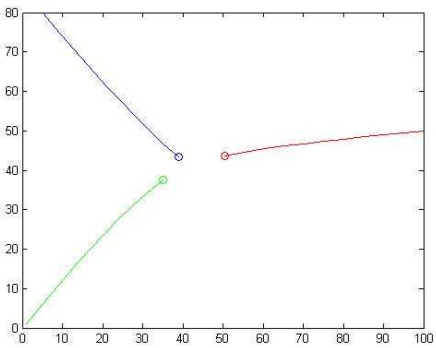

(c)

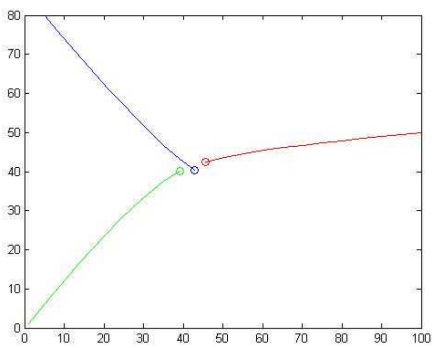

(d)

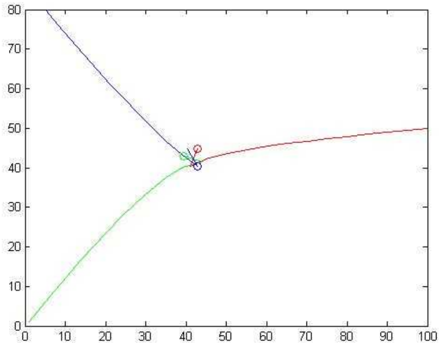

(e)

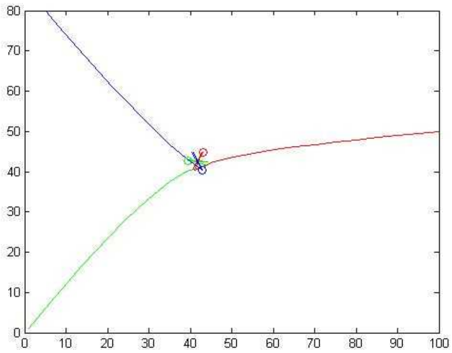

(f)

Fig.3 The Simulation of aggregation process

6. Experiment

Based on the theoretical basis of the multi-robot system and the simulation analysis, the research team carried out an experiment on campus. The three intelligent cars we used are shown in Fig. 4.

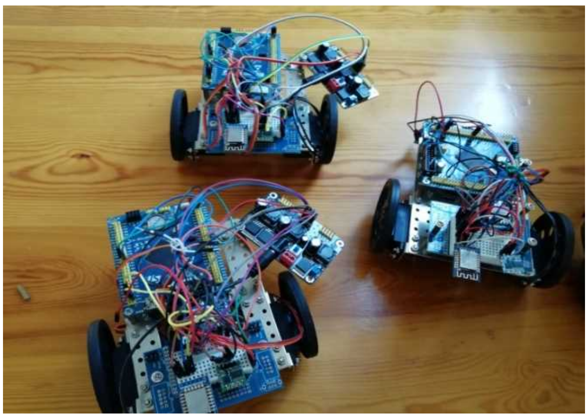

Fig.4 The intelligent cars used in the experiment.

Before the experiment, three intelligent cars were randomly placed on the road at a certain distance. Then start each car program at the same time to observe the motion situation of the multi-car system. The intelligent cars were constantly aggregate to the center. Finally, the cars were very close to each other, and no longer have obvious displacement, it means that the aggregation is successful. Fig.5 shows the aggregation process

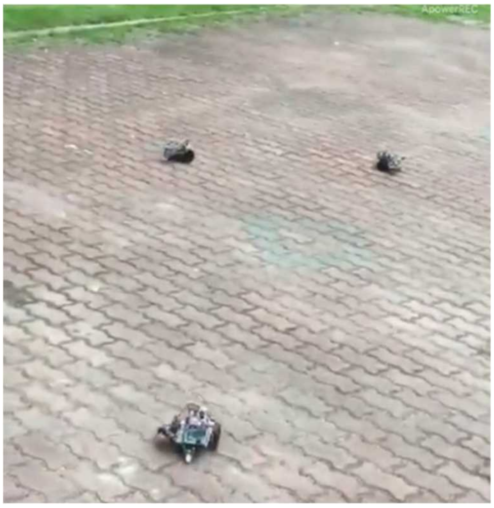

(a)

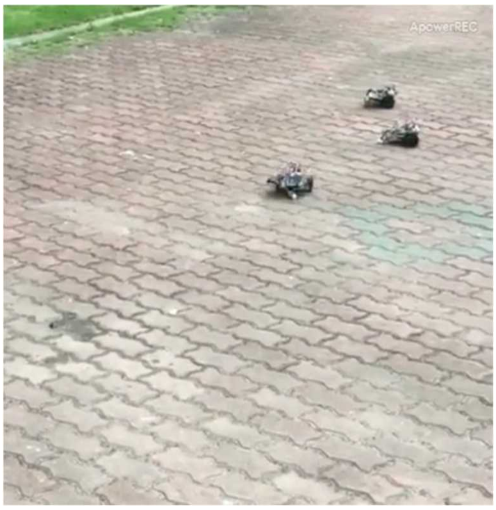

(b)

Fig.5 The aggregation process of the intelligent cars:(a) the initial position of the three cars; (b) the aggregation position of three cars

Through the experiment, some conclusions are put forward as follows:

(1) Regardless of the initial placement of the three cars, they can aggregate successfully, which shows the stability of the system.

(2) The initial position of three smart cars will affect the experimental results, including the final location and speed of aggregation, which means the initial state has a direct impact on the aggregation results.

7. Conclusion

This topic takes multi-robot system as the research object, and takes aggregation as the main task, and realizes the aggregation control of multi-robot in simple environment. After the specific centroid aggregation control algorithm was designed, not only the simulation analysis was carried out, but also the experimental results were carried out in the actual environment. The expected aggregation effect is achieved, which verifies the feasibility of the multi-robot system. The topic embodies the swarm intelligence.

References

1. Huailin Zhao, Yangguang Guo, Masanori Sugisaka. Design of the Multi-Car Collaboration System[C], *the 2017 International Conference on Artificial Life and Robotics (ICAROB 2017)*, 2017.01, Japan. 186-190.
2. Wei Tingting. Research on the surround control problem of multi-agent system [D]. *University of Electronic Science and Technology of China*, 2014.
3. Shi Xiaoxing. *Research on Formation and Coordination of Group Robots* [D]. Lanzhou University of Technology, 2011.
4. Dimos V. Dimarogonas, Kostas J. Kyriakopoulos Connectedness. Preserving Distributed Swarm Aggregation for Multiple Kinematic Robots[C]. *IEEE Transactions on Robotics,* VOL. 24, NO. 5, OCTOBER 2008, 1213-1223.
5. Huailin Zhao, Wei Ren. Consensus Problem of Distributed Multi-agent Systems[C], *Proceedings of the 2015 International Conference on Artificial Life and Robotics (ICAROB 2015)*, 2015.01, Japan. 201-206.
6. Yang Ping, Guo Chunyang, Li Cuiming. Swarm Robots Aggregation Formation Control Based on K-means Clustering Algorithm[J]. *Modular Machine Tool & Automatic Manufacturing Technology*, 2012, 8:89-92.
7. Zhu Guoqing. *Study on Control on strategy for Self-Organized Formation of Swarm Robotics Systems*[D]. Shandong University, 2017.
8. Huailin Zhao, Zheng Wu, Xiaoxing Wang. A Multi-robot Rescuing System[C]. *The 2018 International Conference on Artificial Life and Robotics (ICAROB 2018)*, 2018.02, Japan. 582-586.
9. Wang Wenming, Zhou Shuai. Research on Multi-Robot Cooperative Control and Formation Method[J]. *Netinfo Security*: 2014, 6:59-66.
10. Luo Jing, Liu Chenglin, Liu Fei. Pilot-following formation and obstacle avoidance control of multi-mobile robots[J]. *CAAI Transactions on Intelligent Systems*, 2017, 12(2): 202-212.
11. Fengzhi Dai, Yuxing Ouyang, Yiqiao Qin, Baochang Wei, Yujie Yan. The Design of Intelligent Vehicle System Based on STM32. [C], J*ournal of Advanced Control, Automation and Robotics* 4 (1): 145-148, April 5, 2018.
12. Fengzhi Dai, Yuxing Ouyang, Yiqiao Qin, Ce Bian, Baochang Wei, Shengbiao Chang, Bo Liu. Development of Integral Smart Home Appliances[J]. *Journal of*

Robotics, Networking and Artificial Life, Vol 4, No. 4 (March 2018), 291-294.

Research on Trajectory Planning Problem of Robot in Spherical Cutting

Min Jun
School of electrical and Electronic Engineering,Shanghai Institute of technology,
No. 100, Haiquan Road, Fengxian District， Shanghai 201418,China
E-mail: 15205182192@163.com

Jiang Wenping
School of electrical and Electronic Engineering,Shanghai Institute of technology,
No. 100, Haiquan Road, Fengxian District， Shanghai 201418,China
E-mail: jiangwenping@sit.edu.cn

Zhao Huailin
School of electrical and Electronic Engineering,Shanghai Institute of technology,
No. 100, Haiquan Road, Fengxian District， Shanghai 201418,China
E-mail: zhao_huailin@yahoo.com

Abstract

For cylindrical shape cutting of spherical surface vessel a kind of 5-DOF cutting method of cylindrical shape for spherical surface is provided in this paper. Based on the kinematics model of cutting robotthe mathematic relations between cutting tool cylindrical shape and spherical surface are built using Eulertransformation and the intersection line model of cylindrical and spherical surface is presented. The roboticcutting trajectory is computed according to the position and attitude relation of robot and spherical sphereand simulations and experiments of cutting trajectory for robot are provided in the end. Experiments resultsverified the rightness of robot kinematics and cylindrical shape cutting algorithm,and will promote the robot-is application in cutting field.

Key words: spherical surface;Kinematics;cylindrical shape;cutting;Trajectory planning;robo

1. Introduction

Metal pressure vessels are widely used in chemical, petroleum, mechanical, metallurgical, nuclear, aerospace and aerospace sectors, and are essential equipment in the production process. The can body container is generally composed of a cylinder, a spherical surface, and a head, and the cylindrical surface is usually required to be cut in the manufacturing process. At present, most of China's spherical cutting uses manual operation or CNC cutting machine. The former has the disadvantages of high labor intensity, dependence on operator experience, low precision and poor consistency. Although the latter greatly improves cutting quality and work efficiency, it still exists. Some disadvantages, such as the complicated structure of the cutting aid, the large footprint of the cutting machine, and poor cutting suitability and flexibility. Compared to CNC cutting machines, cutting robots offer greater flexibility and adaptability[1]. analytical method to study the problem of theorthogonal intersecting line between the cylinder and the sphere. However, this algorithm is limited to the orthogonality of the cylinder and the spherical surface. It can not solve the intersection of the cylinder and the spherical surface in any direction, and lacks versatility. At present, the algorithm for solving the intersecting line between the cylinder and the spherical surface is more focused on mathematical theory. The algorithm is more complicated and is not suitable for the engineering application of the cutting robot. Therefore, based on a 5-DOF robot, this paper proposes a cylindrical cutting scheme for the spherical surface of the robot. Based on the kinematics model of the robot, the cutting trajectory planning algorithm for the spherical surface and the arbitrary position and direction cylinder is designed, and the robot The cutting algorithm has been simulated and can be adapted to practical engineering applications[2].

2. Cutting robot motion model

The research object of this paper is a 5-DOF robot, which adopts Cartesian coordinates. The robot with this structure has the characteristics of good rigidity, high precision and low cost. Among them, the first joint is a moving joint along the X axis, the second joint is a moving joint along the Y axis, the third joint is a moving joint along the Z axis, the fourth joint is a rotating joint, and the fifth joint is a swing joint.

When the robot uses the laser cutting method to cut the spherical crown, the robot moves along the intersecting line of the cylinder and the cylinder, and the end posture is consistent with the cylinder axis, so that the straight and oblique cutting of the cylinder and the sphere can be completed. The cutting process of the robot is shown in Figure 1[3].

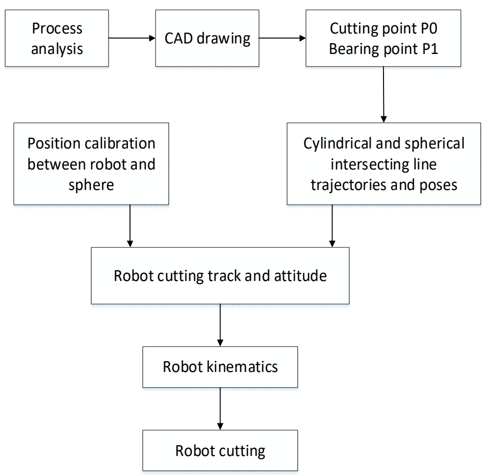

Figure.1. Schematic diagram of the robot cutting process

The structural diagram of the robot is shown in Figure 2, where X, Y, and Z are the basic coordinate systems centered on the robot base, x_1, y_1, z_1、x_2, y_2, z_2、x_3, y_3, z_3、x_4, y_4, z_4 and x_5, y_5, z_5 are the coordinate system of the cutting robot joint coordinates 1, 2, 3, 4, 5 respectively, x_1, y_1, z_1 is the robot end tool coordinate system, d_1, d_2, d_3, d_4, d_5, d_6 is the length of each rod of the robot[4].

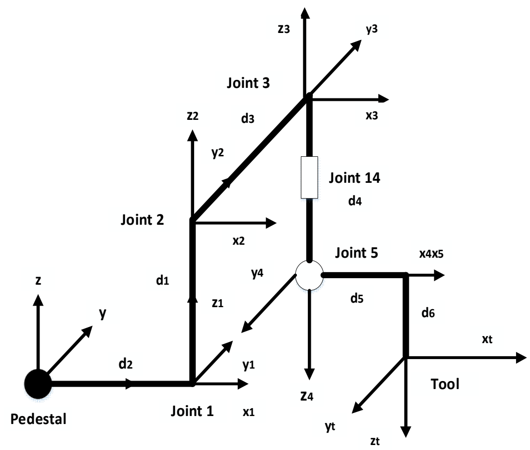

Figure.2. Schematic diagram of the robot structure

2. 1 *Robotic Kinematics*

It is assumed that the motion variables of the joints are X, Y, Z, θ_1, and θ_2 are the motion variables of the first joint, the second joint, the third joint, the fourth joint, and the fifth joint of the robot, respectively. Obviously, $d_2 = X$, $d_3 = Y$, $d_4 = -Z$, so that the coordinate system transformation matrix of adjacent joints can be obtained.

$$^0T_1 = Trans(X,0,0)$$

$$^1T_2 = Trans(0,0,d_1)$$

$$^2T_3 = Trans(0,Y,0)$$

$$^3T_4 = Rot(x,180)Tran(0,0,-Z)Rot(z,\theta_1)$$

$$^4T_5 = Rot(x,90)Rot(z,\theta_2)$$

$$^5T_t = Rot(x,-90)Tran(d_5,0,0)Trans(0,0,d_6)$$

Thus, the pose matrix of the robot end cutting tool in the basic coordinate system can be obtained,just like formula (1).

$$T = {}^{0}_{1}T\,{}^{1}_{2}T\,{}^{2}_{3}T\,{}^{3}_{4}T\,{}^{4}_{5}T\,{}^{5}_{t}T = \begin{bmatrix} c\theta_1 c\theta_2 & -s\theta_1 & -c\theta_1 s\theta_2 & c\theta_1 c\theta_2 d_5 - c\theta_1 s\theta_2 d_6 + X \\ -s\theta_1 c\theta_2 & -c\theta_1 & s\theta_1 s\theta_2 & -s\theta_1 c\theta_2 d_5 + s\theta_1 s\theta_2 d_6 + Y \\ -s\theta_2 & 0 & -c\theta_2 & -s\theta_2 d_5 - c\theta_2 d_6 - Z + d_1 \\ 0 & 0 & 0 & 1 \end{bmatrix} \quad (1)$$

2. 2 *Robot inverse kinematics*

Assume that the end pose matrix of a 5-DOF robot is:

$$P = \begin{bmatrix} n_x & o_x & a_x & p_x \\ n_y & o_y & a_y & p_y \\ n_z & o_z & a_z & p_z \\ 0 & 0 & 0 & 1 \end{bmatrix} \quad (2)$$

According to equations (1) and (2), the inverse solution of the robot can be obtained according to the principle that the corresponding elements of the matrix are equal:

$$\theta_1 = \arctan 2(-o_x, -o_y)$$

$$\theta_2 = \arctan 2(-n_z, -a_z)$$

$$X = p_x - \cos\theta_1 \cos\theta_2 d_5 + \cos\theta_1 \sin\theta_2 d_6$$

$$Y = p_y + \sin\theta_1 \cos\theta_2 d_5 - \sin\theta_1 \sin\theta_2 d_6$$

$$Z = d_1 - p_z - \sin\theta_2 d_5 - \cos\theta_2 d_6$$

3. Rrobot cutting algorithm

The intersection of the sphere and the arbitrary orientation cylinder is shown in Figure 4. Among them, x_s , y_s , z_s is the spherical coordinate system with the spherical center as the origin, x_s' , y_s' , z_s' is the coordinate system with the spherical center as the origin, and the z_s' axis coincides with the axis of the cutting cylinder. x_s' , y_s' are respectively x_s , y_s Rotated around the Euler axis. $p_0(x_0, y_0, z_0)$ is the intersection of the cylinder axis and the spherical surface, $p_1(x_1, y_1, z_1)$ is an arbitrary point in the direction of the cylinder axis, K is the equivalent rotation axis, and θ is the rotation angle around the equivalent axis[5].

3.1 ***x_s , y_s , z_s and x_s' , y_s' , z_s' coordinate system conversion matrix A_s***

The transformation matrix A_s consists of a rotation matrix R_s and a translation matrix T_s , which can be obtained from Figure 3.

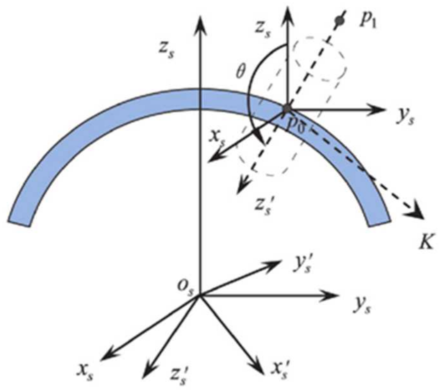

Figure.3. Schematic diagram of the intersection of the spherical surface and the cylinder surface

Here, the rotation matrix R_s is obtained by the equivalent axis angle transformation representation. It can be seen from the robot coordinate system transformation that the two coordinate systems can be obtained by rotating a certain angle around an Euler axis. For the convenience of calculation, the coordinate system origin o_s is translated to the p_0 point, and the equivalent rotation axis K is perpendicular to the z_s and z_s' axes, so that the angle between the z_s and the z_s' axis is the equivalent rotation angle θ [6]. Since the z_s' axis coincides with the axis of the cutting cylinder, in the x_s , y_s , z_s coordinate system, the z_s' vector can be expressed as:

$$z_s' = \begin{bmatrix} v_x & v_y & v_z \end{bmatrix}^T = \begin{bmatrix} \dfrac{x_0 - x_1}{|p_1 p_2|} & \dfrac{y_0 - y_1}{|p_1 p_2|} & \dfrac{z_0 - z_1}{|p_1 p_2|} \end{bmatrix}$$

among them,

$$|p_1 p_0| = \sqrt{(x_0 - x_1)^2 + (y_0 - y_1)^2 + (z_0 - z_1)^2}$$

take the z_s axis vector as $\begin{bmatrix} 0 & 0 & 1 \end{bmatrix}^T$, then $K(k_x, k_y, k_z)$ is:

$$K = z_s \times z_s' = \begin{bmatrix} -v_y & v_x & 0 \end{bmatrix}^T$$

further can get its standard form:

$$K=\left[-\frac{v_y}{\sqrt{v_x^2+v_y^2}} \quad \frac{v_x}{\sqrt{v_x^2+v_y^2}} \quad 0\right]$$

obviously, $\cos\theta = v_z$. Therefore, the rotation matrix R_s can be obtained:

$$R_s = Rot(K,\theta) =$$

$$\begin{bmatrix} k_x k_y v\theta + c\theta & k_x k_y v\theta - k_z s\theta & k_x k_z v\theta + k_y s\theta \\ k_x k_z v\theta + k_z s\theta & k_y k_y v\theta + c\theta & k_y k_z v\theta - k_x s\theta \\ k_x k_z v\theta - k_y s\theta & k_y k_z v\theta + k_x s\theta & k_z k_z v\theta + c\theta \end{bmatrix}$$

in the formula, $v\theta = 1-\cos\theta$,

$\sin\theta = \sqrt{1-\cos\theta^2}$. Thus obtains the pose transformation matrix A_s :

$$A_s = \begin{bmatrix} R_s & T_s \\ 0 & 1 \end{bmatrix} \qquad (3)$$

3.2 *Coordinate system* x_s' , y_s' , z_s' *lower cylinder and sphere intersecting line equation*

In the x_s', y_s', z_s' coordinate system, the z_s' axis coincides with the cylinder axis, and the intersection of the sphere and the cylinder becomes orthogonal. As shown in Fig. 4, the projection of the cylinder in the x_s' , y_s' plane is a circle. Among them, $p_0' = (x_0', y_0', z_0')$ is the intersection of the cylinder axis and the spherical surface, and the radius of the sphere is R , and the radius of the cylinder is r [7].

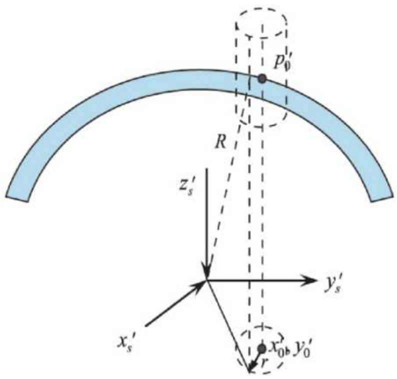

Figure.4. Schematic diagram of spherical intersection in the x_s' , y_s' , z_s' coordinate system

According to the conversion relationship between the x_s , y_s , z_s and x_s' , y_s' , z_s' coordinate systems, p_0' can be obtained in the x_s', y_s', z_s' coordinate system：

$$(x_0', y_0', z_0', 1)^T = A_s^{-1}(x_0, y_0, z_0, 1)^T \qquad (4)$$

According to Figure 5, the equation of the sphere can be obtained：

$$x_s'^2 + y_s'^2 + z_s'^2 = R^2 \qquad (5)$$

At the same time, the geometric equation of the cylinder can be obtained：

$$(x_s' - x_0')^2 + (y_s' - y_0')^2 = r^2 \qquad (6)$$

According to equations (5) and (6), the intersection line data of the sphere and the cylinder can be obtained. To solve the above equations, the value of z_s' must be known, and x_s' and y_s' respectively have two sets of values, which are solved. select. Therefore, the geometric projection method is used here to
olve. In Figure 5, the cylinder is projected on the x_s' , y_s' plane. Consider the value of the entire intersecting line[8]. Here, for equation (6), take:

$$x_s' = x_0' + r\cos\alpha$$

$$y_s' = y_0' + r\cos\alpha \qquad (7)$$

Among them, $\alpha \in (0°,360°)$, so you can get:

$$z_s' = -\sqrt{R^2 - x_s'^2 - y_s'^2} \qquad (8)$$

3.3 *Coordinate line position of the cylinder and the sphere under the coordinate system* x_s, y_s, z_s

After obtaining the data (x_p', y_p', z_p') of the intersecting line in the x_s' , y_s' , z_s' coordinate system, according to the conversion relationship between the x_s , y_s , z_s and the x_s' , y_s' , z_s' coordinate system, (x_p, y_p, z_p) of the (x_p', y_p', z_p') data in the x_s, y_s, z_s coordinate system can be obtained:

$$(x_p, y_p, z_p, 1)^T = A_s(x_p', y_p', z_p', 1)^T \qquad (9)$$

3.4 *Intersecting line cutting posture under coordinate system* x_s, y_s, z_s

When the robot performs a cylindrical cut on the spherical surface, the cutting tool space vector is the axis of the cylinder and remains unchanged. Therefore, the robot end tool coordinate system can be regarded as rotaing α degree around the z_s' axis, so that the attitude transformation matrix of the intersecting line equation in the x_s', y_s', z_s' coordinate system can be obtained:

$$R_y = Rot(z,a) = \begin{bmatrix} \cos\alpha & -\sin\alpha & 0 \\ \sin\alpha & \cos\alpha & 0 \\ 0 & 0 & 1 \end{bmatrix}$$

$$,\alpha \in (0°,360°) \qquad (10)$$

Thus, according to the conversion relationship between the x_s , y_s , z_s and x_s' , y_s' , z_s' coordinate systems, the posture of the cutting tool in the x_s , y_s , z_s coordinate system can be obtained:

$$R_p = R_s R_y \qquad (11)$$

3.5 *Robot intersection line cutting position and attitude calculation*

$$A_t = A_t \begin{bmatrix} R_p & P_p \\ 0 & 1 \end{bmatrix} \qquad (12)$$

In the robot cutting process, firstly, the mounting position of the robot base and the ball is calibrated to obtain its position and attitude transformation matrix A_t , and the movement trajectory of the robot is:

Where R_p is the attitude matrix shown in equation , $P_p = (x_p, y_p, z_p)^T$ [9].

4. Experiment

This paper takes 5 degree of freedom cutting robot as the research object, d_1=800mm, d_5=100mm, d_6 =200mm. Take the radius of the ball R=1000mm, cutting cylinder radius r=150mm, Point p_0= (14.88, -4.83, -98.77) mm on the sphere, point p_1= (24.88, -24.83, -128.77) mm in the direction of the cylinder axis. In the robot cutting process, take the robot and sphere coordinate system conversion matrix:

$$A_t = \begin{bmatrix} 1 & 0 & 0 & 500 \\ 0 & 1 & 0 & 300 \\ 0 & 0 & 1 & 200 \\ 0 & 0 & 0 & 1 \end{bmatrix}$$

Note that during the cutting process, the Z-axis direction of the robot's cutting tool attitude is determined by $p_0 p_1$ and remains unchanged. The data for points p_0 and p_1 can be obtained from the CAD drawing parameters of the sphere[10].

5. Conclusion

In this paper, based on a 5-DOF cutting robot, the kinematics model of the robot is established, and the forward and inverse kinematics algorithm of the robot is given. According to the cylindrical cutting process requirement of the spherical tool at any orientation, the equivalent axis Euler transform method is used to establish the pose transformation matrix of the coordinate system and the spherical coordinate system which coincides with the axis of the cutting cylinder, and then the cylinder is solved according to the geometric projection method. The orthogonal intersecting line equation of spherical cutting is given, and the attitude planning algorithm of spherical cutting is given, so that the intersecting line model and cutting attitude of the spherical and arbitrary azimuth cylinders in the spherical coordinate system can be obtained. On this basis, based on the pose transformation matrix of the robot and the sphere, the robot's cylindrical cutting trajectory algorithm for spherical surface is designed. Finally, the simulation experiment of the cutting trajectory and the kinematics model of the robot is carried out. The experimental results verify the correctness of the spherical cutting algorithm of the cutting robot.

References

1. Liao Weidong, Li Chengneng, Wang Qiang, Liao Wei. Kinematics Modeling and Simulation of 6R Robot Tool End[J]. *Mechanical Design & Manufacturing,* 2018(09): 108-111.
2. Wang Yubao, Wang Shiyu, Li Beibei, Guo Fangda. A Time Optimal Trajectory Planning Algorithm for Industrial Robots with Improved Particle Swarm[J]. *Small Computer Systems*, 2018, 39(08): 1878-1881.
3. Zhang Yonggui, Li Hailong. Research on Trajectory Planning of Milling Robot to Remove Cracks in Forgings[J]. *Combined Machine Tool and Automatic Machining Technology,* 2018(07):1-4+9.
4. Wang Jun, Chen Zhilong, Yang Zhiyong, Qin

Zhengzheng, You Ying, Wei Qiong. Time Optimal Trajectory Planning of Industrial Robot Based on Improved DE Algorithm[J]. *Combined Machine Tool & Automated Machining Technology*, 2018(06): 42-46.

5. LIANG Zilong, DING Yufeng. A trajectory planning method for free-surface polishing robots [J/OL]. Mechanical Science and Technology: 1-7[2018-10-09].https://doi.org/10.13433/j .cnki.1003-8728.20180071.
6. Chen Xuefeng. Research on trajectory planning algorithm of palletizing robot[J]. *Control Engineering*,2018,25(05):925-929.
7. Liao Weiqiang, Zhao Changming, Ma Wenbiao, Zhang Tie. Trajectory Planning of Industrial Robots in Five-Star Welding Process[J]. *Machinery Design & Manufacture*, 2018(04):231-234.
8. LI Li, SHANG Junyun, FENG Yanli, HUA Yawen. A review of trajectory planning research for articulated industrial robots[J]. *Computer Engineering and Applications*, 2018, 54(05): 36-50.
9. FANG Jian, SONG Yu, ZHU Maofei, ZHU Dequan, LIU Yongbo, JIAO Jun. Time-optimal trajectory planning for palletizing robots[J]. *Control Engineering*, 2018, 25(01):93-99.
10. Dong Jiajia, Wang Taiyong, Dong Jingchuan, Zhang Yongbin, Tao Hao. Improved B-spline curve applied to 6R robot trajectory optimization[J]. *China Mechanical Engineering*, 2018, 29(02): 193-200.

Research on Trajectory Planning Problem of Robot in Spherical Cutting

Min Jun
School of electrical and Electronic Engineering,Shanghai Institute of technology,
No. 100, Haiquan Road, Fengxian District，Shanghai 201418,China
E-mail: 15205182192@163.com

Jiang Wenping
School of electrical and Electronic Engineering,Shanghai Institute of technology,
No. 100, Haiquan Road, Fengxian District，Shanghai 201418,China
E-mail: jiangwenping@sit.edu.cn

Zhao Huailin
School of electrical and Electronic Engineering,Shanghai Institute of technology,
No. 100, Haiquan Road, Fengxian District，Shanghai 201418,China
E-mail: zhao_huailin@yahoo.com

Abstract

For cylindrical shape cutting of spherical surface vessel a kind of 5-DOF cutting method of cylindrical shape for spherical surface is provided in this paper. Based on the kinematics model of cutting robot the mathematics relations between cutting tool cylindrical shape and spherical surface are built using Euler transformation and the intersection line model of cylindrical and spherical surface is presented. The robotic cutting trajectory is computed according to the position and attitude relation of robot and spherical sphere,and simulations and experiments of cutting trajectory for robot are provided in the end. Experiments results verified the rightness of robot kinematics and cylindrical shape cutting algorithm,and will promote the robot-is application in cutting field.

Key words: spherical surface;Kinematics;cylindrical shape;cutting;Trajectory planning;robot

1. Introduction

Metal pressure vessels are widely used in chemical, petroleum, mechanical, metallurgical, nuclear, aerospace and aerospace sectors, and are essential equipment in the production process. The can body container is generally composed of a cylinder, a spherical surface, and a head, and the cylindrical surface is usually required to be cut in the manufacturing process. At present, most of China's spherical cutting uses manual operation or CNC cutting machine. The former has the disadvantages of high labor intensity, dependence on operator experience, low precision and poor consistency. Although the latter greatly improves cutting quality and work efficiency, it still exists. Some disadvantages, such as the complicated structure of the cutting aid, the large footprint of the cutting machine, and poor cutting suitability and flexibility. Compared to CNC cutting machines, cutting aid, the large footprint of the cutting machine, and poor cutting suitability and flexibility. Compared to CNC cutting machines, cutting robots offer greater flexibility and adaptability[1].

At present, there are few researches on spherical cutting of robots, mainly focusing on the intersection line solving algorithm of cylinder and spherical surface. Xu Yuanlong used the analytical method to study the problem of the orthogonal intersecting line between the cylinder and the sphere. However, this algorithm is limited to the orthogonality of the cylinder and the spherical surface. It can not solve the intersection of the cylinder and the spherical surface in any direction, and lacks versatility. At present, the algorithm for solving the intersecting line between the cylinder and the spherical surface is more focused on mathematical theory. The algorithm is more complicated and is not suitable for the engineering application of the cutting robot. Therefore, based on a 5-DOF robot, this paper proposes a cylindrical cutting scheme for the spherical surface of the robot. Based on the kinematics model of the robot, the cutting trajectory planning algorithm for the spherical surface and the arbitrary position and direction cylinder is designed, and the robot The cutting algorithm has been simulated and can be adapted to practical engineering applications[2].

2. Cutting robot motion model

The research object of this paper is a 5-DOF robot, which adopts Cartesian coordinates. The robot with this structure has the characteristics of good rigidity, high precision and low cost. Among them, the first joint is a moving joint along the X axis, the second joint is a moving joint along the Y axis, the third joint is a moving joint along the Z axis, the fourth joint is a rotating joint, and the fifth joint is a swing joint.

When the robot uses the laser cutting method to cut the spherical crown, the robot moves along the intersecting line of the cylinder and the cylinder, and the end posture is consistent with the cylinder axis, so that the straight and oblique cutting of the cylinder and the sphere can be completed. The cutting process of the robot is shown in Figure 1[3].

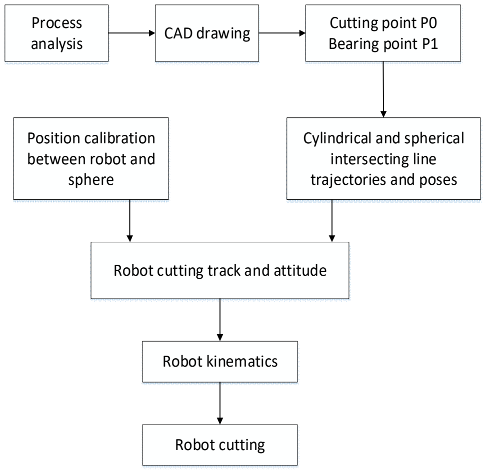

Figure.1. Schematic diagram of the robot cutting process

The structural diagram of the robot is shown in Figure 2, where X, Y, and Z are the basic coordinate systems centered on the robot base, x_1, y_1, z_1、x_2, y_2, z_2、x_3, y_3, z_3、x_4, y_4, z_4 and x_5, y_5, z_5 are the coordinate system of the cutting robot joint coordinates 1, 2, 3, 4, 5 respectively, x_1, y_1, z_1 is the robot end tool coordinate system, d_1, d_2, d_3, d_4, d_5, d_6 is the length of each rod of the robot[4].

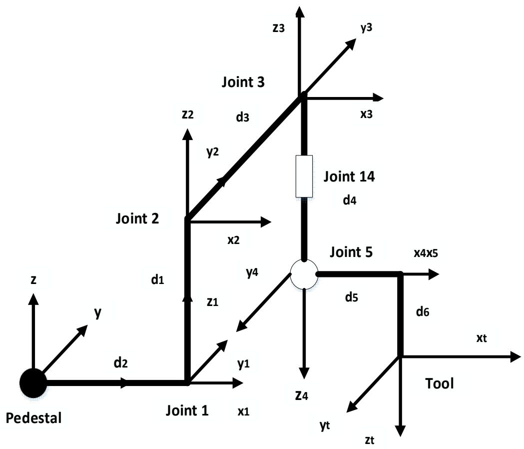

Figure.2. Schematic diagram of the robot structure

2. 1 *Robotic Kinematics*

It is assumed that the motion variables of the joints are X , Y , Z , θ_1 , and θ_2 are the motion variables of the first joint, the second joint, the third joint, the fourth joint, and the fifth joint of the robot, respectively. Obviously, $d_2 = X$, $d_3 = Y$, $d_4 = -Z$, so that the coordinate system transformation matrix of adjacent joints can be obtained.

$$^{0}T_1 = Trans(X,0,0)$$

$$^{1}T_2 = Trans(0,0,d_1)$$

$$^{2}T_3 = Trans(0,Y,0)$$

$$^{3}T_4 = Rot(x,180)Tran(0,0,-Z)Rot(z,\theta_1)$$

$$^{4}T_5 = Rot(x,90)Rot(z,\theta_2)$$

$$^{5}T_t = Rot(x,-90)Tran(d_5,0,0)Trans(0,0,d_6)$$

Thus, the pose matrix of the robot end cutting tool in the basic coordinate system can be obtained,just like formula (1).

$$T={}^{0}T_1{}^{1}T_2{}^{2}T_3{}^{3}T_4{}^{4}T_5{}^{5}T_t=$$

$$\begin{bmatrix} c\theta_1 c\theta_2 & -s\theta_1 & -c\theta_1 s\theta_2 & c\theta_1 c\theta_2 d_5 - c\theta_1 s\theta_2 d_6 + X \\ -s\theta_1 c\theta_2 & -c\theta_1 & s\theta_1 s\theta_2 & -s\theta_1 c\theta_2 d_5 + s\theta_1 s\theta_2 d_6 + Y \\ -s\theta_2 & 0 & -c\theta_2 & -s\theta_2 d_5 - c\theta_2 d_6 - Z + d_1 \\ 0 & 0 & 0 & 1 \end{bmatrix}$$

(1)

2. 2 ***Robot inverse kinematics***

Assume that the end pose matrix of a 5-DOF robot is:

$$P=\begin{bmatrix} n_x & o_x & a_x & p_x \\ n_y & o_y & a_y & p_y \\ n_z & o_z & a_z & p_z \\ 0 & 0 & 0 & 1 \end{bmatrix} \quad (2)$$

According to equations (1) and (2), the inverse solution of the robot can be obtained according to the principle that the corresponding elements of the matrix are equal:

$$\theta_1 = \arctan 2(-o_x, -o_y)$$

$$\theta_2 = \arctan 2(-n_z, -a_z)$$

$$X = p_x - \cos\theta_1 \cos\theta_2 d_5 + \cos\theta_1 \sin\theta_2 d_6$$

$$Y = p_y + \sin\theta_1 \cos\theta_2 d_5 - \sin\theta_1 \sin\theta_2 d_6$$

$$Z = d_1 - p_z - \sin\theta_2 d_5 - \cos\theta_2 d_6$$

3. Rrobot cutting algorithm

The intersection of the sphere and the arbitrary orientation cylinder is shown in Figure 4. Among them, x_s , y_s , z_s is the spherical coordinate system with the spherical center as the origin, x_s' , y_s' , z_s' is the coordinate system with the spherical center as the origin, and the z_s' axis coincides with the axis of the cutting cylinder. x_s' , y_s' are respectively x_s , y_s Rotated around the Euler axis. $p_0(x_0, y_0, z_0)$ is the intersection of the cylinder axis and the spherical surface, $p_1(x_1, y_1, z_1)$ is an arbitrary point in the direction of the cylinder axis, K is the equivalent rotation axis, and θ is the rotation angle around the equivalent axis[5].

3.1 x_s **,** y_s **,** z_s ***and*** x_s' **,** y_s' **,** z_s' ***coordinate system conversion matrix*** A_s

The transformation matrix A_s consists of a rotation matrix R_s and a translation matrix T_s , which can be obtained from Figure 3.

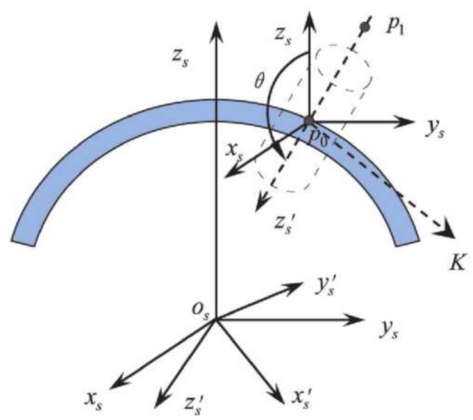

Figure.3. Schematic diagram of the intersection of the spherical surface and the cylinder surface

Here, the rotation matrix R_s is obtained by the equivalent axis angle transformation representation. It can be seen from the robot coordinate system transformation that the two coordinate systems can be obtained by rotating a certain angle around an Euler axis. For the convenience of calculation, the coordinate system origin o_s is translated to the p_0 point, and the equivalent rotation axis K is perpendicular to the z_s and z_s' axes, so that the angle between the z_s and the z_s' axis is the equivalent rotation angle θ[6].

Since the z_s' axis coincides with the axis of the cutting cylinder, in the x_s , y_s , z_s coordinate system, the z_s' vector can be expressed as:

$$z_s{}' = [v_x \quad v_y \quad v_z]^T = \begin{bmatrix} \frac{x_0 - x_1}{|p_1p_2|} & \frac{y_0 - y_1}{|p_1p_2|} & \frac{z_0 - z_1}{|p_1p_2|} \end{bmatrix}$$

among them,

$$|p_1p_0| = \sqrt{(x_0 - x_1)^2 + (y_0 - y_1)^2 + (z_0 - z_1)^2}$$

take the z_s axis vector as $[0 \quad 0 \quad 1]^T$, then $K(k_x, k_y, k_z)$ is:

$$K = z_s \times z_s' = [-v_y \quad v_x \quad 0]^T$$

further can get its standard form:

$$K = \begin{bmatrix} -\frac{v_y}{\sqrt{v_x^2 + v_y^2}} & \frac{v_x}{\sqrt{v_x^2 + v_y^2}} & 0 \end{bmatrix}$$

obviously, $\cos\theta = v_z$. Therefore, the rotation matrix R_s can be obtained:

$$R_s = Rot(K, \theta) =$$
$$\begin{bmatrix} k_xk_yv\theta + c\theta & k_xk_yv\theta - k_zs\theta & k_xk_zv\theta + k_ys\theta \\ k_xk_zv\theta + k_zs\theta & k_yk_yv\theta + c\theta & k_yk_zv\theta - k_xs\theta \\ k_xk_zv\theta - k_ys\theta & k_yk_zv\theta + k_xs\theta & k_zk_zv\theta + c\theta \end{bmatrix}$$

in the formula, $v\theta = 1 - \cos\theta$, $\sin\theta = \sqrt{1 - \cos\theta^2}$. Thus obtains the pose transformation matrix A_s:

$$A_s = \begin{bmatrix} R_s & T_s \\ 0 & 1 \end{bmatrix} \qquad (3)$$

3.2 *Coordinate system x_s', y_s', z_s' lower cylinder and sphere intersecting line equation*

In the x_s', y_s', z_s' coordinate system, the z_s' axis coincides with the cylinder axis, and the intersection of the sphere and the cylinder becomes orthogonal. As shown in Fig. 4, the projection of the cylinder in the x_s', y_s' plane is a circle. Among them, $p_0' = (x_0', y_0', z_0')$ is the intersection of the cylinder axis and the spherical surface, and the radius of the sphere is R, and the radius of the cylinder is r [7].

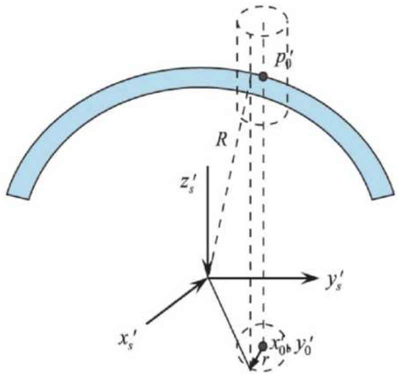

Figure.4. Schematic diagram of spherical intersection in the x_s', y_s', z_s' coordinate system

According to the conversion relationship between the x_s, y_s, z_s and x_s', y_s', z_s' coordinate systems, p_0' can be obtained in the x_s', y_s', z_s' coordinate system:

$$(x_0', y_0', z_0', 1)^T = A_s^{-1}(x_0, y_0, z_0, 1)^T \qquad (4)$$

According to Figure 5, the equation of the sphere can be obtained:

$$x_s'^2 + y_s'^2 + z_s'^2 = R^2 \qquad (5)$$

At the same time, the geometric equation of the cylinder can be obtained:

$$(x_s' - x_0')^2 + (y_s' - y_0')^2 = r^2 \qquad (6)$$

According to equations (5) and (6), the intersection line data of the sphere and the cylinder can be obtained. To solve the above equations, the value of z_s' must be known, and x_s' and y_s' respectively have two sets of values, which are solved. select. Therefore, the geometric projection method is used here to solve. In Figure 5, the cylinder is projected on the x_s', y_s' plane. Consider the value of the entire intersecting line[8]. Here, for equation (6), take:

$$x_s' = x_0' + r\cos\alpha$$
$$y_s' = y_0' + r\cos\alpha \qquad (7)$$

Among them, $\alpha \in (0°, 360°)$, so you can get:

$$z_s' = -\sqrt{R^2 - x_s'^2 - y_s'^2} \qquad (8)$$

3.3 *Coordinate line position of the cylinder and the sphere under the coordinate system x_s, y_s, z_s*

After obtaining the data (x_p', y_p', z_p') of the intersecting line in the x_s', y_s', z_s' coordinate system, according to the conversion relationship between the x_s, y_s, z_s and the x_s', y_s', z_s' coordinate system, (x_p, y_p, z_p) of the (x_p', y_p', z_p') data in the x_s, y_s, z_s coordinate system can be obtained:

$$(x_p, y_p, z_p, 1)^T = A_s(x_p', y_p', z_p', 1)^T \quad (9)$$

3.4 *Intersecting line cutting posture under coordinate system* x_s, y_s, z_s

When the robot performs a cylindrical cut on the spherical surface, the cutting tool space vector is the axis of the cylinder and remains unchanged. Therefore, the robot end tool coordinate system can be regarded as rotaing α degree around the z_s' axis, so that the attitude transformation matrix of the intersecting line equation in the x_s', y_s', z_s' coordinate system can be obtained:

$$R_y = Rot(z,a) = \begin{bmatrix} \cos\alpha & -\sin\alpha & 0 \\ \sin\alpha & \cos\alpha & 0 \\ 0 & 0 & 1 \end{bmatrix}$$

$$,\alpha \in (0°, 360°) \quad (10)$$

Thus, according to the conversion relationship between the x_s, y_s, z_s and x_s', y_s', z_s' coordinate systems, the posture of the cutting tool in the x_s, y_s, z_s coordinate system can be obtained:

$$R_p = R_s R_y \quad (11)$$

3.5 *Robot intersection line cutting position and attitude calculation*

In the robot cutting process, firstly, the mounting position of the robot base and the ball is calibrated to obtain its position and attitude transformation matrix A_t, and the movement trajectory of the robot is:

$$A_r = A_t \begin{bmatrix} R_p & P_p \\ 0 & 1 \end{bmatrix} \quad (12)$$

Where R_p is the attitude matrix shown in equation, $P_p = (x_p, y_p, z_p)^T$ [9].

4. Experiment

This paper takes 5 degree of freedom cutting robot as the research object, d_1=800mm, d_5 =100mm, d_6=200mm. Take the radius of the ball R=1000mm, cutting cylinder radius r=150mm, Point p_0 = (14.88, -4.83, -98.77) mm on the sphere, point p_1 = (24.88, -24.83, -128.77) mm in the direction of the cylinder axis. In the robot cutting process, take the robot and sphere coordinate system conversion matrix:

$$A_t = \begin{bmatrix} 1 & 0 & 0 & 500 \\ 0 & 1 & 0 & 300 \\ 0 & 0 & 1 & 200 \\ 0 & 0 & 0 & 1 \end{bmatrix}$$

Note that during the cutting process, the Z-axis direction of the robot's cutting tool attitude is determined by $p_0 p_1$ and remains unchanged. The data for points p_0 and p_1 can be obtained from the CAD drawing parameters of the sphere[10].

5. Conclusion

In this paper, based on a 5-DOF cutting robot, the kinematics model of the robot is established, and the forward and inverse kinematics algorithm of the robot is given. According to the cylindrical cutting process requirement of the spherical tool at any orientation, the equivalent axis Euler transform method is used to establish the pose transformation matrix of the coordinate system and the spherical coordinate system which coincides with the axis of the cutting cylinder, and then the cylinder is solved according to the geometric projection method. The orthogonal intersecting line equation of spherical cutting is given, and the attitude planning algorithm of spherical cutting is given, so that the intersecting line model and cutting attitude of the spherical and arbitrary azimuth cylinders in the spherical coordinate system can be obtained. On this basis, based on the pose transformation matrix of the robot and the sphere, the robot's cylindrical cutting trajectory algorithm for spherical surface is designed. Finally, the simulation experiment of the cutting trajectory and the kinematics model of the robot is carried out. The experimental results verify the correctness of the spherical cutting algorithm of the cutting robot.

References

1. Liao Weidong, Li Chengneng, Wang Qiang, Liao Wei. Kinematics Modeling and Simulation of 6R

Robot Tool End[J]. *Mechanical Design & Manufacturing*, 2018(09): 108-111.

2. Wang Yubao, Wang Shiyu, Li Beibei, Guo Fangda. A Time Optimal Trajectory Planning Algorithm for Industrial Robots with Improved Particle Swarm[J]. *Small Computer Systems*, 2018, 39(08): 1878-1881.
3. Zhang Yonggui, Li Hailong. Research on Trajectory Planning of Milling Robot to Remove Cracks in Forgings[J]. *Combined Machine Tool and Automatic Machining Technology*, 2018(07):1-4+9.
4. Wang Jun, Chen Zhilong, Yang Zhiyong, Qin Zhengzheng, You Ying, Wei Qiong. Time Optimal Trajectory Planning of Industrial Robot Based on Improved DE Algorithm[J]. *Combined Machine Tool & Automated Machining Technology*, 2018(06): 42- 46.
5. LIANG Zilong, DING Yufeng. A trajectory planning method for free-surface polishing robots [J/OL]. Mechanical Science and Technology: 1-7[2018-10-09].https://doi.org/10.13433/j .cnki.10 03-8728.20180071.
6. Chen Xuefeng. Research on trajectory planning algorithm of palletizing robot[J].*Control Engineering*,2018,25(05):925-929.
7. Liao Weiqiang, Zhao Changming, Ma Wenbiao, Zhang Tie. Trajectory Planning of Industrial Robots in Five-Star Welding Process[J].*Machinery Design & Manufacture*, 2018(04):231-234.
8. LI Li, SHANG Junyun, FENG Yanli, HUA Yawen. A review of trajectory planning research for articulated industrial robots[J]. *Computer Engineering and Applications*, 2018, 54(05): 36-50.
9. FANG Jian, SONG Yu, ZHU Maofei, ZHU Dequan, LIU Yongbo, JIAO Jun. Time-optimal trajectory planning for palletizing robots[J].*Control Engineering*,2018,25(01):93-99.
10. Dong Jiajia, Wang Taiyong, Dong Jingchuan, Zhang Yongbin, Tao Hao. Improved B-spline curve applied to 6R robot trajectory optimization[J]. *China Mechanical Engineering*, 2018, 29(02): 193-200.

Emotional prosody processing between artificial voices and human voices

Qiang Wei[1*], Xiaoyu Zhang[1], Xiao Yang[1], Yixin Lin[2], Qingming Liu[3]

[1] *School of Education, Jianghan University, China;*

[2] *School of Energy and Power Engineering, Huazhong University of Science and Technology, China；*

[3] *Wuhan Rayson School, China*
*E-mail: * weiqiang@jhun.edu.cn*

Abstract

To evaluate the time course of changes in emotional prosody processing between artificial voices and human voices (happy, neutral), the present study examined behavior experience and event related potential component. The emotion of artificial human voice and brain signal were evaluated while the presentation of audio from each conditions (happy-natural, neutral-natural, and synthetic speech). The results showed that there were differences in the time-course distribution of P800 and the intensity of amplitude between emotional prosody processing induced by artificial voices and human voices.

Keywords: P800, artificial voice, synthetic speeches, human voice, emotional prosody processing, event related potential

1. Introduction

Human emotional voice materials are generally divided into three categories: natural speech, performance speech and induced speech. Natural speech refers to the natural expression of the speaker's emotions in real situations. Compared with the latter, the emotional information of natural speech is real and direct. Researchers generally use the speaker's speech to simulate the pronunciation of a specific emotional state in the laboratory as the natural voice material[1].

Speech Interface (SPIN) is also expected to have the function of transmitting emotional information. There are two forms of speech interface, one is real recording, the other is synthetic speech that is kind of artificial voice. Synthetic speech refers to the use of human vocal channel sound mechanism, resonance frequency or the resonance peak produced by the "voice" to simulate the human pronunciation of the speech. Compared with the real recording, the synthetic speech generated by the text-to-speech technology has the advantages of less resource consumption, flexibility, objective reality and so on[2]. In order to bring users a more real and effective interactive experience, the developers of synthetic speech and researchers are devoted to the study of the relationship between emotion, natural voice and artificial voice.

There are many factors would affect the emotional information in speech, such as volume, pause, syntax and so on. Among them, it is generally considered that one of the most influential factors is prosody[3]. The semantic is related to the content, grammar and context of the sentence itself, and often has an impact on the prosody[4]. In order to exclude the semantic influence, this study chooses those speech materials which have the same grammar and have no semantic tendency in their own content.

At present, many of the methods to evaluate the emotional information in synthetic speech are often compare the synthetic speech build by new technology with the real recording models, using EMOS, for example. But there is little evaluation based on cognition processing of the consumers, users of SPIN or audiences.

In this study, we analyzed the EEG recorded during listening to natural and artificial speech materials, in order to understand the differences in the processing of natural speech and synthetic speech. Furthermore, it provides a standard for evaluating the emotional information of synthetic speech and promotes the development of affective artificial voice.

2. Experiment

2.1. Stimuli

Total 150 sentences were on the same syntactic pattern (subject + predicate + object). Every single sentence was moderated in length (6 ± 1 Chinese characters) and without semantic orientation in emotion.

The natural voice is 100 speeches chose from CHEAVD (Chinese natural emotional audio-visual database) developed by the Institute of Automation of the Chinese Academy of Sciences. Half of the speeches were labeled as happy, and others were neutral.

The artificial voices were 50 synthetic speeches build by text-to-speech conversion software. After denoise methods, the total speeches (128bps) had same decibel quantity.

To verify the validity of speeches of natural voice classification, 35 students without dysaudia participated in evaluation test. Participants were required to score the emotion in speeches when the 150 speeches were random broadcasted, using the 7-point Likert scale. 33 data sets were tested by One-way ANOVA. The result shows significant difference between Happy-natural speech and Neutral-natural speech ($p=0.032<.05$), Happy-natural speech and Synthetic speech ($p=0.027<.05$). But Synthetic speech wasn't different from Neutral-natural speech. ($p=0.827>.05$).

2.2. Participants

29 right-handed undergraduate students were participated the experiment. After data analysis, there are still data of 19 participants (10 male, 9 female; average age 19.9 years) can be used.

2.3. Procedure and data acquisition

Using Stereo speakers, participants were presented aurally with speeches in three conditions (happy-natural, neutral-natural and synthetic). The 150 speeches were divided into three blocks of 50 trials in random order.

Participants were required to score every speech after of which presentation was finished by pressing numeric key (1 (very angry), 2 (angry), 3 (neutral mood), 4 (happy), 5 (very happy)) with right hand.

The EEG was recorded from 64 scalp electrodes located at standard International 10/20 system by Brain Amp (Brain Products, Germany) for 2200ms/trial (500 Hz sampling rate; 0.05-100 Hz band-pass), and was re-referenced by FCz. EEG recording started 200ms before the presentation of first word in speeches. The impedances were below 5kΩ. And the positions of electrodes were located by the left and right mastoids. The vertical and horizontal electrooculograms (IO) were recorded to exclude the amplifier saturation, ocular artifacts, and movement artifacts from averaged ERP of trials.

2.4. Data analyses

The Independent Component Analysis (ICA) was applied and returned the artifacts induced by eye-blinks and muscular movement. Averaging the EEG amplitude that responded correctly by participants in different three conditions (happy-natural, neutral-natural, and synthetic speech).

Descriptive statistics was applied to five point scales. According to the averaged ERPs, the research picked following electrodes: FCz, FZ, Cz, F3, F4, FC1 and FC2 as one of the within-subject factors, and the time point of the vertex between 400-1000ms as independent variable.

Than Root Mean Square (RMS) of voltage value at the sampling time points (400-1000ms) recorded from the seven electrodes (FCz, FZ, Cz, F3, F4, FC1 and FC2) was computed in three conditions (happy-natural, neutral-natural, and synthetic speech). After averaging the RMS of electrodes, a repeated measures ANOVA was performed to compare the averaged RMSs in three conditions.

3. Results

3.1. Behavioral data

The descriptive statistics was applied to present the mean and standard deviation (SD) of the emotion evaluation collected from participants in three conditions (happy-natural, neutral-natural, and synthetic speech). The descriptive statistics is shown in Table 1.

	score
Happy-natural	3.94±0.57
Neutral-natural	2.97±0.33
Synthetic	2.98±0.14

Table 1 descriptive statistics of the emotion evaluation

3.2. Electrophysiological results

Starting from the first word onset, ERPs had covered all emotional processing. Averaging the ERP trace in three conditions (happy-natural, neutral-natural, and synthetic speech), from which the emotion processing between different conditions had time course difference (see Fig.2).

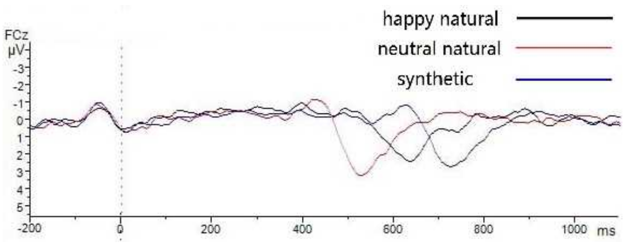

Fig. 2 the averaged ERPs in tree conditions of a typical electrode

3.2.1. Time-related characteristics of vertex

There is a positive amplitude peak presenting between 400-1000 ms in three conditions. The time point of vertex between 400-1000 ms from the electrodes (FCz, Fz, Cz, F3, F4, FC1 and FC2) of 15 participants in three conditions (happy-natural, neutral-natural, and synthetic speech) was computed as independent variable. Two factors repeated measures ANOVA taking conditions and electrodes as repeated measures were applied to verify the interaction and significant effects.

No interaction effect between conditions and electrodes (F(12,7)=.83; p=.63＞05). The main effect of electrodes wasn't significant (F(6,13)=1.38; p=.29＞.05). But the main effect of three conditions (happy-natural, neutral-natural, and synthetic speech) is significant (F(2,17)=52.70; p=.00<.05), and the results of paired comparison for three conditions was shown in following Table (see Table 3).

	Mean	SD	p
Happy -Neutral	49.13	5.90	.00*
Synthetic–Happy	30.61	6.12	.00*
Synthetic–Neutral	79.74	7.75	.00*

Table 3 main effect of three conditions

3.2.2. RMS analysis

The results showed that the time-course differences also presented in averaged RMSs of voltage value in three conditions (see Fig.4). Comparing the RMSs through one-way repeated ANOVA, the significant difference existed in three conditions (F(1,15)=28.95, p<0.05).

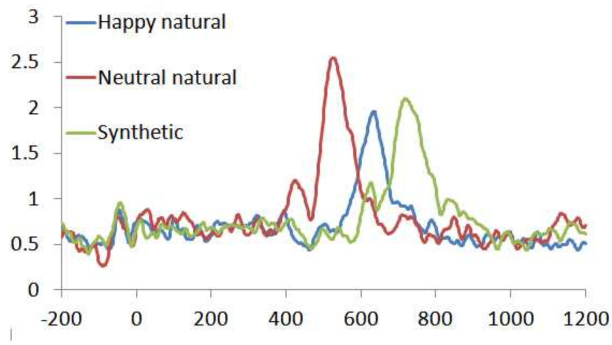

Fig .4 averaged RMS in three conditions

4. Discussion

The results showed that there were differences in the intensity and the late processing between cognitive processing induced by artificial voices and human voices, which provided the proof that the ERPs can be used to evaluate the emotion information included by the prosody of synthetic speech.

4.1. Comparison between behavioral and electrophysiological results

The results of five point scale for emotional evaluation showed that the self-report can distinguish the neutral speech from happy speech, but can't tell the differences between emotional information communicated by neutral natural speech and synthetic speech. ERP covered the shortage of behavioral evaluation by a different time distribution of positive amplitude peak in which the vertex of neutral natural speech was closer to the onset than synthetic speech.

The comparison proved the rationality of the classification that affective synthetic speech can be divided into emotional speech and neutral speech.

4.2. Positive amplitude peak presenting between 400-1000ms

Electrophysiological results demonstrated that positive amplitude peak presenting between 400-1000ms had made the time-course difference in three conditions (happy-natural, neutral-natural, and synthetic speech) significant. To better understand the function of the positive amplitude peak during emotion processing, we compared the component with other typical positive component related to emotion and language processing.

Because of the experimental paradigm that the onset was the beginning of the first word in each sentence and participants should react after the end of whole sentence, it is hard to judge the exact time position of positive amplitude peak presenting between 400-1000ms. So first at all, we take it as P600, a ERP component elicited by syntactic errors, which didn't square with the fact that the syntactic factor was controlled[4.5.6].

Closure Positive Shift (CPS), a late positive component was taken into consideration, who is related to the prosodic boundary showing in long sentence with complexity of syntactic. And it also was usually founded in the interaction of syntactic and prosodic in sentence comprehension. Comparing with the CPS, the positive amplitude peak in our research was founded in sentence with the same simple structure (subject + predicate + object), hardly needed using prosodic boundary[4.5.6].

P800 is an important signal of prosodic processing, founded in cross-splicing paradigm of semantically incongruous and prosodically incongruous. But it can only be induced in the situation where the participants were required to pay attention to prosodic of sentences. Some of the researchers take it as a component that is a real-time conversion from neutral to emotional stimulation[4]. But it was also founded in the incongruous of modality prosody (assertion- question)[7].

Controlling the syntactic and structure of sentence, our research asked participants focused on the emotion information conveyed by speech, which may lead to the attention of participants paid on intonation that is a main communicated way for prosody. So the positive amplitude peak can be P800 the component demonstrated the attention processing of prosodic, emotional prosodic especially.

It would be doubt that P800 who is a late positive component didn't show at 800ms in our research. However, considering the difference of paradigm that our participants were asked to focused on the emotion of whole sentence while the participants of other research reacted in the middle of material presentation, it is reasonable there was a hurry presentation of peak.

The time-course difference of P800 distribution in three conditions suggested that:

The synthetic speech had deficiency of emotional prosody, which didn't trigger the attention of emotional prosody earlier than natural voice. And there may was a negative correlation between task difficulty of attention and the presented time of P800, because the P800 in neutral-natural speech condition showed earlier than happy-natural speech.

4.3. RMS reflexed the intensity of attention

While P800 component demonstrated the attention processing of emotional prosody, the RMS difference may show the intensity difference of attention triggered by processing of emotional prosody. The RMS differences were significant which proved that ERP can be used to evaluate the synthetic speech.

5. Conclusion

The results of present study suggested a new way using ERP to evaluate the emotion information included by voice, especially the intonation difference induced by emotional prosody in speech. In this way, the synthetic speech can be tested by audiences and users of speech interface. P800 can be a successful standard to classify emotional prosody.

References

1. Xiao Yang. ERP study on the difference of emotion perception induced by natural voice and artificial voice [J]. *Journal of Wuhan Vocational and Technical College*, 2017, 16(5):84-90.
2. Jianxiong Chen, Youhong Jian, Shimiao Wang, *a study on emotion conveyed in synthesized voice* (Shandong, Shandong University of Science and Technology, 2007)
3. Zhuangluan Su. Affective Speech Synthesis[D]. *University of Science and Technology of China*, 2006: P19-P25.
4. Aish Chen, Xuhai Chen, Yufang Yang. The Time Course of Verbal Emotional Prosody *Processing[J]. Progress in Psychological Science*, 2009, 17(6):1109-1115.
5. Ze Yu, Guiqin Ren. Overview on ERP Research of Prosody Processing[J]. *Journal of Liaoning Normal University (Social Science Edition)*, 2012, 35(2):201-205.
6. Xuhai Chen, Xiaohong Yang, Yufang Yang. Neurophysiological Mechanism of Implicit Processing of Vocal Emotion Transition [J]. *Acta Psychologica Sinica*, 2013, 45(4):416-426.

7. Corine Astésano, Besson M , Alter K . Brain potentials during semantic and prosodic processing in French[J]. *Cognitive Brain Research*, 2004, 18(2):172-184.
8. Pihan, H. Cortical activation patterns of affective speech processing depend on concurrent demands on the subvocal rehearsal system A DC-potential study[J]. *Brain*, 2000, 123(11):2338-2349.
9. Dutoit T . *An Introduction to Text-to-Speech Synthesis*[M]. Kluwer Academic Publishers, 2001.

How people are affected by emoticons: An ERP study

Qiang Wei[1]*, Jingxuan Huang[1], Yu Han[1], Yixin Lin[2]

([1] School of Education, Jianghan University, China
[2] School of Energy and Power Engineering, Huazhong University of Science and Technology, China)
**weiqiang@jhun.edu.cn*

Abstract

The aim of this study was to investigate the ERP component evoked by emoticons with different attributes and the reaction times during the LDT. The behavioral results demonstrated the significant promoting effect of emoticon for language processing with shorter reaction time under both a positive emoticon and a negative emoticon compared to participants under a nonsense emoticon. The greater amplitude on N170, P300 provided more evidence for the promoting effect of emoticons.

Keywords: emoticon, Lexical decision task, ERP, language processing

1. Introduction

Emotion is an essential project in psychological research. It is generally considered to be the subjectively experienced and conscious mental reaction of individuals to the relationship between external events and internal needs which usually directed toward a specific object and typically accompanied by psychological and behavioral changes in the body.[1]Furthermore, in the field of Man-machine dialog and network information mining, the emotions of network users and publishers have been trying to be predicted by researchers through several different means such as models establishment and text analysis. According to this, effects arising from emotion-related information in the network gain more and more interests.

Emoticons, as a new kind of emotion-related text punctuation, became increasingly popular and were commonly used on internet forums with the development and widespread of internet. Different from stylized pictures (such as Emoji, QQ face) , emoticons are consist of characters including punctuation marks, numbers and letters to express a person's feelings or mood. This resulted in that emoticon combined advantages of stylized pictures and text messages.On the one hand, it holds a natural salience as face pictures did, which means that it is an stimulus that attracts more attention and expresses more emotion-related information than normal text stimuli[2]. On the other hand, it can be easily retrieved, summarized and analyzed within different social networks and forms.

The LDT is a common instrument to measure implicit emotional processing which commonly used in affective priming paradigms to evaluate the emotional state of subjects.Previous studies showed shorter RT of participants for emotion-related targets when compared to neutral targets.

In this study, we used the emoticons of different attributes for prime stimuli on Lexical Decision Task, in order to reveal a corresponding relationship between emoticons and behavioral results of LDT. And then, reveal the specific impact of emoticons during language processing by compare the amplitude and regions within EEG data.

2. Experiment

2.1. Participants

Seventeen right-handed healthy undergraduates (9 males and 8 females) from Jianghan University were recruited to participate in the study. All of the participants were native Chinese speakers free from any history of mental diseases or neurological disorders. Their visual acuity was normal or corrected-to- normal. Their age ranged from 18 to 22 years with mean age of 19.42 years. All participants provided written informed consent and were compensated for their participation.

2.2. Stimulus materials

The entire experiment consisted of 150 emoticons as prime stimuli and 300 words as target stimuli. The emoticons contained three conditions: 50 emoticons of positive mood (e.g., ヽ(￣▽￣)ﾉ), 50 emoticons of negative mood (e.g., (╥╯^╰╥)) and 50 random characters without any mood (e.g.,(=’+)).For the LDT a set of 300 target stimuli were used. 150 neutral words were extracted from the Modern Chinese Dictionary(e.g., “桌子(table)” “药品(medicine)”). 150 Pseudo-words were also generated out of a words listed which composed of those neutral words in this study. Here, neutral words with a length of two Chinese ideograph were manipulated by changing single Chinese ideograph with another word(e.g., “桌药”).Additionally, the selected emoticons in this study were based on the SOHO Pinyin IME 7.5.

The stimuli and recording triggers were presented using the E-prime 2.0 software package.

2.3. Procedure

The subjects were asked to sit in a sound-attenuated room 200 cm away from a computer-controlled screen, on which the stimuli were presented centrally. Before the ERP experiment formally started, they were requested to look at a fixation cross in the centre of the screen.

As shown in Fig.1, each trial began with a fixation cross against a black background for 1000 ms, followed by a black screen for 800ms.Then, a emoticon with different moods appeared for 500ms followed by a black screen for 300 ms. In this step, there is no need to do any button pressing for subjects but staring at the screen. The written stimuli was then shown, and the participants had to determine whether that written stimulus was a Real-Word or not by pressing a keypad (key “Z” for Real-words, key “X” for Pseudo-words) within 3000ms.The stimuli would then disappear as soon as the subjects pressed button. After that, a black screen appeared for 800 ms again. This experiment consisted of 300 trials and include 4 breaks after each 60 trials.

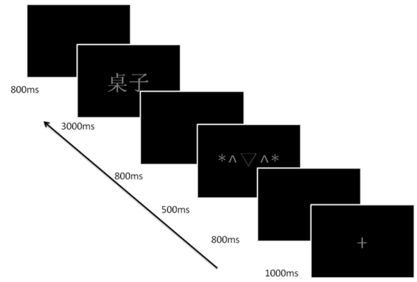

Fig.1.Experimental design

2.4. Electroencephalogram(EEG) recording and analysis

An EEG was continuously recorded for each participant during the task. The reference electrodes were placed on the left and right mastoid, whereas the ground electrode was placed on the center point between Fpz and Fz.An electrooculogram (EOG) was recorded from electrodes placed at 10 mm from the lateral canthi of right eye.Only when the electrode impedances were maintained below 5 kΩ would this experiment started. The high pass filter of the EEG signal was set to 0.5 Hz, and the low pass filter was set to 100 Hz with a sample rate of 500Hz. Data were transferred off-line and vertical electrooculogram and horizontal electrooculogram were corrected .

EEG data sets were segmented for the epoch from 200 ms before the onset of the target appearing on the video monitor to 1000 ms after the onset, with the first 200 ms pre-targets as a baseline. Trails containing amplifier clipping, bursts of electromyography activity, or peak-to-peak deflection exceeding ±50μV were excluded.

3. Results

3.1. Behavioral results of LDT

The results of 3×2 two-way ANOVA on emoticons (positive/negative/random characters) and written stimuli(real-word/pseudo-word) showed a significant main effect of the emoticons [$F(2,5) = 3.302$; $p < 0.05$]; a significant main effect of the written stimuli. The [$F(1,2) = 531.471$; $p<0.0001$]; and no significant emoticons × written stimuli interaction [$F(2,2) = 0.748$; $p>0.05$]. The results of ANOVA on emoticons revealed shorter RT for the subjects under the positive stimuli($p=0.017<0.05$) and the negative stimuli(p=0.047<0.05) compared to random character. However, there are no significant difference between the RT of the positive stimuli and the negative stimuli(p=0.56).

3.2. Electrophysiological data

There were clearly N170 component at all positions , P300 and LPP(Late Positive Potential) at centro-parietal region, N300 component at frontal region during the LDT.

According to the GFP (Global field power) curve on Figure 2, the event-related potential data at the three time windows including: 140ms-180ms, 230ms-300ms, 300ms-330ms were analyzed. The value of global field power were obtained by computing the quadratic sum of electrical activity over chosen electrodes [Centro-parietal(Cz,CP1,CP2,P3,P4);Frontal(Fp1,Fp2,Fz)] at the time windows.

A repeated measures ANOVA on mean amplitude for 140-180ms time window at centro-parietal region showed a significant greater amplitude for positive-emoticons and negative-emoticons when compared to random characters. [positive(p=0.000<0.0001), negative(p=0.000< 0.0001)]. However, there are no significant differences between the positive condition and negative condition.(p=0.115 > 0.05)

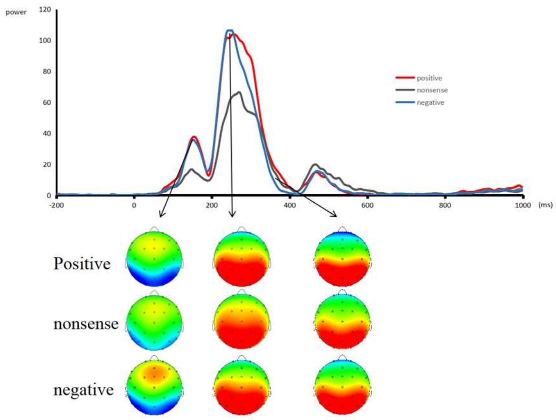

Fig.2 Global field power and amplitude topographies (Cz,Cp1,Cp2,P3,P4) for positive emoticons, nonsense emoticons and negative emoticons.

A repeated-measures ANOVA on mean amplitude for 230-300ms time window showed a significant greater amplitude for positive-emoticons than random characters[p=0.009<0.05], a significant greater amplitude for negative-emoticons than random characters(p=0.040 < 0.05) and no significant differences between the positive condition and negative condition(p=0.586 > 0.05).

Further analysis showed no significant differences between the amplitude of responses to positive-mood target, negative mood target and nonsense target in 300ms-330ms time window at frontal region.

4. Discussion

In this study, the participants browsed emoticons that expressed either the positive, negative or neural mood, and then recorded their reaction time and EEG data of lexical decision task. The behavioral results of LDT showed that the participants had a significant longer response time for nonsense target compared to emotion-related targets.

The difference of the reaction time on LDT could be further interpreted by evidences from EEG data. In the 140-180ms time window identified as N170 component, difference be detected and emotion-related target elicited significant larger amplitude responses than nonsense target, whereas the similar pattern of results was observed in the 230ms-300ms time window.

The results suggests that emotion-related target exert an influence to the visual-orthographic processing and working memory in Lexical decision task[3], which may be related to more effort have been devoted in these two processing[4]. Compared to the nonsense characters, emoticons hold more emotional information and semantic information[1], which might initiate affective priming effect or semantic priming effect.

Different emotional types showed a general consistent trend in these two part. More research is needed to further detect the relationship between emotion types and vocabulary processing.

References

1. Lane R D , Reiman E M , Bradley M M , et al. Neuroanatomical correlates of pleasant and unpleasant emotion[J]. *Neuropsychologia*, 1997, 35(11):1437-1444.
2. Wagenbreth C , Rieger J , Heinze H J , et al. Seeing emotions in the eyes – inverse priming effects induced by eyes expressing mental states[J]. *Frontiers in Psychology*, 2014, 5(3):1039.
3. L. Carretié, et al. "N300, P300 and the emotional processing of visual stimuli." *Electroencephalography and Clinical Neurophysiology* 103.2(1997):0-303
4. Van H S , Seyffarth S , Pexman P M , et al. An ERP Investigation of Vertical Reading Fluency in Scrabble(®) Experts.[J]. *Brain Research*, 2017, 1667:1-10.

Single Chinese Character fragments: An ERPs Study On Orthographic Neighborhood Effect

Qiang Wei [1*], Yunfei Wang[1], Chen Song [1], Yixin Lin[2]

[1] 1 School of Education, Jianghan University, China;

[2] School of Energy and Power Engineering, Huazhong University of Science and Technology;
*E-mail: * weiqiang@jhun.edu.cn*

Abstract

This study is aimed at discussing Orthographic Neighborhood Effect and brain activity during the processing of Chinese characters. In this experiment, event-related brain potentials (ERPs) triggered by Chinese single-word fragments in Chinese character completion and naming experiments were observed and compared. The results showed that the "multiple solutions" caused N400 to be larger than "one solution." Multiple-solution -word are analogized to large families, they are more intense than the Pseudo-words and single-words, which are in line with the interaction activation model and have more resources in the cognitive processing process. The glyph processing, the association process, and the memory phase of Chinese characters have an impact.The N400 component may not only mean the integration of the meaning of the word, but may also be related to the process of adjusting the orthographic of Chinese character fragments.

Keywords: Chinese character fragments, orthographic neighborhood effect, ERP

1. Introduction

How to input text into the computer more accurately and efficiently makes the computer able to quickly and correctly identify the input text has become an important research issue. In general, Chinese characters contain more visual information than alphabetic writing. Due to the particularity and complexity of Chinese characters, it cannot be directly and accurately recognized by computers like alphabetic writing. When there is damage or stain, it is difficult for the computer to recognize Chinese characters quickly and accurately by the current method. The recognition of words can still be improved in accuracy. On the contrary, humans tend to have higher accuracy when performing Chinese character recognition.For this reason, exploring the neuroscience mechanism of the human body in the process of Chinese character recognition may helps us to provide new ideas for the input and recognition of Chinese characters in computers.

The orthogonal neighborhood effect of words is an important evidence to support parallel processing in human Chinese character recognition mode. However, the orthographic neighborhood effect is more thoroughly studied in the phonetic alphabet, and the conclusions of the opposite are found in the existing Chinese. Therefore, the orthographic neighborhood effect of studying Chinese characters can not only be explained the cognitive processing of Chinese characters and can explore the differences between phonetic and ideograms. This study is aimed to explores the influence of the size of the orthographic neighborhood effect on the extraction of Chinese characters through the naming experiment of the residual word, and use Event-related potentials (EPRs) to explore the time course associated with glyph extraction.

2. Experiments

2.1. Subjects

17 undergraduate students (10 males, no disease, normal vision after correction, no history of physical or mental illness, all right-handed, 18 to 22 years old, with an average age of 19.11 years old 10 females participated in the experiment. They will be given some compensation after participating in the trial.

2.2. Stimulate

In this experiment, 100 words were selected from the appendix of the Modern Chinese Dictionary "7000 High Frequency Words" as materials, including Multi-words, pseudo words and single words. Multi-word means that a residual word can be complemented into multiple Chinese characters. Multi-word control position changes. A single word means that the word can only be completed as one Chinese character. Pseudo-words cannot make up for common Chinese characters but conform to Chinese characters' orthographic Chinese characters. The specific information of these materials are shown in Fig.1. There is no statistical difference between single word and multi-word, number of residual words, number of pens, and total number of pens. The residual word is produced by Microsoft's own software Educed. It is presented in the PowerPoint by Song, the 34th word is displayed in 960×720 pixels, 96dpi×96dpi, and the BMP format is exported.

Fig.1. Examples of character Stimuli

2.3. Procedure

Experimental materials were presented by E-prime 2.0 from Psychology Software Tools, Inc. There were 5 experimental groups in the experiment. Pilot study contained two types of two Chinese characters, and four formal experiments randomly appeared one of 300 three types of residual characters. Participants were asked to report their answers as soon as possible when they saw the Chinese characters displayed on the screen.

Fig.2. Experimental procedure

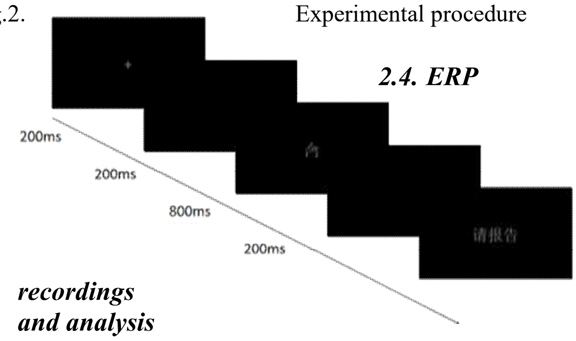

2.4. ERP recordings and analysis

EEG was recorded by the ERP recording and analysis system of Brain Products, Germany, in accordance with the 64-electrode cap of the International 10-20 system. The left and right mastoids are used as reference electrodes. When measuring, In addition, the recording of the horizontal electrocochleogram (HEOG) was recorded on the outside of the eyes, and the vertical electrocochleogram (VEOG) was recorded under the placement electrode and the right eye. The scalp resistance of each electrode was kept below 5 kΩ. The filter band passes through 0.05 to 100 Hz and the sampling frequency is 500 Hz. After continuous recording is completed, the data is processed offline, and VEOG and HEOG are automatically corrected to exclude other artifacts.

The analysis time course is 1000ms after the occurrence of the residual word, and the baseline is corrected for 200ms before the occurrence of the residual word. Data with artifacts such as blink, eye movement, and electricity were excluded, and the exclusion criterion was ±50 μV.

The total average amplitude of ERP and the difference topographic map of multi-word, pseudo-word and single-word conditions showed that there were significant differences between the left and right hemisphere midline and brain forehead conditions, and O1, C3, Cp1, Cz, Fc1, Fz, Pz and FCz performs average volatility statistics.

Three-factor GLM Repeated Measures for ERP wave-forms with SPSS 17.0 statistical software, factors including type (multi, pseud word and single), electrode position (7 electrodes selected) and 18 time windows (100ms-1000 ms) Two-way ANOVA was then performed on different time periods and three types of materials according to different electrodes. Finally, one-way ANOVA was performed for the three conditions of each time period.

3. ERP Results

The three-way ANOVA analysis between the condition × electrode point × time period was performed on the experimental data. The main effect of the condition was found to be significant ($F(2,102)=4.249$, $P=0.014$); the main effect of the electrode was significant ($F(6,34) = 62.553$, $p< 0.001$); the main effect of time was significant ($F(17, 12) = 35.478$, $p< 0.001$). At the same time, the conditional and electrode interaction effects were significant ($F(12,204)=3.622$, $p<0.001$); time and electrode interaction were significant ($F(102,204)=4.180$, $p<0.001$), conditions and time The interaction was not significant; the three interactions of condition, electrode and time were not significant.Differential topographic map of three conditions is shown in the Fig.3.

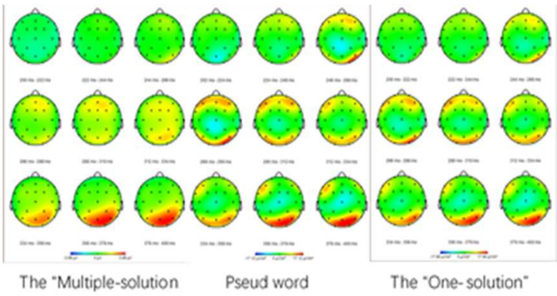

Fig.3. Differential topographic map of three conditions

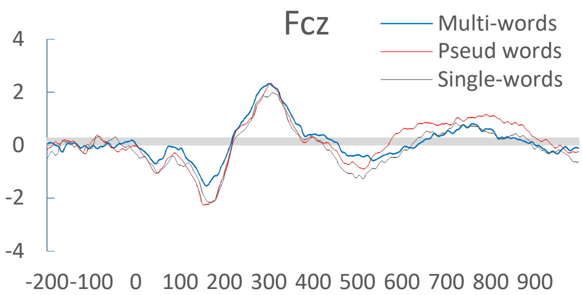

Fig.4. the averaged ERPs in tree conditions of FCz channel

3.1. Time-related characteristic

An N1 component appeared during the early 100-200 ms window, which has the largest amplitude in the unilateral Occidental region and also in the posterior and frontal scalp. There was a significant difference between the conditions of the Occidental lobe during the 200-250 ms period ($p<0.01$), and the the "Multiple-solution" can caused a larger negative wave than the Pseud word and the "One-solution".

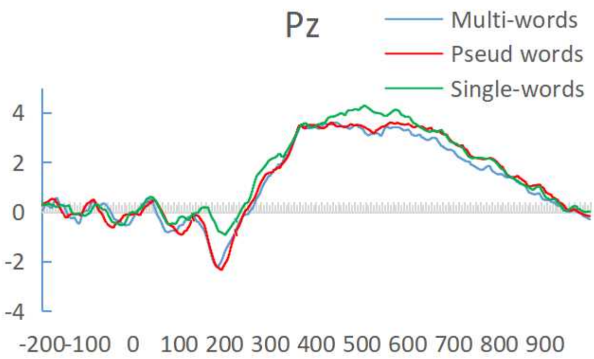

Fig.5.the averaged ERPs in tree conditions of Pz channel

In this study, the difference between the Pseud words and the true words in the 300ms-400ms parietal electrodes (P3/P4, P7/P8) was significant ($p<0.05$).

In this study, multi-words stimulated more negative waves, in the 400-550 ms time window, compared to single words. Moreover, the P600 component appeared in this experiment, and the component was most obvious at the Fz point, and the multi-word and the single word were significantly different ($p<0.05$).

After the P600 component, there is a gentle slow wave with an upward trend, which can be regarded as an LNC component. In this experiment, the three types of conditions are significantly different in the window of 750ms-800ms. Multi-words lead to larger amplitude LNC components.

4. Discussion

There were no significant differences in the three types of materials in the early compositions. Explain that the true word and the Pseud word are combined with the positive character, and it does not cause the difference caused by the non-conformity. In the subsequent of 200-250ms window, the the "Multiple-solution" caused more negative waves than the "One-solution" and the Pseud words. It can be understood that since the Chinese characters are stored according to the template, the more negative the collision occurs, the more negative waves are generated. strong.

Donchin proposed an updated theoretical model of the psychological mechanism of P300 component. That is, when a certain information appears, it is necessary to correct the original psychological representation to adapt to the strategy of the future task. The process of this correction produces P300 component, the greater the magnitude of the correction, the more inconsistent with the original cognitive representation, the greater the amplitude1. In this experiment, the difference between the Pseudo-words and the true words in the 300ms-400ms parietal electrodes (P3/P4, P7/P8) was significant (p<0.05). This result is consistent with Wei Jinghan's research[2], P300 appeared only after the subjects completed the classification or evaluation.

In this study, multi-words stimulated more negative waves, in the 400-550 ms time window, compared to single words. The waveform and latency of this component are consistent with previous studies of the N400 component[3]. However, it is not consistent with the Holcomb's study. In his study, the N400 effect can last up to 1000ms, but there was a P600 component appeared in Huang's study and this study. This may be due to a different type of task.The P600 component was originally called syntactic drift. It is related to the difficulty of syntactic integration. Recently, some studies have suggested that the P600 component is greatly affected by semantic or lexical processing mismatch. And this effect is often accompanied by the emergence of the N400. In Wang's research, the type of task does not involve the semantics of vocabulary, but the glyph. Holcomb's experiments involve vocabulary judgment. In this experiment, the P600 effect was most obvious at the Fz point, and there was a significant difference between the multi-word and the single word (p<0.05).

5. Conclusion

The results of this experiment can basically outline the time course of Chinese character processing in the brain. Between the 100ms-200ms window, the Chinese characters near the parietal lobe undergo preliminary visual feature processing, and the residual characters are decomposed into feature information according to the orthographic rule. At this time, semantic processing is not involved. Between the 200ms-400ms window, the characterization of the working memory is performed in the parietal and frontal lobes, i.e., the characterization similar to the residual is extracted and updated, given the hypothesis.A Pseud word will cause a larger positive bias volatility than a true word. The glyph information obtained before is adjusted in the vicinity of the frontal lobe and the parietal lobe between 400 ms and 600 ms to conform to the task. Multi-word cause a larger negative wave than a single word. During the 600ms-1000ms window, the obtained Chinese character voice information is maintained on the vicinity of the parietal lobe and the frontal lobe. Multi-words are more volatizing in window time than Single words and Pseud words. The conclusions of the study support an interactive activation model in which multi-word processing appears to induce a larger N400.

At the same time, the results of this study also remind us to pay attention to the influence of orthographic neighborhood effect on Chinese character recognition in the future. When designing the computer Chinese character recognition program, the difficulty of the “Multiple-solution” retrieval is also should be considered to improve the recognition efficiency.

References

1. Fabiani M, Karis D, Donchin E. Effects of mnemonic strategy manipulation in a Von Restorff paradigm[J]. *Electroencephalography and clinical Neurophysiology*, 1990, 75(1): 22-35.
2. Wei Jinghan, Pei Peiyu, Zhang Dongsong, Pan Yitian. ERP Features of the Meaning of Chinese Characters in Full-view Chinese Characters and ERP Screening of Chinese Character Recognition[J]. Acta *Psychologica Sinica*,1995,04:413-421.
3. Wang Q, Zhang J. N400 solution effect of Chinese character fragments: An orthographic neighborhood size effect[J]. *Brain research bulletin*, 2011, 86(3): 179-188.
4. Jinrui Zhang, *Research and implementation of intelligent transportation system gateway based on Internet of things* (JlLin, Changchun University of Science and Technology, 2014)

Research On Embedded Electrical Impedance Measurement System

Tong Yin [1], Xiaoyan Chen [1]*, Hongyi Yin[1]

[1] College of Electronic Information and Automation,
Tianjin University of Science and Technology, China;

*E-mail: * cxywxr@tust.edu.cn*
Www.tust.edu.cn

Abstract

This paper develops an impedance measurement system based on S3C6410 processor. An OK6410 host board as the controller platform and an AD5933 chip is used to collect impedance data, and the data is exchanged with the controller with IIC bus protocol. Comparing with the measuring result of the Wayne Kerr 6800B impedance analyzer with the accuracy of 0.05%. The system has the behaviors as lower relative error 0.422% and higher signal-to-noise (SNR) ratio 64.11dB. After calculation, the average absolute error of the impedance phase of the system is 0.527°. The tests results verified that the system is reliable and flexible with a wide application prospect.

Keywords: impedance measurement, embedded system, AD5933, S3C6410

1. Introduction

1.1. *Impedance measurement technology*

Impedance measurement technology is an important part of electronic measurement technology.

In the field of industrial production, the oil moisture content can be measured by measuring the impedance of multi-phase flow [1-2]. In the field of biomedicine, the pulmonary respiratory process can be visualized and monitored by measuring the impedance information of human lungs [3-4].

It is widely used in biomedical, electrochemical, industrial control, power grid control, etc.

1.2. *Principle of impedance measurement*

Impedance plays a very important role in the related research on the electrical properties of materials. From the impedance, a large number of electrical parameters can be deduced to comprehensively analyze the substances. In physical electronics, impedance indicating the degree of obstruction of an object by current, and is the ratio of voltage U to current I, expressed in ohms (Ω), represented by the letter Z. In general, the impedance is a complex, the real part representing the resistance features, labeled by R; the imaginary part represents feature, labeled by X. Z can be expressed as follow:

$$Z = \frac{U}{I} = R + jX = \left|Z\right|\angle\theta \tag{1}$$

Where, is the amplitude of impedance, is the phase angle, and the formulas for calculating and are according to Eqs. (2) and (3).

$$\left|Z\right| = \sqrt{R^2 + X^2} \tag{2}$$

$$\theta = \arctan\frac{X}{R} \tag{3}$$

The conversion formulas of the real part and the imaginary part are using Eqs. (4) and (5).

$$R = |Z| \cos\theta \tag{4}$$

$$X = |Z| \sin\theta \tag{5}$$

1.3. *Measuring system frame*

In the research, an OK6410 board with embedded processor S3C6410 is responsible for running the operating system and measuring programs. The data acquisition and signal conditioning are carried out by AD5933 chip. When it working, the instructions are sent to the AD5933 chip through the analog IIC bus, which make the measurement circuit [5-6] simple. The AD5933 transmits a measured signal to the host board. After a series of conversions and measurements, the signal is returned to the host board and a measurement is finished. Finally, the controller output the processing results to the operating platform. The system frame is shown as Fig. 1.

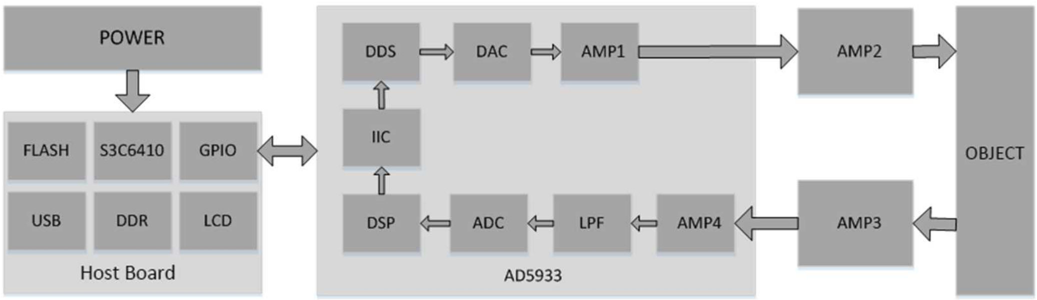

Fig. 1. Hardware system frame.

2. Hardware design

2.1. *Data collection*

We use a direct digital frequency synthesizer (DDS) to generate an alternative exciting current with short conversion time, high frequency resolution and flexible output. The signal is sampled using a high-speed analog to digital converter (ADC). Then, the digital signal processor (DSP) inside the AD5933 demodulate the signals BY Fourier transform, the real and imaginary information of the signals are extracted from the measured impedance [7-8].

2.2. *DC-blocking drive circuit*

When measuring an object which unknown impedance, the AD5933 will output a sinusoidal excitation signal with a significant DC component, which will cause polarization and affect the measuring precision in TABLE 1. It shows the output impedances at different gains and frequencies at 5V and 2.7V. In addition, the internal amplifier of the AD5933 has a high output impedance, which can affect the output signal adversely. The DC bias and output impedance of different output voltages under the voltage supply of 3.3V are shown in Table 1.
The output voltage of this system is 1.98V. The DC offset is fixed to 1.48V, and the DC bias voltage of the receiving end of AD5933 is 1.65V. There is a potential difference of 0.17V, which is easy to cause polarization occurs at the output and receiver.

Table 1. DC bias and output impedance of each excitation voltage.

Output excitation voltage	DC bias voltage	Output impedance typical
1.98V	1.48V	200Ω
0.97V	0.76V	2.4kΩ
383mv	0.31V	1.0kΩ
198mv	0.173V	600Ω

To eliminate the 1.48V DC bias, a 47nF capacitor and two 50kΩ resistors are used to obtain a DC bias VDD/2 = 1.65V, equivalent resistance R = 25KΩ. The circuit is shown in the Fig. 2. The cut-off frequency is set to 135 Hz, which is much lower than the lowest system measuring frequency 10 kHz. The interference to the excitation signal can be ignored. Resetting the DC offset reduces the polarization and improves the accuracy of the device.

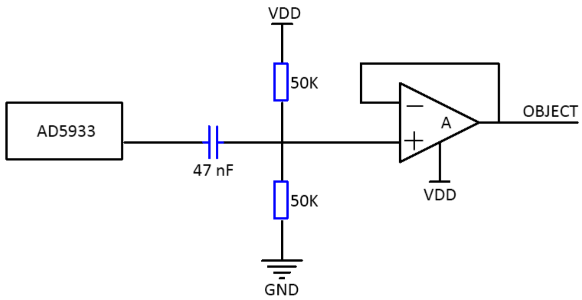

Fig. 2. Signal excitation circuit.

2.3. *Receiving circuit*

The current-voltage amplifier of the AD5933 is susceptible to the bias current, offset voltage, and CMRR of itself, which resulting in inaccurate measurements. By setting an amplifier with excellent characteristics such as low offset voltage and low bias current at the receiving port of the AD5933, the adverse effects of the self-integrated amplifier can be eliminated and the measurement accuracy can be improved. In this design, an AD8606 chip is adopted to build the excitation circuit. The AD8606 has dual channels that can be designed as a voltage follower and the required external converter simultaneously on a single chip, which can reduce the circuit complexity, save the manufacturing costs, and avoid the dual channels unbalance. It also can avoid inconsistencies caused by the using different amplifiers. The circuit is shown in Fig.3.

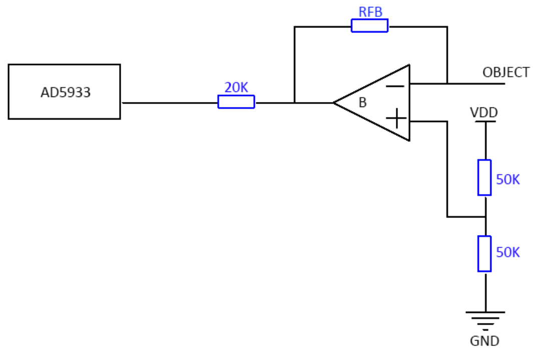

Fig. 3. AD5933 receiver circuit.

2.4. *Feedback resistor*

The measured signal is transferred to the ADC for analog-to-digital conversion. In this step, the input voltage of the ADC needs to be adjusted by some setting parameters such as feedback resistor and gains to ensure it within the linear input range of the ADC. If the input voltage is too large, the ADC can be saturated and errors occurs. If the input voltage is too small, it cannot carry enough measuring information and is susceptible to noise and reduces measurement accuracy.

Due to the requirements of the measurement parameters and the several factors affecting the output voltage, the excitation voltage and the PGA gain can be fixed to a setting point. The feedback resistor needs to be properly selected according to the magnitude of the unknown impedance to ensure the input voltage within the range of the ADC. The feedback resistor needs to select a precision resistor with high precision, capacitive and inductive impedance.

A series of feedback resistor is considered to support 100Ω-200kΩ measurement listed in Table 2, and the overall design of the data acquisition circuit is shown as Fig. 4.

Table 2. Feedback resistance and its impedance measurement range.

Measurement Range	Feedback Resistor
100Ω-1kΩ	100Ω
1kΩ-10kΩ	1kΩ
2kΩ-20kΩ	2kΩ
10kΩ-100kΩ	10kΩ
20KΩ-200kΩ	20kΩ

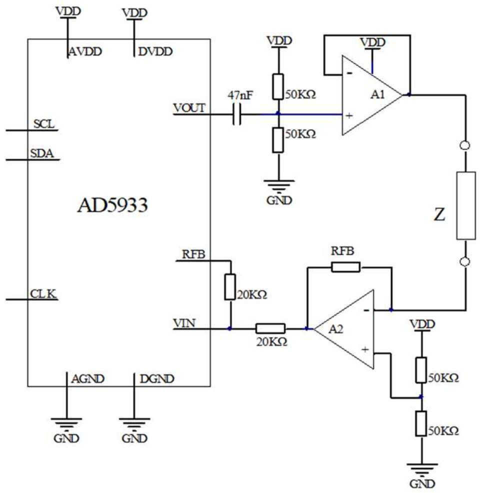

Fig. 4. Data acquisition circuit. Including AD5933 chip and signal conditioning circuit, DC amplifier circuit, receiver circuit and feedback resistor

In measuring, one of the feedback resistor is selected to guarantee most approximate to the measured object. The hardware module is shown as Fig. 5.

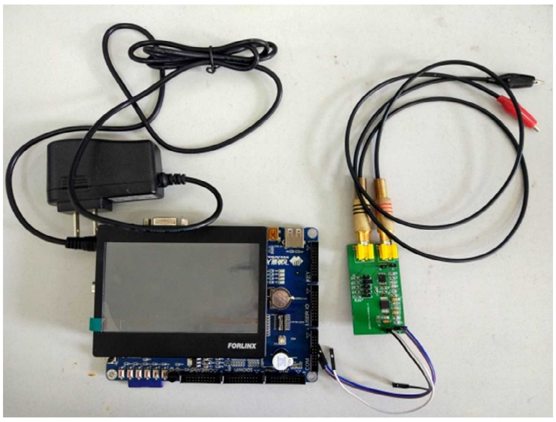

Fig. 5. Hardware module. Including operation platform, data acquisition module, and fixture.

3. System test

3.1. *Accuracy and SNR*

Taking 2kΩ testing as an example, we select 4.7kΩ as the feedback resistor, the excitation voltage is 1.98 V, and the PGA gain is 1. The test begins at 10 kHz with 1kHzincremental increase until 100 kHz. There are 91 testing values acquired. The testing is repeated 100 times. The relative error and SNR ratio at each frequency are calculated according to Eq. (6) and (7).

$$E_i = \frac{\bar{X}_i - X_t}{X_t} \times 100\% \tag{6}$$

$$SNR_i = -20lg\left(\sqrt{\frac{1}{n-1}\sum_i^n (X_i - \bar{X}_i)^2} / \bar{X}_i\right) \tag{7}$$

$\bar{X}_i$ is the average value of the measured impedance at the ith frequency, X_t is the actual value measured by the Wayne Kerr 6500B impedance analyzer, $\bar{X}_i$ is the measured impedance at the ith frequency, E is the relative error, and SNR is the signal noise ratio, n is the number of measurements.

The Wayne Kerr 6500B impedance analyzer measures the actual impedance of the resistor with an accuracy of 0.05%. Then the average relative error and signal to noise ratio of the feedback path are calculated. The other four feedback paths are tested in the same way as above. The performance specifications of the five feedback paths are shown in Table 3.

Table 3. Relative error and snr ratio of each of the five feedback paths.

Tested resistance	Feedback resistance	Relative error (%)	SNR(dB)
100	330	0.56	68.14
1k	4.7k	0.50	65.63
2k	4.7k	0.52	70.55
10k	51k	0.34	54.59
20k	51k	0.19	61.66

The average error of the system as 0.422%, and the SNR ratio is 64.11dB. The results show that the system has higher accuracy and signal to noise ratio.

3.2. *Phase Accuracy Test*

The system excitation voltage to 1.98 V. The test begins at 10 kHz with 1 kHz incremental till 100 kHz and there are 91 testing values acquired. The testing is repeated 100 times. After taking the average of the measured values, the absolute error of each frequency point is calculated. The Wayne Kerr 6800B impedance analyzer with an accuracy of 0.05% measures the phase data used for calibration. The calculated phase absolute error is shown in Table 4, where P indicates parallel and S indicates series.

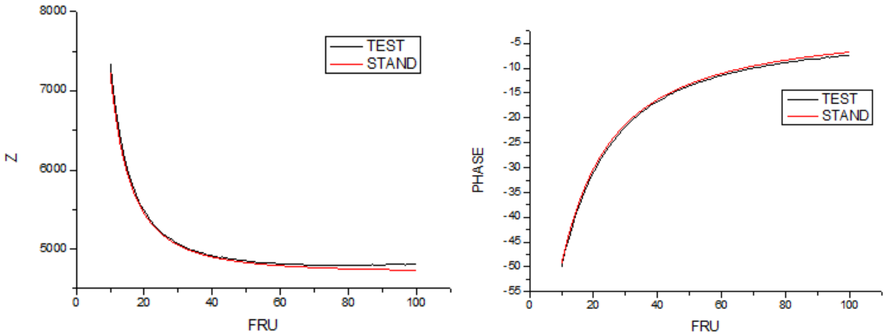

(a) (b)

Fig. 6. Comparing the measurement results of this system with the measurement results of the impedance analyzer, the black line is the result of the system, and the red line is the Wayne Kerr 6800B impedance analyzer result. Flow (a) is impedance data, and (b) is phase data.

Table 4 Absolute phase error of each r-c circuit.

R(Ω)	C(nF)	Connect type	Absolute error (°)
330	28	Parallel	1.664
330	32	Series	0.266
4.7k	3	Parallel	1.048
4.7k	3	Series	0.229
4.7k	16	Parallel	0.441
4.7k	16	Series	0.222
20k	3	Parallel	0.754
20k	3	Series	0.132
20k	16	Parallel	0.382
20k	16	Series	0.132

Finally, calculate the average phase absolute error of the system. The applied experiments on 4.7kΩ and 3nf series R-C circuits, and use origin 8.5 to compare the two data, is shown in Fig. 6.

After calculation, the average absolute error of the impedance phase of the system is 0.527°, which indicates that the system has good measurement performance for phase.

Acknowledgements

The authors would like to thank the EIT research group from Tianjin University of Science and Technology. This paper was supported by a grant from the National Natural Science Foundation of China (Grant No.61301246) and a grant from the Science and Technology Project of Tianjin (12JCYBJC19300). It was also supported by the Reform in Education from Tianjin Municipal Education Commission of China (171005704B).

References

1. Paolinelli LD, Yao J, Rashedi A. Phase wetting detection and water layer thickness characterization in two-phase oil-water flow using high frequency impedance measurements [J]. *Journal of Petroleum Science & Engineering*, 2017, 157: 671-679.
2. Gao ZK, Dang WD, Xue L. Directed weighted network structure analysis of complex impedance measurements for characterizing oil-in-water bubbly flow [J]. *Chaos,* 2017, 27 (3):74-81.
3. Liu N, GJ Saulnier,JC Newell. A multichannel synthesizer and voltmeter for electrical impedance tomography [J]. *International Conference of the IEEE Engineering in Medicine & Biology Society*, 2003, 4:3110-3113 Vol.4.
4. Saulnier GJ, Blue RS, Newell JC, Isaacson D. Electrical impedance tomography [J]. *Signal Processing Magazine IEEE*, 2006, 18 (6):231-43.
5. Hoja J, Lentka G. Interface circuit for impedance sensors using two specialized single-chip microsystems [J]. *Sensors and Actuator A: physical*, 2010, 163(1): 191-197.
6. Hoja J, Lentka G. Portable analyzer for impedance spectroscopy [C]// *XIX IMEKO World Congress on Fundamental and Applied Metrology*, Lisbon: 2009:497-502.
7. Kohout J, George AD. A high-performance communication service for parallel computing on distributed DSP systems [J]. *Parallel Computing*, 2003, 29 (7): 851-878.
8. Witte RA. *Electronic Test Instruments: Theory and Application* [M]. Prentice Hall 1993, 186-203.

Flock Guiding of Hybrid Agents via Root Block

Yunzhong Song†, Ziyi Fu, Fuzhong Wang
College of Electrical Engineering and Automation, Henan Polytechnic University,
2001 Century Avenue, Jiaozuo 454003, P.R.China
E-mail: songhpu@126.com, fuzy@hpu.edu.cn, wangfzh@hpu.edu.cn
www.hpu.edu.cn

Abstract

The convergent equilibrium of flocking agents is vital importance for their collective behavior, where flock guiding of hybrid agents, which are composed by both first order and second order agents, can only be boiled down to the root node agents, is touched upon here. Both the theoretical analysis and the simulation results are provided to verify the suggested scheme.

Keywords: Flock guiding, matrix block, hybrid order agents, collective behavior

1. Introduction

The collective behavior of agents has been a long and lasting spotlight in systems and control field. The underpinning knowledge was introduced by Murray[1], which including graph theory, adjacent matrix as well as consensus concepts, made clear intuitively. Leader follower agent systems, which have been a focus by many experts, were still being improved up to now. The networks of networks scheme of leader follower systems was made possible by Song[2], which demonstrating interdependence of agents, turned into reality via socialized status of the agents. For the engineering complexity, the agents should be different, and only by this difference, the engineering systems can function well, and in this kind of sense, hybrid agents, especially hybrid agents with heterogenous dynamics, were explored in detail. Hybrid agents with both first order and second dynamics, under auspices of augmented matrix operation[3], could be assumed unified.

In spite of collective behavior of hybrid agents has been explored so deeply, there are still some rooms to be filled in. Among those, the ultimate goal of collective behavior will stand out, for its essential value in planning of agent goal. Generally speaking, all the members of the agents should and could contribute their roles, however, counter intuitively, in this paper, in directed networks of hybrid agents, only the root block member agents can dominate the final equilibrium of the flock. And this finding seems promising in today's real world, for the authorized agents, their number should be made as less as possible in case of security.

To be distinguished from the already existed results, our points here have at least three standing out viewpoints. At first, block guiding which extends the concept of leader guiding in flocking control has been

† Corresponding author

reported so less often. And secondly, that ultimate goal position is invariant from the leaf block points will be awarded these days for security of the networks. And the third, network of hybrid agents are borrowed to verify the suggested scheme, is much more promising, for the first order agents can be anchor points sometimes and the second order agents can be the mobile agents, which will be guided by the anchor agents.

The structure of this paper is arranged as follows. At first, problem formulation, together with the main results as well as some comments on the main results will be presented in the second part of this paper. Then followed that will be some conclusions, which will be the final part to end up this paper.

2. Flock Guiding of Hybrid Agents

This part will start with the flock guiding of hybrid agents, which will be covered by subsection 2.1, the theorem will be demonstrated at first, and then some notes about it. Then the main results will be followed at 2.2, both the topology of the agent networks and the simulation results will be provided, and after that some comments will be made ready to clarify the idea further in 2.3.

2.1. *Problem formulation*

For the directed networks, it is composed of root block nodes and leaf block nodes. For the root block nodes, as a whole, they only have output degrees to connect with the other blocks. Intuitively, the nodes of leaf block, as a whole they only have input degrees to connect with the other blocks.

Theorem 1 *Suppose that the coupling matrix A can be turned into the following form:*

$\mathbf{A}=\begin{bmatrix}\mathbf{A}_1 & \mathbf{0}\\ \mathbf{B} & \mathbf{D}\end{bmatrix}$, *and the row summation of* $\boldsymbol{A_1}$ *be zero,* $\mathbf{D}$ *is non-singular. And we also assumed the left eigen vector corresponding to eigen value zero of* $\boldsymbol{A}$ *be* $\xi=[\xi_1 \quad \xi_2]^{\mathrm{T}}$, *then* ξ_2 *will be vector* $\boldsymbol{0}$. *And going into further, if sub matrix* $\boldsymbol{A_1}$ *is symmetrical, then, we can get* $\xi=[\xi_1 \quad \xi_2]^{\mathrm{T}}=[1, \ 1, \ \cdots, \ 1, \ 0, \ \cdots, \ 0]^{\mathrm{T}}$.

Proof: Since ξ is the left eigen vector corresponding to eigen value zero of matrix $\mathbf{A}$, then we can get $\mathbf{A}^{\mathrm{T}}\xi=\mathbf{0}$, and this can be translated into the following form

$$\begin{bmatrix}\mathbf{A}_1^{\mathrm{T}} & \mathbf{B}^{\mathrm{T}}\\ \mathbf{0} & \mathbf{D}^{\mathrm{T}}\end{bmatrix}\begin{bmatrix}\xi_1\\ \xi_2\end{bmatrix}=\mathbf{0} \tag{1}$$

To be concrete, we can have

$$\begin{aligned}&\mathbf{A}_1^{\mathrm{T}}\xi_1+\mathbf{B}^{\mathrm{T}}\xi_2=\mathbf{0}\\ &\mathbf{D}^{\mathrm{T}}\xi_2=\mathbf{0}\end{aligned} \tag{2}$$

For $\mathbf{D}$ is invertible, ξ_2 must be zero vector. And in this sense, we can get $\mathbf{A}_1^{\mathrm{T}}\xi_1=\mathbf{0}$, in case of symmetry of $\mathbf{A}_1$, we have $\mathbf{A}_1\xi_1=\mathbf{0}$. Referring that row summation of $\mathbf{A}_1$ is zero, so there must exist vector $\xi_1=[1, \ 1, \ \cdots, \ 1]^{\mathrm{T}}$, that makes

$$\mathbf{A}_1\xi_1=\mathbf{0} \tag{3}$$

Notes: Theorem1 points out that if sub-matrix A_1 has no input degrees and is symmetric, then its corresponding nodes can be named as root nodes and the ultimate state of the networks can be determined by those sub block nodes; if sub matrix $\mathbf{D}$ is invertible, and it does not have output degrees connected with the other sub blocks, the nodes corresponding to $\mathbf{D}$ can be named as leaf nodes, leaf nodes can not affect the ultimate state of the networks.

2.2. *The main results*

Consider the network, which consists of 5 agents, among which node 1 and node 2 are root block nodes, while node 3, node 4 and node 5, are leaf block nodes, this can be referred to Fig.1.

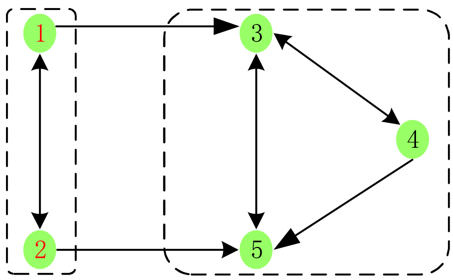

Fig.1 Network consists of 5 nodes

To be further, the nodes 1 and 2 are assigned as the first order agents, while nodes 3 to 5 are assigned as the second order agents, respectively.

The coupling matrix of Fig.1 is easily to be gotten as

$$\mathbf{A}=\begin{bmatrix} -1 & 1 & 0 & 0 & 0 \\ 1 & -1 & 0 & 0 & 0 \\ 1 & 0 & -3 & 1 & 1 \\ 0 & 0 & 1 & -1 & 0 \\ 0 & 1 & 1 & 1 & -3 \end{bmatrix}$$

The left eigen vector to the zero eigen value of $\mathbf{A}$ is $[1/2\ \ 1/2\ \ 0\ \ 0\ \ 0]^{\mathrm{T}}$. The dynamics of the system can be described as

$$\begin{aligned} &\dot{x}_i = u_i,\ \ i\in\{1,2,\cdots,n\};\\ &\dot{\mathbf{x}}_j=\begin{bmatrix}\dot{x}_{j1}\\ \dot{x}_{j2}\end{bmatrix}=\begin{bmatrix}x_{j2}\\ u_j\end{bmatrix}, j\in\{m,m+1,\cdots,N\}; \qquad (4)\\ &n=2, m=n+1, N=5. \end{aligned}$$

Which can be ensemble as compact as

$$\dot{\mathbf{x}}=\begin{bmatrix} 0&0&0&0&0&0&0&0\\ 0&0&0&0&0&0&0&0\\ 0&0&0&1&0&0&0&0\\ 0&0&0&0&0&0&0&0\\ 0&0&0&0&0&1&0&0\\ 0&0&0&0&0&0&0&0\\ 0&0&0&0&0&0&0&1\\ 0&0&0&0&0&0&0&0 \end{bmatrix}\mathbf{x}+\begin{bmatrix} 1&0&0&0&0\\ 0&1&0&0&0\\ 0&0&0&0&0\\ 0&0&1&0&0\\ 0&0&0&0&0\\ 0&0&0&1&0\\ 0&0&0&0&0\\ 0&0&0&0&1 \end{bmatrix}\mathbf{u}$$

Where

$\mathbf{x}=[x_1\ \ x_2\ \ x_{31}\ \ x_{32}\ \ x_{41}\ \ x_{42}\ \ x_{51}\ \ x_{52}]^{\mathrm{T}}$,

$\mathbf{u}=[u_1\ \ u_2\ \ u_3\ \ u_4\ \ u_5]^{\mathrm{T}}$.

To be concise, the control action can be expressed as

$$\mathbf{u}=\begin{bmatrix}u_1\\u_2\\u_3\\u_4\\u_5\end{bmatrix}=\begin{bmatrix} a(x_2-x_1)\\ a(x_1-x_2)\\ a(x_1+x_{41}+x_{51}-3x_{31})\text{-}bx_{32}\\ a(x_{31}-x_{41})\text{-}bx_{42}\\ a(x_2+x_{41}+x_{31}-3x_{51})\text{-}bx_{52} \end{bmatrix}$$

The introduced control action for agents 1 and 2 are easily to be understood, for agents 1 and 2, they make up of the undirected sub network of root block, and they tend to be convergent to each other. Control action added for agents 3, 4 and 5 can make a little nervous at first glimpse, but they still can be made tractable in this way, first we decomposed the added control function into two different parts, and the first part is employed to realize the consensus among themselves and their neighbours, and these consensus actions are scaled by proportional factor a, and the second term is velocity damping part, which is also scaled by proportional factor , and the scaled value can be varied from a, and in this case we named the factor as b. The consensus term plus the damping term collaboratively turn the flock guiding of hybrid agents possible. Among which, we assigned a=1 and b=2, respectively. The simulation results can be seen as Fig.2.

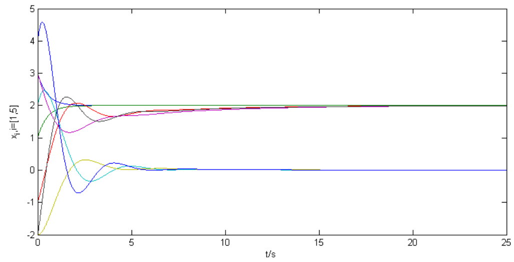

Fig.2 Flock guiding of 5 hybrid agents

During simulation, the initial values of the agents were listed as follows

$$\begin{aligned}\mathbf{x_0}&=[x_{10}\ \ x_{20}\ \ x_{310}\ \ x_{320}\ \ x_{410}\ \ x_{420}\ \ x_{510}\ \ x_{520}]^{\mathrm{T}}\\ &=[3\ \ 1\ \ \text{-}1\ \ 2\ \ 3\ \ \text{-}2\ \ \text{-}2\ \ 4]^{\mathrm{T}}\end{aligned}$$

From Fig.2, the ultimate flock guiding position is 2, it is the average of the initial values of agents 1 and 2. So, in this respect, only the root block agents have their role being played in the ultimate goal of flock guiding. It is much more interesting about the second sub variables of agents 3, 4 and 5, all of them were rendered to zero because of the damped factor of theirs. It seems frustrated that, the velocity signals of the agents at leaf block are not available sometimes. However, all of the second sub system states can be observed, it is a standard way to design observers for them. And in this point, this should not be an excuse to devalue our contribution here. And this is customary, because for the fixed ultimate goal position, the velocity sub variable must be ceased. Of course, the ultimate goal can be adjusted if we like, we can regulate the ultimate goal position by manipulation the coupling coefficients of root block nodes.

2.3. *Some comments*

Flock guiding of hybrid agents via root block has its potential contributions at the following respects: First of all, in the easy to get and easy to use style of the contemporary network world, privacy protection problems are becoming more and more pressing, in helps of our idea here, the key information are strongly suggested to be kept in root block agents. Secondly, infrastructure cyber physical system like smart grid networks, transportation networks, can be kept immune from the injected attacks if only the small number of the key root block nodes are kept shield from the hackers. And the third, root block agents and leaf block agents have different dynamics, can conveniently be specified, paired connections of root block nodes and leaf block nodes can be tagged into block chain, which then strengthened the safety further. Pros of our suggested scheme are so obvious, and without doubt, we should continue our pursuing to this amazing topic. And some cons should be overcome in the near future, such as the injected invaders in the leaf nodes could not change the ultimate goal position indeed, but they could make the process to the ultimate goal position so difficult, via disturbing the topology of the leaf block agents connected graph. Problems like this one would be kept as our focus.

3. Conclusion

In conclusion, in order to realize the security of the flock guiding, the ultimate goal of the flock, should be exposed to only several key agents, and they can be assigned as the root node agents, as to the leaf agents, for their popularity is so massive, they should be kept from the secrets of the ultimate goal. Flock with secrets keeping is made possible here with root node and leaf node decomposition.

System complexity, which is so elusive, could not be easily explained if we are unwillingly exposed to the concrete systems. The road to clarify the complexity can be made tractable through the following exemplified engineering systems as well as the theoretical exploration. Instance like high performance vehicle driving, which was spearheaded in Jia[4] and thereafter individualized designed in Jia[5], can be the justified pilot scale systems. As to the large quantities complex systems, not only the object itself, but also the endured hostile environment, will be an impediment for the successful manipulation of them. Time varying delays, uncertain and unreliable information, annoying disturbances, and multi-inputs multi-outputs, can also be the adversary factors. Adaptive scheme was born to fix them, and this can be referred to Jia[6]. Reductionism should not be the only way to deal with the complex system, but it should be kept in mind at first, for the first step we should know the system locally in detail in order to grasp the whole system globally, and in this way, refined analysis and control of the complex systems are necessary. Refined control of leader follower system according their roles of the leader agent, follower agents that have connected path with the leaders, the follower agents that are failed with the connection of the other agents, and the targeting agent which represent the ultimate goal position are recommended also[7]. So, flock guiding of hybrid agents via root block, the suggested strategy here together with the other champion achievements of complex systems can see its prosperity in the near coming years.

Acknowledgements

This work is partially supported by NSFC Grant (61340041 and 61374079) and the Project-sponsored by SRF for ROCS, SEM to Yunzhong Song as well as Natural Science Fund of Henan Province (182300410112). The root block and leaf block flock guiding idea is benefited from the monograph, written by Prof. Junan Lu, et al.[8]

References

1. R. Olfati, R. Murray, Consensus problems in networks of agents with switching topology and time delays, *IEEE Transactions on Automatic Control*, **49**(2004) 1520-1533.
2. Y. Song, Z. Fu, F. Wang, Socialized multi-agent system rendezvous via networks of networks, *Journal of Robotics, Networking and Artificial Life*, **3** (2016) 136-139.
3. Y. Song, Consensus of agents with mixed linear discrete dynamics, *International Journal of Control, Automation and Systems*, **14** (2016) 1139-1143.
4. Y. Jia, Robust control with decoupling performance for steering and traction of 4WS vehicles under velocity-varying motion, *IEEE Transactions on Control Systems Technology*, **8**(2000) 554-569.
5. Y. Jia, Alternative proofs for improved LMI representations for the analysis and the design of continuous-time systems with polytopic type uncertainty: a predictive approach, *IEEE Transactions on Automatic Control*, **48**(2003) 1413-1416.
6. Y. Jia, General solution to diagonal model matching control of multi-output-delay systems and its applications in adaptive scheme, *Progress in Natural Science*, **19**(2009), 79-90.
7. Y. Song, W. Zhao, Multi-agent system rendezvous via refined social system and individual roles, *WSEAS Transactions on Systems and Control*, **9**(2014),526-532.
8. J. Lu, H. Liu and J. Chen, *Synchronization in Complex Dynamical Networks* (Higher Education Press, Beijing, 2016).

Multiple Model Adaptive Control of Flexible Arm

Yingzhao Zhang*
College of electrical engineering, Guizhou University
Guiyang, 550025, China

Weicun Zhang
School of Automation and Electrical Engineering, University of Science and Technology Beijing
Beijing, 100083, China

Xiao Wang, Handong Li
College of electrical engineering, Guizhou University
Guiyang, 550025, China
E-mail: 15600233121@163.com, weicunzhang@ustb.edu.cn
http://www.gzu.edu.cn/

Abstract

In this paper, dynamic model of a flexible arm is built through Lagrange theory. Then, based on the platform of SIMULINK, model of the flexible arm is established and the states of the flexible manipulator under multiple model adaptive control are simulated. Finally, to compare the control effect (like stability and accuracy) of multiple model adaptive control method with other control methods, some simulation results are given.

Keywords: Flexible arm, MMAC(Multiple Model Adaptive Control), nonlinear system, system identification

1. Introduction

Most of the traditional industrial robots are made of rigid materials, with huge mass and heavy weight. With the continuous progress of science and technology, there are higher requirements for robots. Many industries also require intelligent robots with light weight, high precision, high efficiency and high adaptability. Therefore, the concept of flexible robot was put forward, which is a kind of flexible manipulator with light weight, less energy consumption and small inertia. Flexible manipulator has gradually become an important research object in control field in recent years. At present, the research on flexible robots is still in its infancy, so it is very important to realize the precise control of flexible manipulators [1].

In the classical control field, the change of internal characteristics and the influence of external disturbances can be restrained by feedback control. In the design of controllers, the parameters are always fixed, so if sensor faults, characteristics changes, sudden disturbances and other conditions occur during the operation of the system, the overall performance of the system will decline, or even be unstable. Because of the characteristics of flexible manipulator's material structure and external disturbance, there are some problems in its mathematical model, such as parameter jump. In order to produce better control effect for the

* Corresponding author

controlled object when the parameters jump, this paper adopts multi-model adaptive control method to control the flexible manipulator and studies it with other controllers. The characteristics of multi model adaptive control are summarized.

2. The Main Text

2.1. *Modeling*

Generalized flexible manipulators are mainly divided into two kinds: one is that the link of the manipulator is made of elastic material, and the link itself has flexibility, i.e. distributed flexible manipulator; the other is that the link of the manipulator is rigid, and the flexibility mainly exists in the joint, which is called flexible joint manipulator [2]. The object of this paper is the second flexible joint. The reason for the flexibility of robots is that harmonic gear reducers and moment sensors are widely used in the transmission system of robots. These components are flexible, so the joint of robots is flexible. We can imagine a flexible joint as a spring so that a simplified model of the flexible joint manipulator can be obtained.

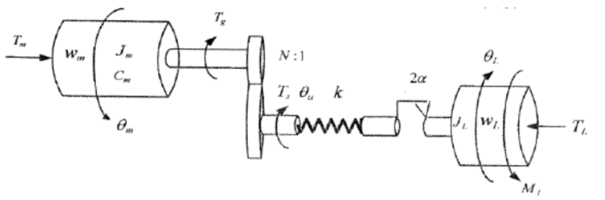

Fig. 1. Simplified model of flexible joint

Aiming at the simplified model mentioned above, this paper uses Lagrange-Euler method to solve the dynamic equation of flexible manipulator. The first thing to do is to write the expression of potential energy and kinetic energy of the manipulator system. When formulating the potential energy expression of flexible manipulator, not only the gravitational potential energy but also the elastic potential energy produced by joint flexibility should be considered.

$$T_1(q,\dot{q}) = \frac{1}{2}\dot{q}^T M_1(q)\dot{q} \tag{1}$$

Eq. (1) is the kinetic energy equation, q is the position vector of the connecting rod. $M_1(q)$ is inertia matrix of connecting rod.

Converting Eq. (1) into vector situation

$$T_r(\dot{\theta}, q, \dot{q}) = \frac{1}{2}\begin{pmatrix}\dot{q}\\ \dot{\theta}\end{pmatrix}^T \begin{bmatrix} M_r(q) & S(q) \\ S(q)^T & J\end{bmatrix}\begin{pmatrix}\dot{q}\\ \dot{\theta}\end{pmatrix} \tag{2}$$

$M_r(q)$ is generalized inertia matrix of rotor. J is rotor inertia matrix of motor rotor, $s(q)$ is inertia matrix of coupling part. The potential energy equation is as follows:

$$V_p(q,\theta) = \frac{1}{2}(\theta - q)^T K(\theta - q) + V_g(q) \tag{3}$$

Substituting Eq. (2) and Eq. (3) into Lagrange's kinetic equation we can get the following formula:

$$H(q)\begin{pmatrix}\ddot{q}\\ \ddot{\theta}\end{pmatrix} + T(q,\dot{q})\begin{pmatrix}\dot{q}\\ \dot{\theta}\end{pmatrix} + \begin{pmatrix} g(q) - K(\theta - q) \\ K(\theta - q)\end{pmatrix} = \begin{pmatrix}\tau_{ext}\\ \tau_m\end{pmatrix} \tag{4}$$

$H(q)$ is the inertia matrix of the model, $g(q)$ is the gravitational function.

It is important to note that we set up the flexible manipulator under the following assumptions:

Hypothesis 1: Consider the rotor of the motor as a whole with the axis as the center, avoiding the rotation process of the rotor. It has a bad effect on motor rotation.

Hypothesis 2: Consider only the mechanical dynamics of flexible manipulator system; assume that the motor dynamics is fast enough to be ignored. Adverse effects on the system is treated as a whole.

Hypothesis 3: A virtual spring is used to simulate joint flexibility, spring elasticity and sum in the derivation of mathematical model. The flexible deformation of the joint achieves a linear relationship, and the corresponding proportional coefficient is the elastic coefficient of the joint. In addition, the spring has damping force, and the deformation velocity is linearly proportional to the damping force.

Finally, by simplification, we can get the following kinetic equations:

$$\begin{cases} M(q)\ddot{q} + C(q,\dot{q})\dot{q} + g(q) = K(\theta - q) + \tau_{ext} \\ J\ddot{\theta} + K(\theta - q) = \tau_m \end{cases} \tag{5}$$

2.2. *Control System*

2.2.1. *Control structure*

$\Omega = \{M_i \mid i = 1,2,\cdots,n\}$ represents a model set with M_i as its element, which can be understood as a

generalized model set in which M_i can represent not only the transfer function model, but also state feedback matrices.
$C = \{U_i \mid i = 1,2,\cdots,n\}$ C is a controller set designed according to Ω, C_i is a controller corresponding to M_i. The overall controller can be expressed as $U_{svs} = f(U_1, U_2, \cdots, U_N, \theta)$

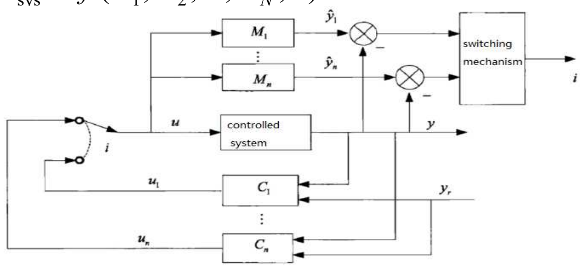

Fig. 2. Multi model adaptive control structure diagram

In this paper, f represents a nonlinear function. θ is a parameter vector. Switching mechanism represents the switching function. According to the error between the output of the models and the outputs of actual plant, the switching mechanism is used to determine the current effective model and the corresponding controller [3].

2.2.2. *Model set*

MMAC is based on multiple models to approximate the uncertainties of the system and establish controllers on the basis of multiple models. Therefore, the model set and the number of element models will directly affect the accuracy and performance of the control. According to the nature of the model, the model set can be divided into the following types: 1. all fixed models; 2. multi-fixed models and one adaptive model; 3. all adaptive models.

In practical problems, because the external environment of the controlled system and the changes of system model parameters are not described by a few models, such problems arise. Without a large number of model systems, it is impossible to describe them accurately. If there are too many models, a large part of the model and the current system will be centralized in each step of the control process. The real models are far from each other, which not only waste the computation of the controller, but also reduce the performance of the controller by excessive competition of the redundant models. In order to avoid the above problems, this paper uses Moving Back method, which constructs the controller based on only one subset of the model set at each time and adjusts the subset dynamically at any time so that it can cover the real model parameters of the controlled object.

2.2.3. *Control strategy*

There are two different control methods, one is weighted MMAC, one is switched MMAC. In this paper, we use switched MMAC. The principle of switched MMAC is to find the model closest to the controlled object based on the performance index function at each sampling time and switch the controller based on this model to the current controller. This multi-model controller can ensure the stability of the controlled system when switching for finite or infinite times [4].

2.2.4. *Switching function*

The core of the switching mechanism is the performance index function. The performance index is used to judge the approximation degree between each model and the actual state of the controlled object at the present stage, and the most suitable model is chosen as the approximation model at the present stage. The establishment of the performance index function is not unique, the performance index function in this article is

$$J_i(t) = \alpha e_j^2(t) + \beta \int_0^t e^{-\lambda(t-\tau)} e_j^2(\tau) d\tau \tag{6}$$

α and β are constants. λ is the forgetting factor, and e_j is the output error between the j model and the actual system. The controller which has the minimum value of switching function will be selected as an effective controller.

3. Simulation Results and Conclusion

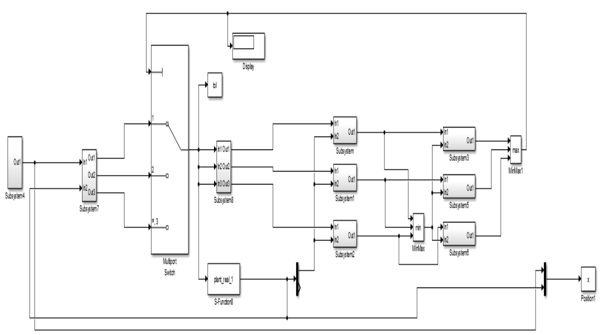

Fig. 3. Simulation diagram

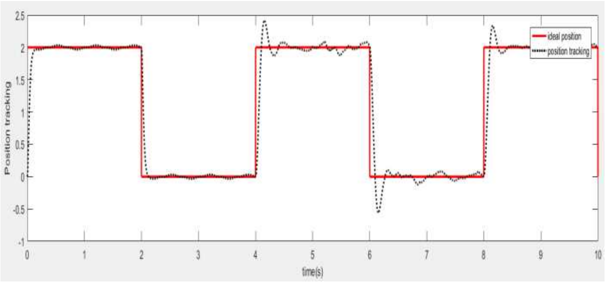

Fig. 4. Control effect using three models.

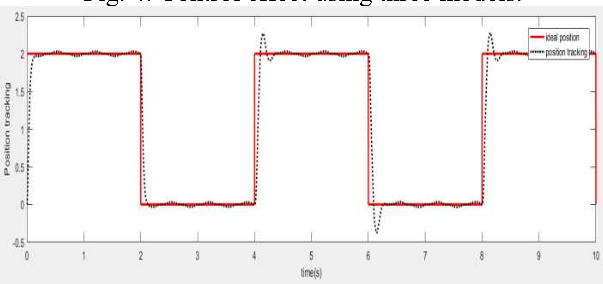

Fig. 5. Control effect using ten models.

Fig. 3 is the basic structure of the simulation system. The control effect of the multi-model control system is studied below. In the following experiments, the only change is the number of centralized models and the corresponding controllers. Parameter jumps occurred at 3 second of the simulation time.

From the above pictures, we can see that with the increase of the number of models in the control system, the control performance is getting better. In this control system, when the number of models reaches 40, the jump of parameters has little effect on the control performance.

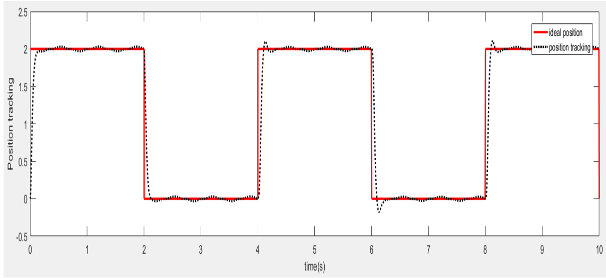

Fig. 6. Control effect using twenty models.

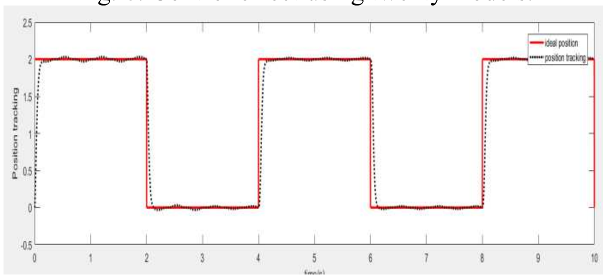

Fig. 7. Control effect using thirty models.

References

1. H. Huang, *Research on Modeling and control of flexible joint manipulator* (Hunan University of Technology, Hunan, 2014).
2. Y. H. Wang, H. S. Li, W. Zhang, Sliding mode variable structure control of flexible joint manipulator, *J. MMTAMT.* **10(1)** (2017) 91–95.
3. X. L. Li, W. Wang, W. Sun, Multi model adaptive control, *J. CONTROL AND DECISION.* **15**(4) (2000) 390–394.
4. W. R. Li, *Multiple Model Adaptive Control and Application for a Class of Nonlinear System* (China Jiliang University, Hangzhou, 2015).

Time-Varying Lyapunov Function for Mechanical Systems

Bin Zhang*
School of Automation, Beijing University of Posts and Telecommunications, Beijing, 1008760, China

Yingmin Jia
The Seventh Research Division and the Center for Information and Control, School of Automation Science and Electrical Engineering, Beihang University (BUAA), 37 Xueyuan Road, Haidian District, Beijing, 100191, China
E-mail: zb362301@126.com, ymjia@buaa.edu.cn
www.bupt.edu.cn, www.buaa.edu.cn

Abstract

In this paper, a general method for constructing time-varying Lyapunov functions is provided for mechanical systems. Sufficient conditions of uniform asymptotical stability are established. Different from the existing results on this subject, we remove the periodic restrictions and persistency of excitation restrictions in our work. It is shown that the time-varying mechanical systems remain uniformly asymptotically stable with the control input provided in our work.

Keywords: Mechanical systems, time-varying systems, strict Lyapunov function, subsystems.

1. Introduction

Controller design for time-varying mechanical systems has emerged as a hot research area. A lot of theoretical and practical results for controller design have been proved based on Lyapunov methods. Several approaches for construction of strict Lyapunov functions have been proposed under various frameworks and control objectives[1,2].

In Ref.3, a new method for estimation the domain of attraction was shown by using non-strict Lyapunov functions. In Ref.4, an extension of invariance principle with non-strict Lyapunov functions was provided for power systems with transmission losses. In Ref.5, strict Lyapunov functions were established for finite-time control problem of robot manipulators. In Ref.6, two kinds of weak-invariance principles for nonlinear switched systems were developed and accurate convergent regions were obtained. The readers can refer to Refs. 7 and 8 for more detailed discussions on this topic and a list of related references.

In recent decades, it is recognized that non-strict Lyapunov functions suffer from some essential disadvantages[9]. On the one hand, non-strict Lyapunov functions are not well suited to robustness analysis, since their negative semi-definite derivatives along trajectories could become positive under arbitrarily small perturbations of the dynamics. On the other hand, non-strict Lyapunov functions are usually insufficient to analyze nonlinear time-varying systems, since their derivatives depend on the time parameters.

*Corresponding author.

Motivated by the above considerations, we provide a general method for constructing time-varying Lyapunov functions for mechanical systems in this paper. We divide the closed loop system into two subsystems. Time-varying Lyapunov function is established for one of the subsystems. Based on the derivatives of the time-varying Lyapunov function along different subsystems, we provide the time-varying Lyapunov function for the closed loop system. It is shown uniform asymptotical stability can be obtained with the control input provided in this paper.

2. Problem Statement

Consider the following mechanical system with time-varying friction

$$M\ddot{q}+C\dot{q}+(F_c(t)+F_s(t)e^{-\rho\mu(\dot{q})})sat(\dot{q})+k(t)q=\tau \quad (1)$$

where $q(t),\dot{q}(t),\ddot{q}(t)\in R^n$ represent the position, velocity, and acceleration, respectively; $M\in R^{n\times n}$ is the positive definite inertia of the system; ρ is a positive constant; $\mu(\cdot)$ is a positive definite function related to the Stribeck effect; $k(t)$ denotes a time-varying spring stiffness. For system (1), it is assumed that the following properties hold.

Property 1. The matrix M is positive definite. Moreover, we define $\lambda_{\max}$ as the maximum eigenvalue of M and $\lambda_{\min}$ as the minimum eigenvalue of M .

Property 2. The derivative of $k(t)$ is bounded such that

$$|k(t)|\leq\hat{k}\quad\forall t\geq 0 \quad (2)$$

where $\hat{k}$ is a positive constant.

Before presenting the main results, we give some lemmas first.

Lemma 1. [10] Let a,b,p,q be positive real numbers. If $\frac{1}{p}+\frac{1}{q}=1$, then

$$ab\leq\frac{a^p}{p}+\frac{b^q}{q}. \quad (3)$$

Lemma 2. [10] Let $a_i>0,b_i>0,i=1,2,...,n,p>1$, and $q>1$. If $\frac{1}{p}+\frac{1}{q}=1$, then

$$\sum_{i=1}^n a_ib_i\leq(\sum_{i=1}^n a_i^p)^{\frac{1}{p}}(\sum_{i=1}^n b_i^q)^{\frac{1}{q}} .$$

(4)

Lemma 3. [10] For $x_i\in R,i=1,2,...,n,$ and $0<m<1$, then the following inequality holds:

$$|x_1|^m+\cdots+|x_n|^m\leq(|x_1|+\cdots+|x_n|)^m.$$

(5)

Lemma 4. For $x_i\in R,i=1,2,...,n,$ and $0<m<1$, then the following inequality holds:

$$|x_1|^m+\cdots+|x_n|^m\leq n^{1-m}(|x_1|+\cdots+|x_n|)^m. \quad (6)$$

Proof. Let $a_i=|x_i|^m,b_i=1,i=1,2,...,n,p=\frac{1}{m},$ and $q=\frac{1}{1-m}$. Then based on Lemma 2, we obtain

$$\begin{aligned}&|x_1|^m+\cdots+|x_n|^m\\&\leq(\sum_{i=1}^n(|x_i|^m)^{\frac{1}{m}})^m(\sum_{i=1}^n 1^{\frac{1}{1-m}})^{1-m}\\&=n^{1-m}(|x_1|+\cdots+|x_n|)^m\end{aligned} \quad (7)$$

which completes the proof. □

3. Subsystems

For the uniform asymptotic stability problem of time-varying mechanical system (1), we propose the following control input

$$\tau=-\alpha M\dot{q}+C\dot{q}-k_0q \quad (8)$$

where α and k_0 are control parameters. Let $q=x_1$ and $\dot{q}=x_2$. Then the closed-loop system (1) and (8) can be written in a compact form as

$$\begin{aligned}&\dot{x}_1=x_2\\&\dot{x}_2=-(k(t)+k_0)M^{-1}x_1-\alpha x_2\\&\quad-M^{-1}(F_c(t)+F_s(t)e^{-\rho\mu(x_2)})sat(x_2).\end{aligned} \quad (9)$$

We define

$$f(t,x)=\begin{pmatrix}x_2\\\tilde{f}(t,x)\end{pmatrix} \quad (10)$$

where function $\tilde{f}(t,x)=-(k(t)+k_0)M^{-1}x_1-\alpha x_2$

$-M^{-1}(F_c(t)+F_s(t)e^{-\rho\mu(x_2)})sat(x_2)$ .We also define $f_1(t,x)=\begin{pmatrix} x_2 \\ -(k(t)+k_0)M^{-1}x_1-\alpha x_2 \end{pmatrix}$ and $f_2(t,x)=\begin{pmatrix} 0 \\ -M^{-1}(F_c(t)+F_s(t)e^{-\rho\mu(x_2)})sat(x_2) \end{pmatrix}$.

Then, we can see that $f(t,x)=f_1(t,x)+f_2(t,x)$. In this subsection, we consider two subsystems $\dot{x}=f_1(t,x)$ and $\dot{x}=f_2(t,x)$, respectively.

Inspired by the results in Ref.7, we consider the following Lyapunov function

$$V(t,x)=A((k(t)+k_0)x_1^Tx_1+x_2^TMx_2)+x_1^Tx_2 \quad (11)$$

where $A>0$ is a positive constant. In this paper, we choose $A>\max\{\frac{1}{\lambda_{\min}},\frac{1}{k_1+k_o}\}$.

It can be verified directly that

$$\begin{aligned} V(t,x)&=A((k(t)+k_0)x_1^Tx_1+x_2^TMx_2)+x_1^Tx_2 \\ &\geq A((k(t)+k_0)x_1^Tx_1+x_2^TMx_2) \\ &\quad -\frac{1}{2}(x_1^Tx_1+x_2^Tx_2) \\ &> -\frac{1}{2}(x_1^Tx_1+x_2^Tx_2). \end{aligned} \quad (12)$$

The derivative of $V(t,x)$ along subsystem $\dot{x}=f_1(t,x)$ shows:

$$\begin{aligned} \dot{V}(t,x)&=\frac{\partial V}{\partial t}+\frac{\partial V}{\partial x}f_1(t,x) \\ &\leq A\hat{k}x_1^Tx_1+2A(k(t)+k_0)x_1^Tx_2+x_2^Tx_2 \\ &\quad -2Ax_2^T((k(t)+k_0)x_1+\alpha Mx_2) \\ &\quad -x_1^T((k(t)+k_0)M^{-1}x_1+\alpha x_2) \\ &\leq -((k_1+k_0)\frac{1}{\lambda_{\max}}-A\hat{k})x_1^Tx_1 \\ &\quad -(2\alpha AM-1)x_2^Tx_2+\alpha\,|x_1^Tx_2| \\ &\leq -l_1x_1^Tx_1-l_2x_2^Tx_2 \end{aligned} \quad (13)$$

where we have $l_1=(k_1+k_0)\frac{1}{\lambda_{\max}}-\frac{1}{2}\alpha-A\hat{k}$ and $l_2=\frac{3}{2}\alpha-1$. Therefore, we can see that if we choose $\alpha>\frac{2}{3}$ and $k_0>(\frac{1}{2}\alpha+A\hat{k})\lambda_{\max}-k_1$, subsystem $\dot{x}=f_1(t,x)$ is uniformly asymptotically stable.

Similarly, the derivative of $V(t,x)$ along subsystem $\dot{x}=f_2(t,x)$ shows:

$$\begin{aligned} &\frac{\partial V}{\partial x}f_2(t,x) \\ &\leq -2x_2^TM^{-1}(F_c(t)+F_s(t)e^{-\rho\mu(x_2)})sat(x_2) \\ &\quad -x_1^TM^{-1}(F_c(t)+F_s(t)e^{-\rho\mu(x_2)})sat(x_2) \\ &\leq 2\sqrt{n}\frac{1}{\lambda_{\min}}\|F_c(t)+F_s(t)\|\|x_2\| \\ &\quad +\sqrt{n}\frac{1}{\lambda_{\min}}\|F_c(t)+F_s(t)\|\|x_1\| \\ &\leq \sqrt{n}\frac{1}{\lambda_{\min}}\|F_c(t)+F_s(t)\|(\|x_1\|+\|x_2\|) \\ &\leq 2\sqrt{n}\frac{1}{\lambda_{\min}}\|F_c(t)+F_s(t)\|V^{\frac{1}{2}}. \end{aligned} \quad (14)$$

In the following, we define time-varying parameter

$$w(t)=\sqrt{n}\frac{1}{\lambda_{\min}}\|F_c(t)+F_s(t)\|.$$

4. Main Results

From (13) and (14), we can see that $V(t,x)$ is not a Lyapunov function for system (1), because it is not easy to verify the negativity of the derivative of $V(t,x)$ along system $\dot{x}=f(t,x)$, which is shown as follows

$$\dot{V}(t,x)\big|_{f(t,x)}=\frac{\partial V}{\partial t}+\frac{\partial V}{\partial x}(f_1(t,x)+f_2(t,x)). \quad (15)$$

Therefore, motivated by the results in Ref.7, we provide the following time-varying Lyapunov function

© The 2019 International Conference on Artificial Life and Robotics (ICAROB2019), Jan. 10-13, B-Con Plaza, Beppu, Oita, Japan

$$V^{\#}(t,x)=\int_0^V \frac{1}{(1+s)^{0.5}}ds$$
$$+\phi\int_{t_0}^{t}(\frac{1}{T}\int_{\tau}^{\tau+T} w(v)dv-w(\tau))d\tau\ln(1+V) \quad (16)$$

where T,ϕ are positive constants. It can be verified directly that if k_0 and α are chosen large enough, then there exist T and ϕ such that

$$\dot{V}^{\#}(t,x)\Big|_{f(t,x)}=\frac{\partial V}{\partial t}+\frac{\partial V}{\partial x}(f_1(t,x)+f_2(t,x))$$
$$<0. \quad (17)$$

Therefore, we conclude with the following theorem.

Theorem 1. Consider time-varying system (1). If the control input is chosen as (8), then the closed loop system is uniformly asymptotically stable. Moreover, (16) is a strict Lyapunov function.

Proof. This result can be verified by taking the derivative of $V^{\#}(t,x)$ given in (16) directly. The detailed process is omitted here. □

5. A Numerical Example

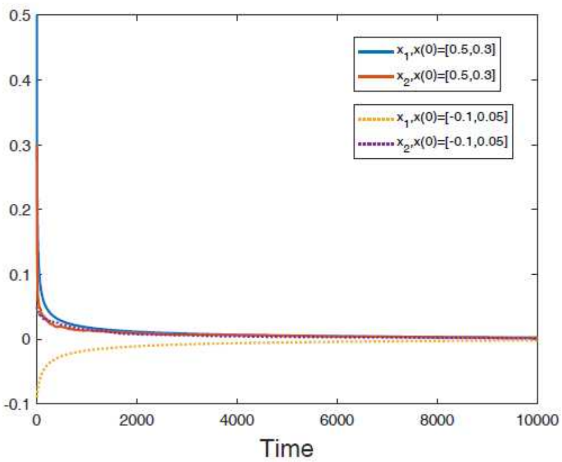

Fig. 1. The state trajectories of system.

We give a numerical example to demonstrate the effectiveness of the proposed theoretical results under different initial values. Two different initial values are chosen as $x(0)=(0.5,0.3)$ and $x(0)=(-0.1,0.05)$, respectively. By using the control input (8), we can see that the state trajectories converge to the origin asymptotically. The simulation clearly illustrate the exactness of our results.

6. Conclusions

In this paper, the stability problems of nonlinear time-varying mechanical systems have been studied by using strict Lyapunov functions. Control input and sufficient conditions for uniform asymptotical stability have been provided. A numerical example has been presented for illustration.

Acknowledgements

This work is supported by National Natural Science Foundation of China (Grant No. 61603050).

References

1. H. K. Khalil, *Nonlinear Systems* (Upper Saddle River, NJ: Prentice-Hall, 2002).
2. A. Bacciotti and L. Rosier, *Liapunov functions and stability in control theory* (New York: Springer Verlag, 2005).
3. D. Han, A. Guindy and M. Althoff, Estimating the domain of attraction based on the invariance principle, in *Proceedings of the 2016 IEEE Conference on Decision and Control*, (Las Vegas, USA, 2016), pp.5569-5576.
4. N. G. Bretas and L. F. Alberto, Lyapunov function for power systems with transfer conductance: Extension of the invariance principle, *IEEE Transactions on Power Systems*, 18(2) (2003) 769-777.
5. Y. G. Hong, Y. S. Xu and J. Huang, Finite-time control for robot manipulators, *Systems and Control Letters*, 46(4) (2002) 243-253.
6. B. Zhang and Y. M. Jia, On weak-invariance principle for nonlinear switched systems, *IEEE Transactions on Automatic Control*, 59(6) (2014) 1600-1605.
7. M. Malisoff and F. Mazenc, *Constrictions of Strict Lyapunov Functions* (New York: Springer Verlag, 2009).
8. F. Mazenc, Strict Lyapunov functions for time-varying systems, *Automatica*, 41(11) (2005) 1973-1978.
9. P. Giesl and S. Hafstein, Review on computational methods for Lyapunov functions, *Discrete and Continuous Dynamical Systems-Series B*, 20(8) (2015) 2291-2331.
10. B. Zhang, Y. M. Jia, J. P. Du and J. Zhang, Finite-time synchronous control for multiple manipulators with sensor saturations and a constant reference, *IEEE Transactions on Control Systems Technology*, 22(3) (2014) 1159-1165.

Optimizing Control Parameters of Space Robot Manipulator for Pulsar X-ray Interference Measurement

Qiang Chen, Hengbin Zhang, Xiaomin Bei
Qian Xuesen's Lab of Space Technology, Chinese Academy of Space Technology, Beijing, 100190, China

Hanwen Zhang*
Beijing Institute of Control Engineering
104# Youyi Road 104, Haidian district, Beijing, 100190, China
Email:cq_01@sina.com, zhanghengbin@qxslab.cn,beixiaomin@qxslab.cn,hanwen96888@163.com
www.qxslab.cn

Abstract

In paper, a pulsar X-ray observation plan of using two detectors installed in two sides of space station is given. Dynamic model of the space robot manipulators and an adapt control method are described. An orthogonal array experimental design method is developed to optimize the control parameters. Simulations are carried out by L_{81} (3^{40}) orthogonal array while fourteen adaptive control parameters are selected. The optimization results show that the parameters expected value can be acquired and computationally efficiency is improved.

Keywords: Control parameters optimizing, coordinated control, attitude and position control, space robot manipulator, pulsar x-ray measurement.

1. Introduction

Pulsars as sources of X-ray are observed with detect devices in spacecraft[1,2,3]. The time of arrival (TOA) measurement of their periodic pulse could be applied to deep space navigation in future. In 2017 NASA has carried out a test named the Neutron star Interior Composition ExploreR Mission (NICER) with a payload in international space station (ISS) using space robot manipulator to make the detectors point to the pulsars. From the pulsar navigation formula it can be proved that the navigation precision is influenced by the angle position of target pulsars. The measurement precision of pulsar angle position is important and could be greatly improved with intensity interference method by two devices observing a pulsar jointly at the same time[4]. In this paper, a pulsar X-ray observation plan of using two detectors installed in two sides of space station is given. Dynamic model of the space robot manipulators and an adapt control method is described in detail. Two manipulators are used to set the relative attitude and position of two detectors respectively and coordinately while observing jointly. The attitude of two detectors are controlled for pointing to the same pulsar dynamically. And the relative position of two detectors, as the intensity interference baseline ranged from 10m to 100m, should be controlled precisely. In fact, attitude and position control system of the space robot manipulators is nonlinear and uncertain. Some control parameters are not easy to obtain or design precisely, especially the couple parameters, so that it is necessary to acquire the coordinated control system parameters of two manipulators by mathematic test. There was a lot of researchers who studies about the control method for

*Corresponding author

space robot[5,6,7,8], especially Chen[9] has given a control method for space robot with two manipulators and Wang[10] has proposed an adaptive Jacobian control method for free floating space robot. In this paper an orthogonal array experimental (OAE) design method is developed to optimize the parameters. Simulations are carried out by L_{81} (3^{40}) orthogonal array while fourteen adaptive control parameters are selected randomly.

2. The Pulsar X-ray Interference Measurement System

The pulsar X-ray interference measurement system consists of space station, two- joint manipulator B1, two-joint manipulator B2, X-ray detector D1 and X-ray detector D2. Each part is connected by a rotating joint. The system centroid is C, and the centroid of every component is C_i. An inertial coordinate system is established (O-xyz) for the system. The mass of two part of every manipulator are m_{b11}, m_{b12} and m_{b21}, m_{b22}. The moment of inertia are J_{b11}, J_{b12}, J_{b21}, J_{b22}. The mass of two detectors are m_{d1} and m_{d2}, the moment of inertia are J_{d1} and J_{d2}. The vector of the component centroid C_i relative to the origin O of the inertial coordinate system is P_i. The vector of the total centroid C relative to the origin O is Pc, as shown in Fig.1.

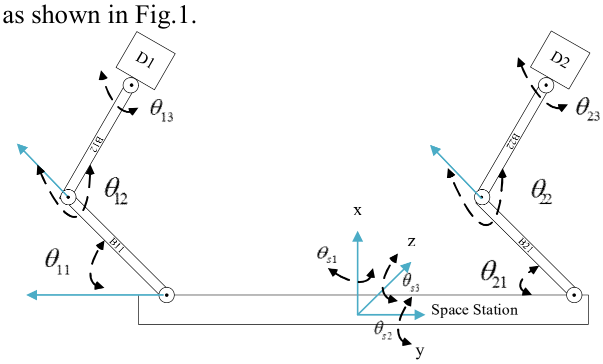

Fig.1. The configuration of pulsar x-ray measurement system

3. Dynamics Model of Two Manipulators Space Robot

Vector q_b is used to describe the attitude of the space station, and q_m is used to describe the angle of the hinge of two manipulators and the attitude of the detector.

$$\begin{aligned} q &= [q_b \quad q_m]^T \\ &= [\theta_{s1} \quad \theta_{s2} \quad \theta_{s3} \quad \theta_{11} \quad \theta_{12} \quad \theta_{13} \quad \theta_{21} \quad \theta_{22} \quad \theta_{23}]^T \end{aligned} \tag{1}$$

The system dynamic equation can be written as Lagrangian form as follows.

$$M(q)\ddot{q} + C(q,\dot{q})\dot{q} = \boldsymbol{\tau} \tag{2}$$

The torque vector $\boldsymbol{\tau}$ is used to represent the actuator input. $\boldsymbol{\tau} \in \mathbf{R}^{3+6}$

Since the space station is free floating with microgravity, the above formula can be separated into two parts.

$$M_{bb}\ddot{\boldsymbol{q}}_b + M_{bm}\ddot{\boldsymbol{q}}_m + C_{bb}\dot{\boldsymbol{q}}_b + C_{bm}\dot{\boldsymbol{q}}_m = 0 \tag{3}$$

$$M_{bm}^{\mathrm{T}}\ddot{\boldsymbol{q}}_b + M_{mm}\ddot{\boldsymbol{q}}_m + C_{mb}\dot{\boldsymbol{q}}_b + C_{mm}\dot{\boldsymbol{q}}_m = \boldsymbol{\tau}_m \tag{4}$$

$M(\boldsymbol{q})$——The total Inertia matrix

$C(\boldsymbol{q},\dot{\boldsymbol{q}})$——Centrifugal force and Coriolis force matrix

$$M(\boldsymbol{q}) = \begin{bmatrix} M_{bb} & M_{bm} \\ M_{bm}^T & M_{mm} \end{bmatrix} \in \mathbf{R}^{9\times 9}$$

$$C(\boldsymbol{q},\dot{\boldsymbol{q}}) = \begin{bmatrix} C_{bb} & C_{bm} \\ C_{mb} & C_{mm} \end{bmatrix} \in \mathbf{R}^{9\times 9}$$

M_{bb}——Inertia matrix of space station, $M_{bm} \in \mathbf{R}^{3\times 6}$

M_{mm}——Inertia matrix of two manipulators, $M_{mm} \in \mathbf{R}^{6\times 6}$

C_{bb}——Centrifugal force and Coriolis force matrix of space station, $C_{bb} \in \mathbf{R}^{3\times 3}$

C_{bm}——Centrifugal force and Coriolis force matrix from space station to two manipulators, $C_{bm} \in \mathbf{R}^{3\times 6}$

C_{mb}——Centrifugal force and Coriolis force matrix from two manipulators to space station, $C_{mb} \in \mathbf{R}^{6\times 3}$

C_{mm}——Centrifugal force and Coriolis force matrix of two manipulators, $C_{mm} \in \mathbf{R}^{6\times 6}$

$\boldsymbol{\tau}_m$——Drive torque of the joint of two manipulators, $\boldsymbol{\tau}_m \in \mathbf{R}^6$

4. The Design of Adaptive Controller

Vector $\boldsymbol{q}_{md} \in \mathbf{R}^6$ is used to describe the desired rotation angle of the manipulators. $\dot{\boldsymbol{q}}_{md}$ is the velocity and $\ddot{\boldsymbol{q}}_{md}$ is the acceleration. $\boldsymbol{q}_{md}$, $\dot{\boldsymbol{q}}_{md}$ and $\ddot{\boldsymbol{q}}_{md}$ are bounded in value. $\dot{\boldsymbol{q}}_{br} \in \mathbf{R}^3$ is the reference angular velocity of space station, and $\dot{\boldsymbol{q}}_{br}(0) = \dot{\boldsymbol{q}}_b(0)$

$$\Delta\boldsymbol{q}_m = \boldsymbol{q}_m - \boldsymbol{q}_{md} \text{ , } \dot{\boldsymbol{q}}_{mr} = \dot{\boldsymbol{q}}_{md} - \beta_0\Delta\boldsymbol{q}_m \tag{5}$$

In the formula, β_0 is a positive constant. Then

$$\ddot{\boldsymbol{q}}_{mr} = \ddot{\boldsymbol{q}}_{md} - \beta_0\Delta\dot{\boldsymbol{q}}_m \tag{6}$$

Assumed that

$$\hat{M}_{bb}\ddot{\boldsymbol{q}}_{br} + \hat{M}_{bm}\ddot{\boldsymbol{q}}_{mr} + \hat{C}_{bb}\dot{\boldsymbol{q}}_{br} + \hat{C}_{bm}\dot{\boldsymbol{q}}_{mr} = K_b(\dot{\boldsymbol{q}}_b - \dot{\boldsymbol{q}}_{br}) \tag{7}$$

In the formula $K_b \in \mathbf{R}^{3\times 3}$ is a symmetric semi-positive matrix.

Definite that $\dot{\boldsymbol{q}}_r = \left[\dot{\boldsymbol{q}}_{br}^{\mathrm{T}} \quad \dot{\boldsymbol{q}}_{mr}^{\mathrm{T}}\right]^{\mathrm{T}}$.

Definite a matrix $\boldsymbol{Y}_b(\boldsymbol{q},\dot{\boldsymbol{q}},\dot{\boldsymbol{q}}_r,\ddot{\boldsymbol{q}}_r)$, $\boldsymbol{Y}_m(\boldsymbol{q},\dot{\boldsymbol{q}},\dot{\boldsymbol{q}}_r,\ddot{\boldsymbol{q}}_r)$ as that

$$\begin{aligned}&\hat{M}_{bb}\ddot{\boldsymbol{q}}_{br}+\hat{M}_{bm}\ddot{\boldsymbol{q}}_{mr}+\hat{C}_{bb}\dot{\boldsymbol{q}}_{br}+\hat{C}_{bm}\dot{\boldsymbol{q}}_{mr}\\&=\boldsymbol{Y}_b(\boldsymbol{q},\dot{\boldsymbol{q}},\dot{\boldsymbol{q}}_r,\ddot{\boldsymbol{q}}_r)a_d\end{aligned} \tag{8}$$

$$\begin{aligned}&M_{bm}^{\mathrm{T}}\ddot{\boldsymbol{q}}_{br}+M_{mm}\ddot{\boldsymbol{q}}_{mr}+C_{mb}\dot{\boldsymbol{q}}_{br}+C_{mm}\dot{\boldsymbol{q}}_{mr}\\&=\boldsymbol{Y}_m(\boldsymbol{q},\dot{\boldsymbol{q}},\dot{\boldsymbol{q}}_r,\ddot{\boldsymbol{q}}_r)a_d\end{aligned} \tag{9}$$

a_d is the unknown dynamic parameter vector of free floating manipulator.
So that the controller is designed as

$$\boldsymbol{\tau}_m=-K_m\boldsymbol{s_m}+Y_m(\boldsymbol{q},\dot{\boldsymbol{q}},\dot{\boldsymbol{q}}_r,\ddot{\boldsymbol{q}}_r)a_d \tag{10}$$

The kinetic parameter update law is selected as

$$\dot{\hat{a}}_d=-\Gamma_d Y^{\mathrm{T}}(\boldsymbol{q},\dot{\boldsymbol{q}},\dot{\boldsymbol{q}}_r,\ddot{\boldsymbol{q}}_r)\boldsymbol{s} \tag{11}$$

In the above formula,

$$\boldsymbol{Y}(\boldsymbol{q},\dot{\boldsymbol{q}},\dot{\boldsymbol{q}}_r,\ddot{\boldsymbol{q}}_r)=[\boldsymbol{Y}_b^{\mathrm{T}}(\boldsymbol{q},\dot{\boldsymbol{q}},\dot{\boldsymbol{q}}_r,\ddot{\boldsymbol{q}}_r)\quad \boldsymbol{Y}_m^{\mathrm{T}}(\boldsymbol{q},\dot{\boldsymbol{q}},\dot{\boldsymbol{q}}_r,\ddot{\boldsymbol{q}}_r)]^{\mathrm{T}}$$

Γ_d is a symmetric positive matrix of appropriate dimension.

$$\boldsymbol{s}=\begin{bmatrix}\boldsymbol{s}_b^{\mathrm{T}} & \boldsymbol{s}_m^{\mathrm{T}}\end{bmatrix}^{\mathrm{T}}=\begin{bmatrix}(\dot{\boldsymbol{q}}_b-\dot{\boldsymbol{q}}_{br})^{\mathrm{T}} & (\dot{\boldsymbol{q}}_m-\dot{\boldsymbol{q}}_{mr})^{\mathrm{T}}\end{bmatrix}^{\mathrm{T}}$$

It can be proved that the tracking errors of free-floating manipulators converges to zero asymptotically by the controller (10) and the parameter update law (11).
When $t\to\infty$， $\Delta\boldsymbol{q}_m\to 0$， $\Delta\dot{\boldsymbol{q}}_m\to 0$

5. System Mathematic Simulations and The Controller Parameters Optimizing

The physical parameters of the space free floating mechanical arm are shown in the following table.

Tab.1 Physical parameters of free-floating space manipulator

	$m_i(kg)$	$I_i(kg\cdot m^2)$	$l_i(m)$	$r_i(m)$
Space Station	59000	2220000	70	15
B11	6.3	1.11909	10	0.72
B12	5.1	0.88128	5	0.71
B21	6.3	1.11909	10	0.72
B22	5.1	0.88128	5	0.71
D1	7.6	0.22800	0.30	0.60
D2	7.6	0.22800	0.30	0.60

According to the data in the above table, the real value of the dynamic parameters of the space manipulator can be calculated.

$$\begin{aligned}a_d&=[13.1746\ 19.3587\ 9.4486\ -1.3261\\&-0.6473\ 77.4449\ 47.1541\ 22.3990]^{\mathrm{T}}\end{aligned}$$

Assumed that initial value of a_d is

$$a_{d0}=[1\ 1\ 1\ 1\ 1\ 160\ 82\ 40]^{\mathrm{T}}$$

The desired rotation angles of the manipulators are

$$q_{md1}(t)=\frac{\pi}{3}(1-\cos(\pi t))$$

$$q_{md2}(t)=\frac{5\pi}{18}(1-\cos(\pi t))$$

Set the Minimum $ITAE=\int_0^T t\left|e(t)\right|dt$ as target performance index.
The controller parameters is $\beta_0=10I$, $K_m=20I$, $K_b=20I$
The simulation results show that the two manipulator can be controlled as expected curves and the parameters expected value can be acquired, as Fig.2, Fig.3, and Fig.4.

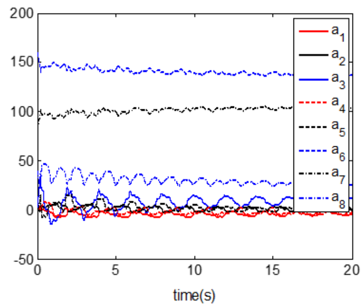

Fig.2. a_d parameter estimating

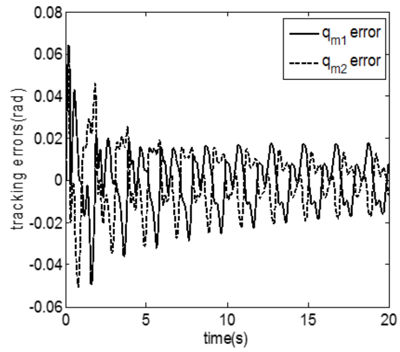

Fig.3. Tracking errors of the manipulator

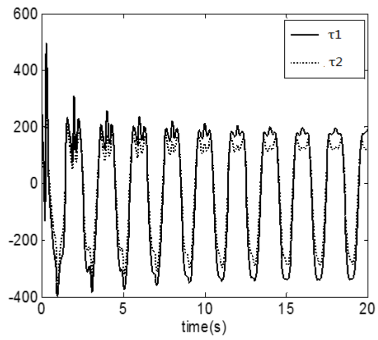

Fig.4. Control moments of the manipulator

Tab.2 Optimized results with orthogonal array design

Parameters	Manipulator 1		Manipulator 2	
	Before optimizing	After optimizing	Before optimizing	After optimizing
β_{01}	5～15	14.9219～15	5～15	5～5.0781
β_{02}	5～15	9.9219～10	5～15	14.9219～15
K_{m1}	15～25	24.9219～25	15～25	24.9219～25
K_{m2}	15～25	24.9219～25	15～25	24.9219～25
K_{b1}	15～25	24.9219～25	15～25	24.9219～25
K_{b2}	15～25	19.9219～20	15～25	24.9219～25
Γ_{d1}	15～25	15～15.0781	15～25	19.9219～20
Γ_{d2}	15～25	15～15.0781	15～25	19.9219～20
Γ_{d3}	15～25	15～15.0781	15～25	18.3594～18.4375
Γ_{d4}	15～25	19.9219～20	15～25	19.9219～20
Γ_{d5}	15～25	17.4219～17.5	15～25	23.0469～23.1250
Γ_{d6}	15～25	24.9219～25	15～25	24.9219～25
Γ_{d7}	15～25	24.9219～25	15～25	24.9219～25
Γ_{d8}	15～25	19.9219～20	15～25	24.9219～25
ITAE MAX	3.612994	0.809579	3.481480	0.909619
ITAE MIN	0.994762	0.797814	1.076619	0.897425

Tab.3 Comparison between optimizing results with orthogonal array experimental method and optimizing on the full scale

	Optimizing with orthogonal array experimental method	Optimizing on the full sacle
Times of ITAE function	81	3^{14}=4782969
loop	7	7
All times	567	33480783

6. Conclusion

From Tab.2 to Tab.3, the optimization results show that the expected value of the parameters are acquired and the test times decreased rapidly in approaching the appropriate value of every control parameter with the orthogonal array experimental design method. The method is useful and effectively to apply to offline optimizing control parameters of complex systems.

Acknowledgements

This work was supported by the National Key Research and Development Program of China (Grant No. 2017YFB0503300, 2017YFB0503304).

References

1. A.G. Lyne, Francis Graham-Smith. *Pulsar Astronomy*. Cambridge University Press.2006.
2. Sheikh. *The use of variable celestial X-ray sources for spacecraft navigation*. University of Maryland.2005.
3. P. Shuai, M. Li, S.L. Chen, Z. Huang. *Principle and method of X-ray pulsar navigation system*. China Aerospace Publishing Press, Beijing, 2009.
4. Q. Chen, S.L. Chen, X.M. Bei, H.W. Zhang, H.B. Zhang. Satellites formation flying for pulsar X-ray interference measurement. *4th IAA conference on Dynamics and Control of Space Systems (DYCOSS2018)*, Changsha，Hunan，China，2018.
5. W. Michael, M. Walker. Adaptive Control of Space-based Robot Manipulators. *IEEE Transactions on Robotics and Automation*. 1992, 7(6):828-835
6. B.L. Ma, W. Huo. *Adaptive control of space robot system. Control theory and the application*，1996，13 (2) ：19l-197.
7. Y.M. Jia. Robust Control with Decoupling Performance for Steering and Traction of 4WS Vehicles under Velocity-Varying Motion. *IEEE Transactions on Control Systems Technology*. 2000(3): 554-569.
8. Y.M. Jia. Alternative Proofs for Improved LMI Representations for the Analysis and the Design of Continuous-Time Systems with Polytopic Type Uncertainty: A Predictive Approach. *IEEE Transactions on Automatic Control*. 2003(8): 1413-1416.
9. L. CHEN，X.T. TANG. Robust Variable Structure Control for Free-floating Space Robot System with Dual-Arms in Joints Space. *Proceedings of the 26th Chinese Control Conference*，Zhangjiajie，Hunan，China，2007.
10. H.L. Wang. Adaptive Jacobian control for robot. *Beijing Institute of Control Engineering*. Beijing, 2009.

Pulse Pose Follow Control and Simulation for a 4-DOF Pulse Diagnosis Robot

Qunpo Liu*, Guanghui Liu, Hongqi Wang, Xianzhe Liu
School of Electrical Engineering and Automation, Henan Polytechnic University, 2001 Century Avenue Jiaozuo, (454003), Henan, P.R.China,

Hanajima Naohiko
College of Information and Systems, Muroran Institute of Technology, 27-1 Mizumoto-cho,Hokkaido Muroran-shi, Hokkaido (050-8585), Japan
E-mail: lqpny@hpu.edu.cn, 211807020075@home.hpu.edu.cn, wanghq2013@yeah.net, 311508070330@home.hpu.edu.cn, hana@mondo.mech.muroran-it.ac.jp
www.hpu.edu.cn, www.muroran-it.ac.jp

Abstract

Pulse diagnosis has been proved to have great practical value in the past dynasties. The key of high-quality pulse diagnosis is how to dynamically adjust the vertical relationship between the pulse and the sensor. The design adopts a four degree of freedom manipulator combined with a matrix sensor to form a diagnostic robot, so as to achieve rapid adjustment and keep the diagnostic pulse sensor perpendicular to the pulse. Kinematics analysis and simulations are performed and the results show feasibility.

Keywords: Pulse diagnosis, robot, follow control, simulation

1. Introduction

For more than two thousand years, pulse diagnosis has played a very important role in the practice of diagnosis and treatment[1]. The theory of pulse diagnosis has been through the physiology, pathology, diagnosis, treatment and other aspects of Chinese medicine. The quality of pulse diagnosis is related to the effect of "syndrome differentiation and treatment" in all clinical departments, which is of great significance to the guidance of TCM theory in medical practice. Since the 1960s, with the development of modern science and technology, many domestic and foreign researchers have been committed to promoting the modernization of TCM pulse diagnosis and expected to improve the situation of "difficult to identify" by using modern medical instruments[2].

2. Composition of the Pulse Diagnosis Robot

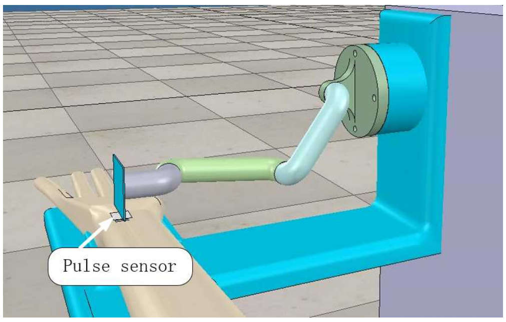

Fig.1 The robot is made up of a four DOF manipulator and a pulse diagnosis sensor matrix.

* Corresponding author

The key of high-quality pulse diagnosis is how to dynamically adjust the vertical relationship between the pulse and the sensor (only the vertical relation between sensor and pulse can guarantee accuracy of pulse diagnosis). The robot is made up of a four degree of freedom (DOF) manipulator and a pulse diagnosis sensor matrix, as shown in Fig.1 and Fig.2.

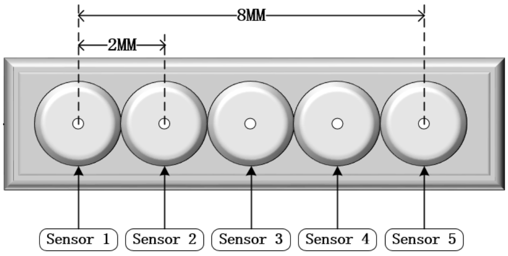

Fig.2 The pulse diagnosis matrix sensor is composed of 5 pressure sensors in a row. The matrix sensors are fitted on the end of the manipulators.

3. Kinematics of the Four DOF Manipulator

According to the standard D-H parameter table method, the coordinate system of the manipulators as shown in Fig.3. The coordinate system 1 is coincide with the origin of the base coordinate system 0, and the origin of the coordinate system of the pulse sensor coincides with the origin of the wrist coordinate system. The D-H parameters are obtained as shown in Tab.1.

The length of the connecting rod is a_i: the distance from the Z_{i-1} axis to the Z_i axis is moved along the X_i axis. The angle of the connecting rod is α_i: the angle of rotation of the Z_{i-1} axis to the Z_i axis around the X_i axis. Connecting rod offset d_i: along the Z_{i-1} axis, the distance between the X_{i-1} axis and the Xi axis is moved. Joint angle θ_i: around the Z_{i-1} axis, rotate the X_{i-1} axis to the angle of the X_i axis.

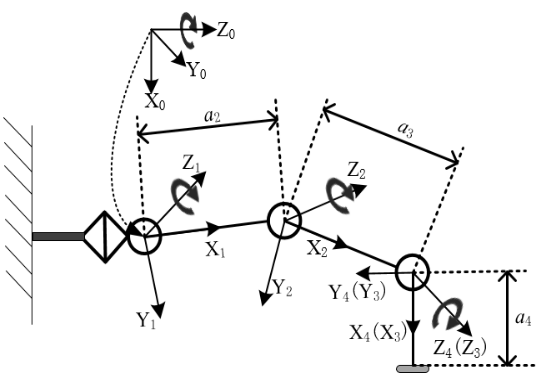

Fig.3 Manipulators structure and its coordinate systems of joints.

3.1. *Forward kinematics of the manipulator*

Tab.1 Parameters of D-H

i	α_i	a_i	d_i	θ_i
1	$-\pi/2$	0	0	θ_1
2	0	a_2	0	θ_2
3	0	a_3	0	θ_3
4	0	0	0	θ_4

According to the standard D-H parameter method, the general equation of the link homogeneous transformation matrix is:

$$ {}^{i-1}_{i}T = \begin{bmatrix} c\theta_i & -c\alpha_i s\theta_i & s\alpha_i s\theta_i & a_i c\theta_i \\ s\theta_i & c\alpha_i c\theta_i & -s\alpha_i c\theta_i & a_i s\theta_i \\ 0 & s\alpha_i & c\alpha_i & d_i \\ 0 & 0 & 0 & 1 \end{bmatrix} \tag{1} $$

Where, c=cos, s=sin.

From the Eq. (1) and the established D-H parameter table, the homogeneous transformation matrix equation of each adjacent joint can be obtained:

$$ {}^{0}_{4}T = {}^{0}_{1}T\,{}^{1}_{2}T\,{}^{2}_{3}T\,{}^{3}_{4}T = \begin{bmatrix} c_1c_{234} & -c_1s_{234} & -s_1 & a_3c_1c_{23}+a_2c_1c_2 \\ s_1c_{234} & -s_1s_{234} & c_1 & a_3s_1c_{23}+a_2s_1c_2 \\ -s_{234} & -c_{234} & 0 & -a_3s_{23}-a_2s_2 \\ 0 & 0 & 0 & 1 \end{bmatrix} \tag{2} $$

Where, $c_{234} = \cos(\theta_2+\theta_3+\theta_4)$, and the others are similar.

3.2. *Inverse kinematics of the manipulator*

The common methods of inverse kinematics solving are mainly include algebraic method and geometric method[3]. Compared with the algebraic method, the geometric method have advantages of simple calculation and avoids the discussion of range of values by using the constraint relationship between the joints[4]. In this paper, the inverse kinematics of the 4-DOF pulse diagnosis robot is solved by geometric method.

Before solving the kinematics with the geometric method, the first rule is that θ_1 has rotated to a position parallel to the target position. According to the establishment rule of D-H, it can be obtained of the schematic diagram of the plane based on the geometric method as shown in Fig.4.

Assume that the position coordinates (x_p, y_p) of the end point P and the azimuth angle γ of the point P are known. According to the geometric relation, it can be obtained:

$$x_{o3} = x_p - a_4 \cos\gamma \tag{3}$$

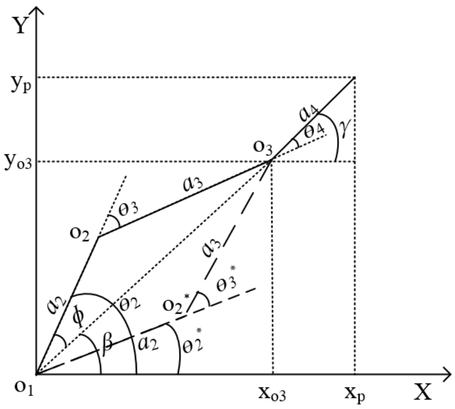

Fig.4 Geometric relationship of three joints in XY plane

$$y_{o3} = y_p - a_4 \sin\gamma \tag{4}$$

By using the cosine theorem in $\triangle o_1o_2o_3$, it can be draw that:

$$\theta_3 = \arccos\frac{\left(x_{o3}^2 + y_{o3}^2 - a_2^2 - a_3^2\right)}{2a_2a_3} \tag{5}$$

$$\theta_2 = \arctan\left(\frac{y_{o3}}{x_{o3}}\right) \pm \frac{x_{o3}^2 + y_{o3}^2 + a_2^2 + a_3^2}{2a_2\sqrt{x_{o3}^2 + y_{o3}^2}} \tag{6}$$

$$\theta_4 = \gamma - \theta_2 - \theta_3 \tag{7}$$

4. Modeling and Simulation

4.1. *Modeling in V-REP*

The robot model is established in V-REP as shown in Fig.1. Set the parameters of the robot model: $a_2 = 0.08$ m, $a_3 = 0.1$ m, $a_1 = -90$ °. The initial posture of the robot can be calculated by assigning the Angle of each joint to 0°:

$${}^{0}_{4}T_{\text{initial position}} = \begin{bmatrix} 1 & 0 & 0 & 0.18 \\ 0 & 0 & 1 & 0 \\ 0 & -1 & 0 & 0 \\ 0 & 0 & 0 & 1 \end{bmatrix} \tag{8}$$

This data is identical to the data obtained in the v-rep simulation.

The pulse diagnosis matrix sensor adopted in this simulation is composed of 5 pressure sensors in a row,

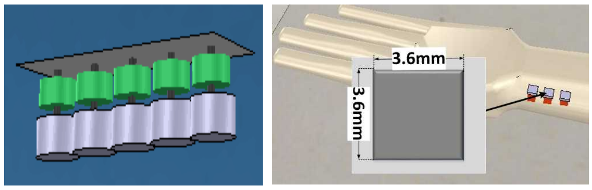

(a) Pulse sensor model (b) Pulse model

Fig.5 Pulse sensor and pulse model in V-REP

which is shown in Fig.5 (a). Each point of the sensors can sense the corresponding pulse. In the simulation, the pulse sensor is exposed to the pulse at different positions to obtain the simulation data. By analyzing these data, the relative pose of sensors with respect to the pulse can be drawn, which will be used to adjust the posture of the joints.

Pulse model is also established with similar dynamic properties to the human pulse, as shown in Fig.5 (b). The width of the pulse model is set as 3.6 *3.6mm^2 according to average adult's size.

4.2. *Pulse detect simulation*

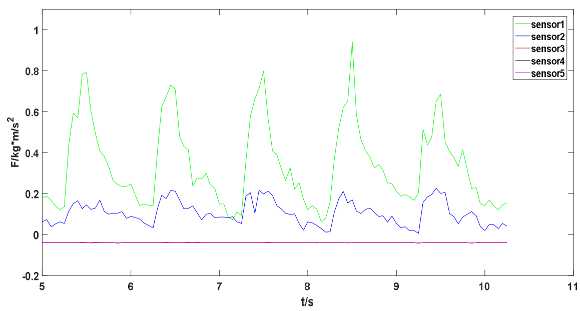

Fig.6 The first sensor is aligned with the pulse

In the V-REP simulation, the pulse beat curve at different positions is measured with changing the relative position of the pulse matrix sensor relative to the pulse model. When the first sensor of the pulse matrix sensor is aligned with the pulse model, the pulse curve obtained is shown in Fig.6. It is very obvious from the figure that the value of sensor 1 is the largest, and the center of the pulse matrix sensor is not perpendicular to the pulse model.

When the third sensor of the pulse matrix sensor is aligned with the pulse model, the pulse curve is shown in Fig.7. It is clear that the intensity of sensor 2, sensor 3 and sensor 4 are same to each other. When the curve similar to Fig.8 is obtained, the pulse matrix sensor can be considered as perpendicular to the pulse, and the third sensor is aligned with the pulse.

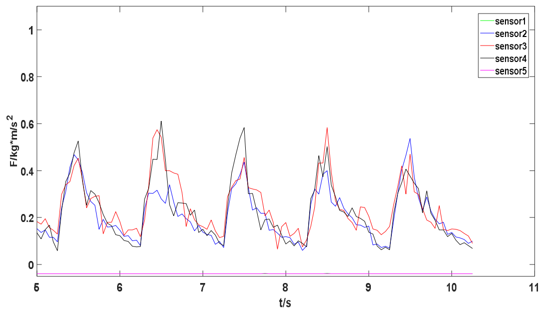

Fig.7 Beating curves of sensors when the third sensor is aligned with the pulse

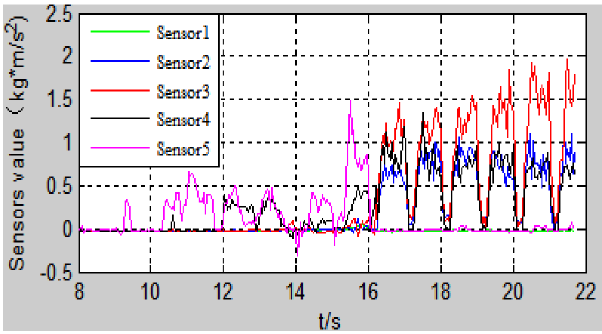

Fig.8 Curve change of each sensor point during pulse pose following control

4.3. *Pulse pose follow control simulation*

Fig.8 shows that the posture curves of the pulse sensors. The values changes related to the relative position between sensors and the pulse, until the matrix sensor is perpendicular to the pulse, and sensor3 is aligned with the pulse. Fig.9 shows that the joints were adjusted to move from sensor5 to sensor3, and finally sensor3 is perpendicular to the pulse as expected.

5. Conclusion

In this paper, a diagnostic robot with a four degree of freedom manipulator and a pulse diagnosis matrix sensor is introduced. The kinematic was analyzed and the model is simulated on V-REP. Simulation results show that the proposed robot can find the position of pulse, and adjust the joints to the posture as expected according to the feedback information from the pulse diagnosis matrix sensor.

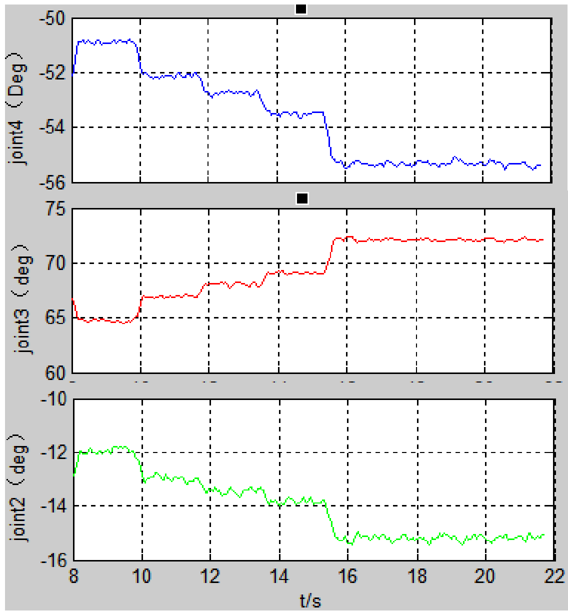

Fig.9 Curve change of θ_2, θ_3 and θ_4 during pulse pose following control

Acknowledgement

This work is partially supported by Innovation Scientists and Technicians Troop Construction Projects of Henan Province (Grant No. CXTD2016054).

References

1. Y. Zhang, H.Y. Wang, Z.l. Lv, Q. Zhang, C.M. Jia, Y. Wang. Research on automatic identification system of traditional Chinese medicine *constitution based on pulsewave. Modernization of Traditional Chinese Medicine and Materia Medica-World Science and Technology (J.)*. 19(10) (2017) 1687-1691.
2. H. Chang and JX. Chen. Piezoelectric pulse diagnosis transducer of 9x9 sensing arrays and pulse signal processing, in *Proc. Int. Conf. Applied Informatics and Communication (2011).*
3. Ghosal A. *Manipulator Kinematics.* (In: Nee A. (eds) Handbook of Manufacturing Engineering and Technology. Springer, London 2015).
4. W.l. Li and N. Li, Kinematics analysis and inverse kinematics solution of a 5-DOF manipulator, *Mechatronics (J.).* 23(11) (2017) 3-7&14.

A New Adaptive Control System Design Method Based on Neural Network Prediction

Weicun Zhang*, Sufang Wang, Yongnan Jia, Qing Li
School of Automation and Electrical Engineering, University of Science and Technology Beijing
30 Xueyuan Road, Haidian District, Beijing, China
E-mail: weicunzhang@ustb.edu.cn, s20170610@xs.ustb.edu.cn
www.ustb.edu.cn

Abstract

In this paper, a new control system design method is proposed, in which, the controller is designed according to a model with un-modeled uncertainties, an artificial neural network (error back propagation neural network) was adopted to predict the model output error, and the predicted model output error is considered in the control law. This control system design can be used to both linear and non-linear systems. The simulation results verified the effectiveness of the proposed method.

Keywords: Adaptive control, BP artificial neural network prediction, linear and non-linear.

1. Introduction

Many contributions have been made to adaptive control[1-4]. But there are still some problems in this important control field, such as, for a general nonlinear system, it is difficult to design an adaptive controller with guaranteed stability and performances[5-8]. In this paper, we present a new frame as a trial to address the problem. In this frame, a simple self-tuning or non-adaptive controller and an artificial neural network are adopted to form a parallel adaptive control system, as shown in Figure 1.

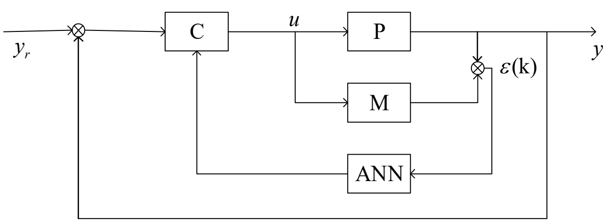

Fig. 1 The parallel adaptive control system structure

In Fig. 1, y_r is reference input of system, y is output value of system, C is controller, P is controlled plant, M is system model, ANN is an Artificial Neural Network. ε(k) is the difference between the output value of the controlled plant and the output value of the model, which is called model output error or parameter tracking error.

2. The Details of the Controller

Consider a plant to be controlled

$$A(q^{-1})y(t) = q^{-d}Bu(t) + C(q^{-1})e(t) \tag{1}$$

where

$$\begin{cases} A(q^{-1}) = 1 + a_1 q^{-1} + \cdots + a_n q^{-n} \\ B(q^{-1}) = b_0 + b_1 q^{-1} + \cdots + b_m q^{-m} \\ C(q^{-1}) = 1 + c_1 q^{-1} + \cdots + c_l q^{-l} \\ d \geq 1, b_0 \neq 0 \end{cases} \tag{2}$$

Suppose we have the following on-line estimated model

*Corresponding author.

$$A_m(q^{-1})y(t) = q^{-d}B_m u(t) + C_m(q^{-1})e(t) \quad (3)$$

According to this model, we can design a minimum variance controller to minimize

$$J = E\{[y(k) - y_r(k)]^2\}$$

Set

$$C_m(q^{-1}) = A_m(q^{-1})F(q^{-1}) + q^{-d}G(q^{-1}) \quad (4)$$

Where

$$\begin{cases} F(q^{-1}) = 1 + f_1 q^{-1} + \cdots + f_{d-1}q^{-d+1} \\ G(q^{-1}) = g_0 + g_1 q^{-1} + \cdots + g_{n-1}q^{-n+1} \end{cases} \quad (5)$$

Then we obtain

$$y_m(k+d) = \frac{Gy(k) + B_m Fu(k)}{C_m} + Fe(k+d) \quad (6)$$

Accordingly, we get the optimal prediction

$$y_m(k+d/k) = \frac{G}{C_m}y(k) + \frac{B_m F}{C_m}u(k) \quad (7)$$

Then we have the control law

$$u(k) = \frac{-G}{FB_m}y(k) + \frac{C_m}{FB_m}y_r(k+d) \quad (8)$$

Next, we consider a general case, i.e. to control an arbitrary non-linear plant, then there must exists an error signal:

$$\varepsilon(k) = y(k) - y_m(k) \quad (9)$$

Then we have

$$y(k+d/k) = y_m(k+d/k) + \varepsilon(k+d/k) \quad (10)$$

Accordingly the control law (8) can be modified by

$$u(k) = \frac{-G}{FB_m}y(k) + \frac{C_m}{FB_m}[y_r(k+d) - \varepsilon(k+d/k)] \quad (11)$$

Generally speaking, $\varepsilon(k+d/k)$ can be obtained by any methods, in this paper, we give two approaches to generate $\varepsilon(k+d/k)$ and we will give the simulation result with BP neural network prediction approach.

3. Simulation Results

In this section we first consider the case where the difference between the system output and the model output is a stationary time series. In this case, an adaptive prediction model can be established. The model can be in the form of an AR model or an ARMA model.

The following is described in conjunction with a specific controlled object and a corresponding parallel adaptive control system. Consider the following plant:

$$\begin{aligned} &y(t) - 1.5y(t-1) + 0.3y(t-2) + 0.04y(t-3) \\ &= u(t-1) + 0.5u(t-2) + e(t) + 0.4e(t-1) + d(t) \end{aligned} \quad (12)$$

Where e(t) is white noise with a zero mean and a variance of 0.01; d(t) is a constant interference, taken $d(t) = 1$. Using low-order modeling:

$$\begin{cases} \deg A_m(q^{-1}) = 2 \\ \deg B_m(q^{-1}) = 1 \\ \deg C_m(q^{-1}) = 0 \end{cases} \quad (13)$$

The prediction model is taken as the AR(2) model:

$$\varepsilon(k) = l_1\varepsilon(k-1) + l_2\varepsilon(k-2) + e(k) \quad (14)$$

In the two parts, the parameters of the model are estimated by recursive least square method.

$$\begin{cases} \hat{\theta}_1(t) = \hat{\theta}_1(t-1) + P_1(t)\varphi_1(t)\left[y(t) - \varphi_1^T(t-1)\hat{\theta}_1(t-1)\right] \\ P_1(t)\varphi_1(t) = P_1(t-1)\varphi_1(t)\left[1 + \varphi_1^T(t)P_1(t-1)\varphi_1(t)\right]^{-1} \\ P_1(t) = \left[1 - P_1(t)\varphi_1(t)\varphi_1^T(t)\right]P_1(t-1) \end{cases}$$

$$\theta_1^T = [-a_1, \cdots, -a_n, b_0, b_1, \cdots, b_m]$$

$$\varphi_1^T(t) = [y(t-1), y(t-2), \cdots, y(t-n), \cdots, u(t-m)]$$

$$\begin{cases} \hat{\theta}_2(t) = \hat{\theta}_2(t-1) + P_2(t)\varphi_2(t)\left[\varepsilon(t) - \varphi_2^T(t-1)\hat{\theta}_2(t-1)\right] \\ P_2(t)\varphi_2(t) = P_2(t-1)\varphi_2(t)\left[1 + \varphi_2^T(t)P_2(t-1)\varphi_2(t)\right]^{-1} \\ P_2(t) = \left[1 - P_2(t)\varphi_2(t)\varphi_2^T(t)\right]P_2(t-1) \end{cases}$$

$$\theta_2^T = [l_1, l_2]$$

$$\varphi_2^T(t) = [\varepsilon(t-1), \varepsilon(t-2)]$$

Control strategy is developed as follows:

$$u(k) = -\frac{G(q^{-1})}{FB_m} y(k) + \frac{C_m}{FB_m} \left[y_r(k+d) - \varepsilon(k+d/k) \right]$$

Secondly, a three-layer B-P neural network can be used to approximate any continuous function as long as there are enough hidden layer nodes. The structure of the three-layer B-P neural network is shown in Fig. 2.

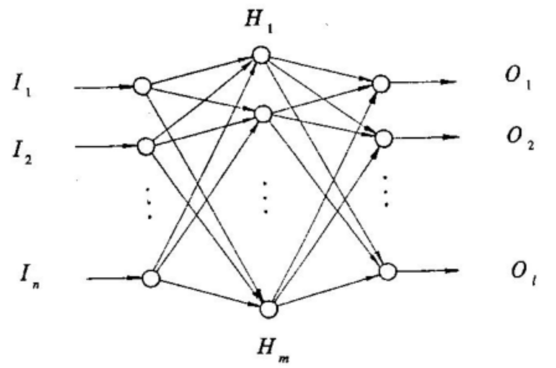

Fig. 2 The structure of B-P neural network

Then, when we consider controlling a complex non-line ar system, we may use a B-P neural network to predict $\varepsilon(k+d/k)$

In the formula (12), consider $d(\mathrm{t}) = 0.2\sin(0.5\,\mathrm{t})$, reference input $y^*(\mathrm{t}) = 1$, neural network parameters are selected as the following:

Input node 20
Hidden layer node 10
Output layer node 3

The initial weights are set as random numbers whose absolute values are selected less than 0.3.

The first 80 steps of the system are used to train the neural network, and then to start the prediction. The simulation result is shown in Fig. 3. If the noise item in the formula (12) is removed, the simulation effect is shown in Fig. 4. From the simulation results, it can be seen that the effect of the neural network prediction is significant.

From the simulation results (especially the result of Fig. 4), it can be seen that the system performance using the parallel adaptive scheme based on neural network prediction is significantly improved compared to system performance of the traditional adaptive (minimum variance self-tuning) scheme.

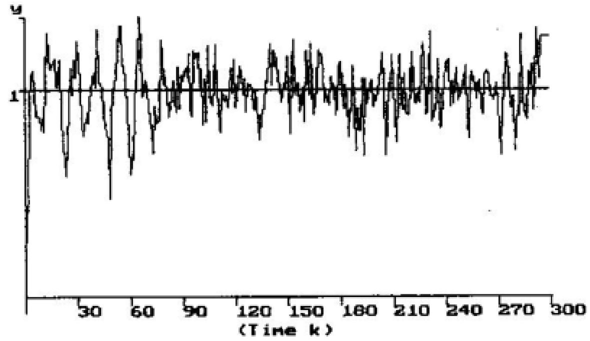

Fig. 3 Simulation result of B-P neural network prediction (plant with noise)

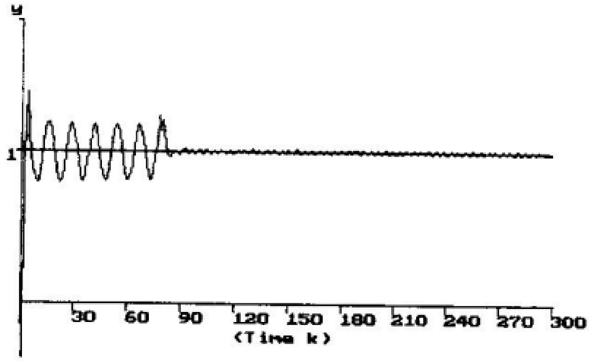

Fig. 4 Simulation result of B-P neural network prediction (plant without noise)

4. Conclusions

In this paper, a new adaptive control system design method based on time series prediction or B-P neural network prediction is proposed to expand the capability of adaptive control. From the effects of simulation experiments, the use of neural network predictors can effectively suppress nonlinear interference, thereby improving the performance of the adaptive control system.

Acknowledgements

This work was partly supported by National Natural Science Foundation of China (No. 61520106010; 61741302).

References

1. Z. D. Yuan, Adaptive Control Theory and Its Application, East China Normal University Press, Shanghai, (1988).
2. R. H. Middleton, G. C. Goodwin, D. J. Hill and D. Q. Mayne, Design issues in adaptive control, IEEE Transactions on Automatic Control (Volume: 33, Issue: 1, Jan. 1988), pp. 50-58
3. C. C. Fu, H. Khalil, Adaptive control of nonlinear systems using neural networks, International Journal of Control, 55(6), (1992) pp. 1299-1317.
4. K. S. Narendra, S. Mukhopadhyay Adaptive control using neural networks and approximate models, Neural Networks IEEE Transactions on, 1997, 8(3), pp.475-485.
5. P. V. Kokotovic, Adaptive Control Design and Analysis., Wiley-Interscience [John Wiley &Sons], Hoboken, NJ, 60(3)(2003) 211.
6. Bar Kana I, Parallel feed-forward and simplified adaptive contro, International Journal of Adaptive Control & Signal Processing, 1(2), (2010) 95-109.
7. Alvarez - Ramírez J, Adaptive control of feedback linearizable systems: amodelling error compensation approach, International Journal of Robust & Nonlinear Control,9(6), (2015) 361-377.
8. L. Xing, C. Wen and H. Su, A new adaptive control scheme for uncertain nonlinear systems with quantized input signal, Journal of the Franklin Institute,352(12), (2015) 5599-5610.

Mean-Square Quasi-Composite Rotating Formation Control of Second-Order Multi-Agent Systems under Stochastic Communication Noises

Lipo Mo, Xiaolin Yuan
School of Science, Beijing Technology and Business University, Beijing, 100048, China

Yingmin Jia*
The Seventh Research Division and the Center for Information and Control, School of Automation Science and Electrical Engineering, Beihang University (BUAA), 37 Xueyuan Road, Haidian District, Beijing, 100191, China

Shaoyan Guo
School of Intelligent Engineering, South China University of Technology, Guangzhou, 510641, China
E-mail: beihangmlp@126.com, 1171681540@qq.com, ymjia@buaa.edu.cn, sanj8023@163.com
www.btbu.edu.cn, www.buaa.edu.cn, www.scut.edu.cn

Abstract

This paper mainly concerns the mean-square quasi-composite rotating formation problem of second-order multi-agent systems (MASs) with stochastic communication noises. Firstly, the definition of mean-square quasi-composite rotating formation is proposed. Afterwards, a distributed control protocol with time-varying control gains is designed. And then, the origin closed-loop system is changed into an equivalent closed-loop system by taking coordinate transformation. Under some mild assumptions, sufficient conditions are deduced. Eventually, numerical simulations are provided to confirm the effectiveness of the proposed theoretical results.

Keywords: Quasi-composite, rotating formation, multi-agent systems, stochastic communication noises.

1. Introduction

Over the past few decades, distributed coordination control of MASs is a research focus and attracts lots of attentions from various of fields, such as Refs. 1, 2. It is common to find that there always exist lots of collective motions in nature, such as the distributed formation flight of satellites around the moon while the moon moving around the earth. Meanwhile, groups of agents may be required to maintain desired formation during this process. Recently, to imitate or explain such kinds of motions, the collective rotating motions[3-5], composite-rotating consensus[6] and formation control[7] of second-order MASs were investigated. Moreover, notice that the communications among different agents may be interfered by stochastic communication noises in reality, it is necessary to design proper control protocol such that the stochastic communication noises can be countered, and numerous of good results have been reported[8, 9]. However, up to date, it is a pity to find that there is no

*Corresponding author.

result on composite-rotating formation control of MASs with stochastic communication noises.

Motivated by the above discussions, the mean-square quasi-composite rotating formation control of second-order MASs with stochastic communication noises is considered in this paper, by using which the actual physical system can be described more precisely. In contrast with Ref. 10, where the quasi-composite rotating formation control of MASs was solved without communication noises, the results of this paper are more realistic. Besides, the definition of the mean-square quasi-composite rotating formation of MASs is first proposed. Moreover, a novel distributed control protocol by local information with a time-varying control gain is designed, by using which the stochastic communication noises can be attenuated, and all agents will surround a moving point with a desired structure and a constant angular velocity $\omega_1 > 0$ while the moving point surrounds the origin with a constant angular velocity $\omega_2 > 0$ asymptotically. Finally, the theories of stochastic differential equation and proper coordination transformation are used to prove that under some mild conditions, the desired formation can be achieved.

2. Preliminaries

Theories of algebraic graph[11]. Let $(\mathcal{V}, \varepsilon, \mathcal{A})$ be an undirected graph with n nodes, $\mathcal{V} = \{1,2,\ldots n\}$ represents the set of nodes, and $\varepsilon \subseteq \mathcal{V} \times \mathcal{V}$ represents the set of edges. $\mathcal{A} = [a_{ij}]$ represents the weighted adjacency matrix. Let $N_i = \{j \in \mathcal{V}: (j,i) \in \varepsilon\}$ denotes the neighbors set of node i, $\mathcal{L} = [l_{ij}]$ denotes the Laplacian of graph $\mathcal{G}$. Graph $\mathcal{G}$ is said to be connected if there exists a path between every two distinct nodes.

Lemma 1. [12] *If $\mathcal{G}$ is a connected undirected graph, then the Laplacian $\mathcal{L}$ of $\mathcal{G}$ has a simple zero eigenvalue, and $\mathbf{1}_n$ is the corresponding eigenvector. Additionally,*

$$0 = \lambda_1(\mathcal{L}) \le \lambda_2(\mathcal{L}) \le \cdots \le \lambda_n(\mathcal{L}).$$

3. Model and Problem Statement

Consider a multi-agent system with n agents, the dynamics of each agent are given as follows:

$$\dot{r}_i(t) = \tilde{v}_i(t), \tag{1}$$

$$\dot{\tilde{v}}_i(t) = u_i(t), \tag{2}$$

where $i = 1,2\ldots,n$, vectors $r_i(t) \in \mathbb{C}, \tilde{v}_i(t) \in \mathbb{C}, u_i(t) \in \mathbb{C}$ respectively denotes the position, velocity and control input of the ith agent.

4. Main Results

In this section, the mean-square quasi-composite rotating formation control of MASs (1) and (2) is investigated.

Let $v_i(t) = \frac{\omega_1}{\omega_1+\omega_2}(\tilde{v}_i(t) + j\omega_2 r_i(t))$, $c_i(t) = r_i(t) + j\omega_1^{-1}v_i(t)$, $i = 1,2\ldots,n$ denotes the relative velocity and the center of the rotation of the ith agent respectively.

Suppose that the information exchange among the agents is affected by the stochastic communication noises. The information of the ith agent received from its neighbor agents is defined as follows:

$$\begin{pmatrix} Y_{rik}(t) \\ Y_{\tilde{v}ik}(t) \end{pmatrix} = \begin{pmatrix} r_k(t) + \sigma_{rik}\eta_{rik} \\ \tilde{v}_i(t) + \sigma_{\tilde{v}ik}\eta_{\tilde{v}ik} \end{pmatrix}, \tag{3}$$

where $k \in N_i$, $\{\eta_{rik}, \eta_{\tilde{v}ik}\}$, $i,k = 1,2\ldots,n$ are independent standard white noises, $\{\sigma_{rik}, \sigma_{\tilde{v}ik}\}$ are the finite noise intensities.

Definition 1. *Let $h = (h_1, h_2, \ldots, h_n)^T = (\rho_1 e^{j\theta_1}, \rho_2 e^{j\theta_2}, \ldots, \rho_n e^{j\theta_n})^T \in \mathbb{C}^n$ denotes the desired formation, where $\rho_i > 0, \theta_i \in [0,2\pi)$, $i = 1,2\ldots,n$. The MASs (1) and (2) are said to achieve mean-square quasi-composite rotating formation if for each $i,k = 1,2\ldots,n$.*

$$\lim_{t\to+\infty} \mathrm{E}\|c_i(t) - c_k(t)\|^2 = 0, \tag{4}$$

$$\lim_{t\to+\infty} \mathrm{E}\left\|\frac{v_i(t)}{\rho_i e^{j\theta_i}} - \frac{v_k(t)}{\rho_k e^{j\theta_k}}\right\|^2 = 0, \tag{5}$$

$$\lim_{t\to+\infty} \mathrm{E}\|\dot{v}_i(t) - j\omega_1 v_i(t)\|^2 = 0, \tag{6}$$

$$\lim_{t\to+\infty} \mathrm{E}\|\dot{c}_i(t) + j\omega_2 c_i(t)\|^2 = 0, \tag{7}$$

and $\lim_{t\to+\infty} Var[r_i(t)] < \infty$, $\lim_{t\to+\infty} Var[v_i(t)] < \infty$, *for given* $\omega_1 > 0$ *and* $\omega_2 > 0$.

In this paper, the following distributed control protocol is proposed:

$$\begin{aligned} u_i(t) &= j(\omega_1 - \omega_2)\tilde{v}_i(t) - \omega_1\omega_2 r_i(t) \\ &-a(t)\sum_{k\in N_i} a_{ik}[r_i(t) - Y_{rik}(t) + j\omega_1^{-1}(\tilde{v}_i(t) - Y_{\tilde{v}ik}(t))] \\ &-a(t)\sum_{k\in N_i} a_{ik}[\tilde{v}_i(t) - \frac{\rho_i}{\rho_k}e^{j(\theta_i-\theta_k)}Y_{\tilde{v}ik}(t) + j\omega_2(r_i(t) \\ &-\frac{\rho_i}{\rho_k}e^{j(\theta_i-\theta_k)}Y_{rik}(t))], \end{aligned} \tag{8}$$

where $a(t) > 0$ is the time-varying consensus control gain. To continue, we need the following assumptions.

Assumption 1. *The communication topology graph $\mathcal{G}$ is connected.*

Assumption 2. $\sum_{i=1}^n \rho_i e^{j\theta_i} \ne 0$ *when* $|\theta_i - \theta_k| = 0$ *or* $|\theta_i - \theta_k| = \pi$, $i,k = 1,2\ldots,n$.

Assumption 3. [8] $\int_0^\infty a(s)ds = \infty$.

Assumption 4.[8] $\int_0^\infty a^2(s)ds < \infty$.

Combining the above equations, then we arrive at

$$\begin{aligned}\dot{v}_i(t) &= j\omega_1 v_i(t) - a(t)\sum_{k\in N_i} a_{ik}[c_i(t)-c_k(t)] \\ &-a(t)\sum_{k\in N_i} a_{ik}\left[v_i(t)-\frac{\rho_i}{\rho_k}e^{j(\theta_i-\theta_k)}v_k(t)\right] \\ &+\frac{a(t)}{1+\omega_1^{-1}\omega_2}\sum_{k\in N_i} a_{ik}\left[(1+j\omega_2\frac{\rho_i}{\rho_k}e^{j(\theta_i-\theta_k)})\sigma_{rik}\eta_{rik}\right] \\ &+\frac{a(t)}{1+\omega_1^{-1}\omega_2}\sum_{k\in N_i} a_{ik}\left[(j\omega_1^{-1}+\frac{\rho_i}{\rho_k}e^{j(\theta_i-\theta_k)})\sigma_{\tilde{v}ik}\eta_{\tilde{v}ik}\right]\end{aligned} \tag{9}$$

$$\begin{aligned}\dot{c}_i(t) &= -j\omega_2 c_i(t) - j\omega_1^{-1}a(t)\sum_{k\in N_i} a_{ik}[c_i(t)-c_k(t)] - j\omega_1^{-1}a(t)\sum_{k\in N_i} a_{ik}\left[v_i(t)-\frac{\rho_i}{\rho_k}e^{j(\theta_i-\theta_k)}v_k(t)\right] \\ &+\frac{j\omega_1^{-1}a(t)}{1+\omega_1^{-1}\omega_2}\sum_{k\in N_i} a_{ik}\left[(1+j\omega_2\frac{\rho_i}{\rho_k}e^{j(\theta_i-\theta_k)})\sigma_{rik}\eta_{rik}\right] \\ &+\frac{j\omega_1^{-1}a(t)}{1+\omega_1^{-1}\omega_2}\sum_{k\in N_i} a_{ik}\left[(j\omega_1^{-1}+\frac{\rho_i}{\rho_k}e^{j(\theta_i-\theta_k)})\sigma_{\tilde{v}ik}\eta_{\tilde{v}ik}\right]\end{aligned} \tag{10}$$

Let $\delta(t) = (v_1(t), c_1(t), \dots, v_n(t), c_n(t))^T$, then the closed-loop system (9) and (10) can be rewritten as

$$\dot{\delta}(t) = \big(I_n\otimes A + a(t)\tilde{\mathcal{L}}\otimes B_1 + a(t)\mathcal{L}\otimes B_2\big)\delta(t) + a(t)\Omega\eta, \tag{11}$$

where $A = \begin{pmatrix} j\omega_1 & 0 \\ 0 & -j\omega_2\end{pmatrix}$, $B_1 = \begin{pmatrix} -1 & 0 \\ -j\omega_1^{-1} & 0\end{pmatrix}$, $B_2 = \begin{pmatrix} 0 & -1 \\ 0 & -j\omega_1^{-1}\end{pmatrix}$, $\tilde{\mathcal{L}} = F^{-1}H\mathcal{L}H^{*}F^{-1}$, $F = \mathrm{diag}\{\rho_1,\dots,\rho_n\}$, $H = \mathrm{diag}\{e^{j\theta_1},\dots,e^{j\theta_n}\}$, $\eta = (\eta_1^T,\dots,\eta_n^T)^T \in \mathbb{C}^{2n^2}$, where $\eta_i = (\sigma_{ri1},\sigma_{\tilde{v}i1},\dots,\sigma_{rin},\sigma_{\tilde{v}in})^T \in \mathbb{C}^{2n}$, $\Omega = \mathrm{diag}\{\Omega_1,\dots,\Omega_n\} \in \mathbb{C}^{2n\times 2n^2}$, $\Omega_i =$

$$\frac{\omega_1}{\omega_1+\omega_2}\left(a_{i1}\begin{pmatrix}\frac{\rho_1+j\omega_2\rho_i e^{j(\theta_i-\theta_1)}}{\rho_1} & \frac{j\omega_1^{-1}\rho_1+\rho_i e^{j(\theta_i-\theta_1)}}{\rho_1} \\ \frac{j\rho_1-\omega_2\rho_i e^{j(\theta_i-\theta_1)}}{\omega_1\rho_1} & \frac{-\omega_1^{-1}\rho_1+j\rho_i e^{j(\theta_i-\theta_1)}}{\omega_1\rho_1}\end{pmatrix}, \dots, a_{in}\begin{pmatrix}\frac{\rho_n+j\omega_2\rho_i e^{j(\theta_i-\theta_n)}}{\rho_n} & \frac{j\omega_1^{-1}\rho_n+\rho_i e^{j(\theta_i-\theta_n)}}{\rho_n} \\ \frac{j\rho_n-\omega_2\rho_i e^{j(\theta_i-\theta_n)}}{\omega_1\rho_n} & \frac{-\omega_1^{-1}\rho_n+j\rho_i e^{j(\theta_i-\theta_n)}}{\omega_1\rho_n}\end{pmatrix}\right),$$

$i = 1,2\dots,n$.

Lemma 3. *Under Assumptions 1, 2, $\tilde{\mathcal{L}}\otimes B_1 + a(t)\mathcal{L}\otimes B_2$ has zero eigenvalue with algebraic multiplicity 2, and all other eigenvalues have negative real part.*

Proof. The proof is similar to the proof in Ref. 10, so we omit it here. □

Theorem 1. *Suppose that Assumptions 1, 2, 3 and 4 are fulfilled. The desired mean-square quasi-composite rotating formation control of MASs (1) and (2) can be achieved by taking the control protocol (8).*

Proof. Let $\beta_1 = \left(FH\mathbf{1}_n\otimes\begin{bmatrix}1\\0\end{bmatrix}\right)$, $\beta_2 = \left(\mathbf{1}_n\otimes\begin{bmatrix}0\\1\end{bmatrix}\right)$, it is clear that

$$\big(I_n\otimes A + \tilde{\mathcal{L}}\otimes B_1 + \mathcal{L}\otimes B_2\big)\beta_1 = j\omega_1\beta_1, \tag{12}$$

$$\big(\tilde{\mathcal{L}}\otimes B_1 + \mathcal{L}\otimes B_2\big)\beta_1 = 0, \tag{13}$$

$$\big(I_n\otimes A + \tilde{\mathcal{L}}\otimes B_1 + \mathcal{L}\otimes B_2\big)\beta_2 = -j\omega_2\beta_2, \tag{14}$$

$$\big(\tilde{\mathcal{L}}\otimes B_1 + \mathcal{L}\otimes B_2\big)\beta_2 = 0. \tag{15}$$

Take invertible matrix $U = [\beta_1,\beta_2,\bar{U}] \in \mathbb{C}^{2n\times 2n}$ with $U^{-1} = [\gamma_1^T,\gamma_2^T,\bar{V}^T]^T \in \mathbb{C}^{2n\times 2n}$ such that

$$U^{-1}\big(\tilde{\mathcal{L}}\otimes B_1 + \mathcal{L}\otimes B_2\big)U = diag\{0,0,\Lambda\}, \tag{16}$$

where $\Lambda \in \mathbb{C}^{(2n-2)\times(2n-2)}$ is a Jordan matrix. From Lemma 3, all eigenvalues of Λ have negative real parts.

Let $\zeta(t) = U^{-1}\delta(t)$, $\zeta(t) = (\zeta_1(t),\zeta_2(t),\bar{\zeta}^T(t))^T$, $\bar{\zeta}(t) = (\zeta_3(t),\dots,\zeta_{2n}(t))^T$. Then the origin system can be decoupled into the following system:

$$\dot{\zeta}_1(t) = j\omega_1\zeta_1(t) + \gamma_1 a(t)\Omega\eta, \tag{17}$$

$$\dot{\zeta}_2(t) = -j\omega_2\zeta_2(t) + \gamma_2 a(t)\Omega\eta, \tag{18}$$

$$\dot{\bar{\zeta}}(t) = [j\bar{V}(I_n\otimes\bar{A})\bar{U} + a(t)\Lambda]\bar{\zeta}(t) + \bar{V}a(t)\Omega\eta. \tag{19}$$

In view of the theory of stochastic differential equation, the solution of (17) (18) and (19) is

$$\zeta_1(t) = e^{j\omega_1 t}\zeta_1(0) + \int_0^t e^{j\omega_1 t}\gamma_1 a(\tau)\Omega\, dW(\tau), \tag{20}$$

$$\zeta_2(t) = e^{-j\omega_2 t}\zeta_2(0) + \int_0^t e^{-j\omega_2 t}\gamma_2 a(\tau)\Omega\, dW(\tau), \tag{21}$$

$$\begin{aligned}\bar{\zeta}(t) &= e^{\int_0^t [j\bar{V}(I_n\otimes\bar{A})\bar{U}+a(\tau)\Lambda]d\tau}\bar{\zeta}(0) \\ &+\int_0^t e^{\int_\tau^t [j\bar{V}(I_n\otimes\bar{A})\bar{U}+a(s)\Lambda]ds}\bar{V}a(\tau)\Omega\, dW(\tau),\end{aligned} \tag{22}$$

where $\bar{A} = jA$, $W(t) = (W_{r11}(t), W_{\tilde{v}11}(t),\dots,W_{r1n}(t), W_{\tilde{v}1n}(t)\dots,W_{rn1}(t),W_{\tilde{v}n1}(t),\dots,W_{rnn}(t),W_{\tilde{v}nn}(t))^T$, and $W_{rik}(t), W_{\tilde{v}ik}(t)$, $i,k = 1,2\dots,n$ are standard Brownian motions. Therefore, we have

$$\begin{aligned}&\lim_{t\to+\infty} E\|\bar{\zeta}(t)\|^2 \\ &\le \lim_{t\to+\infty} E[\|\bar{\zeta}(0)\|^2 e^{2Real(\lambda_{max}(\Lambda))\int_0^t a(\tau)d\tau}] \\ &+\lim_{t\to+\infty} E[(2n-2)\int_0^t a^2(\tau)\, e^{2Real(\lambda_{max}(\Lambda))\int_\tau^t a(s)ds}d\tau \\ &\times\lambda_{max}(\bar{V}\Omega\Omega^*\bar{V}^*).\end{aligned} \tag{23}$$

Together Lemma 3 with Assumptions 3 and 4, we have

$$\lim_{t\to+\infty} E\|\bar{\zeta}(t)\|^2 = 0. \tag{24}$$

Together $\delta(t) = U\zeta(t)$ with (20) and (21), we have

$$\lim_{t\to+\infty} E\|\delta(t) - \beta_1\zeta_1(t) - \beta_2\zeta_2(t)\|^2 = 0. \tag{25}$$

Let $v(t) = \big(v_1(t), v_2(t),\dots,v_n(t)\big)^T$, $c(t) = (c_1(t), c_2(t),\dots,c_n(t))^T$, then we can obtain that

$$\lim_{t\to+\infty} E\left\|v(t) - FH\mathbf{1}_n e^{j\omega_1 t}\zeta_1(0)\right\|^2 = 0, \tag{26}$$

$$\lim_{t \to +\infty} E\left\| c(t) - \mathbf{1}_n e^{-j\omega_2 t} \zeta_2(0) \right\|^2 = 0, \tag{27}$$

which indicates that conditions (4-7) are satisfied, i.e., the desired formation control of MASs (1,2) is achieved. □

5. A Numerical Example

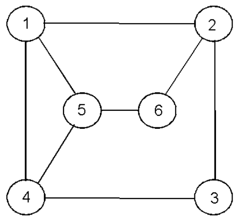

Fig. 1. The communication topology graph.

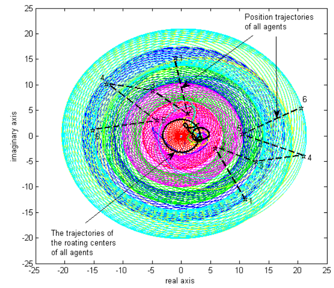

Fig. 2. Whole trajectories of the position and moving rotating centers of the MASs.

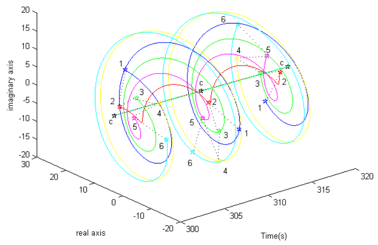

Fig. 3. Local trajectories of the position and moving rotating centers of the MASs.

To demonstrate the effectiveness of the proposed theoretical results, consider MASs with 6 nodes. The communication topology graph of the MASs is shown in Fig. 1, which is connected. Assuming that the weight of each edge is 1. Consider the MASs (1) and (2) with the distributed control protocol (8). The initial conditions of the system are taken as $r_1(0) = -2.8 - 4.8j, r_2(0) = 1.7 + 4.2j, r_3(0) = -1.1 + 6.2j, r_4(0) = 3 + 5j,\ r_5(0) = -1 + 6j, r_6(0) = 3 + 5.3j, \tilde{v}_1(0) = 2.1, \tilde{v}_2(0) = 2.8, \tilde{v}_3(0) = -0.9, \tilde{v}_4(0) = -2, \tilde{v}_5(0) = -1, \tilde{v}_6(0) = -2.2$. Take $a(t) = \frac{2}{1+t}, \omega_1 = 0.8, \omega_2 = 0.02, \theta_i = \frac{\pi i}{6}, i = 1,2,\ldots,6$ and choose $\rho_1 = 2, \rho_2 = 0.5, \rho_3 = 1.5, \rho_4 = 2.5, \rho_5 = 1, \rho_6 = 2.5$. We could see the whole (Fig. 2) and local (Fig. 3) trajectories of the position and moving rotating centers of the MASs for more intuitive, which implicates that Theorem 1 is effective.

6. Conclusions

The mean-square quasi-composite rotating formation problem of second-order MASs with stochastic communication noises was investigated in this paper. A novel distributed control protocol with a time-varying control gain was designed. And then, corresponding sufficient conditions were deduced. Besides, the effectiveness of the proposed theoretical results was confirmed by providing a numerical example.

Acknowledgements

This work is supported by National Natural Science Foundation of China (Grant No. 61304155).

References

1. R. Olfati-Saber, J.A. Fax, and R.M. Murray, Consensus and cooperation in networked multi-agent systems, *Proc. IEEE*, **95**(1) (2007) 215-233.
2. Y. Jia, Robust control with decoupling performance for steering and traction of 4WS vehicles under velocity-varying motion, *IEEE Trans. Control Syst. Technol*, **8**(3) (2000) 554-569.
3. P. Lin and Y. Jia, Distributed rotating formation control of multi-agent systems, *Systems Control Lett*, **59**(10) (2010) 587-595.
4. L. Mo and Y. Yu, Finite-time rotating encirclement control of multi-agent systems, *Acta Automat. Sinica*, **43**(9) (2017) 1665-1672.
5. Y. Li, Y. Huang, P. Lin, and W. Ren, Distributed rotating consensus of second-order multi-agent systems with nonuniform delays, *Systems Control Lett*, **117**(2018) 18-22.
6. P. Lin, W. Lu, and Y. Song, Collective composite-rotating consensus of multi-agent systems, *Chin phys B*, **23**(4) (2014) 040503.
7. F. Xiao, L. Wang, J. Chen, and Y. Gao, Finite-time formation control for multi-agent systems, *Automatica*, **45**(11) (2009) 2605-2611.
8. T. Li and J. Zhang, Mean square average-consensus under measurement noises and fixed topologies: necessary and sufficient conditions, *Automatica*, **45**(8) (2009) 1929-1936.
9. L. Mo, S. Guo, and Y. Yu, Mean-square composite-rotating consensus of second-order systems with communication noises, *Chin phys B*, **27**(7) (2018) 070504.
10. L. Mo, X. Yuan, and Y. Yu, Quasi-composite rotating formation control of second-order multi-agent systems, (submitted).
11. C. Godsil and G. Royle, *Algebraic graph theory*. (New York, Springer Verlag, 2001).
12. W. Ren and R. Beard, Consensus seeking in multiagent systems under dynamically changing interaction topologies, *IEEE Trans. Autom Control*, **50**(5) (2005) 655-661.

Distributed Energy Resource Control Based on Multi-Agent Group Consensus

Yize Yang
School of Electrical Engineering and Telecommunications, The University of New South Wales
Sydney, Australia
School of Information and Electrical Engineering, Ludong University
Yantai 264025, China

Hongyong Yang*, Fan Liu, Yuling Li, Yuanshan Liu
School of Information and Electrical Engineering, Ludong University
Yantai 264025, China
E-mail: yangyz1994@126.com,hyyang@ldu.edu.cn
www.ldu.edu.cn

Abstract

In this paper, a cooperative control strategy of distributed energy resources based on the group consensus of multi-agent systems is proposed. Considering the disturbance effects in actual energy transportation, a multi-agent dispatch model of energy networks with the matched disturbances and mismatched disturbances is designed. The control of energy distribution and safe transportation with multiple disturbances is achieved for a group distributed energy resources. Finally, the numerical simulation results verify the validity of the model and algorithm.

Keywords: Energy resource; distributed control; group consensus; matched disturbances; mismatched disturbances.

1. Introduction

As an important part of the smart grid, distributed energy resources play an irreplaceable role in alleviating grid power supply pressure, balancing peak power loads and storing excess energy. However, distributed energy resources also have hidden dangers because of large quantities, and random geographical locations. The group cooperative control strategy of multi-agent systems provides a new idea for solving the technical difficulties of the distributed energy grid connection.

With the increasing complexity of networked systems, the research on the group movement of multi-agent systems has attracted much attention. Supposing the complex network system with multiple subnets, the convergence of all the agents is achieved by the communication protocol, while the different subnets converge to different states. In Ref. 1, iterative algorithms for reaching acceptable levels of consensus in group decision making is investigated. The heterogeneous agents are governed by the Euler-Lagrange system and the double-integrator system is

*Corresponding Author

investigated in Ref. 2. Group consensus for multi-agent systems with switching topologies and time-varying delays is addressed in Ref. 3. Group consensus problem with discontinuous information transmissions among different groups of dynamic agents is investigated in Ref. 4. A group consensus problem for a multi-agent network with time-varying topologies is concerned in Ref. 5. Many results of multi-agent systems can be consulted the Ref. 6-9 and their references.

2. Preliminaries

Let the graph $G=(V,\omega,A)$ be a weighted undirected graph of nodes n . $V=\{1,2,\cdots,n\}$ is a collection of vertices (or nodes). $\omega \subseteq V\times V$ is a collection of edges. $A=\left[a_{ij}\right]\in R^{n\times n}$ is the node adjacency matrix ($\forall i\in V$, $a_{ii}=0$).If $(i,j)\in\omega$, so $a_{ij}>0$, otherwise $a_{ij}=0$. The Neighbor collection of node i is defined as $N_i=\{j\in V|(i,j)\in\omega\}$. Let $D=diag\{d_1,d_2,\cdots,d_n\}$ be a degree matrix. The analogous Laplacian matrix of the diagram G is defined as $\tilde{L}=D+A\in R^{n\times n}$,where D is the degree matrix corresponding to the topological structure between the intelligent bodies, and A is the corresponding adjacency matrix.

Definition 1. A network with topology $G_1=\{V_1,\omega_1,A_1\}$ is said to be a sub-network of a network with topology $G=\{V,\omega,A\}$ if (i) $V_1\subseteq V$, (ii) $\omega_1\subseteq\omega$ and (iii)the weighted adjacency matrix A_1 inherits A . Correspondingly, we call G_1 a sub-graph of G . Furthermore, if the inclusion relations in (i) and (ii) are strict, and $\omega_1=\{(v_i,v_j):i,j\in v_1,(v_i,v_j)\in\omega\}$, we say that the first network is a proper sub-network of the second one. Correspondingly, we call G_1 a proper sub-graph of G .

Definition 2. For a given initial condition $x(0)=\left[x_1(0),\ldots,x_n(0)\right]^{\mathrm{T}}$, where $x_i(0)\in R$. There is a collection $\{X_1,X_2,\ldots,X_m\}$ satisfy (i) $X_i\cap X_j=\phi$ and (ii) $\bigcup_{k=1}^{m}X_k=X=\{x_1,\ldots,x_n\}$. If the states of agents satisfy(i) $\lim_{t\to\infty}\left|x_i(t)-x_j(t)\right|=0$, $\hat{i}=\hat{j}$ and (ii) $\lim_{t\to\infty}\left|x_i(t)-x_j(t)\right|>0$, $\hat{i}\neq\hat{j}$. It is said to solve a group consensus problem asymptotically.

3. Group Consensus of Distributed Energy Resources with Mismatched Disturbances

Assuming a networked system composed of n agents, the network topology of n agents can be represented as the connected two-bipartite graph. Consider the following form of the second-order multi-agent dynamic equation:

$$\begin{cases}\dot{x}_i(t)=v_i(t)+d_{i1}(t)\\ \dot{v}_i(t)=u_i(t)+d_{i2}(t),\ i=1,\ldots,n\\ y_i(t)=x_i(t)\end{cases}\tag{1}$$

where $x_i(t)$ is the position states of the agent i , $v_i(t)$ is the speed states of the agent i , $u_i(t)$ is the control input of the system, $y_i(t)$ is the control output of the system, $d_{i1}(t)$ and $d_{i2}(t)$ are the mismatch disturbances and the matching disturbances in the system respectively.

3.1. *Design for disturbance observers*

For a dynamic system (1), the disturbances can be estimated by the observers, for $i=1,\ldots,n$.

$$\begin{cases}\hat{d}_{i1}=l_{i1}(x_i-p_{i1})\\ \dot{p}_{i1}=v_i+\hat{d}_{i1}\\ \hat{d}_{i2}=l_{i2}(v_i-p_{i2})\\ \dot{p}_{i2}=u_i+\hat{d}_{i2}\end{cases}\tag{2}$$

where $\hat{d}_{i1}$ and $\hat{d}_{i2}$ are the estimated vectors of mismatched disturbances and matching disturbances in the system respectively, p_{i1} and p_{i2} are intermediate vectors, l_{i1} and l_{i2} are positive observational gains.

Let the error estimation be $e_{d_{ik}}(t)=d_{ik}(t)-\hat{d}_{ik}(t)$, $k=1,2$. The estimation error system is obtained from the system (3) and the observer (4).

$$\begin{cases}\dot{e}_{d_{i1}}=-l_{i1}e_{d_{i1}}+\dot{d}_{i1}\\ \dot{e}_{d_{i2}}=-l_{i2}e_{d_{i2}}+\dot{d}_{i2}\end{cases},\ i=1,2,\cdots,n\tag{3}$$

Assumption 1. The disturbances $d_{ik}(t)$ and $\dot{d}_{ik}(t)$ are limited. That is, there are $d_{ik}^*=\sup_{t\geq0}\{|d_{ik}(t)|\}$ and $\varphi_{ik}=\sup_{t\geq0}\{|\dot{d}_{ik}(t)|\}$.

Assumption 2. The disturbance of dynamic system (3) is $\lim_{t\to\infty}\dot{d}_i(t)=0$, $i=1,2,\cdots,n$.

Remark 1. Assumption 2 is used to prove that the disturbance estimation error system (3) is asymptotically convergent. However, if the observer is dynamic enough, the disturbance observer (2) can also estimate the fast time-varying disturbances by selecting the appropriate observation gain.

Assumption 3. Each agent can receive the information of state and estimated disturbance from its neighbors.

Theorem 1. *(1) If Assumption 1 is established, the observer (4) estimates the error is limited. That is, there are* $e^*_{d_{ik}} = \sup\{|e_{d_{ik}}(t)|\}$ *and* $|e_{d_{ik}}(\infty)| \le \varphi_{ik}/l_{ik}$, $i \in \{1,2,\cdots,n\}^{\ge 0}$, $k = 1,2$.

(2) If Assumption 1-2 is established, the error estimate $\hat{d}_{ik}$ *will asymptotically converge to the disturbance* d_{ik} *of the dynamic system (1).*

Proof. The proof is omitted. □

3.2. *Design of control protocol for dynamic system*

Based on the design of the disturbance observer, this section will design the compound control protocol combined with the sliding mode control, to drive the dynamic system (1) to achieve group consensus flocking.

Based on the disturbance estimation of disturbance observer (2), a compound control protocol is designed:

$$u_i = -c_2^{-1} k_i sgn\left[\sum_{j=1}^{n} a_{ij}\left(s_i + s_j\right)\right] - c_2^{-1}\left[c_1\left(v_i + \hat{d}_{i1}\right)\right] - \hat{d}_{i2},\quad i = 1,\ldots,n \tag{4}$$

where $c_1, c_2 > 0$, $k_i = (c_1 + c_2 l_{i1})e^*_{d_{i1}} + c_2 e^*_{d_{i2}} + \varepsilon_i$, $\varepsilon_i > 0$, $\hat{d}_{i1}$ and $\hat{d}_{i2}$ are respectively the estimated disturbance values of the disturbance observer (2). The dynamic sliding mode surface equation is designed:

$$s_i = c_1\left[\sum_{j\in N_i}^{n} a_{ij}(x_i + x_j)\right] + c_2\left(\sum_{j\in N_i}^{n} a_{ij}\left[\left(v_i + \hat{d}_{i1}\right) + \left(v_j + \hat{d}_{j1}\right)\right]\right) \tag{5}$$

Theorem 2. *Considering the formation of a second-order dynamic multi-agent system (1), it is assumed that the network topology composed of n agents can be represented as the two-bipartite graph* (G_1, V_1, A_1) *and* (G_2, V_2, A_2). *If Assumption 1, Assumption 2, and Assumption 4 are established for the dynamic system with the composite control protocol (4), there are many results as follows:*

(1) The multi-agent systems eventually converge to a limited area. That is, there are $H_1 > 0$ *and* $\lim_{t\to\infty}\sum_{i=1}^{n}\sum_{j=1}^{n} a_{ij}(y_i + y_j)^2 \le H_1$.

(2) The system output consistency is asymptotically achieved. That is $\lim_{t\to\infty}(y_i + y_j) = 0$, $i \in V_1$, $j \in V_2$. *the multi-agent system can finally realize the group consensus flocking movement.*

Proof. The proof is omitted. □

4. Numerical Simulation

Consider a topological structure consisting of 7 distributed energy resources, as shown in Fig. 1. Assuming that the weights of all the lines in the topology diagram are 1, the system's analogous Laplacian matrix is

$$\tilde{L} = \begin{bmatrix} 3 & 0 & 0 & 1 & 1 & 0 & 1 \\ 0 & 2 & 0 & 1 & 0 & 1 & 0 \\ 0 & 0 & 2 & 0 & 1 & 0 & 1 \\ 1 & 1 & 0 & 2 & 0 & 0 & 0 \\ 0 & 0 & 1 & 0 & 1 & 0 & 0 \\ 0 & 1 & 0 & 0 & 0 & 1 & 0 \\ 1 & 0 & 1 & 0 & 0 & 0 & 2 \end{bmatrix}$$

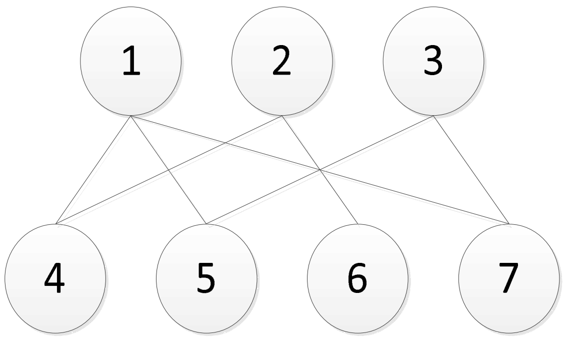

Fig.1. Graph of multiple distributed energy resources.

To verify the validity of the conclusion, it is assumed that all the agents are affected by different disturbances. The disturbances of the agent 1 are $d_{1,1} = 4\tanh(2t)$, $d_{1,2} = 2sigmoid(t)$. The disturbances of the agent 2 are $d_{2,1} = \tanh(t)$, $d_{2,2} = sigmoid(t)$. The disturbances of the agent 3 are $d_{3,1} = 3sigmoid(t)$, $d_{3,2} = 2sigmoid(2t)$. The disturbances of the agent 4 are $d_{4,1} = 5sigmoid(t)$, $d_{4,2} = \tanh(t)$. The disturbances of the agent 5 are $d_{5,1} = 4\tanh(2t)$, $d_{5,2} = 2\tanh(t)$. The disturbances of the agent 6 are $d_{6,1} = 2\tanh(t)$, $d_{6,2} = 3\tanh(t)$. The disturbances of the agent 7 are $d_{7,1} = sigmoid(t)$, $d_{7,2} = sigmoid(2t)$. Where d_{i1} and d_{i2} are respectively represented as mismatched disturbances and matching disturbances.

The parameters in the control protocol are set to $k = 50$, $c_1 = 10$, $c_2 = 8$. For the topology shown in

Fig. 1, we assume that the initial state of 7 agents are $x(0)=[5,8,6,12,4,2,-3]^{T}$, the initial speeds are $v(0)=[5,8,6,9,4,2,-3]^{T}$. The multi-agent dynamic system equation (1) and the control protocol (4) are applied, and the simulation results of the system motion are shown in Fig.2 and Fig.3. The observational estimation errors of the disturbance observer are calculated in Fig.2. The mismatch disturbances can be estimated quickly. The transport status of each distributed energy resource finally converges to the two-equilibrium state in Fig.3. Multi-agent systems achieve the group consensus, which verifies the effectiveness of the theoretical results. accurately.

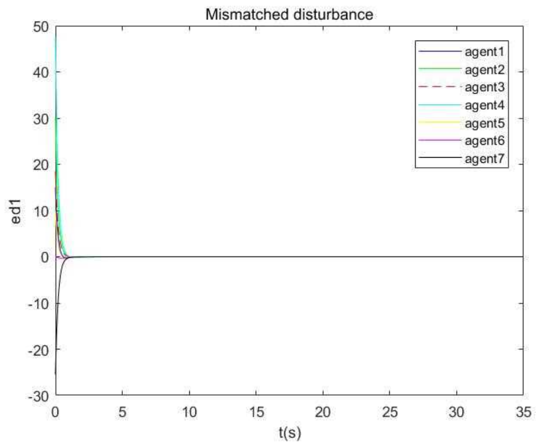

Fig. 2. Errors of mismatched disturbances

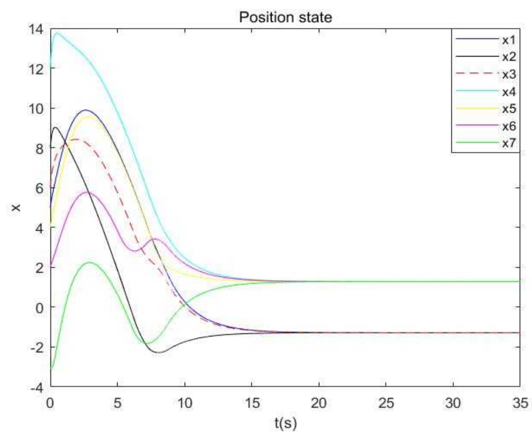

Fig. 3. Group flocking motion states of multi-agent system.

5. Conclusion

A group cooperative control strategy is proposed for cooperative optimal control of multiple distributed energy resources. Considering the situation of multiple disturbances in the actual power supply system, a disturbance observer and a state observer are designed to stabilize load fluctuations and resist external disturbances in the energy supply system.

Acknowledgements

This paper is supported by the National Natural Science Foundation of China (61673200, 61771231), Natural Science Foundation of Shandong Province of China (ZR2018ZC0438, ZR2017MF010, ZR2017PF010).

References

1. Z. Xu and X. Cai, Group consensus algorithms based on preference relations. Information Sciences, 181(1)(2011) 150-162.
2. H. Hu, W. Yu W, Q. Xuan, et al. Group consensus for heterogeneous multi-agent systems with parametric uncertainties. Neurocomputing, 142(1) (2014) 383-392.
3. Y. Gao, J. Yu, J. Shao, et al. Group consensus for second-order discrete-time multi-agent systems with time-varying delays under switching topologies. Neurocomputing, 207(2)(2016) 805-812.
4. H. Hu, L. Yu, W. Zhang, et al. Group consensus in multi-agent systems with hybrid protocol. Journal of the Franklin Institute, 350(3) (2013) 575-597.
5. J. Yu and L. Wang, Group consensus in multi-agent systems with switching topologies. Systems & Control Letters, 59(6) (2010) 340-348.
6. H. Yang, F. Wang, F. Han, Containment control of fractional order multi-agent systems with time delays. IEEE/CAA Journal of Automatica Sinica, 5(3)(2018) 727–732.
7. H. Yang, Y. Yang, F. Han, et.al., Containment control of heterogeneous fractional-order multi-agent systems. Journal of the Franklin Institute, (2017). https://doi.org/10.1016/j.jfranklin.2017. 09.034
8. H. Yang, F. Han, M. Zhao, et.al., Distributed containment control of heterogeneous fractional-order multi-agent systems with communication delays. Open Physics, 15 (2017) 509–516.
9. H. Yang, Z. Zhang and S. Zhang, Consensus of second-order multi-agent systems with exogenous disturbances. International Journal of Robust and Nonlinear Control, 21(9) (2011) 945–956.

Robust Adaptive Control of Air-to-air Refueling Boom with State-dependent Output Constraints

Liang Chang, Yingmin Jia[*]
The Seventh Research Division and the Center for Information and Control, School of Automation Science and Electrical Engineering, Beihang University (BUAA), 37 Xueyuan Road, Haidian District, Beijing, 100191, China
E-mail: chlchang01@163.com, ymjia@buaa.edu.cn
www.buaa.edu.cn

Abstract

In this paper, a robust adaptive controller design method is presented for the uncertain air-to-air refueling boom system with output constraints and disturbance. One advantage of this design method is that the output constraints are state-dependent, which can extend the workspace of the boom while avoiding collision between the boom and the receiver. Backstepping method and barrier Lyapunov function(BLF) are used in this design method. Simulation results show the effectiveness of the proposed controller design method.

Keywords: Air-to-air refueling, robust adaptive control, output constraints, barrier Lyapunov function.

1. Introduction

During aerial refueling operation, the boom is too close to receiver aircrafts[1], thus collision avoidance problem is one of the most important problem in air-to-air refueling.

The most effective method to deal with the collision avoidance problem is output constrained control method. There have been plenty of works about this method. Ref. 2 employed a log-type BLF to ensure the output constraints never be violated and a tan-type BLF was presented in Ref. 3. However, the output constraints in these works are constants, which will limit the aerial refueling boom's workspace. Ref. 4 presented a neural network controller to solve the robotic manipulator control problem with time-varying output constraints, but the constraints require to be known in advance.

In this paper we concern the control problem of air-to-air refueling boom with state-dependent output constraints, unknown parameter and disturbance. Compared with other output constraints, the state-dependent output constraints extend the workspace of the boom while avoiding collision between the boom and the receiver, furthermore, the constraints can be unknown in advance.

This paper is organized as follows: Section 2 formulates the control problem studied in this paper; Section 3 solves this control problem and presents the controller design method; an illustrative example is presented in Section 4 and Section 5 has the conclusions.

2. Problem Formulation

2.1. *Aerial refueling boom model*

The aerial refueling boom is shown in Fig. 1, which is fitted to the rear of the tanker. Its azimuth and elevation can be adjusted arbitrarily, and it can be extended to make

[*] Corresponding author

contact with the receptacle of the receiver. Thus, the aerial refueling boom can be regarded as a 3-DOF robotic manipulator. Setting $-\bar{d} \le d_i \le \bar{d}$ as the disturbance, where $\bar{d} > 0$ is a known constant, q_{di} as the desired position of the ith joint (i.e. the joint position when the boom is contacted with the receptacle), which is second order differentiable. Define $q = [q_1, q_2, q_3]^T$ as joint variables vector, $q_d = [q_{d1}, q_{d2}, q_{d3}]^T$ as joints desired position vector, $\tau = [\tau_1, \tau_2, \tau_3]^T$ as control input vector, $d = [d_1, d_2, d_3]^T$ as disturbance vector, $y = q - q_d = [y_1, y_2, y_3]^T$ as output vector, then the model of the aerial refueling boom can be expressed as

$$\begin{cases} M(q)\ddot{q} + C(q,\dot{q})\dot{q} + G(q) = \tau + d, \\ y = q - q_d. \end{cases} \tag{1}$$

Notice that the elevation of the boom is controlled by control surfaces (See Fig. 1), thus model (1) should be rewritten as

$$\begin{cases} M(q)\ddot{q} + C(q,\dot{q})\dot{q} + G(q) = L\tau + d, \\ y = q - q_d, \end{cases} \tag{2}$$

where $l > 0$ is a unknown constant, $L = diag\{l,1,1\}$, $M = diag(M_{11}, M_{22}, M_{33}), C = diag(C_{11}, C_{22}, C_{33})$, $G = [G_1, G_2, G_3]^T$, the specific expressions of these matrices are not given due to space limitations.

2.2. *State-dependent output constraints*

During aerial refueling operation, the boom is contacted with the receptacle to refuel receiver aircrafts. This

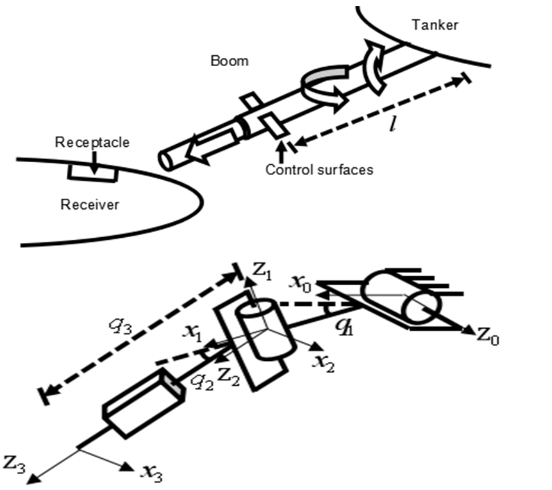

Fig. 1. The aerial refueling boom and its mechanical structure model.

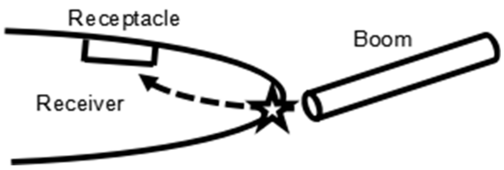

Fig. 2. The aerial refueling boom may cause collision with the receiver if the output y is not constrained.

process may cause collision if the trajectory of the boom relative to the receptacle is not constrained (or, equivalently, the output y is not constrained), as shown in Fig. 2, thus the control problem of air-to-air refueling boom should consider output constraints.

Instead of adopting the traditional output constraints, we propose a set of novel state-dependent output constraints (as shown in Fig. 3) in this paper as follows:

$$\begin{cases} -k_{oi} \le y_i \le k_{oi}, \quad i = 1,2 \\ k_{o3l} \le y_3 \le k_{o3r}, \end{cases} \tag{3}$$

where

$$k_{oi} = \begin{cases} (\overline{k_{oi}} - \underline{k_{oi}}) y_3^2 / k_{o3l}^2 + \underline{k_{oi}}, & y_3 \le 0 \\ \underline{k_{oi}}, & y_3 > 0 \end{cases} \quad i = 1,2 \tag{4}$$

$$k_{o3r} = C_1 > 0, \quad k_{o3l} = C_2 < 0, \tag{5}$$

$C_1, C_2, \overline{k_{oi}}, \underline{k_{oi}}$ are known constants. Compared with those traditional output constraints, the state-dependent output constraints extend the workspace of the boom while avoiding collision between the boom and the receiver.

Thus, the problem under study in this paper is as follows: find a controller τ such that the closed-loop system (2) achieves the following two objectives:

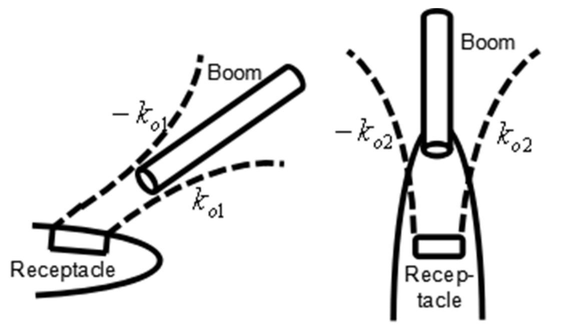

Fig. 3. State-dependent output constraints of air-to-air refueling boom.

(i) All the signals in the closed-loop system are global uniformly bounded with unknown parameter l and disturbance d.
(ii) The state-dependent output constraints (3)-(5) are not violated.

The following lemma is needed in the proof of our main results.

Lemma 1.[5] *For any* $\varepsilon > 0$ *and* $\eta \in \Re$ *, the following inequality always holds,*

$$0 \le |\eta| - \eta \tanh(\eta/\varepsilon) \le k_p \varepsilon, \tag{6}$$

where $k_p = 0.2785$.

3. Controller Design

The backstepping design approach is adopted to design our controller. Define $z_1 = y = [z_{11}, z_{12}, z_{13}]^T$, $z_2 = \dot{q} - \alpha_1 = [z_{21}, z_{22}, z_{23}]^T$, where $\alpha_1 = [\alpha_{11}, \alpha_{12}, \alpha_{13}]^T$ is a virtual controller to be designed later. The dynamics of z_1 is given by

$$\dot{z}_1 = \dot{q} - \dot{q}_d = z_2 + \alpha_1 - \dot{q}_d. \tag{7}$$

Choose the following BLF

$$\begin{aligned} V_1 = & \frac{1}{2}\sum_{i=1}^{2} \ln \frac{k_{oi}^2}{k_{oi}^2 - z_{1i}^2} + \frac{1}{2} q(z_{13}) \ln \frac{k_{o3r}^2}{k_{o3r}^2 - z_{13}^2} \\ & + \frac{1}{2}(1 - q(z_{13})) \ln \frac{k_{o3l}^2}{k_{o3l}^2 - z_{13}^2}, \end{aligned} \tag{8}$$

where

$$q(z_{13}) = \begin{cases} 1, & z_{13} > 0 \\ 0. & z_{13} \le 0 \end{cases}$$

Then the time derivative of V_1 is as follows

$$\begin{aligned} \dot{V}_1 = & \sum_{i=1}^{2} \left[\frac{z_{1i}(z_{2i} + \alpha_{1i} - \dot{q}_{di})}{k_{oi}^2 - z_{1i}^2} - \frac{z_{1i}^2 \dot{z}_{13}\, \partial k_{oi} / \partial z_{13}}{(k_{oi}^2 - z_{1i}^2) k_{oi}} \right] \\ & + q(z_{13}) \frac{z_{13}(z_{23} + \alpha_{13} - \dot{q}_{d3})}{k_{o3r}^2 - z_{13}^2} \\ & + (1 - q(z_{13})) \frac{z_{13}(z_{23} + \alpha_{13} - \dot{q}_{d3})}{k_{o3l}^2 - z_{13}^2}, \end{aligned} \tag{9}$$

where

$$\frac{\partial k_{oi}}{\partial z_{13}} = \begin{cases} 2\dfrac{(\overline{k_{oi}} - \underline{k_{oi}}) z_{13} \dot{z}_{13}}{k_{o3l}^2}, & z_{13} \le 0 \\ 0. & z_{13} > 0 \end{cases}$$

Design virtual controller α_1 as

$$\begin{cases} \alpha_{1i} = -k_{1i} z_{1i} + \dot{q}_{di} + 2\dfrac{(\overline{k_{oi}} - \underline{k_{oi}}) \dot{z}_{13}^2}{k_{o3l} \underline{k_{oi}}} z_{1i}, \\ \alpha_{13} = -k_{13} z_{13} + \dot{q}_{d3}, \qquad i = 1,2 \end{cases} \tag{10}$$

where $k_{1i} > 0$ are parameters. Therefore Eq. (9) becomes

$$\begin{aligned} \dot{V}_1 \le & \sum_{i=1}^{2} \frac{-k_{1i} z_{1i}^2 + z_{1i} z_{2i}}{k_{oi}^2 - z_{1i}^2} + \left(\frac{q(z_{13})}{k_{o3r}^2 - z_{13}^2}\right. \\ & \left. + \frac{1 - q(z_{13})}{k_{o3l}^2 - z_{13}^2}\right)(-k_{13} z_{13}^2 + z_{13} z_{23}). \end{aligned} \tag{11}$$

The dynamics of z_2 is given by

$$\dot{z}_2 = M^{-1}(-C\dot{q} - G + d + L\tau) - \dot{\alpha}_1. \tag{12}$$

Then consider the following Lyapunov function:

$$V_2 = \frac{1}{2} z_2^T z_2, \tag{13}$$

and its time derivative is:

$$\dot{V}_2 = z_2^T (M^{-1}(-C\dot{q} - G + d + L\tau) - \dot{\alpha}_1). \tag{14}$$

We design the controller τ as:

$$\tau = \hat{L}_{inv} \overline{\tau} = \hat{L}_{inv} [\overline{\tau_1}, \overline{\tau_2}, \overline{\tau_3}]^T, \tag{15}$$

where

$$\begin{aligned} \overline{\tau} = & C\dot{q} + G + M[u_1, u_2, u_3]^T, \\ u_i = & -k_{2i} z_{2i} + \dot{\alpha}_{1i} - \frac{z_{1i}}{k_{oi}^2 - z_{1i}^2} \\ & - \tanh(3 z_{2i} M_{1i}^{-1} \overline{d} / \varepsilon) M_{1i}^{-1} \overline{d}, i = 1,2 \\ u_3 = & -k_{23} z_{23} + \dot{\alpha}_{13} - \left(\frac{q(z_{13}) z_{13}}{k_{o3r}^2 - z_{13}^2} + \frac{(1 - q(z_{13})) z_{13}}{k_{o3l}^2 - z_{13}^2}\right) \\ & - \tanh(3 z_{23} M_{13}^{-1} \overline{d} / \varepsilon) M_{13}^{-1} \overline{d}, \end{aligned}$$

$\hat{L}_{inv} = diag\{\hat{l}_{inv}, 1, 1\}$, $\hat{l}_{inv}$ is an estimate of $1/l$, k_{2i} , ε are positive design parameters. By using Lemma 1, we have

$$\begin{aligned} \dot{V}_1 + \dot{V}_2 \le & \varepsilon k_p - \sum_{i=1}^{2} \frac{k_{1i} z_{1i}^2}{k_{oi}^2 - z_{1i}^2} - k_{13}\left(\frac{q(z_{13})}{k_{o3r}^2 - z_{13}^2}\right. \\ & \left. + \frac{1 - q(z_{13})}{k_{o3l}^2 - z_{13}^2}\right) z_{13}^2 - \sum_{i=1}^{3} k_{2i} z_{2i}^2 - l \tilde{l}_{inv} z_{21} M_{11}^{-1} \overline{\tau}_1. \end{aligned} \tag{16}$$

For the estimate parameter $\hat{l}_{inv}$, the adaptive law is chosen as

$$\dot{\hat{l}}_{inv} = -z_{21} M_{11}^{-1} \overline{\tau_1} - k_l (\hat{l}_{inv} - l_{inv0}), \tag{17}$$

where k_l , l_{inv0} are positive design parameters.

Then we can present our main results.

Theorem 1. *Consider the closed-loop system (2)(10)(15), and parameter update law (17). For any positive parameters* $k_{1i}, k_{2i}, \varepsilon, k_l, l_{inv0}$, *the following properties hold:*

(i) All the signals in the closed-loop system are global uniformly bounded with unknown parameter l and disturbance d.

(ii) The state-dependent output constraints (3)-(5) are not violated.

Proof. Consider the following BLF:

$$V = V_1 + V_2 + (l/2)\tilde{l}_{inv}^2, \tag{18}$$

where $\tilde{l}_{inv} = 1/l - \hat{l}_{inv}$. And its time derivative is:

$$\dot{V} \le -CV + C_0, \tag{19}$$

$$C = \min(2k_{1i}, 2k_{2i}, k_l),$$

$$C_0 = \varepsilon k_p + (k_l/2)l(1/l - l_{inv0})^2.$$

Then from Eq. (19) we can have the conclusion that the two properties above hold. □

4. Simulation

The joints desired position $q_{d1} = \pi/8 + (\pi/18)\sin(t)$, $q_{d2} = \pi/2 + (\pi/9)\sin(t)$, $q_{d3} = 13 + 0.5\sin(t)$, the disturbance $d_i = 2000\sin(t)$, $\overline{d} = 2000$, the constraints parameters $\overline{k_{o1}} = \pi/6$, $\underline{k_{o1}} = \pi/18$, $\overline{k_{o2}} = \pi/4$, $\underline{k_{o2}} = \pi/18$, $C_1 = 1$, $C_2 = -6$, the initial condition is $q(0) = [0, \pi/3, 8]^T$, the design parameters are $k_{1i} = k_{2i} = k_l = 1$, $l_{inv0} = 1/8$, $\varepsilon = 0.1$.

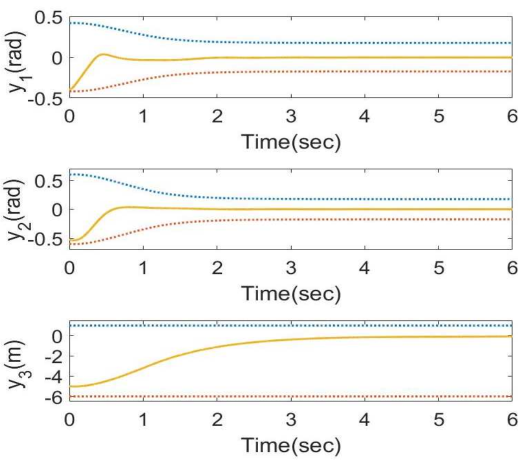

Fig. 4. The output of the air-to-air refueling boom.

Fig. 4 shows the output of the air-to-air refueling boom. The solid lines are the output and the dashed lines are state-dependent output constraints. We can find that under the proposed controller (10)(15) the state-dependent output constraints are not violated with unknown parameter *l* and disturbance *d,* and the state-dependent output constraints provide a larger workspace for the boom than constant output constraints.

5. Conclusions

The control problem of air-to-air refueling boom with state-dependent output constraints, unknown parameter and disturbance has been addressed in this paper. Backstepping method and BLF are used for the state-dependent output constraints problem, the unknown parameter and disturbance are dealt with by adaptive control method and hyperbolic functions. Simulation results show the effectiveness of the proposed controller design method.

Acknowledgements

This work was supported by the NSFC (61327807, 61521091, 61520106010, 61134005) and the National Basic Research Program of China (973 Program: 2012CB821200,2012CB821201).

References

1. J. Doebbler, T. Spaeth et al., Boom and receptacle autonomous air refueling using visual snake optical sensor, *J. Guid. Control Dyn.*, **30**(6) (2007) 1753–1769.
2. K. P. Tee, S. S. Ge and E. H. Tay, Barrier lyapunov functions for the control of output-constrained nonlinear systems, *Automatica.* **45**(1) (2009) 918–927.
3. Z. L. Tang, K. P. Tee and W. He, Tangent barrier lyapunov functions for the control of output-constrained nonlinear systems, in *3rd IFAC Int. Conf. on Intell. Control and Autom. Sci.*, (Cheng-du, China, 2003), pp. 449-455.
4. H. F. Huang, W. He and S. Zhang, Neural network control of a robotic manipulator with time-varying output constraints by state feedback, *IFAC-PapersOnLine*, **50**(1) (2017) 8969-8974.
5. P. Li and G. H. Yang, Fault-tolerant control of uncertain nonlinear systems with nonlinearly parameterized fuzzy systems, In *Proc. of 2009 IEEE Control Appl., (CCA) & Intell. Control, (ISIC),* (Saint-Petersburg, Russia, 2009), pp. 382-387.

Skill Model Estimation of Ability for Reading Drawings

Kazuo Kawada
Department of Technology and Information Education, Hiroshima University,
1-1-1 Kagamiyama, Higashi-Hiroshima, Hiroshima 739-8524, Japan
E-mail: kawada@hiroshima-u.ac.jp
https://www.hiroshima-u.ac.jp

Tsukasa Hiyama
Graduate School of Education, Hiroshima University,
1-1-1 Kagamiyama, Higashi-Hiroshima, Hiroshima 739-8524, Japan
E-mail: m160404@hiroshima-u.ac.jp
https://www.hiroshima-u.ac.jp

Teruyuki Tamai
Faculty of Education, Ehime University,
3 Bunkyo-Cho,Matasuyama, Ehime 790-8577, Japan
E-mail: tamai.teruyuki.xq@ehime-u.ac.jp
https://www.ehime-u.ac.jp

Abstract

In Japan, students are studying various drawing educations in junior high school technical education, high school industrial education and university engineering education. However, it is very difficult to read the drawing without understanding trigonometry. Moreover, it is also very difficult to draw wish parts. Because of this, there are many research studies, but these are before-after analysis, and none analysis by time-series data. Therefore, this study aims to develop a new quantitative evaluation method of 3D recognition ability.

Keywords: List four to six keywords which characterize the article.

1. Introduction

In Japan, technical education of junior high schools, industrial education of high schools, industrial colleges of technology, and engineering department of universities, the engineering drafting education is conducted. If students can not understand trigonometry handled in engineering drawing, they can not read or draw drawings. From this, there are many efforts to improve the read ability and drawing ability. However, these efforts were carried out only before-and-after evaluation, not the one handling the learning curve (time series evaluation).

In order to effectively acquire skills by a teaching guidance, proper support through modeling of learning is important. If it is possible to evaluate the learning process from initial learning performance, the learning support according to individuals is possible. One of the authors proposed a method to regard the skill acquisition process in the model between teacher and student as "first-order + time delay" system based on the control engineering approach[1]. However, in past studies to evaluate the learning process, exponential functions or exponential functions are used as learning curves.

Therefore, we propose a new method to evaluate the reading skill of engineering drawings.

2. Proposed Reading Skill Model

A power function and an exponential function of typical 2 equations are often used as a learning curve in the skill evaluation.
The power function is following equation.

$$T_R = a + b\ N^{-c} \quad (1)$$

where T_R denotes the response time, a denotes the asymptotic value, b denotes the difference between initial and asymptotic performance, N denotes the number of trials, and c denotes the learning rate parameter.
The exponential function is following equation.

$$T_R = a + b\ \mathrm{e}^{-c\,N} \quad (2)$$

where a again denotes the asymptotic value, b denotes the amount that learning can reduce T_R, c denotes the rate at which asymptotic level performance is approached as a proportion, and N again denotes the number of trials. We employed the Eq.(2) for evaluating the reading skill of engineering drawings. However, in order to evaluate skill based on the real learning time rather than the amount of learning (practice), we proposed following equation by changing from N to real time R_T (total learning time) in Eq.(2).

$$T_R[n] = a + b\ \mathrm{e}^{-c\,R_T[\mathrm{n}]} \quad (3)$$

where the relationship between T_R and R_T when the amount of learning is n is as follows.

$$R_T[n] = \sum_{i=0}^{n} T_R[i] \quad (4)$$

3. Skill Model Parameters Estimation using a Real-Coded Genetic Algorithm

The parameters of skill model a, b and c are arranged as cells included in a string. These parameters included in the string are given by real values. The real-coded GA is employed, which is explained as follows.

(i) Initialization

The generation number G is set, and the initial individuals are produced with random real-codes within the initial domain which is set in advance. Here, the number of population is set as N_P.

(ii) Selection

The fitness value $f(l)$ is calculated which is given by

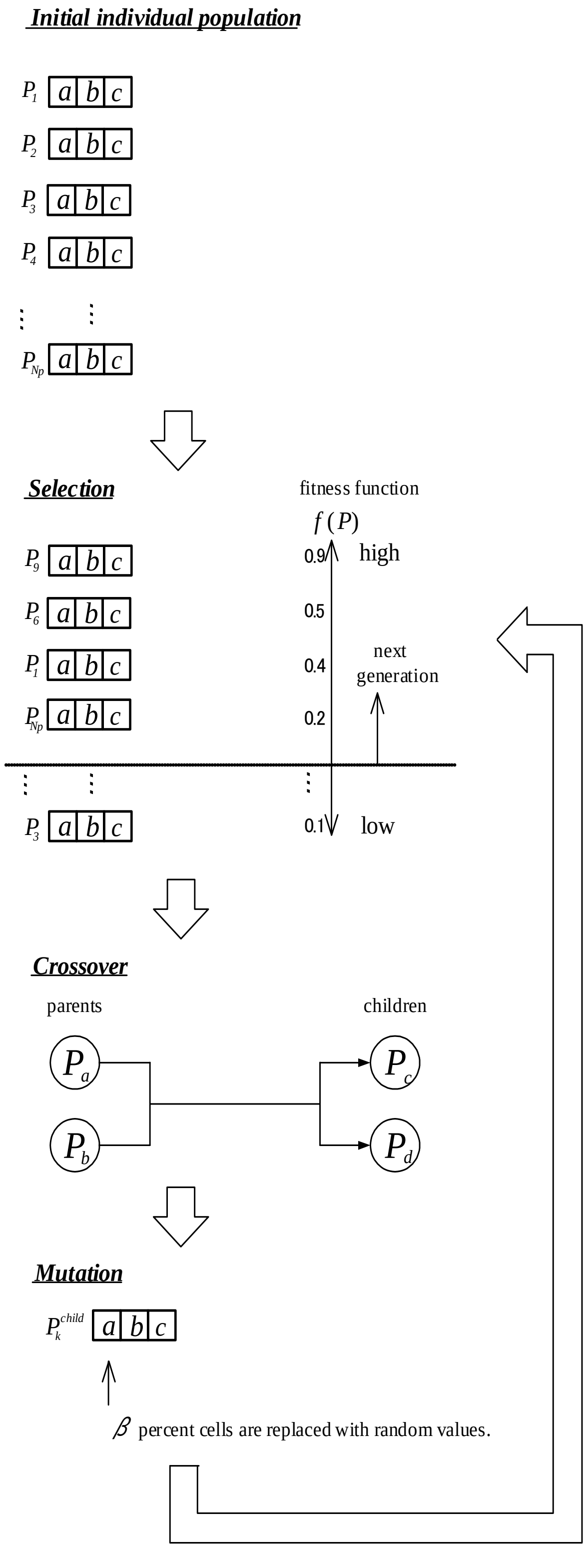

Fig. 1. Schematic figure of GA flow chat.

$$f(l) = 1/\{1 + \sum_{t=1}^{t_{end}} \{\hat{T}_R(k) - T_R(k)\}^2 . \qquad (7)$$

where $\hat{T}_R$ and T_R respectively denote the learning time and the estimated learning time by the parameters of skill evaluation model a, b and c. Each individual P_l is arranged in order, based on the fitness value. Then, α percent individuals with superior fitness values are selected, and saved in the next generation.

(iii) Crossover

The $(100-\alpha)$ percent remaining are generated by the crossover. Two individuals, P_a and P_b are chosen from among the superior α percent, and new individuals P_c and P_d are generated by employing the following procedure:

$$P_c(i) = P_{\sup}(i) - \frac{|P_a(i) - P_b(i)|}{4}, \qquad (8)$$

$$P_d(i) = P_{\sup}(i) + \frac{|P_a(i) - P_b(i)|}{4} \qquad (9)$$

where $P_{\sup}$ in Eq.(8) and Eq.(9) refers to the individual with the superior fitness value, *i.e.*, P_a or P_b. Note that this procedure is employed for every cell included in P_a and P_b.

(iv) Mutation

Of all individuals which are randomly selected and given by the crossover, β percent are chosen and replaced with randomly determined values within the initial domain.

(v) Update

The procedure from (i) through (iv) is repeated for generations.

This procedure is summarized in Fig. 1.

4. Evaluation of Proposed Reading Drawings Skill Model

The effectiveness of the proposed reading drawings skill model was evaluated from the relationship between the learning time and the reading time (response time) of drawing. 2 university students who learned the basics of engineering drawing were the research participants.

The procedure of the experiment is explained as follows.

(1) 17 kinds of 3D models of 30 mm square shown in Fig. 2 and drawings by third angle projection method shown in Fig. 3 are prepared.

(2) The participants randomly showed the drawing, and worked to match the three-dimensional model and the drawing. At this time, the time (response time) required for matching work was measured.

The procedure from (1) through (2) was repeated for 15 times.

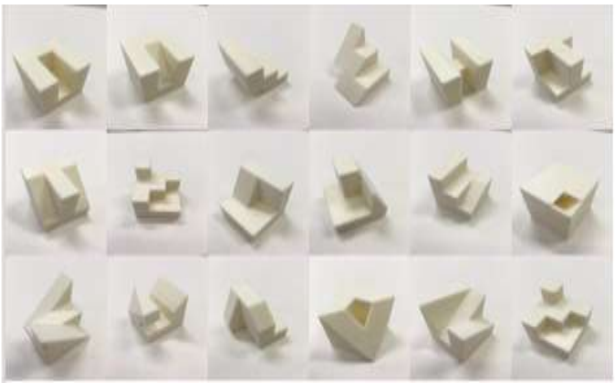

Fig. 2. 3D models of 30 mm square.

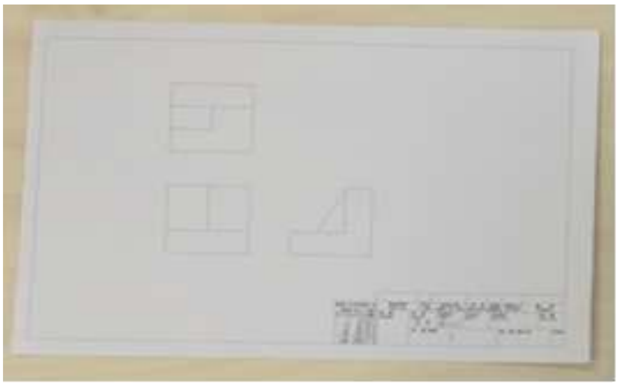

Fig. 3. Drawing of 3D model.

The total learning time R_T and the response time T_R of participants (A and B) measured by experiment are shown in Table 1. Figures 4 and 5 are graphs of Table 1. From these total learning time R_T and response time T_R, the red lines in Figs. 4 and 5 were estimated the reading skill model by using the real-coded GA. Then, estimated parameters (a, b and c) were showed in Table 2.

It is clear that the estimated read skill models of A (Fig. 4) and B (Fig. 5) fit almost to the response time. Furthermore, the reading skills of A and B can be understood from the parameters of Table 2. Specifically, although A has a shorter response time than B, the response times of A and B are almost equal. This shows that B has a higher learning rate than A. From the above, it was found that the proposed reading skill model suggested individual characters.

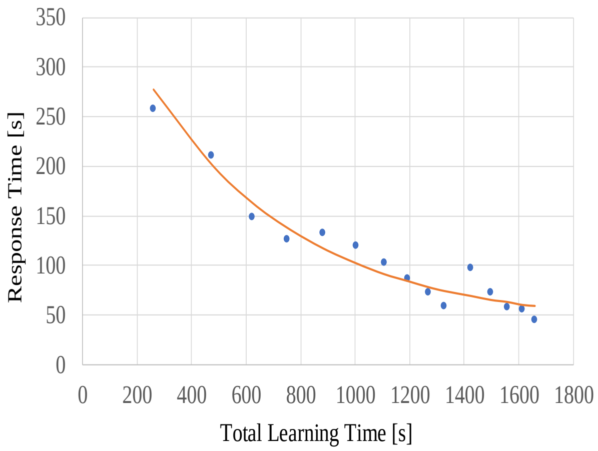

Fig. 4. Learning curve of A.

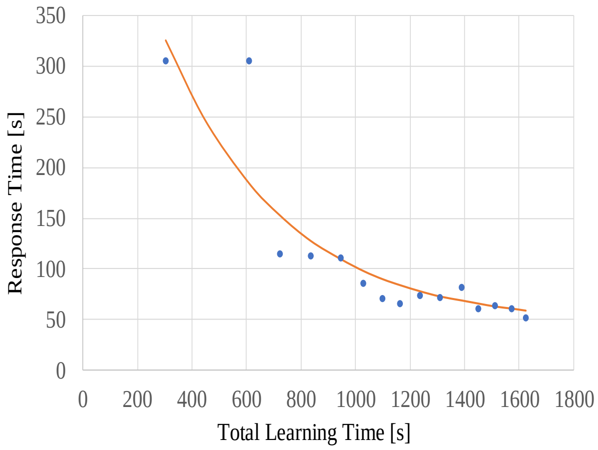

Fig. 5. Learning curve of B.

Table 2. The parameters of drawing skill model.

	a	b	c
A	40	379	0.0018
B	46	566	0.0023

5. Conclusions

We proposed a model to evaluate reading skills of drawings and verified its effectiveness. Specifically, the reading ability of the two participants was evaluated individually by using the proposed skill model. In the future, we plan to develop a learning support system using this reading skill model.

This work was supported by JSPS KAKENHI Grant Number JP16K12760.

References

1. M. Nagamatsu, T. Usuzaka, K. Kawada and T. Yamamoto, Consideration on a Model Between Teacher and Student Based on Control Engineering Approach, *IEEJ Trans. EIS*, **134**(10) (2014), pp.1537-1542. (in Japanese)
2. A. Rosenbaum, R. A. Carlson, and R. O. Gilmore, Acquisition of Intellectual and Perceptual-Motor Skills, Annual Review of Psychology, **52** (2001) , pp.453-470.
3. W. Schneider and R. M. Shiffrin, Controlled and Automatic Human Information Processing: I. Detection, Search, and Attention, *Psychological Review*, **84**(1) (1977), 1-66.
4. J. Cohen, K. Dunbar and J. L. McClelland, On the control of automatic processes: A parallel distributed processing model of the Stroop effect, *Psychological Review*, **97**(3) (1988), 332-361.
5. I. G. Dobbins, D. M. Schnyer, M. Verfaellie and D. L. Schacter, Cortical activity reductions during repetition priming can result from rapid response learning, *Nature*, **428** (2004), 316-319.
6. A. Newell and P. S. Rosenbloom, Mechanisms of Skill Acquisition and the Law of Practice, *Cognitive Skill and Their Acquisition*, J. R. Anderson (Ed.), Erlbaum, Hillsdale, N. J. (1981).

Learning Simulation based on a Computational Model of Neuromodulators

Yuki Moriguchi
Hiroshima University, 1-1-1 Kagamiyama,
Higahsi-hiroshima, Hiroshima 739-8524, Japan

Masayasu Nagamatsu
Hiroshima University, 1-1-1 Kagamiyama,
Higahsi-hiroshima, Hiroshima 739-8524, Japan
E-mail: m176972@hiroshima-u.ac.jp, nagamatu@hiroshima-u.ac.jp

Abstract

Reinforcement learning, and its biological basis are key to understand human learning. Here we illustrate learning processes of the tower of Hanoi based on the computational model of neuromodulators (Doya, K. 2002). The model assumes hypothetical roles for the following parameters of reinforcement learning. 1) Dopamine signals TD error, 2) Serotonin controls discount factor, 3) Noradrenaline controls the inverse temperature, and 4) Acetylcholine controls the learning rate. We have compared the two learning situations. Case a) the reward is given at the goal state only, and Case b) the reward is divided and placed at the intermediate state and goal state. The resulting learning curves shows that b) divided reward enhanced the learning. This result shows an example of learning simulation with a variety of learners who have their own learning characteristics.

Keywords: Tower of Hanoi task, Neuromodulator, Reinforcement Learning,

1. Introduction

Dopamine reward system plays an essential role for a constellation of findings on human behaviors including learning processes, addiction, and adaptation to unknown environments[1-8]. In artificial systems, recent seminal papers on complex cognitive tasks indicate the possibility of such algorithms for modelling the human behavior [9-13]. One of the remaining problems is the modelling of the variety of human learning characteristics for a variety of task structures. As for learning characteristics, three basic parameters need to be considered. First, credit assignment problem, which is called the "notorious" technical problem for problem solving and cognitive skill acquisition[14]. Second, the trade-off between exploration and exploitation. To explore all possibilities, we require that the behavior policy be soft (*i.e.*, that it select all actions in all states with nonzero probability), while exploiting the past[15]. Third, the balance between memory storage and renewal, which corresponds to the most basic parameter of learning.

2. Simulation

2.1. *Reinforcement Learning*

In reinforcement learning, a learner in some state take

$$Q(s_t, a_t) \leftarrow (1-\alpha)Q(s_t, a_t) + \alpha\left[r_t + \gamma \max_a Q(s_{t+1}, a)\right] \quad (1)$$

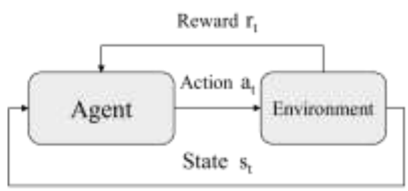

Fig. 1. Agent-Environment interaction in Reinforcement Learning

some action, and in typical case, proceed to the next step and some fortunate learners get some reward(Fig.1). The goal of the learners is to maximize the total reward. The typical algorithm is to model the value of possible actions at each state (Eq.1).

α is learning rate, and γ is discount rate parameter which models the effect of future reward.

By Eq.2, the action with highest preference for each state are given highest probability. This policy parametrization is called soft-max[16]. β is inverse temperature.

$$\pi(s_t, a) = \frac{\exp\left(Q(s_t, a)\beta\right)}{\sum_{a' \in A} \exp\left(Q(s_t, a')\beta\right)} \qquad (2)$$

2.2. *Roles of the neuromodulators*

With the parameters α, β, γ in Eq.1 and Eq.2, we can model the characteristics of heterogeneous agents. Doya[17] proposed the functional model of neuromodulators listed below.

1. Dopamine represents the global learning signal for prediction of rewards and reinforcement of actions.
2. Serotonin controls the balance between short-term and long-term prediction of reward.
3. Noradrenaline controls the balance between wide exploration and focused execution.
4. Acetylcholine controls the balance between memory storage and renewal.

These functions have one to one correspondence to the parameters in Eq.1 and Eq.2.

2.3. *Tower of Hanoi task*

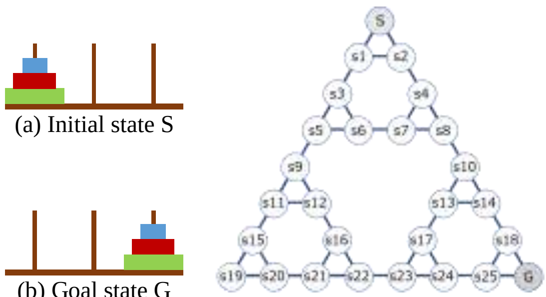

(a) Initial state S

(b) Goal state G

(c) State space

Fig. 2. State space of 3-disk Tower of Hanoi.

The state space of three-disc tower of Hanoi is shown in Fig.2. Agents of Q-learning start from state S, and moves to G. The number of moves is counted. As a reward design, (a)the reward is given at goal state only (Concentrated reward), and (b)reward is divided and additional reward is given at intermediate state S8 (Distributed reward). The condition is given by all possible combination of α (0.1, 0.3, 0.5, 0.7, 0.9), β (0.5, 1, 5, 10, 50), γ (0.1, 0.2, 0.3, 0.4, 0.5, 0.6, 0.7, 0.8, 0.9). The number of combination is 225. The number of agent for each combination is 100. The pattern of reward is two. In sum, total of 45000 independent learners are tested.

2.4. *Result*

Figure3 shows effect of reward design on different learners. In Fig3(a) best performance is achieved at 25 trials. But the performance become worse at later trial.

In Fig 3(b), learning is enhanced in distributed reward condition. But the effect of reward design is very

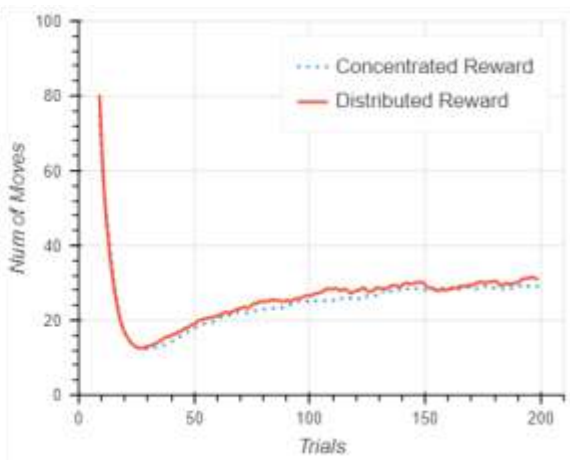

Fig. 3. (a) Learning curves (α = 0.5, β = 5, γ = 0.9)

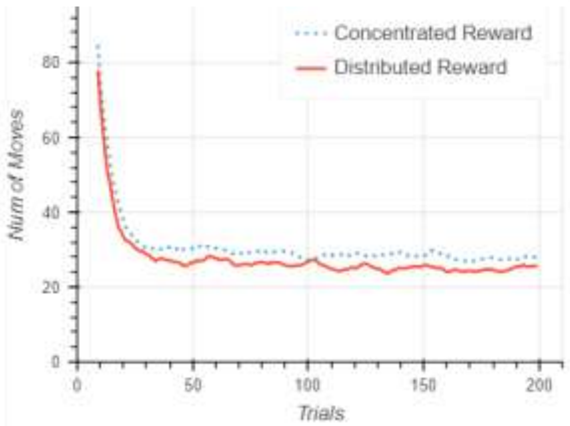

Fig. 3. (b) Learning curve (α = 0.5, β = 10, γ = 0.5)

different by the individual learners. Effect sizes (Hedges' d) of different reward plan are shown in Fig.4. Error bars indicate 95% confidence interval. Distributed reward plan is effective for learners who have large β(tendency to choose the same action) and small γ(leaners who tend to neglect the future reward). But this reward design is not effective for learners of another learning characteristics

3. Conclusion

Based on the computational model of neuromodulators (Doya, K. 2002), learning processes of the tower of Hanoi task for different learning characteristics are simulated. The same reward design had different effect on different learners. This is an example of learning simulation for biologically inspired numerical experiments.

References

1. Barto, AG., and Sutton, RS., *Reinforcement Learning* 2nd, ed. (MIT Press, Cambridge MA, 2018), 341-458.
2. Schultz, W., Neuronal Reward and Decision Signals : From Theories to Data, *Physiol. Rev*. 95 (2015) 853–951.
3. Schultz, W., Dopamine reward prediction error signaling: a two-component response, *Nature Reviews Neuroscience*, 17 (2016) 183-195.
4. Baldassarre, G. and Mirolli, M., *Intrinsically Motivated Learning in Natural and Artificial Systems*, (Springer 2013)
5. Todd M. Gureckis and Bradley C. Love, Computational Reinforcement Learning, In *Oxford handbook of computational and mathematical psychology*, 99-117, (Oxford University Press 2015)

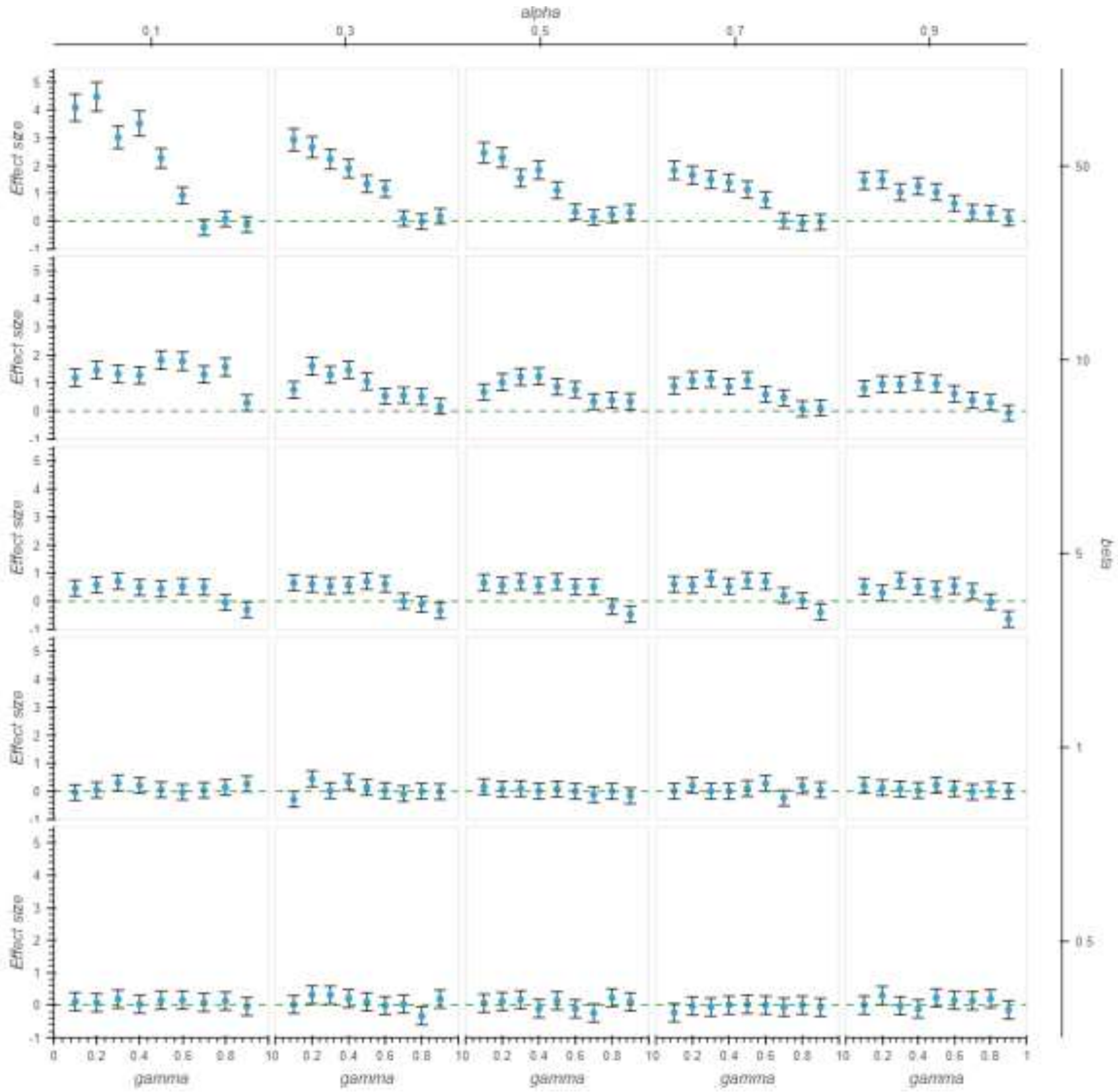

Fig. 4. Effect sizes for various learning characteristics.

6. Bromberg-Martin, ES., Matsumoto, M. Hikosaka, O., Dopamine in Motivational Control: Rewarding, Aversive, and Alerting, *Neuron* 68(5) (2010) 815-834.
7. Westbrook, A., and Todd S. Braver, TS., Dopamine Does Double Duty in Motivating Cognitive Effort, *Neuron* 89, (2016) 695-710.
8. Shenhav, A., Musslick, S., Lieder, F., Kool, W., Griffith, TL., Cohen, JD., and Botvinick, MM., Toward a Rational and Mechanistic Account of Mental Effort, *Annu. Rev. Neurosci*. 40(2017) 99–124.
9. Silver,D. Huang, A. Maddison,CJ, Guez,A, Sifre, L. George van den Driessche, Schrittwieser, J, Ioannis Antonoglou, I., Panneershelvam, V., Lanctot, M, Dieleman, S, Grewe, D., Nham, J, Kalchbrenner, N, Sutskever, I, Lillicrap, T, Leach, M, Kavukcuoglu, K, Graepel, T & Hassabis, D., Mastering the game of Go with deep neural networks and tree search, *Nature* 529 (2016) 484-489.
10. Silver, D., Huang, A., Maddison, C., Guez, A., Sifre, L.,van den Driessche, G., Schrittwieser, J., Antonoglou, I.,Panneershelvam, V., Lanctot, M. , Dieleman, S., Grewe, D.,Nham., Kalchbrenner, N., Sutskever, I., Lillicrap, T., Leach, M., Kavukcuoglu, K., Graepel, T. and Hassabis, D., Mastering the game of Go without Human Knowledge, *Nature* 550(2017) 354-359
11. Yamins, DLK, DiCarlo, JJ., Using goal-driven deep learning models to understand sensory cortex, *Nature Neuroscience*,19(3) (2016) 356-365.
12. Kumaran, D., Hassabis, D., McClelland, JL., What Learning Systems do Intelligent Agents Need? Complementary Learning Systems Theory Updated, *Trends in Cognitive Sciences*, 20(7) (2016) 512-534.
13. Hassabis, D., Kumaran, D., Summerfield, C., Botvinick, M., Neuroscience-Inspired Artificial Intelligence, *Neuron*, 95(2) (2017) 245-258.
14. VanLehn, K., Problem solving and Cognitive Skill Acquisition, In M.J. Posner (ed.) *Foundations of Cognitive Science*, MIT Press (1989) 529-579.
15. Barto, AG., and Sutton, RS., *Reinforcement Learning* 2nd, ed. (MIT Press, Cambridge MA, 2018), 91-103.
16. Barto, AG., and Sutton, RS., *Reinforcement Learning* 2nd, ed. (MIT Press, Cambridge MA, 2018), 321-338.
17. Fum, D., Missier, F.D., & Stocco, A.: Why a model is sometimes better than 10000 words, *Cognitive Systems Research* vol.8 (2007) 135-142 .

Estimation of Programming Learning Achievement by Line Tracing Robot

Yoshihiro Ohnishi
Faculty of Education, Ehime University, 3, Bunkyocho
Matsuyama, Ehime 790-8577,JAPAN
E-mail: ohnishi@ehime-u.ac.jp,
*www. ehime-u.ac.jp**

Teruyuki Tamai
Faculty of Education, Ehime University, 3, Bunkyocho
Matsuyama, Ehime 790-8577,JAPAN
E-mail: tamai.teruyuki.xq@ehime-u.ac.jp
www. ehime-u.ac.jp

Kazuo Kawada
Graduate School of Education, Hiroshima University, 1-1-1, kagamiyama
Higashi-hiroshima, Hiroshima 739-8524,JAPAN
E-mail: kawada@hiroshima-u.ac.jp
www. hiroshima-u.ac.jp

Abstract

How to estimate learning outcomes of programming learning is an important problem. However, quantitative evaluation method according to learning outcome is difficult. On the other hand, "work" of a control program influences the control performance of the plant by petrochemical industry, and to have an influence on the operation cost, Improvement of a program and am planning for productivity improvement are suggested by evaluating the control performance quantitatively. In this paper, evaluation of the program itself is attempted with hints on this concept of control performance assessment. In particular, the higher the degree of difficulty of the program is raised, the better the result is given to the learner. From this result, a method that can estimate the degree of difficulty of the program and the achievement of learning is considered. The teaching material is a robot that performs line tracing. Depending on the degree of difficulty of the program, use a route whose traveling route is different and whose goal time changes.

Keywords: programming learning, control performance assessment, learning achievement, line tracing robot

1. Introduction

How to estimate learning outcomes of programming learning is an important problem. However, quantitative evaluation method according to learning outcome is difficult. On the other hand, in the process control area represented by petrochemical industry, "work" of a control program influences the control performance of the plant. And it also influences on the operation cost. Therefore, the idea of control performance assessment (CPA) [1]-[6] is becoming important in the process control area. In other words, in the process control, CPA is used as a program evaluation. CPA is to calculate the quantitative evaluation of "performance of control", which tends to be subjective to the conventional operator, as "performance index". This method defines the control performance related to economic indicators such as product quality and expenditure of the plant as an index and defines that a good program efficiently earns money. In other words, the "effect" by the program is "visualized" as a continuous number "performance index".

Technical education at junior high school is expected to incorporate "problem solving" activities into programming learning. In programming learning, evaluation criteria tend to be whether a task has been cleared. With this, it is impossible to grasp how much the learner is approaching the problem solving. This is a factor that makes learning difficult for both learners and instructors.

In this paper, evaluation of the program itself is attempted with hints on this concept of control performance assessment[7]. In particular, the higher the degree of difficulty of the program is raised, the better the result is given to the learner. From this result, a method that can estimate the degree of difficulty of the program and the achievement of learning is considered. The teaching material is a robot that performs line tracing. Depending on the degree of difficulty of the program, use a route whose traveling route is different and whose goal time changes.

2. Basic concept

This research develops teaching materials that can be evaluated with "performance index" which quantifies the "work" of the program. "Performance index" considered

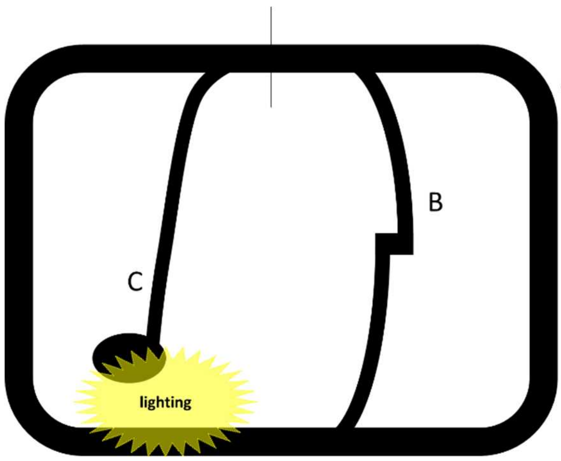

Fig. 1. Line trace course that allows to select a route according to difficulty level of the program.

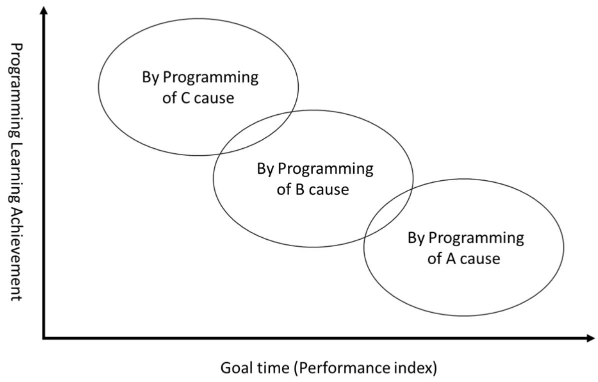

Fig. 2. Diagram correlating program achievement level and goal time (performance index).

in this research is an index that can express "work" of a program on some measure. As an example, consider a robot teaching material that performs line tracing with an infrared sensor as shown in Fig. 1 as a clue. The program following the course on the outside like the trajectory shown in A performs only the right turn. This program cannot be expected the good(short) goal time. Therefore, if a program that follows inner courses like the trajectory shown in B and can turn right and to the left, the goal time can be shorten a little more. Furthermore, if the program which uses a lightness sensor mounted on the robot is used and put in a function that runs in a bright place and enables shortcuts that shown in C, the time can be further shortened. In this task, the time required until the goal is "performance index", which means a program with a short time. At this time, there is a limit to the goal time with the A type program, and in order to obtain a shorter goal time, a type B program is required. In order to achieve a shorter time, a C type program is required. In other words, as shown in Fig. 2, if the goal time is shown as the "performance index", the learner's achievement level is estimated which shown as Fig.2.

3. Practice result

This chapter examines the concepts introduced in Chapter 2. The undergraduate students were charged with the task of programming the robot to trace the line in Figure 1. Undergraduate students who attend this practice belong to the teacher training course and do not receive specialized programming education. The objective robot is shown in Fig. 3, has ‘Arduino’ compatible ‘studuino mini’ [8] as the control board, and has two running

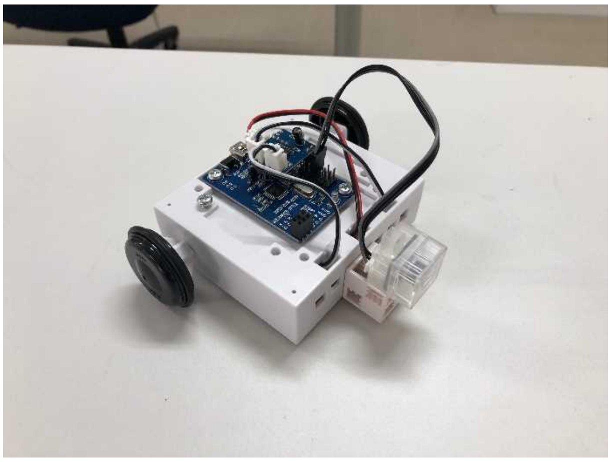

Fig. 3. Line trace robot with control board and sensor.

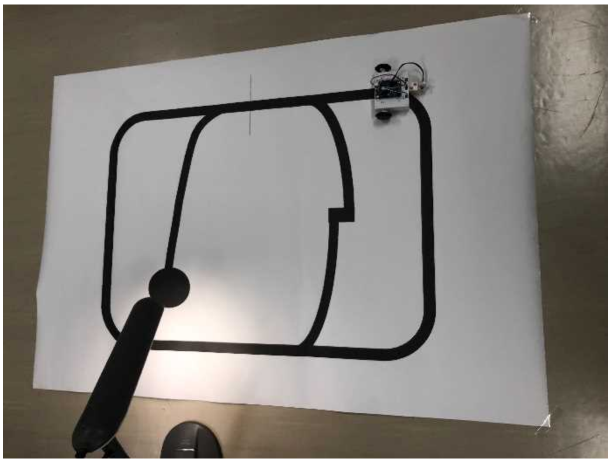

Fig. 4. Line tracing by Robot.

motors, an infrared sensor and a lightness sensor. The students who made the program were able to select the three routes shown in Fig.1. In other words, route A is the simplest program, route B in the next simple program, and route C in the most difficult program. In the route A, only the right turn is performed, but in the route B, it is necessary to perform left and right turns. In order to pass through Route C, not only the robot recognizes the black line under the robot, but also recognizes the brightness,

Table 1. Measurement result of the goal time divided for each degree of difficulty.

A	41.82	1’24.63	--	--
B	35.10	43.18	1’04.32	--
C	19.95	20.00	22.83	23.80

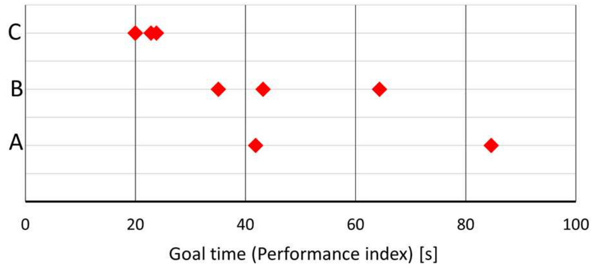

Fig. 5. Diagram visualized by program difficulty based on Table 1.

and if it gets brighter, it must take the right turn movement. Fig. 4 shows the line tracing run of the robot. Table 1 shows the results of students' line tracing robot. Also, a diagram visualized by difficulty level based on Table 1 is shown in Fig. 5. Comparing Fig. 5 with Fig. 2, rough trends are similar. In the line trace course in Fig.1, it can be said that it is possible to roughly estimate the degree of achievement of programming learning with the goal time as the performance index. However, some data reverses between difficulty and goal time. It is necessary to proceed verification with more data.

4. Conclusions

In this paper, to estimate the achievement of programming learning was considered. It was challenged to estimate the degree of difficulty the goal time as a performance index using the line tracing robot programming. Better goal time was obtained by more complex movements and programming with multiple sensors, was confirmed. In the future, verification will be carried out at the actual school site.

Acknowledgements

This work was supported by JSPS KAKENHI Grant Number JP18K02980.

References

(1) B. Huang and S. L. Shah : *Performance Assessment of Control Loops: Theory and Applications*, Springer, London (1999)
(2) M. Jelali : An overview of control performance assessment technology and industrial applications, *Control Engineering Practice*, Vol.14, pp. 441-466 (2006)
(3) M. Jelali : *Control Performance Management in Industrial Automation* ,Springer, London (2013)

(4) T. J. Harris: Assessment of Closed Loop Performance, Canadian *Journal of Chemical Engineering*, Vol.67, pp. 856-861 (1989)
(5) M. J. Grimble : Controller performance benchmarking and tuning using generalized minimum variance control。 *Automatica*, Vol. 38, pp.2111-2119 (2002)
(6) L. Desborough and T. J. Harris : Performance assessment measures for univariate feedback control, *The Canadian Journal of Chemical Engineering*, Vol 70, pp.1186-1197 (1992)
(7) Y. Ohnishi: Control Performance Assessment Method as Assessment of Programming Learning Achievement, *Proceedings of The 2018 International Conference on Artificial Life and Robotics (2018)*
(8) https://www.artec-kk.co.jp/studuino/en/ (Access Nov.10, 2018)

Development of Cultivate Computational Thinking using Finger Robot

Kaito Omata
Faculty of Education, Tokyo Gakugei University,
4-1-1, Nukuikita-machi, Koganei, Tokyo, 184-8501, Japan.[*]

Shinichi Imai
Graduate school, Tokyo Gakugei University,
4-1-1, Nukuikita-machi, Koganei, Tokyo, 184-8501, Japan.

E-mail: a151404s@st.u-gakugei.ac.jp, shimai@u-gakugei.ac.jp
http://www.u-gakugei.ac.jp/

Abstract

Computational Thinking is one of the necessary skills for children who live in modern times. Therefore, in this research, we aim to design lesson that can cultivate Computational Thinking. In this research, design a lesson that cultivates Computational Thinking by moving a robot to the specified finger state using a finger robot. At that time the children can know that by using the notion of "binary" you can count many numbers by bending and extending your fingers. By using a finger robot, it is thought that children will motivate themselves to teach and to understand easily.

Keywords: Computational Thinking, Programming Education, Binary number, Robot, CS Unplugged

1. Introduction

In modern times, it is said to be called the fourth industrial revolution. In Japan, the National Curriculum was revised in 2017, and in the elementary school a new national curriculum will be implemented from FY 2020. In the new national curriculum, programming education at elementary school level is compulsory. Worldwide, in England the subject "Computing" has already been compulsory in the primary education stage since 2014 [1]. From the world viewpoint, it can be seen that knowledge, skills, qualities and abilities of computers and programming are considered necessary in future times.

Towards 2020, lessons using visual programming languages, lessons using robots, etc. have been tried as practices of programming education in various regions of Japan [2, 3]. According to a lesson using a robot, a robot can draw interest even if the degree of interest and understanding of the scientific concept of the child is not high. It is also excellent for thinking trial & error. And it is reported that children can work on programming with enjoying.

Many of the robots used in programming lessons are mobile robots. The mobile robot has the advantage that the operation at the time of program execution can be observed as the behavior of the robot and it is possible to understand the control structure and its necessity in stages by repetition or case classification at the time of collision.

However, there are problems that teachers who can instruct robot programming are few, and it is difficult for children to understand and program sensors and motors.

By developing robot teaching materials that are simple in programming and operate without having a deep understanding of sensors and motors, robot programming with many advantages in programming education becomes easy.

As an approach to teaching information science to primary school students, there is "COMPUTER SCIENCE Unplugged" (Next, CS Unplugged) developed by Dr. Tim Bell of New Zealand and others [4].

CS Unplugged is a method that learns basic principles of computers easily in elementary school students. Examples include binary numbers, image representations, text compression, and the like. In the world of computers, information is represented in binary notation. In the process of learning programming, learning the structure of the computer makes it possible to deepen the understanding of computers and programming.

It is thought that educational materials that can learn programming and basic principles of computers simultaneously are necessary in the future. In this research, we develop robot teaching materials that can simultaneously learn binary numbers and learn programming.

2. Educational robot teaching materials

Fig. 1 shows the appearance of the robot teaching material (Next, finger robot). The finger robot uses ARTEC Corporation's parts of ARTEC Robo. Finger robot model human hands. By programming, children can move each finger. By associating the hand shape of the finger robot with the binary number representation, the child can know the binary number representation. A decimal number stretched over the front of a finger robot is an aid for associating the shape of a hand with a binary number and a decimal number. Children associated with finger shape and binary numbers can also associate binary numbers with decimal numbers.

2.1. *Binary number*

Binary number is a number expressed using two numbers of "0" and "1". In the method of counting binary numbers with fingers, "0" and "1" correspond to the bending and stretching of the finger [5]. Fig. 2 shows the idea of binary numbers using fingers. Fig. 2 (a) shows the correspondence between fingers and digits, and (b) shows an example of representing binary numbers with fingers.

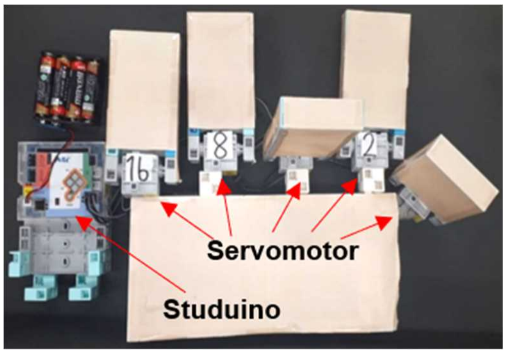

Fig. 1. Finger robot

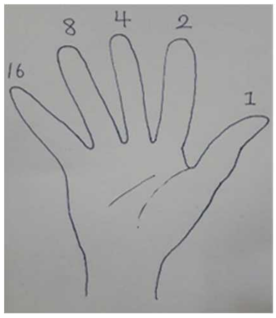

(a)Digit correspondence

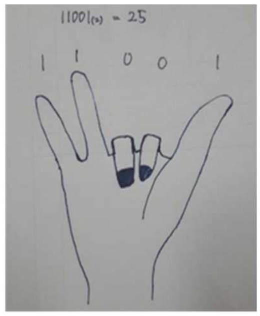

(b) An example

Fig. 2. Concept of expressing binary numbers with fingers

Until now, efforts to teach elementary school students binary numbers using CS unplugged have been done. What has been used in CS unplugged is a method of expressing binary numbers on the front and back sides of a card on which points corresponding to the decimal number are drawn. In the CS unplugged, the back of the card corresponds to "0" and the front corresponds to "1". In the finger robot, the front and back of the card are replaced by bending and extending the fingers. Also, by moving the finger of the finger robot, the decimal number stretched on the front of the finger robot can be seen / disappeared. This also corresponds to representing on the front and back of the card.

2.2. *Hardware*

The hardware configuration is shown in Fig. 3. The finger robot uses four AAA batteries as a battery. The computer uses Studuino which is Arduino compatible base. Studuino is connected to a personal computer (PC) to use. As shown in Fig. 4, the PC is used to create a program to transfer to Studuino and to display the status of the finger robot.

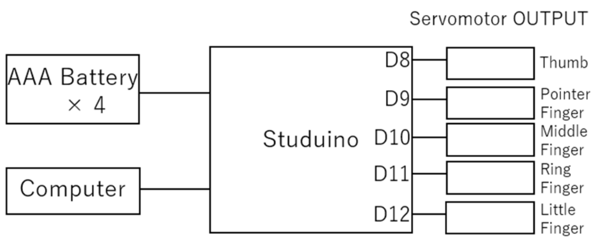

Fig. 3. System diagram

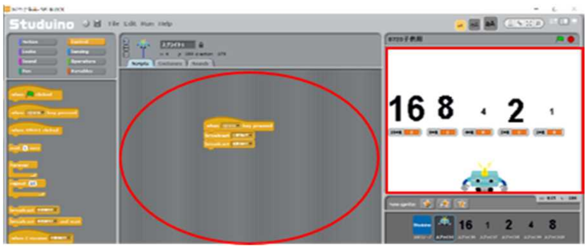

Fig. 4. Program creation screen

Fig. 5. Block that specifies the angle

In the finger robot, one servo motor is used for each finger, and a total of five servo motors are used. Human hand fingers, the thumb has two joints, and the other fingers have three joints. However, as it is considered difficult for elementary school students to think of multiple joints when programming, only one joint of a finger robot is considered. By connecting the terminal of the servo motor to the port of Studuino, it becomes possible to move the servomotor. To control the servo motor, usually adjust the pulse interval. In Studuino, as shown in Fig. 5, the servomotor can be moved by directly inputting the angle (arc degree). There are two states of the finger part of the finger robot, that is, a bent state and an extended state. In the case of Fig. 1, the fingers (thumb) at the right end and the third finger (middle finger) from the right are bent and the other fingers are in a stretched state. The servo motor is in a state in which the finger is bent by 180 ° and the state in which the finger is extended by 90 °.

2.3. *Software*

In the finger robot, each finger moves independently. The software that moves the finger robot uses Studuino

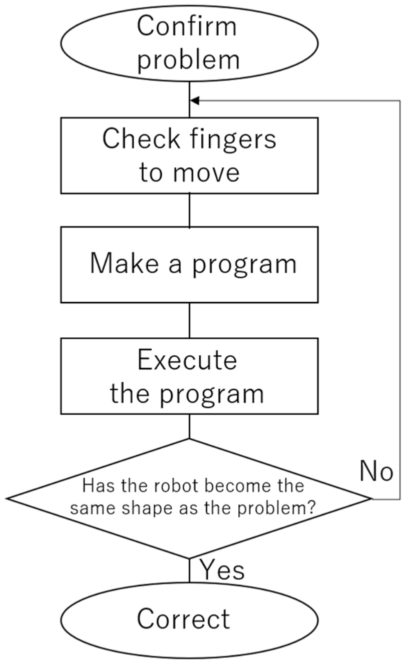

Fig. 6. Program creation flowchart

Software, a visual programming software based on Scratch. As shown in Fig. 4, Studuino Software creates a program by combining blocks. Therefore, even elementary school students can easily experience programming. Although it is written in English in the figure, when used by a child, it is used in Japanese notation. The boxed portion in Fig. 3 is a space called "stage". The decimal number displayed on the stage changes the appearance of the number corresponding to the state of each finger of the finger robot. In Fig. 4, "4" and "1" are small. This indicates that the finger robot is bent with fingers corresponding to "4" and "1". In addition, under the decimal number, the value corresponding to the state of the finger and the notation of the binary number is displayed. "0" is displayed below "4" and "1" in Fig. 4 so that it can be seen that the current finger state is "11010" when expressed in binary.

Children use Studuino Software for programming. As shown in Fig. 6, the child creates a program for moving the finger portion of the robot to a designated state (eg, a state in which only the ring finger and the thumb are bent). In the program that moves the finger part, we use functions prepared beforehand by the authors. As an example, the function to move the thumb is shown in Fig.7. This function is a function that changes the value

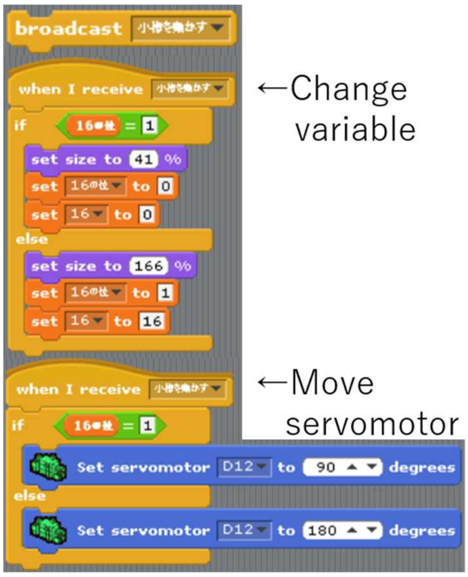

Fig. 7. Function example: To move thumb

of a variable when called. The variable has two variables, a variable representing the state of the servomotor and a variable representing whether the finger portion represents binary "0" or "1". The child does not create the contents of the function. The servomotor can be moved by merely using the function.

3. Activity

In lesson, children use finger robots in pairs of two child. The problem is presented from the teacher to move the finger robot to the specified state. The question is presented in four kinds of represents. Four kinds of problems are problems of fingers represented by photographs, letters, binary numbers, and decimal numbers. To these problems, consider a program in pairs. To get to the state expressed by the problem, think about which finger to move. From the current state to the state of the problem, execute the program once and transform it. Therefore, instruct that every time you make a mistake, the current state will not change.

4. Results of using teaching materials

The correspondence between the program and the movement of the finger robot is shown in Fig. 8. In the state shown in Fig. 8, when the program on the left of Fig. 8 is executed, the state is changed to the state shown in the lower part of Fig. 8.

Fig. 8. Program(left) Before robot(above) After robot(under)

5. Conclusion

In this research, we developed a teaching material called a finger robot which can be used for programming education in elementary school. Elementary school students can use the finger robot to know the idea of counting binary numbers with fingers while experiencing programming. Children can deepen their understanding of correspondence between binary numbers and decimal numbers by associating the state of the finger robot with the representation of binary numbers and decimal numbers. In the future, we plan to conduct durability tests assuming the use of children and setting tasks to cope with various developmental stages.

References

1. QCA, National curriculum in England: computing programmes of study, 2013.
2. Katsuyuki HAGIWARA, *Robot Programming for Elementary School Children*, Mie University Faculty of Education Departmental Bulletin Paper, Vol. 68, 2017, pp. 307-315.
3. KOUJI KAI, YOSHIHIKO KIMURO, YOSHIFUMI SAKAGUCHI, HIROTO YASUURA, An Educational Method of Computer Principles for Elementary and Junior High School Students, *Transactions of Information Processing Society of Japan*, Vol.43, No.4, 2002, pp.1121-1131.
4. Tim Bell, Ian H.Witten, Mike Fellows, *COMPUTER SCIENCE unplugged,* 2015.
5. Frederik Pohl, *The best of Frederik Pohl*, Ballantine Books Co., Ltd., 1975.

Different Type of Interaction or Decision Error Contribute to Functional Differences

Saori Iwanaga
Department of Safety Technology, Japan Coast Guard Academy, 5-1 Wakaba
Kure, Hiroshima 7378512, Japan

Masao Kubo
Department of Computer Science, National Defense Academy of Japan, 1-10-20 Hashirimizu
Yokosuka, Kanagawa 2398686, Japan
E-mail:s-iwanaga@jcga.ac.jp, masaok@nda.ac.jp

Abstract

There are many situations where interacting agents can benefit from coordinating their actions, that is, agents gain payoffs by taking the same action as others. These situations can be modeled as coordination games. Another situations is modeled as complementary game, asymmetric coordination games or minority games. In complementary game, agents gain payoffs by taking the different action from others. We deal with these coordination games and asymmetric coordination games as type of interaction and each agent can change the interaction type. And each agent can change the interaction partner. We show that population changes to a mixed population comprised of 80% cooperative agents and 20% complementary agents. A mixed population diversify the collective behavior, type of interaction and preference. There, opposite type of interaction plays a role of small decision error, and it is inefficient to adopt both.

Keywords: Collective behavior, decision error, diversity, payoff matrix, type of interaction, preference.

1. Introduction

Studies into multi-robot and multi-agent simulations began in the late 1980s. Reynolds[1] shows that collective behavior occurs when three rules are used simultaneously by Boids and that the collective behavior is a complex system. Sims' study[2] of virtual block creatures and Terzopoulos' study[3] of artificial fish provide examples of emerged physical or functional characteristics. Kubo et.al[4] demonstrates the emergence of unique individuals in a competition for food between ant colonies. However, individual heterogeneity is often ignored in most studies[5]. For example, a recent study investigated the formation by multi robots. In a multi-robot system, if heterogeneous robots exist, such robots are removed[6]. There are limits to the adaptation performance of multi robot systems with heterogeneous robots, and computer simulations rarely reproduce emerged diversity in population.

There are many situations where interacting agents can benefit from coordinating their actions, that is, agents gain payoffs by taking the same action as others. Examples where coordination is important include trade alliance and the choice of compatible technologies or conventions, such as the choice of a software or language. These situations can be modeled as coordination games[7, 8]. Complementary games that have received attention recently are asymmetric coordination games or minority games. In these games agents gain payoffs by taking the different action from others. Examples where asymmetric coordination is important is division of labor, traffic congestion or site selection in opening shops. The Santa Fe bar problem and the minority games are also modeled in the same manner.

We deal with these coordination games and asymmetric coordination games as type of interaction. In this study, we deal with population in which each agent can change the interaction type. We show that small decision error makes collective behavior efficient. We also show that with without error is good for population in which each agent can change the interaction type.

2. Model

2.1. *Social Network*

We consider the lattice structure for social network of agents and each agent interacts with only its neighbors. We deal with the von Neumann neighborhood model, in which each agent interacts with its nearest four neighbor agents all at once. Lattice model is used to make the ecological characteristic of living beings clear [9].

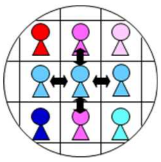

Fig.1. von Neumann neighborhood model.

2.2. *Type of Interaction*

There are two behavior, S1 and S2, for each agent. We adopt the payoff matrix given in Table 1[10], which describes the outcome of the interaction between agents. In this matrix, if two agents chose the same behavior, agent Ai can receive a positive payoff 1- θi or θi, or agent Ai receive payoff 0 where $0 \leq \theta i \leq 1$. This is coordination game. Contrastingly, there is another game, if two agents chose a different behavior, agent Ai can receive a positive payoff. This is a complementary game. The payoff matrix is given by Table 2[11].

3. Behavior of Agents

3.1. *Decision of the Choices: Best Response Rule*

Agents are not aware of the behavior the neighbor agents will take, but know the last behavior the neighbor agents took. We define the proportion of agents having chosen S1 at time t as pi (t) ($0 \leq pi(t) \leq 1$) in four neighbors of agent Ai. Each agent acts to maximize the utility and takes the best response against the behavior which the neighbor agents took by calculating the expected payoff. In a coordination game, rational agent Ai calculates the expected utilities by S1 and S2 at time t, which is given as follows,

$$Uc(S1, t) = pi(t)(1-\theta i),\ Uc(S2, t) = (1-pi(t))\,\theta i. \quad (1)$$

Agent Ai chooses S1 if $Uc(S1, t) > Uc(S2, t)$, or chooses S2 if $Uc(S1, t) < Uc(S2, t)$ at next time t +1. The decision rule of agent Ai at time t +1 is described as follows. Agent Ai chooses[10],

$$\text{S1 if } pi(t) > \theta i,\ \text{S2 or if } pi(t) < \theta i. \quad (2)$$

That is the best response rule and the decision depends on the parameter θi. When pi (t) = θi, we assume that the agent chooses the same behavior as at time t. We define the parameter θi as threshold of agent Ai. According to the threshold, behavior of the agents differentiate from each other. Moreover, the proportion of agents having chosen S1 among the partners pi (t) of agent is different from each other. Then, the decision of the agent different from each other. That is, the threshold and social network of agent effects on the behavior of the agent, they form the collective behavior, which is the behavior of the whole population. We define the collective behavior p(t) as the proportion of agents having chosen S1 in population at time t. We call the agent with payoff matrix of Table 1 as cooperative agent.

Table 1 The payoff matrix of agent Ai (cooperative).

Coordination Game		Behavior of Other Agent	
		S1	S2
		pi (t)	1- pi (t)
Behavior of Agent Ai	S1	1- θi	0
	S2	0	θi

Table 2 The payoff matrix of agent Ai (perverse).

Complementary Game		Behavior of Other Agent	
		S1	S2
		pi (t)	1- pi (t)
Behavior of Agent Ai	S1	0	θi
	S2	1- θi	0

In contrast, Agent Ai in a complementary game calculates the expected utilities by S1 and S2 at time t, which is given as follows,

$$Ua(S1, t) = (1-pi(t))\,\theta i,\ Ua(S2, t) = pi(t)(1-\theta i). \quad (3)$$

Then, agent Ai chooses[11],

$$\text{S1 if } pi(t) < \theta i,\ \text{S2 or if } pi(t) > \theta i. \quad (4)$$

When pi (t) = θi, we assume that agent chooses the same behavior as at time t. We call the agent with payoff matrix of Table 2 as perverse agent.

3.2. *Decision Error*

We set very small probability an agent will make a mistake. If agents are not absolutely rational, there are possibility to make mistakes, which we call decision error. We define the probability as ε[12]. And each agent make decision depending on (2) or (4) with probability 1- ε. With probability ε, each agent make decision opposite from (2) or (4).

3.3. *Movable for New Neighbors*

If an agent wants to receive a high payoff, it is an effective method to move to another site and change its partners with which it interacts[7, 13]. If the average payoff of agent Ai received through and interaction with four neighbor agents is above the threshold μ, agent Ai stays the site. Or agent Ai moves to another site. In cooperative or complementary games, the expected utilities by S1 and S2 at time t, which are given as (1) or (3). The rule of change neighbor agents is as follows, where v = a, c and k = 1, 2. Then, at next time t +1 agent Ai[13],

stays at the site if Uv (Sk, t) ≥ μ,
moves to another site if Uv (Sk, t) < μ. (5)

Previously, we showed that movability of agent is effective for collective behavior[13].

3.4. *Self-Reinforcement of Preference*

Each agent can update the payoff parameter through interaction. We define this as self-reinforcement of preference. As for the coordination game in Table 1, if Agent Ai[13] has been chosen S1 for T times in succession, the agent increases the payoff 1- θi for S1 by delta Δ and decreases the payoff θi for S2 by delta Δ. Or if agent Ai has been chosen S2 for T times in succession, the agent increases the payoff θi for S2 by Δ and decreases the payoff 1- θi for S1 by Δ.

In contrast, in the complementary games in Table 2, if Agent Ai has been chosen S1 for T times in succession, the agent increases the payoff θi for S1 by Δ and decreases the payoff 1- θi for S2 by Δ. Or if agent Ai has been chosen S2 for T times in succession, the agent increases the payoff 1- θi for S2 by Δ and decreases the payoff θi for S1 by Δ.

3.5. *Type of Interaction*

3.5.1 When agent chooses S1 at time t

Agent Ai chooses cooperative game if Uc (S1, t) > Ua (S1, t), or chooses complementary game, or if Uc (S1, t) < Ua (S1, t) at next time t +1. The decision rule of agent Ai at time t +1 is described as follows. Agent Ai chooses

cooperative game if pi (t) > θi,
complementary game or if pi (t) < θi. (6)

When pi (t) = θi, we assume that agent chooses the same game as at time t.

2.5.2. When agent chooses S2 at time t

In contrast, agent Ai chooses cooperative game if Uc (S2, t) > Ua (S2, t), or chooses complementary game if Uc (S2, t) < Ua (S2, t) at next time. The decision rule of agent Ai at time t +1 is described as follows. Agent Ai chooses

cooperative game if pi (t) < θi,
complementary game or if pi (t) > θi. (7)

When pi (t) = θi, we assume that agent chooses the same game as at time t.

4. Simulation settings

We arrange agents for an area of 50×50 (2500 agents) with no gap, four corners and ends of an area connect it with an opposite side. First, we set the same threshold θi =0.5 for all agents. The Initial collective behavior p(0), which is the proportion of agents having chosen S1 in population, from 0.0 to 1.0 at intervals of 0.125, where we assume that each agent chooses at random. Each agent makes its decision depending the best response rule (2) (4) each time step, and then collective behavior p(t) changes. We simulate 10,000 time steps for a trial. We simulate 100 trials per one Initial collective behavior and investigate Final collective behavior p*. We set three cases, in which agents make decision with no noise, with noise 0.001 and with noise 0.01.

The rule of moving agents is given by (5). For each case, we set the initial ratio of agents adopting a cooperative game, 100%, 50% and o%. Each agent can select the game (6) (7). We set parameters as follows based on preliminary experiments, the threshold to move μ as 0.3, interval of self-reinforcement T as 10, increasing delta Δ as 0.01 and interval of value change R as 20. Increasing delta Δ must be slower than decision speed for emergence of preference diversity. Similarly, we set a greater interval of value change R than an interval of self-reinforcement T for emergence of type of interaction diversity. We evaluate the average utility at last time step.

5. Simulation results

Simulation results are shown below. The results are when initial collective behavior p(0) was 0.5 as represents. In these figures, x-axis is the average final collective behavior p* and y-axis is the average utility. Simulation result when agent makes decision error is shown in Fig.2. All results show that about 50 % of agents choose S1 at last. Without error, in population with 100% or 0% of cooperative agents, which described by "co" or "per", the average utilities with error 0.001 are higher than that without errors or with error 0.01. But, "50% mix" population of both types shows the opposite result.

Simulation result when agent can change interaction type is shown in Fig.3. Without error, the average utilities are higher than that of with decision error. There, the ratio of cooperative agents become about 80% at last.

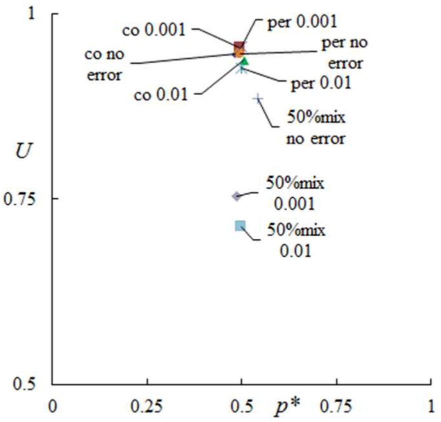

Fig.2. Effect of decision error.

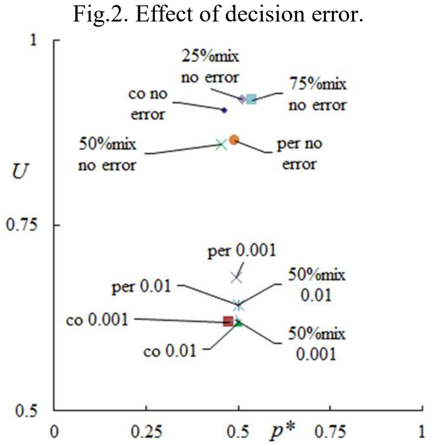

Fig.3. Effect of different type of interaction.

6. Conclusion

We deal with these coordination games and asymmetric coordination games as type of interaction and each agent can change the interaction type. We show that population changes to a mixed population comprised of 80% cooperative agents and 20% complementary agents. A mixed population diversify the collective behavior, type of interaction and preference. There, opposite type of interaction plays a role of small decision error, and it is inefficient to adopt both.

References

1. C. Reynolds, Flocks, Herds, and Schools: A Distributed Behavioral Model, Computer Graphics, in *SIGGRAPH '87 Proceedings of the 14th annual conference on Computer graphics and interactive techniques*, ACM (USA, New York, 1987), pp.25-34.
2. K. Sims, Evolved Virtual Creatures, Computer Graphics, in *SIGGRAPH '94 Proceedings of the 21st annual conference on Computer graphics and interactive techniques*, ACM (USA, New York, 1994), pp.15-22.
3. D. Terzopoulos, X. Tu and R. Grzeszczuk, Artificial Fishes: Autonomous Locomotion, Perception, Behavior, and Learning in a Simulated Physical World, *Artificial Life*. **1**(4) (1994) 327-351.
4. M. Kubo and Y. Kakazu, Evaluation of Coordinated Motions of Multi-Agent Systems on Competition for Food between Ant Colonies, *IPSJ Journal* (in Japanese). **35**(8) (1994) 1555-1566.
5. R. Axelrod and M.D. Cohen, *Harnessing Complexity* (Free Press, New York, 2001).
6. M. Rubenstein, A. Cornejo and R. Nagpal, Programmable self-assembly in a thousand-robot swarm, *Science*, **345** (6198) (2014) 795-799.
7. T. Schelling, *Micromotives and Macrobehavior* (Norton, New York, 1978).
8. B. Huberman and N. Glance, Diversity and Collective Action, in *Interdisciplinary Approaches to Nonlinear Complex Systems, Springer Series in Synergetics* 62, (Springer, Berlin, 1993), pp.44-64.
9. M.A. Nowak, *Evolutionary Dynamics: Exploring the Equations of Life* (Harvard University Press, Cambridge, 2006).
10. S. Iwanaga and A. Namatame, The Complexity of Collective Decision, *Journal of Nonlinear Dynamics and Control*. **6**(2) (2002) 137-158.
11. S. Iwanaga and A. Namatame, Emergent Division of Labor and Evaluation of Its Efficiency and Equity, *International Journal of Knowledge-Based Intelligent Engineering Systems*. **7**(3) (2003)115-123.
12. R. Selten, Reexamination of the perfectness concept for equilibrium points in extensive games, *International Journal of Game Theory*. **4**(1) (1975) 25–55.
13. S. Iwanaga and A. Namatame, Influence of Partner Selection on Functional Differentiation: Emergence of Diversity by Isolated Interaction and Preference Change, *Journal of Robotics, Networking and Artificial Life*. **3**(4) (2017) 257-264.

Evaluation for the Synchronization of the Parade with OpenPose

Yohei Okugawa
Dep. of Computer Science, National Defense Academy of Japan
Yokosuka, Kanagawa, 239-8686, Japan
Masao Kubo
Dep. of Computer Science, National Defense Academy of Japan
Yokosuka, Kanagawa, 239-8686, Japan
Hiroshi Sato
Dep. of Computer Science, National Defense Academy of Japan
Yokosuka, Kanagawa, 239-8686, Japan
Bui Duc Viet
Dep. of Computer Science, National Defense Academy of Japan
Yokosuka, Kanagawa, 239-8686, Japan
E-mail: em57037@nda.ac.jp, masaok@nda.ac.jp
www.nda.ac.jp/cs/

Abstract

In military organization, the synchronization in the parade is important for showing their majesty. However, we don't have any quantitive evaluation methods for the parade. In this research, we propose an evaluation method focusing on the synchronization level of the parade with OpenPose. In order to measure the synchronization level, our method is based on the timing of arm swing data in the parade, and the result shows our method is appreciable for measuring the synchronization level.

Keywords: OpenPose, Unity, Parade, Synchronization, Multi-person Pose Estimation, Multi-Agent

1. Introduction

In the military parade, the synchronization level of each member is a major factor of the performance. Shimohagi et al. conducted scientific analysis for the synchronization of the parade[1],[2],[3], however, measuring synchronization level of the parade requires a large number of posture data at same time and is difficult. We don't have any quantitive evaluation methods for the synchronization. In this research, we propose the evaluation method focusing on the synchronization level of the parade with OpenPose. OpenPose [4] can measure many kinds of postures from movies simultaneously, therefore it is much easier to acquire data than conventional motion analysis with motion capture [5],[6], and it is suitable for parade analysis, which is a cooperative operation of multiple people (Fig. 1).

Fig.1 Military Parade with OpenPose
(https://www.youtube.com/watch?v=zaviumhF7aA)

As a first step of the research, in order to measure the synchronization level, we focus on the arm swing data of each cadets in the parade and analyze "Marking Time". Marking Time is a military step in which soldiers march in place, moving their legs as in marching, but without step forward.

In this paper, we analyze the synchronization of two members. When we evaluate the synchronization level of the two members appropriately, in the case of multiple people, we evaluate it in combination of two members.

This paper is organized as follows. After introducing OpenPose in the next section, we describe the data processing method from OpenPose. In the section 4, we propose the evaluation method for the synchronization level. After explaining the two experiments with 3D CG and real behavior of Marking Time in the section 4, we show our results from the experiments. Considering the results, our evaluation method is appreciable for real Parade.

2. OpenPose

OpenPose represents simultaneous posture recognition of multiple people on single images. The left side of Fig.2 shows an example of pose estimation with OpenPose. If the movements of the two are synchronized, it can be expected that the same trend data can be obtained.

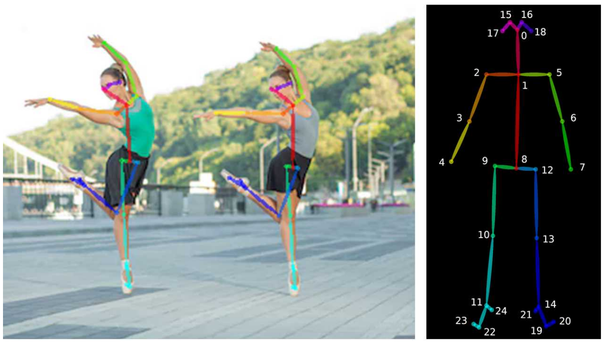

Fig.2 Multi-person Pose Estimation with OpenPose

The right side of Fig. 2 shows the points of posture data. As a three-dimensional data of $[x,\ y,\ likelihood]$ on the image according to the number of points, we can obtain 85 points of data for one piece of posture information. It is difficult to measure the synchronization because the values and accuracy of the posture data are different depending on the position and body size. Therefore, it is necessary to use a trend which is not influenced by position or height as an index.

3. Proposed Method

In this section, we propose the measurement method using indicators focusing on inflection point of movement. In the following, we will explain the proposed method in order.

3.1. *Focus Points*

Focusing on the synchronized arm swing of the left hand during the parade, we obtain the data of each shoulder (5 in Fig. 3), elbow (6 in Fig 3) and perm (7 in Fig.3). We converted the data into 4 angles: φ, ψ, λ, θ (Fig. 3)

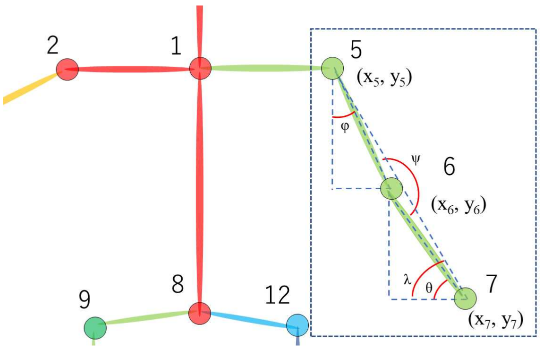

Fig 3. Focus Points of OpenPose

3.2. *K-means Clustering*

In order to get time series data of each person's arm swing angle in the image, we conduct the clustering using K-means method (1) for the angle data. In this section, we analyze the Marking Time movies for two members, thus we set K=2 for the cluster analysis using K-means method.

$$\arg\min_{V_1,V_2} \sum_{i=1}^{n} \min_{j} \left\| x_i - V_j \right\|^2 \tag{1}$$

3.3. *Smoothing*

In order to read the inflection point of the time series data of arm swing angle accurately, we conduct the smoothing process for the angle data (2).

$$\mathrm{ma}_i = \left\{x_i + 0.5 \times (x_{i-k} + x_{i+k}) + \sum_{j=1}^{k-1}(x_{i-j} + x_{i+j})\right\} \quad (2)$$

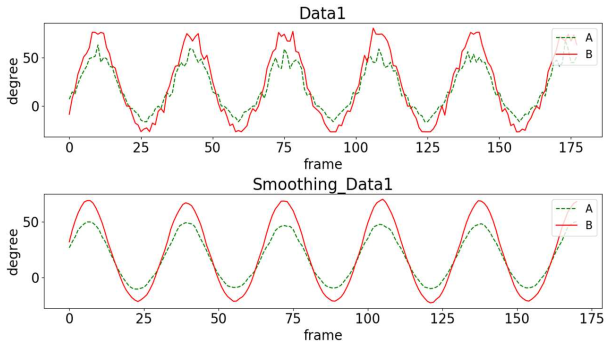

Fig. 4 Data Smoothing Before and After

Fig. 4 shows an outline of the data before and after the smoothing process. It can be seen that the outline is smooth, and the inflection points are easy to read.

3.4. *Evaluation*

We get the time series data of arm swing angle (3).

$$\vec{A} = [Ang_{A1}, Ang_{A2}, \cdots, Ang_{Ai}] \quad (3)$$

$\vec{A}$ is the time series data of arm swing angle of member A in a image, and Ang_{A1} is the arm swing angle of member A at the first frame of the movie.

From each time series data of the arm swing angle, we use correlation coefficients for evaluation.
We define the synchronization level *r* as below,

$$\mathrm{r} = \frac{\sum_{i=1}^{n}(x_i-\bar{x})(y_i-\bar{y})}{\left((\sum_{i=1}^{n}(x_i-\bar{x})^2)(\sum_{i=1}^{n}(y_i-\bar{y})^2)\right)^{\frac{1}{2}}}. \quad (4)$$

We use Pearson's moment correlation coefficient as the synchronization level. If *r* approaches 1, it is synchronized. If *r* approaches -1, it is expected that the phase will be in opposite.

4. Experiment

In this chapter, we conducted two kinds of experiments. In Experiment 1, we examine measurement accuracy and evaluation index of our method using 3D CG models. After confirming the effectiveness of the evaluation method, in Experiment 2, we evaluate the synchronization level *r* in real Marking Time behavior with our method.

4.1. *Experiment 1: The Accuracy of Our Method*

For measuring the effectiveness of our method, we analyze the 3DCG models. Since we can adjust the synchronization level between two models, it can be an ideal analysis target. Evaluation using 3DCG created by Unity is appropriate because we can completely control human-like model. In the 3D CG, the two models are doing the Marking Time (Fig. 5).

Fig. 5 An example of 3D CG Models with OpenPose

The arm swing angle of the models during the Marking Time was implemented according to the simple vibration equation (5). In this section, the phase difference of the arm swing angle is expressed by changing the initial condition of θ_0 as 0, π / 8, π / 4, π / 2 and π.

$$\mathrm{x} = \mathrm{A}\sin(\omega t + \theta_0) \qquad (\omega = 2\pi) \qquad (5)$$

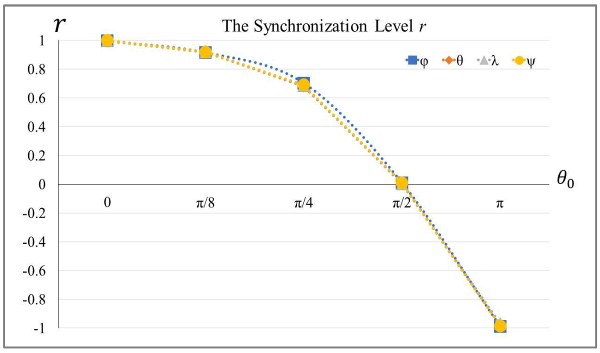

Fig. 6 The Synchronization Level r of 3D CG

Fig. 6 shows the synchronization level *r* in Eq. (4) in time series angle data of two models. As the initial value of θ_0 shifts, the value of *r* decreases. Also, when the initial value of θ_0 is π, that is, each arm swing angle is in opposite phase, it approaches -1. From the result, the synchronization level r is monotonically decreasing according to the value of θ_0. Therefore, it was confirmed that our evaluation method is appreciable as a measuring the synchronization level in the 3D CG Marking Time movie.

4.2. *Experiment 2:The Evaluation of Real Parade*

Since we can show our evaluation method is appreciable, we experiment for real Marking Time with our method which is appreciable for evaluation the synchronization. As in Experiment 1, we analyze Marking Time for two members. We experiment for two cadets of the National Defense Academy, which have parade training every day, and their height is 10 cm different (Fig. 7).

Fig. 7 A Capture of Real Marking Time with OpenPose

For Experiment 2, we have three types of arm swing: *Phase Synchronization*, *Phase Difference* and *Phase Opposition*. Fig 7 shows a snap shot of *Phase Opposition*. We can see both cadet arm swing is opposite in Fig. 7.

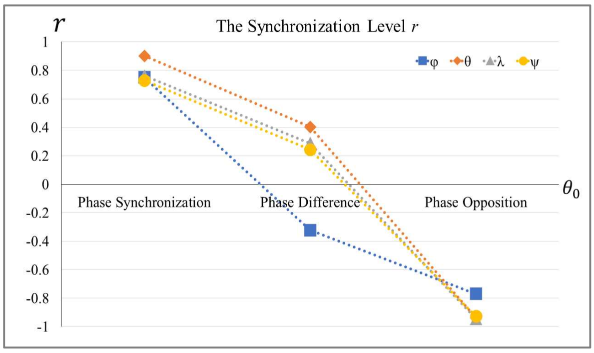

Fig. 8 The Synchronization Level r of Marking Time

Fig. 8 shows the synchronization level *r* of Marking Time. As shown in Fig. 8, we can confirm that as the difference of the arm swing angle shifts, the synchronization level *r* decreases. This shows the same trend as the result of Experiment 1, and it is our evaluation method is appreciable for measuring the synchronization in real Parade. In addition, although it was suggested that measuring the synchronization level with armpit angle has good sensitivity for evaluation, further consideration is needed as future task.

5. Conclusion

We propose the evaluation method for the synchronization level of the Parade with OpenPose. We focus on the arm swing data and analyze the Marking Time for two members. Through the simulation experiment using 3DCG, it was confirmed that our method based on time series angle data is appreciable for measuring the synchronization level. Moreover, through the real Marking Time of Parade, our evaluation method is appreciable for measuring the synchronization level. In addition, it was suggested that measuring the synchronization level with armpit angle has good sensitivity for evaluation.

References

1. Takato Shimohagi (2017), Parade Analysis based on Network System, *In Proceedings of National Defense Academy of Japan Graduation Thesis*, pp. 61-62(in Japanese).
2. Tento Ishihara (2018), Development of VR parade training system, *In Proceedings of National Defense Academy of Japan Graduation Thesis*, pp. 47-48(in Japanese).
3. Yohei Okugawa, Masao Kubo, Takato Shimohagi, Tento Ishikawa, and Hiroshi Sato (2018), Analysis of a Parade with the Kuramoto Model -For Better Performance without Trainings-, *In Proceedings of IEEE SMC* 2018.
4. Z. Cao, T. Simon, S.E. Wei, and Y. Sheikh (2017), Realtime multi-person 2d pose estimation using part affinity fields. *In Proceedings of the 2017 IEEE Conference on Computer Vision and Pattern Recognition.*
5. Kentaro Inada, Takaaki Ishikawa and Hiroshi Watanabe (2018), Coincidence Evalustion of Multiple People's Dance Using OpenPose, *In Proceedings of the 80th National Convention of IPSJ.*
6. Masato Nakai et al. (2018), Prediction of Basketball Free Throw Scoring by OpenPose, *In Proceedings of the 32nd Annual Conference of the Japanese Society for Artificial Intelligence.*

Phase shift estimation of the bifurcating neuron from superimposed chaotic spike sequences

Akihiro Yamaguchi*, **Yutaka Yamaguti**
Department of Information and Systems Engineering, Fukuoka Institute of Technology,
3-30-1 Wajiro-higashi, Higashi-ku, Fukuoka, 811-0295, JAPAN

Masao Kubo
Department of Computer Science, National Defense Academy of Japan,
1-10-20 Hashirimizu, Yokosuka, Kanagawa, 239-8686, JAPAN

*E-mail: *aki@fit.ac.jp*

Abstract

For the bifurcating neuron, the phase shift value of background oscillation is one of the typical parameters that determine the shape of dynamics. In this research, we propose an estimation method of the phase shift values from superimposed chaotic spike sequences generated by the bifurcating neuron. The proposed method was examined by the numerical experiments for the estimation of the phase shift values and the identification of superimposed chaotic spike sequences up to 12 spike sequences under additive noise.

Keywords: bifurcating neuron, neural coding, background oscillation, chaotic dynamics

1. Introduction

In the view point of neural coding, temporal structure of spike firing is regarded to play important role for representation of neural information in the brain[1]. In our previous research[2,3], authors have studied the decomposition method of the superimposed chaotic spike sequences and selective synchronization for the phase shift value of the bifurcating neuron. The bifurcating neuron was introduced by Lee and Farhat[4] and exhibits chaotic inter-spike interval dynamics that depends on the phase shift value of the background oscillation. Therefore, if we correctly estimate each phase shift values from the superimposed chaotic spike sequences, we can characterize the dynamics of the bifurcating neuron and identify each spike sequence from the other superimposed spike sequences.

In this study, we propose an estimation method of the phase shift value from superimposed spike sequences generated by the bifurcating neuron. In Sec. 2, we explain the bifurcating neuron model. In Sec. 3, we propose an estimation method of the phase shift value. In Sec. 4, the numerical simulation is performed to evaluate performance of our proposed method. Then, we summarize results.

2. Bifurcating neuron

The bifurcating neuron was introduced by Lee and Farhat[4]. We define the bifurcating neuron as a form of the spike response model[2,5]. Let $n^{(i)}$ be the i-th bifurcating neuron, where $i = 0,1,\cdots,N-1$ and N is the number of neurons. The dynamics of the i-th bifurcating neuron is defined as follows:

$$u^{(i)}(t) = u_{rest} + \eta^{(i)}(t) + \nu^{(i)}, \quad (1)$$

where $u^{(i)}$, u_{rest}, $\eta^{(i)}$ and $\nu^{(i)}$ denotes the internal potential of $n^{(i)}$, the resting potential, the kernel function of internal dynamics, and the external noise, respectively. The kernel function $\eta^{(i)}$ is defined as

$$\eta^{(i)}(t) = \alpha\left(t - t_{last}^{(i)}\right) + \eta_0\left(t_{last}^{(i)}, \phi^{(i)}\right); \qquad (2)$$

$$\eta_0(t, \phi) = A_\eta \sin(2\pi\omega\, t + \phi)\,, \qquad (3)$$

where α is the time constant of the kernel $\eta^{(i)}$, and $t_{last}^{(i)}$ is the last firing time of $n^{(i)}$. The internal potential $u^{(i)}$ is linearly increasing by the kernel $\eta^{(i)}$. The neuron $n^{(i)}$ fires when $u^{(i)}$ exceeds the threshold θ, and then $u^{(i)}$ is reset to the initial potential given by the back ground oscillation $\eta_0(t, \phi)$. The constants A_η, ω, and $\phi^{(i)}$ is the amplitude, the frequency, and the phase shift value of background oscillation, respectively. The bifurcating neuron exhibits various chaotic dynamics of the inter-spike interval. The phase of the next firing time is determined by the chaotic one dimensional map of the phase of the last firing time[4]. Let $T_k^{(i)}$ be a phase of the firing time $t_k^{(i)}$. $T_k^{(i)}$ is defined as

$$T_k^{(i)} = t_k^{(i)} \bmod 1/\omega\,, \qquad (4)$$

and $t_{k+1}^{(i)}$ and $T_{k+1}^{(i)}$ is determined by the chaotic one dimensional map such as

$$t_{k+1}^{(i)} = f(t_k^{(i)};\ \phi^{(i)}), \qquad (5)$$

and

$$T_{k+1}^{(i)} = f(T_k^{(i)};\ \phi^{(i)}) \bmod 1/\omega, \qquad (6)$$

where

$$f\left(t;\ \phi^{(i)}\right) = t + \frac{\theta - u_{rest} - \eta_0\left(t, \phi^{(i)}\right)}{\alpha}. \qquad (7)$$

The bifurcation diagram of the map of the firing phase (Eq.(6)) and the Lyapunov exponents of this map are shown in Fig. 1.The shape of chaotic map Eq.(6) is determined by the phase shift value $\phi^{(i)}$. Examples of this chaotic map is shown in Fig. 2.

3. Phase shift estimation

In this section, we explain our proposed method of phase shift estimation from the superimposed spike sequences for two cases. One is the case that the phase shift values are completely unknown. The other is the case that the candidates of phase shift values are given in advance and select the optimal one by the estimation.

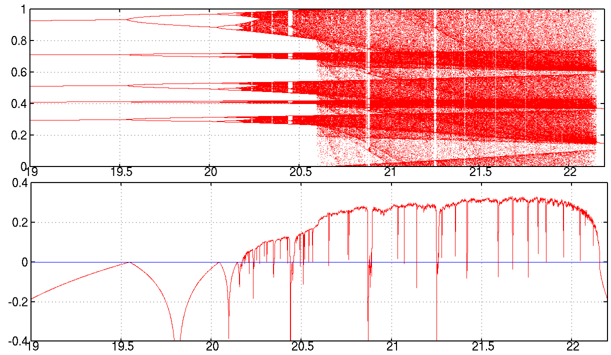

Fig. 1. The bifurcation diagram for the amplitude of the background oscillation and the Lyapunov exponents of the the phase map of the bifurcating neuron.

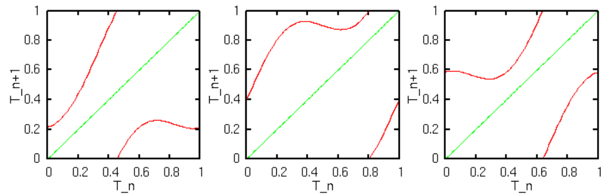

(a) $\phi = \pi/3$ (b) $\phi = \pi$ (c) $\phi = 5\pi/3$

Fig. 2. Examples of the one dimensional chaotic map of the phase of firing time.

3.1. *Superimposition of spike sequences*

Let the set $S^{(i)} = \{t_0^{(i)}, t_1^{(i)}, t_2^{(i)}, \cdots\}$ be a set of firing time of the neuron $n^{(i)}$, where $t_j^{(i)}$ is the firing time of j-th spike of $n^{(i)}$. The superimposition of spike sequences S is defined as a set of firing time of the all bifurcating neuron such that

$$S = \bigcup_{0 \le i < N} S^{(i)}. \qquad (8)$$

The elements of S are denoted $\{t_0, t_1, t_2, \cdots\}$ and $t_j < t_k$ if $j < k$.

3.2. *Direct estimation of the phase shift value*

For the neuron $n^{(i)}$, the time $t_{k+1}^{(i)}$ is determined by the previous firing time $t_k^{(i)}$ as mentioned in the previous section. If successive firing times $t_k^{(i)}$ and $t_{k+1}^{(i)}$ are given, we can solve Eq.(5) and directly obtain the phase shift value $\phi^{(i)}$ such that

$$\phi^{(i)} = \sin^{-1}(\beta(t, t_{k+1}^{(i)})/A_\eta) - 2\pi\omega\, t_k^{(i)}, \qquad (9)$$

where

$$\beta(v_0, v_1) = (\theta - u_{rest} - \alpha(v_1 - v_0))\,. \qquad (10)$$

For the superimposed spike sequences, we have no knowledge about the source neuron of each spike. Furthermore, the inverse function of sin has two values within the range from 0 to 2π. Therefore, we estimate candidates of the phase shift value for each pair of firing times (v_0, v_1) in the superimposition of spike sequences S as follows:

$$\hat{\phi}_1(v_0, v_1) = 2\pi + \sin^{-1}(\beta(v_0, v_1)) - 2\pi\omega\, v_0 \bmod 2\pi, \quad (11)$$

and

$$\hat{\phi}_2(v_0, v_1) = \pi - \sin^{-1}(\beta(v_0, v_1)) - 2\pi\omega\, v_0 \bmod 2\pi, \quad (12)$$

where $-\pi/2 \le \sin^{-1}(\cdot) \le \pi/2$. From Eq. (5),if the pair of the phase of firing time v_0 and v_1 is the successive firing time $t_k^{(i)}$ and $t_{k+1}^{(i)}$, then v_0 and v_1 satisfy the condition

$$|\beta(v_0, v_1)| \le A_\eta\,, \quad (13)$$

where noise less dynamics is assumed in Eq.(1). By using this condition, we could restrict pairs of firing time v_0 and v_1 for the estimation of the phase shift values (Eq.(11) and (12)).

The direct estimation method of the phase shift values is as follows:

(1) Choose all possible pairs of firing times $v_0, v_1 \in S$ that satisfy the condition Eq.(13).
(2) Calculate $\hat{\phi}_1$ and $\hat{\phi}_2$ from chosen pairs (v_0, v_1).
(3) Make a histogram of the calculated phase shift values.
(4) Obtain estimated phase shift values that correspond to local peaks of the calculated histogram.

If the pair of firing times v_0, v_1 is the successive firing time of a certain neuron, one of the phase shift values $\hat{\phi}_1$ and $\hat{\phi}_2$ is correct and the other false one widely distributes within the range from 0 to 2π. Therefore, the frequency of the correct phase shift values become higher than the others.

3.3. *Selection of the optimal phase shift value*

In this section, we propose a selection method of the optimal phase shift value for each spike firing time from given candidates. In order to select the optimal phase shift value, we evaluate the distance between the estimated phase shift value and candidates for the successive K spike firing times. A set of the possible K-tuples of spike firing times is defined as

$$V = \{(v_0, \cdots, v_{K-1}) \mid v_i \in S, |\beta(v_i, v_{i+1})| \le A_\eta\}. \quad (14)$$

The candidates of the phase shift value is given as

$$\Phi = \{\varphi_0, \varphi_1 \cdots, \varphi_{M-1}\}, \quad (15)$$

where M is the number of candidates.

The distance between the candidate φ and the estimated phase shift value from K-tuple of firing times is defined as

$$d(v_0, v_1, \cdots, v_{K-1}; \varphi) = \sum_{j=0}^{K-2} \min_{i=1,2} \left|\hat{\phi}_i(v_j, v_{j+1}) - \varphi\right|. \quad (16)$$

For the specified firing time $v \in S$, we calculate the score of the candidate φ such as

$$score(\varphi; v) = \min_{(v_0, v_1, \cdots, v_{K-2}, v) \in V} d(v_0, v_1, \cdots, v_{K-2}, v;\ \varphi)\,. \quad (17)$$

Then we obtain the optimal phase shift value $\phi^*(v, \Phi)$ that gives the minimal score for the given firing time v. The definition of $\phi^*(v, \Phi)$ is

$$\phi^*(v, \Phi) = \arg\min_{\varphi \in \Phi} score(\varphi; v)\,. \quad (18)$$

By using this method, it becomes to be possible to identify spike sequence which generated by the same neuron from the other superimposed spikes.

4. Numerical experiments

4.1. *Experimental setting*

We numerically simulate M bifurcating neurons and construct the superimposition of chaotic spike sequence (Eq.(8)). The phase shift value of each neuron is assigned as

$$\phi^{(i)} = 2\pi(i + 0.5)/M \ \ (i = 0, \cdots, M-1). \quad (19)$$

We examine the direct estimation method of the phase shift value and evaluate a performance of selection method of optimal one. Numerical simulation was performed with the following setting: $\alpha = 100$, $\theta = -30$, $u_{rest} = -70$, $A_\eta = 21.5$, and $\omega = 1$. The distribution of external noise in Eq. (1) was the Gaussian distribution with the average $\mu = 0$ and the variance $\sigma^2 = 0.3$.

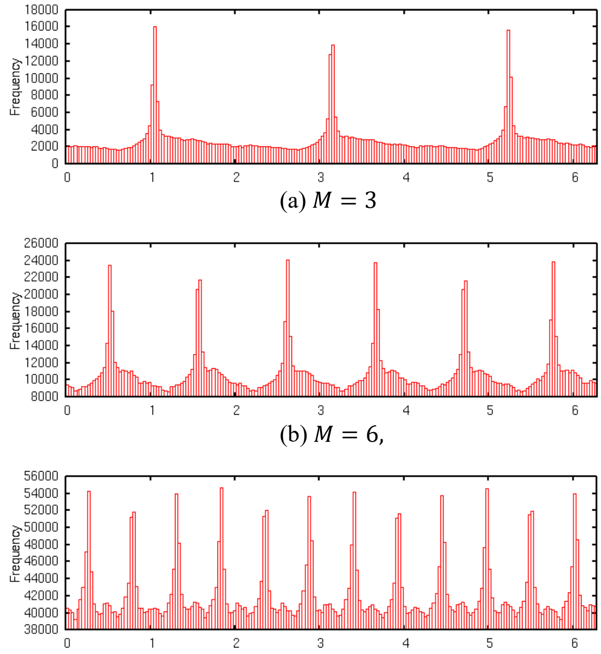

(a) $M = 3$

(b) $M = 6$,

(c) $M = 12$

Fig. 3. Histograms of the directly estimated phase shift values for (a) $M = 3$, (b) $M = 6$, and (c) $M = 12$.

Table. 1. The ratio of correct identification of the superimposed chaotic spike sequences.

M	$K = 2$	$K = 3$	$K = 4$	$K = 5$
2	***98.2±0.5%***	96.3±0.6%	93.9±0.7%	91.3±0.9%
3	***91.6±0.8%***	***92.1±0.9%***	88.9±1.2%	86.5±1.5%
4	86.1±0.8%	***90.4±0.8%***	87.7±1.0%	84.5±1.2%
5	80.4±1.0%	***87.2±1.0%***	***86.5±1.3%***	83.9±1.6%
6	72.8±1.4%	***83.5±0.9%***	***83.4±1.0%***	***82.1±1.5%***
9	54.1±1.3%	72.5±1.4%	***75.0±1.3%***	***75.5±1.4%***
12	41.0±1.8%	60.3±1.4%	***66.0±1.2%***	***67.7±1.8%***

4.2. *Experimental results*

Results of the direct estimation of the phase shift values are shown in Fig. 3 for the cases $M = 3$, $M = 6$, and $M = 12$ as examples. For these three cases, histograms of the estimated phase shift values have significant peaks that correspond the correct phase shift values. The valiance of the estimated phase shift values depends on the amplitude of the external noises. When the variance of external noise decreases, the variance of the estimated phase shift value also decreases.

Next we evaluated the performance of selection method of the optimal phase shift value. The candidates were given as $\Phi = \{\phi_0, \phi_1, \cdots \phi_{M-1}\}$. Results are shown in Table 1. Here, for each firing time in the superposition of spike sequences, the source neuron was identified by the estimated phase shift value. More than 90% of spikes are correctly identified up to $M = 4$. The maximal correct identification ratios are highlighted by italic bold style. Although these results also depends on the amplitude of the external noise, our proposed selection method based on the successive K firing times is effective when the number of superimposed spike sequences M is increased.

5. Conclusion

For the bifurcating neuron, the estimation method of the phase shift value was proposed and the identification performance of superimposed spike sequences based on the estimated phase shift value was evaluated. Numerical results show correct estimation of the phase shift values of superimposed spike sequences and good performance for the identification of them. Since the performance of estimation and identification depend on the amplitude of external noise, analysis of relation between the noise amplitude and the performance of estimation is one of our future works.

Acknowledgements

This work was partially supported by MEXT KAKENHI Grant Number 15H05878, 16K00409 and 17H01794.

References

1. Fuji, H., Ito, H., Aihara, K., Ichinose, N., and Tsukada, M., Dynamical cell assembly hypothesis – Theoretical possibility of spatio-temporal coding in the cortex, *Neural Networks*, Vol.9, No.8, pp.1303-1350, 1996.
2. A. Yamaguchi, Y. Yamaguti, and M. Kubo, *Decomposition of superimposed chaotic spike sequences by using the bifurcating neuron, Advances in cognitive neurodynamics (VI)*, Springer, pp.3-9, 2018.
3. A. Yamaguchi, Y. Yamaguti, and M. Kubo, Selective synchronization of coupled bifurcating neurons for phase shift of background oscillation, *J. Robotics, Networking and Artificial Life*, Vol.5, No.2, pp. 79-82, 2018.
4. Lee G., and Farhat, N.H., The Bifurcating Neuron Network 1, *Neural Networks*, Vol. 14, pp. 115-131, 2001.
5. Gerstner, W., and Kistler, W., *Spiking Neuron Models: Single Neurons Populations Plasticity*, Cambridge University Press, 2002.

Design of a Data-driven Predictive-PI Controller

Yoichiro Ashida
Graduate School of Engineering, Hiroshima University,1-4-1 Kagamiyama
Higashihiroshima city, Hiroshima, Japan

Shin Wakitani
Graduate School of Engineering, Hiroshima University,1-4-1 Kagamiyama
Higashihiroshima city, Hiroshima, Japan

Toru Yamamoto
Graduate School of Engineering, Hiroshima University,1-4-1 Kagamiyama
Higashihiroshima city, Hiroshima, Japan
E-mail: ashida-yoichiro@hiroshima-u.ac.jp, wakitani@hiroshima-u.ac.jp, yama@hiroshima-u.ac.jp
http://www.cse.hiroshima-u.ac.jp/

Abstract

PID controllers have been widely employed in real processes. However, for processes with long dead time, the control performance obtained by PID controllers are limited. The predictive PI controller can control such processes efficiently and have only three parameters. However, it is desired to determine the parameters automatically. In this paper, a data-driven design method for a predictive PI controller is proposed. The effectiveness of the proposed scheme is evaluated by a simulation example.

Keywords: Predictive control, predictive PI controller, data-driven, process control, long dead time.

1. Introduction

PID controllers[1] have been widely employed in real processes. Especially in chemical processes, 90% of the control loops are controlled by PID controllers. However, for processes with long dead time, the control performance obtained by a PID controller is limited. This is because prediction by a derivative element is not very efficient for such processes. Furthermore, the derivative part is sometimes switched off because the part amplifies the influence of noise, and it is not easy to tune the derivative gain suitably. Nevertheless, PID controllers are main controllers because PID controllers only have three parameters and can be tuned by "trial and error". To derive good control performance from the processes with long dead time, some predictive controllers have been proposed. Among them, a predictive PI controller[2-4] has only three parameters, and the controller can be tuned manually like a PID controller. Although a predictive PI controller can be tuned by "trial and error", it is desired to determine control parameters automatically. The authors have proposed a data-driven design method of PID controllers[5]. This method can be employed in designing predictive PI controllers.

In this paper, the properties of a discrete predictive PI controller are explained. In addition, a data-driven design method for a predictive PI controller is proposed. In the proposed method, control parameters of the predictive PI controller are calculated automatically from one set of operation data. The effectiveness of the proposed scheme is evaluated by a simulation example.

$$W(z^{-1}) = \frac{\{b_0(K_P + K_I)z^{-1} + b_0K_Pz^{-2}\}z^{-d}}{1 + (K_{pred} - 1 + a_1)z^{-1} + a_1(K_{pred} - 1) - \{K_{pred} - b_0(K_P + K_I)\}z^{-(d+1)} - (a_1K_{pred} + b_0K_P)z^{-(d+2)}} \quad (6)$$

2. Predictive PI controller

2.1. *Definition of the predictive PI controller*

A control law of a PID controller is written as follow:

$$u(t) = K_Pe(t) + K_I\frac{e(t)}{\Delta} + K_D\Delta e(t), \quad (1)$$

where $u(t)$ and $e(t)$ denotes a controlled error and input, respectively. Δ denotes the differencing operator defined by $\Delta := 1 - z^{-1}$, where z^{-1} is the shift operator which means $z^{-1}e(k) = e(k-1)$. The last term is a derivative element, and it compensate a dead time. However, the derivative does not effective for a long dead time. In addition, the derivative amplifies high frequency signals such as sensor noise. Therefore, PI controllers are sometimes used.

To tackle this problem, a predictive PI controller has been proposed as follows:

$$\begin{aligned} u(t) &= K_Pe(t) + K_I\frac{e(t)}{\Delta} \\ &\quad + \frac{K_{pred}}{\Delta}\{u(t-1) - u(t-d-1)\} \quad (2) \\ &= k_c[e(t) + \frac{T_s}{T_i}\frac{e(t)}{\Delta} \\ &\quad + \frac{T_{pred}}{T_s}\frac{1}{\Delta}\{u(t-1) - u(t-d-1)\}], \quad (3) \end{aligned}$$

where L denotes a dead time, and a prediction term of the predictive PI controller is based on a smith predictor. This controller has only 3 parameters.

2.2. *Properties of the predictive PI controller*

The controlled system is assumed to be the following stable first order system with a dead time:

$$G(z^{-1}) = \frac{b_0z^{-1}}{1 + a_1z^{-1}}z^{-d}, \quad (4)$$

and a reference model is designed as follows:

$$G_m(z^{-1}) = \frac{(1 + p_1)z^{-1}}{1 + p_1z^{-1}}z^{-d}. \quad (5)$$

The closed-loop transfer function obtained by the predictive PI controller is shown as e. q. (6). The influence of the dead time appears at the third and fourth terms of the denomination of e. q. (6). The control parameters should be determined to remove the influence. Therefore, K_P and K_I should be determined as follows:

$$K_P = -\frac{b_0}{a_1}K_{pred}, K_I = \frac{1}{b_0}K_{pred}. \quad (7)$$

By using these parameters, e. q. (6) can be rewritten as follows:

$$W(z^{-1}) = \frac{K_{pred}(1 + a_1z^{-1})z^{-(d+1)}}{1 + (K_{pred} - 1 + a_1)z^{-1} + a_1(K_{pred} - 1)z^{-2}}. \quad (8)$$

When K_{pred} is set as $K_{pred} = 1 + p_1$, the following relation is obtained because the system is stable:

$$\begin{aligned} W(z^{-1}) &= \frac{(1 + p_1)(1 + a_1z^{-1})z^{-(d+1)}}{1 + (p_1 + a_1)z^{-1} + a_1p_1z^{-2}} \\ &= \frac{(1 + p_1)}{1 + p_1z^{-1}}z^{-(d+1)}. \quad (9) \end{aligned}$$

Therefore, the predictive PI controller can control a first order and dead time system.

3. Tuning of the control parameters

3.1. *Design of the predictive PI controller*

If the system parameters are known, control parameters can be determined as discussed above. However, they are rarely known. In this section, a data-driven design method is proposed.

E. q. (2) is rewritten as follows:

$$\begin{aligned} r(t) &= \frac{1}{K_P + K_I}\Delta u(t) + \frac{K_P}{K_P + K_I}\{r(t-1) - y(t-1)\} \\ &\quad + \frac{K_{pred}}{K_P + K_I}\{u(t-1) - u(t-d-1)\} + y(t). \quad (10) \end{aligned}$$

Augmented output $\Phi(t)$ is defined as follows:

$$\begin{aligned} \Phi(t) &= a_1\Delta u(t) + a_2\{\Phi(t-1) - y(t-1)\} \\ &\quad + a_3\{u(t-1) - u(t-d-1)\} + y(t), \quad (11) \end{aligned}$$

where coefficients a_1, a_2, and a_3 are defined as follows:

$$a_1 := \frac{1}{K_P + K_I}, a_2 := \frac{K_P}{K_P + K_I}, a_3 := \frac{K_{pred}}{K_P + K_I}. \quad (12)$$

From e. q. (10) to (12), the following relationship can be obtained:

$$r(t) = \Phi(t). \quad (13)$$

The evaluation function J is defined as follows:

$$J = \frac{1}{N}\sum_{j=1}^{N}\varepsilon(j)^2, \quad (14)$$

where N denotes the number of data and augmented error $\varepsilon(t)$ is defined as follows:

$$\varepsilon(t) := y(t) - G_m(z^{-1})\phi(t). \quad (15)$$

By minimizing the evaluation function J, the following relationship can be obtained:

$$G_m(z^{-1})\phi(t) \to y(t). \qquad (16)$$

From e. q. (11), parameters to be optimized are a_i $(i = 1, 2, 3)$. When the minimization has been finished, it leads the following relationship:

$$y(t) \to G_m(z^{-1})\phi(t). \qquad (17)$$

Therefore, the reference response is realized by using the optimized a_i. a_i can be converted to control parameters using the following equations:

$$K_P = \frac{a_2}{a_1}, K_I = \frac{1 - a_2}{a_1}, K_{pred} = \frac{a_3}{a_1}, \qquad (18)$$

$$k_c = \frac{a_2}{a_1}, T_i = \frac{a_2}{1 - a_2}T_s, T_{pred} = \frac{a_3}{a_2}T_s. \qquad (19)$$

3.2. *Extend the design method*

If the system is strictly first order and the dead time is known, the above discussions are directly applicable. However, most controlled systems are high order and have unknown dead times. Then, the design method is extended in this section.

In the previous design method, the augmented error is defined as e. q. (15). As a result, a purpose of the minimization of e. q. (14) is exact model matching. However, sometimes control parameters are calculated too large when the system is a high order or the dead time of the controller is incorrect.

To tackle this problem, e. q. (13) is rewritten as follows:

$$\varepsilon(t) \coloneqq y(t) - G_m(z^{-1})\phi(t) + \lambda G_m(z^{-1})\Delta u(t). \quad (20)$$

The third term denotes a variation of the input signal. λ is a weight of the variation of the input, and it is a user-specified parameter. E. q. (16) is rewritten as follows:

$$\begin{aligned}\varepsilon(t) \coloneqq y(t) &- (a_1 - \lambda)G_m(z^{-1}) \\ &- a_2 G_m(z^{-1})\{\Phi(t-1) - y(t-1)\} \\ &- a_3 G_m(z^{-1})\{u(t-1) - u(t-d-1)\}. \quad (21)\end{aligned}$$

By using e. q. (21), control parameters are as follows:

$$K_P = \frac{a_2}{a_1 + \lambda}, K_I = \frac{1 - a_2}{a_1 + \lambda}, K_{pred} = \frac{a_3}{a_1 + \lambda}, \qquad (22)$$

$$k_c = \frac{a_2}{a_1 + \lambda}, T_i = \frac{a_2}{1 - a_2}T_s, T_{pred} = \frac{a_3}{a_2}T_s. \qquad (23)$$

Normally, the weight λ is set as $\lambda \geq 0$. From e. q. (23), a_1 affects only k_c. This means that by tuning λ, an entire gain of a controller is tuned. When the system is a high order or dead time is unknown, λ should be large value and a conservative controller should be designed.

The influence of λ for dead time compensation is considered below. The third and fourth terms of the denomination of e. q. (6) must be zero. By using e. q. (18), the terms become zero, and the following relationships are obtained by substituting e. q. (18) to the terms of e. q. (6):

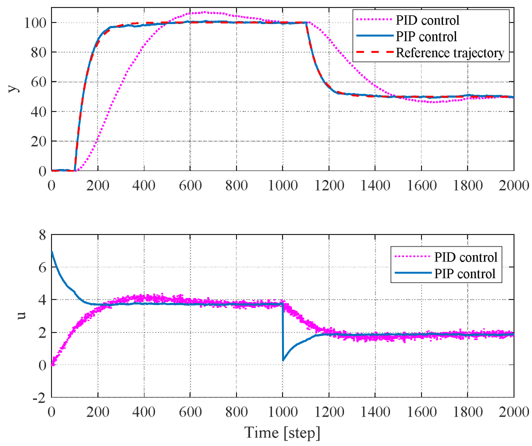

Fig. 1. Control result using PID and predictive PI controllers.

$$K_{pred} - b_0(K_P + K_I) = 0 \Leftrightarrow a_3 - b_0 = 0, \qquad (24)$$

$$a_1 K_{pred} + b_0 K_P = 0 \Leftrightarrow a_1 a_3 - b_0 a_2 = 0. \qquad (25)$$

When e. q. (22) is substituted instead of e. q. (18), the terms are rewritten as follows:

$$K_{pred} - b_0(K_P + K_I) = \frac{a_3 - b_0}{a_1 + \lambda}, \qquad (26)$$

From e. q. (24) to (27), the third and fourth terms of the denomination of e. q. (6) are zero regardless of the value of λ.

Hence, λ does not affect the performance to compensate for the influence of the dead time.

4. Simulation example

In this section, a simulation example is shown by using the following controlled system.

$$G(s) = \frac{18s + 27}{10s^3 + 30s^2 + 100s + 1}e^{-100s}. \qquad (28)$$

The system was discretized by sampling time $T_s = 1$ s, and the following discrete system is obtained:

$$G(z^{-1}) = \frac{0.38z^{-1} + 0.04z^{-2} - 0.02z^{-3}}{1 - 0.57z^{-1} - 0.37z^{-2} - 0.05z^{-3}}z^{-100}. (29)$$

A Gaussian white noise with zero means and 0.1^2 variance was added in the simulation.

The control result is shown as Fig. 1. There are two results using PID control with Chien, Hrones, and Reswick method and the proposed control. An initial operating data is required to apply the proposed method. The operating data obtained by PID control was used as the initial data.

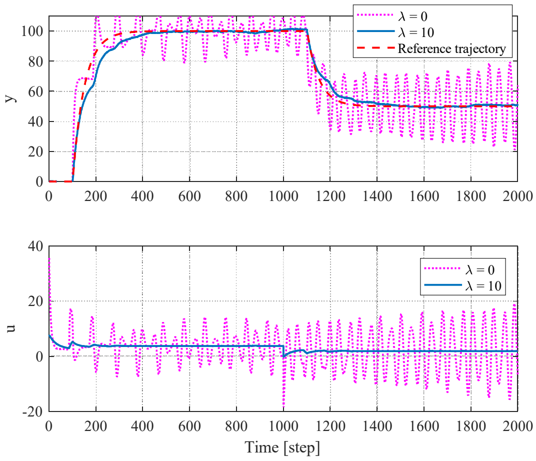

Fig. 2. Control result of predictive PI controller designed as $\lambda = 0$, and $\lambda = 10$.

In the proposed method, the reference model was made as $p_1 = -0.98$ with known dead time, and $\lambda = 0$. The optimization method is *fminserch* function of MATLAB R2017b. Control parameters were as follows:

$$\text{PID: } K_P = 0.02, K_I = 0.0002, K_D = 1.11, \quad (30)$$

$$\text{Predictive PI: } K_P = 0.07, K_I = 0.0007, K_{pred} = 0.02. \quad (31)$$

By using the proposed predictive PI control, the more aggressive response was realized than PID control and tracked the reference trajectory. In addition, the predictive PI controller did not amplify the influence of noise in contrast to the PID control. This is because there are no derivative elements in the predictive PI controller.

Next, the dead time used in designing predictive PI controller was set as 85. The other parameters were set as the same as the previous result, and the initial data was also the same. The control results by setting $\lambda = 0$, and $\lambda = 10$ are shown as Fig. 2. When $\lambda = 0$, the closed loop transfer function became unstable. In contrast, when $\lambda = 10$, the transfer function was stable while the control performance was worse than the reference model.

The calculated control parameters were as follows:

$$\lambda = 0: K_P = 0.35, K_I = 0.003, K_{pred} = 0.14, \quad (32)$$

$$\lambda = 10: K_P = 0.08, K_I = 0.0008, K_{pred} = 0.03. \quad (33)$$

The parameters are rewritten to the form of e.q. (19) as follows:

$$\lambda = 0: k_c = 0.35, T_i = 102.5, K_{pred} = 0.39, \quad (34)$$

$$\lambda = 10: k_c = 0.07, T_i = 102.5, K_{pred} = 0.39, \quad (35)$$

It is clear that only k_c was varied by changing λ. This result confirms the discussion at **3.2**.

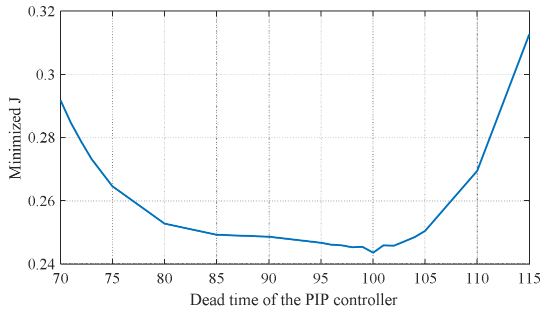

Fig. 3. The minimized evaluation values J corresponding to the dead time of the predictive PI controller when $\lambda = 0$.

At last, the minimized evaluation values J corresponding to the dead time of the predictive PI controller when $\lambda = 0$ are shown as Fig. 3.

The minimum evaluation value is calculated when dead time is 100 steps, and 100 steps are the same as the true dead time of the system. Then, the dead time can be determined based on the evaluation function. However, in the actual systems, it is considered that exact dead time cannot be calculated because of various reasons like nonlinearity. Therefore, it is recommended that λ is set as a nonzero value.

5. Conclusions

In this paper, a consideration of a predictive PI controller is presented, and a data-driven design method is proposed. The controller is effective for systems with long dead time. The effectiveness of the proposed method is confirmed by a simulation example.

References

1. K. J. Åström and T. Hägglund, *Advanced PID Control*, (International Society of Automation, North Carolina, 2006).
2. T. Hagglund, A predictive PI controller for processes with long dead times, *IEEE Control Systems Magazine* **12**(1) (1992) 57–60.
3. T. Hagglund, An industrial dead-time compensating PI controller, *Control Engineering Practice* **4**(6) (1996) 749–756.
4. P. Airikka, Robust Predictive PI Controller Tuning, *IFAC Proceedings Volumes* **47**(3) (2014) 9301–9306.
5. Yoichiro Ashida, Kayoko Hayashi, Shin Wakitani, and Toru Yamamoto, A novel approach in designing PID controllers using closed-loop data, *Proc. of the American Control Conference 2016* (2016) 5308–5313.

Improvement in Intersample Response of Multirate Optimal Control

Takao Sato, Natsuki Kawaguchi, Nozomu Araki, Yasuo Konishi
Graduate School of Engineering, University of Hyogo
2167, Shosha, Himeji, Hyogo, 671-2280, Japan

Abstract

In this study, the dual-rate sampled-data control system is designed, where the sampling interval of a plant output is an integer multiple of the holding interval of a control input. Because the discrete-time linear quadratic integrator (LQI) is used for optimizing the discrete-time control performance, intersample output might oscillate. In order to eliminate the oscillation of the intersample ripple caused by the input oscillation, the designed LQI controller is extended. Finally, the original LQI control law and the extended control laws are quantitatively compared.

Keywords: Sampled-data control system, dual-rate system, intersample response, discrete-time response, null-space, redundancy.

1. Introduction

In the sampled-data control system[1], the continuous-time plant is controlled using the discrete-time controller. In the single-input/single-output system, there are two intervals: the holding interval of a control input and the sampling interval of a plant output. This study discusses a design method for controlling a dual-rate control system, where the sampling interval is longer than the holding interval.

In such dual-rate control systems, intersample ripples might occur even if the sampled output converges to the reference input because the control input can be changed between the sampling intervals[2]. Therefore, the condition for eliminating the intersample ripples caused by the input oscillation has been proposed[3].

This study proposes two design methods for eliminating the intersample ripples: one is an extension method based on the null-space[4], and the other is to weight on the input deviation.

Finally, the effectiveness of the proposed method is demonstrated through numerical examples, and the control performances are quantitatively evaluated based on the numerical results.

2. Controlled Plant Model

A controlled plant is an unknown linear continuous-time single-input single-output time-invariant system given as follows:

$$\dot{\boldsymbol{x}}(t) = A_c\boldsymbol{x}(t) + \boldsymbol{b}_c u(t) \tag{1}$$

$$y(t) = \boldsymbol{c}_c^T\boldsymbol{x}(t) \tag{2}$$

where $\boldsymbol{x}(t) \in \boldsymbol{R}^n$ is the state variable, $u(t) \in R$ is the control input, and $y(t) \in R$ is the plant output, respectively. $A_c \in \boldsymbol{R}^{n\times n}$ is a coefficient matrix, and $\boldsymbol{b}_c \in \boldsymbol{R}^n$ and $\boldsymbol{c}_c \in \boldsymbol{R}^n$ are coefficient vectors. Because the sampled-data control system is designed, a continuous-time plant output is sampled, and a discrete-time control input is held. Since the sampling interval of the plant output is an integer multiple of the holding interval of the control input, the following lifted dual-rate model is obtained.

$$\boldsymbol{x}(k+l) = A_l\boldsymbol{x}(k) + B_l\boldsymbol{u}(k) \tag{3}$$

$$\boldsymbol{u}(k) = [u(k) \quad \cdots \quad u(k+l-1)]^T \tag{4}$$

$$y(k) = \boldsymbol{c}_l^T\boldsymbol{x}(k) \tag{5}$$

where l is a positive integer. The dual-rate model is assumed to be known, and a sampled-data control system is designed based on this model. It is assumed that (A_l, B_l) is stable.

3. Optimal Controller Design

The control system is designed using the following state feedback control law:

$$\boldsymbol{u}(k) = -F\boldsymbol{z}(k) \tag{6}$$

$$\boldsymbol{z}(k) = [\boldsymbol{x}(k) \quad x_i(k)]^T \tag{7}$$

$$x_i(k+l) = x_i(k) + \big(r(k) - y(k)\big)T_s \tag{8}$$

where $r(k) \in \boldsymbol{R}$ is the reference input to be followed by the plant output, and T_s denotes the sampling interval of the plant output. $F \in \boldsymbol{R}^{l\times(n+1)}$ is the feedback gain, and it is designed using the linear quadratic integrator (LQI)[5]:

$$J = \textstyle\sum_{k=0}^{\infty}\big(\boldsymbol{z}(k)^T Q\boldsymbol{z}(k) + \boldsymbol{u}(k)^T R\boldsymbol{u}(k)\big) \tag{9}$$

where $Q \in \boldsymbol{R}^{(n+1)\times(n+1)}$ is a positive definite matrix, and $R \in \boldsymbol{R}^{l\times l}$ is a positive semi-definite matrix. The performance index is rewritten as follows:

$$J = J_z + J_u \tag{10}$$

$$J_z = \textstyle\sum_{k=0}^{\infty} \boldsymbol{z}(k)^T Q\boldsymbol{z}(k) \tag{11}$$

$$J_u = \textstyle\sum_{k=0}^{\infty} \boldsymbol{u}(k)^T R\boldsymbol{u}(k) \tag{12}$$

The closed-loop system using control law (6) is obtained as follows:

$$\boldsymbol{z}(k+l) = (A_z - B_zF)\boldsymbol{z}(k) + Er(k) \tag{13}$$

$$A_z = \begin{bmatrix} A_l & 0 \\ -T_s\boldsymbol{c}^T & 1 \end{bmatrix}, B_z = \begin{bmatrix} B_l \\ \boldsymbol{0}_{1\times l} \end{bmatrix}, E = \begin{bmatrix} \boldsymbol{0}_{n\times 1} \\ T_s \end{bmatrix} \tag{14}$$

4. Two Intersample Suppression Methods

To eliminate the intersample ripples caused by the input oscillation between the sampling instants, two extension methods are proposed.

4.1. *Null-space method*

One extension method is based on the null-space. $B_\perp \in \boldsymbol{R}^{l\times(l-1)}$ is defined as follows:

$$Im(B_\perp) = Ker(B_l) \tag{15}$$

$$Ker(B_l) = \{\boldsymbol{b}_\perp \in \boldsymbol{R}^l | B_l\boldsymbol{b}_\perp = \boldsymbol{0}_{n,1},\ \boldsymbol{b}_\perp \neq \boldsymbol{0}\} \tag{16}$$

Using the defined $B_\perp$, the control law is extended as follows:

$$\boldsymbol{u}(k) = -F\boldsymbol{x}(k) + B_\perp\boldsymbol{w}(k) \tag{17}$$

where $\boldsymbol{w}(k) \in \boldsymbol{R}^{l-1}$ is a newly introduced vector.
The closed-loop system using the extended control law (11) is obtained as follows:

$$\boldsymbol{z}(k+l) = (A_z - B_zF)\boldsymbol{x}(k) + Er(k) + B_zB_\perp\boldsymbol{w}(k) \tag{18}$$

From the definition of $B_\perp$, the last-term in the right-hand side of Eq. (18) is $\boldsymbol{0}_{(n+1)\times 1}$. As a result, the closed-loop system is not affected by $\boldsymbol{w}(k)$. In this study, $\boldsymbol{w}(k)$ is designed so that all the elements in $\boldsymbol{u}(k)$ are equivalent.

4.2. *Input-weighting method*

In the other extension method, the deviation of the control input is suppressed in LQI. To this end, the difference between $u(k+i)$ and $u(k+i+1)$ is penalized as follows:

$$\delta_i\big(u(k+i-1) - u(k+i)\big)^2 = [u(k+i-1) \quad u(k+i)]\Delta_i \begin{bmatrix} u(k+i-1) \\ u(k+i) \end{bmatrix} \tag{19}$$

$$\Delta_i = \delta_i \begin{bmatrix} 1 & -1 \\ -1 & 1 \end{bmatrix} \tag{20}$$

where $\delta_i \in \boldsymbol{R}$ is a non-negative weighting factor. To evaluate the weighted input deviation in LQI, J_u in Eq. (12) is replaced with the following criterion:

$$J_u = \textstyle\sum_{k=0}^{\infty} \boldsymbol{u}(k)^T(R+\Delta)\boldsymbol{u}(k) \tag{21}$$

where Δ is a matrix which satisfies the next equation:

$$\textstyle\sum_{i=1}^{l-1} \delta_i\big(u(k+i-1) - u(k+i)\big)^2 = \boldsymbol{u}(k)^T\Delta\boldsymbol{u}(k) \tag{22}$$

In the proposed weighting method, J_u must be redesigned. Therefore, the Riccati equation is resolved by replacing Eq. (12) by Eq. (21).

5. Discussion on Discrete-time and Intersample Control Performance

In the dual-rate sampled-data control system, the discrete-time model is available, and the continuous-time model is not always obtained. In such a case, when the discrete-time performance is optimized, the intersample ripples might be caused by the input deviation between the sampling instants, although the discrete-time performance is optimized.
In this study, the discrete-time performance is optimized based on the known lifted dual-rate model, and the designed control law is extended so that the intersample

performance is improved. In the discrete-time performance evaluation, because the discrete-time performance function consists of J_x and J_u, two indices are quantitatively evaluated.
In the first extension method based on the null-space, the intersample ripples can be eliminated by introducing the new design parameter. Further, the parameter is designed independent of the discrete-time closed-loop system. Therefore, J_x is maintained and J_u is changed. Hence, the optimization on the control input is not maintained
In the second extension method, since the difference of the control input is always penalized, the input deviation is suppressed. As a result, the intersample ripples caused by the input deviation is eliminated. However, both J_x and J_u are affected by the weighting factor δ_i.

6. Numerical Example

Consider a continuous-time system given as follows:

$$G(s) = \frac{1}{3s+1} \tag{23}$$

The sampling interval and the holding interval are 2s and 1s, respectively, and the following lifted dual-rate system is given:

$$x(k+2) = 0.51x(k) + \begin{bmatrix} 0.72 \\ 1.0 \end{bmatrix} \boldsymbol{u}(k) \tag{24}$$

$$y(k) = 0.28x(k) \tag{25}$$

The feedback gain is obtained by solving the LQI problem with $Q = R = I_2$. The reference input is a unit step function.
The control result using the original feedback control law (6) is shown in Fig. 1. This figure shows that the sampled output converges to the reference input at the sampling instants. However, the control input oscillates, and the intersample output hence oscillates. In the LQI design, the amount of the control input is evaluated, but the intersample output is not evaluated. Therefore, the deviation of the control input is not attenuated, and the intersample ripples occur.
To eliminate the intersample ripples caused by the input deviation, the extended controllers are applied. The result using the extended controller designed in 4.1 is shown in Fig. 2. The lower figure shows that the control input is constant between the sampling instants, and the upper figure shows that the intersample ripples are eliminated. Furthermore, the sampled output response is the same as Fig. 1 even though the control input is redesigned.
The control results using the extended controller designed in 4.2 are shown in Fig. 3 and Fig. 4, where δ_1 is set to 10^0 and 10^5, respectively. In both figures, the amplitude of the difference in the control input is attenuated since the control input deviation between the sampling instants is penalized. The larger δ_1, the smaller the amplitude of intersample ripples.
For comparing the controllers, the performance indices are quantitatively evaluated in Table 1, where the evaluation length is 50 steps. Table 1 shows that the index J^{50} of the original LQI is best, and that of the extended methods are increased, although the intersample ripples are suppressed. In the index of state $\boldsymbol{z}$, J_z^{50}, the original LQI is best and it is the same as the extended method of 4.1 because the original closed-loop system is maintained in the extended controller designed in 4.1.

Table 1. Index values

Controller	$J_z^{50}(\times 10^3)$	J_u^{50}	J^{50}
Original	3.029	93.82	3.122
4.1	3.029	96.38	3.125
4.2($\delta_1 = 10^0$)	3.034	95.49	3.130
4.2($\delta_1 = 10^5$)	3.037	96.35	3.133

7. Conclusion

This study has discussed the design methods for controlling a dual-rate sampled-data control system. Firstly, an optimal control law is designed using LQI. Secondly, the designed control law is extended using two methods: one is based on the null-space, and the other is to weight the input deviation between the sampling instants. Finally, the effectiveness of the proposed method is demonstrated through the numerical examples, and the control performances are quantitatively evaluated.

Acknowledgements

This study was supported by JSPS KAKENHI Grant Number 16K06425.

References

1. T. Chen and B. Francis, *Optimal Sampled-Data Control Systems* (Springer-Verlag, London, 1995).

2. A.K. Tangirala, D. Li, R.S. Patwardhan, S.L. Shah and T. Chen, Issues in Multirate Process Control, *in Proc. of the American Control Conference* (1999), pp.2771–2775.
3. A.K. Tangirala, D. Li, R.S. Patwardhan, S.L. Shah and T. Chen, Ripple-Free Conditions for Lifted Multirate Control Systems, *Automatica*, **37**(10) (2001), pp.1637–1645.
4. L. Zaccarian, Dynamic Allocation for Input Redundant Control Systems, *Automatica*, **45** (2009), pp.1431–1438.
5. P. C. Young and J. C. Willems, An approach to the linear multivariable servomechanism problem, *Int. J. Control* **15**(5) (1972), pp.961–979.

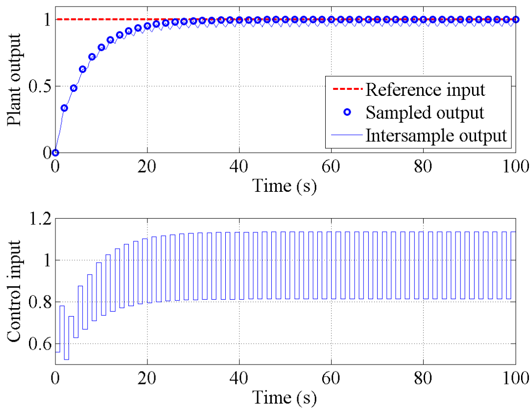

Fig. 1. Simulation result using the original state feedback control law (upper: output trajectory, lower: input trajectory)

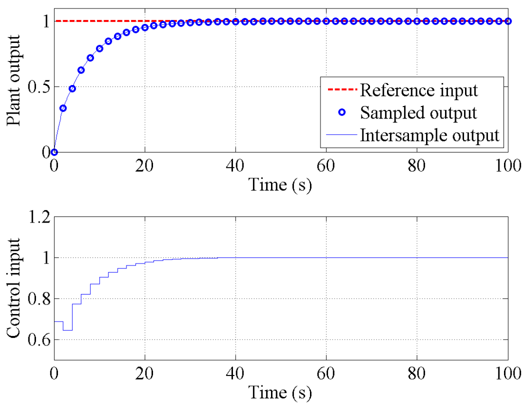

Fig. 2. Simulation result using the extended method given 4.1

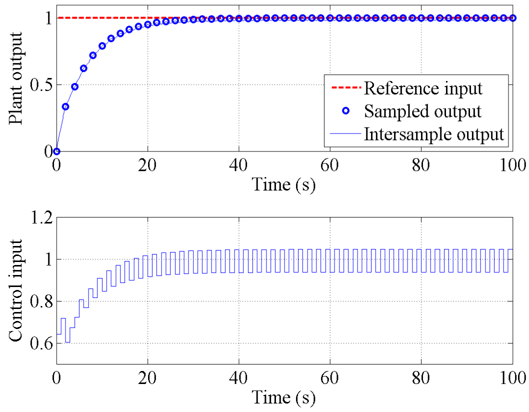

Fig. 3. Simulation result using the extended method given 4.2 with $\delta_1 = 10^0$

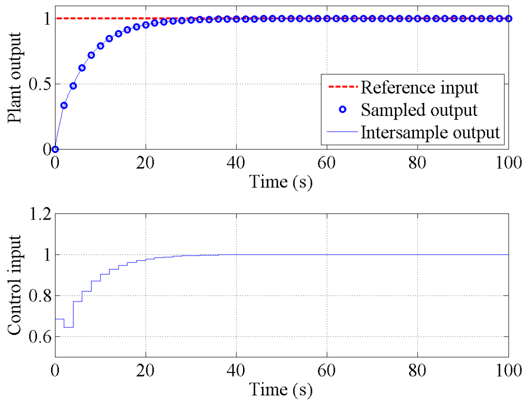

Fig. 4. Simulation result using the extended method given 4.2 with $\delta_1 = 10^5$

Design of a PID Controller using a Fictitious Exogenous Signal for a Fluctuation System

Masatoshi Kozui
Graduate School of Engineering, Hiroshima University
1-4-1, Kagamiyama, ,Higashi-Hiroshima, Hiroshima, Japan
E-mail: kozuim@hiroshima-u.ac.jp

Takuya Kinoshita
Graduate School of Engineering, Hiroshima University
1-4-1, Kagamiyama, ,Higashi-Hiroshima, Hiroshima, Japan
E-mail: takuya-kinoshita@hiroshima-u.ac.jp

Toru Yamamoto
Graduate School of Engineering, Hiroshima University
1-4-1, Kagamiyama, ,Higashi-Hiroshima, Hiroshima, Japan
E-mail: yama@hiroshima-u.ac.jp

Abstract

It is possible to design PID controller to achieve the desired behavior of industrial machines by the FRIT. However, in the steady state, if the system characteristics are changed, the desired control performance can not be obtained by the FRIT. In this paper, it is assumed that a disturbance is input when system characteristics are changed. A PID controller used the Fictitious Exogenous Signal calculated by the operational data is proposed. The effect has been verified by numerical example.

Keywords: PID Control, Fictitious Exogenous Signal, Fictitious Reference Iterative Tuning

1. Introduction

A lot of industrial machines are controlled by a PID control in order to obtain the desired performance. In particular, the response of the system output is important. It is necessary to set appropriate PID parameters for a good characteristic. However, it is difficult to decide these parameters with trial and error. Therefore, the CHR method can be mentioned as a conventional method for determining these parameters. In this method, the proportional gain, the integral gain and the differential gain are respectively determined based on the system parameters to be controlled. However, this method can be applied only when the system parameters is known, and desired response characteristics can not necessarily be obtained. Recently, the Fictitious Reference Iterative Tuning (FRIT) method which calculates PID parameters directly using the closed loop data obtained by a set of operational data attracts attention.[1] The method can be applied, even when the characteristic of the system are unknown. The fictitious reference input is calculated from acquired system input and output, and input to reference model. It is a method of designing an optimum controller by adjusting the PID parameters so that the output obtained from the reference model is closer to the output of the experiment data. However, in many industrial machines, especially the system characteristics of machines operated by human are often changed as the

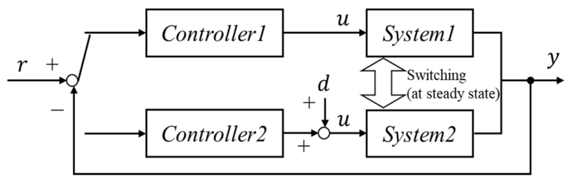

Fig.1 Switching system

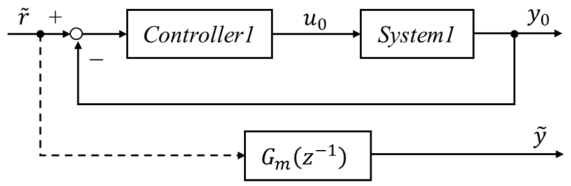

Fig.2 Block diagram of FRIT.

operating environment changes. When such system fluctuation occurs, it is necessary to change the controller before and after the system fluctuation.

In this paper, it is assumed that the system to be controlled is switched in a steady state, and the controller is constituted by a PID controller. PID parameters before system switching are set by the FRIT method. After system switching in the steady state, the method setting PID parameters by the Fictitious Exogenous Signal is proposed. Specifically, it is regarded system fluctuation in the steady state as disturbance like impulse virtually inputted. At this time, the transfer function from the disturbance to the control error is constructed. The optimum controller is designed by adjusting PID parameters so that the characteristic of the closed loop system approaches a reference model. Genetic algorithm was used to calculate PID parameters. Moreover, the effectivity of the proposed method has been verified by numerical examples.

2. Control System

2.1. *Control Objective*

As shown in Fig.1, the control objective is a switching system in which the system changing occurs in the steady state. Initial state is system1, and System2 is after switching. It is assumed that the switching of the system occurs at the known time. Controllers for these systems are Controller1 and Controller2, respectively. PID parameters are set for these controllers.

2.2. *Control law*

The controllers for system1 and system2 use the following I-PD controller.

$$\Delta u(k) = K_i e(k) - K_p \Delta y(k) - K_d \Delta^2 y(k) \qquad (1)$$

$u(k)$, $e(k)$ and $y(k)$ are control input, control error and system output. K_p, K_i and K_d are proportional gain, integral gain and differential gain, respectively. The difference operator is $\Delta := 1 - z^{-1}$. Furthermore, the control error $e(k)$ is calculated as following equation. $r(k)$ is reference.

$$e(k) = r(k) - y(k) \qquad (2)$$

2.2.1. *FRIT method*

The controller1 for system1 is set as K_{p1}, K_{i1} and $K_{d1}$by the FRIT method. The FRIT method can be calculated the controller parameters directly from one experimental data, and block diagram is shown in the Fig.2. $u_0(k)$ and $y_0(k)$ are system input and system output in closed loop data. $\tilde{y}(k)$ is the output of the reference model $G_m(z^{-1})$. $\tilde{r}(k)$ indicates the fictitious reference input to the reference model $G_m(z^{-1})$. $G_m(z^{-1})$ and $\tilde{r}(k)$ are defined as the following equations.

$$\tilde{y}(k) = G_m(z^{-1})\tilde{r}(k) = \frac{z^{-1}P(1)}{P(z^{-1})}\tilde{r}(k) \qquad (3)$$

$$P(z^{-1}) = 1 + p_1 z^{-1} + p_2 z^{-2} \qquad (4)$$

$$\tilde{r}(k) = y_0(k) + \frac{\Delta u_0(k) + K_p \Delta y_0(k) + K_d \Delta^2 y_0(k)}{K_i} \qquad (5)$$

p_1 and p_2 are designed by the following equations.[2]

$$\left.\begin{aligned} p_1 &= -2exp\left(-\frac{\rho}{2\mu}\right)\cos\left(\frac{\sqrt{4\mu-1}}{2\mu}\rho\right) \\ p_2 &= exp\left(-\frac{\rho}{\mu}\right) \\ \rho &= \frac{T_s}{\sigma} \\ \mu &= 0.25(1-\delta) + 0.51\delta \end{aligned}\right\} \qquad (6)$$

σ is the rising characteristic of control, δ is the parameter related to the attenuation characteristic, and can be arbitrarily set by a designer.

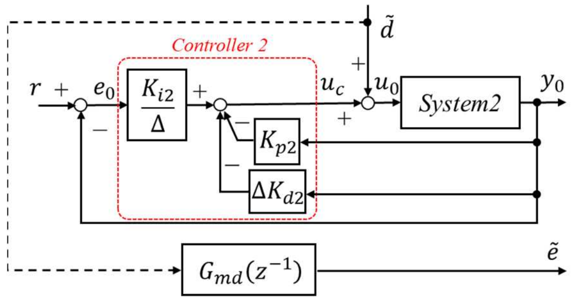

Fig.3 Block diagram of Fictitious Exogenous Signal.

2.2.2. *Fictitious Exogenous Signal method*

The controller2 for system2 is set as K_{p2}, K_{i2} and K_{d2} by a method using the Fictitious Exogenous signal. The proposed method can be calculated the controller parameters directly from a set of experimental data similar to the FRIT method, and block diagram is shown in the Fig.3. As shown in Fig.3, the reference model $G_{md}(z^{-1})$ is constructed by the transfer characteristic from disturbance to control error when $d(k)$ is the input and $e_0(k)$ is the output. The $\tilde{d}(k)$ is a Fictitious Exogenous signal, and the output of the reference model $G_{md}(z^{-1})$ when this is input is $\tilde{e}(k)$. The Fictitious Exogenous signal $\tilde{d}(k)$ and the reference model $G_{md}(z^{-1})$ can be expressed by the following equations.[3]

$$\tilde{d}(k) = u_0(k) - \Big(u_c(k-1) + K_{i2}e_0(k) - K_{p2}\Delta y_0(k) - K_{d2}\Delta^2 y_0(k)\Big) \tag{7}$$

$$\tilde{e}(k) = G_{md}\tilde{d}(k) = -\frac{z^{-1}P_d(1)}{P_d(z^{-1})}\left(\frac{K_i}{\Delta}\right)^{-1}\tilde{d}(k) \tag{8}$$

The setting method of $P_d(z^{-1})$ is the same as the FRIT method, and parameters different from system1 can be set for σ and δ.

2.3. *Genetic Algorithm*

The genetic algorithm(GA) was used to minimize the evaluation function value.[4,5] The evaluation function is defined by the following equations.

【System 1】

$$J_1 = \frac{1}{2}\sum_1^{N_1}\big(y_0(k) - \tilde{y}(k)\big)^2 \tag{9}$$

【System 2】

$$J_2 = \frac{1}{2}\sum_1^{N_2}\big(e_0(k) - \tilde{e}(k)\big)^2 \tag{10}$$

N_1 and N_2 indicate the total number of steps of experimental data in the system1 and the system2. In the system1, a desired response characteristic can be obtained by defining the difference between the reference model output $\tilde{y}(k)$and $y_0(k)$ as an evaluation function and setting the controller parameters so as to minimize the evaluation value. When the evaluation value is low, the fitness is high and PID parameters is better. The system2 is also the same. First, initial individuals with K_p, K_i and K_d as genes are randomly generated. Next, initial evaluation is performed, and elite selection, crossover, tournament selection, and mutation are performed based on the evaluation values. These procedures are repeated, and PID parameters are obtained as the gene of the individual with the highest fitness in the final generation. In this paper, the GA was calculated with 200 individuals and 200 generations.

3. Numerical Example

In order to verify the effect of the proposed method, the switching system of the first order lag systems were set the following equations and a simulation is carried out.

【System 1】

$$G_1 = \frac{1}{1+50s}e^{-2s} \tag{11}$$

【System 2】

$$G_2 = \frac{1}{1+60s}e^{-2s} \tag{12}$$

3.1. *Conventional method (CHR method)*

Above equations are discretized at the sampling time $T_s = 1$ [sec], and following equations are obtained. Furthermore, in 250 step, the system1 is switched to the system2. The effect of control in responsiveness has been verified. Reference is $r(k) = 10$.

$$y(k) = 0.980y(k-1) + 0.0990u(k-3) \tag{13}$$

$$y(k) = 0.984y(k-1) + 0.0165u(k-3) \tag{14}$$

First, a simulation was performed on the system1 with the PID gain calculated by the CHR method. The result was shown in Fig.4, and the set PID parameters were shown in Table 1.

As shown in Fig.4, it took long time to follow the target value, and the responsiveness of the system1 is no good. The output variation after switching to the system2 was

Table 1. PID gain calculated by CHR method.

	K_p	K_i	K_d
System1&2	3	0.06	3

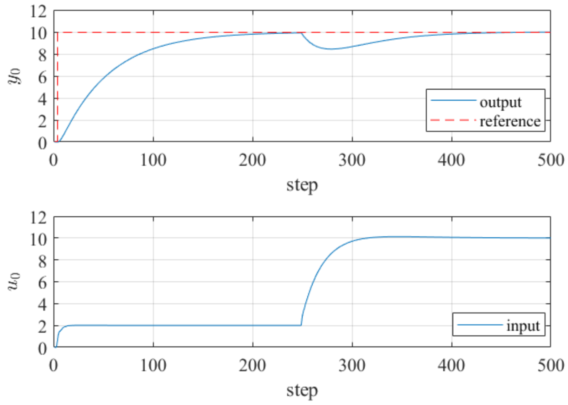

Fig.4 Simulation result by using CHR method.

large and recovery time is long, the control performance is no good.

3.2. *Proposed method*

Next, the result of the proposed method using the FRIT method for the system1 and the method of controller adjustment with the Fictitious Exogenous Signal for the system2 is shown in Fig.5. The control result by the CHR method was used as the operation data $u_0(k)$ and $y_0(k)$. Table 2 shows the set PID parameters. As shown in Fig.5, the response of the system1 is faster than the conventional method, and the desired output is obtained. In addition, the output variation after switching to the system2 is less than 1/4 as compared with the conventional method, and good control performance is obtained.
It was confirmed that responsiveness after switching of the system is improved by considering the system fluctuation as disturbance input and applying the adjustment law using the Fictitious Exogenous Signal.

4. Conclusion

In this paper, a method of controller adjustment law using the Fictitious Exogenous Signal for a system that switched characteristics in steady state has been proposed. The system fluctuation is regarded as the input of the disturbance, and the transfer function from the disturbance $d(k)$ to the control error $e(k)$ is configured as the reference model $G_{md}(z^{-1})$. The Fictitious

Table 2. PID gain tuning by the FRIT and Fictitious Exogenous Signal.

	K_p	K_i	K_d
System1	1.22	0.05	1.21
System2	15.9	0.60	20

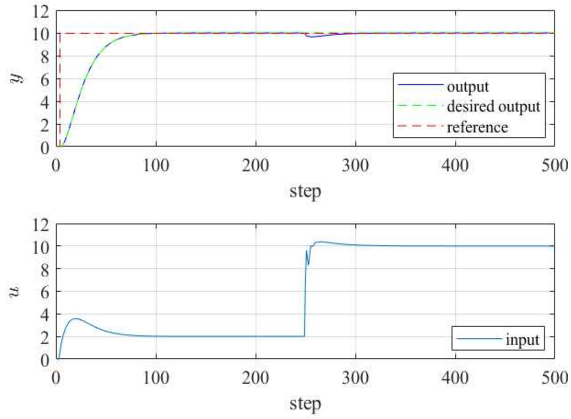

Fig.5 Simulation result by using the FRIT and Fictitious Exogenous Signal.

Exogenous Signal calculated from one experimental data is input to the reference model. A controller with a good disturbance responsiveness can be obtained by adjusting the PID parameters as approximating the reference model output to the control error $e_0(k)$.
In the future, the proposed method will apply to the actual machine and confirm the effect.

Reference

1. O. Kaneko, K. Yoshida, K. Matsumoto and T. Fujii, A New Parameter Tuning for Controllers Based on Least-Squares Method by using One-Shot Closed Loop Experimental Data: An Extension of Fictitious Reference Iterative Tuning, *in ISCIE Journal*, **18**(11) (2005), pp.400-409.
2. K. Hayashi and T. Yamamoto, Evolutionary Design of a PID Controller Using Closed-loop Data, *Trans. of IEEJ C*, **131**(4) (2011), pp.794-799.
3. S. Masuda and K. Takeda, An FRIT Method for Disturbance Attenuation Using Input-Output Data Generated from Disturbance Responses, *Trans. of IEEJ C*, **131**(4) (2011), pp.788-793.
4. D.E.Goldberg, *Genetic Algorithms in search, optimization, and machine learning* (Addison-Wesley Publishing Company, 1989)
5. K. Kawada, H. Sogo, T. Yamamoto and Y. Mada, Robust PD Sway Control of a Lifted for a Crane Using a Genetic Algorithm, *Trans. of IEEJ D*, **123**(10) (2003), pp.1097-1103.

Izhikevich Model Based Self-Repairing Control for Plants with Sensor Failures and Disturbances

Masanori Takahashi
Department of Electrical Engineering and Computer Science, Tokai University
9-1-1 Toroku, Higashi-ku, Kumamoto,862-865, Japan
E-mail:masataka@ktmail.tokai-u.jp

Abstract

In the previous works, several types of the self-repairing control systems (SRCS) have been developed against unknown sensor failures. The SRCS can automatically detect the failure, and replace the failed sensor with the healthy backup so as to maintain the system stability. This paper presents a new SRCS, whose fault detector is constructed based on a spiking neuron model proposed by E. M. Izhikevich. The sensor failure induces the spikes in the detection filter. Hence, only counting up the number of spikes makes it possible to find the sensor failure. Also, in this paper, the robustness with respect to disturbances is theoretically analyzed, and it is shown that self-repairing control can be accomplished in the presence of unknown disturbances.

Keywords: Self-repairing control, sensor failure, fault detection, dynamic redundancy, spiking neuron model.

1. Introduction

Stabilities of control systems are guaranteed under the natural assumption that the feedback loops are healthy. Obviously, if just one loop has the broken sensor, then the control system would lose its stability. Hence, failure detection for sensors plays an important role in maintaining the control system. In the previous works, several types of the self-repairing control systems (SRCS) have been developed against unknown sensor failures[1,2]. The SRCS can automatically detect the failure, and replace the failed sensor with the healthy backup so as to recover the system stability. Compared with existing active fault tolerant controls, the SRCS has the following advantages: (1) the structure of the detection filter can be simple independently of the mathematical model of the plant, and (2) the maximum time of detection can be specified arbitrarily in advance, that is, early fault detection can be accomplished. However, in order to detect failures, an unstable detection filter has been utilized[1], but this is contrary to the idea of the strong stability, which claims that control systems should be constructed by stable elements[3].

In this paper, for the SRCS against sensor failures, a new design method for the detection filter is presented based on a simple spiking neuron model by E. M. Izhikevich[4], and also a concrete detection of failures by counting the number of spiking waves from the filter is shown. This method is solid for strong stability concept, because boundedness of the filtered signal is always guaranteed. Furthermore, this paper shows the high-gain feedback controller stabilizing both the plant and the above-mentioned detection filter. It is shown that the overall control system could have robustness with respect to disturbances in spite of its simple structure.

Throughout this paper, with $x \in \mathbb{R}$, we define the ‘sgn’ function by

$$\mathrm{sgn}[x] = \begin{cases} 1 & (x \geq 0) \\ -1 & (x < 0) \end{cases}$$

Notice that this is slightly different from the ordinary one.

2. Spiking Neuron Model

The spiking neuron model proposed by E. M. Izhikevich[4] is represented as,

$$\dot{v} = 0.04v^2 + 5v + 140 - w + I$$
$$\dot{w} = \varepsilon(\gamma v - w) \quad (1)$$

$$\text{if } \ v \geq 30 \text{ [mV]} \ \text{ then } \begin{cases} v \leftarrow v_R \\ w \leftarrow w + w_R \end{cases} \quad (2)$$

where $v \in \mathbb{R}$ is the membrane potential of the neuron, $w \in \mathbb{R}$ is the recovery variable, $I \in \mathbb{R}$ is the stimulus, and $\varepsilon \in \mathbb{R}$ and $\gamma \in \mathbb{R}$ are the parameters for the recovery dynamics. The auxiliary after-spike resetting is expressed by (2), where $v_R \in \mathbb{R}$ and $w_R \in \mathbb{R}$ are the reset values.

Fig. 1 shows the numerical example for the parameters $\varepsilon = 0.02, \gamma = 0.2, v_R = -50, w_R = 2$, the initial values $v(0) = -50, w(0) = 2$ and the stimulus $I = 10$ [mV]. In the figures, the point 'A' indicates the first spike in the bursting pattern, and the red two lines are nullclines.

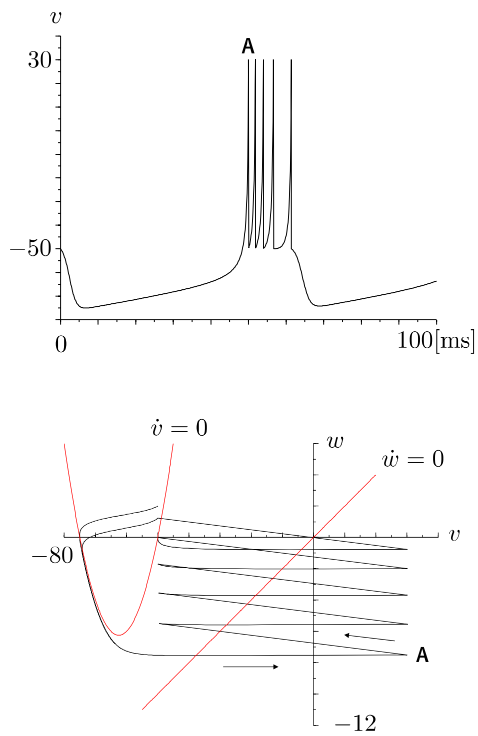

Fig. 1. A 'bursting' pattern by Izhikevich spiking neuron model: the time history (top) and the trajectory (v, w) of the $v - w$ plane (bottom).

This result shows the 'bursting' pattern, which will be exploited in fault detection of the proposed SRCS.

3. Problem Statement

Consider the following linear time invariant system with unknown disturbances.

$$\Sigma_P : \ \dot{y} = ay + bu + \boldsymbol{h}^T\boldsymbol{z} + d_y$$
$$\dot{\boldsymbol{z}} = \boldsymbol{F}\boldsymbol{z} + \boldsymbol{g}y + \boldsymbol{d}_z \quad (3)$$

where $y \in \mathbb{R}$ is the actual output, $u : \mathbb{R}^+ \to \mathbb{R}$ is the control input, and $\boldsymbol{z} \in \mathbb{R}^{n-1}$ is the state. Also, $d_y \in \mathbb{R}$ and $\boldsymbol{d}_z \in \mathbb{R}^{n-1}$ are unknown but bounded disturbances. Here, it is assume that the high frequency gain $b \in \mathbb{R}$ is positive, and that $\boldsymbol{F} \in \mathbb{R}^{(n-1)\times(n-1)}$ is the stable matrix (*i.e.*, all eigenvalues lie in $\mathbb{C}^-$).

For measurement of the output y, the two sensors are prepared. One is the primary sensor #1, and the other is the backup #2 for occasion of failure. Then, the feedback signal $y_S : \mathbb{R}^+ \to \mathbb{R}$ can be expressed as follows.

$$y_S(t) = \begin{cases} y_1(t) & (t \leq t_D) \\ y_2(t) & (t > t_D) \end{cases} \quad (4)$$

where $t_D \in \mathbb{R}^+$ is the detection time, whose detail will be discussed later. Each $y_i \in \mathbb{R}, i \in \{1, 2\}$ is the output of the sensor $\#i$. Obviously, the healthy output is $y_i = y$. Based on dynamic redundancy (4), we usually use the primary sensor #1, but switch to the backup when the failure of the primary one is detected.

The failure scenario to be consider here, is expressed as follows.

$$y_1(t) = \varphi, t \geq t_F \quad (5)$$

where $t_F \in \mathbb{R}^+$ is the unknown failure time, and $\varphi \in \mathbb{R}$ is the unknown stuck value.

The problem is to design the SRCS, which can replace the failed sensor with the backup to maintain the control stability and guarantee the convergence property of y:

$$\lim_{t\to\infty} \sup|y(t)| \leq \lambda \quad (6)$$

for arbitrarily given $\lambda \in \mathbb{R}^+$.

4. Control System Design

First of all, the detection filter is introduced based on the spiking neuron model (1) and (2).

$$\Sigma_D : \ \dot{v} = \text{sgn}[y_S](\theta_2 v^2 + \theta_0 - \eta w) + \theta_1 v$$
$$+\sigma(\dot{y}_S + p y_S)$$
$$\dot{w} = \varepsilon(\gamma_1 \text{sgn}[y_S] v + \gamma_0 - w) \quad (7)$$

$$\text{if }\ \gamma_1\mathrm{sgn}[y_S]v \geq v_T\ \text{ then } \begin{cases} v \leftarrow \mathrm{sgn}[y_S]v_R \\ w \leftarrow w + w_R \end{cases} \tag{8}$$

where the parameters, $\theta_0 \in \mathbb{R}, \theta_1 \in \mathbb{R}, \theta_2 \in \mathbb{R}$, $\gamma_0 \in \mathbb{R}, \gamma_1 \in \mathbb{R}$, $\sigma \in \mathbb{R}^+$ and $\eta \in \mathbb{R}^+$ are positive constants. Also, $v_T \in \mathbb{R}$ is the threshold for auxiliary resetting. For stability, the resetting rule (8) should be invalid before the steady state.

Next, the high-gain feedback controller is designed by

$$\Sigma_C\,:\, u = -p(y_S + v) - y_S^3 - v^3 \tag{9}$$

where $p \in \mathbb{R}^+$ is the feedback gain to stabilize the plant and the detection filter.

Then, we have the following representation of the overall control system with the healthy sensor, *i.e.*, $y_S = y$.

$$\begin{aligned}
\dot{y} &= -(bp - a)y - bpv - by^3 - bv^3 \\
&\quad + \boldsymbol{h}^T\boldsymbol{z} + d_y \\
\dot{\boldsymbol{z}} &= \boldsymbol{F}\boldsymbol{z} + \boldsymbol{g}y + \boldsymbol{d}_z \\
\dot{v} &= -(\sigma bp - \theta_1)v + \mathrm{sgn}[y]\theta_2 v^2 - \sigma b v^3 \\
&\quad + \mathrm{sgn}[y](\theta_0 - \eta w) + \sigma a y + \sigma \boldsymbol{h}^T\boldsymbol{z} + \sigma d_y \\
\dot{w} &= \varepsilon(\gamma_1 \mathrm{sgn}[y]v + \gamma_0 - w)
\end{aligned} \tag{10}$$

Here, consider the positive definite function $S\,:\, \mathbb{R}^+ \to \mathbb{R}^+$ as,

$$S := \frac{1}{2}\left\{y^2 + \delta \boldsymbol{z}^T\boldsymbol{P}\boldsymbol{z} + \frac{1}{\sigma}v^2 + \delta w^2\right\} \tag{11}$$

where $\boldsymbol{P} \in \mathbb{R}^{(n-1)\times(n-1)}$ is the positive definite matrix which satisfies $\boldsymbol{F}^T\boldsymbol{P} + \boldsymbol{P}^T\boldsymbol{F} = -2\boldsymbol{Q}$ for any positive definite $\boldsymbol{Q} \in \mathbb{R}^{(n-1)\times(n-1)}$. Taking the time derivative of S gives

$$\begin{aligned}
\dot{S} &\leq -\frac{1}{2}\left(\alpha_1 y^2 + \delta\alpha_2\|\boldsymbol{z}\|^2 + \alpha_3 v^2 + \frac{1}{2}\delta\varepsilon w^2\right) \\
&\quad + \delta\left(2 + \varepsilon\gamma_0 + \frac{1}{2}\|\boldsymbol{P}\|^2\right)
\end{aligned} \tag{12}$$

where

$$\begin{aligned}
\alpha_1 &= bp - 2a - \|\boldsymbol{h}\|^2 - \frac{1}{\delta}\|\boldsymbol{P}\boldsymbol{g}\|^2 - a^2 - \frac{1}{\delta}\bar{d}_y^2 \\
\alpha_2 &= 2\lambda_{\min}[\boldsymbol{Q}] - 3 - \bar{d}_z^2 \\
\alpha_3 &= bp - \frac{\theta_1}{\sigma} - \frac{\theta_2^2}{b\sigma^2} - \frac{\theta_0^2}{4\delta\sigma^2} \\
&\quad - 1 - \frac{1}{\delta}\|\boldsymbol{h}\|^2 - \delta\varepsilon\gamma_1^2 - \bar{d}_y^2
\end{aligned}$$

and $\bar{d}_y \geq |d_y(t)|, \bar{d}_z \geq \|\boldsymbol{d}_z(t)\|$. Choosing sufficiently large p, we have all $\alpha_i > 0, i = 1,2,3$. Hence, from (12), it follows that

$$\dot{S}(t) \leq -\alpha S(t) + \delta\beta, \qquad t \in [0, t_F) \tag{13}$$

where

$$\alpha = \min\left\{\alpha_1, \frac{\alpha_2}{\lambda_{\max}[\boldsymbol{P}]}, \sigma\alpha_3, \frac{1}{2}\varepsilon\right\}$$

$$\beta = 2 + \varepsilon\gamma_0 + \frac{1}{2}\|\boldsymbol{P}\|^2 \tag{14}$$

Solving the differential inequality (13), we have

$$S(t) \leq S(0)e^{-\alpha t} + \frac{\delta\beta}{\alpha}, \qquad t \in [0, t_F) \tag{15}$$

Therefore, we can conclude that all the signals in the control system are bounded although the disturbances exist. Moreover, if no sensor fails, that is, $t_F = \infty$, then

$$\lim_{t\to\infty} \sup|y(t)| \leq \lim_{t\to\infty} \sup\sqrt{2S(t)} \leq \sqrt{\frac{2\delta\beta}{\alpha}} \tag{16}$$

For sufficiently small δ, we have $\sqrt{2\delta\beta/\alpha} < \lambda$. This means that the inequality (6) holds if no failure occurs. The overall control system is illustrated in Fig. 2.

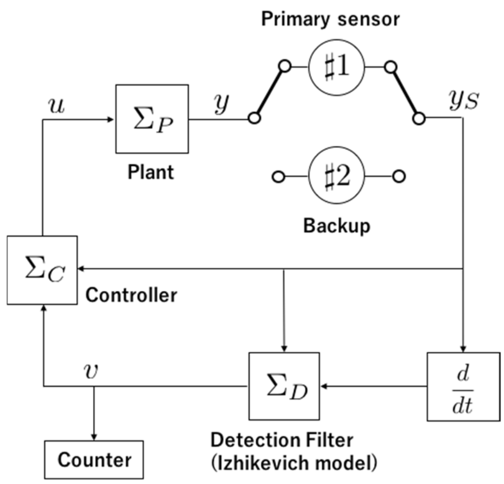

Fig. 2. The block diagram of the proposed SRCS with the Izhikevich spiking neuron model.

5. Fault Detection

This section shows the concrete detection method by using the detection filter by (7) and (8).

Refer to the 'bursting' as shown in Section 2. Roughly speaking, when the two nullclines in (1) run apart from each other by the large stimulus I, the bursting pattern appears. Then, suppose that the parameters in (7) are chosen so that the following two nullclines run with a sufficient distance each other.

$$\begin{aligned}
0 &= \theta_2 v^2 + \theta_1 v + \theta_0 - \eta w \\
0 &= \gamma_1 v + \gamma_0 - w
\end{aligned} \tag{17}$$

If the sensor fails, then the bursting pattern appears just like Fig. 1. Such a pattern does not occur as far as the sensor is healthy. It does not depend on the disturbances. Therefore, counting the number of the spikes in the bursting pattern, makes it possible to find the sensor failures. Thus, the detection time t_D is defined by

$$t_D := \min\{t \mid c_R(t) \geq n_R\} \quad (18)$$

where $c_R \in \mathbb{N}$ is the counted number of the spikes in the filtered signal v from the detection filter, and $n_R \in \mathbb{N}$ is the specified minimum number of spikes.

After replacing the failed sensor, the boundedness of all the signals in the control system are guaranteed again, and the convergence (6) can be obtained.

6. Numerical Examples

To confirm the effectiveness of the proposed method, the numerical simulation is explored.

Consider the following plant with disturbances.

$$\dot{y} = -y + u + z + 0.5 + \sin(0.01t)$$
$$\dot{z} = -2z + y + \cos(0.1t) \quad (19)$$

The initial values are $y(0) = 1$ and $z(0) = -1$.

The failure scenario (5) is supposed that

$$t_F = 25\ [s],\ \varphi = y(t_F) \quad (20)$$

Of course, these are assumed to be unknown.

For the above plant, the parameters for the detection filter are selected as follows.

$$\theta_0 = -0.06, \theta_1 = -0.6, \theta_2 = 4, \gamma = \delta = 1$$
$$\varepsilon = 0.02, \gamma_0 = -6, \gamma_1 = 20$$

Also, the parameters for resetting are

$$v_T = 1, v_R = 0.2, w_R = 2$$

The specified number of the spikes in the bursting pattern is supposed to be five, that is, $n_R = 5$ within almost 1 [s]. In order to stabilize the plant and the detection filter mentioned above, the controller gain is chosen as

$$p = 30$$

The simulation results are shown in Fig. 3. In this figure, the measured output y_S, the actual output y (top) and the filtered signal v (bottom) are shown. From this result, it is clear that the control system can be well stabilized in spite of existence of disturbances, and the actual output y converges to a very small ball before and after the failure. The self-repairing control can be accomplished, and the failed sensor is replaced at $t_D \cong 26$ [s] that is, early fault detection can be achieved by using the spiking neuron model.

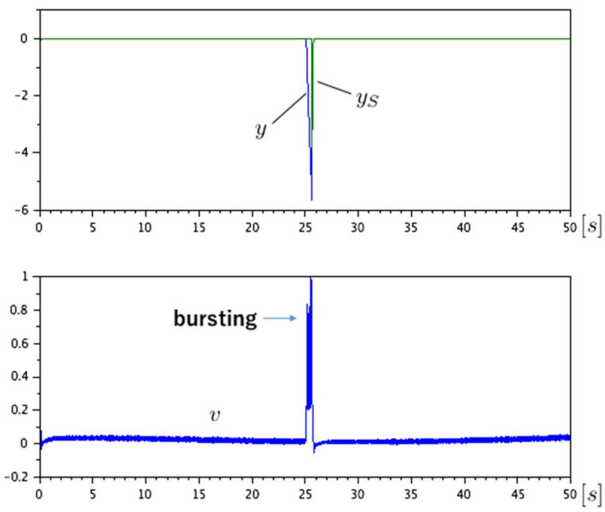

Fig. 3. Simulation results: the measured output and the actual output (top) and the filtered signal (bottom).

7. Conclusions

In this paper, a new SRCS has been developed that has the detection filter based on the spiking neuron model by E. M. Izhikevich. In this method, the sensor failure can be found by counting the spikes from the filter. The applications to nonlinear systems with noise, MIMO systems and so on are still left in the future works.

Acknowledgements

This work is supported by JSPS KAKENHI Grant Number JP16K06429.

References

1. M. Takahashi: Self-repairing control against unknown sensor failures and biases, Asian J. Control, Vol. 15, Issue 4, pp. 1215-1223 (2013).
2. M. Takahashi: Self-repairing PI/PID control against sensor failures, *Int. J. Innovative Computing, Information and Control*, Vol. 12, No. 1, Feb. pp. 193-202 (2016)
3. A. Yanou, M. Minami, and T. Matsuno: "Strong Stability Rate for Control Systems Using Coprime Factorization", *Trans. of the Society of Instrument and Control Engineers*, Vol.50, No.5, pp.441–443 (2014) (in Japanese)
4. E. M. Izhikevich: Simple model of spiking neurons, *IEEE Trans. on Neural Networks*, Vol. 14, No. 6, pp. 1596-1572 (2003)

Design of a Data-Driven Controller with Evaluating Controller Performance

Takuya Kinoshita
Graduate School of Engineering, Hirosihma University,
1-4-1, Kagamiyama, Higashihiroshima city, Hiroshima, Japan

Toru Yamamoto
Graduate School of Engineering, Hirosihma University,
1-4-1, Kagamiyama, Higashihiroshima city, Hiroshima, Japan
E-mail: takuya-kinoshita@hiroshima-u.ac.jp, yama@hiroshima-u.ac.jp
http://www.hiroshima-u.ac.jp

Abstract

Data-driven controller systems have been proposed to achieve the desired control performance without using any system identifications. The effectiveness of these control schemes has been shown through experimental results. For time-variant and nonlinear systems, it is important to evaluate the controller performance and redesign controller when the performance is poor. According to the proposed scheme, the controller performance calculator and controller design are integrated using only input and output data.

Keywords: PID controller, controller assessment, data-driven controller, least squares method.

1. Introduction

In most industries, it is very important to get desired control performance. Data-driven control schemes[1, 2, 3] have been proposed to achieve the aforementioned desired control performance without using any system identifications. For time-variant systems, performance-driven controller[4] has been proposed to improve the steady state control performance only when the performance is poor. However, performance-driven controller cannot evaluate the transient state.

In this paper, the scheme of evaluating controller performance without using any system identifications is proposed. According to the proposed scheme, the control performance is evaluated system output error including transient state. Furthermore, the controller performance calculator and controller design are integrated using only input and output data.

2. Schematic figure of the proposed scheme

The schematic figure of the proposed control system is shown in Fig. 1. $C(z^{-1})$, $G(z^{-1})$, $G_m(z^{-1})$, and $\hat{G}(z^{-1})$ are the controller, controlled system, reference model and estimated system model, respectively.

The purpose of the proposed control system is to achieve the desired control performance by minimizing the following criterion J_r:

$$J_r = \frac{1}{2}\phi_r(t)^2 \tag{1}$$

$$\phi_r(t) = y(t) - y_r(t), \tag{2}$$

where $y(t)$ and $y_r(t)$ are the control output and reference output, respectively.

Another purpose is to design the estimated system model $\hat{G}(z^{-1})$ by minimizing the following equation:

$$J_r = \frac{1}{2}\hat{\phi}(t)^2 \tag{3}$$

$$\hat{\phi}(t) = y(t) - \hat{y}(t), \tag{4}$$

where $\hat{y}(t)$ is the estimated output. In the proposed scheme, $\hat{G}(z^{-1})$ can be introduced by using the controller parameters and reference model parameters

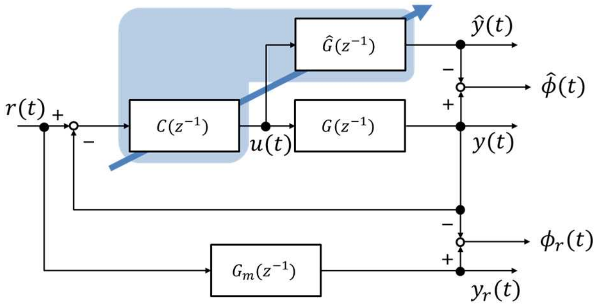

Fig. 1. Schematic figure of the proposed control system.

without any system identifications. Therefore, controller and estimated system model can be designed simultaneously.

In addition, user set a desired reference model expressed by following equation:

$$y_r(t) = G_m(z^{-1})r(t) \tag{5}$$

$$G_m(z^{-1}) := \frac{z^{-(1+d)}P(1)}{P(z^{-1})} \tag{6}$$

where $r(t)$ is the reference signal and $P(z^{-1})$ is user-specified polynomial. $P(z^{-1})$ is designed based on the reference design[5] as follows:

$$P(z^{-1}) := 1 + p_1 z^{-1} + p_2 z^{-1} \tag{7}$$

$$\begin{cases} p_1 = -2\exp\left(-\dfrac{\rho}{2\mu}\right)\cos\left(\dfrac{\sqrt{4\mu-1}}{2\mu}\rho\right) \\ p_2 = \exp\left(-\dfrac{\rho}{\mu}\right) \\ \rho := \dfrac{T_s}{\sigma} \\ \mu := 0.25(1-\delta) + 0.51\delta \end{cases}, \tag{8}$$

where σ is a parameter related to the rise-time and δ is a parameter related to the damping oscillation. User set them arbitrarily. σ denotes the time when output reaches about 60% of the step reference value. Moreover, δ is set between $0 \le \delta \le 2.0$ desirably. In particular, $\delta = 0$ indicates the response of Butterworth model and $\delta = 1.0$ indicates the response of Binominal model.

3. Relationship between controller and estimated system model

The following equation can be obtained by introducing the optimized controller $C^*(z^{-1})$ which achieves $\phi_r(t) = 0$:

$$\frac{G(z^{-1})C^*(z^{-1})}{1 + G(z^{-1})C^*(z^{-1})} = G_m(z^{-1}). \tag{9}$$

The controlled system $G(z^{-1})$ is expressed as follows by using the aforementioned equation:

$$G(z^{-1}) = \frac{G_m(z^{-1})}{C^*(z^{-1})\{1 - G_m(z^{-1})\}}. \tag{10}$$

Here, the following estimated system model $\hat{G}(z^{-1})$ is defined using a controller $C(z^{-1})$ instead of $C^*(z^{-1})$ because it is difficult to obtain the optimized controller $C^*(z^{-1})$:

$$\hat{G}(z^{-1}) = \frac{G_m(z^{-1})}{C(z^{-1})\{1 - G_m(z^{-1})\}}. \tag{11}$$

Note that the estimated controlled system $\hat{G}(z^{-1})$ is expressed by using a controller $C(z^{-1})$ and reference model $G_m(z^{-1})$ without any system identifications.

$\hat{G}(z^{-1})$ equals to $G(z^{-1})$ when the optimized controller $C^*(z^{-1})$ is obtained. It mentions that $\hat{\phi}(t) = 0$ because of $\hat{G}(z^{-1}) = G(z^{-1})$. Therefore, the optimized controller $C^*(z^{-1})$ achives $\phi_r(t) = 0$ and $\hat{\phi}(t) = 0$ simultaneously.

4. Evaluation of the controller performance

The optimized controller $C^*(z^{-1})$ makes $\hat{\phi}(t)$ equals to zero. In contrast, $\hat{\phi}(t)$ becomes large when the performance of the controller $C(z^{-1})$ is poor. Hence, this paper considers the performance of the controller $C(z^{-1})$ based on $\hat{\phi}(t)$.

5. Tuning scheme of the PID gains

In this paper, the controller is utilized as following I-PD controller:

$$\Delta u(t) = K_I e(t) - K_P \Delta y(t) - K_D \Delta^2 y(t) \tag{12}$$

$$e(t) := r(t) - y(t), \tag{13}$$

where K_P, K_I and K_D are the proportional gain, integral gain and derivative gain, respectively.

The estimated system model $\hat{G}(z^{-1})$ is expressed by using I-PD controller is as follows:

$$\hat{G}(z^{-1}) = \frac{G_m(z^{-1})}{\frac{K_I}{\Delta} - C(z^{-1})G_m(z^{-1})}, \tag{14}$$

where

$$C(z^{-1}) = \frac{K_P\Delta + K_I + K_D\Delta^2}{\Delta}. \tag{15}$$

The estimated output is calculated as follows:

$$\hat{y}(t) = \frac{G_m(z^{-1})}{\frac{K_I}{\Delta} - C(z^{-1})G_m(z^{-1})} u(t), \tag{16}$$

where $u(t)$ is control input. In order to apply the least squares method, $\hat{\phi}(t) = 0$ is considered and the following equation is derived by using Eq. (2) and (18):

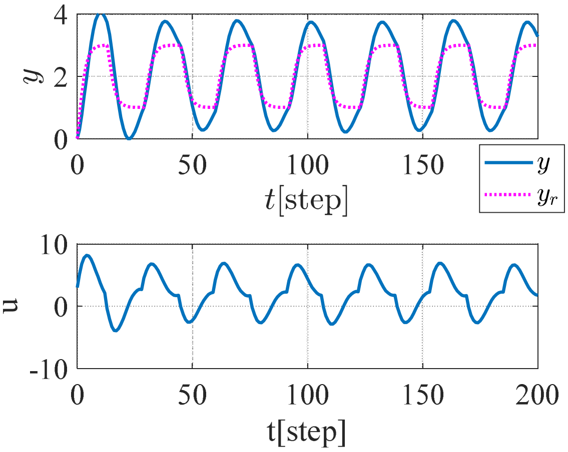

Fig. 2. Control result by using the initial PID gains.

$$G_m(z^{-1})u(t) = \left\{\frac{K_I}{\Delta} - \frac{K_P\Delta + K_I + K_D\Delta^2}{\Delta}G_m(z^{-1})\right\}y(t) \tag{17}$$

$$\Delta G_m(z^{-1})u(t) = K_I\{1 - G_m(z^{-1})\}y(t) - (K_P\Delta + K_D\Delta^2)G_m(z^{-1})y(t). \tag{18}$$

Therefore, the PID gains are calculated by using the following least squares method:

$$\boldsymbol{\theta} = (\boldsymbol{\Phi}^T\boldsymbol{\Phi})^{-1}\boldsymbol{\Phi}^T\boldsymbol{v}, \tag{19}$$

$$\begin{cases} \psi(t) = \begin{bmatrix} -\Delta G_m(z^{-1})y(t) \\ \{1 - G_m(z^{-1})\}y(t) \\ -\Delta^2 G_m(z^{-1})y(t) \end{bmatrix}^{\mathrm{T}} \\ \boldsymbol{\Phi} = [\psi(1), \psi(2), \cdots, \psi(N)]^T \\ \boldsymbol{v} = [\Delta G_m(z^{-1})u(1), \cdots, \Delta G_m(z^{-1})u(N)]^T \\ \boldsymbol{\theta} = [K_P,\ K_I,\ K_D]^T \end{cases}. \tag{20}$$

6. Numerical example

The controlled system $G(s)$ is given as follows:

$$\begin{cases} G(s) = \dfrac{1}{1 + 10s}\ (t < 100) \\ G(s) = \dfrac{2}{1 + 20s}\ (t \geq 100) \end{cases}. \tag{21}$$

The parameters of the reference model $G_m(z^{-1})$ are set as follows:

$$\sigma = 3.0, \delta = 0. \tag{22}$$

Finally, the initial PID gains are set as follows:

$$K_P = 1.0, K_I = 1.0, K_D = 1.0. \tag{23}$$

In this section, the following three simulations are shown.

A) Fig. 2: Control result by using initial PID gains of Eq. (23).

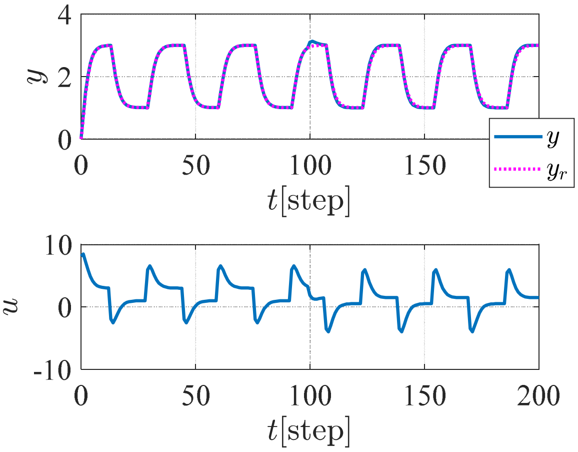

Fig. 3. Control result of the proposed scheme without controller retuning.

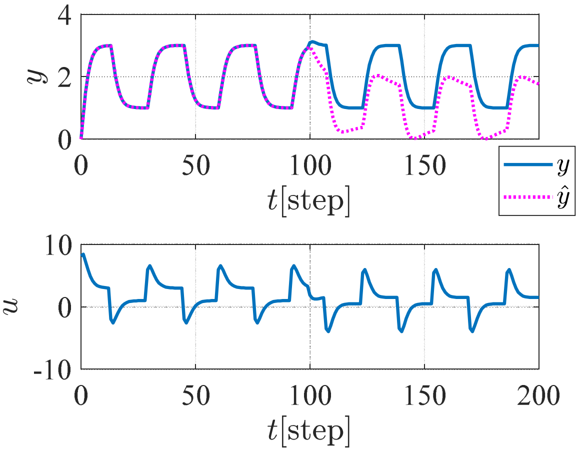

Fig. 4. Trajectory of the estimated output $\hat{y}(t)$ corresponding to Fig. 3.

B) Fig. 3: Control result of the proposed scheme without controller retuning.

C) Fig. 5: Control result of the proposed scheme with controller retuning.

Control results

Fig. 2 shows the control result by using initial PID gains of Eq. (23). The control performance is poor because control output $y(t)$ does not track to reference output $\hat{y}(t)$.

Fig. 3 shows the control result of the proposed scheme. The following PID gains were calculated applying Eq. (19) by using the data between t = 0 to 100 [step] in Fig. 2:

$$K_P = 6.74, K_I = 2.49, K_D = 0.0. \tag{24}$$

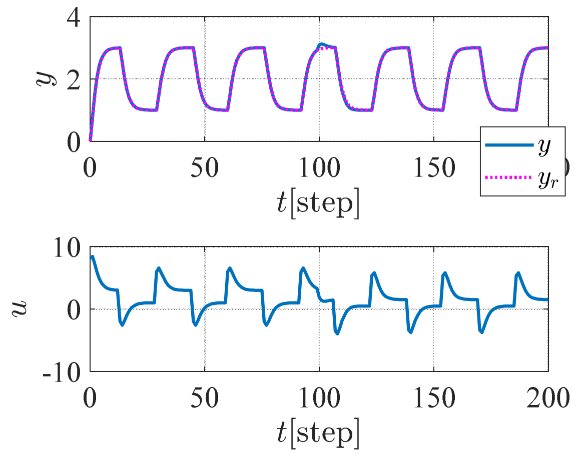

Fig. 5. Control result of the proposed scheme with controller retuning at 120 [step].

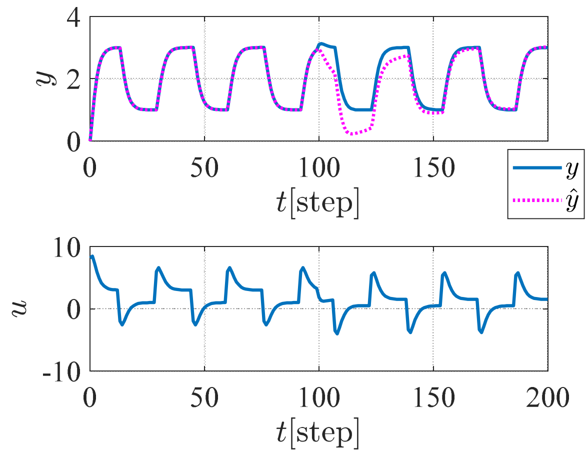

Fig. 6. Trajectory of the estimated output $\hat{y}(t)$ corresponding to Fig. 5.

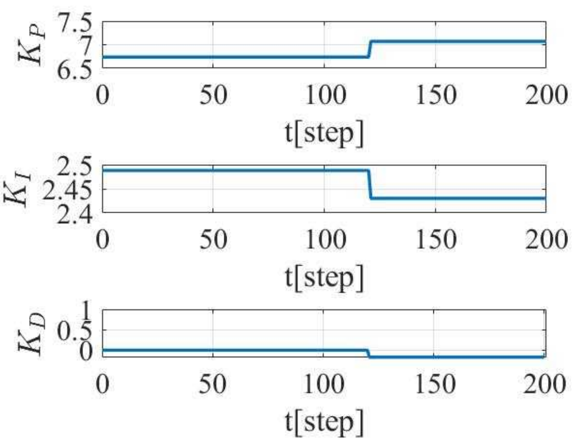

Fig. 7. Trajectories of the PID gains corresponding to Fig. 5.

In Fig. 3, the control performance is good even though the system $G(z^{-1})$ is changed at $t = 100$ [step]. It mentions that it is difficult to detect the system parameters are changed. On the other hand, Fig. 4 shows the trajectories of the estimated output $\hat{y}(t)$. It easier to detect the system parameters are changed than Fig. 3.

Finally, Fig. 5 shows the control result with controller retuning at 120 [step]. Fig. 6 shows the estimated output $\hat{y}(t)$, and Fig. 7 shows the trajectories of the PID gains corresponding to Fig. 5. In Fig. 7, each PID gains are slightly adjusted, however, the estimated output $\hat{y}(t)$ of Fig. 6 is significantly improved. Therefore, the proposed scheme can diagnose the system parameters are changed strictly.

7. Conclusions

This paper has proposed the design of data-driven control system with evaluating controller performance The features of the proposed scheme are as follows:

- Controller and estimated system model can be designed simultaneously.
- Satirical diagnosis of that system parameters are changed.

The proposed scheme has been verified by numerical examples.

References

1. S. Soma, O. Kaneko and T.Fujii, “A New Approach to Parameter Tuning of Controllers by Using One-Shot Experimental Data: A Proposal of Fictitious Reference Iterative Tuning (in Japanese)”, *Trans. of the Institute of systems, Control and Information Engineers*, **17**(2) (2004) 528–536.
2. T. Yamamoto and K. Takao and T. Yamada, “Design of a Data-Driven PID Controller”, *IEEE Trans on control systems Technology*, **17**(1) (2009) 29–39.
3. M.C. Campi, A. Lecchini and S.M. Savaresi, “Virtual Reference Feedback Tuning: A Direct Method for the Design of Feedback Controllers”, *Automatica*, (38) (2002), 1337-1346.
4. T. Kinoshita, Y. Ohnishi, T. Yamamoto and S. Shah, “Design of a Performance-Driven Control System based on the Control Assessment”, *Proceedings of the IECON 2018 - 44th Annual Conference of the IEEE Industrial Electronics Society, Washington D.C.*, (2018).
5. T. Yamamoto and S. L. Shah, “Design and Experimental Evaluation of a Multivariable Self-Tuning PID Controller”, *IEE Proc. Control Theory and Applications*, **151**(5) (2004) 645–652.

The Actual Car Driving Evaluation System using Combined with Eyeball and Face Angle

Keiko Sakurai
Faculty of Engineering, University of Miyazaki,
1-1,Gakuen-kibanadai-nishi, Miyazaki-shi ,Japan

Hiroki Tamura
Faculty of Engineering, University of Miyazaki,
1-1,Gakuen-kibanadai-nishi, Miyazaki-shi ,Japan

Koichi Tanno
Faculty of Engineering, University of Miyazaki,
1-1,Gakuen-kibanadai-nishi, Miyazaki-shi ,Japan

Yukio Hattori
OFA SUPPORT INC, 3535-2,Shimanouchi, Miyazaki-shi, Japan

E-mail: sakurai.keiko.u6@cc.miyazaki-u.ac.jp, htamura@cc.miyazaki-u.ac.jp,
tanno@cc.miyazaki-u.ac.jp,

Abstract

The lack of automobile driving standards of persons with brain dysfunction and the increase of car accidents by the elderly are problems. Under these circumstances, to evaluate brain dysfunction and driving ability of elderly people is needed. So, gaze estimation research is rapidly developing. In this paper, we proposed the actual car driving evaluation system which can be evaluated by combining eye movements using eye tracking device (TalkEyeLite) and face movement estimated using template matching. In order to the evaluate our proposal method, we carried out the actual car driving experiments. The subjects were one instructor of the car driving school, and 6 general drivers (three of the elderly, three of 40 people). We compare the gaze range of the 6 general subjects and the instructor. As a result, we confirmed that one male in the 40s and one elderly narrow the gaze range.

Keywords: actual car driving evaluation system, eye tracking, template matching.

1. Introduction

Development of a system for evaluating the driving ability of a car is proceeding from the necessity of evaluating the traffic accident of elderly people and the resumption of operation of patients with higher brain functions.When a person sees a specific direction, in most cases the position of the head and eyes simultaneously moves [1] [2], so to consider the movement of the head and eyes in evaluating the driving of the car is necessary. Therefore, we proposed the facial pose detection method by using camera [3] in previous research. Further, we proposed a system that selects the RGB-D sensor to determine the direction of the head, estimates both directions simultaneously using the RGB-D sensor and the EOG sensor, and estimates high precision gaze [4][5]. However, this proposed system had not high accurate that could be used for car driving evaluation. In addition, the existing system is necessary to place the RGB-D sensor, there is a problem that is specialized for use in a limited space.

In this paper, we propose the car driving evaluation system using gaze by using combined eyeball and face angle. We use the eye tracking device (TalkEyeLite [6]) to get the eyeball angle and the image processing technique to get the face angle. In this image processing technique, we proposed the face angle estimate method using template matching method. We have constructed a system that can be evaluated by actual car driving using eye tracking device and proposed face angle estimation method. In this paper, we consider the results of actual car driving evaluation for one instructor at a driving school and 6 general subjects (three elderly people and three men in their forties). By using eye tracking device and proposed face angle estimate method, we built a system that can be evaluated by actual car driving. In this paper, we consider about the results of actual car driving evaluation.

2. Measurement System

2.1. *Measurement system using TalkEyeLite[6]*

TalkEyeLite [6] is a wearable eye movement measurement system that uses a USB camera for eyeball detection and visual field and connects directly to the processing computer. Fig. 1(a) is a picture of TalkEyeLite goggles including a view camera and eyeball camera which is a goggle type device. The gaze of both eyes is blue cross points of Fig.1(b).

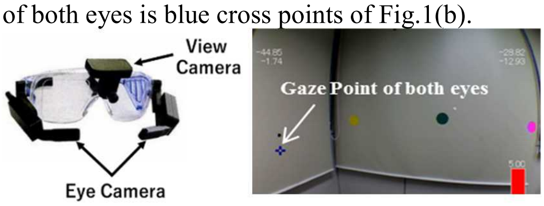

(a) TalkEyeLite Goggles (b) The operation imageof .

Fig. 1. The measurement system of TalkEyeLite

Through USB camera, TalkEyeLite is able to track the pupil of subject, therefore through the eye motion analysis software we can able to know which target the subject was looking at. The angle of convergence can possibly be calculated with angle data of both eyes.

2.2. *The face angle estimation method using template matching method*

We proposed the face angle estimate method using template matching method. We use the viewing camera of TalkEyeLite to obtain the head movement. The face angle estimate method using template matching method does not need to set up the camera. Therefore, there is a merit that it is easily usable in various environment. We prepare three templates (Marker1,2 and 3) as shown Fig.2. with downward triangle and upward triangle and circle on the front glass of the car. Fig. 3 shows the coordinate position of each markers and the range of calibration.

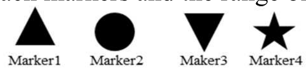

Fig. 2. Types of markers.

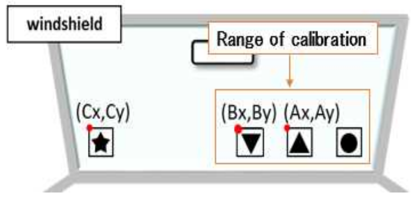

Fig. 3. The markers positions and the range of calibration

We perform the template matching method using these three template images and estimate the face angle.

The inclination of the face has three tilt axes, the yaw axis, the pitch axis, and the roll axis, but when the roll axis is tilted, the error occurs in the yaw angle and the pitch angle. In order to solve this problem, the coordinates calculated by the template matching are converted into the coordinates corresponding to the change of the roll axis, and the angle of the movement of the face is estimated from the coordinates.

3. Proposal Driving Evaluation Method

In this section, we introduce the evaluation method of this system. The fixation point is obtained by adding the estimation result of the line of sight and the angle of the face estimated from TalkEyeLite. Fig. 4 shows the animation of the analysis result after performing the template matching.

Fig.4. The display of our proposal system.

To evaluate the performance of this system, an actual vehicle experiment was conducted at the driving school. The subjects were one driving school instructor and 6 general subjects (Subject A: 60s, Subject B: 60s, Subject C: 60s, Subject D: 40s, Subject E: 40s, Subject F: 40s). The driving school instructor ran four times on actual cars, and 6 general subjects each ran on an actual car once. The data of the driving school instructor was taken as teacher data. In order to evaluate, we compare teacher data and 6 general subjects in the time in case of face angle, eyes movement angle and gaze. Fig.5 and 6 are histograms of the face angle, the eye movement, and gaze during car driving, which means the face angle, the line of sight, and the line of sight are distributed in the area during running. The vertical axis represents the number of times, the horizontal axis represents the X direction (left and right: plus is right, minus is left), and the depth is Y direction (upper and lower: plus is upper, minus is down).

Fig. 5 is an instructor of driving school, and Fig. 6 is subject B(60s). The numbers of data differ depending on subjects. Also, the hatched portion on each graph is the range during running calculated based on the result of Gaussian fitting with the confidence interval set to 95%.

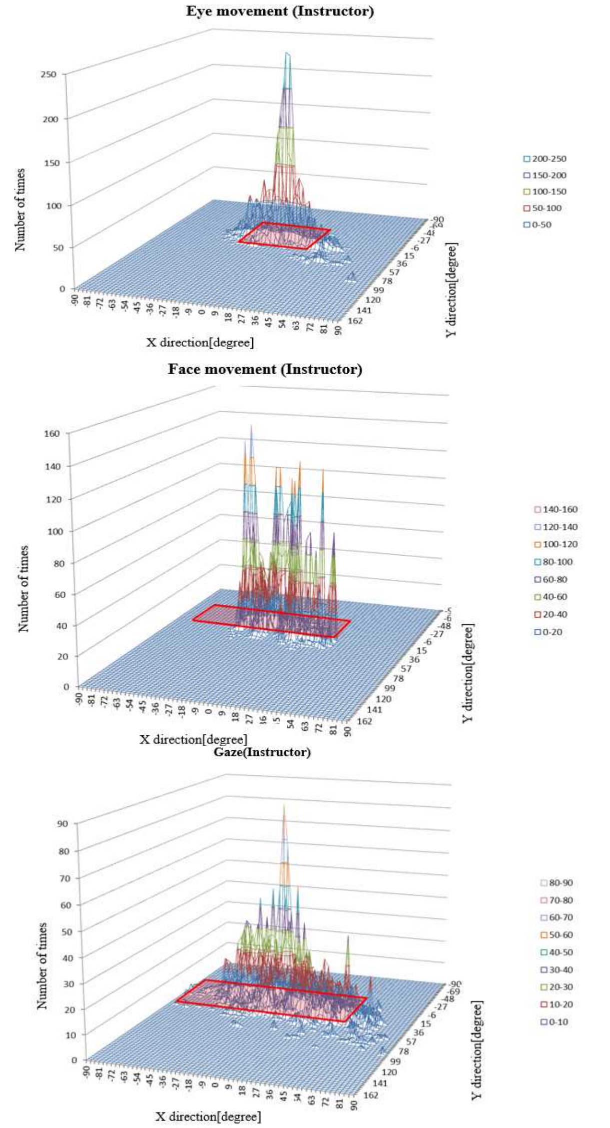

Fig.5. Histograms during car driving (Instructor)

In other words, we assumed that the range of 5% or less is not seen. The maximum value in the X direction is X_{max}, the minimum value is X_{min} when the threshold value is 5%, and X is defined as X_{max}-X_{min}. Similarly, Y is Y_{max}-Y_{min} in the Y direction.

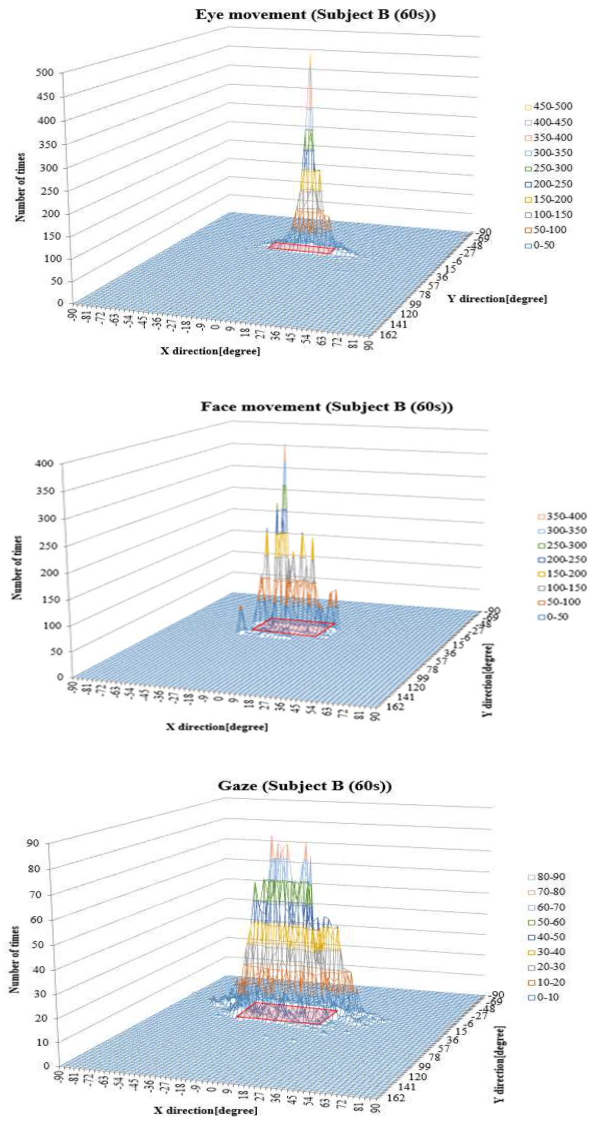

Fig.6. Histograms during car driving (Subject B(60s))

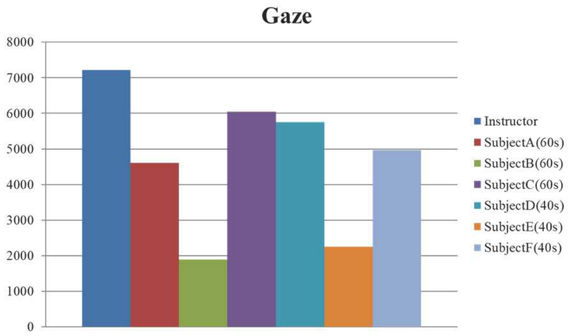

Fig.7. Compare the X*Y value

4. Conclusion

In this paper, we introduced the actual car driving evaluation system using gaze by using combined eyeball and face angle during car driving. We extended previous proposed method and constructed the car driving evaluation system by actual car. We also investigate the system.

Previous studies, we could not measure the range of accurate gaze during actual cars driving, but in this paper, we measured the gaze while driving with one instructor and 6 general subjects on actual car. And compare with the teacher data, we constructed a system that can accurately show the range of gaze during driving. In the evaluation, we found that subject B (60's) and subject E (40's) had narrower gaze range than the instructor. By performing Gaussian fitting, a certain driving evaluation may be possible by comparing the gaze range of instructors and general subjects.

In addition, the scores of each subject's car driving evaluation system (Smart Driving Assessment Program: SDAP) are as follows. Subject A (60s): -840, Subject B (60s): -887, Subject C (60s): -720, Subject D(40s): -770, Subject E(40s): -808, Subject F(40s): -405. The scores are calculated by subtraction method. Therefore, lower score means better result. Experimental results in this paper suggest that subjects with poor SDAP scores may have narrow field of view.

5. Future Work

The final objective of this paper is to construct a car driving evaluation system which is the standard for resuming the driving of people with higher brain dysfunction. For that purpose, to find clear differences between the driving of healthy people and people with higher brain dysfunction is necessary. However, since the number of subjects is small, our system is greatly influenced by the individual's driving. Therefore, we consider that the investigation on the gaze point movements and the collection of actual cars driving data by expert drivers, healthy people and people with higher brain dysfunction are required.

Acknowledgements

Funding and support from the OFA SPPORT INC is gratefully acknowledged.

References

1. C.J.S.Collins and G.R.Barnes, "Independent control of head and gaze movements during head-free pursuit in humans," *Journal of Physiology*, February 1999; Volume 515, Part1, pp 299-314.
2. S. Ron, A. Berthoz,"Eye and head coupled and dissociated movements during orientation to a double step visual target displacement," *Experimental Brain Research*, May 1991, Volume 85, Issue 1, pp 196–207.
3. Min Gyo CHUNG, Jisook PARK and Jiyoun DONG," A Simple Method for Facial Pose Detection", *IEICE TRANSACTIONS on Fundamentals of Electronics, Communications and Computer Sciences* Vol.E87-A No.10, October 2004, pp.2585-2590.
4. Keiko Sakurai , Mingmin Yan, Kazuhiko Inami, Hiroki Tamura and Koichi Tanno, "A study on human interface system using the direction of eyes and face", *Artificial Life and Robotics*, December 2015, Volume 20, Issue 4, pp 291-298.
5. Keiko Sakurai, Mingmin Yan,Hiroki Tamura and Koichi Tanno," Comparison of two techniques for gaze estimation system using the direction of eyes and head", *2016 IEEE International Conference on Systems, Man, and Cybernetics (SMC)*, October 2016, DOI: 10.1109/SMC.2016.7844609.
6. Takei Scientific Instruments Cooperation: URL http://www.takei-si.co.jp/en/ (access 2018.9.10)

A Study on Speaker Identification Approach by Feature Matching Algorithm using Pitch and Mel Frequency Cepstral Coefficients

Barlian Henryranu Prasetio
Interdisciplinary Graduate School of Agriculture and Engineering, University of Miyazaki, 1-1 Gakuen Kibanadai-nishi, Miyazaki-shi, 889-2192, Japan

Keiko Sakurai
University of Miyazaki, 1-1 Gakuen Kibanadai Miyazaki-shi, 889-2192, Japan

Hiroki Tamura
University of Miyazaki, 1-1 Gakuen Kibanadai Miyazaki-shi, 889-2192, Japan

Koichi Tanno
University of Miyazaki, 1-1 Gakuen Kibanadai Miyazaki-shi, 889-2192, Japan

E-mail: barlian@ub.ac.id, sakurai.keiko.u6@cc.miyazaki-u.ac.jp, htamura@cc.miyazaki-u.ac.jp, tanno@cc.miyazaki-u.ac.jp

Abstract

In this paper, we grouping the words based on the speaker in a sequence of speech in a conversation. There are two speakers in each conversation. The first speech assumed spoken by speaker-1. In recognizing the speakers, we use pitch detection and Mel Frequency Cepstral Coefficients feature extraction with 13 filters. Furthermore, we examine the distance of the second speech vector with the first speech vector using the Feature matching algorithm. Previously, we had experimented on each speaker to find out the mean and variance of the Feature matching. Based on the experimental results, the Standard Deviation of Euclidean, Mahalanobis and Manhattan Distance are 0.0383, 0.0254, and 0.0341. Hence, if the Feature matching value deviates is not more than variance value then the speech is assume spoken by speaker-1. Otherwise, the speech assume spoken by speaker-2.

Keywords: Speaker identification, Pitch, MFCCs, Euclidean, Mahalanobis, Manhattan.

1. Introduction

Stress is a mental disorder that occurs in a person due to pressure.[1] Stress is one of emotion. Emotions divided into two types, conscious and unconscious emotions.[2] Conscious emotions are emotions that we can feel like anger, sadness and happiness. Unconscious emotions are emotions that we cannot feel like stress and depression. It means, we cannot know when we are under stress. It makes relatively difficult to recognize stress.

Speech is one of methods that can be recognizing a stress.[3] It focuses on speech features in the frequency domain. Human voice signals have a very high level of variability.[4] A speech signal issued by different speakers produces different speech patterns. It makes a problem when we recognize a stress in a conversation. As we know, the conversation is a sequence of words spoken by more than one speaker. Therefore, in this paper, we present a simple method of identifying the speaker in a conversation that indicated to have a stress speech on the speaker.

2. Materials and proposed method

2.1. *Proposed method*

In this paper, we used a sequence of words that has been segmented from two-pilot conversation in an Apache helicopter cockpit.[5] This conversation is recorded and collected by the Linguistic Data Consortium (LDC) in the Speech Under Simulated and Actual Stress (SUSAS) database.[6] This conversation indicates the stress condition of the speaker. The speaker identification consists of two stages, feature extraction and feature matching.[7] The process of our proposed method can be seen in Fig. 1.

The Fig. 1 shows that the speech conversations consisting of sequence words. The first speech extracted the frequency fundamentals pitch and Mel Frequency Cepstral Coefficients (MFCCs). Furthermore, we do the same thing in the second speech. We assume that the first speech spoken by the speaker-1. Furthermore, we examine the distance between the first speech and the second speech vector using the feature-matching algorithm (Euclidean[8], Mahalanobis[9] and Manhattan[10]). In the preliminary experiment, we have analyzed the standard deviation of each speaker. Therefore, if the distance between the two vectors is less or equal to the standard deviation, we decide that the second speech spoken by the speaker-1, otherwise spoken speaker-2.

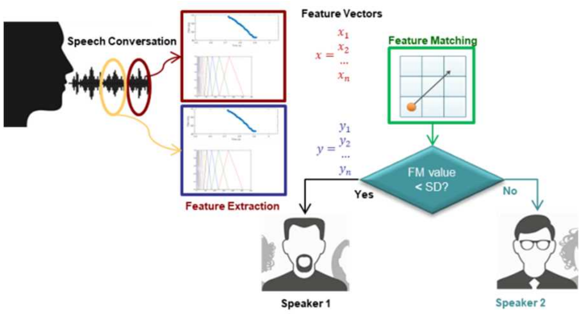

Fig. 1. Proposed method process.

2.2. *Feature extraction*

2.2.1. *Pitch*

The Pitch is the fundamental frequency of the vocal cord vibration (called F_0) followed by formants bandwidth at higher frequencies.[11] Typically, the male voice pitch is around 85-155 Hz and the female is about 165-255 Hz.[12]

$$F_0 = \frac{1}{2L}\sqrt{\frac{\sigma}{\rho}} \tag{1}$$

Where: L is length of vocal folds
σ is longitudinal stress
ρ is Tissue density

2.2.2. *Mel Frequency Cepstral Coefficients (MFCCs)*

The MFCC can use as a characteristic vector to represent human sound and musical signals. The sound analysis on Mel-Frequency based on the perception of human hearing,[13] because the human ear has observed to function as a filter at a certain frequency. The filters have a frequency response forming a triangle, and the space between their bandwidth determined by a constant mel-frequency interval.[14]

The triangular filters applied to computing filter banks.[15] We used 13 filters to extract frequency bands on a Mel-scale to the power spectrum. The model of filter bank on a Mel-Scale can be express as:

$$H_m(k) = \begin{cases} 0, & k < f(m-1) \\ \frac{2(k-f(m-1))}{f(m)-f(m-1)}, & f(m-1) \le k \le f(m) \\ \frac{2(f(m+1)-k)}{f(m-1)-f(m)}, & f(m) < k \le f(m+1) \\ 0, & k > f(m+1) \end{cases} \tag{2}$$

Where: m is the number of filters we want, *f()* is the list of $m+2$ Mel-spaced frequencies.

The frequency band of the filter[16] shows in Table 1.

Table 1. The frequency band of the filter.

Filters	Passband Edges (Hz)
Filter1	[133 267]
Filter2	[200 333]
Filter3	[267 400]
…	…
Filter12	[867 999]
Filter13	[933 1071]

© The 2019 International Conference on Artificial Life and Robotics (ICAROB2019), Jan. 10-13, B-Con Plaza, Beppu, Oita, Japan

2.3. *Feature Matching Algorithm*

2.3.1. Euclidean Distance

The Euclidean distance between points x and y is the length of the line segment connecting $(\overline{xy})$. In Cartesian coordinates, if $x = (x_1, x_2, \dots, x_n)$ and $y = (y_1, y_2, \dots, y_n)$ are two points in Euclidean *n-space*, then the distance (d_{ED}) from x to y, is given by the Pythagorean formula:[17]

$$d_{ED}(x,y) = \sqrt{\sum_{i=1}^{n}(x_i - y_i)^2} \qquad (4)$$

2.3.2. Mahalanobis Distance

The Mahalanobis distance is a measure between two samples point. The Mahalanobis distance between a vector x and y with covariance σ is[18]

$$d_{MD}(x,y) = \sqrt{\sum_{i=1}^{n}\left(\frac{x_i - y_i}{\sigma_i}\right)^2} \qquad (3)$$

2.3.3. Manhattan Distance

The distance between two points measured along axes at right angles. In a plane with x at (x_1, x_2) and y at (y_1, y_2), it is:[19]

$$d_{MH}(x,y) = \sum_{i=1}^{n}|x_i - y_i| \qquad (5)$$

3. Results and Discussions

In this work, we used three conversations between two speakers. Therefore, we have from six speakers feature vector data. Furthermore, we calculate the standard deviation for each speaker in each distance algorithm, as follows:

- Euclidean Distance = 0.0383,
- Mahalanobis Distance = 0.0254,
- Manhattan Distance = 0.0341.

This standard deviation value is the threshold for determining speaker identification.

In the features extraction, each speech extracted from its pitch and MFCC features. The feature vector sample from feature extraction can be seen in Fig. 2.

Then on, we calculated the vector distance both of speech vector. Feature matching of each speech in the first conversation can be seen in Fig. 3.

Finally, we compare the number of speeches that have grouped with the actual number of speeches for each distance algorithm to determine the accuracy of our proposed method. The accuracy based on its features extraction. The system accuracy can be seen in Fig. 4.

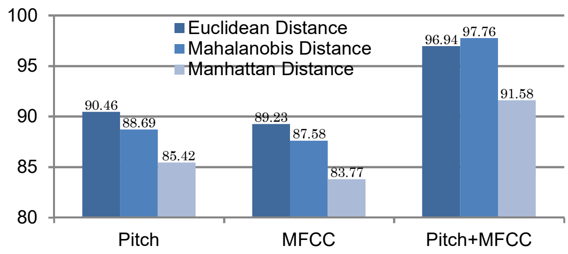

Fig. 4. The system accuracy.

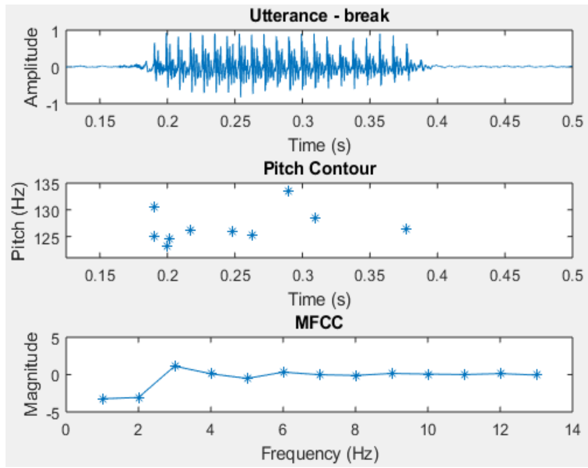

Fig. 2. The feature vector sample. The utterance is "*break*". Pitch features is 10 feature vectors and 13 feature vectors for MFCC

In Fig. 4 can be seen that in general the accuracy reaches above 80%. Accuracy for multi-feature extraction is better than single features, above 90%.

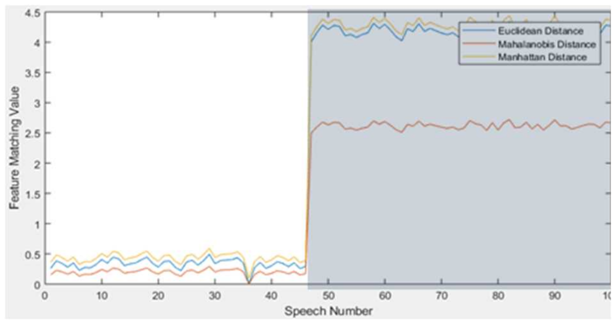

Fig. 3. The distance value on feature matching process of each speech in the first conversation.

Euclidean distance is better for single feature extraction. Mahalanonbis distance is better on multi-features.

4. Conclusion

The experiment involves three conversations between two speakers. The system accuracy rate calculated from the number of words clustered in both speakers by comparing pitch feature, MFCC feature and combination of pitch and MFCC with self-calculation. The experimental result shows that Euclidean Distance is better for single feature extraction and Mahalanobis Distance is better for multi-features extraction.

Acknowledgements

Thank you for Tamura Laboratory that has supported us in this study. Thank you to LDC that has given us the SUSAS Data.

References

1. N. Schneiderman, G. Ironson and S. D. Siegel, Stress And Health: Psychological, Behavioral, and Biological Determinants, *Annu Rev Clin Psychol,* 2005(1) (2005) 607-628.
2. A. K. Tiwari, Non-Verbal Communication-an Essence of Interpersonal Relationship at Workplace, *SMS Varanasi Management Insight,* 11(2) (2015) 109-114.
3. N. R. Prakash and J. Kaur, A Study on Physiological Parameters Used To Monitor Stress in Experimentally Induced Stimuli, *International Journal of Computer Science and Information Technologies,* 6(6) (2015) 5244-5246.
4. M. Latinus and P. Belin, Human voice perception, *Current Biology,* 21(4) (2011) 143-145.
5. J. H. L. Hansen, Composer, *SUSAS Transcripts LDC99T33.* [Sound Recording] (Philadelphia: Linguistic Data Consortium. 1999).
6. J. H. L. Hansen, Composer, *SUSAS LDC99S78. Web Download.* [Sound Recording] (Philadelphia: Linguistic Data Consortium. 1999).
7. S. S. Tirumala, S. R. Shahamiri, A. S. Garhwal and R. Wang, Speaker identification features extraction methods: A systematic Review, *Expert Systems With Application* 2017(90) (2017) 250-271.
8. A. . S. Thakur and N. Sahayam, Speech Recognition Using Euclidean Distance, *Proc. International Journal of Emerging Technology and Advanced Engineering,* 3(3) (2013) 587-590.
9. G. Aradilla, J. Vepa and H. Bourlard, Using Posterior-Based Features in Template Matching for Speech Recognition, in *Proc. Interspeech ICSLP* (Pittsburgh, Pennsylvania, 2006).
10. M. D. Malkauthekar, Analysis of euclidean distance and Manhattan Distance measure in face recognition, in *Proc. Third International Conference on Computational Intelligence and Information Technology* (Mumbai, India, 2013).
11. N. Peleg, Homepage of Audio-Video Compression Course, 2 2010. [Online]. Available: http://cs.haifa.ac.il/~nimrod/Compression/Speech/S1Basics2010.pdf. [Accessed 23 3 2018].
12. N. Zivic, *Modern Communications Technology, Oldenbourg* (De Gruyter Studium, 2016).
13. L. Muda, . M. Begam and I. Elamvazuthi, Voice Recognition Algorithms using Mel Frequency Cepstral Coefficient (MFCC) and Dynamic Time Warping (DTW) Techniques, *Journal of Computing* 2(3) (2010) 138-143.
14. A. V. Bhalla and S. Khaparkar, Performance Improvement of Speaker Recognition System, *International Journal of Advanced Research in Computer Science and Software Engineering* 2(3) (2012) 82-87.
15. H. Fayek, Haytham Fayek, 21 4 2016. [Online]. Available: http://haythamfayek.com/2016/04/21/speech-processing-for-machine-learning.html. [Accessed 21 3 2018].
16. L. R. Rabiner and S. Ronald W, *Theory and Applications of Digital Speech Processing* (Upper Saddle River: Pearson, 2010).
17. H. Anton, in *Elementary Linear Algebra (7th ed.)* (John Wiley & Sons, 1994), pp. 170-171.
18. R. Wicklin, SAS Blog, The DO Loop , 15 2 2012. [Online]. Available: https://blogs.sas.com/content/iml/2012/02/15/what-is-mahalanobis-distance.html. [Accessed 24 10 2018].
19. P. E. Black, xlinux, NIST, 31 5 2006. [Online]. Available: https://xlinux.nist.gov/dads/HTML/manhattanDistance.html. [Accessed 21 10 2018].

A Study on Breathing and Heartbeat Monitoring System during Sleeping using Multi-Piezoelectric Elements

Praveen Nuwantha Gunaratne
University of Miyazaki, 1-1 Gakuen Kibanadai-nishi, Miyazaki-shi, 889-2192, Japan

Chika Yoshida
Graduate School of Engineering, University of Miyazaki, 1-1 Gakuen Kibanadai-nishi, Miyazaki-shi, 889-2192, Japan

Keiko Sakurai
University of Miyazaki, 1-1 Gakuen KibanadaiMiyazaki-shi, 889-2192, Japan

Hiroki Tamura
University of Miyazaki, 1-1 Gakuen KibanadaiMiyazaki-shi, 889-2192, Japan

Koichi Tanno
University of Miyazaki, 1-1 Gakuen KibanadaiMiyazaki-shi, 889-2192, Japan

E-mail: praveennuwantha@gmail.com, hi13049@student.miyazaki-u.ac.jp, sakurai.keiko.u6@cc.miyazaki-u.ac.jp, htamura@cc.miyazaki-u.ac.jp, tanno@cc.miyazaki-u.ac.jp

Abstract

We propose a method to monitor breathing and heartbeat during sleeping using piezoelectric elements. The signal acquired from the piezoelectric elements during sleeping is separated into a breathing signal and a heartbeat signal using biomedical signal processing software. In the previous experiment, two subjects slept for one and a half hours. The data from the piezoelectric elements during sleep were extracted. We compared the true value with the count results from these data using the proposed method. The error rate of the breathing count was 0–13%, and the error rate of the heartbeat count was 0–8.2%. In this paper, we show the proposal system to apply the diagnosis of sleep Apnea-syndrome. From this experiment, our proposal method clearly makes sense given that on diagnosis of sleep Apnea-syndrome and the developed system has already been able to verify the 80% of non-breathing/stopped-breathing time intervals.

Keywords: *Piezoelectric Element, Breathing Waveform, Heartbeat Waveform.*

1. Introduction

Polysomnography is considered the gold standard for routine monitoring of physiological parameters of persons in bed and evaluation of the sleeping state. Its basic elements are electroencephalography, eye movement, and mentum electromyography, and it can simultaneously record respiration, electrocardiography, oxygen saturation, pretibial electromyography, snoring, body position, motion, and temperature, and other parameters; however, it requires the attachment of many sensors to the individual in an array designed for performance of the measurements, and thus, its routine use is generally not practicable.

In the present study, we constructed and assessed the accuracy of a system that incorporates thin, high-sensitivity, piezoelectric elements to obtain real-time output and analysis of respiration and heartbeat counts and information on body movement without imposing movement restrictions on the subject or invading their privacy. We already found experimentally that the proposal method using fuzzy logic can yield respiration and heartbeat counts with mean error rates of 0-13% and 0-8.2%, respectively [1]. In this paper, we show the proposal system to apply the diagnosis of sleep Apnea-syndrome.

2. Measurement system

2.1. System

In the present study, respiration and heartbeat were measured using six PE elements, which were placed between the bed and a bed mat, to facilitate acquisition and transmission of their voltage signals. They are placed so that the subject's chest area lies vertically above them and thus close to the chest region to facilitate acquisition of respiration signals by related changes in the position of the chest surface and heartbeat signals by fine heart pulsations. Six voltage signals underwent analog-to-digital (A/D) conversion by the A/D converter followed by recording on a personal computer (PC). The sampling frequency for the A/D conversion was 1,000 Hz. In the present study, respiration and heartbeat were thus measured from the voltage signals of the six elements in the above layout and stored in the PC.

2.2. Acquisition of respiration and heartbeat signals

For an adult at rest, respiratory movement occurs approximately 13 to 20 times per min with a respiration signal frequency of 0:23–0:33 Hz, and heartbeat occurs approximately 50–90 times per min at a frequency of 0.83–1.5 Hz. As shown in Fig. 1, signals obtained using a PE element contain a respiration signal frequency of 0.23–0.33 Hz, a heartbeat signal frequency of 0.83–1.5 Hz [2], and a commercial power noise frequency of 60 Hz. With this information, the digital signal processing to extract the respiration signal from the signal obtained by the elements is performed in the following process flow.

The signals obtained by the six elements undergo 10 Hz cutoff low-pass filtration, followed by 0.8 Hz cutoff low-pass filtration, and then 0.05 Hz cutoff high-pass filtration. The respiration signal is extracted in this digital signal process of respiration extraction signal filtering. The respiration extraction signal is characterized by periodic increases in amplitude, as illustrated by the example in Fig. 2, which shows a signal after respiration extraction filtering.

To extract the heartbeat from the signal obtained by the PE element, the digital signal was next subjected to the following process flow using software. The signals obtained by the six elements undergo 7 Hz cutoff low-pass filtration, followed by 5 Hz cutoff high-pass filtration, full-wave rectification processing, and finally, 2.5 Hz cutoff low-pass filtration.The heartbeat signal is extracted in this digital signal process of heartbeat extraction signal filtering. The heartbeat extraction signal is characterized by periodic increases in amplitude, as illustrated by the example in Fig. 3, which shows a signal after heartbeat extraction filtering.

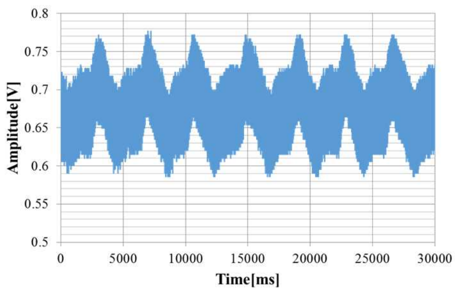

Fig. 1. Sample raw waveform

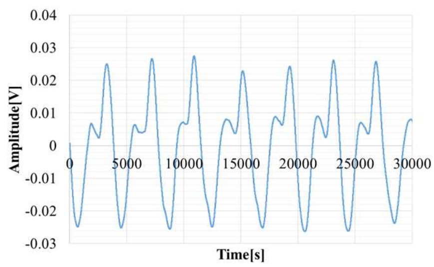

Fig. 2. Breathing waveform

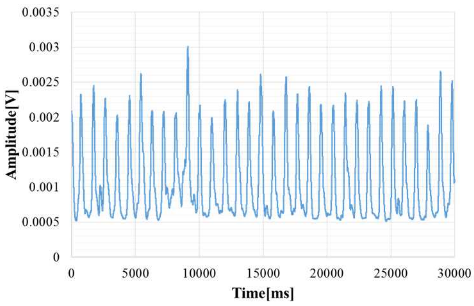

Fig. 3. Breathing waveform

3. EXPERIMENT AND RESULTS

3.1. Proposed bio-signal measurement method

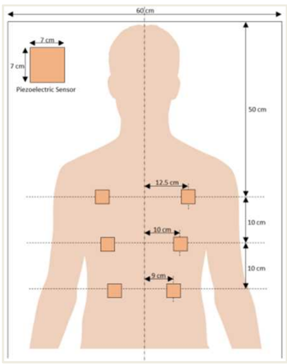

Fig. 4. Sensor arrangement of the prototyped sensory bed

Measurement and performance evaluation were conducted using a prototyped sensory bed arrangement and 5 persons, having different age, gender as well as physical height & weight were subjected to the examination process. In the development of sensory bed arrangement, 6-piezoelectric sensors have been placed on a mattress by considering the most reliable contact areas during the state of sleeping position (Back position with arms down) of an average person for precise bio-signal data acquisition. Fig. 4 depicts the sensor placements that have been used for data acquisition.

Fig. 5 portrays the system configuration of the measurement system. In the signal acquisition process, the obtained bio-signal data will be directed through a commercially available A/D convertor device before the process of signal processing is being executed and after that heart-rate & breathing waveforms will be extracted mainly based on their frequency characteristics.

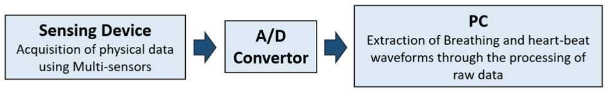

Fig. 5. Basic system configuration process flow

3.2. Testing

In accordance with the proposed bio-signal measurement method, the experiment on selected test users was performed. The total experiment time per one test user was 180 sec. and within that period, pre-selected 15 sec. time intervals have been considered as non-breathing/stopped breathing for the waveform differentiation. 3 time intervals starting from 70th second of the experiment time, were considered as the stopped-breathing and test users were instructed to perform accordingly. 70-85, 100-115 & 130-145 were the pre-set stopped-breathing time intervals taken while performing the experiment. Further we managed to execute all these experiments at a steady state, with minimal body motion in order to minimize any distraction.

3.3. Results

Fig. 6 presents a sample raw waveform acquired through a piezoelectric sensor in the examination of bio-signals during sleep test of 1st test user. The acquired test result shows a significant variation in the raw waveform during the above mentioned non-breathing/stopped breathing time intervals. Further it depicts considerably similar waveform during the rest of the time. Figs. 7(a) and 7(b) respectively portray the extracted breathing and heart-beat waveforms based on their frequency bands.

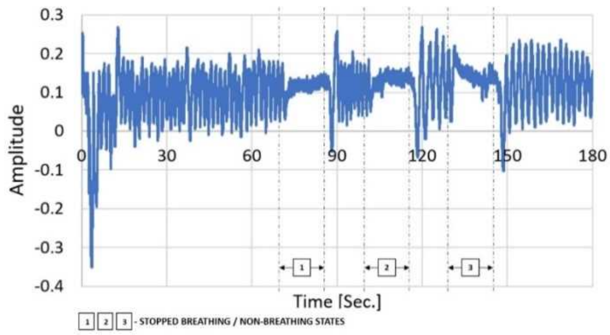

Fig. 6. Sample raw waveform of 1st test user

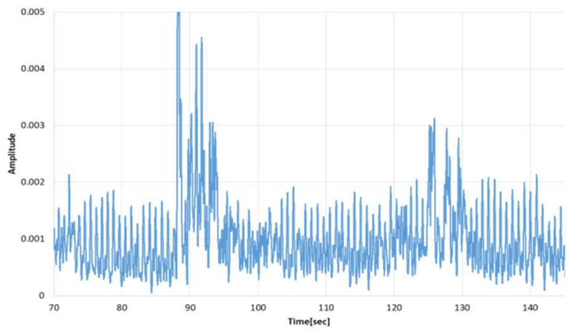

Fig. 7(b). Heart-beat waveform (70[sec] to145[sec]) of 1st test user

The visual inspection of these extracted waveforms clearly shows the successful and effective capture of breathing and heart-beat waveforms. This approach clearly makes sense given that on diagnosis of sleep Apnea-syndrome and the developed system has already been able to verify the 80% of non-breathing/stopped-breathing time intervals of the above mentioned examination. Apart from that, the measurement result has showed that the pressure waves acquired at the custom designed piezoelectric transducer can be used to observe any slight change in heart-beat and body motions as well.

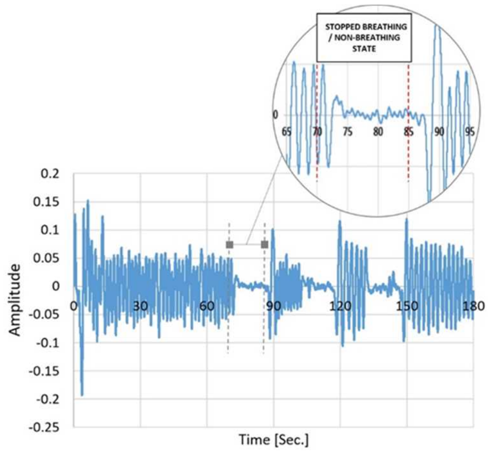

Fig. 7(a). Breathing waveform of 1st test user

4. Conclusion

In the present study, we have proposed and investigated a method of using multiple PE elements for respiration and heartbeat measurements during sleep. This proposed method clearly makes sense given that on diagnosis of sleep Apnea-syndrome and has already been able to verify the 80% of non-breathing/stopped-breathing time intervals. The dismissal of system constraint of state of sleeping position and further improvement on accuracy of diagnosis of sleep Apnea-syndrome can be obtained by adopting a piezoelectric transducer array, which is a task for future work.

.

References

1. Kiyotaka Ho, Naoki Tsuchiya, Hiroshi Nakajima, Kei Kuramoto, Syoji Kobashi and Yutaka Hata, Heartbeat Rate and Respiratory Rate Detection based on Fuzzy Logic by Air Pressure Sensor, *Japan Society for Fuzzy Theory and Intelligent Informatics, Fussy Symposium,* 25(0), 54-54, 2009
2. Hiroki Tamura, Hiroaki Matsumoto, Chika Yoshida, Nobuya Takahashi, Breathing and Heartbeat Monitoring during Sleeping using Piezoelectric Elements, *Japanese Society for Medical Engineering, Medical Engineering Symposium,* 2P-1-4,2016

Field Robot and Sensing system

Eiji Hayashi*
Mechanical Information Science and Technology, Kyushu Institute of Technology
680-4, Kawazu, Iizuka, Fukuoka, 820-8502, Japan
haya@mse.kyutech.ac.jp

Abstract

Labors in which forestry and agriculture and factory, are working in severe circumstance. So, such workers are necessarily declines and decreases. However, it is important for us to keep going economy, life and nature. Therefore, to prevent a devastation of the forest, the safety and the lack of food and work in harsh environments, we are thinking alternative technologies that a part of severe and dangerous works are taken robot instead of such workers. Something changes are needed that they are seen innovation such as the generation of a new industry by new technologies using AI and intelligent to improve how to recognize and express more and more of the things that we have various desires.

Keywords: List four to six keywords which characterize the article.

1. Introduction

Japan's population is decreasing after a peak in 2008 due to aging of the population and declining birthrates. Such shrinking population will be having a major impact to build a sustainable economy and society over a long-term period, but almost all people feel that the effects for a short term are small and negligible. Japan's economy and society will require more development in technologies such as artificial intelligence and robots to make up for a decline in the labor force. However, the decline of the labor force already invites the labor shortages in the industries. Therefore, the Japanese government aims to introduce a new residence status that the foreign workers are accepted in the fourteen business sectors which are restaurants, hotels, nursing care, building cleaning, agriculture, fishery, food and beverage, materials processing, industrial machinery, electronics and electric machinery, construction, shipbuilding, vehicle maintenance, and airport ground handling and aircraft maintenance.

The technology of robotics has provided efficient productivity, quality and safety in factory as well as improved operability so far. The developing robots in forestry, agriculture and food factory are active nowadays since AI and robotics technologies has progressed rapidly. Robot in the future has to have the work capacity or the co-operation cooperativeness equivalent to the skilled worker. It is too difficult to make up for the labor shortages only in such robotics technologies at the present.

This paper reports on field robot and sensing system as applications of the robotics and AI to the agriculture, the forestry, the food factory and future industrial factory.

2. Agriculture

A decline of Japan's Agriculture has 2 big problems related to work in the severe environmental conditions such as hot summer climate and labor shortage. Foreign agriculture employs a large-scale management represented by United states, Australia and Netherlands

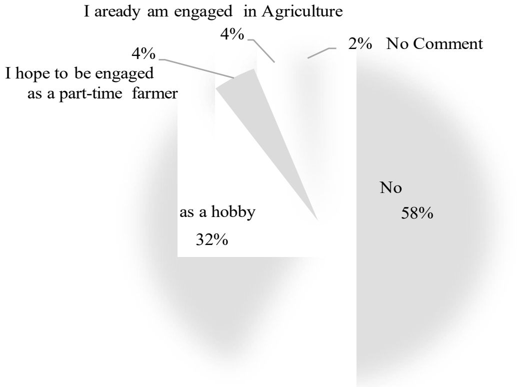

Fig.1 Question : Do you hope to be engaged in the agriculture?

using the agricultural machines or the environmental control technology introduced the latest technologies.

2.2. *Present State of Japan*

4.42 million ha of The Japanese are of the cultivated land in 2018 is estimated to be 54.4 % of paddy fields, 45.6 % exclusive use for meadows and 6.3 % land under permanent crops of the total amount of the fields.
A survey results are described in the meeting's materials of Cabinet Secretariat of Government of Japan as is shown in Fig.1.
The famers who mainly engaged in farming is estimated to be 1.50 million persons, average age:66.7 in 2017, compared to 2.05 million persons, average age: 66.7 in 2010. Taking Japan's rapidly decreasing working population to consideration, it will be too severe in realty for the future agriculture to substantially decrease the formers. The age structure of farmer in each country shown in Fig.2 reveals that the Japanese farmers of this kind are more likely to be "mainly and significantly aged farmers" than other countries.

2.3. *Agricultural Technology*

Nowadays it is important to improve the labor productivity and the local adaptability so that the agriculture product can be produced in quantity. The technology in the agriculture has promoted the introductions of management and automation system [1-2], enviromental control for the green house like a plant factory, especially in Netherlands. The plant factory cultivates plant in the facility utilizing artificial control of

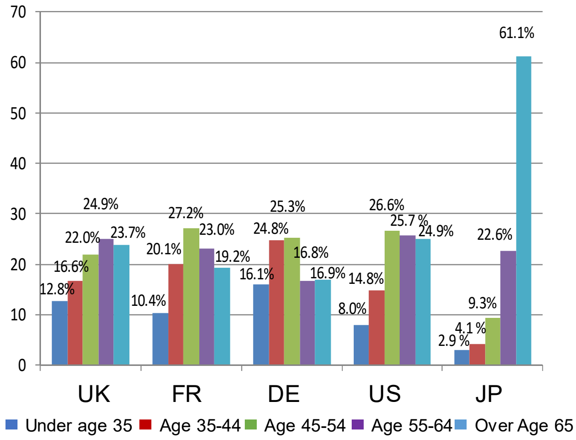

Source : 3rd. meeting's materials of Cabinet Secretariat of Government of Japan, No.4, 2015
https://www.cas.go.jp/jp/seisaku/kataro_miraiJPN/dai3/gijisidai.html

Fig.2 The age structure of farmer in each country. The Japanese farmers are more likely to be "mainly and significantly aged farmers"

light, temperature, moisture, and carbon dioxide concentrations all year around. The producing crops almost are vegetables which are divided into of a fruit vegetable such as tomato, strawberry, cucumber or eggplant, and a green vegetable such lettuce, spinach, green onion and herbs.
Such a plant factory has the issues as follows.

- Almost all work is done from raising seedling to harvesting by hand.
- Initial cost and running cost

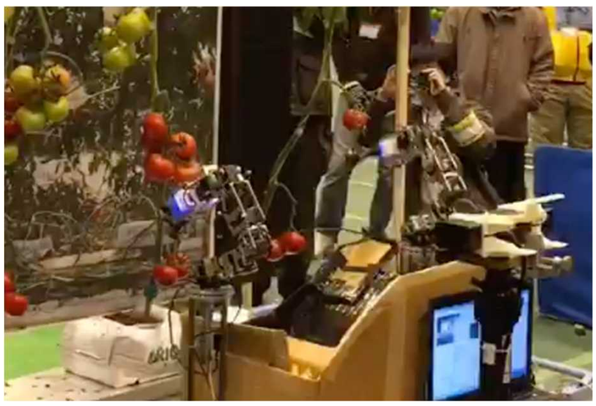

Fig.3 The tomato harvesting robot picks a tomato. This robot can pick one of the tomatoes around 20 seconds.

2.4. *Automation*

All work from seedling to harvesting is difficult to automatically do by robotic technology because the influence of light in the various situation. [3-6] It is important for robot to reduce and suppress the influence of light including infrared. The influence of light occurs due to regular reflection light bounces off from the smooth surface. If the intensity of the regular reflection increases, a color of object is recognized as different color. Human usually sees a color of the smooth surface from an angle occurring no regular reflection to reduce and suppress.

This phenomenon has various influences on the recognition for degree of mutilation of crop, controlling pests and inspect, crop disease diagnosing, robot's posture and travelling for the harvesting as shown in Fig.3.

2.4. *Malaysia*

In mainly Malaysia and Indonesia, the palm oil industry has developed more active with the palm plantation because oil palm is a kind of tropical plants is grown on a large scale as the commercial crops.

Fig.4 The plantation and Dropped fruit bunches in Sime Darby's plantation

The infield FFB in the plantation of Sime Darby in Fig.4 has 2724 ha in Sepang Estate. This area's acclivity occupies 42.5 % (1,158 ha) of 0 – 6 degree from flat to undulating, 19.4% of 6-12 degree.

In case of SD2 (1699 ha) in Sepang Estate, the mature oil palm area is broken into 9 blocks to maintain the harvesting rounds within approximately 10 days.

The robot [7] has to be aimed autonomously 2 - 2.5 hours / task (including traveling time) , depending on a terrain and weather. If such robot can achieve, dozens of work rate and people would be reduced, and would be provided more efficient to the plantation.

3. *Forestry*

Japan has one of the world' largest forests, and the amount of the forests area accounts approximately 25 million ha and 66 % of Japan's land area of 37.8 million ha. However, the labor force population of Japan declines with the aging over the long term, and is about 45,000 people in 2015.

The forests in Japan are almost the plantation forests made by planting the seedings which cover the area of 10 million ha of the forests in Japan, and are consisted of Japanese cedar, Japanese cypress which are a type of leaved tree.

Although the forestry cycle is plant, glow and harvest, nowadays the Japanese government has promoted the cyclical use of the forests as circulative resources in Fig.6 in facing the all-out harvest of the plantation forests that it will cause the vicious cycle in large scale logging as well as deterioration of the forest.

3.1. *Forestry Technology*

The forestry is need as the follows

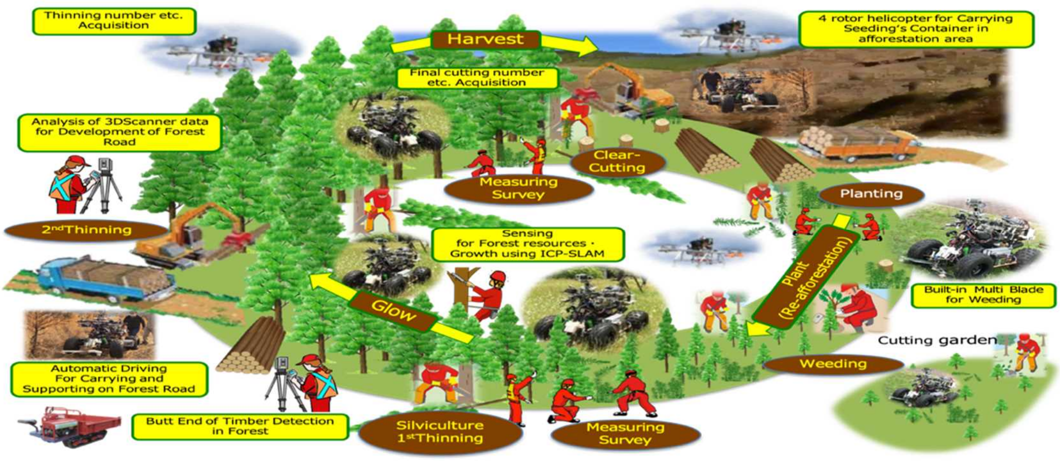

Fig. 5 The cyclical use of the forests as circulative resources

- forest information system to measure the timber
- volume and the height of trees and to analyze the tree community in the forest
- Carrying system of the pot for the seedings using the drone etc.
- Weeding robot [7] system for a steep mountain slope

Since the Japanese mountain has the steep slope, the workers are too taught to operate the planting and the weeding under the blazing the sun as well as the forcing various painful work postures.

4. Conclusions

Recently, although there are various issues in global, robotics has potential for development and improvement to solve them using networks and AI. This paper is described that there are only a few example of the agricultural and the forestry robots and systems as the field robotics and sensing system. As the related issues, the robotic technologies are needed the robotic arm for factory automation or food factory with the teaching less and the autonomous motion using AI processing, the autonomous moving type robot for iron ores and cokes in ironworks, cleaning robot for the drifted garbage on the seashore and so on.

5. References

1. K. Imou, "Automatization and Robotization of Agricultural Machinery," *J. of the Robotics Society of Japan*, Vol.35, No.5, pp. 376-378, 2017.
2. H. Sori, H.Inoue , H. Hatta and Y. Ando, Effect for a Paddy Weeding Robot in Wet Rice Culture, *Journal of Robotics and Mechatronics*, Vol.30 No.2, pp198-205, 2018.
3. W. Nakagawa, "Robots of Agricultural Implement and Machinery. Current State, Problem, and View in the Future," *J. of the Robotics Society of Japan*, Vol.35, No.5, pp. 387-389, 2017.
4. R. Fukui, K. Kawae and S. Warisawa, Development of a Tomato Volume Estimating Robot that Autonomously Searches an Appropriate Measurement Position – Basic Feasibility Study Using a Tomato Bed Mock-Up –, *Journal of Robotics and Mechatronics,* Vol.30 No.2, pp173-179, 2018.
5. A. Shinjo et al., "The practical use of IT in agriculture: The movement into high-value-added crops and integrated solutions," *The J. of the Institute of Electronics, Information and Communication Engineers*, Vol.96, No.4, pp. 280-285, 2013 (in Japanese).
6. R. Loren and D. B. Benson (eds.), *Introduction to String Field Theory*, 2nd edn., Springer-Verlag, New York, 1999.
7. T. Fujinaga, S. Yasukawa, B. Li, and K. Ishii, Imagecs Mosaicking Using Multi-Modal Images for Generation of Tomato Growth State Map, *Journal of Robotics and Mechatronics*, Vol.30 No.2, pp187-197, 2018.
8. A. Mowshowitz, A. Tominaga and E. Hayashi, Robot Navigation in Forest Management, *Journal of Robotics and Mechatronics*, Vol.30 No.2, pp223-230, 2018.

Proposition of Saliency map Based on the Maximization of Center-Surround Difference*

Ryuugo Mochizuki†
Graduate School of Life Science and Systems Engineering, Kyutech, 2-4 Hibikino Wakamatsu-ku
Kitakyushu-City, 808-0135/Fukuoka, Japan‡

Shinsuke Yasukawa§
Graduate School of Life Science and Systems Engineering, Kyutech, 2-4 Hibikino Wakamatsu-ku
*Kitakyushu-City, 808-0135/Fukuoka, Japan***

Kazuo Ishii
Department of Human Intelligence System., Kyutech, 2-4 Hibikino Wakamatsu-ku
Kitakyushu-City, 808-0135/Fukuoka, Japan
E-mail: mochizuki-ryuugo@edu.brain.kyutech.ac.jp, s-yasukawa@brain.kyutech.ac.jp, ishii@brain.kyutech.ac.jp
www.lsse.kyutech.ac.jp

Abstract

Saliency is a property of images which attracts human attention. The tendency is expressed as distribution in a saliency map. Traditionally saliency map is calculated by obtaining and merging Center-Surround Differences, where, the Center and Surround are calculated through the convolution by the finer, coarser Gaussian Filter respectively. However, Saliency depends on the filter scales, furthermore, requires adjustments of Gaussian Filter scales. Ideal Saliency is difficult to define. We propose to maximize the Center-Surround Difference to calculate saliency.

Keywords: Saliency map, Maximization of Center-Surround Difference, Image Feature, Feature Stability

1. Introduction

In the domain of image processing, researches of finding salient features are ongoing. Saliency means the tendency of features in images to attract human attentions. One of a method of creating saliency map utilizes Gaussian Filter. In the example, saliency is evaluated according to across-scale difference (Center-Surround Difference) [1], that is, the difference of images which were smoothed by finer filters (the Center) and by coarser smoothing filters (the Surround). Itti's method[1] is typical of the example. They proposed a method of creating saliency map by utilizing Gaussian Pyramid, and calculated image saliency by convolution of different scales of filters, then operated across-scale differences with the smoothed images and merged them to form saliency map. The maps created under the process is categorized as a bottom up saliency map, which was inspired by a model originated from biological visual mechanism. Including the method[1], the response of saliency depends on the filter size or scale.

As the result, trial and error is required for smoothing filter selection. Selecting appropriate filters is a problem to obtain desirable saliency. Under fixed scale, the saliency varies by changing object size in the scene.

We propose to select filter automatically so as to maximize the Center-Surround Difference. Filter scale is dynamically adjusted according to the frequency, then, unstable saliency by various object size and distance can be prevented.

2. Related Research

Itti proposed a method of obtaining saliency map, by adopting Gaussian Pyramid, whose filters were fixed to the power of two (σ_s, σ_c=2^0, 2^1, 2^2, …), and, input image was smoothed with different scales of Gaussian Filter[1]. Here, σ_s and σ_c correspond to the filter scales for the Center and the Surround, respectively.

Since then, saliency map has been developed so that objects in scenes are highlighted in intact shapes[2-6]. For example, arbitral scale selection of Gaussian Filters is a strategy to the purpose. R. Achanta stated that high-resolution saliency map can be created with enhanced object edges, where objects were monotonously highlighted by finely tuning the frequency of band path filters[2]. S. Frintrop enabled free ratio σ_s/σ_c selection of Gaussian Filters' scales for the Center and Surround as VOCUS2(Visual Object detection with a CompUtational attention System)[6]. However, from the point of view, the saliency changes according to the scale ratio, then, ideal ratio is difficult to determine.

We propose to adopt maximization of the Center-Surround Difference by enabling dynamic adjustment of the filter sizes according to frequency components in local regions in an image, that is, maximization of Center-Surround Difference. The function differs from the examples enumerated above. Thus, empirical filter selection can be omitted.

3. Proposed Method

3.1. *Outline*

We show some examples of saliency maps M_{Sal} in Itti's and proposed method, in Fig. 1, which were generated from two Lenna Images (Size: 512x512 [Pixels]). The Lenna was resized in the black background each other. The variation of saliency emerged under the variation of the object (=Lenna) size, when the image was smoothed with fixed scale of Gaussian Filters in conventional saliency map generation. The cause of the variation is changing frequency band of the image emerged from the resize. The characteristics of Gaussian Filters differ in a nine levels of Gaussian Pyramid. Thus, the differences of the responses by each filter reflect to M_{Sal}. In case of the application of saliency map into object detection with robot vision, oversight may be occurred depending on distance differences between camera and objects. On the other hand, proposed method can highlight the object uniformly also in the case of distance change. Robust object detection can be realized under the condition.

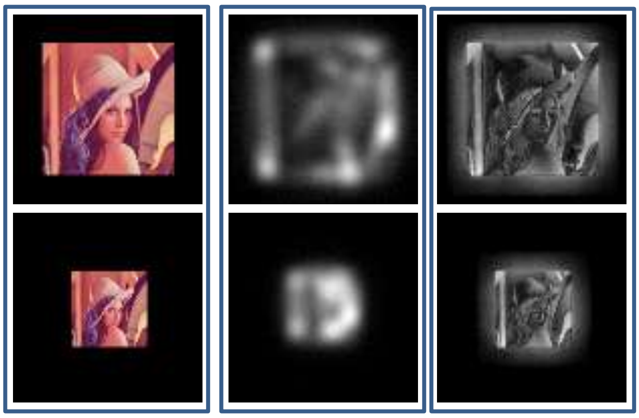

Fig. 1 Examples of saliency map generations
(Upper row: Resized to70% Lower row: Resized to 40%)

We propose to introduce Center-Surround Difference Maximization into the algorithm for saliency map generation.

The flow of proposed method is indicated in Fig. 2. Firstly, input image I_{IM} is converted from RGB to CIELab system, and distributed to Intensity Channel I_L, Color Channel I_a (Red-Green), I_b (Yellow-Blue). I_a and I_b indicate the contrast of Red and Green, Yellow and Blue, respectively. We use Integral Image[5] to obtain the Surround and the Center. Integral Image is obtained by summing up pixel values from the origin to arbitral location (x, y). Integral Image is prepared for each channel, then, the calculation of the Center and the Surround is done using Integral Image together with Box Filter. Frequency component differs according to local regions in the input image. We adjust the filter size while scanning the filter so as to maximize the Center Surround

Difference. The difference is reflected to Feature Maps M_I for Intensity Channel, M_{Ca}, M_{Cb} for Color Channels. These Fearute Maps are normalized and merged to form saliency map M_{Sal}.

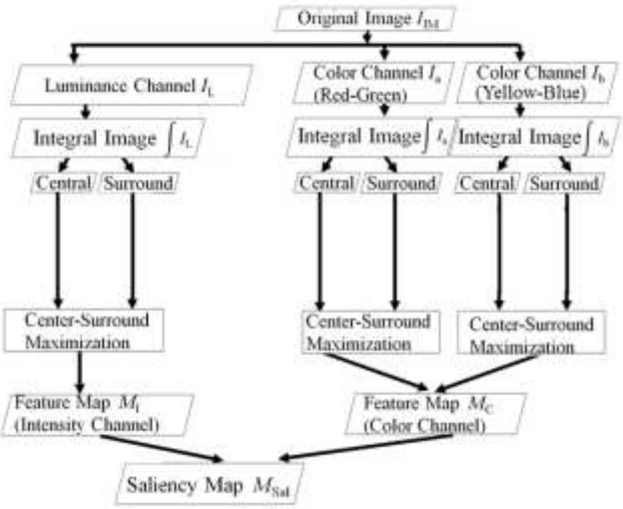

Fig. 2. Procedure of proposed saliency map generation method

3.2. *Procedure*

3.2.1. *The center and the surround*

I_{IM} is converted from RGB to CIELab System, then, decomposed into three components, that is, Luminance L, Color (Red-Green) a, (Yellow-Blue) b, to handle colors easily to compute Center-Surround Difference in the Color Channel. The contrasts of a, b are the same as the Color Channel in Itti's method[1]. Integral Image L_{INT} is generated, then, region p (W_{pmax} x H_{pmax} [pixel]) is prepared. Two box filters F_{Bc}(for the Center), F_{Bs}(for the Surround) whose centers are common to p (center $\boldsymbol{p}_p$) are prepared (Fig. 3). The size of F_S is optimized within p so as to maximize Center-Surround Difference at $\boldsymbol{p}_p$. Integral Image was adopted for the face recognition method proposed by Viola[8] to speed up the calculation of Haar-Like feature. S. Frintrop also adopted Integral Image for fast calculation to obtain the Center and the Surround[9]. Smoothing by convolution requires large computational cost. The cost rises up proportionally to the square of filter width. For this reason, we utilize the combination of Integral Image and box filter for smoothing. Integral Image is obtained by Eq.(1).

$$I_{INT,i'}(x,y) = \sum_{y'=0}^{y'=y} \sum_{x'=0}^{x'=x} I_{Ret,i'}(x',y') \qquad (1)$$

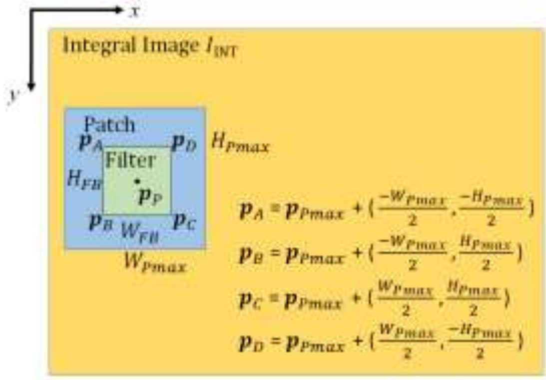

Fig. 3. Smoothing with Integral Image and Box Filter

Pixel value at (x, y) in a smoothed image is denoted as Eq.(2) shows.

$$I_{Blr,i'}(x,y) = \frac{I_{INT,i'}(\boldsymbol{p}_C) - I_{INT,i'}(\boldsymbol{p}_D) - I_{INT,i'}(\boldsymbol{p}_B) + I_{INT,i'}(\boldsymbol{p}_A)}{W_F H_F} \qquad (2)$$

$$i' \in \{L, a, b\}$$

With the help by Integral Image, only five arithmetic operations are required to obtain a pixel value of a smoothed image.

3.2.2. *Maximization of center-surround difference*

We state the process of Center-Surround Maximization in the section. The filter sizes are W_{Bc} xH_{Bc}, W_{Bs} xH_{Bs}, respectively. The matrice are shown in Eq. (3), (4). We show matrix fully one as ${}^{W_{Bc}\,x H_{Bc},}[1]$ etc.

$$F_{Bc} = \frac{1}{W_{Bc} H_{Bc}} * {}^{W_{Bc} \times H_{Bc}}[1] \qquad (3)$$

$$F_{Bc} = \frac{1}{W_{Bs} H_{Bs}} * {}^{W_{Bs} \times H_{Bs}}[1] \qquad (4)$$

The two Box Filters are centered with $\boldsymbol{p}_p = (x, y)$, and F_{Bs} is magnified up to W_{Pmax} xH_{Pmax} at maximum. The size is changed depending on the spectrum at region P. For the reason, F_S is altered to F_S ($\boldsymbol{p}_p$) and expressed in Eq. (5)-(7). Thus, we select W_{Bs} so that Center-Surround Difference is maximized at each $\boldsymbol{p}_p$. The maximization is plotted to feature map $M_I(\boldsymbol{p}_p)$, $M_{Ca}(\boldsymbol{p}_p)$, $M_{Cb}(\boldsymbol{p}_p)$ at each $\boldsymbol{p}_p$.

$$M_I(\boldsymbol{p}_p) = \max_{W_s(\boldsymbol{p}_p)} \left| I_L(F_s, \boldsymbol{p}_p) \ominus I_L(F_s(\boldsymbol{p}_p), \boldsymbol{p}_p) \right| \quad (5)$$

$$M_{Ca}(\boldsymbol{p}_p) = \max_{W_s(\boldsymbol{p}_p)} \left| I_a(F_s, \boldsymbol{p}_p) \ominus I_a(F_s(\boldsymbol{p}_p), \boldsymbol{p}_p) \right| \quad (6)$$

$$M_{Cb}(\boldsymbol{p}_p) = \max_{W_s(\boldsymbol{p}_p)} \left| I_b(F_s, \boldsymbol{p}_p) \ominus I_b(F_s(\boldsymbol{p}_p), \boldsymbol{p}_p) \right| \quad (7)$$

3.2.3. *Merging feature maps*

$M_{Ca}(\boldsymbol{p}_p)$, $M_{Cb}(\boldsymbol{p}_p)$ are merged to $M_C(\boldsymbol{p}_p)$ as shown in Eq.(8).

$$M_C(\boldsymbol{p}_p) = \frac{1}{2}\left(M_{Ca}(\boldsymbol{p}_p) + M_{Cb}(\boldsymbol{p}_p)\right) \quad (8)$$

Only for the generation of saliency map M_{Sal}, M_I and M_C are normalized in order to prevent extra extension of luminance amplitude when each of $M_{Ca}(\boldsymbol{p}_p)$, $M_{Cb}(\boldsymbol{p}_p)$ is extremely narrower to the other in amplitude.

$$M_{Sal}(\boldsymbol{p}_p) = \frac{1}{2}\left(f_{Norm}(M_I(\boldsymbol{p}_p)) + f_{Norm}(M_C(\boldsymbol{p}_p))\right) \quad (9)$$

We just magnify the amplitude of the feature map to 255(unsigned 8bit) to simplify the calculation. The normalization is denoted with f_{Norm}

4. Experiment

In the experiment, as described in Fig. 4, we evaluated the effect to saliency map as saliency variation $|\Delta M_{Sal}|$ (in image) and $||\Delta M_{Sal}||$ (in scalar) caused by changing object size W_{obj} x H_{obj} ($W_{obj} = H_{obj}$), respective Itti's method[1], VOCUS2[6], and proposed method.

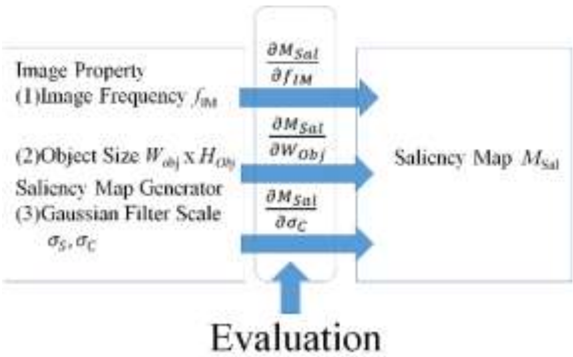

Fig. 4 Influences for M_{Sal}

In the event of changing W_{Obj}, we cropped the area in M_{Sal}, where object (Lenna image) was located, and, magnified the cropped saliency map to original size. Thus, we evaluated $||\Delta M_{Sal}||$, respecting conventional and proposed saliency map by varying W_{Obj} and changing the ratio of σ_C/σ_S for each Gaussian Filters in Twin Pyramid in VOCUS2[6]. Fig. 5 and Eq. (10)-(12) explain the procedure to obtain $|\Delta M_{Sal}|$ and $||\Delta M_{Sal}||$.

$$||\Delta M_{Sal}|| = \frac{\sum_{y=1}^{H_{IM}} \sum_{x=1}^{W_{IM}} |\Delta M_{sal}|(x,y)}{W_{IM} H_{IM}} \quad (10)$$

$$|\Delta M_{sal}| = \frac{\sum_{n=1}^{N-1} |\Delta M_{sal,n}|}{N-1} \quad (11)$$

$$|\Delta M_{sal,n}| = |M_{sal,n+1} - M_{sal,1}| \quad (12)$$

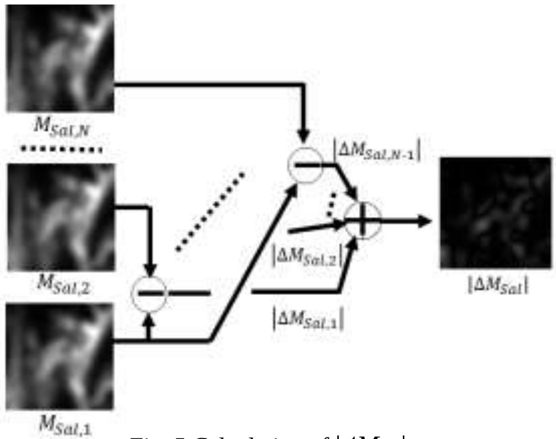

Fig. 5 Calculation of $|\Delta M_{Sal}|$

4.1. *Effect for saliency by resized object*

4.1.1. *Experimental condition*

Fig. 6 shows an example of changing object (=Lenna Image) size W_{Obj} x H_{Obj}[Pixel] ($W_{Obj} = H_{Obj}$) in the input image (size: W_{IM} x H_{IM}[Pixel]). The object size is changed equally R_s times in its height and width. R_s is calculated based on W_{IM} x H_{IM}[Pixel]. The object size is shown as Eq. (13)

$$W_{Obj} \times H_{Obj} = R_S W_{IM} \times R_S H_{IM} \quad (13)$$

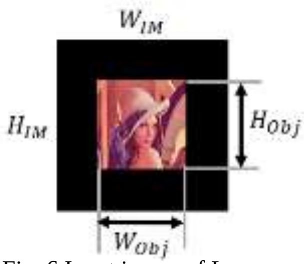

Fig. 6 Input image of Lenna

In this experiment, R_s is varied as following, $(R_S=R_{S,1}, R_{S,2}, R_{S,3}, R_{S,4}, R_{S,5}, R_{S,6})$=(1.00, 0.90, 0.80, 0.70, 0.60, 0.50), Number of the variation N_S is 6. We used the source code from[7] to use Itti's method.

4.1.2. *Results*

Table 1 shows the variation of M_{Sal}, that is, $\|\Delta M_{Sal}\|$. Proposed method marked the smallest $\|\Delta M_{Sal}\|$ than other

Table 1. Comparison of $\|\Delta M_{Sal}|$

Saliency Method	$\|\Delta M_{Sal}\|$
VOCUS2 (σ_c: σ_s)=(1:10)	50.00
VOCUS2 (σ_c: σ_s)=(3:10)	57.22
VOCUS2 (σ_c: σ_s)=(5:10)	63.81
Itti	44.91
Proposed $W_{PMax}=0.25W_{IM}$	**32.30**
Proposed $W_{PMax}=0.50W_{IM}$	**32.30**

conventional methods. The table indicates that M_{Sal} in our method is the steadiest against changing W_{Obj}. On the other hand, under VOCUS2, $\|\Delta M_{Sal}\|$ rose up as σ_s increased.

4.1.3. *Discussion*

The transition of $\|\Delta M_{Sal,n}\|$ is shown in Fig. 7. And the procedure to calculate $|\Delta M_{Sal}|$ (i.e. Difference image of M_{Sal}) is shown in Fig. 8, 9 and 10 under VOCUS2 (σc:σs =1:10), (σc:σs =5:10) , and proposed

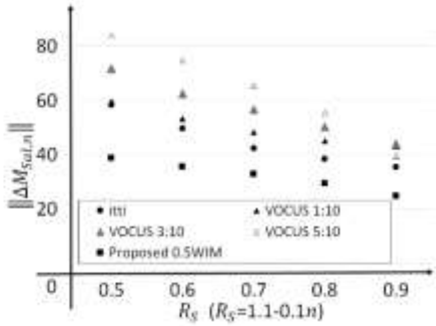

Fig. 7 Transition of $\|\Delta M_{Sal}\|$

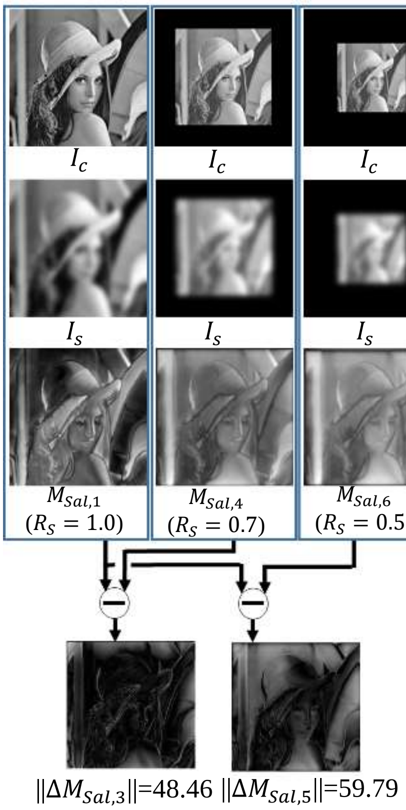

Fig. 8 Transition of $|\Delta M_{Sal,n}|$ (VOCUS2 1:10)

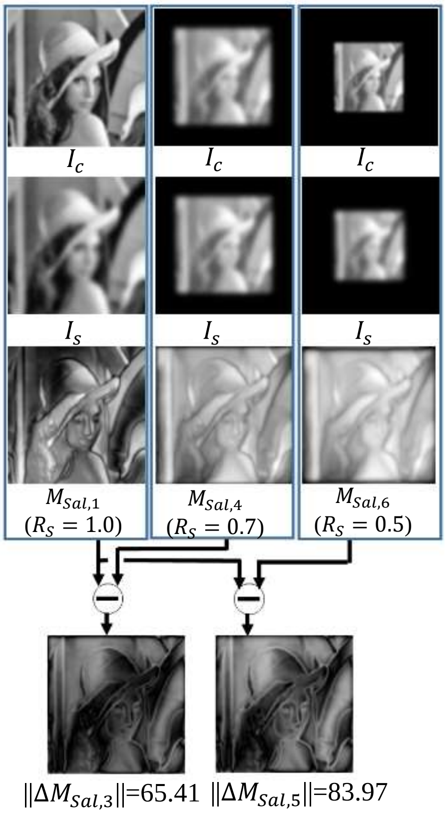

Fig. 9 Transition of $|\Delta M_{Sal,n}|$ (VOCUS2 5:10)

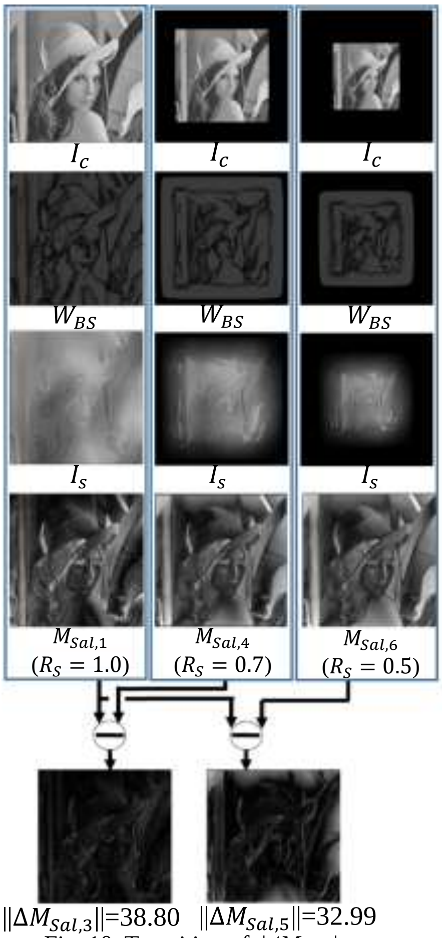

Fig. 10 Transition of $|\Delta M_{Sal,n}|$ (Proposed Method $W_{Pmax}=0.5W_{IM}$)

method respectively. I_c and I_s correspond to the image of the smallest filter scale in Gaussian Pyramid. According to the transition of $\|\Delta M_{Sal,n}\|$, commonly to all saliency maps, $\|\Delta M_{Sal,n}\|$ increased in the surrounding area of Lenna, as R_s becomes farer from 1.0, because, the luminance gradient became less steep as the Lenna image with black background is smoothed. In the case of R_s = 1.0, without background, the attenuation of the luminance does not occur near the border of Lenna. The difference of the attenuation is one of the reason for increasing $\|\Delta M_{Sal,n}\|$. As W_{Obj} becomes smaller, the area of the black background is larger. Thus, the luminance gradient becomes milder. That is why $\|\Delta M_{Sal,n}\|$ increases as R_s decreases. Next, we explain the cause of the difference in $\|\Delta M_{Sal}\|$ between in the case of increasing the ratio of σ_c under VOCUS2 method, and, applying proposed method. When σ_c:σ_s was set to 1:10, high-frequency spectrum remained more in Ic than under the condition of (σ_c:σ_s)=(5:10). When R_s decreased from 1.0 to 0.7, only high-frequency component was cut. On the other hand, when (σ_c:σ_s) was equal to (5:10), much more frequency component was cut in I_c. The effect was serious since R_s was set to 0.7. Downsizing an image corresponds to the increase of high-frequency component. However, the higher frequency was cut by larger σ_c of Gaussian Filter. Thus, M_{Sal} is affected by various ratio of σ_c in VOCUS2. While, when proposed method was applied, F_{Bs} was optimized so that the contrast between the Center and the Surround would be maximized. As Lenna was downsized and the background becomes larger, F_{Bs} was enlarged. For the reason, the surrounding area can be affected to lose intensity by the background. Particularly, the variation of $|\Delta M_{Sal}|$ was large when R_s was 0.5. The contrast is relatively small only considering on inside Lenna image, compared to the image with background. However, in proposed method, F_{Bs} was optimized also inside Lenna, so that the contrast between the Center and the Surround can be well enhanced by the maximization of the Center-Surround Difference. This phenomenon is opposite to the situation that larger σ_c of Gaussian Filter is cutting high-frequency component in Lenna. The maximum difference between the Center and the Surround is reflected to M_{Sal}. Thus, M_{Sal} is less affected by the combination of f_{IM} σ_c and σ_s.

5. Conclusion

We proposed to introduce smoothing filter optimization into saliency map creation, that is adaptive to various image frequency. In experiment, we compared the saliency variation under conventional and proposed methods. The maximization of the Center-Surround Difference was effective to suppress the variation. However, proposed method has the limitation to enlarge the Box Filter F_{Bs}. Our method is not completely free of the constraint by the filter size.

References

1. L. Itti, C. Koch, and E. Niebur, "A Model of Saliency-based Visual Attention for Rapid Scene Analysis", *IEEE TPAMI* 20(11)(1998), pp.1254-1259.
2. M. Cheng, N. J. Mitra, X. Huang, P. H. S. Torr, S. Hu, "Global Contrast based Salient Region Detection", *IEEE TPAMI* 37(3)(2015), pp.569-582.
3. G. Yildirim, S. Susstrunk, "FASA: Fast, Accurate, and Size-Aware Salient Object Detection", In *Proceedings of the 12th Asian Conference on Computer Vision*, (Singapore, 2014), pp. 515-528.
4. F. Perazzi, P. Krähenbühl, Y. Pritch, and A. Hornung, "Saliency Filters: Contrast Based Filtering for Salient Region Detection", In *IEEE Conference on Computer Vision and Pattern Recognition* (Providence, Rhode Islande, USA, 2012), pp. 733-740.
5. R. Achanta, S. Hemami, F. Estrada, and S. Seusstrunk, "Frequency-tuned Salient Region Detection". *the 2009 IEEE Computer Society Conference on Computer Vision and Pattern Recognition*, (Miami, Florida, USA, 2009), p.1597–1604.
6. S. Frintrop, T. Werner, and G. M. Garcia, "Traditional Saliency Reloaded: A Good Old Model in New Shape", *Proceedings of IEEE Conference on Computer Vision and Pattern Recognition*, (Boston, Massachusetts, USA, 2015) pp. 82-90.
7. Caltech HP, Introduction of Software"Simpsal" http://www.vision.caltech.edu/~harel/share/gbvs.php
8. P. Viola, M. Jones, "Rapid Object Detecton Using a Boosted Cascade of Simple Features", Proc. *IEEE Computer Society Conference on Computer Vision and Pattern Recognition*, (Kauai, Hawaii, USA, 2001), pp. 511-518.
9. S. Frintrop, M. Klodt, and E. Rome, "A Real-time Visual Attention System Using Integral Images. ", *In International Conference on Computer Vision Systems*(Bielefeld, Germeny, 2007).

Evaluation of Multi-Drone Wireless Network Properties for Tunnel Inspection

Raji Alahmad
Department of Human Intelligence System, Graduate School of Life Science and Systems Engineering,
Kyushu Institute of Technology,
2-4 Hibikino, Wakamatsu-ku, Kitakyushu, 808-0196, Japan

Kazuo Ishii
Department of Human Intelligence System, Graduate School of Life Science and Systems Engineering,
Kyushu Institute of Technology,
2-4 Hibikino, Wakamatsu-ku, Kitakyushu, 808-0196, Japan
E-mail: alahmad.raji941@mail.kyutech.com , ishii@brain.kyutech.ac.jp
www.lsse.kyutech.ac.jp

Abstract

Communication is one of the challenges for UAVs during operations inside tunnels. In this paper, a wireless network system using multiple drones functioning as repeaters is proposed. A number of measurements for Wi-Fi signals are conducted to confirm the effect of different scenarios on the signal in virtual tunnel and real life tunnel. As a result, RSS with -64 dBm can provide five Mbps of bandwidth.

Keywords: Tunnel inspection, wireless network, multi-drones.

1. Introduction

Since all infrastructures are gradually damaged by time, environment, and human factors that cause deterioration in the underpinnings, the need for inspection and maintenance is very important. Humidity, dust, and reduced visibility are the main defects that operators face in such areas. In addition, the collapses, accidents, and natural disasters arose the exigency of sending robots for performing the inspection tasks. Conventional methods depend on special ground vehicles that have many limitations in mobility see Refs.1,2. Unmanned aerial vehicles (UAVs) on the other hand, can overcome these limitations due to their small size and high maneuverability.[3]

Communication is of the challenges for UAVs, due to signal attenuation, which is a result of many factors such as distance, free-space loss, absorption, reflection and interference. Furthermore, the waveguide effect plays an important role in influencing the signal propagation due to receiving different number of reflected rays of signal that cause multipath propagation which lead to interference phenomenon.[4]

There are many documented studies about communication in subways and tunnels see Refs.5-11. However, none of the previous researches and methods have tackled the problem of communicating with the robots for long distances inside the tunnels.

In this paper, a number of measurements for Wi-Fi signals are conducted to confirm the effect of different scenarios on the signal.

2. Concept of multi-drone network

We propose providing a communication link to create a dynamic wireless network using multiple drones. The basic idea is to distribute a number of supporting drones equipped with signal transmitters and receivers, which will act as repeaters. Each drone will receive the transmitted signals and retransmit it with more power. As a result, we can transmit and receive the signals between the base station (at the gate of the tunnel) and the main drone, which is supposed to perform the main task. The network topology is illustrated in the figure 1.

The procedure of building a dynamic network can be described as follows:

(i) Start with sending the group of all drones together inside the tunnel.

(ii) When the drones face a weak received signal strength (RSS) from the base station, one of the supporting drones (repeaters) will stop and the others will continue. In a similar manner, the second supporting drone will stop when the signal, repeated by the first repeater, is recognized as weak, and so on.

3. Experiments and Results

In order to find out the characteristics of wireless signals in the tunnel, a number of measurements for Wi-Fi signals is conducted with several scenarios.

3.1. Experimental setup

In nonrealistic tunnel with square shape and dimensions as illustrated in the figure 2. five different scenarios are implemented to find out their effect on the RSS.

Aterm WG 1800 HP2 is used as a transmitter, with Built-in antenna (transmission 3×reception 3), and frequency band is 2.4 GHz. For receiving terminal, Raspberry Pi 3 model B is used with built-in antenna.

More details for experimental setup are illustrated in table 1.

3.1.1. Straight case

We measured RSS versus the distance in the case of straight tunnel. At each meter we calculate the averages of measured signal strength for 65 points as shown in the figure 3. We can see that as distance increases, RSS decreases, which is the result of the factors that have been mentioned above affecting signal propagation and causing signal attenuation.

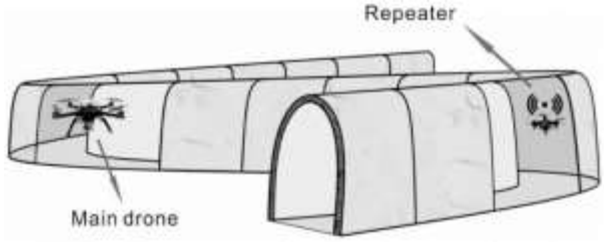

Fig. 1. Wireless Network topology using multiple drones.

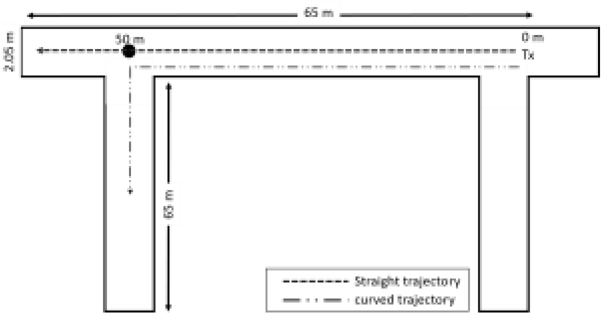

Fig. 2. Nonrealistic Tunnel shape and dimensions.

Table 1. Experimental setup in Virtual Tunnel

Parameter	Equipment / Value
Tunnel length	65 meter
Tunnel width	2.05 meter
Tunnel Height	2.78 meter
Transmitter	Aterm WG 1800 HP2
Receiver	Raspberry PI 3 model B - AWUS036h
Rx speed	0.3 - 1.93 m/sec
Sampling freq.	450 -750 - 1073 sample/pint
Frequency	2.4 GHz
Tx altitude	0.2 – 1 meter
Rx altitude	0.2 – 1 – 2 meter
Sampling freq. of BW	60 sample/point

3.1.2. With 90 degree of curvature

In order to check out the effect of curvature on the signal, at the distance of 50 meter, we turned by 90 degrees and continue measuring the average of signal strength. Figure 3 illustrates RSS before and after 90 degree of curvature. As clearly shown in the figure, the RSS curve slopes rapidly and the signal is lost after 15 meters. Which can see the big impact of curvature on the signal strength.

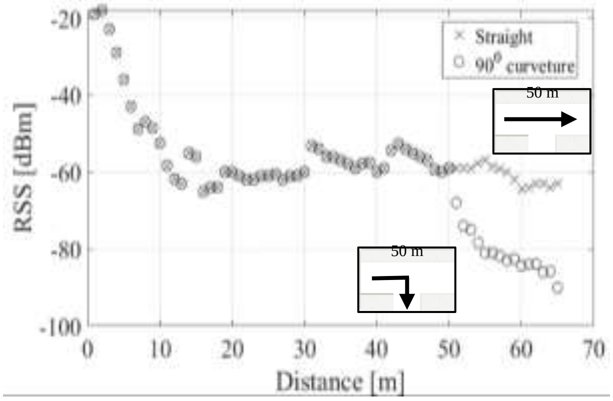

Fig. 3. RSS VS Distance in case of straight and 90° of curvature.

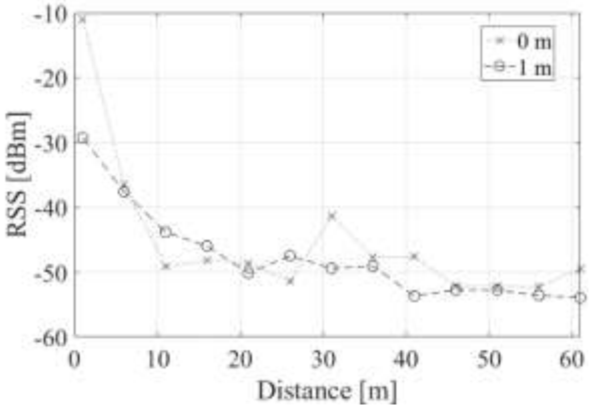

Fig. 4. RSS VS Distance with Tx-Rx altitude difference.

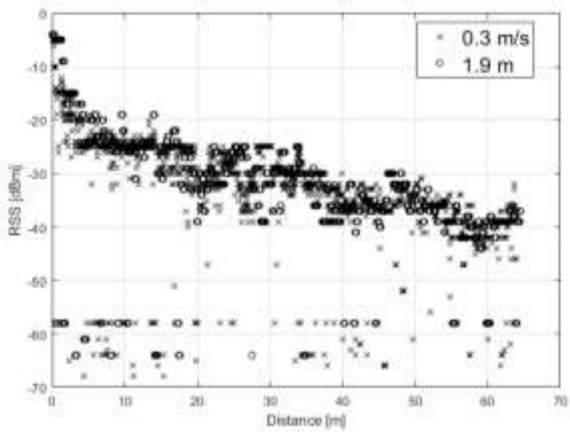

Fig. 5. RSS VS Distance with two different speeds of receiver.

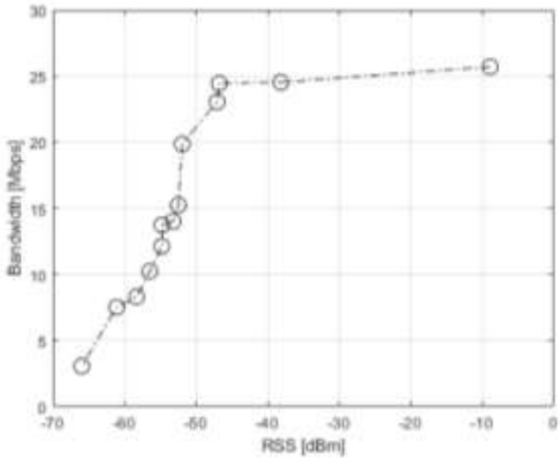

Fig. 6. Bandwidth VS RSS.

3.1.3. Tx-Rx altitude difference

Figure 4 shows RSS versus distance while changing the altitude between the transmitter Tx and the receiver Rx, and measuring the signal strength at each 15 meter and then calculate the average of RSS, the figure shows that Tx-Rx altitude difference has a very small effect on RSS.

3.1.4. Different speed of receiver

To confirm the moving speed effect of Rx on RSS, two different speeds, 0.3 m/s and 1.9 m/s, are implemented using Alfa AWUS036h Wi-Fi adapter. Figure 5 shows RSS versus the distance for different Rx speeds. We can see that Rx speed has almost no effect on the RSS.

3.1.5. Bandwidth VS RSS

Iperf tool is used to see the relationship between bandwidth BW and RSS. This tool sends and receives packets between the server and the client to measure the bandwidth. As it is illustrated in Figure 6, as RSS decreases, BW also decreases. In addition, the point with -64dBm can provide 5Mbps, which is recommended for HD video streaming.

4. Discussion

Based on the experiments results with several scenarios, we could make the following discussion:

- Signal strength: Distance and waveguide effect are the important factors effect on the signals. The drops and increasing of RSS curve accrues due to receive different number of reflected rays of transmitted signal.
- Curvature: the curvature has a big effect on the signal strength since it blocks the main transmitted ray, and then the reflected rays from the tunnel's walls will be dominant.
- Rx speed: different speeds of receiving terminal does not change the RSS. The different could be happened depending on the receiver sensitivity.
- Different altitude of Rx: we found that different height of receiver with constant height of transmitter causes a relatively small difference in received signal strength due to the propagation models.
- Bandwidth: With the experiment conditions and equipment, we found the point with -64 dBm of signal strength met 5 Mbps. However, using different equipment and different environments the signal strength that can provide HD video streaming might be different.

5. Conclusion

In this paper, we proposed a dynamic wireless network system using multiple drones in order to communicate with the drone inside a tunnel during an inspection task. We discussed the effects of speed, altitude, and curvature on the received signal strength. The results show that for our specific communication equipment in a nonrealistic tunnel, placing a repeater at the point where signal strength is -64dBm allows a longer distance communication.

References

1. Lee, S. Y., Lee, S. H., Shin, D. I., Son, Y. K., & Han, C. S. (2007). "Development of an inspection system for cracks in a concrete tunnel lining." *CAN. J. CIVIL. ENG.* 34.8 (2007): 966-975.
2. Minichan, R., Fogle, R., & Marzolf, A. "H-Canyon Air Exhaust Tunnel Inspection Vehicle Development." (No. SRNL-STI-2011-00078). *SRS*. 2011.
3. Mitchell, J., & Marshall, J. A.. "*Design of a Novel Auto-Rotating UAV Platform for Underground Mine Cavity Surveying.* " (2017).
4. Goldsmith, Andrea. "Wireless communications. " Cambridge university press, 2005.
5. Guan, K., Ai, B., Zhong, Z., López, C. F., Zhang, L., Briso-Rodríguez, C., ... & Tang, T. "Measurements and analysis of large-scale fading characteristics in curved subway tunnels at 920 MHz, 2400 MHz, and 5705 MHz." *IEEE Trans. Intell. Transp. Syst*. 16.5 (2015): *2393-2405*.
6. Val, I., Arriola, A., Rodriguez, P. M., Gonzalez-Plaza, A., Alonso, D., Zhang, L., ... & Goikoetxea, J. "Wireless channel measurements and modeling for TCMS communications in metro environments." *Antennas and Propagation (EUCAP), 2017 11th European Conference on. IEEE, 2017.*
7. Jinxing, L., Youping, Z., Jing, Z., Rui, J., Cheng, T., & Zhenhui, T. "Radio channel measurements and analysis at 2.4/5GHz in subway tunnels." *China Commun*. 12.1 (2015): 36-45.
8. Guan, K., Zhong, Z., Alonso, J. I., & Briso-Rodríguez, C. "Measurement of distributed antenna systems at 2.4 GHz in a realistic subway tunnel environment. " *IEEE Trans. Veh. Technol.* 61(2), 834-837.
9. El-Maghrabi, H. M., Attiya, A. M., & Hashish, E. A. "Indoor Wave Propagation Prediction for Corridors Segments with Partially Reflecting Walls by Using 3D Waveguide Modal Analysis." *Appl Comput Electromagn Soc J*, 31(3). (2016).
10. Hrovat, A., Kandus, G., & Javornik, T. "A survey of radio propagation modeling for tunnels." *IEEE Commun. Surveys Tut.* 16(2), 658-669. (2014).
11. Nurminen, H., Dashti, M., & Piché, R. "A survey on wireless transmitter localization using signal strength measurements." *WIREL COMMUN MOB COM*, 2017. (2017).

Counting Crops under Cultivation using Drone

Yasunori Takemura
Department of Engineering, Nishinippon Institute of Technology, 1-11 Aratsu, Kanda Miyako-gun, Fukuoka, 800-0394, Japan

Yusuke Hirata
Graduate School of Life Science and System Engineering, Kyushu Institute of Technology, 2-4 Hibikino, Wakamatsu Kitakyushu, Fukuoka, 808-0196, Japan

Eiji Mizoe
Sky Canvas Co. Ltd. , 3B 3F, 1-9-10, Sakaimachi, Kokurakita-ku Kitakyushu, Fukuoka802-0005, Japan

Masao Tashiro
Project Skyeye LLC. , 2243-55 Kamishinyu Nogata, Fukuoka 822-0033, Japan

Yousuke Nagai
Aruku Agriculture LLC, 415-1, Oaza Hirosue, Chikujo-machi Chikujo-gun, Fukuoka, 829-0100, Japan
E-mail:takemura@nishitech.ac.jp, hirata-yusuke@edu.brain.kyutech.ac.jp, m.1978.eiji@ked.biglobe.ne.jp, contact@arknougyou.com

Abstract

In recent years, agricultural workers in Japan are decreasing year by year. Also, rising the average age of agricultural workers is a problem in Japan. As a solution to this problem, there is promotion of new agriculture (smart agriculture) that realizes super-energy saving and high quality production by utilizing robot technology and IoT technology. The authors are promoting technology by operating forest drone competition and tomato harvesting robot competition. Through robot competition, we are currently paying attention to the use of drone in the agricultural field.

In this research, we aim to automatic detect the number of agricultural crops by image processing from image data of aerial photographs taken by drone. In this paper, we will report a method to discriminate agricultural crops by color and to detect the number.

Keywords: Field Robotics, Sensing System, Agriculture robot, Drone, Image processing

1. Introduction

In recent years, agricultural workers in Japan are decreasing year by year (Fig.1) [1]. Also, rising the average age of agricultural workers is a problem in Japan. As shown Fig.1, agricultural workers are declining, the elderly population aged 65 and older is flat. It is expected that this trend will continue in future, and problems in agriculture are labor shortage and reduction in production efficiency.

The actual condition of the agricultural field is severe. A lot of works are relied on manually. Although the

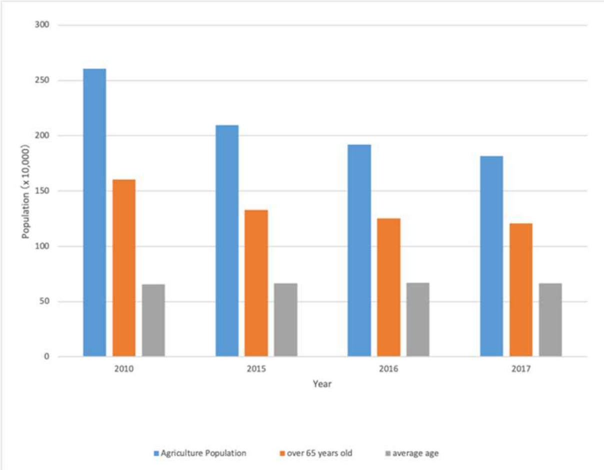

Fig.1 Population of the agriculture in japan

mechanization of agriculture is depending on item, horticultural crops such as vegetables and fruit trees rely on manual works such as harvesting and management.

In this situation, securing new workers is very important. However, current agriculture requires a lot of hard work that depends on hands, takes time to acquire skills, and many farming techniques are difficult to manualize. Normally in a crop, a worker can only experience all the work one a year. It takes a long time for new workers to acquire known-how like experienced workers [2].

As a solution to this problem, there is promotion of new agriculture (smart agriculture) that realizes super-energy saving and high quality production by utilizing robot technology and IoT technology [3,4,5]. The authors are promoting technology by operating forest drone competition and tomato harvesting robot competition [6]. Through robot competition, we are currently paying attention to the use of drone in the agricultural field.

In this research, we aim to automatic detect the number of agricultural crops by image processing from image data of aerial photographs taken by drone. In this paper, we will report a method to discriminate agricultural crops by color and to detect the number.

2. Field Survey and Previous Research in Agriculture

The author conducted a survey on issues and work on agricultural sites at a farmer who is a coauthor in working in Aruku agriculture service.

When surveying, one of the biggest problems is income instability. Because, regular farmers do not count the number of settled plants after planting crops. The reason is that counting the number of crops manually is too time consuming and laborious. For that reason, it is very difficult for farmers to make a profit plan. Farmers usually ship to wholesalers after harvesting. However, wholesalers do not buy everything they harvested. Therefore, we usually discard the remaining crops.

Also, the price of the crop changes according to the harvest time of the crop. How much crops can be harvested at any time is one of the important factors in planning income and expenditure. Knowing the number of settled crops makes it easier to predict the number of harvests and make it easier for business planning. When it is possible to plan a processing plan assuming the number of agricultural crops considered to be unsold, loss due to disposal will decrease, it is thought that this will lead to improvement of production efficiency and stabilization of management.

As an example of previous research in agriculture, there is a study that explores the possibility of some trait evaluation by processing the image of the field from the drone aerial image [7]. In this research, he used a drone equipped with a camera with eight rotating blades with a size of 100 [cm] x 100 [cm] x 30 [cm] and a mass of 1.6 [kg]. Drone flying automatically with a pre-programmed flight path of 4 hectares of field. In this research, photographs of the whole field are created by synthesizing about 60 images taken from 100 m above the sky. Growth data such as sprouting timing, initial growth rate, and dead time can be obtained from this growth amount, which measures the growth amount of the crop from the time series image taken regularly by the same flight route. In this way, Drone's aerial image is said to be suitable for data collection by regular photography because it has high definition and low operation cost.

In this hearing survey and previous research, we thought that we could shoot color images taken of agricultural crops using drone to count the number of planted crops. We also thought that we can grasp the number of settled plants and the growth situation of crops from the area of crops extracted by image processing.

3. Algorithm of counting crops

Figure 2 shows the algorithm for counting crops using image processing. First, the drone flies the field automatically and takes pictures of the crop. At this time, the drone moves along the ridge if keeping a certain altitude. The photograph is taken offline into a personal computer and processed as image data.

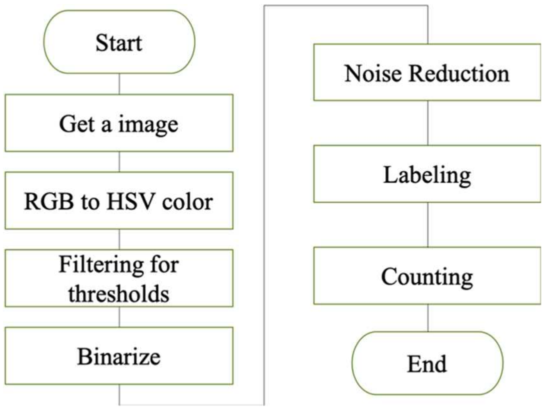

Fig.2 Algorithm for image processing

Because the read data is RGB image, it converts to HSV hue system. Because, this time, identification of crops is done with emphasis on hue data. Next, binary conversion is performed by determining the threshold value by hue. Filter the binarized image to identify the size of the crop. In the filter, filling up the hole is done to grasp the area of the object to be crop, before removing the noise. Some noise or crops or unknown things remain in the binary image detected as crop even if noise removal processing is done. Therefore, in order to make the number of crops accurate, labeling is performed on candidate images and a histogram is created with area.

Figure 3 shows the histogram example of result. The horizontal axis is the object area (number of pixels) and the vertical axis is the number of objects (pieces) Note that the number of classes in the histogram is the Sturges' formula. Sturges' formula [8] is expressed by the following equation. N is the sample size, and k is the number of classes.

$$k = log_2 N + 1$$

The formulas determine the appropriate number of classes in the histogram. As can be seen from Figure 3, the first class has concentrated areas that are not crops in the field, so treat the class width as a threshold and treat it as noise. Figures 4 shows the processed images of image processing. Figure 4 (a) shows the raw image of picture. (b) shows after the binarize of image. (c) shows after the filtering process, and (d) shows the end of image processing.

4. Experiment of counting crops of Lettuce field

This experiment was conducted to examine the validity of the program to calculate the number of plantings from images of agricultural crops taken with drone. In the experiment, the accuracy of the program is evaluated by obtaining the relative error between the number (true value) from the actual image and the number calculated from the program.

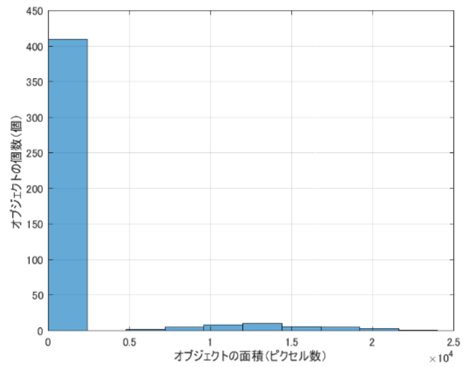

Fig. 3 histogram of image processing binarized object

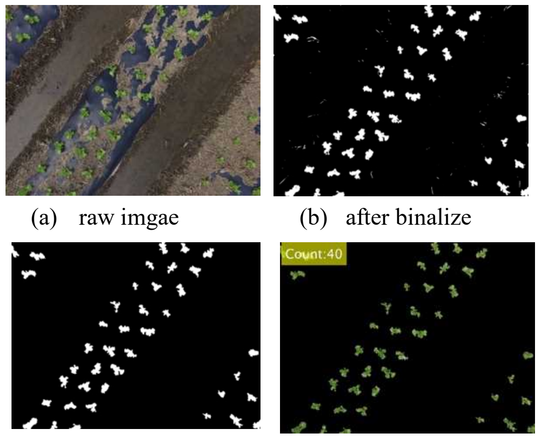

(a) raw imgae (b) after binalize

(c) after noise reduction (d) counting result

Fig.4 Image processing process

Fig.5 DJI Drone and experimental view

4.1. *Usede equipment*

For this experiment, "Phantom 3 Advance" which is a drone of DJI company was used (Fig.5). The specifications of the camera mounted on Phantom 3 can

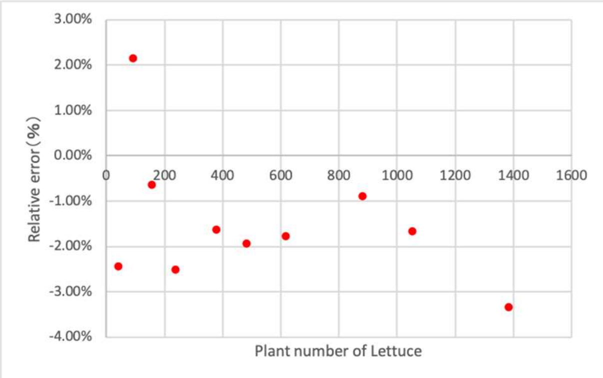

Fig.6 Experimental result

be taken with a maximum still image of 4000 x 3000 [pixcel].

4.2. *Experiment method and result*

Experiments were conducted by changing the altitude at a fixed point. By changing the altitude of the drones the range of shooting widens and the shooting ability changes. At that time, we conducted an experiment to verify to what extent the height can be measured to see if it is appropriate. Height was changed 5 m at a time and shooting was performed from 5 [m] to 50 [m]. In the experiment, 41 lettuces could be taken for shooting at 5 [m], and 1384 lettuces could be taken when shooting at 50 [m].

Figure 6 shows the experimental results. Changing the height, errors increased as the number of settled lettuce increased. However, the relative error was within 4% at the most. When the height is high, the relative error tends to be in the minus direction. Changing the height makes crops smaller. Therefore, it is difficult to discriminate from noise.

At about 50 [m], it was found that the relative error was not greatly affected. In addition, it was found that a minus error of several percent is generated than the actual planting number. In the future, we need to make improvements to distinguish it from weeds as a measure. In the situation where photography was actually done, there were no weeds in the ridge, and there were many weeds on the sidewalk. Therefore, we believe that improvement of accuracy can be expected by adding improvements such as finding ridges.

5. Summary

In this research, we aim to automatic detect the number of agricultural crops by image processing from image data of aerial photographs taken by drone.

As a result of the experiment, it was found that the number of settled plants can be calculated from the program with an error of a few percent. However, some algorithms such as removal of weeds and others by noise elimination algorithms remove some crops from the image. Therefore, as a future works, we need to improve the algorithm for improvement of accuracy. For example, we try to find ridges and weeds.

Acknowledgements

This works is supported by COC (Center of Community) Project in Nishinippon Institute of Technology and Sky Canvas Co. Ltd., Aruku Agriculture LLC., and Project Skyeye LLC.

References

1. Homepage in Ministry of Agriculture, Forestry and Fisheries, "Statistics of Agricultural Workers", in Japanese, "http://www.maff.go.jp/j/tokei/sihyo/data/08.html"
2. Sumito Yasuoka, "Promotion of "Smart Agriculture"", *Journal of Robot Society Japan*, Vol35, No.5, pp.2-5, 2017, in Japanese
3. JETRO Homepage, "Market Report: Smart agriculture", https://www.jetro.go.jp/ext_images/en/invest/attract/pdf/mr_smartagri_en.pdf", 2017
4. E.Morimoto, K.Hayashi, "Design of Smart Agriculture Japan Model", *Advances in Animal Biosciences*, Vol.8, Special Issue 2), pp.713-717, 2017
5. T.Fujinaga, S.Yasukawa, B.Li and K.Ishii, "Image Mosaicing Using Multi-Modal Images for Generation of Tomato Growth State Map", *Journal of Robotics and Mechatronics*, Vol.30, No.2, 2018, pp187-197
6. K.Ishii, Y.Takemura, T.Matsuo and T.Sonoda, "Tomato Harvesting Robot Competition", pp.537-542, *SCIS-ISIS*, 2016, Hokaido
7. Ryo Sugiura, "High-Throughput Field Phenotyping Using Aerial Imagery from Drone", *Journal of Robotics Society Japan* (JRSJ), Vol.35, No.5, pp.369-371, 2017
8. H.Sturges, "The choice of a class-interval", *Journal of American Statistical Assoc.*, Vol.21, pp.65-66, 1926

Soil Compaction and Rolling Resistance Evaluation of a Locomotion System with an Adjustable Contact Patch for a Grape Transporting Robot

Enrico di Maria
Department of Human Intelligence System, Graduate School of Life Science and Systems Engineering,
Kyushu Institute of Technology,
2-4 Hibikino, Wakamatsu-ku, Kitakyushu, 808-0196, Japan

Kazuo Ishii
Department of Human Intelligence System, Graduate School of Life Science and Systems Engineering,
Kyushu Institute of Technology,
2-4 Hibikino, Wakamatsu-ku, Kitakyushu, 808-0196, Japan
E-mail: e.dimaria.srt@gmail.com , ishii@brain.kyutech.ac.jp
www.lsse.kyutech.ac.jp

Abstract

Soil compaction is a form of soil degradation which causes soil erosion, drainage difficulties, and loss of nutrients. To mitigate this issue, in agricultural farms several methods have been adopted. In this paper the preliminary study of a locomotion system with adjustable contact patches is proposed. Aim is to reduce the compaction and optimize the rolling resistance of a grape transporting robot employed in vineyard. A Finite Element Method model supported by experimental results is developed to study the system.

Keywords: Soil Compaction, Rolling Resistance, Finite Element Method, Cone Penetrometer.

1. Introduction

Soil compaction of agricultural soil is a result of the increase in mechanization and the usage of heavy vehicles exerting high forces onto the soil. As a porous material, soil consists of a solid part which includes pores containing air or water. Excessive compression causes the reduction of pore space and the loss of air and water, important for plants roots growth, and determines infiltration difficulties, loss of nutrients and soil erosion. Soil compaction resulted to be related to a significant reduction in the yield, and it was estimated a crop yielding reduction of 25-50% in some districts of Europe and North America, [1]. To solve these issues many methods have been proposed, with different results and different costs, [2]. The problem can be addressed by direct interventions, such as subsoiling and plough, or by avoiding compaction using low ground pressure tyres, tracked tractors or controlled traffic farming (CTF). Avoiding the compaction resulted to be the best solution in terms of cost benefits. With CTF, not only compaction itself is avoided, but energy consumption is reduced because of the lower rolling resistance of vehicles on permanent traffic lane, [2]. Different levels of mechanization can be adopted in the farms, and soil compaction is often neglected.

Target of this work are the canopied vineyards, in which the trees form a roof and the small and closed environment makes more difficult a full mechanization. Here harvester machines are rarely employed, unlike the espalier vineyards where big harvester machines are widely used. Usual tractors don't improve the harvesting

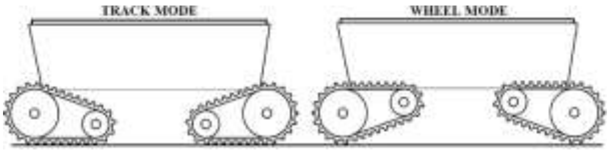

Fig. 1. System configurations in track and wheel mode.

process, but yet they cause a huge compaction.

The system proposed here consists of an autonomous kart aimed to optimize the rolling resistance while avoiding the compaction. It consists of four small track modules which can be partially lifted so as to reduce their contact patch and act as a wheel, depending on the soil conditions and vehicle payload, Fig. 1. Tracks are more suited for soft or wet soils, while wheels show better performance on hard soils.

In this paper the system is studied in terms of rolling resistance (RR) and compaction, evaluated by empirical equations and a Finite Element Method model (FEM). FEM simulations have been widely employed for RR evaluation on soft and hard soils, [3]. Experiments in the field are carried out to find some of the soil parameters.

The empirical equations for RR evaluation, derived from Terramechanics, are considered in the second section. In the third section the experiments carried out in the field are explained. These results, together with a non-linear regression equation, are used in section 4 for evaluating soil Young moduli and modelling the soil. Finally, in section 5, static simulations to determine the soil deformation and stress are carried out and explained.

2. Rolling resistance on soft soils

Rolling resistance on soft terrains can be seen as the work done in compacting the soil and making a rut of area *A* and depth *z*,[4], as in Eq. (1):

$$Rl = bl\int_0^{z_0} pdz. \qquad (1)$$

Where *z* is the depth, *p* the pressure, *b* the contact patch width, *l* the contact patch length of the track and R the rolling resistance. In case of wheel, the length considered is the distance traveled by one revolution. The pressure-sinkage relation proposed by Bekker requires a series of empirical parameters, such as: the cohesion modulus k_c, the frictional modulus k_ϕ and the exponent of sinkage *n*. These parameters are determined by means of the Bevameter test, [4]. Because the equipment required is big and the interpretation of the results is not trivial, often the usage of the Cone Penetrometer (CP) is preferred to estimate the rolling resistance and performance of off road vehicles,[5]. CP is a portable device to measure the strength of the soil. It consists of a circular cone at the end of a metal stick and a load cell for measuring the force required to push the cone into the ground. The parameter obtained is the Cone Index (CI) [kPa]. Based on the CI the following empirical equations for estimating the RR on soft terrains have been proposed for track vehicles, [6]:

$$C_n = \frac{CI \times b \times l}{W},\ \ R = W\left(\frac{0{,}45}{C_n} + 0{,}045\right). \qquad (2)$$

And for wheel vehicles,[7]:

$$C_n = \frac{CI \times b \times D}{W},\ \ R = W\left(\frac{1{,}2}{C_n} + 0{,}04\right). \qquad (3)$$

Where C_n is the track numeric, *b* and *l* the contact patch width and length respectively, *D* the wheel diameter, W the weight supported from each wheel or track, and *R* the rolling resistance. As a first tentative choice for the design, the product HS-200 developed by Shangai Puyi Industrial Co. is considered. Main dimensions and load bearing are shown in Table 1:

Table 1. HS-200 Track module

Ground contact length	400 mm
Width	200 mm
Outer sprocket diameter	370 mm
Load bearing	100 kg

Considering this track module and a vehicle weight of 400 kg, for a CI between 500 kPa and 7000 kPa the comparison in terms of RR between track mode and wheel mode is shown in Fig. 2.

As expected, on soft soil tracks outperform wheels, while on stiff soil wheels have better performance.

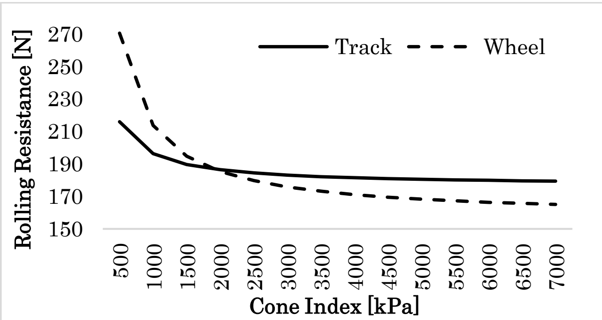

Fig. 2. Rolling resistance comparison between wheel mode and track mode for different soil strength.

The difference between the two modes depends on track module sizes and vehicle weight, and in the design a set of best parameters has to be decided in order to maximize this difference.

3. Experiments in the vineyard

Soil strength measurements have been carried out in a vineyard in the South of Italy, at Latiano in Puglia region. Hand-held digital cone penetrometer SC900 developed by Spectrum Technologies was employed. It allows to investigate the soil until a depth of 45 cm and a CI of 7000 kPa. Moisture sensor VG Meter 200 has been used for measuring the volumetric water content percentage. Moisture content affects soil behavior and rolling resistance considerably, and for this reason it is monitored in the analysis.

The measurements were taken with sets of 9 points from row to row every 6 m as shown in Fig. 3, so as to get a profile of compaction, for a total of 63 measurements. The distance between the trees is 2 m, while the space among each measurement point is of 22 cm. The points are in the middle between the trees for avoiding the roots. Because the average CI for the first 15 cm is widely used for rolling resistance evaluation, [5], a depth of 15 cm is considered here. On the wheel tramlines some of the measurements could not be completed because the resistance exceeded the limit of the sensor. In the analysis a value of 7000 kPa (sensor limit) is considered for those points.

The results in terms of range of CI measured and profile along the road are reported in Fig. 4 and Fig. 5 respectively. Moisture content average was of 6,5 % in a range of [2% - 17%]. High variability in the overall CI results is due to the higher compaction at the wheel tramlines, as it can be seen from the two peaks in the strength profile.

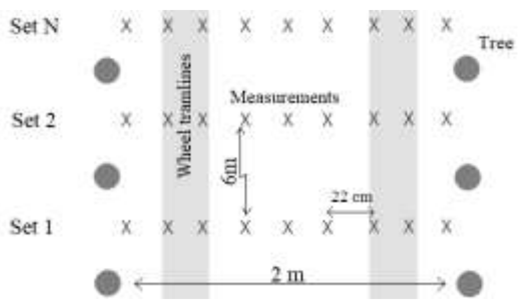

Fig. 3. Experimental layout.

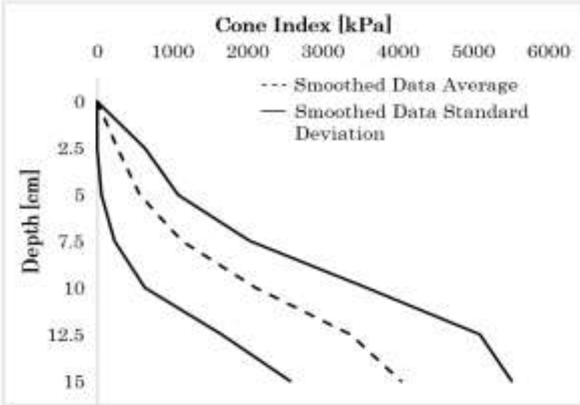

Fig. 4 Cone Index overall results.

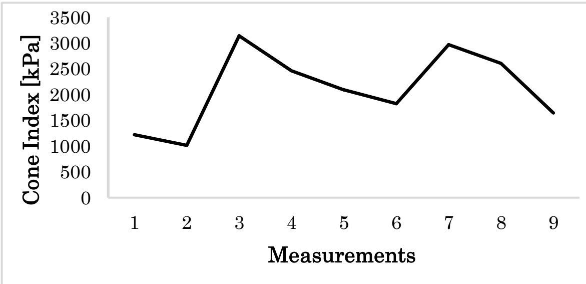

Fig. 5. Soil strength profile AVG 15 cm

4. Soil modelling and simulations

Soil under stress presents an elastoplastic behavior. Drucker-Prager criterion (DP), outer cone approximation of the Mohr-Coulomb criterion, is used in this work, [3].

A method adopted for developing a FEM soil model is to divide it into layers. Based on the experimental results, 3 layers have been identified. First 2.5 cm with low strength, 2.5 cm to 7.5 cm with medium strength and from 7.5 cm to 50 cm with high strength. Density and Young Modulus E (in case of soils also called Modulus of deformation) are different in each layer. The relation between CI and E for cohesive and non-cohesive soils was found from Melnikov,[8], by the non-linear regression equation shown in Eq. (4), based on the soil classes classification proposed by Robertson,[8], using a soil type function I_c. From the average CI of the experiments and considering a clay soil class, the Young moduli for the 3 layers were estimated.

$$E = 24{,}60 - 6{,}005 \times I_c - 0{,}5811 \times {I_c}^2 + (1{,}084 - 1{,}511 \times I_c + 1{,}090 \times {I_c}^2) \times CI \quad (4)$$

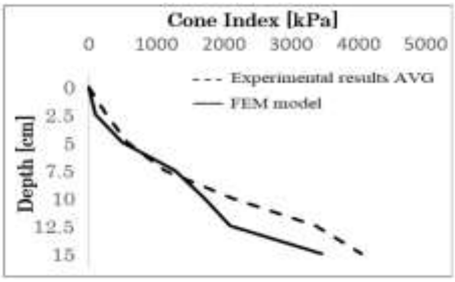

Fig. 6. CI comparison between experiments and FEM model.

At first soil is described as an isotropic elastic medium, as indicated in [9], with a specific Young Modulus and Poisson ratio. With these assumptions the CP test was simulated by FEM with the Young moduli found by Eq. (4), slightly adjusted for a better match with the experimental results, as shown in Fig. 6. DP model was completed with the soil data available at [10]. Then two static simulations were carried out to evaluate: soil deformation, to estimate the rolling resistance, and soil stress, as a measure of the compaction. Track modules are considered as stiff bodies and their deformation and contribute to the total RR is neglected in this study.

5. Discussion

With a sinkage of 4.3 mm and 13.8 mm, RR for the track and wheel mode were 43 N and 47,6 N respectively. With an average CI of 1800 kPa the two RR are almost the same as expected, and the values lower than those from empirical equations. In this analysis only the soil deformation due to a static vertical load is considered, while the deformation due to shear forces, the slip and the bulldozing effects are neglected.

Further experiments in the field and more complex analyses are required to improve and refine the model and consider all the contributes.

Regarding the stress results, in track mode the peak was 13,3 kPa while for wheel mode it was 60 kPa. Values are high only for the first layer, while the stress propagated to the deeper layers decreases rapidly in both cases, and the difference in the value is not high. As from other research,[2], contact pressure affects mainly the first layers while the load determines the stress reached at the deeper ones. Contact patch shapes are shown in Fig. 7.

6. Conclusions and future works

In this paper the preliminary study for the development of a locomotion system with an adjustable contact patch was presented. Soil stress and RR by means of empirical equations and a FEM model were evaluated, and the results in line with the expectations. The aim of the study is developing a tool for analyzing the performance of such system by identifying the soil conditions in which one mode outperforms the other, and finding the best parameters for the final design, such as track module dimensions and vehicle weight. After performing other experiments in the field, more complex analyses, also with multiple passes of the vehicle, will be carried out in different soil conditions, with different vehicle weights.

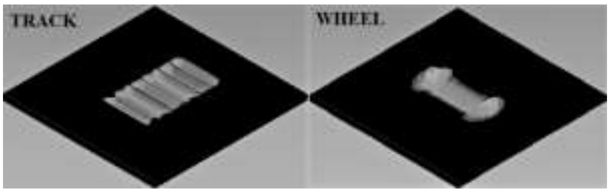

Fig. 7. Contact patch in track mode and wheel mode.

Acknowledgements

I thank my friend Daniele Ciccarese for allowing to carry out the experiments in his farm and for his support.

References

1. J. Eriksson et al., 1974. The Effect of Soil Compaction on Soil Structure and Crop Yields. *Bullettin 354. Swedish Institute of Agricultural Engineerin*g, Uppsala. R.
2. W.C. Tim Chamen, et al., Mitigating arable soil compaction: A review and analysis of available cost and benefit data, *Soil & Tillage Research* 146 (2015) 10-15.
3. Sally A. Shoop, Finite Element Modeling of Tire-Soil Interaction, *US Army Corps of Engineers*, 2001.
4. J.Y. Wong, *Theory of Ground Vehicles*, (John Wiley & sons, Inc).
5. G. L. Mason et al., Improved sinkage algorithm for powered and unpowered wheeled vehicles operating on sand, *J. Terramechanics* 67 (2016) 25-36.
6. S. Al-Milli et al., Track-terrain modelling and traversability prediction for tracked vehicles on soft terrain, *J. Terramechanics* 47 (2010) 151-160.
7. H. Taghavifar, A. Mardani, *Off-road Vehicles Dynamics*, (Springer)
8. A.V. Melnikov, G.G. Boldyrev, Correlations between CPT resistance and Young Modulus of soils, *Soil Mechanics and Foundation Engineering*, 2015.
9. P. Defossez, G. Richard, Models of soil compaction due to traffic and their evaluation, *Soil & Tillage Research* 67 (2002) 41-64.
10. www.jsg.utexas.edu, Some Useful Numbers on the Engineering Properties of materials (Geologic and Otherwise).

Robot Navigation in Forest Management Based on Graph

Ayumu Tominaga, Ryusuke Fujisawa and Eiji Hayashi
Department of Computer Science and Technology, Kyushu Institute of Technology, 680-4,
Iizuka,, Fukukoka, 820-8502, Japan
tominaga@mmcs.mse.kyutech.ac.jp, Fujisawa@mmcs.mse.kyutech.ac.jp, haya@mse.kyutech.ac.jp

Abbe Mowshowitz
Department of Computer Science, The City College of New York
New York, NY10031,USA
abbe@cs.ccny.cuny.edu

Abstract

This paper reports on an application of robotics to the management of a trees intended for eventual harvest. Such management requires periodic cutting extraneous growth around the trees. We proposes the trajectory computation for guidance of the robot in the forest is carried out based on a weighted undirected graph G with trees as vertices. The graph to be used in the navigation system is $L(G)$, the line graph of G. The vertices of $L(G)$ represent the midpoints of the edges of G and the midpoints of each tree pair. The $L(G)$ would be safety paths for the robot pass through. Our robot was able to follow a part of the trajectory computed in experimental forest, thus demonstrating the feasibility of forest maintenance by an autonomous.

Keywords: Forestry Robotics, Autonomous Robot, Graph, Navigation

1. Introduction

The application of robotics in management of forest resources is well-established [1]. Especially, improvements in Simultaneous Localization and Mapping (SLAM) techniques allow for the automatic creation of a precise forest inventory that includes individual tree locations trunk diameters, and tree height [2,3]. Such these applications have been introduced to increase productivity, enhance safety and in some cases, to compensate for the lack of available forest workers. However, there are not so many discuss the automation about a work with travelling on a rough terrain. Particularly, eliminate weed plants work aimed at promoting the growth of trees must be periodic performed. Currently, it have been done manually. Such work have being placed large labor on the employees, so it is expected that introducing the autonomous land vehicle in forest management. [4].

This paper reports an application of robotics to the maintenance of trees and forest intended for eventual harvest. The weeding robot our focused is required to have a mechanism for weeding, and traveling in the forest without damage to the tree. Navigation is most challenging part of this process.

A navigation system is requires 1) localization, 2) path planning and 3) path-following with obstacle avoidance. This paper assumes that the localization is achieved by using GPS, and mentions regard for the path planning method and the path-following with obstacle avoidance behavior. In the path planning, we propose using trees consisting a forest as a landmark. Trees are resources that the subjects of management, its location will unchanged in long period of time. Trees are resources that the subjects of management, its location will unchanged in long period of time. Using a SLAM techniques or a identify locations of each tree by GPS will allow for utilizing in a navigation system. There are not many changes in short term, so the landmark based map would be created at low labor. Therefore, in this research, we made the landmark based map in advance of the robot entrances into the forest. Therefore, in this research, we made the landmark based map in advance of the robot entrances into the forest. The map contains only position information of each tree without other objects (i.e. rocks or any obstacles). The path planning is performed by a graph consisted by the individual trees as vertices. We have been developed the robot having reactive path-following with obstacle avoidance behavior system. We show how it can be done and report on an experiment using our method in the setting of a small experimental forest located on the campus of the Kyushu Institute of Technology.

2. Computing the trajectory based on graph

Computation of a trajectory in a forest to make it follow the robot would be facilitated by treating the tree as vertices in a graph. Trees can be represented by a graph $G = (V, E)$, where V is the set of vertices and E is the set of edges [5]. A vertex $s \in V$ represents an individual tree, and and edge $e \in E$ joining vertices s and t represents a path between trees. The graph used in the robot's trajectory is $L(G)$, the line graph of G. A line graph is a graph having vertices that correspond one-to-one to edges in G, and connected two vertices of line graph corresponding to adjacent two edges [6]. In constructing the trajectory, we superimposed the natural geometry over the line graph, considering the position of the vertices of L(G) to be the midpoints of the edges of G. If the case of G with an Eulerian property, all vertices in G have even degrees, and an Euler circuit can be found. In addition, a Hamilton circuit can be used to represent the vertices in the line graph corresponding to the order to follow the edges in the Eulerian graph [6, 7].

To ensure the existence of Hamiltonian circuit in $L(G)$, the graph G will be made to be Eulerian. Any line of sight path between two trees can define an edge of G so there are sufficiently many choices of edges to allow for obtaining an Eulerian graph. Every pair of trees between which there is an unobstructed path in the forest that would allow the robot to navigate safety could contribute an edge.

In large scale forest applications it might be advisable to divide the trees into sections and treat each one separately. Criteria for subdividing the forest would naturally include section sizes, location of robot staging areas, and terrain issues such as steepness and presence of potential obstacles (e.g., rocks). For example, there were 3000 trees in the forest, it could be subdivided into 150 clusters each containing 20 trees. Such a subdivision

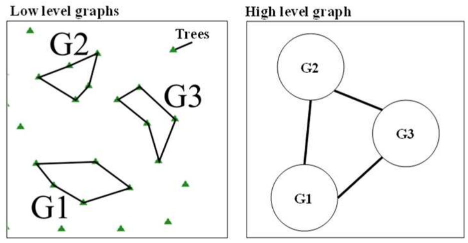

Fig. 1. Concept of two layered graph structure for trajectory in large forest

would allow for simplifying the computation of the robot's trajectory. We created a set of graphs containing several trees as vertices, and created a high-level graph consisted these as vertices, as shown in Fig.1.

3. Forestry Robotic System "SOMA"

The autonomous robot "SOMA" shown in Fig.2 is built on the platform of an All-Terrain Vehicle (ATV). An ATV was chosen for its robust design for outdoor use in rough terrain. The power source is 90cc gasoline engine. The throttle, brake lever and steering are controlled by DC motors to propel the robot. The weeding operation is realized by a specialized mechanism attached to the front of the ATV. Included sensors are RTK-GPS for localization, IMU in order to measurement the robot's heading, rotary encoder to measure the velocity, and RGB-D camera is to recognize an surrounding external situation. The final dimensions of the robot are 0.9×1.4 × 1.2m (Width × Length × Height). It is sufficiently smaller than a standard planting interval (2.5m), and allows for the robot to enter the interior of a forest.

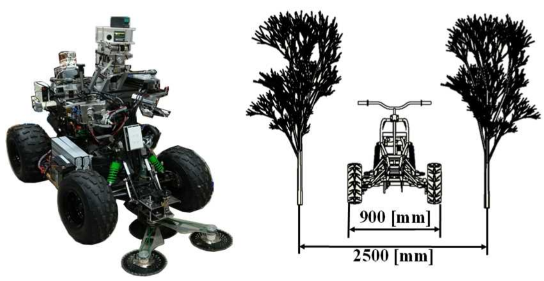

Fig. 2. Forestry robotic system "SOMA"

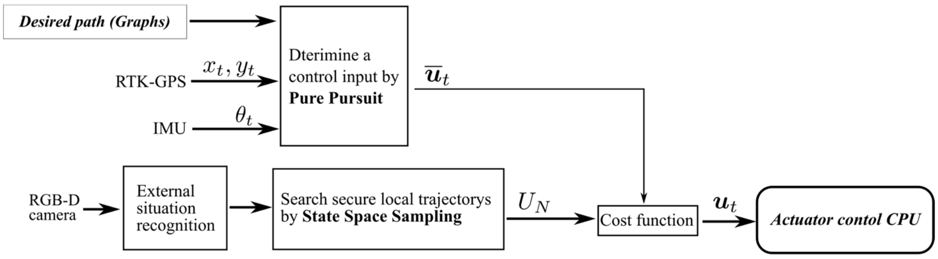

Fig. 3. System block diagram

4. Autonomous Moving System

The overview of the system is shown in Fig.3. In this research, the robot moves on two dimensional plane, and its state vector in the discrete time t is represented by $\boldsymbol{x}_t = [x_t, y_t, \theta_t]$. Here, x_t, y_t represent a location of the robot obtained by RTK-GPS, and θ_t is the robot's heading measured by IMU. The control input is represented by $\boldsymbol{u}_t = [\lambda_t, v_t]$, λ_t is a steering angle and v_t is a moving velocity. Each actuator control systems are built on another CPU in order to improve development efficiency. The navigation system is consisted by three subsystems as follows.

- External situation recognition
- Search secure trajectories
- Determine the control input for path following

Each subsystem are described below.

4.1. *External Situation Recognition*

The robot recognizes the external situation via the point cloud obtained from the RGB-D camera. We are using R200 (Intel Corporation) for our vision system. Figure 4 shows the procedure from the point cloud to the obstacle recognition around the robot. First, after acquiring the point cloud, performing the noise remove processes. Then each three-dimensional point is projected on the xz plane. Next, the clustering process of points is performed based on euclidean distance between

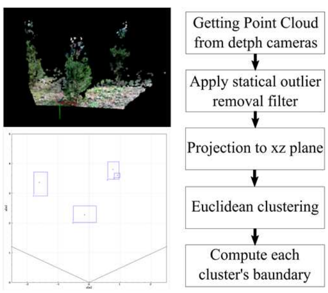

Fig. 4 External situation recognition procedure

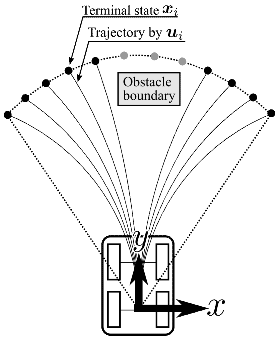

Fig. 5. Search secure trajectory based on State Space Sampling

each point, finally, obstacle boundaries approximated to rectangular are obtained.

4.2. *Search secure trajectories based on State Space Sampling*

After recognition the external situation, searching secure trajectories capable avoiding collision with obstacles is performed based on State Space Sampling method. State Space Sampling method creates a set of terminal state vector on an arc around the robot, and a set of control input allowing for reach to these state vectors are also computed [10]. The searching space of it is defined by a shape parameter $\boldsymbol{p}_{ss}$. The details of the procedure of sampling the terminal state vectors and $\boldsymbol{p}_{ss}$ are see [8].

In this research, as shown in Fig.5, The set of control input $U_N = [\boldsymbol{u}_1, \boldsymbol{u}_2, \dots, \boldsymbol{u}_n]$ that ensured safety is extracted via applying State Space Sampling to the local coordinate of the robot.

4.3. *Determine the control input for path following*

Pure Pursuit algorithm [9] is used make the robot follow the desired path based on graph described in Section 2. In each discrete time, the destination point is set on an edge in desired paths. The control input $\overline{\boldsymbol{u}}_t$ which the robot could follow the path is obtained, however it is not always output because of the obstacle avoidance behavior is high priority more than path-following. In many situations, obstacles exist surrounding the robot. Therefore, the robot should be took detour and return to paths. In the system, the final control input to propel the robot is determined by the cost function shown in Eq. (1) and (2).

$$\boldsymbol{u}_{\mathrm{t}} = argmin\{C(\overline{\boldsymbol{u}}_t, \boldsymbol{u}_j)|\boldsymbol{u}_j \in U_M\} \tag{1}$$

$$C(\overline{\boldsymbol{u}}_t, \boldsymbol{u}_j) = \overline{\lambda}_t - \lambda_j \tag{2}$$

5. Experimental results

The experimental forest on the campus of the Kyushu Institute of Technology consists of 39 trees spread over a 35×35 meter square. There are no objects other than trees. The maximum degree of slope is about 5°.

Based on these dimensions and the width of the path between trees, an undirected graph was developed, as shown in Fig.6. The adjacencies represent pairs of trees at a line-of-sight distance from each other. We created three graphs using by trees having label shown in Table.1 as for graphs of lower layers.

Table 1. Trees used in each graph

Graph	Used trees
$G1$	22,23,25,24,29
$G2$	33,38,39,40,44
$G3$	27,34,35,36,37

As shown the experimental results (Fig.8), the robot traverses around each graph in low layer, and performed transition between the graph and adjacent graph of its. These suggests it is feasible The result suggest it is feasible that the robot will be able to traverse a whole of forest by subdividing to small scale region and based on reactive motion control.

6. Conclusion

In this paper reported we have demonstrated the feasibility of designing an autonomous forestry robot to service trees meant for eventual harvest. A paths for an autonomous robot to follow can be computed based on graph from initial geographic map of trees in a forest. In the future work, we will improve the accuracy of path-following to decline the error between trajectories and desired paths.

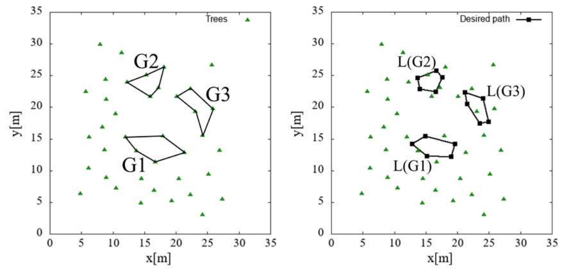

Fig. 6. Desired graphs

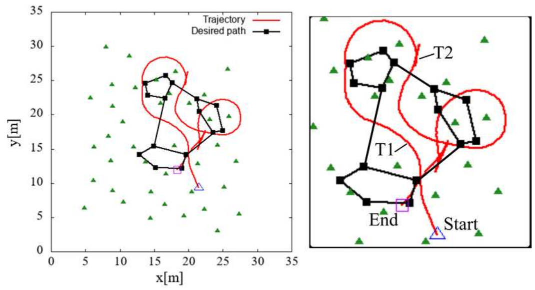

Fig. 7. The experimental results

References

1. R. Parker, K. Bayne, and P. W. Clinton, "Robotics in Forestry", *New Zealand Journal of Forestry*, No.60, pp.8-14, 2016.
2. J. Tang, et al., "SLAM-Aided Stem Mapping for Forest Inventory with Small-Footprint Mobile Li-DAR", *Forests*, Vol.6, No.12, pp.4588-4606, 2015.
3. T. Ritter, et al., "Automatic Mapping of Forest Stands Based on Three-Dimensional Point Clouds Derived from Terrestrial Laser-Scanning", *Forests*, Vol.8, No.8, pp.1-19, 2017.
4. T. Tatsuo, "Recent Research Issues in Forestry Robotics", JRSJ, Vol.12, No.7, 1994.
5. F. Harary, "*Graph Theory*", Reading MA:Addison-Weslay, 1969.
6. F. Fujie and P. Zhang, "*Line Graphs and Power of Graphs", in Covering wlks in graphs*, Springer, 2014.
7. S. Skiena, *"Line Graph", in Implementing Discreate Mathematics: Combinatorics and Graph Theory with Mathematica*, Addison-Wesley, 1990.
8. T. M. Howard, C. J. Green, and A. Kelly, "State Space Sampling of Feasible Motions for High-Performance Mobile Robot Navigation in Complex Environments", *Journal of Field Robotics*, Vol.25, pp.325-345, 2008.
9. M. Samuel, M. Hussein and M. B. Mohamad, "A Review of Some Pure-Pursuit Based Path Tracking Techniques for Control of Autonomous Vehicle", *International Journal of Computer Applications*, Vol.135, No.1, 2016.

Development of Autonomous Moving System for Field Robot

Kengo Kawazoe, Ryusuke Fujisawa, Eiji Hayashi
Department of Mechanical Information Science and Technology, Kyushu Institute of Technology
680-4, Kawazu, Iizuka-City, Fukuoka, 820-8502, Japan

E-mail: kawazoe@mmcs.mse.kyutech.ac.jp, fujisawa@ces.kyutech.ac.jp, haya@mse.kyutech.ac.jp

Abstract

Forestry go into a decline by labor shortage in Japan. We have been developing autonomous moving robot with all-terrain vehicles (ATV). And we designed an obstacle avoidance behavior to move around in the forest. Moreover, by adding a pan angle control actuator to the visual system, we increased the degree of freedom in external situation recognition. This made it possible the robot to the target coordinates specified on the global map based on the obstacle avoidance behavior.

Keywords: Autonomous Moving System, Forest

1. Introduction

SLAM (Simultaneous Localization and Mapping) technology which simultaneously performs self-location estimation and construction of environmental map is applied to resource management for forestry activity in artificial forest[1][2]. As a result, the mapping of the trees in the artificial forest and the automation of the growth amount measurement of the trees have been realized. However, the development of a robot that make it possible to circulate inside an artificial forest instead of a worker by utilizing such a technique has not advanced. This is due to the fact that artificial forests are developed in steep middle mountainous areas, and their planting density is also high[3]. On the other hand, in the forestry industry in Japan, the decline of forestry due to labors has decreased, and mechanization and automation of forestry work are required.

In this research, we developed an autonomous moving robot with platform of all-terrain vehicle with high moving ability in rough terrain. With this robot, we aim to automate the planting work and resource management within the forest. We designed an obstacle avoidance behavior to move around in the forest. Moreover, by adding a pan angle control actuator to the visual system, we increased the degree of freedom in external environment recognition. The robot achieves to guide to the target on the global map, and to cover the work area with the obstacle avoidance behavior by this function and mechanism.

2. The Robot Platform

Fig. 1. Outline of robot appearance

Figure 1 shows the robot developed in this study. We will operate the robot on a steep slope in the actual mountain hillside, and the road is rough. Thus, the robot is based on an ATV (Kawasaki, Inc.) to handle on the rough terrain. The size of robot is following; length: 1400 mm, width: 900 mm, height: 1200 mm. In the Japanese forestry work, the planting interval is approximately 2.5 m, which is narrow compared to forestry regulations in other countries. As shown in Fig. 1, the size of our developed robot is sufficiently small compared to the planting interval that it can easily travel into the native forest. The robot has four wheels, the front two wheels are turning and the rear two wheels are driving. The external environment is recognized by RealSence R200 (Intel, Inc.) which is constructed with a depth sensor and a RGB-CCD camera, and equipped on the ATV. The depth sensor can acquire an object's position as three-dimensional (3D) point-cloud data via an infrared laser measurement. The maximum measurable depth direction of the sensor is 15 m. In addition, the robot has an inertial measurement unit (IMU) for pose detection and RTK-GPS for global localization. The power source is gasoline engine. The brake lever, accelerator lever, and steering are all controlled by DC motors. A weeding task is performed by a weeding mechanism that has multi blades and attached on the front of the ATV.

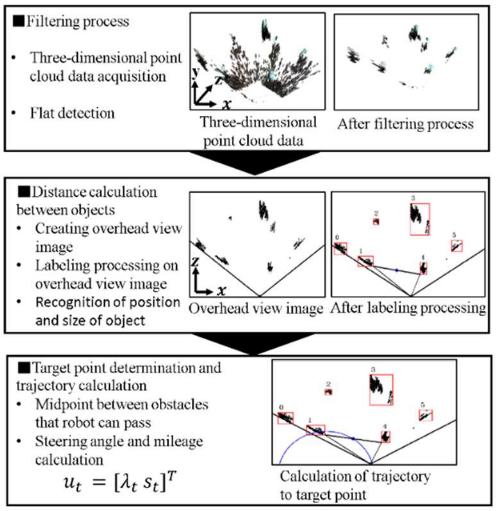

Fig. 2. Outline of obstacle avoidance

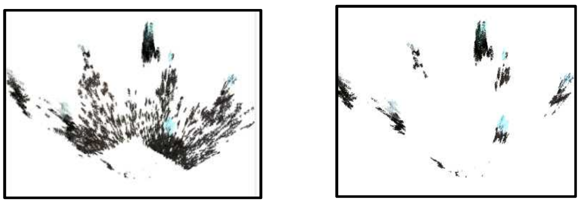

Fig. 3. Raw point cloud data (left) and after removing plane (right)

3. External Environment Recognition and Obstacle Avoidance

Outline of obstacle avoidance is shown in Fig. 2. First, three-dimensional point cloud data is acquired from the RealSence R200, and filtering processing is performed on the point cloud. Next, three-dimensional coordinate transformation is performed to make a top-down view image. By labeling processing on this top-down view image, the size and position of each object in front of the robot is recognized. Then, a distance between each object is calculated. Let the midpoint of this segment be the target point of the robot at time *t*. Finally, steering angle is obtained, and actuator control is performed. Filtering processing and target point determination are described as following.

3.1. *Filtering Process*

By filtering processing on the obtained three-dimensional point cloud data, the obstacle is recognized accurately. The plane detection as a ground surface and removal on three-dimensional point cloud data was implemented using RANSAC (Random Sampling Consensus) algorithm. Fig. 3 shows raw data obtained from RealSence R200, and the result after the plane removal.

By the plane filtering processing, it is possible to remove the point cloud data of the robot ground contact surface and to extract only the point cloud data of the obstacle at every moment.

3.2. *Determination of Target Point*

There are a lot of obstacles in traveling in the forest, the robot needs to travel like sewing between obstacles and travel with straightness. Fig. 4 shows the flow of processing for determining the target point.

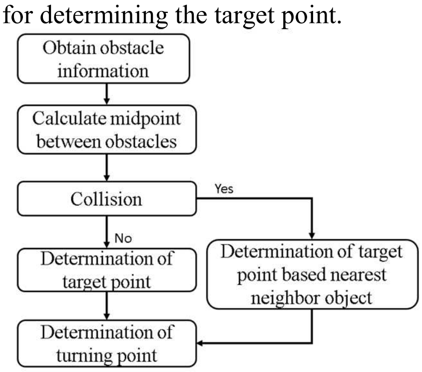

Fig. 4. Flow-chart of processing for determining target point

First, we calculate the midpoint between obstacles based on the results after labeling processing in the top-down view shown in Fig. 2. Next, the route of the robot to the midpoint of the obstacle is determined, and a collision with an obstacle is judged. When there are multiple midpoints that can go through, the target point is the midpoint with the shortest distance between the robot and the midpoint. When the robot cannot go through between all obstacles, it sets a target point to the wider space which is selected the left or right of the nearest object. As a process after determining the target point, there is determination of the target point and turning point and the travel route of the robot are shown in Fig. 5.

If an operator has a destination on the global map, the operator cannot go to the final destination simply by going around avoiding obstacles. Thus, it is necessary to approximate the attitude angle of the robot to the current attitude angle of the robot. As a result, obstacle avoidance with straight traveling is accomplished. The target point coordinate is $P_r(x_r, y_r)$, the turning point coordinate is $P_s(x_s, y_s)$, and x_s, $y_s$is obtained by using the equation (1, 2) .

$$x_s = x_r/2.0 \quad (1)$$

$$y_s = y_r/2.0 \quad (2)$$

Steering angle λ_s for heading to the turning point, travel distance s_s. The rotary encoder judges arrival at the turning point. After arrival of the turning point, the robot runs to the target point.

4. Moving Method in Work Area

The robot goes outside the work area because it just avoids obstacles. As a solution to this problem, we set up a work area using RTK-GPS data and developed a system towards the center point within that area using IMU and RTK-GPS when a robot comes out from that area.

For determination of whether the robot is located within the area or outside the area, the immediate result of RTK-GPS is used. First, a rectangular work area is set. When existing from the work area, control the pan rotation angle of the sensor so that the field of vision of the sensor faces the direction closer to the directional data of the robot from the IMU, the center point in the work area and the robot. By orienting the visual field range of the sensor toward the center point side of the work area, and as a result, the robot can return to the work space.

5. Experiment

For the experiment of the autonomous moving system, we carried out the robot autonomously at the experiment site in our university. A map showing the position of the trees was prepared beforehand in the experimental field of 35 m^2 and the x and y coordinates of each tree were measured by RTK-GPS. Fig. 6 shows the travel route of the robot at each time obtained from RTK-GPS. The result of autonomous movement with work area is shown in Fig. 7. A rectangle in the map indicates a work area.

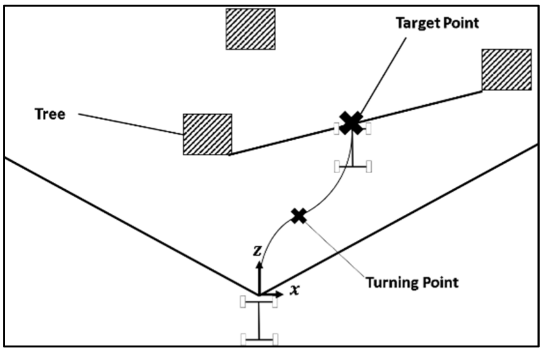

Fig. 5. Determination of target point and turning point and travel route of robot

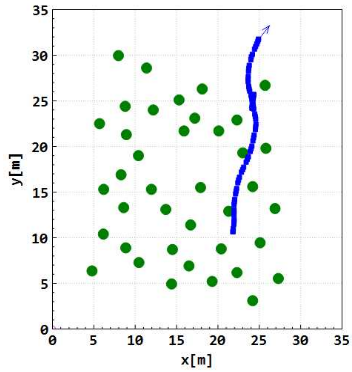

Fig. 6. Obstacle avoidance

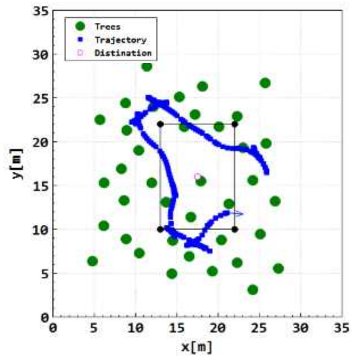

Fig. 7. Obstacle avoidance in work area

6. Conclusion & Future work

In this study, we constructed an obstacle avoidance behavior based on a lot of obstacle information in autonomous moving robot that do weeding and investigate in the forest.

With the constructed obstacle avoidance behavior, the robot did not proceed to escape to the outside of the experiment site, resulting in running with improved straightness. In addition, when the robot is located outside the work area, it is possible to return to the work area. In the future, when we reach the target point we will improve the method of determining the route to the target point to control the posture of the robot.

References

[1] H.-G. Maas, A. Bienert, S. Scheller, and E. Keane, "Automatic forest inventory parameter determination from terrestrial laser scanner data," *International Journal of Remote Sensing*, 29 (5), pp.1579-1593, 2008.

[2] G. Brolly, and G. Király,. "Algorithms for stem mapping by means of terrestrial laser scanning," *Acta Silv. Lign. Hung*. 5, pp.119-130, 2009.

[3] 新エネルギー・産業技術総合開発機構, “ロボット白書 2014”, p5-38, 2014.

[4] Martin A. Fischler, and Robert C. Bolles, “Random Sample Consensus: A Paradigm for Model Fitting with Applications to image Analysis and Automated Cartography”, *ACM*, Vol. 24, No. 6. (June 1981), pp. 381-395

Development of the Sense System That Is Combined Force and Vision Feedback

-Improvement Reproducibility of Deformation Simulation by Using LEM-

Tamon Shigeyama, Ryusuke Fujisawa, Eiji Hayashi
Department of Mechanical Information
Science and Technology
Kyushu Institute of Technology
680-4, Iizuka City, Fukuoka, Japan, 820-8502
E-mail: shigeyama@mmcs.mse.kyutech.ac.jp, *fujisawa@ces.kyutech.ac.jp, haya@mse.kyutech.ac.jp*

Abstract

The purpose of this research is to develop a combined senses system that uses both force and visual feedback on a deformation simulation. Especially, focus on a way to produce a force that is calculated in simulation of deformation using a haptic device. As the first stage, our simulation of deformation was improved by using LEM (Long Element Method) and evaluated accuracy of a virtual object's deformation.

Keywords: force feedback, haptic interface, simulation, LEM

1. Introduction

In the medical treatment and bio-technology field, doctors and researchers need technologies that can accurately perform microscale works, like a cell injection. But there are some problems, the operators rely only on sight through the microscope, and cannot feel the sense of forces. And the operators cannot see the all states of the samples. As a result, the operators have to work for a long time, and need expert skills for microscale works.

With the improvement of virtual reality technology and development of haptic devices, we can obtain haptic and visual of virtual object on computers. And implementation of force and visual feedback can improve efficiency and reproducibility in microscopic operations.

Our aim is to develop the combined system that uses both force feedback from the manipulator and visual feedback on a cell's deformation simulation. By reproducing force and visual sense of a sample, an operator can perceive these sense of a virtual object. For this research, we focus on a way to produce a force which calculated in simulation of deformation using a haptic device. Deformable virtual objects simulation, model of a sample object and reproduction of the deformation were calculated by the spring-mass-damper model in previous studies.[1] However, it is difficult to construct the model of a sample object with complicated shape, and measure spring-damper coefficient between mass points. Thus, the modeling of an object is performed by LEM(Long Element Method)[2]. LEM is an object filled with incompressible fluid is modeled based on Pascal's principle and volume preservation and deriving deformation results of semi-static state. LEM suitable for reproducing deformation of living tissue like surgical simulation. As the first step, we implemented simulation

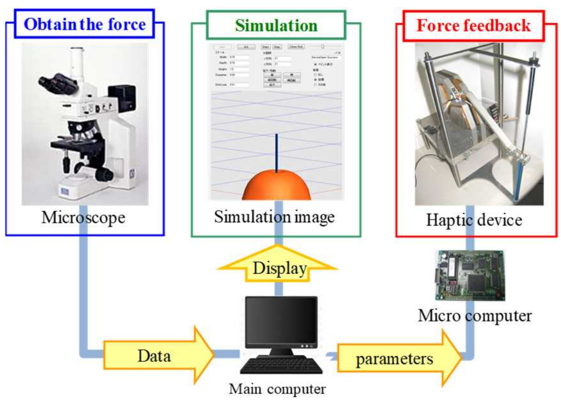

Fig. 1 The system structure

method which compute deformation of samples using LEM and evaluate accuracy of a virtual object's deformation.

2. System Structure

Figure 1 shows the system structure of our research. The main computer also sends parameters to the haptic device. The parameters are obtained by measuring dynamic characteristics of a sample using microscope. This system consists of a force feedback part and a simulated virtual visual feedback part. At a force feedback part, this system is equipped with the haptic device and a microcomputer for controlling the haptic device. At a simulated virtual visual feedback part, it shows a simulated video from a main computer.

3. Haptic Device

Figure 2 shows a diagram of the haptic device. It consists a rotor, a laser module, and a PSD module. The angle of the rotor can be measured by the laser and the PSD. The haptic device has a coil on the rotor with a polarity magnet. When electric current flows through the coil, the coil generates a Lorentz force which towards according to Fleming's left hand rule. The rotor moves depend on a waveform input, less than 36 Hz. An operator holds a moving part like a pen and receives the vertical force. Hereinafter, the moving part is called a pen slide. Figure 3 shows the connection between the haptic device and a microcomputer. The haptic device is controlled by command signals from the microcomputer process.

4. Simulation Interface

In this study, we integrate the working system using a microscope, a haptic device and a simulation. A fundamental element was simulating the deformation of sample object. Figure 4 shows the GUI of the implemented simulator. A sample object model is rendered using OpenGL.

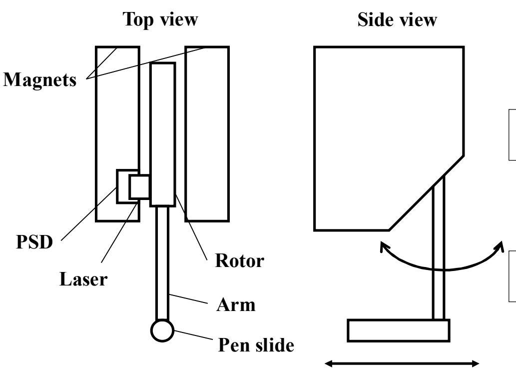

Fig.2. The structure of the haptic device

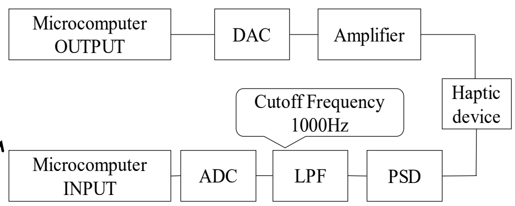

Fig. 3 The connection between the haptic device and a microcomputer

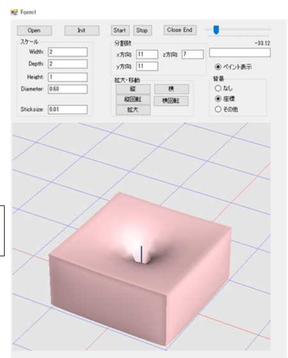

Fig.4. Simulator

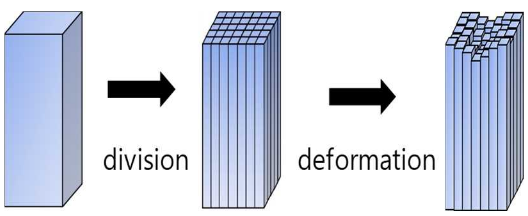

Fig.5. LEM model

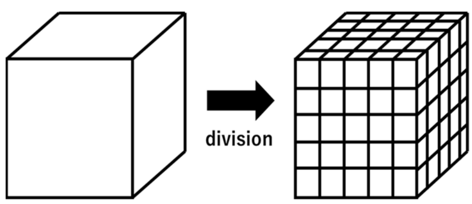

Fig.6. 3-dimensional LEM model

5. Modeling by Using LEM

The deformation of the object is also reproduced using LEM. Fig. 5 shows a method of reproducing the deformation. The object is divided into LE(Long Element), and the surface shape is reproduced by the set of deformation of each LE. Each LE deforms only in one axis direction. Modeling is divided by LE for each surface to be deformed. In 3-dimensional deformation, divide 5 faces by LE. Fig. 6 shows the 3-dimensional deformation.

6. Deformation simulation

We reproduced the deformation of silicon gel. Table 1 shows the size of the silicon gel (Taika α gel ® Co., Ltd.) and the necessary physical properties for modeling. Figure 7 shows the results of the deformation simulation.

Table 1 Parameter of the silicon gel

Parameter	Explanation	Value
Size[mm]	Width × Depth × Height	20 × 20 × 10
E[kPa]	Elasticity	28.9
d[kg/m^3]	Density	980

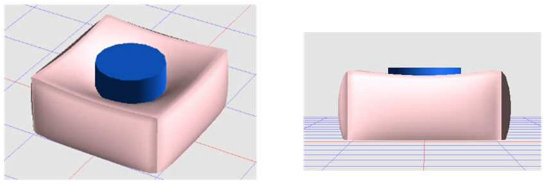

(a) Overall view (b)Front view

Fig.7 Deformation simulation of silicon gel

7. Evaluation Experiment

We experimented to evaluate the simulation. We deformed the gel by stick's pushing the top surface and measured the displacement of side surface. We extracted deformation by image processing software for measurement. Figure 8 shows an example of the observed image. Figure 9 and Figure 10 show measured and simulation values (stick diameter 10 mm and 18 mm). These values were compared and the simulation was evaluated.

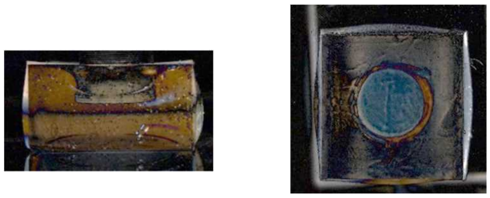

(a)Front view (b)Bottom view

Fig.8 Deformation of the silicon gel

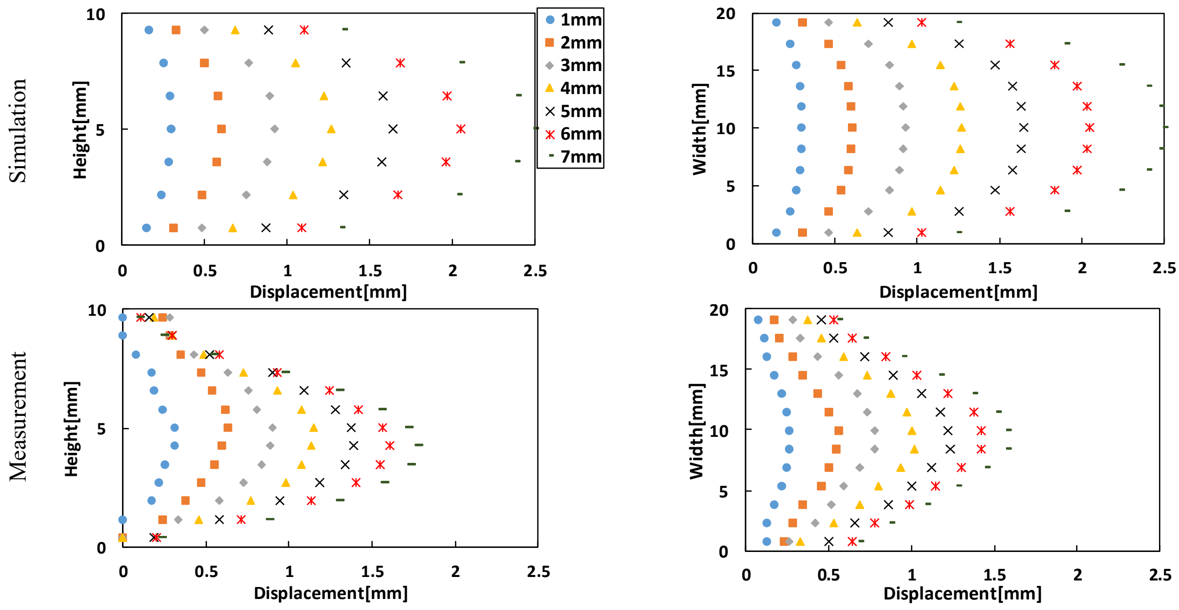

From Side From Bottom

Fig.9 Experiment result (Diameter 10mm)

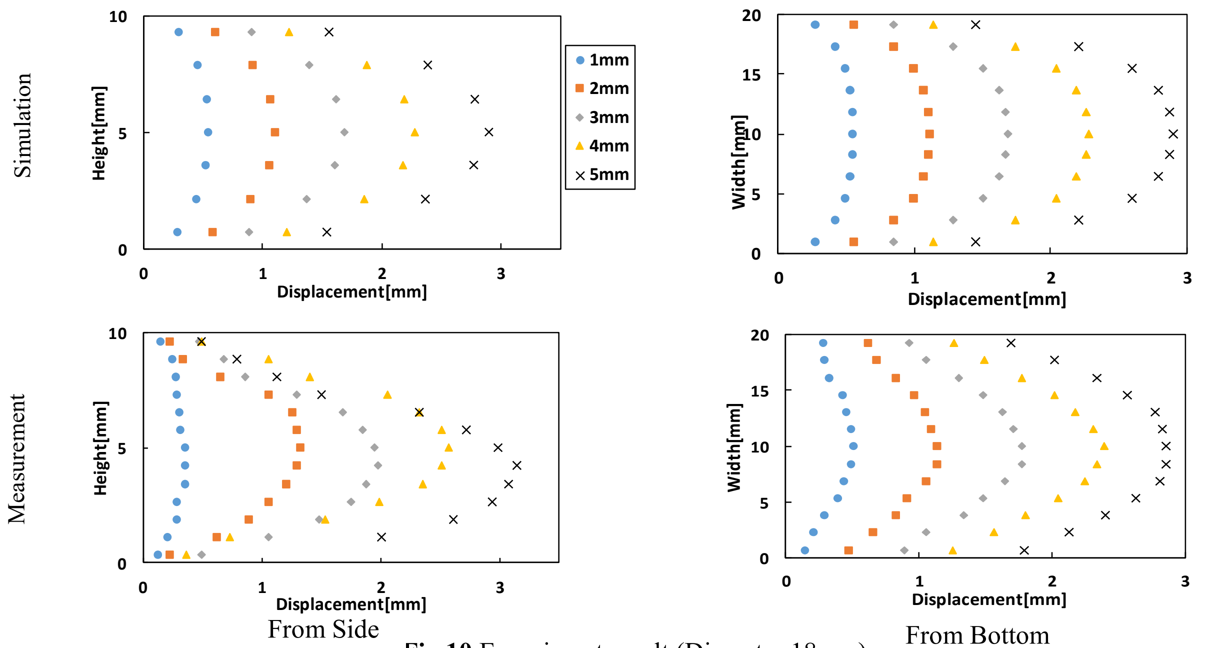

Fig.10 Experiment result (Diameter 18mm)

8. Discussion

The comparison result is different depending on the stick diameter. The stick diameter is 10 mm, the edge is drawn inward by pushing the top side. But the stick diameter is 18 mm, the area which the top surface is pushed is large so that it isn't drawn inward. In the measurement result of From Side, the displacement of top surface's edge is smaller than other points, and the peak value is lower than middle. However, the simulation value has no tendency and it can't be reproduced.

Moreover, the results of From Bottom, measurement value of edge's displacement is smaller than simulation. This is due to the gel deformation of edge is deformed in the oblique direction, but this deformation can't be reproduced in LEM.
From these facts, it was found that LEM simulation deformation of the edge is a problem.

9. Conclusion

In this study, modeling an object and reproducing the deformation of a sample is performed using by LEM. The deformation of silicon gel was reproduced. And we conducted an evaluation experiment to evaluate the simulation. Since the error is large, it is necessary to improve it.

Future research should focus on calculating force from equations of LEM and generating calculated force with the haptic device. Such a system would make it possible to test smaller samples easily.

References

1. T.OKADA, Re-creation of a membrane puncture's sense of an object constituted of liquid and an outer membrane by a haptic device and a deformation simulation of the virtual objects (*International Conference on Artificial Life and Robotics (ICAROB2017)*, Jan 19-22, Miyazaki, Japan, 2017).
2. Costa IF, Balaniuk R, LEM-An Approach for Real Time Physically Based Soft Tissue Simulation (*Proc of IEEE ICRA 2001*, Korea, pp. 2337-2343, 2011).

System Development of AUV's Sampling Device Controller Employing MATLAB/Simulink Toolboxes

Takashi Sonoda*
Faculty of Engineeing, Nishinihon Institute of Technology, 1-11, Aratsu, Kanda-machi Miyako-gun, Fukuoka, 800-0344, Japan

Shinsuke Yasukawa, Jonghyun Ahn, Yuya Nishida, Kazuo Ishii
Graduate School of Life Science and Systems Engineering, Kyushu Institute of Technology, 2-4 Hibikino, Wakamatsu-ku, Kitakyushu, Fukuoka, 808-0196, Japan
E-mail: sonoda@nishitech.ac.jp, s-yasukawa@brain.kyutech.ac.jp, ahn@brain.kyutech.ac.jp, ynishida@lsse.kyutech.ac.jp, ishii@brain.kyutech.ac.jp

Abstract

We developed an AUV's sampling device control system. It is employed the any toolboxes provided in MATLAB/Simulink by Mathworks. The toolboxes are powerful, useful, and functional. "Robotics System Toolbox" in theirs supports the ROS middle ware. It provides the cloud data communication. "Parallel Computing Toolbox" can struct a multi process and parallel computing on script base and Simulink model base program. "Stateflow" is a powerful tool for design of state transition control method. The toolboxes are employed in the sampling device control system of the AUV. This method with using the toolboxes of MATLAB/Simulink realize the rapid prototyping of the system designs, developments and system test. The developed system mounted on an AUV was powered in several real sea areas. Report on the results and problems when operating in real environments.

Keywords: System development, AUV, Sampling device.

1. Introduction

We have developed a sampling device that can be mounted on the AUV (Autonomous Underwater Vehicle) in order to accomplish sampling missions of livings on the ocean floor[1-5]. In order to operate it, we need to assume a collision with the undersea surface and various unexpected situations. For robots working in an underwater environment, the development of a system that controls the robot and some devices is very important. In development of the system, it is necessary to consider not only safety and certainty but also development speed, reusability and maintainability. Our development team has challenged system development based on MATLAB / Simulink. The toolboxes provided in MATLAB / Simulink are powerful, useful, and functional. In addition, "Robotics System Toolbox" in theirs supports the ROS middle ware. ROS provides many software which are

Fig. 1. Photograph of AUV "Tuna-Sand2" with the sampling device (manipulator type).

*Corresponding author

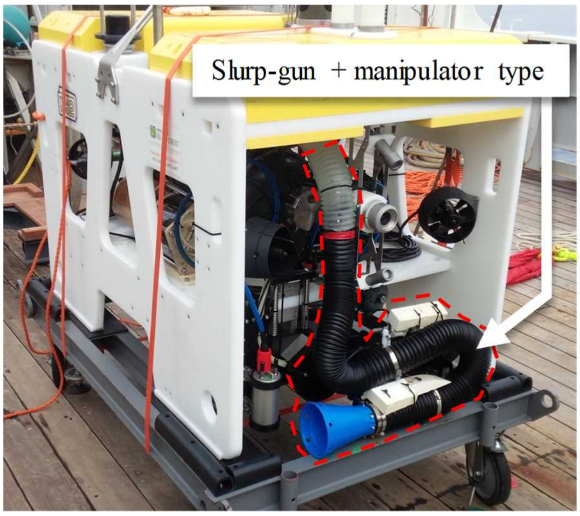

Fig. 2. The 2nd type of the sampling device (Slurp-gun and manipulator type) on the AUV.

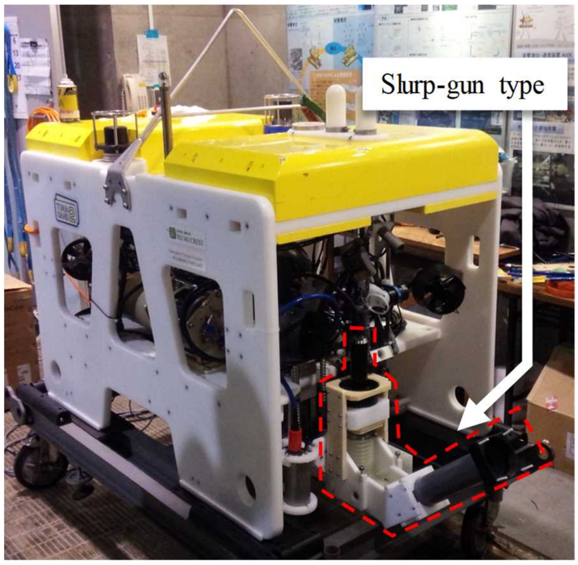

Fig. 3. The 3rd type of the sampling device (Slurp-gun type) on the AUV.

regarding to robotics such as navigation, manipulation, machine vision etc. It is possible to achieve both system extensibility and development speed by linking MATLAB / Simulink toolboxes and ROS.

We applied this system development method to the control system of the sampling device mounted on the AUV "Tuna-Sand 2" (see Fig. 1). The developed system was mounted on the AUV which operated in several real sea areas. In this paper, we discuss about the results and problems when operating in real environments.

2. Sampling device structure

There are several types of the sampling device developed. Fig. 1 is “Manipulator type” of the sampling device. Fig. 2 is “Slurp-gun and manipulator type”. Fig. 3 is “Slurp-gun type”. Fig. 4 shows the schema diagram of the sampling device. The control computer is built into the control hull.

2.1. *Manipulator type*

In this type, it has a 3 DOF manipulator with a robotic hand. The joints are actuated by hydraulic cylinders[3]. The hydraulic system is structed by 2 types of cylinder. The slave cylinder is pushed and pulled by the master cylinder. The joint angles are measured by magnetic encoders. However, there are no slurp-gun. The manipulator was designed for underwater conditions only. To launching, the manipulator must lock to avoid opening of joint angle. For the control system, monitoring lock status is very important. The type is very difficult to catch the livings.

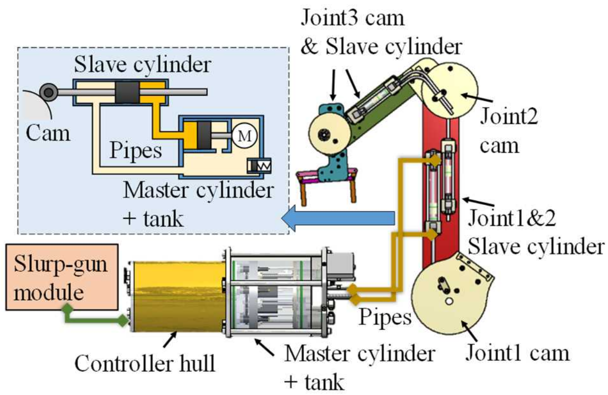

Fig. 4. Schema of the sampling device. The device has the controller hull including a computer and microcomputers. And there are hydraulic actuation system and a slurp-gun module.

2.2. *Slurp-gun and manipulator type*

In this type, it has the manipulator and a slurp-gun module. The slurp gun module is constructed by a suction hose, a canister and a suction device. Sampling by suction is easier than hand. However, this type requires a long suction hose. The suction performance of this is not efficient.

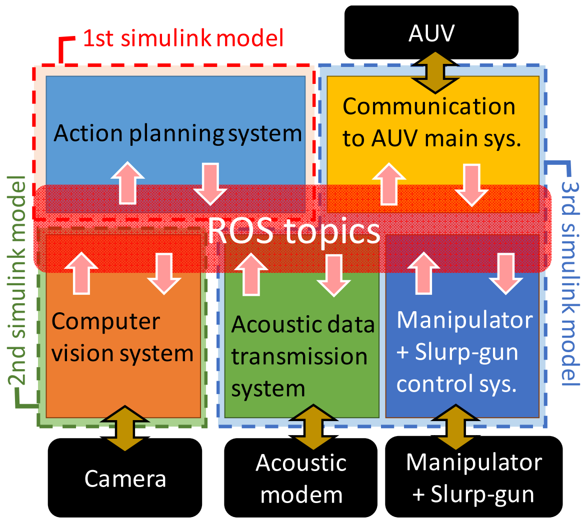

Fig. 5. The system diagram of the sampling device. The system has three Simulink models which are separated by category of works. Each model can communicate by ROS blocks which are supported in Robotics System Toolbox.

2.3. *Slurp-gun type*

In this type, it has the slurp-gun only. The suction hose is devised so that it can also be used as a canister. This configuration realizes a strong suction force. However, it is difficult to control while fine-tuning the position of the target aimed at.

3. System structure

Fig. 5 shows the system diagram of the sampling device. The sampling device is optional equipment for the AUV. It can't control the AUV and it does not have control authority. The system of the sampling device can just send any request commands to the main system of AUV. The system has three Simulink models that run parallel. "Parallel Computing Toolbox" can struct a multi process and parallel computing on script base and Simulink model base program. Each model can communicate by ROS topics. It provides the cloud data communication on ethernet in the AUV. We developed the system based on Simulink that is visual programing. This can easily be expressed as a Simulink software component.

3.1. *1st Simulink model (Action plan)*

The 1st Simulink model has an action plan system using "Stateflow" toolbox that provides state transition and flow chart editing functions. "Stateflow" is a powerful tool for design of state transition control method. The model controls and monitor the action states.

3.2. *2nd Simulink model (Computer vision)*

The 2nd Simulink model is connected to a GIGE vision system. In the model, computer vision system recognizes and trach some living objects on underwater surface. Data related to the captured object is transmitted as a message of the ROS topic.

3.3. *3rd Simulink model (Commuication to AUV, Acoustic data transmission, Manipulator and slurp-gun control)*

This Simulink model controls the hardware devices (AUV, Acoustic modem, manipulator and slurp-gun) other than the vision camera. There is the communication block to AUV main system with TCP/IP. Acoustic modem for data transmission is employed to send image taken by vision system. The manipulator and the slurp-gun connected to a microcomputer and two motor drivers with serial communications.

4. System operation in real environments

We operated this system in several real sea environments (Okinawa, Shizuoka, Hokkaido etc.).

4.1. *Data visualization*

We developed a data visualization model using Simulink. Fig. 6 shows the log file viewer using the log file when operated in real environment at Hokkaido off sea. Simulink can save time-series log data. The viewer can load the time-series log data. Because we can't use communication by radio waves in underwater situation, visualization tools that easy to understand is important. However, as a problem, the log file is generated independently from each model and the start time is different. Therefore, it takes time and effort to adjust the start time of the time.

4.2. *Flexibility to change missions*

In a real environment, the situation changes from moment to moment. When changing the configuration of the system, Simulink makes it easy to avoid mistakes because it can be changed on a block basis. It is the same when developing software components. Since the Action

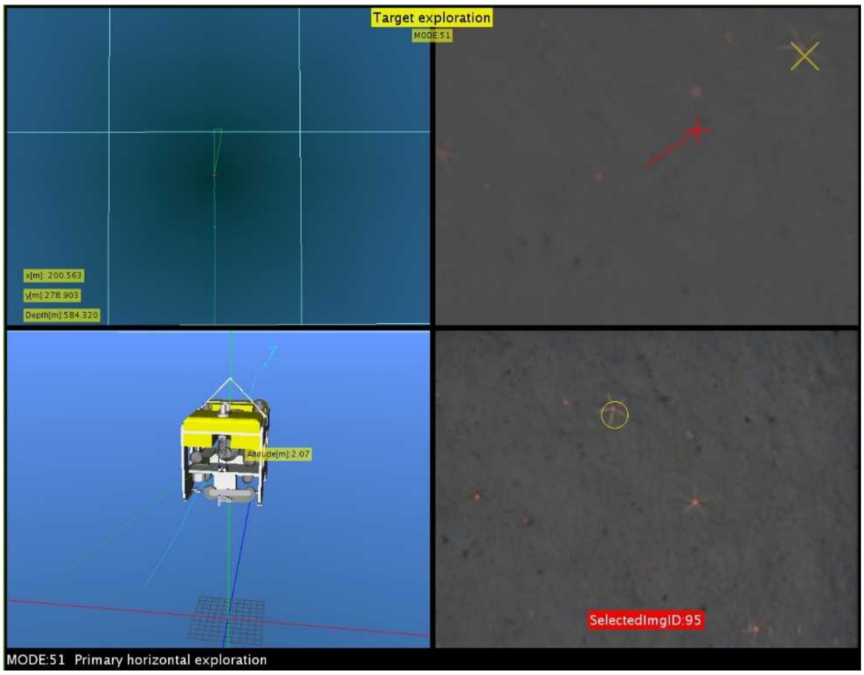

Fig. 6. Developed log file viewer for underwater cruises of AUV with sampling mission. In a deep sea, we can't see the states of the AUV and sampling device easily. Data visualization is important in term of understanding the behavior of systems in underwater. This viewer has the 4 view windows. (The upper right is camera view. The red line in the view shows a control direction and amplitude. The bottom right is the sampling target view found by machine vision system, the yellow circle is the target. The upper left is the location and trajectory view from surface of sea. The bottom left is the zoom view by the 3D model.)

planning system can be executed separately from other systems, offline checking of mission tasks is also possible. However, as a matter of value, you need to open the block with the value of the property, and you need to be careful when changing property values not described in the value change script.

5. Conclusions

I explained the sampling device I developed. In this system, it is based on MATLAB / Simulink and can be extended by ROS. As a result, it became a system that can be operated under the actual environment. However, initial cost and delays in sampling time are future tasks.

Acknowledgements

This research is supported by JST CREST "Establishment of core technology for the preservation and regeneration of marine biodiversity and ecosystems".

References

1. J. Ahn, S. Yasukawa, T. Sonoda, Y. Nishida, K. Ishii, T. Ura: Image Enhancement and Compression of Deep-Sea Floor Image for Acoustic Transmission, in in *Proc. OCEANS 2016 MTS/IEEE* (2016).
2. Y. Nishida, S. Yasukawa, T. Sonoda, J. Ahn, K. Ishii, T. Ura: Development of an Autonomous Underwater Vehicle with Human-Aware Robot Navigation, in *Proc. OCEANS 2016 MTS/IEEE* (2016), pp.1-4
3. K. Ishii, A. A. F. Nassiraei, I. Godler, T. Sonoda, T. Weerakoon: Development of a Hydraulic Underwater Manipulator for Deep-Sea Survey AUV, *The 2018 International Conferrence on Artificial ALife and Robotic*s, OS7-1 (2018).
4. K. Ishii, T. Sonoda A. Nishjima, K. Watanabe: Development of End-effector for Sampling-AUV "TUNA-SAND2", *The 2018 International Conference on Artificial Life and Robotics*, OS7-6 (2018).
5. J. Ahn, S. Yasukawa, T. Sonoda, T. Ura, K. Ishii: Enhancement of deep-sea floor images obtained by an underwater vehicle and its evaluation by crab recognition, in *Journal of Marine Science and Technology* (2017), pp 1–13.

Inspection System for Underwater Structure of Bridge Pier

Takumi Ueda, Hiyoyasu Hirai, Kazuki Fuchigami, Ryoma Yuki, Ahn Jonghyun, Shinsuke Yasukawa, Yuya Nishida, Kazuo Ishii
Dept. of Human Intelligence Systems, Kyusyu Institute of Technology
2-4 Hibikino, Wakamatsu, Kitakyushu, Fukuoka, 808-0196, Japan
Email: {ueda.takumi964, hirai.hiroyasu467}@mail.kyutech.jp
ynishida@lsse.kyutech.ac.jp, {ahn, s-yasukawa, ishii}@brain.kyutech.ac.jp

Takashi Sonoda
Faculty of Engineering, Nishinippon Institute of Technology
1-11 Niizu, Kanda-cho, Kyoto-gun, Fukuoka, 800-0394, Japan
Email: sonoda@nishitech.ac.jp

Katsunori Higashi, Katsunori Tanaka, Tomomasa Ikeda
West Nippon Expressway Engineering Kyushu, Japan
1-2-22 Maizuru, Chuo-ku, Fukuoka, Fukuoka, 810-0073, Japan
Email: {k.higashi.a, k.tanaka.a, t.ikeda.a}@w-e-kyushu.co.jp

Abstract

Inspection of underwater infrastructure of bridge pier is important for bridge maintenance, however, the underwater environment is dangerous and their observation is one of difficult problems. We have been developing the underwater inspection system which consists of an unmanned surface vehicle (USV) and a remotely operated vehicle (ROV). The concepts of the system are (1) Operation is executable with a small number of persons, (2) USV and ROV are controllable from land or bridge, (3) Build 3D model and images for crack detection. The ROV observes the status of whole infrastructure using cameras and control its posture using a depth sensor and IMU sensor. The USV vertically lifts up and down ROV by winch and carries ROV to the infrastructure. USV has GPS, LRF and IMU for horizontal positioning and pan-tilt control of the camera. In this paper, we discuss the results of the inspection operation test by the robot.

Keywords: Infrastructure inspection, ROV, USV,

1. Introduction

Most of Japan's infrastructure were built during the high economic growth period, which brings a concern of aging problems of the structures to be over 50 years within the next 20 years. In order to extend the lifetime of infrastructure facilities, it is important to understand the current damages and the deterioration progress by inspections. Then, it is effective to decide the repair countermeasure method from future prediction of degradation progression estimated from the inspection data[1].

Especially the inspection of underwater parts of the infrastructure facilities are not conducted as the dangerous area, or done by divers in the emergency cases. However, divers cannot work for a long period of time due to the high risk which in fact is critical to the efficiency of the work. It is difficult to continuously observe a specific damaged portion in order to predict degradation. Therefore, inspection of underwater infrastructure facilities using underwater robots has been attracting attention as one of new methods[2-6].

One of the difficulties is position estimation of the underwater robot due to the unavailability of GPS (Global Positioning System). Most of self-localization method use acoustic positioning. In the operating around underwater infrastructure facilities, acoustic positioning becomes difficult due to the sound reflection problems such as multi-path and water surface.

We introduce a system that involves an ROV (Remotely Operated Vehicle) for underwater survey and inspection and an USV (Unmanned Surface vehicle) for the ROV transport towards the underwater infrastructure, which is equipped with GPS and LRF for self-positioning estimation.

In this paper, we report on the results of the operation confirmation test and current problems.

2. Operation and required specification

The underwater infrastructure inspection robot system proposed in this paper consists of a ROV for camera observation attached to USV acting as an auxiliary boat that guides ROV towards the infrastructure and is equipped with remote control system.

Following is the development concept of the system.

- Minimum number of operator required
- Ability to generate panorama image with abnormality detection information attached
- Ability to send data to an operator on site

The flow of inspection using the underwater infrastructure inspection system proposed in this paper is shown in Fig.1. The method of our inspection consists of (1) deploy / navigation, (2) investigation, (3) return.

After deployment of robot from (1) in the figure, the operator navigates the auxiliary boat remotely towards the target bridge to be inspected.

At this time, the auxiliary boat performs assistance in orientation and position control from the information of GPS (Global Positioning system), IMU (Inertial Measurement Unit) and LRF (Laser range finder) to the operator.

After approaching to the bridge, underwater robot is lowered by a winch from auxiliary boat as shown in figure 2 to lower the underwater robot to surveil the infrastructure and washing condition using Front and Bottom Camera. The operator checks the image sent from the camera robot in real time and performs inspection. The auxiliary boat and the camera robot can keep the position from the bridge piers constant by the guide rollers.

After the survey of the underwater infrastructure equipment, the auxiliary boat returns back to injection point and recovers the robot.

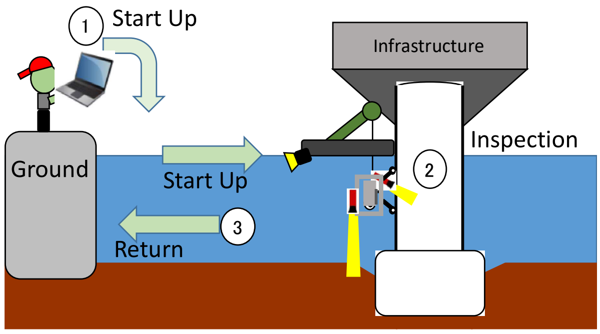

Fig.1 Flow of Infrastructure inspection

3. Underwater infrastructure inspection system

3.1 Overview

Table 1 shows the specification of the support boat developed.

Table 1 The specification of the support boat

Voltage	AC240V
Size	970*1030*1140 mm
Mass	64.0 kg
Buoyancy	89.0 kg
Propeller	300W Thruster*4
Observation equipment	GPS IMU sensor Laser range finder Winch

The support boat is equipped with Inertial Measurement Unit (IMU), GPS, LAF for recognizing the operating environment as well as a winch for depth control of ROV and four 300W thruster for maneuver.

Table 2 shows the specification of the Camera robot developed.

Table 2 The specification of the Camera robot

Voltage	AC240V
Size	477.5*510*551.1mm
Mass	17.0kg
Propeller	90W Thruster*2
Underwater weight	4.5kg
Observation equipment	Front camera Bottom camera Depth sensor IMU sensor

As for image observation robot has an IMU, and a Depth sensor for recognizing the operating environment. Front and bottom camera are mounted to bridge piper inspection. In order to make the captured image of the image observation robot more stable, two Thruster (90 W) are used as a thruster for sticking to the wall.

Figure 2 shows the image of infrastructure inspection system. The robot uses AC240V. This power is also the source of communication through PLC (Power Line Communication), making it possible to send the images from the two cameras to the operator on ground station in real time.

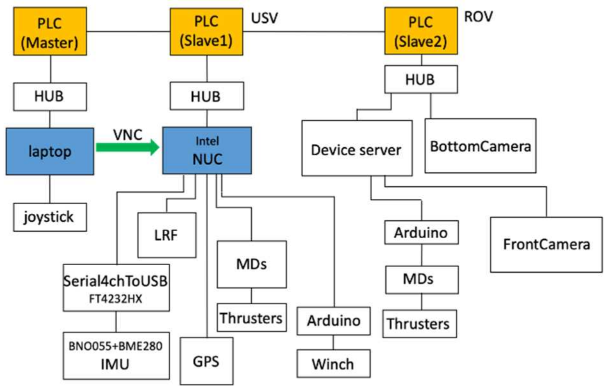

Fig. 2 System diagram of the bridge inspection system

Fig.3 The camera robot on of bridge inspection system.

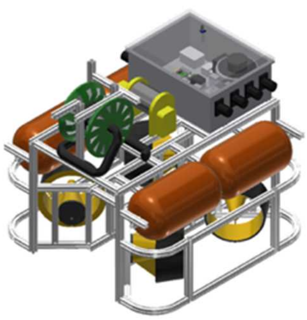

Fig.4 The support boat on of bridge inspection system.

3.2 Using underwater camera

Necessity of repair may vary depending on the inspection site and the position. Generally, cracks occurring in underwater infrastructure increase and the condition degrades over time. Due to this fact, it is important to monitor and recognize any micro cracks that currently exist. Table 3 shows the necessity of repair for each environment [7].

Table 3 Necessity of repair for crack scale

	Environment		
	Hard	Normal	Soft
Need repair[mm]	0.4	0.4	0.6
Not need repair[mm]	0.1	0.2	0.2

The environment which is considered to be the most severely degraded refers to under severe rain, dry moisture, repeated wet and freezing, or in a corrosive environment. Under such circumstances, there is a possibility that concrete and reinforcing bars will crack, rust and peel off where it is thought that the frequency of inspection and the level of degrade increase. The underwater infrastructure equipment covered in this paper includes ports, estuaries, coastal areas where chloride ion is present in the air these areas require a frequent inspection.

The image observation robot developed in this paper observes cracks that are already getting serious as well as micro cracks. The minimum inspection target was defined as a hair crack with 0.1 mm in width at which may become more severe in the future.

4. Experiment and results

In order to confirm the effectiveness of hair crack recognition by the proposed method, a resolution evaluation experiment was conducted. For the subject, we used resolution chart ISO 12233 shown in Fig.5 and HD Pro Web Camera C 920 for camera. The resolution of the captured image is 5168 × 2907 pixels. Experiments were conducted in water, and the distance between the subject and the image observing robot was fixed at 120 mm.

Fig.6 shows the images taken from experiments and the analysis results. The image in Fig. 6 was taken of region A in Fig. The result in Fig. 6 (a) is obtained by plotting pixel values after grayscale conversion of the photographed image. From this result, the influence of aliasing increases from the vicinity of Fig. 6 (d), and the original waveform can not be recognized.

Fig.7 shows the image of area B in Fig.5, which is taken of a continuously changing scale. The results in Fig. 7 show that the original waveform can be seen in the sections 1 to 5, but it can be confirmed that the sections after the section 7 are collapsed.

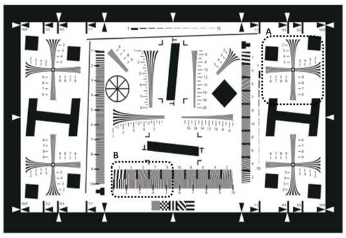

Fig.5 Using ISO12233 test image

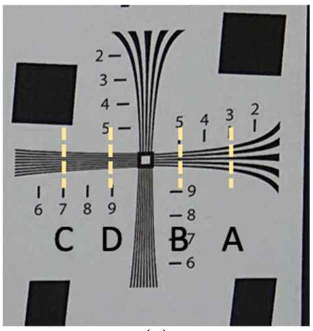

(a)

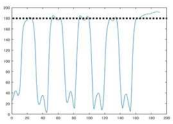

(b) Point A

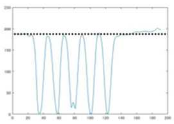

(c) Point B

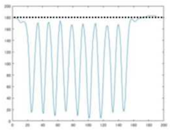

(d) Point C

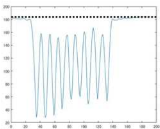

(e) Point D

Fig.6 Obtained images of A

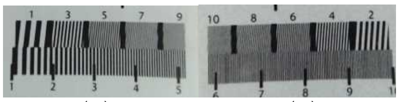

(A) (B)

Fig.7 Obtained images of B

5. Discussion

From the results of the experiment in Fig. 7, the discriminable pattern is section 6 in Fig. 7 (b), and the pattern width at that time is 0.3 to 0.4 mm. Observing cracks that need repair is It is possible. In order to observe cracks of 0.3 mm or less where follow-up observation is required, it is necessary to make the angle of view smaller than the current angle and enlarge the drawing distance per pixel.

6. Conclusion

In this paper, we propose a new underwater infrastructure inspection system and conducted an evaluation experiment using resolution chart ISO 12233. Firstly, we describe required specifications of underwater infrastructure inspection, and defined the targeted hair cracks in the proposed system. In order to investigate whether it is possible to shoot according to the defined hair crack width, evaluation experiment using resolution chart ISO 12233 was carried out and showed a range strongly affected by aliasing.

Based on the results obtained in this experiment, we plan to further develop underwater infrastructure inspection system corresponding to finer cracks and apply it to inspection of underwater infrastructure in the future.

7. Reference

(1) Ministry of Land, Infrastructure, Transport and Tourism, "*Present state and future of aging of social capital*" Ministry of Land, Infrastructure, Transport and Tourism,2016

(2) Tetsuya Sumi , "Introduction to On-site Demonstrations of Next-generation Robotic Technologies for Social Infrastructures, Organized by Advisory on Underwater Structures' Maintenance" *Journal of the Robotics Society of Japan*., Vol.34, No.10, pp.7-12. 2016

(3) Hiroshi Shiramizu, Shinya Kusuhara, "Underwater infrastructure inspection system using image sharpening technology" *Journal of the Robotics Society of Japan*, Vol.34, No.8, pp.503-504. 2016

(4) Taro Furutono, Atsuo Oono, "Maintenance Management and Inspection Using 3D Laser Scanner and 3D Multibeam Scanning Sonar", *Journal of the Robotics Society of Japan*, Vol.34, No.8, pp.509-510. 2016.

(5) Hideki Sugimoto, Tetsuya Ogasawara, Youichi Moriya, "Underwater Structure Diagnosis System by Remotely Operated Vehicle". *Journal of the Robotics Society of Japan*, Vol.34, No.8, pp.505-506. 2016.

(6) Hideki Sugimoto, Tetsuya Ogasawara and Yoichi Moriya "Underwater Structure Diagnosis System by Remotely Operated Vehicle", *Journal of the Robotics Society of Japan*,Vol.34, No.8, pp.15-16.

(7) Japan Concrete Engineering Society, "Survey of cracks in concrete, repair and reinforcement guidelines -2003-, *Japan Concrete Engineering Society*.

Three-dimensional Measurement Using Laser Pattern And Its Application to Underwater Scanner

Yuya Nishida, Tomoya Shinnoki, Shinsuke Yasukawa, Kazuo Ishii
Kyushu Institute of Technology
2-4 Hibikino, Wakamatsu, Kita-kyushu, Fukuoka 808-0196, Japan
E-mail: ynishida@lsse.kyutech.ac.jp, n237038t@mail.kyutech.jp, s-yasukawa, ishii@brain.kyutech.ac.jp

Abstract

In order to measure an accurate volume of the resources, the authors developed a new three-dimensional instrument consisting of a laser projector and a camera. The laser projector irradiates a sharp two-dimensional laser pattern independent the distance to the target object. Our instrument was able to measure three-dimensional shape of the target object with maximum error of 5% in the water, at one scan

Keywords: Three-dimensional measurement, structured light, Underwater instrument, Resource investigation

1. Introduction

Japan's exclusive economic zone is in rich in resources including mineral such as hydrothermal deposit, energy such as methane hydrate and biological resources [1]. For measurement of accurate volume of those resources, many institutes and have researched underwater instrument which is able to measure three-dimensional shape of target objects. A sonar such as synthetic aperture and multi-beams sonar measure sea bottom topographical of wide area with the resolution of a several meters, and is suited for survey of large resources [2]. An optical instrument using underwater camera measures object shape with high resolution, and its swath width is the smaller than the sonar. Light cutting method using a camera and a sheet laser [3], and stereo vision using two cameras [4], are able to measure three-dimensional shape of millimeter order. Because measurement accuracy of two methods depend on accuracy of self-localization of underwater vehicle with instrument, those are not suited for measurement of moving objects such as fish.

In order to measure actual volume biological resources, this research developed a new underwater optical instrument consisting of a laser projector and a camera. The laser projector irradiates a sharp laser pattern independent the distance to the target object. The instrument can measure three-dimensional shape of the target object using the laser pattern of several color beam at one scan. Thus, measurement accuracy of the instrument doesn't depend on position accuracy of mounted vehicle. This paper explains the principle of three-dimensional measurement of the instrument, and shows the results of its experiment for evaluating accuracy.

2. Principle of three-dimensional measurement

2.1. *Measurement model*

Our three-dimensional consist a laser projector inside a PC hull and a network camera inside a camera hull, and the position of the place where the laser beam hits is measured in camera coordinate. Although basic principle is the similar to general light cutting method, measurement area of the instrument is larger than the general by multi colors laser beam from the projector. Camera model in the instrument is shown in Fig.1, and Z axis direction of the camera coordinate which is located on the optical center inside the camera is same as the camera direction. The projector which is located y axis in the camera coordinate be inclined to pitch direction of φ_p

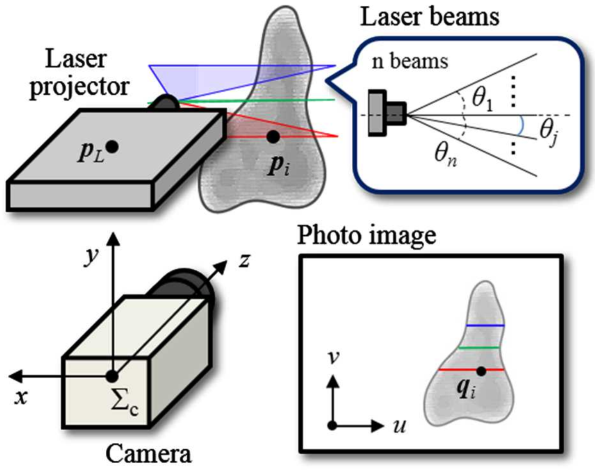

Fig. 1. Measurement model in our instrument

degrees, and n color beams be irradiated from the projector. The position $\boldsymbol{q}_i = [u_i\ v_i]^T$ in image coordinate denotes the position $\boldsymbol{p}_i = [x_i\ y_i\ z_i]^T$ where laser beam inclined at θ_j degree hits on the target object. Let the target object and its photo image be related by pinhole camera model. x_i and y_i in $\boldsymbol{p}_i$ are expressed by following equation:

$$x_i = \frac{su_i}{f} z_i \tag{1}$$

$$y_i = \frac{sv_i}{f} z_i \tag{2}$$

where f is focal length, and s denote the size per one pixel in image coordinate respectively. z_i is geometrically calculated using the projector position and beam angle.

$$z_i = \frac{y_L - y_i}{\tan(\varphi + \theta_j)} \tag{3}$$

y_L denotes the position of y axis of the projector. Then, equation (1) is substituted for equation (3), and z_i is represented by following equation.

$$z_i = \frac{f y_L}{f \tan(\varphi + \theta_j) + s v_i} \tag{4}$$

The camera capture photo image of laser reflection, and the position of each laser reflection in image coordinate is detected by binarization of HSV model. The shape of the target object can be measured by applying equation (1), (2) and (4) to all the pixels of the detected laser reflection.

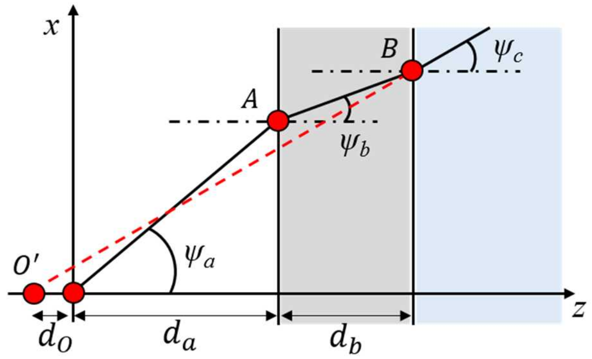

Fig.2 Schematic diagram of light path

2.2. *Water influence*

In our three-dimensional instrument, the network camera is installed inside acrylic housing for water proof, and it take underwater image from in air. Light refracts based on Snell's law when the medium though which light passes changes. In our instrument, light goes from air to acrylic, from acrylic to water, shown in Fig.2. Based on Snell's law, the view angle of the camera in air and water is related as following equation.

$$\frac{\sin \Psi_a}{\sin \Psi_c} = \frac{v_a}{v_b}\frac{v_b}{v_c} = \frac{v_a}{v_c} \tag{5}$$

ψ_a, ψ_b and ψ_c denote the view angel in air, acrylic and water, and v_a, v_b and v_c are light velocity in air, acrylic and water. The angle in water is obtained by solving equation (6) for ψ_c.

$$\psi_c = \sin^{-1}\left(\frac{v_c}{v_a}\sin\psi_a\right) \tag{6}$$

Because v_a and v_c are a parameter determined by physical property values, ψ_c is obtained from ψ_a by using equation (6).

Not only the view angle, but optical center also is affected by water. Using the distance d_a between optical center and acrylic and acrylic thickness d_b, the offset d_o of z axis of optical center is expressed by following equation.

$$d_0 = d_a + d_b - \left(\frac{d_a \tan\Psi a + d_b \tan\Psi b}{\tan\Psi c}\right) \tag{6}$$

ψ_b in equation (6) is obtained in the same way as ψ_c.

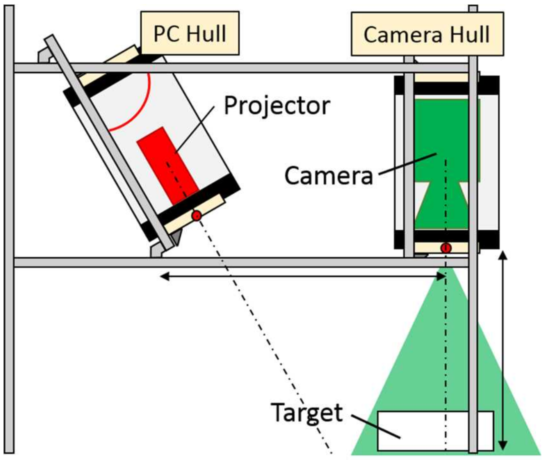

Fig.3 Experimental setup

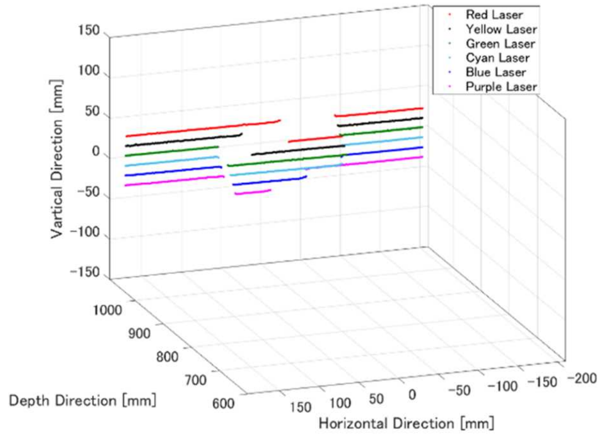

Fig.4 The position of laser reflection

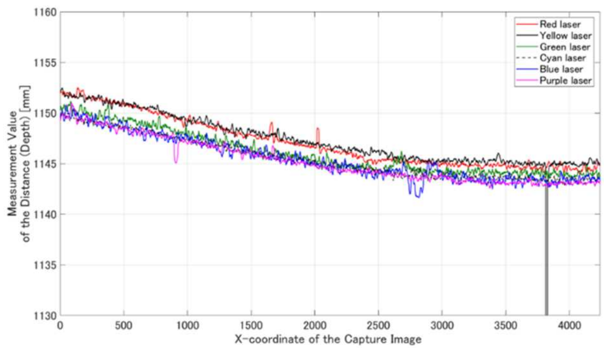

Fig.5 The distance measured with each laser beams

3. Experiment and evaluation

3.1. *Dry test*

To evaluate the performance of our three-dimensional instrument, the shape of a box which 55.4 mm wide, 150.6 mm length and 30.8 mm height was measured using setup shown in Fig.3. The box was putted on the bottom which 1,137 mm distance from the optical center of the center, and the projector inclined at 60 degrees is located at 600 mm distance from the camera. The projector irradiated 6 color beams including red, yellow, green, light blue, blue and purple to target object for measurement. Figure 4 shows the position of laser reflection calculated using equations in chapter 2.1. The instrument measured the distance to the bottom less than 5% error rate. As the box dimension was estimated based on measurement results, error rate of wide, length and height were 7%, 5% and 5% respectively.

3.2. *Wet test*

The distance to the bottom was measured in water by the setup same as Fig.3, and equations considering water influence shown in chapter 2.2 were used. Then, actual distance between the optical center and the bottom was 1,096 mm. Figure 5 shows measurement results with each laser beams. The instrument measured the distance in water with less than 5% error rate in each laser beam. Even though parameters and lens distortion had was calibrated before wet test, measurement results depended on the position of x axis. This cause is considered that the distortion of the projector lens was not calibrated.

4. Conclusions

We developed new three-dimensional instrument that can measure the shape of target located in 1,000m away with less than 5% error rate, in air. The instrument measured the distance to target with high accuracy.

References

1. Yuya Nishida, et al., Autonomous underwater vehicle "BOSS-A" for acoustic and visual survey of manganese crusts, *Journal of Robotics and Mechatronics*, Vol.28, No.1, pp.91-94, 2016.
2. Akira Asada, et al., Expanded interferometry and synthetic aperture applied to a side scanning sonar for seafloor bathymetry mapping, *Proc. Of International Symposium on Underwater Technology*, 8281046, Taipei, 2004.
3. Blair Thornton, et al., Instruments and methods for acoustic and visual survey of manganese crusts, *Journal of Oceanic Engineering*, Vol.38, No.1, pp.186-203, 2013.
4. Mathew Johson-Roberson, et al., Generation and visualization of large-scale three-dimensional reconstructions from underwater robotic surveys, *Journal of Field Robotics,* Vol.27, Issue 1, pp.21-51, 2009.

Development of dam inspection underwater robot

Hiroyasu Hirai
Dept. of Human Intelligence Systems, Kyushu Institute of Technology
2-4 Hibikino, Wakamatsu, Kitakyushu, Fukuoka, 808-0196, Japan
E-mail: hirai.hiroyasu467@mail.kyutech.jp

Kazuo Ishii
Dept. of Intelligence Systems, Kyushu Institute of Technology
2-4 Hibikino, Wakamatsu-ku, Kitakyushu, Fukuoka, Japan
E-mail:ishii@brain.kyutech.ac.jp

Abstract

Maintenances of social infrastructures such as dam, bridge are important subjects. The more aging problem going on, the more the effective inspection methods have been expected. In the inspection of dams, divers observe the conditions of their surface manually, however underwater structure deeper than 30m is limited and their inspections are insufficient. In this paper, we propose the ROV whose functions are video capture, indirect measurement using laser, target depth keeping, heading keeping. The ROV is applied into the dam inspection and showed the effectiveness to find cracks. In this study, The Remotely Operated Vehicle (ROV) is developed with the aim of practical application of technologies capable of replacing and supporting dam inspection by diver. Using the developed ROV, we conducted in the 'Verification field of the next generation social infrastructure robot' which was publicly offered by the Ministry of Land, Infrastructure and Transport in FY 2015 and examined its usefulness. In the verification on-site, it was able to satisfy about half of the required inspection items.

Keywords: Underwater robot, dam inspection, underwater robot positioning, remotely operated vehicle

1. Introduction

Social infrastructures such as dams and bridge is an important existence that becomes the foundation of the state, and it requires a great deal of cost and time for restoration and conservation[1]. However, many are built during the high economic growth period and aging due to aging is progressing[1]. Meanwhile, efficiency of maintaining and managing social infrastructure is required by the declining population and the aging of the population. Among them, in the underwater inspection work of the dam, dam damage and the function of the drainage gate are inspected by visual confirmation by a diver but at the depth of more than 30 m depth, the diving work is restricted for safety so have not been able to carry out sufficient confirmations[2]. To solve such problems, inspection methods utilizing underwater robots have been developed and researched[3].

The author have developed and researched Remotely Operated Vehicle (referred to as ROV) with the aim of practicing technologies capable of replacing and supporting diver inspection work by a diver. The developed ROV has functions such as underwater moving image photographing function by the camera, object size indirect measurement, depth and maintaining the distance and direction with respect to the dam body. Also accompanied by a floating unit for measuring the horizontal coordinate position during ROV diving.

In this paper, the authors report on the results of underwater examination using ROV at actual dam participating in 'Verification field of the next generation social infrastructure robot' publicly invited by Ministry of Land, Infrastructure and Transport in FY 2015..

2. Dam inspection underwater robot

2.1. *Configuration of ROV system*

In development of ROV, we focused on not being able to take time and effort for lightweight preparation, on the premise of operation with two people. Fig.1 present the appearance of the ROV system and Fig.2 shown in the system configuration diagram. In Fig.2 shows three elements that make up the system. The Ground Station operated on the ground and the underwater ROV are connected by a neutral buoyancy cable and power is transmitted. Moreover, communication is performed via power line by using Power Line Communication.

Floating unit operates with batteries and is connected to Ground Station wirelessly using ZigBee. Use the controller for operations such as movement of ROV, lighting of LEDs, shooting still images.

Fig.1 The dam inspection underwater robot

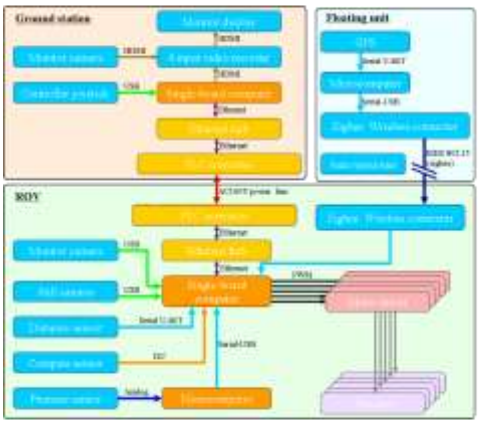

Fig.2 System architecture of ROV

2.2. *ROV*

ROV has azimuth sensor, depth sensor, USB camera. The control of ROV is carried out by built-in one-board computer, numerical value acquisition from sensor, operation of motor driver and LED projector by PWM output, transfer of operation video from USB camera and photographing of still picture.

2.3. *Floating Unit*

The appearance of the floating unit is shown in Fig.3

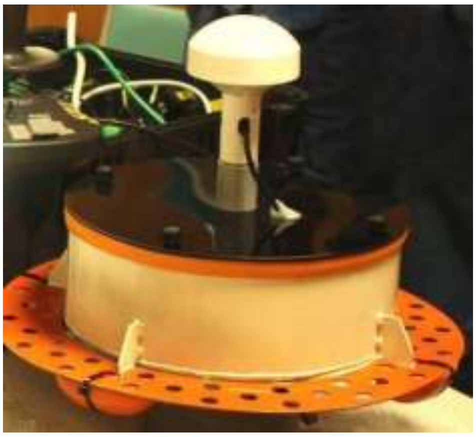

Fig.3 Overview of Floating Unit

Floating unit is fixed to ROV via fishing line. By sending out the fishing line according to the movement of the ROV and keeping a constant tension, it moving in the direction corresponding to the horizontal position of the ROV. In addition, it incorporates a GPS and transmits the output value to the Ground Station via Zigbee.

2.4. *Ground Station*

Fig. 4 shows the display contents of Ground Station. The contents displayed are the image of the monitor camera installed in the ROV, the image of the camera , the shipboard camera, the output values of the sensor and the current direction of the ROV drawn on the map, the direction facing it. Automatically start recording of the display contents simultaneously with powering on the system.

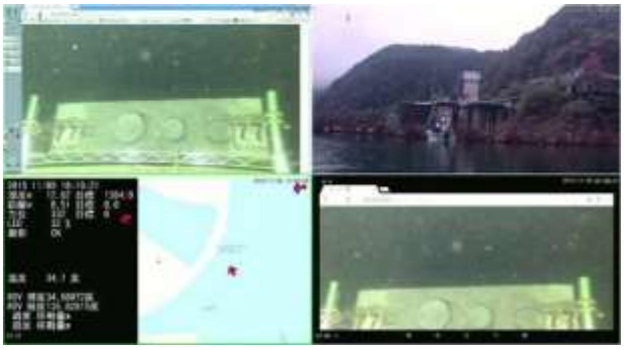

Fig.4 Display contents of Ground Station

3. Underwater infrastructure inspection method

3.1. *Outline of inspection method*

In the inspection of the dam using the ROV, although the dam body is continuously photographed using the built-in camera, it is necessary to simultaneously record the coordinates of the object at the time of photographing. Furthermore, it is desirable to be able to measure the size of the object to be imaged, and estimation was done by post processing. Also, in order to photograph a wide range continuously and smoothly, position keeping of a robot by feedback control was mounted on ROV and verified.

3.2. *Estimation of shooting coordinates*

The output values of the GPS mounted on the floating unit and the depth sensor, orientation sensor, underwater distance sensor mounted on the ROV are recorded at the same time stamp and the coordinates of the object at the time of camera shooting are estimated by post processing.

3.3. *Estimation of size of photographing object*

Estimate the size of the object indirectly by using the fixed laser mounted on the ROV. The fixed laser was composed of two pieces, and the interval distance was set to 300 mm. Fig. 5 shows the result of calculating the size of the object to be photographed from the photographed image. We calculated the size of the object by deriving the size of each pixel in the photographed image by using the distance between two points of the fixed laser shown in the image.

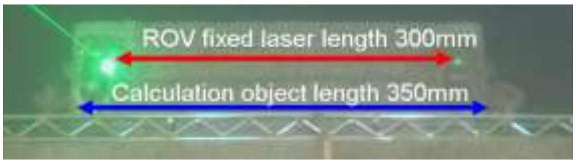

Fig.5 Calculated object size result

3.4. *Stabilize the attitude*

In order to maintain the positional relationship with the object to be photographed, feed-back control is used to stabilize the attitude of the ROV. Control consists of depth, azimuth, and horizontal distance from the dam wall. PID control was used for feedback control, and the control gain was adjusted by actual movement in pool and dam. In the maintenance control of the horizontal distance from the dam body, since it is necessary for the underwater distance sensor to be opposite to the dam body, it is performed simultaneously with the maintenance control of the azimuth.

4. Evaluation of system using real dam inspection

To confirm the effectiveness of the developed ROV, we conducted a test at the Amagase Dam in Kyoto Prefecture on November 24, 2015. Amagase dam is an arched concrete dam. The state of the test at the Amagase dam is shown in Fig.6.

Fig.6 Amagase dam and boat

The inspection target in the test is to check the position coordinates, the surface shape, and the size by photographing the concrete block installed in the preliminary conduit gate in a state of falling into the water. In the test, the ROV dropped from the boat was brought close to the dam wall and the submarine began using the guide rail of the preliminary conduit gate exposed on the water as a marker. Fig. 7 shows the state of the boat and ROV at the start of the inspection.

Fig.7 Approach to dam with ROV

In Fig.7, we see ROV and Floating unit on the water surface indicated by red circle. We tried diving by manual operation and attempted maintenance by autonomous control about heading and horizontal distance from the dam body. As a result of the test, we succeeded in photographing four concrete blocks with a working time of about 3 hours. Concrete blocks were not informed of the number, position and current in advance, but the total was 4 and it was possible to discover everything, and on the concrete block surface slits and protrusions imitating cracks were printed I was able to confirm the numbers. The four concrete blocks found in Fig. 8 are shown.

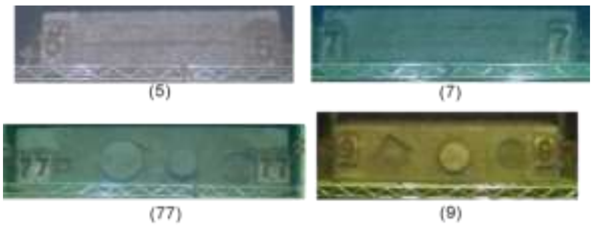

Fig.8 Inspection target concrete block and dummy clacks

In Fig. 8, it is understood that the numbers 5, 7, 9, 77 are printed on the concrete block.

Table 1 shows the calculation results of the position coordinates of the four concrete blocks from the sensor output values at the time of shooting. As shown in the error of Table 1, although it is larger than the visual observation, it got results that endure use.

Table 1. Concrete block position and difference

Block		Position (JGD2011 VI plane rectangular co-ordinates)		
		x[m]	y[m]	Difference[m]
5	measured	-124157.849	-15709.042	0.470
5	exact	-124157.410	-15709.042	
7	measured	-124156.738	-15709.955	0.470
7	exact	-124155.226	-15710.195	
9	measured	-124155.630	-15709.039	0.600
9	exact	-124155.139	-15709.383	
77	measured	-124156.738	-15709.955	0.650
77	exact	-124156.131	-15709.188	

5. Equations

In this paper, in order to confirm whether ROV developed and researched can be used for efficient underwater inspection work, the result of participating in the verification test at actual dam was described.

In the verification test, We were able to estimate the coordinates of the shooting position by still image of the concrete block installed in the dam body by ROV within a predetermined time and checking with the sensor information based on the shooting time .In addition, We were able to estimate the size of 12 simulated cracks from the captured image, respectively.

As a result, it was possible to show that there is possibility of efficient inspection of the dam by ROV.

Acknowledgements

This research is promoted by the Nissui Marine Kogyo Co., Ltd.

References

1. MLIT, "*White paper on land, infrastructure, transport and tourism in Japan 2013*"(Japan,2013),pp.28-30. Available:http://www.mlit.go.jp/common/001063075.pdf.
2. National Institute of Occupational Safety and Health, Japan.,*JICOSH*,Available: https://www.jniosh.johas.go.jp/icpro/jicosh-old/japanese/country/japan/laws/03_rel/08_selectedchemicals_reg/index.html
3. N. A. Cruz, A. C. Matos, R. M. Almeida, B. M. Ferreira, and N. Abreu, TriMARES – A hybrid AUV/ROV for dam inspection, *OCEANS2011 MTS/IEEE(*Waikoloa, Hawaii, 2011), pp. 1-6.

Conceptual Design of Small ROV for Sky to Water System

Keisuke Watanabe*
School of Marine Science and Technology, Tokai University, 3-20-1 Orido Shimizu-ku Shizuoka-shi, Shizuoka, Japan†

Koushi Utsunomiya
School of Marine Science and Technology, Tokai University, 3-20-1 Orido Shimizu-ku Shizuoka-shi, Shizuoka, Japan

Kazumasa Harada
School of Marine Science and Technology, Tokai University, 3-20-1 Orido Shimizu-ku Shizuoka-shi, Shizuoka, Japan

Shuhei Nakajima
School of Marine Science and Technology, Tokai University, 3-20-1 Orido Shimizu-ku Shizuoka-shi, Shizuoka, Japan
E-mail: keisuke@tsc.u-tokai.ac.jp

Abstract

Long term and wide range monitoring of coral reef is necessary for the research of coral bleaching. Researchers diving for investigation, they need to hire a boat whose port is not always near the target site where is sometimes near a beach. We are developing a new method which uses a set of Multicopter-USV-ROV. We named this concept as Sky to Water System. In this paper, we introduce the conceptual design of the SWS and its Small ROV.

Keywords: Sky to Water System, Coral bleaching, Unmanned Surface Vehicle, RTK GNSS, Multicopter, Floating LBL

1. Introduction

Long term and wide range monitoring of an area of coral reef is necessary for investigation of coral bleaching. The researchers usually use underwater cameras to record the reef's present condition using a ROV or diving by themselves. In those cases, they need to hire a boat whose port is not always near the target investigation site where sometimes near a beach. The researcher diving is effective from the viewpoint of precise investisation of a limited spot, however, it is impossible for divers to investigate such wide area like the Great Barrier Reef simultaneously. Though satellite image can be used to monitor the vast area, needless to say, it is difficult for us to measure the underwater environmental parameters such as time, conductivity, pH, color of reefs etc.

To breakthrough these limitations we are developing a new method which uses a combined system of multicopter-USV(Unmanned Surface Vehicle)-ROV. We named this concept as Sky to Water System(STWS).

*Corresponding author

In this paper, we introduce the conceptual design of SWS, the conceptual design of the Small ROV which can be delivered with its mother USV by a multi-copter from the nearest beach, and some experimental results of precise RTK GNSS positioning which is essential for determination of the underwater coordinate of ROV by our developing floating LBL system.

2. STWS concept

STWS consists of a multi-copter for USV/ROV system transportation, multi-copters for taking pictures from the sky, USVs, ROVs or AUVs and the floating LBL system[1] for determination of underwater vehicle's position.[2] Each module is delivered by the multi-copter from a mother vessel or seashore.[3] The ROV or AUV is docked to the unmanned surface vehicle (USV) when the multi-copter transports it. The USV has wireless LAN so that we can control the USV and ROV remotely and monitor the underwater images which the ROV films by its video camera. The USV also equips a kind of winch system to release and wind up the umbilical cable attached to the ROV. If an AUV is deployed, the winch system can be omitted. Each USV has ultrasound ranging module, RTK GNSS and communication device (XBee module). The communication device is used to communicate between USVs for collision avoidance and transmission of acquired data to calculate the base line distance or underwater coordinate of the ROV or AUV.

3. Conceptual Design of ROV

Our ROV is delivered by a multicopter UAV with an interface USV. So it must be designed as light weight as possible. The schematic view and drawing are shown in Fig.1 and Fig.2 respectively. The equipment of ROV and its architecture is shown in Fig.3. The total weight in air is around 3.5kgf.

The ROV has its own battery inside to be able to be used for a kind of AUV in the next experiment. A single board computer controls sensor/actuator systems. We implemented a video camera to capture the underwater images of corals and the acryl pressure hull is hired for this purpose. The supposed water depth is up to 100m from the strength estimation using its thickness of the wall. At this stage, conductivity, temperature and depth (CTD) sensors are implemented for recording of environmental condition data that should be recorded with the picture taken.

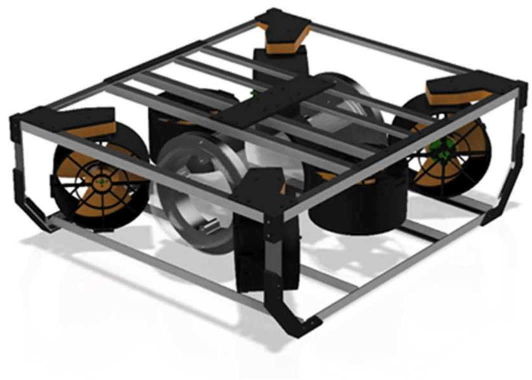

Fig. 1. Principal dimension of designed ROV.

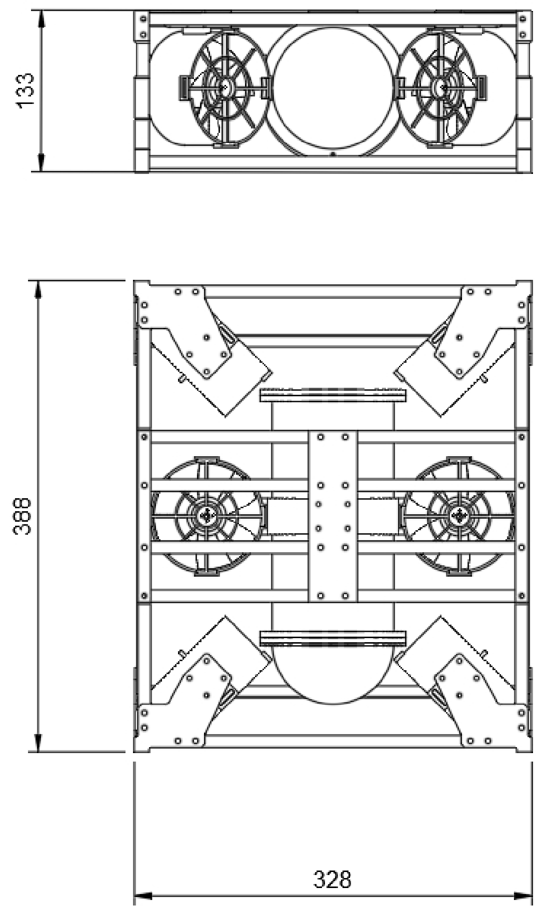

Fig. 2. Principal dimension of designed ROV.

Six thrusters are hired to control its underwater position. The underwater position is determined by the floating LBL using ROV's transponder ultrasound signal.

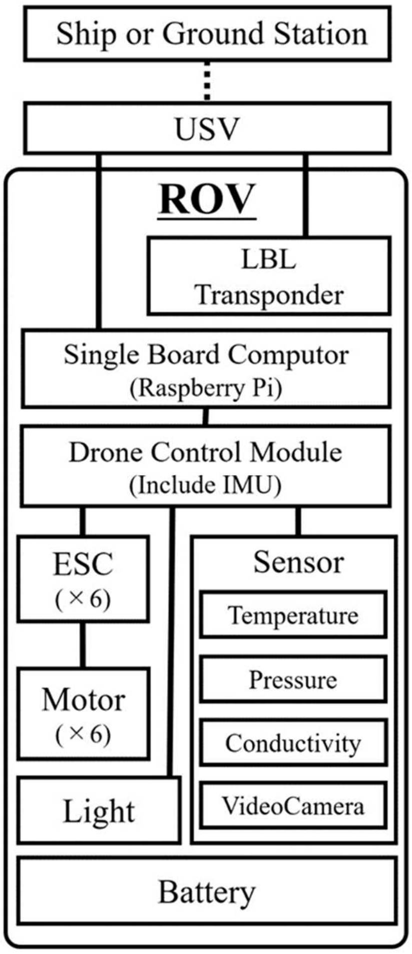

Fig. 3. Equipments of ROV.

4. GNSS baseline detection experiments

In our floating LBL system, the baselines are measured using each USV's GNSS (N,E) coordinate. Recent progress in GNSS receiver enables us to measure the distance with centimeter accuracy. The accuracy of baseline distance is crucial in our underwater position calculation, we confirmed the accuracy of RTK GNSS is enough to develop our floating LBL system.

The experiments were carried out on our school field as shown in Fig.4. GNSS base station is fixed as the origin of the coordinate. Two rover antennas are arranged on the orthogonal lines and each distance from the base station is changed from 2m, 5m, 10m, 20m, 30m.

Figures 5-7 show the time series of measured distance between base-rover1, base rover2, rover1-rover2, when the setup distance is 2[m].

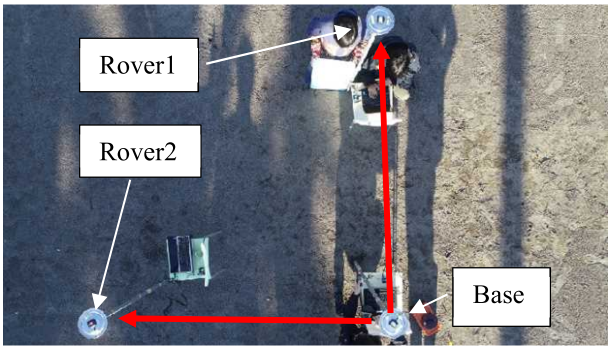

Fig. 4. RTK GNSS distance measurement experiment

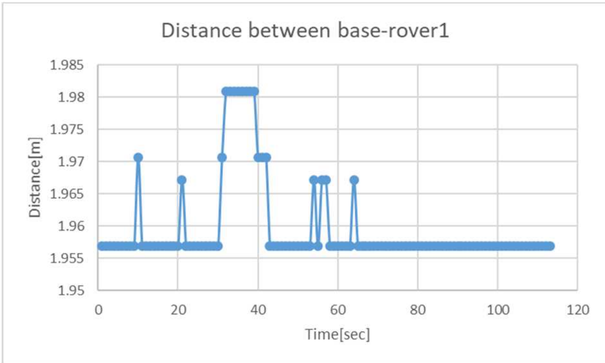

Fig. 5. Base-rover1 distance case 2[m].

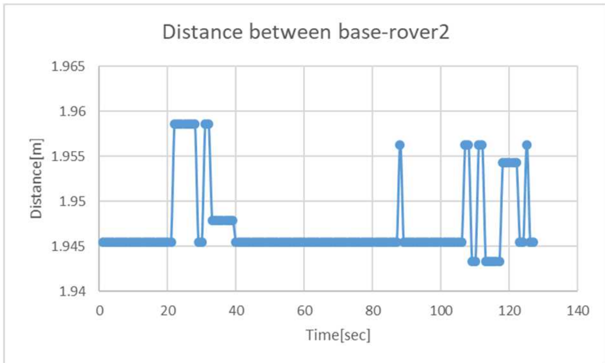

Fig. 6. Base-rover2 distance case 2[m].

In these experiments, the relative height of each GNSS module was almost zero, so we calculated the distance as follows.

$$disance = 1852.196 \times (N1 - N2) \times (E1 - E2) \times \cos(Nbase) \quad (1)$$

Here, (N1, E1) shows longitude and latitude

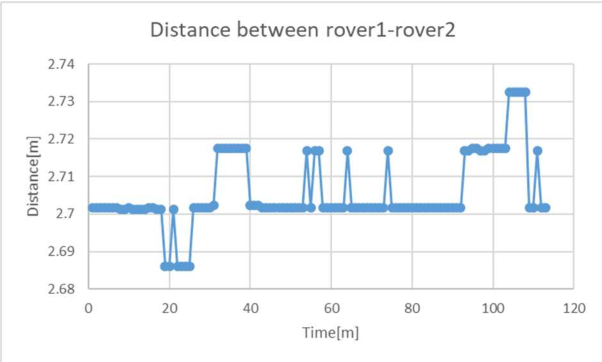

Fig. 7. Rover1-rover2 distance case 2[m].

Figures 8-10 show the time series of measured distance between base-rover1, base rover2, rover1-rover2, when the setup distance is 30[m]. From these experiments, we confirmed we can implement the RTK GNSS modules in our floating LBL baseline measurement system in very good accuracy.

5. Conclusion

We designed small ROV concept for STWS. The fabrication is ongoing and we will carry out first sea experiment in the near future. The underwater position determination is essential for this ROV and the baseline accuracy of the floating LBL is desirable within several centimeters order. The RTK GNSS experimental results showed our current system can measure relative length from 2[m] to 30[m] less than 2[cm]. Distance measurement using ultrasound transponder is our next step.

Acknowledgements

We sincerely thank to our laboratory members to help field experiments. This research is supported by the Tokai University Supporters Association Research and Study Grant. ext.

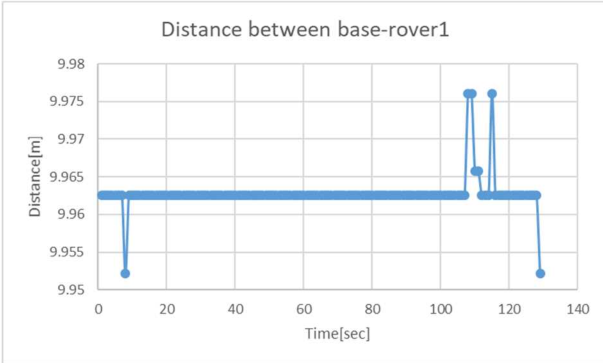

Fig. 8. Base-rover2 distance case 10[m].

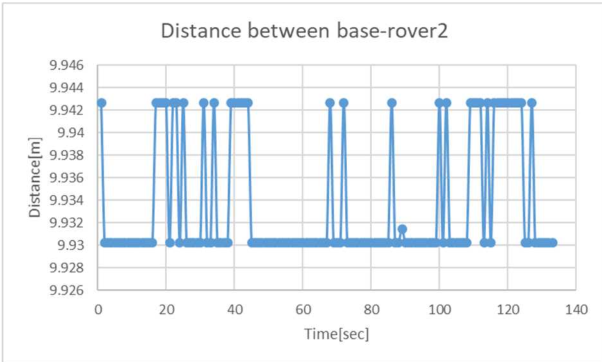

Fig. 9. Base-rover2 distance case 10[m].

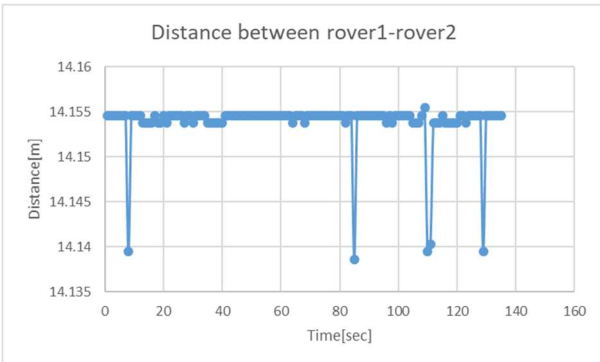

Fig. 10. Rover1-rover2 distance case 10[m].

References

1. K. Watanabe, K. Ishii, "Floating LBL concept for underwater position detection", *Proc. of the 2017 International Conference on Artificial Life and Robotics*, Miyazaki, ICAROB, OS7-2(2017), pp.245-249
2. K. Watanabe, K. Mitsumura, K. Utsunomiya and S. Takasaki, "Experiments of Floatable UAV for Wave Dissipating Block Inspection", *Journal of Robotics, Networking and Artificial Life,* Vol.4, No.3(2017), pp.234-238
3. K. Watanabe, K. Utsunomiya, K. Harada, Y. Watanabe, "A Concept of Coastal Sea Monitoring System from Sky to Water", *Proc. of the 3rd World Congress on Civil, Structural, and Environmental Engineering (CSEE'18) (2018)*, Paper No. ICESDP 136
4. K. Watanabe, K. Mitsumura, K. Utsunomiya, K. Harada, "An Experiment of Multicopter and Small ROV Combined Monitoring System for Coastal Area Environment", *Proc. of the 28th International Ocean and Polar Engineering Conference*, (2018), pp.373-378

Study on Position Estimation Using Small Size ZigBee Module

Atsushi Sanada
Nishinippon Institute of Technology,
1-11, Aratsu, Kanda, Miyako-gun, Fukuoka, 800-0934, Japan
E-mail: sanada@nishitech.ac.jp

Abstract

Position information is very important information that can be utilized in various fields. In this research, we propose a location estimation system using low cost ZigBee compact radio module. The position is estimated based on the radio wave intensity for the plurality of antennas. Since the radio wave intensity is nonlinear with distance, the distance was estimated using a neural network. As a result, it was confirmed that the distance can be estimated correctly.

Keywords: Position Estimation, Small Size Wireless Module, TWELITE, Neural Network

1. Introduction

In recent years, services based on location information have become widespread, and are used in all situations of life. For example, the navigation system[1] is installed not only in automobiles but also in smartphones, indicating an efficient route to the destination. For this purpose, position information by GPS is mainly used. Additionally, Bluetooth is installed for near distance search in GPS tags for loss prevention. In addition to location services using satellite radio waves and radio waves like this, a system used in sports such as football that detects and displays the positions of players and balls is realized by analyzing a plurality of camera images set around the field. As described above, location services are deployed by various technologies, but as shown in Table 1, each has advantages and disadvantages.

GPS can be used mostly outdoors and has a very wide detection area, but it cannot be used indoors. Further, if it is tried to obtain accuracy of cm unit, an auxiliary device such as a fixed station is required. The camera is highly accurate if the shooting range is the detection area and the detection area is narrow, but it is impossible to detect a wide range while maintaining accuracy with one camera. In order to detect a wide range, it is necessary to cooperate with plural cameras, resulting in high cost. Wireless radio waves are used for rough location detection[2,3] when ZigBee, Bluetooth or WIFI is used, and not until detection in cm. This is because it is difficult to simply obtain the distance from the radio wave intensity because the radio wave changes due to fading caused by reflection on a wall or the like. Considering the influence of this fading, the accuracy of position detection using

Table 1. Comparison of position detection methods

Position Detection Method	Area	Indoor Use	Accuracy	Cost
GPS	◎	×	○	○
Camera	×	○	◎	×
Radio Wave	△	○	△	○
Proposed Method	○	○	◎	◎

radio waves should improve. In this research, we aim to improve position detection accuracy by learning the radio field strength including fading with a neural network.

2. System overview

2.1. *Transmitter and Receiver*

As shown in Fig. 1, the present system is composed of a receiver set at known coordinates and a transmitter that moves. ZigBee is used as a wireless system. Signals are periodically transmitted from the transmitter, and the signals are received by the respective receivers. At the receiver, a value of LQI (Link Quality Indicator) indicating the quality of the received signal is obtained when the signal is received. Since the approximate value of the radio field strength can be obtained from LQI using Eq. (1), LQI is used in this system. In the equation, P_{dBm} represents radio field intensity, and Q represents LQI.

$$P_{dBm} = \frac{7Q\text{-}1970}{20} \tag{1}$$

The LQI information is gathered in one antenna, and the position of the transmitter is estimated using a neural network learned beforehand.

2.2. *Neural Network*

As shown in Fig. 2, the neural network used in this system consists of an input layer, two intermediate layers, and an output layer. The number of input layers is 4 according to the number of receivers used in later experiments, the number of intermediate layers is 500 and 100, respectively, and the output layer outputs two coordinates because it outputs coordinates.

3. Experiments and results

3.1. *Confirm directionality*

Experiments were conducted to confirm that neither the transmitter nor the receiver had directivity. The transmitter and the receiver were installed at a distance of 10 m, and the radio field strength was measured while rotating the transmitter. The experimental results are shown in Fig. 3. From the figure, the measured value is shifted in the direction of 315 °, but this is considered to be due to a small inclination of the receiver, and it was confirmed that neither transmitter nor receiver has directivity.

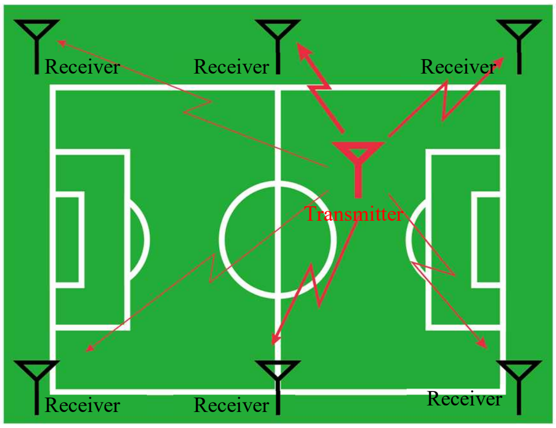

Fig. 1. System overview

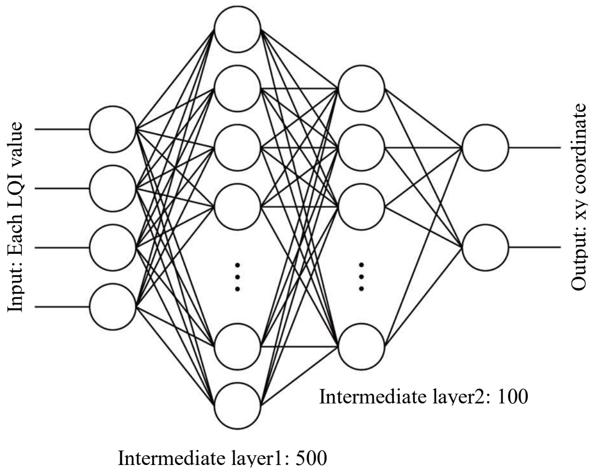

Fig. 2. Neural Network

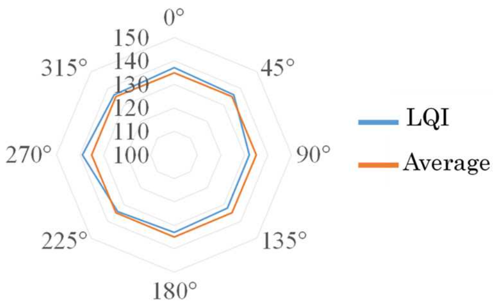

Fig. 3. Directionality

3.2. *Relationship between the distance and the radio wave intensity*

In order to confirm the relationship between the distance and the radio wave intensity, the radio field intensity was measured every 1 m from 1 m to 100 m for the transmitter and the receiver. The measurement result is shown in Fig. 4. The LQI value decreases as the distance increases, and it decreases while bouncing. It is thought that this is caused by fading due to reflection to the ground. Since fading occurs not only due to the ground but also due to walls, it is difficult to express it by mathematical formulas including all causes. Therefore, we decided to estimate the position by learning the radio field strength including the influence of fading using the neural network.

3.3. *Position estimation*

As shown in Fig. 5, the receivers (R_1 to R_4) were installed at the four corners of the half of the field, the fields were divided into meshes with intervals of 10[m], and the radio field intensity at each point was measured. Since the measurement range is bilaterally symmetrical, it is set as a half area surrounded by a broken line. 50 samples were taken at each point. The relationship between LQI and coordinates was learned using the neural network shown in Fig. 2. Normalization was performed by dividing by the value (160) which is larger than the maximum value of the measured LQI by using the LQI of the signal received by each receiving antenna. The coordinates were also divided by 70 to normalize. Therefore, the output is multiplied by 70 to output coordinates. 40 samples at each point were used for learning and the remaining 10 samples were used as unlearned data to confirm the learning result. Therefore, since there are 24 measuring points, 960 samples of learning data and 240 samples of unlearned data are obtained. In addition, the learning rate was 0.01, learning was done with batch learning, and learning was done using 10 random samples. The transition of the learning error is shown in Fig. 6. The CPU of the used PC is Core i5-4300 U (1.9

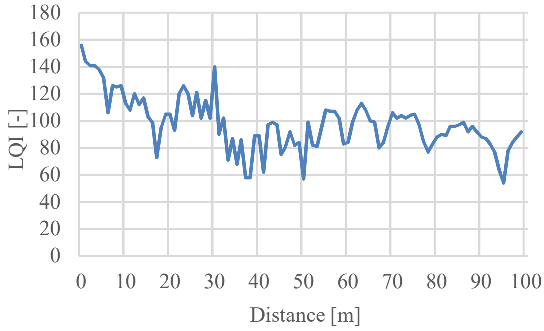

Fig. 4. Relationship between the distance and the radio wave intensity

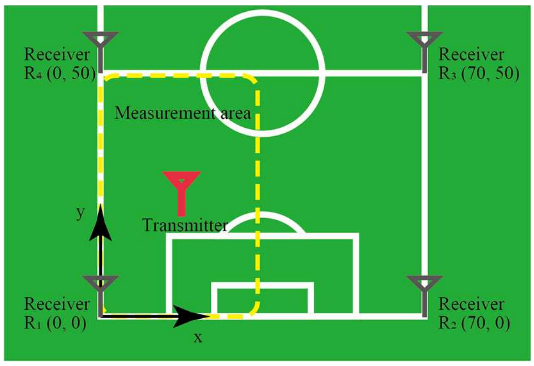

Fig. 5. Receiver position

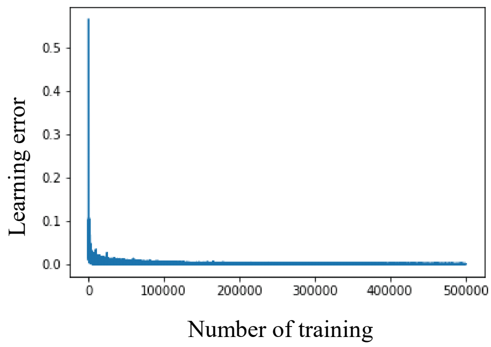

Fig. 6. Transition of the learning error

Table 2. Maximum error and average error

Number of training	x-axis error (maximum) [m]	y-axis error (maximum) [m]	x-axis error (average) [m]	y-axis error (average) [m]
50000	4.79	2.51	0.99	0.85
100000	4.01	2.67	0.53	0.58
500000	1.46	1.47	0.22	0.38

GHz - 2.5 GHz). Also, the learning time was 951 seconds at 500,000 times. We obtained the result of inputting unlearned data to the learned neural network. Fig. 7 shows the results when the learning number is 500000 times. In the figure, the true value is indicated by a blue square and the estimated value is indicated by an orange triangle. Also, the dispersion at each point is indicated by a bar. The dispersion tended to increase at the center of the field far from the receiving antenna. Table 2 shows the maximum error and average error depending on the number of learning. It is understood that the error decreases as the number of times of learning increases. Also, the average error is within 0.5m. In this experiment, we cannot verify the interpolation by the neural network, but not only the measured points but also the coordinates between the measured points should be able to be estimated, so confirmation is necessary.

4. Conclusion

In this research, the location was estimated from radio field intensity using a compact radio module. By using a neural network for estimation, we were able to estimate the position without concern for complicated fading effects. Good results were obtained, such as estimation with an error within 0.5 m with a learning number of 500000, using a 3-layer neural network with an intermediate layer of about 500. In addition, since we conducted experiments only in a quarter of the football field this time we want to do it in the whole area next time. And, I would like to improve position estimation accuracy by increasing the number of receivers. When this system is moved to another field, the influence of fading varies, so it may be considered that it does not work well. However, we believe that the neural network that has learned sufficiently can shorten the additional learning time in the destination field. I would like to examine the shortening of learning time from now on.

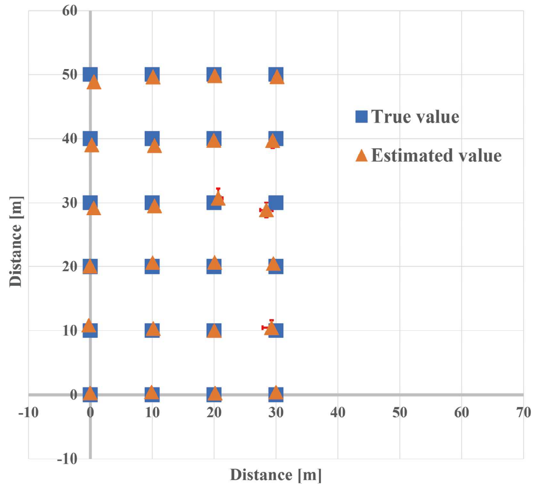

Fig. 7. Experiments result

References

1. Robert Bosch GmbH, BOSCH Automotive Handbook, p.1116, 2007.
2. Erin-Ee-Lin Lau and Wan-Young Chung, Enhanced RSSI-Based Real-Time User Location Tracking System for Indoor and Outdoor Environments, *2007 International Conference on Convergence Information Technology*, 2007.
3. Oziel Hernandez, Varun Jain, Suhas Chakravarty and Prashant Bhargava, Position Location Monitoring Using IEEE® 802.15.4/ZigBee® technology, *Beyond Bits*, Issue 2 Summer 2009, pp. 67-73, 2009.

Report of the 4th Tomato Harvesting Robot Competition

Takayuki Matsuo
National Institute Technology, Kitakyushu College
2-20-1, Shii, Kokuraminami-ku, Kitakyushu-shi, Fukuoka, Japan

Takashi Sonoda and Yasunori Takemura
Nishinippon Instituite of Technology
1-11Aratsu, kanda-tyo, Miyako-gun, Fukuoka, Japan

Masanori Sato
Nagasaki Institute and Applied Science
536, Aba-matchi, Nagasaki-Shi, Nagasaki, Japan

Kazuo Ishii
Kyushu Institute of Technology
2-4, Hibikino, Wakamatsu-ku, Kitakyushu-shi, Fukuoka, Japan

E-mail: matsuo@kct.ac.jp, sonoda@nishitech.ac.jp, takemura@nishitech.ac.jp, ishii@brain.kyutech.ac.jp
http://www.lsse.kyutech.ac.jp/~sociorobo/ja/tomato-robot2017

Abstract

Tomato is one of important fruit vegetables and most tomatoes are produced in the greenhouses, or large scale farms, where the high temperature and humidity, and long harvest age force the famers heavy works. In this paper, we report on the results of 4th tomato harvesting robot competition.

Keywords: robots for socio synthesis, robot competition and agriculture robot

1. Introduction

Recently, the aging and depopulation of famers grow worse in Japanese agriculture, as results the shortages of future famers and manpower become big problems. Tomato is one of important fruit vegetables and most tomatoes are produced in the greenhouses, or large-scale farms, where the high temperature and humidity, and long harvest age force the farmer heavy works.

As the research of tomato harvesting robots in Japan, Kawamura et. al. developed a mobile robot with manipulator[1] and proposed the tomato harvesting method using image processing and visual feedback[2][3]. Kondo et. al. proposed the method to improve the success ratio of tomato harvesting and speed-up technique[4][5]. Ota et. al. proposed the path planning method to pick up tomato[6].

We organized the tomato harvesting robot competition for an aim to promote the automation of tomato harvesting until 2014. In this paper, we will report on the result of the 4th tomato harvesting robot competition.

2. Competition regulations

The tomato harvesting robot competition consists of two leagues which are he Senior League and the Junior League. The target competitors for Senior League are supposed to the team with automated and remote-controlled robots, and the Junior League are for high school or junior high school students who build robot using LEGO Mindstorm. In this section, competition regulations of both reargues will be introduced.

2.1. *Senior League*

The Senior League supposes that teams composed of undergraduate, graduate students or developers join the competition with their tomato harvesting robots. Two kind of competition field are designed, the one is rail-style area and the another one is fee-style area as shown in Fig.1 and Fig.2. The rail-style area is designed to have the similar environment with the tomato factory. Free-style area is for the robots of general tomato fields in outdoor environment. Tomatoes are set on height from 800mm to 1200mm. The required specification of tomato harvesting robot is shown in Table 1. In first stage, a tomato is suspended as shown in Fig.3 and the team is able to advance to the second stage when an end-effecter of the robot is able to touch the tomato. In second stage, a bunch of tomato is suspended as shown in Fig.4. Teams compete with each other for the harvesting number of the tomato. Even if the robot can harvest many tomato, the score of the team is added to the score when the tomato has no damage. However, When the tomato harvested by the robots are not redder than a tomato shown by an executive committee, and the basic point of the team is decided. Final score of second stage is the score multiplied the basic score and the coefficient decided by a combination of choice between the control method which are remotely and autonomous control and the areas which are the rail area and the free style area. The five highest team can advance to the final stage. In final stage, the robots harvest tomato from plant body as shown in Fig.5.

Table 1 Specifications of a robot

Size	W:800mm D:800mm (H: No limitation)
Equipment	Emergency stop switch
Weight	Max. 50kg (recommend)
Motor Power	Max. 70W (recommend)

Fig.1 Free-style area

Fig.2 Rail-style area

Fig.3 1st Stage

Fig.4 2nd Stage

Fig. 5 Final Stage

2.2. *Junior League*

In Junior League, we have selected an autonomous transport system of tomato harvesting robot as the subject of Junior League. Students should develop the robot using LEGO Mindstorm. Competition subjects include Line Trace Challenge, Color Identify Challenge, Mechanism Design and Control Challenge and Object Detection Challenge. In Line Trace Challenge, robots should detect white line in the competition area and move along the line using a color sensor. The robot starts from the starting point. In the middle of the course, the tomato-box- harvesting field (harvest field) exists, where tomato boxes are arranged. The robot must move to the harvest field in order to get the tomato boxes. In Color Identifying Challenge, robots should explore and recognize color signs in the middle of the course and the same color of three boxed tomatoes (tomato box). As guidance to harvest field, red, yellow and blue lines are drawn in the field. It is necessary for the robots to detect guidance line by color sensor. The robot gets the tomato boxes of the same color. Along the white line for line trace, each color is signed. The robot can move to the harvest field from the lone detecting the color. In Mechanism Design and Control Challenge, robot should manipulate a tomato box using manipulator and carry to the storage location. To pick up the tomato box by using a manipulator equipment which is made by each team, participants are expected to design and make a device to get a tomato box on their idea. The robot is required to store, transport and relocation depending on tomato box colors. After picking up the box, the robot should return to the course. Then, the robot carries the box to the specific storage location of the tomato box. In Object Detection Challenge, robots should detect a battery charging station and stop there. Each team consists of 3 or 4 students and make a robot using LEGO Mindstorms EV3 and also do robot programming for solving the competition subjects. The basic specification for robot is that the size of the robot is within 300mm x 300mm on ground.

3. Result of 4th tomato harvesting robot competition

Teams which could proceed to final stage are 5 teams including Hibikinno Toms's R (Category T5, Kyushu Institute of Technology), Nagasaki GANBARANBA (Category T4, Nagasaki Institute of Applied Science), KPC2017A, KPC2017B (Category T5, Kyushu Polytechnic college) and HAYASHI-LAB (Category T5, Kyushu Institute of Technology). 1st place of rail-style division is HAYASHI-LAB, 2nd place is Hibikino Tom's R and 3rd place KPC2017A 1st place Nagasaki GANBARANBA as the result of free-style. 2nd and 3rd are no eligible teams. Finally, Overall winner is HAYASHI-LAB and Overall runner-up is Hibikino-Tom's R.In Senior League, number of the participated teams were 18 teams and the result is Table 5 and Table 6

Table 2 Final result of the Senior League

Ranking	Team
Overall winner	HAYASHI-LAB
Overall runner-up	Hibikino-Tom's R

Table 3 Result of rail-style division

Ranking	Team
1st place	HAYASHI-LAB
2nd place	Hibikino-Tom's R
3rd place	KPC2017 A

Table 4 Result of free-style division

Ranking	Team
1st place	Nagasaki GANBARANBA
2nd place	-
3rd place	-

Table 5 Result of rail-style division

Ranking	Team
1st place	Ohnishi lions (Fukuoka Technical Hischool
2nd place	Ooita kogyo C(Ooita Technical High School)
3rd place	NiAScience (High school attached Nagasaki Institute of Appied Science)

Table 6 Special award

Ranking	Team
Best presentation award	J-Tech2 (Joto high school)
Special Jury Award	Team ROSA (Ooita Technical High School)
Challenge award	Team Daiichi (Fukuoka Daiichi High School)

4. Discussion

In Senior League of 4th tomato harvesting robot competition, scores are evaluated as shown in Eq.(1)

$$P = C(2\alpha + \beta) - 2(\gamma + \delta) - \varepsilon \qquad (1)$$

, where P is score, C is coefficient of magnification depending on selecting class as shown in Table Ta, $\alpha$is the number of tomatoes which is no damaged and correct color, β is the number of damaged tomatoes, γ is the number of drop tomatoes and γ is the number of damaged tomatoes which are not harvested. ε is a deducted point when robots damage stalks of tomato plants and the point is deducted in Final Stage. However, if the teams select high class such as T5 and T6, Total score P is almost not influenced from γ, δ and ε. This means that teams selected high class can get high score if robot damage tomatoes and drop tomatoes. In actual tomato factory, damaged tomatoes and drop tomatoes have no commercial value. Therefore, famer need to treats tomatoes with care. In next competition, we will employ concept of carefully dealing with tomatoes. We proposed new equation for next competition as shown in Eq.(2).

$$\boldsymbol{P} = \frac{\alpha}{\alpha+\beta+\gamma+\delta}\boldsymbol{C}(2\boldsymbol{\alpha}+\boldsymbol{\beta}) - 2(\boldsymbol{\gamma}+\boldsymbol{\delta}) - \boldsymbol{\varepsilon} \qquad (2)$$

Equation (2) is employed harvest rate and if robot damage and drop tomatoes magnification C is decreased.

Table 7 The class number and coefficient at choosing remote control

Method of View	Directly		Indirectly	
Area	Rail	Free	Rail	Free
Number of Category	T1	T2	T3	T4
Coefficient C	1	2	2	4

Table 8 The class number and coefficient at choosing autonomous control

Area	Rail	Free
Number of Category	T5	T6
Coefficient C	8	16

5. Conclutions

In this paper, Tomato robot competition for robot socio-synthesis was introduced. The tomato harvesting robot competition has two leagues which are Senior League and Junior League. In Junior League, number of the participated teams were 18 teams. In Senior League, number of participated team 9 team. In next competition, concept of carefully dealing with tomatoes will be employed and we proposed new equation employed harvest rate and if robot damage and drop tomatoes magnification C is decreased.

Acknowledgements

This works was supported by Kyushu Institute of Technology, Center for Socio-Robotics Synthesis, The University of Kitakyushu, Nippon Bunri University, Nishinippon Institute of Technology(This support was including The Ministry of Education, Culture, Sports, Science and Technology(MEXT), Center of Community), Kitakyushu College of Technology, Hibikinada-Saien, City of Kitakyushu, The Kitakyushu Chamber of Commerce and Industry, Institute of Systems, Information Technologies and Nanotechnologies (ISIT), Japan Chapter of IEEE Society on Systems, Man, and Cybernetics, The Japan Society of Mechanical Engineers(JSME), The Robotics Society of Japan(RSJ), Kitakyushu Foundation for the Advancement of Industry Science and Technology (FAIS), IT and Mechatoronics Chapter and Kyushu Chapter of Japanese Society of Agricultural Machinery and Food Engineers, The MathWorks Co. Ltd., and Ministry of Agriculture, Forestry and Fisheries(MAFF).

References

1. Kawamura et. al. Study on agricultural robot (1st report), *The journal of JASM*, vol. 46 No.3, pp.353-358, 1984 in Japanese
2. Kawamura et. al. Study on agricultural robot (2nd report), *The journal of JASM*, vol.47 No. 2, pp.177-182, 1985 in Japanese
3. Kawamura et. al., Fruit harvesting robot, *The journal of JASM*, vol.47 No.2, pp. 237-241, 1985 in Japanese
4. Kondo, et.al., A Machine Vision System for Tomato Cluster Harvesting Robot, *Engineering in Agriculture, Environment and Food*, Vol. 2, No. 2, pp.60-64, 2009
5. Kondo, et.al, Development of an End-Effector for a Tomato Cluster Harvesting Robot, *Engineering in Agriculture, Environment and Food*, Vol. 3, No. 1, pp.20-24, 2010
6. Ota et. al., Development of a Tomato Harvesting Robot with a Vision System Using Specular Reflection (Part 1), *the journal of JASM*, vol. 72 No.6, pp.595-603, 2010
7. Ota et. al., Development of a Tomato Harvesting Robot with a Vision System Using Specular Reflection (Part 1), *the journal of JASME*, vol. 72 No.6, pp.587-594, 2010

End-effector for robotic harvesting of a tomato fruit with calyx

Bingh Li
Dept. of Human Intelligence Systems, Kyushu Institute of Technology
2-4 Hibikino, Wakamatsu, Kitakyushu, Fukuoka, 808-0196, Japan
E-mail: li-binghe@edu.brain.kyutech.ac.jp

Shinsuke Yasukawa
Dept. of Human Intelligence Systems, Kyushu Institute of Technology
2-4 Hibikino, Wakamatsu, Kitakyushu, Fukuoka, 808-0196, Japan
E-mail: s-yasukawa@edu.brain.kyutech.ac.jp

Takuya Fujinaga
Dept. of Human Intelligence Systems, Kyushu Institute of Technology
2-4 Hibikino, Wakamatsu, Kitakyushu, Fukuoka, 808-0196, Japan
E-mail: s-yasukawa@edu.brain.kyutech.ac.jp

Kazuo Ishii
Dept. of Human Intelligence Systems, Kyushu Institute of Technology,
2-4 Hibikino, Wakamatsu, Kitakyushu, Fukuoka, Japan
E-mail: ishii@brain.kyutech.ac.jp

Abstract

Tomato fruit harvesting is a labor-intensive process, and therefore robotic automation is required. For tomato fruit harvesting robot, we developed three types of end-effectors (EEs): scissor type, cylinder type and suction-cutting type. It is necessary to harvest the tomato fruit with calyx especially in Japan. Therefore, the proposed EE has a cutter mechanism for cut the peduncle. The results show that the scissor type and the cylinder type EE can cut the peduncle; however, it is difficult to separate one fruit from the cluster. On the other hand, the suction-cutting type can separate and cut one fruit from the cluster and therefore it is useful for harvesting tomato fruit with calyx.

Keywords: *Tomato-Harvesting Robot, End-effector, Cutting, Suction*

1. Introduction

Population of workers in agricultural field in Japan has been drastically decreasing each year from 260,600 in 2010 and 2097,000 in 2015[1]. The primary industries have also been suffering from population aging due to high rate of departure of young workers. Various agricultural machines have been introduced to solve the labor shortage and the increase in burden on agricultural workers so far. In recent years, the introduction of new technologies such as robot to the primary industry has become essential, and has high expectations from agricultural site. Among various agricultural crops, tomatoes require a long harvesting work time and high labor load. Therefore, automation for harvesting by robots is desired. In this research, we develop a tomato harvesting robot aiming at practical application at Hibikinada vegetable garden Co., Ltd. for the first time at a tomato production facility with large infrastructure.

In this paper, we focus on the tomato harvesting end effector and describe the development of a harvesting mechanism capable of harvesting tomato containing the calyx.

2. Related Researches

In the fruit harvesting robot, the end effector makes direct contact to fruit. Various types of mechanisms are being introduced to safely harvest, without damaging both the stem and the fruit. For example, there is a mechanism that cuts fruit pattern by electric burning method and harvests [2]. Some mechanisms utilize the characteristics of tomatoes taken out from abscission layer and pick off from the cluster [3]. Suction method can be added to pull a single fruit and pick off with fingers [4]. Other mechanisms cut each tassel with a blade [5] [6], which can also be combined with suction [7]. From these studies, the harvesting mechanism can be divided as follows, and the end effector is developed with reference to these methods.
1) Fruit harvesting method: peeling type, cutting type.
2) Fruit guiding method: finger type, sucker type, suction type.

3. Work condition and Target tomato

3.1. *Work condition*

Hibikinada vegetable garden Co., Ltd. is a large-scale indoor vegetable garden (Fig.1). Tomatoes are cultivated in a system that can be harvested for a long time. The harvestable tomatoes are adjusted to about 0.8 m to 1.2 m in height and the leaves between them are removed for easy access to the fruits. There is a rail between tomato plants where workers performs work while using dollies. The target tomato in this study is medium size tomato.

3.2. *Tomato with calyx*

There are two types of harvesting tomato. One is to harvest a cluster of tomato and another to harvest each fruit one by one. In countries that produce a large amount of tomato such as Netherlands, many tomatoes are sold in clusters. However, in Japanese market, single fruits with the calyx attached are preferred. In fact, the condition of the calyx indicates freshness of the fruit. Therefore, it is essential to preserve each fruits' calyx when harvesting.

Fig. 1 Hibikinada vegetable garden Co., Ltd. and harvesting tomato with calyx

4. Harvesting robot and End-effector system

4.1. *Harvesting robot system*

The developed robot is shown in Fig. 2 The robot consists mainly of a manipulator, a moving cart, a camera, an end effector and a control PC.
In the harvest flow, the carriage moves on the rail until a desired tomato is detected from the image obtained by the camera. When finding the tomato it stops, the manipulator moves to the measured tomato position, and a single fruit is harvested from the cluster by the end effector.

4.2. *End-effector system*

Following is considered to be requirement of end effector for harvesting tomato.
① All tomato must include the calyx in order to maintain its full value.

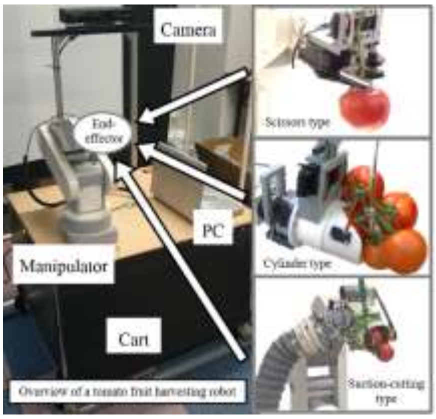

Fig. 2 Overview of tomato harvesting robot and End-effectors

② A single frit must be harvested at a time.
③ The mechanism must not damage any part of the plant or fruit during and after harvesting.
As a way to realize ①, there is picking off and cutting of peduncle. The picking off method is designed to separate fruit and peduncle at the part of abscission layer, but there is a possibility of damaging calyx. Therefore, cutting is desirable to ensure the harvesting of fruits with a calyx. Since there are several methods to realize ②, we developed three types of prototype harvesting mechanism.

4.3. *Scissor type*

The appearance and operation principle of the scissor type are shown in Fig.3. This end effector consists of fingers and rotary blades, a DC motor and a servomotor that drive them. The rotary blade rotates from the DC motor via a pulley and a timing belt. The fingers are opened and closed by a servomotor using a link mechanism.
The fingers are divided into top and bottom, during which there is a gap through which the rotary blade can enter when the finger is closed. The upper finger is made into a shape that makes it easier to take the peduncle up to the position of the rotary blade. The lower finger can grasp the peduncle with the base part from the moment of cutting.

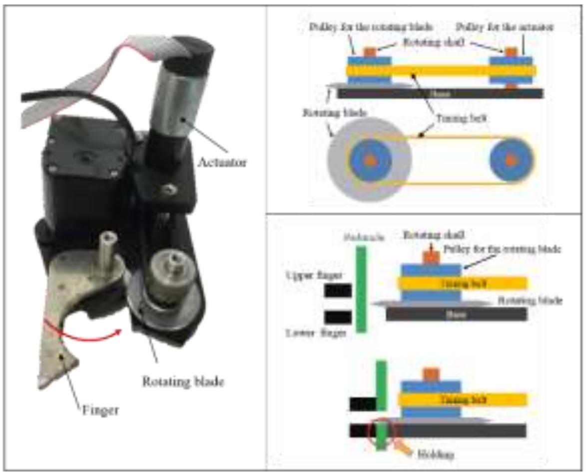

Fig. 3 Overview of scissor type and mechanism

4.4. *Cylinder type*

The appearance and operation principle of the cylinder type are shown in Fig.4. This type consists of a fixed cylinder and a rotating cylinder. The rotary cylinder has a function of moving by the motor and cutting the peduncle.

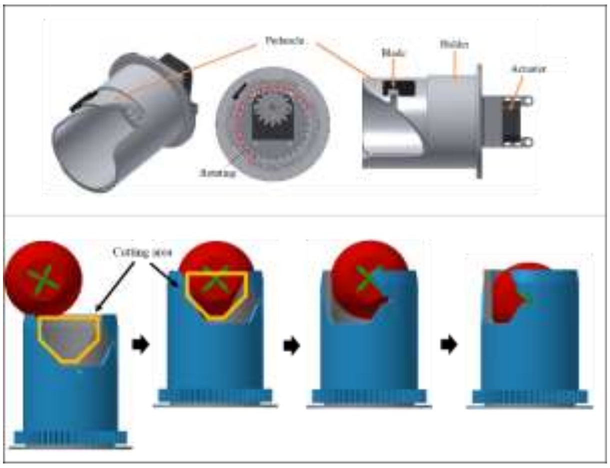

Fig. 4 Overview of Cylinder type and mechanism

As shown in the Fig.4, there is a cutting area in the upper part of the cylinder, and it has a shape that can guide the peduncle to the cut section. By pressing the cylinder against the cluster, the tomato fruit enters the cylinder. At that time, since the peduncle also enters the cutting area, it is possible to harvest the fruit by cutting the peduncle by rotating the cylinder.

4.5. *Suction-cutting type*

The appearance and operating principle of the suction-cutting type are shown in Fig.5 and Fig.6. This type consists of a suction port, a finger with a U-shaped blade, a suction hose and a suction device.
EDF Ducted fan for radio control is used for suction device. It has an inner diameter of 69 mm and a maximum of approximately 2.65 kg. The EDF and the

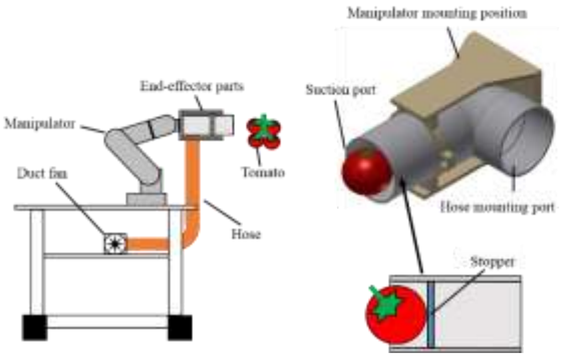

Fig. 5 Overview of Suction-cutting type

end effector are connected by a hose. The diameter of the tomato to be harvested was about 65 mm at the maximum, and the suction part at the tip was set to 72 mm, which is the size that can tomatoes can be drawn.
This system utilizes suction force to separate a single fruit from a cluster and hold it in position for cutting. A stopper is installed in the suction port to prevent separation of the fruit and its calyx and stopping it from entering further into suction hose.
When the tomato is in place, the peduncle is cut by rotating the U-shaped blade-attached finger as shown in Fig.6.

5. Conclusions

In this paper, we described three prototypes of end effectors. All three types of mechanism are proven to be able to harvest the tomato fruit with the calyx attached. However, figure type requires more accurate image processing and precision manipulation due to the difficult in pinpointing the exact place on peduncle from cluster of tomatoes. It is relatively easier to harvest using cylinder type, however, some tomato may fail to enter into the cylinder due to the structure of the cluster. Therefore, we found that a mechanism that can actively separate tomatoes like suction cut type is necessary.
For further studies, it is essential to examine each type of end effectors and consider the optimal harvest approach with consideration of their characteristics.

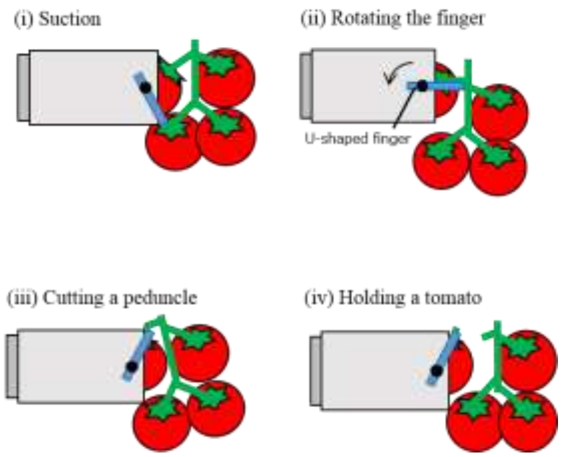

Fig. 6 Suction-cutting mechanism

References

1. http://www.maff.go.jp/j/tokei/index.html
2. Kollenburg-Crisan, L. M. V, et al, Robotic systems for cutting fruit and leaves in greenhouse, *Proceedings of Workshop on European Scientific and Industrial Collaboration*, pp.113~122, Netherlands (2001)
3. Shumpei Uegaki, Hidekazu Araki, Ryo Toshima, Makoto Shinzaki, Daisuke Ueta, Ryuji Yamazaki, Tomato-Harvesting Robot using AI for Environment Recognition, *Panasonic Technical Journal*, Vol. 64, No. 1, May 2018
4. M. Monta, et.al., “End-Effectors for Tomato Harvesting Robot”, *Artificial Intelligence Review*, Vol. 12, Issue 1, pp.11-25, 1998
5. Kondo, N., Yata, K., Iida, M., Shiiji, T., Monta, M., Kurita, M., Omori, H., Development of an End-Effector for a Tomato Cluster Harvesting Robot, *Engineering in Agriculture, Environment and Food*, 3(1), (2010), 20-24
6. Qingchun Feng, Wei Zou, Pengfei Fan, Chunfeng Zhang, Xiu Wang, Design and test of robotic harvesting system for cherry tomato, *International Journal of Agricultural and Biological Engineering*, vol 11, No 1(2018), 96-100
7. Arima, S. et al. Harvesting robot for strawberry grown on table top culture. (Part 1) Harvesting robot using 5 DOF manipulator. *J. SHITA*, 13(3), 159-166, 2001

Evaluation for Ball Dribbling Mechanism of RoboCup Middle Size League Soccer Robot in The World Teams

Kenji Kimura, Shota Chikushi, Kazuo Ishii

Department of Human Intelligence Systems
Kyushu Institute of Technology
2-4 Hibikino ,Wakamatsu-ku, Kitakyushu, Fukuoka, 808-0196 Japan
E-mail: kimura_kenji@edu.brain.kyutech.ac.jp,

Abstract

RoboCup is a platform designed to promote such research fields as artificial intelligence (AI) and robotics. In recent years the Middle size league soccer robot has a ball dribbling mechanism. This mechanism controls the ball with two driving rollers and in order to play soccer games well, ball control capability and holding capacity are indispensable. As the result of a survey at the 2017 World Cup, all teams in the world have determined the rollers arrangement heuristically, and no mathematical consideration has been made. In this research, we focus the sphere slip velocity and derive relationship sphere slip speed and sphere mobile speed. and evaluated the roller arrangement in the world teams.

Keywords: *The ball dribbling mechanism, sphere slip velocity, dynamical friction*

1. Introduction

RoboCup is an international project that promotes AI, robotics, and related domains. It is an attempt to develop AI and autonomous robotics research by providing a fundamental problem where a wide range of technologies can be integrated. Even among then, Middle Sized League soccer competition makes a goal in the dynamical environment where many robots corporate with the human in same space.

In recent years, the world teams have mounted a ball dribbling mechanism for controlling the rotation of the ball. Their performances have to be good in order to win in competition. The rollers are arranged on the upper half of the ball, enabling them to keep pulling on the ball when driving reverse. A friction between the ball and rollers generated by spring in lever supporting roller get the ball toward the robot. When the robot is dribbling with the ball, it is required that the roller rotate in the ball has approximately the same speed and moves in the same direction as the robot.

The authors conducted an investigation of the ball dribbling mechanisms of the world teams (2017 Nagoya in Japan). **Table 1** shows the investigation results such as team name, symbol (pair of figure and team’s initial letter), roller types and roller arrangement angle. **Fig. 1** shows rollers axis arrangement patterns with respect to plane including two contact points and center of sphere. As show in

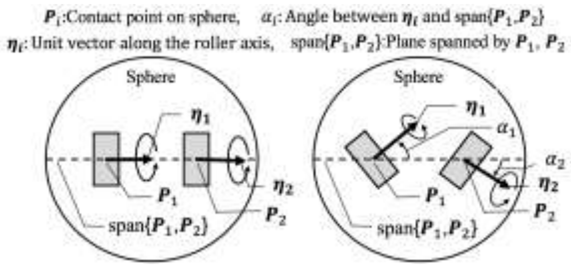

(a) Case of $|\alpha_i| = 0°$ (b) Case of $|\alpha_i| > 0°$

Fig. 1 Two rollers arrangement in ball dribbling mechanism

Table 1 Roller type and angle in world teams

Team name	Symbol	Roller type	$\lvert\alpha_i\rvert$
RV-infinity[1]	■R	constraint	0°
Tec United Turtles[4]	●T	constraint	10°
Falcons	●F	constraint	10°
Hibikino-Musashi[5]	▲H	constraint	20°
NuBot[6]	▲N	constraint	20°
Water	◆W	constraint	30°
CAMBADA[3]	−	unconstraint	50°

Fig.1(a), RV-Infinity[1] is adopted non-slip roller arrangement as $|\alpha_i| = 0°$. Because it is condition that two rollers axes are on the same plane (See[2]). On the other hand, as show in Fig.1 (b), the others teams are adopted slip roller arrangement as $|\alpha_i| > 0°$. Because it is condition that two rollers axes are not on the same plane (See[2]). But, CAMBADA[3] doesn't cause slip by using unconstraint rollers(omni-rollers).

Most of the teams including Tec United Turtles[4], Hibikino-Musashi[5] and NuBot[6] and focus ball Handling force and discuss roller arrangement. However, they discuss it without slip and determine roller arrangement by experiments, heuristically. Slip can cause sphere mobile speed efficiency loss. But, it can cause friction and improve ball holding force and sphere rotational stability. In this way, both are related to transactions and slip thought to be important factor for ball holding force.

In this study, we focus to sphere slip velocity with respect to rollers and reveal relationship sphere slip speed and sphere mobile speed on horizontal plane in backward movement and evaluate the roller arrangement in the world teams by experiment using device robot.

2. The sphere rotational motion by two constraint rollers

In this chapter,using sphere angular velocity vector allow for slip caused by two constraint rollers, we calculate sphere slip velocity and sphere mobile speed.

2.1 *The sphere angular velocity vector by two constraint roller allow for slip*

As show in **Fig. 2**, the sphere which have radius r and center $\boldsymbol{O}$ is fixed as origin of coordinate system $\Sigma - xyz$. *i-th* constraint roller is contacted with sphere at the position vector $\boldsymbol{P_i}$, and *i-th* roller is arranged such that mass of roller, $\boldsymbol{P_i}$ and $\boldsymbol{O}$ are on the same line. $\boldsymbol{\omega}$ denotes the sphere angular velocity vector. $\boldsymbol{\eta_i}$ denotes the unit vector along *i-th* roller's axis. α_i $(-90° \le \alpha_i \le 90°)$ denotes roller arrangement angle between $\boldsymbol{\eta}_i$ and $\mathbf{span}\{\boldsymbol{P_1}, \boldsymbol{P_2}\}$ (see Fig.1). When peripheral speed v_1 and v_2 are given. $\boldsymbol{\omega}$ can be represented by eq.(1).

$$\boldsymbol{\omega} = \frac{1}{\sqrt{r^4 - \langle \boldsymbol{P}_1, \boldsymbol{P}_2 \rangle^2}}[(v_2 \cos\alpha_2)\boldsymbol{P_1} - (v_1 \cos\alpha_1)\boldsymbol{P_2}] + \frac{v_1 \sin\alpha_1 + v_2 \sin\alpha_2}{2r}\frac{\boldsymbol{P}_1 \times \boldsymbol{P}_2}{\|\boldsymbol{P}_1 \times \boldsymbol{P}_2\|} \quad (1)$$

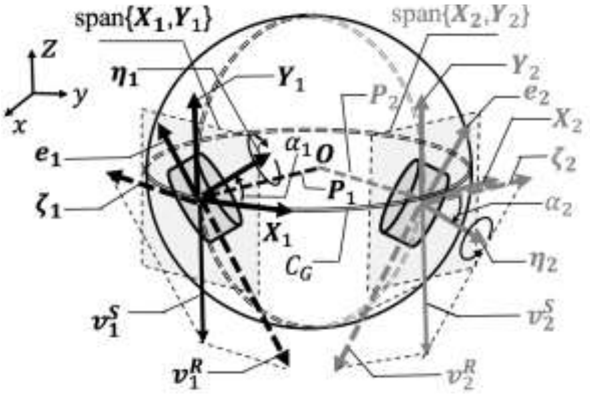

Fig. 2 Variables related to sphere rotational movement

Where

$$\boldsymbol{P_i} = r\left[\cos\theta_{1,i} \cos\theta_{2,i}, \sin\theta_{1,i} \cos\theta_{2,i}, \sin\theta_{2,i}\right]^T \quad (2)$$

2.2 *The sphere slip velocity and sphere mobile speed*

In each roller, slip occurs when two contacting surfaces (roller and sphere) move such that the roller velocity $\boldsymbol{v_i^R}$ and the sphere velocity $\boldsymbol{v_i^S}$ at the tangent plane at point $\boldsymbol{P_i}$ are different (See Fig. 2). $\boldsymbol{e}_i$ denotes unit vector along roller velocity. Using $\boldsymbol{\omega}$, sphere slip velocity $\boldsymbol{\zeta_i}$ which is relative speed with respect to $\boldsymbol{v_i^R}$ can be represented by eq.(3).

$$\boldsymbol{\zeta_i} = \boldsymbol{v_i^S} - \boldsymbol{v_i^R} \quad (3)$$

Where

$$\boldsymbol{v_i^R} = v_i\boldsymbol{e_i}\ ,\ \ \boldsymbol{v_i^S} = \boldsymbol{\omega} \times \boldsymbol{P}_i \quad (4)$$

$\boldsymbol{X_i}$ is tangential unite vector of great circle $\boldsymbol{C_G}$(pass through $\boldsymbol{P}_1$ and $\boldsymbol{P}_2$), $\boldsymbol{Y_i}$ is unit normal vector of $\mathbf{span}\{\boldsymbol{P_1}, \boldsymbol{P_2}\}$. $\boldsymbol{\zeta_i}$ can be represented as linear combination of $\boldsymbol{X_i}$ and $\boldsymbol{Y_i}$ as follow.

$$\boldsymbol{\zeta_i} = S_i\boldsymbol{X_i} + T_i\boldsymbol{Y_i} \quad (5)$$

Where

$$S_i = \langle \boldsymbol{\zeta_i}, \boldsymbol{X}_i \rangle, \quad T_i = \langle \boldsymbol{\zeta_i}, \boldsymbol{Y}_i \rangle \ \text{[m/s]} \quad (6)$$

Thus. $\|\boldsymbol{\zeta_i}\|$ can be calculated by eq.(7).

$$\|\boldsymbol{\zeta_i}\| = \sqrt{S_i^2 + T_i^2} \ \text{[m/s]} \quad (7)$$

And. Using components ω_x, ω_y of $\boldsymbol{\omega}$, norm of sphere mobile velocity $\boldsymbol{V}$ on the xy-plane (horizontal plane) can be represented by eq.(8).

$$\|\boldsymbol{V}\| = r\sqrt{\omega_x^2 + \omega_y^2} \ \text{[m/s]} \quad (8)$$

Table 2 Target values in $v_1 = v_2 = -0.91$ [m/s]

$\lvert\alpha_i\rvert$	0°	10°	20°	30°
S_1 [m/s]	0	-0.16	-0.30	-0.41
T_1 [m/s]	0	0	0	0
S_2 [m/s]	0	0.16	0.30	0.41
T_2 [m/s]	0	0	0	0
$\lVert\boldsymbol{\zeta_1}\rVert$ [m/s]	0	0.16	0.30	0.41
$\lVert\boldsymbol{\zeta_2}\rVert$ [m/s]	0	0.16	0.30	0.41
$\lVert\boldsymbol{V}\rVert$ [m/s]	1	0.98	0.93	0.81

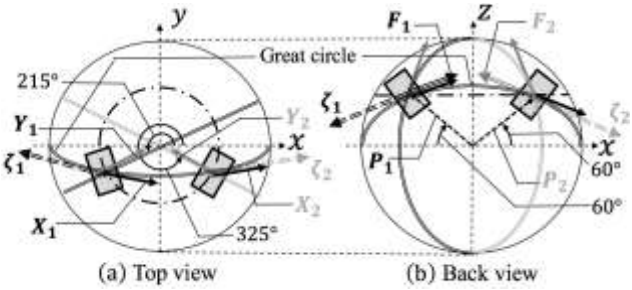

Fig. 3 Roller positions on sphere, existence of sphere slip vector and dynamical friction in backward movement

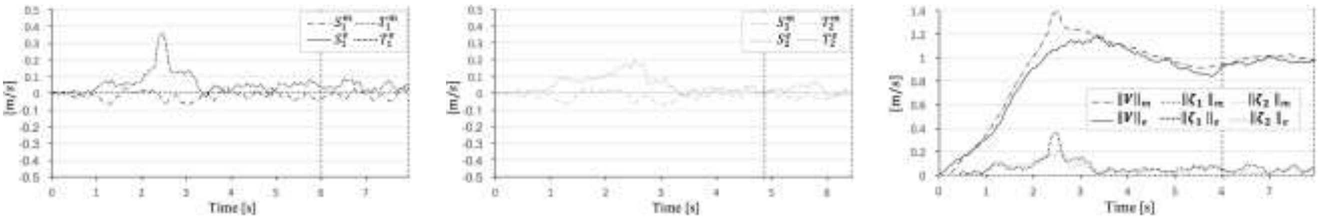

(a) Shpere slip velocity (left side roller) (b) Shpere slip velocity (right side roller) (c) Shpere mobile speed and slip speed

Fig. 4 Comparison theoretical value and experimental value case of $\lvert\alpha_i\rvert = 0°$

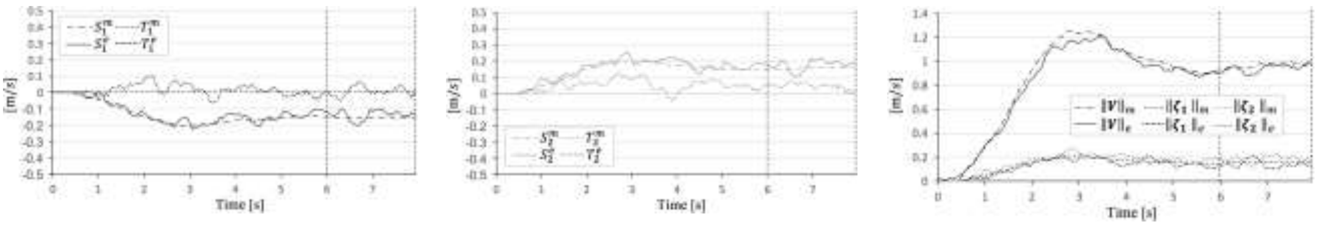

(a) Shpere slip velocity (left side roller) (b) Shpere slip velocity (right side roller) (c) Shpere mobile speed and slip speed

Fig. 5 Comparison theoretical value and experimental value case of $\lvert\alpha_i\rvert = 10°$

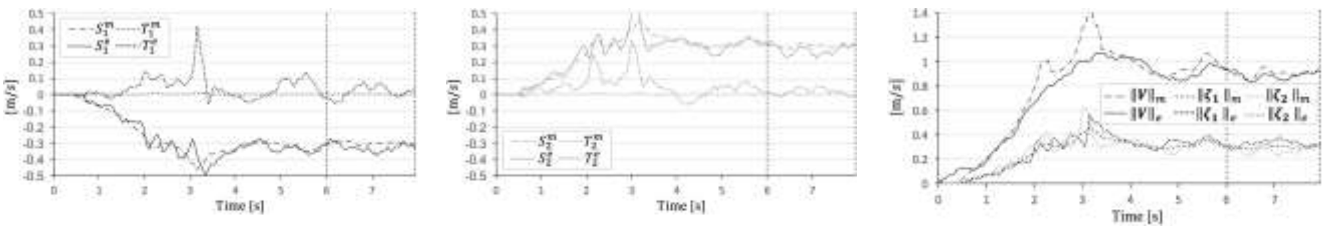

(a) Shpere slip velocity (left side roller) (b) Shpere slip velocity (right side roller) (c) Shpere mobile speed and slip speed

Fig. 6 Comparison theoretical value and experimental value case of $\lvert\alpha_i\rvert = 20°$

3. Experiment

In this chapter. Using device robot, we experimented to measure sphere mobile speed, sphere slip velocity to verify theoretical formula and consider distribution sphere slip velocity in backward movement. Finally, we evaluate world team's roller arrangement.

3.1 *Verify theoretical formula*

As show in **Fig. 3,** the conditions are given as follows: $\theta_{1,1} = 215°, \theta_{1,2} = 325°, \theta_{1,2}, \theta_{2,2} = 60°$, $r = 0.1$[m]. Five experiments were conducted, each at the same four different degrees angles (α_i= 0°, 10°, 20°, 30°) . As shown in **Table 2**, S_i , T_i, $\lVert\boldsymbol{\zeta_i}\rVert$ and $\lVert\boldsymbol{V}\rVert$ are ideal target values calculated using $v_1 = v_2 = -0.91[m/s]$ from eq.(6)(7)(8). **Fig. 4-6** are indicated theoretical data: S_i^m , T_i^m , $\lVert\boldsymbol{\zeta_i}\rVert_m$ $\lVert\boldsymbol{V}\rVert_m$ and experimental data: S_i^e , T_i^e, $\lVert\boldsymbol{\zeta_i}\rVert_e$, $\lVert\boldsymbol{V}\rVert_e$ (calculated in interval 0-8[s]).

In the evaluation of case ($\lvert\alpha_i\rvert = 0°, 10°, 20°$), S_i^e , T_i^e,

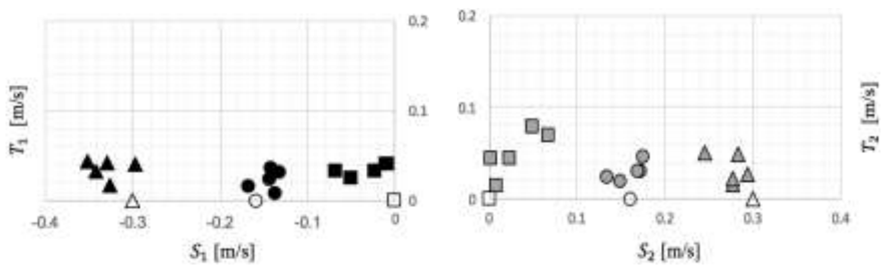

(a) End points of $\boldsymbol{\zeta_1}$ on $\mathbf{span}\{\boldsymbol{X_1}, \boldsymbol{Y_1}\}$ (b) End points of $\boldsymbol{\zeta_2}$ on $\mathbf{span}\{\boldsymbol{X_2}, \boldsymbol{Y_2}\}$

Fig. 7 The distribution of end points of sphere slip velocity

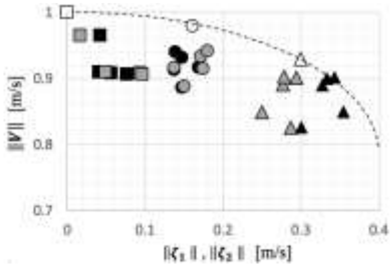

Fig. 8 Relationship sphere slip speed and sphere mobile speed

$\|\boldsymbol{\zeta_i}\|_e$ and $\|\boldsymbol{V}\|_e$ are close to S_i^m, T_i^m, $\|\boldsymbol{\zeta_i}\|_m$ and $\|\boldsymbol{V}\|_m$, respectively (see Fig. 4-6).

In the evaluation of $|\alpha_i| = 30°$, By limited motor drivers and influence of intense dynamical friction which caused between roller and sphere and roller surface could have heat. So, we had stopped the second and subsequent experiments. However, S_i^e, T_i^e, $\|\boldsymbol{\zeta_i}\|_e$ and $\|\boldsymbol{V}\|_e$ are close to S_i^m, T_i^m, $\|\boldsymbol{\zeta_i}\|_m$ and $\|\boldsymbol{V}\|_m$.

Therefore. The validity of theoretical formulas is verified.

3. 2 *Consideration of sphere slip velocity*

Theoretically, In case of $v_1 = v_2 = -0.91[m/s]$, $\boldsymbol{\zeta_1}$ and $\boldsymbol{\zeta_2}$ are tangent to great circle $\boldsymbol{C_G}$ pass thorough $\boldsymbol{P_1}$ and $\boldsymbol{P_2}$ on sphere from $T_1, T_2 = 0$ in Table 2). The validity of this fact is verified by experiment as follow.

Fig 7 shows distribution end point of sphere slip velocity $\boldsymbol{\zeta_i}$ on $\mathbf{span}\{\boldsymbol{X_i}, \boldsymbol{Y_i}\}$. The horizontal axis and the vertical axis show S_i and T_i, respectively. All the values show mean value of 6-8[s]. □○△ indicated as coordinate by using target values in Table 3. ■●▲ indicated as coordinate by using experimental mean values calculated in interval 6-8[s](See Table 1).

1) horizontal coordinate

In ■R , S_i^e are almost ± 0.04[m/s]. In ●T and ●F, S_i^e are almost ± 0.16[m/s]. In ▲H and ▲N, S_i^e are almost ± 0.30[m/s].

2) vertical coordinate

In all dates, T_i^e are almost 0.04[m/s] and close to zero. From **1), 2),** $\boldsymbol{\zeta_1}$ and $\boldsymbol{\zeta_2}$ are almost equal to tangential vector on great circle and turn round to outward (See Fig. 3). Therefore, the validity of the sphere slip velocity was verified. And, dynamical friction $\boldsymbol{F_i}$ are generated by $\boldsymbol{\zeta_i}$ in opposite direction. These can exert like grabbing ball (See Fig. 3(b)).

3. 3 *Evaluation of world teams' rollers arrangement*

Fig. 8 shows relationship sphere slip speed and sphere mobile speed. The horizontal axis and the vertical axis show $\|\boldsymbol{\zeta_i}\|$ and $\|\boldsymbol{V}\|$, respectively. Dotted line is theoretical curve.

1) vertical coordinate (mobile speed efficiency)

In ■R, ●T and ●F, Sphere mobile speed $\|\boldsymbol{V}\|_e$ are almost distributed in the range of 0.95 to 0.97 [m/s]. In ▲H and ▲N, sphere mobile speed $\|\boldsymbol{V}\|_e$ are distributed in the range of 0.89 to 0.90 [m/s]. Thus. ■R, ●T and ●F have sphere speed efficiency better than ▲H and ▲N.

2) horizontal coordinate (sphere slip speed)

In ■R, $\|\boldsymbol{\zeta_i}\|_e$ are almost distributed in the range of 0 to 0.05[m/s]. Thus, dynamical friction $\boldsymbol{F_1}$ and $\boldsymbol{F_2}$ are almost zero. In ●T and ●F, $\|\boldsymbol{\zeta_i}\|_e$ are almost distributed in the range of 0.12 to 0.15 [m/s]. Thus, dynamical friction $\boldsymbol{F_1}$ and $\boldsymbol{F_2}$ can exist moderately. In ▲H and ▲N, $\|\boldsymbol{\zeta_i}\|_e$ are almost distributed in the range of 0.28 to 0.35 [m/s], dynamical friction $\boldsymbol{F_1}$ and $\boldsymbol{F_2}$ can't exist moderately. In fact, that roller surfaces have heat and be worn away by such dynamical friction. From **1), 2),** it is determined that ●T and ●F are adopted optimum arrangement as $|\alpha_i| = 10°$.

4. Conclusion

In this study, we focus the sphere slip velocity and derive relationship sphere slip speed and sphere mobile speed. and evaluated the roller arrangement in the world teams. As a result , Tech United Turtles, Falcons have adopted optimum roller arrangement. As a future task, we will propose kinetic model allow for the friction between sphere and rollers in detail.

Reference

[1] H. Suzuki, T. Yoshida, K. Watanabe et al., RV-Infnity Team Description Paper 2017, *RoboCup 2017 Nagoya* (Nagoya, 2017)

[2] K. Kimura, K. Ishii, Y. Takemura, M. Yamamoto, "Mathematical Modeling and motion analysis of the wheel based ball retaining mechanism", *SCIS & ISIS* (2016), pp.4106-4111

[3] B. Cunha, A. J. R. Neves, P. Dias et al., CAMBADA'2015: Team Description Paper, *RoboCup 2015 Hefei* (Hefei, 2015)

[4] Rob.Hoogendijk: "*Design of a Ball Handling Mechanism for Robocup*" Bachelor End Project, departement Mechanical Engineering, Technische Universiteit Eindhoven

[5] K. Fujimoto, K. Ishii, Y. Kitazumi, Development of a ball handling mechanism for a RoboCup Soccer Robot, *Robotics and Mechatronics Conference (Okayama,2011)*

[6] R. Junkai, X. Chenggang, X. Junhao et al., A Control System for Active Ball Handling in the RoboCup Middle Size League, *2016 Chinese Control and Decision Conference (CCDC)*, (IEEE, Yinchuan, 2016), pp. 4396-4402

Robot-Control Method Based on Personal Space

Kota Kawamoto, Ryusuke Fujisawa, Eiji Hayashi
Department of Mechanical Information Science and Technology, Kyushu Institute of Technology
680-4, Kawazu, Iizuka-City, Fukuoka, 820-8502, Japan

E-mail: kawamoto@mmcs.mse.kyutech.ac.jp , fujisawa@.ces.kyutech.ac.jp, haya@.mse.kyutech.ac.jp

Abstract

In our daily life, we unconsciously adjust our personal space according to the intimacy with others. It is also said that personal space is classified into non-verbal communication. In this research, we analyzed the distance that a person can tolerate when the robot approaches to identify the minimum distance that the person is able to interact comfortably. As a result, we could get parameters which can be index of initial distance between robot and users.

Keywords: personal robot, personal space, nonverbal communication, intimacy

1. Introduction

Nowadays, the rapid development of high technology has produced robots not only for industrial factories (industrial robots) but also for museums, homes, healthcare institutions and so on (non-industrial robots). Among various types of non-industrial robots, recently, service and personal robots have attracted global attention[1]. What makes them unique is that they are required to have "user affinity" that gives the user a sense of affinity as well as functions such as intellectual behavior and communication ability. Generally, human communication can be divided into two simple categories verbal communication and nonverbal communication. Moreover, it is said that almost 60 percent of the human communication consists of nonverbal communication whether through facial expression, the tone of voice or body movement[2]. All of these are essential to conveying intent or emotional state. Thus, robot control system should be considered the impression from the standpoint of users.

E.T. Hall introduced for the first time the concept of interpersonal distances[3]. People create their own territories around them unconsciously, which define and determine the interactions they can have with other people. In a word, we all are creating our own portable bubble in public space to keep others far from each other. Interpersonal distances are classified into non-verbal communication. Furthermore, the interpersonal distance between them is reflected the social relationship they have. E.T. Hall has proposed a model to represent these different spaces; it divides the space around a person in 4 distinct zones (i), (ii), (iii), (iv), as shown in Figure 1.

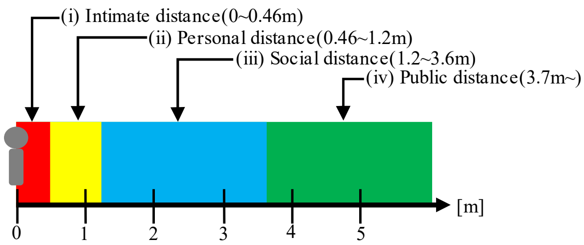

Fig. 1. Definition of Hall's personal space model.

He defined that the Intimate distance is for embracing, touching or whispering, the Personal distance is for interactions among good friends or family, the Social distance is for interaction among acquaintances, the Public distances used for public speaking. Moreover, space within (i) intimate distance and (ii) personal distance is called personal space.

In this research, we designed the robot system and conducted an experiment with considering the personal space between human and robots.

2. Structure of the Robot

The robot we developed is depicted in Figure 2. This robot consists of 4 major parts: the head with 2 degrees of freedom, the Body with 3 degrees of freedom, the Arm with 6 degrees of freedom and the Base with a 4-wheel-drive. The height of the robot is approximately 1.5 m.

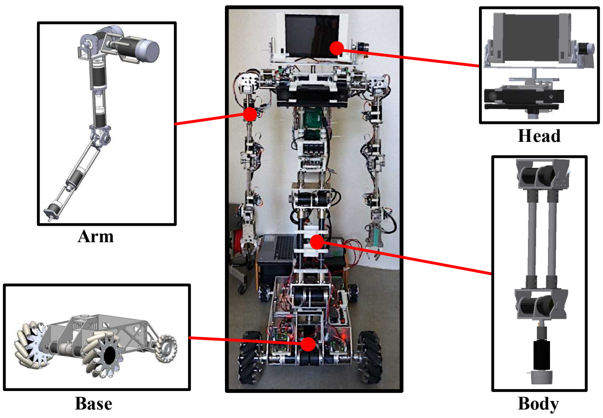

Fig. 2. Structure of the robot

3. System Configuration

The control diagram is depicted in Figure 3. In this system, each part of the robot constructs a control system. The control flow of the Base part is as follows. First, a user is detected by the Kinect V2 sensor, and a target vector command is sent from the PC to the microcomputer according to the information received from the sensor. The microcomputer calculates speed and direction from each parameter and control the motors via the servo controller.

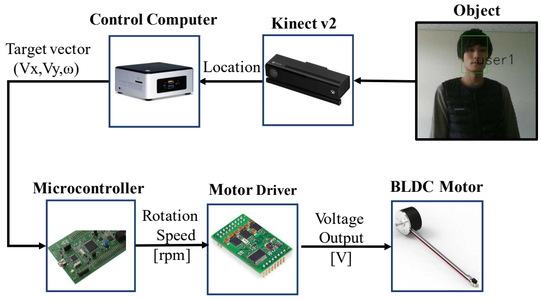

Fig. 3. Control diagram

4. Motion Model of the Moving Device

The mecanum wheel adopted for the Base part is covered with a barrel whose surface is inclined at 45 degree with respect to the axle. By controlling the rotation direction of each wheel as shown in Figure 4, omnidirectional movement is realized by a combination of rotation of the wheel and movement of the barrel on the circumference.

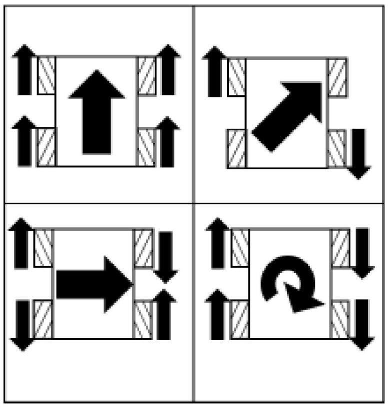

Fig. 4. Various combination of wheel rotation

Let V_0 be the vector according to the angular velocity. Let V_w be a velocity vector in rectangular coordinates. In equation (3), "I" represents the distance from the center of gravity to the lateral edge, and "L" represents the distance to the longitudinal edge.

$$V_w = [\,V_{1w}V_{2w}V_{3w}V_{4w}\,]^T \in R^{4\times1} \tag{1}$$

$$V_0 = [\,V_x\;V_y\;\omega_z]^T \in R^{3\times1} \tag{2}$$

$$J_0 = \begin{bmatrix} 1 & -1 & -(l+L) \\ 1 & 1 & (l+L) \\ 1 & 1 & -(L+l) \\ 1 & -1 & (L+l) \end{bmatrix} \tag{3}$$

V_w can be expressed by using the equation (2), (3).

$$V_w = J_0 \cdot V_0 \tag{4}$$

Here, the speed control of the moving device gives the vector (V_x, V_y, ω_z) as input to the microcomputer and controls the speed V_w of each wheel by PWM output.

5. System Flow of the Movement Control

Figure 5 shows the flowchart of the movement control of the Base part. In the movement control, base part is controlled so as to keep a specific position according to the sensor value. Specifically, the distance and angle are calculated, and the robot approaches the user until the distance of the threshold.

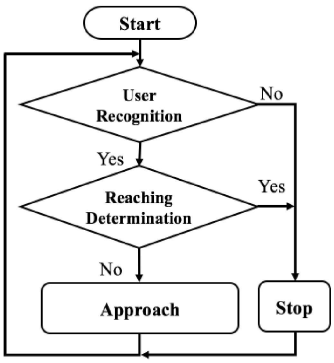

Fig. 5. Flow chart of location control

6. Measurement of the personal space

As I said in chapter 2, People update, control, and adjust their personal spaces continuously. Therefore, psychological strains between human to robot could be measured by physical distances.

In this time, the personal space between robot and subject were measured using the following procedures.

(i) The robot approached at each velocity (0.2, 0.3, 0.4, 0.5, 0.6[m/s]) to a subject who was standing
(ii) The subject raised his hands as a signal if he felt uncomfortable (too close to the robot).
(iii) The distance was measured by a sensor installed at the front of the robot and these procedures were repeated for the 10 subjects.

The measurement result is depicted in Figure 6.

As the velocity increased, the standard deviation tended to be higher. However, there was no significant relationship between the velocity and the distance. The average distance was almost same as any velocity.

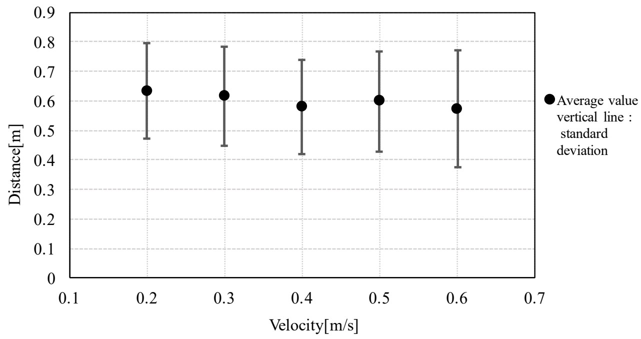

Fig. 6. Measurement result

7. Evaluation of the personal distance

Based on the measurement values obtained from the previous experiment, the evaluation experiments were conducted. The moving speed was controlled within the range of 0.0 ~ 0.3 [m/s] so that the boundary of the personal space was kept about 0.6 m, which was the average distance of the previous experiment.

The evaluation experiment was conducted as follows.

(i) A subject sat on the chair on casters in front of the robot.
(ii) The subject moved freely in the specified range for a minute.
(iii) The robot kept the distance as shown in Figure 7.
(iv) After the experiment, the subject answered the questionnaire of the impression about the robot's approach. Repeat for the 12 subjects.

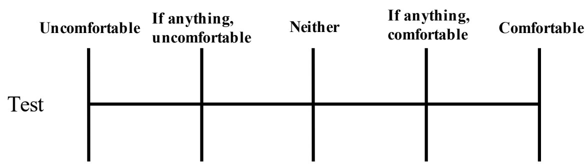

Fig. 7. Evaluation questionnaire

The result of the evaluation experiment is depicted in Figure8. Each result of the questionnaire was quantified as shown in Table 2.

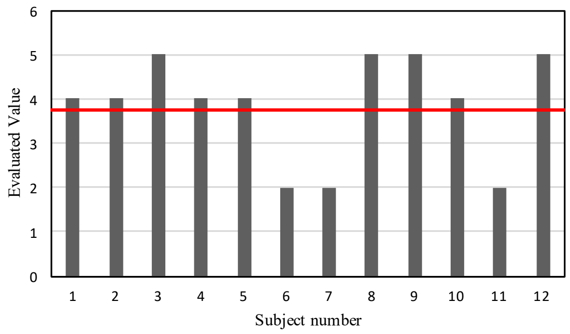

Fig. 8. Evaluation result

Table. 2. Conversion table for the result

	Uncom-fortable	-----	Nei-ther	-----	Com-fortable
Evaluated value	1	2	3	4	5

Table.3.Average and standard deviation of the result

average	3.8
Standard deviation	1.1

The average score is shown by a red horizontal line. The average score was 3.8 and close to “comfortable”.

8. Conclusion and Future work

It is considered that the velocity range and the distance could be adapted to realize the appropriate approach to most of the users. It means that the distance can be index of initial distance between robot and users. However, to optimize the personal space for each users, we need to create the database to store the information.

References

[1] S.Yumitori, *Overview of Robot R&D in NEDO*
[2] K.Buhardwaj, *Professional Communication*
[3] E.T. Hall, *The Hidden Dimension* (Vol. 609. Garden City, NY: Doubleday, 1966).
[4] J.leroy, M.mancas and B.gossel, Personal Space Augmented Reality Tool

Recognition Method of Target Objects for Autonomous Tomato Harvesting Robot

Keiji Kamei*
Department of Production Systems, Graduate School of Engineering, Nishinippon Institute of Technology
1-11 Aratsu, Kanda, Miyakogun, Fukuoka 800-0394, Japan†

Hiroyuki Moriyama
Department of Information Systems, School of Engineering, Nishinippon Institute of Technology
1-11 Aratsu, Kanda, Miyakogun, Fukuoka 800-0394, Japan
E-mail: kamei@nishitech.ac.jp
www.nishitech.ac.jp/~kamei/

Abstract

Recently, the shortage of agricultural workers and depression of agricultural production efficiency have been said in Japan. To solve those problems, the researches that apply information and robot technology are studied actively. The aim of our research, we focus on the autonomous tomato harvesting robot, and develop the recognition method for target objects. The color identification from a camera and distance measurement between target tomatoes and a robot are key points. To solve those problems, we propose to identify color based on HSV values using Look-Up-Table for acceleration of calculation and to measure distance for tomatoes using depth camera. From the experiments, we succeeded in acquiring a tomato from a camera and in measuring distance.

Keywords: Computer Vision, Recognition of Target Objects, Autonomous Robot, Harvesting of Field Crops.

1. Introduction

According to the report from Japanese Ministry of Agriculture, Forestry and Fisheries(MAFF)[1], the shortage of agricultural workers and depression of agricultural production efficiency have been said in recent Japan. From that report, the number of agricultural and forestry workers decreases steadily with each passing year; in addition, the number of that elderly workers who are over 65 years old have been increasing. To solve those problems, the researches that apply information and robot technology are studied actively, and those are called “Smart Agriculture.” In this research, we focus on the automation system for harvesting, which is the harvesting robot, of field crops in Smart Agriculture.

The common aims for the harvesting robots which have been researched and developed so far are development of the functions for full automation harvesting of crops in order to increase production efficiency. Generally, those robots use cameras for recognition of crops color and shape, and use sensors, e.g., laser range finder, to measure distance between a robot and crops. However, those robots have problems of economic feasibility. In addition, those take slowly actions, so that the number of harvesting crops within unit time is a small amount compared with agricultural workers. For this, it can be said that the autonomous harvesting robots have not yet put into use on actual farm.

In this research, our aim is development of the recognition system of target crops for the harvesting

*In 2007 he obtained his PhD at the Department of Brain Science and Engineering, Kyushu Institute of Technology. From April, 2007 to March, 2014, he was a lecturer. Since April, 2014, he has been an associate professor, Nishinippon Institute of Technology.

robot, and target crop is tomatoes because our harvesting robot participate in "Tomato Robot Competition[2]." Our harvesting robot is developed by joint team of laboratories at Nishinippon Institute of Technology, and we take charge of the recognition system on that robot. The color identification from a camera and the distance measurement between target crops and a robot are key points. To solve those problems, we propose to identify the color based on "HSV values" using "Look-Up-Table(LUT)" for acceleration of calculation and to measure distance for target crops using "Depth camera." From the experiments on Tomato Robot Competition, we succeeded in recognizing a tomato from camera and in measuring distance.

2. Tomato Robot Competition

In Tomato Robot Competition, there are two categories for the harvesting robot style, i.e., "Rail Style" and "Free Style," and there are two sections for the control of a robot in each category, i.e., "Remote Control" and "Autonomous Control." We participate in "Rail Style" and "Autonomous Control." Rail style category is that a harvesting robot moves on the rail which is laid in advance. The competition is that a robot harvests as many tomatoes as possible in the time limitation. In addition to the number of tomatoes, the states of tomatoes, i.e., color of tomatoes, bruises on skin of tomatoes, etc., are elements of deduction or addition to the score. The competition consists of 3 stages, i.e., qualifier 1(Q1), qualifier 2(Q2) and final stage. Table 1 shows the specifications of field for all of stage of competition, and Fig. 1 illustrates the overview of competition field.

Table 1. Specifications for competition field(Rail Style category). Unit is millimeter.

Stage	Q1	Q2	Final
Distance between rail and tomatoes rack	200		
Distance between rail and tomatoes	200		100 ~ 400
Distance between floor and tomatoes	800 ~ 1200		
Diameter of pipe for rail	∅50		
Rail gauge	600(±5)		

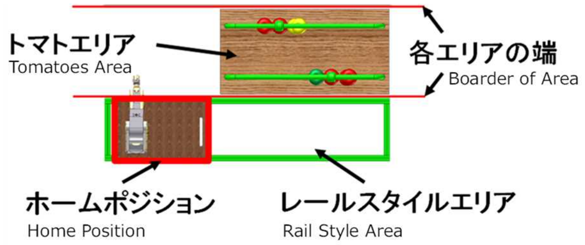

Fig. 1. Overview of competition field. (Ref. The homepage of "5th Tomato Robot Competition[2].")

2.1. *Qualifier 1*

Tomatoes are hung separately one by one in the tomatoes area. A harvesting robot moves from the home position toward front of a tomato, then harvests tomatoes. The minimum requirement to pass the qualifier 1 stage is to touch a tomato. The teams that pass the qualifier 1 stage are able to go on the qualifier 2 stage.

2.2. *Qualifier 2*

The difference of the condition for the tomato area between the qualifier 1 stage and the qualifier 2 stage is that tomatoes are hung as bunches of tomatoes. The minimum requirement to pass the qualifier 2 stage is to harvest at least one tomato. The teams that pass the qualifier 2 stage are able to go on the final stage.

2.3. *Final stage*

In the final stage, there are several plants of tomatoes in the tomato area, and a robot harvests ripe tomatoes which are selected by recognition system from plants. The score will be deducted if a robot harvests tomatoes are not ripe.

3. Tomato Harvesting Robot and Recognition System

Our harvesting robot is developed by joint team of laboratories at Nishinippon Institute of Technology. We explain our harvesting robot and recognition system for target tomatoes in this section.

3.1. *Hardware of harvesting robot*

The hardware of our harvesting robot is developed by Takemura Laboratory at Nishinippon Institute of Technology. Fig. 2 shows the overview of our harvesting robot. This robot has a pair of harvesting scissors, and that scissors are able to expand and contract by air cylinder. A sensor for recognition of tomatoes is set on upper side of a harvesting arm.

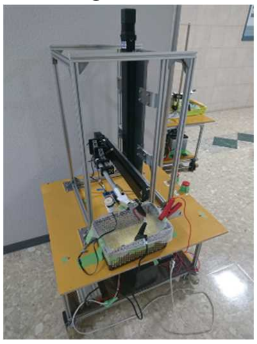

Fig. 2. Overview of tomatoes harvesting robot.

3.2. *Recognition system of target crops*

We take charge of the recognition system on our harvesting robot. We have to recognize tomatoes and to measure the exact distance between a robot and tomatoes; therefore, we propose to apply a sensor that is integrated camera and depth sensor to recognition and measuring. There are several types of such sensor, we choose "Intel RealSense R200[3, 4]" because that sensor connects via USB3.0 and so does not need external power source. Table 2 and Fig. 3 shows the specifications of Intel RealSense R200 and overview, respectively.

Table 2. Specifications for Intel RealSense R200[3, 4]

	Camera sensor (Color image)	Distance sensor (Depth image)
Resolution	1920, 1080	640, 480
Aspect ratio	16 : 9	4 : 3
Viewing angle	H:70, V:43, D:77	H:59, V:46, D:70
Frame rate	30[fps]	60[fps]

Fig. 2. Overview of Intel RealSense R200.

Fig. 3 illustrates the flowchart of a tomato recognition and the process of distance measurement. Firstly, the recognition system attempts to sample red area from taken color image in order to find tomatoes. That system sends moving signal to robot controller if it does not find red area or red area is not center of a taken image. Robot moving signal is sent until red area is centered in an image. Subsequently, that system attempts to sample green area that is neighboring to red area in order to find stem. Then, it measures the distance to red and green area from depth sensor, and selects red and green objects which have similar distance. Finally, recognition system determines red as a tomato and green as stem.

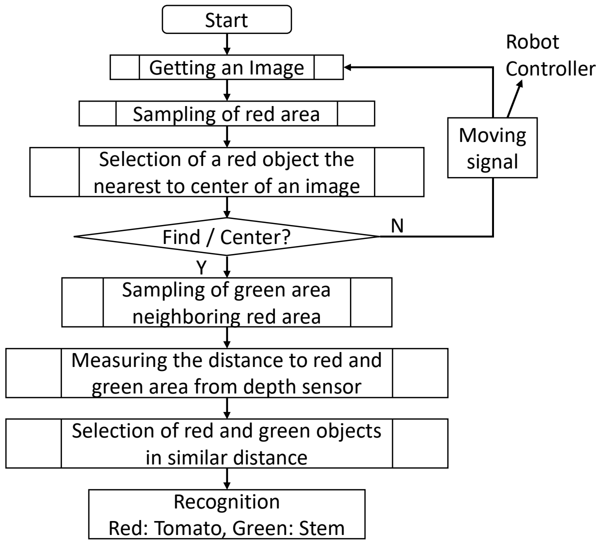

Fig. 3. The flowchart of recognition of a tomato.

We apply conversion of color space of taken images, i.e., RGB to HSV, because HSV images have robustness for alternation of luminance. In process of conversion, we apply Look-Up-Table(LUT) method to conversion of color space. LUT method converts color space based on conversion table that is calculated in advance; therefore, a pixel value in RGB is converted by a corresponding value in HSV on conversion table. As a consequence, LUT method allows calculation for recognition of red area(tomatoes) and stem to accelerate.

4. Experiments

We conduct 2 kinds of exmpriments, i.e., in laboratory and in Tomato Robot Competition. This section shows those results.

4.1. *Experiment 1: In Laboratory*

This experiment demonstrates capability of recognition for a tomato and stem, and validates accuracy of measurement distance between the sensor and a tomato from depth image. We use an imitation tomato in this experiment. Fig. 4(a), (b) and (c) show the original image(input), recognition of red area(tomato) and recognition of green area(stem), respectively.

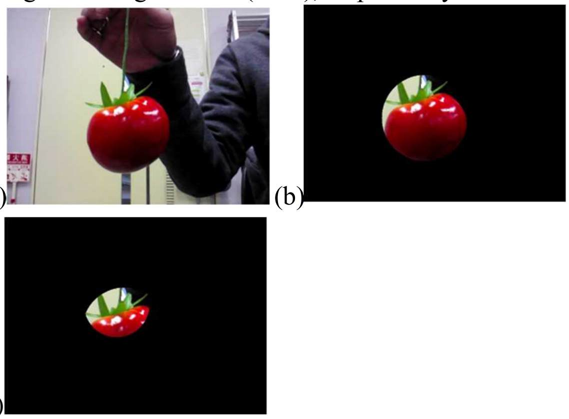

Fig. 4. Original and Processed images. (a)Original(input), (b)Recognition of red area, (c)Recognition of green area.

From the result of comparison of Fig. 4(a) and (b), it is able to recognize a tomato from red area, and so our proposal succeeded in extracting the image of a tomato. The center of visible region in Fig. 4(c) shows the stem at the joint to a tomato, so that succeeded in finding the cutting point. Next, we validate accuracy of measurement distance by 2 kinds of distance between cutting point of stem and sensor; those are set to 200[*mm*] or 500[*mm*]. The number of trials for validation is 10 times for each distance. Table 3 shows the results of validation.

Table 3. The results of validation of measuring distance

Distance	200[*mm*]	500[*mm*]
Trial 1	202.531	510.031
Trial 2	203.188	517.313
Trial 3	204.125	514.469
Trial 4	213.719	515.938
Trial 5	214.031	510.250
Trial 6	213.656	514.188
Trial 7	214.188	509.281
Trial 8	214.156	517.031
Trial 9	213.938	516.719
Trial 10	214.938	512.125
Average	210.847	513.735
Standard deviation	5.246	3.100

From the results in Table 3, the measurement error is about 10[*mm*], and measurment distances tend to be long distance compared with actual diatances. The reason for those results is that there are occasional times that sensor measures the distance between a leaf behind stem on hull of a tomato and sensor. However, this measurement error does not affect to harvest because harvesting scissors moves to the farther than actual distance.

4.2. *Experiment 2: Tomato Robot Competition*

In the competition, our harvesting robot was not able to touch and to harvest a tomato in time limitation, so that our robot failed to pass the qualifier 1. The reason for failure is that our robot was not able to move until red area(a tomato) is centered in a color image due to programming failure of robot controller; namely, our robot continued to move back and forth so that a tomato is at the center of an image. We took part in to the qualifier 2 as an open participant. In the qualifier 2, we modified the program of robot controller. The result of qualifier 2 is that our robot was able to move toward front of a tomato and to touch that stem; consequently, it can be said that the proposal in this research succeeded in recognizing of a tomato and in measuring of distance.

5. Conclusions

The shortage of agricultural workers and depression of agricultural production efficiency have been said. To solve those problems, the researches that apply the information and robot technology are studied actively.

The aim of in this research is development of tomato harvesting robot. Our robot is developed by joint team, and we take charge of the recognition of tomato. From the results in laboratory, our proposal succeeded in recognizing a tomato and in finding the cutting point. In addition, our proposal were able to measure the distance for cutting point within allowable error. By contrast, our robot was not good results in Tomato Robot Competition; however, our robot was able to touch the stem of a tomato in the end, so that our proposal succeeded in recognizing of a tomato and in measuring of distance.

References

1. Ministry of Agriculture, Forestry and Fisheries, Statistics on agricultural labor force(in Japanese), http://www.maff.go.jp/j/tokei/sihyo/data/08.html.
2. Center for Socio-Robotic Synthesis, Tomato Robot Competition, http://www.lsse.kyutech.ac.jp/~sociorobo/ja/tomato-robot2017.
3. Intel Corporation, RealSense, https://realsense.intel.com/.
4. R. Hatsune et. al., *Intel RealSense SDK Sensor Programming(in Japanese)*, 1st edn. (SE Book, 2015).

Color Image Arrangement Based on Histogram Matching Using Smoothed Brightness Histogram (I) --- Overall Smoothing ---

Yusuke Kawakami*, **Tetsuo Hattori, Yoshiro Imai, Koji Kagawa, Yo Horikawa**
Graduate School of Kagawa University, 2217-20 Hayashi
Takamatsu City, Kagawa 761-0396, Japan

R. P. C. Janaka Rajapakse
Tainan National University of the Arts, 66 Daci
Guantian District, Tainan 72045, Taiwan
E-mail: riverjp2002@gmail.com, {hattori imai, kagawa, horikawa}@eng.kagawa-u.ac.jp, janaka@mail.tnnua.edu.tw

Abstract

Although we have already reported that automated color image arrangement by Histogram Matching based on Gaussian Distribution (HMGD) gives good feeling impression if the brightness histogram of the original image has a single peak. However, if there are multiple peaks in the histogram, the HMGD processing does not always bring good results. In this paper, we propose a Histogram Matching method using overall smoothing over the brightness histogram of original image as the reference one instead of using Gaussian distribution. Also in this paper, we present the experimental results.

Keywords: Image processing, Brightness Histogram, Histogram matching, HMGD

1. Introduction

These days, automated image processing for enhancement of color images has been more familiar to us, for example, Digital Signage, Smart Phone, etc[1-3].

In the previous paper, we have already presented that the Histogram Matching based on Gaussian Distribution (HMGD) processing is one of the automated image arrangement method using Elastic Transformation[4-5] based on the brightness axis and gives good feeling impression if the original images have single peak[6].

However, we have understood that if the original images have multiple-peak brightness histogram, HMG-D processing does not always give good feeling impression. Through the experimental results, we have considered if the reference histogram make change to satisfy brings good results whether or not the number of original image brightness histogram peaks[7].

In this paper, we propose a Histogram Matching method using overall smoothing over the brightness histogram of original image as the reference one instead of using Gaussian distribution. Also in this paper we illustrate the experimental results using proposed Histogram Matching method.

2. Principle of Histogram Matching based on Gaussian Distribution (HMGD)

In the section, we describe the principle of HMGD processing.

Fig. 1 shows the conceptual image of HMGD. Let $f(x)$ and $h(y)$ be two probabilistic density functions (PDF) on real variables x and y, respectively. The PDF is corresponding to histogram of image brightness level which is discretely defined.

In addition, let $y=\phi(x)$ be a continuous and monotonic increase function corresponding to cumulative histogram of image brightness level between variables x and y [7-9]. And let $y=\phi(x)$ be defined by Eq. (1).

$$y = \phi(x) = L\int_0^x f(x)dx. \tag{1}$$

At first, we have to expand brightness level of original image histogram and convert into uniform distribution histogram, because we aim to match Gaussian distribution. From Eq. (1) and Fig. 1, we can derive Eq. (2) and (3).

$$f(x) = h(y)\phi'(x) = h(y)Lf(x). \tag{2}$$

$$h(y) = \frac{1}{L}. \tag{3}$$

We understand the histogram of original image $f(x)$ becomes uniform distribution $h(y)$ by Eq. (3). This means that brightness level of original image $f(x)$ is expanded to $h(y)$.

Then, let $Gauss(z)$ and $\gamma(z)$ be the function that is defined by Eq. (4) and (5), respectively.

$$Gauss(z) = \frac{1}{\sqrt{2\pi\sigma^2}}\exp\left(-\frac{(z-\mu)^2}{2\sigma^2}\right). \tag{4}$$

$$\begin{aligned} y = \gamma(z) &= L\int_0^z Gauss(z)dz \\ &= \frac{1}{\sqrt{2\pi\sigma^2}}\int_0^z \exp\left(-\frac{(z-\mu)^2}{2\sigma^2}\right)dz. \end{aligned} \tag{5}$$

Here, Fig.1 shows the relationship between $y=\phi(x)$ and $y=\gamma(z)$. So we can be obtained following Eq. (6).

$$L\int_0^x f(x)dx = \frac{L}{\sqrt{2\pi\sigma^2}}\int_0^z \exp\left(-\frac{(z-\mu)^2}{2\sigma^2}\right)dz. \tag{6}$$

And we can derive Eq. (7) from differential of Eq. (6).

$$\frac{d}{dx}L\int_0^x f(x)dx = \frac{d}{dz}\frac{L}{\sqrt{2\pi\sigma^2}}\int_0^z \exp\left(-\frac{(z-\mu)^2}{2\sigma^2}\right)dz. \tag{7}$$

If we perform Eq. (7),

$$L\phi'(x) = L\gamma'(z) \tag{8}$$

That is, we understand that $f(x)$ becomes Gaussian distribution $Gauss(z)$ when we take the transform function as (1) and (5). Thus, HMGD processing is the function which defined by cumulative histogram transformation the original histogram into Gaussian histogram[6,7].

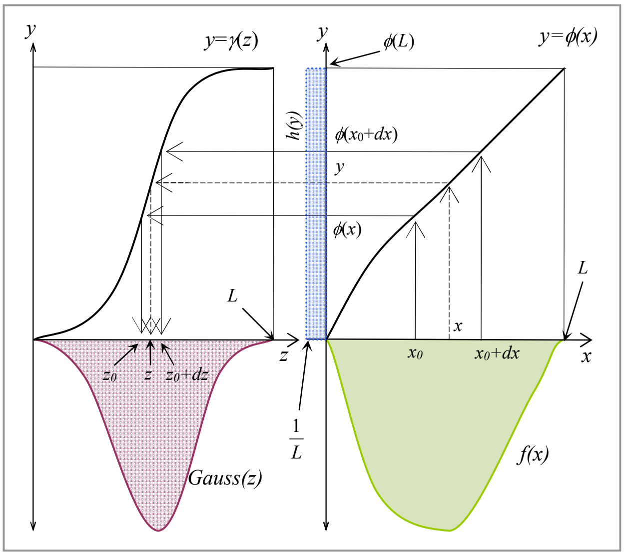

Fig. 1. Conceptual image of HMGD[6, 7].

3. Histogram Matching Using Smoothed Brightness Histogram

In the previous section, we have described about the principle for HMGD processing. In this section, we propose the concrete process of Histogram Matching using smoothed brightness histogram

(i) Input original image and calculate moving average of brightness histogram of the one.

(ii) If not need to calculate moving average of it further (if it satisfies number of times recursive), proceed to (iii). Otherwise, calculate moving average of the brightness histogram recursively.

(a) Image: Original[6, 7] (far left), Histogram Matching using Moving Average (5 times: second from left, 10 times: second from right, 100 times: far right)

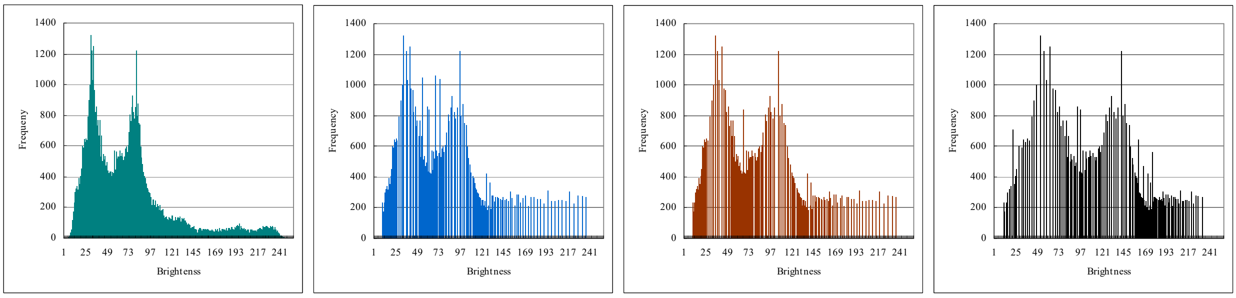

(b) Histogram: Original (far left), Histogram Matching using Moving Average (5 times: second from left, 10 times: second from right, 100 times: far right)

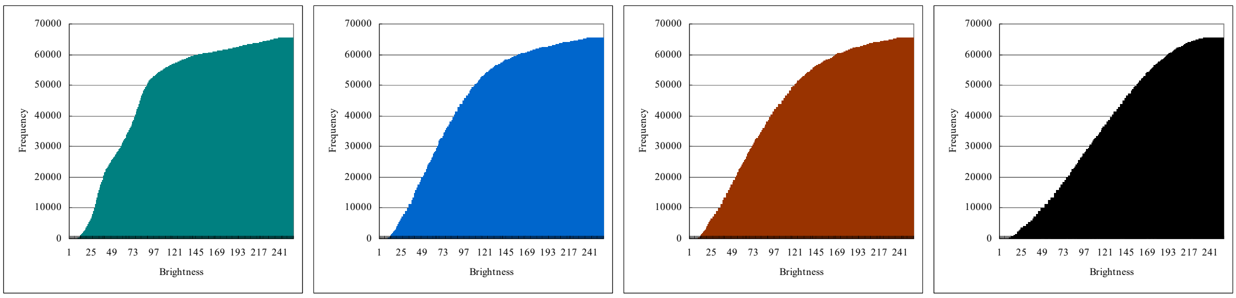

(c) Cumulative Histogram: Original (far left), Histogram Matching using Moving Average (5 times: second from left, 10 times: second from right, 100 times: far right)

Fig. 2. Example of results and the corresponding histogram.

(iii) Generate the reference histogram h_r from the result of (ii).
(iv) Perform Histogram Matching processing of using reference histogram as h_r.
(v) Output processed image.

4. Experimentation

In this experimentation, we perform moving average a range of ± 25 with respect to each brightness value of original image histogram.

Fig. 2 shows the example of results and the corresponding histogram. In this case, we understand that Histogram Matching processing image using moving average of brightness histogram is enhancing contrast than original image.

From far right of Fig. 2(a) ~ (c), we notice that these results like Histogram Equalization (HE) or Histogram Matching based on Gaussian Distribution (HMGD). That is, we consider that this processing result will get close to HE or HMGD if we increase in the number of times moving-average recursive. And we consider that the processing result does not always give us good Kansei impression in such case.

5. Conclusion

In this paper we have proposed the color image arrangement based on histogram matching using moving average of original image brightness histogram. As for the concrete processing method, we have used moving average recursively from the original image brightness histogram to generate reference histogram. Then we have taken a histogram-matching processed image.

From the experimentation, histogram matching processed image is enhancing contrast from original image and this processing result will get close to HE or HMGD if we increase in the number of times moving-average recursive. That is, we consider that proposed method is simple and convenient as Kansei impression enhancement instead of HMGD.

References

1. R. C. Gonzalez and R. E. Woods, *Digital Image Processing* (Addison-Wesley Publishing Company, 1993).
2. B. Jahne, *Digital Image Processing --Concepts, Algorithms, and Scientific Applications-- 4th edition* (Springer, 1995).
3. E. S. Umbaugh, *Computer Vision and Image Processing: A Practical Approach Using CVIP tools* (Prentice Hall PTR, 1998).
4. W. Burger and J. M. Burge, *Principles of Digital Image Processing: Fundamental Techniques* (Springer 2009).
5. T. Izumi, T. Hattori, S. Sugimono, and T. Takashima, Color Image Arrangement Using Elastic Transform on Principal Component Axis (in Japanese), *Journal of Japan Society of Kansei Engineering* **8**(3) (2009) 667-674.
6. Y. Kawakami, T. Hattori, D. Kutsuna, H. Matsushita, Y. Imai, H. Kawano, R.P.C. Janaka Rajapakse, Automated Color Image Arrangement Method Based on Histogram Matching - Investigation of Kansei impression between HE and HMGD -, *International Journal of Affective Engineering* **14**(2) (2015) ISSN 2187-5413, 85-93.
7. Y. Kawakami, T. Hattori, Y. Imai, K. Ando, Y. Horikawa, R. P. C. Janaka Rajapakse, Reference Histogram Matching Based on Moving Averaged Brightness Histogram, *IEEJ Transactions on Electronics Information and Systems* 138(9) (2018) ISSN 1348-8155, 1131-1132.

Color Image Arrangement Based on Histogram Matching Using Smoothed Brightness Histogram (II) --- Piecewise Smoothing ---

Yusuke Kawakami*, **Tetsuo Hattori, Yoshiro Imai, Koji Kagawa, Yo Horikawa**
Graduate School of Kagawa University, 2217-20 Hayashi
Takamatsu City, Kagawa 761-0396, Japan

R. P. C. Janaka Rajapakse
Tainan National University of the Arts, 66 Daci
Guantian District, Tainan 72045, Taiwan
E-mail: riverjp2002@gmail.com, {hattori imai, kagawa, horikawa}@eng.kagawa-u.ac.jp, janaka@mail.tnnua.edu.tw

Abstract

Although we have already reported that automated color image arrangement by Histogram Matching based on Gaussian Distribution (HMGD) gives good feeling impression if the brightness histogram of the original image has a single peak. However, if there are multiple peaks in the histogram, the HMGD processing does not always bring good results. In this paper, we propose a Histogram Matching method using piecewise smoothing over the brightness histogram of original image as the reference one, after Histogram Analysis by curvature computation. Also in this paper, we present the experimental results.

Keywords: Image processing, Brightness histogram, Histogram matching, HMGD

1. Introduction

These days, automated image processing for enhancement of color images has been more familiar to us, for example, Digital Signage, Smart Phone, etc[1-3].
In the previous paper, we have already reported that the Histogram Matching based on Gaussian Distribution (HMGD) processing is one of the automated image arrangement methods[4-5] on the brightness axis and gives good feeling impression if the original images have single peak[6].
However, we have understood that if the original images have multiple-peak brightness histogram, HMG-D processing does not always give good feeling impression. Through the experimental results, we have considered if the reference histogram make change to satisfy brings good results whether or not the number of original image brightness histogram peaks[7-8].
In this paper, we propose a Histogram Matching method using piecewise smoothing over the brightness histogram of original image as the reference one, after Histogram Analysis by curvature computation. Also in this paper we illustrate the experimental results.

*1882-36, Yashima-nishi, Takamatsu, Kagawa 761-0113 Japan

2. Principle

In another paper, we have described principle of Histogram Matching based on Gaussian Distribution (See Ref. 8). In this section, we describe the principle of peaks and valleys detection method, and variance estimation by regression analysis.

2.1. *Peaks and Valleys Detection of Histogram*[9]

Fig. 1 shows the conceptual image of the original image histogram which is variance σ^2 and average a. And Fig. 2 shows its cumulative histogram.

Let y be a function with respect to x, the definition curvature $R(x)$ is given by Eq. (1)

$$R(x)=\frac{d^2y}{dx^2}\left(1+\left(\frac{dy}{dx}\right)^2\right)^{-\frac{3}{2}}. \qquad (1)$$

Let $g(x)$ and K be a Gaussian distribution function approximated at a peak and its coefficient that are defined by the following equations.

$$g(x)=\frac{K}{\sqrt{2\pi\sigma^2}}\exp\left(-\frac{(x-a)^2}{2\sigma^2}\right)$$

$$\left(\frac{K}{\sqrt{2\pi\sigma^2}}\int_0^L \exp\left(-\frac{(u-a)^2}{2\sigma^2}\right)du=1\right) \qquad (2)$$

Next, let $y=f(x)$ be a function representing the cumulative histogram which is represented Eq. (3). That is, dy/dx and d^2y/dx^2 be described as Eq. (4) and (5), respectively. From Eq. (4) and (5), we obtain the approximation of curvature $R(x)$ as Eq. (6).

$$f(x)=\int_0^x g(u)du=\frac{K}{\sqrt{2\pi\sigma^2}}\int_0^x \exp\left(-\frac{(u-a)^2}{2\sigma^2}\right)du. \qquad (3)$$

$$\frac{dy}{dx}=g(x)=\frac{K}{\sqrt{2\pi\sigma^2}}\exp\left(-\frac{(x-a)^2}{2\sigma^2}\right). \qquad (4)$$

$$\frac{d^2y}{dx^2}=\frac{dg(x)}{dx}=\frac{(a-x)}{\sigma^2}g(x) \qquad (5)$$

$$R(x)=\frac{\frac{(a-x)}{\sigma^2}g(x)}{\left(1+g(x)^2\right)^{\frac{3}{2}}}\approx\frac{(a-x)}{\sigma^2}g(x). \qquad (6)$$

From Eq. (6), we understand that the curvature $R(x)$ varies the sign according to the value of x. That is, if $x<a \rightarrow R>0$ (downward convex shape), and if $x>a \rightarrow R<0$ (upward convex shape).

As for valley detection, we can approximate the shape of the neighbor points at the valley point as 1.0 - $g(x)$. So, around the valley point, the curvature $R(x)$ is shown as follows:

(a) $x<0 \rightarrow R<0$ (upward convex shape)
(b) $x>a \rightarrow R>0$ (downward convex shape)

In any case, it holds that if R>0, the shape of the original histogram curve is downward convex. In this way, from the value of curvature over the cumulative histogram, we can detect peaks and valleys in the original histogram curve.

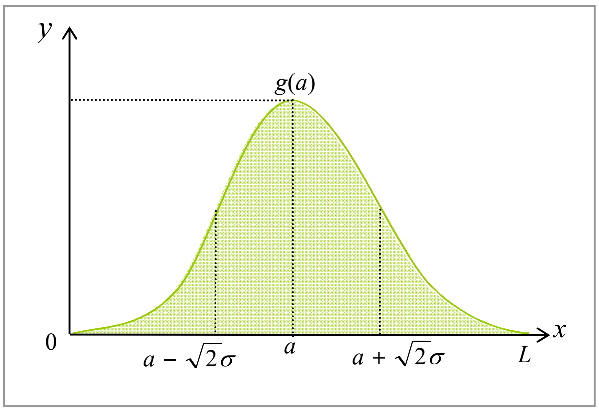

Fig. 1. Conceptual image of the original image histogram[9].

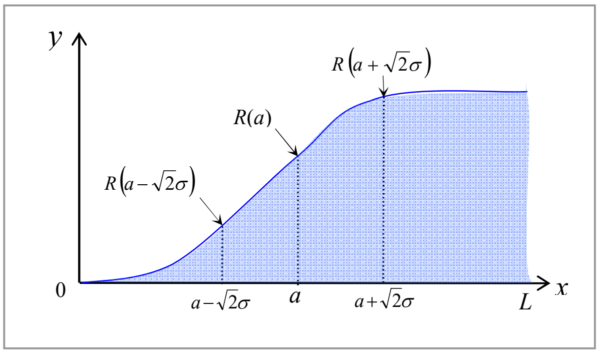

Fig. 2. Conceptual image of the original image cumulative histogram[9].

(a) Image: Original[6] (far left), Histogram Matching using Moving Average (5 times: second from left, 10 times: second from right, 100 times: far right)

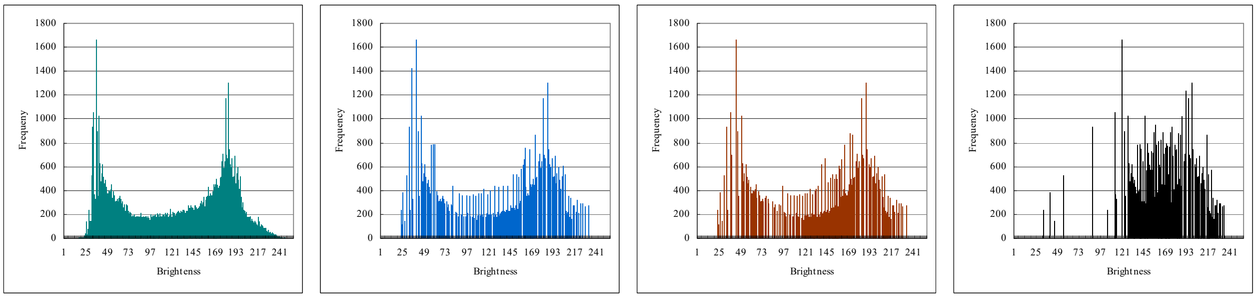

(b) Histogram: Original (far left), Histogram Matching using Moving Average (5 times: second from left, 10 times: second from right, 100 times: far right)

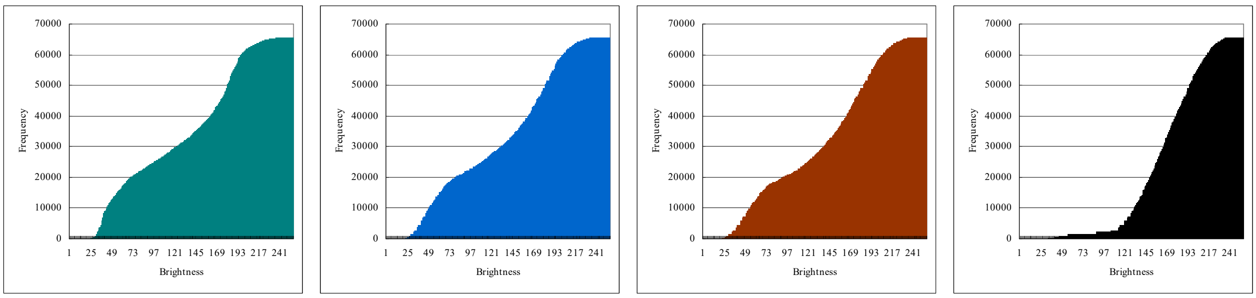

(c) Cumulative Histogram: Original (far left), Histogram Matching using Moving Average (5 times: second from left, 10 times: second from right, 100 times: far right)

Fig. 3. Example of results and the corresponding histogram.

2.2. *Variance Estimation by Regression Analysis*[9]

From Eq. (6), the $R(x)$ can be shown as the following Eq. (7).

$$R(x) \approx \frac{(a-x)}{\sigma^2} g(x) = \frac{1}{\sigma^2}(a-x)g(x). \quad (7)$$

And, let $C=1/\sigma^2$ and $H(x) = (a\text{-}x)g(x)$ respectively, we have Eq. (8).

$$R(x) \approx CH(x) \quad (8)$$

Now, we can calculate a constant C by using least-square regression analysis as in the following Eq. (9).

$$\begin{aligned} &R_i = CH_i + \varepsilon_i , \\ &\varepsilon_i \sim N(0, \sigma^2) \quad (i = 1, \ldots n) \end{aligned} \quad (14)$$

Thus, we can evaluate σ^2 as the following Eq. (10).

$$C = \frac{\sum_{i=1}^{n} (H_i R_i)}{\sum_{i=1}^{n} (H_i)^2}, \quad \sigma^2 = \frac{1}{C} \quad (15)$$

3. Histogram Matching Using Smoothed Brightness Histogram

In this section, we propose the concrete process of Histogram Matching using piecewise smoothed brightness histogram.

(i) Input original image and peaks and valleys detection, and then perform variance estimation of each peak.
(ii) Calculate piecewise moving average of brightness histogram.
(iii) If not need to calculate piecewise moving average of it further (if it satisfies number of times recursive), proceed to (iv). Otherwise, calculate them recursively.
(iv) Generate the reference histogram h_r from the result of (iii).
(v) Perform histogram matching processing of using reference histogram as h_r.
(vi) Output processed image.

4. Experimentation

In this experimentation, we perform moving average a range of ± 10 with respect to each valley-to-valley brightness value of original image histogram.
Fig. 3 shows the example of results and the corresponding histogram. In this case, we understand that histogram matching processing image using piecewise moving average of brightness histogram is enhancing contrast than original image naturally.
From far right of Fig. 3(a) ~ (c), we notice that these results turn unnatural color from original image and each peak shifted to higher brightness.
That is, we consider that this processing will get enhance brightness if we increase in the number of times piecewise-moving-average recursive. And if we increase number of it too much, we consider that the processing result does not always give us good Kansei impression in such case.

5. Conclusion

In this paper we have proposed the color image arrangement based on histogram matching using piecewise moving average of original image brightness histogram.
As for the concrete processing method, we have detected each peak and valley, and estimated each variance of original image histogram by regression analysis. Then, we have used piecewise moving average recursively from the original image brightness histogram to generate reference histogram. Finally we have taken a histogram-matching processed image.
From the experimentation, we consider that histogram matching processed image by proposed method is enhancing brightness from original image naturally, unless we increase number of piecewise-moving-average recursive times too much. That is, we consider that proposed method is simple and convenient as Kansei impression enhancement instead of HMGD.

References

1. R. C. Gonzalez and R. E. Woods, *Digital Image Processing* (Addison-Wesley Publishing Company, 1993).
2. B. Jahne, *Digital Image Processing --Concepts, Algorithms, and Scientific Applications-- 4th edition* (Springer, 1995).

3. E. S. Umbaugh, *Computer Vision and Image Processing: A Practical Approach Using CVIP tools* (Prentice Hall PTR, 1998).
4. W. Burger and J. M. Burge, *Principles of Digital Image Processing: Fundamental Techniques* (Springer 2009).
5. T. Izumi, T. Hattori, S. Sugimono, and T. Takashima, Color Image Arrangement Using Elastic Transform on Principal Component Axis (in Japanese), *Journal of Japan Society of Kansei Engineering* **8**(3) (2009) 667-674.
6. Y. Kawakami, T. Hattori, D. Kutsuna, H. Matsushita, Y. Imai, H. Kawano, R.P.C. Janaka Rajapakse, Automated Color Image Arrangement Method Based on Histogram Matching - Investigation of Kansei impression between HE and HMGD -, *International Journal of Affective Engineering* **14**(2) (2015) ISSN 2187-5413, 85-93.
7. Y. Kawakami, T. Hattori, Y. Imai, K. Ando, Y. Horikawa, R. P. C. Janaka Rajapakse, Reference Histogram Matching Based on Moving Averaged Brightness Histogram, *IEEJ Transactions on Electronics Information and Systems* **138**(9) (2018) ISSN 1348-8155, 1131-1132.
8. Y. Kawakami, T. Hattori, Y. Imai, K. Kagawa, Y. Horikawa, R. P. C. Janaka Rajapakse, Color Image Arrangement Based on Histogram Matching Using Smoothed Brightness Histogram (I) --- Overall Smoothing ---, *in Proceedings of International Conference on Artificial Life and Robotics* (ICAROB 2019) (Oita, Japan, 2019), To Be Published.
9. Y. Kawakami, T. Hattori, Y. Imai, K. Ando, Y. Horikawa, R. P. C. Janaka Rajapakse, Histogram Analysis Method Based on Gaussian Distribution and Curvature Computation (I) ---- Peaks and Valleys Detection ----, *in Proceedings of International Conference on Artificial Life and Robotics* (ICAROB 2018) (Oita, Japan, 2018) ISBN 978-4-9908350-3-3, 367-370.

Parameter Estimation Method for Compartment Model
---- PET Inspection ----

Tetsuo Hattori*, Yoshiro Imai*, Koji Kagawa*, Yo Horikawa*, Yusuke Kawakami**
Kagawa University
2217-20 Hayashi Takamatsu City, Kagawa 761-0396, Japan

Hiromichi Kawano†
NTT Advanced Technology Company Ltd.
1-19-8 Nakamachi, Musashino City, Tokyo 180-0006, Japan

**E-mail: {hattori, imai, kagawa, horikawa}@eng.kagawa-u.ac.jp*
***E-mail: riverjp2002@gmail.com, †E-mail: hiromichi.kawano@ntt-at.co.jp*

Abstract

This paper proposes a new general method for parameters estimation in compartment model using DOC (Differentiation of Convolution). In this paper, we apply the DOC method to the parameter estimation in PET (Positron Emission Tomography) inspection especially. Pet inspection is done for getting physiological and biochemical information of organs. The PET camera acquires the image of radioactive distribution inside the human body. In this paper, we make a mathematical analysis of the PET compartment model and describe the DOC method.

Keywords: Compartment model, PET Inspection, Parameters estimation, Difference of Convolution

1. Introduction

Compartment model is used in a wide variety of fields such as pharmacokinetics, chemical kinetics, modeling of neurons, epidemiology, and simulation of natural phenomena, etc [1-6].

And in many cases, the parameter estimation of the model is performed from actual measurement data, based on the adopted compartment model.

Moreover, parameters to be estimated are often the exponent of the exponential in the convolution integral such as 3-component model ones of FDG (fluoro-deoxyglucose) PET (Positron Emission Tomography) inspection in the field of nuclear medicine.

This paper newly proposes a method for such parameter estimation using DOC (Differentiation of Convolution) operation.

2. Compartment Model

2.1. *Multi-compartment*

The compartment model, especially, multi-compartment model is a type of mathematical model used for describing the way that materials or energies are transmitted among the compartments of a system (Fig.1). Such compartment models are mostly described as in the form of simultaneous differential equation system with respect to time *t* that contains some parameters of the transmission flow.

And, in most cases, the parameters estimation of the transmission flow is quite an important problem to know the situation of the compartment modelled objects such as PET inspection in medicine.

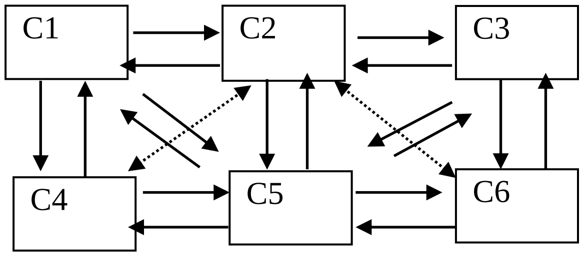

Fig.1. Multi-compartment model.

2.2. *Compartment Model in FDG PET Inspection and Parameter Estimation*

The 3-compatment model used in FDG PET inspection is shown in Fig.2. The simultaneous differential equation system at time *t* [*min*] used in the FDG PET model is also shown in Fig.2.(b). The flow parameters K_1, k_2, k_3, k_4, ($[ml \cdot g^{-1} \cdot min^{-1}]$ or $[min^{-1}]$) show the transport and binding rates of the tracer between two compartments.

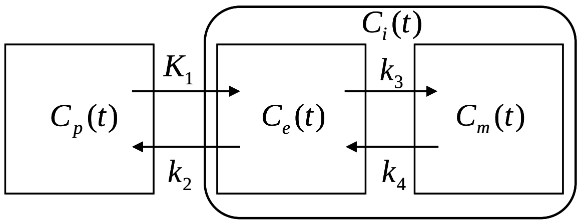

(a)

$$\begin{cases} \dfrac{dC_e(t)}{dt} = K_1 C_p(t) - (k_2 + k_3) C_e(t) + k_4 C_m(t) \\ \dfrac{dC_m(t)}{dt} = k_3 C_e(t) - k_4 C_m(t) \\ C_i(t) = C_e(t) + C_m(t) \end{cases}$$

(b)

Fig.2. Compartment model in FDG PET inspection. (a) 3-Compartment model of the FDG PET with four tracer's flow parameters. (b) Simultaneous differential equations on the FDG PET compartment model.

The solution including the flow parameters K_1, k_2, k_3, k_4, is described in the following Eq.(1).

$$C_i(t) = \frac{1}{\beta - \alpha}\left[(k_3 + k_4 - \alpha) e^{-\alpha t} + (\beta - k_3 - k_4) e^{-\beta t} \right] \otimes K_1 C_p(t)$$

$$\left(\alpha, \beta = \left\{ (k_2 + k_3 + k_4) \mp \sqrt{(k_2 + k_3 + k_4)^2 - 4 k_2 k_4} \right\} \cdot 1/2 \right)$$

where $\otimes$ means the convolution. (1)

3. DOC Method

3.1. *Fundamental Theorem and its Corollary*

Our DOC (Differentiation of Convolution) method is based on the following Theorem 1 and its Corollary 1.

Theorem1:

Let $f(x,t)$ and $\dfrac{\partial}{\partial t} f(x,t)$ be a continuous function and its partial derivative function that is also continuous over the intersection $a \le x \le b$, respectively.
Then

$$\frac{d}{dt}\int_a^b f(x,t)dx = \int_a^b \frac{\partial}{\partial t} f(x,t)dx$$

If the *a* and *b* are the functions *a*(*t*) and *b*(*t*) with respect to *t*, respectively, then

$$\frac{d}{dt}\int_{a(t)}^{b(t)} f(x,t)dx = \int_{a(t)}^{b(t)} \frac{\partial}{\partial t} f(x,t)dx + f\left(b(t),t\right)\frac{db(t)}{dt} - f\left(a(t),t\right)\frac{da(t)}{dt}$$

(We omit the description of the proof of Theorem1.)

From Theorem 1, we obtain the following Corollary 1.

Corollary 1:

Let $J(t)$ be the convolution between e^{-kt} and $C(t)$ as show in the following.

$$J(t) = e^{-kt} \otimes C(t) = \int_0^t e^{-k(t-\tau)} C(\tau) d\tau$$

Then

$$\frac{dJ(t)}{dt} \equiv J'(t) = (-k)J(t) + C(t)$$

Proof.

Let $a(t)=0,\ b(t)=t$, $f(x,t)\ =e^{-k(t-x)}C(x)$.
Then from Theorem1, we have

$$
\begin{aligned}
&J'(t)\\
&=\int_a^{b(t)}\frac{\partial}{\partial t}f(x,t)dx+f(b(t),t)\frac{db(t)}{dt}-f(a,t)\frac{da}{dt}\\
&=\int_0^{t}\frac{\partial}{\partial t}f(x,t)dx+f(t,t)\frac{dt}{dt}-f(0,t)\frac{d0}{dt}\\
&=(-k)\int_0^t e^{-k(t-x)}C(x)\,dx+e^{-k(t-t)}C(x)-f(0,t)\cdot 0\\
&=(-k)\int_0^t e^{-k(t-x)}C(x)\,dx+C(t)\\
&=(-k)J(t)+C(t)
\end{aligned}
$$

Accordingly, we have

$$J'(t)=(-k)J(t)+C(t) \tag{2}$$

Q.E.D.

3.2. *Parameter Estimation Using DOC Method*

Let $r(t)$ be the measured value by PET camera at time *t*. Then $r(t)$ is approximately represented as shown in the following equation, where the parameters are the same as shown in Eq.(1).

$$r(t)=C_i(t)=\frac{1}{\beta-\alpha}\{J_1(t)+J_2(t)\} \tag{3}$$

where

$$J_1(t)=(k_3+k_4-\alpha)e^{-\alpha t}\otimes K_1C_p(t) \tag{4}$$

$$J_2(t)=(\beta-k_3-k_4)e^{-\beta t}\otimes K_1C_p(t) \tag{5}$$

Applying the aforementioned Corollary 1 to the Eq.(3)-(5), we have the following equations.

$$r'(t)\equiv\frac{dr(t)}{dt}=\frac{1}{\beta-\alpha}\{J'_1(t)+J'_2(t)\} \tag{6}$$

$$J'_1(t)=(-\alpha)J_1(t)+(k_3+k_4-\alpha)K_1C_p(t) \tag{7}$$

$$J'_2(t)=(-\beta)J_2(t)+(\beta-k_3-k_4)K_1C_p(t) \tag{8}$$

Then we have

$$r'(t)=\frac{1}{\beta-\alpha}\left[(-\alpha)J_1(t)+(-\beta)J_2(t)\right]+K_1C_p(t) \tag{9}$$

Similarly,

$$
\begin{aligned}
r''(t)&\equiv\frac{d^2r(t)}{dt^2}\\
&=\frac{1}{\beta-\alpha}\left[(-\alpha)J'_1(t)+(-\beta)J'_2(t)\right]+K_1C'_p(t)\\
&=\frac{\left(\alpha^2J_1(t)+\beta^2J_2(t)\right)}{\beta-\alpha}\\
&\quad+\{(k_3+k_4)-(\beta+\alpha)\}K_1C_p(t)+K_1C'_p(t)
\end{aligned} \tag{10}
$$

Since $J_1(t)$ and $J_2(t)$ are represented by $r(t)$, $r'(t)$ and $C_p(t)$ from Eq.(3) and Eq.(9), we can obtain Eq.(11) by substituting those representation into Eq.(10).

$$
\begin{aligned}
r''(t)=&(k_3+k_4)K_1C_p(t)+K_1C'_p(t)\\
&-(k_2+k_3+k_4)r'(t)-k_2k_4r(t)
\end{aligned} \tag{11}
$$

Then, integrating both sides twice with respect to time *t*, we obtain the following Eq.(12).

$$r(t)=AC_p^{II}(t)+BC_p^{I}(t)+Cr^{I}(t)+Dr^{II}(t) \tag{12}$$

where

$$\begin{cases} r^I(t)=\int_0^t r(\tau)d\tau\\ r^{II}(t)=\int_0^t r^I(\tau)d\tau\end{cases} \tag{13}$$

$$\begin{cases} C_p^I(t)=\int_0^t C_p(\tau)d\tau\\ C_p^{II}(t)=\int_0^t C_p^I(\tau)d\tau\end{cases} \tag{14}$$

$$\begin{cases} A=K_1(k_3+k_4)\\ B=K_1\\ C=-(k_2+k_3+k_4)\\ D=-k_2k_4\end{cases} \tag{15}$$

Since the time series data $r(t)$ and $C_p(t)$ are given by PET Camera and blood sampling respectively, we can obtain the values of parameters A, B, C, D in Eq.(15) by least squares method based on the Eq.(12). So, we can estimate the parameters K_1, k_2, k_3, k_4 from the computed A, B, C, D.

4. Experimentation

We have experimented for parameters estimation using the simulated time series data $C_p(t)$ that means the tracer plasma radioactivity concentration and $r(t)$ that is the computed PET Camera's time series data according to Eq.(1) where the values of parameters K_1, k_2, k_3, k_4 are set beforehand.

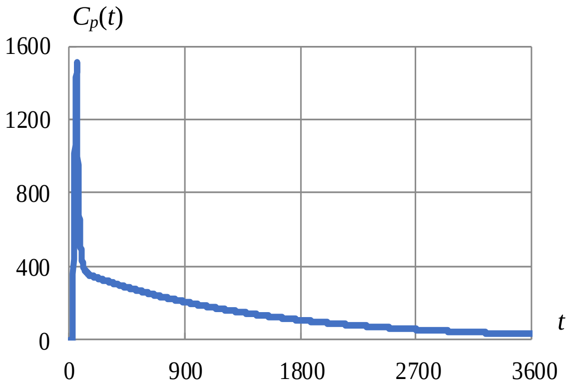

Fig.3. Model function of $C_p(t)$ (plasma)[Bq/ml] at time t [sec] for numerical experimentation.

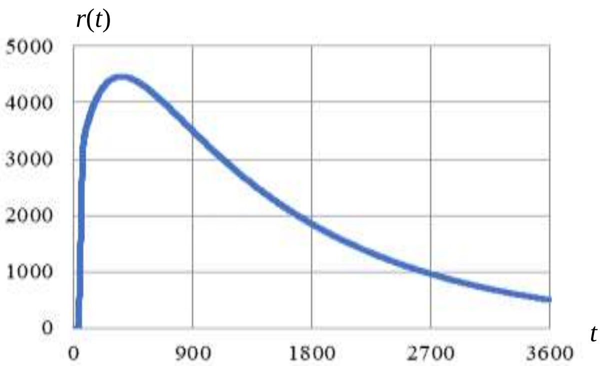

Fig.4. Computed $r(t)$ [Bq/ml] at time t [sec] from $C_p(t)$ without Gaussian noise addition.

The results are shown in Table 1. As a result, we have found that the relative error rate of parameters estimation using the proposed DOC method is less than 0.4 [%], if we use the time series data of $r(t)$ and $C_p(t)$ for more than 600 seconds (10 minutes).

Table 1. Estimated value from $r(t)$ and $C_p(t)$ for 60 minutes' measurement, and its accuracy.

$r(t)$ and $C_p(t)$: 60 minutes' time series data

parameter	true value	estimated value	relative error [%]
K_1	0.2000	0.2004	0.2024
k_2	0.1300	0.1304	0.3737
k_3	0.0600	0.0601	0.0952
k_4	0.0070	0.0070	0.0956

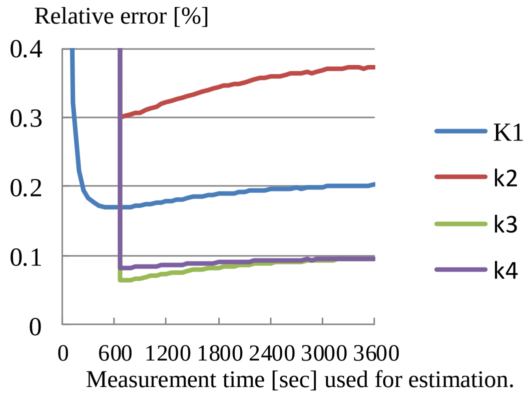

Fig.5. Accuracy of the parameters estimation for K_1, k_2, k_3, k_4 with respect to the measurement time in the case where Gaussian noise are not added to $r(t)$.

References

1. Godfrey, K., *Compartmental Models and Their Application*, (Academic Press, 1983).
2. R. P. Maguire and K. L. Leenders, ed., PET Pharmacokinetic Course Manual, (*International Society of Cerebral Blood Flow and Metabolism*, Summer School 2007, May 2007).
3. https://en.wikipedia.org/wiki/Multi-compartment_model.
4. Hiroshi WATABE, Yoko IKOMA, Yuichi KIMURA, Mika NAGANAWA, and Miho SHIDAHARA, PET kinetic analysis—compartmental model, *Annals of Nuclear Medicine*, Vol. 20, No. 9, 583–588, 2006.
5. Kudomi N, Choi E, Yamamoto S, Watabe H, Kim K, Shidahara M, et al., Development of a GSO detector assembly for a continuous blood sampling system, *IEEE Trans. Nuclear Science*, Vol. 50, No.1, pp.70–73, 2003.
6. Naganawa M, Kimura Y, Ishii K, Oda K, Ishiwata K, Matani A, Extraction of a plasma time-activity curve from dynamic brain PET images based on independent component analysis, *IEEE Trans. Biomedical Engineering*, Vol. 52, No.2, pp.201–210, 2005.

Application and Trial Evaluation of Document Writing Support System to Avoid Emotional misUnderstanding

Shunsuke Doi, Yoshiro Imai*, Koji Kagawa, Tomohiko Takagi, Yusuke Kawakami, Tetsuo Hattori
Graduate School of Engineering, Kagawa University,
2217-20 Hayashi-cho, Takamatsu, Kagawa, 631-0396, Japan

**Corresponding author. E-mail: imai@eng.kagawa-u.ac.jp*
Tel: +81-87-864-2244, Fax: +81-87-864-2244

Abstract

This paper describes a newly developed system of document designing, handling and self-checking in order for writers to avoid their readers' unnecessary emotional misunderstanding and possible repulsion which may occur as a result. It is realized as server-client computing system, namely its server is written in Perl and PHP just like LAMP (Linux-Apache-MySQL-PHP/Perl) and its client is implemented in JavaScript executing on the major Browsers. The server can obtain user document through the client, scan and separate the regarding document into word-level expressions, check each word while matching it with our sentiment dictionary, calculate the relevant sentimental values for the document and then generate the corresponding radar chart based on emotional axis such as delight, anger, sorrow, pleasure etc. on the relevant user's Web. This is one of examples of his/her document visualization. Document writers utilize such a system before transferring and/or archiving, they can check sentimental values for their documents and recognize how their ones have a lot of emotional feelings which would probably include non-suitably emotional expressions. With this facility, the user can check his/her document and recognize whether the document possibly generates readers' unnecessary emotional misunderstanding and moreover repulsion which may occur as a result.

Keywords: Sentimental value, Sentiment analysis, Visualization, Japanese Language processing, Document transferring, Document archiving..

1. Introduction

People used to be writing several kinds of documents such as memoranda, message, e-mail etc. for the third persons to read possibly with emotional feeling. After they prepared such documents, sometimes some of their documents might unintentionally hurt other's heart due to their careless emotional expressions. If some kind of checking services were available, people could check their documents, recognize whether their documents included careless emotional expressions, and avoid to write documents which would unintentionally hurt other's heart.

Data mining becomes more and more popular and then big data analysis has been consistent with the trend of information processing. Data mining and big data analysis seem to be excellent approaches to reveal hidden relation behind phenomena people have never found before and bring new recognition about such a relation to our daily lives for possible decision-making.

Sentiment analysis1 can play another important role of information processing for sentences, expressions and documents not only from SNS/Internet but also from normal, daily verbal communication. Due to preprocess related with sentimental analysis, we can find whether our writing document includes "unnecessary or non-suitable" emotional expressions or not. So we would be relieved to transfer our documents as well as archive ones if we had employed any preprocess to detect such emotional expressions and then had removed these expressions.

This paper describes our Document Transferring and Archiving Service with Sentiment Analysis-based Preprocessing Facility. Such service is designed and implemented as server-client computing model and for users to manipulate it through Web-based application. The paper introduces a whole system and then explains a preprocess service to generate Sentimental Dictionary and to perform Sentimental Analysis to detect emotional expressions graphically. It illustrates some trial of visualization of documents through sentimental analysis in the third section. It demonstrates document transferring and archiving by means of our services in the fourth section. And finally it concludes our summaries in the last section.

2. Detail of System Configuration and Process

Our system has been design and implemented as a typical server-client computing model, where the server is realized in the LAMP type and the client executes on the major browsers written by JavaScript. Fig.1 shows a main flow of the system, the three major menus, namely input menu, show graph one and e-mail transfer one, are provided on the client and then the related three procedures, namely sentimental analyzing, simple mail transferring and PDF generating are invoked on the server and performed as server tasks written in PHP and Perl scripts. The system has two major database managing modules which execute on the server together with SQL database.

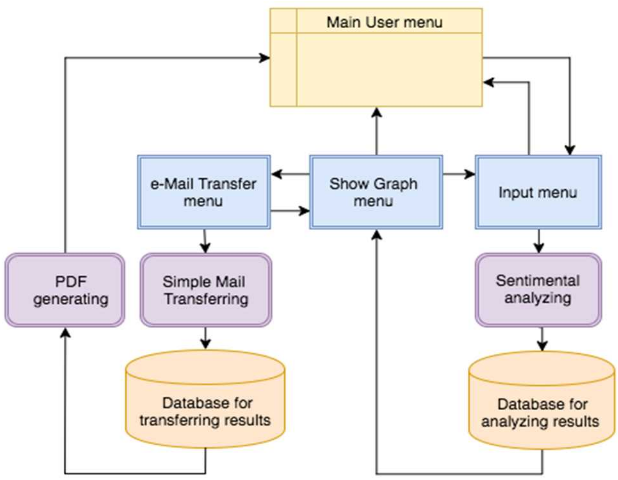

Fig.1. Main flow of the system.

Before describing our sentimental analysis for preprocessing, this subsection explains how to define sentimental dictionary and how to calculate sentimental value for each focused sentence. With Japanese language processing, our system obtains some documents in the target domain, decomposes such a document into sentences and decompose them into a series of words by MeCab. Such words are classified into cluster and computed with sentimental values according to sentimental dictionary[2].

3. Visualization through Sentimental Analysis

3.1 *Process flow for sentimental analysis*

Process for Sentimental Analysis starts decomposing the obtained document into sentence, decomposing each sentence into a series of words by MeCab, and then checks whether each word is registered in the sentimental dictionary or not. If each word of the sentence is registered, then sentence is calculated with sentimental values according to the conditions including "Negation" and/or "Conjunction". Because Negation and/or Conjunction is included in the sentence, calculation of whole sentimental value for the relevant sentence must be modified in the ways shown in Fig.2 and Fig.3.

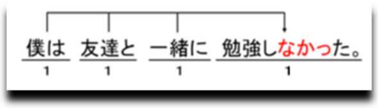

Fig.2. Example for Determination of Negation.

Fig.3. Example for Determination of Conjunction.

3.2 *Computing and assigning of sentimental values*

After picking up the relevant sentimental value for each word from sentimental dictionary together with detection of "Negation" and "Conjunction", calculation of sentimental values for a whole sentence can be performed in the following way. Real example of calculation of sentimental value for simple document is illustrated in Fig.4. A lots of emotional feelings have been classified and categorized into 10 clusters, for example, \`**delight**', \`**anger**', \`**sorrow**' and \`**pleasure**' are the four major axis, and then we have defined other four clusters, some of them seem to be combined and modified with the four major axis. The bottom two lines of 5 clusters shown in Fig.4, which indicate the sentimental values for 10 clusters, are the results of calculated sentimental values for the relevant document described in the expression at the top line of Fig.4.

Fig.4. Example of Calculation and Assignment of Sentimental Values for Simple Document.

3.3 *Visualization based on Sentimental Analysis*

Users understand what kinds of emotional feelings are included in their writing document, so it is more convenient for them to understand emotional feeling whether their writing document includes emotional expressions or not through graphical expression rather than through Fig. 4. Carefully using with those information, writers, namely users of our system, would be able to avoid such non-suitable emotional expressions thank to visualization of emotional feeling in the relevant document.

As you know, it is more useful for visualization to show the results of sentimental analysis graphically than to show them in the ways of calculated tabulation or numerical expression just like Fig.4. So our system can obtain document by user through input mode. And then it can calculate sentimental value and visualize the result of sentimental analysis graphically just like Fig.5. Users can modify their writing documents with emotional feeling into more acceptable contents which includes suitably emotional expressions and reduces non-suitable ones according to visualized results of calculating sentimental analysis for their previous written documents. Each user can check how his/her writing document varies in chronological order from the viewpoint of sequential line graph for the results of calculating sentimental analysis. Fig.6 shows sequential line graph for the results of calculating sentimental analysis. It is very useful and attractive for each user to understand what kind of emotional expressions in his/her writing documents vary in chronological order and to obtain a meaningful hint to modify his/her documents into more suitable not only for himself/herself but also for those who shall probably read his/her documents near future.

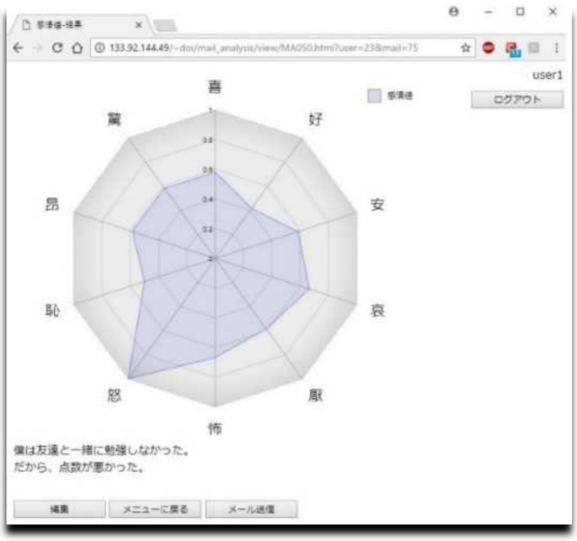

Fig.5. Example for Visualization of Sentimental Values.

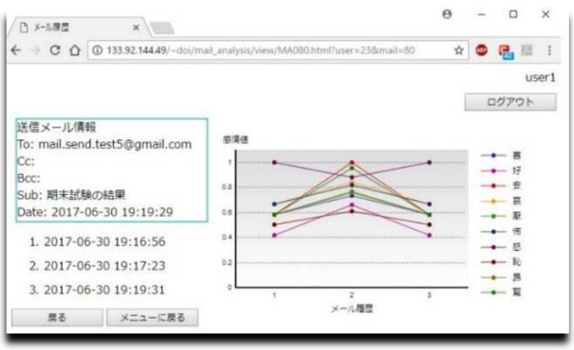

Fig.6. Another Visualization of Sentimental Values.

4. Application of System and its Evaluation

This section describes typical application of the system with other useful services for document transferring and archiving after sentimental analysis and visualization of its calculated results. And it reports the last but not least description about trial evaluation of our system.

At first, document transferring service has been implemented in the system through invocation of server-side e-mail handling facilities called "Postfix" as MTA

(Mail Transfer Agent) and "Dovecot" as MUA (Mail User Agent). A user write his/her document onto the Web-based client of the system, check what kinds of emotional feelings are included in his/her writing document, and then instruct to let the relevant document, which has been already checked by Sentimental analysis, be transferred into someone's e-mail address. Fig.7 shows e-mail transfer menu of the system. With our system, the document to be transferred shall be modified without non-suitable emotional feelings for anyone.

Fig.7 Mail Transferring on Web application of the system.

Secondarily, document archiving service has been also implemented in the system in order to generate a PDF style, namely the system can support to transform the documents into PDF. By means of usage of LaTeX typesetting software, the relevant document can be formed into more easily readable together with dating, signature and other important information automatically. Fig.8. shows PDF generating menu of our system.

Fig.8. PDF generating by LaTeX.

As trial evaluation of our system, we have heard from users about the two types of comments for our system as follows;

(1) "In the case of e-mail writing, I used to be afraid my expression would be probably harmful for the friends who received my e-mail. Therefore this system will be very useful for such my case to write e-mail very comfortably and moreover it will be able avoid my careless expression to hurt others' feeling."

(2) "The system would let us write such documents that did not get offended against others and support us to transfer our documents into PDF styled articles automatically through LaTeX typesetting tool."

5. Conclusion

Our system provides sentimental analysis to calculate sentimental values for each document in order to visualize what kinds of emotional feelings are included in such a document. And it also performs to transfer the relevant documents without non-suitable emotional expressions as well as to archive such documents as PDF files, for example to form them through external LaTeX facility. With our system, users, namely writers of documents, can realize document management effectively and efficiently.

References

1. T. Kumamoto, et al., "Proposal of Impression Mining from News Articles", *Lecture Notes in Computer Science* Volume 3681, pp 901–910, 2005.
2. M. Kyokane, et al., "A Study of Visualization for Hidden Relation between Published Documents and Message from Twitter," *International Journal of E-Learning and Educational Technologies in the Digital Media* Vol.2, No.1, pp.217– 224, 2016.
3. S. Doi, et al., "Calculation and Comparison of Sentimental Values for Tweeting Message during Multiple Years," *Proc. of The Second International Conference on Electronics and Software Science*(ICESS2016@ Takamatsu), pp. 165 – 169, Nov.2016.
4. E. Cambria, et al., "Statistical approaches to concept-level sentiment analysis," I*EEE Intelligent Systems* Volume 28, No.3, pp.6 - 9, 2013.
5. P. Bo and L. Lee, "Opinion mining and sentiment analysis," *Foundations and Trends in Information Retrieval*, Volume.2, No.1–2, pp.1-135, 2008.

A Method of Haiku Generation Using Deep Learning for Advertising Generation

Jumpei Ono
Vocational School of Digital Arts Sendai
Sendai, Miyagi, 980-0014, Japan

Takashi Ogata
Iwate Prefectural University
Sugo, Iwate, 020-0693, Japan
E-mail: j.ono@sugawara.ac.jp, t-ogata@iwate-pu.ac.jp

Abstract

We tried various approaches to story generation. One of them was haiku generation using deep learning. The method we tried had several tasks, one of which was to use only word time-series data as training data. Therefore, the result of training can be a model similar to generation based on simple word-transition probability. Consequently, we organized the current tasks, tried to study the features used for training, and generated by applying the learned results. Furthermore, we consider how to use the method proposed in this paper in advertisement generation and in generating different types of stories.

Keywords: Haiku, Haiku Generation, Deep Learning

1. Introduction

In this study, we attempted to generate various types of stories using both artificial intelligent techniques and narratological models. One of the approaches proposed story generation with a framework of mutual conversion between a haiku and a narrative. We approached this from two perspectives—a generation method based on haiku practices and a generation method based on a deep learning method. Here, we describe the generation of haikus using deep learning. Based on an attempt to generate haikus by Ito, Igarashi & Ogata[1,2], we increased training data and confirmed the change that occurred in the generated result.

2. Background

A haiku is a poem composed of relatively short phrases. As a formal feature, an ordinary haiku consists of three phrase, whereby, the first, second, and third phrases contain five, seven, and five mora, often rhyming to some extent. Furthermore, the number of mora are filled by including "kireji." Semantic features include "kigo" (seasonal words), which directly or indirectly imply scenes to some extent (There are also haiku which deviates from the above characteristics). Fig.1 is a haiku written by Matsuo Basho. The haiku reads as "A frog jumped in an old pond. Sound of water echo." (Because a haiku can describe scenes in extremely short phrases, it must be stated here that English translations can vary greatly depending on the translator).

古 池 や		蛙 飛 び 込 む		水 の 音
Furuike ya	/	kawazu tobikomu	/	mizu no oto

Fig.1 An example of a haiku
(Matsho Basho, "Oku no hosomichi")

Haiku generation using training is a method that uses deep learning by Yoneda et al.[3] and seqGAN by Hirota, et al.[4] among others. In addition, Rzepka & Araki proposed a system to present not only artificial haiku but also sounds and images related to the haiku[5].

We used statistical methods based on deep training; however, from the perspective of the entire framework of haiku generation, differentiation is also achieved by incorporating the approach from the narrative theory. The aspect of that is discussed in Ito & Ogata[6], Ito, Ono & Ogata[7]. Our proposed haiku generation mechanism proposed is single and incomplete. In the haiku generation mechanism, our developed system is linked to the integrated narrative generation system[8], and it has the possibility of being linked to the generation of haikus, stories, music, and video. Ultimately, we treat haiku as one of the inputs to and outputs from story generation, and the haiku generation mechanism is integrated as a mechanism for generating a more versatile story.

3. Haiku Generation

As demonstrated in Igarashi[1,2], this paper uses a method that uses "Chainer," a deep training framework. Previous research[1,2] used 62 phrases in "Oku no Hosomichi" as training data. learned pattern is the appearance pattern of words and characters.

In this paper, 2000 haikus from the "modern haiku database" (http://www.haiku-data.jp/) were used as training data. LSTM was used as the training method. By dividing a haiku into word units using the morphological analyzer "MeCab," a time-series data of word sequence is achieved.

We generated haikus based on data from 100 training iterations. In addition, we generated haikus based on data from 900 training iterations. Therefore, word training of 900 training iterations is the intersection point of the approximate straight line (inverse proportionality relationship between the understandability of haiku and interesting haiku). Fig.2 shows the result of previous research[2].

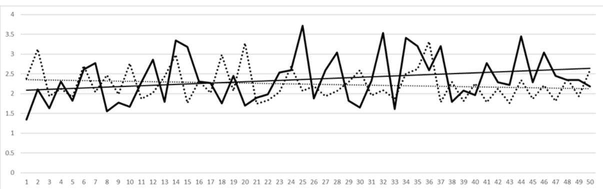

Fig.2 Deep training based on words[2]
(X-axis is each Haiku/ Y-axis is averages of evaluations each Haiku. The solid line: understandability / The broken line: interest)

Fig.3 shows the generation results of 100 iterations of training, and Fig.4 shows the generation results of 900 iterations of training.

(a). [洗い髪 のせ哭く後ろ 向き背中]
(b). [込むアパート ゆるめし眠れ アンデルセンやわらかい]
(c). [十一月投ず梅]

Fig.3 A haiku based on words training (100 iterations)

(d). [生涯に あざやか秋切る は哀しり]
(e). [夏野笑ぐ の峯日のコップ]
(f). [はじまりて 会うとや見える]

Fig.4 A haiku based on words training (900 iterations)

Subsequently, we attempted to generate a haiku without controlling the number of mora, but as in (a) of Fig.3, a haiku suitable for the number of mora with meaning was generated. Furthermore, (b) in Fig.3, where the number of mora is large, these can be used as a haiku if you adjust them using any method. Conversely, the examples in (c) in Fig.3, (e) in Fig.4, and (f) in Fig.4 have meaning and a form that can be considered to have generated parts of haiku. Consequently, in the narrative approach, it is considered to be a generation result useful for generating parts of haiku. Generation results of Igarashi[1,2] concluded that many data existed that were the same as input data due to overtraining, and the overall results thus resulted in potentially useful results for future development.

4. Conclusion

In this paper, we attempted to generate a haiku by training using LSTM. This improved training data from previous trials. Compared with previous attempts, the variance of the quality of the generated haiku increased, but we succeeded because we aimed to generate a haiku irrespective of the input. In the future, while trying to control the formal aspect, we will try to create haikus from the fused narrative approach.

References

1. K. Igarashi, T. Ito and T. Ogata, An attempt of Haiku generation by deep learning. *Proc. of Special Interest Group on Language Sense Processing Engineering*, **57** (2018), 35-37.
2. J. Ono, T. Ito and T. Ogata, Considering a Haiku Generation Process Using Deep Learning. *Proc. of the*

28th Annual Conference of the Japanese Neural Network Society, (2018), 166-167.

3. K. Yoneda, S. Yokoyama, T. Yamashita and H. Kawamura, 2018. Generated haiku distinctions by deep learning. *IPSJ SIG Technical Report*, 2018-ICS-192 (8) (2018).
4. A. Hirota, N. Oka, M. Araki and K. Tanaka, Haiku generation by seqGAN that divided learning data set. *Proc. of the Twenty-fourth Annual Meeting of the Association for Natural Language Processing*, (Okayama, Japan, March 2018), 1292-1295.
5. R. Rzepka and K. Araki, Haiku Generator That Reads Blogs and Illustrates Them with Sounds and Images, *Proc. of the Twenty-Fourth International Joint Conference on Artificial Intelligence* (IJCAI 2015)
6. T. Ito, and T. Ogata, On haiku/narrative generation. In *Proc. of the 56th Special Interest Group on Language Sense Processing Engineering*, (Morioka, Japan, Dec. 01-06, 2017), 35-37.
7. T. Ito, J. Ono and T. Ogata, Haiku Generation Using Gap Techniques, *2018 International Conference on Artificial Intelligence and Virtual Reality,* V-004.
8. T. Ogata, The Integrated Narrative Generation System -From Mechanism to Contents-. In T. Ogata, Y. Kawamura & A. Kanai *Information Narratology*, (Tokyo, HAKUTO-SHOBO publishing, 2018), 247-288.

The Pragmatic Features of Onomatopoeias in the Recipe Corpus

Hiroki Fukushima*
University Department, Kyushu Women's University,1-1, Jiyugaoka, Yahata Nishi Ward, Kitakyushu City, 807-0000, Japan†

E-mail: fukushima@kwuc.ac.jp
www.hiroki.fukushima.jp

Abstract

In this study, we analyzed the pragmatic features of the onomatopoeias in the recipe corpus.As a clear result is that the onomatopoeias tend to co-occur with the words for taste or flavor (i.e. sweetness, acidity, umami, flavor, and so on.). This tendency suits to the function of the onomatopoeias in the tasting description corpus which the author have revealed.

Keywords: Onomatopoeia, recipe, form-masking method

1. Introduction

In a natural language, the connection between form and meaning is said to be arbitrary. There is a rich vocabulary whose form (i.e., sound) is suggestive of its meaning. In English, for example, flare and glare are different in intensity, and the semantic difference is due to the sound difference between f- and g-. The same goes for the difference between sarasara (i.e., smooth) and *zarazara* (i.e., rough) in Japanese. Thus, in the case of sound symbolism, the meaning of a word is partially influenced by the sound of the word. Sound symbolic expressions are often used to describe the perception of taste and smell in Japanese.

In this study, we focus on Japanse sound symbolic words relating to tastes. Onomatopoeia is a typical exemplar of sound symbolism, and yet, the sphere of sound symbolism is much broader. Chip and slit sound smaller than chop and slot. Thus, vowels have something to do with sound symbolism.

In the previous studies[1], researchers focused on collecting symbolic expressions and grouping them into categories, identifying what sound corresponds to what meaning. Cross-linguistic studies have been conducted to show if there are universal trends in sound symbolism. However, little systematic research has been done to show how symbolic words are used in a perceptual domain.

2. Method

In other to identify the semantic functions of sound symbolism in text, the author have developed a new method or what we call "the form-masking method, " by which we were able to reveal the co-occurrence relationships within corpora, without considering specific meanings of symbolic words. [2]

By this method, we can reveal the pragmatic features such as “what do onomatopoeias modify in general?”, or “what is the pragmatic difference between the onomatopoeia-containing sentences and the non-onomatopoeia-containing sentences”, rather than the individual usage of the onomatopoeias.

2.1. *Procedure*

0. Prepare and cleansing the corpus
1. Extract the onomatopoeias in the corpus
2. Replace each onomatopoeia with a masking word
3. Extract only the “onomatopoeia(masking word)-containing sentences” from the whole corpus. Remains are the sub-corpus that is “non-onomatopoeia-containing sentences”.

2.2. *Data*

In this study, we analyze the recipe database of Cook Pad, the recipe-posting website in Japan.The “whole corpus” consists of the title and abstract of the posted recipe.

Table 1 shows the detail of the corpora. Note that the OS (onomatopoeia-containing sentences corpus) and the nonOS (non-onomatopoeia-containing sentences corpus) are the sub corpus of the Whole Corpus.

Table 1

	Whole Corpus	OS	nonOS
token	9,928,126	1,310,839	8,617,286
type	83,868	22,467	80756
total sentences	2,726,551	304,145	2,422,405

2.3. *Analyzed words*

In order to reveal the pragmatic features of OS and nonOS (i.e. co-occurrence features of onomatopoeia), following words are examined:

- Top 150 words of both OS and nonOS
- Characteristic words of each corpus (75words for each, by Jaccard Index)

3. Result

The result of Chi-square test (with Yate’s correction) is shown in the Appendix A and B. Note that Bonferroni correction for the multiple comparisons is adopted.

4. Conclusion

In this study, we analyzed the pragmatic features of the onomatopoeias in the recipe corpus.

As a clear result is that the onomatopoeias tend to co-occur with the words for taste or flavor (i.e. sweetness, acidity, umami, flavor, and so on.). This tendency suits to the function of the onomatopoeias in the tasting description corpus which the author have revealed[2].

Reference

[1] L. Hinton, J. Nichols and J. J. Ohala, *Sound symbolism*. Cambridge University Press, 2006.

[2] H. Fukushima, M. Imai and S. Tanaka, "The Usage Mechanism of Japanese Ideophones in the Description of Taste: Morphological and co-occurrence analysis of the description of wines and sakes", *International Journal of Computational Linguistics Research*, vol. 8, no. 3, pp. 109–122, 2017.

Appendix A.

	word	χ2	p	
1	eat	7477.34	<.0001	*
2	vegetable	18277.38	<.0001	*
3	taste	5322.53	<.0001	*
4	sweet	5506.43	<.0001	*
5	summer	8365.9	<.0001	*
6	texture	9443.46	<.0001	*
7	ginger	1409.64	<.0001	*
8	juicy	2006.38	<.0001	*
9	vitamin	1456.31	<.0001	*
10	nutrition	6603.2	<.0001	*
11	outside	8594.99	<.0001	*
12	feeling	22571.46	<.0001	*
13	finished	1669.46	<.0001	*
14	umami	1923.03	<.0001	*
15	umami taste	3102.72	<.0001	*
16	hot	5006.83	<.0001	*
17	fiber	4832.19	<.0001	*
18	matching	2389.91	<.0001	*
19	morning	5012.83	<.0001	*
20	tasty	1380.17	<.0001	*
21	dough	1365.36	<.0001	*
22	volume	1326.29	<.0001	*
23	body	1219.9	<.0001	*
24	finish	1174.17	<.0001	*
25	(ranked)	939.67	<.0001	*
26	smell	927.63	<.0001	*
27	lemon	840.1	<.0001	*
28	stew	829.07	<.0001	*
29	effective	799.22	<.0001	*
30	aromatic	793.22	<.0001	*
31	vinegar	791.57	<.0001	*
32	softly	790.29	<.0001	*
33	flavor	734.93	<.0001	*
34	put into	706.24	<.0001	*
35	smell(V)	705.59	<.0001	*
36	appetite	688.95	<.0001	*
37	acidity	667.59	<.0001	*
38	rich	647.83	<.0001	*
39	flesh	611.91	<.0001	*
40	rich taste	548.25	<.0001	*
41	soft	542.19	<.0001	*
42	sweetness	529.02	<.0001	*
43	add	491.86	<.0001	*
44	cookie	458.61	<.0001	*
45	season	410.63	<.0001	*
46	feeling	402.08	<.0001	*
47	fresh	392.69	<.0001	*
48	bread	381.98	<.0001	*
49	ponzu sauce	377.3	<.0001	*
50	hot(spicy)	364.74	<.0001	*
51	a dish	332.52	<.0001	*
52	get cold	321.55	<.0001	*
53	gentle	312.77	<.0001	*
54	differ	233.14	<.0001	*
55	broil	215.72	<.0001	*
56	soup	204.96	<.0001	*
57	cake	199.74	<.0001	*
58	labor	185.88	<.0001	*
59	adult	165.19	<.0001	*
60	skin	162.24	<.0001	*
61	egg	156.1	<.0001	*
62	bread	140.59	<.0001	*
63	roll	129.83	<.0001	*
64	go forward	115.69	<.0001	*
65	Welsh onion	112.87	<.0001	*
66	beer	110.02	<.0001	*
67	leef	107.27	<.0001	*
68	seasoning	107.24	<.0001	*
69	chill	104.72	<.0001	*
70	cheese	80.56	<.0001	*
71	healthy	74.53	<.0001	*
72	breakfast	67.6	<.0001	*
73	ume plum	66.5	<.0001	*
74	salad	61.35	<.0001	*
75	water	61.17	<.0001	*
76	cabbage	53.73	<.0001	*
77	hamburger	44.1	<.0001	*
78	salty-sweet	23.83	<.0001	*
79	sake	19.97	<.0001	*
80	Chinese cabbage	17.55	<.0001	*
81	good	17.3	<.0001	*
82	sauce	12.3	0.0005	
83	use	11.72	0.0006	
84	bit hot	11.05	0.0009	
85	time	10.08	0.0015	
86	deep-fry	9.72	0.0018	
87	chicken	8.78	0.003	
88	butter	6.13	0.0133	
89	yoghurt	5.93	0.0149	
90	mayonnaise	5.79	0.0161	

df = 1, * p < .00026

Appendix B.

	Words	$\chi 2$	p	
1	easy	13889.69	< .0001	*
2	home	2616.29	< .0001	*
3	microwave oven	2549.44	< .0001	*
4	character Bento	1902.71	< .0001	*
5	toast	1836.53	< .0001	*
6	topics (fn.)	1825.70	< .0001	*
7	bacon	1770.35	< .0001	*
8	regular dishes	1761.51	< .0001	*
9	Natto	1724.92	< .0001	*
10	thank	1711.19	< .0001	*
11	de (fn.)	1658.44	< .0001	*
12	left over	1638.78	< .0001	*
13	canned tuna	1626.43	< .0001	*
14	green pepper	1612.86	< .0001	*
15	diet	1590.76	< .0001	*
16	soya milk	1589.39	< .0001	*
17	frying pan	1551.74	< .0001	*
18	cut	1545.64	< .0001	*
19	avocado	1536.34	< .0001	*
20	spinach	1429.80	< .0001	*
21	gratin	1419.13	< .0001	*
22	perfection	1412.12	< .0001	*
23	cookpot	1402.67	< .0001	*
24	soy sauce	1398.10	< .0001	*
25	carrot	1384.23	< .0001	*
26	corn	1381.03	< .0001	*
27	original	1368.23	< .0001	*
28	salmon	1342.17	< .0001	*
29	eggplant	1328.15	< .0001	*
30	balsam pear	1319.16	< .0001	*
31	mayonnaise	1287.92	< .0001	*
32	think(fn.)	1255.01	< .0001	*
33	sauce	1233.68	< .0001	*
34	chicken	1231.09	< .0001	*
35	freezing	1222.56	< .0001	*
36	left over	1205.04	< .0001	*
38	baby food	1196.35	< .0001	*
39	cheep	1172.89	< .0001	*
40	many	1165.58	< .0001	*
41	boil	1162.38	< .0001	*
42	kimchi	1160.85	< .0001	*
43	ingredients	1151.25	< .0001	*
44	calorie	1150.34	< .0001	*
45	preference	1149.27	< .0001	*
46	cook	880.23	< .0001	*
47	stir-fry	811.39	< .0001	*
48	love(V)	780.48	< .0001	*
49	recipe	673.15	< .0001	*
50	ingredients	669.48	< .0001	*
51	remake	607.09	< .0001	*
52	dress	510.49	< .0001	*
53	OK	467.08	< .0001	*
54	easy-made	373.65	< .0001	*
55	Bento	363.52	< .0001	*
56	rice cooker	320.40	< .0001	*
57	broccoli	303.19	< .0001	*
58	miso	290.29	< .0001	*
59	mix together	259.54	< .0001	*
60	home	255.45	< .0001	*
61	-like (fn.)	253.49	< .0001	*
62	simple	218.44	< .0001	*
63	one bowl meal	215.26	< .0001	*
64	pasta	213.03	< .0001	*
65	cook	204.61	< .0001	*
66	boiled food	202.36	< .0001	*
67	Kimpira	201.42	< .0001	*
68	usage (fn.)	179.00	< .0001	*
69	jam	175.67	< .0001	*
70	handmade	171.04	< .0001	*
71	pizza	151.40	< .0001	*
72	delited	136.93	< .0001	*
73	seasoning	134.07	< .0001	*
74	like	128.51	< .0001	*
75	on the market	128.35	< .0001	*
76	recommend	127.54	< .0001	*
77	salted Koji	118.29	< .0001	*
78	Kombu kelp	109.91	< .0001	*
79	curry	93.34	< .0001	*
80	lol (fn.)	86.04	< .0001	*
81	pork	78.22	< .0001	*
82	Chinese	68.19	< .0001	*
83	fridge	48.73	< .0001	*
84	pudding	48.31	< .0001	*
85	pork	47.88	< .0001	*
86	potato	45.17	< .0001	*
87	made (fn.)	42.45	< .0001	*
88	children	42.30	< .0001	*
89	arrange	41.46	< .0001	*
90	tomato	29.31	< .0001	*
91	spring	20.93	< .0001	*
92	salt	20.17	< .0001	*
93	go well	13.82	< .0001	*
94	boil	13.26	< .0001	*
95	chicken	6.27	0.012	

Storytelling in the Conversation of Aged People

Yuki Hayashi
Graduate School of Science and Engineering, Chiba University, 1-33 Yayoi-cho, Inage-ku, Chiba-shi Chiba, 261-0004, Japan[*]
E-mail: yu@chiba-u.jp

Akinori Abe
Faculty of Letters, Chiba University, 1-33 Yayoi-cho, Inage-ku, Chiba-shi Chiba, 261-0004, Japan / DWANGO Artificial Intelligence Laboratory, Tokyo, Japan [†]
E-mail: ave@ultimaVI.arc.net.my

Abstract

For early detection of dementia, we regarded dementia as a type of communicative problem which was gradually articulated through communication with people concerned. From the viewpoint of that, we examined narrative data stored in DIPEx-Japan and classified characteristic phrases into several categories.

Keywords: early detection of dementia, analysis of semi-structured interview data, illness narrative.

1. Introduction

It is said that early detection of dementia is important. For example, Honma pointed out the importance of the early detection as follows[1].

- In case of Alzheimer's dementia, its progress will be delayed by Donepezil hydrochloride, which is a type of medicine. Therefore, a period of in-home care will be able to be extended.
- The right of self-determination will be respected. For example, the elderly people will be able to communicate with their family in regard to wealth management or nursing before they will suffer from several symptoms of dementia.
- QOL (Quality of Life) will be preserved. If care-givers (including family members) recognize the state of dementia in advance, they will be able to keep communicating with a person with dementia.

To detect dementia, several tools have been recommended. For example, fundamental check list is shown in Manual for preventing nursing[4]. According to this list, if an elderly person is often pointed out that he/she is forgetful, his/her cognitive functions will be suspected to decline. However, it is difficult to determine whether an elderly person is dementia or not. Generally, dementia is defined as ``the sustainable decline of intelligent abilities and the state which interfere with daily life and social life due to several types of cognitive disorders''[6]. We think early detection of dementia is difficult due to the ``sustainable'' decline of intelligent abilities. In this paper, we will discuss the difficulty of early detection of dementia based on narrative data.

2. Dementia problem

Alzheimer's disease, Lewy body disease or cerebrovascular disease are known as the factor of dementia. However, an appearance of these disease is not

No.	Question	Yes	No
	(...)		
16	Do you go outside at least once per week?	0	1
17	This year do you go outside less than last year?	1	0
18	Are you often pointed out that you are forgetful?	1	0
19	Can you make a telephone call by yourself?	0	1
20	Sometimes aren't you sure when is today?	1	0
21	Your daily life is vivid in this 2 weeks.	1	0

Fig. 1. Fundamental Check List[4]

always equal to the beginning of dementia. Deguchi interpreted dementia ``not just as physical and somatic problem for the elderly people but as interactive problem due to communicative disorder between the elderly people and people concerned"[5]. So we regard dementia as communicative problem which is gradually articulated through communication with people concerned. Through an interview data, Deguchi illustrated the phases of dementia troubles as follows.

- Zero point of an unspecialized trouble,
- Variation of an interpretation or definition about the trouble,
- Confusing how to deal with the trouble,
- Regarding the trouble as a claim,
- Discussing how to deal with the trouble among people concerned,
- Determining how to deal with the trouble among people concerned

To discover the beginning point of dementia trouble (``Zero point of an unspecialized trouble"), Deguchi interviewed the elderly people with dementia and their family. However, there are not so many samples in Deguchi (1999) so we'll analyze the other type of interview data in the next chapter.

Furthermore, in articulation and cognitive anomie hypothesis, Nakagawa examined the process of dementia. According to his hypothesis, ``a claim on unspecialized trouble will refuse a process of normalization. Then the claim will gradually be articulated and be classified into deviation, social problem or the other type of problems. Finally, the factor and solution for the claim will also be articulated"[3]. In the following chapter, we will analyze communicative aspect of dementia and examine the difficulties of early detection of dementia.

3. Analysis

3.1. *Method*

We have analyzed semi-structured interview data stored in DIPEx-Japan[2]. DIPEx is a database of personal experiences of health and illness. It contains patient interviews data and the database is opened to public through the Internet. So patients, their family members and medical professionals can access the narrative. DIPEx-Japan has various theme of narrative shown in Fig~\ref{dipex}. In each section, there are voice data (some interviewees hide their face) and text data like Fig~\ref{dipex_sample}. In this chapter, we will focus on narrative about ``beginning of dementia".

Fig. 2. The construction of interview data. Upper side is voice data and lower side is text data (in Japanese).

3.2. *Results*

We examined how caregivers (including family members) noticed the beginning of dementia before some type of troubles are clearly classified into dementia. In the following analysis, characteristic phrases will be shown in several categories.

The first type of narrative is the narrative in which people didn't regard as dementia. There are some examples as follows (with Japanese translations).

- I didn't imagine the possibility of disease. (病気の予想なんかしてなかった。)
- I think our family had never considered the possibility of dementia. (認知症かどうかっていう

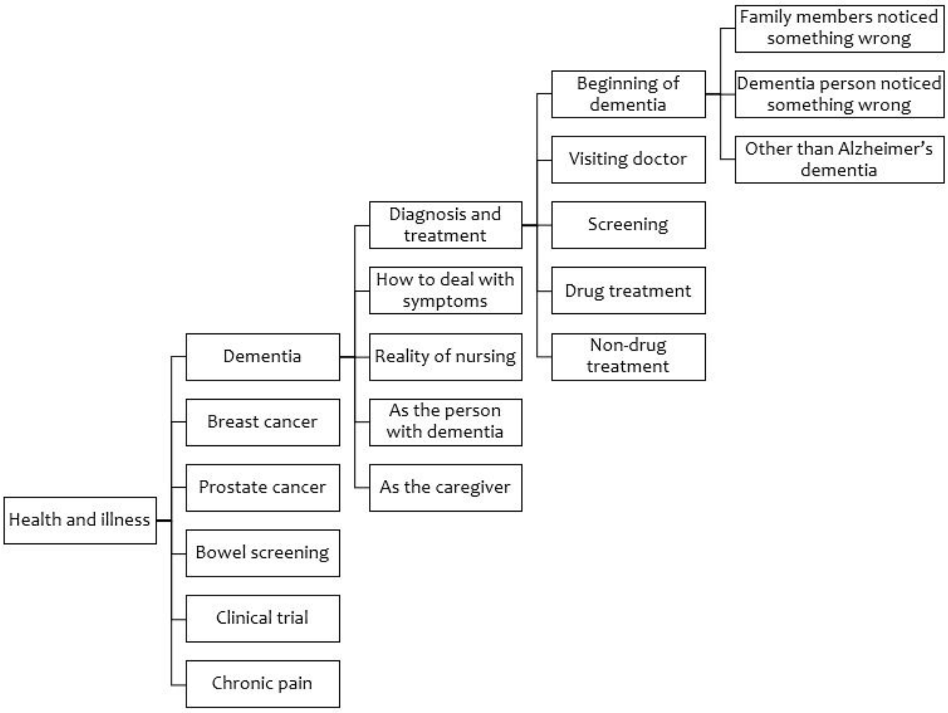

Fig. 3. The construction of narrative in DIPEx-Japan.

ような風にはみんな捉えてなかったんじゃないかと思う。)

In several cases, we observed the reason why people had not regarded as dementia.

- My mother had depression and saw her doctor regularly. So I was not sure whether she was dementia or not. (うつになって以来神経科とかにかかってて、それでずーっと来たので、その異変ていうのが、どこから異変ていうのがわからなくて。)
- I thought she looked strange due to her age. (年をとって、そういうふうになっているみたいな。)
- On that day, he might be not feeling very well. (その日は、体調が悪いのかなとか思って。)

Secondly, there are the narrative in which people pointed out some specific events they felt wrong or strange as follows (with Japanese translations).

- I think she often left her belongings. (置き忘れとかはね、結構あったと思う。)
- It took so long time for my husband to search his belongings. (あれどこいったんだろうって、探す時間が長くなって。)
- He sometimes forgot a password for ATM. (たまに暗証番号忘れてお金が下ろせなかったりとか。)
- He made a phone call to a certain person and did soon again to the same person. (さっき電話をかけたところにまたかけ直す、みたいなことがあって。)

These behaviours are nearly equal to the dementia symptoms which are known as typical ones. In addition, some people focused on the other type of behaviour.

- Her bahaviours, especially in the way of walking, looked wrong for me. (やっぱり挙動ですかねえ。歩き方がおかしいとか。)
- Her sleeping hours gradually increased. (睡眠時間がだんだん長くなってきたようなのを覚えています。)

As we mentioned, the beginning point of dementia is usually not clear. In fact, the following examples shows the aspect of dementia and a type of confusion for family members.

- I'm not sure when is the beginning of dementia. (いつごろ始まったかっていうのは、はっきりしない。)
- In those days, I was not sure whether my husband is dementia or not. (そのときは、やっぱり、分からなかった。)

However, there are the narrative in which people pointed out something wrong or strange as follows (with Japanese translations).

- A few years ago before my husband was diagnosed with dementia two years ago, I think something strange happened around him. (その診断の 2, 3 年前には、何かいろいろあったような気がする。)
- My mother was mature for her age. However, there were something strange with her. (しっかりした母親やったんですよ。ところが、何か様子がどうも。)
- When I visited my mother, I felt something wrong with her. (訪ねて行ったときに、どうもいつもと様子が違う感じを受けた。)

3.3. *Discussion*

Usually people didn't determine whether their family member was dementia or not because they compared their family with common people. In addition, it may be difficult for them to detect the differences between normal state and wrong state.

In the second type of narrative, people pointed out some specific events they felt wrong or strange. However, these behaviours are nearly equal to the dementia symptoms which are known as typical ones. So it is not so suitable for early detection of dementia. On the other hand, in the last type of narrative, people told they felt something wrong or strange. These narrative seem not to have significant meanings, but feelings which family members as caregiver may feel are important. We think these narrative are less influenced by cognitive bias.

4. Conclusion

For early detection of dementia, we regarded dementia as a type of communicative problem which was gradually articulated through communication with people concerned. From the viewpoint of that, we examined narrative data stored in DIPEx-Japan and classified characteristic phrases into several categories.

References

1. A. Honma, Early detection of senile dementia and future prospect in local cities, *Gerontology New Horizon*, vol. 15, pp. 20--23, 2003.
2. DIPEx-Japan, Narrative on health and illness, referred on 27th April 2017.
3. N. Nakagawa, *Social problem game and researcher's game, the Bulletin of faculty of liberal arts*, Toyama University, vol. 25, pp. 57--81, 1995.
4. Revision committee on manual for preventing nursing, On preventing nursing, in *Manual for preventing nursing*, pp. 1--37, March 2012.
5. Y. Deguchi, *Micro politics of troubles about senile dementia---retrospective narrative on family care-givers' trouble experiences---, Sociologist*, faculty of sociology, Musashi University, vol. 1, pp. 39--75, 1999.
6. Y. Takebayashi, H. Ueno, Development of fundamental technology for understanding emotions of people with dementia and its applications to communication support, *The 27th Annual Conference of the Japanese Society for Artificial Intelligence*, 3A1-NFC-03-2, 2013.

Expression of the taste of Japanese sake and metaphor

Akinori Abe
Division of Behavioral Science, Faculty of Letters, Chiba University, 1-33 Yayoi-cho, Inage-ku, Chiba 263-8522, Japan

Dwango Artificial Intelligence Laboratory, Tokyo, Japan

E-mail: ave@ultimaVI.arc.net.my, ave@chiba-u.jp

Abstract

Seto explained ``tasting expression'' from the aspects of synesthetic expressions (both direction), which are metaphor, metonoymy, and synecdoche. When we express the taste of Japanese sake, we sometimes use the expression ``Refreshing scent such as the scent of muskmelon and pear is elegant...'' It is rather easy to express the taste by using the well-known taste. However, how we control the path of the metaphor flow? For instance, we frequently use the expression ``cheek like apple.'' Why we assume the colour is red? Similarly, for the taste of the sake, we frequently use the expression ``taste like apple.'' Which apple we assume? In this paper, I will discuss the flow of the metaphor from the aspect of discussion above..

Keywords: expression of taste, metaphor, Japanese sake, affordance

1. Introduction

Seto explained ``tasting expression'' from the aspects of synesthetic expressions (both direction), which are metaphor, metonoymy, and synecdoche [1]. When we express the taste of Japanese sake, we sometimes use the expression ``Refreshing scent such as the scent of muskmelon and pear is elegant...'' It is rather easy to express the taste by using the well-known taste. For the description of the taste of Japanese sake, I previously discussed in [2] and [3]. I discussed taste has a shape. Several researchers have discussed the taste by very simple shape such as round and rectangle (For instance, [4]). However, I thought more complex shape should be dealt with for the taste. Because the taste is rather complicated and it is not easy to express only by simple shape such as round and rectangle. In addition, the shape can be extended to metaphoric expression. In this paper, I will discuss the taste of sake from the aspect of metaphor and flow from the source to target.

2. About the expression of taste

Sommeliers have several words for the expression of the taste of wines. These words can be regarded as poetic, emotional or affective words. Accordingly they can express the taste better but sometimes are not easy to understand. Seto explained ``tasting expression'' from the aspects of synesthetic expressions (both direction), which are metaphor, metonoymy, and synecdoche. It means that taste can be expressed by the figurative expression, and that taste is expressed by using touch, smell, sight, and hearing [1]. For instance, in the description ``[t]he taste of chat masala is explained that the rounded spicy taste of Aji Amarillo is added to the spicy taste of garam masala,'' sight is used to explain the taste. The description can be regarded as a metaphor. The shape is used as a metaphor to express the non-sharp taste. Thus when we express the taste, we frequently use a metaphor, because it is rather difficult to find or create a nice word. A metaphor is a good tool to express novel concept.

3. Expression of the taste of wine

There exist several dictionaries for the wine tasting. All definitions in the dictionary are clear. For instance, taste is defined by using well known taste such as butter. When we describe the taste of wine, we usually use the phrases in the dictionary. For instance, in BC Liquor Stores, Vol. 19, Issue 2 (summer 2017), the following descriptions can be found:

Quail's Gate Pinot Noir (2015)

> Elegant and sophisticated, this Burgundian-style Pinot Noir expresses bright strawberry, red cherry and spice with hints of forest floor and earth. Medium-bodied with fine tannins, this will pair well with salmon.

We can easily imagine the taste of wines. In fact, ``hints of forest floor'' is frequently used phrase for nice wines. In addition, ``forest floor'' is used for matured wine. In general, the phrase is used for the (nice) wines produced in Bourgogne. A forest floor is defined as the above-ground layer of a forest made up of tree roots, soil and decaying matter (Collins English Dictionary). Thus the taste of wine can be imagined as a *soil and decaying* (matured) taste and flavour. The richly organic layer of soil and debris is a characteristic of forested land. This will also be a characteristic of the wine. This phrase can become a type of a good metaphor. Readers may understand correctly the taste of wines by the above descriptions. As for the metaphor of the wine taste, there seems very few misunderstandings. For instance, the wine taste is strictly defined as follows:

Apple: A smell often found in young white wines. Unripe apple is often a sign that a wine has not undergone malolactic fermentation.

Apricot: Common in the white Rhone's of Condrieu and Chateau Grillet and other examples of the Viognier grape, and in wine from botrytis-affected grapes.

In addition, the cultural difference is understood as follows:

Pear drop is a term often used by wine writers to describe the flavor of Beaujolais Nouveau. These writers would all be British since pear drops are virtually unknown in North America. They're a traditional type of candy that the British call boiled sweets and Americans call hard candy (https://www.delongwine.com/blogs/de-long-wine-moment/14610411-tasting-terms-pear-drop). Thus all are strictly defined.

4. Expression the taste of Japanese sake

For the taste of Japanese sake, according to Fukushima, there exist only critical words such as rough taste (雑味 (zatsumi)) which can express a bad taste. This is because such words are usually used for (critically) checking the taste of sake in sake factories. Thus words for a good taste have not been established yet. In addition, there exists a textbook for studying to pass the master of sake examination. It will not be used as a general dictionary. Fukushima has built the ``Japanese Sake Tasting Dictionary'' [5], but it is not large dictionary. Accordingly, when we express the taste of Japanese sake, we will use our own expression. For instance, in ``LOVE ♡ Japanese sake!, 2014, 2 Gakken,'' the taste of Isojiman Junmai ginjo (磯自慢 純米吟醸) was described as follows:

Refreshing scent such as the scent of muskmelon and pear is elegant...

(マスクメロンや洋ナシを思わせる爽快とした香りは気品すら感じさせるもの....)

The phrase describes the taste by borrowing the taste of fruits. Perhaps, the taste of muskmelon and pear will be the same for everybody. However for a certain sake, ambiguous express can be used. Since we do not have a dictionary, in such case, the impression may be different according to the culture. As pointed above, a strict definition may be required in such cases. However sometimes without such a strict definition, we can understand the meaning of metaphor.

5. Metaphors are common?

In [6], I discussed the process of understanding metaphor. When we use the phrase including metaphor ``a cheek like an apple,'' we assume that the cheek belongs to a pretty young girl and its colour is red. Actually there are several colour of apples, for instance, red, yellow etc. Why we can understand the colour is red? I discussed the process of understanding metaphor by using the concept of metaphor. Jung et al. discussed the metaphor in an interface (human computer interaction) design as shown in figure 1.

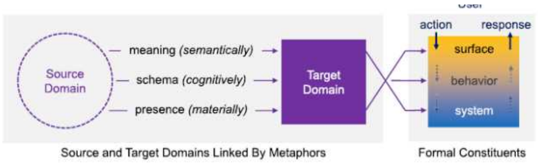

Figure 1: User interaction mediated through different formal aspects

The process is for an interface design, it will not possible to apply this structure to the normal metaphor, but the concept is interesting. From source to target, three links are connected and the understanding is performed by the following three aspects:

--The surface aspect of interactive forms is about *how a digital application is represented* through its interface to indicate what a user can do with it.

--The behavioral aspect is about *how an artifact responds to interaction events* by unfolding corresponding formal changes that are coded behind the surface.

--The systemic aspect of an interactive form is about *how its multiple states are connected to each other* in a coherent structure.

Thus Jung et al. claimed that forms and meanings of artifacts are connected across various material domains and that metaphors implicitly or explicitly play a key role in bringing a new design perspective from one domain to another, sometimes reified as design conventions. Their investigation extended the perspective on affordances from perceivable action possibilities to invitations for interpreting forms and meanings of an interactive artifact. They also highlighted the role of metaphors as a systematic strategy for exploring materialities and affordances of digital media.

This position is for the HCI design, so, as pointed out above, it is rather different from the metaphor understanding in our domain. However, the concept of affordance can be applied to our domain and the application will be significant.

6. Metaphor understanding by affordance selection

As discussed in the above, the function (selection) of affordance will be important in metaphor understanding. However, how to select the proper affordance for metaphor understanding? As shown in the previous section, the meaning of pear drop differs according to the country. The phenomenon can be considered by the concept of affordance. Affordance was introduced by Gibson [7] [8]. Gibson ecologically introduced the concept of affordance for perceptional phenomena. It emphasizes the environmental information available in extended temporal pattern in optic arrays, for guiding the behaviors of animals, and for specifying ecological events. Thus he defined the affordance of something as ``a specific combination of the properties of its substance and its surfaces taken with reference to an animal."

I described the taste of Kagatobi just-squeezed raw non-additional-water Ai (加賀鳶 しぼりたて生原酒 藍) as follows (part of):

The taste is nicely and strongly harmonized. At last, a taste of fruit (pear) repeats in the mouth. Before that a pungent taste slightly comes on the top of tongue. (うまく、濃くまとまっている。最後に口の中に薄く果実(梨)の味が残る。その前に舌先に軽くピリ感。)

I used the word ``pear'' in the description. We have several types of pear in Japan. For instance, niju-ichi-seiki (二十一世紀), kosui (幸水), and tyoujurou (長十郎). A niju-ichi-seiki is rather sour and others are rather sweet. In the above description, for pear I imagined the taste of niju-ichi-seiki, which is fresh and clear. Perhaps, even if a person has not taste the sake, he/she will imagines the taste of niju-ichi-seiki. Because the taste of such a just-squeezed raw sake is usually fresh and clear. As discussed in [6], if we mention a pear, there should be several possibilities in taste. However, why we can determine the taste of a pear as one exact taste? For this situation I think it is possible to consider the same procedure as in the determination of the colour of an apple. For the interpretation of the taste of a pear, we can see several affordance to select a proper one by abduction. If it is formalized by Theorist [9], the formalization is as follows:

$$F \cup affordance \vdash ideal\ feature.$$

$$F \cup affordance \nvdash \square.$$

In the case of the taste of pear, the following can be considered.

$$F \cup pear \cup \{affordance{=}\ niju\text{-}ichi\text{-}seiki\} \vdash fresh\ and\ clear\ taste.$$

$$F \cup pear \cup \{affordance{=}\ niju\text{-}ichi\text{-}seiki\} \nvdash \square.$$

Thus when tasting ` Kagatobi just-squeezed raw non-additional-water Ai ' and image the taste of pear, we can select an affordance that pear is niju-ichi-seiki. Then we can determine the type of pear is niju-ichi-seiki.

7. Conclusions

In this paper, I discussed the interpretation of metaphor. In fact metaphor is used to express the taste of food. The metaphor is used for instance based on shape and familiar things. When we use a word ``rounded'' for the spicy taste, the metaphor is used to reduce the level of spicy. That is, to remove the sharpness from the taste, rounded is used as a metaphor. For the taste description, familiar fruits are frequently used as a metaphor. For instance, for wine tastings, apple and apricot are used as a metaphor. A phrase `` a smell often found in young white wines.'' is used. In fact in Japan there are various types of apples. Perhaps this description is made in Europe. Accordingly the apple will be a Jonathan. However, in Japan, if we read this phrase, we will be wonder which apple they mention. If we properly select an affordance from apples, such a wondering will be solved.

The main theme of this paper is affordance and abduction based metaphor understandings. Such ambiguous metaphor can be determined by selecting a proper affordance and the affordance is abductively selected.

This paper mainly deals with a metaphor in tasting. In addition, a metaphor in poems will be dealt with in the same or similar way as in tasting. In the next paper, I will also deal with interpretations of metaphors in poems. Furthermore it can be extended interpretations of metaphors in stories.

References

[1] K. Seto, Ed., *Language will be over the taste, A quest for a description of a good taste*, Kaimeisha, 2003.

[2] A. Abe, "About the better expression of taste," *Proc. of the 2nd. Int'l Workshop on Language Sense on Computer in IJCAI2017,* pp. 28--34, 2017.

[3] A. Abe, "Is the expression of taste abstract or representational?," *Proc. of SMC2018 Workshop on Narratology and Cognitive Content Generation,* pp. 18--23, 2018.

[4] C. Velasco, A. T. Woods, O. Deroyc and C. Spence, "Hedonic mediation of the crossmodal correspondence between taste and shape," *Food Quality and Preference,* vol. 41, pp. 151--158, 2015.

[5] H. Fukushima, *Japanese Sake Tasting Dictionary*, Keio Gijuku University, 2013.

[6] A. Abe, "Why a young girls cheek is red?," *Technical Report of JSAI,* Vols. SIG-LSE-B803, pp. 1--8, 2018.

[7] J. J. Gibson, "The Theory of Affordances," in *Perceiving, Acting, and Knowing*, R. Shaw and J. Bransford, Eds., Lawrence Erlbaum Association Publishers, 1977, pp. 67--82.

[8] J. J. Gibson, *The Ecological Approach to Visual Perception*, Houghton Mifflin, 1979.

[9] D. Poole, R. Goebel and R. Aleliunas, "Theorist: A Logical Reasoning System for Defaults and Diagnosis," in *The Knowledge Frontier: Essays in the Representation of Knowledge*, N. J. Cercone and G. McCalla, Eds., Springer-Verlag, 1987, pp. 331--352.

[10] H. Jung, H. Wiltse, M. Wiberg and E. Stolterman, "Metaphors, materialities, and affordances: Hybrid morphologies in the design of interactive artifacts," *Design Studies,* vol. 53, no. C November, pp. 24--46, 2017.

An Analysis on Advertising Techniques of Beverages Using Positive Factors of Evaluation Database System

Yoji Kawamura
Faculty of Business Administration, Kindai University, 3-4-1 Kowakae
Higashi-osaka, Osaka 577-8502, Japan
E-mail: kawamura@bus.kindai.ac.jp
www.kindai.ac.jp

Abstract

This study aims to systematically shed light on what kind of effects are brought about by the film techniques in individual CMs. Based on audiovisual experiments, with positive factors as the evaluation index, we considered what could be analyzed from film techniques and their effects. For this study, we conducted audiovisual experiments of communication effects (positive factors, interest, and the willingness to buy) by using 100 commercials for beverages (tea, canned coffee, and beer), and analyzed the relationships between film technique and product and category characteristics, historical transitions, interest, and the willingness to buy. Subsequently, we examined the results of the audiovisual experiments. According to the tabulation results, the tea Sokenbicha (Coca Cola) and Namacha (Kirin) tended to focus on "atmosphere 2 (sexy or cute)"; canned coffee Boss (Suntory) tended to focus on the "story," "mise-en-scène (person)," and "atmosphere 1 (humor)"; canned coffee Wonda (Asahi) tended to focus on "message" and "mise-en-scène (person)"; and Super Dry beer (Asahi) tended to focus on "message," "mise-en-scène (background)," and "empathy." These kinds of film techniques and effects structure a product's brand image or "identity." According to our quantitative formulation, "mise-en-scène (person)," "mise-en-scène (background)," "story," and "sound" are important for increasing the level of interest. "Empathy," "mise-en-scène (background)," and "message" are important for increasing the level of willingness to buy.

Keywords: Commercial Film, Film Technique, Effect, Positive Factor, Beverage

1. Introduction

Even though film techniques and effects of television commercial message (CM) have been studied by researchers such as Stewart and Furse[1] and Kawamura,[2, 3, 4, 5, 6] CMs are complex information media, and hence it takes a significant amount of time and effort to evaluate a CM comprehensively. Therefore, attempts to systematically study film techniques and their effects have been largely unsuccessful. Meanwhile, in the advertising business, the CM Soken Consulting built a system for evaluating CM expressions comprehensively, using CM likability studies within the framework of positive factors. The positive factors of the CM Soken Consulting have by no means one to one correspondence with film techniques, but a number of them involve film techniques. Probably, the institute also has a research approach that examines the effects and transitions in film techniques based on a comprehensive evaluation database by using positive factors as the evaluation index. However, the CM likability surveys of the CM Soken Consulting depend on the ad placement frequency and social environment (such as trends and current affairs), and hence they do not evaluate the film technique of an individual CM.

This study aims to systematically shed light on what kind of effects are brought about by the film techniques in individual CMs. Based on audiovisual experiments, with positive factors as the evaluation index, we considered what could be analyzed from film techniques and their effects. For this study, we conducted audiovisual experiments of communication effects (positive factors, interest, and the willingness to buy) by using 100 commercials for beverages (tea, canned coffee, and beer), and analyzed the relationships between film technique and product and category characteristics, historical transitions, interest, and the willingness to buy. Subsequently, we examined the results of the audiovisual experiments.

2. Positive Factors and Film Techniques

The CM Soken Consulting conducts monthly CM likability surveys and provides a database service for evaluating CM expressions. The CM likability surveys study likability by gender and age groups, by using 15 types of positive factors.[7] Our study evaluated impressions (feelings) after viewing the CMs, with items relating positive factors to effects (impressions and feelings from the commercial as a whole) and items relating to film techniques (such as story, mise-en-scène, and sound). The positive factors were set empirically, and hence a challenge was that the questions about items related to film techniques did not cover film techniques precisely or exhaustively. However, due to the existence of questions relating to major film techniques, we believe that the questionnaire provides a valuable database for the analysis of film techniques. According to film theory,[8, 9, 10, 11, 12] films are composed of stories (how the intended content is constructed by means of cinematic expression), mise-en-scène (how shots [information elements and compositions on the screen] are structured), editing (how shots are connected), and sound (what type of sound is added to shots and the edited video products). In this study, we performed our analysis by taking into account these considerations and mapping the positive factors to the film techniques/effects shown in Table 1.

Table 1. The film techniques/effects and positive factors.

Film techniques/effects (9 categories)		Positive factors (15 indicators)
Film tech-nique	Message	"impressive catch phrases"
	Story	"a good story"
	Mise-en-scène (person)	"talents or characters"
	Mise-en-scène (background)	"good visual images/videos"
	Sound	"impressive music/sound"
Effect	Emphathy	"attracted by the product" "it is pleasantly persuasive"
	Atmosphere1	"it is humorous" "not fashionable but likeable" "reassuring"
	Atmosphere2	"because it is sexy" "cute"
	Other	"it feels at the cutting-edge of time" "good surrounding reputation" "the firm's attitudes appear to be sincere"

Table 2. The targets for analysis.

Category	Product (Company)
Tea	Oolongcha (Suntory), Namacha (Kirin), Sokenbicha (Coca Cola)
Canned coffee	Boss (Suntory), Fire (Kirin), Wonda (Asahi)
Beer	Moltz (Suntory), Lager (Kirin), Super Dry (Asahi), Kuro Label (Sapporo)

3. Analysis Method

3.1. *Analysis Targets*

Beverages are low involvement products, and compared to CMs for other products, CMs for beverages make full use of film techniques. Therefore, we chose 10 major products (Table 2) within the beverage category (tea, canned coffee, and beer) as targets for analysis. To investigate from a diachronic perspective, we surveyed a total of 100 CMs created during a span of 10 years from 1997 to 2006 (number of samples: 10 CM' for each product).

3.2. *Subjects*

The subjects were students between the ages of 20 and 23 years. The number of samples was 100 human subjects for each of these commercials.

3.3. *Indicators and Evaluation*

As positive factor indicators for the audiovisual experiments, we used the CM Soken Consulting's indicators (15 indicators) (Table 1). We used a 2-point scale for evaluating the positive factors ("left an impression" and "did not leave an impression"). For tabulation and analysis, we also analyzed indicators classified from the standpoints of film techniques and effects (film techniques/effects: 9 categories). To measure the level of interest, we used a 5-point scale (1: Not interested, 2: Not particularly interested, 3: Fairly interested, 4: Pretty interested, 5: Extremely interested). To measure the level of willingness to buy, we used a 5-point scale (1: Definitely would not buy, 2: Probably would not buy, 3: Might buy, 4: Probably would buy, 5: Definitely would buy).

3.4. *Audiovisual Experimental Method*

We showed the CM to 100 subjects and got them to evaluate their level of interest (5-point scale), willingness to buy (5-point scale), and positive factors (2-point scale, 15 types). For tea and canned coffee, we aired six CMs (CMs for three products, created in two different years) to the same subjects and gathered evaluations. For beer, we aired and evaluated eight commercials (commercials for four products, created in two different years). We elicited responses from subjects concerning their attributes of gender and consumption frequency (daily, two to three times per week, once a week, once a month, and almost never consumed).

3.5. *Tabulation and Analysis Method*

Based on the collected evaluation data, we tabulated film techniques and effect categories and analyzed characteristics by product, characteristics by category, and historical transitions. We also performed a regression analysis of the relationships between the interest and willingness to buy and film techniques and effect categories.

4. Results and Analysis

4.1. *Summary*

A total of 10,000 samples were tabulated, comprising 50.5% and 49.5% of males and females, respectively. The totals for the interest level and the willingness to buy are shown in Fig. 1. The proportion of subjects interested (3~5 scales) and those who expressed a willingness to buy (3~5 scales) accounted for 70.2% and 58.7%, respectively. The positive factors' totals are shown in Fig. 2. Overall, the highest-rated factor (left an impression) by positive factors was "impressive music/sound." This was followed by "talents or characters," "good visual images/videos," "it is

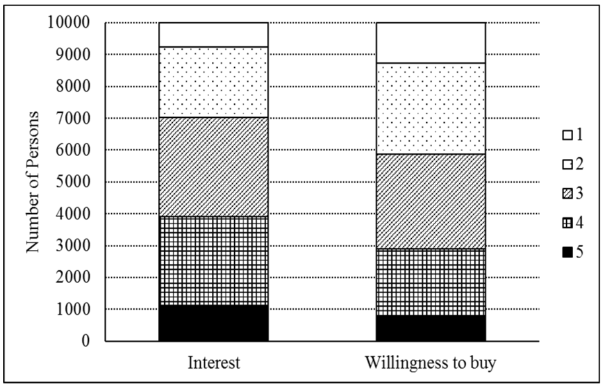

Fig. 1. The totals of interest level and the willingness to buy.

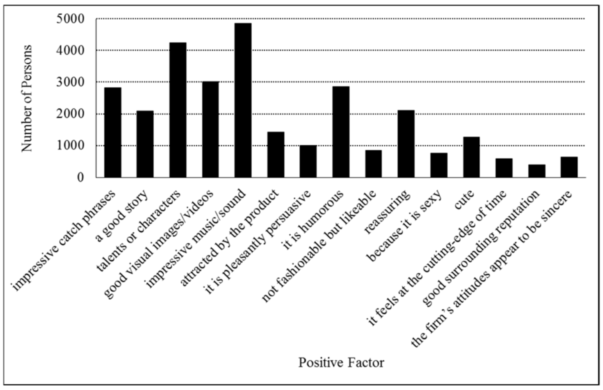

Fig. 2. The positive factors' totals.

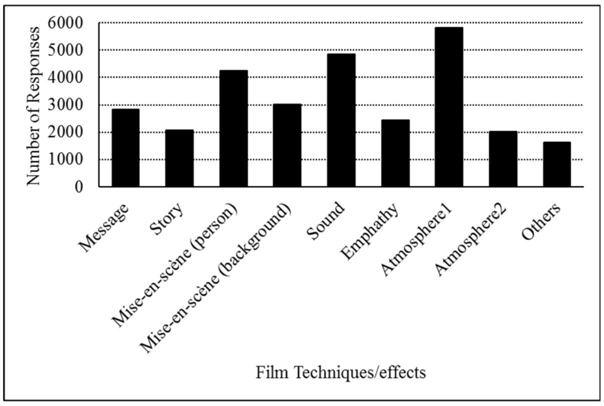

Fig. 3. The results of tabulation of film techniques/effects.

humorous," and "impressive catch phrases." Based on the categories shown in Table 1, the results of tabulation of film techniques/effects are shown in Fig. 3. For film techniques/effects, overall, the "atmosphere 1" received a very high evaluation. In these categories, the next highest were " sound," "mise-en-scène (person)," "mise-en-scène (background)," and "message."

4.2. *Relationship between the Interest Level and Willingness to Buy and the Positive Factors*

We performed regression analysis, with the interest level and the willingness to buy as explained variables (5-point scale) and positive factors as explanatory variables. Fig. 4 shows the level of influence (the regression formula coefficient) of interest and willingness to buy on the positive factors. "Talents or characters" had the highest impact on interest, followed in order by "attracted by the product," "a good story," and "good visual images/videos." "Attracted by the product" had the highest impact on the willingness to buy, followed in order by "it is pleasantly persuasive," "because it is sexy," "good visual images/videos," and "impressive catch phrases." Overall, the "impressive music/sound" was most highly evaluated, but it did not have a very significant impact on the interest or willingness to buy.

4.3. *Characteristics of Film Techniques/effects Categories by Product*

Figure 5 shows the totals by the product of film techniques/effects. Sokenbicha (Coca Cola) and Namacha (Kirin) had the highest evaluation among the teas for "atmosphere 2," and the canned coffee Boss (Suntory) had the highest evaluations for "story," "mise-en-scène (person)," and "atmosphere 1," and canned coffee Wonda (Asahi) had the highest evaluations for "message" and "mise-en-scène (person)." Super Dry beer (Asahi) had the highest evaluations for "message," "mise-en-scène (background)," and "empathy."

4.4. *Characteristics by Film Techniques/effects by Category*

Figure 6 shows the totals by category of film techniques/effects. Tea had the characteristic of being highly evaluated for "atmosphere 2," and canned coffee had the characteristic of being highly evaluated for "story," "mise-en-scène (person)," and "atmosphere 1."

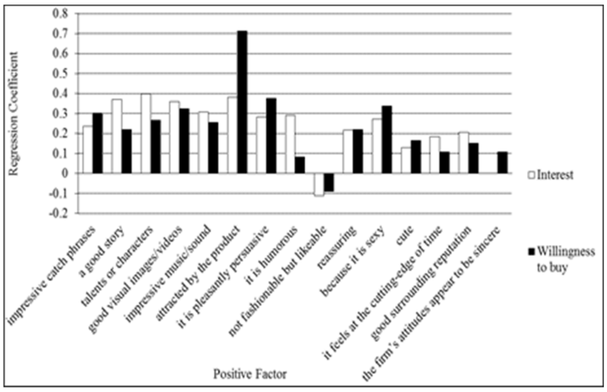

Fig. 4. The regression formula coefficient of interest and willingness to buy on the positive factors.

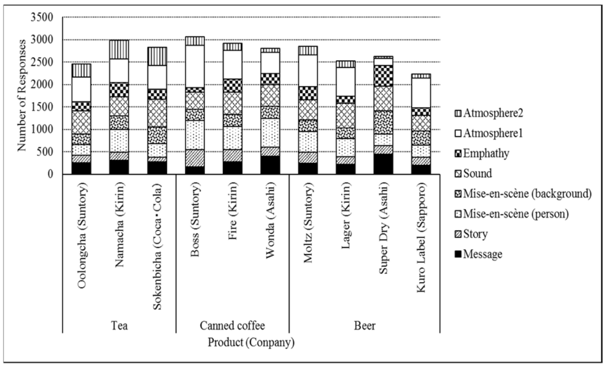

Fig. 5. The totals by the product of film techniques/effects.

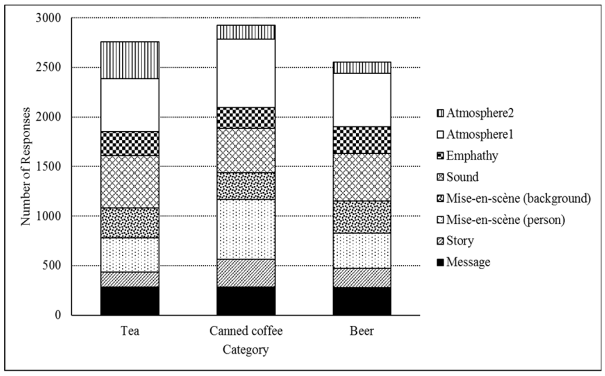

Fig. 6. The totals by category of film techniques/effects.

4.5. *The Historical Transition of Film Techniques/effects*

Fig. 7 shows the historical transition of film techniques/effects. Compared to 1997, in 2006, there was an increasing trend in the ratio of “mise-en-scène (person)” and “empathy” and a decreasing trend in the ratio of “atmosphere 1.’

4.6. *Relationships between the Interest and the Willingness to Buy and Film Techniques/effects*

Fig. 8 shows the relationships (cross tabulation) between interest and willingness to buy and film techniques/effects. Depending on the level of interest and willingness to buy, the proportion of which film technique or effect category being influenced underwent a change. When the levels of interest and willingness to buy become higher, the proportions of "atmosphere 1" and "sound" become smaller. When the levels of interest and willingness to buy become higher, the proportions of “mise-en-scène (background)” and “empathy” tend to become larger.

We performed a regression analysis, with the level of interest and willingness to buy as explained variables and film techniques/effects as explanatory variables.

The regression formula was:

(1) Interest
= 2.30 + 0.24 x Message + 0.39 x Story
+ 0.41 x mise-en-scène (person)
+ 0.39 x mise-en-scène (background)
+ 0.32 x Sound + 0.36 x Empathy
+ 0.18 x Atmosphere 1 + 0.20 x Atmosphere 2

(2) Willingness to buy
= 2.09 + 0.31 x Message + 0.21 x Story
+ 0.27 x mise-en-scène (person)
+ 0.35 x mise-en-scène (background)
+ 0.28 x Sound + 0.59 x Empathy
+ 0.09 x Atmosphere 1 + 0.27 x Atmosphere 2

Fig. 9 shows the level of influence (regression formula coefficient) of film techniques/effects on the interest and willingness to buy. “Mise-en-scène (person)” had the greatest impact on interest, followed by “mise-en-scène (background),” “story,” “empathy,” and “sound.” “Empathy” had the greatest impact on willingness to buy, followed by “mise-en-scène (background)” and “message.” Mise-en-scène (person and background) and story fulfill large roles in gaining interest. It is important to obtain empathy in order to drive the willingness to buy, and the message that forms the context for the mise-en-scène fulfills an important role.

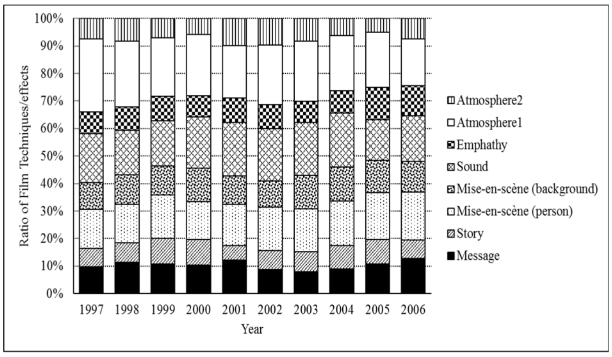

Fig. 7. The historical transition of film techniques/effects.

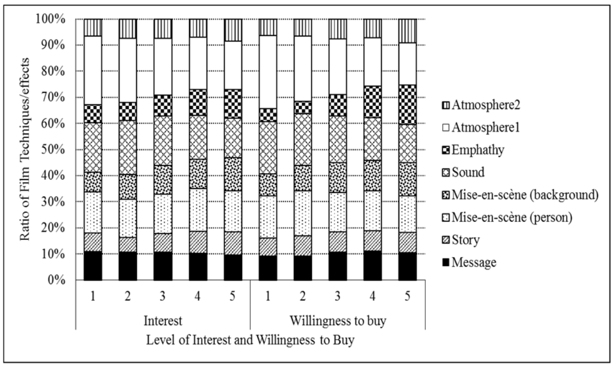

Fig. 8. The cross tabulation between interest and willingness to buy and film techniques/effects.

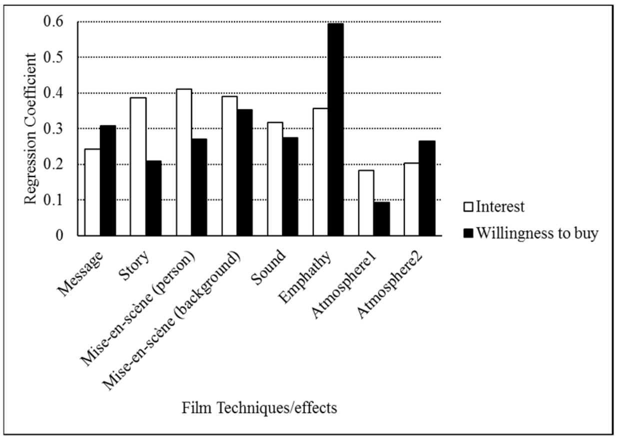

Fig. 9. The regression formula coefficient of film techniques/effects on the interest and willingness to buy.

5. Outcomes and Future Challenges

5.1. *Quantification of Brand Images*

This study conducted audiovisual experiments of communication effects (positive factors, interest, and the willingness to buy) by using 100 CMs for beverages (tea, canned coffee, and beer) and analyzed the relationships between film technique and product and category characteristics, historical transitions, interest, and the willingness to buy, based on the evaluation of positive factors. When compared to a large number of CMs created in a 10-year period (said to exceed 30,000), 100 CMs represent a small number, but they have significance in that their effects for advertising the same brands over the period of 10 years were evaluated. According to the tabulation results, the tea Sokenbicha (Coca Cola) and Namacha (Kirin) tended to focus on “atmosphere 2 (sexy or cute)”; canned coffee Boss (Suntory) tended to focus on the “story,” “mise-en-scène (person),” and “atmosphere 1 (humor)”; canned coffee Wonda (Asahi) tended to focus on “message” and “mise-en-scène (person)”; and Super Dry beer (Asahi) tended to focus on “message,” “mise-en-scène (background),” and “empathy.” These kinds of film techniques and effects structure a product’s brand image or “identity.” Our study is significant because it was able to elucidate this in a quantitative way. It is possible to utilize these techniques and effects as quantitative indicators for maintaining and innovating brand images. This study does not specifically address this point, but it is possible to use this methodology to analyze the historical transitions of brand images for each brand.

5.2. *Quantitative Formulation of Relationships between Interest and the Willingness to Buy and Film Techniques/effects*

It is not easy to quantitatively evaluate the effects of film techniques, but this study attempted a quantitative formulation of the relationship between interest and the willingness to buy and film techniques/effects. Our study is significant because it could shed quantitative light on the kinds of film techniques on which efforts must be focused in order to trigger interest and the willingness to buy. According to our quantitative formulation, “mise-en-scène (person),” “mise-en-scène (background),” “story,” and “sound” are important for increasing the level of interest. “Empathy,” “mise-en-scène (background),” and “message” are important for increasing the level of willingness to buy. A creator of advertising would probably see these results as obvious, but the significance of the results is that they clearly demonstrate the impact in a quantitative way.

5.3. *Automation of Communication*

In other studies, through a variety of audiovisual experiments, in addition to the formulation demonstrated in 5.3., Kawamura[13, 14] has attempted to extract the film techniques that draw interest and those that drive the willingness to buy. If these techniques (rules) can be made specific and used with information systems technologies, then they would significantly contribute toward upgrading marketing automation.

5.4. *Analysis of Film Techniques and their Effects Using a CM Evaluation Database Using Positive Factors as an Evaluation Index*

At present, the CM Soken Consulting do not cover any survey items regarding interest or willingness to buy in its CM likability surveys, but it is possible to calculate the interest and willingness to buy based on the formulated functions. The formulation clearly depicts relationships between levels of interest and “mise-en-scène (person),” “mise-en-scène (background),” “story,” “empathy,” and “sound,” and there is a strong relationship between the level of willingness to buy and “empathy.” Simply put, we believe that “film technique” (= “a good story” + “talents or characters” + “good visual images/videos” + “impressive music/sound”) is an indicator for evaluating interest, and “empathy” (= “attracted by the product” + “it is pleasantly persuasive”) is an indicator for evaluating the willingness to buy. If we use these methods of analysis as the basis for analyzing data in a comprehensive system for evaluating CM expressions, then we would be able to analyze the film techniques comprehensively and quantitatively and analyze their effects for diverse product categories and from a variety of time periods.

5.5. *Future Challenges*

This study targeted beverages for analysis, and hence it will also be necessary to attempt to analyze other product categories. Additionally, our subjects comprised the younger generation (aged 20 to 23 years), and hence it will also be necessary to attempt to analyze other age groups. Based on these analysis, in the medium- and long-term, we would like to conduct a comprehensive analysis of film techniques and their effects using an advertising evaluation database, and formulate a system out of these.

Acknowledgements

This work was supported by JSPS KAKENHI Grant Number 22500102.

References

1. D. W. Stewart and D. H. Furse, *Effective Television Advertising: A Study of 1000 Commercials* (Lexington Books, Lexington, MA, 1986).
2. Y. Kawamura, An analysis of the rhetoric of commercial film: Toward the building of a commercial film production support system based on image rhetoric, in *Proc. 2003 IEEE Int. Conf. on Systems, Man and Cybernetics*, (USA, Washington DC., 2003), pp.993-1000.
3. Y. Kawamura, An analysis of the rhetoric of commercial film: Toward the building of a commercial film production support information system, *J. of Advertising Sci.*, (45) (2004), pp.122-139. (In Japanese)
4. Y. Kawamura, An analysis on rhetoric of the commercial film of beer and personal computer: A symbolic approach on rhetoric of commercial film, *J. of Advertising Sci.*, (47) (2006), pp.33-48. (In Japanese)
5. Y. Kawamura, A study on the technique-rhetorics and effects of commercial film, *Cognitive Studies*, **14**(3) (2007), pp.409-423. (In Japanese)
6. Y. Kawamura, An analysis on the story and editing techniques of commercial film: Toward the building of a commercial film production support information system, *J. of Advertising Sci.*, (50) (2009), pp.16-32. (In Japanese)
7. CM Soken Consulting, Monthly top 10 CM of new works, *CM INDEX*, **12**(1)-**21**(12) (1997-2006). (In Japanese)
8. R. Whitaker, *The Language of Film*, (Prentice-Hall, Englewood Cliffs, NJ, 1970).
9. J. Monaco, *How to Read a Film: the Art Technology, Language, History and Theory of Film and Media*, (Oxford University Press, New York, NY, 1977).
10. G. Deleuze, *Cinéma 1: L' Image-mouvement*, (Les Editions de Minuit, Paris, France, 1983).
11. D. Bordwell, *Narration in the Fiction Film*, (University of Wisconsin Press, WI, 1985).
12. K. Asanuma, Techniques for image text, *For Movie II*, (Suiseisha, Tokyo, Japan, 1990), pp.130-247. (In Japanese)
13. Y. Kawamura, A viewing experiment on the effects of advertising story, *J. of Robotics, Networking and Artificial Life*, **3**(2) (2016), pp.92-95.
14. Y. Kawamura, Rhetoric of commercial film and the response of viewers, *J. of Robotics, Networking and Artificial Life*, **4**(2) (2017), pp.158-162.

High-Performance Computing for Visual Simulations and Rendering

Jasmine Wu
National Center for High-performance Computing, National Applied Research Laboratories, Hsinchu 300, Taiwan

Chia-Chen Kuo, Shu-Hsin Liu, Chuan-Lin Lai, Chiang-Hsiang Lien, Ming-Jen Wang, Chih-Wei Wang
National Center for High-performance Computing, National Applied Research Laboratories, Hsinchu 300, Taiwan

1803040@narlabs.org.tw, 1803031@narlabs.org.tw

www.narlabs.org.tw

Abstract

National Center for High-performance Computing (NCHC) built a render farm that provides a platform for the industry to render their work in a much more efficient timeframe. It allows not only CPU rendering, but also GPU rendering. The throughput is also greatly improved to support complex and large scale simulations. The main goal of this session is to introduce scientific discoveries and technical innovation through prospective computing technology and platform.

Keywords: render farm, visual simulation, virtual desktop infrastructure, high-performance computing

Introduction

We have a reputation for global technology manufacturing and professionals in Taiwan. But, more importantly, we bring forward the culture aspect of Taiwan with our developing technology. The central thinking of National Center for High-performance Computing (NCHC) is whether technology may be closer to people, and how it can act as a tool for preservation and creativity in culture[1].

NCHC built a render farm, a cluster of networked computers with a high performance speed and enormous amount of data storage devoted to rendering images, with hopes to help improve the film industry in Taiwan. The render farm can be directly accessed through Virtual Desktop Infrastructure (VDI), allowing users to take advantage of this platform with any device available to them at any location. This was intended for students who may not have access to an equipped device when needed. It also means that users can use the render farm and still do work on their own device with no interference, allowing companies to work more efficiently.

So far, over 100 films in Taiwan were rendered using our platform by animation students in Taiwan, as well as companies from the industry.

Fig. 1. An animation contest conducted once a year by NCHC since 2011, providing contestants services of the render farm.

The newest Render Farm was launched in March of 2018, which allowed not only CPU rendering, but also GPU rendering. The throughput is also greatly improved to support complex and large scale simulations.

1. Background

A lot of movies and TV productions today involve computer generated imagery (CGI), because most of the time it is cheaper and easier to create virtual props in the computer than it is to build them in real life. These visual effects can be so realistic that the audiences are fooled into thinking that it is an actual footage filmed with real-life setups. Not only props and backgrounds can be made with CGI, but also actors and creatures. For example, in a lot of action films, it is often too dangerous and risky to ask the actor/actress to do certain moves. In this case, CGI artists will build a 3D model of the actor/actress, and animate it to do the job.

Any image generated by means of computer programs, whether it's photorealistic or non-photorealistic, needs to go through the process of rendering in order for the details created to be seen. To render a video means to render a sequence of images each second the video plays. The more details an image have, whether it is geometry, texture, lighting or shadows, the more render time will be requires.

Rendering is the way a computer draws an image by calculating the color of each pixel. The process of rendering, for example, is when an image contains a pixel that is red, and a filter is added to make the red pixel blue, the software will have to recreate this blue pixel when it exports the finished image[2].

When creating CGI that involves visual simulations, a powerful computing system is required to render the images. Simulation is an imitation of a real-world process generated through computer calculations. For example, the computer can simulate a water crown splash through computing. Instead of animating fluid by hand, a simulation can be generated with information such as the size and the speed of the water drop. Once all the information is gathered, the computer can imitate the reaction of a drop of fluid hitting surface from some distance above.

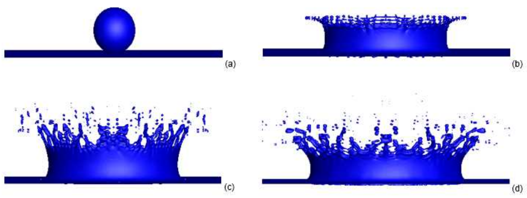

Fig. 2. The way the water drop is predicted through time. (a) t = 2.0; (b) t = 3.0; (c) t = 4.0; (d) t = 5.0.[3]

2. Concerned Contents

In order to achieve cloud studios on HPC, the GPU render farm in NCHC, mainly based on VMware Horizon, comprises vSphere ESXi hypervisor, vCenter server, View Connection server, View Composer service, etc. Despite the complex structure, end users can access remote desktop via VMware Horizon Client, simply typing in the IP, username, and password. On account of limited network discharge for some user, H.264 encoding, accelerated by GPU, of video stream is used to make himself at home.

Just like some traditional render farms, Deadline scheduler manages batch rendering on the GPU render farm in NCHC, and many authorized software programs here are ready-to-use, including animation software (Maya, 3ds Max), ray-tracing renderers (Arnold, V-Ray), visual effects simulators (RealFlow, Houdini), etc.

3. Importance or Significance of Tutorial

Modern film and TV footage runs at 24 frames per second, a single frame from Monsters University can take up to 29 hours to render[4]. This means that the film, which is 1h44m long, would have taken about 10,000 years to finish if it was rendered with one CPU. This explains why render farms are needed in the film industry.

Visual simulation, also known as 3D visualization, are created through computer computation by taking the input data and run it through algorithms base on given variables. Visual simulations are not only used for movies or animations, but they also allow researchers to make a more accurate prediction of an experiment without having to run the test physically. It can also simulate population, traffic, or human behaviors[5].

Simulations can also be done in real-time. When creating any experience that involves interaction, the rendering process will have to be in real-time, because the video react base on the action detected.

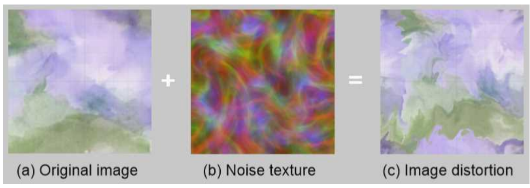

Fig. 3. Texture Distortion Method[6].

The texture distortion method shown in figure 3 is an example of real-time rendered simulation. The project was to create a shader for materials that distorts its UV to create a water effect.

Thanks to remote virtual desktop, complete production pipeline, and batch renderer cluster, frequently network transportation of high poly models, which is one of the bottlenecks of traditional render farms, is avoided on the GPU render farm in NCHC. Cooperating is available as well for a group of users in the cloud studio, with high throughput and IOPS of the storage system supporting multi-user performance.

4. Possible Outcome

NCHC is ready to inquire more advanced software and plugin for the render farm. Provided software/ plugin are used for creating a more realistic visual content. For example, a grooming plugin allows user to create more realistic fur, and is able to simulate the way it moves or reacts with objects.

With new tools at hand, users can create a more advanced visual for their content. The amount of time render farm can save in terms of rendering, provides the opportunity to create a better product with the same amount of time spent.

5. Conclusion

Simulation is very important to many fields today. Rendering is especially needed for visual focused content such as animated films, movies, or video games. Whether it is rendering for videos or real-time rendering for interactable experiences, a high-performance computing system is required for an efficient workflow.

6. Reference

1. Maxim- Eden- Robyned- TomaszMSwidzinski-Sareesh Sudhakaran – https://wolfcrow.com/blog/what-is-a-render-farm/
2. Lin, Shi-Min, Wang, Chih-Wei, and Kuo, Chia-Chen. 2018. "HPC Rendering for Culture Recreation – An Example of Koji Pottery in Taiwan" *In Proceedings of SEAIP* 2018.
3. Chang, Chih-Wen, Chiu, Pao-Hsiung, and Kuo, Chia-Chen. 2014. "Milkcrown Simulation using OpenACC Accelerated Framework." *In Proceedings of SIGGRAPH* 2014.
4. Takahashi, Dean. "How Pixar Made Monsters University, Its Latest Technological Marvel." VentureBeat, 24 Apr. 2013, venturebeat.com/2013/04/24/the-making-of-pixars-latest-technological-marvel-monsters-university/.
5. Lytle, Sam. "What Is a Visual Simulation?" CivilFX, 26 Jan. 2015, http://www.civilfx.com/visual-simulation/
6. Hsiao, Shao-Ting and Kuo, Chia-Chen. 2018. "Real-time Rendering for New Media Art" *In Proceedings of SEAIP* 2018.

Virtual Reality as an Art Form

R.P.C. Janaka Rakapakse, Yi-Ping Hung
Tainan National University of the Arts, 66 Daci,
Guantian District, Tainan 72045, Taiwan
E-mail: janakaraja@gmail.com, hung@csie.ntu.edu.tw

Abstract

After introducing content creations in the immersive environments, the VR content creation process has been changed dramatically. It has enhanced the direct engagements of the artists and reduces the time it takes to get a part from the idea stage to the production stage. Time consuming VR content creation process has been reduced to hours or days. Not only is the time reduced, but the cost is also significantly reduced. The reduced time and cost allows artist to work in near real-time, with the design and production happening at nearly the same time. This section of the session is focused on VR content creation process and its artistic perspectives. Especially, not only concerning VR contents creation in immersive environment is an alternative to find new form of art. And the last part of the speech concerns about the role of VR in the live performance and new form of theater.

Keywords: virtual reality, art form, VR contents, immersive, interaction, content creation

1. Introduction

According the Cambridge Advanced Learner's Dictionary, the abbreviation of VR for *virtual reality*: a set of images and sounds, produced by a computer, that seem to represent a place or a situation that a person can take part in virtual experience. Generally, people may think of VR as an experience on the computer using a headset. But according to the literature, interactive virtual experiences have been around for several decades. In 1962, the Sensorama[1] introduced a 3D experience that included motion, color, stereo-sound, aromas, wind, vibrations, etc. The ViewMaster allowed us to view an image in stereo which is the same principle as a today's VR headsets as shown Fig. 1.

Fig. 1. Evaluation of VR headsets.

Nowadays, VR-application[2] are using in many fields. VR can be used as a training application in the medical field where doctors can experience surgery on a virtual human before performing the real cases. The military extensively use VR as a training tool. The VR can aid in physical therapy for children as well as adults. Recently, researchers in the U.S. have developed an ingenious system that uses VR to help prevent falls by detecting and reversing balance impairments in elderly people. In Entertainment, VR was being incorporated into music videos for more than a passive experience. Also popular TV-Star programs incorporated 360-degree VR with Dancing Stars. VR gaming is becoming more mainstream now as well. VR can be used as a design support tool in the fields of architecture and interior design. It can be used to evaluate the state of a new design, or it can be used to modify a design with the feedback of customer in a real-time virtual 3D space. VR can also be used to sell a product or a building.

However, authors do not think VR should be construction software or all your modeling should be in there. There are methodologies to working in VR related to software, hardware, and techniques. Therefore, this

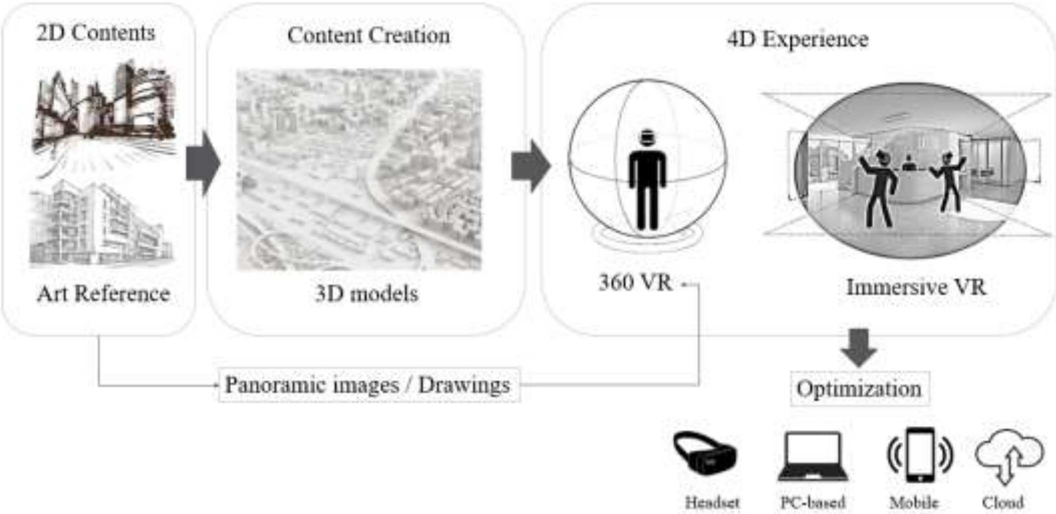

Fig. 2. VR workflows and optimizations

paper of the tutorial session is focused on VR content creation process and its artistic perspectives.

2. Objectives

One lesson learned early on was that VR can feel overwhelming. If anyone is going to drop someone in a virtual experience, it is important to have clear goals and not let them feel lost in the woods. There is no technology that can compensate for lackluster content or the absence of a clear idea or strategy. we think that there's a lot of people, across many industries that basically see VR as a big fad that they need to get a piece of. It is a hard task, because it only takes one bad experience for user to forever after feel weary of VR. So here, we are very specifically concerning the VR workflow as shown in fig. 2. And there is a misconception that many have that doing anything with VR requires a totally separate workflow from what creators are used to do in content creation. But the reality is, if creator's workflow already includes 3D modeling, texturing of some kind, lighting of some kind, or rendering, maybe from commodity 3D applications, he or she is on the way. Actually, building for VR is an extension of what creator is already doing. In order to clear all misconceptions, this tutorial concerns following listed objectives.

- To understand the power of designing in VR over traditional methods, tutorial contents considers the affordances of VR: scale, presence, design options, experiencing decisions while creators are in process.
- To study how to communicate design intent with relatively simple VR preproduction, teaching contents to consider a complex or photo-realistic content experience.
- To learn how to use VR at every stage of the design process, tutorial contents focuses some open source content creation applications too.
- To understand how to cycle a VR methodology into workflows, tutorial concerns two major workflows such as static VR and immersive VR, probably focuses already using software that has VR capabilities, and even those that don't can interface well with more specialized VR software.

3. VR Workflows

There are different workflows for virtual reality currently being utilized in the content creation industry. This tutorial would share a few of them here and discuss how an artist try to build and incorporate them into their production process.

3.1. *Static VR (Panorama or 360 Degree VR)*

Panoramas and 360 images are most often displayed on phones, tablets, and untethered head mounted displays (HMD), similar to google cardboard and other Gear VR as shown in Fig. 3. Based on the devices people choose they have the choice between a simple 2D spherical image or 3Dstereoscopic image.

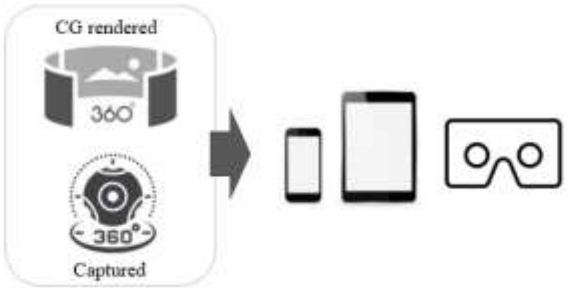

Fig. 3. Static VR workflow

CG (Computer Graphics) generated or captured panoramic or spherical renderers display cleanly on mobile devices such as phones and tablets with accelerometers. This functionality allows the user to hold the device in the air and experience the space by moving the device side to side and up and down. People also have the option to control the display of the device by using user's finger on the face of the screen to rotate and scale the image. As shown in Fig 3. once your render is created, upload it to an app that is built for viewing on your chosen hardware. The extension of static VR with 3D stereoscopic, new cinematography of VR movies, strength and weakness will be described in this section.

Fig. 4. HTC VIVE equipped with VR-Ready Notebook PC (image courtesy: RoadToVR: https://goo.gl/c7zJLc)

3.2. *Immersive VR*

Immersive VR provides fully immersive experiences. User has ability to interact with the VR environment. This part of tutorial uses the HTC Vive[3], but learners can concern other options like the Oculus Rift. These HMD's offer a much more immersive experience, where almost anything is possible. As shown in Fig. 4, the headset is currently wired to computer, although there are third party add-ons being released soon allowing the Vive to become wireless. We chose the Vive because of the room scale mobility and stable VR headset that came with tracked controllers. Room scale allows the user to walk and explore in a real-time interaction.

To getting started start out the immersive VR project, there are several application and authoring tools. If you are creating a VR application, you should be considering it from the beginning. This is to confirm that most of creator's time can be spent creating fun experiences and troubleshooting, rather than re-modeling other creative parts. Therefore, this tutorial will be explained following workflows in step by step.

- Unity[4] Workflow
- Autodesk Stingray/ Max Interactive[6] Workflow
- Unreal Workflow[7]

Tutorial also focuses on the building contents in Maya-2018 or Blender Application softwares. This is the basic workflow for Unity VR builds that we have found successful. We recommend additional training if you have never used Unity before. And we have found that our VR builds do not need to be photo real. For most of our VR needs a very simple ambient light and a sun setup works best, we don't fill our scenes with artificial lighting. This keeps the project simple and optimized. The contents don't usually include reflection probes or complex effects. The simpler you keep your project the more geometry you can load into it. We will provide some model data which can use for initial VR project. Teleportation vs. Locomotion: Motion sickness is one of the biggest problems developers have to contend with in VR. Tutorial will cover teleporting and VR content navigation techniques. The advantages of teleporting are obvious, a disadvantage worth noting is the way teleporting bypasses the passing of time. The participants can experience our recent project works which used different teleporting techniques with LeapMotion[8] sensor interaction for hand and figures.

4. Possible Outcomes

The participants of this tutorial primarily get a training and knowledge about the VR workflows as well as on-hand experience in the provided VR demonstrations. Hopefully, shared knowledge and experience helps to choose a path into VR that works for their future research directions. After VR is proven valuable there is a rich potential to use VR as a creativity support tool in the creative industry. By our experience (as shown in Fig. 5.), VR is a presentation tool, design tool, communication and creativity support tool

Fig. 5. VR as a creativity support tool.

To set up the true learning experience in this tutorial, we will go through a few our research examples[9,10] and we are trusting that the audience of this tutorial will have the ability to connect the dots and apply these methods to more complex projects in their research carrier. Fig. 6 shows a snap of a group of people taking experiencing VR content design in our earlier held tutorial session in Taiwan 2018. Lastly, this tutorial will show you how to turn VR model into a Social VR model, and describe some case studies[11] which create a personal VR experience in where multiple media integration with live performances, review the recent projects virtually that support recall memories and take some selfies all while immersed in Virtual Reality.

Fig. 6. VR as a creativity support tool.

5. Conclusion

The contents we have covered in this tutorial, have emphasized the major workflows and processes you can take to optimize the experience and create VR contents for your research areas. This session encourages you to continue to explore new ways to adapt and work with real-time contents creations for achieving endless possibilities. If you approach each aspect with the same attention and consideration, from the learning of different workflows and mastering them, what you can accomplish in VR has no limits.

Acknowledgements

The tutorial is supported by the project (E984704): Research of Advanced Interaction Technologies for VR/AR and Their Applications to Revitalizing Cultural Heritage, MOST Grant- in-Aid, Ministry of Technology, Taiwan.

References

1. Sensorama, https://en.wikipedia.org/wiki/Sensorama
2. A.B. Craig, W. R. Sherman and J. D. Will, *Developing Virtual Reality Applications: Foundations of Effective Design*, 1st edn. (Morgan Kaufmann, 2009)
3. HTC VIVE, https://www.vive.com/eu/
4. Unity, https://unity3d.com/
5. Maya-2018, https://www.autodesk.com/products/maya/overview
6. 3ds max interactive, https://area.autodesk.com/blogs/the-3ds-max-blog/get-3ds-max-interactive/
7. Unreal engine, https://www.unrealengine.com/en-US/what-is-unreal-engine-4
8. LeapMotion interaction for the hands, http://leapmotion-developer.squarespace.com/
9. J. Lee, R. P. C. J. Rajapakse, Y. Hung and Y. Tokuyama, The Development of a Virtual Doll Companion for Haptic Interaction, in *Proc. 2018-Nicograph International (NicoInt),* (Tainan, Taiwan, 2018), pp. 9292. doi: 10.1109/NICOINT.2018.00038
10. J. Lee, R. P. C. J. Rajapakse, Y. Hung and Y. Tokuyama, The Development of an Interactive Device for Tactile Sensation with Haptic Companion Doll(poster), in *Proc. of the 16th ACM SIGGRAPH International Conference on Virtual-Reality Continuum and its Applications in Industry (VRCAI2018)*, (Tokyo, Japan, 2018) Tokyo, Japan.
11. Draw Me Close: a VR Application for performance https://www.drawmeclo.se/

TS-3 Using Quill as a Tool for Real-Time Rendering

Jasmine Wu
National Center for High-performance Computing, National Applied Research Laboratories, Hsinchu 300, Taiwan

Chia-Chen Kuo, Shu-Hsin Liu, Chuan-Lin Lai, Chiang-Hsiang Lien, Ming-Jen Wang, Chih-Wei Wang
National Center for High-performance Computing, National Applied Research Laboratories, Hsinchu 300, Taiwan

1803040@narlabs.org.tw,

www.narlabs.org.tw

Abstract

Real-time rendering are performed through interactive videos such as in video games, Virtual Reality (VR), and Augmented Reality (AR). Oculus Quill can be used as a tool to create content for VR, which can then be transformed into AR using game engines such as Unity. The intuitiveness of Quill allows a greater possibility for developers.

Keywords: render farm, visual simulation, virtual desktop infrastructure, high-performance computing

1. Introduction

We value art and culture as much as the effort we put into our developments in technology, so we built a render farm as a tool that allows the entertainment industry in Taiwan to prosper. With the provided rendering service at National Center for High-performance Computing (NCHC), related fields are presented with much bigger possibilities.

Render farm is a cluster of networked computers with a high performance speed and enormous amount of data storage devoted to rendering images, typically used for producing animated films. We made render farm accessible through Virtual Desktop Infrastructure (VDI), allowing users to take advantage of this platform with any device available to them at any location. This was intended for students who may not have access to an equipped device when needed. This also means that users can use the render farm and still do work on their own device with no interference, allowing companies to work more efficiently.

So far, over 100 films in Taiwan were rendered using our platform by students and companies from the industry. The newest Render Farm was launched in March of 2018, which allowed not only CPU rendering, but also GPU rendering. The throughput is also greatly improved to support complex and large scale simulations.
For having a reputation for global technology manufacturing and professionals in Taiwan, we constantly update ourselves with the newest technological trends. Virtual Reality (VR) is one of the most talked about topics in the technological industry, and it has been utilized in many fields, but most successfully in film, animation, and video game.

2. Background

Rendering is the way a computer draws an image by calculating the color of each pixel. The process of rendering, for example, is when an image contains a pixel that is red, and a filter is added to make the red pixel blue, the software will have to recreate this blue pixel when it exports the finished image[1]. This means that any image edited or generated through computer programs, whether it's photorealistic or non-photorealistic, needs to go through the process of rendering.

Videos are a sequence of images played in order, so to render a video means to render a sequence of images. When it comes to movies or animations that involves Computer Generated Imagery (CGI), the more details an image have, whether it is geometry, texture, lighting or shadows, the more render time will be requires.

To put it in perspective, modern film and TV footage runs at 24 frames per second, a single frame from Monsters University can take up to 29 hours to render[2]. This means that the film, which is 1h44m long, would have taken about 10,000 years to finish if it was rendered with one CPU. This explains why render farms are needed in the film industry, because it can shorten this time to couple of years.

VR is like a monitor, but instead of having a still screen in front of the user, the screen is all around. The VR devices today typically come in headsets that cover the eyes to prevent peripheral vision, cutting out any context that would disconnect the user from the virtual world. The user may spin their head, and the camera would follow, pointing to the direction the user wants to see in a scene, thus giving the user an immersive experience.

Having a 360 degree video also means that the render needs to cover all around instead of one direction. When VR content is created in 3D, the user may not only see an environment in 360, but also move around in the virtual space. Any interactive experience will require real-time rendering.

Quill is an example of a VR experience. It provides a creative platform for users to illustrate and animate using the Oculus Rift. It allows users to paint directly inside a 3 dimensional virtual space. Users can create animated content by using the Oculus Touch to paint 3D materials, and move them frame by frame to create an animation.

Fig. 1. The interface and produced content of Quill.

3. Concerned Contents

For interactive video such as video games and most VR experiences, the rendering process cannot be done ahead of time, because what the user sees corresponds with the way the user moves in the scene. Rendering process that is done as the video plays are called real-time rendering, and this requires a high-performance computing system.

Another example to demonstrate NCHC's real-time render farm was by performance art. It has a high data throughput that can help the performer to do a large scale VFX simulation and to create new kinds of cross-disciplinary performances. A project that was done at NCHC shows the performer dancing with projected visual effects, which reacts in response to the performer. The rate of how the visual effects plays and reacts shows the performance speed of the real-time renderer.

The render farm computers at NCHC provides real-time rendering supported by both Unity and Unreal, which are two of the most used game engines by the public today[3]. Using the real-time rendering engines on the render farm computers present a faster frame rate.

Render farm may help with the render time, as well as the speed of software provided by a stronger machine which improves the workflow. However, the production time cannot be decreased. The steps in the animation production pipeline before the point of rendering from a typical animation studio includes but not limited to the following[4]:

- Modeling
- Surfacing
- Rigging
- Layout/ Set dressing/ Anim Prep
- Character Animation
- Crowds
- Character Effects/ Simulation
- Effects
- Technical Director
- Matte Painting
- Lighting

For big animation studios such as Disney, there are enough members in the team to distribute the worktime. But, for one creator or a small studio, it is a lot harder to create a complete animation even when they have created a great concept to animate.

Today, there are a few illustration/3D modeling and animation tool for the VR, which can shorten the traditional 3D animation process done in 3D software. It is a new way of animating that is more intuitive, which has an easier transition to using our real-time renderer. Quill is one of the more intuitive tools that will be introduced.

4. Importance or Significance of Tutorial

Quill is a great tool to create content for Unity or Unreal, which can then be rendered in real-time by the super computers at NCHC. Render is normally the last step to the production pipeline, and each step is important for the next. For example, if a 3D model is not rigged properly, it will not animate properly. This makes it harder for one person to complete the job without any help.

The traditional 3D animation pipeline would most likely take years to master each step. Oculus Quill can skip the steps of modeling, rigging, texturing, and go directly into animating. Even though it may not have a final product as realistic or as detailed as an animation made with 3D software, but it is a great option for making quick and simple animations, which can then be used for other purposes.

At NCHC, animations created with Oculus Quill are imported into game engines supported by the render farm, which can be built into VR or even Augmented Reality (AR).

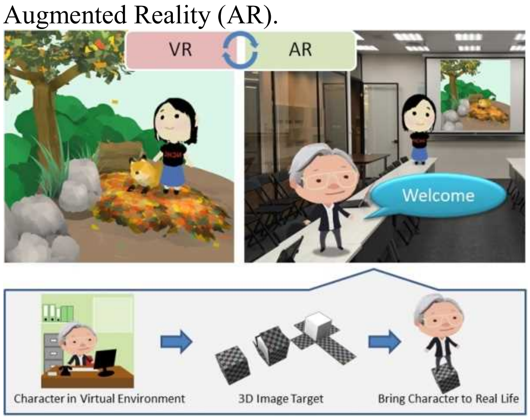

Fig. 2. An example of how content created by Quill can be applied into VR/AR.

Although VR/AR is beginning to emerge with the animation industry, most AR developers are not animators who can create 3D models. Moreover, a lot of applications of AR do not necessarily require detailed models, since there are still limitations to most AR devices available that restricts files that are too big. Quill is a great tool for such users to quickly create their own IP for demonstration purposes.

Fig. 3. Quill is also a great tool for creating contents for smartglasses.

5. Possible Outcome

One specialty about Quill is that there is no limit to the canvas size; it can be zoomed in and out endlessly. The only limit to Oculus Quill is the system that it is running on. A powerful computer is required to run the Oculus Rift, and its processor and graphics card determines how smoothly Quill runs on the Oculus Rift.

NCHC are finding ways to connect VR equipment to the render farm through virtual desktop. If succeeded, this opens up a whole new way of using the render farm, and extends the possibility of VR creations to the next level.

6. Conclusion

The central thinking of NCHC is to fill the gap between technology and art. However, it has been a hard task due to the limited people who have knowledge to both sides. Thanks to the developers of Quill, the bridge between technology and art seem to be found.

7. Reference

1. Maxim- Eden- Robyned-TomaszMSwidzinski-Sareesh Sudhakaran – https://wolfcrow.com/blog/what-is-a-render-farm/
2. Takahashi, Dean. “How Pixar Made Monsters University, Its Latest Technological Marvel.” VentureBeat, 24 Apr. 2013, venturebeat.com/2013/04/24/the-making-of-pixars-latest-technological-marvel-monsters-university/.
3. Unreal Engine 4 Vs. Unity: Which Game Engine Is Best For You? https://www.pluralsight.com/blog/film-games/unreal-engine-4-vs-unity-game-engine-best
4. Willett, Nora, et al. “Animation Production Pipeline.” Physbam, 29 Mar. 2011, physbam.stanford.edu/cs448x/old/Animation_Production_Pipeline_(2d)_Nora_Willett.html.

System to decide unit's layout of cell assembly machine by GA (Big Mutation in mutation process)

Yoshiki Ito
Department of Human Information Systems, Gifu University, Yanagido 1-1, Gifu, Gifu 501-1194, JAPAN

Hidehiko Yamamoto
Department of Mechanical Engineering, Gifu University, Yanagido 1-1 Gifu, Gifu 501-1194, JAPAN

Takayoshi Yamada
Department of Mechanical Engineering, Gifu University, Yanagido 1-1 Gifu, Gifu 501-1194, JAPAN

E-mail: w4525008@edu.gifu-u.ac.jp, yam-h@gifu-u.ac.jp, yamat@gifu-u.ac.jp

Abstract

This study develops the system which assists the unit placement decision of the automatic assembling equipment to assemble efficiently. The unit is a part supply or a robot hand constituting assembling equipment. Conventional research has used reinforcement learning to determine efficient unit placement but this research adopts Genetic Algorithm (GA) instead of Reinforcement Learning. First, as input data, information such as an arrangeable region of each unit is input, and the input region is divided into fixed sizes. Next, the unit is placed in the divided region. Prepare a group of individuals whose genes are the placement of each unit, and repeat selection, crossover, mutation, and evaluation to improve placement. This system introduces the concept of Big Mutation that changes the mutation rate of GA every certain generation. As a result, the possibility of searching for an optimal unit placement increased, and it is expected that the system simulation time is shortened.

Keywords: Unit placement decision, Big Mutation, Double arm robot, Cell assembly machine,Genetic algorithm

1. Introduction

In recent years, it has been demanded to produce a large quantity of products in a short time at the production site. So, automation of the assembling work by the assembling apparatus has been carried out. When developing an automatic assembling machine, production efficiency changes depending on the arrangement of each unit. However, in many factories, the placement of units is based on the experienced engineers It remains questionable whether the determined placement by the experienced engineers is really efficient. In this research, the layout decision system that supports unit layout determinations of efficient cell type assembly machine is developed by using genetic algorithm (GA).

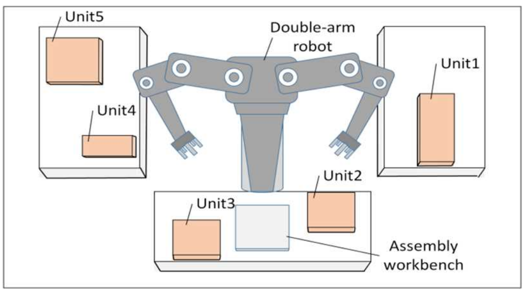

Fig. 1. Cell type assembly machine

2. Cell type assembly machine

As shown in Fig. 1, the cell type assembly machine to be used in this study has a configuration in which an assembly machine is arranged at the center, a work stand at the front and assembly units on the periphery. Therefore, after each arm chucks the needed unit, the arm carries it to the workbench to assemble the parts. In this research, approach 1, approach 2 and the chuck position of the robot arm movement route are defined as the three points that exist on the arm moving route as follows

・Chuck position ... position to position and grip unit
・Approach 1 ... position upward away from the chuck position
・Approach 2 ... position further upward than Approach 1

As shown in Fig. 2, the arm passes from approach 2 to approach 1 and arrives at the chuck position.

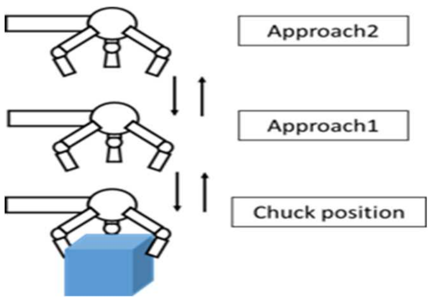

Fig. 2. Movement of arm

3. Layout determination system

The layout determination system we develop decides the arrangement of each unit with the best operation efficiency during designing a cell type part assembly machine by using GA. The system consists of two modules, the condition creation module and the GA module. The condition creation module performs to read the arrangement possible area of the unit and work contents, to divide the arrangement possible area and to decide various necessary GA parameters. The GA module determines the arrangeable place of the units, evaluates the working time and outputs coordinates of the arrangement place of the unit and the layout image of the unit.

3.1 Condition creation module

The procedure of the condition creation module is as follows.

Step Ⅰ: Read work data of parts assembly, placement possible area, parts arrangement data and create their database.

Step Ⅱ: Divide possible placement area into a lattice shape to create possible placement place.

Step Ⅲ: Carry out genes coding.

Step Ⅳ: Define the fitness function.

Step Ⅴ: Determine various parameters.

3.2 GA module

The process flowchart of the GA module is shown in Fig. 3. The process procedure is shown below.

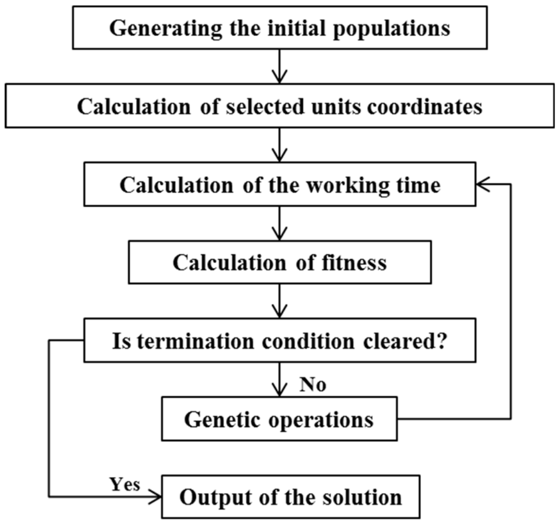

Fig. 3. Flowchart of GA module

Step 1: Generate an initial population.

Step 2: Calculate the placement coordinates of each unit.

Step 3: Calculate the time taken for each work.

Step 4: Calculate fitness.

Step 5: Apply genetic operations (selection, crossover, mutation).

Step 6: Judge whether the termination condition is satisfied. If it is, go to Step 8. If not ,go to step 3.

Step 7: The unit arrangement of individuals with the smallest operation time is adopted as the optimum arrangement and the output as a solution.

3.3 Big mutation in mutation process

In general, the phenomenon of local solution convergence occurs when a considerable number of generations in GA elapse. Therefore, we call Big mutation that only some superior individuals are carried over to the next generation as they are and a certain generation is given a high mutation rate. Because of Big mutation, it is expected to escape local solution convergence and to have a high possibility easy to converge to an excellent solution. Also, the simulation time can be shortened. However, if the mutation rate is increased too much, it is difficult to converge the solution and it is not possible to expect the effect. Therefore, it is necessary to carry out the trial and error decisions of the Big mutation rate according to work contents and GA parameters. The setting method of the Big mutation rate is shown below.

Step i :Set the mutation rate as k% which is generally adopted
Step ii :Set the interval m which occurs Big mutation between generation to generation
Step iii :Set the Big mutation rate as j% which occurs Big mutation.
Step iv :Carry out Big mutation
3.2 Step 5 of the GA module into the process of mutation in genetic manipulation incorporate Big mutation.

Fig. 4 shows the Big mutation outline. The horizontal axis of the Fig. 4 is the number of generations, the vertical axis is the mutation rate

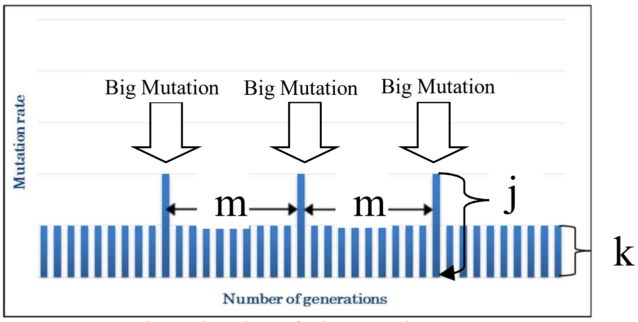

Fig.4 Situation of Big Mutation

4. Application examples of system and performance comparisons

The layout decision system developed in the research was applied to the assembly machine and production simulations were carried out. As a comparison, simulations of the following two systems were carried out.

- The system that determines unit layout by reinforcement learning
- The system that determines unit layout by using GA without Big mutation

The units that determine the placement has eight left tray, right part tray, left parallel hand, left three nail hand, right parallel hand, right four nail hand, jig A, jig B and also the assembly work. The layout map is shown in Fig. 5. Fig. 6 is the left and right part trays with 52 parts. Each number represents each part.

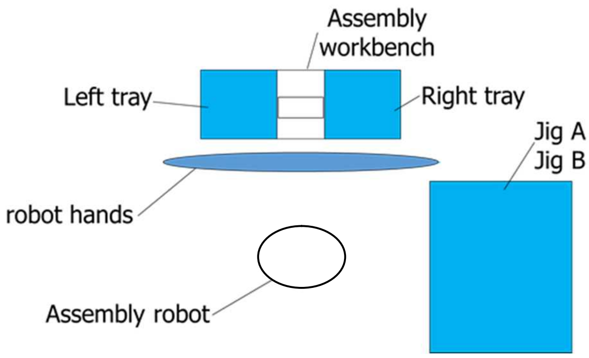

Fig. 5. Units layout

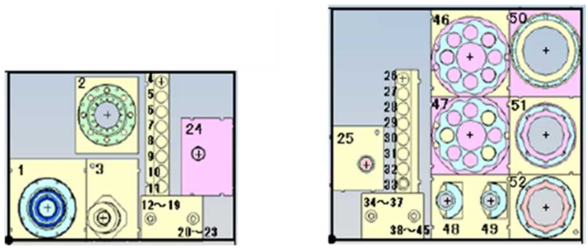
Fig. 6. Parts trays

Next, Table 1 and Table 2 show the position data and placeable area data of the dual arm robot.

Table 1. Coordinates of double arm robot

	x[mm]	y[mm]	z[mm]
Dual arm Robot	2,210	915	740

Table 2. Placement area of each unit

Unit	x1[mm]	y1[mm]	z1[mm]	x2[mm]	y2[mm]	z2[mm]
Left tray	1,811.5	1,760	740	1,918.5	1,804.5	740
Right tray	2,522	1,806.5	740	2,628	1,807.5	740
Left parallel hand	1,280	1,480	629	2,320	1,480	629
Left three claw hand	1,280	1,480	629	2,320	1,480	629
Right parallel hand	2,100	1,480	629	3,140	1,480	629
Right four claw hand	2,100	1,480	629	3,140	1,480	629
Jig A	3,034	83	740	3,656	1,117	740
Jig B	3,034	83	740	3,656	1,117	740

4.1 Simulation results

Simulations were carried out ten times in each of the three systems. The results of the simulations are described below.

・Minimum cycle time：
The smallest work time in each simulation
・Average cycle time：
Average work time of simulation for 10 times
・Average simulation time：
Average time taken for 10 simulations
・Standard deviation ：
Indicator indicating variation of the data

From Table 3, in all simulation results, the values of the systems using GA were calculated systems using GA beter than that of reinforcement learning. Table 4 shows reduced simulation time and stability of simulation results by using Big mutations.

Table.3 Comparisons with reinforcement learning

	Reinforcement learning	Two point crossover
Minimum cycle time[s]	237.287	237.147
Average cycle time[s]	237.332	237.168
Average simulation time[s]	495.327	28.072
Standard deviation of Cycle time	0.027449	0.013559

Table.4 Comparisons with GA system not using Big mutation

	Two point crossover	Two point crossover (Big Mutation)
Minimum cycle time[s]	237.251	237.147
Average cycle time[s]	237.262	237.168
Average simulation time[s]	31.088	28.072
Standard deviation of Cycle time	0.015394	0.013559

Fig. 7 shows the output diagram of the unit arrangement with the highest efficiency in two-point crossover using Big mutation.

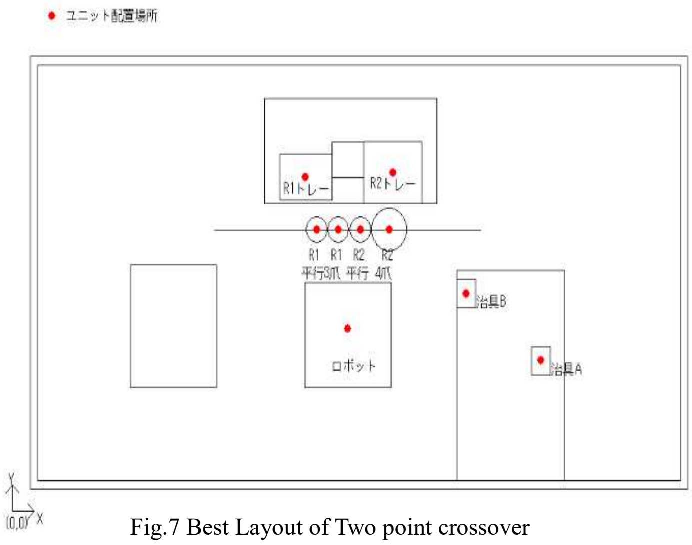

Fig.7 Best Layout of Two point crossover (Big Mutation)

5. Conclusions

The layout determination system developed in this research is the system aiming at improvement of design and production efficiency by automating the unit arrangement determination of a cell type assembly machine by GA.

As a result of comparing the performance of the system using reinforcement learning and the GA system without Big mutation and the layout decision system, the layout determination system was able to obtain a more efficient unit arrangement than the other two systems. Therefore, it was found that the layout determination system is useful for determining the arrangement of units in a cell type assembly machine.

Autonomous decentralized FMS that adopts priority order structure based on AGV's lie

Kento Uejo
Department of Mechanical Engineering Gifu University, Yanagido 1-1 1-1,Yanagido,Gifu, 501-1194, JAPAN

Hidehiko Yamamoto*1
Department of Mechanical Engineering, Gifu University, Yanagido 1-1 1－1, Yanagido, Gifu 501-1194, JAPAN

Takayoshi Yamada*2
Department of Mechanical Engineering, Gifu University, Yanagido 1-1 1－1, Yanagido, Gifu 501-1194, JAPAN

*E-mail: *1; yam-h@gifu-u.ac.jp *2; yamat@gifu-u.ac.jp*

Abstract

We introduce the model of AGV mind to eliminate path interferences between AGVs when running an autonomous decentralized FMS and have carry out behavior controls. The conventional autonomous decentralized FMS believes all information sent by agents as correct. However, the information sent by some agents may be incorrect due to malfunctions. We define this incorrect information as a "lie" and carry out the AGVs action controls which doesn't decrease the outputs of autonomous decentralized FMS even if lies occur.

Keywords: Autonomous decentralized FMS, AGV, Priority order structure

1. Introduction

We have researched an autonomous decentralized flexible manufacturing systems(FMS) factory [1]. Here, when operating an autonomous decentralized FMS, we researched avoiding route interferences between AGVs. Especially, we controlled AGVs by inserting two models of mind, an arrogant mind and a modest mind, into AGV[1].

In this research, all information transmitted by agents is treated as true. In the actual operations of an autonomous decentralized FMS, it is the possible situation that incorrect information is sent due to machine breakdowns. In order to solve this problem, we define this incorrect information as a "lie" of AGV. We study how to control the AGVs not to decrease the productivity in spite that AGVs sometimes lies

The control method is to give an order to each AGV according to the number of lies. We propose the "priority order structure" and the AGV whose priority order structure belongs to a higher position has the higher possibility to be given a job.

We carry out the production simulations of the autonomous decentralized FMS with the proposed method and get the productivity to prove the goodness of the proposed method. As a comparison, we also calculate the productivity by using AGVs that adopted the "reliability structure" which is the past research that our lab developed and verify the effectiveness of this proposal method.

2. Mechanism of autonomous decentralized FMS

2.1. *Description of autonomous decentralized*

Fig.1 shows the example of an autonomous decentralized FMS factory. The factory floor is divided into a grid pattern where an AGV moves on the line. FMS manufactures the products by carrying the parts from the warehouse to machining centers (MCs).

An autonomous decentralized FMS does not have a management mechanism that controls the whole system between agents that constitute the system to the knowledge exchange, to determine the behavior by coordination.

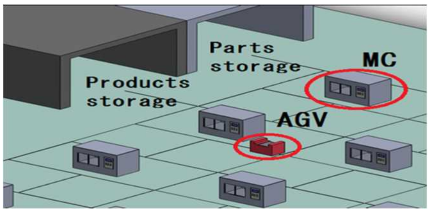

Fig.1 Example of autonomous decentralized FMS

2.2. *Model of mind and behavior of AGV*

As multiple AGVs in the autonomous decentralized FMS autonomously determine the behavior, this research gives the AGV a mind and realize the AGVs moving control by a mind. That is, some AGVs have arrogant minds and others have modest minds to move.

AGV with an arrogant mind moves forcibly to the destination. AGV with a modest mind gives way to other AGVs.

We express the mind as the mind model of Fig.2, Minimum Unit of Mind (MUM). A1 and A2 of Fig.2 are the units, X is the load and the arrow is a stimulation vector. If the internal value of the unit reaches the threshold, we call it "satisfied". And if it does not reach the threshold, we call it "normal".

When the signal is sent to the unit, MUM sends the signal to the direction of the arrow if it is satisfied, and MUM does not send if it is normal.

The load has the function to change the internal value of the unit. When the signal is sent to the load, the value of the unit is increased by the value of X.

The stimulation vector is a line connecting the load and the unit and a signal is sent to the load or unit when the signal comes. When A1 is kept satisfied, we call it "modest mind" and when normal, we call it “arrogant mind”. Also, by the amount of the signal input to the unit, MUM changes the mind frequently, arrogant or modest.

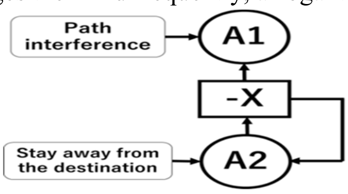

Fig.2 Model of Mind

We describe the internal functions of MUM. When the arrogant AGV has a path interference, A1 is increased by 1. Keeping the situation of the interference, the A1 value repeats to be increased by 1. When the A1 value finally becomes the threshold value, the A1 becomes satisfied and the AGV is changed to a modest mind. As humble AGVs give way each other and continue to give way, we increase the A2 satisfaction by one. When modest AGVs try to make way for each other and A2 becomes satisfied, MUM sends a signal to the load. The load that received the signal will change the units A1 and A2 from satisfied to normal. As a result, AGV will become an arrogant AGV from a modest AGV.

In this way, a mind switching between arrogant mind and modest mind avoids path interferences between AGVs of autonomous decentralized FMS.

3. AGV’s lie and its reliability structure

We define the AGV as “liar” when the AGV sends an incorrect information and as “honest” when the AGV sends a correct information. We also define the lies as the following three kinds of lies that the AGV has

1. Sending incorrect location information(USO1).
2. Reading incorrect location information(USO2).
3. Do not send location information(USO3).

The reliability structure which is our past study[2] determines which AGV can be trusted by counting the number of lies and is the hierarchical structure including the hierarchical relationship in the AGV group. This reliability structure gives the job to the AGVs with high hierarchies. The AGVs with lower hierarchies take actions to give way to other AGVs.

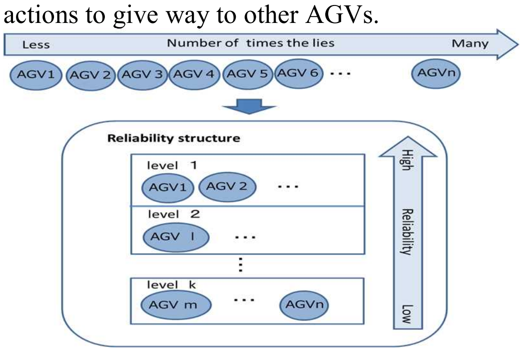

Fig.3 Example of reliability structure AGV

4. Priority order structure

4.1 Concept of priority order structure

When we carry out jobs at a company or a school, the efficiency of carrying out jobs is needed. In order to carry out the high efficiency jobs, assigning a priority to works and choosing the high priority works are one of the ideas. We propose the priority order structure(POS) to "prioritize the AGVs based on the number of lies and construct POS".

The POS gives a move to the AGV that does not lie and AGV which often lies makes a movement not to disturb other AGVs actions. In spite there are AGVs that lie, it is thought that a production can be smoothly carried out without decreasing production efficiency.

4.2 Formation of POS

In order to make POS in the AGVs, as shown in Fig.4, every AGV adds the information on the number of times that AGV lied and the order of AGV.

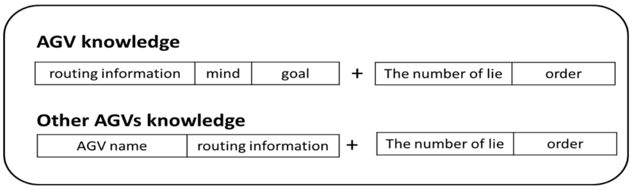

Fig.4 AGV Knowledge

The following algorithm shows how to make POS.
Step 1. At the end of production, information about the n umber of lies described in AGV knowledge is transmitte d to all other AGVs.
Step 2. Save the number of lies received from other AGVs in the AGV knowledge of other AGVs.
Step 3. Arrange from a small number of AGV lies of myself and other AGVs.
Step 4. Form POS according to the above arrangement.
Step 5. Check the order of each AGV from the formed priority structure and save it as a knowledge of myself and a knowledge of other AGVs.

In this way, if each AGV performs Step1 to Step5, the order of each AGV is generated as the order shown in Fig.4. As a result, the POS as shown in Fig.5 is constructed.

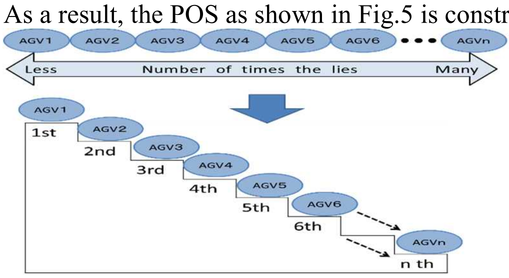

Fig.5 Example of priority order structure AGV

4.3 Behavior control using POS

When the AGV group that formed the POS interferes with the path, the order in the knowledge of myself and the knowledge of other AGVs that interfere with the myself route are compared. If the order is higher, the AGV becomes arrogant mind and if the order is lower, the internal value of the unit of MUM is changed in order to become a modest mind. This is the mind change and the change can shorten the time for avoiding route interference.

4.3.1 Case 1:Two AGVs interference

When the AGV1 and the AGV2 interfere with each other as shown in Fig.6, the order in myself knowledge of AGV1 and the order of AGV2 in myself knowledge of other AGVs are compared. Finding AGV1 order is high, AGV1 keeps the arrogance and does not change the mind. As AGV2 compares the order in knowledge of myself with the order of AGV1 in knowledge of other AGVs and finds the order is lower than AGV1, AGV2 turns into a modest mind, gives way and avoids a route interference.

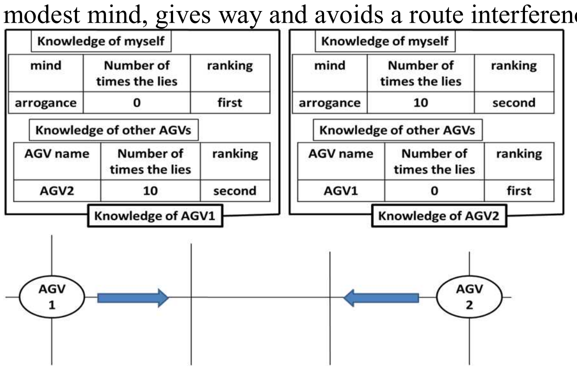

Fig.6 Example of path interference

4.3.2 Case 2:Interference of the same order AGV

When AGV1 and AGV2 that have the same order interfere each other as shown in Fig.7 below, their order in the knowledge of myself of AGV1 is compared with the order of AGV2 in the knowledge of other AGVs. Because it is the same, the mid of arrogance is kept. AGV2 also compares in the same way and the arrogant mind of AGV2 is kept because the order is the same. In this case, using MUM shown in Section 2.2, route interference by mind change is avoided.

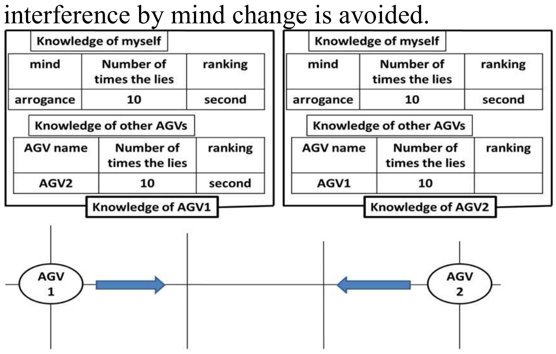

Fig.7 Example of the same order

4.3.3 Case 3:Multiple AGVs interference

When multiple AGVs (n) interfere with each other as shown in Fig.8, first the AGV1 compares the order in knowledge of myself with the order of all AGVs that interfere. Finding that the order is the highest, the arrogant mind of AGV1 is kept. Secondly, the AGV2 compares the order in knowledge of myself with the order of all AGVs that interfere. Finding that there is an AGV with a higher order than my order, the modest mind is changed. In this way, every AGV that interferes with each other compares orders as described above. If there is no higher AGVs, the arrogant mind is kept. If there is a higher AGV, the modest mind is changed. This action is performed n times and only AGV of an arrogant mind goes forward. Other AGVs of modest mind takes action to give way. As AGV1 with the highest order passes, (n-1)AGVs with modest minds will interfere, similarly, (n-1)AGVs compare the order each other. The AGV mind with the highest order among (n-1)AGVs is changed to arrogant. This mind change is repeated until an interference is disappeared.

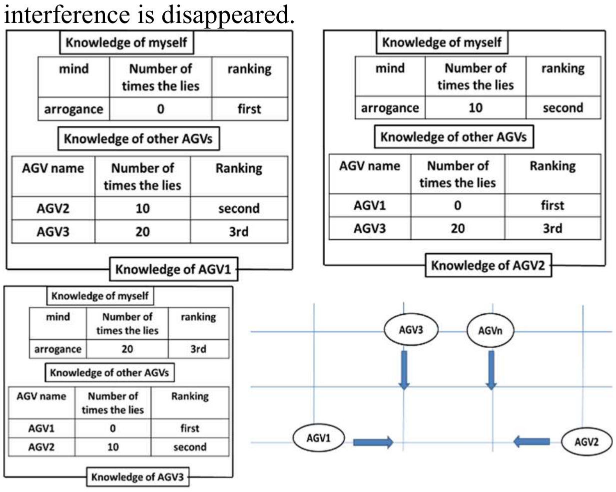

Fig.8 Example of multiple AGVs

5. Simulation and results

We carried out production simulations of autonomous decentralized FMS with POS and the reliability structure. The reliability structure adopted the model in which the number of hierarchies is three, the number of hierarchies 1 is one, the number of hierarchies 2 is three, and the number of hierarchies 3 is five.

In this production simulation, the number of AGVs was 9, the number of MCs was the 24 MCs have 3 type of the same MC. The operating time was 8 hours a day, and carried out 20 days.

The probability that AGV lies shows in Table 1. This is the probability that each lie occurs when the AGV passes through the intersection.

Table 1 Probability of occurrence of lies

	USO1	USO2	USO3
AGV1	0	1/2	1/2
AGV2	0	0	0
AGV3	0	1/20	1/20
AGV4	1/20	0	0
AGV5	1/2	0	1/200
AGV6	0	0	0
AGV7	0	1/200	1/200
AGV8	1/200	0	0
AGV9	1/2	0	0

The Table 2 shows the production simulation outputs of FMS with reliability structure and POS.

Table 2 Simulation results of production outputs

	FMS reliability structure	FMS priority order structure
Production outputs (20 days)	4,397	4,440

From the simulation outputs results, it is found that the outputs of POS is more than that of the reliability structure. The difference was 43. It is ascertained that POS is useful.

6. Conclusions

In order to prevent the production output decrease of FMS which lies occurs. We proposed POS. After the production simulations, it is found POS is useful.

Reference

[1] Hidehiko YAMAMOTO, Takayoshi YAMADA and Shinsuke KATO, AGV Mind Model and its Usage for Autonomous Decentralized FMS by Change of Mind, *Proceeding of Third KES International Symposium*, KES-AMSTA 2009, Agent and Multi- Agent Systems : Technologies and Applications, Lecture Notes in Artificial Intelligence, Edited by Anne Hakansson, Ngoc Thanh Nguyen etc. , ISSN 0302-9743, Uppsala, Sweden, pp.744-753, June(2009), Springer.

[2] Moving Robots Lies and Their Minds with Degree of Confidence in a Decentralized Autonomous FMS, Shizuka Tanaka, Hidehiko Yamamoto and Takayoshi Yamada, Proceedings of The 2016 International Conference

CULET: Cubelet Lego Turing Machine

Ricardo Q. Figueroa
Artificial Life Robotics Lab, Escuela Superior de Cómputo, Instituto Politécnico Nacional, México

Daniel A. Zamorano
Artificial Life Robotics Lab, Escuela Superior de Cómputo, Instituto Politécnico Nacional, México

Genaro J. Martínez
Artificial Life Robotics Lab, Escuela Superior de Cómputo, Instituto Politécnico Nacional, México. Unconventional Computing Laboratory, University of the West of England, Bristol, United Kingdom

Andrew Adamatzky
Unconventional Computing Laboratory, University of the West of England, Bristol, United Kingdom

E-mail: qf7.ricardo@gmail.com, daz23ayala@gmail.com, genaro.martinez@uwe.ac.uk, andrew.adamatzky@uwe.ac.uk

Abstract

In this paper, we show the construction of CULET: a robot that simulates the execution of any 2-symbols Turing machine. CULET is constructed with Cubelets (small autonomous robot-cubes used for teaching basic robotics and programming for kids) and Lego bricks. Cubelets are a kind of high level programming where you do not use traditional code but rather achieves different robots trough the concatenation of blocks, i.e. robots assembled. CULET is designed to performance the read and write of a Turing machine.

Keywords: Turing machine, Robotics, Cubelets, Lego, Cellular Automata.

1. Introduction

In the history of Turing machines an ample number of physical mechanical devices have been developed. Indeed, during the Turing's 100th birthday, Lego built an autonomous mechanical Turing machine adding binary numbers in 2012 year[1]. So we, inspired in the idea of machines self-reproducing from cellular automata theory[2], construct the robot CULET, a robot based in small robots-cube Cubelets and some pieces Lego. The main feature of this proposal is that it is the first machine constructed with robots and bricks. This way, *this robotic machine* is able to simulate the function of other machine: *machines simulating machines*. Cubelets, helped with pieces Lego, proof how a robotic machine is able to simulate an abstract computable machine. The brain of this robot is concentrated in a cube which can read and other two cubes that move the head and the arm (write). Of course, these cubes need be re-programed for each table of transitions.

For the implementations we programming two special Turing machines. The first one is a universal Turing machine able to simulate the behaviour of a complex elementary universal cellular automaton known as Rule 110[3]. The second Turing machine programmed in CULET doubles the number of ones in the tape.

The paper has the next structure. In Section 2 we introduce quickly the Cubelet robots and describe the Turing machines implemented. Section 3 describes the design (hardware and software) and finally in Section 4 we give some final remarks.

2. Preliminaries

2.1 The Cubelets

The Cubelets are small cubes designed to teach fundaments of robotics and programming to kids. Each cube has a different functionality; the general idea is to construct robots only through the concatenation of different cubes, this way Cubelets can be represented as a formal language, where every valid construction is a valid expression in the language, thus we can see an unlimited number of possible robots. This can be seen as a high level of programming: the child does not modify the original program of each cube, but instead, use this program together with the interaction among cubes for produce a new robot. The different cubes are classified in three categories[4]:

- Input sensors: cubes used for obtain data from the environment. The most common are the distance and light sensors.
- Actuators: cubes used for make movements, e.g. drives or rotators.
- Thinkers: cubes for make computations. Some of them are inverters, maximum, minimum, etc.

A single cube communicates with his neighborhoods through a shared channel that is established in the concatenation of blocks. The input sensors publish his reading thought the channel; the thinkers obtain these readings, make his computation, and send the information to the actuators.

Another, less popular, approach is to reprogram the cubes for obtain different behaviors. This reprogramming is done in C or Scratch-like code. The CULET, which is described in the next section, follows this approach. In Ref 5 is described the API for programming the cubes.

2.2 Universal Turing machines

The Turing machines was invented by Turing in 1936[6] to solve problems about completeness and decidability. A Turing machine is a finite-state machine associated with an external memory medium, an infinite tape divided in squares. The machine move in the tape and the head read the value in each square sequentially[7]. Formally, the Turing machine is a set of quintuples of the form:

$$(q_0, s_0, q_{i+1}, s_{i+1}, d) \qquad (1)$$

Where q is the set of states, s is the set of symbols and d indicates the direction of movement of the head in the tape (right or left); i is the time step. So, the first two elements of the quintuple indicate the current state and symbol, the next two elements indicate the following state and symbol, and the last one indicates the direction of movement[a].

One of the greatest achievements of Turing's work is the conceptualization of the so called *universal machines.* A universal machine *U* can do everything that any machine can do. *U* receives as input two things, a description of a machine *A*, and the input for that machine *M*; and, as output *U* puts on the tape the same thing that the machine *A* would put when have as input *M*.

2.3 Elementary cellular automata

Cellular automata were invented by von Neumann in Ref. 2 as, ironically, a mean for study decentralized systems and been able of design non-von-Neumann-style computers. The cellular automata consist of a grid of square cells, each of which is a finite-state automaton (the same rules for all the cells simultaneously) and where the state of each cell in the next generation depends on his current close neighborhood. Von Neumann was developed a very complex automaton with 29 states evolving in two dimensions.

Another important event in cellular automata history is the popularization of Conway's Game of Life in the 70's[9]. This is a cellular automaton with only two states and a neighborhood of eight cells (Moore neighbourhood). The popularity of this automata comes given his very complex and unpredictable behavior from simple rules. Conway demonstrated the universality of this automata constructing a register machine in Ref. 10.

In the 80's years, Wolfram invented the elementary cellular automata as an effort for understanding the dynamics of cellular automata[11]. This is an extremely simplified version of the previous studies: the space is unidimensional (a row of cells) and the neighbourhood consist exclusively on the two closest cells of each.

[a] Some other standard literature, like Ref. 8, defines the machine in terms of quadruples instead of quintuples.

Wolfram hypothesis was that if we cannot understand such minimal models, then we could never understand bigger ones. The interesting part comes when even in those small automatons are still, in some of them, very complex behavior.

2.4 Universal ECA: rule 110

In Ref. 12 Cook proofed that the elementary cellular automaton Rule 110 is universal. The proof consists in showing how, with particle interactions[13] typical of the rule, emulate the operation of a cyclic tag system. This one is the smallest cellular automaton proofed computationally universal simulating a very sophisticated sequential machine by particle collisions in one dimension. This way, a new machine was invented to simulate a computable function known as cyclic tag system in this automaton, for details see Ref. 12 and 14. This way, Rule 110 can simulate a cyclic tag system[12], cyclic tag systems can simulate tag systems[12,14], tag systems can simulate Turing machines[7], and a Turing machine (developed by Eppstein in Ref. 12) can simulate Rule 110 and therefore such a Turing machine is universal. Finally, CULET can simulate the universal Turing machine which simulate the behavior of Rule 110, complex behavior, and collisions of particles[15,16].

Table 1. 7x2 Rule 110 Turing Machine.

	0	1
S_{x0}	$(0, T_{x0}, R)$	$(1, T_{01}, R)$
S_{01}	$(1, T_{x0}, R)$	$(1, T_{11}, R)$
S_{11}	$(1, T_{x0}, R)$	$(0, T_{11}, R)$
S_L	$(0, T_{x0}, L)$	$(1, T_{x0}, L)$
T_{x0}	$(1, S_{x0}, R)$	$(0, S_L, L)$
T_{01}	$(1, S_{01}, R)$	X
T_{11}	$(1, S_{11}, R)$	X

The Table 1 shows the transition table of the machine implemented. Every generation in which the head of the machine reaches a right end, a new generation of the rule 110 is computed. There are some considerations with respect to this machine: the initial condition and the representation of the cellular automata symbols. The initial condition of the machine must be, from left to right, an infinite string of zeros, the encoded version of the initial that the machine is going to emulate, and an infinite repetition of the string "10". A "1" of the cellular automata is represented like "11" in the machine, and a "0" like "00"; the symbol "10" is used like a blank symbol.

2.5 A duplicator Turing machine

A duplicator Turing machine was used by Rendell as part of the Turing machine constructed in the Game of Life cellular automaton, for details see Ref. 17. We implement this machine in CULET. In Fig. 1, we show a 3-symbols version: it starts advancing to the right, for each one scanned, it put another one in the left until there is no more ones to the right. For the implementation in the CULET we used a 2-symbols version of this machine.

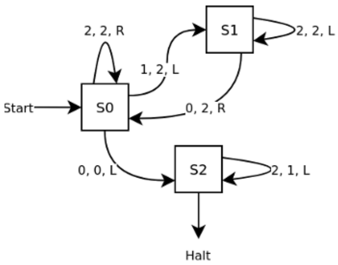

Figure 1. Duplicator machine.

3. CULET Design

3.1 General description

In the Fig. 2.1 we show a snapshot of CULET. The tape is represented as an array of Lego blocks over rectangles of black paper; the position of the block (front or back) indicates the symbol on the cell (zero or one respectively). The Cubelet car moves through the tape reading and writing in the tape; the read process is achieved with a distance sensor that test the position of the Lego block under scanning; the writing is done with a lever of Lego and a rotate cube: depending on the desired symbol, the leaver push or pull the block of the tape. The movement across the tape is done with a couple of wheels that move in right or left direction. In the backwards of the car is attached a rail that helps to maintain the alienation of the car with respect to the tape.

3.2 Hardware

In the Fig 2.2 we show a picture of the cubes needed by the CULET: a couple of batteries, a couple of drives, two distance sensors, one rotator, one passive and one light. In figure 2.3 are shown the Lego components needed (from left to right): a rail of 4 blocks width; a stabilizer car (it must go over the rail); a leaver; the symbols of the

Figure 2. (1) The CULET; (2) and (3) Cubelets and Lego.

cells.

3.3 Software

As we point out in the previous section, we reprogram some of the cubes for obtain the desired behavior. The central cube, the one that has encoded the production rules of the Turing machine, is the rotator. In the state diagram of the Fig. 3 we show the stages of the program of this cube. The scan operation is achieving reading the value of the sensor that is pointing to the cell; the other sensor, the one that is pointing up, control the movement of the leaver: it stablishes when stop moving the rotator motor; both sensors have the original program. The other two cubes that have custom programs are the motors; they receive instructions from the rotator: if they receive a 1, they move to the right; if they receive a 2, they move to the left; a 0 indicates stop moving.

The car starts with a cell below the reading sensor; it scans the position of the block and determine the next action: write a one, write a zero, or doesn't write anything; then, it moves left or right and start over again. The decisions of this automaton (the symbols to write, the directions to move) are determined accordingly to the automaton of the machine that is being executed; thus, in any moment, there are two descriptions of the program working at different levels: the low level one, that determines the behavior of the hardware components (move left, move right, scan, write); and the high level one, which is given by the rules of the Turing Machine.

4. Final Remarks

We develop a robotics Turing machine named CULET, able to simulate any 2-symbols Turing machine. CULET is constructed with autonomous cube robots Cubelets and Lego bricks. A video showing the function of the Turing machine simulating Rule 110 with CULET is available in Ref. 18 and the duplicator Turing machine in Ref 19. The full code to reprogram Cubelets is available from Ref. 20. In the future work, we will develop machines reading more than two states.

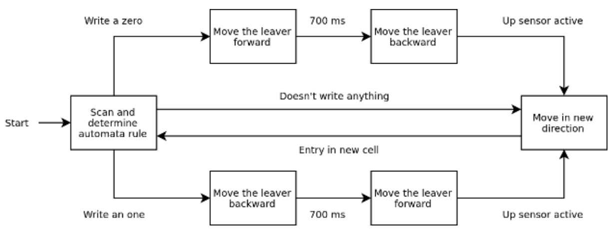

Figure 3. State diagram of the main program.

References

1. *Lego Turing Machine*. https://www.ecalpemos.nl/filmmaking/lego-turing-machine/, consulted in 04/10/2018.
2. J. von Neumann, *Theory of Self-Reproducing Automata*, edited and completed by A.W. Burks (University of Illinois Press, London, 1966).
3. *Rule 110 repository*. http://uncomp.uwe.ac.uk/genaro/Rule110.html, Consulted in 05/10/2018.
4. *The Cubelets*. https://www.modrobotics.com/cubelets/, Consulted in 3/10/2018.
5. *Cubelets API*. http://api.modrobotics.com/cubelets/, Consulted in 3/10/2018.
6. A.M. Turing, On Computable Numbers with an Application to the Entscheidungsproblem, in *Proc. of the London Mathematical Society* **2(1)** (1936), pp. 230-265.
7. M. Minsky, *Computation: finite and infinite machines* (Prentice-Hall, 1967).
8. M. Davis, *Computability and Unsolvability* (McGraw-Hill, 1958).
9. M. Gardner, Mathematical Games: The Fantastic Combinations of John H. Conway's New Solitaire Game 'Life', in *Scientific American* (224) (1970), pp. 120-123.
10. E.R. Berlekamp, J.H. Conway, R.K. Guy, *Winning Ways for Your Mathematical Plays*, 2nd ed. (Academic Press, London, 1982).
11. S. Wolfram, *Cellular Automata and Complexity* (Addison-Wesley Publishing Company, 1994)
12. M. Cook, Universality in Elementary Cellular Automata in *Complex Systems* **15(1)** (2004), pp. 1-40.
13. A. Adamatzky, *Collision-Based Computing* (Springer, 2002).
14. S. Wolfram, *A New Kind of Science* (Wolfram Media, Champaign Illinois, 2002).
15. G.J. Martínez, J.C.S.T. Mora, H. Zenil, *Computation and Universality: Class IV versus Class III Cellular Automata* **7(5-6)** (2013) pp. 393-430.
16. G.J. Martínez, A. Adamatzky, H.V. McIntosh, A Computation in a Cellular Automaton Collider Rule 110, In *Advances in Unconventional Computing: Volume I Theory*, edited by A. Adamatzky (Springer, 2017), pp. 391-428.
17. P. Rendell, *Turing Machine Universality of the Game of Life* (Springer, 2016).
18. *CULET: Cubelets Lego Universal Turing Machine ECA Rule 110,* https://youtu.be/GIQDA5Gnxkc, Consulted in 05/10/2018.
19. *CULET: Cubelets Lego Doubler Turing Machine*, https://youtu.be/CrUrKtIw34w, Consulted in 05/10/2018.
20. Code developed for CULET, http://www.comunidad.escom.ipn.mx/ALIROB/CULET , Consulted in 03/12/2018.

Automated Guided Vehicle System Analysis in Foam Manufacturing Plant Using Petri-net

Amornphun Phunopas*, Wisanu Jitviriya, Noppadol Pudchuen and, Sutee Kumjaikong
Faculty of Engineering, King Mongkut's University of Technology North Bangkok, 1518 Pracharat 1 Road, Bangsue, Bangkok 10800, Thailand†

Songklod Tunsiri
Urban Community Development College, Navamindradhiraj University, Wachira Phayaban, Khao Road, Dusit, Bangkok 10300, Thailand

Eiji Hayashi
Computer Science and Systems Engineering, Kyushu Institute of Technology, 680-4 Kawazu Iizuka, Fukuoka 820-0067, Japan
E-mail: amornphun.p@eng.kmutnb.ac.th, haya@mse.kyutech.ac.th
www.kmutnb.ac.th

Abstract

The logistic robot is very popular nowadays. The robots run in autonomous, reactive, and parallel situations. These kinds of work are defined as a stochastic problem. We focus on task distribution, routing, scheduling, and queueing. This paper presents a multi AGVs operational analysis in the foam manufacturing plant using the Petri-net. Each robot is designed a role-assignment supervisor with the role of a robot fixed in a zone. According to the work capacity, the supervisor assigns the role of high capacity work to another robot to help in a new zone. To monitor the work situation, the supervisor continually receives feedback information of the system. The analysis is necessary for preventing any failure that can make the central software go down. The results show system management for robotic assistants in the foam manufacturing process.

Keywords: AVG, EPS manufacturing, Central Software, Petri-net

1. Introduction

Nowadays, the Automated Guide Vehicle (AGV) is becoming popular and important in manufacturing applications, and it is one of the key machines for automated logistic transportation systems [1]-[2]. The AGV operates without any human intervention [3]. AGVs are dynamic and synchronized to other systems throughout the entire process. There is a central system to link and control every module. Meanwhile, the central system has to respond to the modules concurrently to obtain the highest productivity. Commonly, the operational area is static; therefore, the path can be marked with permanent methods such as magnetic guide tape, inductive loop optical marks, etc. The advantage of these methods is fast execution, but the disadvantage is the fixed path, which is difficult to modify. Path planning is a vital role for AGV. It is vital to find the optimal path from the starting point to the goal point in the workspace area based on optimal criteria such as minimum time, shortest distance, collision avoidance with other AGVs (multi-robot) and obstacles, etc. [4]-[6]. In this paper, an

*Amornphun Phunopas, Department of Production Engineering, King Mongkut's University of Technology North Bangkok, 1518 Pracharat 1 Road Bangsue, Bangkok, 10800, Thailand. Email: amornphun.p@eng.kmutnb.ac.th

© The 2019 International Conference on Artificial Life and Robotics (ICAROB2019), Jan. 10-13, B-Con Plaza, Beppu, Oita, Japan

overview system is proposed in section 2. The main controller of all AGVs is the central software, which is described in section 3. In section 4, the Petri-net model is used to find the shortest path for AGVs and the implementation in Zone1 and Zone2. Finally, the conclusion shows in section 5.

2. Process Overview

This paper describes applying AGVs to the manufacturing process of EPS (expandable polystyrene) products. Foam is widely used for protecting fragile products in packaging. It is cheap, light and simple to shape in molding. In Fig.1 the process starts to put EPS raw material to the machine to pre-expand EPS by the stream. The EPS can be shaped in various products such as protective packaging and home appliance components. Next step, the products go to the drying room and packing. All finished products will be stored in the warehouse waiting for sending to the customers. AGV operates after the products come out from the machine to deliver them to the drying room and packing zone by containing in a cart. AGV carry the cart to do the next process.

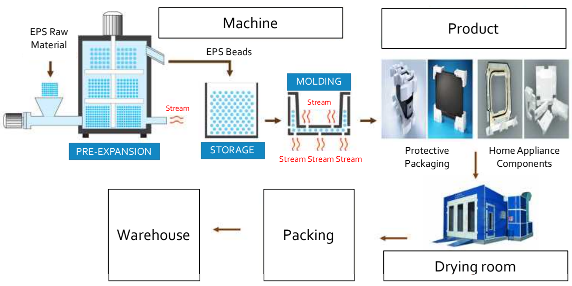

Fig. 1. The manufacturing process of EPS products.

The manufacturing process of EPS is defined in the zones in Table.1 and Fig.2. The AGV moves from zone to zone using magnetic line detection. There are nine molding machines to feed new products in Zone2. The workers check the product quality and arrange the products into the empty carts for each molding machine. When a cart is full, the worker will push a button to tell the central software to call an AGV to take the full cart to Zone3. The drying process takes one to two hours as per the schedule plan to open and close the door of two drying rooms in Zone4. When the products are done with the drying process, the AGV takes the cart from the drying room to Zone5. The workers pack the products for sending to the customers.

Table 1. Defined zones and operations

Zone	Operation
Zone0↔Zone1	Zone0 is the rest area of the AGVs. Zone1 is the empty cart area.
Zone1→Zone2	The AGV delivers the empty cart to Zone2 where the products come out from the molding machine.
Zone2→Zone3	Zone3 is the waiting zone before entering the drying room according to the schedule plan.
Zone3→Zone4	Zone4 is the drying room.
Zone4→Zone5	Zone5 is the packing area.
Zone5→Zone1	After packing, the worker delivers the empty carts to Zone1.
Zone2→Zone5	*Special0, the products do not need to go to the drying room.

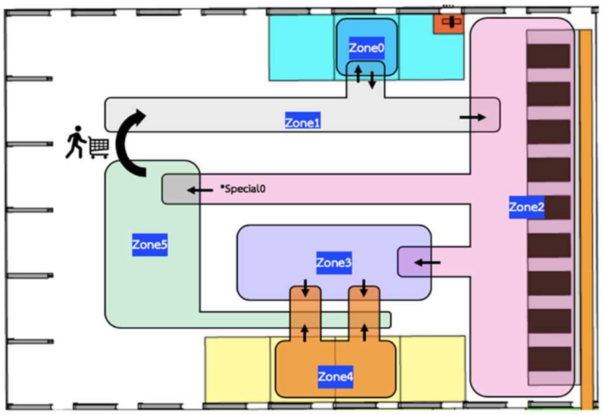

Fig. 2. AGV operation zones in the plant.

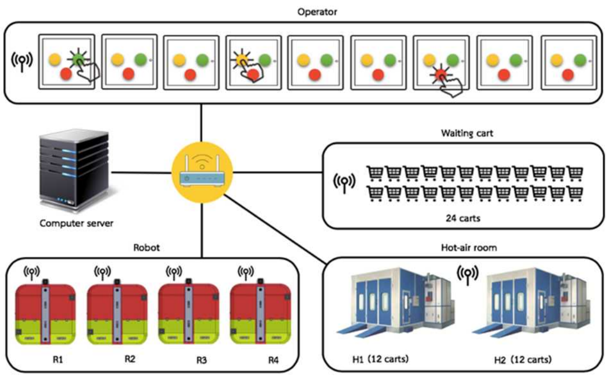

Fig. 3. The central software and connected modules.

3. Central Software

The computer server is the central control unit that communicates to every module, including push buttons, waiting carts, AGVs, and drying room, as shown in Fig. 3. This paper shows an implementation in Zone1 and Zone2. Therefore, there are two related modules: push buttons and AGV.

3.1. *Push buttons*

The initial condition is that the empty carts are in front of every molding machine. The box of the push button is installed in front of all molding machines. There are three buttons for a worker to push to communicate to the central software in Fig. 4. When the yellow button is pushed, the AGV comes to take a full cart to the waiting zone. When the green button is pushed, the AGV comes to take a full cart to the packing zone. When the red button is pushed, it clears the state, and another AGV carries the empty cart to replace the full cart. The queue of the push button is ordered by FIFO.

Fig. 4. (Left) The push buttons. (Right) The cart in front of the molding machine with the products inside.

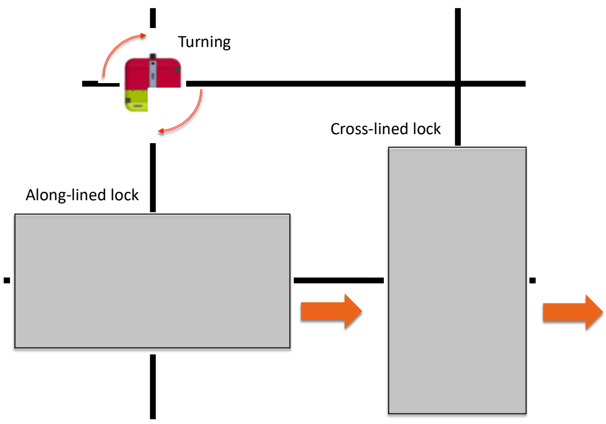

Fig. 5. AGV movement on the magnetic line and the cart-carrying configuration.

3.2. *AGV*

There are four AGVs in the system that operate in different zones. An AGV is a differential wheel platform that can take a payload of 100 kg. It takes a cart by hooking and locking under the cart. An AGV has two cart-carrying configurations: along-lined lock and cross-lined lock. An AGV can turn together with a carrying cart in Fig. 5. To verify the AGV's position, there are RFIDs under every junction to sense its current location. The AGV receives all commands from the central software, such as go to a generated shortest path, go to hook, go to lock, and turn itself at its current position.

4. Petri Net

The Petri Net is a tool that verifies that the system's operation is a stochastic problem to ensure that a deadlock condition does not occur. We focus on task distribution, routing, scheduling, and queueing.

4.1. *Shortest path*

The central software can generate the shortest path for each AGV using the undirected graph in Fig. 6. After pushing the button, the central software defines the destination as the position in front of the molding machine. Then, the central software selects the appropriate AGV for the task and sends the current position of the AGV to generate the shortest path. However, it is possible for paths to conflict when all of the AGVs are operating. The central software will assign a new path to the AGV or wait for another AGV to pass.

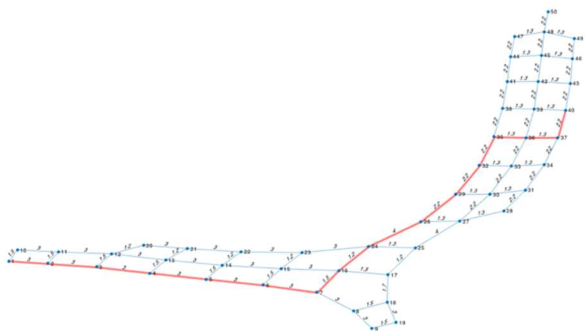

Fig. 6. The shortest path is generated from the central software.

4.2. *Petri-net Model of Zone1 and Zone2*

The model is triggered by pushing the buttons. There are tasks for two AGVs to deliver a full cart and take an empty cart. The following places and transitions are defined for a Petri net model C^s of the supervisor in Fig. 7.

Structure : $C^s = (P, T, I, O)$.
Places : $P = \{P_1, P_2, P_3, P_4, P_5, P_6\}$.
Transitions : $T = \{T_1, T_2, T_3, T_4, T_5, T_6\}$.
Input function : $I(T_1) = \{P_1\}, I(T_2) = \{P_2\}, I(T_3) = \{P_1, P_3\}, I(T_4) = \{P_4\}, I(T_5) = \{P_6\}, I(T_6) = \{P_2, P_5\}$.
Output function : $O(T_1) = \{P_2\}, O(T_2) = \{P_1\}, O(T_3) = \{P_1, P_4\}, O(T_4) = \{P_3\}, O(T_5) = \{P_5\}, O(T_6) = \{P_2, P_6\}$.

The following places are defined to model the supervisor.
P1 : AGV1 delivering a full cart, AGV2 taking an empty cart,
P2 : AGV1 taking an empty cart, AGV2 delivering a full cart,
P3 : AGV1 taking an empty cart,
P4 : AGV1 delivering a full cart,
P5 : AGV2 delivering a full cart,
P6 : AGV2 taking an empty cart.
The transitions are defined as follows.
T1 : AGV1 is in a good position to deliver a full cart,
T2 : AGV2 is in a good position to deliver a full cart,
T3 : AGV1 presently finishing tasks, it is a good position to delivering role,
T4 : AGV1 presently finishing tasks, it is a good position to taking role,
T5 : AGV2 presently finishing tasks, it is a good position to taking role,
T6 : AGV2 presently finishing tasks, it is a good position to delivering role.

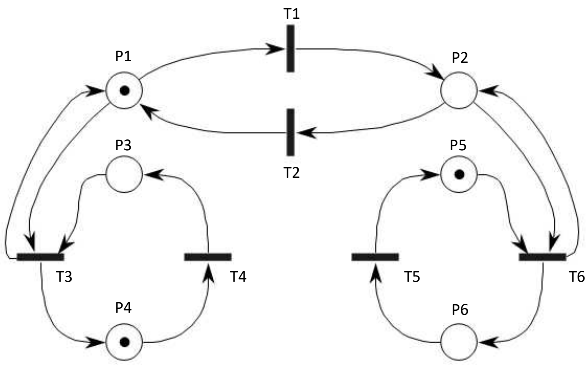

Fig. 7. A petri-net graph for role assignment supervision.

The Petri-nets model must be clear and verified in many software tools, for example, CPN tools and PIPE. For real implementation, this research uses Java language. Table 2 shows the relation of the Petri-net model to Java language.

Table 2. Petri-net and Java programming

Petri-net	Java
Autonomous transition	Runnable Class
Event-Driven transition	Class Method
Place	Block, semaphore, Blocking Queue, Synchronized channel
Token	Thread-safe data and resources
Deadlock-free PN	Deadlock-free program

5. Conclusion

This research successfully created an example case of a Petri-net model in Zone1 and Zone2 to verify the operation without deadlock. The tasks are complicated and have more conditions to complete the whole system. The next step is to convert the Petri-net model to Java programming for real implementation for AGVs.

Acknowledgements

This work is supported by the Thai Research Fund (TRF) and Polyfoam Manufacturing Co., LTD under the contract no. RDG6050047.

References

1. Handke G, Production flexibility and modern AGV system[J], *Proc of 6th Int Conf on AGVS*, IFSLtd.UK, 1988:pp344-347
2. T. L. Bui, P. T. Doan, H. K. Kim, V. G. Nguyen and S. B. Kim, "Adaptive Motion Controller Design for an Omnidirectional AGV Based on Laser Sensor", *Lecture Notes in Electrical Engineering*, Vol. 282, pp. 509-523, 2013.
3. Mantel. Ronald, Design and operational control of an AGV system[J], *International Journal of Production Economics*, 1995(41):pp257-256
4. P. Bhattacharjee, Multi-Robot Path-Planning Using Artificial Bee Colony Optimization Algorithm, *IEEE conference*, 2011.
5. M. Likhachev, S. Koenig, Lifelong Planning A* and Dynamic A* lite: The proofs. *Technical report*, Atlanta, 2001.
6. M.S. Alam and M. U. Rafique, Mobile robot path planning in environment cluttered with non-convex obstacles using particle swarm optimization, *In Control, Automation and Robotics (ICCAR)*, 2015.

Preliminary Comparative Experiments of Support Vector Machine and Neural Network for EEG-based BCI Mobile Robot Control

Yasushi Bandou, Takuya Hayakawa, Jun Kobayashi
Department of Systems Design and Informatics, Kyushu Institute of Technology
Kawazu 680-4, Iizuka, 820-8502, Japan
E-mail: jkoba@ces.kyutech.ac.jp
lab.jkoba.net

Abstract

This study aims at achieving a practical EEG-based BCI for mobile robot control by means of machine learning. To this end, the authors had conducted experiments for collecting EEGs as training/test dataset and built some neural networks (NN) using the data; however, satisfactory performance has not been obtained yet. We have employed Support Vector Machine (SVM) for further improvement and compared the performance with the NNs. As a result, the SVMs outperformed the NNs in almost all cases.

Keywords: brain computer interface, electroencephalography, support vector machine, neural network, mobile robot control

1. Introduction

Brain Computer Interface (BCI) provides you with a means to convey your intention and volition to a computer via electroencephalogram. The technology not only makes up for impairments but also expands and enhances abilities of human beings. Electric wheelchair control and robotic arm control are typical application examples of BCI. R. Single et al. developed a SSVEP-based BCI for controlling a wheelchair using multi-class SVM[1,2]. J. Meng et al. experimentally investigated a noninvasive BCI for reach and grasp task of robotic arm[3]. Mobile robot control by EEG-based BCI is also a challenging and promising technology[4].

The authors have been developing an EEG-based BCI for mobile robot control by means of machine learning techniques, especially multi-layered neural networks (NNs)[5,6]. We experimented with an omnidirectional mobile robot to collect brain waves of persons picturing a movement of the mobile robot in their brains. Then, we trained multilayered NNs with the measured brain waves in order to obtain brain wave pattern classifiers used in BCI and evaluated them. However, practical classification performance could not be achieved in the NNs.

Support Vector Machine (SVM) is also a popular machine learning method that has been applied to various fields and accomplished tremendous results. In this study, we employ SVM as classifiers for EEG patterns and compare their performance with the multi-layer NN we used in the previous studies.

2. Experiments for EEG Data Collection

The authors carried out EEG measurement experiments in order to collect EEG signals for training NNs and SVMs. The same experiments had been conducted for 3 subjects in the previous study[5]. For this study, we have newly obtained EEG signals from 3 other subjects, a 21-year-old and two 22-year-old male college students; EEG signals recorded from totally 6 subjects (named A, B, C, D, E, F) were used in this study. As with the previous EEG measurement experiments, the EEG headset shown in Fig. 1 were used for recording EEG signals, and the omni-wheel mobile robot shown in Fig. 2 that moves following predetermined commands was employed. Commands for move forward, backward, to right, and to left were given to the mobile robot in these experiments.

Fig. 1. EMOTIV EPOC (wireless portable EEG headset)

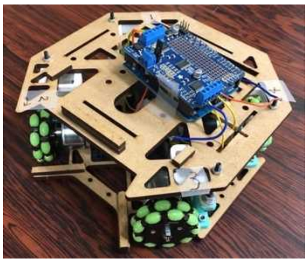

Fig. 2. Omni-wheel mobile robot

Each subject imagined 30 trials per direction, i.e. 120 trials in total, at each day for 5 different days; therefore, we collected EEG data of 600 trials for each subject. One trial consists of about 5 sec rest, 5 sec task (imagining), and 5 sec rest again. Brain waves of a subject were recorded throughout the 15 sec trials. The subject silently counted 5 sec during the first rest, and then pressed a key of a keypad just before getting started the task so that a PC for EEG recording could recognize the timing. When a beep sounded after 5 sec, the subject stopped the task and took a rest until the next trial for about 5 sec.

The subjects were given two different imagining tasks, called CLOSED-EYES and OPEN-EYES.

- CLOSED-EYES: close your eyes and imagine a specified arrow
- OPEN-EYES: watching the mobile robot moving to a certain direction, imagine the robot's motion

The CLOSED-EYES experiment was carried out first, then the OPEN-EYES one. Fig. 3 shows arrows, one of which the subjects imagined in a trial of the CLOSE-EYES task in the EEG measurement experiment. Up, down, right, and left arrows correspond to moving forward, backward, to right, and to left for the mobile robot, respectively.

↑	↓	→	←

Fig. 3. Arrows indicating directions (up, down, right, and left)

Fig. 4 shows the procedure of the trials in the experiments for OPEN-EYES task. At the beginning of the procedure, a subject counts 5 sec silently while gazing the mobile robot being at rest. During the task period, the subject keeps gazing at the mobile robot moving to a certain direction and imagine the robot's motion for 5 sec. As the task finish, the subject closes their eyes for rest and the mobile robot automatically moves back to the initial position. The subject can notice when they should end the rest even with closed eyes because the mobile robot emits a sound during the return movement.

The EEG signals recorded with 14 electrodes of the EPOC for 5 sec were preprocessed according to the following methods. First, EEG signal components in the frequency range from 8 to 30 Hz were extracted by a band-pass filter. Second, power spectrum of the filtered EEG signals was calculated, and then moving average was applied to them. Finally, the power spectrum was normalized between 0 and 1, and resampled with 1 Hz. This preprocessing produces a 322-dimensional feature vector from 5 sec EEG signals, which was used as an input into the EEG pattern classifiers.

3. EEG Signal Classification with Multi-layered Neural Network and Support Vector Machine

Stacked Autoencoder (SAE) with a softmax layer at the output was adopted as multi-layered NN for EEG pattern classification. In the training process of the NNs, the hyperparameters were optimized by Bayesian optimization[7]. Table 1 describes the optimized hyperparameters and their options. The SAEs and Bayesian Optimization were implemented using Chainer14 (ver. 1.18.0)[8] and GPyOpt13 (ver. 1.2.0)[9].

As another EEG pattern classifier, nonlinear SVM with RBF kernel function was employed. In the training process of the SVMs, input feature vectors were scaled, and parameters of RBF function and regularization were optimized using grid search. LIBSVM (ver. 3.22)[10] was used for implementing the SVMs.

The classification performance of the NNs and SVMs trained in this study was evaluated using 5-fold cross validation. Table 2 shows the computation environment for development of the SAEs and SVMs.

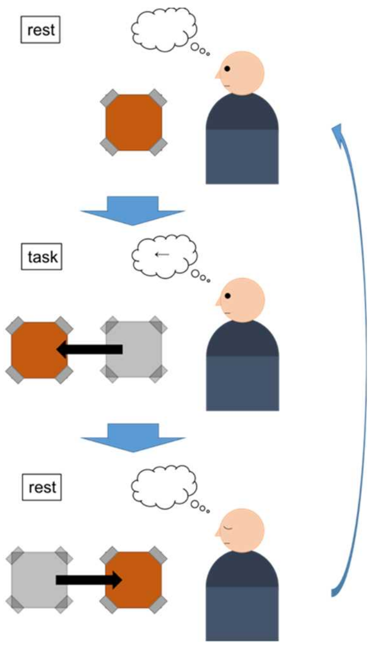

Fig. 4. Procedure of trials in experiments for OPEN-EYES

Table 1. Hyperparameters and options

Hyperparameter	**Options**
Number of hidden layers	1 ~ 3
Number of nodes in 1st hidden layer	250 or 300
Number of nodes in 2nd hidden layer	150 or 200
Number of nodes in 3rd hidden layer	50 or 100
Iteration of pretraining each AE (epoch)	1000 or 2000
Iteration of finetuning (epoch)	5000 or 10000
Dropout 50% in pretraining AEs	OFF or ON
Dropout 50% in finetuning	OFF or ON

Table 2. Specifications of computation environment for development of SAEs and SVMs

CPU	Intel® Core^{TM} i7-6800K CPU @ 3.40GHz
Memory	16GB (DDR4-2133 4GBx4)
Storage	SSD 240GB + HDD 1TB
GPU	NVIDIA GeForce GTX1060 6GB GDDR5
OS	Ubuntu 16.04 LTS

4. Results and Discussion

Table 3 and Table 4 shows results of the comparative experiments of the NNs and SVMs trained with the EEG signals recorded in CLOSED_EYES task. The values in the rightmost columns are averaged classification rate percentages of the 5 experiment days. The better averaged classification rate between the NNs and SVMs are shown in red. Comparative results in the case of OPEN_EYES are shown in Table 5 and Table 6.

These results clearly show that the SVMs outperformed the NNs regardless of the task types, CLOSED_EYES and OPEN_EYES. The averaged classification rate percentages of all subjects were 55.03% for the NNs and 63.49% for the SVM in CLOSED_EYES; 50.61% for the NNs and 61.17% for the SVM in OPEN_EYES.

Table 3. Classification rate percentages of NNs trained with Bayesian optimization using 120 samples recorded in CLOSED_EYES

Subject	**1st day**	**2nd day**	**3rd day**	**4th day**	**5th day**	**Ave.**
A	55.00	57.50	66.67	79.17	92.50	70.17
B	50.00	70.00	53.33	66.67	54.17	58.83
C	44.17	49.17	51.77	76.67	33.33	51.02
D	58.34	70.00	54.17	50.83	40.83	54.83
E	45.83	45.00	56.67	44.17	29.17	44.17
F	76.67	42.50	40.00	39.17	57.50	51.17

Table 4. Classification rate percentages of SVMs trained using 120 samples recorded in CLOSED_EYES

Subject	**1st day**	**2nd day**	**3rd day**	**4th day**	**5th day**	**Ave.**
A	57.97	49.04	64.40	58.80	62.74	58.59
B	64.70	63.04	71.79	72.50	56.61	65.73
C	93.63	86.73	55.36	59.70	62.02	71.49
D	52.44	49.94	55.95	61.25	55.71	55.06
E	64.64	71.43	65.00	72.32	58.33	66.34
F	65.18	68.16	65.18	63.40	56.79	63.74

Table 5. Classification rate percentages of NNs trained with Bayesian optimization using 120 samples recorded in OPEN_EYES

Subject	1st day	2nd day	3rd day	4th day	5th day	Ave.
A	95.83	48.33	45.83	41.67	75.00	61.33
B	66.67	57.50	60.83	33.33	43.33	52.33
C	60.00	40.00	49.17	76.67	38.33	52.83
D	52.50	79.17	37.50	38.34	35.00	48.50
E	49.17	33.34	45.84	19.17	31.67	35.84
F	51.67	62.50	55.84	48.34	45.83	52.84

Table 6. Classification rate percentages of SVMs trained using 120 samples recorded in OPEN_EYES

Subject	1st day	2nd day	3rd day	4th day	5th day	Ave.
A	63.04	56.61	62.68	66.31	65.83	62.89
B	68.75	73.57	66.90	63.75	77.02	70.00
C	65.00	58.57	67.20	60.24	69.40	64.08
D	69.52	49.88	55.06	52.86	60.00	57.46
E	62.62	67.50	63.39	54.94	72.20	64.13
F	54.64	56.67	45.24	43.21	42.62	48.48

The input feature vectors to the classifiers were extracted from the EEG signals obtained in the experiments as mentioned in Section 2. The EEG signals were recorded when the subjects were imagining one of the 4 motions of the mobile robot. That means the extracted feature vectors belongs to one of the classes representing mobile robot motions, such as move forward, backward, to left, and to right. The NNs and SVMs were trained to recognize the class of the input feature vectors. Nonlinear SVM transforms input feature vectors into a higher dimensional feature space so that a decision boundary can linearly separate the feature vectors into classes more easily. The transformation is called kernel trick. In this study, the nonlinear SVMs were constructed with RBF kernel function. The kernel trick, transforming the input feature vectors into a higher dimensional space, might have led to the results that the SVMs performed the better classification performance.

5. Conclusion

This paper presented the comparative experimental results of the SVMs and NNs that were trained to be able to work as an EEG-based BCI for mobile robot control. Consequently, in almost all cases, the SVMs with RBF kernel function have outperformed the NNs trained with hyperparameter optimization. The SVMs transformed the input feature vectors into a higher dimensional feature space using RBF kernel function in order to make the feature vectors be linearly separable as far as possible. The authors have assumed that the kernel trick, i.e. transforming feature vectors into a higher dimensional feature space, was the key factor for the results of this study. Therefore, from that point of view, the authors will design an EEG pattern classification method including feature extraction in order to achieve practical EEG-based BCI mobile robot control.

References

1. R. Singla et al., Influence of stimuli color on steady-state visual evoked potentials based BCI wheelchair control, *J. Biomedical Science and Engineering* **6**(11) (2013) 1050–1055.
2. R. Singla et al., Influence of stimuli color in SSVEP-based BCI wheelchair control using support vector machines, *J. Medical Engineering & Technology* **38**(3) (2014) 125–134.
3. J. Meng et al., Noninvasive Electroencephalogram Based Control of a Robotic Arm for Reach and Grasp Tasks, *Scientific Reports* **6**(38565) (2016).
4. L. Bi et al., EEG-Based Brain-Controlled Mobile Robots: A Survey, *IEEE Trans. On Human-Machine Systems* **43**(2) (2013) 161–176.
5. T. Hayakawa and J. Kobayashi, Open Eyes Influence on Electroencephalography Signals for Constructing Neural Network Classifiers as Mobile Robot Control Brain-Computer Interface, in *Proc. of Int. Conf. on Advanced Mechatronic Systems* (Xiamen, China, 2017), ThuM01-03.
6. T. Hayakawa and J. Kobayashi, Improving EEG-based BCI Neural Networks for Mobile Robot Control by Bayesian Optimization, *J. Robotics, Networking and Artificial Life* **5**(1) (2018) 41–44.
7. J. Snoek et al., Practical Bayesian Optimization of Machine Learning Algorithms, in *Proc. of Int. Conf. on Neural Information Processing Systems* (Lake Tahoe, Nevada, 2012), pp. 2951–2959.
8. Chainer: A Powerful, Flexible, and Intuitive Framework for Neural Networks, https://chainer.org/.
9. GPyOpt: A Bayesian Optimization framework in Python, http://github.com/SheffieldML/GPyOpt.
10. LIBSVM: A Library for Support Vector Machines, https://www.csie.ntu.edu.tw/~cjlin/libsvm/.

Position Tracking Error Constrained Super-Twisting Dynamic Surface Control with Disturbance Observer for Robot Manipulators

Seong Ik Han
Mechanical System Engineering, Dongguk University Gyeongju, 123 Dongdae-ro
Gyeongju, Gyeongsangbuk-do 38066, Korea Republic
E-mail: skhan@dongguk.ac.kr

Abstract

A tracking error constrained dynamic surface control (DSC) with a super-twisting algorithm (STA) and a nonlinear disturbance observer is proposed for robot manipulator systems, where the system dynamics are partially known. The stabilizing controls of the DSC were designed by combining the STA with the virtual tracking errors defined from the DSC design concept. A nonlinear disturbance observer was designed to estimate the unknown nonlinear function and external disturbance instead of using parameterization of the nonlinear function or adaptive law in the conventional STA and DSC schemes. Moreover, a simpler tracking error constraint method is also proposed. The proposed tracking error constrained STA-DSC scheme combined with a nonlinear disturbance observer has better tracking error performance and robustness to uncertainty of robot manipulator system than control systems with a conventional DSC and disturbance observer. The control scheme was evaluated through simulations with the articulated manipulator system.

Keywords: Dynamic surface control, super-twisting algorithm, nonlinear disturbance observer, robot manipulator.

1. Introduction

In recent years, backstepping control (BSC) has been developed to control manipulator systems with matched or unmatched uncertainties without neglecting or linearizing nonlinear terms by using recursive design procedures [1]. However, the repeated differentiation of the virtual controls appeared in the BSC design steps result in the “explosion of complexity”. In order to overcome this drawback, dynamic surface control (DSC) was proposed by introducing a first-order filter in each step of BSC scheme [2]. A conventional DSC is also designed using the ordinary Lyapunov stability theorem, so the convergence for such systems is at best exponential with infinite settling time. In this study, we considered a DSC system combined with STC [3] (SDSC) and propose a nonlinear disturbance observer (NDO). This approach achieves finite-time convergence of both estimation and tracking errors and improves upon the weakness of uncertainty problems with the conventional DSC system by exploiting the merits of both DSC and STA systems. Next, to avoid this complex variable transformation, a simple constraining control method is considered. Simulations for two-link manipulator system present to show the efficacy of the proposed control scheme.

2. Dynamics of Manipulator and Actuator

The manipulator dynamics are described as follows:

$$M(q)\ddot{q} + C(q,\dot{q})\dot{q} + G(q) + F_d = \tau , \qquad (1)$$

$$L\frac{di}{dt} + Ri + k_b\dot{q} = V , \qquad (2)$$

where $q, \dot{q}, \ddot{q} \in R^{n\times 1}$ are the joint position, velocity, and acceleration vectors, respectively; $M(q) \in R^{n\times n}$ denotes a positive definite symmetric moment of the inertia matrix; $C(q,\dot{q}) \in R^{n\times n}$ is the centripetal Coriolis matrix; $G(q) \in R^{n\times 1}$ is the gravity vector; $F_d \in R^{n\times 1}$ the disturbance torque vector including external disturbance and joint friction; $\tau \in R^{n\times 1} = nk_t i$ is the control torque vector obtained from the joint actuators; L_m and R_m are the inductance and resistance of the motor drive, respectively; k_b is the back emf constant; i is the motor current; and V is the voltage applied to the motor drive.

Property 1. The symmetric and positive definite inertia matrix $M(q)$ is bounded by $\|M(q)\| \le K_M$ for all q, where K_M is a diagonal positive constant matrix.

Property 2. $\dot{M}(q) - 2C(q,\dot{q})$ is a skew- symmetric matrix and $s^T[\dot{M}(q) - 2C(q,\dot{q})]s = 0$.

Property 3. $C(q,\dot{q})$ and $G(q)$ are bounded by some positive constants, K_C and K_G, such that $\|C(q,\dot{q})\| \le K_C \|\dot{q}\|$ and $\|G(q)\| \le K_G$.

The objectives of the controller design are:

(i) All signals of the closed-loop system converge to zero in finite-time.

(ii) The position tracking errors are constrained within the prescribed boundary without depending on a high control gain

3. Design of Nonlinear Disturbance Observer and Controller

3.1. *Transformation of the tracking error*

A smooth decreasing positive performance function $\mu_i(t)$ can be defined to satisfy the partial error constraints as follows:

$$\mu_i(t) = (\mu_{0i} - \mu_{\infty i})e^{-a_i t} + \mu_{\infty i}, \tag{3}$$

where μ_{0i}, $\mu_{\infty i} = \lim_{t\to\infty} \mu_i(t)$, and a_i are appropriately defined positive constants. The constant $\mu_{i\infty}$ confines the size of the tracking errors under a steady state. The decreasing rate a_i of $\mu_i(t)$ regulates the required speed of convergence of the tracking errors. A error transformation is defined as

$$T_{pi}(t) = \tan\left(\kappa_i \frac{e_i(t)}{\mu_i(t)}\right), \; i = 1,\ldots,n, \tag{4}$$

where $T_{pi}(t)$ is a smooth and strictly bounded function and $0 < \kappa_i < \pi/2$ is a constant gain.

3.2. *Design of nonlinear disturbance observer*

The dynamics of a nonlinear disturbance observer is proposed as follows:

$$\hat{\rho} = \psi + p(x), \; i = 1,\ldots,n, \tag{5}$$

$$\dot{\psi} = -\eta(x)\psi - \eta(x)[p(x) + f(x) + g(x)\tau - z], \tag{6}$$

where $p(x)$ are nonlinear functions to be designed and $\eta(x) = \partial p(x)/\partial x$ or $p(x)$ are chosen such that $\eta(x) = \partial p(x)/\partial x > \eta > 0$ for all $x \in R^n$. By using $\tilde{\rho} = \rho - \hat{\rho}$ and $\dot{\tilde{\rho}} = -\dot{\hat{\rho}}$, it follows that

$$\begin{aligned}\dot{\tilde{\rho}} &= -\dot{\hat{\rho}} = -\dot{\psi} - \frac{\partial p(x)}{\partial x}\dot{x} \\ &= \eta(x)\psi + \eta(x)[p(x) + f(x) + g(x_i)\tau - z] - \eta\dot{x} \\ &= -\eta(\tilde{\rho} + z),\end{aligned} \tag{7}$$

The result in (7) can remove the coupled residual estimation error term that appears in the derivative equation of the Lyapunov function candidate as shown later.

3.3 *Design of super-twisting dynamic surface controller*

The strict-feedback state space form of (1) and (2) is represented as

$$\begin{aligned}\dot{x}_1 &= x_2, \\ \dot{x}_2 &= f_{02}(x) + g_{02}x_3 + \rho_2, \\ \dot{x}_3 &= f_3(x) + g_3 u, \\ y &= x_1,\end{aligned} \tag{8}$$

where $x_1 = q$, $x_2 = \dot{q}$, $x_3 = i$, $u = V$, $g_3 = L_m^{-1}$, $f_{02}(x) = -M_0^{-1}G_0(q)$, $\rho_2 = M_0^{-1}[-\Delta M\dot{x}_2 - \Delta G(x_1) - F_d]$, $g_{02} = M_0^{-1}nk_t$, $f_3(x) = -L_m^{-1}(R_m x_3 + k_b x_2)$, and $u = V$. The command tracking error and new states are defined as

$$z_1 = x_1 - \varpi_1, \; z_2 = x_2 - \varpi_2, \; z_3 = x_3 - \varpi_3, \tag{9}$$

$$\zeta_{i,1} = k_{i,1}z_i + |z_i|^{1/2} sign(z_i), \tag{10}$$

$$\zeta_{i,2} = -k_{i,2}\int_0^t [k_{i,1}^2 z_i + \frac{3}{2}k_{i,1}|z_i|^{1/2} sign(z_i) + \frac{1}{2}sign(z_i)]d\tau, \quad i = 1,2,3, \tag{11}$$

where $\varpi_1 = y_d$, $k_{i,1} > 0$ and $k_{i,2} > 0$ are constants. The stabilizing controls and final controller are selected as

$$\alpha_1 = -c_{1,1}\zeta_{1,1} - c_{1,2}T_p\zeta_{1,1} + \dot{\varpi}_1 + \zeta_{1,2} \ , \tag{12}$$

$$\alpha_2 = g_{02}[-c_{2,1}\zeta_{2,1} - f_{02} - \hat{\rho}_2 - \frac{\varphi_1\phi_1}{\varphi_2\phi_2}(z_2 + y_2) + \dot{\varpi}_2 + \zeta_{2,2}], \tag{13}$$

$$u = g_{03}[-c_{3,1}\zeta_{3,1} - f_3 - \frac{\varphi_2\phi_2}{\varphi_3\phi_3}(z_2 + y_2) + \dot{\varpi}_3 + \zeta_{3,2}], \tag{14}$$

where $c_{i,j} > 0$ are constants, α_i are passed through first-order filters with a time constant κ_i as

$$\kappa_i\dot{\varpi}_i + \varpi_i = \alpha_{i-1},\ \varpi_i(0) = \alpha_{i-1}(0),\ i = 2,3\ , \tag{15}$$

$y_i = \varpi_i - \alpha_{i-1}$, and $\varphi_i = k_{i,1} + \frac{1}{2}|z_1|^{1/2}$.

4. Stability Analysis

We define the Lyapunov function candidate as

$$V = \sum_{i=1}^{3} V_i \ , \tag{16}$$

$$V_i = \frac{1}{2}\zeta_i^T P_i \zeta_i \ , \tag{17}$$

where $\zeta_i = [\zeta_{i,1}\ \zeta_{i,2}]^T$, $P_i = \begin{bmatrix} \beta_i + 4\varepsilon_i^2 & -2\varepsilon_i \\ -2\varepsilon_i & 1 \end{bmatrix}$, and the constants $\beta_i > 0$ and $\varepsilon_i > 0$. A Lyapunov description of finite-time is given as the following inequality:

$$\begin{aligned} \dot{V}(\zeta) &= \sum_{i=1}^{3}\dot{V}_i \\ &\le -\sum_{i=1}^{3}\varphi_i\zeta_i^T Q_i \zeta_i \\ &\le -\eta_1 V(\zeta) - \eta_2 V^{1/2}(\zeta)\ , \end{aligned} \tag{18}$$

where $\eta_1 > 0$ and $\eta_2 > 0$. $V(t)$ converges to an equilibrium point in finite-time T_f given by [4]

$$T_f \le \frac{2}{\eta_1}\ln\frac{\eta_1 V^{1/2}(\zeta(0)) + \eta_2}{\eta_2}\ . \tag{19}$$

Theorem 1. *Consider the closed-loop states of a strict feedback system (9) consisted by a plant (1), nonlinear estimate law, virtual stabilizing functions, and control law. The following conditions then holds: if the gains for guaranteeing the positive definiteness of Q_i satisfy*

$$\begin{aligned} &c_{1,1} > \frac{2\varepsilon_1^3}{\beta_{i,1}} + \frac{\beta_1}{8\varepsilon_1} + \varepsilon_1 - c_{1,2}T_p\ , \\ &k_{1,2} > 2\varepsilon_1(c_{1,1} + c_{1,2}T_p)\ , \end{aligned} \tag{20}$$

$$\begin{aligned} &c_{i,1} > \frac{2\varepsilon_i^3}{\beta_i} + \frac{\beta_i}{8\varepsilon_i} + \varepsilon_i,\ i = 2,3, \\ &k_{i,2} > 2\varepsilon_i c_{i,1},\ i = 2,3\ , \end{aligned} \tag{21}$$

then, $z_i = 0$ and $\zeta_i = 0$ are equilibrium points that are strongly and globally asymptotically stable, and the Lyapunov function candidate in (19) is a global and strong Lyapunov function. The convergence time is given by (19).

Proof. See [3]. □

5. Simulation Results

The manipulator parameters are presented in Table 1. The constraint functions were selected as follow: $\mu_1(t) = (0.5 - 0.008)e^{-5t} + 0.008\,(rad)$ and $\mu_2(t) = (0.5 - 0.008)e^{-5t} + 0.008\,(rad)$. The joint position commands are selected as $q_{d1} = 0.1\sin(0.8\pi t)$ (rad) and $q_{d2} = 0.15\sin(0.8\pi t)$ (rad) . Among the four links of the robot manipulator, only two links (upper arm = link1, forearm=link2) were selected for experimental verification. Hence, the dynamic parameters of the articulated manipulator are given as follows:

$$M(q) = \begin{bmatrix} M_{11} & M_{12} \\ M_{21} & M_{22} \end{bmatrix},$$

$$M_{11} = (m_1 + m_2)L_1^2 + m_2L_2^2 + 2m_2L_1L_2cos(q_2),$$

$$M_{12} = m_2L_2^2 + L_1L_2m_2cos(q_2),$$

$$M_{21} = m_2L_2^2 + L_1L_2m_2cos(q_2), M_{22} = m_2L_2^2,$$

$$C(q,\dot{q}) = \begin{bmatrix} -2m_2L_1L_2sin(q_2)\dot{q}_2 & -m_2L_1L_2sin(q_2)\dot{q}_2 \\ m_2L_1L_2sin(q_2)\dot{q}_1 & 0 \end{bmatrix},$$

$$G(q) = \begin{bmatrix} m_2L_2gcos(q_1 + q_2) + (m_1 + m_2)L_1gcos(q_1) \\ m_2L_2gcos(q_1 + q_2) \end{bmatrix}.$$

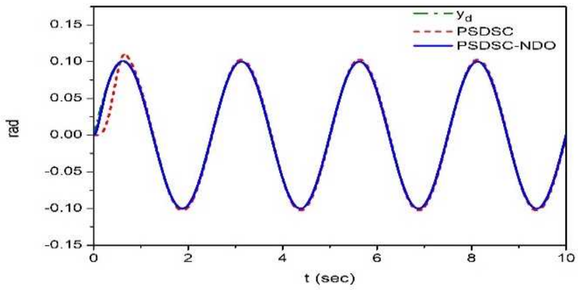

(a)

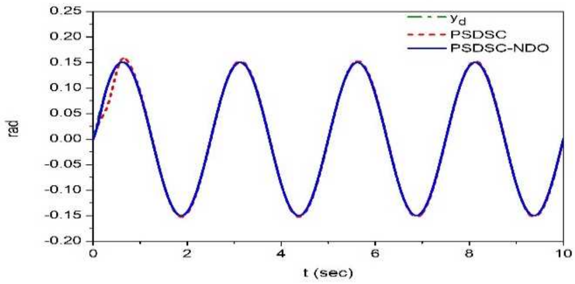

(b)

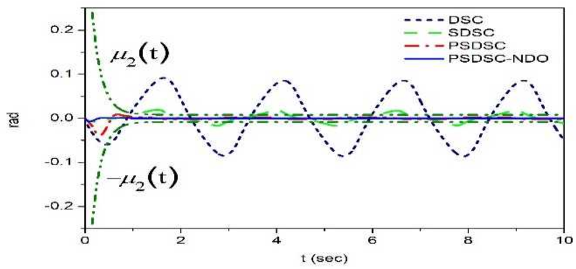

(c)

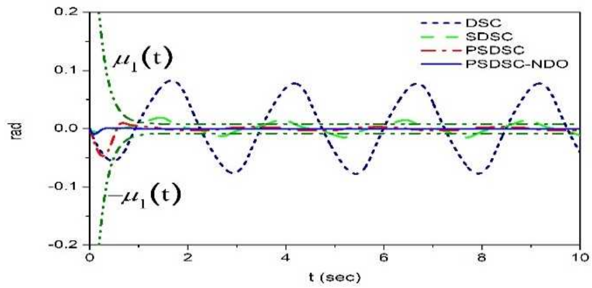

(d)

Fig. 1 Simulation results for two-link manipulator system. (a) Tracking output for link 1 of the PSDSC and PSDSC-NDOB systems. (b) Tracking output for link 2 of the PSDSC and PSDSC-NDOB systems. (c) Tracking errors for link1 of the DSC, SDSC, PSDSC, and PSDSC-NDO systems. (d) Tracking errors for link1 of the DSC, SDSC, PSDSC, and PSDSC-NDO systems.

Fig. 1 shows the joint tracking simulation results for two-link articulated manipulator. The SDSC system has more improved performance than the DSC system. The tracking errors of the PSDSC system and PDSC-NDO systems remain within the prescribed error boundaries, but the PSDSC-NDO system reveals more advanced performance due to compensating effect on the nonlinear disturbance.

Table 1. Manipulator parameters

Symbol	Parameter	Value
m_1, m_2	mass of link1 and 2	$12.1kg$, $3.59kg$
L_1, L_2	mass of link1 and 2	$0.3m$, $0.41m$
n_i	gear ratio of reduction gea r	65.5
R_{mi}	resistance of motor	0.8294 Ω
k_{ti}	torque constant	0.0182 *Nm/A*
k_{bi}	back emf constant	0.182 *V/rad/sec*

6. Conclusions

A hybrid DSC scheme was combined with the STA and the nonlinear disturbance observer. The tracking and virtual tracking errors in the recursive DSC design were taken as the error component of the error state surfaces of the STC. The virtual and final controllers were derived without introducing differentiation of the filtered output disturbance were estimated by the super-twisting nonlinear disturbance observers with tracking error constraint.

Acknowledgements

This work has supported by the National Research Foundation of Korea (NRF) grant funded by the Korea government (MSIT) (No. NRF-2018R1A2B6005128)

References

1. M. Kristic, I. Kanellakopoulos, P. V. Kokotovic, *Nonlinear and adaptive control design* (Wiley, NY, 1995).
2. D. Swaroop, J. K. Hedrick, P. P. Yip, and J. C. Gerdes, Dynamic surface control of a class of nonlinear systems, *IEEE Trans. Automatic Control*, **45**(10) (2000) 1893-1899.
3. J. A. Moreno, and M. Osorio, Strict Lyapunov functions for the super-twisting algorithm, *IEEE Trans. on. Automatic Control*, **57**(4) (2012) 1035-1039.
4. S. Yu, X. Yu, B. Shirinzadeh, and Z. Man, Continuous finite-time control for robotic manipulators with terminal sliding mode, *Automatica*, **41** (2005) 1957–1964.

Image Processing for Picking Task of Random Ordered PET Drinking Bottles

Chen Zhu
Graduate School of Information, Production and Systems, Waseda University, 2-7 Hibikino, Wakamatsu Kitakyushu 808-0135 Fukuoka, Japan

Takafumi Matsumaru
Graduate School of Information, Production and Systems, Waseda University, 2-7 Hibikino Wakamatsu Kitakyushu 808-0135 Fukuoka, Japan
E-mail: zhuchen@toki.waseda.jp, matsumaru@waseda.jp
www.waseda.jp

Abstract

In this research, six brands of soft drinks are decided to be picked up by a robot with a monocular RGB camera. The drinking bottles need to be located and classified with brands before being picked up. A Mask R-CNN is pretrained with COCO datasets to detect and generate the mask on the bottles in the image. The Inception v3 is selected for the brand classification task. Around 200 images are taken, then, the images are augmented to 1500 images per brand by using random cropping and perspective transform. The results show that the masked image can be labeled with its brand name with at least 85% accuracy in the experiment.

Keywords: Image Processing; Robotics Picking; Deep Learning; COCO Dataset

1. Introduction

Under the lower birth rate and aging society, the cost of human labor is becoming higher. In a warehouse, the picking task for goods sorting takes more than half of the total cost (1). During the festival and special events, the drinks are randomly put in a big box or a cooler box with water and ice. The existing picking robot can hardly process the overlapping of the objects without modeling or the same objects (2). In this paper, the image processing for the robot picking task is discussed.

1.1. *Related Works*

Random picking is a challenging problem in the robotics and computer vision fields. The aim of this task is to pick up objects which are manipulated under structured layout by using a robot arm's end-tip effector. Bin picking was studied when Amazon started the picking challenge. By using a 3D image sensor, the position and pose of the object to be picked up are calculated (3).

On the other hand, for the industrial random picking robots, FANUC, YASKAWA, etc. have developed the bin picking robot by using the structured light or binocular camera.

1.2. *Contributions*

In some special application such as bottles being put in the ice water, a normal 3D sensor cannot get the correct depth information. In this paper, a deep-learning-based image processing method is purposed to detect and segment the randomly ordered PET bottles by using a monocular RGB camera instead of a depth sensor.

Additionally, this research also discusses the brands' recognition under the overlapped conditions by using the Inception v3 without the knowledge on the target.

2. Methodology

In this research, random piled up drinking bottles of different sizes and brands are required to be picked up. The bottle is not limited to one type of bottle, so deep learning-based detection method are used to solve this problem. The whole process is divided into two stages: the training stage and the detection stage. The training stage is to train the network in order to get the corresponding kernel and bias value. The detection stage is to detect and generate a mask on each bottle and find out the brands of the bottle.

2.1. *Network Training Stage*

The network training is divided into five steps as shown in Fig. 1. First, the Mask R-CNN (Regional Convolutional Neural Network) (4) is pretrained by the Microsoft COCO (Common Object in Contest) dataset. The COCO dataset has a large number of images with labels and segmentation lines. To prevent overfitting, the Mask R-CNN is trained with all 80 classes of COCO dataset. Second, around 200 photos are taken or found for each brand of bottle. Next, the dataset of bottles is used for fine tune the Mask R-CNN. Then, all the images are augmented with random cutting and perspective transform to increase the dataset size to 1500 brands per brands. Finally, the augmented images are used for training for brand recognition.

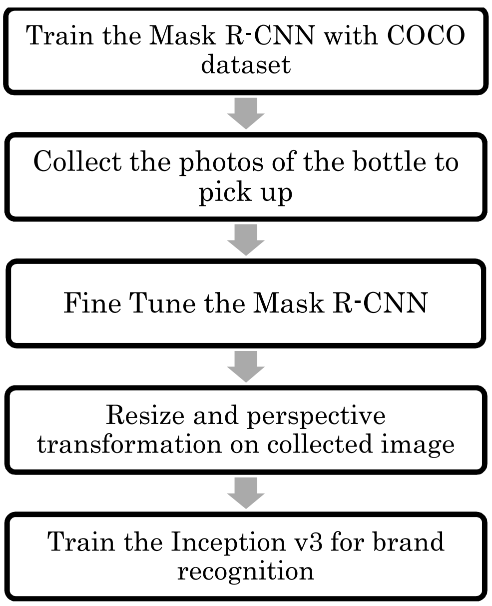

Fig. 1. The network training process

The training of Mask R-CNN takes 160 epochs in total, where 40 epochs for the classification head, and 120 epochs for the ResNet-101 backbone.

Around 80% of the images are randomly selected for the training, and the remaining 20% of images are used for validation. The training is stopped when the validation accuracy no longer rising along with the training accuracy.

2.2. *Detection Stage*

The detection stage contains four steps as shown in Fig. 2. First, the ROI (Region of Interest) box and the mask are needed to be generated by using Mask R-CNN. Next, the mask is bitwise-AND with the original image. Then, by using the ROI generated in the first step, a bottle is cut out from the image with a black background. Finally, for each image with only one bottle visible are sent to the Inception v3 network for brand recognition.

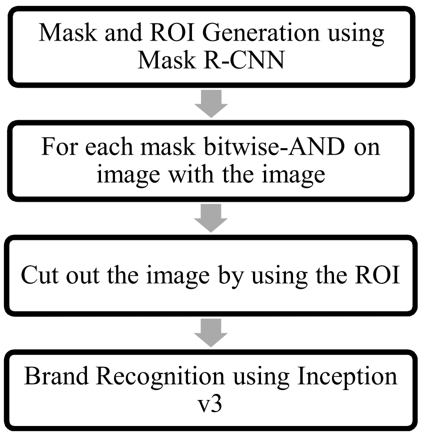

Fig. 2. Detection Process

The evaluation of the brand recognition is based on the comparison between the human and the network output, so that it can filter out the overlapped bottles that cannot be recognized by a human. Assume the number of objects detected from the image is N_d; the number of correct brands recalled by the Inception v3 is N_r; the number of which brands cannot be recognized by a human is $\overline{N_h}$ in which correctly recalled by Inception v3 is $\overline{N_e}$. Then the accuracy P of the brand recognition is calculated by the following formula.

$$P = \frac{N_r - \overline{N_e}}{N_d - \overline{N_h}} \times 100\% \tag{1}$$

3. Result

Based on the method mentioned in the previous section, the experiment is performed. To run the different network on the same machine, a library called "Protocol Buffer" is used as data exchange.

3.1. *Training of Mask R-CNN*

The bottles are the primary detection target in this research. However, the number of images that can be used to retrain the whole network is limited. The COCO dataset comes with 80 classes for object detection plus 1 class for background. So, all 81 classes are used for training the whole network at first. Then the bottles taken from the test subject are labeled with a class name and a mask as shown in Fig. 3.

Fig. 3. Image Segmentation for Training

The training rate in this step is set to 0.01 and only training the mask and classification parts in the network.

3.2. *Training for brand recognition*

The brand recognition is implemented by the Inception v3. Retraining the whole network will cause too much time and easy to get overfitted. So, the initial weight of Inception v3 is transferred from the object recognition network. In this research, six kinds of drinking in the Japan market including Oiocha, Coca-Cola, Calpis, Afternoon tea, Irohasu, and Nama cha are selected as test subject. For each brand, around 150-200 images are collected from the Internet or taken directly. Then, the images are processed randomly with cropping, perspective transform, rotation and zooming to increase the number of images up to 1500 for each brand as shown in Fig. 4.

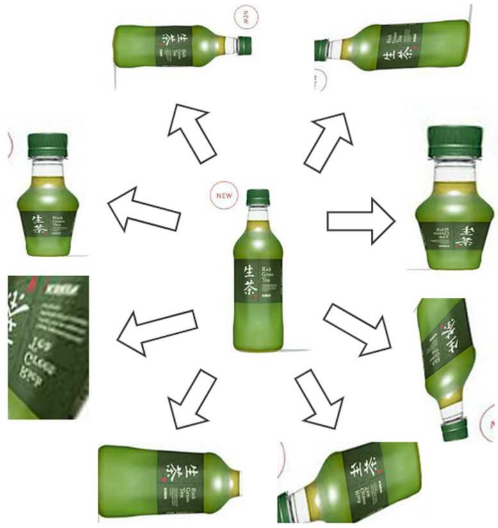

Fig. 4. Image Augmentation

The training of the Inception v3 stops, based on the accuracy that convergence to around 0.85 as shown in Fig. 5. The blue line shows the validation result of the 20% of the images which can be used to indicate the best fitting point.

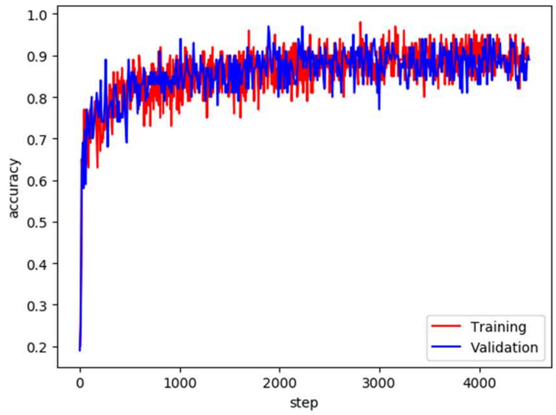

Fig. 5. Training accuracy and validation accuracy

Continuing the training steps will increase the training accuracy but not validation accuracy, which will lead to overfitting of the network. In this dataset, validation accuracy reaches the top when the training steps are 4000 steps.

3.3. *Evaluation of Mask and ROI Generation*

Fig. 6 shows the result of the mask and ROI generation. The evaluation is based on the real image taken from a normal monocular camera as shown in Fig. 6(a). By using the mask and ROI generated from the network shown in Fig. 6(b), the original image can be masked and cut off as shown in Fig. 6(c) and (d).

(a) Original Image

(b) Mask Generation

(c) Masked Image

(d) Image Cut out by ROI

Fig. 6. Mask and ROI cutting on the original image

As shown in the result, bottles with color can be correctly detected from the image. However, bottles with a transparent appearance have a lower detection rate.

3.4. *Evaluation of the brand recognition*

The brand recognition is based on the image cut off from the Fig 6(d). These images are resized to 299x299 and sent to Inception V3 for the brand recognition one by one. The output with the highest score is selected as the result. Here, we select one more group of test data besides the images in "Fig. 6. Mask and ROI cutting on the original image", and the result of the brand recognition is shown in Table 1.

As the result shows, although the network gives out all the correct result, the score of output is not very satisfying in some cases, because the score under 0.6 will be seen as unacceptable result.

Table 1 Labeled result and output score

Human Labeled	**Top Result**	**Score**
Oiocha	Oiocha	0.66
Calpis	Calpis	0.94
Namacha	Namacha	0.93
Namacha	Namacha	0.56
Coca cola	Coca Cola	0.87
Irohasu	Irohasu	0.98
Afternoon Tea	Coca Cola	0.62
Namacha	Namacha	0.99
Calpis	Calpis	0.92
Namacha	Namacha	0.97
Coca Cola	Coca Cola	0.96
Coca Cola	Coca Cola	0.29
Irohasu	Irohasu	0.91
Number of correct answers		**10**

4. Conclusion & Discussion

The combination of the Mask R-CNN and Inception V3 can detect and recognize the brand of the bottles with overlapping in at least 80% accuracy. Based on the mask center point and the area of the mask, the robot can be guide for the picking task.

Acknowledgements

This research is supported by Japan Society for The Promotion of Science (KAKENHI-PROJECT-17K06277), to which we would like to express our sincere gratitude.

References

1. JJ. Bartholdi and ST. Hackman, *Warehouse & Distribution Science* (The ISyE department Georgia Institute of Technology, Atlanta, GA, 2014).
2. K. Kim, J. Kim, S. Kang, J. Kim and J. Lee, Vision-based bin picking system for industrial robotics applications, *9th International Conference on Ubiquitous Robots and Ambient Intelligence*. (Daejeon, South Korea, 2012).
3. N. Correll and K.E. Bekris et al, Analysis and Observations From the First Amazon Picking Challenge, *IEEE Transactions on Automation Science and Engineering*. **15**(1) (2016) 172-188.
4. K. He, G. Gkioxari, P. Dollár and R. Girshick, Mask R-CNN, *2017 IEEE International Conference on Computer Vision (ICCV)*, (Venice, Italy).
5. C. Szegedy, V. Vanhoucke, S. Ioffe, J. Shlens and Z. Wojna, Rethinking the Inception Architecture for Computer Vision, *2016 IEEE Conference on Computer Vision and Pattern Recognition (CVPR),* (Las Vegas, NV, USA, 2016)

The Use of Importance Ranks to Derive Suitable Timing of Visual Sensing in Manipulation Task Containing Error Recovery

Akira Nakamura[1], **Kazuyuki Nagata**[1], **Kensuke Harada**[2], **Yukiyasu Domae**[1]

[1]*Intelligent Systems Research Institute*
National Institute of Advanced Industrial Science and Technology (AIST)
Central 2, 1-1-1 Umezono, Tsukuba, Ibaraki, 305-8568 Japan

[2]*Robotic Manipulation Research Group, Systems Innovation Department*
Graduate School of Engineering Science, Osaka University
1-3 Machikaneyama, Toyonaka 560-8531, Japan

E-mail: a-nakamura@aist.go.jp, k-nagata@aist.go.jp,
harada@sys.es.osaka-u.ac.jp, domae.yukiyasu@aist.go.jp
www.aist.go.jp

Abstract

In general, a manipulation task can be composed of many skill primitives. Therefore, it is desirable to perform plural visual sensing in most skill primitives; however, performing sensing all the time is difficult. In this paper, we propose the addition of importance ranks to the attribute of skill primitives to derive a suitable timing for performing sensing. Furthermore, we show that the skill primitives distinguished by their high importance ranks considerably correlates with error recovery.

Keywords: manipulation skill, task stratification, error recovery, error classification, physical distribution

1. Introduction

In recent years, studies on robotic manipulation for performing required tasks have been conducted in various fields. The use of robotic manipulation to perform plant-maintenance tasks and produce industrial products (Fig. 1) has been researched upon considerably.[1-3] These manipulation tasks tend to be complex, necessitating the formulation of composition rules for the entire work process.

By analyzing the assembly and disassembly sequences performed by humans, those tasks were determined to be composed of several significant motion primitives, each of which is called a “skill.” Furthermore, most maintenance tasks were shown to be composed of a number of skills.[1-3]

Ideally, a robotic task must be successfully completed as planned. However, in actual tasks of complicated plant maintenance, the execution of a task may terminate before completion. Therefore, as error recovery is an important research theme for robots that must perform actual tasks, various techniques have been reported.[4-7] However, most of the reports on error recovery are related to orbit adjustment and only few studies have reported on the application of complicated error recovery in maintenance tasks.

We have researched error recovery technique in robotic tasks so that robots can be used for such complicated tasks.[8, 9] In our method, error recovery through a forward correction process is used by slightly correcting the preplanned task. Also, error recovery

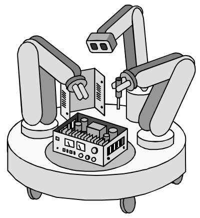

Fig. 1 Maintenance robot

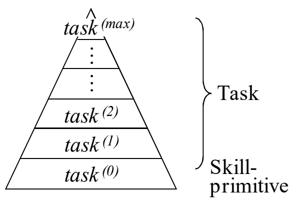

Fig. 2 Manipulation hierarchy

through a backward correction process is used for significantly correcting the preplanned task.

A manipulation task consists of several skill primitives, most of which require the use of visual sensing. However, performing sensing all the time is difficult because of some restrictions. In this paper, we propose to distinguish skill primitives according to their importance ranks to select the primitives with suitable timing of visual sensing. Furthermore, we show that the skill primitive distinguished according to a high rank is deeply related to the skill primitive in which error recovery is considered in advance. In addition, visual sensing is assumed to be performed precisely to stop movement before and after execution of skill primitive.

The next section explains manipulation skills and the stratification of manipulation tasks. The procedure of marking manipulation skill according to the importance ranks is proposed in Section 3, and a concept of error recovery and a method of error classification are described in Section 4. Section 5 presents the effectiveness of applying importance ranks to skill primitives through examples of repacking tasks.

2. Task Stratification

Let us first explain our concept of skills and stratification of tasks; the details can be found in Ref. 1.

2.1. *Concept of skills*

We analyzed human motions in tasks, such as disassembly and reassembly, and found that the movements consisted of several significant motion primitives. We call such motion primitives “skills”.[1] We considered three fundamental skills, namely move-to-touch, rotate-to-level, and rotate-to-insert, all of which play an important part in the tasks. A specific task is composed of sequences of skill primitives. The skill sequences can be decided through several methods. In our previous study, we presented a method that uses variations of the number of contact points in the skill primitives.[2] Moreover, many skills can be defined based on modified versions of these three fundamental skills.

2.2. *Stratification of tasks*

Figure 2 shows a hierarchy of manipulation tasks.[8] If we ignore the servo layer, the *skill* layer comprising elements, such as the three skills mentioned earlier, is located in the lowest layer called the $task^{(0)}$ layer. Further, the $task^{(1)}$ layer is located one tier above the $task^{(0)}$ layer. Similarly, $task^{(i+1)}$ is composed of sequences of $task^{(i)}$ elements. The top layer, in which the error recovery loop is closed, is called $task^{(max)}$.

3. Addition of Importance Ranks in Skill Primitives to Derive Suitable Timing for Visual Sensing

Ideally, visual sensing should be performed twice in each skill primitive to derive the exact posture of the objects before execution and confirm the last state of objects after execution. However, in actuality, it is difficult to perform sensing at all sensing points because of the restrictions of time and hardware.

We researched the suitable timing of visual sensing in skill sequences with error recovery in Ref. 10. It is efficient that a visual sensing is performed by considering the difficulty in accomplishing a skill primitive, as shown in Case 4 of Section 4 of Ref. 10. The degree of necessity of a visual sensing is derived based on the consideration of the following idea in this paper. An importance rank derived from the degree of the necessity of sensing was added to the attribute of each skill primitive. Moreover, the priority of performing visual sensing in each skill primitive can be derived by deciding the whole value of the importance rank in the total task. To decide the value of an importance rank, an operator’s teaching is allowed, although it is desirable to decide the value automatically.

Let us consider, for example, importance ranks with a transfer task (Fig. 3) and grasping and gripper-open tasks (Fig. 4). In the transfer task, a skill primitive in which strict visual sensing is needed is designated as first priority and a skill primitive with the task of grasping one or more objects has second priority (Table 1). In the grasp and gripper-open skills, the skill primitive in which the contact state, with the grasped object, changes has the top priority (Table 2). The timing of efficient visual sensing in a total task can be

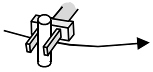

Fig. 3 Transfer task

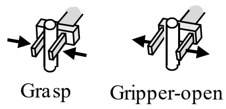

Fig. 4 Grasping and Gripper-open task

Table 1 Importance rank of transfer skill

Importance rank	Conditions
$H^T(1)$	The target position and orientation are demanded strictly.
$H^T(2)$	The hand is grasping one or more objects.
L^T ($= H^T(3)$)	Other than the above.

$H^T(1) > H^T(2) > L^T (= H^T(3))$

Table 2 Importance rank of grasp and gripper-open skills

Importance rank	Conditions
$H^G(1)$	The contact state with the grasped object changes.
L^G ($= H^G(2)$)	Other than the above.

$H^G(1) > L^G (= H^G(2))$

derived by considering an importance rank in each skill primitive according to Tables 1 and 2.

4. Error Recovery Through Classification

The real performance may differ from the ideal performance. In actual manipulation, errors often occur from various causes. This section describes the proposed concept of error classification and process flow, with error recovery in the task hierarchy (for more details, please refer to Ref. 8).

4.1. *Classification of errors*

The causes of manipulation failures can be attributable to several kinds of errors. We grouped the error states into several classes, namely execution, planning, modeling, and sensing, according to the possible causes.[8]

Merely remedying the causes of these errors does not always solve the problem. It may be necessary to return to a previous step when the working environment greatly changes because of the error.

4.2. *Error recovery based on classification*

A generalized process flow of stratified tasks that considers error recovery was proposed in Ref. 8. Figure 5 illustrates the central portion of Figure 10 in Ref. 8. This process is performed based on error recovery through *a backward correction process*. At the Confirmation step in each skill primitive $task^{(0)}_{(i0)}$, the result is judged as correct or incorrect by an automatic process or a human operator. Error recovery is performed using the following error classifications.

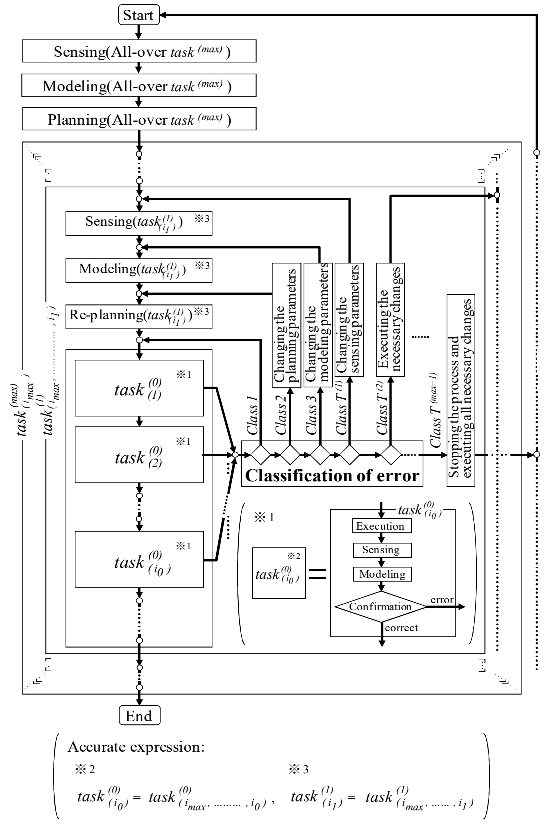

Fig. 5 Process flow with error recovery

Class 1: The error is judged to be an execution error, and $task^{(1)}_{(i1)}$ is executed again without correcting the parameters.

Class 2: The error is judged to be a planning error, and $task^{(1)}_{(i1)}$ is executed again with different planning parameters.

Class 3: The error is judged to be a modeling error, and $task^{(1)}_{(i1)}$ is executed again with different modeling parameters.

Class $T^{(1)}$: The error is judged to be a sensing error, and $task^{(1)}_{(i1)}$ is executed again with different sensing parameters.

Class $T^{(2)}$: $task^{(2)}(i_2)$ is executed again after the execution of the necessary changes and returns to the initial position one tier above layer $task^{(1)}_{(i1)}$.

:

:

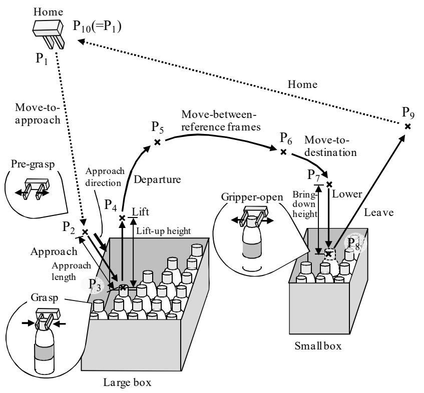

Fig. 6 Picking and placing task using a gripper

Class $T^{(max)}$: $task^{(max)}_{(imax)}$ is executed again after the execution of the necessary changes and returns to the initial position at (max – 1) tier above layer $task^{(1)}_{(i1)}$.

Class $T^{(max+1)}$: When it is judged that too many changes will be required, the process being executed is aborted.

5. Importance Ranks in Skill Primitives with Illustration of Repacking Tasks

Let us consider robots playing an active role in physical distribution. Then, consider tasks involved in repacking objects from a large box into a small box at a distribution center and the processes of error recovery for the robot tasks. Here, a typical task of picking up an indicated object by using the parallel jaw gripper on the robot[11] is selected, and an importance rank is considered for each skill primitive according to Section 3.

This section describes the main errors in the repacking tasks. In addition, we explain the process of recovery with respect to each error. Moreover, we consider the relation between typical errors of the task and skill primitives with high importance degrees.

A. Sequence of repacking tasks

Figure 6 shows the processes of picking up and placing objects such as PET bottles by using a manipulator with a gripper. The flow of the skill sequence if there is no error is shown in Fig. 7. These primitive motions are as follows.

($Skill_1$) Move-to-approach: Moving to the starting point of the approach motion.

($Skill_2$) Pre-grasp: Opening to grasp the object.

($Skill_3$) Approach: Moving to the grasping point at low speed.

($Skill_4$) Grasp: Grasping the target object.

($Skill_5$) Lift-up: Lifting the grasped object.

($Skill_6$) Departure: Moving to a specific point in a reference frame of a box from which the object is taken.

($Skill_7$) Move-between-reference-frames: Moving to a specific point in a reference frame of a box, in which the object must be placed.

($Skill_8$) Move-to-destination: Moving to the destination point.

($Skill_9$) Lower: Bringing down the grasped object.

($Skill_{10}$) Hand-open: Opening to place the object.

($Skill_{11}$) Leave: Moving to the safe area.

($Skill_{12}$) Home: Returning to the starting point for the next approach motion.

B. Importance ranks of skills in repacking tasks

Here, we consider the importance ranks of skills in the repacking task. An importance rank of each skill primitive is derived (Section 3) as follows:

$Skill_1$: L^T, $Skill_2$: L^G, $Skill_3$: $H^T(1)$,
$Skill_4$: $H^G(1)$, $Skill_5$: $H^T(2)$, $Skill_6$: $H^T(2)$,
$Skill_7$: $H^T(2)$, $Skill_8$: $H^T(2)$, $Skill_9$: $H^T(1)$,
$Skill_{10}$: $H^G(1)$, $Skill_{11}$: L^T, $Skill_{12}$: L^T

Let us suppose that the following relation exists among the importance ranks.

$$H^T(1) > H^G(1) > H^T(2) > L\ (= L^T = L^G) \qquad (1)$$

These skill primitives, in turn, can be arranged as follows based on the importance ranks with inequality (1).

First priority: $Skill_3$, $Skill_9$
Second priority: $Skill_4$, $Skill_{10}$
Third priority: $Skill_5$, $Skill_6$, $Skill_7$, $Skill_8$
Fourth priority: $Skill_1$, $Skill_2$, $Skill_{11}$, $Skill_{12}$

C. Candidate errors in repacking tasks

Next, we will consider the main types of errors in the tasks.

(1) Errors when grasping and lifting

(1. a) error of height; the gripper does not reach a PET bottle in $Skill_3$ (Fig. 8 (a))

(1. b) error of parallel movement to the bottom of the box; the open gripper is not positioned around the cap of a PET bottle in $Skill_3$ (Fig. 8 (b))

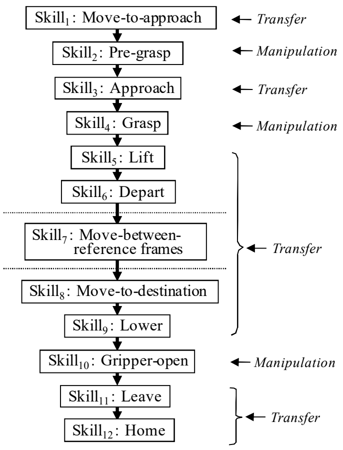

Fig. 7 Task sequence of picking and placing a bottle

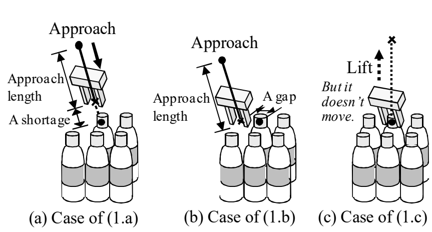

Fig. 8 Errors when grasping and lifting

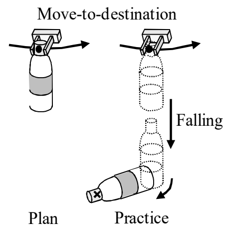

Fig. 9 Errors when carrying

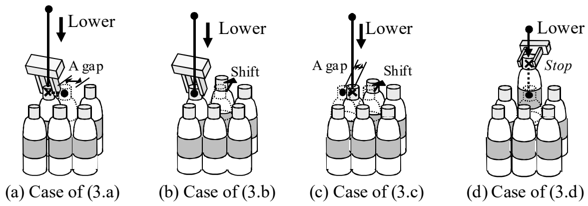

Fig. 10 Errors when packing

(1. c) error in which a PET bottle cannot be extracted owing to tight packing in $Skill_5$ (Fig. 8 (c))

(2) Errors when carrying an object

(2. a) error in which a PET bottle is dropped in $Skill_i$ (i = 6, 7, 8) (Fig. 9)

(3) Errors when packing

(3. a) error of parallel movement to the bottom of the box; a gap exists between the target position in $Skill_9$. No movement of another bottle is performed (Fig. 10 (a)).

(3. b) error in which the grasped PET bottle pushes the surrounding PET bottles in the box in $Skill_9$ (Fig. 10 (b)).

(3. c) error in which (3. a) and (3. b) occur simultaneously (Fig. 10 (c)). Gaps occur both between the positions of the grasped bottle and surrounding bottles.

(3. d) error in which $Skill_9$ is stopped before completion (Fig. 10 (d)) because the available space is too small.

D. Error-recovery processes

This section presents the explanation of the recovery process from each error. The following numbers and letters in brackets coincide with those describing the candidate errors in the previous section. The corrections were performed based on definite or indefinite causes derived from the error classification, and the process restarts from the corresponding step.

(1) Cases (1. a), (1. b), and (3. a)

Class 1: Execution is simply repeated.

Class 2: The process is re-executed from the planning step after the planning parameters are modified from the gap.

Class 3: The process is restarted from the modeling step after modification of the geometric models of the bottles.

Class $T^{(1)}$: The process is re-executed from the sensing step after modification of the coordinate system.

(2) Cases (1. c) and (3. d)

Class 1: Execution is simply repeated.

Class 2: The process is re-executed from the planning step after the modification of the planning techniques such as the motion with slightly shaking in lifting or lowering.

Class 3: The process is restarted from the modeling step after modification of the geometric models of the bottles or box.

Class $T^{(1)}$: (The same as (1))

(3) Case (2. a)

In most cases, the task of picking up a bottle in the box is changed to the task of lifting the bottle that has dropped to the bottom of the path; Class $T^{(2)}$ is chosen. The skill sequence of this task is executed from the beginning.

(4) Cases (3. b) and (3. c)

The original task is completed, and the process returns to the start of the flow. Next, the task to move the bottle to the correct position is executed. When the movement of many bottles is demanded, it is desirable to consider whether or not the paths converge efficiently.

E. Sensing time in repacking tasks

We considered typical errors in *C* and recovery processes of errors in *D*. Furthermore, we introduced the importance ranks of skill primitives in *B* so that $Skill_3$ (Approach skill) and $Skill_9$ (Lower skill) became high priority tasks. Then, these are included in skill primitives treated in *C* and *D*. That is, $Skill_3$ is relevant to (1. a) and (1. b), and $Skill_9$ is relevant to (3. a), (3. b), (3. c), and (3. d). Thus, the skill primitive in which error recovery is almost considered has a deep relation with the skill primitive in which visual sensing is needed. Moreover, skill primitives that are important alongside the above-mentioned skills are grasp and gripper-open skills, i.e., $Skill_4$ and $Skill_{10}$, respectively, and transfer skills: $Skill_5$, $Skill_6$, $Skill_7$ and $Skill_8$. Especially, $Skill_5$ and $Skill_7$ are skill primitives with high importance ranks, as in (1) and (2) in *C*, respectively.

When considering error recovery processes in the task composed of several skill primitives, the total number of skill primitives in which our error-recovery procedure[8, 9] can be applied increases considerably. It is difficult to consider all the recovery processes as great effort is necessary for planning them. When using the importance ranks proposed in Section 3, the selection of skill primitives, for which considering an error-recovery procedure is suitable, becomes relatively easy.

6. Conclusion

In general, a manipulation task can be composed of many skill primitives. It is desirable to perform plural visual sensing in most skill primitives as geometric modeling and task planning are performed before execution, and task achievement is confirmed after execution. However, the performance of sensing at all sensing points is difficult because of the restrictions of time and hardware. In this paper, we proposed the addition of importance ranks to the attribute of skill primitives to derive suitable timing to perform visual sensing. The use of the proposed method eases the selection of skill primitives in which visual sensing should be performed. Furthermore, we showed that skill primitives distinguished according to their high importance ranks considerably correlate with those in which error recovery is considered in advance. This characteristic can be used for selecting skill primitives in which error recovery is planned in advance.

In the future, we will apply our proposed procedure to sensing, modeling, planning, and execution tasks and attempt to apply our error-recovery method to actual maintenance robots.

References

1. T. Hasegawa, T. Suehiro and K. Takase, A model-based manipulation system with skill-based execution, *IEEE Trans. Robot. Autom.*, 8(5) (1992) 535-544.
2. A. Nakamura, T. Ogasawara, T. Suehiro and H. Tsukune, Skill-based backprojection for fine motion planning, in *Proc. IEEE/RSJ Int. Conf. on Intell. Robots Syst.*, (Osaka, Japan, 1996), 2, 526-533.
3. A. Nakamura, T. Ogasawara, K. Kitagaki and T. Suehiro, Using robust and simplified geometric models in skillbased manipulation, in *Proc. IEEE/RSJ Int. Conf. on Intell. Robots Syst.*, (Hawaii, USA, 2001), 1, 138-145.
4. B. R. Donald, Planning multi-step error detection and recovery strategies, Int. *J. Robot. Res*., 9(1) (1990) 3-60.
5. C. M. Baydar and K. Saitou, Off-Line error prediction, diagnosis and error recovery using virtual assembly systems, in *Proc. IEEE Int. Conf. Robot. Autom*., (Seoul, Korea, 2001), 818-823.
6. M. Scheutz and J. Kramer, Reflection and reasoning mechanisms for failure detection and recovery in a distributed robotic architecture for complex robots, in *Proc. IEEE Int. Conf. Robot. Autom.*, (Roma, Italy, 2007), 3699-3704.
7. P. Pastor, M. Kalakrishnan, S. Chitta, E. Theodorou and S. Schaal, Skill learning and task outcome prediction for manipulation, in *Proc. IEEE Int. Conf. Robot. Autom.*, (Shanghai, China, 2011), 3828-3834.
8. A. Nakamura and T. Kotoku, Systematization of error recovery in skill-based manipulation, *Artificial Life and Robotics*, Springer, 14(2) (2009) 203-208.
9. A. Nakamura, K. Nagata, K. Harada, N. Yamanobe, T. Tsuji, T. Foissotte and Y. Kawai, Error recovery using task stratification and error classification for manipulation robots in various fields, in *Proc IEEE/RSJ Int. Conf. on Intell. Robots Syst*., (Tokyo, Japan, 2013), 3535-3542.
10. A. Nakamura, K. Nagata, K. Harada and N. Yamanobe, The Suitable Timing of Visual Sensing in Error Recovery Using Task Stratification and Error Classification, *J. Robotics, Networking and Artificial Life,* 4(2), (2017) 134-137.
11. A. Nakamura, K. Nagata, K. Harada and N. Yamanobe, Error recovery using task stratification and error classification for manipulation robots in physical distribution, *Trans. Control and Mechanical Syst*., 3 (2014) 122-131.

Electronic Measurement and Gamification of Balance Tests

Yan−Xin Liu, Massimiliano Leggieri, Henrik Hautop Lund
Center for Playware, Technical University of Denmark, Building 326,
2800 Kgs. Lyngby, Denmark
E-mail: s161642@student.dtu.dk, maxleggieri@gmail.com, hhl@playware.dtu.dk
www.dtu.dk

Abstract

We gamified three common balance tests for fall risk diagnosis, Timed Up & Go (TUG), Chair Stand (CS), and Four Square Step Test (FSST), by using the Moto Tiles. The embedded pressure sensor of the Moto Tile was used to detect the movement of subjects and to time the tests. The proposed Moto measurement was compared with traditional stopwatch measurement. A total of 51 samples were analyzed. The intraclass correlation coefficients of the TUG and CS tests were very high (0.98 and 0.94). The FSST was analyzed by Pearson's correlation coefficient and the result also indicated strong correlation (0.79). Based on the results, we concluded that the proposed Moto tests are as reliable as traditional tests.

Keywords: Playware, gamification, balance test, fall risk.

1. Introduction

Fall is one of the most common threaten of injures of the elderly. About 30% elderly aged over 65 fall at least once a year.[1, 2] Serious falls can even result in disability or death.[3, 4] The causes of falls are often associated with impaired balance ability.[5] Hence, the assessment of balance is a critical part of fall prevention.

There are many broadly accepted standardized balance tests which have been proved to be accurate predictions of fall risks. These balance tests usually require nurse practitioners or physiotherapists to instruct subjects to accomplish a physical movement task in a specific test environment. Such test environment is normally stressful and boring, which prevents the best performance of subjects and may also make high frequency regular test (e.g., daily) impractical.

In order to let subjects fully engage in balance tests and reduce the workload of testers, we applied the Moto Tiles[6] to set the test sites and time the test. The Moto Tiles is a modular distributed system, which consists of ten tiles and a tablet. The tiles are controlled by the tablet wirelessly. Typical usage of the Moto Tiles is to place the tiles on ground and step on the tiles to play games. In the past years, the Moto Tiles has been proved to be an effective tool for physical and cognitive training.[7-10] The Moto Tile trainings produced significant improvement with less training times than traditional training.[9, 11] The amazing effects were resulted from the essence of play, which allows subjects to forget that they are training and to be able to devote themselves into the play.

We selected three typical balance tests and gamified them by the Moto Tiles. They are Timed Up & Go (TUG)[12], Chair Stand (CS)[13], and Four Square Step Test (FSST)[14]. A total of 51 older subjects took the three tests and their times were measured by both stopwatch and the Moto Tiles. The two time measurements were compared to examine the validity and reliability of the Moto tests.

2. The Design of the Moto Balance Test

There are numerous balance tests developed over the years. We selected balance testes for the gamification based on the following criterion:

- The critical steps of the test can be measured by pressure sensors (e.g., sit down to a chair or step to a particular position).

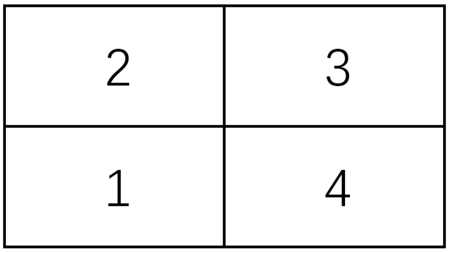

Fig. 1. Schematic diagram of the FSST test.

- The test is relatively simple and can be done within minutes
- The validity and reliability of the test are widely accepted.

Then the TUG, CS, and FSST tests were selected. The TUG test measures the time that a subject takes to rise from a chair, walk three meters, turn around, walk back to the chair, and sit down. Typical cut point of the TUG test is 14 seconds[12]. The TUG test has been proved to have a high inter-rater reliability (intraclass correlation coefficient [ICC] = 0.99)[15], and significant association with falls.[16] The CS test measures the time that a subject takes to stand up from a chair and sit down five times. The cut point of the CS test for fall risk is 15 seconds[17]. The CS test has a high correlation with the TUG test(r=0.64, p<0.001) and a strong reliability (ICC=0.95).[18] In the FSST test, the floor is divided into four squares as Fig. 1 shows. At the start of the test, subjects stand with both beet on the Square 1 and face to Square 2. Then, subjects are required to step as fast as possible into each square with both feet in the following sequence: Square 2, 3, 4, 1, 4, 3, 2, 1 (clockwise and counterclockwise). The cut point of the FSST test for fall risk is 15 seconds[14]. Goh et al.[19] showed that the FSST test has a high correlation with TUG scores (r = 0.59; P = 0.02), and a high intrarater reliability (ICC = 0.83).

Fig. 2. The Moto Tile for the TUG and CS test.

Traditionally, the time of the above tests are measured by stopwatch by an operator manually pressing start and stop on the stopwatch. By contrast, the Moto balance tests use the Moto Tiles to automatically measure the timing of subjects' physical movement. For the TUG and CS tests, a Moto Tile is placed on the chair to detect the rise and sit down movement of the subject (see Fig. 2). For the FSST test, four Moto Tiles are place on the floor to form the four squares (see Fig. 3). One tile is lit in green to indicate next target step, while other tiles are lit in blue. The detail of the time measurements can be found in Table 1.

Table 1. Comparison between stopwatch measurement and the Moto measurement.

Test name	Ordinary test	Moto Test
TUG	Start: when the instructor says go. End: when the subject sit down to the chair	Start: when the Moto tile on the chair is released. End: when the Moto tile on the chair is pressed.
CS	Start: when the instructor says go. End: when the subject sit down to the chair 5th time	Start: when the Moto tile on the chair is released. End: when the Moto tile on the chair is pressed 5th times.
FSST	Start: when the first foot reach the Square 2. End: when both feet touch the Square 1.	Start: when the Moto tile No. 2 is pressed. End: when the Moto tile No. 1 is pressed.

3. Validity and Reliability of the Moto Physical Test

In order to examine the validity and reliability of the proposed Moto balance tests, we presented the tests in cooperation with a number of elderly care institutes around Copenhagen area. Totally 51 older adults (average age 80.1 years) participated the tests. Two of them took only TUG test due to their impaired mobility and endurance.

Since the proposed Moto TUG and CS tests do not change any test standard, the subjects took only the TUG and CS test once but they were timed by both stopwatch and the Moto Tiles, and therefore it was the reliability of the Moto measurements that were analyzed. However,

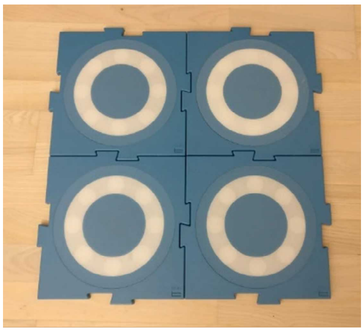

Fig. 3. The Moto Tiles for the FSST test.

the proposed Moto FSST test is not exactly the same as ordinary FSST test, which allows participants to step on larger squares than the Moto Tiles. Therefore, subjects were required to take an ordinary FSST and a Moto FSST separately. The sequence of the two FSST tests were determined by coin flipping in order to compensate the test-retest improvement. Due to the small difference of the two FSST tests, they were regarded as two different tests and it was the validity of the Moto FSST in association with the traditional FSST that were analyzed

Fig. 4 shows the relationship between the stopwatch measurement and the Moto measurement of the three tests. The reliability of the TUG and CS tests were examined by ICC, and the validity of the Moto FSST was examined by Pearson's Correlation Coefficient. The differences between stopwatch and the Moto measurement are evaluated by Wilcoxon Signed-Rank Test.

For the TUG test, there was no significant difference between stopwatch and the Moto measurement ($p = 0.84$). A consistent relationship between the two times can be observed (ICC = 0.98, 95% CI = [0.97, 0.99]).

For the CS test, the Moto measurement was significantly faster than stopwatch measurement ($p = 0.01$). This is because a few seniors with poor limb strength had unsuccessful risings, which were not counted by instructor, but triggered the Moto tile. However, the correlation between the two measurements were also very strong (ICC = 0.94, 95% CI = [0.89, 0.96]).

For the FSST test, the difference between the traditional and the Moto tests was marginally insignificant ($p = 0.06$). The mean value of the Moto time was faster than that of the stopwatch time, which meet the fact that the Moto time is one step less than the stopwatch time (see Table 1). The correlation between the two measurements were also strong ($r = 0.79$).

4. Discussion & Conclusion

The presented results indicate that the proposed Moto balance tests are very reliable and can be a good replacement of traditional test method. The Moto balance tests allow seniors to take the physical test along with

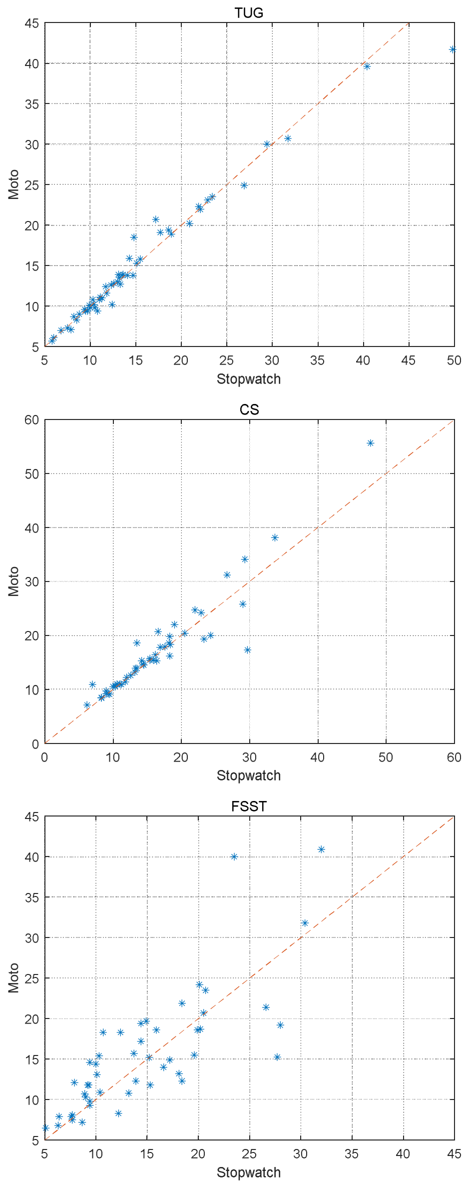

Fig. 4. Relationship between the stopwatch and the Moto measurement. Dotted line represents unity. (a) TUG (b) CS (c) FSST.

regular Moto playful training. The digital solution can also record and track the test performance automatically and thus can easily present the improvement in the tests to users, which would motivate users to engage more in the training.

Further possibility of the Moto balance tests can be the development of more standardized test (e.g., 30 Second Chair Stand, Tandem walk, etc). All the Moto balance tests can be later integrated together as an overall assessment of fall risk like the Berg Balance Scale,[20] which evaluates both the static and dynamic balance abilities.

Acknowledgements

The authors would like to thank Dagcentret På Tværbommen, Dagcenter Vennerslund, Daghjemmet Blåklokkevej, Betaniahjemmet, Hillerød Sundhedscentret, and Omsorgscentret Toftehøjen for the cooperation of the trial and also thank all participants of this experiment.

Part of the work was produced as part of the EU Horizon 2020 project REACH under grant agreement no. 690425.

References

1. A.J. Milat, W.L. Watson, C. Monger, M. Barr, M. Giffin, M. Reid, Prevalence, circumstances and consequences of falls among community-dwelling older people: results of the 2009 NSW Falls Prevention Baseline Survey, *New South Wales public health bulletin*, 22 (2011) 43-48.
2. M.G. Amin, Y.D. Zhang, F. Ahmad, K.D. Ho, Radar signal processing for elderly fall detection: The future for in-home monitoring, *IEEE Signal Processing Magazine*, 33 (2016) 71-80.
3. R.W. Sattin, D.A. LAMBERT HUBER, C.A. DEVITO, J.G. RODRIGUEZ, A. ROS, S. BACCHELLI, J.A. Stevens, R.J. Waxweiler, The incidence of fall injury events among the elderly in a defined population, *American journal of epidemiology*, 131 (1990) 1028-1037.
4. P.K. Canavan, L.P. Cahalin, S. Lowe, D. Fitzpatrick, M. Harris, P. Plummer-D'Amato, Managing gait disorders in older persons residing in nursing homes: a review of literature, *Journal of the American Medical Directors Association*, 10 (2009) 230-237.
5. K.B. Foreman, O. Addison, H.S. Kim, L.E. Dibble, Testing balance and fall risk in persons with Parkinson disease, an argument for ecologically valid testing, *Parkinsonism & related disorders*, 17 (2011) 166-171.
6. http://www.moto-tiles.com/
7. H.H. Lund, J.D. Jessen, Effects of short-term training of community-dwelling elderly with modular interactive tiles, *GAMES FOR HEALTH: Research, Development, and Clinical Applications*, 3 (2014) 277-283.
8. H.H. Lund, Modular interactive tiles for rehabilitation: evidence and effect, in *Proceedings of the 10th WSEAS international conference on Applied computer science* (2010), pp. 520-525.
9. Y. Liu, H.H. Lund, L. Wu, Playful Cognitive Training with Physical Interactive Tiles for Elderly, in *2018 International Conference on Information and Communication Technology Robotics (ICT-ROBOT)* (2018), pp. 1-4.
10. Y. Liu, H.H. Lund, Effect of Playful Physical Interactive Tiles on Cognition, in *2018 International Conference on Information and Communication Technology Robotics (ICT-ROBOT)* (2018), pp. 1-4.
11. H.H. Lund, Play for the elderly-effect studies of playful technology, in *International Conference on Human Aspects of IT for the Aged Population* (2015), pp. 500-511.
12. A. Shumway-Cook, S. Brauer, M. Woollacott, Predicting the probability for falls in community-dwelling older adults using the Timed Up & Go Test, *Physical therapy*, 80 (2000) 896-903.
13. J.M. Guralnik, E.M. Simonsick, L. Ferrucci, R.J. Glynn, L.F. Berkman, D.G. Blazer, P.A. Scherr, R.B. Wallace, A short physical performance battery assessing lower extremity function: association with self-reported disability and prediction of mortality and nursing home admission, *Journal of gerontology*, 49 (1994) M85-M94.
14. W. Dite, V.A. Temple, A clinical test of stepping and change of direction to identify multiple falling older adults, *Archives of physical medicine and rehabilitation*, 83 (2002) 1566-1571.
15. S.S. Ng, C.W. Hui-Chan, The timed up & go test: its reliability and association with lower-limb impairments and locomotor capacities in people with chronic stroke, *Archives of physical medicine and rehabilitation*, 86 (2005) 1641-1647.
16. T. Nakamura, K. Meguro, H. Sasaki, Relationship between falls and stride length variability in senile dementia of the Alzheimer type, *Gerontology*, 42 (1996) 108-113.
17. S.L. Whitney, D.M. Wrisley, G.F. Marchetti, M.A. Gee, M.S. Redfern, J.M. Furman, Clinical measurement of sit-to-stand performance in people with balance disorders: validity of data for the Five-Times-Sit-to-Stand Test, *Physical therapy*, 85 (2005) 1034-1045.
18. A. Goldberg, M. Chavis, J. Watkins, T. Wilson, The five-times-sit-to-stand test: validity, reliability and detectable change in older females, *Aging clinical and experimental research*, 24 (2012) 339-344.
19. E.Y. Goh, S.Y. Chua, S.-J. Hong, S.S. Ng, Reliability and concurrent validity of four square step test scores in subjects with chronic stroke: a pilot study, *Archives of physical medicine and rehabilitation*, 94 (2013) 1306-1311.
20. K. Berg, S. Wood-Dauphinee, J. Williams, The Balance Scale: reliability assessment with elderly residents and patients with an acute stroke, *Scandinavian journal of rehabilitation medicine*, 27 (1995) 27-36.

Playful Body and Brain Test with the Moto Tiles

Yan-Xin Liu, Massimiliano Leggieri, Henrik Hautop Lund
Center for Playware, Technical University of Denmark, Building 326,
2800 Kgs. Lyngby, Denmark
E-mail: s161642@student.dtu.dk, maxleggieri@gmail.com, hhl@playware.dtu.dk
www.dtu.dk

Abstract

We propose novel playful body and brain test. The test includes a series of standardized Moto Tiles games, which cover both physical and cognitive abilities. Reference scores of the tests were modeled by data collected from a large number of participants of different ages. The reference scores can be applied to evaluate a user's body and brain abilities in comparison with the average performance at the same age. By inversing this model, a new model was obtained. The input of the new model was game score and output was user's body and brain age, which provides an interesting and attractive manner to present the test results.

Keywords: Playware, cognition, aging, game.

1. Introduction

Aging is becoming a prevalent social issue in many developed countries. There were 27.3% of Japanese aged over 65 years old by 2016.[1] The figure at the global level was also predicted to reach 22% by 2050.[2] A direct consequence of population aging is the increased public expense of medical resources, which will become a serious social burden. There can be two possible directions to reduce the stress from the technology perspective. First is the development of economic personal health facilities which can improve a person's health level and delay the aging. Second is the development of intelligent hardware and software which can detect disease, impairment, and any characteristics of aging at an early stage. Based upon the early detection, a prevention or treatment plan can be established in order to avoid some of the aging-related health problems.

During the past decade, the Moto Tiles[3] has been proved to be an effective training tool which meets the first direction described above. Early investigation showed that the Moto Tiles training significantly improved the balance of older adults with less training period than ordinary training.[4-6] Later Liu et al.[7] presented a Moto training regime which could enhance the reaction speed of the elderly. The versatility of the Moto Tiles can be attributed to its modular and minimalistic design which allows both developer and users to create their games and usages with infinite possibilities. Based on this feature, we propose a novel Moto body & brain age (BBA) test, which is aimed at providing an early detection solution in a user friendly, enjoyable, and attractive environment.

2. The Design of the Moto BBA Test

The Moto Tiles Bode & Brain Age test includes four short Moto Tiles games which can evaluate different aspects of body and brain abilities. Each game lasts for only 30 seconds so that participants can complete the test quickly within 2 minutes. The four games and their descriptions are listed below:

- Color Race: One tile lights up in red. Player steps on the lit tile. Each correct press is counted as one point.
- Special One: One tile lights up in a special color (another color than the rest of the tiles). Player steps on this special tile. Then all colors change and next round begins. Each correct press is counted as one point.

- Final Countdown: All tiles light up in red. The tiles count down by turning off the LEDs in sequence. Player keeps light in all tiles by pressing on them before any tile count down to zero. Each correct press is counted as one point.
- Remember: Four tiles light up in different colors. Player remembers the color and position. After four seconds, the tile are turned off. Player has to step on the tiles according to a color sequence displayed on the tablet. Each correct press is counted as one point. Besides, wrong presses are also recorded and error rate is calculated for analysis.

3. The Moto BBA Model

We propose two models for the BBA evaluation. The first model is an age-score model, where the input is age and the output is a normative performance at the input age. The model is able to evaluate if a user performs better or below average and based on this recommend a training program to the user. The second model is a score-age model, which is the inverse of the first model. That is, the input is a user's game performance and the output is the user's body & brain age. This model presents a user's performance in an interesting and fun manner, which can motivate the user's further training and obtain better effects.

In order to construct an accurate model which can reflect the average performance of overall population, we conducted a large-scale test with over 100 participants enrolled. At the moment of handing this paper, totally 127 samples aged from 4 to 97 were collected.

The models are constructed by polynomial fitting. The data was randomly divided into a training set, a validation set, and a testing set, each of which accounts for 70%, 20%, and 10% respectively. The training set was used for calculating the polynomial coefficients. The validation set was used for finding the best order of the polynomial and avoiding overfitting. The testing set was used for a final evaluation of the model.

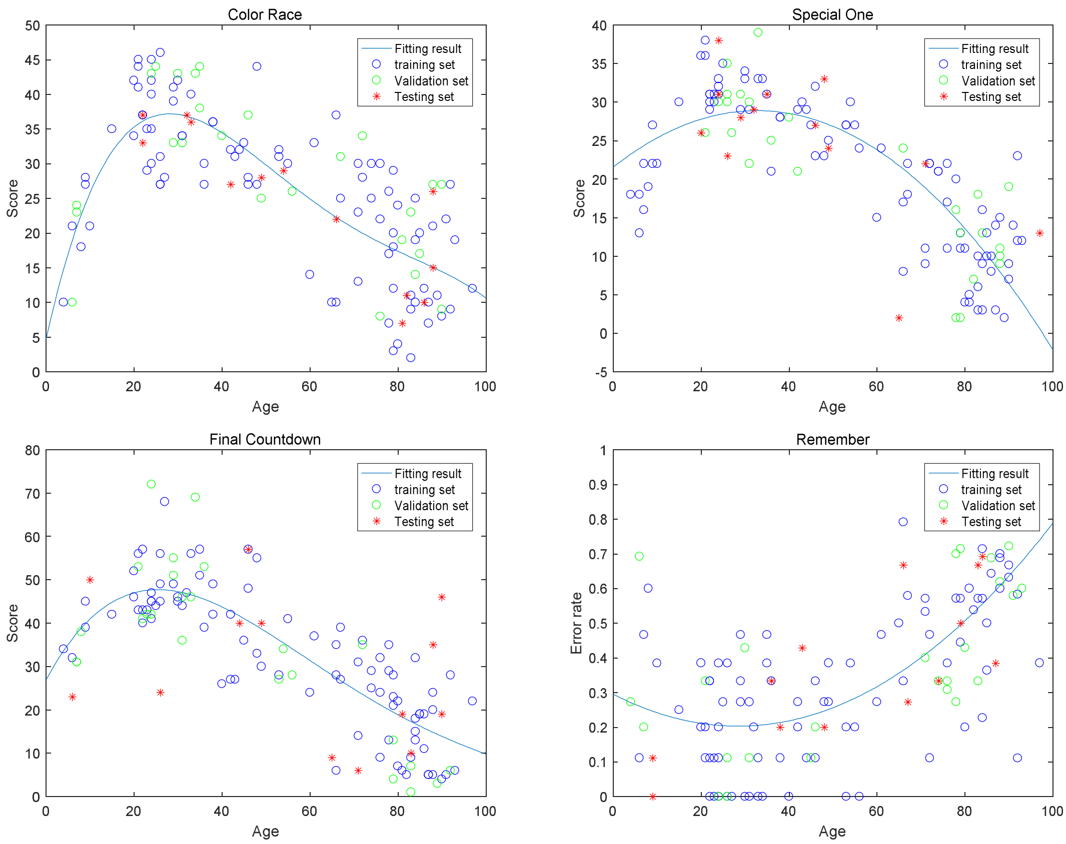

Fig. 1. The age-score model.

Fig. 1 shows the age-score model of the four games. The fitted formula of the Color Race game is:

$$-3.1 \cdot 10^{-6} \cdot x^4 + 8.5 \cdot 10^{-4} \cdot x^3 - 0.081 \cdot x^2 + 2.8 \cdot x + 4.7 \quad (1)$$

The formula of the Special One game is:

$$-0.0069 \cdot x^2 + 0.45 \cdot x + 21.56 \quad (2)$$

The formula of the Final Countdown game is:

$$-1.39 \cdot 10^{-6} \cdot x^4 + 4.63 \cdot 10^{-4} \cdot x^3 - 0.053 \cdot x^2 + 1.89 \cdot x + 26.92 \quad (3)$$

And the formula of The Remember game is:

$$1.14 \cdot 10^{-4} \cdot x^2 - 0.0065 \cdot x + 0.30 \quad (4)$$

In general the fitting results match the growth and aging process of human. Abilities grow as age increases until maturity. Then after 30 years old the abilities gradually decrease. This models of the first three games can be used as a judge of physical abilities such as speed, mobility, balance, etc. Scores below the model output indicate that the participant may need some training to improve corresponded abilities. For the senior users, a low score may also indicate potential age-related diseases or fall risk. The model of the Remember game provides a reference of short-term memory, which can be used for the early diagnosis and screen of certain types of dementia.

Fig. 2 shows the score-age model of the four games. The fitted formula of the Color Race game is:

$$-1.454 \cdot x + 91.257 \quad (5)$$

The formula of the Special One game is:

$$-2.035 \cdot x + 94.006 \quad (6)$$

The formula of the Final Countdown game is:

$$-1.198 \cdot x + 90.794 \quad (7)$$

And the formula of The Remember game is:

$$74.627 \cdot x + 26.581 \quad (8)$$

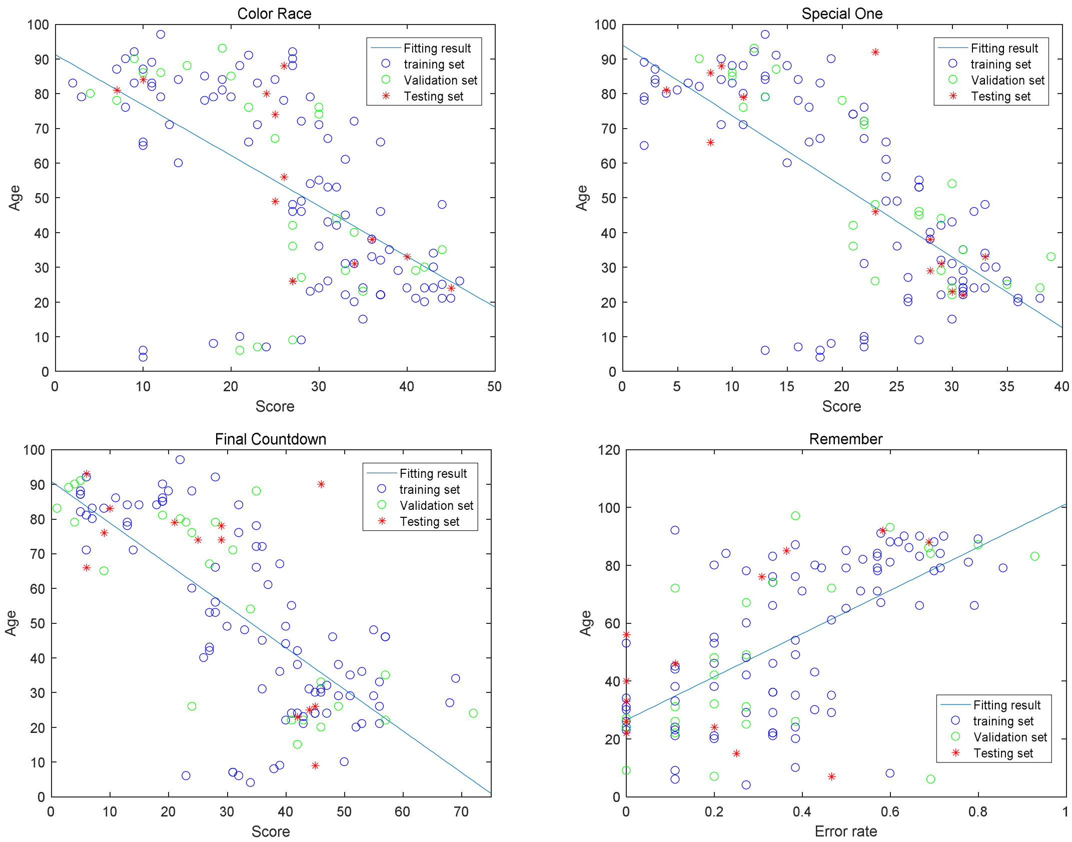

Fig. 2. The score-age model.

Fig. 3. Flow diagram of the Moto BBA test and analysis.

Note that all the four score-age models are first order polynomials. This is because both children and seniors performed at a relatively low level, which means certain scores are connected with both very low and high ages. Thus, higher orders of polynomials would easily cause overfitting. When more children and teenager samples are available, the model can be further improved by dividing it in two parts for fitting: a youth part where scores have a positive correlation with age, and an adult part where scores have negative correlation with age.

4. Discussion & Conclusion

The perspective of the tests when these correlations have been verified as above, is that we will be able to perform, for instance, test, risk analysis and recommendation for motivating treatment, as indicated in Fig. 3.

This may be incorporated in the Moto Tiles as a tests, which provides the analysis and provides the automatically generated training protocols indicating which Moto Tiles games to play and for how long in order to improve on the abilities that may be recommended to improve upon. An initial example of such an integration into the Moto Tiles system is shown Fig. 4.

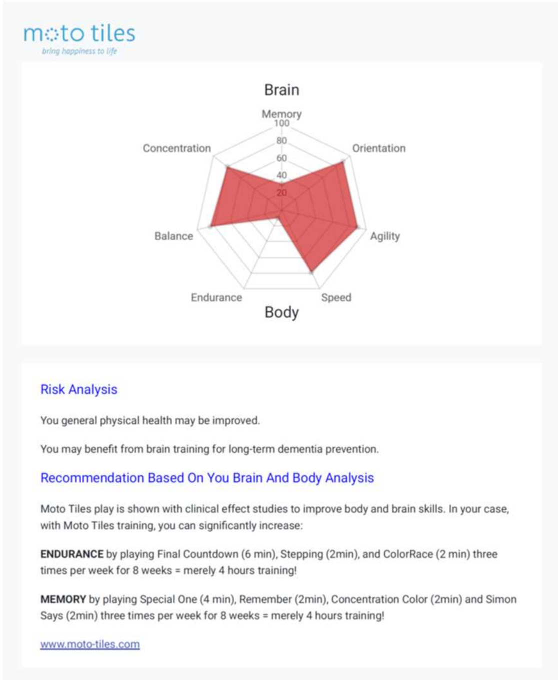

Fig. 4. The Moto BBA analysis and recommendation.

Acknowledgements

The authors would like to thank all participants of this experiment. Part of the work was produced as part of the EU Horizon 2020 project REACH under grant agreement no. 690425.

References

1. *Japan Statistical Yearbook 2018*, Statistics Bureau, Ministry of Internal Affairs and Communications, 2018.
2. D.E. Bloom, A. Boersch-Supan, P. McGee, A. Seike, Population aging: facts, challenges, and responses, *Benefits and compensation International*, 41 (2011) 22.
3. http://www.moto-tiles.com/
4. H.H. Lund, J.D. Jessen, Effects of short-term training of community-dwelling elderly with modular interactive tiles, *GAMES FOR HEALTH: Research, Development, and Clinical Applications*, 3 (2014) 277-283.
5. H.H. Lund, Play for the elderly-effect studies of playful technology, in *International Conference on Human Aspects of IT for the Aged Population* (2015), pp. 500-511.
6. H.H. Lund, J.D. Jessen, Effect of playful balancing training-a pilot randomized controlled trial, *2013 ISAROB*, (2013).
7. Y. Liu, H.H. Lund, L. Wu, Playful Cognitive Training with Physical Interactive Tiles for Elderly, in *2018 International Conference on Information and Communication Technology Robotics (ICT-ROBOT)* (2018), pp. 1-4.

Extracting Co-occurrence Feature of Words for Mail filtering

Seiya Temma
Graduate School of Sciences and Technology for Innovation, Yamaguchi University, 1677-1 Yoshida Yamaguchi, Yamaguchi 753-8512, JAPAN

Manabu Sugii
Faculty of Global and Science Studies, Yamaguchi University,1677-1 Yoshida Yamaguchi, Yamaguchi 753-8541, JAPAN

Hiroshi Matsuno
Graduate School of Sciences and Technology for Innovation, Yamaguchi University, 1677-1 Yoshida Yamaguchi, Yamaguchi 753-8512, JAPAN
E-mail: p040de@yamaguchi-u.ac.jp, manabu@yamaguchi-u.ac.jp, hmatsuno@yamaguchi-u.ac.jp

Abstract

Spam mail filters often take advantage of appearance frequency of words in a text for mail classification. However the appearance frequency is one of the most important attribute information with which the mail can be characterized, not a few spam mails can not be distinguished with only the appearance frequency of words. In order to search new attribute information to characterize and classify the mails, we analyzed relationship between words in a text of mails by text data mining. Also we visualized the word network by the co-occurrence and multi-dimensional scaling analysis with the jaccard coefficient in real mails. The co-occurrence network analysis showed important word connections with noun and verb in the same kinds of mails. Multi-dimensional scale analysis showed some word clusters extracted from the same kind of mails.

Keywords: mail-filtering, attribute information, text mining, co-occurrence network.

1. Introduction

We are still getting many spam mails from the Internet, nevertheless a lot of kinds of mail filtering system have been developed by using database or machine learning based on Bayes' theorem[1-3]. It seems kind of like "a cat-and-mouse game" because spam mail senders release new spam mails by taking advantage of vulnerability of a new filtering method based on features extracted from past spam mails.

We investigated the method for characterizing mails with machine learning, and we developed a new filtering system which could break out of the bad loop of "a cat-and-mouse game" by using features in ham mails for filtering[4]. The system uses appearance frequency of each word and its sequence patterns in a mail body. These features (the appearance frequency and its sequence patterns) are attributes of words, and these attributes can contribute to characterize and classify each mail.

We focused on three advantages for mail filtering method based on the attribute information[5] as follows;

1. reducing information
2. protection of private information and privacy
3. easy apply to multi-language

For example, amount of information of a mail body can be reduced to about 1/4 by converting each word into a single character as an attribute symbol represented its appearance frequency. Then, it is not easy to recover the original mail body from the converted attribute symbols. Finally, it is not necessary to process natural language analysis by this method because the attribute conversion does not depend on specific language. As a result, it is easy to apply the system to any languages.

Some attributes of words like appearance frequency, a part of speech, tf-idf value, cosine similarity and the Jaccard index are known as important factors to characterize words and documents, and they are applied to mail filtering system to characterize spam mails. But it is still difficult to classify some kinds of spam mails similar to ham mails like unsolicited mails about “Online dating service”.

In this study, we are trying to find better attributes for the spam mail filtering by text mining. We considered that it is possible to extract the new attributes which can cluster the same kind of mails, and we focused on a co-occurrence network of words as the one of the attributes.

2. Method of Searching attributes

In order to find new attributes that can remove typical spam mails or perform high accuracy mail filtering, it needs to search not only characteristics of words in mails, but also characteristics of groups based on the connection of words in mails. Thus, we visualized a co-occurrence network with the Jaccard index and analyzed clusters extracted by multidimensional scaling with it. The Jaccard index is represented by the equation (1) and it indicates co-occurrence intensity between two words in this study.

$$\boldsymbol{J}(\boldsymbol{A},\boldsymbol{B}) = \frac{|\mathbf{A} \cap \mathbf{B}|}{|\mathbf{A} \cup \mathbf{B}|}, \tag{1}$$

for given sets **A** and **B**.

The Jaccard index between each two words are calculated from a number of mails which contain these words according to equation (1). In both methods, co-occurrence network analysis and multidimensional scaling, some clusters of words are visualized on two dimensional space with similarity values between two words. The result of the visualization is useful to grasp the whole image of the relationship between each word in sample mails.

2.1. *KH coder*

KH coder[6] is a free software for analyzing text data statistically. And it was produced to analyze various social survey data such as free description of questionnaire, interview article, newspaper article etc.

KH coder has functions of aggregating and searching words in data, and multivariate analysis and visualization by using R and morphological analysis module, Chasen or MeCab. The Jaccard index was calculated by KH coder, and a part of speech of each word was also identified with MeCab in KH coder. We visualized co-occurrence networks and words distribution by multidimensional scaling with the Jaccard index.

2.2. *Co-occurrence network*

Co-occurrence network is a network diagram composed of edges and nodes with the Jaccard index over a threshold. Some clusters are usually formed in the co-occurrence network which is produced with the words from mail bodies. The words in the cluster represent a strong relationship and similarity between these words in the sample mails.

2.3. *Multidimensional scaling*

Multidimensional scaling is a method to visualize similarity of individual elements of dataset. Similarity between each element is regarded as distance of them, and all elements are laid on the N-dimensional space depending on the distance without contradiction. As a result, high similarity elements are laid from a short distance on the space. In this study, we applied the Jaccard index to the similarity between words in sample mails.

2.4. *Sample mail*

In this study, we used the 2007 TREC Public Spam Corpus[7]. It is composed of 30,338 mails (spam: 50,199 mails, ham: 25,220 mails) accepted from 2007/4/4 to 2007/7/6. Two thousand mails were extracted from each spam and ham partial set of TREC07 as a sample mail set, and input them into KH coder.

3. Result

Fig. 1 shows a co-occurrence network with all words from whole TREC07 mail samples. There are many clusters composed of co-occurrence words (the Jaccard index >= 0.3) in the same kind of sample mails. For example, the words extracted from the mails about software development or advertising mails or having the same topic mails show a tendency to make one cluster. But it is too complicated to see details of each cluster components in Fig. 1 because too many words are shown in the network, and the layout of words in each cluster is too small.

Fig. 2 shows the re-construction of the co-occurrence network with only nouns from ham mails. It has two major clusters, A and B. The words in the cluster A and B are extracted from the mails with a common mail signature and system log announcement, respectively. This result shows that each cluster in co-occurrence network is composed of the words extracted from similar kinds of mails. In other words, a mail can be characterized with the co-occurrence word set which composes such clusters in the co-occurrence network.

Fig. 3 shows the re-construction of the co-occurrence network with nouns and verbs from ham mails. It has still two major clusters, A and B extracted from the same mail set. However these clusters have nouns and verbs (red under line) as well, a lot of co-occurrence connections between nouns and verbs are shown in the cluster A. But there is only one verb in cluster B because the mails which compose the cluster B contain few verbs in the first place. This result suggested that the co-occurrence network between nouns and verbs might indicate an important feature to characterize a certain mail.

Fig. 4 shows the result of multidimensional scaling. Each word is distributed on the 2-dimensional space which has unknown coordinates, and high similarity words are located at the close region. We focused on three regions and words in these regions, A, B and C. The words in region A, B and C are extracted from the mails about CNN news, the mails with a common mail signature and the system log announcement, respectively.

When nouns and verbs are distributed on 2-dimensional space by multidimensional scaling (Fig. 4b), the verbs are located around the center region, and they are close to the region B. Fig. 4c shows the result of multidimensional scaling without the words from the system log announcement. The distribution of the words changed completely but verbs were still located around the center region.

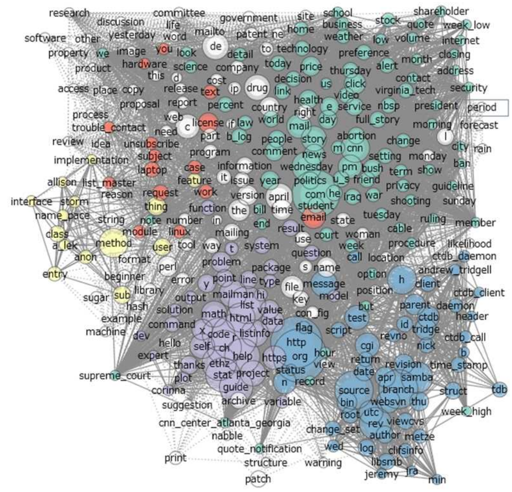

Fig. 1. Co-occurrence network of TREC07 mail sample

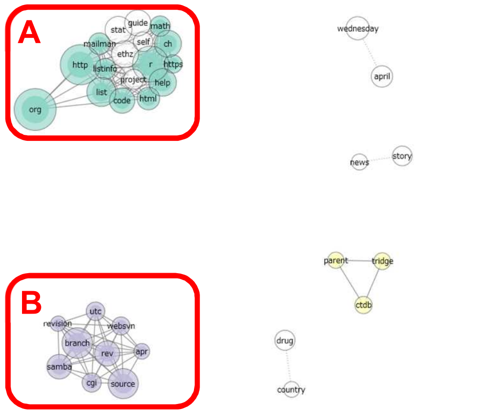

Fig. 2. Co-occurrence network with only nouns from ham mails

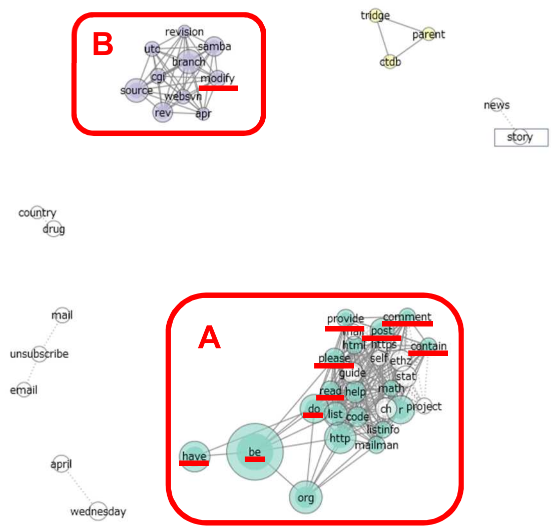

Fig. 3. Co-occurrence network with nouns and verbs from ham mails

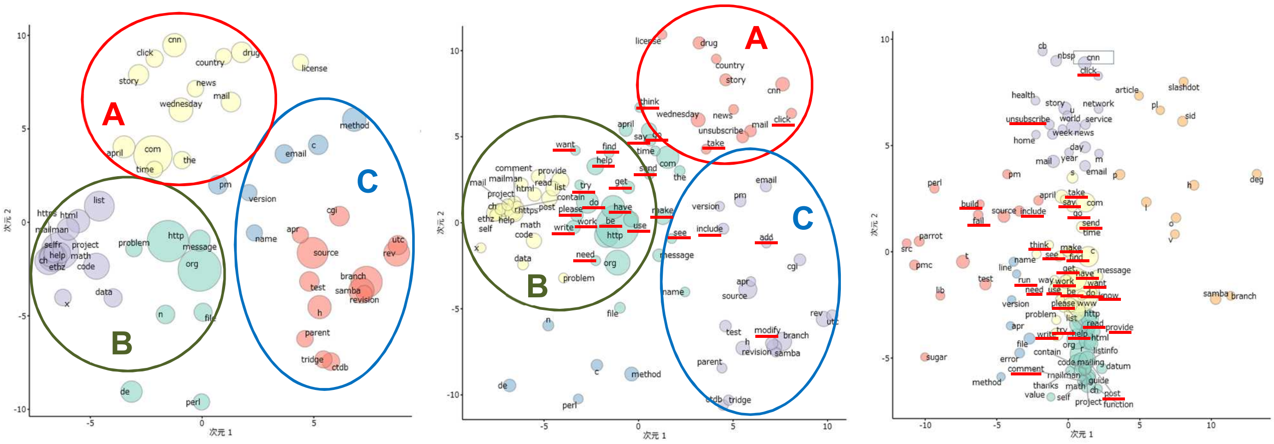

a : only nouns.

b : nouns and verbs

c : nouns and verbs without system log announce mails

Fig. 4. The distribution of words on 2-dimensional space by multidimensional scaling

4. Discussion

Most of all mail filtering system try to characterize mails as only two categories, spam or ham. Of course, it is the very simple method for the mail filtering but it might be also difficult process to find features because there are too many kinds of mails to characterize as two categories in both spam and ham. In other words, it is very difficult to find common features from all spam mails or ham mails.

The result of this study shows that it is possible to group mails into several types with the combination of co-occurrence words because the words extracted from the same kind of mails cluster easily in the co-occurrence network. Then, the words with the low level co-occurrence index can be visualized as a cluster in the co-occurrence network by removing the mails which contain the high level co-occurrence words[8].

Some kinds of spam mails like the system log announcement and advertising mails which contain only URL can be removed by checking the co-occurrence connection between nouns and verbs. They have the quite few connections between them.

We do not have a concrete measure to use the co-occurrence connection set between nouns and verbs as the attribute but we considered that the combination of them is very important to characterize the type of mails. At least, it could be better attribute than an appearance frequency of words for the filtering of unsolicited mails like “Online dating service” because these mails have similar use of words in ham mails. We will plan how to utilize it for mail filtering as our future work.

5. Acknowledgements

This work was supported by JSPS KAKENHI Grant Number JP16K12438.

6. References

1. P. Graham, “A Plan For Spam”, 2002: http://www.paulgraham.com/spam.html
2. P. Graham, ”Better Bayesian Filtering”, 2003: http://www.paulgraham.com/better.html
3. bsfilter-bayesian spam filter: https://ja.osdn.net/projects/bsfilter/
4. M. Sugii, H. Matsuno, Decision Tree Representation of Spam Mail Features by Machine Learning, 2007(16(*2007-DPS*-130)), 183-188, 2007-03-01,2007.
5. N. Fujii, M. Sugii, and H. Matsuno, Finding the Candidates of Attributes in Mail Words Filtered by Bayesian Method, *IEICE Technical Report*, vol. 116, no. 525, MSS2016-89, pp. 43-48, 2017.
6. KHcoder : http://khc.sourceforge.net/
7. TREC 2007 Public Corpus : http://plg.uwaterloo.ca/~gvcormac/treccorpus07/
8. S. Temma, M. Sugii, H. Matsuno, Searching Attribute Information for Mail Filtering based on Text Mining, *ITC-CSCC2018 proceedings*, 596-599, 2018.

Learning Style Classification with Weighted Distance Grey Wolf Optimization

Duangjai Jitkongchuen
College of Innovative Technology and Engineering
Dhurakij Pundit University, Thailand

Piyalak Pongtawevirat
College of Innovative Technology and Engineering
Dhurakij Pundit University, Thailand
E-mail: duangjai.jit@dpu.ac.th, piyalak.pot@dpu.ac.th
http://cite.dpu.ac.th

Abstract

This research aims to improve the performance of multiclass classification by using grey wolf optimization algorithm. The proposed algorithm presents a solution to improve the grey wolf optimization performance using weighted distance and immigration operation. The weight distance is used for the omega wolves movement is defined from fitness value of each leader. The proposed technique is based on learning style prediction which addresses multiclass classification problem. The results showed that the proposed technique obtained the higher accuracy rate than other classification techniques.

Keywords: Data mining, Classification, Grey wolf optimization algorithm, Learning style

1. Introduction

The one of the most important areas in machine learning is classification. The classification goal is to find determinations of classes to un-classified and unseen instances (data samples) based on information previously learned. Solving classification problems intends to design good classifier(s) which make right determinations as often as possible[1].

Generally, the classification techniques can be divided into two categories. The binary classification identifies the output class from two possible classes. The second category is the multiclass classification which predicts the result from multiple classes. Hence, the techniques to improve the classification performance in terms of accuracy for multiclass classification should be investigated.

There are many commonly used classification techniques that have been used to deal with classification problems and predictions in various areas. Examples of these techniques are decision trees (DT), naïve bayes (NB), artificial neural networks (ANN) and support vector machines (SVM)[2]. In addition, the algorithm in the group of evolutionary algorithm has been also introduced to solve the classification problem[3]. However, in each classification techniques have many advantages and disadvantages. As a result, the most appropriate technique for each dataset and its data types should be examined in order to obtain the appropriate built classification model for specific problem.

The remainder of this paper is organized as follows. In Section 2, learning domain, learning style and the original grey wolf optimizer algorithm is provided. In Section 3, the proposed algorithm weighted distance grey wolf optimization is described. In Section 4, a performance evaluation of our proposed methods is done compared to other classification techniques (cAnt-Miner, PART, C4.5) on dataset of learners' information related to classification model prediction. Finally, in Section 5, the conclusions will be discussed.

2. Related work

2.1. *Learning Domain and Learning Style*

The cognitive learning which refers to human knowledge is one of the learning domains for human[4]. The cognitive learning focuses on individual level of knowledge. The individual learning is difference which is based on personal learning style. As a result, everyone prefers different kind of learning content based on their learning style. This conduces to more developing learners' abilities.

The learning style refers to an individual's unique approach to learning based on strengths, weaknesses, and preferences. Several researchers have been worked to define the learning style for learner. Many learning styles such as the Felder-Silverman Index of Learning Styles have been proposed[5]. There are two approaches to identify a learning style which are questionnaire and computer model prediction. Firstly, the questionnaire approach needs the learner to fill in their information respecting the available model[6]. Secondly, the learner's learning style is determined using computational techniques and the learning style prediction model is created based on available information.

2.2. *Grey wolf optimization algorithm*

The grey wolf optimizer algorithm (GWO)[7] is intelligence algorithm which simulates the hierarchy structure and hunting mechanism of wolf pack. The social dominant hierarchy of the wolf pack is divided into four levels. From top level to bottom grade are alpha (α) wolves, beta (β) wolves, delta (δ) wolves and omega (ω) wolves. An ability of grey wolves has to recognize the positions of prey and to encircle them. The hunting (optimization) is guided by alpha, beta and delta. The omega wolves are iteratively improved by following the other dominant wolves.

Grey wolves encircle prey during the hunt. The mathematically of model encircling behavior as follows

$$\vec{X}(t+1) = \vec{X}_p(t) - \vec{A} \cdot \vec{D} \tag{1}$$

$$\vec{D} = \left| \vec{C} \cdot \vec{X}_p(t) - \vec{X}(t) \right| \tag{2}$$

where t is the iteration number, $\vec{X}$ is the grey wolf position and $\vec{X}_p$ is the prey position. The vectors $\vec{A}$ and $\vec{C}$ are coefficients are calculated as follows

$$\vec{A} = 2a \cdot \vec{r}_1 - a \tag{3}$$

$$C = 2\vec{r}_2 \tag{4}$$

The value of a is decreased linearly from 2 to 0 over the course of iterations and $\vec{r}_1, \vec{r}_2$ are random vectors in the range [0, 1]. The vector $\vec{C}$ is used to furnish a random weight to mention attractiveness of prey is a random value in the range [0, 2].

Hunting strategy of the grey wolves can be mathematically modeled by approximating the prey position with the help of alpha, beta and delta solutions. The first three best solutions get so far and force the other search agents (including the omegas) to update their positions according to the position of the three best search agents. Each wolf can update their positions by following equations.

$$\vec{X}(t+1) = \frac{\vec{X}_1 + \vec{X}_2 + \vec{X}_3}{3} \tag{5}$$

where $\vec{X}_1, \vec{X}_2, \vec{X}_3$ are determined as in Eq. (6)-(8), respectively.

$$\vec{X}_1 = \left| \vec{X}_\alpha - \vec{A}_1 \cdot \vec{D}_\alpha \right| \tag{6}$$

$$\vec{X}_2 = \left| \vec{X}_\beta - \vec{A}_2 \cdot \vec{D}_\beta \right| \tag{7}$$

$$\vec{X}_3 = \left| \vec{X}_\delta - \vec{A}_3 \cdot \vec{D}_\delta \right| \tag{8}$$

where $\vec{X}_\alpha, \vec{X}_\beta, \vec{X}_\delta$ are the first three best solutions at a given iteration t, $\vec{A}_1, \vec{A}_2, \vec{A}_3$ are determined as in Eq. (3), and $\vec{D}_\alpha, \vec{D}_\beta, \vec{D}_\delta$ are determined as in Eq. (9)-(11), respectively.

$$\vec{D}_\alpha = \left| \vec{C}_1 \cdot \vec{X}_\alpha - \vec{X} \right| \tag{9}$$

$$\vec{D}_\beta = \left| \vec{C}_2 \cdot \vec{X}_\beta - \vec{X} \right| \tag{10}$$

$$\vec{D}_\delta = \left| \vec{C}_3 \cdot \vec{X}_\delta - \vec{X} \right| \tag{11}$$

where $\vec{C}_1, \vec{C}_2, \vec{C}_3$ are determined as in Eq. (4). The parameter a that controls the tradeoff between exploration and exploitation is linearly updated to range from 2 to 0 in each iteration as shown in Eq. (12)

$$a = 2 - t\frac{2}{MaxIter} \tag{12}$$

where t is the iteration number and $MaxIter$ is the total number of iteration.

3. The proposed approach

The process of traditional grey wolf algorithm has only one wolf pack and has opportunity of local optimum problems. The proposed algorithm presents grey wolf algorithm with more than one pack and integrate the immigration operation between pack to improve the exploration and exploitation.

The position of omega wolves in traditional grey wolf algorithm are identified by the position of three leaders, alpha, beta and delta wolf while the position of omega wolves in proposed algorithm are identified using weight value difference of three leaders. The omega wolves positions are updates by following equations.

$$\vec{X}(t+1) = \frac{W_1\vec{X}_1 + W_2\vec{X}_2 + W_3\vec{X}_3}{3} \tag{13}$$

where W_1, W_2, W_3 is the weight value of alpha, beta and delta wolf, respectively. The weight value of each leader are calculated as follows

$$W_1 = \frac{f_\alpha}{f_\alpha + f_\beta + f_\delta} \tag{14}$$

$$W_2 = \frac{f_\beta}{f_\alpha + f_\beta + f_\delta} \tag{15}$$

$$W_3 = \frac{f_\delta}{f_\alpha + f_\beta + f_\delta} \tag{16}$$

where f_α, f_β, f_δ is the fitness value of alpha, beta and delta wolf, respectively.

The immigration operation is active in next process to use to distribute value to expand the search space. The omega wolves which low fitness value would be immigrated to create new pack and generate new wolves member to fill up the old pack. The center value of pack is used to generate the new wolves members for sustain the boundary of pack.

The immigration has an effect on continually increasing pack amount in each iteration. Therefore, pack which have maximum weak member would be removed by mean of weak member is member that have fitness value less than the average fitness value of pack.

The all process is repeated until the termination criteria are convinced or a predefined number of iterations are achieved.

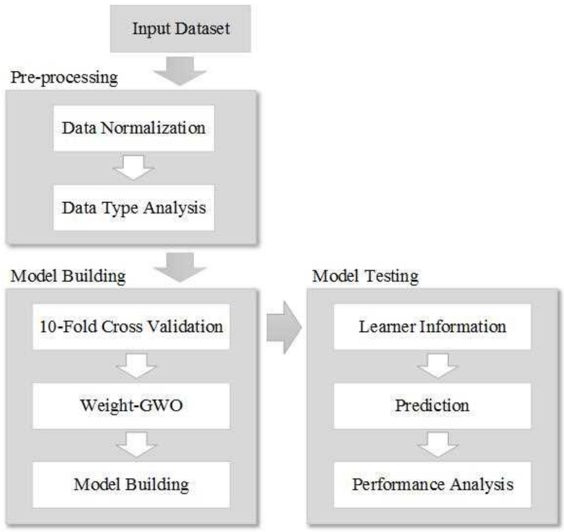

Fig. 1. The framework of learning style classification with weighted distance grey wolf optimization.

4. Experimental results

The learning style can be classified into 4 class, Active and Reflective, Sensing and Intuitive, Visual and Verbal, and Sequential and Global. Nevertheless, some students can grouped as multiple classes so this class of learning style is classified as others. The experiment used data source from published research work on learning style classification in university students[8]. The attributes of data consists of learners' information related to classification model prediction such as gender, age, educational background, current grade point average, major unit's enrolment and major unit's grade point average. There are 400 records in this dataset and the information related to this dataset can be seen from Table 1.

Table 1. Datasets used in experiments.

Learning Style	Instances
Active and Reflective	66
Sensing and Intuitive	81
Visual and Verbal	122
Sequential and Global	67
Others	64
Total	**400**

The training data have three hundred randomly selected records and the remains one hundred records were used for testing data. The classification model is built by using training data and evaluates performance of model by using testing data.

The proposed algorithm was evaluated performances with cAnt-Miner, C4.5 and PART. The metric to determine the performance of the classification is based on accuracy rate. The experimental results are shown in Table 2.

The experimental results shown that the proposed algorithm can perform better in terms of accuracy rate compared to other classification techniques. In addition, it performed better than C4.5 and PART. The proposed algorithm can improve classification performance by analyzing and predicting the continuous attributes in the dataset so can used to predict the dataset, learning style of learner, efficiently.

Table 2. Comparison of accuracy rate.

Dataset	cAnt-Miner	C4.5	PART	Proposed
A	86.75	82.00	73.44	**92.15**
B	85.50	71.70	70.59	**91.45**
C	84.50	76.92	73.56	**91.75**

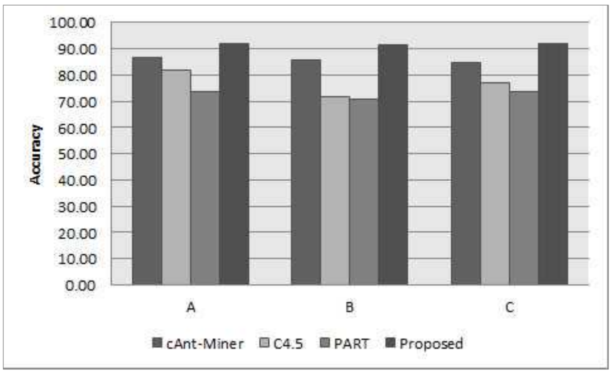

Fig. 2. A comparison of accuracy between proposed algorithm and other classification techniques.

5. Conclusions

The multiclass classification seems to be difficult to improve the performance of the built classification model. One of the novel approaches in recent years is bio-inspired algorithm. Grey wolf optimization algorithm is one of bio-inspired algorithm which good capacity to distinguish between an exploration phase and an exploitation phase. This research aims to improve the performance of multiclass classification by using weighted distance grey wolf optimization algorithm and integrate immigration operation. This which leads to generate new candidate individuals in order to enhance the classification performance. The results from the experiments based on learning style datasets have shown that the proposed technique can perform better in terms of accuracy rate compared to other classification techniques.

References

1. C. M. Bishop, *Pattern Recognition and Machine Learning*, (Springer-Verlag GmbH, Berlin, Germany, 2006).
2. X. Wu, et al., Top 10 Algorithms in Data Mining, *Knowledge and Information Systems*, vol. 14(1) (2008), pp. 1-37.
3. D. Jitkongchuen, and A. Thammano, *A Hybrid DE-ACO Approach for Discovering Classification Rules* (Proc. International Technical Conference on Circuits/Systems, Computers and Communications (ITC-CSCC), 2012).
4. B.S. Bloom, *Taxonomy of educational objectives: the classification of educational goals* (David McKay, 1956).
5. R. M. Felder and L. K. Silverman, Learning and Teaching Styles in Engineering Education, *Engr. Education*, vol. 78(7) (1988), pp. 674-681.
6. A. Klašnja-Milićević, B. Vesin, M. Ivanović, and Z. Budimac, E-Learning personalization based on hybrid recommendation strategy and learning style identification, *Computers & Education*, vol. 56(3) (2011), pp. 885-899.
7. S. Mirjalili, S.M. Mirjalili and A. Lewis, Grey Wolf Optimizer, *Advances in Engineering Software*, vol.69 (2014), p.46-61.
8. W. Paireekreng and T. Prexawanprasut, *An Integrated Model for Learning Style Classification in University Students Using Data Mining Techniques* (Proc. 12th International Conference on Electrical Engineering /Electronics, Computer, Telecommunications and Information Technology (ECTI-CON), 2015).

The Relevance Research among Destination Image, Brand Trust and Satisfaction: Tainan Festival in Taiwan as Example

Shang-Hui Li
Department of Food and Beverage Management, Far East University, Taiwan (R.O.C.)
E-mail :a0956358700@gmail.com

Shu-Fang Hsu
Department of Food and Beverage Management, Far East University, Taiwan (R.O.C.)

Yi-Tai Shang
Department of Food and Beverage Management, Far East University, Taiwan (R.O.C.)

Abstract

In recent years, all local governments of Taiwan have held sightseeing festivals to enhance their popularity, promote their economy, to establish their brand. Tainan, the second biggest city in southern Taiwan, also promotes the various agricultural products and sightseeing to serve customers as the region's annual event. This study took Tainan Festival as an example to explore the relevance of the destination image, brand trust, and satisfaction. The participants for those who took part in 2017 Tainan Festivals, from May to July, were the main subjects on this study. 500 questionnaires were issued, 465 valid questionnaires collected, 93%. The finding results showed that the destination image of Tainan festival activities had a positively effects on satisfaction, brand trust had a positive effects on satisfaction, destination image had a positive effects on brand trust, brand trust had the intermediary effect to the satisfaction and destination image.

Keywords: Festival, Destination Image, Brand Trust, Satisfaction

1. Introduction

In recent years, the Taiwan government has actively promoted the development of agricultural products in various regions with local characteristics and encouraged to hold the festival with combining the local industry to activate the economy and culture. The festival also promoted food-related activities which could increase the economic impact of tourism. In addition to promote local specialty industries, local festivals can also take advantage of opportunities to increase industrial revenues and achieve marketing goals. Festivals are held in every administrative district of Tainan, Taiwan every year.

For example, the Dongshan District Farmers' Day in May, the Mango Festival was held in conjunction with Yujing, Nanxi, Nanhua, Danei and Zuozhen from June to July and Baihe Lotus Festival from July to August etc. It is hoped to promote the development of local and urban tourism culture through the integration of resources in industry, tourism and culture. This study took Tainan festivals as an example to explore destination image, brand trust and satisfaction in order to understand the consumer's satisfaction with the festival activities. Did the first impression and the feeling of participating in the event affect their satisfaction with the activity? Will it affect the satisfaction of consumption on the festival brand if consumers generate trust in the festival brand?

2. Literature Review

Taiwan local governments will like to hold the unique folk culture, festivals and industrial cultural activities to attract tourists to consume. It is not only shaping the local characteristics, but also activating the local economy, it can also promote the development of the local tourism industry for local marketing purposes [1]. The destination image is an important indicator in the visitors' eyes [2]. It is also the emotional connection between the tourist destination and the consumers' psychology, with positive, neutral and negative feelings respectively [3].
Destination image is a key factor in the tourism decision-making process and destination selection behavior [4] [5]. Destination image contains a multidimensional oriented construct of cognition, emotion, and intention [6] [7]. Qu, Kim, and Im argued that destination brand imagery should contain unique images, and unique images refer to images with impressive attributes or traits [8]. In recent years, food tourism has developed rapidly and diet has become a motivation for people to travel [9]. Therefore, the destination food image and the destination tourist image are parts of the destination image. Morgan and Hunt defined trust as the reliability and costiveness of trading partners [10]. The transaction will take place under the consumer clearly feels the sincerity of the other party and has a sense of security for the brand. Arjun & Morris believed that consumers are willing to take the initiative to trust and trust the products offered by the brand [11]. The idea of customer satisfaction was first proposed by [12]. Cardozo believed that customer satisfaction was the degree of customer satisfaction with the product's expectations and results [13]. Day considered customer satisfaction as a perception in which customers evaluate the pre-purchase expectations and post-purchase actual performance [14].

3. Research Method

This study explored the relevance among destination image, brand trust and satisfaction. The research structure was constructed after basing on the research background, research purposes and related literature, as shown in Figure 1.

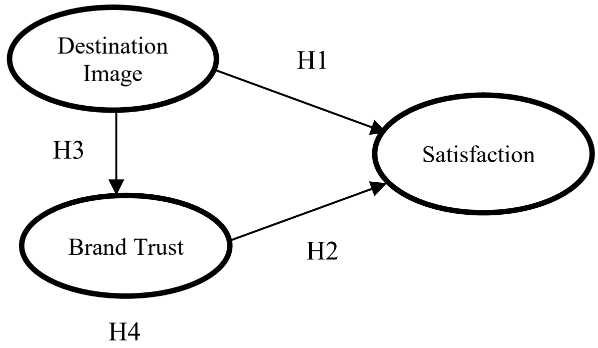

Figure 1. Research Structure

Various hypotheses are proposed based on the purpose of this study, and the results of the data analysis will verify if the hypothesis was true. The research hypothesis was as follows:

H1: destination image has a positive impact on satisfaction.
H2: brand trust has a positive impact on satisfaction.
H3: destination image has a positive impact on brand trust.
H4: The brand trust has a mediating effect between satisfaction and destination image.

Destination image refers to the consumer's perception and thoughts about the activity. The scale was based on the questionnaires of G'omez, Lopez and Molina (2015), with a total of 16 questions. Brand trust refers to the consumer's trust to the brand. The scale was based on the questionnaires of Chaudhuri and Holbrook (2001), a total of 4 questions. Satisfaction refers to the consumers' satisfaction in participating this activity. The scale was based on the questionnaires of Lu, Chi and Liu (2015), with a total of 4 questions. The study objects and scope were mainly for the consumers who participated in the Tainan festivals from May to July, 2017. 500 questionnaires were distributed under convenient sampling method, and 465 valid questionnaires (93%) were collected. The version 12.0 of SPSS (Statistical Package for the Social Science) was used for empirical data analysis.

4. Running Heads

The study used regression analysis to analyze if destination image has a significant correlation to satisfaction. Destination image predicted the 42.7% explanatory power of satisfaction, F=347.342, P=.000, reaching a significant level. It was shown that the explanatory power had the statistical significance, and the result of the coefficient estimation indicated that the destination image can effectively affect satisfaction. The beta coefficient was 0.655 (t=18.637 p=0.000) which indicated that the higher the consumer's destination image, the higher the satisfaction. The result supported hypothesis 1.

The study examined if the brand trust of Tainan's festival activities affected satisfaction (Table 2). Brand trust predicted the explanatory power of 27.2% of satisfaction, F=177.727, P=.000, reached a significant level which indicated that the explanatory power was statistically significant. Therefore, the brand trust can effectively affect the satisfaction. The Beta coefficient reached 0.527 (t=13.331 p=0.000), indicated that the higher the consumer's brand trust, the higher the satisfaction. The result supported hypothesis 2.

The study examined if the destination image of the festival affected the brand trust, predicting the explanatory power of the brand trust 30.4% with the destination image, F=202.698, P=.000, reached a significant level which was shown that explanatory power had statistical significance. The results of the coefficient estimation indicated that the destination image can effectively affect the brand trust, and the beta coefficient was 0.552 (t=14.237 p=0.000), indicated that the higher the consumer's destination image, the higher the brand trust. The result supported hypothesis 3.

Regression Analysis was used to verify if the brand trust had a mediating effect on destination image and satisfaction. Incorporating destination image, brand trust and satisfaction into regression mode, shown that destination image and brand trust had no significant effect on satisfaction, and then compare β value, the latter β=0.527 is smaller than the former β=0.655. Overall, the results supported hypothesis 4, which indicated that the brand trust had a mediating effect on destination image and satisfaction.

5. Conclusions and Recommendations

The higher on destination image, and the higher on the consumer's satisfaction. The industry can strengthen the destination image of festivals of Tainan, for example, a large number promotion on media, online, Facebook, IG and Line to enhance consumer impressions of festivals which could help consumers recognize their destinations and increase satisfaction.

The higher on destination image, the higher on the consumer's brand trust, and the better regional image and reputation could enhance the trust of visitors.

Some suggestions could be offered by this study such as local government and the Council of Agriculture, COA, could cooperate with public welfare organizations to enhance the trust of tourists in Tainan area.

The higher on the brand trust of consumers in Tainan's festivals, the higher on their satisfaction. It may be that the activities are mostly organized by government agencies and have a certain sense of trust for consumers. It could be believed that more consumers could be attracted to the festivals if local farmers could be invited to support and publicize their products in the future activity. It is difficult to explore one by one item due to manpower considerations. It is recommended that the follow-up researchers can add more different variables to conduct the further study, so that the research can be more complete.

References

1. Chen, P. T., Chen, F. D. & Pei, L., Evaluation of Place Marketing Effects Induced by Festivals. *Journal of Sport, Leisure and Hospitality Research.* 9(3), 2014, pp. 23-28.
2. Hunt, J. D., Image as a factor in Tourism Development. *Journal of Travel Research*. 13, 1975, pp. 1-7.
3. Woodside, A. G. & Lysonski, S., A general model of traveler destination choice. *Journal of Travel Research*. 17(4), 1989, pp. 8-14.
4. Echtner, C. M. & Ritchie, J. R. B., The meaning and measurement of destination and the influence of geographical location upon that image. *Journal of Travel Research*. 14(4), 1991, pp. 18-23.
5. Baloglu, S. & Mangaloglu, M., Tourism destination images of Turkey, Egypt, Greece and Italy as perceived by US-based tour operators and travel agents. *Tourism Management.* 22, 2001, pp.1-9.
6. Beerli, A. & Martin, J. D., Factors influencing destination image. *Annals of Tourism Research*. 31(3), 2004, pp. 657-681.

7. Prayag, G. (2007). Exploring the relationship between destination image and brand personality of a tourist destination: An application of projective techniques. *Journal of Travel and Tourism Research.* 7(2), 111-130.
8. Qu, H., Kim, L. H. & Im, H. (2011). A model of destination branding: Integrating the concepts of the branding and destination image. *Tourism Management*. 32(3), 465-476.
9. Lin, Y. C., Pearson, T. E. & Cai, L. A. (2011). Food as a form of Destination Identity: A Tourism Destination Brand Perspective. *Tourism and Hospitality Research*. 11(1), 30-48.
10. Morgan, R. M. & Hunt, S. D. (1994). The commitment-trust theory of relationship marketing. *Journal of Marketing.* 58, 20-38.
11. Arjun, C. & Morris, B. H. (2001). The Chain of Effects from Brand Trust and Brand Affect to Brand Performance: The Role of Brand Loyalty. *Journal of Marketing.* 65, 81-93.
12. Drucker, P. F. (1950).*The new society.* William Heinemann, Ltd.
13. Cardozo, R. N. (1965). An experimental study of customer effort, expectation, and satisfaction. *Journal of Marketing Research*. 24, 244-249.
14. Day, R. L. (1984). Modeling choices among alternative responses to dissatisfaction. In Thomas C. Kinnear (ed.). *Advances in Consumer Research*. 496-499.

Third-party Logistics Service Supply: Catering Service Trade as Example

Shu-Fang Hsu
Department of Food and Beverage Management, Far East University, Taiwan (R.O.C.)
E-mail:h99582004@gmail.com

Shang-Hui Li
Department of Food and Beverage Management, Far East University, Taiwan (R.O.C.)

Abstract

With the development of third-party logistics, refrigeration technology, and transportation which made the food to obtain easily, and improve the quality of food preservation. Now, the catering chefs just ordered his needed foods by line, telephone, fax, or fill the order list etc., to inform the third-party logistics suppliers and there will be someone assigned to the designated location which could save purchasing time and catering chefs don't need to rush around to procure foods. This study analyzed the collected information through literature, in-depth interviews, and observation methods. Third-party logistics suppliers conducted the information, logistics, and cash flow by the different deal due to the different nature of suppliers. Third-party logistics suppliers could be exhaustive on the quality management, logistics activities, interactive mode of trust mechanism, which could not only win the good reputation by the catering chefs, but the professional core competence.

Keywords: Supply Chain, Third-party logistics Service Supplier, Catering

1. Introduction

Recently, the quality of food preservation has been enhanced by the frozen technology and the developed transportation. The demand for refrigeration facilities are even more urgent due to the traditional catering service is held outdoors. With the continuous development of cryogenic equipment, from refrigerator to frozen car, not only the preservation of food got more secure, but the availability of fresh foods throughout the country [1]., and this was attributed to the development of low-temperature technology and transportation [2].
Comparing the past time, catering chefs needed to rush around the procurement of foods, now, catering chefs obtained simply the food by line, telephone, fax, fill orders, etc., telling third-party logistics suppliers and the needed foods will be delivered to the designated location which could save a lot of procurement time. Fresh foods are made easier to obtain and there are more changes in the dishes with the development of the third-party logistics supply. In this case study, Catering Chef Lee (hereinafter refers to as Chef Lee), in Pingtung County, Taiwan, has been engaged in catering service for more than 40 years. And all his partners including vegetables supplier, meat supplier, and seafood supplier are referred to the third-party logistics service.

2. Literature Review

Table-keeping activities have long existed in Taiwanese society. The general discussion will be explained by the meaning of "co-food": a group of people prepare dishes together and enjoy dishes together, and enhance the relationship between family members and friends by sharing food, or increase popularity and popularity. Actually, "Do table" was not only to serve the good dishes for the guests, but contained many taboos and etiquette. Different dishes and different etiquette are for different theme. Each catering service had its certain rules including tableware, tables and chairs furnishings etc. Even the purpose of catering service can be seen from the menu. And the owner did not require to pay the rental space cost except the catering expense [3].

American Logistics Management Association (1998) proposed that logistics was a part of the supply chain process which focused on items, services, and the related information. In other words, logistics refers to the effective circulation, storage planning, execution, and management from starting to consumption to meet customer's requirements. Taiwan Association of Logistics Management (TALM, 1996) considered that logistics as an entity's physical circulation activities. During the process of circulation, it could create value to meet the needs of customers through the effective combination of transportation, storage, packaging, distribution, and information such as from supply to production facility, then to distribution facilities, and finally to the sales market. The different logistics network was provided through the establishing international logistics service system which including intra-regional and inter-regional maritime, land and air transport and warehousing complex system. And gradually complete international logistics network provided a more diversified international logistics service options [4]. According to [5]., the so-called logistics outsourcing referred to the business owners who organized the operation of logistics operations within the organization and appointed to the third-party logistics companies for planning and service which encompassed the warehouses of the third-party logistics supplier, used mass or contractual transport, and provided the business owner with the best logistics supplier to fulfill their needs. To effectively use the limited resources was the main reason for logistics outsourcing, the third-party logistics supplier would take all the responsibility of transportation, warehousing, or other logistics activities of the company. In addition, the third-party logistics supplier made their efficient management via the professional logistics solutions, the developed transport networks, as well as a variety of information technology. [6].argued that third-party logistics was mainly a collection of all important logistics services including transportation, warehousing, packaging, material management, and various auxiliary management [7]. Therefore, it can be argued that advancements in the field would benefit from the development of a systematized conceptual base consisting of common definitions of important constructs and variables.

3. Research Method

Triangulation test refers to the same conclusion, using different methods, in different situations and time, to test different people in the sample, the purpose is to carry out the conclusions that have been established through as many channels as possible. Test to obtain the maximum degree of truth of the conclusion. In qualitative research, the most typical way to conduct correlation tests is to combine both interviews and observations [8]. Observations allow us to see the behavior of the researcher, and interviews can help us understand the motivations of their behavior. By comparing the results of the interviews, we can test the relationship between what the researcher said and what he did. This study uses semi-structured interview studies through in-depth interviews, case studies, observations, etc., plus the multiple views of the literature-supported triangulation. The research framework was shown as Figure 1. Based on logistics activities between catering service and third-party logistics supply such as logistics, money flow, and information flow as well. Meanwhile, study the supply process between the two sides and the third-party logistics supply concerning on warehouse management of goods（such as inventory control, product management, packaging, and inventory management）, and quality management (good, save etc.).

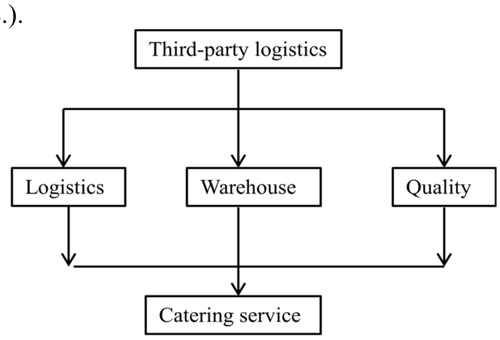

Figure 1. Research framework

4. Data Analysis

4.1 On-site Workflow of Catering Service

This case study explored some basic information as catering for thirty tables (and a table can be seated for ten guests), will start the catering service at 12:30p.m. there are six infield workers. Usually, the working members will bring their own knives and wearing kitchen suits to collect at the scene during 5-6a.m. and Chef Lee will bring dry food to the scene. Then, all of them will begin their work such as inspect the cook tools, washing pan and bowl, and other cleaning actions. Then, wait for all the suppliers to deliver the goods to the scene. All the delivered goods must be inspected by Chef Lee personally, and any unqualified foods will be returned directly to supplier. Supplier will then replace the qualified food to the scene. Actually, it had a very low rate of return from the scene due to the food will be inspected by the supplier from the wholesale. Chef Lee always processed the vegetable first no matter which one of three suppliers came the first because seafood and meat took some time to de-ice, however, the live seafood was left aside for processing. And fruit and sweet soup were cold in the fridge, waiting for dish. Cleaning was the first step, and then drained. Cutting was responsible by the six workers, they worked together to deal with cleaning and cutting. All vegetables are required to be blanched in a pot of boiled water for a short time by Chef Lee personally, then, mushrooms, shark's fin, squid, meat, chicken, and finally seafood in order. Cold dish was followed. As for chicken soup, lobster mushroom soup, and steamed groupers were produced and insulated with the different steamers to cook at the same time. The last one was sweet soup.

4.2. Goods Quality Management and Warehousing Management of the Third-party Logistics Supply

Food can be distinguished from the appearance, shape, weight, color, smell, taste, and vacuum. Chef Lee believed that seafood was good as long as it was the living body while sent to the scene. All the fresh fish, shell, raw meat will be kept at 2-2ºC while they sent to the catering scene regardless of circulation, trafficking, or vacuum packaging. The low temperature gas storage method was the most commonly used for fresh fruits and vegetables. The three suppliers had placed their orders to their upstream suppliers after Chef Lee ordered. Based on the geographical sake, most of customers of Chef Lee were from Linbian Township, Pingtung, and all adjacent townships. The living seafood supplier, therefore, could be supplied within 1 to 2 hours. The paper orders will be transformed into electronic files by the seafood supplier after receiving the order from Chef Lee. Vegetable order was confirmed by paper list and telephone. Meat supplier made a special notebook to confirm the order details instantly. Usually, the seafood needed to be frozen under -18ºC after seafood supplier purchased from the wholesale supplier and some are stored in 5-0ºC. Living food must be delivered to catering scene within one hour after purchasing from wholesale supplier. As for meat, all the meat must be frozen under at -18ºC according to the various parts of meat. Fruit and vegetable supplier provided an on-site delivery of their items to the designated scene after purchasing from whole market at the same day.

4.3 Logistics Activities

Chef Lee needed to give the exact orders to all suppliers five days in advance. This could give enough time for the three suppliers to place orders to their upstream suppliers. For example, seafood for 3 days, meat for 1 day, however, vegetable and fruit are at the same day. Under such arrangement, the error rate for the delivery time of the above suppliers, therefore, was very low. As for the inspection, seafood could be checked by its color, and touched the body by hand if was still alive or not. Meat could be viewed by its color, and touched by hand to make sure there was no sticky feeling. Vegetable could be checked by the fresh appearance or use hand-flick to the surface for testing solid sense. Seafood supplier delivered the frozen and live food through freezer at below 5℃ to the catering scene. Meat supplier used refrigerated trucks delivered the meat to the scene. Vegetable supplier trucked vegetable to the scene at room temperature. As for the price, all the product prices were based on the price of middle-wholesale. Chef Lee paid to all the suppliers by cash. The delivery of third-party logistics service saved a lot of time for catering service businessmen, and enhanced the quality of food management.

5. Conclusions and Recommendations

The finding results showed that both the third-party logistics suppliers and Chef Lee can’t be sloppy regarding the quality requirements and inspection details of food. Only under this condition, then can maintain the food safety for guests. The error rate was very low for all the suppliers, and they asked themselves to keep independent quality management to the food which, therefore, reduced the quality and quantity of inspection, Chef Lee could focus on his cuisine of cooking. The ingredients are shipped from the third-party logistics service to the catering scene. And all kinds of food packaging was to protect the product to avoid being contaminated, and facilitate the handling of warehousing to ensure the correctness of the quantity of food, the quality, the safety of work, and timely supply to the designated place.

The results also found that the logistics center has the function to short the upstream and downstream industry on circulation process in the vertical integration of production and marketing, which has the intermediary function could reduce the production and marketing gap, but also for the horizontal relationship between the same industry, and the different industry exchange and integration support, it has become a pivotal player in the modernization path revolution. In addition, the responsibility attribution would transfer from the supplier to Chef Lee when all the logistics supplier and Chef Lee had completed the inspection. Especially the double quality requirements, from quality requirement of the third-party logistics supplier to quality requirement of Chef Lee, were the long-term core competence for catering service career.

References

1. Kuo, J. C. & Chung, C. C. (2006). Cool storage type low temperature home delivery system. *China Hydropower Refrigeration Air Conditioning Monthly*. April, 1-10.
2. Chen, K. H. & Huang, D. H. (2011). Eat, Eat Well, Eat Cleverly, and Eat Healthfully-Study on the Development of Menu Items in Taiwanese Banto. *Journal of Hospitality and Truism*. 8(2), 97-126.
3. Lin, X. Y. (2013). *Taiwan's table culture*. Ph.D. Thesis, Department of History, College of Liberal Arts, China University of Culture, Taipei.
4. Su, H. I. (2012). *Supply Chain Management*. Taipei, Taiwan: Zhisheng Culture Business Co., Ltd.
5. Yeh, C. C. & Lai, M. C. (2005). Logistics and supply chain management. Taipei, Taiwan: San Min Book Co., Ltd.
6. Liu, W. L. (2008). *Supply Chain Management*. Taipei, Taiwan: Yufeng Information Co., Ltd.
7. Marasco, A. (2008). Third-party logistics: A literature review. *International journal Production Economics.* 113, 127–147.
8. Chen, H. M. (2011). *Social science qualitative research.* Wunan Book Publishing Co., Ltd.

Pedal Scale Control Device for Weighing Food Ingredients or Chemical Materials

Shang-Hui Li, Shu-Fang Hsu, Yi-Tai Shang, Kuan-Ying Chen
Department of Food and Beverage Management, Far East University, Taiwan (R.O.C.)
E-mail:a0956358700@gmail.com

Abstract

Safety and hygiene is one of the most important elements when weighing ingredients or chemical materials. It may cause cross-contamination when preparing them if the operators conduct the scale button and hold the food ingredients or chemical materials by using both hands. The invention relates to a pedal scale control device comprising a scale body and a foot unit. The wireless signal on the foot unit can be connected to the scale body to zero and buckle the function without using of both hands. This invention has obtained Taiwan's invention patent, which is more hygienic and safety for the users when weighing the food ingredients or chemical materials.

Keywords: Scale, Invention, Patent

1. Introduction

It is often necessary to use scales to weigh the raw materials when making baked ingredients, preparing pharmaceuticals or chemicals material etc., so that they can be made into uniform specifications. However, it is necessary to repeatedly use the finger to touch the button when using the electronic scale which is not only easy to have health concerns, but also may cause pollution, especially in pharmaceutical or chemical raw materials. And the study found a way to solve this problem. The study designed for using the pedal control device to scale food ingredients, chemical, medical or pharmaceutical materials which will be enable to measure the weight without the hands to maintain cleanliness, safety and hygiene. This device has obtained the patent certificate No. I588458 from Taiwan, and hopes it will give some contribution to the weighing of raw materials in various industries such as food, chemical and pharmaceutical fields.

2. Pre-case Discussion

Scales are closely related to the daily lives of consumers. It will be used in various fields such as warehousing, freight, chemical, pharmaceutical and food etc. Usually, the scale is one of the most important elements as the basis for pricing in market transaction, and it is also announced as the statutory weighing instrument that should be verified [1]. There are many types of scales, and the electronic scales is the most commonly used one in market, which measures the weight of the object by the gravity of the object, saving manpower and time. Furthermore, the common electronic scales are divided into electronic counting scales, electronic weighing scales, electronic pricing scales, electronic balances, electronic crane scales, electronic medical scales and electronic small scales [2]. The weighing of different electronic scales is different. For example, electronic scales need precise weighing. Usually, the sensitivity is 1 to 5 digits (0.1g-0.01mg), and the maximum weighing is less than 60kg. However, the electronic platform scales are used for weighing large goods, and range from 500kg to 10 tons. In general, electronic scales are equipped with some functions such as returning to zero which could measure the net weight of articles for the users. This function is important for referring to recipes or cooking etc.

In other word, the weight required for various materials are generally marked whether it is in chemical, pharmaceutical or recipe formula. It is often necessary

to continuously use the weight-reduction function in the process of blending materials. According to the users experience, when the user prepares the materials with both hands, the electronic scale must be touched by the user's hand, which will lead the operation interface of the electronic scale often contaminates the material. Moreover, the operation interface of the electronic scale often has the pollution of greasy and fouling if the cleaning is not performed after repeated using. It is inevitable that there is a concern about hygiene and safety. One of similar patents No. 326771 "Electronic Scales Improved Structure" announced by Intellectual Property Office, Ministry of Economic Affairs, Taiwan, 2015[3] which could pull out the display platform independently, and is convenient for transaction use.
However, the operation interface is easy to be dirty, and the interface is damaged by long-term use when used for the raw materials of the food. And sometimes it is not operate for one person. When used repeatedly, it may cause health and safety concerns. Therefore, a pedal-type scale control device was proposed through continuous experiment and research to improve the above-mentioned defects.

3. System Design

The pedal scale control device comprises a scale body, which divided into a processing unit and a return-to-zero module, and a pedal unit. The pedal unit is separated from the scale body. The pedal unit is provided with a tread portion, which could connect its signal to the scale body to be zeroed. And a radio frequency (RF) connects between the scale body and the pedal section, which has high-frequency electromagnetic waves with long-distance transmission capability, and radio frequency technology is widely used in the field of wireless communication (Fig.1).
In other words, the pedaling transmits a signal to the scale body, and a wireless transmission interface signal A is set on the scale body, and the A is connected to the zero return module for zeroing or deduction. The pedal section also has another wireless transmission interface signal B, which connects the pedal section and A, to transmit the pedal signal to the zeroing module. The Pedal Scale Flow Chart for the pedal scale control device is shown as Figure 2.

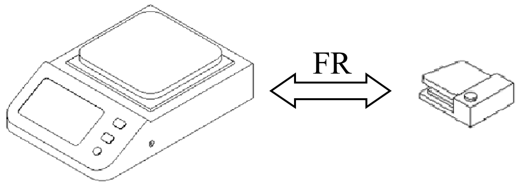

Figure 1 System architecture diagram

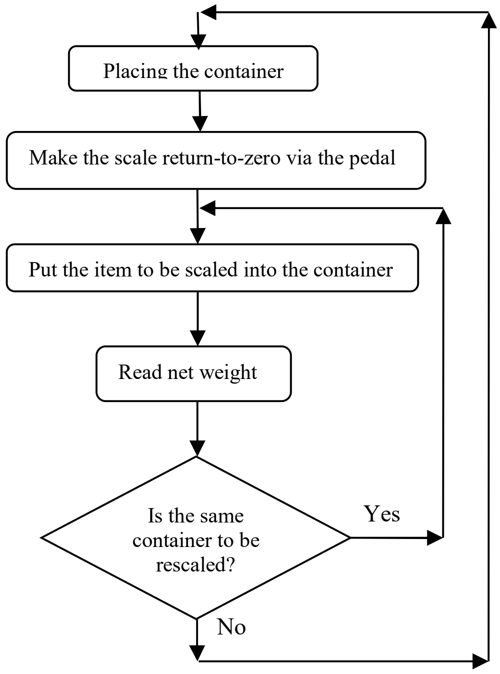

Figure 2. Pedal Scale Flow Chart

The pedal scale control device was subjected to actual simulation experiments. The actual finished product was shown as Figure 3 and the actual operation was shown as Figure 4. The study showed that the expected results can be achieved. Described as follows:

(1).Obviously, the return-to-zero function could be operated by the pedal scale control device, and the operator can empty the hands to prepare the ingredients without touching the scale body, which is more hygienic and clean when cooking.

(2).The operation mode is more intuitive and simpler than returning to zero or weighing by hands, and the process of deduction is smoother and faster.

(3).The scale body also has an operation button, and the pedal unit can be removed, and the scale body is used as a general scale.

(4).Connect the scale body and the pedal unit by wireless to avoid possible interference such as wire interference and easy tripping during using.

Figure 3. Actual operation diagram of the pedal scale control unit

4. Results and Discussion

The results of this study propose an isolation system between the pedal control device and the scale, which can effectively isolate the safety distance between the scale and the sanitary. This design has the following features：

(1). The design utilizes the wireless method to improve the traditional electronic scales operation which needs to use both hands to repeatedly touch the screen interface, and thus obtained the certificate of Taiwan invention patent No. I588458.

(2). The pedal scale control device has been turned into a specific product from the concept, and is currently seeking cooperation with manufacturers, and it is expected to commercialize the product in the future.

(3). The pedal scale control device can be used in chemical, medical, food industry.

(4). This design allows the operator to avoid touching the scale body and reduce cross-contamination. Obviously, it makes the scale body more hygienic, clean and safe, and more secure for consumers.

Figure 4. Actual operation diagram of the pedal scale control unit

5. Reference

[1]Bureau of Standards, Metrology & Inspection, Ministry of Economic Affairs, Taiwan.(2018). “Weights and Measures”, July 30, 2018 from https://www.bsmi.gov.tw/bsmiGIP/wSite/ct?xItem=36623&ctNode=4077&mp=1

[2]T-Scale Company limited. (2018). “Electronic Scales” July 25, 2018 from http://www.tscale.com.tw/index.php?do=product_details&id=174 .

[3]Intellectual Property Office, Ministry of Economic Affairs, Taiwan. (2015). Taiwan Patent Search System. May 18, 2015 from https://twpat7.tipo.gov.tw/tipotwoc/tipotwkm.

Convolution Neural Network Based Fault Diagnosis of Induction Motor

Jong-Hyun Lee
School of Electronics Engineering Kyungpook National University
Daegu, Korea

In-Soo Lee
School of Electronics Engineering Kyungpook National University
Daegu, Korea
E-mail: whdugs8428@knu.ac.kr, insoolee@knu.ac.kr

Abstract

Induction motors are one of the most important components for machine and industrial equipment in modern industrial applications. Therefore, it is necessary to develop a fault diagnosis system that detects the operating condition and fault of the induction motor early. This paper presents a induction motor fault diagnosis system using a CNN (Convolution Neural Network) model. In the proposed method, the fault diagnosis of the induction motor is performed by using the vibration signal data obtained from the induction motor experiment environment as the input value of the convolution neural network model. And then the fault diagnosis was made using convolution neural network. In this paper, fault diagnosis of normal state, rotor and bearing fault of induction motor is performed. From the experimental results, it is confirmed that the proposed method is suitable for diagnosis of rotor and bearing fault of induction motor.

Keywords: Induction motor, Convolution neural network, Rotor fault, Bearing fault, Fault diagnosis system

1. Introduction

Induction motors are one of the most important components for driving DC motors, rectifiers and DC motor systems and industrial equipment. However, the shutdown of the plant due to an unexpected induction motor fault results in significant economic losses. Therefore, it is necessary to develop a fault diagnosis system that detects the operating condition and fault of the induction motor early.[1]

Fault diagnosis is to detect faults in the system and to classify faults, which can be largely classified into model-based methods and non-model-based methods. In the model-based method, the fault of the system is diagnosed based on the mathematical model of the system, but it is not easy to obtain an accurate mathematical model due to the nonlinearity of the system. Non-model-based methods include fault diagnosis based on measurements, experience, or physical reviews in the target system, and thresholding, expert system techniques, and neural networks.[2]

In particular, neural networks have advantages such as parallel processing ability, nonlinear function description and learning function, and there have been many studies to use neural network for trouble diagnosis based on this. However, the structure of the neural network model of the perfect connection layer can't learn the invariant property. This leads to a problem in that it can't be learned by extracting effective features from periodic vibration signals.[3]

In this paper, CNN model with local connectivity is used for fault diagnosis. And the vibration signals of three states normal, rotor fault and bearing fault are obtained from the induction motor, and the vibration signals are used for fault classification. The performances of the proposed fault diagnosis method are verified through the experiment and simulation.

2. Experimental environment for fault diagnosis of induction motor

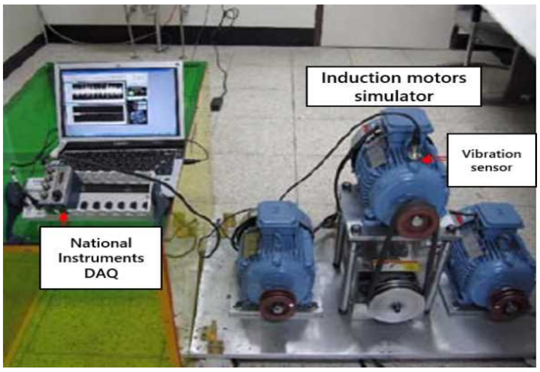

Fig. 1. Experimental set up.

For the fault diagnosis of the induction motor, a simulator was constructed as three three-phase induction motors that caused normal, rotor fault, and bearing fault as shown in Fig. 1. The induction motor located at the center is in the normal state. The induction motor located on the left side of the induction motor is in the state of rotor fault, and the induction motor located on the right side is in the state of fault of the bearing. We acquired the vibration data from induction motor by using NI9234 and vibration sensor.

(a) Rotor fault (b) Bearing fault

Fig. 2. Fault types of induction motor.

As shown in Fig. 2, there are two types of faults occurring in induction motors: rotor fault and bearing fault. As shown in Fig. 2 (a), the rotor bar of the induction motor was punctured by a drill, and the bearing was worn by putting powder into the bearing as shown in Fig. 2 (b).

3. The proposed fault diagnosis method for induction motor

3.1. *CNN based fault diagnosis system*

The proposed fault diagnosis system consists of a vibration sensor part for measuring the vibration signal generated by the induction motor as shown in Fig. 3, a data collection part for digitizing and storing the vibration signal obtained from the vibration sensor, And a Convolution Neural Network (CNN) based fault classification unit which classifies the types of faults generated in the induction motor.

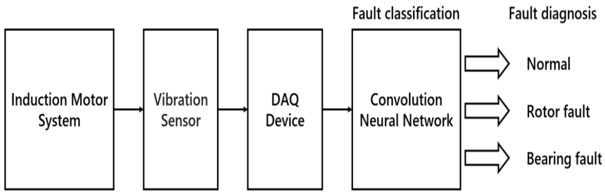

Fig. 3. Structure of the proposed fault diagnosis method.

3.2. *Convolution neural network*

Convolution neural network (CNN) is a model that integrates feature extraction and classification, which are separate from existing pattern recognition methods. CNN is basically composed of a plurality of convolution layer and a subsampling layer. [4] The structure of the CNN used in the induction motor fault system consists of one input layer, two convolution layers, two max polling layers and one fully connected layer and three output layers as shown in Fig. 4.

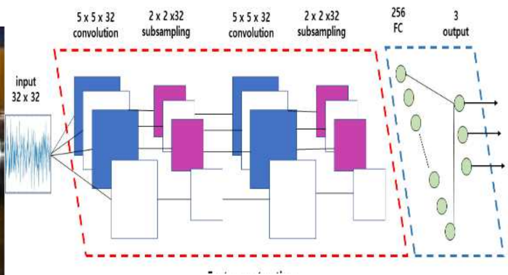

Fig. 4. Structure of the proposed CNN model.

The convolution layer extracts features from the input data. The convolution layer consists of a filter that extracts features. The filter detects the characteristics of the data and maps the detected features to the feature map. The extracted feature map applies the activation function. In this paper, Relu function is used as an activation function.[5]

The subsampling layer performs the process of reducing the dimension of the extracted feature map. There are various techniques for pooling. In this paper, It use the max pooling method which extracts the maximum value from the feature map. Using the max pooling technique reduces the size of the entire data, which reduces the amount of computation and extracts only the necessary data. [6]

In CNN, when the convolution layer and the max pooling layer are repeated, only the main features are extracted, and the extracted characteristics are transmitted to the Fully connected Layer. Since the convolution layer and the max pooling layer have two-dimensional data, they are transformed into a one-dimensional layer for transmission to the fully connected layer and then transferred to the output layer.

Softmax function was used for the output layer. softmax is used to transform the class classification problem, that is, the output from the previous layer, into the probability of each state when solving the state classification problem. Take the exponent on each output and divide by the normalization constant so that the sum is 1.

4. Simulation and Results

The simulation environment was implemented using Python 3.5 and Keras library in Windows 10 OS. The CNN model used in the simulation consists of an input layer with 1024 nodes, a first convolution layer and a max pooling layer, a second convolution layer and a max pooling layer, and finally, it consists of a fully connected Layer with 256 nodes and an output layer with 3 nodes. The two convolution layers and the fully connected layer use the activation function ReLU and the output layer uses the softmax function.

In order to test the performance of the proposed induction motor fault system, vibration signal data were acquired using a vibration sensor by artificially generating normal, rotor fault, and bearing fault in the experimental apparatus shown in Fig. 5. The vibration signal data can be obtained with 1024 data per 0.1 second. As a result, 1024 pieces of data are used as a model input. The data of the three states obtained from the experimental apparatus are shown in Fig. 5 (a), (b) and (c).

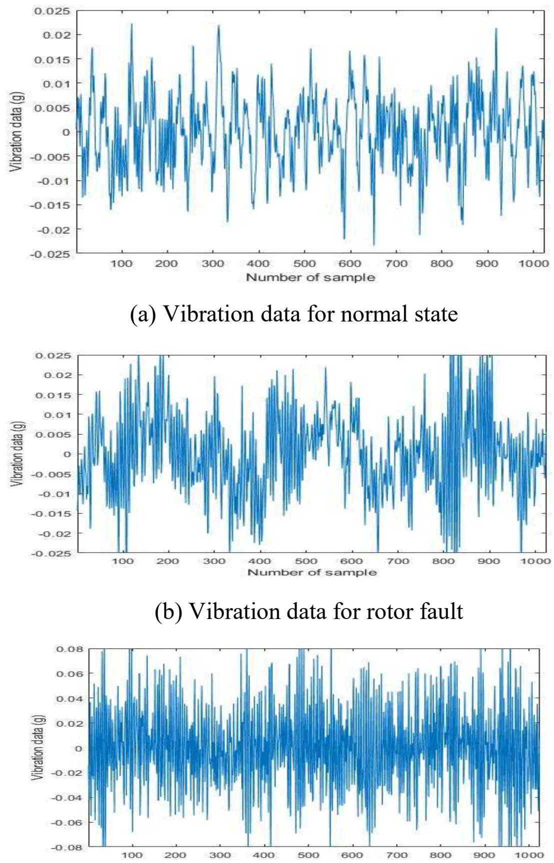

(a) Vibration data for normal state

(b) Vibration data for rotor fault

(c) Vibration data for bearing fault

Fig. 5. experimental data.

The data used for learning and verification data are data of normal, rotor fault and bearing fault state acquired from the experimental apparatus as shown in Table 1. For learning, 200 pairs of each state, that is, a total of 614,400 data, are used. The vibration data used in the learning was used without the frequency domain transformation. The epoch is 30. In the case of the test, data of 100 pairs for each state, that is, a total of 307,200 samples, were used. The results of the test are shown in Fig. 6, which shows two cases of fault diagnosis when the inverter changes from the normal state to the rotor fault state and when the inverter changes from the normal state to the bearing fault state. In Fig. 6, the x-axis represents the number of vibration data, and the y-axis represents the diagnostic value of the model. If classification result is 1, it is in the normal state. If 2 is output, it is the rotor fault state. If 3 is output, it is the bearing fault state.

Fig. 6 (a) shows the simulation result when the rotor is changed from the normal state to the rotor fault state. It can be confirmed that the model correctly determines the rotor fault state when the vibration signal inputted at the 102,400 samples changes to the rotor fault state. Fig. 6 (b) shows the simulation results when the normal state changes to the bearing fault state. It can be confirmed that the model accurately determines the fault state of the bearing when the vibration signal inputted at 102,400 samples changes into the bearing fault state.

Table 1. The data pares for simulation.

Induction motor state	Number of training data	Number of test data
Normal	204,800	102,400
Rotor fault	204,800	102,400
Bearing fault	204,800	102,400
Total	614,000	307,200

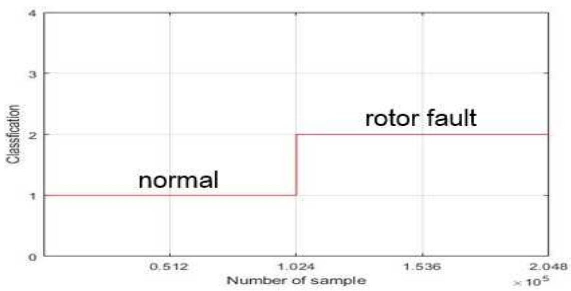

(a) Result of rotor fault diagnosis

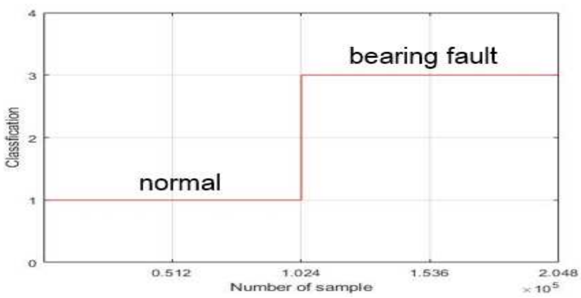

(b) Result of bearing fault diagnosis

Fig. 6. Result of the Induction motor fault diagnosis.

5. Acknowledgment

This study was supported by the BK21 Plus project funded by the Ministry of Education, Korea (21A20131600011).

6. Conclusion

In this paper, an induction motor fault diagnosis system using CNN was proposed. In the proposed method, the fault diagnosis of the induction motor was performed by using the data obtained from the simulator as the input of CNN. As a result of the simulation, it was confirmed that the state of the motor was completely diagnosed by the motor data obtained from the simulator and the fault diagnosis can be performed without frequency domain transform process. The further study will need to apply the proposed method to the industrial equipment.

References

1. In Soo Lee, “Fault Diagnosis System Development of Induction Motors Using Discrete Wavelet Transform and Neural Network”, Journal of Korean Institute of Information Technology, vol. 9, no. 8, pp. 53-61, 2011.
2. In Soo Lee, “Fault Diagnosis of Induction Motors Using Discrete Wavelet Transform and Artificial Neural Network”, HCI International 2011, Florida, USA, 9-14 July 2011.
3. In Soo Lee, "Diagnostic system development for state monitoring of induction motor and oil level in press process system", Journal of Fuzzy Logic and Intelligent Systems, vol. 19, no. 5, 2009.
4. Abien Fred Agarap, “An Architecture Combining Convolutional Neural Network (CNN) and Support Vector Machine (SVM) for Image Classification”, arXiv preprint arXiv:1712.03541, 2017
5. Wenjun Sun, Rui Zhao, Ruqiang Yan, Siyu Shao, Xuefeng Chen, “Convolutional Discriminative Feature Learning for Induction Motor Fault Diagnosis”, IEEE Transactions on Industrial Informatics, vol.13, no. 3, June 2017.
6. Rui Zha, Ruqiang Yan, Zhenghua Chen, Kezhi Mao, Peng Wang, Robert X.Gaoc, “Mechanical Systems and Signal Processing”, Mechanical Systems and Signal Processing vol. 115, pp. 213–237, January 2019.

Analysis of Value Chain on Food and Beverage Micro-enterprises: Mobile Diner as Example

Shu-Fang Hsu
Department of Food and Beverage Management, Far East University, Taiwan (R.O.C.)
E-mail:h99582004@gmail.com

Shang-Hui Li
Department of Food and Beverage Management, Far East University, Taiwan (R.O.C.)

Abstract

This study was based on the theory of value chain proposed by Porter, 1985, in conjunction with the mobile diner industry from the value activities created in the value chain. The main activity was to analyze the competitive advantage of the mobile diner and the added value to meet customers' need. In this study, the Delphi method was used, and then conducted with interview and observation method on 10 homogeneous mobile diners to gain an in-depth understanding of the development and current situation in southern Taiwan. Exploring their competitiveness, and discovering that the businessmen purchased the necessary food by themselves, which could ensure safety. In terms of marketing and sales, due to the mobility and easy acceptance of customization, the relative value of products and services are relatively improved. This study could provide a practical reference for micro-entrepreneurs who want to invest in food and beverage in the future.

Keywords: Supply Chain, Third-party logistics Service Supplier, Catering

1. Introduction

Most micro-entrepreneurs used vans to become as the mobile diner when Taiwan began to introduce the concept of mobile dining cars. However, it was illegal to convert the regular car into a mobile diner and ran it on the road. It would be taken as a general street vendor to drive away by police, unlike the restaurant which has a general location, if it parked for a long time. In recent years, Taiwan's traffic laws have been revised to allow the mobile diner owners (hereinafter as "owner"), to have more room to operate. Entrepreneurship itself requires a lot of capital and must bear a lot of risks. Every entrepreneur wants to create the greatest economic benefits with the least amount of capital. The mobile diner can move freely, and also drive to crowded places to do business opportunities with high mobility, and save store rent. In recent years, attention has been paid to the coffee mobile diners in Taiwan. Gradually, other types of mobile diners have begun to appear, such as selling coffee, sandwiches, Japanese ramen or American meals. The overall value presented by the value chain is made up of various value activities and margins. Value chains are all kinds of material and technical specific activities carried out by enterprises, and also the basis for enterprises to create valuable products for customers. The purpose of this study was to find out the value in the main activities of the mobile diners in value chain, and to (1) to explore the logistics and production operation management of the mobile diner. (2) to explore the shipping logistics, marketing and service value of the mobile diner.

2. Literature Review

In recent years, Taiwan has promoted the "Micro-Startup Phoenix Project". The Project was to improve the labor force participation rate of Taiwan female labors, middle-aged nationals, outlying island residents, and to build a friendly environment for entrepreneurship. Moreover, assist in the development of micro-enterprises and create employment opportunities. Provide entrepreneurial loan interest subsidy, entrepreneurial companionship service and financing credit guarantee project [1]. For this reason, 22 classes of "Entrepreneurship and Development Classes" and 15 classes of "Entrepreneurship Advanced Classes" had been launched throughout Taiwan in 2016. The classes provided the necessary professional knowledge of entrepreneurship, upgraded the credit rate of youth entrepreneurial loans, and implementing youth entrepreneurship to enhance the policy goal of youth entrepreneurship [2]. Many business newcomers were eager to run their mobile diners, and regarded it as a way to realize their own value, and then they were willing to dedicate themselves to it which was able the mobile diner to achieve their goal of self-realization.

The value chain was proposed by Michael Porter in 1985. It needs to resolve the business process of the enterprise into a series of value creation processes if a company wants to develop its unique competitive advantage or create higher added value for shareholders, and the conjunction of this value process is the value chain. If the value of the product or service that the company holds is higher than all the costs it uses to create the product, then the company is a profitable company. In other words, all the various "value activities" and "profits" constitute the overall value of the value chain [3].

Enterprises can differentiate themselves from others through each link in the value chain. The construction and purchase as the underlying value chain model combined with marketing effectiveness and demand supply chain management, thereby enhancing the overall competitive advantage [4]. It mentioned that the value created by a company for its customers may come from many aspects, such as manufacturing, research and development, logistics, branding, advertising or access etc. The companies can attach all aspects of their advantages to products or services through a variety of potential sources of value, and differentiate themselves from others to form a unique competitive advantage.

3. Research Method

In this study, the Delphi Method was used to design and interview the questionnaires, and the data was collected and collated by the re-validation method. Triangulation was used to strengthen the theoretical basis and improve the intrinsic validity of the research in the process of data collection and analysis. Triangulation test refers to the same conclusion, using different methods, in different situations and time, to test different people in the sample, the purpose is to carry out the conclusions that have been established through as many channels as possible. Test to obtain the maximum degree of truth of the conclusion. In qualitative research, the most typical way to conduct correlation tests is to combine both interviews and observations [5]. In detail, methods triangulation, data triangulation, and analyst triangulation were used to improve the reliability and objectivity of the research data in the process of collection and analysis. In the method of triangulation, various data collection methods are used included in-depth interviews with experts, special lecture speeches, expert TV interview records, written documents and other sources of information to enhance integrity [6]. There were 10 mobile diners for this studies coded A, B, C, D, E, F, G, H, I, J respectively. Because value creation is not a single activity that can be formed, it must be complemented by relevant departments and closely related to each other. How to pursue production innovation and marketing sales is the target of this study.

During the interview, there were 10 mobile dining cars. Each interviewee had a different personality during the interview. For example, one of the respondents was more conservative, and such respondents were less willing to provide information and more likely to refuse to accept and answer. Part of the problem, when faced with private issues, usually do not want to answer, even if the respondent is willing to provide information, may not be able to provide the correct information The research framework was shown as Figure 1.

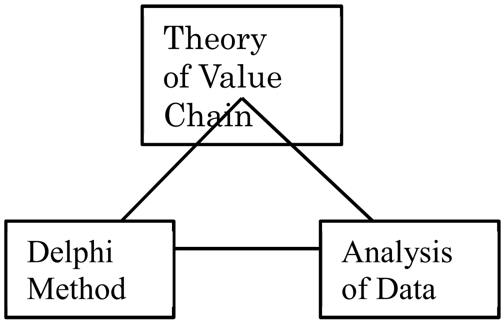

Figure 1. Research framework

4. Data Analysis

4.1 General Review

The mobile diners need to overcome various tasks and difficulties, such as weather factors, storage space, and the single nature of the goods, which will affect the business income. In this study, there were four mobile diners sold chicken cakes, two offered sandwiches, and four others provided simple meals. As for gender, 4 were female and 6 for male. Half a year was the shortest period for running diner business, and the longest was 8 years. Most owners graduated from high school and college, and two of them graduated from food-related department. Most of the mobile diners are modified their car body based on Varica and Veryca. The high mobility were the mainly considered by most of owners, which is lower than the operating cost of the store. As for venture capital, 8 were below NT$500,000, and the other two were between NT$ half million to 1 million. Among these owners, 6 received the traffic ticket. And H owner rent the space for his business, and B and E paid particular attention to the annual activities of department stores because of being invited, there was no traffic ticket problem.

Among these operators, a total of 6 received a fine, and the remaining four did not receive a ticket; the H operator chose to operate in the leased area, and the B and E operators were mainly located in the department store activities, due to the invitation, No ticket issue. Among the 10 mobile diners, only E and I operators have not returned to the book, 8 operators have graduated from the catering-related departments, and the other two operators have not contacted the catering-related departments, and four of them have not engaged in catering-related industries. . Due to the long working hours of the business car, a total of 9 are full-time, only the I business is semi-retired, and the work attitude is more casual.

4.2. Feed Logistics and Production Operations

6 of the 10 owners purchased the fresh ingredients by themselves except A owner. The reason for A was that the mass fresh ingredients were not easy to preserve. In addition, there was no bargaining space due to the frequent purchase of small number ingredients. Most owners purchased their raw ingredients from food stores or suppliers, which are more expensive than supermarket. J owner bought his raw ingredients from traditional market because he needed a variety of fresh food. In terms of purchasing time, most owners chose to buy before business, mostly in the morning. All owners separated food ingredients between business and household to ensure hygiene and quality. 7 owners changed the new flavors within one month. A owner showed his new taste in half a year, A considered that he was no time to develop the new taste because of his long business hours. As for B, E, F, J owners, they introduced a new product at least one month. Of 6 of 10 diner cars were equipped with refrigeration equipment, and the rest were not refrigerated, but with the related equipment for storing raw ingredients and semi-finished products. Most of the owners prepared their related ingredients before the business except F, and F owner did his work before and after the business since F owner's prepared materials was close to the finished products which could be prepared and stored after the business. Most of the mobile diner sold the simple products with a short preparing time. E, F, and I owners did their food with more cumbersome process. Most of the owners ran their business within 6 hours daily. A and D owners divided their business time and locations into two sections, so their business hours are longer than others.

The mobile diner has a low investment amount and is easy to get started. Because of its small scale, it can maintain flexible and adaptable environment and can be quickly reformed. The dining car needs to introduce new tastes to attract consumers from time to time. Competitive, but there may be difficulties in being imitated by the industry or not thinking about new ideas.

4.3 Marketing, Sales and Service

9 mobile diners operated on social networking or professionally marketed via fans except H. Because H has done his business for 10 years with the simple products and easy to produce, and he has the regular customers. The A, B, C and D owners were different from the traditional chicken cake. Their price was higher than the traditional ones through diversified the appearance, ingredients and stuffing. B was the most famous ones with the high price because the ingredients he used in the stuffing were special and innovative. Seven owners often showed their new products, seasonal and daily limited products, and used hunger marketing techniques to attract customers' attention except H, I, and J, they offered the regular products. All owners accepted customized services and were willing to accept the return and exchange products. However, G owner, without customized services, can be presented to the customers only after heating because the goods were already semi-finished products.

After the modified diner has a unique style, it can quickly attract the attention of consumers, so there is no need for DM and advertising, and nowadays the network is more developed to increase exposure. The mobile dining car has a single product type and a fast meal speed, but the customer selection will be limited. The 10 mobile diner visited by the group were all prepared after the materials were prepared. All the operations were completed by the operators themselves. The front-end operations of the mobile dining cars were not shorter than the general restaurant preparation time. As [7] puts forward the view of Taiwanese service, the customization of Taiwanese service is not only for high-priced products, but also for the top-level customer, but for ordinary products, it can be tailored to customers. The dining car operator is also using this concept regardless of the price level. And the action dining car is less rent-free, even if the ticket is received, it is cheaper than the store rent.

5. Conclusions and Recommendations

It is known from the conclusion of this study that the weather factors are uncontrollable. When the rain is rainy, the shelter can be sheltered from the rain, but the operators can change their attitudes and find ways to deal with them. Furthermore, if you want to move the system flow of the storefront into the dining car, you will not be able to fully utilize the integrity of the process and finished product due to insufficient space for the mobile car.

Mobile diner owners must face the pressure of real losses while realizing self-worth. It’s impossible to go all the way on the road to entrepreneurship, and there will be an off-season time in the face of this business. If there are no regular customers, the owners must adjust their mood at any time, optimistically face and maintain the initial intention of starting-up a business in addition to the daily pressure. However, the mobile diners have a low amount of capital with high mobility and free business hours. The owners can choose the most appropriate time and place for sale according to their product category and customer group. It is also relatively easy to change the business location.

This study results showed that “chicken cake” is a suitable choice for micro-enterprise beginners because “chicken cake” has traditional characteristics, an easy way to make, and with a wide range of consumer groups. The cost waste will not be occurred due to the product can be produced and sold out on the same day. Therefore, the maximum benefit can be obtained in the shortest time with the least cost.

References

1. Micro-Startup Phoenix (2017). Introduction to the project. 2017 Retrieved from https://beboss.wda.gov.tw/cht/index.php?code=list&ids=262
2. Implementation Notes for the 105-Year Government Project Plan (2016). Taiwan Youth Entrepreneur Association. 2017 Retrieved from http://www.careernet.org.tw/modules.php?name=web&file=project&op=105
3. Porter, M. E. (1995) The Competitive Advantage of the Inner City. *Harvard Business Review.* May-June.
4. Ssu Tu, T. H. (2011) *A new theory of strategic management-conceptual architecture and analytical methods*. Taipei, Taiwan: Zhisheng Culture Business Co., Ltd.
5. Chen, H. M. (2011). *Social science qualitative research.* Taipei, Taiwan: Wunan Book Publishing Co., Ltd.
6. Yen, C., & Lin, S. Y. (2010) A discussion of the impact of packaging design benefits on brand equity. *Journal of Design Research*.10, 71-79.
7. Shen, F. C. (2016) *Taiwan taste service: Shen Fang-Cheng leads the way.* Taipei, Taiwan: World Magazine.

Suppression of Roll Oscillation in Turning of Quadruped Robot by Asymmetric Amplification of Central Pattern Generator Output Waveform

Makoto Kitani, Ryo Asami, Noritaka Sato, and Yoshifumi Morita
Morita and Sato Laboratory, Electrical and Mechanical Engineering, Nagoya Institute of Technology,
Gokiso-cho, Showa-ku, Nagoya, Aichi, 466-8555 Japan
E-mail: m.kitani.810@nitech.jp
http://watt.web.nitech.ac.jp/index_2.html

Tomofumi Fujiwara, Takahiro Endo, and Fumitoshi Matsuno
Matsuno Laboratory, Kyoto university,
Kyoto daigaku-Katsura, Nishikyo-ku, Kyoto, 615-8530 Japan
E-mail: matsuno@me.kyoto-u.ac.jp
http://www.mechatronics.me.kyoto-u.ac.jp/index.php?ml_lang=en

Abstract

Quadruped robots experience excessive vibrations in the roll direction when turning by controlling their hip yaw joint. To overcome this problem, we proposed the asymmetric amplification of the output waveforms of central pattern generators. We implemented the proposed method on a robot by using a simulator and verified the effectiveness during the turning operation.

Keywords: CPG, quadruped robot, suppression of roll oscillation

1. Introduction

Legged robots can move on various terrain because they have several degrees of freedom. They are controlled by planning their motion based on a strict model of a robot and an environment. However, planning their motion for various environments is quite complex, and they are inefficient at moving on various terrains at high speed.

To overcome this problem, central pattern generators (CPGs) can be used. It was observed that this mechanism is related to rhythmical movements such as walking and swimming.[1,2] The CPG, an animal motion generation method, enables the motion of legged robots on various terrain by using only one algorithm because of a pull-in phenomenon.

Because of the above advantages, CPGs have been used in robots in several studies. Kimura et al. implemented the CPG on a real robot. The robot "Patrush" can walk[3] and "Tekken4" can turn[4] on rough terrain. The turning motion is realized by controlling the hip yaw joint. However, the vibrations of the robot body are large because this method uses falling in the roll direction.

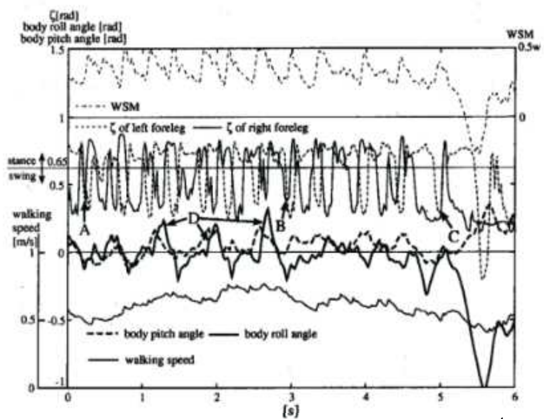

Fig. 1 Tekken body angle in turning on flat land[4 a]

In teleoperation, an operator controls a robot while watching the images from a camera mounted on the robot. Therefore, the image vibration should be small. In the experiment conducted by Kimura et al.,[4] the robot experiences vibration in the roll direction. Fig. 1[a] shows the graph of the posture of the main body and walking speed when turning on a flat ground.[4] The vertical axis of the graph corresponds to the roll angle of the robot body, the pitch angle, and the walking speed. The horizontal axis corresponds to time. According to the body roll angle (thick black line) in the graph, the robot vibrates, and it is finally overturned.

In the method proposed by Kimura et al., the camera image will vibrate making teleoperation difficult. According to the study conducted by Tsubaki,[5] if the frequency of the image vibration is the same, a larger amplitude makes the operator uncomfortable. Therefore, in teleoperation, the image vibration should be small. Fig. 2[b] illustrates a graph showing the relation between the subjective evaluation and the rotation angle for motion sickness.[6] Vibration in the roll direction is most likely to cause motion sickness at any speed of rotation.

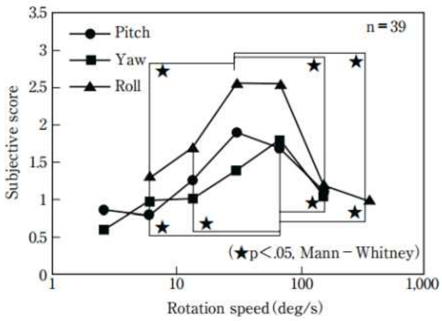

Fig. 2 Subjective evaluation value of motion sickness with respect to speed of rotation when rotation relative to yaw, pitch, and roll axis is given in video[6 b]

The vibration of the robot body causes discomfort to the operator. Therefore, the purpose of this study is to suppress roll vibration in legged robots. To suppress roll vibration, we proposed a turning method using the asymmetric amplification of the CPG output waveform. In this study, we verified the previous method[4] that uses the yaw hip joint and the proposed method by using a simulator.

2. Walking on flat ground by using CPG

2.1. *Nonlinear first-order simultaneous differential equations constituting CPG*

The basic formula of the CPG is a nonlinear first-order simultaneous differential equation shown in Eq. (1)–(3).[3]

$$\tau \dot{u}_i = -u_i - \beta v_i + \sum_{j=1}^{n} w_{ij} y_j + u_0 + Feed_i \quad (1)$$

$$\tau' \dot{v}_i = -v_i + y_i \quad (2)$$

$$y_i = max(0, u_i) \quad (3)$$

u_i, v_i, and y_i are the value, fatigue state, and output of the ith neuron, respectively, u_0 is the steady input that generates oscillation, $Feed_i$ is the feedback such as the joint angle, β is the fatigue state factor, τ and $\tau'$are the time constants of u_i and v_i, respectively, and w_{ij} is the connection factor that determines the influence of the other neurons. A pair of CPGs was mounted on each joint, and four equations were formed corresponding to each leg. This method is based on the biped walking program[7] of the CPG where the connection factor is defined as follows. The first character [R: Right, L: Left], the second character [F: Fore, H: Hind], the third character [H: Hip, K: Knee], the fourth character [E: Extensor, F: Flexor].

w_1 - Between the extensor and flexor of the same joint
w_2 - Between the right and left of the same extensor and flexor
w_3 - Between the knee and hip joints of the extensor
w_4 - Between the knee and hip joints of the flexor
w_5 - Others

Fig. 3 shows the proposed CPG configuration. We generated a waveform for walking by multiplying the difference in the output of the CPG of each extension muscle flexor and the amplification gain. The walking waveform is given by Eq. (4).

$$\theta_{joint} = K_{joint}(y_E - y_F) \quad (4)$$

θ_{joint} is the target angle of the joint, K_{joint} is the amplification gain at the joint, y_E and y_F are the CPG output values of the extensor and flexor, respectively.

[a] Adapted from "Realization of dynamic turning motion on irregular terrain of a quadruped robot "TEKKEN4" with neural oscillators" by Yasuhiro Fukuoka and Hiroshi Kimura, 2006, Journal of the Robotics Society of Japan, 72(724) p.3852, Copyright 2006 by The Japan Society of Mechanical Engineers

[b] Adapted from "Visually induced motion sickness" by Hiroyasu Ujike, 2007, Information and Television Engineers, 61(8) p.1124, Copyright 2007 by The Institute of Image Information and Television Engineers

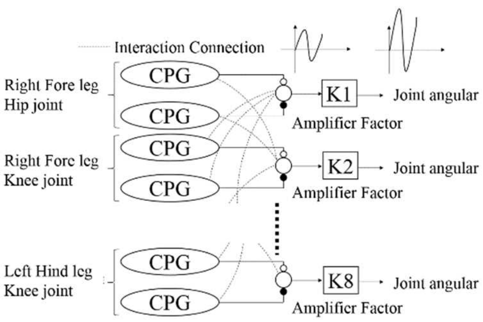

Fig. 3 Proposed CPG configuration

2.2. *Robot for experiment*

A verification robot implementing the CPG is shown in Fig. 4. We developed the robot using a simulator called Gazebo. The CPG parameters are listed in Table 1.

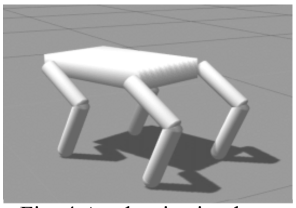

Fig. 4 A robot in simulator

3. Turning movement

3.1. *Turning method with yaw joint (conventional method)*

In the conventional method, the degree of freedom in the yaw direction is added to the hip joint. The turning radius can be changed by the angle of the yaw axis of the leg. However, in this method, the left front leg protrudes outside the robot. This increases the moment around the falling axis. We assumed that large vibrations would occur because of the increase in the moment.

3.2. *Turning method without yaw joint (proposed method)*

In order to reduce the moment around the falling axis, we suggest a change in the amplification factor of the CPG output between the left and right legs. The robot is able to turn when the amplification factor of the joint angle on the outside of the turning circle is increased. The turning radius can be changed by changing the amplification factor. Table 2 lists the amplification factors at straight and turning.

Table 1 CPG parameters

Parameter	Value	Parameter	Value
u_0	3.0	w_1	-2.0
β	2.5	w_2	-1.0
τ	0.10	w_3	-0.50
τ'	0.080	w_4	-0.30
		w_5	0

Table 2 Amplification factor

<table>
<tr><td colspan="2"></td><td colspan="2">Gain (straight)</td><td colspan="2">Gain (turn)</td></tr>
<tr><td colspan="2">Joint name</td><td>Right</td><td>Left</td><td>Right</td><td>Left</td></tr>
<tr><td colspan="2">FH</td><td>2.2</td><td>2.2</td><td>4.2</td><td>1.2</td></tr>
<tr><td colspan="2">FK</td><td>0.8</td><td>0.8</td><td>1.8</td><td>0.8</td></tr>
<tr><td>HH</td><td>2.2</td><td>2.2</td><td colspan="2">4.2</td><td>1.2</td></tr>
<tr><td>HK</td><td>0.8</td><td>0.8</td><td colspan="2">1.8</td><td>0.8</td></tr>
</table>

4. Verification

4.1. Verification condition

To verify the proposed method, we used the Gazebo simulator as described in Section 2. We made the robot walk on a flat ground using the simulator and evaluated its performance in the following sequence: adjusting the steady input to have the same turning radius, measuring the roll angle of the robot body when the robot walks on the turning trajectory, and comparing the data. The following conditions were applied so that the robot can walk on the same turning radius.

- Conventional method
  Rotation angle of front leg - 0.15 [rad]
  Stationary input - 2.7
- Proposed method
  The amplification factor of the joint angle - The "gain(turn)" column of Table 2
  Stationary input - 3.0

4.2. *Results and discussion*

Figs. 5 and 6 show the graph of the robot posture when turning in orbit shown as Fig. 7. The peak-to-peak value of the roll angle in the conventional method is -0.2 to 0.15 [rad] and that in the proposed method is -0.1 to 0.1 [rad].

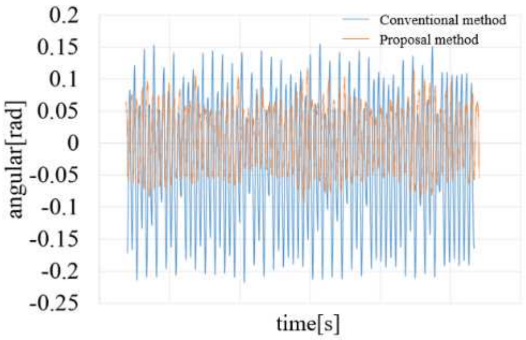

Fig. 5 Robot body roll angle

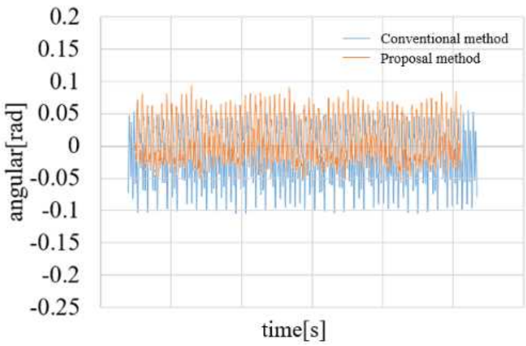

Fig. 6 Robot body pitch angle

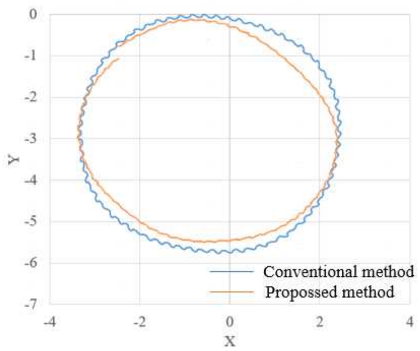

Fig. 7 Orbit of robot turning

In this study, we compared the conventional and proposed methods. As shown in the graph, the vibration in the roll direction could be suppressed. By comparing the maximum peak-to-peak value of both methods, we observed that the proposed method is able to suppress 43.7% vibration in the roll direction. Moreover, the proposed method suppressed 7.4% vibration in the pitch direction compared to the conventional method because of the suppression of vibration around the falling axis. Moreover, motion sickness can be reduced because the vibration in the roll direction can be suppressed.

5. Conclusions and future work

The purpose of this study is to suppress roll vibration in the turning motion of legged robots. We suggest a turning method that changes the amplification factor of the joint angle between the left and right legs to suppress the robot body vibration. We verified the two methods using a simulator. As a result, we succeeded in suppressing 43.7% vibration in the roll direction and 7.4% in the pitch direction when compared to the conventional method. The proposed method will reduce the motion sickness caused by the image vibration during remote operation. In the future, we will realize walking of legged robots on rough terrain by installing CPG feedback.

References

1. G. S. Stent, W. B. Jr.Kristan, W. D. Friesen, C. A. A. Ort, M. Poon and R. L. Carabrese, Neuronal generation of the leech swimming movement, *Science*, 200 (1978) 1348–1357
2. J. T. Bachanam and S. Grillner, Newly identified glutamate interneurons and their role in locomotion in lamprey spinal cord, *Science*, 236 (1987) 312–314
3. Hiroshi Kimura, Seiichi Akiyama and Kazuaki Sakurama, Dynamic walking on irregular terrain and running on flat terrain of the quadruped using neural oscillator, *Journal of the Robotics Society of Japan*, 16(8) (1998) 1138–1145
4. Yasuhiro Fukuoka and Hiroshi Kimura, Realization of dynamic turning motion on irregular terrain of a quadruped robot "TEKKEN4" with neural oscillators, *Journal of the Robotics Society of Japan*, 72(724) (2006) 3848–3854
5. Ikuko Tsubaki, Toshiya Morita, Kiyoharu Aizawa and Takahiro Saito, The analysis of oscillatory motion of videos affected by camera shaking for visually induced motion sickness, *The Journal of the Institute of Electronics, Information and Communication Engineers*, J89-A (3) (2006) 262–267
6. Hiroyasu Ujike, Visually induced motion sickness, *Image Information and Television Engineers*, 61(8) (2007) 1122–1124
7. Open dynamics engine http://www.koj-m.sakura.ne.jp/ode/index.php?

Tumble avoidance system for rescue robot by estimating the contact points using a 3D depth sensor

Noritaka Sato[*], Kotaro Ohshima, Yoshifumi Morita
Department of Electrical and Mechanical Engineering, Nagoya Institute of Technology, Gokiso-cho, Syowa-ku Nagoya, Aichi 466-8555, Japan
E-mail: sato.noritaka@nitech.ac.jp
http://hi.web.nitech.ac.jp[†]

Abstract

Rescue robots are expected to perform works in hazardous areas. However, when the robot runs on a rough terrain, fatal rollover falling sometimes occurs. Therefore, we propose a tumble-risk-assessment system, which calculates a normalized energy stability margin by using a 3D depth sensor. Moreover, a control system to avoid the tumble situation by moving the sub-crawlers automatically is proposed. We implemented the proposed systems to a real robot, carried out experiments, and confirmed the effectiveness of the proposed method.

Keywords: Rescue robot, Tumble avoidance, Normalized energy stability margin, 3D depth sensor

1. Introduction

Recently, times of emergency have necessitated rapid searches for victims in collapsed buildings. However, searches conducted by humans involve risks of secondary disasters. Therefore, it is expected that rescue robots search for victims before entry by humans [1].

Most existing rescue robots are controlled by teleoperation, because fully autonomous control may be dangerous in uncertain disaster environments. However, full teleoperation is difficult for a human operator, because a rescue robot has multiple degrees of freedom in general. Therefore, human support control system, “semi-autonomous control” in other words, is needed [2].

One of most critical incidents is falling down of the robot. Figure 1 shows a robot which falls down in the RoboCup Rescue Robot League competition. As shown in Fig. 1, the fallen robot cannot run again without someone’s supports.

Fig. 1. Fallen robot in RoboCup Rescue Competition.

Okuda et al. proposed a semi-autonomous control system to avoid the falling-down situation [3] by using the normalized energy stability margin (S_{NE}) proposed by

.

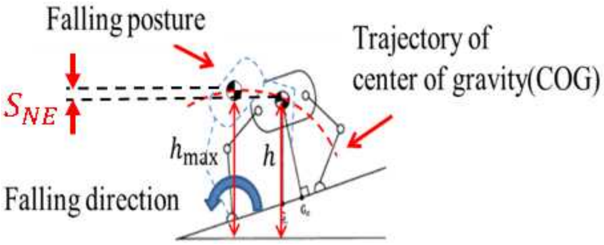

Fig. 2. Normalized energy stability margin.

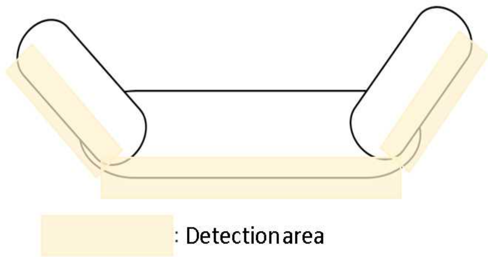

Fig. 3. Detection area for contact points.

Hirose et al. [4]. However, the authors assume that the circumference of the robot contacts with the ground. Therefore, the system often cannot calculate the risk of the fall precisely, when the robot runs on a rough terrain, because the contact point between the robot and the ground may locate on the inner part of the robot.

In the existing works, the assumption about the contact points between the ground and the robot are necessary because S_{NE} is obtained from the position of the contact points and it is difficult to get the precise position of the contact point. However, the assumptions of existing studied do not often satisfy when the robot runs on a rough terrain.

In our previous work, we developed estimating system of the contact points by using a reconstructed 3D map from the point cloud data of a 3D depth sensor, such as KINECT [5]. Therefore, the purpose of this study is to develop a semi-autonomous system to avoid the falling-down situation. In our system, we use partial differentiation of the S_{NE}. The contact points are estimated by the system which is developed in our previous work.

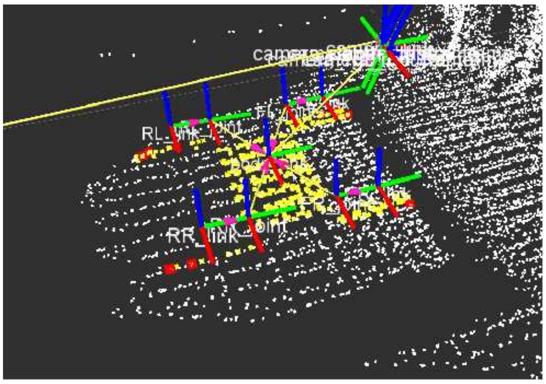

Fig. 4. Estimation result of contact points and axes of fall. (White points are environment points of 3D map, yellow points are contact points between ground and robot, and red points are points which configure axes of fall.)

2. Calculation Method of Normalized Energy Stability Margin

2.1. *Normalized Energy Stability Margin*

The normalized energy stability margin proposed by Hirose et al. [5] is one of the most popular indexes of risk of fall because the calculation is very simple. The normalized energy stability margin S_{NE} is obtained by

$$S_{NE} = h_{max} - h, \tag{1}$$

where h_{max} is the highest height of the COG (center of gravity) of the robot when the robot falls down and h is the current height of the COG of the robot, as shown in Fig. 2. As mentioned in Section 1, to calculate SNE, the positions of the contact points are necessary because the axis of the fall is obtained by the positions of the contact points.

2.2. *Estimation of Contact Points*

To estimate the contact points between the ground and the robot, the 3D map is reconstructed by using a 3D depth sensor. The SLAM (Simultaneous Localization and Mapping) technique is used for the map building with ROS (Robot Operation System) by Willow Garage. By using ROS, a developer can easily use someone's open-source programs. In this study, we use RTAB-Map developed by Labbe et al. [6]. And since we also use ROS, other developers can easily use our system, only putting a 3D depth sensor on the robot.

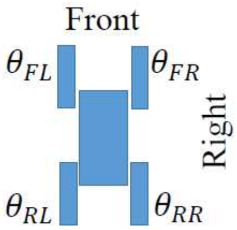

Fig.5. Definition of $\theta_{YX} = \theta_{FR}, \theta_{FL}, \theta_{RR}, \theta_{RL}$ (Top view)

2.3. *Estimation of Axis of fall*

We set the detection area along with the shape of the bottom part of the robot as shown in Fig. 3. If a point in the 3D map exists in the detection area, the point is set as a contact point as shown in Fig. 4. A convex polygon is made from the contact points and the edges of the convex polygon are set as the axes of fall. After obtaining the axes of fall, the normalized energy stability margin SNE is calculated by Eq. 1.

3. Control Method of Sub-crawlers

To avoid the tumble situation, S_{NE} should be increased by moving the sub-crawlers, when the S_{NE} becomes almost zero. Therefore, the sub-crawlers should be moved so that

$$\frac{\mathrm{d}S_{NE}}{\mathrm{dt}} > 0. \quad (2)$$

S_{NE} is a function of the contact points and the angle of the sub-crawlers. In this study, we assume that the contact points are known by the proposed estimation system described in Section 2 and S_{NE} is the function of the angle of the sub-crawlers only. Therefore,

$$\frac{\mathrm{d}S_{NE}}{\mathrm{dt}} = \frac{\partial S_{NE}}{\partial \theta_{FR}}\frac{d\theta_{FR}}{dt} + \frac{\partial S_{NE}}{\partial \theta_{FL}}\frac{d\theta_{FL}}{dt} + \frac{\partial S_{NE}}{\partial \theta_{RR}}\frac{d\theta_{RR}}{dt} + \frac{\partial S_{NE}}{\partial \theta_{RL}}\frac{d\theta_{RL}}{dt}. \quad (3)$$

The definition of $\theta_{YX} = \theta_{FR}, \theta_{FL}, \theta_{RR}, \theta_{RL}$ is shown in Fig. 5. The target angle of the sub-crawlers are set as Eq. (4) in this study.

$$\frac{d\theta_{YX}}{dt} = K\frac{\partial S_{NE}}{\partial \theta_{YX}} \quad (K: Constant\ value) \quad (4)$$

By applying Eq. (4) to Eq. (3), we obtain following equation:

$$\frac{\mathrm{d}S_{NE}}{\mathrm{dt}} = K\left\{\left(\frac{\partial S_{NE}}{\partial \theta_{FR}}\right)^2 + \left(\frac{\partial S_{NE}}{\partial \theta_{FR}}\right)^2 + \left(\frac{\partial S_{NE}}{\partial \theta_{FR}}\right)^2 + \left(\frac{\partial S_{NE}}{\partial \theta_{FR}}\right)^2\right\} \quad (5)$$

Therefore, in the case of $K > 0$, the right side of Eq. (5) is always positive, i.e. to avoid the tumble situation by

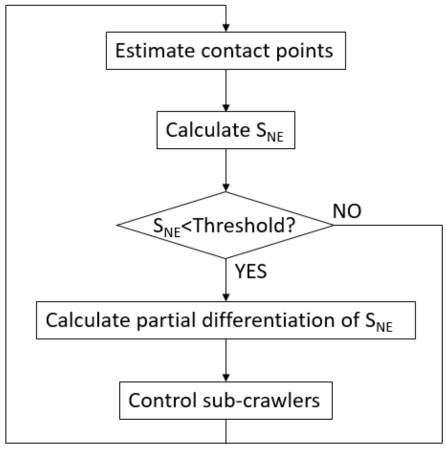

Fig. 6. Flow chart of the proposed control system.

satisfying Eq. (2), the target angle of the sub-crawlers should be set as Eq. (4).

In the proposed control system, the robot is tele-operated by an operator. However, when the S_{NE} becomes almost zero, the target angles of the sub-crawlers are used as Eq. (4) instead of the input by the operator to avoid the tumble situation. Figure 6 shows the control flow chart of the proposed control system.

4. Experiment

4.1. *Experiment method*

The purpose of the experiment is to verify the effectiveness of the proposed method compared to the existing method [3]. The experiment environment and the motion of the robot is shown in Fig. 7. The left side of the robot is on the concrete block and the other side is on the ground. The robot repeats stop and go for 2.5 seconds. The evaluation index is S_{NE}.

4.2. *Result*

The result of the experiment is shown in Fig. 8. The horizontal axis is time and the vertical axis is S_{NE}. The green and orange line shows the SNE by the existing method and the proposed method, respectively. As shown in Fig.8, in the case of the proposed method, the decrease of the S_{NE} becomes gradual after 9.2 s and the S_{NE} increases after 10 s. On the other hand, in the case of the existing method, the S_{NE} continues to decrease after 9.2 s.

Fig. 7. The experiment environment and the motion of the robot (Proposed Method).

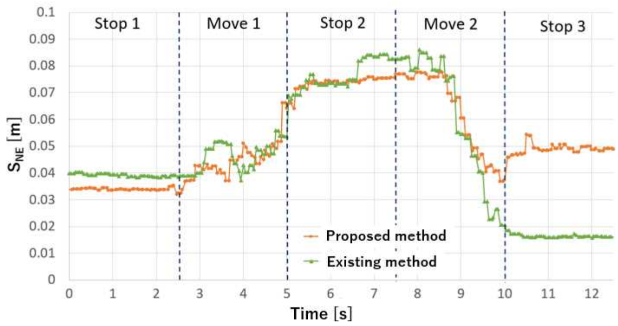

Fig. 8. The result of the experiment.

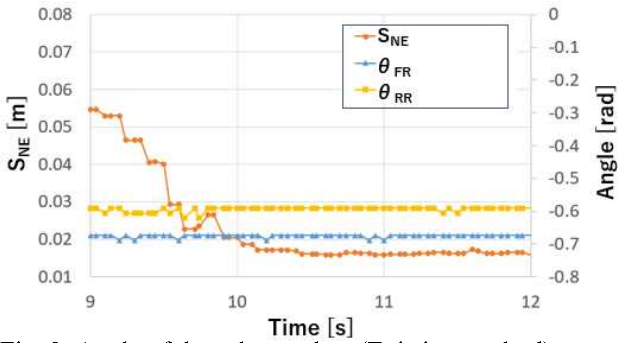

Fig. 9. Angle of the sub-crawlers (Existing method).

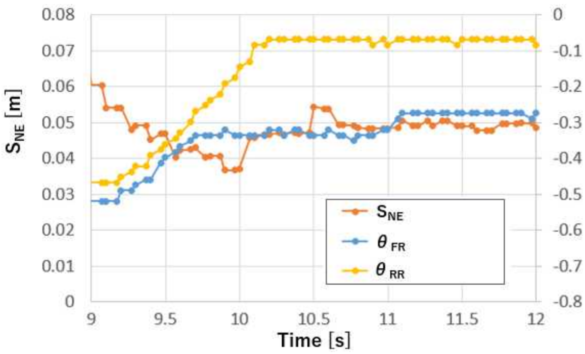

Fig. 10. Angle of the sub-crawlers (Proposed method).

4.3. *Consideration*

As shown in Fig. 8, the large difference between the proposed method and the existing method is observed after 9 s. Therefore, Fig. 9 and Fig. 10 show the angle of the sub-crawlers after 9 s in the case of the existing method and the proposed method, respectively.

As shown in Fig. 9, the sub-crawlers did not move because of the assumption that the circumference of the robot contacts with the block and the ground. On the other hand, as shown in Fig. 10, in the case of the proposed method, the front-right and rear-right sub-crawlers are moved after 9.2 s, and then the S_{NE} increases, because the contact points and the axis of the fall are precisely estimated and the motions of the sub-crawlers are correct.

5. Conclusion

In this study, we propose a tumble-risk-assessment system, which calculates a normalized energy stability margin by using a 3D depth sensor. Moreover, a control system to avoid the tumble situation by moving the sub-crawlers automatically is proposed. We implemented the proposed systems to a real robot, carried out experiments, and confirmed the effectiveness of the proposed method.

The future works are to carry out the experiment on rough terrains and to develop a system not to become a dangerous situation by predicting the S_{NE}.

References

1. S. Tadokoro, Special Project on Development of Advanced Robots for Disaster Response (DDT Project), *Proc. of IEEE Workshop on Advance Robotics and its Social Impacts* (2005) 66–72.
2. K. Ohno et al., Semi-autonomous control system of rescue crawler robot having flippers for getting over unknown-steps, *Proc. of the 2007 IEEE/RSJ Int. Conf. on Intelligent Robots and Systems* (2007) 3012–3018.
3. Y. Okada et al., Semi-autonomous operation of tracked vehicles on rough terrain using autonomous control of active flippers, *Proc. of IEEE/RSJ Int. Conf. on Intelligent Robots and Systems* (2009) 2815–2820.
4. S. Hirose et al., Normalized energy stability margin and its contour of walking vehicles on rough terrain, Proc. of *IEEE Int. Conference on Robotics and Automation* (2001) 181–186.
5. N. Sato et al., Assessment System of Tumble Stability Risk for Rescue Robot Using a 3D Depth Sensor, *Proc. Of Int. Conf. on Mechatronics and Information Technology* (2015) 146–150.

Rule based Intrusion Detection System by Using Statistical Flow Analysis Technique for Software Defined Network

Mahnoor Ejaz, Osama Sohail, Talha Naqash, Zain ul Abideen, Sajjad Hussain Shah

Department of CS
Bahria University,Islamabad, Pakistan
mahnoorejaz96@gmail.com, sohailosama71@gmail.com, talhanaqashtn@gmail.com, Zain@bahria.edu.pk, sajjadshah@ieee.org

Abstract

Network Security is a vast field making progress around the globe very fast. In every progressing year, developers have implemented different tools, which include Intrusion detection systems. Nowadays Intrusion Detection System (IDS) is one of the popular tools, which are drawing the attention of many researchers. Applying it in Software Defined Networking (SDN) facilitates network management and enables to enhance the productivity of network monitoring. Classifying packets based on their statistics and separating the forward process of network packets from the routing process is the main challenge. In this paper, rule-based classification is done in order to differentiate between viruses and normal packets. Statistical analysis of different network traffic flows are done through which segregation is made and intrusion is detected in Software Defined Networking. The proposed system is experimentally tested on UNB ISCX datasets

*Keywords*__ Network Security, Software Defined Networking (SDN), Intrusion Detection System (IDS), Network Monitoring, Network traffic flows

1. Introduction

The predominance of the Internet and nearby systems, intrusions plays an important role in computer systems. Exposure of such attacks is an important issue in computer network security. Intrusion Detection Systems (IDS)[1] innovation is a powerful methodology in managing the issues of system security. An intrusion discovery framework scans for strange or malignant practices in the examples of action in the review trail. Most intrusion detection systems are programming projects. Individuals use screen to monitor the happening in a computer framework or system, examination the framework events, recognize suspected interruption, and afterwards generates an alarm. Intrusion Detection System (IDS) on the exactness of this depiction explains the framework execution in a huge extent, and this portrayal is a trouble in research region of intrusion identification. Unlike traditional networks, Software Defined Networking (SDN) has introduced centralized controller that is making SDN beneficial in terms of simplified network hardware, efficient infrastructure and programmable architecture [3] that help in deployment of new applications due to which it is becoming common in big companies. This evolution occur with the upbringing Open Flow protocol that is used in SDN [2] to control and regulate traffic in controller. Having a view on root cause to write this research paper up brings the study of all work done by researchers in this objective. Different techniques are being used in this context that are fuzzy logic, machine learning, genetic algorithms etc. For the security hazards our focus is to design an application for software defined network that will be efficient enough to detect the intruders in network thus making it safe from malicious attacks. When it comes to SDN architecture unlike traditional networks they don't distribute the decision making power among the routers and switches rather it is all done by the centralized controller that uses Open Flow protocol[4] which tells the switches to regulate the traffic to most suitable path in network. Most important aspect that comes to mind using any network is to have reliable and secure communication. SDN provides programmable platform to develop an application that can detect the malicious traffic. For that purpose many work has been done at hardware level by the researchers that is an efficient way to secure the networks from intruders. Authorized Authentication Authority [8] is one of these devices that are used for intrusion detection in networks but are very costly. To avoid this disadvantage many solutions are provided, we are developing an application that will run in SDN controller and doesn't require a separate device and it is a cost effective remedy to it.

2. Software Defined Networking

Software defined networking is regulating the traffic via controller, instead of using large number of routing devices. SDN constitutes three layers connected to north and south bound API's to build a communication between the application and devices. SDN controller is a software that is regulating the traffic in network. SDN programmable environment bring an ease to program a software like controller for reliability and security issues. SDN is trending in present era whose many applications are developed and deployed by many service providers like Amazon, Facebook etc. thus replacing the traditional networks. Controllers [9] are efficient enough to administrate the traffic from single instance and can be deployed to various hardware devices. SDN have the capability to support 5 different type of controllers.

- Open Daylight open-source SDN controller
- Open Contrail SDN controller.
- Floodlight open SDN controller
- Ryu SDN controller
- FlowVisor SDN controller

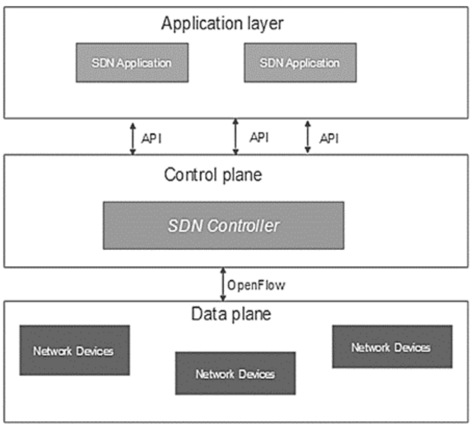

Fig 1: Software Defined Networking Outline

A. Ryu SDN OpenFlow Controller.

Different categorized controllers are used by separate developers in Software Defined network to build their componential architecture for developing their applications for several areas. It provides programmable environment in python for SDN operating system. Ryu controller [6] provides a platform for developing in application in SDN frameworks with many API's that are well-defined for understanding by the developers. The conventions utilized by the controller are Open Flow protocol that is responsible for tasking the SDN to regulate the traffic to optimized path. The versions of Open Flow that are fully supported by RYU are V1.0, V1.2, and V1.3. The one that is used in this research is V1.3.This version provides many messages and structures that are utilized to get the statistical information regarding traffic. We have used OFPFlowStatsReply message to get the required statistics.

3. Related Work

As the study begins related to Intrusion Detection System we came across many techniques that might have used by many researchers and developers for its development. Typically, IDS [4] is required to this concern instead using a simple firewall tool. Intrusion detection system that is responsible to take care of the network from the unwanted data manipulation. IDS is programmed using different knowledge based techniques like machine learning. In order to detect the manipulated traffic that is caused either by malicious attack by attacker or by an application that intrudes the network and get it damage IDS tools are in recent market. IDS can be distributed IDS in which results from disseminate junctions are then governed by IDS administer or it can be parallel IDS that is monitoring the traffic on a single point. Several anomaly based and signature based methodologies are used and giving adequate results as per developers need. Detection and prevention further based on protocols (TCP, ICMP, UDP), attacks (DOS, DDOS, UDP flood attack)[10]. In order to follow a signature or rule based methodology to develop IDS require different tools like SNORT, BASE [13] etc. These tools provide overall analysis of network and help detecting the malicious flow. Different rules according to understanding regarding harmful traffic can be written and implemented in any language. In result to these rules results are generated thus detecting the intruders in network. SNORT tool is the most common tool used in signature based technique that is being used in implementing many IDS. It can also be used merged with other frameworks regarding intrusion detection. In Signature rule based[12,16] model is developed using SNORT sensors that have rules databases that are further updated keeping in view the results of previous rules to bring efficiency and improvement to detect the malicious traffic. SNORT provides fast single-threaded and multi-threaded versions.

IV. Proposed Framework to Detect Viruses using rules

We are going to develop an application in Ryu SDN controller that will be able to detect the malicious packets and play a role of NIDS [7, 15] in any network system. When a traffic flow is send IP and MAC addresses are learned by the controller to regulate the next flows. Major technique observed by us in classification of virus and normal traffic is stating the rules based on five statistical information obtained from Open Flow message structure that are Pckt_Count, Byte_Count and

Duration. Other two features are calculated using them. Passing through the rules established using these features; traffic is classified into virus and normal. A separate database is maintained containing all the IP and MAC addresses that is used by our application to separate the addresses of those that are malicious to network. Which are then placed in grey list database and are temporarily blocked, if the same action repeated than placed to black list database result the permanent blockade. Features that are obtained using OFP Flow Stats Request[5] message gives the following flow statistics. Table no.1 shows the features.

Table No.1: Traffic Flows features

S.NO	**Feature Name**	**Explanation**
1	Flags	Kept zero
2	Match	Instance of OFP match
3	Duration_nsec	Duration of flow in seconds
4	Idle_timeout	ime out for a flow
5	Hard_timeout	Hard time out for a flow
6	Pckt-Count	Pcaket count of a flow
7	Byte-Count	Byte count of a flow
8	Cookie	Matching entry values
9	Out_port	Output port for new entries
10	Out_group	Output group for new entries

For our application these OFP Flow Stats Request and Reply messages are used to parameters as per our requirements to develop the rules are separated, observed, and stored in a separate database. Some of the basic features, which are required to build an IDS. Using some of the basic features we can derive other features such as *bit-rate* and *packet-rate.* Applying basic formulas to produce bit-rate can help us making decision about the malicious packets. Formulas are used to calculate the required features.

Suppose x is the bytes from the traffic flow and t is the duration in which it is communicating. Then $x=1,2,3....n$ and $t=1s,2s,3s,4s$...then

$$\sum_{i=0}^{n} \frac{x_i * 8}{t_i} \qquad (1)$$

Can be used to derive the bit-rate from the traffic flow.
Similarly for the packet-rate

$$\sum_{i=0}^{n} x_i / t_i \qquad (2)$$

A. Rules To Detect The Attacks/Viruses

Attacks are of different types with different vulnerabilities. One of the famous attacks is the Denial of Service (DoS) attack [11], which makes the system hang up as the number of pings is way too much in less duration. By this general hypothesis we can assume that if the duration is less and pckt-count is high then it is a DoS attack [14]. To define the high and low, statistical analysis is applied on the data to check the difference in behavior of viruses and normal packets. During this analysis we realized that pckt-count, byte-count are very important with respect to duration in which packets are send. A basic rule is as follows:

If duration isLOW && pckt-count isHIGH then attack==DoS

If pckt_count isLOW && byte-count isHIGH then attack == DOS

B. Flow of the Application

Any application has a flow in which it is executed. The flow of this application is explained by this flow diagram

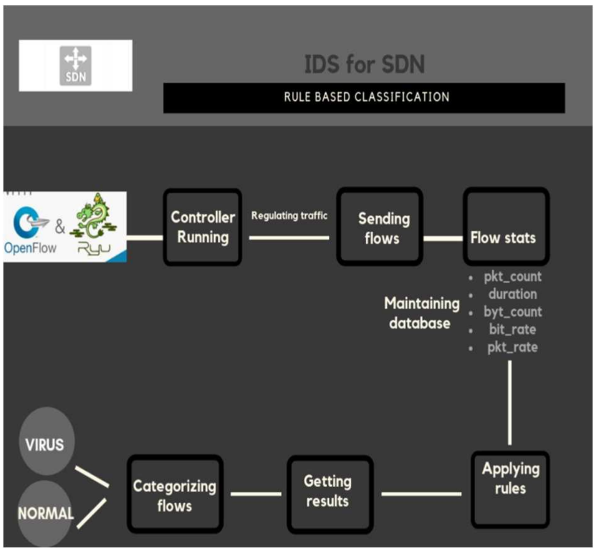

Fig 2: Flow Diagram of Proposed Solution

In fig no.2 the basic flow is defined of the application where controller is set on at the start of the procedure. After controller is set on, now to make the network virtually, topology is made. After topology is created now the application is ready to let ongoing traffic pass through it. As soon as traffic is sent, if the file is sent completely then it will apply rules on the ongoing traffic otherwise it will be again directed towards controller.

For the evaluation of the proposed solution, we utilized the UNB-ISCX data set this dataset consist of various malware traffic recorded in complex scenarios. The detail of the attack available in the data set is given in table II also the flow instances with malware launched by these attacks are given in table III.

Table 2 : Malware Traffic Used in the Experiment

Alien Spy Rat Version 1-4	Blackhole Version 2-6	Cutwail Version 1-3	Darkness DDOS	Drower Worm
Kuluoz	Load money	Ponyzeus	Purplehaze	Pony Loader
Power Loader	Salty Version 1-4	Spy Eye	Tbot Version 1-5	Tiny Zbot
Trojan	Zeus	Zero access Version 1-2		

Table 3 : Malware Quantities Used in the Experiment

Virus	Flows	Packets
Alien Spy Rat Version 1-4	7111	9124
Blackhole Version 2-6	482	7429
Cutwail Version 1-3	1801	35358
Kuluoz	18913	178353
Purplehaze	6872	294810
Pony Loader	289	3798
Power Loader	221	4740
Sality Version 1-4	9448	19881
Tbot Version 1-5	474	9993
Zeus	382	6892
Zero access Version 1-2	481	5111
Normal Traffic		
Normal 1	4982	25587
Normal 2	21842	1750963
Normal 3	23691	216332
Normal 4	36721	1063445

We recoded the normal traffic (without virus traffic) in a secure environment and mix the files with malware to check the accuracy of the algorithm. The proposed system successfully detected the flows as shown in the figure 3. Both rules detected the malware traffic by using their statistical values, which proves the accuracy of the system.

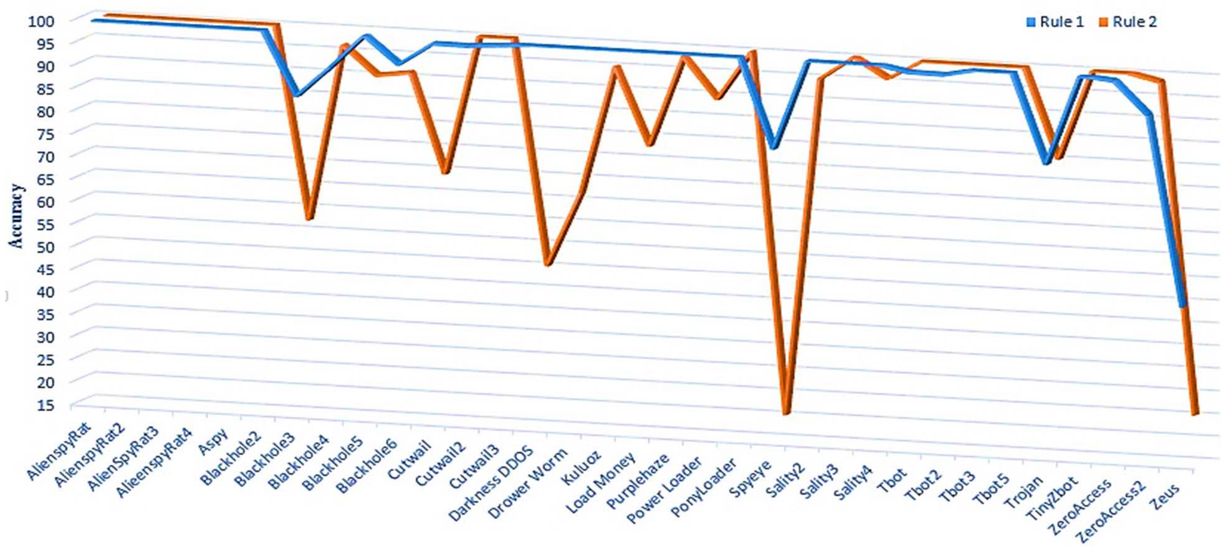

Figure 3: Accuracy of Rules against the Various Malwares of ISCX2012

4 Conclusion

Intrusion Detection systems (IDS) nowadays are the basic need for the network security. Monitoring network traffic flows and detecting the malicious packets was the main challenge. In this paper, we devised an Intrusion Detection System (IDS) by applying statistical analysis based on flow statistics extracted by using OFPFlowStatsReply message. Our system incorporates the concept of rule based classification of virus and normal traffic. The developed application have defined rules when flow passes through these rules will be detected if the flow is malicious and is blocked permanently on repetition. Two databases for grey and black list flows are maintained. We use Low and high keywords for defining rules for features that are packt_count,byte_count and duration_nsec which are first used to train the system and then used to classify the test data. We have used UNB ISCX datasets for training and evaluating our system. Results that are generated after experimentation depicts the effectiveness of our system. Detection rates of the developed application shows that it can be widely applicable at larger data sets. In addition to detection, this system can further be used in order to develop a software to prevent the networks from intruders, which will enhance the reliability and demand of IDS systems.

.References

1. M. Z. Masoud, Y. Jaradat, I. Jannoud, "On preventing ARP poisoning attack utilizing Software Defined Network (SDN) paradigm", *Jordan Conference on Applied Electrical Engineering and Computing Technologies (AEECT)*, pp. 1-5, 2015

2. https://www.edgewaternetworks.com/blog/2014/07/benefits-sdn-solving-network-infrastructures-root-canal-problem/. Available at www.edgewaternetworks.com Accessed on:[13-10-18]

3. www.sdxcentral.com"what is SDN" Available https://www.sdxcentral.com/sdn/definitions/sdn-controllers/openflow-controller/. Accessed on:[13-10-18]

4. M.Hellman, "*Fuzzy logic introduction*", Laboratoire Antennes Radar Telecom, F.R.E CNRS 2272, Equipe Radar Polarimetrie.

5. M. Erel; E.Teoman and Y. Özçevik etal **"**Scalability analysis and flow admission control in mininet-based SDN environment" . *IEEE Conference on Network Function Virtualization and Software Defined Network*. 2015 pp 18-19

6. M. Enamul, K. Jiankun "A statistical Framework for Intrusion Detection System" *IEEE 11th International Conference on Fuzzy Systems and Knowledge Discovery*, 2014 , pp. 941-946

7. www.sdxcentral.com,"Software Defined Networking", 2017. Available at: https://www.sdxcentral.com/sdn/definitions/what-the-definition-of-software defined-networking-sdn/ Accessed:[10-07-18].

8. www.cisco.com,"What is a network switch or router",Available: https://www.cisco.com/c/en/us/solutions/small-business/resource-center/connect-employees-offices/network-switch-what.html Accessed:[21-07-18

9. M.Hellman, "*Fuzzy logic introduction*", Laboratoire Antennes Radar Telecom, F.R.E CNRS 2272, Equipe Radar Polarimetrie.

10. V.Ali,R.Maryam,S.Babak,"A fuzzy Intrusion Detection System based on Categorized of Attacks", *6th Conference on Information and Knowledge Technology (lKT 2014)*, May 28-30, 2014, Shahrood University of Technology, Tehran, Iran, pp. 50-55

11. Meng, Y., & Kwok, L. F. "Adaptive context-aware packet filter scheme using statistic-based blacklist generation in network intrusion detection.", *7th International Conference on Information Assurance and Security (IAS)* 2011, pp. 74-79.

12. H.Yajam, K.Younes, A.Mohammadali , "Deniable Encryption based on Standard RSA with OAEP", *2016 8th International Symposium on Telecommunications (IST'2016)* pp. 84-88

13. H.Khalid, S.Jawad, V.Dillshad, M.Nafees, M.Awais, "An Adaptive SYN Flooding attack Mitigation in DDOS Environment", *IJCSNS International Journal of Computer Science and Network Security*, VOL.16 No.7, July 2016.pp 27

14. Shanmugavadivu, R., & Nagarajan, N. "Network intrusion detection system using fuzzy logic". *Indian Journal of Computer Science and Engineering (IJCSE)* 2011, 2(1),pp 101-111.

15. S.Kritsanapong , "The Improving Decryption Process of RSA by Choosing New Private Key", *8th International Conference on Information Technology and Electrical Engineering (ICITEE)*, Yogyakarta, Indonesia.2016, pp1-4

Development of Test-bed for SDN to know its feasibility of deployment on access layer

Rafay Shah, M Osama Shaikh, TalhaShaikh
BE Telecommunication, MUET (Mehran University of Engineering & technology),
Jamshoro, Pakistan 76090
Email: rafayshah26@gmail.com, osama.shaikh12369@gmail.com,talhaazmatshaikh21@gmail.com
https://www.muet.edu.pk

Abstract

Today, the network requirement of organizations includes enhancing performance, realizing broader connectivity and security regulations. SDN technology makes easier for an IT Administrator to easily deploy and update regulatory policies. We have developed a Test-bed kit using Zodiac-FX OpenFlow Switch for SDN and have tested SDN feasibility on Access Layer. We have also simulated a network of Faculty of Electrical Electronics Computer Engineering of MehranUET and have found that SDN performs better than traditional network architecture of FEECE of MehranUET.

Keywords: SDN, Network, OpenFlow, SDN Controllers, Zodiac-FX

1. Introduction

Nowadays, organizations have been challenged by the need of scalability in their network in order to make growth of application. When OpenFlow Protocols were implemented on the data centers, since then service providers have been implementing OpenFlow Protocols to ease their operations [6]. Today, the network requirement of organizations includes:

- Enhancing performance
- Realizing broader connectivity
- Security regulations

In order to comply with all of these criteria, Networking Protocols have been evolving significantly over the last few decades.

2. Software Defined Network Architecture

Yet, northbound interfaces allow devices to communicate among the higher level components. While the traditional networks uses 2 mechanisms to control packets on data plane.

- Load Balancing
- Firewall

Implementing SDN on Northbound interface of controller, it lets the installed applications to communicate with the controller. Northbound APIs are used by different types of organizations including,

- Non-profit
- Educational
- IT Organization and others

In SDN, Southbound Interfaces are the OpenFlow protocol which enables communication between controllers, switches and other network nodes. This further lets the router to,

- Identifies the topology of Network
- Determine the Flows on the Networks

Some of the popular southbound APIs are OpenFlow, Cisco, and OpFlex and other vendors that support

OpenFlow include IBM, Dell, Juniper, Arista and more [7].

3. Openflow Controllers

Controllers are the core of an SDN Network. In SDN, Controller is an application that manages FlowControl to enable networking. SDN Controllers are based on protocols such as OpenFlow which allows server to tell switches where to send packets [1]. It provides communication between applications and devices. Any communication between them goes through the controller as it chooses optimal path for traffic applications. Controllers act as OS in networks. Controller facilitates automated network management and makes it easier to integrate and administrate. Vendors of SDN Controller include:

- Big Switch Networks
- HP
- IBM
- VM Ware
- Juniper

RYU is a component based open source frame work implemented via Python. It supports various component including OpenFlow Protocols (version 1.1, 1.2, 1.3 and 1.4), event management, applications management and different services [4]. At API layer RYU has Open Stack Quantum Plugin which supports the configurations based on VLANs or GRE based overlay and supports REST interfaces for its OpenFlow operations.

POX controller is also referred as NOX and was developed by Nicira. It was the known as the first open source OpenFlow Controller. It provides APIs to interact with OpenFlow Switches including connection handler. Additional components checks the availability ofAPIs, provides Host Tracking, Routing, Creating and Analyzing Topology. NOX/POX applications are

- **SANE:** SANE is an approach to represent network as a file system.
- **Ethane:** Ethane is a Stanford University research application for centralized network security [13].

4. Openflow Protocol

The OpenFlow protocol defines the communication between an OpenFlowcontroller and an OpenFlowswitch.It has various versions from version 1.0.0 to version 1.5.0 [6]. Thisprotocol is what most uniquely identifies OpenFlow technology. At its essence, the protocol consists of a set of messages that are sent from the controller to the switch and a corresponding set of messages that are sent in the opposite direction. The messages, collectively, allow the controller to program the switch so as to allow fine-grained control over the switching of user traffic [9]. The most basic programming defines, modifies and deletes flows. The OpenFlow protocol has evolved significantly with each version of OpenFlow, so we will cover the detailed messages of the protocol in the version-specific sections that follow. The specification has evolved from development point release 0.2.0 on March 28, 2008 through release V.1.5.0, released in 2014. Numerous point releases over the intervening years have addressed problems with earlier releases and added incremental functionality. OpenFlow was viewed primarily as an experimental platform in its early years. As such, there was little concern on the part of the development community advancing this standard to provide for interoperability between releases. As OpenFlow began to see more widespread commercial deployment, backwards compatibility has become an increasingly important issue. There are many features, however, that were introduced in earlier versions of OpenFlow that are no longer present in the current version. Since the goal of this chapter is to provide a roadmap to understanding OpenFlow as it exists today, we will take a hybrid approach of covering the major releases that have occurred since V.1.0. We focus on those key components of each release that became the basis for the advances in subsequent releases and do not focus on functionality in earlier releases that has been subsumed by new features in subsequent releases [10].

5. Implementation of SDN on Access Layer

Access layer provides a communication path and connects hosts computer to the network. Access layer is referred as third tier model of network. It uses TCP/IP protocol hierarchy which defines network how to transmit IP datagram [11]. Typically a logical network ID is created by associating physical port of a switch or VLAN to a specific logical network ID with its own routing protocol and forwarding tables. Whenever packets will be transmitted it will destined to that port associated to VLAN ID on logical network. With SDN, a controller can determine the logical network of every flow and then tunnels the traffic to top the end of logical networks.

To check the performance of SDN first of all we will conFig. Zodiac FX switch and bind the controller with the switch. We have used HPE Van SDN and RYU OpenFlow Controllers to check the connectivity between controller and switch through ping command from controller to switch. Once we get a stable connection between switch and controller we added the flows by using GUI of controllers.

6. SDN Controllers and their integration

As shown in Fig.1, Zodiac FX switch has four ports in which port number 4 is native port and other ports are used to connect end devices. Connect port number 4 with controller using UTP cable as connection is established so port status will become up.

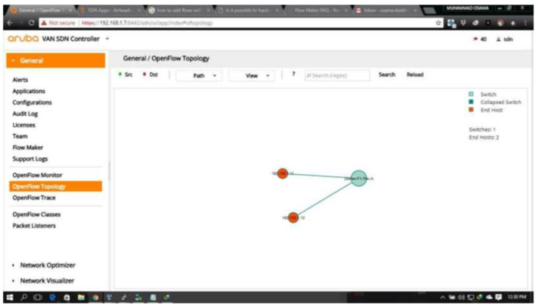

Fig. 1: Zodiac FX Topology in HPE Van SDN Controller

Zodiac-FX switch has four ports in which port number 4 is native port and other portsare used to connect end devices. Connect port number 4 with controller using UTP cable as connection is established so port status will become up.

Zodiac FX OpenFlow Switch has four ports in which port number 4 is native port and other ports are used to connect end devices. Connect port number 4 with controller using UTP cable as connection is established so port status will become up.

7. Zodiac FX Switch based Test-bed kit

Zodiac FX is a 4 port network development hardware kit designed for network development and SDN implementations. It is an open source firmware which allows the user to modify or create Zodiacs firmware according to their work of projects. For example

- Router and Bridge
- Web Server
- VPN Connector

SPI connector allows zodiac fx to connect other devices using the industry standard Serial Peripheral Interface (SPI) and is a collection of 8 pins whereas JTAG Debugger is used for developing zodiac firmware and uploading using specially designed cable. The zodiac fx provides serial connectivity through USB port for performing changes/configuration in switch. Zodiac FX also provides web interface for the configurations in GUI. Our SDN Test-bed Kit consists of Zodiac FX OpenFlow SDN Switch and SDN Controllers. Firstly we have conFig.d Zodiac FX IP Address, Subnet Mask, OF-Controller IP Address and Gateway. After configuring Zodiac FX OpenFlow SDN Switch we integrate it with different SDN Controllers i.e. HPE Van SDN Controller, RYU SDN Controller and POX SDN Controller. Once, successfully integrated we have tested SDN Test-bed Kit and calculated various results.

8. Results

Graph in Fig.2 shows the percentage of usage of CPU by different controllers. This experiment was performed on Zodiac-FX kit. Higher the percent of CPU Usage the lower will be the performance.

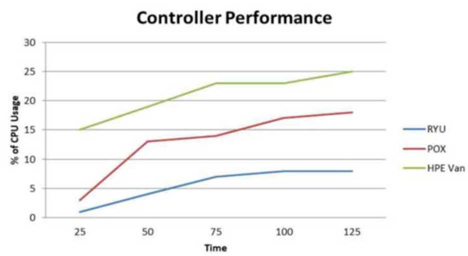

Fig. 2: CPU usage VS Time

The values of graph in Fig. 2 is calculated using SDN Controllers Usage Tool and shows that the performance of RYU SDN Controller is better than other SDN Controllers.

Throughput is calculated using IPERF tool. The graph in Fig. 3 shows that the throughput of SDN is better than Traditional network.

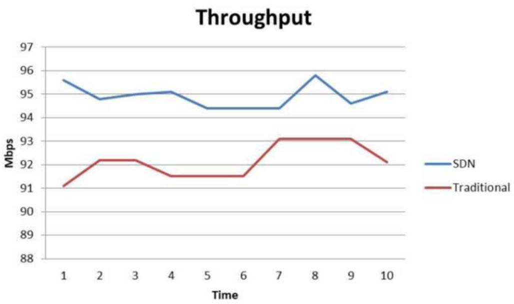

Fig. 3: Throughput comparison

Here it can be observed in Fig. 3that Traditional Network, throughput, at 6 ms interval of time, was 91.5 Mbps whereas in SDN it was 94.5 Mbps. Hence, it can be concluded that the SDN can perform much better than Traditional Network.

The graph in Fig.4 shows the Throughput of SDN and traditional network of FEECE Faculty.

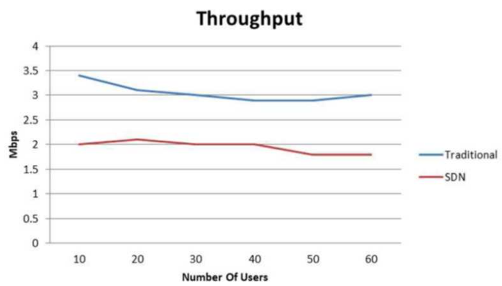

Fig. 4: Number of User versus Throughput

This graph show that the throughput of SDN is better than Traditional Network. Here it can be observed that in Traditional Network when the number of user was 40 throughput is 2 Mbps whereas in SDN throughput is 2.9 Mbps. Here it is also observed that SDN Switches have maintained the throughput even the number of users exceed up to 60 Users. Hence, it can be concluded that the SDN Networking can perform much better than Traditional Networking.

As shown in Fig. 4, the latency of the packets is less in SDN than the latency of the packets in traditional networks. This result is calculated on Zodiac-FX especially for SDN and for traditional network, we have just used simple common devices.

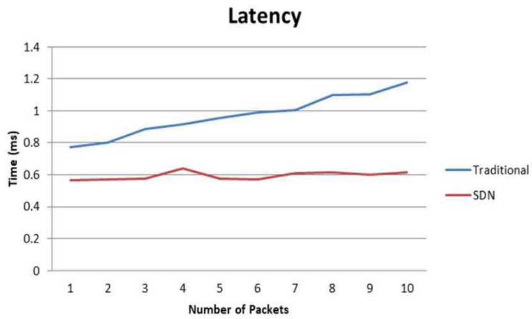

Fig. 5: Latency

To calculate latency we just use ping test. The graph in Fig. 5 shows that the SDN Switches transfers 10 packets within just 0.6 (ms) but the traditional switches took 0.8 (ms) to 1.2 (ms) time to transfer 10 packets from source to the destination.

9. Conclusion and Future Work

In our work, we have developed a Test-bed for SDN andis based on Zodiac-FX OpenFlowswitch, on which students can gain hands on experience on SDN and do research on it. We have tested the feasibility of deploying SDN on access layer. The performance is evaluated in terms of delay, throughput and scalability. We also have simulated FEECE faculty of MUET on SDN using mininet with different controllers. Three different controllers have been used and these are HPE VAN SDN Controller, RYU SDN Controller and POX SDN Controller.

In this test-bed, we have used single Zodiac FX OpenFlow switch and in future multiple switches can be installed to test various/multiple topologies. We have installed controller on a laptop but in future, controller can be install on a dedicated Raspberry pi. We have simulated FEECE faculty on mininet but in future, deployment with hardware switches is also possible.

References

1. H. Huang, S. Guo, P. Li, W. Liang, and A. Y. Zomaya. *Cost minimization for rule caching in software defined*

2. K. Salah, K. Elbadawi, and R. Boutaba. Performance modeling and analysis of network firewalls. *IEEE Transactions on Network and Service Management*, 9(1):12–21, March 2012.

3. G. Hampel, M. Steiner, and Tian Bu. applying software-defined networking to the telecom domain. *In 2013 IEEE Conference on Computer Communications Workshops (INFOCOM WKSHPS)*, pages 133–138, April 2013.

4. S. Asadollahi, B. Goswami, and M. Sameer. Ryu controller's scalability experiment on software defined networks. *In 2018 IEEE International Conference on Current Trends in Advanced Computing (ICCTAC*), pages 1–5, Feb 2018.

5. J. Alcorn, S. Melton, and C. E. Chow. Portable sdnTest-bed prototype. *In 2017 47th Annual IEEE/IFIP International Conference on Dependable Systems and Networks Workshops (DSN-W)*, pages 109–110, June 2017.

6. A. Bianco, R. Birke, L. Giraudo, and M. Palacin. Openflow switching: Data plane Performance. *In 2010 IEEE International Conference on Communications*, pages 1–5, May 2010.

7. T. Huang, F. R. Yu, C. Zhang, J. Liu, J. Zhang, and Y. Liu. A survey on large-scale software defined networking (sdn) Test-beds: Approaches and challenges. *IEEE Communications Surveys Tutorials*, 19(2):891–917 Second-quarter 2017.

8. S. Khorsandroo and A. S. Tosun. An experimental investigation of sdn controller live migration in virtual data centers. *In 2017 IEEE Conference on Network Function Virtualization and Software Defined Networks (NFV-SDN)*, pages 309–314, Nov 2017.

9. V. Tanyingyong, M. Hidell, and P. Sjdin. Improving pc-based openflow switching performance. *In 2010 ACM/IEEE Symposium on Architectures for Networking and Communications Systems (ANCS)*, pages 1–2, Oct 2010.

10. R. Gopakumar, A. M. Unni, and V. P. Dhipin. An adaptive algorithm for searching in flow tables of openflow switches. *In 2015 39th National Systems Conference (NSC)*, pages 1–5, Dec 2015.

11. S. Zerrik, D. El Ouadghiri, and M. Bakhouya. Performance evaluation of software defined networking architectures using network calculus. *In 2016 5th International Conference on Multimedia Computing and Systems (ICMCS)*, pages 543–547, Sept 2016.

12. Y.Wang, Y.Dar, and G.Chang. Sdn-based dynamic multipath forwarding for interdata center networking. *In 2017 IEEE International Symposium on Local and Metropolitan Area Networks (LANMAN)*, pages 1–3, June 2017.

13. R. Jain and S. Paul. Network virtualization and software defined networking for cloud Computing: a survey. *IEEE Communications Magazine*, 51(11):24–31, November 2013

Spectrum Sensing using Unsupervised Learning for Cognitive Radio

Asmara Shaukat, DanishKhan, TalalArshad, Haseeb Ahmad
College of Electrical Engineering, PAF Karachi Institute Of Economics And Technology, Karachi, Pakistan

E-mail: *asmarashaukat93@gmail.com,maddanish2050@gmail.com, Sam.samad22@gmail.com, mianhaseebahmad149@gmail.com*

Abstract

Cognitive Radio is the type of wireless communication which has the ability to learn from its surrounding and reconfigure its operating parameters. It uses radio spectrum efficiently by detecting which communication channels are in use and which are not, and instantly move into vacant channels while avoiding occupied ones. This optimizes the use of available radio-frequency (RF) spectrum while minimizing interference to other users. Spectrum sensing is one of the most important tasks performed by the CR.Spectrum sensing refers to the ability of a CR to measure the spectrum activities due to ongoing transmissions over different spectrum bands and to capture the related parameters, it tells us about spectrum usage and existence of primary users in a geographical area. In this work we perform Spectrum sensing using k-mean clustering and find vacant spectrum.

Keywords: Cognitive Radio, Radio frequency spectrum, Primary user, Spectrum sensing, K mean clustering

1. Introduction

Usable radio spectrum is a precious natural resource whose allocation is governed by various government bodies.This fixedassignmentof the frequencies has caused spectrum scarcity [1].CR is an innovative approach to wireless networking in which the radio device is aware of its environment and has the ability to establish and adjust its parameters autonomously. It has the ability to observe and learn from its environment, adapt to the environmentalconditions, and make decisions to use the radio spectrum moreefficiently [2]. One of the most important task of CR is spectrum sensing and detect Primary user activity. As soon as the Primary user activity is detected, they have to vacate the channel [3].

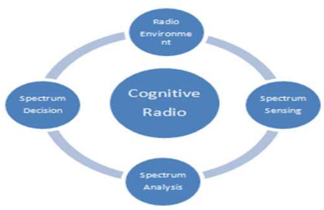

Fig.1.Cognitive Radio Working Principle.

2. Spectrum sensing

Spectrum sensing is one of the most important task performed by the CR. Spectrum sensing refers to the ability of a CR to measure the spectrum activities due to ongoing transmissions over different spectrum bands and to capture the related parameters. The ultimate objective of the cognitive radio is to obtain the best available spectrum through Cognitive Capability and Re-configurability as described above. Since there is already a shortage of spectrum, the most important challenge is to share the licensed spectrum without interfering with the transmission of other licensed users. The cognitive radio enables the usage of temporally unused spectrum, which is referred to as spectrum hole or white space. If this band is further used by a licensed user, the cognitive radio moves to another spectrum hole or stays in the same band, altering its transmission power level or modulation scheme to avoid interference.Machine learning algorithms have been widely used for the pattern classification problems, where the feature vector extracted from the training data is fed into the classifier to categorize the pattern into a certain class. Spectrum sensing can be thought of as a binary-class classification problem. Weare using k-mean clustering.

In general, two types of learning algorithms exist, namely the “supervised” and the “unsupervised”. In case of the supervised learning, the training feature vectors are fed to the classifier with their actual labels; while in case of the unsupervisedlearning, the same are fed without any label [4].

3. K-mean clustering

K-means clustering is a type of unsupervised learning, which is used to characterize data points in groups. This characterization is done on the basis of features similarity. After every iteration, each data points are assigned to a particular cluster. Two main tasks performed by K-mean clustering algorithm are:

1. To obtain the centroids of the *K* clusters, which can be used to label new data

2. Assign cluster to every data point.

3.1. *K-mean clusteringAlgorithm*

k-means is oneof the simplest unsupervised learning algorithms that solve thewell-known clustering problem. The procedure follows a simple way to classify data in certain number of clusters.

3.2. *Algorithmic steps for k-means clustering*

- Recalculate diatance between each data point and obtain new cluster center
- Randomly select cluster centers
- Assign data point to each cluster center whose distance from the center is minimum
- Recalculate the new cluster center
- calculate distance beteen data point and cluster centers

After we have these k new centroids, a new binding has to be done between the same data set points and the nearest new center. A loop has been generated. As a result of this loop we may notice that the k centers change their location step by step until no more changes are done or in other words centers do not move any more. Finally, this algorithm aims at minimizing an objective function knows as squared error function given by:

4. Simulations and Results

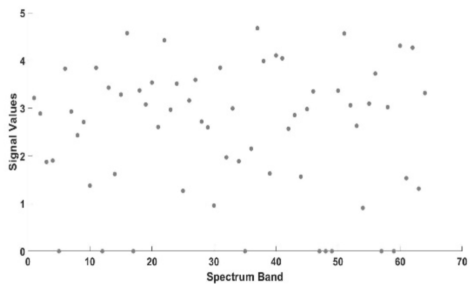

Fig.2: Signal values some are zero

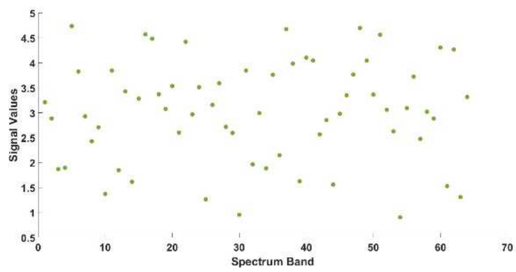

Fig. 3: Signal values

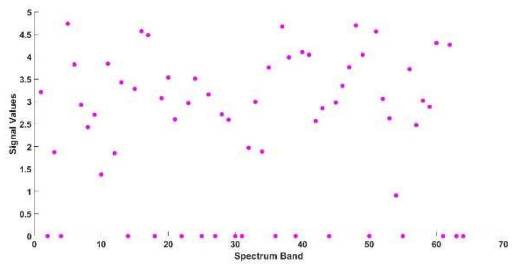

Fig. 4: Signal values more values are zero

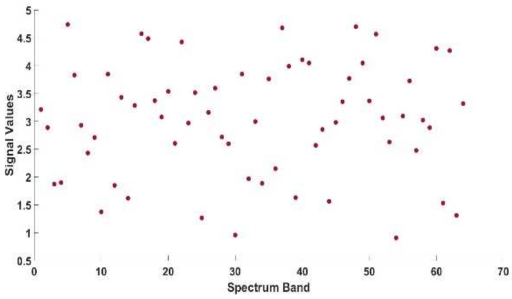

Fig. 5: Signal values no values are zero

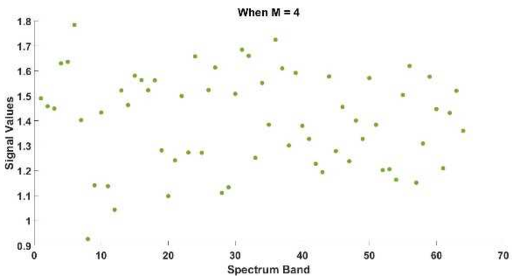

Fig.6: Signal values no values are zero

References

1. *Techniques for Dealing with Uncertainty in Cognitive Radio Networks* Fatima Salahdine1,2, Naima Kaabouch1, Hassan El Ghazi21Electrical Engineering Department, University of North Dakota, Grand Forks, USA2STRS Laboratory, National Institute of Posts and Telecommunication, Rabat, Morocco

2. *Markov Model Based Jamming and Anti-Jamming Performance Analysis for Cognitive Radio Networks* Wednel Cadeau, Xiaohua Li, Chengyu Xiong, Department of Electrical and Computer Engineering, State University of New York at Binghamton, Binghamton, USA.

3. K-mean clustering based cooperative spectrum sensing in generalized κ-μ fading channels,V. Kumar, D. C. Kandpal, M. Jain, R. Gangopadhyay and S. Debnath, *2016 Twenty Second National Conference on Communication (NCC)*, Guwahati, 2016,pp.1-5.doi: 10.1109/NCC.2016.7561130

Tracking Secondary User in Cognitive radio for 5G Communication

Muhammad Adnan,Muhammad Umair,Sameed bin Junaid
College of Engineering PAF-KIET
Karachi ,Pakistan

E-mail: adnan13july1995@gmail.com, Engr.umairshahbaz@gmail.com

Abstract

Cognitive Radio (CR) is a promising technology which resolves the spectrum scarcity issues and allows secondary user (SU) to use the vacant spectrum space without causing interference to the primary user (PU). Many secondary users are allocated different spectrum bands to enhance spectrum utilization. SU co-exists with the PU in the CR network and continuously monitors PU activities in order to use vacant space of PU in the spectrum. The movement of SU in the CR network is random and therefore it is necessary to track the position of SU and measure radio signal strength indicator (RSSI) in order to avoid interference with the PU. In this work, we present the implementation and comparison of two algorithms KALMAN Filter and State Space Least Mean Square (SSLMS) to track the position of SU in the CR network under log distance and log normal shadowing path loss models. Both algorithms track the position of SU by measuring RSSI and Signal to Noise Ratio (SNR) from the PU; however SSLMS gives better performance as compared to KALMAN Filter.

Keywords: Cognitive radio, Spectrum sensing, Energy detection, SSLMS

1. Introduction

In the most latest research paper on the behave of attacker which create disturbance to the functionally of Cognitive Radio network, because of several of user at the same time detect the spectrum and utilize it for different reasons and applications .cognitive Radio is to solve the issues of the spectrum and design the prediction sense of availability of the channel in wireless communication.

However, Cognitive Radio potentially solve the spectrum utilization for the users which is directly related to the secondary user and primary user .spectrum sensing is the major part of Cognitive Radio and it helps to find the primary user whether it is present or not due to this approach most of the research work on detecting algorithm to track the secondary user as quick as possible and to track it accurately, previously on different detection techniques which are used to the sensing purpose of the primary user such as cyclostationary detection, wavelet detection , match filter energy detection [1, 2, 3].

Between the transmitter and receiver both have same fading effect which can create a problem of fluctuating during sensing and by acknowledging these different paths used for fading effect such as log distance path loss and log normal shadowing ,these are the effected propagation model between the transmitter and receiver . In this paper we tried to approach the flexibility of Cognitive Radio in receive signal strength based on the different position of moving secondary user with respect to primary user receive signal strength depends on the different factor and

areas we are focusing on the distance between primary user and secondary user .
Most of the research is based on usage of KALMAN filter for the detection of moving secondary user to estimate the position and velocity but KALMAN filter have some covariance which is the main disadvantage throughout the estimation because there are different errors which are continuously effecting on the behavior of estimation. KALMAN filter is used to detect the fault on the industrial fields and robotic system, image and signal processing [4, 5] and in the field of different criteria like navigation system, automation, stock marketing.
Throughout the research we are interested to track the S.U to estimate the secondary user with the help of STATE SPACE LEAST MEAN SQUARE algorithm is better than KALMAN filter like less computational cost and in this algorithm there is no covariance which means that there is no effect to estimate the position of secondary user, after that we use energy detection method to sense the primary user from probalistic method using signal noise ratio (SNR).
The goal of this paper is to contribute the sensing purpose to make the performance better in low cost as compared to KALMAN filter of the real time detection of primary user with respect to the moving mobility of secondary user.

2. System Model

We describe our scenario networks model in Fig. 1 which we point out our purpose in this paper, this model is solve by the mathematical equations. In our study we have describe two basic approaches in cognitive radio networks

- The fixed primary user (base station).
- Random movement mobility (secondary user) in different direction.

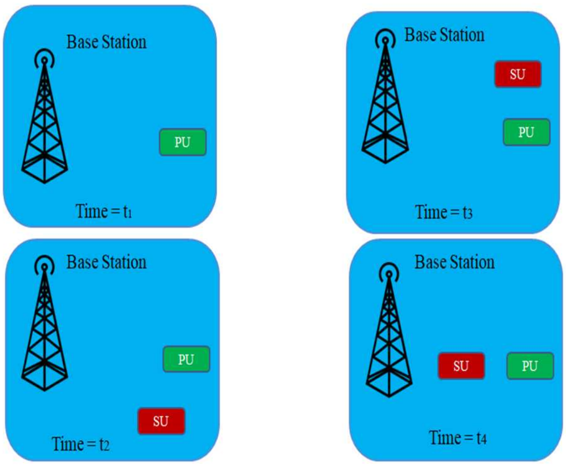

Fig. 1 Moving S.U around primary user

2.1 Propagation Model

Log-distance path loss is generic model which is used to finding the path losses between the transmitter and receiver. The Receive Signal Strength (RSS) is represented in dB between primary user and secondary user

$$RSS_{(SU)} = P_{r_{(SU)}} = P_{t_{(PU)}} \text{-}(\mathrm{P}L_0 + 10\beta log_{10}(\frac{d}{d_0})) \quad (1)$$

Log-distance model Eq. (1) we also represented by,

$$\left[\frac{P_{r_{(SU)}}(d)}{P_{r_{(SU)}}(d0)}\right]_{dB} = \text{-}10\beta log_{10}(\frac{d}{d_0}) \quad (2)$$

$$P_{r_{(SU)}}(d_0) = P_{t_{(PU)}} \text{ - } \mathrm{P}L_0 \quad (3)$$

$$\mathrm{P}L_0 = 20log_{10}\left(\frac{4\pi d_0}{\lambda}\right) \quad (4)$$

We assume the shadowing effect in log-distance path loss, so we get the log normal shadowing due the one additional part so the Eq. 2 is represented by,

$$\left[\frac{P_{r_{(SU)}}(d)}{P_{r_{(SU)}}(d0)}\right]_{dB} = \text{- } 10\beta log_{10}(\frac{d}{d_0}) + X_\sigma \quad (5)$$

Where $P_{r_{(SU)}}$ is the receive power, β is the path loss exponent in different areas, d_0 is the reference distance so we set the $(d_0 = 1)$, d is the distance between transmitter and receiver, λ is the wavelength of the signal, $\mathrm{P}L_0$ reference path, these parameter are used to determine the path losses propagation model and X_σ is the Gaussian distribution with zero means and standard deviation [6–7]. , we calculate the signal to noise ratio (SNR) by using the restive signal strength (RSS) between primary user and secondary user is represented by

$$SNR_{(PU,SU)} = \left(\frac{P_{r_{(SU)}}(d)}{P_{noise}}\right) \quad (6)$$

$$SNR_{(PU,SU)}(dB) = P_{r_{(SU)}}(d)\,(dB) - P_{noise}(dB) \quad (7)$$

$P_{noise}(dB)$ is the noise power, so the SNR in dB is Eq. 7 .

2.2. Spectrum Sensing Model

In this model we represent local spectrum sensing in energy detection, the sensing process or the detection of the primary user divide into two parts first one is cooperative spectrum sensing (CSS) and the second part is local spectrum sensing (LSS).for the local spectrum we take the secondary user each has energy detector which is used to sensing purpose for primary user and identifying the primary user is absent (H_0) or present (H_1),

•When the primary user is absent so the output signal at the secondary user is defined as

$$Y(t) = w(t) \longrightarrow H_0 \quad (8)$$

•When the primary user is present so the output signal at the secondary user is defined as

$$Y(t) = x(t) + w(t) \longrightarrow H_1 \quad (9)$$

$Y(t)$ is the receive signal strength at the secondary user under the AWGN channel which are use in both cases log distance path loss and log normal shadowing, after the receiving signal the secondary user decided to H_0 or $H_1$and sense the primary user with respect to the energy at the secondary user ,

$$E = \left(\frac{1}{M}\right)\sum_{n-1}^{M}|y_n|^2 \quad (10)$$

y_n is the receive signal with the sample size M, the secondary user mobility continuously moving so that the effect on sensing which is bandwidth of signal, due to this behavior we assume the two energy performance at the secondary user the energy, we can write the Eq. 10 as follows,

$$E = \begin{cases} E1 = \left(\frac{1}{M}\right)\sum_{n-1}^{M}|y_n|^2 \\ E2 = \left(\frac{1}{M}\right)\sum_{n-1}^{M}|x_n + w_n|^2 \end{cases} \quad (11)$$

Eq.11 also expressed in as

$$E = \begin{cases} E1 = x^2{}_M & \rightarrow H_0 \\ E2 = x^2{}_M(2\gamma) & \rightarrow H_1 \end{cases} \quad (12)$$

$x^2{}_M$, $x^2{}_M(2\gamma)$, these parameter to determine using the chi square distribution central and non-central with the degree of freedom M, (γ) is the real value of SNR which are converted to from dB, to check the sensing performance of the primary user, we use the probability of detection against the false alarm detection

$$Pd = P(E > \delta H_1) = Q_M(\sqrt{2\gamma}, \sqrt{\delta})$$
(13)

$$Pf_a = P(E > \delta|H_0)\ \frac{\Gamma(M,\frac{\delta}{2})}{\Gamma(M)} \quad (14)$$

Q_M is the Marcum Q function [9] which directly determine the theoretical value, Γ is the gamma function [8] and δ is the threshold decision to check the against energy of signal.

3. Results

Scenario 1 (log distance path loss)

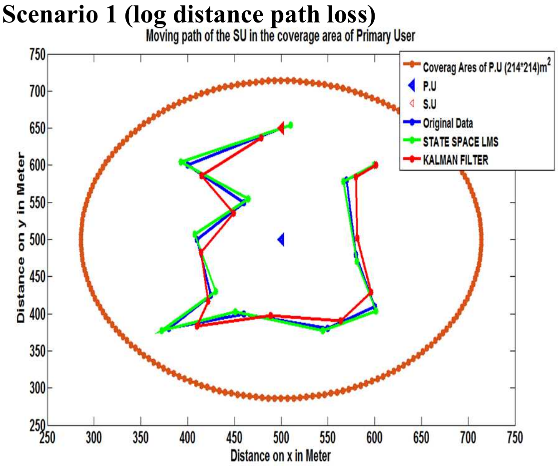

Fig.2 SU movement

In Fig.2 we are tracking secondary user through primary user for that we have to assign a coverage area. If secondary user is in the coverage area the primary user will detect it and then we are predicting the future value of secondary user through KALMAN filter and SSLMS

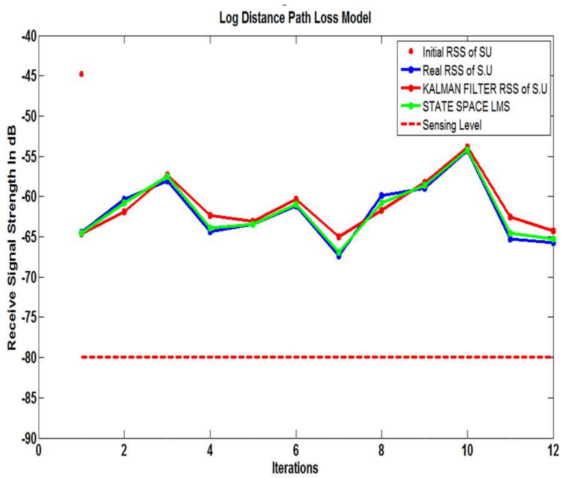

Fig.3 SU RSS measurements

In Fig.3 the graph is in between receive signal strength and iteration. In this figure we have assign a threshold or a reference line that if the signal is above the reference we have high receive signal strength

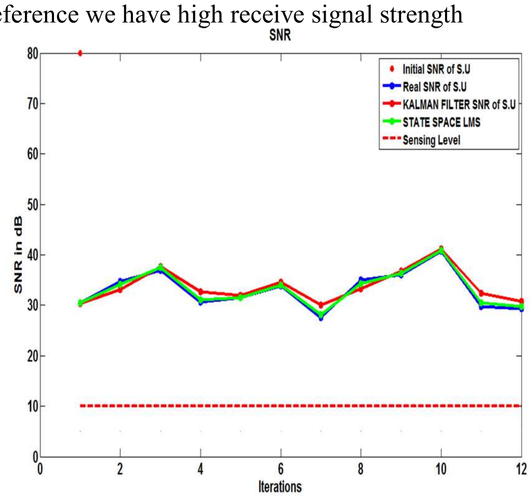

Fig.4 SU SNR measurements

In Fig.4 the graph is in between signal to noise ratio and iteration. In this figure we have assign a threshold or a reference line that if the signal is above the reference we have high signal to noise ratio at different position of secondary user.

Scenario 2 (log normal shadowing path loss)

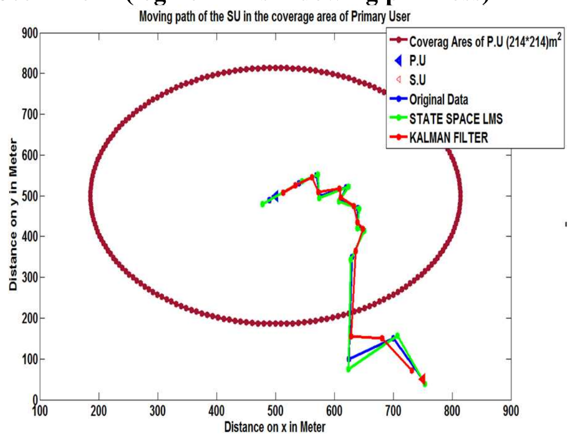

Fig.5 SU movements

In Fig.5 secondary user is out of the coverage area and then we apply KALMAN filter and SSLMS to predict the next value of secondary user through primary user for that we have to assign a coverage area. If secondary user is in the coverage area the primary user will detect it and then we are predicting the future value of secondary user through KALMAN filter and SSLMS

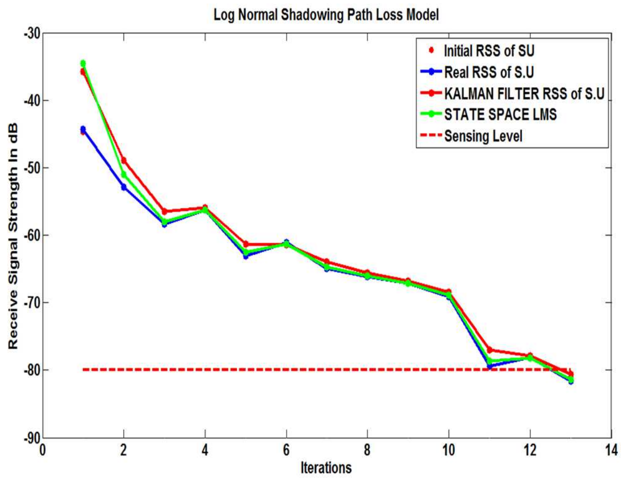

Fig.6 RSSI measurements

In the above Fig. 5 we see that the secondary user is out of the coverage area then we calculate it's receive signal strength through KALMAN filter and SSLMS in Fig. 6 and we see that its graph is decreasing to threshold or reference line. and is also decreasing calculate the receive signal strength then we see that if it goes out of the coverage area the graph will go under the threshold or reference lin

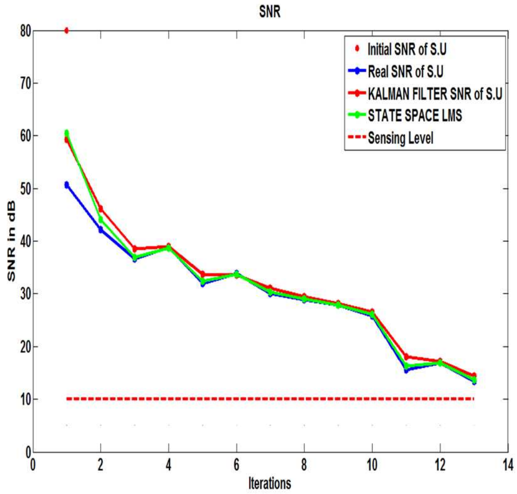

Fig.7 SNR measurements

In Fig.7 the value of signal to noise ratio is decreasing to threshold because the secondary user is out of the coverage area that's why its SNR is decreasing.

The graph is in between signal to noise ratio and iteration. In this figure we have assign a threshold or a reference line that if the signal is above the reference we have low signal to noise ratio at different position of secondary user.

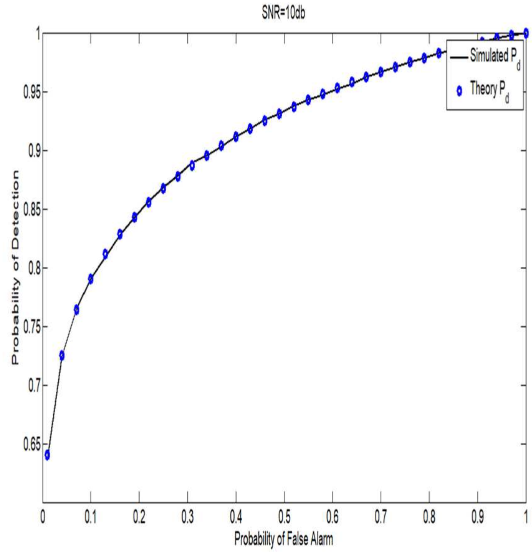

Fig.8 Detection of SU

In Fig.8 this graph shows the probability detection vs. false alarm at 10 dB, we observed that if the graph is away from the diagonal the probability of detection is greater and if it is near to diagonal the probability of false alarm is greater.

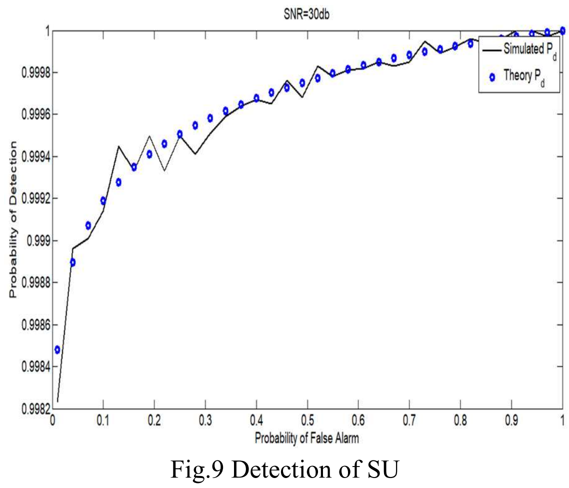

Fig.9 Detection of SU

In Fig.9 this graph shows the probability detection vs. false alarm at 30 dB, we compare both the above graph and observe that which have a greater probability of detection. If the value of signal to noise ratio is greater the probability of detection is greater and vice versa And if this graph is away from the diagonal the probability of detection is greater and if it is near to diagonal the probability of detection is lower.

References

1. Akyildz, I. F., Lo, B. F., & Balakrishnan, R. (2011). Cooperative spectrum sensing in cognitive radio networks: A survey. Physical Communication, 4(1), 40–62.
2. Akyildz, I. F., Lee, W. Y., Vuran, M. C., & Mohanty, S. (2006). NeXt generation/dynamic spectrum access/cognitive radio wireless networks: A survey. *Computer Networks*, 50(13), 2127–2159.
3. Ben Letaief, K., & Zhang, W. (2007). Chapter: *Cooperative spectrum sensing. Cognitive wireless communications networks* (pp. 115–138). Berlin: Springer.
4. Michael, P., & Phillip A. L. (2003). Kalman filter recipes for real-time image processing. *Real-Time Imaging*, 433–439.
5. Abhik, M., Partha, P. A., Nandi, P-K., Pinakpani, P., & Das, J. (2002). Estimation of atmospheric boundary layer using Kalman filter technique. *Signal Processing*, 1763–1771.
6. Andrea, G. (2005). *Wireless communications*. Cambridge: Cambridge University Press.
7. Sohra, S., Mohammed, F., & Abdelmalek, A. (2012). Seamless infrastructure independent multihomed NEMO handoff using effective and timely IEEE 802.21 MIH triggers. *International Journal of Wireless and Mobile Networks (IJWMN)*, 4(3), 119–139.
8. Gradshteyn, I. S., & Ryzhik, I. M. (1994). Table of integrals, series, and products (5th ed.). Waltham: Academic Press
9. Nuttall, A. H. (1975). Some integrals involving the QM function. IEEE Transactions on Information Theory, 21(1), 95–96.

Wireless Power Transfer And Data Communication For Biomedical Application

Hammad Saleem, Muhammad Awais, Siraj Din, Attequa, Asma Mahar
BEelectrical,PAF KIET(Karachi Institute of Economics and Technology),KorangiCreek
Karachi,75190, Pakistan
Email:hammadmughal265@gmail.com,awaischaudhry101@gmail.com,attequa.engineer@gmail.com,
qureshi8932@gmail.com,asmamahar@hotmail.com,www.pafkiet.edu.pk

Abstract

A technique of wireless power transfer(WPT) system for biomedical applications with backscattering communication ,a rectifier use with active bias mechanism(dependent and independent stages) overcome the diode device losses has been presented in this paper .A part from conventional and static Vth cancellation technique rectifiers, it achieve s more than double efficiency and achieves powerless reduction in both forward and reverse biased condition s it decrease turn on voltage in forward bias condition along with decrease in reverse leakage current during reverse bias condition. Under the input conditions (Vin=1Vp-p coupling coefficient's=0.01 at 200MHzfrequency with transmitter and receiver inductanceof22nH),actively biased differential drive rectifier sable to achieve DC voltage of 880mv for 50kΩ load resistance independent stage and achieves DC voltages of 803.2mv for 50kΩ load resistance in independent stage. Backscattering communication has been performed using switch by changing the resonance frequency of the receiver.

Keywords: wireless power transfer (WPT), backscattering communication, inductor, rectifiers.

1. Introduction

Recently, wireless power transfer (WPT) technology has become a very popular research topic, particularly in applications related to portable device chargers and biomedical devices. Since the WPT idea was proposed, many researchers have tested the probability of applying this concept to commercial applications. The WPT has been prevented from widespread used for a number of reasons, but the major issues are the power transfer efficiency. Therefore, the target of all research in the field of WPT is to improve the efficiency of the WPT system so t hat less transmitting power is required for a longer distance between the external transmitting device and the implant device can be facilitated while using the same transmitting power from the external device. To achieve the target, be sides improving the performance of coil transfer, the rectifier also plays a very important role in the total efficiency of the WPT system.

The faraday's law of induction was proposed by Michael Faraday in 1831, provided the basis for advancements in wireless power transfer WPT systems. The concept of WPT was not new, however this concept was first found by Nikola Tesla centuries ago.In1891, Nikola Tesla was performed resonant wireless power transfer experiments and after four year she was received patents in1894.In that patent she was claimed the use of resonance to achieve high efficiency of WPT. In 1960-70s wireless power transfer WPT was utilized in many applications such as Bluetooth, mobile phone, Biomedical and smart watches. In multiple biomedical applications using resonant coupling. With the advancement in CMOS process, the integration of 2 dimensional and 3 dimensional inductors have opened doors for wireless power transfer to these small size devices.

In this work two different techniques are proposed to achieve regulating DC voltage along with enhance backscattering communication. A high Q on-chip custom inductor design is also presented to meet area constraint of bio-medical implants. The on-chip receiver inductor is used for both receiving power and communicating data back to the external device. Both highly efficient approaches are discussed with each of them having its own advantages in certain regard. While striving for high WPT efficiency, receiving circuitry efficiency is taken into account along with the rectifier conversion efficiency. To ensure sufficient wireless power transfer through EM coupling, coupling coefficient 'k' is estimated prior to the circuit design. 'k' for a certain application is determined by the transmitted power, inductor Q factor and distance between coils. To maximize the signal reception at receiving end, high Q inductor design has been proposed in [1]. [2] Suggests an improved resonator with better transmission efficiency in contrast to spiral and helical resonators occupying same volume. Another design methodology integrating rectifier with the antenna (rectenna) for incident power as low as 5- 100uW/cm2 has been presented in [3].

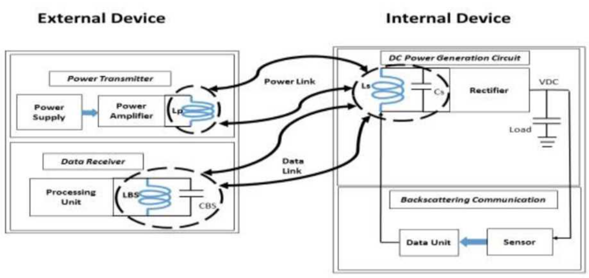

Fig. 1. Inductive Wireless Power Transfer System block diagram

In addition to the forward power link, most of these applications require a reverse data link to acquire information on an external device for processing. The data is sent back on a wireless communication channel using the same on-chip receiver coil. Immense research has been carried out recently to avoid the degradation of power efficiency due to conventional backscattering Techniques [5]. This will be discussed later in section.

A complete pictorial representation of WPT system along with backscattering communication is shown in fig.1. It has an external device and an internal device. The power is transferred through coupling among primary and secondary coil. The primary coil when driven by the power amplifier generates AC magnetic fluxes. This variable flux couples to the secondary coil and produces an AC signal at the receiving end. Received AC signal is rectified to power up device. Most often this dc signal is also processed to send back desired output voltage inside the chip. If the device has sensor in it, and sensor data is required externally, then it is sent instead of DC encoded signal over the backscattering channel. Sensor data proper reception on receiving end also ensures the required power generation.

For backscattering communication, varactor or a switch is connected in parallel to the receiver circuit to vary the peak voltage at data frequency. This data is received externally on a separate coil resonating at frequency of backscattered data. The frequency of data is kept below the WPT frequency to keep the efficiency degradation of WPT minimum. This data is processed to extract required information. For the available area of 710*710um2, highest possible Q, L and SRF is required for a planar inductor design. The planar inductors have many shapes such as square, hexagonal, octagonal or circular. However circular planar inductor has highest Q factor, while square planar inductor has the minimum. But as the required inductor needs to couple with external coil, coupling coefficient 'k' is desired to be maximized and the coupling coefficient 'k' is directly dependent on the area of the coupling inductors. Where, coupling coefficient 'k' is given by: $\boldsymbol{K}=\mathbf{M}\sqrt{\mathbf{L1}*\mathbf{L2}}$ (1) If the area of the coupling coils is not same, 'k' is determined by the area of the smaller coil which signifies the dependence of 'k' on the area of on-chip inductor because off-chip coil could be kept larger. Therefore, the square inductor is most suitable for such applications where device performance is dependent on the coupling among coils. While square inductors Q factor is also accounted for WPT performance, Lower Q factor of the square inductor because of the sharp turns at the edges which increases conduction losses of the inductor. Then the sharp edges are replaced by the diagonally cutting edges which improves Q factor by 3.5%.

Custom inductor design with 25um width, spacing equal to 6um, inner radius of 175um, outer radius of 355um and number of turns equal to 6, Fig 2 shows was simulated on EM Simulator for 150nm 6 metal A1 CMOS technology provided by L Foundry. Ports of inductor are defined on same layer to maintain symmetry as different metal layers have different resistivity and distance from substrate.

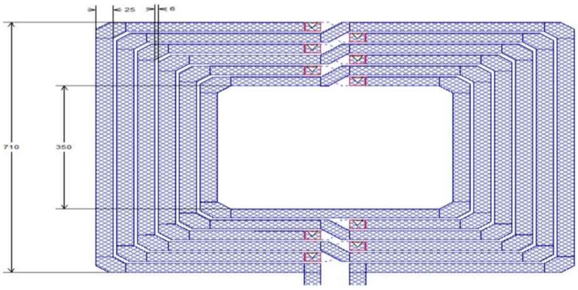

Fig. 2. Inductor Design

2. Major Headings

Major headings should be typeset in boldface with the first letter of important words capitalized.
Sub-headings should be typeset in boldface italic and

3. Differential Drive Rectifier with Active Bias Mechanism

The power conversion efficiency of a rectifier circuit is dependent upon the forward and reverse biased power loss of the diode connected devices. Where forward power loss is due to the turn on voltage of the device and reverse power loss is due to leakage current.
Power conversion efficiency (PCE) of rectifier is defined as.

$$PCE = P\_out / P\_in$$

$$P\_in = P\_out + P\_rectloss \quad (3)$$

Where, P_out and P_in represents output and input power respectively show in eq 2 and P_rectloss represents power loss across rectifier show in eq 3.

4.1. *Active Bias Mechanism (Dependent stages)*

The static Vth cancellation techniques constantly provide Vth at the gate and source of the transistor, irrespective of the instantaneous input AC signal Amplitude. This helps achieve very small forward bias resistance but also increases the reverse leakage current. In ref [4] and [5], an active bias mechanism has been proposed which automatically reduces reverse leakage current by increasing Vth in reverse biased condition while keeping Vth low during forward bias condition. This active mechanism achieves double the efficiency as compared to static Vth cancellation. The rectifier is a cross coupled configuration driven by a differential input signal as shown in fig. 3. The WPT frequency is 200MHz. When Vac+ has its positive cycle, Vac- is negative hence reducing the turn on voltage. Similarly, when Vac+ gets negative, Vac- is positive, hence increasing Vth in the reverse biased condition.

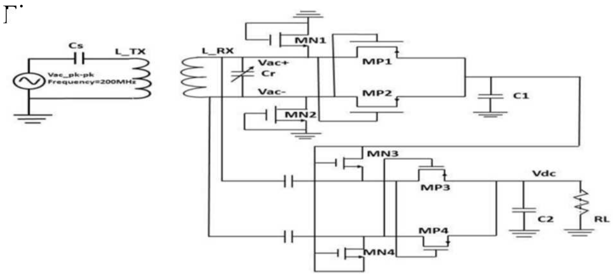

Fig. 3. Differential Drive Rectifier circuit (Dependent Stages)

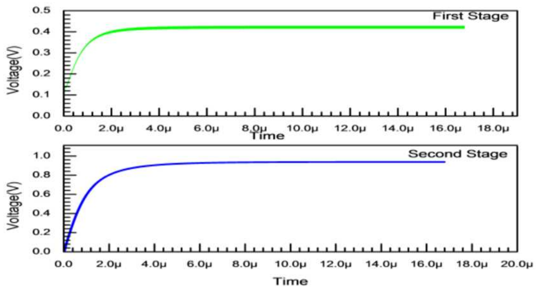

Fig. 4. Voltage at output of stage 1 and stage 2

The stage is copied twice with first stage providing bias voltage to the second stage, shown in fig 4. This is known as self Vth cancellation as the rectifier itself is providing the required bias voltage.
Another interesting feature of this rectifier circuit is that if the first and second stage N and PMOS devices are properly matched, the intermediate stage capacitor can be removed or a small capacitor could be sufficient to reduce the voltage ripple. This is because the forward current of NMOS can be sunk by the PMOS and vice versa.
Also, multiple stages of this rectifier can be used to further improve the output dc voltage according to the requirement. But as this circuit works on self-bias mechanism, the input voltage should be sufficient

enough to provide Vth to the first stage devices to start functioning.

4.2. *Active Bias Mechanism (Independent stages)*

Reconfigurable rectifier (dependent stages) was a good rectifier in respect of voltage, but the problem is by increasing its rectification stages the voltage are increases but due to its dependent stage, the DC shifts and connects to the second stage, By this reason the lower PMOS of second stage starts to lose the current due to unavailability of negative peaks and by the reason the overall power efficiency started to decrease. To avoid this problem, a new design is proposed that is independent stages reconfigurable rectifier.

This rectifier has two stages that are doing individual rectification. First stage generates positive DC and second stage generates negative DC show in fig 5, and we drive a load by these two independent DC voltages. As per its independent stage, voltage isn't shifts to DC at second stage and it's both NMOS works accurately. This circuit gives 80.3% efficiency on 50 K load, 82.2% efficiency on 100 K load and 83% efficiency on 300 K load show in fig 6.The difference voltage at load shown in fig 7.

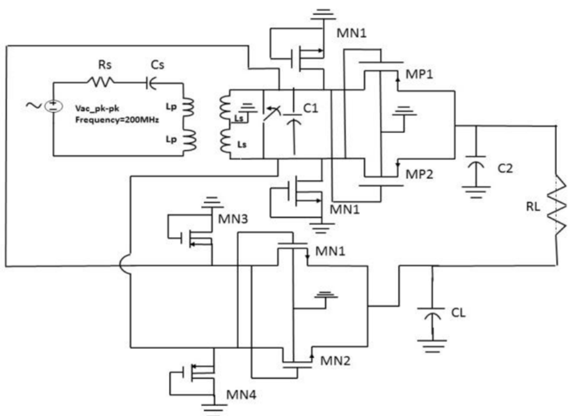

Fig .5. Differential Drive Rectifier circuit (Independent Stages)

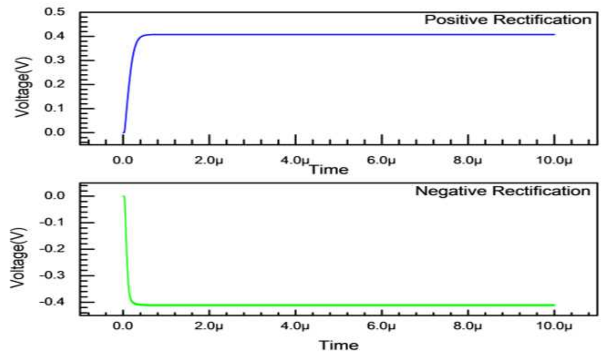

Fig .6. Voltage at output of stage 1 and stage

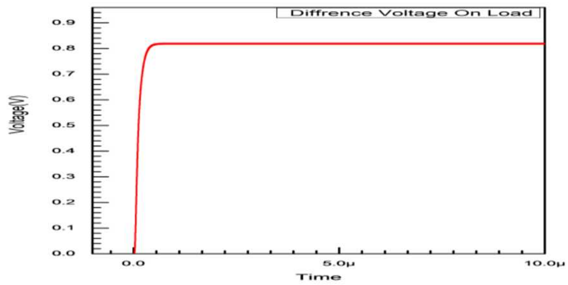

Fig .7. Difference Voltage at Load

5. Backscattering Communication

Conventional backscattering employs a switch in parallel with the receiver coil. The amplitude of the received signal is varied by switching it ON for either '1' or '0' of the data, while keeping it OFF for the other. The ON resistance is usually kept sufficient enough to obtain backscattering signal amplitude of 200-250mV. This is shown in fig 8.The main concern of this paper is that the efficiency of WPT should be least effected by backscattering. Data rate is kept quite low as compared to WPT frequency, but the dc for both '1' and '0' of the data should be sufficient enough to meet the requirements of the device

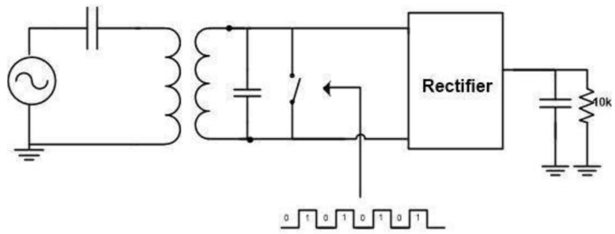

Fig .8. Conventional backscattering technique

6. Conclusion

A differential drive rectifier with active Vth cancellation technique (Dependent and independent stages) has been presented. The output DC voltage generated is 0.835mV. The efficiency improvement is considerable. Along with high efficiency, circuit shows a self- regulated output DC voltage for different coupling conditions. Which adds robustness to the design? But backscattering is possible in dependent stage because of their dependency backscattering not affect the input voltages but their leakage current increase and if number of independent states increased then it reduce their reverse leakage current but backscattering was not efficient. Backscattering using switch by changing the resonance frequency of the receiver has been shown. For a 200mV backscattered data, DC change of only 110mV was observed, effecting WPT efficiency by only 7%.

References

[1] Chia-Chu Wu, Hung-Wei Chiu, Da-Sheng Lee, Min-Hsiang Chang, Chien-Chi Lu, and Chao-N ing Chang, "High Q Inductor Design Using M odified Magnetic Substrate Structure", *IEEE International Conference on Wireless Power Transfer*, pp 284-287, May 2014.

[2] WeiWeiYoshihiro Kawahara and Tohru As ami, "Experimental Analysis of Double Spir al Resonator for Wireless Power Transmissio n", *IEEE transaction*, pp 9-12, 2013.

[3] Zoya Popovic, "Far-Field Wireless Power Deli very and Power Management for Low-Power Sensors", *IEEE transaction,* pp 1-4, 2013.

[4] K. Kotani and T. Ito, "Self-Vth-cancellation high-efficiency CMOS rectifier circuit for UHF RFIDs," *IEICE Trans. Electron.*, vol. E92-C no. 1, pp. 153–160, Jan. 2009

[5] A.Sasaki, K.Kotani, and T.Ito, "Differential-drive CMOS rectifier for UHF RFIDs with 66% PCE at -12 dBm input," in *Proc. IEEE ASSCC*, pp. 105–108, Nov. 2008

.

Feasibility Study of UAV Implementation In Route Surveying

Hazry Desa
Centre of Excellence for Unmanned Aerial Systems (COEUAS), UniMAP, Kangar, Perlis Kangar, Perlis, Malaysia
Mohd Azizi Azizan
Centre of Excellence for Unmanned Aerial Systems (COEUAS), UniMAP, Kangar, Perlis Kangar, Perlis, Malaysia
Safwan Suhaimi
Centre of Excellence for Unmanned Aerial Systems (COEUAS), UniMAP, Kangar, Perlis Kangar, Perlis, Malaysia
Zulaiha Ramli
Centre of Excellence for Unmanned Aerial Systems (COEUAS), UniMAP, Kangar, Perlis Kangar, Perlis, Malaysia
Mohamad Syafiq Abdul Khadir
Centre of Excellence for Unmanned Aerial Systems (COEUAS), UniMAP, Kangar, Perlis Kangar, Perlis, Malaysia
Zainuddin Hat
IP Fokus Sdn Bhd
Bandar Baru Bangi, Selangor, Malaysia
E-mail: aziziazian@unimap.edu.my, msyafiq@unimap.edu.my
www.unimap.edu.my

Abstract

Unmanned Aerial Vehicle (UAV) are widely used in numerous field and the technology keeps growing. Generally, conventional method use in data collection for engineering work is tedious and requires a lot of manpower. This research focuses on the investigation of the suitability of UAV for route survey. Three stages involved: data collection, data processing and data analysis. By using KAMA BETA, the data was collected. For data processing, PIX4D MAPPEER used for point cloud and AutoCAD 2014 for analysis stage. The result is mainly focused on extracting the road profile and test the point cloud data using RMSE. The result from both method, conventional and UAV from the point cloud data using RMSE show only the small difference, with only 6.67% from total 60 points out of tolerance.

Keywords: UAV, engineering work, land survey, drone.

1. Introduction

Engineering survey is a survey undertaken for the purpose of obtaining information essential to the planning of an engineering project. Engineering survey provides accurate and reliable dimension data through the construction process from the base topographical survey, cross-section and ground modeling information to cut and fill calculation, dimensional control to setting-out on-site and finished as-built drawing [1].

Route surveying is comprised of all survey operation required for designing and construction of engineering works such as highways, pipelines, canals or railroads. Survey operations in route survey include topographic survey, cross-section and longitudinal section [2].

Unmanned aerial vehicles (UAVs), also known as "drones", are among the most important technological advances that have been introduced to the land surveying industry in quite some time. It can be piloted by remote and can take detailed survey information while simultaneously transmitting that data back to the head office. UAVs create a highly accurate map and provide valuable data to companies and individuals who are considering major projects on large areas of land. Research about the reliability of these techniques to be used in topographic mapping was conducted in land survey method [3].

2. Methodology

2.1. *Planning and Preparation*

Planning and preparation are needed before the data collection. Planning and preparation cover the scope of work such as planning for the area of the survey and the preparation for the instrument and software used in this project. A good planning and preparation enable to ensure efficiency and maintaining a high quality of the data collection in this study. Furthermore, proper planning and preparation help in saving time and cost as time increase, the cost will increase as well. The figure below shows general planning and preparation for UAV and TS.

2.2. *Data Collection*

Data collection for this study is focused into two methods. The first method of data is used as a conventional method by total station. Besides that, the second method for this study used a new method by Unmanned Aerial Vehicle (UAV).

2.3. *Data Processing*

Data processing for this study refers to processing for the laser and the conventional method. Data processing for a conventional method uses the Civil Design & Survey software. Besides that, for the UAV processing used Pix4D Mapper. Both use AutoCAD as data analysis processing.

3. Result and Analysis

3.1. *Camera Calibration*

The camera calibration is done before do the flight planning. The purpose of camera calibration is to determine the focal length, principal point, and lens distortion from the camera. This process was carried out to figure out the unstable element in the camera like interior orientation and lens distortion parameters [5].

In this project, the camera calibration is processed using PhotoModeler Software. This software is an automatic lens calibration, which uses A1 paper sheet as a calibration target. It supports estimations of the full camera calibration matrix, including non-linear distortion coefficient.

To check the accuracy of the camera calibration results the total final error must be checked. In both methods the data sets are not the same. For lab calibration the data set is the grid of the pattern and for filed calibration are the 67 targets points. According to PhotoModeler tutorial a value less than 1.0 pixel indicates a good calibration and very good calibrations can have a final total error smaller than 0.4 pixels (www.photomodeler.com). In this case, the lab calibration has a final error of 1.940 pixels.

Table 1. Total final error and residuals of the camera calibration projects.

	Lab calibration	Field calibration (50m flight high)
Final total error (pixel)	1.940	0.282
Largest marking residual (pixel)	0.723	0.700
Overall RMS (pixel)	0.245	0.341

The total error a bit higher than the recommended. The field calibration has a total error of 0.282 pixels, which is assumed to be a very good calibration project. Also checking the marking residuals is a good way to test the calibration quality [6]. PhotoModeler tutorial recommended having a largest marking residual less than 1.0 pixel [3]. In both cases the largest marking residuals are less than 1.0 pixel. The lab calibration has 0.723 pixels and the field calibration 0.700 pixels (Table 1).

The accuracy of field calibration was also checked to compare the GPS coordinates of the targets with the coordinates obtained with PhotoModeler. This software only needs three control points to change from relative to absolute coordinates. For this process, the targets number one, two and four were used. The planimetric and the altimetric RMS were calculated. The planimetric RMS was 0.028 m and the altimetric 0.026 m, which is really small and indicates the accuracy level of the project.

3.2. *Georeferencing*

Ground control point (GCP) and verification point (VP) are very important data that are used to involve in aerial triangulation phase, where it can be identified on the ground features and can be georeferenced with the aerial image used in geometric correction of the distorted image [8]. Therefore, pre-marking for GCP's and VP's must be carried out before a flight mission. This is because the processing of the tie point image could be more efficient and accurate. The coordinates and z-value that were observed using leveling method (land survey).

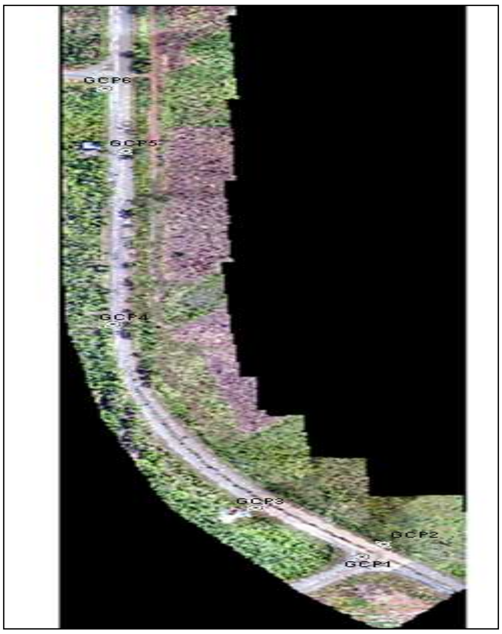

Fig. 2. Location of GCP in UAV images in Chuping, Perlis, Malaysia (Orthophoto).

Figure 2 shows the strategic location of placement six (6) GCP's. The location of GCP was in Chuping, Perlis, Malaysia. Each of GCP is observed by GPS equipment (Topcon – GR5) using Static Method. The reason of this method selection because this method is the most widely used differential technique for control and geodetic surveying, involved 1 hour of observation in order to resolve the integer ambiguities between the satellite and the receiver. By using this method, the accuracies in the sub-centimeter range can be obtained.

3.3. *Digital Surface Model (DSM)*

Aerial image was taken from above with 14 minutes flight duration. To achieve this project the overlap is 80%, sidelap is 70% and the altitude is 110 meters. This overlapping and flight altitude is required to avoid potential missing areas of coverage and to ensure good coverage. Based on the data that has been processed using Pix4D software produced an Orthophoto and DSM in raster as shown in Figure 2 and Figure 3.

Figure 3 shows the sample result road profile of UAV and TS data for CH 1 to CH 10, which is located in Chuping, Perlis, Malaysia. Based on Figure 3, the red color is referring to the highest elevation while soft blue color is referring to the lowest elevation [8].Therefore, it can clearly be seen that the UAV data gives a greater number of point compare to TS data. Besides that, the profile generated by using UAV is denser than the TS data due to the great number of point [9].

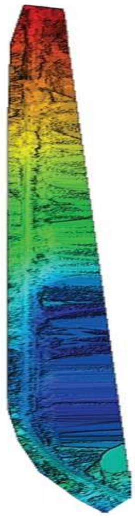

Fig. 3. DSM of the project area (Location: Chuping, Perlis, Malaysia).

3.4. *Statistical Analysis*

The road profiles are tested with Root Mean Square Error (RMSE) which is done by analyzing comparison of differences between and within the group. The road profile is statistically tested by used the RMSE test at each chainage to ensure that the data of UAV and TS is significant to each other.

Root Mean Square Error (RMSE) is the standard deviation of the residuals (prediction errors). Residuals are a measure of how far from the regression line data points are; RMSE is a measure of how to spread out these residuals are. In other words, it tells you how concentrated the data is around the line of best fit. Root mean square error is commonly used in climatology, forecasting, and regression analysis to verify experimental results [9].

The formula is:

$$\boxed{\mathrm{RMSE}_{fo} = [\sum_{i=1}^{N} (z_{f_i} - z_{o_i})^2 / N]^{1/2}} \quad (1)$$

Where:
Σ = summation ("add up")
(zfi – Zoi)Sup>2 = differences, squared
N = sample size

There is three type of sample are tested using RMSE formula, verification point, positioning and elevation. Values from the real measurement are compared with the value from the 3D modeling to get the error of every sample.

Based on Figure 4, it can be seen that the graph values of RMSE Verification Points for minimum and maximum errors. All the VPs are under tolerance which is below ±0.10m.Based on Figure 5, it can be seen that the graph values of RMSE Cross Section for minimum and maximum errors for Different Elevation (H). The best result is ±0.03m (VP5). VP9, VP10, and VP18 are out of tolerance which is above ±0.10m.

The values of RMSE XY for minimum and maximum errors can be referred to Figure 6. All the XY are under tolerance which is below ±0.10m except at VP19 with value ±0.125m. These results might be affected by image matching algorithm that was used in the same software during image processing. The error was usually caused by flying height during image acquisition, image matching during image processing and motion movements such as omega, phi, and kappa [10].

4. Conclusion

As a conclusion, three objectives of this study has been achieved. The first objective to process image capture from Unmanned Aerial Vehicle (UAV). The most important procedure for route survey work is data collection. Planning and preparation in this study focusing on planning for a number of GCP and flight planning. Number of GCP depend on a number of flight planning where need minimum visible from the aerial view and location of GCP. After that, the procedure for route survey by using UAV need to focus on processing the point cloud data. Starting with data registration point cloud data use minimum three images that visible each other. Then, the next process is point cloud densification using PIX4D Mapper software. Then next process produces DSM and Orthophoto. In this research, two methods was applied, land survey and UAV survey.

A land survey is used as a benchmark for this research. Point cloud data produce in 2D data with 3D coordinate which can use to generate road profile for route survey. The third objective for this study to analyses the accuracy between land survey data and UAV data. Series of test and analysis have been conducted in term of the reliability of UAV data in completing route survey. The reliability of UAV data shows in quantitative assessment by comparing result road profile from UAV and TS method.

Acknowledgements

The author acknowledge ICAROB for giving the opportunity to join this conference. Highly appreciation to UAS research team for excellent contribution. A special gratitude to IP Fokus Sdn Bhd for full support in completing this project.

Fig.4. RMSE error verification points.

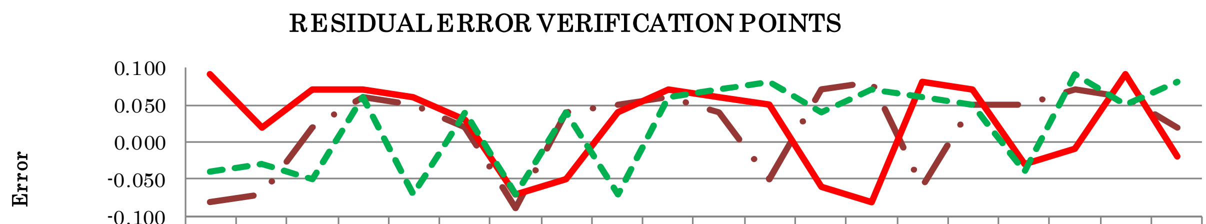

	VP 1	VP 2	VP 3	VP 4	VP 5	VP 6	VP 7	VP 8	VP 9	VP 10	VP 11	VP 12	VP 13	VP 14	VP 15	VP 16	VP 17	VP 18	VP 19	VP 20
Diff Easting (E)	-0.08	-0.07	0.020	0.060	0.050	0.020	-0.09	0.040	0.050	0.060	0.040	-0.05	0.070	0.080	-0.06	0.050	0.050	0.070	0.060	0.020
Diff Northing (N)	0.090	0.020	0.070	0.070	0.060	0.030	-0.07	-0.05	0.040	0.070	0.060	0.050	-0.06	-0.08	0.080	0.070	-0.03	-0.01	0.090	-0.02
Diff Elevation (H)	-0.04	-0.03	-0.05	0.060	-0.07	0.040	-0.07	0.040	-0.07	0.060	0.070	0.080	0.040	0.070	0.060	0.050	-0.04	0.090	0.050	0.080

Fig. 5. RMSE error cross section.

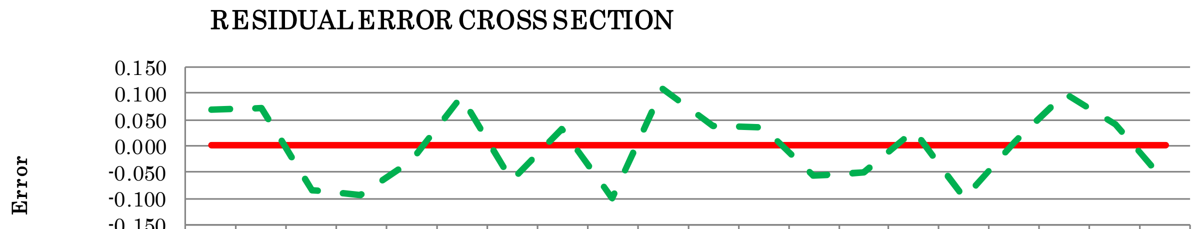

	VP 1	VP2	VP3	VP4	VP5	VP6	VP7	VP8	VP9	VP10	VP11	VP12	VP13	VP14	VP15	VP16	VP17	VP18	VP19	VP20
Diff Easting (E)	0.000	0.000	0.000	0.000	0.000	0.000	0.000	0.000	0.000	0.000	0.000	0.000	0.000	0.000	0.000	0.000	0.000	0.000	0.000	0.000
Diff Northing (N)	0.000	0.000	0.000	0.000	0.000	0.000	0.000	0.000	0.000	0.000	0.000	0.000	0.000	0.000	0.000	0.000	0.000	0.000	0.000	0.000
Diff Elevation (H)	0.070	0.073	-0.08	-0.09	-0.03	0.093	-0.06	0.032	-0.10	0.110	0.038	0.034	-0.05	-0.05	0.030	-0.09	0.008	0.100	0.041	-0.07

Fig. 6. Residual Error XY.

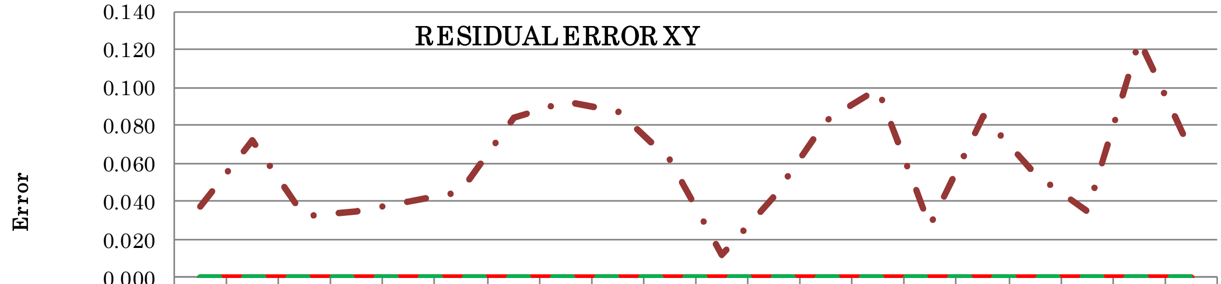

	VP 1	VP2	VP3	VP4	VP5	VP6	VP7	VP8	VP9	VP10	VP11	VP12	VP13	VP14	VP15	VP16	VP17	VP18	VP19	VP20
Diff Distance (m)	0.037	0.072	0.032	0.035	0.040	0.045	0.084	0.093	0.087	0.062	0.012	0.042	0.082	0.099	0.027	0.085	0.054	0.035	0.125	0.066
Diff Northing (N)	0.000	0.000	0.000	0.000	0.000	0.000	0.000	0.000	0.000	0.000	0.000	0.000	0.000	0.000	0.000	0.000	0.000	0.000	0.000	0.000
Diff Elevation (H)	0.000	0.000	0.000	0.000	0.000	0.000	0.000	0.000	0.000	0.000	0.000	0.000	0.000	0.000	0.000	0.000	0.000	0.000	0.000	0.000

References

1. Ahmad, A., Hashim, K. A., & Samad, A. M. (2010).Aerial mapping using high resolution digital camera and unmanned aerial vehicle for Geographical Information System. *2010 6th International Colloquium on Signal Processing & its Applications*. doi:10.1109/cspa.2010.5545303
2. Eisenbeiss, H. (2004). A mini unmanned aerial vehicle (UAV): system overview and *image acquisition*. 1.
3. Everaerts, J. (2008). *The use of unmanned aerial vehicles (UAVs) for remote sensing and mapping*. 1-2.
4. Peterman, V., & Mesaric, M. (2012). Land Survey from Unmanned Aerial Vehicle. *Int. Arch. Photogramm. Remote Sens. Spatial Inf. Sci*, XXXIX-B1, 447-451. doi:10.5194/isprsarchives-xxxix-b1-447-2012
5. Pérez, M., Aguera, F., & Carvajal, F. (2012). Digital Camera Calibration Using Images Taken From an Unmanned Aerial Vehicle. *Int. Arch. Photogramm. Remote Sens. Spatial Inf. Sci,* XXXVIII-1/C22, 167-171. doi:10.5194/isprsarchives-xxxviii-1-c22-167-2011
6. Samad, A. M., Kamarulzaman, N., Hamdani, M. A., Mastor, T. A., & Hashim, K. A. (2013). The potential of Unmanned Aerial Vehicle (UAV) for civilian and mapping application. *2013 IEEE 3rd International Conference on System Engineering and Technology*. doi:10.1109/icsengt.2013.6650191
7. Zulasmin,W. and Ibrahim,W. "Towards a Sustainable Quarry Industry in Malaysia *Limestone and Granite Quarry Industry*," no. December, 2007.
8. Alias, R.B (2013). *Statistic for science and engineering.* Kuala Lumpur, Malaysia : Universiti Technologi MARA
9. Bienert a. s. schiller. keana, e ., mohan f and nugent, c (2007). *Tree detection and diameter estimation by analysis forest*
10. Diego Gonzalez-*aguilera, angle munoz-nieto*, Javier